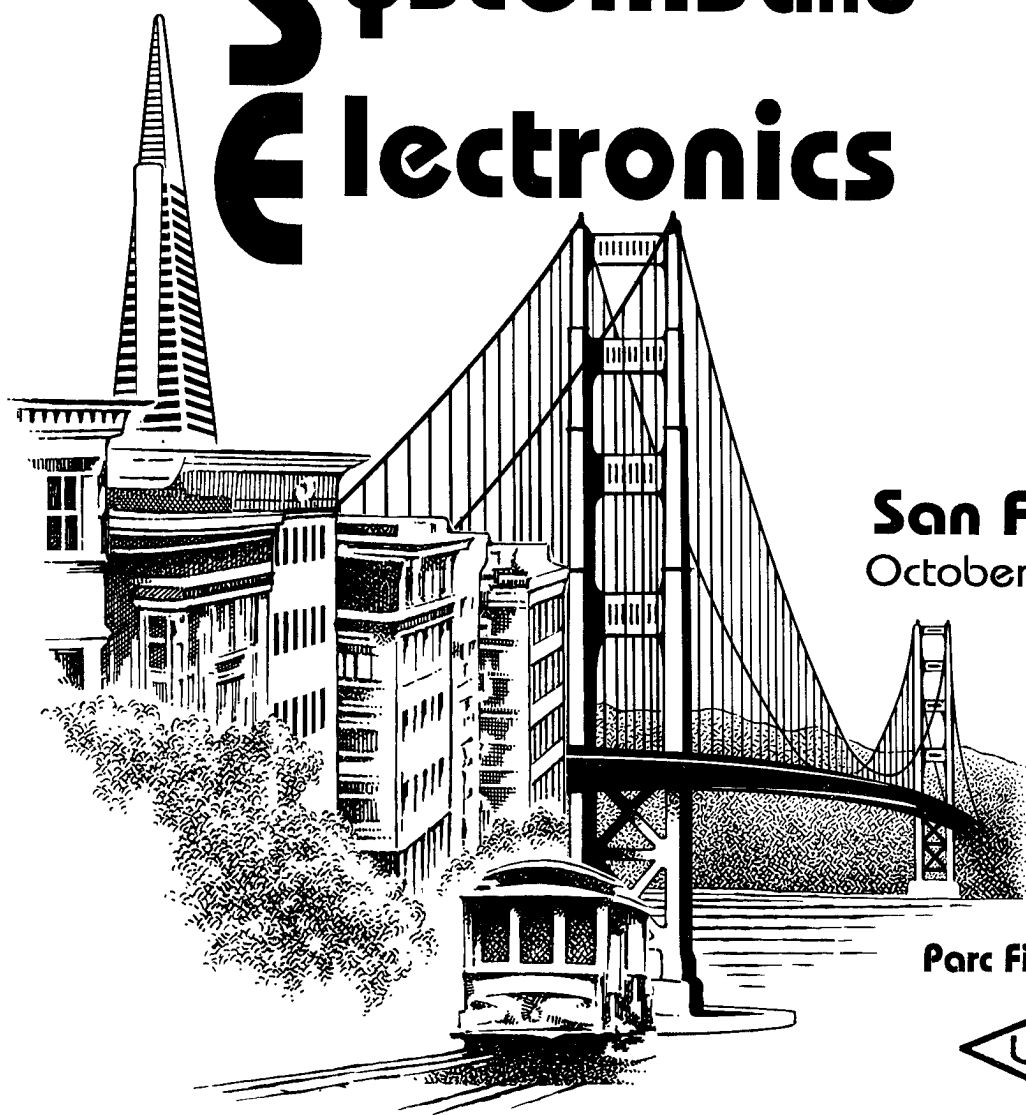


1995 Conference Proceedings of the

International Symposium on Signals, 19951130 101 Systems and Electronics



San Francisco
October 25-27, 1995

Parc Fifty Five Hotel

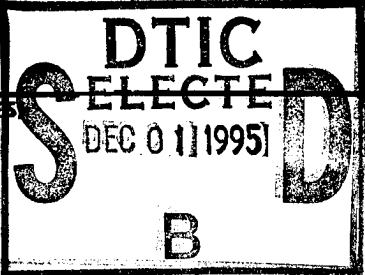
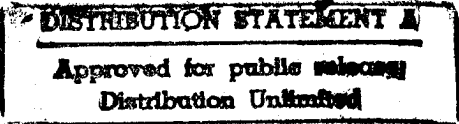


Union Radio-Scientifique Internationale
International Union of Radio Science

REPORT DOCUMENTATION PAGE

Form Approved
OMB No. 0704-0188

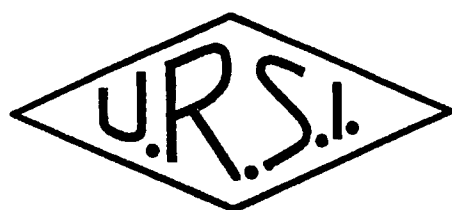
Public reporting burden for this collection of information is estimated to average 1 hour per response, including the time for reviewing instructions, searching existing data sources, gathering and maintaining the data needed, and completing and reviewing the collection of information. Send comments regarding this burden estimate or any other aspect of this collection of information, including suggestions for reducing this burden, to Washington Headquarters Services, Directorate for Information Operations and Reports, 1215 Jefferson Davis Highway, Suite 1204, Arlington, VA 22202-4302, and to the Office of Management and Budget, Paperwork Reduction Project (0704-0188), Washington, DC 20503.

1. AGENCY USE ONLY (Leave blank)		2. REPORT DATE 1995		3. REPORT TYPE AND DATES COVERED Proceeding	
4. TITLE AND SUBTITLE International Symposium on Signals, Systems, and Electronics				5. FUNDING NUMBERS N00014-95-1-0641	
6. AUTHOR(S) Tatsuo Itoh					
7. PERFORMING ORGANIZATION NAME(S) AND ADDRESS(ES) UCLA Electrical Engineering 405 Hilgard Ave. 66-147A, EE IV Los Angeles, CA 90095					
8. PERFORMING ORGANIZATION REPORT NUMBER				9. SPONSORING/MONITORING AGENCY NAME(S) AND ADDRESS(ES) Department of the Navy Office of Naval Research, Code 251A:CLW 800 North Quincy Street, Arlington, VA 22217-5000	
10. SPONSORING/MONITORING AGENCY REPORT NUMBER				11. SUPPLEMENTARY NOTES	
12a. DISTRIBUTION/AVAILABILITY STATEMENT 				12b. DISTRIBUTION CODE	
13. ABSTRACT (Maximum 200 words) <p>This third URSI International Symposium on Signals, Systems and Electronics (ISSSE'95) was held in San Francisco, CA, USA at the Parc Fifty Five Hotel. For this symposium we were fortunate to obtain co-sponsorship from the NAVY with the Institute of Electrical and Electronic Engineers (IEEE), Microwave Theory and Techniques Society, Army as well as the cooperative sponsorship of the IEEE EDS, LEOS, COM and C&S Societies.</p> <p>In response to the call of papers, many high quality papers were submitted. Through the dilligent work of the Technical Program Committee a well balanced technical Program of reasonable size, covering all the research areas of major interest has been developed. Inaddition, to the regular sessions including both invited and contributed papers, a poster session was organized. The symposium invited three world renowned experts for keynote presentations.</p>					
14. SUBJECT TERMS				15. NUMBER OF PAGES	
				16. PRICE CODE	
17. SECURITY CLASSIFICATION OF REPORT		18. SECURITY CLASSIFICATION OF THIS PAGE		19. SECURITY CLASSIFICATION OF ABSTRACT	
				20. LIMITATION OF ABSTRACT	

PROCEEDINGS
1995 URSI INTERNATIONAL
SYMPOSIUM ON SIGNALS,
SYSTEMS, AND ELECTRONICS

ISSSE '95

PARC FIFTY FIVE HOTEL
SAN FRANCISCO, U.S.A.
OCTOBER 25-27, 1995



Union Radio-Scientifique Internationale
International Union of Radio Science

1995 INTERNATIONAL SYMPOSIUM OF SIGNALS, SYSTEMS AND ELECTRONICS

Copyright and Reprint Permission: Abstracting is permitted with credit to the source. Libraries are permitted to photocopy beyond the limits of U.S. copyright law for private use of patrons those articles in this volume that carry a code at the bottom of the first page, provided the per-copy fee indicated in the code is paid through the Copyright Clearance Center, 222 Rosewood Drive, Danvers, MA 01923. Instructors are permitted to photocopy isolated articles for noncommercial classroom use without fee. For other copying, reprint, or republication permission, write to IEEE Copyright Manager, IEEE Service Center, 445 Hoes Lane, P.O. Box 1331, Piscataway, NJ 08855-1331. All rights reserved. Copyright © 1995 by The Institute of Electrical and Electronics Engineers, Inc.

IEEE Catalog Numbers: 95TH8047

Library of Congress Number: 94-74516

ISBN - Softbound: 0-7803-2516-8

Microfiche: 0-7803-2517-6

Additional copies of this Conference Record are available from

IEEE Service Center
445 Hoes Lane
P.O. Box 1331
Piscataway, NJ 08855-1331
1-800-678-IEEE

Accession For	
NTIS GRA&I	<input checked="" type="checkbox"/>
DTIC TAB	<input type="checkbox"/>
Unannounced	<input type="checkbox"/>
Justification	
By	
Distribution/	
Availability Codes	
Dist	Avail and/or Special
A-1	

Welcome Remarks

Since its inception in 1913, when radio techniques were primitive and largely dependent on the ingenuity of its pioneers, URSI, in accordance with the initial stimulus has been promoting international cooperation while expanding and deepening its field of activities. Some of the research it promoted opened up new fields of knowledge in other disciplines, such as metrology, solar physics, meteorology, astronomy and space science. With the increasing inter-disciplinary nature of science, it is indeed almost inevitable that the free pursuit of basic radio research should lead the Union into new fields of endeavor. At the present, the ten scientific Commissions of URSI cover the following broad areas: electromagnetic metrology; fields and waves; signals and systems; electronics and photonics; electromagnetic noise and interference; wave propagation and teledection; ionospheric radio and propagation; waves in plasmas; radioastronomy and electromagnetics in biology and medicine. The primary objective of the Union remains: to stimulate and coordinate, on an international basis, studies in the field of radio telecommunications and electronic sciences. New scientific knowledge arising from these studies often lead to engineering efforts, the consequences of which are far-reaching for our society. Today, on the other hand, the time between discovery and its practical application is getting shorter. With this in mind, a special 1987 conference of URSI officers and outside experts, expressed the opinion that it would be desirable to put greater emphasis on telecommunications, and hence, Commission C on Signal and Systems and Commission D on Electronics and Photonics would have a major roles to play. Each Commission, though in its own field of activity, has in common full participation in the world-wide explosion we see today in telecommunications technology. And each have utilized new knowledge, inventions and discoveries in the radio and electronic technologies often which crosses the perceived boundaries of the Commissions. In accordance with the recommendations made to the URSI General Assembly in Tel Aviv later in 1987, it was decided to initiate a series of triennial international symposia with the aim of covering all the fields of telecommunications, in particular the activities of Commissions C and D and of promoting the exchange of experience and results between scientists and engineers working in these multi-disciplinary areas. The first URSI International Symposium on Signals Systems and Electronics (ISSSE) in the series was held in Erlangen, Germany in 1989. The second Symposium, ISSSE'92, was held in Paris at the Conservatoire National des Arts et M'etiers (CNAM) in 1992.

The third URSI International Symposium on Signals, Systems and Electronics (ISSSE'95) will be held in San Francisco, California, USA at the Parc Fifty Five Hotel. For this Symposium we have the pleasure of co-sponsorship with the Institute of Electrical and Electronic Engineers (IEEE) Microwave Theory and Techniques Society, Army Research Office and Office of Naval Research as well as cooperative sponsorship of the IEEE EDS, LEOS, COM, and C&S Societies. In response to the call for papers, many high quality papers were submitted. Through the diligent work of the Technical Program Committee a well balanced technical program of reasonable size, covering all the research areas of major interest has been developed. In addition to the regular sessions including both invited and contributed papers, a poster session is organized. The symposium invited three world renowned experts for keynote presentations.

As chairman of the Symposium, I would like to take this opportunity to express our thanks to the all authors who have responded to the Call for Papers and to the Technical Program Committee who selected the papers and established the program. In addition I would like to thank all members of the Steering Committee for their untiring efforts to make this Symposium a success. The technical contents of the Symposium cover wide ranges of interest on: Signal and Information Theory; Signal Processing and System Theory; Communications Systems; Electronics; and Photonics. Several sessions cover topics of interest spanning both Commissions C and D. We do hope that the 3rd International Symposium on Signals, Systems and Electronics will attract a great number of participants and we are looking forward to welcoming them in San Francisco in October.

James W. Mink
Chairman of the Steering Committee

Organization

Organizer:

Union Radio-Scientifique Internationale (URSI)
International Union of Radio Science

Co-Sponsored by

IEEE MTT-S
U.S. Army Research Office
U.S. Office of Naval Research

Cooperatively Sponsored by

IEEE Lasers and Electro-Optics Society
IEEE Electron Devices Society
IEEE Circuits and Systems
IEEE Communications Society

CONFERENCE COMMITTEE

Steering Committee

Dr. J. W. Mink	General Chairman, N. Carolina State Univ. Raleigh, USA
Prof. T. Itoh	Vice Chairmen, UCLA, Los Angeles, USA
Prof. P. H. Wittke	Vice Chairmen, Queen's University, Kingston, Canada
Prof. A. N. Willson, Jr.	Technical Program Chair, UCLA, Los Angeles, USA
Prof. M. Shur	Technical Program Chair, Univ. of Virginia, Charlottesville, USA
Dr. A. P. Khanna	Local Arrangements, Avantek Santa Clara, USA
Dr. R. Soohoo	Local Arrangements, Avantek Santa Clara, USA
Dr. H. J. Kuno	Finance, Quinstar, Torrance, USA
Dr. J. Harvey	Publicity, US Army Research Office, Research Triangle Park, USA
Dr. R. Trew	Publicity, Case Western Reserve Univ. Cleveland, USA
Dr. W. Sander	Publications, US Army Research Office, Research Triangle Park, USA
Prof. M. C. Wu	Executive Secretary, UCLA, Los Angeles, USA

Program Committee

M. Akaike, Japan	G. Salmer, France
A. Alwan,	T. K. Sarkar, USA
C. Cox, USA	F. Schuermeyer, USA
B. Evans, UK	M. Shur, USA
T. Fjeldly, Norway	M. Strosio, USA
A. Gersho, USA	D. J. Thomson, USA
E. Kolberg, Sweden	K. Weiser, Israel
M. Levinshtein, Russia	A. N. Willson, Jr., USA
H. Ling, USA	P. Wittke, Canada
E. Martinez, USA	J. Xu, Canada
G. Pottie, USA	K. Yao, USA

Opening Session

Wednesday, October 25, 1995

Dr. James W. Mink
North Carolina State University

Dr. David Chang
Polytechnic University

Keynote Sessions

Wednesday, October 25, 1995

Dr. Charles Rush
Compass Rose International
Global Information Infrastructures:
Challenges and Realities

Thursday, October 26, 1995

Dr. Andrew Viterbi
Qualcomm

Universal Wireless Communication: Convergence of Technology
and Market Forces

Friday, October 27, 1995

Prof. Alwyn Seeds
University College, London
Mining the Optical Fiber Bandwidth Goldmine

TABLE OF CONTENTS

SESSION WA1: Active Antennas For Wireless Communications

Convener: T. Itoh, *UCLA, USA*

Chairman: J. Harvey, *ARO, USA*

WA1 Tutorial: Active Integrated Antennas for Microwave Wireless Systems

C. Pobanz, J. Lin, T. Itoh, UCLA, USA 1

WA1-1: Scanning Oscillator Arrays for Low Cost Transceivers

R. York, UC. Santa Barbara, USA 5

WA1-2 Invited: Active Antenna Elements for Millimeter-Wave Cellular Communications

M. J. Vaughan, W. Wright, R. C. Compton, Cornell University, USA 9

WA1-3 Invited: Integrated Microstrip Active Antennas and Their Applications

K. Chang, TEXAS A&M Univ., USA 13

WA1-4 : A Liquid-Crystal Optoelectronic Phased Array Beam Forming Network

O. Kobayashi, H. Ogawa, NTT, Japan 17

WA1-5: Millimeter-Wave Dielectric Leaky-Wave Antennas

C. Y. Lee, A. Basu, J. Liao, J. Wong, B. Houshmand, T. Itoh, UCLA, USA 21

SESSION WB1: Recent Developments in MMICs

Convener: M. Akaike, *Science Univ., Japan*

Chairman: Y. C. Shih, *Hughes, USA*

WB1 Tutorial: MMICs for Mobile/Personal Communications Applications

M. Aikawa, M. Muraguchi, NTT, Japan 25

WB1-1 Invited: R/D Activities on MMIC's in Europe

C. Rumelhard, CNAM, France 29

WB1-2 Invited: Recent MMIC Developments in Australia

R. A. Batchelor, CSIRO, Australia 33

WB1-3 Invited: MMIC Applications to Satellite Communications

Y. C. Shih, M. Delaney, E. Kato, R. Isobe, Hughes, USA 37

WB1-4 Invited: MMIC Characterization Using Electro-Optic Field Mapping

D. Jager, G. David, Duisburg Univ. Germany 41

WB1-5 Invited: High Power Amplifiers for Mobile Communication Systems

Y. Itoh, Mitsubishi Electric., Japan 45

SESSION WC1: Data Compression

Convener: M. Bellanger, *CNAM, France*

WC1 Tutorial: VLSI Architecture for Video Compression

P. Pirsch, Univ. of Hannover, Germany 49

WC1-1: Transmission of DCT-Coded Images by Multicarrier Modulation for Noisy Channels

K. P. Ho, M. Kahn, Univ. of California, Berkeley, USA 55

WC1-2: Error Concealment Enhancement by Using The Reliability Outputs of A SOVA in MPEG-2 Video Decoder	
<i>S. Aign, German Aerospace Research Establishment, Germany</i>	59
WC1-3 Invited: A DCT/IDCT Processor for HDTV Applications	
<i>A. Madisetti and A. N. Willson, Jr., UCLA, USA</i>	63
SESSION WD1: Computer, Data and Satellite Communications	
Convener: P. Wittke, <i>Queen's Univ., Canada</i>	
*WD1 Tutorial: Multiple-Windows Spectrum Estimates and Detection of Solar g-Modes	
<i>D. J. Thomson, AT&T Bell Labs, USA</i>	
WD1-1: Impact of Tropospheric Scintillations on DS/SS Satellite Communications Networks	
<i>M. S. Alouini, P. G. Steffes, Georgia Inst. of Tech., USA</i>	67
WD1-2: Fade Prediction and Control Systems	
<i>M. Luglio, Univ. of Rome, Italy</i>	71
WD1-3: Rain Attenuation Characteristics on Radio Links	
<i>T. Manabe, T. Yoshida, NTT, Japan</i>	77
SESSION WA2: Quasi-Optical Fundamental Frequency Power Combining	
Convener: J. Harvey, <i>Army Res. Office</i>	
Chairman: T. Itoh, <i>UCLA, USA</i>	
WA2 Tutorial: An Overview of Quasi-Optical Power Combining: Where We Are- and How We Got There	
<i>J. Mink, North Carolina State Univ., USA</i>	81
WA2-1 Invited: Quasi-Optical Power Combining in A Dielectric Substrate	
<i>H. Hwang, T. W. Nuteson, M. B. Steer, J. W. Mink, J. Harvey, A. Paolletta, North Carolina State Univ., USA</i>	89
WA2-2 Invited: Quasi-Optical Components and Subsystems for Communication	
<i>Z. B. Popovic, J. Schoenberg, T. Mader, W. Shiroma, S. Hollung, M. Markovic, Univ. of Colorado, USA</i>	93
WA2-3 Invited: Quasi-optical Microstrip Amplifiers Based on Multilayer Coupled Structures	
<i>T. Ivanov, A. Mortazawi, Univ. of Central Florida, USA</i>	99
WA2-4 Invited: Quasi-Optical Grid Amplifiers and Oscillators	
<i>R. M. Weikle, Univ. of Virginia, USA</i>	103
SESSION WB2: III-V Devices	
Convener: G. Salmer, <i>Universite des Sciences et Technologies de Lille, France</i>	
Chairman: B. Jalali, <i>UCLA, USA</i>	
WB2 Tutorial: Low Temperature Grown GaAs Materials and Devices Present Status and Trend	
<i>E. Kohn, K-M. Lipka, Univ. of Ulm, Germany</i>	107
*WB2-1 Invited: Cryogenically Cooled HEMT's	
<i>L. Graffeuil, Thomson-CSF, USA</i>	*
WB2-2 Invited: Recent Applications of 2D and Quasi 2D Simulations: Evaluation of Performance and Fundamental Limitation of Power FET	
<i>J. C. De Jaeger, Institut d'Electronique et de Microelectronique du Nord, France</i>	111

* Papers not available at the time of printing.

WB2-3 Invited: GaInP/GaAs HBT: State of The Art

S. L. Delage, H. Blanck, S. Cassette, D. Floriot, E. Chartier, M. A. Diforte-Poisson, E. Watrin, P. Bourne, Thomson-CSF Laboratoire, France 115

WB2-4 Invited: High-Performance Millimeter-Wave MMIC's for Wireless Communication Systems

K. Ohata, NEC Corp. T. Saito, Fjitsu Labs. Japan 119

SESSION WC2: Detection and Estimation I

Convener: D. J. Thomson, AT&T Bell Labs, USA

WC2 Tutorial: Algorithms for Blind Identification of Terrestrial Microwave Radio Channels

J.B. Gomez del Moral, E. Biglieri, Inst. of Elect. and Telecom. Poly., Italy. 123

WC2-1: Channel Evaluation from Predicted Zero Crossing Analysis

P. W. Piggin, M. Gallagher, Univ. of Leeds, UK. 127

WC2-2: A New Method for Frequency Detection by Linear Prediction using Total Least Squares

R. P. Lemos, A. Lopes DECOM/FEE/UNICAMP, Brazil 131

WC2-3: A Parametric Set of Nonlinear Methods of Spectral Estimation:

R. Ugrinovskiy, Russian Academy of Science, Russia 135

SESSION WD2: Sigma - Delta Converters

Convener: G. C. Temes, Oregon State Univ., USA

***WD2 Tutorial: S-D Converter Operation and Architectures**

*G. C. Temes, Oregon State Univ., USA **

***WD2-1 Invited: Bandpass S-D Converters**

*R. Schreier, Oregon State Univ., USA **

WD2-2 Invited: Practical Aspects of S-D Converter Design

P. Ferguson, Analog Devices, USA 139

***WD2-3 Invited: S-D Converters in Wireless Devices**

*L. Longo, Oasis Design, USA. **

SESSION WA3: Millimeter Wave Radiometry and Devices

Convener : R. J. Mattauch, Univ. of Virginia, USA

Chairman: S. Jones, Univ. of Virginia, USA

WA3 Tutorial: Active Grids for Quasi-Optical Power Combining

D. Rutledge, J-C. Chiao, M. DeLisio, J. Liu Caltech, USA 141

***WA3-1: SIS Radiometry**

*J. Zmuidzinas, Caltech, USA **

WA3-2: Transferred Electron Oscillators for Heterodyne Receivers

S. H. Jones, J. E. Carlstrom, M.F. Zybura, Univ. of Virginia, J. Carlstrom, Caltech, USA 145

WA3-3: Novel Hot Electron Bolometer Mixers for Submillimeter Applications: An Overview of Recent Developments

W. R. McGrath, JPL, USA 147

WA3-4: Millimeter-Wave Mixers With Schottky Diodes, for Superheterodyne Spaceborne Radiometers- Review and Predictions

I. Galin, Aerojet ElectroSystems, USA. 153

SESSION WB3: Field Effect Transistors

Convener: J. Henaff, *CNET, France*

Chairman: E. Kohn, *Univ. of Ulm, Germany*

WB3 Tutorial: Silicon and Gallium Arsenide in High Temperature Electronics Applications

J. W. Klein, Ruhr-Universitaet, Bochum, Germany. 157

WB3-1: Heterodimensional Technology for Ultra Low Power Electronics

W. C. B. Peatman, M. Hurt, R. Tsai, T. Ytterdal, H. Park, J. Gonzales, M. Shur, Univ. of Virginia, USA 163

WB3-2: Analysis of The Hot Electron Regime of Operation in Heterostructure Field Effect Transistor

E. Martinez, M. Shur+, F. Schuermeyer, Wright Lab., USA (+ Virginia Univ., USA). 167

WB3-3: 60 GHz MMIC Mixer Using A Dual-Gate PM HEMT

R. Allam, C. Kolanowski, D. Langrez, P. Bourne, J. C. De Jaeger, Y. Crosnier, G. Salmer, Institut d'Electronique et de Microelectronique du Nord, France 171

WB3-4: Low-Frequency Noise Performances of SiO₂/InP Metal-Insulator -Semiconductor Field-Effect Transistor

Y. K. Su, S. C. Shei, K. C. Gan, M. Yokoyama, National Cheng Kung University, Taiwan, R. O.C 175

SESSION WC3: Detection and Estimation II

Convener : E. Biglieri, *Inst. of Elect. and Telecom. Poly., Italy*

WC3-1: A New Form of The Fourier Transform for Time-Varying Frequency Estimation

V. Katkovnik, Univ. of South Africa, South Africa. 179

WC3-2: Estimation of The Surface Reflectivity of Sar Images Based on a Marked Poisson Point Process Model

J. S. Daba, M. R. Bell, Univ. of Tech. Sydney, Australia. 183

WC3-3: An Improved Direct Inverse Problem Solver for Fractal Interpolation Functions with Application to Signal Compression

J. Wen, X. Zhu, Tsinghua Univ., China. 187

WC3-4: Optimum CFAR Detection Against Correlated K-Distributed Clutter

T. Bucciarelli, P. Lombardo, S. Tamburrini, Univ. of Rome, Italy 191

SESSION WD3: Applications of DSP to Telecommunications

Convener: P. Pirsch, *Univ. of Hannover, Germany*

WD3 Tutorial: A DSP Perspective of Sigma-Delta Techniques with Applications in Telecommunications

M. Bellanger, CNAM, France 195

WD3-1: Adaptive Change of Code Rate in DS-SSMA Systems

Y. Ryu, S. C. Kim, I. Song, S. Park, H. M. Kim, KAIST, Korea. 199

WD3-2: Modified Delay-Locked Loop for Fading Channels

A. Wilde, DLR Oberpfaffenhofen, Germany 203

WD3-3: Railway Cab Signaling by Track Circuits and Spread Spectrum Modulations

E. Costamagna, P.F. Pellegrini, Univ. of Pavia, Italy 207

* Papers not available at the time of printing.

SESSION ThA1: Mixed Mode Circuit Technology

Convener: F. Schuermeyer, *Wright Lab., USA*

***ThA1-T Tutorial: Compound Semiconductor Technology for Mixed Mode Circuit Applications**

P. Greiling, Hughes, USA

ThA1-1: Microwave Modeling of A Photodetector-Amplifier Used in Optical Communication Systems

V. Anand, University College, London, U.K. 211

ThA1-2 Invited: On The Applicability on The Transimpedance Amplifier Concept for 40Gb/s Optoelectronic Receivers Based on InAlAs/InGaAs Heterostructure Fieldeffect Transistors

R. M. Bertenburg, G. Janssen, S. Waasen Van, R. Reuter, F. J. Tegude, Gerhard-Mercator-Univ., Germany ... 215

***ThA1-3: Info-Theoretic Approach to ADC Circuits**

A. M. Dighe, Visvesvaray Regional Coll. of Eng., India *

ThA1-4: High Electron Mobility Transistor as Electronic Flute

--M. I. Dyakonov, M Shur, Univ. of Virginia, USA 219

ThA1-5: An Algorithm for Quaternary ADCs

A. S. Gandhi, A. M. Dighe, VRCE, India 223

SESSION ThB1: Microwave Systems Components

Convener: J. Henaff, *CNET, France*

Chairman: O. Lloas, *LAAS-CNRS, France*

ThB1-T Tutorial: Time Domain Identification of Non-Linear Systems

M. I. Sobhy, E. A. Hosny, M. W. R. Ng, A. Bakkar E-S, Univ. of Kent at Canterbury, UK 227

ThB1-1: A Computer-Aided Impedance Characterization for Microwave Resonant-Cap Circuits

S. Kar, Inst. of Radio Phys. & Elec, India 231

ThB1-2: New Current Mode Universal Filter

R. Nandi, Jadavpur Univ., India 235

ThB1-3: A New Type CPW-Resonator Bandpass Filter with Widley Suppression Characteristics of Harmonic Resonance Responses

Y. Noguchi, K. Wada, T. Nakamine, N. Okamoto, Kinki Univ., Japan 237

ThB1-4: A Linear Sinewave voo Design and its Digital Control

S. K. Sanyal, R. Nandi, S. K. Debroy, D. Pal, Jadavpur Univ. India 241

***ThB1-5: Optimum Large-Signal Performance of Microwave Field Effect Transistors**

M. C. E. Yagoub, H. Baudrand, E.N.S.E.E.I.H.T., France

SESSION ThC1: Time-Frequency Analysis

Convener: H. Ling, *Univ. of Texas, Austin, USA*

ThC1 Tutorial: Joint Time-Frequency Analysis of Electromagnetic Backscattered Data

H. Ling, Univ. of Texas, Austin, USA 243

***ThC1-1 Invited: Phase-Space Processing of Electromagnetic Scattering Data**

L. Carin, NY Poly Tech, USA *

ThC1-2: Region-of-Interest Tomography Using Biological ZImage Perception Concepts

A. Moghaddar, Ohio State Univ., USA (withdrawn) *

ThC1-3: Joint Time-Frequency ISAR Algorithm for Imaging Targets with Non-Point Scattering Features

L. C. Trintinalia, H. Ling, Univ. of Texas, Austin, USA 247

ThC1-4: Reconstruction of ISAR Image by Time-Frequency Distribution Series	
<i>V. C. Chen, S. Qian, National Instruments, USA</i>	251

SESSION ThD1: Personal and Mobil Communications

Convener: A. Acampora, *UCSD, USA*

ThD1 Tutorial: An Adaptive High-Speed Wireless Transceiver for Personal Communications	
<i>G. Pottie, UCLA, USA</i>	255
ThD1-1: Homodyne Receiver Technology for Small and Low-power Consumption Mobile Communications Equipment	
<i>M. Hasegawa, T. Fukagawa, M. Mimura, M. Makimoto, Matsushita, Japan</i>	259
ThD1-2: System Design for Continuous Cell Coverage in High Density Microcellular Networks	
<i>B. C. Jones, D.J. Skellern, Macquarie Univ., Australia</i>	263
ThD1-3: The Effect of Receiver Collisions on Throughput Performance of Multichannel Multiaccess Protocols	
<i>I. E. Pountourakis, National Technical. Univ. of Athens, Greece</i>	267

SESSION ThA2: New Device Technologies for Future DSP Systems

Convener: E. Martinez, *Wright Lab., USA*

ThA2 Tutorial: Silicon-on-Insulator (SOI) Technology for Low Power Electronics	
<i>Z. Lemnios, ARPA, USA</i>	271
ThA2-1 Invited: Complementary GaAs Technology and Applications	
<i>J. Hallmark, J. Abrokwhah, B. Bernhardt, B. Crawforth, D. Foster, J-H. Huang, M. LaMacchia, R. Lucero, B. Mathes, B. Ooms, Motorola, USA</i>	275
ThA2-2 Invited: Manufacturable GaAs BiFET Technology for High Speed Digital Processing	
<i>F. Chang, Rockwell, USA</i>	279
*ThA2-3 Invited: InP HBT Technology for High Speed Signal Processing in Electronic	
<i>Y. K. Chen, AT&T Bell Labs, USA</i>	*
*ThA2-4 Invited: Title will be announced at the conference	
<i>A. Oki, TRW, USA</i>	*

SESSION ThB2: Photonics: Devices, Links and Applications

Convener: C. Cox, *MIT Lincoln Lab. USA*

ThB2 Tutorial: Techniques and Applications of Analog Fiber Optic Links	
<i>C. Cox, MIT Lincoln Lab. USA</i>	283
ThB2-1 : Novel Photonic Oscillator for Signal Generation and Distribution	
<i>L. Maleki, JPL, USA</i>	*
ThB2-2: Photonic Systems for Antenna Control	
<i>M. VanBlaricam, C. Swann, Toyon, USA</i>	287
*ThB2-3: External Modulators for Cable TV Distribution Applications	
<i>G. Gopalakrishnan, General Instrument, USA</i>	*
*ThB2-4: Insertion of Photonic Technology in RF Phased-Array Antennas	
<i>L. Lembo, TRW, USA</i>	*

* Papers not available at the time of printing.

SESSION ThC2: Optical Communication Networks

Convener: *E. Yablonovitch, UCLA, USA*

***ThC2 Tutorial: A Model Architecture for A Management-Scaleable All-Optical Telecommunications Infrastructure**

<i>A. Acampora, UCSD, USA</i>	*
ThC2-1: Performance Analysis of Optical Fiber TDMA Systems	
<i>J-G Zhang, Asian Institute of Technology, Thailand</i>	291
ThC2-2: An Error Floor Reduction Scheme for DPSK Receivers Impaired by Phase Noise	
<i>K. Kiasaleh, Univ. of Texas, Dallas, USA</i>	295
*ThC2-3: On The Placement of Optical Amplifiers in Digital Links	
<i>H. Waldman, R. N. Ribeiro, A. A. Surerus, DECOM/FEE/UNICAMP, Brazil</i>	*
ThC2-4: Multi-Wavelength, Optical Code-Division-Multiplexing Based on Passive, Linear, Unitary, Filters	
<i>C. F. Lam, E. Yablonovitch, UCLA, USA</i>	299

SESSION ThD2: Image Processing

Convener: *W. Sander, ARO, USA*

ThD2 Tutorial: Application of Antenna Array Processing to Problems in Image Understanding	
<i>T. Kailath, H. Aghajan, Stanford Univ., USA</i>	303
ThD2-1: Phase Retrieval Algorithm Based on Maximum Entropy Method	
<i>A. Bajkova, Institute of Applied Astronomy, Russia</i>	307
ThD2-2: A Method to Decrease Nonlinear Image Reconstruction Distortions Caused by Measurement Errors	
<i>Bajkova A, Institute of Applied Astronomy, Russia</i>	311
ThD2-3: Synthesis of Data-Dependent Filters for Digital Image Processing and Recognition	
<i>A. V. Kovalenko, V. N. Kurashov, N. G. Nakhodkin, Taras Shevchenko Univ., Russia</i>	315

SESSION ThA3: Application of Signal Processing Techniques for Efficient Device Modeling and Characterization

Convener: *E. K. Miller, Los Alamos Lab., USA*

Chairman: *T. Sarkar, Syracuse Univ., USA*

ThA3 Tutorial: The Principle of Analytic Continuation - How To Use It?	
<i>R. S. Adve, T. K. Sarkar, S. M. Rao, E. K. Miller, Syracuse Univ. USA</i>	319
ThA3-1: Time-Domain Signal Restoration and Parameter Reconstruction on An LCRG Transmission Line	
<i>J. Lundstedt, S. Stroem, S. He, Royal Inst. of Tech. Sweden</i>	323
ThA3-2: On Incorporating Signal Processing and Neutral Network Techniques with The FDTD Method for Solving Electromagnetic Problems	
<i>J. Litva, E. Navarro, McMaster Univ., Canada</i>	327
ThA3-3: Simulated Images for Wide Band Appellation, An Alternative to Complex Images of Multilayer Media	
<i>Y. L. Chow, A. Torabian-Esfahani, N. Hojjat, S. Safavi-Naeini, Univ. of Waterloo, Canada</i>	331
ThA3-4: Interpolation/Extrapolation of Frequency Domain Responses Using The Hilbert Transform	
<i>S. M. Narayana, G. S. Rao, R. S. Adve, T. K. Sarkar, M. Wicks, E. K. Miller, Syracuse Univ. USA</i>	335

SESSION ThB3: Microwave Systems Components

Convener: E. Kollberg, *Chalmers Univ. Sweden*

ThB3 Tutorial: Cryogenically Cooled HEMT's From The Device Towards The Applications <i>O. Llopis, L. Escotte, LAAS CNRS, France</i>	339
ThB3-1: High Temperature Microwave Modeling and Circuit Design with MESFET's and HBT's <i>V. Krozer V, M. Schuessler, K. Fricke, W. Y. Lee, H. L. Hartnagel, Tech. Univ. Darmstadt, Germany</i>	343
ThB3-2: AlGaAs/GaAs and GaIn/GaAs HBT for High Temperature Microwave Operation <i>M. Schuessler, V. Krozer, W. Y. Lee, H. L. Hartnagel, Tech. Univ. Darmstadt, Germany</i>	347
ThB3-3: Heterojunction Bipolar Phototransistors for Analog Microwave Photonic Systems <i>A. Paoletta, L. E. M. deBarro, P. Herczfeld, P. Enquist, W. VanMeerbeke, US Army Research Lab., USA</i>	351
ThB3-4: Modeling for Dispersion of Shielded Microstrip Linr Using SLR Technique <i>A. K. Verma, R. Kumar, Univ. of Delhi, India</i>	355

SESSION ThC3: Adaptive Algorithms and Systems

Convener : E. Deprettere, *Tech. Univ. of Delft, Netherland*

ThC3 Tutorial: Adaptive Asymptotic Optimal Algorithms for Detecting Signals in Autoregressive Noise <i>B. B. Shishkov, Y. P. Georgiev, S N. Stoyanor, Tech. Univ. of Sofia, Bulgaria</i>	359
ThC3-1: A Fuzzy-Rule-Based Phase Error Detector <i>F. Daffara, Phillips, France</i>	363
*ThC3-2: An Adaptive Spatial Processing Algorithm Using Special Parametric Form of Reference Signals <i>P. V. Gorev, Radiophys. Research Inst., Novgorod, Russia</i>	*
*ThC3-3: Fast Switching Frequency Synthesizer Employing Adaptive Phase Locked Loop Operating in The Pseudo Linear Region <i>SR. Al-Araji, A. J. Al-Dweik, M. S. AbuRajab, Univ. of Yarmouk, Jordan</i>	*

SESSION ThD3: Recent Advances in Speech Processing

Convener: A. Alwan, *UCLA, USA*

ThD3 Tutorial: Speech Production and Perception Models and their Applications to Synthesis, Recognition, and Coding <i>A. Alwan, S. Narayanan, B. Strobe and A. Shen, UCLA, USA</i>	367
ThD3-1 Invited: Microphone Arrays for Speech Processing <i>E-E. Jan, J. L. Flanagan, Rutgers Univ., USA</i>	373
ThD3-2 Invited: Vocal-Tract Acoustics and Speech Synthesis <i>S. Maeda, CNRS, France</i>	377
ThD3-3 Invited: Digital Signal Processing for An Ear Level Binaural Hearing Aid <i>S. Soli, House Ear Institute, USA</i>	381
ThD3-3 Invited: Recent Advances and Current Challenges in Speech Recognition <i>P. Price, SRI, USA</i>	*

* Papers not available at the time of printing.

SESSION FA1: Modeling and Simulation I

Convener: M. Strosio, *ARO, USA*

*FA1 Tutorial: Confined Phonons

M. Strosio, ARO, USA *

FA1-1: Topological Pulse Modulation of Field and New Microwave Circuits Design for Superspeed Operating Computers

G. A. Kuzaev, V. I. Gvozdev, Moscow Inst. of Ele. and Math., Russia 383

*FA1-2: Modeling of Improvement Self-Protected Microwave Detector

L. M. Drozdovskaia, Special Research Bureau of Moscow, Russia *

*FA1-3: Optimization Criteria of A Microwave Generator Circuit by An Appropriate Choice of The E.F. Transmission

G. Alquie, S. Aidel, A. Said, Univ. of Constantine, Algeria *

FA1-4: Low-power PSA transistors for Microwave Communication Systems: Comparison Among Bias-Dependent Models Extracted form Measured Noise and Scattering Parameters

A. Caddemi, M. Sannino, Univ. of Palermo, Italy 385

SESSION FB1: Modeling and Simulation II

Convener: M. Shur, *Univ. of Virginia, USA*

FB1 Tutorial: Recent Advances in Time-Domain Simulation

B. Houshmand, T. Itoh, UCLA, USA 389

FB1-1 Solution of EM Fields by Asymptotic Waveform Techniques:

M. Li, Q. J. Zhang, M. S. Nakha, Carleton Univ., Canada 393

FB1-2: Design and Simulation of Microwave Filter

A. M. Nassar, A. M. Moselhy, M. A. El-Gazzar, Egyptian Air Academy, Egypt 397

FB1-3: Statistical Modeling of Idd Testing Efficiency of Analogue Integrated Circuits

V. Musil, Univ. of Brno, Czech Republic 401

FB1-4: A Simulated Annealing Algorithm for The Optimization of Communication Networks

E. Costamagna, A. Fanni, G. Giacinto, Univ. of Pavia, Italy 405

SESSION FC1: Array Processors, Modulation and Coding

Convener: R. L. Pickholtz, *George Washington Univ., USA*

FC1 Tutorial: On Optimization of Broadband Beamformer for Hearing Aid Applications

A. Wang, F. Lorenselli, D. Korompis, R. E. Hudson, K. Yao, UCLA, USA 409

FC1-1: Optimum Detection of The Discrete Spectrum Signals, with Applications to Array Beamforming in A Waveguide

A. I. Malekhanov, Russian Academy of Science, Russia *

FC1-2: Pseudo-Random Turbo-Codes

G. Battail, ENST, France 419

FC1-3: An Automatic Procedure to Construct The Optimal Soft-Decision Quantizers and Branch Metrics for Viterbi Decoders

T. F. Wong, D. J. Skellern, L. H. Lee, Macquarie Univ., Australia 423

SESSION FD1: Digital Filters and Filter Banks

Convener: G. Pottie, *UCLA, USA*

FD1 Tutorial: State Space approach in Time-Varying Biorthogonal Filter Banks

A. N. Lemma, E. Deprettere, Tech. Univ. of Delft, Netherland 427

FD1-1: Piecewise-Linear Characteristics of MSLMS Filters

H. Q. Xu, J. N. Lin, R. Unbehauen, Univ. Erlangen-Nuernberg, Germany 435

FD1-2: Variance of Quantization Error at The Output of Recursive Digital Filter

G. Mollova, Higher Inst. of Arch. and Civil Engr., Bulgaria 439

SESSION FA2: Packaging and Amplifiers

Convener: M. Levinshstein, *A. F. Ioffe Institute, Russia*

FA2 Tutorial: RF Characterization of A Low Cost Multichip Packaging Technology for Monolithic Mircrowave and Millimeterwave Integrated Circuits

K. Jayarai, T. E. Noll, Foster-Miller, Inc. And D. Singh, Honeywell Tech. Ctr. USA 443

FA2-1: Novel Approach Using Tapers for High Power FET Chips Characterization

M. Zoyo, C. Galy, A. Darbandi, L. Lapierre, J. F. Sautereau, ALCATEL ESPACE, France 447

FA2-2: High Temperature Operational Amplifier with Low Offset Voltage

J. Bergmann, A. Have ten, Inst. for Electronics, Bochum, Germany 451

FA2-3: Design of A High Gain Power Amplifier Using A Bias Defendent Large Signal Mestet Model and The Describing Function Technique

S. Munoz, J. L. Sebastian, J. L. Sebastian, Univ. of Complutense, Spain 455

FA2-4: Simulation and Characterization of A High Temperature SIMOX-Operational Amplifier

P. Gehse, C. Eisenhut, Inst. for Electronics, Bochum, Germany 459

SESSION FB2: Modeling and Simulation III

Convener: K. Weiser, *Technion, Israel*

FB2 Tutorial: Conformal Mapping Analysis of Microshield Transmission Lines

E. Costamagna, A. Fanni, Univ. of Pavia, Italy 463

FB2-1: Device Models in FDTD Analysis of Microwave Circuits

C. N. Kuo, B. Houshmand, T. Itoh, UCLA, USA 467

FB2-2: A Simple Technique for Determining Transmission Losses in Saw Delay Lines

T. E. Taha, Faculty of Electrical Engineering, Egypt 471

FB2-3: Comparison Study Between A Computer Allied Analysis Program Using State Space Technique and Spice Program

A. M. Nassar, A. M. Moselhy, M. A. El-Gazzar, Egyptian Air Academy, Egypt 477

***FB2-4: Nonlinear Emissions Dynamic of Heterolaser Caused by Nonlinear Waveguiding in The Active Layer**

V. V. Tchernyi, G. A. Zhuravely, Volgograd State Univ. Russia *

* Papers not available at the time of printing.

SESSION FC2: Signal Processing and System Theory

Convener: K. Yao, *UCLA, USA*

FC2-1 Invited: Performance and Convergence Analysis of A CM Signal Canceler with Noise <i>W. Lee and R. L. Pickholtz, George Washington Univ., USA</i>	481
FC2-2: A Wavelet-Based Algorithm for Time Delay and Doppler Measurements <i>X. X. Niu, P. C. Ching, Y. T. Chan, Chinese Univ. of Hong Kong, Hong Kong</i>	485
FC2-3: Sampling Errors and The Influence of Processing After Sampling <i>E. G. Woschni, Tech. Univ. Chemnitz-Zwickau, Germany</i>	489
FC2-4: Optimisation of Orthogonal Low-Rate Convolutional Codes in A DS-CDMA System <i>J. J. Maxey, R. F. Ormondroyd, Univ. of Bath, UK</i>	493

SESSION FD2: Nonlinear and Neural Systems

Convener: A. N. Willson, *UCLA, USA*

FD2 Tutorial: An Efficient Continuation Method for use in Globally Convergent DC Circuit Simulation <i>M. M. Green, SUNY, Stony Brook, USA</i>	497
FD2-1: A Learning Algorithm for Cellular Neural Networks (CNN) Solving Nonlinear Partial Differential Equations <i>F. Puffer, R. Tetzlaff, D. Wolf, Univ. of Frankfurt, Germany</i>	501
FD2-2: An Algorithm to Recognize Numerical Handwritten Characters Isolated and Overlapped <i>L. E. Flores, E. N. Rezende, A. Carrijo, J. B. T. Yabu-uti, UFU, Brazil</i>	505
FD2-3: Neural System for Tracking and Classification of Primary Radar Echo Signals <i>S. Cuomo, P. F. Pellegrini, E. Piazza, Univ. of Florence, Italy</i>	509

SESSION FA3: Photonic Devices

Convener: J. Xu, *Univ. Toronto, Canada*

FA3 Tutorial: Investigation of 1.3um Pr-ion Doped Optical Fiber Amplifier for CATV Subscriber Network <i>J. Y. Cao, Shanghai Jiaotong Univ., China</i>	513
FA3-1: Modelling of Sub-Shot Noise Optocouplers Using Relative Noise Difference <i>W. N. Cheung, P. J. Edwards, T. Zhang, Univ. of Canberra, Australia</i>	517
FA3-2: Microwave Signal Transformation in A Magnetostatic Wave Transmission Line Under Pulsed Laser Irradiation <i>Y. Fetisov, I. Romanov, V. Studenov, Moscow inst. of Radioengineering, Russia</i>	521
FA3-3: Self-Consistent BPM Model of A Waveguide Coupler with Distributed Gain <i>R. F. Ormondroyd, Univ. of Bath, UK</i>	525
FA3-4: An All-Optical CDMA Communication Network by Spectral Encoding of LED Using Acousto Optic Tunable Filters <i>K. Iversen, O. Ziemann, Tech. Univ. of Ilmenau, Germany</i>	529

SESSION FB3: Nanostructures and SAW Devices

Convener: W. C. B. Peatman, *Univ. of Virginia, USA*

FB3 Tutorial: Longitudinal Electron Transport in Nonregular Electron Waveguides for Future Ultra Fast Nanoelectronic Devices

<i>A. S. Tager, SR&PC, Russia</i>	533
*FB3-1: Periodical Nanoscopic Quantum Well Structures for Simulated Light Generation Under Low Excitation Level	
<i>V. G. Litovchenko, D. V. Korvutayak, Y. V. Kryuchenko, Ukrainian Academy of Science, Ukraine</i>	*
*FB3-2: Achievements in The Optics of Multilayer Produce Unequal-Thickness Structures	
<i>Y. O. Pervak, I. V. Fekeshgazi, National Academy of Science, Ukraine</i>	*
*FB3-3: Spectral Analysis of SSBW in Resonant Devices	
<i>M. Benslama, T. E. Taha, H. Baudrand, Faculty of Electrical Engineering, Egypt</i>	*
FB3-4: Analysis of The Monolithic SAW Memory by Using Green's Function	
<i>T. E. Taha, M. El-Kordy, Faculty of Electrical Engineering, Egypt</i>	537

Poster Session:

***Experimental Investigation of GaAs PIN-Diode Properties**

<i>I. V. Levedev, L. M. Drozdovski, N. V. Drozdovski, A. S. Shnitnikov, Special Research Bureau of Moscow, Russia</i>	*
---	---

An Integratable Current-Tunable R-L Oscillator

<i>B. Srisuchinwong, N. V. Trung, Thammasat Univ. Thailand</i>	541
--	-----

Analysis and Design of Microstrip Power Divider

<i>A. M. Nassar, A. M. Moselhy, M. A. El-Gazzar, Egyptian Air Academy, Egypt</i>	545
--	-----

Application of BWO for Excitation of The Intensive Noise Signals of Millimeter Wave Band

<i>V. A. Rakityansky, Kharhov Ukraine</i>	549
---	-----

***Investigation of Millimeter Wave Integrated Circuits**

<i>A. V. Chanakin, Kiev Polutech. Inst., Ukraine</i>	*
--	---

MOSSIM: Metal Oxide Semiconductor Device Simulation Package

<i>U. Kumar, N. B. Singh, ITT, Delhi, India</i>	553
---	-----

***A New Current Mode Universal Filter**

<i>R. Nandi, S. K. Sanyal, S. K. Debbroy, Jadavpur Univ., India</i>	*
---	---

Operational Amplifier for Redundant Analog Systems

<i>V. V. Ivanov, M. V. Ivanov, OES Electronics, Russia</i>	557
--	-----

***Co-Channel Interference in The Frequency Range 30MHz to GHz (Verification of, Using The Land-Separation Method)**

<i>V. S. A. Adeloye, Brunel Univ., UK</i>	*
---	---

The Volume-Meterical Monolithic Integrated Circuits for Microwave Band

<i>V. I. Gvozdev, S. I. Podkovyrin, A. A. Lyalin, G. A. Kuzaev, Moscow Inst. of Electronics and Mathematics, Russia</i>	561
---	-----

An IC for Closed-Loop Micromotor Control

<i>N. K. Rao, K. D. Hartsfield, A. Purushotham, S. L. Garverick, Case Western Reserve Univ., USA</i>	563
--	-----

***Trigger Optical Multistability in The System of The Coupled Nonlinear Waveguide Resonators**

<i>V. V. Tchernyi, G. A. Zhuravely, A. I. Voronko, Volgograd State Univ., Russia</i>	*
--	---

* Papers not available at the time of printing.

*Adaptive Array Processing via Recursive Least Squares Filtering Based upon A Non-Triangular Inverse Decomposition	
<i>P. V. Gorev, Radiophys. Research Inst. , Novgorod, Russia</i>	*
A Novel DCT and FTC Based Hybrid Still Image Compression Algorithm	
<i>J. Wen, X. Zhu, Tsinghua Univ., China</i>	567
Discrete Multiplicative Signals and Their Recognition Algorithms, Based on Vilenkin-Krestenson Functions Spectral Techniques	
<i>N. L. Evgenievich, S. V. Mihailovich, Russian Academy of Science, Russia.</i>	571
Rheoliner System Theory Applied to The Problem of Generation of Extremely Low Frequencies and to Frequency Modulation	
<i>E. G. Woschni, Tech. Univ. Chemnitz-Zwickau, Germany</i>	573
New Architecture for Self-Routing Photonic Switching with Self-Synchronization and Optical Processing	
<i>J-G Zhang, Asian Institute of Technology, Thailand.</i>	575
Effects of Increased Capacity in CDMA Cellular Systems	
<i>W. M. Tam, F. C. M. Lau, Hong Kong Polytech. Univ., Hong Kong.</i>	579
The Algorithm for Image Decomposition and Reconstruction Using Amplitude and Phase Patterns	
<i>A. Buchowicz, Inst. of Radioelectron, Warszawo, Poland.</i>	583
Author Index	587

ACTIVE INTEGRATED ANTENNAS FOR MICROWAVE WIRELESS SYSTEMS

Carl W. Pobanz^{}, Jenshan Lin^{**}, and Tatsuo Itoh^{*}*

^{*} Electrical Engineering Department
University of California, Los Angeles
405 Hilgard Ave., L.A. CA 90095 USA

^{**} High Speed Electronics Research
AT&T Bell Laboratories
600 Mountain Ave.
Murray Hill, NJ 07974 USA

ABSTRACT

Active integrated antennas, in which solid-state devices and antennas are integrated together on a single substrate, offer significant advantages in performance, size and cost for microwave wireless systems. Recent developments include elements for integrated transmitters, heterodyne receivers, transceivers and transponders operating at frequencies from UHF through millimeter-wave. These elements can be used alone or in phased arrays for wireless communication, identification and sensing.

1. INTRODUCTION

In conventional microwave and millimeter wave wireless system design, the signal processing circuitry and the antenna are often treated as separate subsystems. Combining these elements to form integrated active antennas can result in a high-performance circuit with the minimized size, complexity and cost demanded by modern commercial wireless applications [1]. In this approach, a radiating structure serves as both an antenna and a circuit element such as a filter, diplexer, or resonator. This allows a wide assortment of printed antennas to be used to form efficient compact oscillators, mixers, and receivers which interact directly with the radiated fields [2].

2. TRANSMITTERS

A simple radio transmitter is formed when an oscillating active device, such as a Gunn diode or MESFET, is coupled to a printed antenna. In this situation, the antenna may function as both the

load and the resonant element which provides positive feedback for oscillation at a desired frequency. An example is the circuit shown in Figure 1, which comprises a GaAs MESFET coupled to a microstrip slot antenna. The FET is destabilized via reactive loading with mistrostrip stubs, to present a negative resistance to the slot antenna. This results in oscillation at 25 GHz, producing a 10 mW signal which is directly radiated [3]. Many similar circuits have been designed, employing resonant antennas such as rectangular and circular microstrip patches, CPW slots and printed dipoles. Traveling-wave type antennas such as the exponentially-tapered slot have also been used for wideband operation with tunable sources [4]. Much of the recent interest in the area of active antennas has been in using arrays of oscillators in spatial power combining schemes, where the radiated power from many low-power devices is combined in free space to form a powerful beam. This is especially useful at millimeter-wave frequencies, where the power available from each active device is relatively low. For example, with a large array of n sources, the total radiated power as well as the array directivity both increase with n , resulting in an effective isotropic radiated power (EIRP) which increases as n^2 . This EIRP may exceed that which is possible from a conventional waveguide power-combining network feeding an antenna of equal directivity, due to relatively lossless free space propagation. A recent example is a 6-element linear array of oscillators, with elements comprising GaAs MESFETs coupled to rectangular microstrip patches [5]. The array produces a broadside beam at 10.8 GHz, with an EIRP exceeding 100 W.

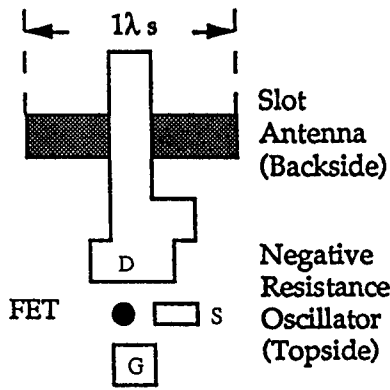


Figure 1. 25 GHz active antenna oscillator with FET and microstrip slot antenna.

The oscillation frequency of an active antenna can be controlled by injection-locking it to a low-power reference signal. This allows a modulated carrier to be effectively amplified and radiated by an element. In an array, injection-locking allows the radiated power from all elements to add coherently and form a beam. This is done by distributing a reference signal, or through electromagnetic coupling between the oscillators that allows the array to self-synchronize. By controlling this coupling and the tuning of selected oscillators in the array, the transmitted beam can be made to scan in various directions. In contrast to conventional phased arrays, this method does not require phase shifters. As the RF source is distributed over the array, the conventional feed network is eliminated as well. This makes possible inexpensive phased arrays for such applications as portable satellite uplink stations, as well as other transmitters that are thin and conformally mountable. One example is an X-band array which uses strong coupling between oscillator elements, in conjunction with detuning the free-running frequencies of the end elements of the array. A progressive interelement phase shift results when the elements injection-lock each other to the same frequency, resulting in a continuously steerable radiated beam [6]. Another recent array uses unilateral injection-locking at 6 GHz, where the phase reference signal is passed from one element to the next in one direction (Figure 2). This results in greater control over the phase progression in the array, allowing the scanning of both sum and difference patterns

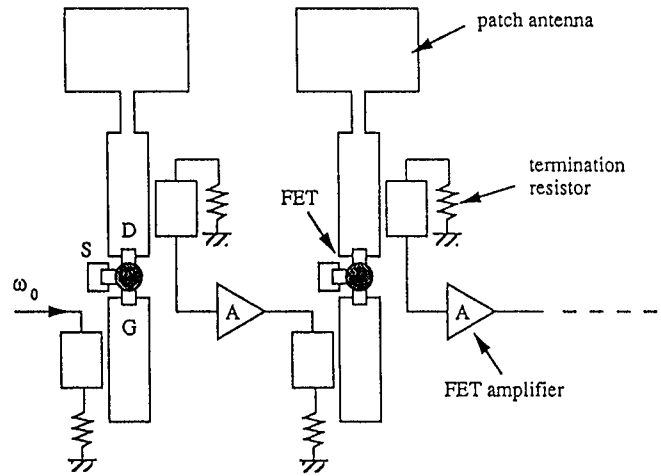


Figure 2. Transmitting phased array using the unilateral injection-locking technique. A reference signal is applied to the first element only.

[7]. Applications include automotive radar, for road sensing and collision avoidance.

3. RECEIVERS

Receivers with integrated antennas include quasi-optical mixers and detectors, which are highly compact frequency-converting circuits. The input RF and local oscillator (LO) signals are coupled into the structure via radiation and the mixing product (IF), usually the difference frequency, is extracted through a printed waveguide. The mixing devices are typically Schottky diodes or MESFETs. At millimeter-wave frequencies and above, the entire antenna structure including the devices may be fabricated monolithically on a single semiconductor substrate. In quasi-optical mixers, the active devices are mounted directly in the antenna or feed structure where the impedance is desirable. Antenna types include various slots (slot ring, tapered slot, and coupled rectangular slots), patches, bowtie dipoles, and log spirals. Since the LO signal must be radiated in, such mixers may be impractical as down-converters in microwave wireless systems (although they can be used "in reverse" as upconverters, such as for a transponder). Instead, self oscillating quasi-optical mixers can be employed which generate their own LO signal, often with the same nonlinear active device used for frequency conversion [8].

Quasi-optical mixers can also be arrayed to form more complex integrated receivers, such as for coherent monopulse tracking (four-quadrant

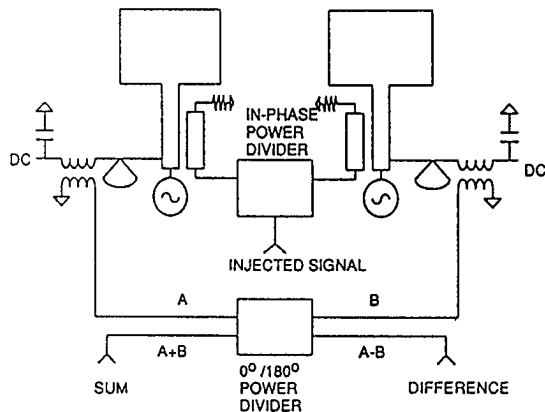


Figure 3. A planar 6 GHz Doppler radar module with azimuth tracking capability.

sum and difference patterns). One such monopulse receiver operates at 35 GHz, using a 2×2 array of slot ring mixers fabricated monolithically on a GaAs substrate [9]. The mixer element uses diodes placed at a $\lambda/4$ interval within a 1λ -circumference annular slot, which is etched into metal that clads the dielectric substrate. This slot-ring acts as both antenna, hybrid and diplexer to provide balanced mixing between orthogonally-polarized RF and LO beams. Feeding a mixer-antenna array with in-phase LO signals results in coherently down-converted IF, such that the array "stares" in a fixed direction. By varying the LO phases, it is possible to steer the receiving beam to a desired angle. This technique has been used in an adaptively-steered receiver array, for reception of Japanese DBS satellite television at 12 GHz [10]. A 216-element rectangular patch array is fabricated in a multilayer structure, which includes low noise downconverters in coplanar waveguide underneath each 9-element subarray. The IF output signals are applied to self-phasing circuits, which combine the subarrays with phasing such that the receiving beam tracks the satellite automatically. This planar circuit replaces a 33 cm.-diameter parabolic dish and its feedhorn electronics.

4. TRANSCEIVERS & TRANSPONDERS

The active antenna approach is especially well suited to wireless-system components where both

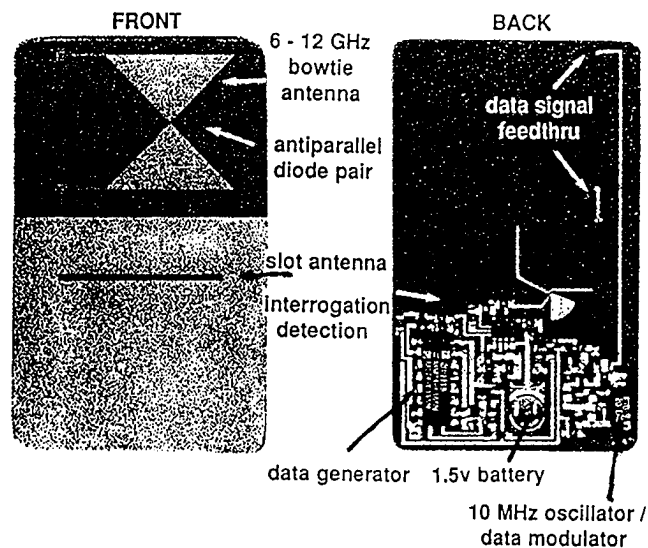


Figure 4. A microwave noncontact identification card, using 6 GHz interrogation.

transmit and receive capabilities are required. In this case, a whole system can be integrated onto a single substrate. An example is the Doppler radar transceiver shown in Figure 3. This 2-element microstrip patch array uses GaAs MESFETs as transmitting oscillators and as receiving mixers, by virtue of their nonlinearity. A sum pattern is transmitted at 6.5 GHz, and both sum and difference patterns are available at the IF (Doppler shift frequency) to obtain the range-rate and rough azimuth tracking of a target [11]. This information can be used by intrusion-detection sensors and process control systems. The circuit is a compact and efficient equivalent to the bulky Gunn oscillator/horn antenna conventionally used. Other transceivers have been designed for point-to-point microwave radio communications. A recent example is the polarization-duplexed 6 GHz transceiver based on an active inverted circular patch [12]. An FET is embedded in a circular microstrip patch to form an oscillator, whose signal is used as the transmitted carrier as well as the local oscillator for downconverting incoming signals from another transceiver. For receiving, a Schottky diode is mounted in the patch at an optimum impedance point to form a microwave mixer. The incoming and outgoing signals are orthogonally polarized as a result of the two resonant modes used for transmitting and mixing by the patch antenna. These signals are also frequency spaced to provide a 200 MHz IF output at each station.

A transponder is a component that transmits a signal only in response to an interrogation signal. The use of small, inexpensive microwave "tag" transponders for non-contact identification (RFID) such as entry systems, toll collection, and inventory control has attracted interest in recent years. An ID card was recently developed which, when illuminated by a 6 GHz signal, transmits a unique digital identification code at a response frequency near 12 GHz. The coded response is readable from a distance of 10 feet away using a simple transceiver, and no microwave source is required on the card (Figure 4). This circuit is based on a quasi-optical mixer originally designed for mm-wave arrays, and demonstrates active-antenna techniques. Only three Schottky diodes are needed for the microwave processing, including interrogation detection for activating the card from a power conserving state [13]. Other transponders have been developed which translate a 12 GHz interrogation signal to 7 GHz to provide a unique response signature, using microstrip patch antennas integrated with two microwave FETs on a single substrate [14]. For long range operation, an 8-element array type transponder was recently demonstrated which uses diode mixers with integrated patch antennas to retro-reflect a 6 GHz interrogation signal back to its source. This circuit provides the function of a radar corner-reflector in a planar, conformal circuit which can be electronically modulated [15].

5. CONCLUSION

Active integrated antennas are compact, efficient circuits that can provide the essential functions required in microwave wireless systems. The advantages of this integrated approach have been demonstrated by several recently developed circuits.

ACKNOWLEDGMENT

This work was supported by the Joint Services Electronics Program (JSEP) under contract F49620-92-C-0055 and the U. S. Army Research Office under contract DAAH04-93-G-0068.

REFERENCES

- [1] C. W. Pobanz and T. Itoh, "Quasi-optical microwave circuits for wireless applications," *Microwave Journal*, pp. 64-86, Jan. 1995.
- [2] J. Lin and T. Itoh, "Active integrated antennas," *IEEE Trans. Microwave Theory Tech.*, vol. 42, pp. 2186-2194, Dec. 1994.
- [3] S. Kawasaki and T. Itoh, "Quasi-optical planar arrays with FETs and slots," *IEEE Trans. Microwave Theory Tech.*, vol. 41, pp. 1838-1844, Oct. 1993.
- [4] J. A. Navarro, K. A. Hummer and K. Chang, "Active integrated antenna elements," *Microwave Journal*, pp. 115-126, Jan. 1991.
- [5] P. Liao and R. A. York, "A high power two-dimensional coupled-oscillator array at X-band," *IEEE MTT-S Int. Microwave Symp. Dig.*, pp. 909-912, 1995.
- [6] P. Liao and R. A. York, "A new phase-shifterless beam-scanning technique using arrays of coupled oscillators," *IEEE Trans. Microwave Theory Tech.*, vol. 41, pp. 1810-1815, Oct. 1993.
- [7] J. Lin, S. T. Chew and T. Itoh, "A unilateral injection-locking type active phased array for beam scanning," *IEEE MTT-S Int. Microwave Symp. Dig.*, pp. 1231-1234, 1994.
- [8] T. Itoh, "Recent progress of quasi-optical integrated microwave and millimeter-wave circuits and components," *Alta Frequenza*, vol. LVIII - N. 5-6, pp. 507-514, 1989.
- [9] R. L. Gingras et al., "Millimeter-wave slot ring mixer array receiver technology," *IEEE Microwave and Millimeter-Wave Monolithic Circuits Symp. Dig.*, pp. 105-107, 1992.
- [10] T. Murata and M. Fujita, "A self-steering planar array antenna for satellite broadcast reception," *IEEE Trans. Broadcasting*, vol. 40, pp. 1-6, Mar. 1994.
- [11] S. T. Chew and T. Itoh, "An active antenna phased array Doppler radar with tracking capability," *IEEE AP-S Int. Symp. Dig.*, pp. 1368-1371, 1995.
- [12] R. Flynt, L. Fan, J. A. Navarro and K. Chang, "Low cost and compact active integrated transceiver for system applications," *IEEE MTT-S Int. Microwave Symp. Dig.*, pp. 953-956, 1995.
- [13] C. W. Pobanz and T. Itoh, "A microwave non-contact identification transponder using subharmonic interrogation," *IEEE MTT-S Int. Microwave Symp. Dig.*, pp. 752-756, 1994.
- [14] K. Cha, S. Kawasaki and T. Itoh, "Transponder using self-oscillating mixer and active antenna," *IEEE MTT-S Int. Microwave Symp. Dig.*, pp. 425-428, 1994.
- [15] C. W. Pobanz and T. Itoh, "A conformal retrodirective array for radar applications using a heterodyne phased scattering element," *IEEE MTT-S Int. Microwave Symp. Dig.*, pp. 905-908, 1995.

SCANNING OSCILLATOR ARRAYS FOR LOW COST TRANSCEIVERS

Robert A. York

Department of Electrical & Computer Engineering
University of California, Santa Barbara, CA 93106, USA
rayork@ece.ucsb.edu

ABSTRACT

Unilateral and bilateral injection-locked oscillator arrays show promise for cost-effective implementation of intelligent scanning antenna systems, especially for emerging millimeter-wave applications. This paper reviews some of these techniques and some remaining technical challenges for practical implementation of the concepts.

INTRODUCTION

A number of commercial opportunities are emerging in the wireless communications, imaging, and automotive electronics markets for active, "smart" antenna array systems. These applications have brought a number of new constraints that could make conventional phased and adaptive array techniques unattractive. Most notably these are cost, size, and efficiency.

It is anticipated that automotive collision avoidance or blind spot indicators should cost less than US\$200 for market viability. Auto manufacturers are also reluctant to allocate more than a few square inches of surface area for possible antenna aperture, which not only makes system integration difficult but also forces the use of higher frequencies in order to satisfy antenna beamwidth requirements. Initial systems are targeting 24 GHz and 77 GHz, but there is already talk of 94–150 GHz systems for further miniaturization. Such high frequencies stress current device technology.

In the wireless sector, compact scanning arrays could be useful in hand-held or mobile systems to reduce power consumption through "adaptive power control", where the array alternates between a low gain "search" mode and a high gain "acquisition" mode much like a tracking radar system. In the high gain mode the array has a high directivity which requires less power for effective communication, and also reduces the susceptibility to interference when receiving. Compact scanning systems could also be used for mobile satellite links which also require high directivity antennas. These wireless applications will likely suffer similar constraints to those mentioned above.

Principles of conventional phased-arrays are well known. Typically coherence is maintained between array elements using a single source distributed to every array element through a corporate feed network. Separate phase shifters are required at each element, each of which requires biasing and multiple control wires (fig 1). It is usually difficult to integrate such systems successfully into a small package since the antennas, feed networks, phase-shifters, and control signals occupy a lot of space. Phase shifters can also add considerable expense to a system, depending on the size of the array and scanning requirements. At millimeter-wave frequencies it is also difficult to generate the required output power with a single solid-state source, and this problem is compounded by large losses in the feed network and phase shifters.

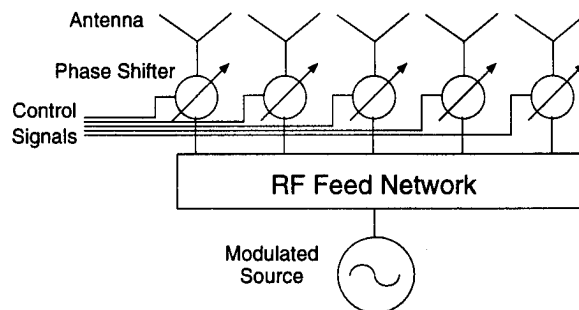


Figure 1 - Conventional approach for an electronically scanned transmitter.

This has led a number of researchers to explore new techniques for beam control that either eliminate or combine the functions one or more components in conventional phased-arrays systems. A number of interesting techniques have been realized using injection-locked or mutually synchronized oscillator arrays, and depend on the unusual phase dynamics of nonlinear oscillators to achieve the scanning objective. The common feature of these alternatives is that they eliminate the phase-shifter circuitry at each array element, and in some cases the RF and control signal distribution networks. The proposed techniques appear to have some advantages over conventional phased arrays, but as with any real system this typically comes at the expense of some other

performance criterion; whether these are acceptable alternatives must be considered on a case-by-case basis.

2. INJECTION-LOCKING TECHNIQUES

The practical use of nonlinear oscillators for phase control is based on the phenomenon of injection locking, sometimes called frequency entrainment. This effect has a long history dating back to observations of synchronized mechanical pendulums by Huygens, and has since been observed in a wide variety of self-sustained (non-linear) biological and physical oscillators.

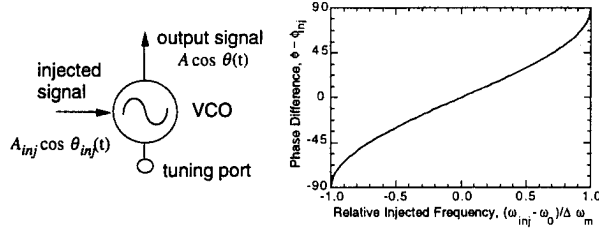


Figure 2 - Injection-locked oscillator and plot showing behavior of oscillator phase as injection frequency is varied relative to the free-running frequency.

Using a simple single-tuned oscillator model it can be shown [1] that the output phase of an oscillator with an injected signal is given by Adler's equation

$$\frac{d\theta}{dt} = \omega_0 + \frac{\omega_0}{2Q} \frac{A_{inj}}{A} \sin(\theta_{inj} - \theta) \quad (1)$$

where $\theta = \omega t + \phi(t)$ and $\theta_{inj} = \omega_{inj} t + \phi_{inj}$ are the instantaneous phases of the oscillator and the injected signal, respectively, A_{inj} and A are the amplitudes, similarly, and Q is the quality-factor of the oscillator resonant circuit. When the oscillator locks onto the injected signal, $d\theta/dt = \omega_{inj}$ in the steady-state, and (1) becomes

$$\omega_{inj} - \omega_0 = \Delta\omega_m \sin \Delta\theta \quad (2)$$

where $\Delta\omega_m = A_{inj}\omega_0/2QA$. $\Delta\omega_m$ is called the *locking bandwidth* of the oscillator, and $\Delta\theta$ is the steady-state phase difference between the oscillator and injected signal. Equation (2) indicates that as the injected signal frequency is tuned over the locking range of the oscillator, $\omega_0 \pm \Delta\omega_m$, the phase difference will vary between $-90^\circ < \Delta\theta < 90^\circ$ (see figure 2).

The most straightforward application of the injection-locking technique to phased arrays is shown in figure 3. Each array element is a self-contained, voltage-controlled oscillator (VCO) that delivers its energy to an antenna. The oscillators are all slaved to a common signal (the desired output signal) which is distributed using a standard feed structure like a corporate feed network. The phase of each oscillator can be changed

relative to the reference signal (and hence the other oscillators) by adjusting the oscillator tuning voltage (the free-running frequency) according to figure 2 above. It should be noted that oscillator arrays like this also serve as efficient power combiners; in fact, most of the techniques described in this paper have evolved from research groups investigating quasi-optical power combining methods [2].

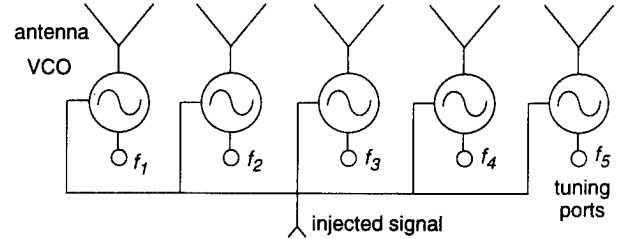


Figure 3 - Injection-locked oscillator array. Output can be scanned through electronic control of each oscillator tuning voltage.

A 4×4 array using the topology of figure 3 has been reported [3], although the emphasis was on the power-combining aspect of the array and not the possible scanning feature. The technique shown in figure 3 will be limited in bandwidth by the locking range of the oscillators, which in turn is related to the injected signal strength. This array topology should degrade gracefully.

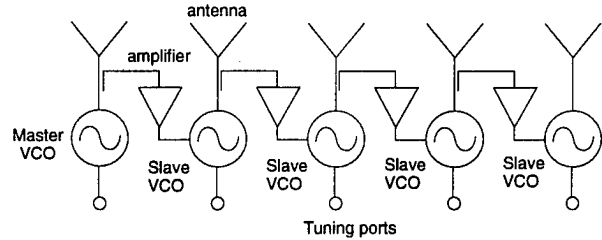


Figure 4 - Cascade of injection-locked VCOs slaved to a low-noise master oscillator, after Itoh [4]. Voltage-tuning each VCO can create a progressive phase shift.

A variation of this idea that eliminates the corporate feed structure involves an injection-locked cascade whereby each array element is slaved to the preceding element in the array. This is shown in figure 4, and has been tested experimentally at UCLA [4]. Amplifiers are used between the oscillators for isolation and also help boost the signal strength for a better locking range. This does increase the circuit complexity. The extension to two-dimensional arrays is straightforward. One feature of all injection-locked arrays is that the oscillators will assume the noise properties of the master oscillator or reference signal, even if the oscillators themselves are quite noisy. Therefore the array in figure 4 will collectively have a low phase noise as long as the injected signal is derived from a "quiet" source.

3. COUPLED OSCILLATOR AND PHASE-LOCKED LOOP ARRAYS

A less obvious extension of the injection-locking concept is an array of mutually synchronized oscillators, such as illustrated in figure 5 below. Each oscillator is bilaterally coupled to neighboring array elements. This system was first proposed by Stephan [5]. Mutual coherence is achieved via the injection-locking process, but the steady-state phase relationships are more difficult to calculate since each oscillator depends nonlinearly on its neighbors.

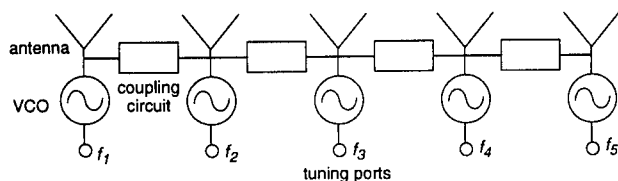


Figure 5 - Coupled-oscillator array

Analysis of the phase dynamics can be simplified by assuming nearest-neighbor interaction and identical oscillators. The mutual interaction between adjacent oscillators is described using a complex coupling coefficient $\epsilon \exp(-j\Phi)$, which can be related to the y - or z -parameters of the coupling circuit that connects the oscillators [7]. The phase dynamics of a system of N coupled oscillators can then be derived as [6,7]

$$\frac{d\theta_i}{dt} = \omega_i - \frac{\epsilon\omega_i}{2Q} \sum_{\substack{j=i-1 \\ j \neq i}}^{i+1} \sin(\Phi + \theta_i - \theta_j) \quad i = 1, 2, \dots, N \quad (3)$$

where ω_i , and θ_i are the frequency and instantaneous phase, respectively, of oscillator i , and Q is the Q -factor of the oscillator embedding circuits. This is obviously just a generalization of Adler's equation (1). When the free-running frequencies, ω_i , are similar enough, then the oscillators can lock to the same frequency so that $d\theta_i/dt = \omega$ in the steady-state. For beam-scanning a constant progressive phase shift of $\Delta\phi$ is required, represented mathematically as $\theta_i - \theta_{i-1} = \Delta\phi$ where $i = 2 \dots N$. Substituting this condition into (3) and assuming $\Phi = 0^\circ$ leads to a set of conditions on the free-running frequencies [6]

$$\omega_i = \begin{cases} \omega_0 / [1 - \Delta\omega_m \sin \Delta\phi] & \text{if } i = 1 \\ \omega_0 & \text{if } 1 < i < N \\ \omega_0 / [1 + \Delta\omega_m \sin \Delta\phi] & \text{if } i = N \end{cases} \quad (4)$$

where ω_0 is the desired steady-state synchronized frequency, and $\Delta\omega_m = \epsilon\omega_0/2Q$ is the locking range. This indicates that a constant phase shift can be programmed by slightly detuning only the end elements of the array in opposite directions. This appears to be the key ad-

vantage of this technique over the unilateral injection-locked oscillators: only peripheral array elements need to be voltage-controlled.

Although (4) seems to imply that any phase shift $\Delta\phi$ can be obtained, a stability analysis of (3) puts limits on this quantity [6]. For the special case of $\Phi = 0^\circ$, the limits are

$$-90^\circ < \Delta\phi < 90^\circ$$

In a typical array with element spacing of $d = \lambda_0/2$, this phase shift is sufficient to scan the beam over a $\pm 30^\circ$ range. This simplified analysis serves to introduce the beam-scanning concept, but in reality the dynamics are complicated by many factors that have been left out of (1), such as amplitude dynamics and non-uniformities, frequency-dependent coupling networks, non-nearest-neighbor interactions, non-uniform tuning profiles of the VCOs, and frequency-dependent device characteristics [7].

Several coupled oscillator arrays have been constructed during the past two years, using packaged MESFET devices and patch antennas. The oscillators are typically coupled with resistively-loaded transmission lines [7]. A recent version was built in collaboration with researchers at the Jet Propulsion Laboratory, operating at 8.4 GHz [8]. It used a novel VCO based on a varactor-tuned patch antenna, and produced over 1 Watt with an 8-element array, and had a total scanning range of 45° (-15° to $+30^\circ$ around broadside).

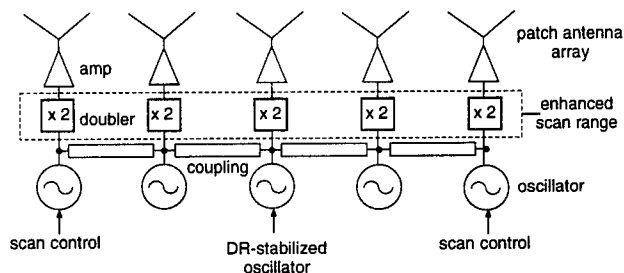


Figure 6 - An improved version of the scanning oscillator concept uses frequency doublers to increase the scan range, and a low-noise source to stabilize the array.

A limitation of both the injection-locked and coupled-oscillator topologies is the limited range of phase shifts that can be synthesized. This can be solved using the topology shown in figure 6 below. A frequency doubler circuit is used at each array element which effectively doubles the inter-element phase shift, which extends the theoretical scanning range to nearly full hemispherical coverage [9].

This technique has other potential benefits: the oscillators are designed at half the desired output frequency, which reduces the cost of the device technology and sim-

plifies design. The range of oscillator tuning required to achieve a given scan range is also significantly reduced. For $\pm 45^\circ$ scanning in a frequency-doubled array (half-wavelength spacing), the relationship between oscillator tunings and interelement phase-shift (fig. 2) is quite linear, which simplifies calibration and scan control circuit design. Doublers (and possibly amplifiers) following the oscillators also provide a desirable measure of isolation between the antenna and oscillator.

Phase noise in a free-running coupled-oscillator array is typically poor, and this is exacerbated by the frequency doublers. Low noise can be achieved by injecting a stable reference signal (which could also contain modulation) into the *center* element of the array, as suggested in the figure 6. Dramatic improvement in phase noise has been measured, suitable for sensitive receiver applications [10].

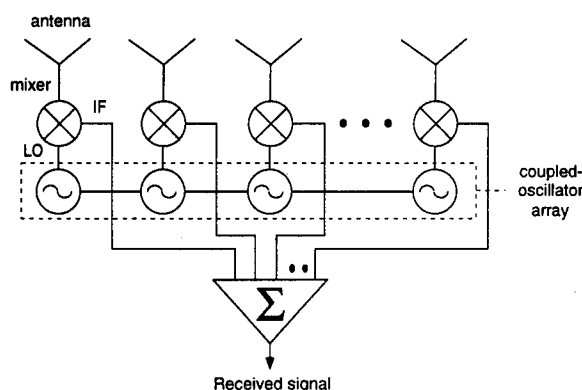


Figure 7 - The coupled-oscillator technique can be used for scanning receivers by using the array as a distributed local oscillator.

The scanning oscillator configurations can also be used for receiving applications [11]. This is accomplished by using the scanning oscillator array as the local oscillator for a set of mixers, as shown in figure 7. Using one of our early array prototypes and some commercial packaged mixers, this concept was tested by first measuring the scanning properties in transmit mode (oscillators coupled directly to antennas), followed by the receive mode as shown. Identical scan ranges and patterns observed in each case, as expected. It may be possible to merge the transmit and receive functions, especially for FMCW imaging arrays, by making each array element a self-contained FMCW transmitter and receiver, where each array element is coupled to its neighbors. This has not yet been tested.

4. CONCLUSIONS

Several interesting new techniques using injection locked and coupled oscillators are currently under investiga-

tion. The technology is still relatively new, and it is not clear whether the benefits of the new techniques outweigh the new difficulties that are introduced. In the near term, these approaches could find use in low cost, low to medium performance mm-wave imaging systems, as they are inherently suited to the FMCW technique. As the understanding of coupled-oscillator systems improve, it may well be possible to achieve high performance with the proposed methods.

5. ACKNOWLEDGEMENTS

This work was supported by the U.S. Army Research Office, Hughes Research Laboratories in Malibu, CA, and the Jet Propulsion Laboratory in Pasadena, CA.

6. REFERENCES

- [1] K. Kurokawa, "Injection-Locking of Solid-State Microwave Oscillators", *Proc. IEEE*, vol. 61, pp. 1386-1409, Oct 1973.
- [2] R.A. York, "Quasi-Optical Power Combining Techniques" in *Millimeter and Microwave Engineering for Communications and Radar*, J. Wiltse, ed., vol. CR54, pp. 63-97, SPIE Press: Bellingham, Washington, 1994.
- [3] J. Birkeland and T. Itoh, "A 16 Element Quasi-Optical FET Oscillator Power Combining Array with External Injection Locking", *IEEE Trans. Microwave Theory Tech.*, vol. MTT-40, pp. 475-481, March 1992.
- [4] J. Lin, S. T. Chew and T. Itoh, "A unilateral injection-locking type active phased array for beam scanning", *IEEE MTT-S International Microwave Symposium Digest* (San Diego), pp. 1231-1234, June 1994.
- [5] K. D. Stephan and W. A. Morgan, "Analysis of Inter-Injection-Locked Oscillators for Integrated Phased Arrays", *IEEE Trans. Antennas Propagat.*, vol. AP-35, pp. 771-781, July 1987.
- [6] R.A. York, "Nonlinear analysis of phase relationships in quasi-optical oscillator arrays", *IEEE Trans. Microwave Theory Tech.*, special issue on quasi-optical techniques, vol. MTT-41, pp. 1799-1809, October 1993.
- [7] R.A. York, P. Liao, J.J. Lynch, "Oscillator array dynamics with broadband N-port coupling networks", *IEEE Trans. Microwave Theory Tech.*, vol. MTT-42, pp. 2040-2045, November 1994.
- [8] P. Liao and R.A. York, "A 1 Watt X-band power-combining array using coupled VCOs", *IEEE MTT-S International Microwave Symposium Digest* (San Diego), pp. 1235-1238, June 1994.
- [9] A. Alexanian, H.C. Chang and R.A. York, "Enhanced scanning range in coupled oscillator arrays utilizing frequency multipliers", *1995 IEEE Antennas and Propagation Society Symposium Digest* (Newport Beach, CA).
- [10] X. Cao and R.A. York, "Phase noise reduction in scanning oscillator arrays", *1995 IEEE MTT-S International Microwave Symposium Digest* (Orlando).
- [11] X. Cao and R.A. York, "Coupled Oscillator Scanning Technique for Receiver Applications", *1995 IEEE Antennas and Propagation Society Symposium Digest* (Newport Beach, CA).

ACTIVE ANTENNA ELEMENTS FOR MILLIMETER-WAVE CELLULAR COMMUNICATIONS

Mark J. Vaughan, Warren Wright, and Richard C. Compton

School of Electrical Engineering
Cornell University, Ithaca, New York 14853
mjv2@cornell.edu, ww24@cornell.edu, rcc7@cornell.edu

ABSTRACT

The direct modulation of oscillators in an active array provides an efficient means of communicating over millimeter-wave carriers. This paper describes how various forms of digital modulation can be applied and gives details of the development of a 28 GHz transmission system designed to operate at 2Mbit/s using frequency shift keying.

1. INTRODUCTION

Millimeter-wave wireless local and wide area networks offer the promise of high-bandwidth communications within small to medium sized cells. However, even for modest data rates and coverage areas, the power requirements exceed the levels possible with existing semiconductor based amplifiers. Several devices must therefore be used in conjunction with power combiners to generate adequate power levels for most applications. These power combiners can be quite lossy though, especially when large arrays of devices are involved. One solution to this problem is to use quasi-optical power combining [1], in which the power generated by each element of an array of solid-state oscillators or amplifiers is radiated into free-space, where power-combining losses are negligible.

Most of the array power combining research done thus far has focused on creating arrays with future application in radar and point-to-point communications. Recently a quasi-optical array which could be used in a multipoint distribution system was presented [2].

Although active antennas capable of both receiving and transmitting have been created [3, 4], separation of these functions into different arrays has a number of benefits. It allows greater isolation, which decreases coupling of the strong transmitted signals into the sensitive receivers, and it simplifies full-duplex operation. Additionally, separating the receive and transmit functions gives more freedom in optimizing the different elements.

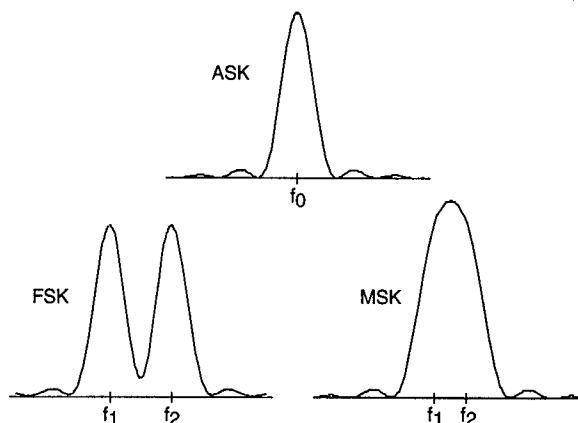


Figure 1: Comparison of power spectra for ASK, FSK, and MSK.

Because most wireless services are migrating towards digital modulation techniques, this paper will discuss the application of active antenna elements to digital communication links. Digital signals are more secure and easier to multiplex, switch, and compress. Also, they can be broadcasted over large distances without degradation, using repeaters which can faithfully reconstruct the original signal [5].

2. FREQUENCY-SHIFT KEYING

Aside from amplitude-shift keying (ASK), which is the modulation scheme of turning the carrier on and off, frequency-shift keying (FSK) is the simplest digital modulation scheme to implement with active antenna elements. In the basic binary FSK, the array frequency is shifted synchronously between two frequencies, f_1 and f_2 , which represent the two data states. Since the operating frequencies of oscillator arrays are sensitive to bias voltage, this modulation is easily implemented by switching the bias voltage between two values. Alternatively, varactors can be incorporated into the circuits to provide frequency control [6]. FSK is

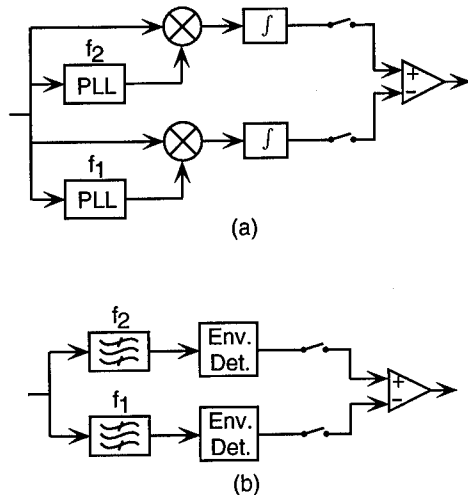


Figure 2: (a) Coherent binary FSK receiver [4]. (b) Noncoherent receiver [3]. The switches are used to sample at intervals of T_0 .

preferred to ASK, even though it generally occupies a larger bandwidth (see Fig. 1), because it has fixed optimum states (f_1 & f_2), unlike the states of ASK which are sensitive to fading.

The separation between the two frequencies, $\Delta f = f_2 - f_1$, should be made as small as possible to reduce the transmission bandwidth. In order to maintain orthogonality between the two states, the minimum value of the separation should be

$$\Delta f = \frac{1}{2T_0}$$

where T_0 is the time allocated per bit (reciprocal of data rate). Modulation using this Δf is referred to as minimum-shift keying (MSK) [5].

FSK receivers can either be coherent or noncoherent. The coherent configuration (Fig. 2a) uses a pair of phase-locked loops (PLL) to generate sinusoids at frequencies f_1 and f_2 which are in phase with the received signal. Each of these is then mixed with the received signal, and the resultant is integrated. The data value (0 or 1) is determined by comparing the outputs of the integrators sampled at intervals of T_0 . The noncoherent receiver (Fig. 2b) instead uses a pair of bandpass filters followed by envelope detectors to generate the signals which are fed to the output comparator.

While noncoherent receivers are substantially easier and cheaper to build, the coherent versions yield better performance. The theoretical difference in the probability of errors between the two is a factor ranging from two to ten, depending upon the signal-to-noise ratio of the received signal.

A practical, inexpensive noncoherent receiver can be constructed for use with a quasi-optical array FSK transmitter fairly easily utilizing an MC13055 "Wide-band FSK Receiver" IC [8]. This integrated circuit contains the detectors and comparator, as well as an input amplifier/limiter. Fig. 3 shows a block diagram for a complete 28 GHz receiver using this IC.

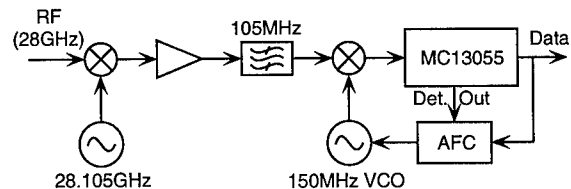


Figure 3: Practical implementation of a noncoherent 28 GHz binary FSK receiver.

The automatic frequency control (AFC) block adjusts the frequency of the 150 MHz LO to compensate for any drift in the transmitter array. It senses the frequency deviations from the center frequency set in the MC13055 and adjusts to maintain a zero average deviation. This circuit has a capacity of 2Mbit/s, but more recent ICs, such as the MC13155, could be used for higher speeds.

Work is currently progressing on implementation of this receiver to demonstrate FSK of a 28 GHz endfire active antenna element [9].

3. LINEAR MODULATION

Frequency shift keying is a nonlinear modulation scheme that is best suited for millimeter-wave systems with carriers that have insufficient phase stability to perform carrier phase estimation[7]. In contrast, linear modulation schemes, such as amplitude and phase modulation, place more stringent requirements on the carrier stability to perform phase-coherent detection. Most microwave digital radio systems use linear modulation schemes to achieve optimal spectral efficiencies (Bits/Sec/Hz) with good power efficiency [10].

Phase modulation can be achieved in several different ways. One approach is to place the active oscillator element into a phase locked loop [11] (see Fig. 4). The oscillator acts as a voltage controlled oscillator. When the loop is locked, the average VCO frequency equals the stable reference frequency. The baseband data is fed into the low-frequency section of the PLL.

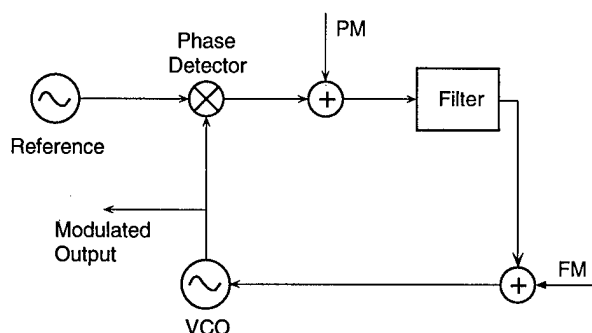


Figure 4: Phase-locked loop for phase modulation of an oscillator element (VCO).

Four-level phase-shift keying (4-PSK), which is identical to four level quadrature amplitude-shift keying, has a spectral efficiency of 2 Bits/Sec/Hz. Higher order modulation schemes, for example 16-PSK and 16-QAM, afford higher data rates but require larger carrier-to-noise ratios (C/N). For these higher order schemes, n-QAM is preferable to n-PSK because it requires a lower C/N than n-PSK. However, the standard rectangular constellation n-QAM (see Fig. 5) is difficult to implement in an active antenna for $n \geq 16$ because it requires both a quadrature and an in-phase oscillator. The circular variation of QAM, on the other hand, can be more easily achieved, by separately phase and amplitude modulating the oscillator element. Another benefit of the circular scheme is that it requires slightly less peak power to achieve the same probability of error.

Constant-phase amplitude modulation can be achieved using a class-C oscillator of the type described in reference [12]. Furthermore, this element can be phase modulated using a PLL circuit which drives a varactor at the gate of the transistor, allowing generation of circular constellation n-QAM.

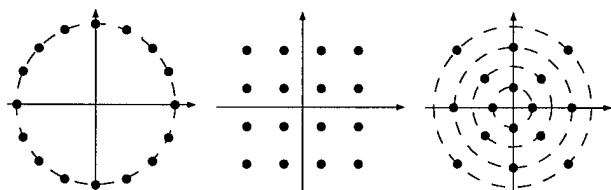


Figure 5: In-phase and quadrature constellation for 16-PSK and rectangular and circular implementations of 16-QAM.

ACKNOWLEDGMENTS

This work was supported by the Army Research Office. Mark Vaughan is supported by a JSEP Graduate Fellowship. The authors would like to thank K. Y. Hur at

Raytheon's Advanced Device Center for supplying the InP HEMTs used in this work.

1. REFERENCES

- [1] J. W. Mink, "Quasi-Optical Power Combining of Solid-State Millimeter-Wave Sources," *IEEE Trans. Microwave Theory Tech.*, vol. 34, no. 2, pp. 273-279, Feb. 1986.
- [2] M. J. Vaughan and R. C. Compton, "28 GHz Omni-Directional Quasi-Optical Transmitter Array," to be published in *IEEE Trans. Microwave Theory Tech.*
- [3] R. Flynt, L. Fan, J. Navarro, and K. Chang, "Low Cost and Compact Active Integrated Antenna Transceiver for System Applications," *IEEE MTT-S Int. Microwave Symp. Dig.*, 1995, pp. 953-956.
- [4] K. Cha, S. Kawasaki, and T. Itoh, "Transponder Using Self-oscillating Mixer and Active Antenna," *IEEE MTT-S Int. Microwave Symp. Dig.*, 1994, pp. 425-428.
- [5] B. P. Lathi, *Modern Digital and Analog Communication Systems*, HRW-Saunders College Publishing, 1989, Philadelphia.
- [6] A. C. Oak and R. M. Weikle, "A Varactor Tuned 16-Element MESFET Grid Oscillator," *Proc. IEEE AP-S Int. Symp.*, 1995, pp. 1296-1299.
- [7] J. G. Proakis and M. Salehi, *Communication Systems Engineering*, Prentice-Hall, 1994, New Jersey.
- [8] G. Elmore and K. Rowett, "Inexpensive Multi-Megabaud Microwave Data Link," *Ham Radio*, Dec. 1989, pp. 9-29.
- [9] M. J. Vaughan and R. C. Compton, "28 GHz Oscillator for Endfire Quasi-Optical Power-Combining Arrays," submitted for publication to *Electronics Lett.*
- [10] L. J. Greenstein and M. Shafi, *Microwave Digital Radio*, IEEE Press, 1988, New York, NY.
- [11] F. M. Gardner, *Phaselock Techniques*, John Wiley & Sons, 1979, New York NY.
- [12] R. D. Martinez and R. C. Compton, "A Quasi-Optical Oscillator/Modulator for Wireless Transmission," *IEEE MTT-S Int. Microwave Symp. Dig.*, 1994, pp. 839-842.

INTEGRATED MICROSTRIP ACTIVE ANTENNAS AND THEIR APPLICATIONS

Kai Chang

Department of Electrical Engineering
Texas A&M University
College Station, Texas 77843-3128
Chang@ee.tamu.edu

ABSTRACT

In this paper, we consider an inverted stripline active antenna configuration for system applications. Solid-state devices can be directly integrated with the antenna to perform various functions. A two-way communication system using two integrated active antenna transceivers was demonstrated.

1. INTRODUCTION

Integrated and active integrated antennas receive a great deal of attention because they can reduce the size, weight and cost of many transmit and receive systems. Passive and active solid-state devices can be configured to provide various functions with several components at the terminals of the antenna. Two- and three-terminal solid-state devices have been integrated with various antennas to form switches, tuners, detectors, mixers, amplifiers, oscillators, Doppler sensors and receivers. The choice between transistors and diodes is not clear cut. It depends on the type of microwave component required, operating frequency range, RF power output desired, available DC power input and other considerations. For integrated antennas, the choice of solid-state device also involves its effect on the radiation characteristics. Although integration can reduce the size, weight and cost of many microwave systems, active integrated antennas have shown a deterioration of both the antenna and component performance. Unlike a passive antenna, an integrated antenna includes the effect of device packages and bias lines on the electromagnetic fields and currents which

flow on it. These effects often cause changes in operating frequencies, lower conversion efficiencies and higher cross-polarization levels (CPL). If an integrated antenna can maintain reasonable component specifications with little degradation in the radiation characteristics, the approach would be attractive for many commercial and military systems.

To meet the performance requirements, an inverted stripline active antenna was developed. The configuration has many advantages over other microstrip antennas such as low cross polarization levels, small disturbances from solid-state device mounting and bias lines, ease of hermetically sealing, and excellent radiation patterns. Solid-state devices such as PIN diodes [1], varactors [1], Gunn [2], FETs [3], and mixers [4] have been successfully integrated with the antennas to perform switching, tuning, oscillation, beam steering, and transceiving functions.

To demonstrate the system applications, a two-way communication system using two integrated active antenna transceivers was built. The transmitter provides 63 mW output power with an estimated maximum link distance of 4.8 km [4].

2. ANTENNA AND CIRCUIT CONFIGURATIONS

Figure 1 shows the inverted stripline antenna integrated with a Gunn diode. A single diode exhibited an output power of 60-70 mW at X-band [2]. Power combining efficiencies of over

89% have been demonstrated for a four-element square array. Beam steering was demonstrated by varying bias voltage to the individual antenna element [5].

The inverted stripline antenna was successfully integrated with an FET as shown in Figure 2 [3]. The FET provides 57 mW at 5.69 GHz with a DC-to-RF efficiency of over 50%. The cross-polarization levels are less than 19 dB compared to the co-polarization levels.

PIN diodes or varactors can be integrated with the inverted stripline to perform switching or tuning functions. Figure 3 shows the integration of these devices at the radiating edges of the antenna [1]. By varying the bias voltages of the PIN diodes, the antenna reflection coefficient at the operating frequency varies from a VSWR of 1.014 to 22.87. For varactor diodes, the operating frequency was tuned over 31% centered at 3.4 GHz.

The integration of an FET oscillator and a mixer diode with the antenna forms a transceiver. Part of the FET output power can be used as the local oscillator pump to the mixer. Figure 4 shows the circuit configuration [4]. The mixer location was optimized for impedance matching. The transmitter provides 63 mW and the mixer has an isotropic conversion loss of 5.5 dB.

3. TWO-WAY COMMUNICATION SYSTEM

Two transceivers described in the previous section were used to build a two-way communication system. The arrangement is shown in Figure 5 [4]. The receive pattern is perpendicular to the transmit pattern for LO to RF isolation. The maximum distance that the two transceivers can be separated was found to be 4.8 km for a bandwidth of 6 MHz.

4. CONCLUSIONS AND ACKNOWLEDGMENTS

In conclusion, inverted stripline active antennas have been developed and integrated with various solid-state devices. The integrated antennas have excellent performance and are useful for system applications.

This work was supported in part by the Army Research Office. The author would like to thank J.A. Navarro, L. Fan and R. Flynt for their good work.

5. REFERENCES

1. J.A. Navarro and K. Chang, "Low-Cost Integrated Inverted Stripline Antennas with Solid-State Devices for Commercial Applications," *1994 IEEE-MTT Microwave Symposium Digest*, San Diego, CA, May 1994, pp. 1771-1774.
2. J.A. Navarro, L. Fan and K. Chang, "Active Inverted Stripline Circular Patch Antennas for Spatial Power Combining," *IEEE Trans. on Microwave Theory and Techniques*, Vol. 41, No. 10, October 1993, pp. 1856-1863.
3. J.A. Navarro, L. Fan and K. Chang, "Novel FET Integrated Inverted Stripline Patch," *Electronics Letters*, Vol. 30, No. 8, April 14, 1994, pp. 655-657.
4. R. Flynt, L. Fan, J.A. Navarro and K. Chang, "Low Cost and Compact Active Integrated Antenna Transceiver for System Applications," *1995 IEEE-MTT Microwave Symposium Digest*, Orlando, Florida, May 1995, pp. 953-956.
5. J.A. Navarro and K. Chang, "Electronic Beam-Steering of Active Antenna Array," *Electronics Letters*, Vol. 29, No. 3, February 4, 1993, pp. 302-304.

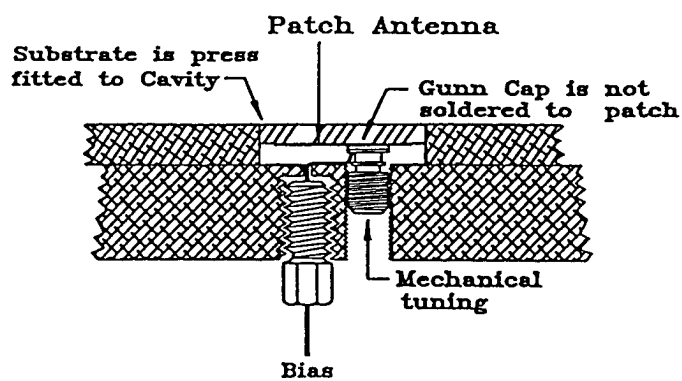


Figure 1. A Gunn diode integrated with an inverted stripline antenna

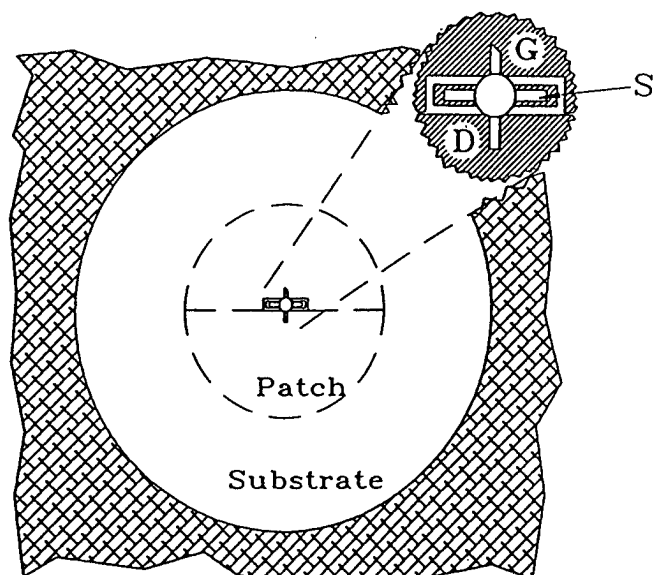


Figure 2. An FET device integrated with an inverted stripline antenna

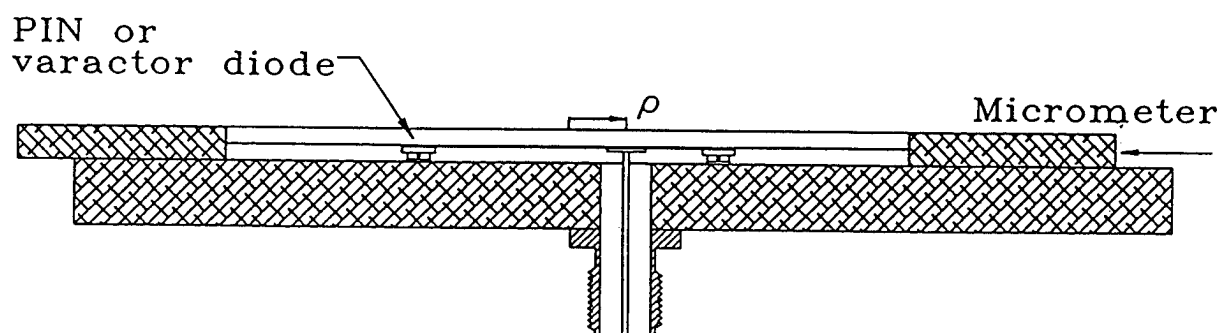


Figure 3. PIN or varactor diodes integrated with an inverted stripline antenna

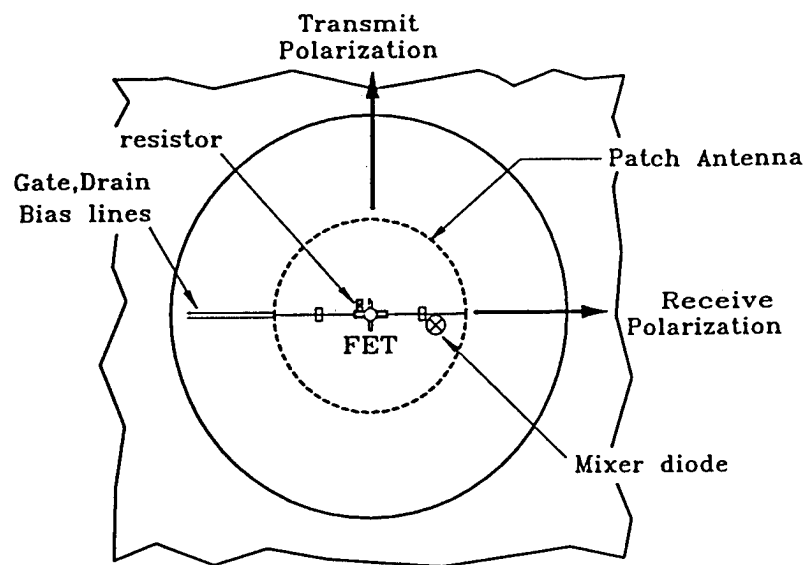


Figure 4. Transceiver integration

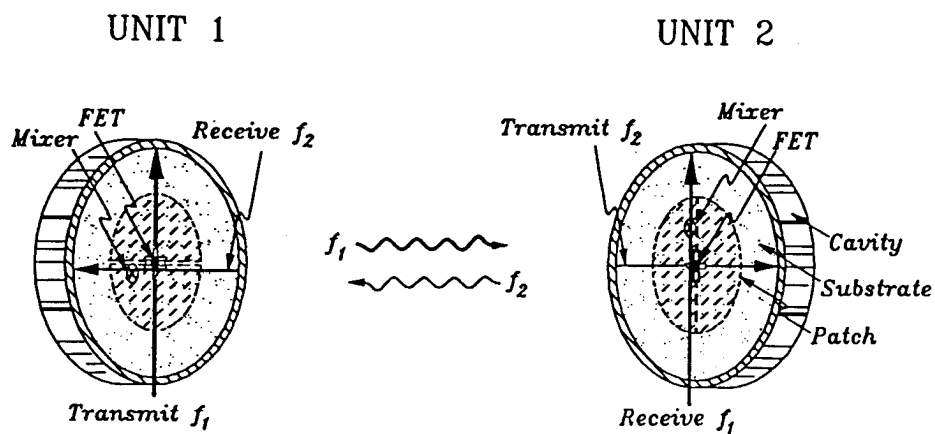


Figure 5. Two-way communication system

A LIQUID-CRYSTAL OPTOELECTRONIC PHASED ARRAY BEAM FORMING NETWORK

Osamu KOBAYASHI and Hiroyo OGAWA

NTT Wireless Systems Laboratories
1-2356 Take, Yokosuka, Kanagawa 238-03 JAPAN

Phone: +81 (468) 59 3352 Fax: +81 (468) 59 3351

ABSTRACT

An optoelectronic beam forming network (BFN) is presented for a 3-element phased array antenna that utilizes electrically controllable birefringence mode nematic liquid-crystal cells (ECB mode NLC cells) for phase shifting and amplitude control. In the circuit, a microwave signal is carried by a pair of orthogonal linearly polarized lightwaves (signal and reference lightwaves) using the optical heterodyning technique. A prototype circuit is built and its performance experimentally examined. With small deviations among the three cells, phase shifts of up to 240 degrees are achieved for MW signals from 0.9 GHz to 20 GHz with good stability; attenuation of more than 18 dB was achieved.

1. INTRODUCTION

We are planning to realize the advanced personal communication service by using the multiple beam geostationary communication satellite system [1]. It offers direct links between the low-cost customer-premises earth stations/handy terminals and the geostationary satellite as depicts in Fig. 1. For realization of that service, the satellite must offer large effective isotropic radiated power (e. i. r. p.). Large deployable reflector antennas with diameters exceeding ten meters [2] fed by active phased array antennas will be adopted as the onboard antennas.

Active phased array antenna systems are suitable and will be widely used not only for satellite onboard antenna systems, but also for microwave (MW)/millimeter-wave (MMW) systems because of the following advantages. First, radiated MW/MMW power level can be increased by the spatial power combining technique (simply increasing the number of antenna elements). The spatial power combining technique is inevitable in MMW transmitting systems where efficient, high-power active devices are hard to obtain by existing technologies, as well as communication satellite onboard antenna systems which must offer very large e. i. r. p. Second, antenna beam shaping/steering can be achieved by changing the amplitude and phase distributions of the antenna array elements. Adaptive antenna beam shaping/steering is regarded as a promising countermeasure to reduce unnecessary and undesired electromagnetic interference.

Unfortunately, the configuration of the BFNs becomes very complex for large scale, multiple beam phased array antenna systems. The number of the input/output ports of the BFNs must increase to achieve large e. i. r. p. The number of the output ports will increase

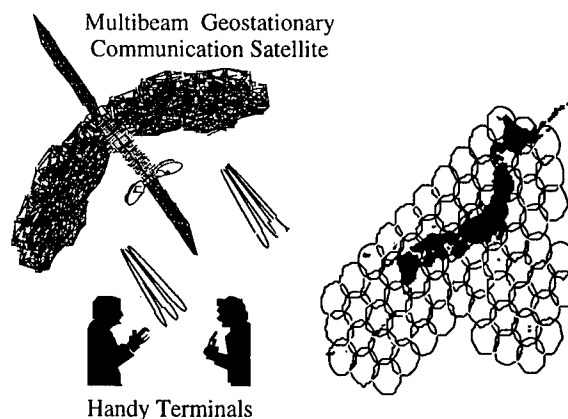


Fig. 1 Multibeam geostationary communication satellite

because the BFN must feed MW/MMW signals to a large number of active elements. As the diameter of the reflector antenna increases, antenna spot beam size reduces, and the required number of antenna beams increases to cover the main islands of Japan and its archipelago. It will increase the number of the input ports. Furthermore, it requires a significant number of phase shifters and attenuators, and the level of interconnection between these components will be very complex.

The approach that utilizes photonic technologies is promising to build large scale phased array antenna BFNs due to the massively parallel signal processing capability of optical systems [3]. Various optoelectronic phased array beam forming networks have been proposed and studied [4]. The BFNs that utilize Fourier optics are reported in [5] and [6]. The BFN that gives true time delay for antenna elements is presented in [7]. Twisted nematic liquid-crystals were used to switch the optical path to give different time delay. Experiments on the phase shifting of a single radio frequency (RF) signal by using a liquid-crystal cell were reported in [8]. Unfortunately, the processed signal was limited to the RF band by the restriction of the acoustic-optical modulator and laser source (He-Ne laser of 633 nm) used in the circuit.

The authors have developed a BFN for a 3-element phased array antenna that deals with MW signals. In the circuit, a microwave signal is carried by a pair of orthogonal linearly polarized lightwaves using the optical heterodyning technique. ECB mode NLC cells are used to control the phase and amplitude of the signals in an analogue manner in the optical domain. The phase shifts and attenuation of the MW signals of 0.9 GHz to 20 GHz were measured. The configuration and performance of the circuit is described in this paper.

2. ATTENUATION AND PHASE SHIFT OF MICROWAVES WITH POLARIZATION MULTIPLEX OPTICAL HETERODYNING

We adopted 'polarization multiplex optical heterodyning' to transmit and process MW signals in the BFN. Fig. 2 shows the scheme that realizes amplitude or phase control of a MW signal with this technique. The MW signal $\cos \omega_{rf} t$ is fed to the E/O converter, and the optical signal $\cos(\omega_{opt} + \omega_{rf}) t$ is obtained. Here, ω_{rf} and ω_{opt} denote the angular frequencies of the input MW signal and the laser source, respectively. The E/O conversion scheme is optical frequency shifting. Therefore, the output optical signal of the E/O converter has the same spectrum as the input MW signal, but the frequency is different. The E/O converter also provides the optical signal $\cos \omega_{opt} t$.

The signal lightwave $\cos(\omega_{opt} + \omega_{rf}) t$ and the reference lightwave $\cos \omega_{opt} t$ are assigned to the orthogonal linear polarizations and combined for transmission through the BFN circuit.

The lightwaves are input to a homogeneous type ECB mode nematic liquid-crystal cell. The LC cell is made by filling liquid-crystals between two parallel glass plates on which transparent electrodes are formed. Nematic liquid-crystal molecules lay parallel to the glass plate when no voltage is supplied, and the direction of the major axes are the same throughout the liquid-crystal layer. An ECB mode NLC cell with local Cartesian coordinate xyz is illustrated in Fig. 2. The glass plates are placed in the plane parallel to the xy plane, and the direction of the major-axes of liquid-crystals become parallel to the y axis. Lightwaves propagate along the z axis. The liquid-crystal molecules begin to raise respect to the glass plate as the voltage applied to the cell increases. The refractive indices of an ECB mode NLC cell for the linear polarization parallel to the x and y axes are written as follows.

$$\begin{cases} n_x = n_o \\ n_y = 1 / \sqrt{\frac{\cos^2 \theta_s}{n_e^2} + \frac{\sin^2 \theta_s}{n_o^2}} \\ \Delta n = n_y - n_x \end{cases} \quad (1)$$

Here, n_x and n_y denote the refractive indices for the respective polarizations. n_e is the refractive index for the polarization parallel to the major axes of the liquid-

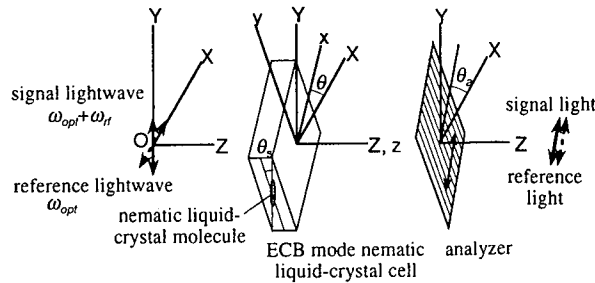


Fig. 2 Polarization Multiplex Optical Heterodyning

crystal molecules, and n_o is for the polarization parallel to the minor axes. θ_s is the declination angle of the liquid-crystal molecules with the respect to the glass plate.

The ECB mode NLC cell is placed on the global Cartesian coordinate XYZ . We set to the z -axis to match the Z -axis, and the cell is rotated by θ around the Z -axis. Behind the cell, an analyzer is placed so that it passes the tilted linear polarization component of θ_a . In that configuration, the complex amplitude of the output lightwaves for the polarization parallel to the X and Y axes are respectively written as follows.

$$E_{//}^X = [\cos^2 \theta + \sin^2 \theta \exp(-jk\Delta n d)] \cos \theta_a + [\sin \theta \cos \theta \{1 - \exp(-jk\Delta n d)\}] \sin \theta_a \quad (2)$$

$$E_{//}^Y = [\sin \theta \cos \theta \{1 - \exp(-jk\Delta n d)\}] \cos \theta_a + [\sin^2 \theta + \cos^2 \theta \exp(-jk\Delta n d)] \sin \theta_a \quad (3)$$

Here, superscripts X and Y denote the input polarizations, and subscript $//$ denotes the output component of the analyzer.

The microwave signal is retrieved as the beat of the two components. The amplitude and phase changes as $k\Delta n d$, i.e. the LC cell applied voltage, is changed. When $\theta = \pm \pi/4$ and $\theta_a = 0, \pi/2$, the circuit works as an MW signal attenuator. When $\theta = 0, \pi/2$ and $\theta_a = \pm \pi/4$, only the phase changes, and the circuit works as a phase shifter. The advantages of polarization multiplex optical heterodyning are as follows:

- The phased array beam forming network requires many optical interferometers for phase shifting. Because an interferometer is formed on a single signal path, the complexity of the optical circuit is reduced.
- Because signal and reference lightwaves propagate over the same path, the phase stability of the output MW signal is very good.
- Because the reference lightwave is provided with the signal lightwave, the O/E conversion block becomes very simple. Only a photodiode and an MW amplifier are required.

3. THE EXPERIMENTAL SETUP

The optoelectronic phased array beam forming network built for the experiments is illustrated in Fig. 3. Two laser diode pumped Nd:YAG lasers of $1.32 \mu m$ were used for the transmission of MW signals in the circuit. Lasers were single mode and single frequency type, and were controlled by a phase locked loop (PLL) so that their optical frequency difference remained constant and corresponded to the MW carrier frequency. One laser output was considered as the signal lightwave, and the other the reference lightwave.

The outputs of the two lasers were input to a 2 by 4 polarization maintaining fiber (PMF) coupler tree. The polarization states of the two input lightwaves were set to be linearly orthogonal, i.e., the polarization plane of the signal lightwave is parallel to one of the two optical axes of the PMF; that of the reference lightwave is parallel to the other optical axis. The signal and reference

lightwaves are combined and divided into two, to be maintained the polarization states by the first PMF coupler. Further division is performed by the PMF couplers of the next stage. The signal and the reference lightwaves propagate the same path through the circuit but with orthogonal polarization state.

The outputs of the PMF coupler tree were input to a pair of collimator arrays. A 1 by 3 ECB mode NLC cell array was installed between the pair of collimator arrays. The LC cells were set so that the direction of the major-axes of the LC molecules when no voltage was supplied was vertical. In that configuration, only the refractive index for y-polarization (vertical polarization) is changed as the LC molecules incline from the vertical, while the refractive index for x-pol. (horizontal polarization) remains constant. Therefore, we can set the phase difference between the signal and the reference light using the ECB mode NLC. The amount of the phase shift is determined by the voltage applied to the LC cell. The two orthogonal components of the outputs of the LC cells were combined by an analyzer whose direction was set to 45 degrees. For the attenuation experiments, the LC cells were rotated by 45 degrees, and the analyzer was set so that y-pol. (or x-pol.) lightwave passed through it.

The combined lightwaves were input to the photodiodes (PDs) to retrieve the MW signals as the beats of the signal and reference lightwaves. The microwave signals preserved the results of phase shifts and amplitude change made in the optical domain. The microwave signals output by the receivers were input to a vector network analyzer in order to measure amplitude and phase difference.

4. EXPERIMENTAL RESULTS AND DISCUSSIONS

We measured phase shifts and amplitude change of the MW signals for the three signal paths as functions of the LC cell applied voltages. Two cases were examined; the case when LCs were used for phase shifts, and the case when LCs were used for amplitude control. The results of phase control experiments of the MW signals of 0.9 GHz are illustrated in Fig. 4(a), and those of the amplitude control experiments are illustrated in Fig. 4(b). Fig. 4(a) shows that phase shifts of about 240 degrees were observed for the three cells. It is also observed that amplitudes remained constant. The deviations among the three cells were small. Note that the identical PD and the MW amplifier were used when measuring the amplitude and phase of the MW signals. From Fig. 4(b), it is observed the amplitude changed with the LC cell applied voltages. More than 30 dB attenuation was achieved for the best, and more than 18 dB attenuation was possible even in the worst case. The phase shifts changed with the MW signals. Phase shifts of π were observed at the maximum attenuation level.

Phase control experiments of MW signals of 0.9 GHz, 5 GHz, and 20 GHz were performed. Results for the same cell are illustrated in Fig. 5. Phase shifts of about 240 degrees were achieved in all cases. The results were independent of MW signal frequency. Small fluctuations in amplitude were observed as the LC applied voltages increased. It was about ± 0.9 dB for the worst case. The fluctuation may be improved by more precisely

aligning the orientation of the LC cells and polarization planes of the lightwaves. Wideband phase controllability of the circuit was confirmed from Fig. 5.

Fig. 6 shows the phase stability of the output MW signal of 0.9 GHz. Because the signal and reference lightwaves propagate through the same path, disturbances that commonly affected the two lightwaves were suppressed, and excellent phase stability of the beat signal was achieved. The fluctuation was about a degree. This includes the phase fluctuation of the laser sources, the fluctuation of the orientations of LC molecules, and the thermal instability of PMF length.

5. CONCLUSION

A 3-element optoelectronic phased array antenna BFN that utilizes ECB mode NLC cells for both phase shifting and amplitude control was presented. A microwave signal is carried by a pair of orthogonal linearly polarized lightwaves using the optical heterodyning technique. Therefore, the configuration of the optical circuit is very simple, and the phase stability of the microwave signals was improved. Phase shifts of up to 240 degrees were achieved for MW signals of 0.9 GHz, 5 GHz and 20 GHz with good phase stability. Attenuation of more than 18 dB was achieved. Deviations among the three cells was small. The described system can be expanded to 2D phased array beam forming network by using a 2D array of LC cells, wherein the parallel signal processing capability of the optical signal processing technique can be fully utilized.

Acknowledgment

The authors would like to thank Mr. Takashi Yamanaka for assistance in the experiments, Dr. Takashi Kurokawa and Mr. Tetsuo Yoshizawa of NTT Optoelectronics Laboratories for providing the liquid-crystal cells and helpful suggestions, and Dr. Kenji Kohiyama and Dr. Shuichi Samejima for their encouragement.

References

- [1] H. Ogawa et al., "Microwave photonics for multibeam satellite communications", Technical digest of the fifth Optoelectronics Conference, pp. 268-269, July 1994.
- [2] M. Watanebe, A. Meguro, H. Tanaka, J. Mitsugi, "Analytical and experimental study on deployable modular mesh antenna structures", Proc. of 45th Congress of the International Astronautical Federation, IAF-94-1.1.172, Oct. 9-14, 1994, Jerusalem, Israel.
- [3] C. Tocci and H. J. Caulfield, "Optical Interconnection", Artech House, 1994.
- [4] H. Zmuda and E. N. Toughlian (ed.), "Photonic aspects of modern radar", Artech House, 1994.
- [5] G. A. Koepp, "Optical processor for phased array antenna beam formation", SPIE vol. 477, pp. 75-81, 1984.
- [6] L. P. Anderson, F. Boldissar, D. C. D. Chang, "Phased array antenna beamforming using optical processor", Proc. of AIAA '92, pp. 1279-1288, Washington D. C., March 1992.
- [7] D. Dolfi, S. Bann, J-P. Huignard, J. Roger, "Two-dimensional optical architecture for phase and time-delay beam forming in a phased array antenna", Proc. SPIE Vol. 1703, pp. 481-489, 1992.
- [8] N. A. Riza, "Liquid crystal-based optical control of phased array antennas", IEEE J. of Lightwave Tech., pp. 1974-1992, vol. 10, no. 12, Dec. 1992.

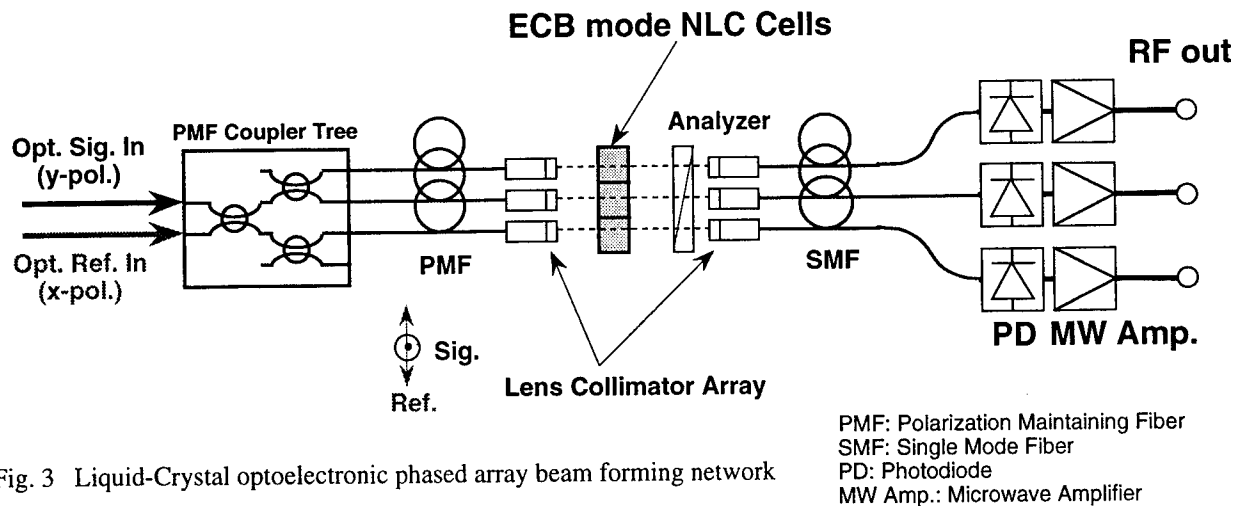


Fig. 3 Liquid-Crystal optoelectronic phased array beam forming network

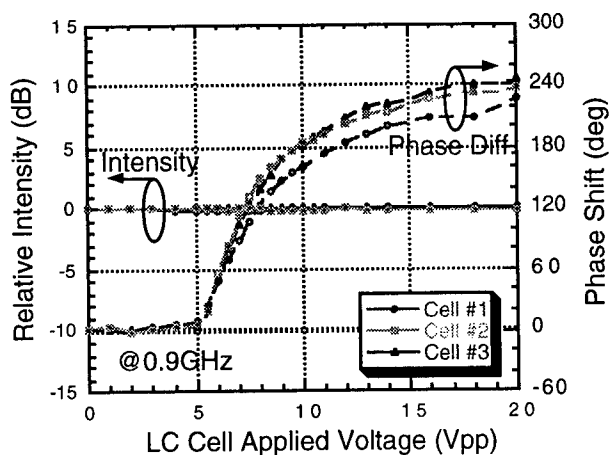


Fig. 4(a) Phase shift as a function of the liquid-crystal cell applied voltage at 0.9 GHz

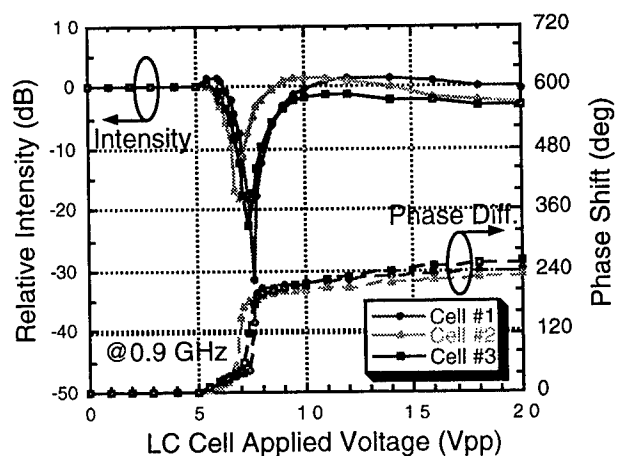


Fig. 4(b) RF attenuation as a function of the liquid-crystal cell applied voltage at 0.9 GHz

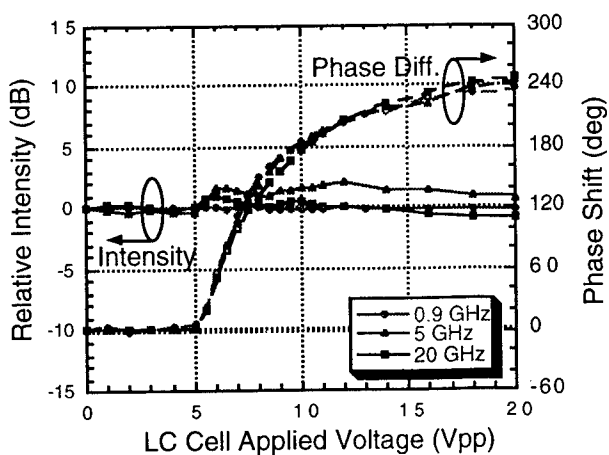


Fig. 5 Phase shift of MW signals of 0.9 GHz, 5 GHz, and 20 GHz

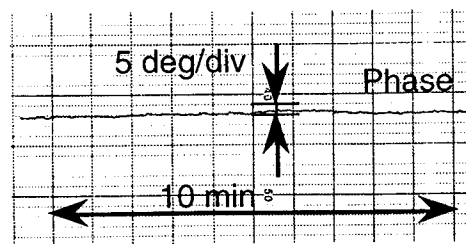


Fig. 6 Phase stability of the output MW signal of 0.9 GHz

MILLIMETER-WAVE DIELECTRIC LEAKY-WAVE ANTENNAS

Chung-Yi Lee, Ananjan Basu, John Liao, June Siey-Mun Wong,
Bijan Houshmand and Tatsuo Itoh

Electrical Engineering Department
University of California, Los Angeles
Los Angeles, CA 90095
TEL:(310)206-4820 FAX:(310)206-4819

ABSTRACT

A dielectric leaky-wave antenna with a new perturbation scheme is developed. The attenuation constant with different gap width between metal patches is determined experimentally. The dielectric waveguide used in this paper is an anisotropic Sapphire rod. The conventional effective dielectric constant (EDC) method is modified to calculate the unperturbed propagation constant and then used to predict the main beam position. Experimental data agree quite well with that of simulation.

I. INTRODUCTION

Dielectric antennas provide superior properties in the low guided-wave loss, simple design, and light weight in the millimeter-wave frequency range. A dielectric leaky-wave antenna also possesses the advantage of electronic scanning of the main beam by simply varying the operating frequency. Directivity or beamwidth of the leaky-wave antenna can be easily controlled by properly designing the antenna length.

The complex propagation constant of a uniform leaky-wave antenna with a finite transverse substrate was analyzed by Mittra and Kastner based on the spectral domain approach [1]. Radiation characteristics of antennas with perturbation strips on either the broad or narrow side of the dielectric rod were studied [2]. The directivity at the transverse plane of an antenna was improved using a pair of metal flares along the longitudinal direction [3]. A series of studies based on a waveguide model for analyzing several dielectric leaky-wave structures was published by Ghomi *et al* [4]-

[7]. The Ritz-Galerkin variational approach was applied to analyze an inset dielectric waveguide antenna [8]. A theory based on a novel multimode transverse equivalent network was proposed by Guglielmi and Oliner to calculate the dispersion behavior of a metal-strip-loaded image leaky-wave antenna [9]. Moreover, mode-matching and point-matching techniques were applied to the analysis of metal-strip-loaded dielectric antennas [10].

It is noticed that metal strips or patches of all pervious references were deposited on the dielectric rod directly. These designs have the advantage of the most antenna elements in the transverse direction if a dense planar array is needed. For applications of a very narrow beamwidth, the dielectric antenna is very long electrically. The attenuation constant of above directly metal-deposited techniques is, however, too high for such a long antenna design. Furthermore, the fabrication process also becomes very difficult for a physically long antenna. In this paper, we use the field coupling mechanism as shown in Fig. 1 to perturb the guided surface wave. Then an appropriate attenuation constant can be obtained for the design of a nearly $300 \lambda_0$ long leaky-wave antenna.

II. ANTENNA DESIGN

Fig. 1 depicts a dielectric leaky-wave antenna with the proposed perturbation scheme which is suitable for a very long antenna design. The metal patches are placed on both sides of a high dielectric constant rod so that a proper attenuation constant can be obtained. The dielectric waveguide used here is a low-loss Sapphire rod with an anisotropic dielectric constant tensor,

$$[\epsilon] = \epsilon_0 \begin{bmatrix} 9.3 & 0 & 0 \\ 0 & 9.3 & 0 \\ 0 & 0 & 11.5 \end{bmatrix} \quad (1)$$

where ϵ_0 is the free space permittivity. The cross dimension of the Sapphire rod is chosen so that only the dominant mode exists in the operating frequency range.

Due to its anisotropy, a rigorous full-wave analysis is necessary to accurately calculate the propagation constant of Fig. 1. However the conventional effective dielectric constant (EDC) method can be modified to quickly give us the approximated but good enough data. In the formulation of the EDC along the y-direction for a multilayered slab waveguide with an anisotropic layer, we assume that only TM modes propagate and there is no x variation. The field is concentrated in the Sapphire region. Derived from Maxwell's equations and compared with the isotropic case, one can have the anisotropic propagation constant as,

$$\beta_{\text{ani}} = \beta_{\text{iso}} \sqrt{\frac{\epsilon_{yy}}{\epsilon_{zz}}} \quad (2)$$

where β_{iso} is calculated from the conventional EDC method by replacing the Sapphire layer with a dielectric constant ϵ_{zz} isotropic material. The conventional EDC method is then used to formulate the eigenvalue equation along the x-direction since there is no E_x component in our assumption. Fig. 2 shows dispersion curves of Fig. 1 without perturbation metal patches and with dimensions: $w = 24$ mil, $t = 23.7$ mil, and $h = 10$ mil. It can be seen that only the dominant mode exists for frequencies less than 100 GHz. The phase constants of Fig. 1 with and without metal patches are assumed to be the same since the leaky constant is usually very small in the leaky-wave antenna design. Therefore, one can use the unperturbed data to predict some important antenna parameters. For example, the main beam position of the -1 space harmonic wave is simply decided by changing the perturbation period d according to the following equation,

$$\theta = \sin^{-1} \left(\frac{\beta}{k_0} - \frac{2\pi}{k_0 d} \right) \quad (3)$$

where θ is the angle with respect to the broad side direction, β/k_0 is the normalized phase constant of the dominant mode.

The attenuation constant of Fig. 1 is studied experimentally by taking the ratio of $|S_{21}|$ with and without uniformly perturbed patches, respectively. The metal patches are fabricated on a custom-made 10-mil thick Teflon sheet. Each metal patch has the dimension: 20 mil x 50 mil. The parameter used to control radiation is the gap width g between a pair of patches. The measured attenuation constant versus gap width is shown in Figs. 3 and 4 for two different frequencies. Solid lines are measured data and dash lines are curve-fitting results. Based on these curves, a new tapering method by changing the gap width between patches is employed and a 36-inch long antenna with linearly tapered gap width is designed. The initial gap width is 62 mil and the final one is 40 mil.

III. ANTENNA PERFORMANCE

The main beam positions of two leaky-wave antennas with different perturbation periods, 80-mil and 50-mil, are assembled and measured. Fig. 5 depicts measured and calculated antenna performance. Although the modified EDC method is an approximated method, this efficient technique can predict the antenna performance quite well. The deviation between theoretical and measured data is about 5° for the 80-mil period antenna and is 3° for the 50-mil one. The measured scanning range from 91 to 97 GHz is about 16.5° and 24.5° for the 80-mil and 50-mil perturbation periods, respectively.

IV. CONCLUSION

A millimeter-wave leaky-wave antenna with an anisotropic Sapphire rod and a new perturbation scheme is analyzed and designed. The conventional EDC method is modified to include the anisotropy of the Sapphire dielectric waveguide. The calculated main beam position

and the scan range agree well with measured data.

ACKNOWLEDGMENT

This work was supported by ThermoTrex Corporation in San Diego, California.

REFERENCES

- [1] R. Mittra and R. Kastner, "A spectral domain approach for computing the radiation characteristics of a leaky-wave antenna for millimeter waves," *IEEE Trans. Antennas Propagat.*, vol. AP-29, pp. 652-654, July 1981.
- [2] S. Kobayashi, R. Lampe, R. Mittra, and S. Ray, "Dielectric rod leaky-wave antennas for millimeter-wave applications," *IEEE Trans. Antennas Propagat.*, vol. AP-29, pp. 822-824, Sept. 1981.
- [3] T. Trinh, R. Mittra, and R. J. Paleta, JR., "Horn image-guide leaky-wave antenna," *IEEE Trans. Microwave Theory Tech.*, vol. MTT-29, pp. 1310-1314, Dec. 1981.
- [4] M. Ghomi, H. Baudrand, and C. Cavalli, "New approach for computing radiation pattern of dielectric leaky-wave antenna," *Electron. Lett.*, vol. 25, no. 5, pp. 345-346, 1989.
- [5] M. Ghomi and H. Baudrand, "Full-wave analysis of microstrip leak-wave antenna," *Electron. Lett.*, vol. 25, no. 13, pp. 870-871, 1989.
- [6] M. Ghomi and H. Baudrand, "Full-wave analysis of coupled microstrip leaky-wave antennas," *IEEE AP-S Int. Symp.*, pp. 322-325, June 1991.
- [7] M. Ghomi, B. Lejay, J. L. Amalric and H. Braudrand, "Radiation characteristics of uniform and nonuniform dielectric leaky-wave antennas," *IEEE Trans. Antennas Propagat.*, vol. AP-41, pp. 1177-1186.
- [8] T. Rozzi and L. Ma, "Scattering by dipoles in inset dielectric guide and application to millimetric leaky wave antennas," *Proc. 17th European Microwave Conference*, pp. 543-548, Sept. 1987.
- [9] M. Guglielmi and A. A. Oliner, "A practical theory for dielectric image guide leaky-wave antennas loaded by periodic metal strips," *Proc. 17th European Microwave Conference*, pp. 549-554, Sept. 1987.
- [10] J. A. Encinar, "Mode-matching and point-matching techniques applied to the analysis of metal-strip-loaded dielectric antennas," *IEEE Trans. Antennas Propagat.*, vol. AP-38, pp. 1405-1412, Sept. 1990.

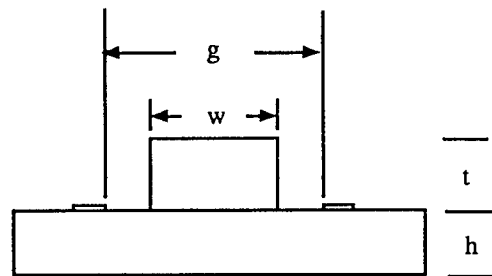
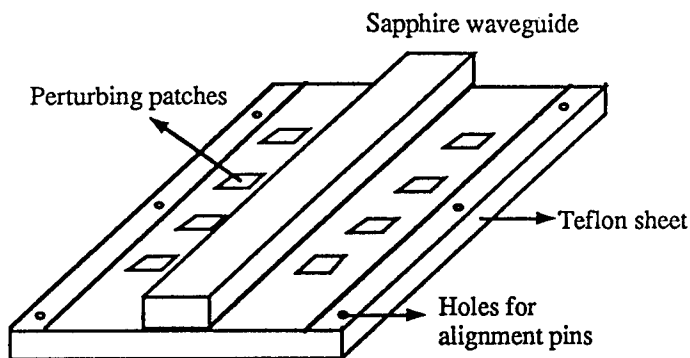


Fig. 1 A dielectric leaky-wave antenna. (a) Schematic plot. (b) Cross dimensions.

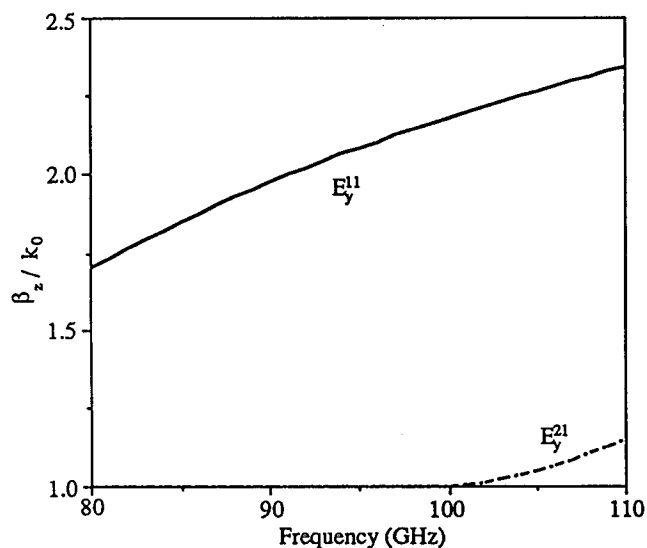


Fig. 2 Dispersion curves of Fig. 1 without perturbation metal patches.

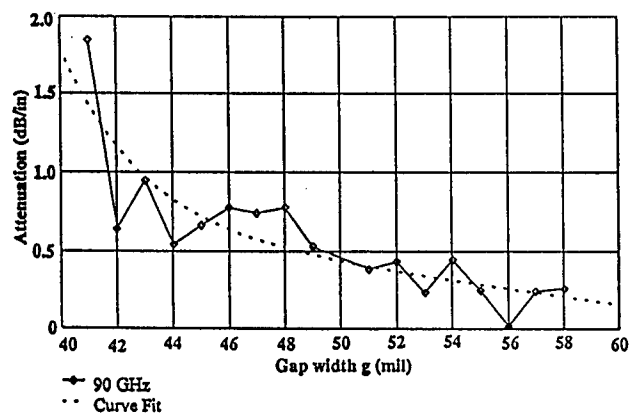


Fig. 3 Attenuation constant versus gap width at 90 GHz.

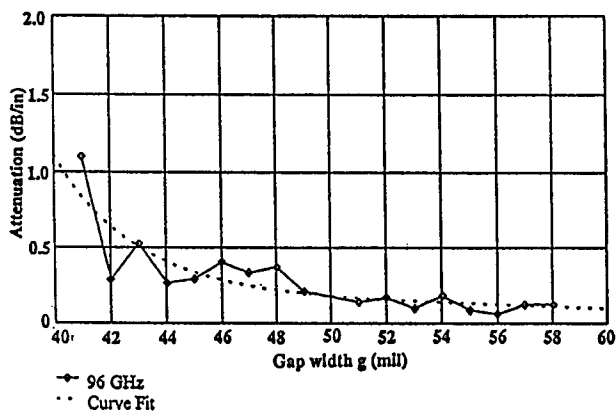


Fig. 4 Attenuation constant versus gap width at 96 GHz.

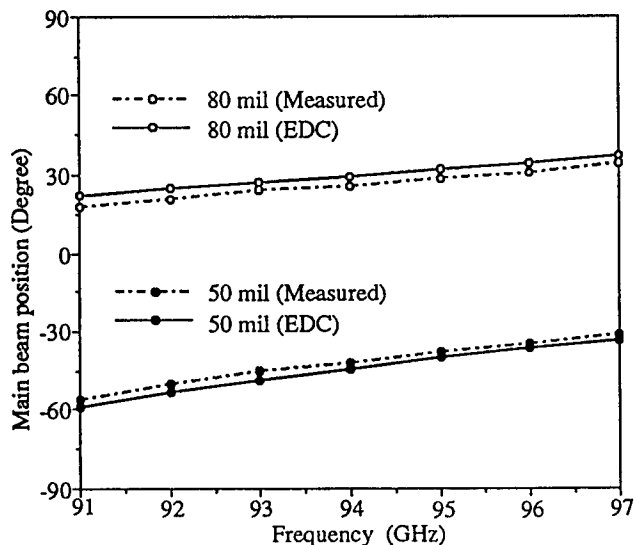


Fig. 5 Measured and calculated main beam position of antennas with different perturbation periods.

MMICs for mobile/personal communications applications (Tutorial, Invited)

Masayoshi Aikawa and Masahiro Muraguchi

NTT Wireless Systems Laboratories
1-2356 Take, Yokosuka, Kanagawa 238-03, Japan
aikawa@mhossun.ntt.jp, murag@mhossun.ntt.jp

Abstract

The demand for mobile and personal communications systems is expected to produce a huge market for handy phone sets and their MMICs in coming years. A number of ICs in silicon bipolar, silicon Bi-CMOS, GaAs MESFET, HBT, and HEMT are now becoming available for system application. There are tradeoffs among the competing technologies with regard to performance, cost, reliability, and time-to-market. This paper describes process selection and requirements of cost and RF performances to MMICs for digital cellular and cordless telephones. Furthermore, new circuit techniques which were developed by NTT are presented.

1. Introduction

Many cellular and cordless systems are presently being planned and operated in the world. Trends for system standards are moving towards a higher frequency and from analog to digital modulation techniques. Cordless systems are being planned as the next generation systems of personal communications. Such systems are called the Personal Handy phone System, or PHS in Japan, the Personal Communication Service, or PCS in the US, and the Digital European Cordless Telecommunication, or DECT in Europe. The concept of the cordless system is to combine mobile communication and public telephones, where handy phone sets can be used in the home as cordless telephones and in town as cellular telephones. Since the base stations of cordless systems cover a very small area, only about 200 meters in diameter, the systems are called microcellular systems.

The 1.9 GHz-band Japanese PHS employs $\pi/4$ -shift QPSK digital modulation, Time Division Multiple Access (TDMA), and the Time Division Duplex (TDD) scheme. The bit rate and the channel spacing are set at 384 kbps and 300 kHz, respectively.

Handy phone sets should be small, light, and provide extended communication service time. In the PHS, talking-time of over 8 hours and standby-time of one week are

expected. A typical block diagram of the PHS handy phone set is shown in Fig. 1. The RF unit consists of a single conversion transmitter and a double conversion receiver. The first and second intermediate frequencies are 1.66 GHz band and 240 MHz band, respectively. Since the transmission frequency and receiving frequency are the same in the PHS, a T/R switch is required.

2. Process Selection for MMICs

In selecting PHS component fabrication processes, there are tradeoffs to consider with regard to performance, cost, reliability, and time-to-market. According to the present market trend, price is the most important factor in employing components. As a result, manufacturers tend to employ a silicon process, as long as silicon circuits can provide acceptable performance. In the RF unit, GaAs is used in the power amplifier, T/R switch, and local oscillator switch, while silicon is used in all the other circuits, i.e., mixers, QPSK modulators, PLLs, IF ICs, and so on. In the baseband unit, all circuits are silicon-based.

3. MMIC Requirements

3.1 Cost and price requirements

MMICs for the PHS are commercially available now from various Japanese, American, and European manufacturers, for example, Matsushita, NEC, Fujitsu, Mitsubishi, and Sony in Japan, National Semiconductor, Pacific communication, Analog Devices, AT&T, and HP in the US, and Philips in Europe. The present market prices are very low: in the neighborhood of 1 to 8 dollars. Just last year, the market prices were 4 to 15 dollars. With the advance of mass production, our guess is that market prices will be reduced to from 1 to 5\$. For example, the price of PHS power amplifiers was around 15 \$ in 1994, but it has dropped to about 5\$. For each RF IC, only one or two manufacturers can provide satisfactory service in this severe cost race. This is because orders tend to be concentrated to specific manufacturers who supply lower-priced or special-performance devices.

3.2 RF Performance Requirements

Digital systems require special performance from microwave components. A transmitter unit for digital systems such as the PHS requires low adjacent channel interference and low modulation vector error. The ideal output spectrum of $\pi/4$ -shift QPSK modulation has a narrow occupied bandwidth of about 200 kHz. However, the output spectrum of a transmitter spreads out because of microwave component distortion, as shown in Fig. 2. Here, the PHS specifications require an adjacent channel interference level of better than -50 dBc at a 192-kHz bandwidth at a 600-kHz off-carrier, and modulation vector error of better than 12.5%rms. Phase noise from VCOs, and phase and amplitude distortion from a mixer, driver amplifier, power amplifier, and T/R switch degrade both adjacent channel interference and modulation vector error. Therefore, the transmitter components are required to have sufficient linearity. This linearity requirement strongly limits the low-power consumption designs of microwave components. For example, power-added efficiency of a commercially available power amplifier is normally 20%. These requirements differ from those of analog cellular systems.

4. Example of MMICs

NTT has developed new RF circuit techniques for the PHS, which overcome the distortion problems that occur with low supply voltages such as 2 V. For example, several MMICs will be presented.

4.1 Low noise amplifier (LNA) [1]

High performance LNAs can be constructed by suitably combining enhancement-mode FETs, or EFETs, with depletion-mode FETs, or DFETs. An EFET is characterized by low noise and high gain under a low operation current. However, a DFET is characterized by low distortion. Therefore, a series connection of the two types of FETs provides low noise, high gain, and low distortion performance under low-voltage and low-current conditions. The developed LNA is shown in Fig. 3. It has a noise figure of 2.0 dB and a gain of 12 dB at 1.9 GHz using a drain voltage of 2 V and a drain current of 1 mA.

4.2 Power amplifier [2]

For low voltage and high efficiency operation, we tried to reduce the phase distortion. It was discovered that, as the input power increases, the phase of the common source FET advances, but that of the common gate FET is delayed.

This led us to believe that a combination of these FETs could compensate for the phase distortion. Indeed, this is the case, the Cascode FET, which is a cascode connection of a common source FET and common gate FET, thoroughly suppresses the phase deviation. Thanks to the phase distortion compensation, the limit of the efficiency for the new power amplifier increases up to 50% at 3 V operation. The new linear power amplifier is shown in Fig. 4. This amplifier has excellent performance with a power-added efficiency of 45%, an output power of 20.5 dBm, and a gain of 30 dB in spite of a low supply voltage of 2.4 V. At a supply voltage of 3 V, the performance of the PA increases. It achieves record performance with a power added efficiency of 50%, an output power of 21.5 dBm, and a gain of 31.5 dB. The chip size of the PA is 2.0 x 1.5 mm.

4.3 Quadrature modulators [3]

The factor preventing low voltage operation for modulators is the use of Gilbert Cell mixers. The supply voltage of less than 3 V of the conventional Gilbert Cell mixer degrades its linearity and modulation accuracy, because the Gilbert Cell mixer employs three series-connected transistors and each transistor requires a supply voltage of more than 1 V, as shown in Fig. 5(a). Figure 5(b) shows our new Gilbert Cell mixer which can operate at a supply voltage of 2 V. The essence for low voltage operation lies in reducing the number of series-connected transistors. Two cross-coupled single-balanced mixers consisting of differential pairs form a double-balanced mixer core similar to the Gilbert cell. A local signal is applied to the differential pairs in the Gilbert Cell core. Each baseband voltage signal is converted into a differential current signal using the current mirror. The sum of the single-balanced mixer tail currents is held constant because the differential current mirror has current sources. Thus, low-distortion mixing is obtained. Since the new double-balanced mixer includes only two series-connected transistors in each circuit branch, it can operate at the low voltage of 2 V. The new quadrature modulator is shown in Fig. 6. The active area is 2.4 x 0.7 mm. At the 1.9 GHz specified for the PHS, the vector error is 6.9%rms. The power consumption of 68 mW at 2 V is about 1/3 of the minimum consumption of previously reported modulator ICs.

5. Conclusion

In selecting MMIC fabrication processes for handy phones, there are tradeoffs to consider with regard to performance, cost, reliability, and time-to-market. According to the present market trend, price is the most

important factor in employing microwave components. As a result, manufacturers tend to employ a silicon process, as long as silicon circuits can provide acceptable performance. Therefore, GaAs MMICs must distinguish themselves by their special performances.

Acknowledgment

We wish to thank Dr. K. Kohiyama and Dr. O. Kurita for their many helpful suggestions and encouragement.

References

- [1] M. Nakatsugawa, Y. Yamaguchi, and M. Muraguchi, "An L-band ultra low power consumption monolithic

low noise amplifier," IEEE GaAs IC Symp. Tech. Digest, pp. 45-48, Oct. 1993.

- [2] M. Muraguchi, T. Tsukahara, M. Nakatsugawa, Y. Yamaguchi, and T. Tokumitsu, "1.9 GHz-Band Low Voltage and Low Power Consumption RF IC Chip-Set for Personal Communications," Proceedings of the 44th IEEE Vehicular Technology Conference, pp. 504-507, June 1994.
- [3] T. Tsukahara, M. Ishikawa, and M. Muraguchi, "A low-voltage 2 GHz Si-bipolar direct-conversion quadrature modulator," IEEE International Solid-State Circuits Conference Digest, Feb. 1994.

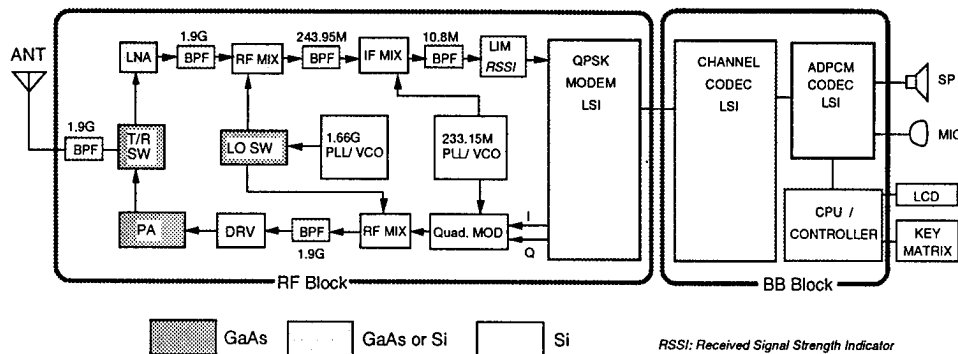


Fig. 1 Typical block diagram of the PHS.

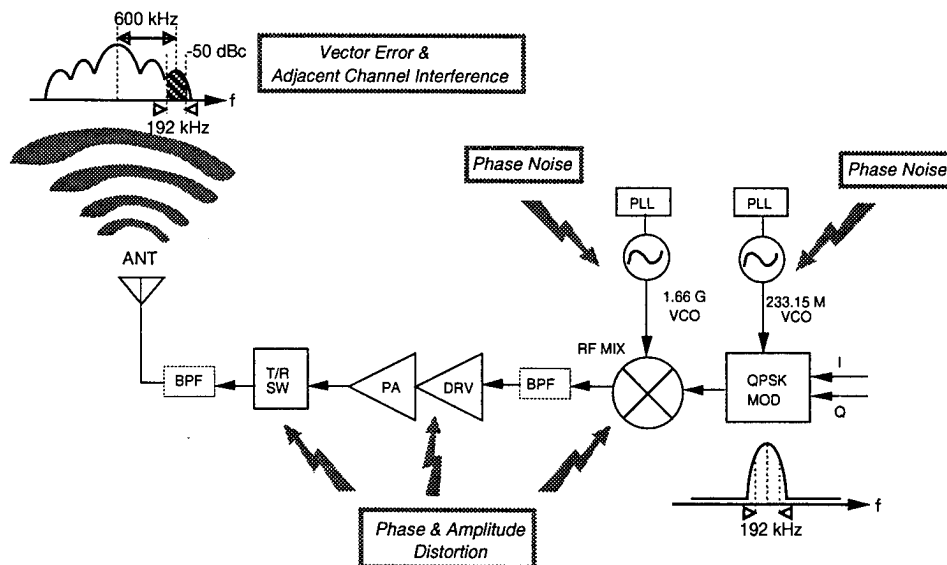


Fig. 2 Transmitter distortion problem.

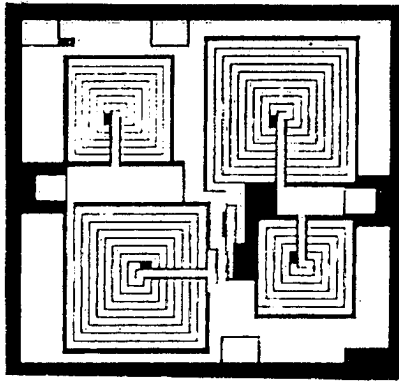


Fig. 3 1.9 GHz low noise amplifier.
Chip size: 1.5 x 1.5 mm

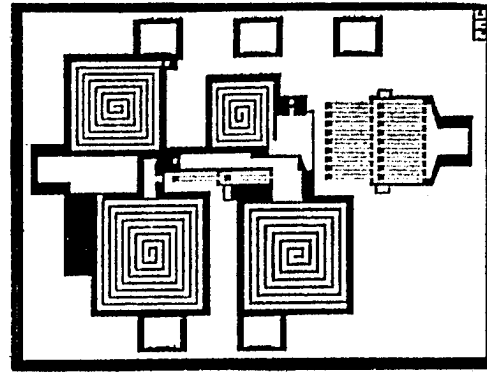
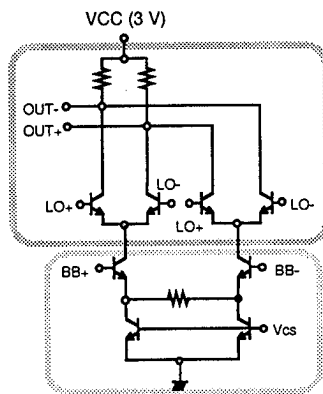
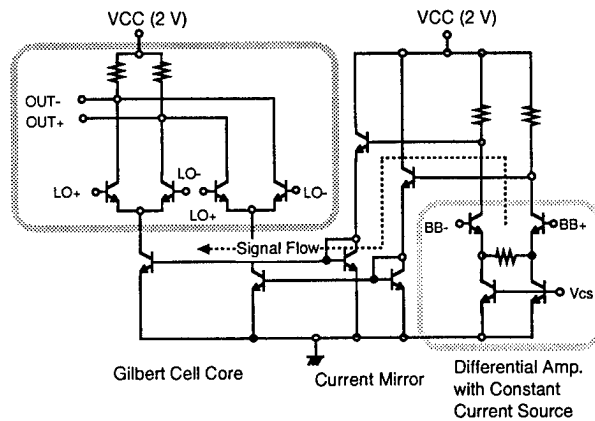


Fig. 4 1.9 GHz power amplifier.
Chip size: 2.0 x 1.5 mm



(a) Conventional Gilbert Cell Mixer
with constant current sources
($V_{cc} \geq 3\text{ V}$)



(b) New Gilbert Cell Mixer
with constant current sources
($V_{cc} \geq 2\text{ V}$)

Fig. 5 New Gilbert cell mixer and conventional one.

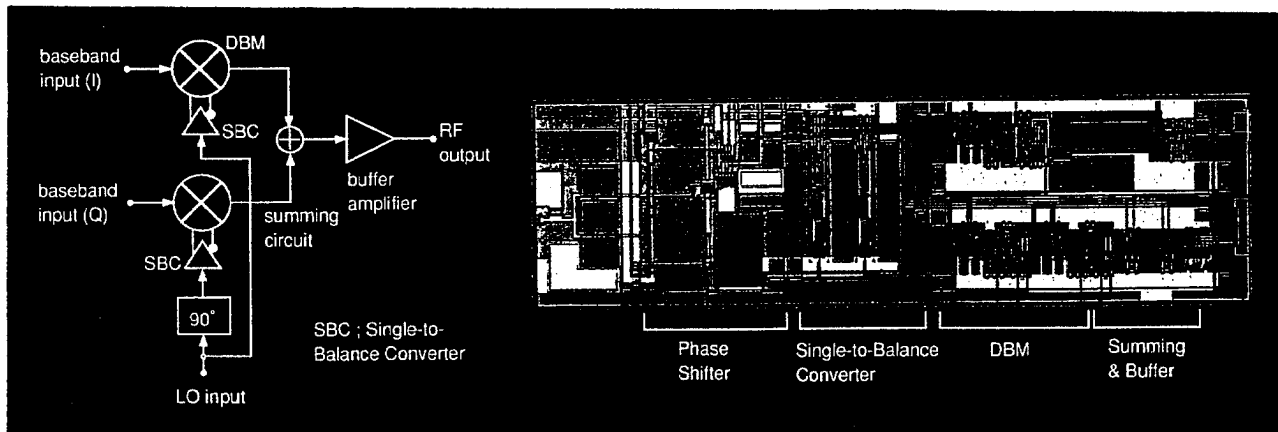


Fig. 6 1.9 GHz quadrature modulator.

R/D ACTIVITIES ON MMICs IN EUROPE

C. Rumelhard

Laboratoire Physique des Composants Electroniques
Conservatoire National des Arts et Métiers
292, rue Saint-Martin, 75141 Paris Cedex 03, France
rumelhard@cnam.fr

ABSTRACT

The R/D activity on MMICs in Europe is presented through three representative aspects. The first one consists in an overview of recent power circuits. The second one shows the developments in millimeter-wave circuits. The third one describes an activity which becomes specially interesting with monolithic circuits: the multifunction chips.

1. INTRODUCTION

Although the activities in MMICs are still changing in Europe, the main sources of MMICs available at present time or the research centres working on MMICs, are listed in Table 1 (F is for foundries and R for research centres):

Company or Institution	Country
IMEC (R)	Belgium
CNET (R); IEMN (R); Philips Microwave Limeil (F); Thomson-CSF (R,F)	France
Daimler-Benz (R,F); F-IAF (R); Siemens (F)	Germany
Alcatel-Telettra (F); Alenia (F)	Italy
GEC Marconi Materials Technology (F), DRA (R), GMMT (F)	U K

Table 1 : Different sources of MMICs in Europ

The monolithic circuits activities are also based on different research centres working on epitaxy or discrete transistors like IEMN (France), F-IAF (germany) and DRA (UK) or suppliers of epitaxial products like Picogiga (France) or Epitaxial Products International (UK). Several research and development programmes from European Community, from European Space Agency, from european military programmes or from the different national governments helped to develop these technologies [1].

The seven major foundries are grouped in an association called EUROGaAs [2].

These recent developments make possible the many applications which are emerging in telecommunications or in consumer applications [3]. The state of the art of these technologies is presented by the description of three aspects of these integrated circuits : the power circuits, the millimeter-wave circuits and the multifunction chips.

2. POWER AMPLIFIERS

According to the frequency, different kinds of power technologies are available [4]:

MESFET technologies with 0.7 μm or 0.5 μm gatelengths give power circuits at 0.9 or 1.8 GHz for cordless and cellular telecommunications or at 5-6 or 10 or 6-18 GHz for phased array radars. With these well stabilized technologies, the research efforts concern the design of the circuits. It consists in increasing the power added efficiency (PAE) by presenting short or open circuits on 2nd or 3rd harmonics. For instance, when working in class F, it is possible to increase the PAE of an X-band power amplifier of 5% [6].

During last years, a big effort has been done in Europe on *HBT technologies* [9][10][11]. Power HBTs for digital mobile communication systems were developed by CNET and Siemens. As for Thomson-CSF, GEC-Marconi, Defense Research Agency, DASA and Daimler-Benz Research, they developed also high efficiency power HBTs but for X band applications. A special cooperation is currently developed between Thomson-CSF and Daimler-Benz to get fully compatible HBT technologies. This gives a GaInP/GaAs technology with a carbon doped base. A basic cell for the power device was optimized with the help of electrical and thermal modelling. It gives a transistor having a cutoff frequency of 60 GHz and a maximum frequency of 90-110 GHz.

Typical results of power amplifiers are shown in table 2.

When the frequency increases, another important technology is based on P-HEMT. Some typical circuits obtained with a P-HEMT power technology with a gate length of 0.25 μm or 0.16 μm are also presented in table 2.

F GHz	Pout dBm	Ga dB	stage numb.	Technology	PAE %	Institution
1.7	32	50	3	MESFET	38	Siemens [5]
4.8	30	12	2	MESFET	-	Alcatel-Telettra [7]
5 - 6	38.2	29	3	MESFET	30	TH-CSF [8]
9 - 11	34	10	2	MESFET	30	Dassault + Siemens
9 - 11	36	17	2	MESFET	38	TH-CSF [8]
10	31	15	2	HBT	34	Daimler-Benz and
9	36	6.5	1	HBT	43	TH-CSF [12][28]
18 - 23	28	17	2	P-HEMT	20	TH-CSF [13]
35 - 39	23	15	2	P-HEMT	-	"
62 - 70	18	11	2	P-HEMT	-	"
71 - 77	16	2.5	1	P-HEMT	-	"
70 - 80	13	9.5	2	P-HEMT	-	F-IAF [29]

Table 2 : Examples of power amplifiers

3. MILLIMETER WAVE CIRCUITS

Within the power circuit shown in the preceding section, some of them work in millimeter wave.

Above 20 GHz, several tens of circuits have been realized in different technologies. At these frequencies, three European Community programmes pushed the research. In the frame of AIMS programme, technologies and circuits were developed to work between 20 and 40 GHz while in the frame of CLASSIC programme for the technology and MBS for the study of a mobile broadband system, circuits between 40 and 80 GHz were developed. The main technologies used at these frequencies are:

- a well stabilized MESFET technology with a $0.5 \mu\text{m}$ gate length which gives circuits like mixers, doublers, switches, oscillators and buffer amplifiers [14],
- a $0.25 \mu\text{m}$ and $0.15 \mu\text{m}$ gate length technology developed at Daimler-Benz, at Thomson-CSF, at GMMT, for MMICs and at IEMN for discrete components,

• a double heterostructure P-HFET technology for power circuits with a $0.25 \mu\text{m}$ gatelength which was introduced in the preceding section,

• the same type of technology was also developed by F-IAF with a $0.16 \mu\text{m}$ gatelength,

• the HBT technology presented in the last section for X band power amplifiers can also be used for oscillators thanks to its good $1/F$ performance and also because of the availability of a good vertical varactor diode between base and collector electrodes [11][17].

Table 3 shows some examples of distributed and low noise amplifiers realized with these technologies. At these frequencies, coplanar technologies present some advantages and some of these circuits are realized in coplanar lines [23].

Some research centres like IEMN, F-IAF and IMEC work on InP based (lattice matched or PM) technologies. A typical result is shown on table 3.

F GHz	Gain db	stage numb.	NF dB	Technology	Institution
2 - 52	9	matrix	7	$0.25 \mu\text{m}$ HFET	F-IAF + Alcatel SEL [21]
2 - 28	13	distributed.	6	$0.25 \mu\text{m}$ HFET	Dassault Electronique + TH-CSF
5 - 80	9	cascade	3.5	$0.25 \mu\text{m}$ HFET	F-IAF [16]
28.6 - 38	13	2	3.5	$0.25 \mu\text{m}$ P-HFET	Thom-EMI + GMMT [22]
24 - 30	16	3	4	$0.2 \mu\text{m}$ P-HFET	Alcatel + PML [19]
28.5	13.5	2	3.2	$0.25 \mu\text{m}$ HFET	Daimler-Benz
34.7	18	3	3	$0.25 \mu\text{m}$ HFET	+ TH-CSF [15]
62 - 69	10	3	-	$0.15 \mu\text{m}$ HFET	TH-CSF
5 - 50	11.5	dual-gate	-	$0.25 \mu\text{m}$ HFET InP	IMEC + ESAT/TELEMIC [32]

Table 3: Examples of distributed and low noise amplifiers

Table 4 shows some examples of oscillators.

F GHz	Tuning range GHz	Phase noise at 100kHz dBc/Hz	Techno.	Institution
30.9	1	-75	HBT	Daimler-Benz + DASA [20]
34.5	1.3	-75	MESFET	TH-CSF [15]
28.5	6.5	-75	HBT	TH-CSF [11]

Table 4 : Examples of VCOs

4. MULTIFUNCTION CHIPS

Another important aspect of the evolution of the MMIC activity is the appearance of multifunction chips. This type of integrated circuits are worth noting because they result from the association of technological progress and of design effort.

Moreover, they have some very important characteristics:

- As all the connections are made on the chip itself, they allow the realization of complex circuits which could not be realized with a hybrid technology.

- With a mature technology, they bring an important reduction in cost.

As frequency is increasing, the interconnection of several chips brings uncertainties which are avoided with a single chip. Moreover, these interconnections can be taken into account in the simulation of the circuits. This fact is very important for millimeter wave circuits.

- The multifunction technique also improves the reliability of the final circuit.

- The design of multifunction circuits implies the development of circuit cells which are introduced in a library. The performances of these blocks can be changed by the variation of some parameters.

Some examples of such circuits are given in table 5 which shows several modulators or demodulators, for telecommunications from 1 to 65 GHz.

Another example is given by a 56.8 GHz phase lock loop chip realized by Thomson-CSF [31]. On this chip, several elementary circuits are found: a doubler oscillator, a band-pass filter, a power divider and an amplifier.

5. CONCLUSION

Some samples of recent results obtained with different MMIC technologies available in Europe have been shown. These results implies a good cooperation between technological and designers teams.

A common trend can be observed for all the categories of circuits which have been presented: a constant increasing in frequency. All the examples showed that the MMIC technology is now ready for the many applications which are emerging, specially at millimeter wave frequencies

Circuit	F GHz	Technology	Dimensions (mm)	Institution
Modulator 4, 16 QAM	1 - 2.8	MESFET 0.7 μ m	1.8 x 2.2	PML [24]
Modulator/Demod /LNA/Medium power amp./4 PSK	1.25 - 3	MESFET 0.5 μ m	2.4 x 5	Alcatel Standard Electrica/GMMT [30]
Vector modul.	5 - 5.6	MESFET 0.7 μ m	1.9 x 2.9	PML + TNO [25]
Modulator/ demodulator 4, 16, 64 QAM	5.9 - 6.8	MESFET 0.5 μ m	2.7 x 3.65	TH-CSF [26]
Modulator 4, 16, 64 QAM	35 - 65	HFET 0.2 μ m	2 x 4	ANT + F-IAF [27]

Table 5 : Examples of modulators / demodulators

BIBLIOGRAPHY

- (1) A. MBaye, G. Gatti: "CEC and ESA activities in the area of GaAs and related compounds", GAAS'92, Noordwijk, april 1992.
- (2) J. Turner: "Gallium arsenide in Europe: a quiet revolution", GAAS'94, pp. 15-16.
- (3) S. Meyer: "Microwave and millimeter-wave technology for consumer applications in Europe", APMC94
- (4) Y. Crosnier: "Power FETs families, capabilities and limitations from 1 to 100 GHz", European Microwave Conference, Cannes, 1994, pp. 88-101
- (5) K.J. Schöpf, E. Pettenpaul, "Recent advances in MESFET MMIC's", GAAS'94, Turino, Apr. 94, pp. 93-96.
- (6) H. BROUZES, J.P. VIAUD, J. OBREGON, Y. MANCUSO, L. REMIRO, C. LABILLE, "Amplificateur MMIC classe F en bande X délivrant 2,5 w avec 30 % de rendement", Journées Nationales Microondes, PARIS, Avril 1995, 3 D9.
- (7) E.M. Bastida et al: "High efficiency and power ion implanted MESFET devices", European Microwave Conference, Cannes, sept. 1994, pp. 1137-1142.
- (8) L. Poteau et al: "Ku-band modular MMICs for up to 5W power blocks for VSAT applications", GAAS'94, pp. 221-224.
- (9) France Télécom CNET, Information sheet CNET-RGA-93/8300, 1993.
- (10) H. Leier, "GaAs HBT power amplifiers: A review of european activities", Workshop on recent advances in microwave high power technology, EuMC, Cannes, sept. 1994, pp. 121-126.
- (11) S. Delage et al, "Le transistor bipolaire à hétérojonction GaInP/GaAs. Technologie et performances hyperfréquences", Revue Technique Thomson-CSF, vol 26, n° 2, juin 1994.
- (12) S.L. Delage et al: "Power GaInP/GaAs HBT MMICs", European Microwave Conference, Cannes, 1994, pp. 1143-1148.
- (13) P. Bourne-Yanoba et al: "Millimeter-wave power amplifiers from 18 GHz to 70 GHz", INMMC'94, 3rd International Workshop on integrated Non-linear Microwave and Millimeter-wave Circuits, oct. 94.
- (14) J.-M. Dieudonne et al: "GaAs MESFET technology based MMICs for Millimetre-wave front-ends", European Microwave Conference, Cannes, pp. 534-541, 1994.
- (15) P. Briere: "Recent european developments programmes for volume applications of millimeter waves IC's", European Microwave Conf., Cannes, 1994, pp. 144-155.
- (16) J. Braunstein et al: "Very broad band TWAs to 80 GHz on GaAs substrate", European Microwave Conference, Madrid, sept. 1993, pp. 372-373.
- (17) H. Blanck et al: "fully monolithic Ku and Ka band GaInP/GaAs HBT wideband VCOs", 1994 MTT Symposium Digest, pp. 127-130.
- (18) H. Buret, et al: "MMICs for 30/20 GHz space equipments", European Microwave Conference, Cannes, sept. 1994, pp. 1967-1972.
- (19) U. Gütlich et al: "Ka band monolithic VCOs for low noise applications using GaInP/GaAs HBTs", 1994 MTT Symposium Digest, pp. 131-134.
- (20) R. Heiling et al: "A monolithic 2-52 GHz HEMT matrix distributed amplifier in coplanar waveguide technology", 1994 MTT Symposium Digest, pp. 459-462.
- (21) R. Lang et al: "Modelling and characterisation of a Ka band monolithic P-HEMT low noise feedback amplifier" GAAS'94, pp. 327-330.
- (22) I. Wolff, "Design rules and realization of coplanar circuits for communication applications", European Microwave Conference, Madrid, sept. 1993, pp. 36-41.
- (23) R. Pyndiah et al: "GaAs monolithic direct linear (1-2.8 GHz) QPSK modulator", European Microwave Conference, London, sept. 1988, pp. 597-602.
- (24) T.C.B. Tieman et al: "A simple chip C band linear MMIC vector modulator on GaAs developed for an airborne active phased-array synthetic aperture radar", GAAS'94, Turino, Apr. 1994, pp. 337-239.
- (25) I. Telliez et al: "A compact, monolithic microwave demodulator-modulator for 64-QAM digital radio links", IEEE Transactions on Microwave Theory and Techniques, vol. 39, n°12, pp. 1947-1954, 1991.
- (26) W. Ehrlinger et al: "wide band monolithic modulator InGaAs/AlGaAs technology", European Microwave Conference, Cannes, sept. 1994, pp. 560-566.
- (27) S.L. DELAGE, H. BLANCK, S. CASSETTE, D. FLORIOT, E. CHARTIER and M.A. diFORTE-POISSON, "GaInP/GaAs HBT MMIC Technology for X-band power applications", Workshop "MMIC Technology and characterization", MIOP 1995.
- (28) M. SCHLECHTWEIG, W. REINERT, A. BANGERT, J. BRAUNSTEIN, P.-J. TASKER, R. BOSH, W.H. HAYDL, W. BRONNER, A. HÜLSMANN, K. KÖHLER, J. SEIBEL, R. YU and M. RODWELL, "High performance MMICs in coplanar waveguide technology for commercial V-band and W-band applications", IEEE 1994 Microwave and Millimeter-wave Monolithic Circuits Symposium, pp. 81-84.
- (29) A. BOVEDA, F. ORTIGOSO, "GaAs Monolithic Single-chip transceiver", IEEE 1995 Microwave and Millimeter-wave Monolithic Circuits Symposium", pp. 31-34.
- (30) I. TELLIEZ, M. CAMIADE, P. SAVARY, P. BOURNE-YAONABA, "Millimeter wave phase locked oscillator for mobile communication systems", IEEE 1995 Microwave and Millimeter-wave Monolithic Circuits Symposium", pp. 49-52.
- (31) Y. BAEYENS, D. SCHREURS, B. NAUWELAERS, M. VAN HOVE, W. DE RAEDT, M. VAN ROSSUM, "Ultra-broad band distributed variable gain amplifiers using Lattice Matched and Pseudomorphic InP cascode HEMTs", MIOP 1995, pp. 345-349.

RECENT MMIC DEVELOPMENTS IN AUSTRALIA

R A Batchelor

CSIRO Division of Radiophysics
PO Box 76, Epping, NSW, 2121, Australia
rbatchel@rp.csiro.au

ABSTRACT

The introduction of new microwave-based technologies such as personal communications systems (PCS), wireless local area networks (WLANs) and the provision to the home and office of broadband services, is focusing the attention of the Australian communications industry on gallium arsenide (GaAs)-based monolithic microwave integrated circuits (MMICs). In order to provide a lower risk entry point into MMIC-based applications, the CSIRO has established a design and fabrication capability at its Division of Radiophysics. This paper will discuss millimetre-wave MMICs developed using this capability.

1. INTRODUCTION

A significant Australian GaAs MMIC program is being carried out at the CSIRO Division of Radiophysics. MMIC design, fabrication and testing services are now available to both Australian and overseas companies for prototype development, and, in the near future, limited production capability will be offered. In addition to this, the Division has established relationships with several US foundries to provide a convenient path to large-scale production.

The CSIRO provides three MMIC processes, 0.25 micron gate, pseudomorphic, high-electron-mobility transistor (PHEMT) providing amplifier performance to ~70 GHz, planar Schottky diode (mixer and varactor) suitable for circuits operating to beyond 100 GHz, and combined PHEMT/Schottky diode. Principal emphasis thus far has been on low-noise, high-frequency applications and establishing accurate models to facilitate the objective of one-pass design.

The paper will describe circuits that have been designed and fabricated using these processes, together with their packaging for application to millimetre-wave

PCS systems and wireless distribution of wideband customer services.

2. MMIC FABRICATION

The principal process offered by the CSIRO GaAs MMIC fabrication facility, the PHEMT process, used 0.25 micron, mushroom-cross-section gates and offers performance to ~70 GHz. An improved process under development will reduce the gate-length to <0.15 micron enabling performance to be extended beyond 100 GHz. Two-inch wafers with epitaxial layers grown in the Division's molecular-beam epitaxy (MBE) system are used. The process incorporates the usual metal-insulator-metal (MIM) capacitors and thin-film resistors, together with air-bridge cross-overs. Dry recess-etching is used for the gate process. Wafers are thinned to either 50 or 100 microns and through-substrate vias are used to provide grounding. This process has been used to fabricate amplifiers operating to ~70 GHz. The example shown in figure 1, a 2-stage amplifier, covers the frequency range of 50 to 67 GHz with ~10 dB gain, as shown in Figure 2.

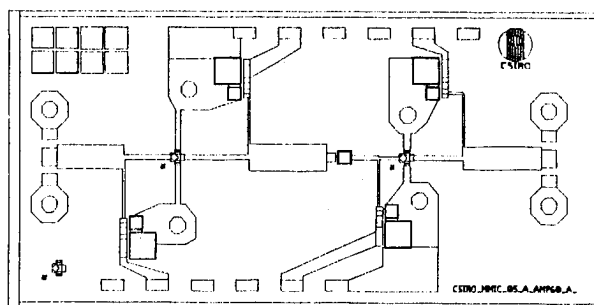


Figure 1 60 GHz 2-stage amplifier

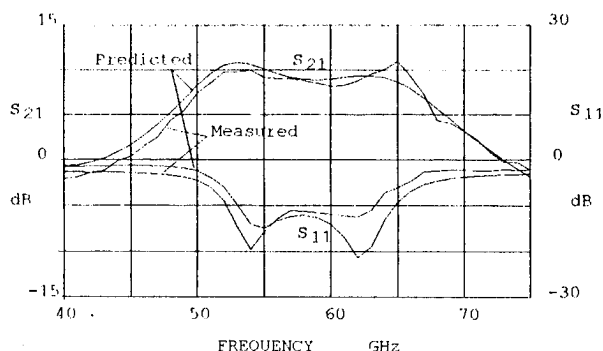


Figure 2 S_{11} and S_{21} measured and predicted for a 2-stage 60 GHz MMIC amplifier.

In addition to the development of shorter length gates (<0.15 micron), research is being done into epitaxial material structures for increased linearity and power handling. Results of this work to date are encouraging with some materials having saturation currents of ~1 A/mm.

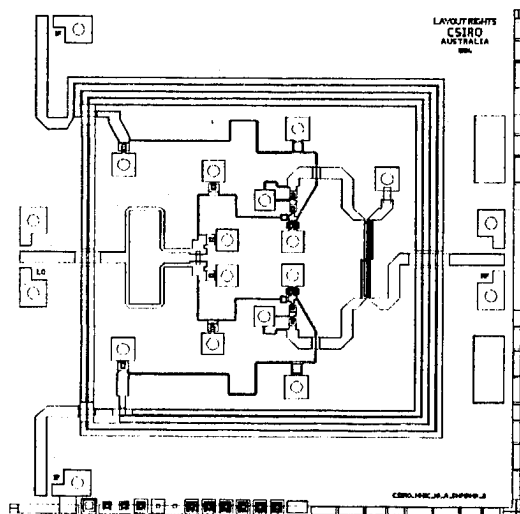


Figure 3 60 GHz image-reject mixer

The Schottky diode process [1] provides both varactor and mixer diodes. This process has been used to produce mixers [1,2] and frequency multipliers operating to 100 GHz and beyond. Figure 3 shows an example of a 60 GHz image-reject mixer. Its performance is illustrated in Figure 4 showing conversion loss of ~10 dB and image rejection of ~20 dB. The mixer is laid out inside a spiral 2.5 GHz IF

coupler providing a compact chip of 3 x 3 mm. Upper or lower sideband operation can be selected by connecting to the appropriate terminal of the spiral coupler.

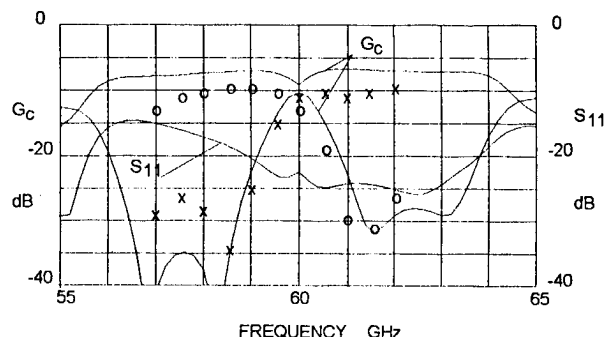


Figure 4 Conversion gain and S_{11} (RF return loss) for a 60 GHz mixer. Circles show measured performance for the lower sideband, crosses show upper sideband performance.

The combined PHEMT/Schottky diode process has been used for voltage-controlled oscillator (VCO) circuits. A 12.5 GHz VCO gave a tuning range of 11.5 to 13 GHz and an output power of +14 dBm. The phase-noise for this circuit was -95 dBc/Hz at 100 kHz. Higher frequency oscillators at 20 and 30 GHz, with a tuning ranges of ~2 GHz and output powers of ~14 dBm, have recently been fabricated.

Other MMICs designed and fabricated in the CSIRO's GaAs facility include:

- 1-25 GHz distributed amplifiers
- 6-20 GHz amplifiers
- 25-50 GHz amplifiers
- 35-45 GHz image-reject mixers.

4. DESIGNS FOR EXTERNAL FOUNDRIES

The Radiophysics Division has established relationships with external foundries to enable it to provide a design service for commercial customers that can lead to large-scale production. One such relationship, with the TRW foundry in the USA, is being used to produce a chip set for 38 GHz transceivers for wireless backhaul applications in PCS systems. In addition to low-noise amplifiers (LNAs), medium-power amplifiers and mixers (both up and

down converters) for this program, other designs fabricated at TRW include:

- 38 GHz receiver (LNA plus mixer) [2]
- 60 GHz amplifiers
- 60 GHz mixers
- 1-20 and 20-45 GHz switches.

All design work and prototype testing for this program has been carried out at the Radiophysics Division.

5. DEVICE TESTING

MMIC testing and active device characterisation is carried out in the Division's MMIC test laboratories. The dc laboratory includes facilities for evaluating materials, using step-and-etch Hall effect and photo-reflectance systems. The microwave test laboratory includes four microwave probe stations (two with auto-stepping capability) and two HP8510C 50 GHz automatic network analysers, one of which is equipped with waveguide extensions enabling on-wafer probing from 40 MHz to 110 GHz for device characterisation and MMIC testing, as well as measurement of waveguide and coaxial packaged devices.

6. DEVICE MODELLING

A significant effort has gone into device measurement and the refinement of active and passive device models with a view to accurate performance prediction and, ultimately, one-pass design. The measured and predicted linear responses for 60 and 40 GHz amplifiers shown in Figures 2 and 5 indicate the progress that has been made in this aspect of the work.

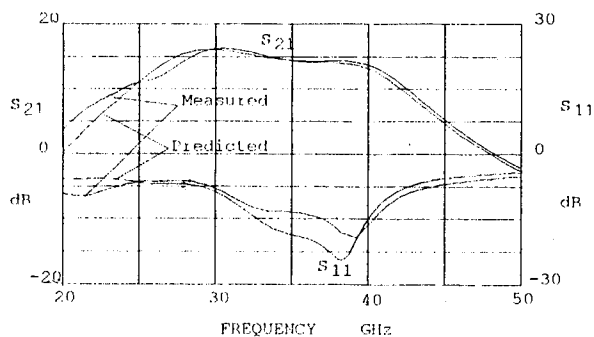


Figure 5 S_{11} and S_{21} measured and predicted for a 2-stage 40 GHz MMIC amplifier.

A physics-based, non-linear HEMT model has been developed in conjunction with Macquarie University, NSW, Australia [3,4]. This model has been coded into HP-EEsof Libra [5] to facilitate accurate non-linear MMIC design. Software tools have also been written to extract circuit elements from measured I-V characteristics and bias-dependent S-parameters for the Libra implementation of the Curtice non-linear FET model and the CSIRO non-linear HEMT model.

7. MMIC APPLICATIONS

The MMIC work at the CSIRO is part of a larger program of system design, and complements other work on antenna design, telecommunications and signal processing. Work in progress at the Division of Radiophysics includes designing MMIC-based transmitter and receiver elements for 38 GHz wireless backhaul applications in personal communications systems, investigating systems for delivery to the home and office of wideband customer services, and developing a 60 GHz WLAN system which is capable of 100 M bit s⁻¹ operation [6]. Each of these tasks includes packaging MMICs, together with designing circuits with higher levels of integration.

Packaging efforts have included optimising transitions between waveguide and other transmission media using the HP HFSS (high-frequency structure simulator) software, miniaturising packages, and developing planar antennas for integration with MMIC transceiver elements.

8. CONCLUSION

While the scale of MMIC design and fabrication in Australia is small compared to the work being carried out in the major GaAs foundries of the world, the levels of quality and innovation are high. Devices and circuits are produced with high performance at millimetre wavelengths, and designs performing at, or close to, specification are produced with a single design cycle. The prototyping services being offered are increasing the use of MMICs in Australian products.

9. ACKNOWLEDGMENTS

The work described in this paper is the joint effort of three groups within the CSIRO Division of Radiophysics: MMIC Design and Test, Radio Systems, and the GaAs IC Prototyping Facility.

10. REFERENCES

- [1] John W. Archer, Robert A. Batchelor, and C. J. Smith, "Low-Parasitic, Planar Schottky Diodes for Millimeter-Wave Circuits", *IEEE Trans. Microwave Theory Tech.*, vol. MTT-38, no. 1, pp. 15-22, January 1990.
- [2] John W. Archer, Simon J. Mahon and Oya Sevimli, "Fully Monolithic Image-Reject Mixers for 38 GHz Wireless Telecommunication Links", *Microwave and Opt. Tech. Lett.*, August 20 1995 in press.
- [3] Simon J. Mahon, David J. Skellern, and Frederick Green, "A Technique for Modelling S-Parameters for HEMT Structures as a Function of Gate Bias", *IEEE Trans. Microwave Theory Tech.*, vol. MTT-40, no. 7, pp. 1430-1440, July 1992.
- [4] Simon J. Mahon and David J. Skellern, "Modelling Drain and Gate Dependence of HEMT 1-50 GHz, Small-Signal S-Parameters, and D.C. Drain Current", *IEEE Trans. Microwave Theory Tech.*, vol. MTT-43, no. 1, pp. 213-216, January 1995.
- [5] Simon J. Mahon and David J. Skellern, "HEMT Model Enhancements for DC I-V and 1-50 GHz S-Parameter Simulation, and Implementation Notes for Circuit Simulators", *Proc 1993 International Semiconductor Device Research Symposium*, Charlottesville VA, pp 803-810, December 1-3 1993.
- [6] Robert A. Batchelor, John W. Archer, Trevor S. Bird, Stephen Giugni, John S. Kot, Nasiha Nikolic, Diet I. Ostry, Terence M. Percival and Alan C. Young, "Australian Activities in Microwave Links for Wireless LANs", *Microwave Theory Tech. Dig.*, Atlanta, GA, pp. 677-680, 1993.

MMIC APPLICATIONS TO SATELLITE COMMUNICATIONS

Yi-Chi Shih, Mike Delaney, Erica Kato and Russ Isobe

Hughes Space & Communications Company
P.O.Box 92919, Los Angeles, CA 90009
Phone: (310)364-5116; Fax: (310)416-5050
email: yshih@ccgate.hac.com

Abstract

This paper summarizes the general requirements of the monolithic microwave integrated circuit (MMIC) for satellite communication applications. It also describes a space qualification procedure being implemented on a 0.25 μm MESFET MMIC process as well as a 0.15 μm InP HEMT process and a few examples of the MMIC's developed using these processes.

MMIC's for satellite communications in order of their importance are: (1) reliability, (2) performance, (3) power consumption, and (4) size and weight.

In this paper, we first summarize a space qualification procedure that we developed for the design and manufacture of MMIC's for satellite communications. Then, we will present examples of MMIC's that we developed for microwave and millimeter-wave applications.

1. Introduction

Communication satellites rely heavily on microwave and millimeter-wave carriers for signal transmission. Therefore, microwave and millimeter-wave components play an important role in communication satellites. Because of the unique environment in space, design requirements of microwave components are also unique. The expensive operation of transporting the satellite to space demands that payloads be small and light. The limited amount of energy from solar cells demands efficient operation of the electronics while radiating sufficient microwave power for signal transmission. The 10 to 15 years of service requirement without the possibility of field repair demands that every component be extremely reliable.

The reliability must not be compromised for any other performance requirement. By employing MMIC's as the functional building blocks, the size and weight of the electronic payload will be dictated by the other electronic circuits and their packages. Therefore, reducing the size of the MMIC's themselves is not a key issue. Higher functional levels of integration are desirable to reduce the size/weight of the MMIC circuit packaging. In addition, having fewer components and wirebonds in the manufacturing process will also improve the system reliability. In summary, the design parameters of the

2. Space Qualification Procedure

Hughes Space and Communications is qualifying for space a 0.25 μm MESFET MMIC process for communication payload applications. Over 23 individual MMIC's have been designed, fabricated, and tested for engineering model (EM) development. These MMIC's are now in flight production. The qualification plan for these MMIC's is based on a tailored version of MIL-I-38535B which has been adopted in part due to specific program requirements and the timing of the Hughes GaAs Operation (GAO) foundry QML certification. The qualification process is broken into generic process qualification and specific MMIC product qualification. Additionally, there are specific lot acceptance test requirements. This procedure can be applied to any process or foundry.

Generic process qualification includes step stress and biased life-test on technology characterization vehicles (TCV) and standard evaluation circuits (SEC). The TCV's include standard FET's, Ohmic contact TLM's, electromigration test patterns, etc. For the process SEC, an X-band two stage LO driver circuit was chosen. The MMIC's for the communication payload can be divided functionally into five classes: low noise, driver, mixer, multiplier, and macrocell. DC and/or RF burnin and life tests are performed as part of a one time functional

qualification. Representative MMIC's from each functional class are chosen to qualify the entire functional class. Additional design validation tests are performed on all MMIC's to verify the reliability of all designs.

In MMIC product qualification, each MMIC product will be individually analyzed to determine the extent of the qualification testing. Product qualification addresses the required tests to demonstrate that the MMIC meets the performance requirements over the expected bias variations, temperature range, and life of the satellite. The accelerated product life-tests described here will demonstrate the acceptability of specific MMIC products for use in space applications. Successful completion of performance and reliability tests will indicate that the specific MMIC product is qualified for space applications. Within each functional class at least one MMIC product will receive more extensive testing. This will typically involve a two or three temperature accelerated life-test. The remainder of the MMICs will have more limited life-testing and will be qualified in part by similarity to the other MMIC products in its class.

The MMIC performance requirements are clearly documented. The MMIC FET DC performance requirements are defined by a MMIC general specification whereas the MMIC RF performance requirements are defined by the MMIC specification control drawing (SCD) for each product. Each MMIC product will have a full functional electrical test consisting of DC and RF performance measured over bias and temperature ranges. This test will ensure that the specific MMIC product design will meet performance over all bias and temperature extremes it is likely to see in operation. The nominal operating bias is defined in the individual MMIC product SCD. This test will vary the drain-source bias voltage (V_{ds}) and gate-source bias (V_{gs}) within five percent. DC and RF performance for each product must be met for these test conditions. The MMIC products will have DC and RF performance measured at three temperatures covering the nominal operating temperature and the upper and lower extremes.

Supplemental accelerated life-tests are performed on individual MMIC products because the SEC life-test described above in the MMIC generic process qualification does not cover all functional operating modes of the MMIC's to be qualified by this plan. The MMIC's to be qualified fall into a number of functional classes differentiated by the operating mode of the FET's. These functional classes include small signal or low noise amplifiers, large signal power devices, dual gate variable gain amplifier, FET mixers, complex

macrocells, voltage controlled oscillators (VCO), FET multipliers, and phase and amplitude modulators.

The DC or RF accelerated life-test and electrical stress for the MMIC product is selected based upon the functionality of each product. All tests include DC and RF characterization. The two temperature life-test will continue until at least 50% of the devices fail at least one parameter. If time is available the devices will be taken well beyond 50% failure. The log normal distribution of percent failures versus failure time will be plotted for each parameter and temperature. The median failure point for each parameter will then be plotted versus temperature as an Arrhenius plot to determine MTTF at mean mission baseplate temperature of 65°C and the activation energy for the degradation mechanism.

Lot Acceptance Test (LAT) is the steady-state life-test which is performed on a minimum of 5 each of the MMIC's utilizing the MMIC product die from each product wafer lot. Test conditions will be at a case temperature of 125°C for 1000 hours with bias as specified in the detailed drawing. Lifetest pass/fail criteria are clearly defined in the detailed drawing.

3. Ku-band MMIC Examples

Using the 0.25 μm MESFET process described above, we developed a family of MMIC microcells and macrocells for Ku-band communication satellite applications. Figure 1a shows a voltage-controlled attenuator (VCA) which consists of two identical shunt FET's sandwiched between two Lange couplers. At zero bias, the drain-source resistance is low (<5 Ohms) to reflect most of the power and set the maximum insertion loss. As the negative bias increases in magnitude, the insertion loss decreases because the FET resistance increases and allows more power through the 50 Ω line. The balanced configuration using Lange couplers directs the reflected power into a 50 Ω load to achieve low return loss (>20 dB). Since the insertion loss is mainly due to the reflected power, only a small amount of power is dissipated in the FET. This results in a low voltage swing across the FET junction and a high IP3 of the attenuator. For the bandwidth of 10.7 to 12.7 GHz, the VCA has about 1 dB insertion loss, 10 dB dynamic range, 17 dB return loss, and greater than 15 dBm of IP3 over the dynamic range.

Combining the VCA circuit with single-stage gain block(s) constitutes the variable gain attenuators (VGA) as shown in Figures 1b-1d. The VGA circuits have 10-dB of dynamic range per VCA and 6-dB of gain per gain

block. Figures 1e and 1f are examples of Ku-band macrocells. Figure 1e is a 17-GHz downconverter consisting of an RF amplifier, LO amplifier, and a passive FET mixer. The IF signal is at 1 GHz. Figure 1f is a singly-balanced up-converter taking a 2 Hz signal through a buffer amplifier and an active splitter to a pair of passive FET mixers. The LO drive is amplified by a two-stage amplifier.

4. V-band MMIC Examples

Future satellite payloads have a need for size and weight reductions in the EHF payload without sacrificing the system performance. InP HEMT's can play a major role in meeting those needs. The InP HEMT structure has produced the lowest device noise figure performance at 60 GHz (about 1 dB) with 9 dB of associated gain and the highest cutoff frequency (> 300 GHz). This section summarizes the circuit design and measured results of four MMIC chips shown in Figure 2.

The V-band LNA design uses a 100 μm device, 4×25 μm , biased for low noise ($V_{ds}=+1.0\text{V}$ at 14 mA) in the first stage and a 50 μm device biased for high gain ($V_{ds}=+1.5\text{V}$ at 10 mA) in the second stage. The 100 μm device was chosen to minimize the matching network required for the best noise match and return loss at V-band. The device were stabilized with a double tuned quarter-wavelength structure on the gate bias for optimum stability. Chip size is 2×2.5 mm^2 and consumes 29 mW of power (Figure 2a). The measured results show a noise figure between 2.2 and 2.4 dB with an associated gain of 14.7 to 16.7 dB from 58 to 62 GHz.

The mixer design uses a single-ended, passive HEMT as the nonlinear element to yield a small mixer with a low LO drive. The drain is biased at zero volts and the mixing function is achieved by creating a linear, time varying channel resistance produced by the LO signal driving the gate. This linear resistance minimizes intermodulation products. The design uses a single 100 μm device. An LO signal of +4 dBm is sufficient to drive the gate which is biased near pinch-off. The drain is designed with a bandpass diplexer network which receives the RF input signal (58 to 64 GHz) through one port, mixes with the LO frequency (48 to 58 GHz), and outputs the IF frequency (6 to 10 GHz) through the second port. The chip size is 2×3 mm^2 (Figure 2b) and consumes no power. The measured result shows a conversion loss from 8 to 10 dB for the IF frequency from 4.5 to 10 GHz with $V_{ds} = 0\text{V}$ and $V_{gs} = -0.4\text{V}$. The 2IF spur is at -32 dBc.

The three-stage LO amplifier design uses a 50 μm device in the first stage and a 150 μm device in the second and third stages. All stages are biased for high gain with $V_{ds}=+1.5\text{V}$ at 10 mA for the 50 μm device and 30 mA for each of the 150 μm devices. The chip size is 2×3 mm^2 and consumes 105 mW of power (Figure 2c). Measurement at 55 GHz shows 21.7 dB of linear gain and +9.65 dBm of output power at 1 dB gain compression.

We also developed a V-band downconverter macrocell by combining the LNA and mixer building blocks with a 50 Ohm line (Figure 2d). The measured result shows 7 dB of gain and 3 dB noise figure for RF signals between 61 to 62 GHz.

5. Conclusion

In this paper, we have summarized the general requirements of the MMIC's for satellite communications. We have also described the space qualification procedure being implemented on a 0.25 μm GaAs MESFET process as well as a 0.15 μm InP HEMT process. A few examples of the MMIC's that were developed using these processes are also given.

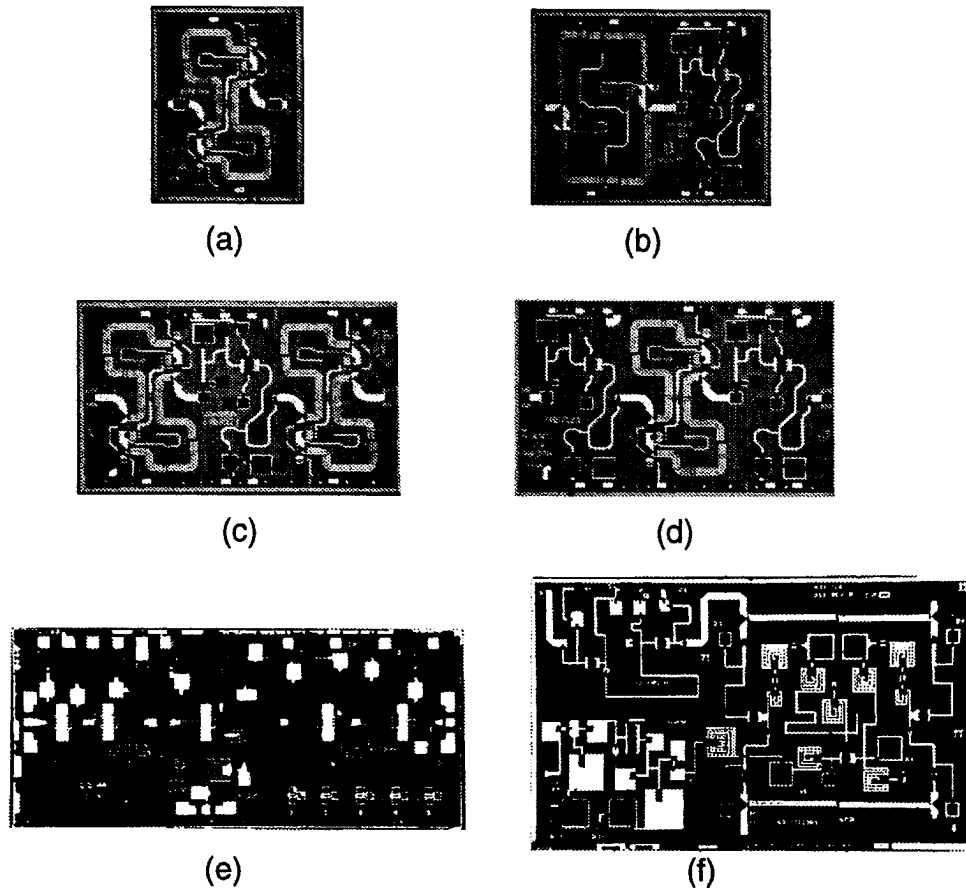


Figure 1. Ku-band MMICs, (a) voltage-controlled attenuator, (b,c,d) variable gain amplifiers, (e) downconverter, and (f) upconverter.

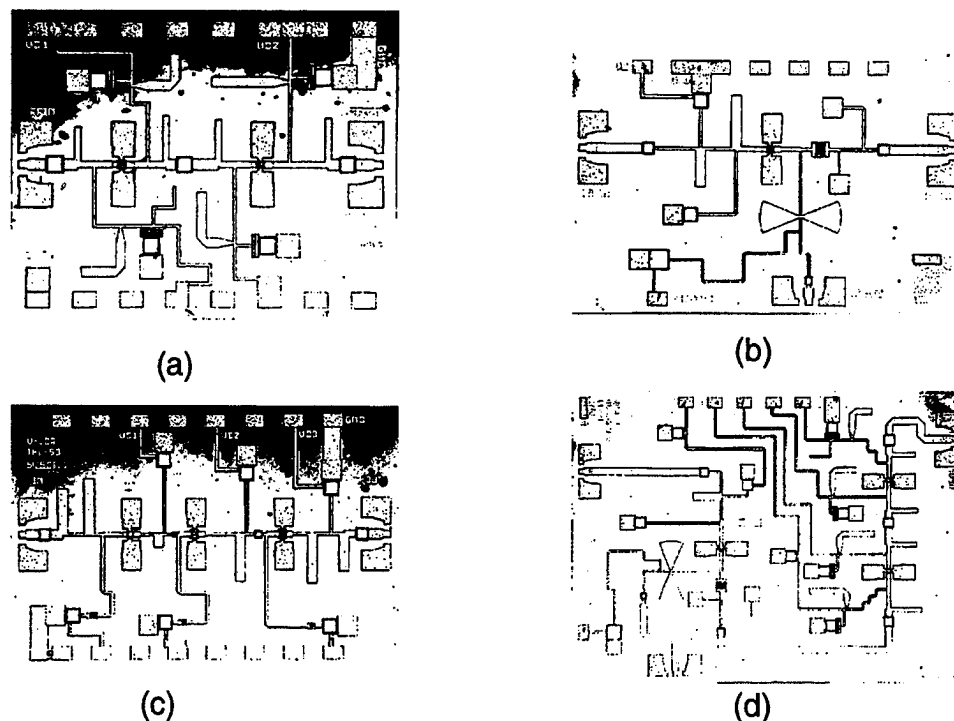


Figure 2. V-band MMICs: (a) Two-stage LNA, (b) mixer, (c) LO amplifier, and (d) downconverter macrocell.

MMIC CHARACTERIZATION USING ELECTRO-OPTIC FIELD MAPPING

D. Jäger and G. David

FG Optoelektronik, Sonderforschungsbereich 254
Gerhard-Mercator-Universität Duisburg
Kommandantenstr. 60, D-47057 Duisburg, Germany
Phone: + 49-203-379-2340
Fax: + 49-203-379-3400
email: jaeger@optorisc.uni-duisburg.de

(INVITED)

ABSTRACT

It has been demonstrated recently that the technique of direct electro-optic probing can successfully be applied to study two-dimensional electric field distributions in MMICs. As a result, each MMIC component can be characterized by on-wafer and in-circuit measurements up to millimeter wave frequencies. In this paper, experimental results performed on a traveling-wave amplifier are presented as an example. Furtheron, different MMIC components are tested in detail and a quantitative comparison with theoretical results is carried out.

1. INTRODUCTION

Rapid progress has recently been made in the simulation, design and processing of monolithic microwave integrated circuits (MMICs) on III-V semiconductors. However, the high-frequency performance test is usually made by conventional network analysis at the input and output ports which only allows an integrated overview of the

electrical behavior of the whole structure. On the other hand, the direct electro-optic measurement technique [1] has been shown to provide a circuit-internal and contactless test with high spatial and frequency or temporal resolution by two-dimensional field mapping of the device under test (DUT) [2]. In this paper, an overview is given on recent results performed on a traveling-wave amplifier (TWA) and on different MMIC components. In particular, the two-dimensional field distributions on the drain transmission line of a three stage amplifier and inside a high-speed MESFET and interdigitated capacitor are presented and discussed. Additionally, the properties of different coplanar waveguide (CPW) modes are studied in detail. Moreover, the paper summarizes preliminary steps towards quantitative comparisons with theoretical results.

2. EXPERIMENTAL SETUP

The fundamental experimental setup (Fig.1) consists of a polarized picosecond Nd:YAG laser system. The optical pulses are focussed

onto the DUT from the backside, the reflected signal being analysed by a polarizer and a photodiode. The output electrical signal is a low-frequency replica of the

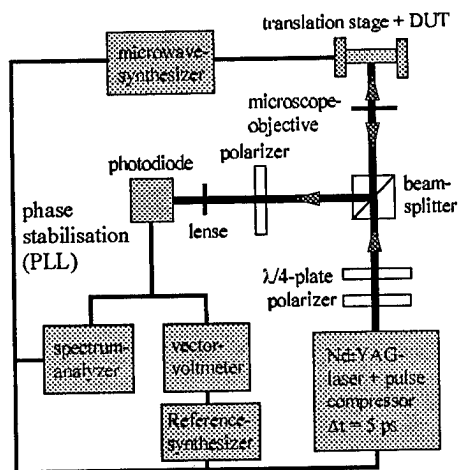


Fig.1 Experiment setup [2,3]

microwave signal at the point of observation, generated by harmonic mixing in the semiconductor as a result of the electro-optic Pockels effect [2,3].

3. EXPERIMENTAL RESULTS

In Fig.2 the 1-12 GHz traveling-wave

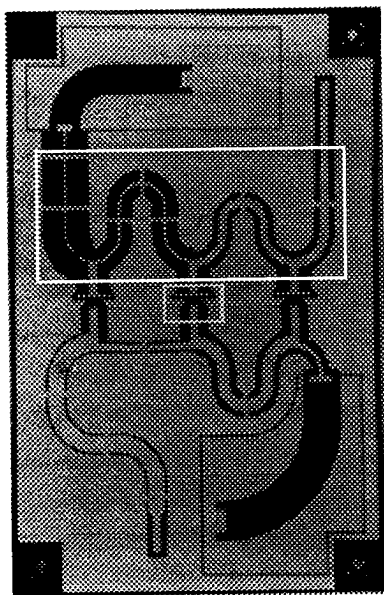


Fig.2 Microwave coplanar TWA [2]

amplifier under test is shown. It consists of transmission lines, terminating resistors, of three MESFETs, gate and drain air bridges, capacitors and dc bias ports. The field distribution inside the circuit has been studied in detail [2]. Two examples are shown in Figs.3 and 4. From the field distribution in Fig.3

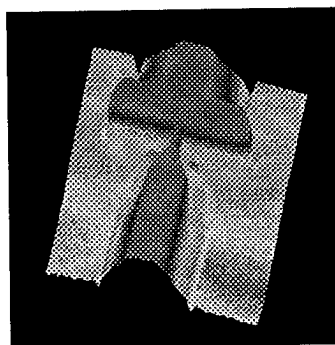


Fig.3 Two-dimensional field map of a MESFET of the TWA in Fig.2, frequency 1 GHz

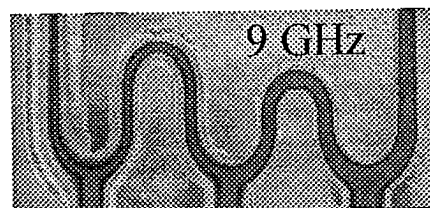


Fig.4 Two-dimensional field map of the drain transmission line of the TWA in Fig.2, frequency 9 GHz

the circuit-internal amplification can directly be determined. The measurement gives also an insight into the potential and phase distribution on the metallization structure at different frequencies. The traveling-wave characterization of the TWA can be obtained from the results in Fig.4, where field maxima and minima reveal the influence of standing wave effects inside the structure. Fig.5 is an example of the high spatial resolution which has been obtained using

conventional optical components. Clearly, the field distributions in a $2\mu\text{m}$ structure can

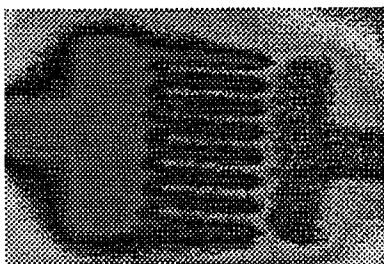


Fig.5 Two-dimensional field map of an interdigitated capacitor ($2\mu\text{m}$ structure)

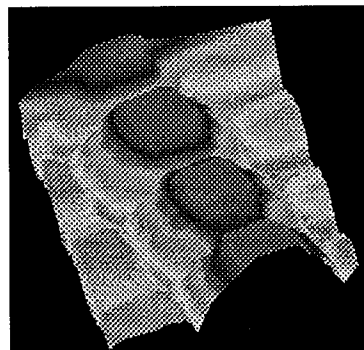
easily be detected.

In Fig. 6 the measured field distribution of different modes on a CPW are plotted [4]. The standing waves clearly show the characteristics of the even and odd mode and the so called microstrip mode [5] which give rise to novel coupling effects, especially at inhomogeneities such as bends, air bridges, etc..

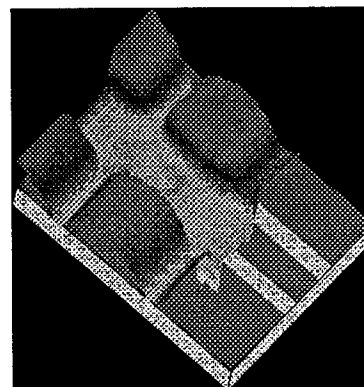
4. QUANTITATIVE COMPARISON WITH THEORY

Preliminary quantitative comparisons of experimental results with those of numerical simulations have been carried out. Particularly, microwave propagation properties on CPWs have been studied in detail including the phase and attenuation coefficient and the characteristic impedance [6]. In Ref. [7] the signal traces in a coplanar 18 - 21 GHz amplifier have been measured and compared with the predictions of a microwave CAD. From the experimental results, the dispersion properties can easily be determined [5]. Additionally, the two-

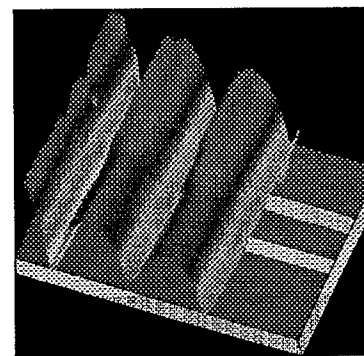
dimensional electro-optic probing has recently been combined with field theory based multimode wave amplitude extraction technique to study mode conversion phenomena in MMIC components [3].



(a)



(b)



(c)

Fig. 6 Two-dimensional field map of even (a), odd (b), and microstrip (c) mode on a CPW

5. SUMMARY AND CONCLUSIONS

It is shown by several examples that two-dimensional electro-optical field mapping can successfully be used to study and characterize MMICs. The method provides circuit-internal, contactless measurements of electrical signals at arbitrary nodes. In addition, a good agreement between experimental and theoretical result has been obtained and it is shown that the electro-optic field mapping is a unique method, not only for the measurement of mode conversion or wave propagation effects but also for a detailed and spatially resolved test of MMICs and relevant devices. This is especially important for frequencies close to and above 100 GHz.

6. ACKNOWLEDGEMENTS

This work has been financially supported by the Deutsche Forschungsgemeinschaft. The authors would like to thank the Fachgebiet Halbleitertechnik / Halbleitertechnologie, the Fachgebiet Allgemeine und Theoretische Elektrotechnik, both Universität Duisburg, and the IMST, Kamp Lintfort, for providing the traveling-wave amplifiers.

REFERENCES

- [1] B.H. Kolner and D.M. Bloom, "Electrooptic sampling in GaAs integrated circuits", IEEE J. Quantum Electron., vol. QE-22, (1986), 79-93.
- [2] G. David, S. Redlich, W. Martin, R.M. Bertenburg, S. Koßlowski, F.J. Tegude, and D. Jäger, "Two-dimensional direct electro-optic field mapping in a monolithic integrated GaAs amplifier", Proc. 23rd EuMC, September 6-9, 1993, Madrid, Spain, 497-499.
- [3] G. David, W. Schröder, D. Jäger, and I. Wolf, "2D electro-optic probing in combination with field theory based multimode wave amplitude extraction: A new approach to on-wafer measurement", 1995 IEEE MTT-S Int. Symposium, May 15-19, 1995, Orlando, USA.
- [4] G. David, P. Schmitz, S. Redlich, J. Buschke, R. Kremer, and D. Jäger, "Mode analysis of wave propagation on coplanar transmission lines using electro-optic field mapping", Proc. Asia-Pacific Microwave Conference, Tokyo, December 6-9, 1994, 149-152.
- [5] H. Shigesawa, M. Tsuji, and A.A. Oliner, "A new mode coupling effect on coplanar waveguide of finite width", 1990 IEEE MTT-S Digest, 1990, 1063-1066.
- [6] G. David, S. Redlich, W. von Wendorff, and D. Jäger, "Electro-optic probing of coplanar transmission lines and optoelectronic microwave devices up to 40 GHz", Proc. of the MIOP'93, May 25-27, Sindelfingen, 1993, 492-496.
- [7] G. David, A. Ising, Y. Kalayci, R. Tempel, I. Wolf, and D. Jäger, "Circuit-internal characterization of MMICs using two-dimensional electro-optic field mapping in combination with microwave CAD", Proc. 24th EuMC, September 5-8, 1994, Cannes, France, 1378-1383.

High Power Amplifiers for Mobile Communication Systems

Yasushi Itoh

Mitsubishi Electric Corporation
Electro-Optics & Microwave Systems Laboratory
5-1-1 Ofuna, Kamakura, Kanagawa, 247 Japan
Tel:+81-467-41-2544, Fax:+81-468-41-2519, E-mail:sei@eml.melco.co.jp

Abstract

This paper introduces our current results of GaAs MESFET high power amplifier modules with low drain bias voltage for use in mobile communications systems. The design and fabrication techniques using HMIC and MMIC technologies are presented, addressing a design method of high power amplifier modules with the stringent requirements for cost, size, and performance. This paper describes three types of high power amplifier modules: UHF-band high efficiency, high power amplifier modules employing a combination of HMIC and MMIC technologies, a UHF-band high efficiency, linear amplifier module employing HMIC technologies, and a 1.9GHz high efficiency, linear MMIC amplifier.

1. Introduction

With the rapid worldwide progress in mobile and satellite communication systems, a number of high power amplifier modules have been developed [1-3]. In such systems, requirements for high power amplifiers are low cost, low operation voltage, low power consumption, small size, and high linearity especially for digital cellular radio systems and the PHS (Personal Handy Phone System) in Japan. In this paper, our current results of GaAs MESFET high power amplifier modules with low drain bias voltage for use in analog/digital handheld telephones and the PHS in Japan are presented, focusing on the design, fabrication and performance of the amplifiers. These amplifiers demonstrate high efficiency, high power, or high linearity under low drain bias operation of 3.3V.

2. High Power Amplifiers Employing a Combination of HMIC and MMIC

A photograph of the UHF-band three-stage high efficiency, high power amplifier module is shown in Fig.1 [4]. The gate peripheries of the 1st, 2nd, and final stage FETs were determined to 0.2, 1.6, and

18.2mm, respectively, to achieve a saturated output power of greater than 31dBm and a power-added efficiency of greater than 50% at UHF-band. The amplifier is operated with low drain bias voltage of 3.3V for reducing battery size of handheld telephones and is biased under class AB operation for achieving long operating time. To achieve high efficiency, the optimum load impedances of the final stage FET for the fundamental and second harmonic waves were obtained by making the fundamental and second harmonic load-pull measurements [5]. Based on the results of the load-pull measurements, the output matching circuit was designed by employing the second harmonic reflection circuit to show the optimum impedances for both the fundamental and second harmonic waves.

The amplifier is comprised of three chips: active circuit chip, passive circuit chip, and output matching circuit chip. The active and passive circuits were designed by using lumped elements and fabricated on GaAs substrates for achieving a miniaturized size. The output matching circuit was designed by using distributed elements and fabricated on a high dielectric substrate ($\epsilon = 38$) to reduce loss and size of the amplifier. These three chips are mounted on a ceramic leadless

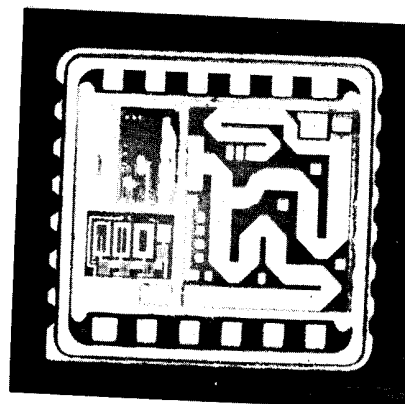


Fig.1 UHF-band three-stage high efficiency, high power amplifier module

package with the dimensions of $9.5 \times 10\text{mm}^2$. The measured output power and power-added efficiency are plotted in Fig.2. A saturated output power of 31.8dBm, and a power-added efficiency of 57.3% have been achieved at UHF.

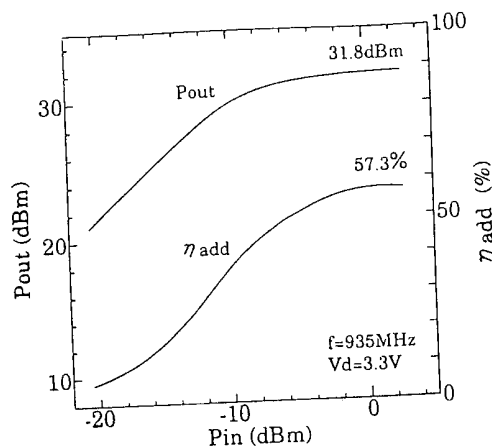


Fig.2 Measured output power and efficiency

Another example of a UHF-band four-stage, high efficiency, high power amplifier module employing a combination of HMIC and MMIC is shown in Fig.3 [6]. It consists of three-stage driver MMIC amplifier and a single-stage power HMIC amplifier. The gate peripheries from the 1st and final stage FETs were optimized to maximize the efficiency for an averaged power of 31dBm and a saturated power greater than 34dBm for $\pi/4$ -shift QPSK modulated signals at UHF. The load impedance of the final stage FET providing the maximum efficiency was obtained by the fundamental and second harmonic load-pull measurements.

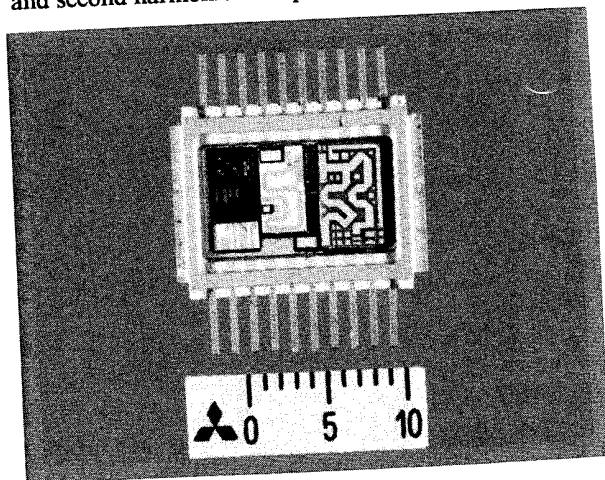


Fig.3 UHF-band four-stage, high efficiency, high power amplifier module

The source impedance providing the minimum insertion phase variation was obtained by the source-pull measurement. Based on the results of the source-pull measurement, the input and output matching circuits of the final stage amplifier were designed to achieve high efficiency and low insertion phase variation.

The amplifier consists of four chips: a three-stage MMIC amplifier chip, a final-stage FET chip, input and output matching circuit chips. The input and output matching circuits were fabricated on high dielectric substrates ($\epsilon = 9.8$ and 38) to reduce loss and size of the amplifier. These chips were mounted on a ceramic package. The measured output power, power-added efficiency, and insertion phase variation are plotted in Fig.4. The amplifier demonstrates a saturated output power of 34dBm, a drain efficiency of 38.1% and an insertion phase variation of 7deg at an averaged power of 31dBm at 950MHz. The measured output spectrum for $\pi/4$ -shift QPSK modulated signals at an averaged power of 31dBm is plotted in Fig.5. An adjacent channel leakage power (50kHz offset) of -48.5dBc has been obtained. The drain voltage is 5.8V.

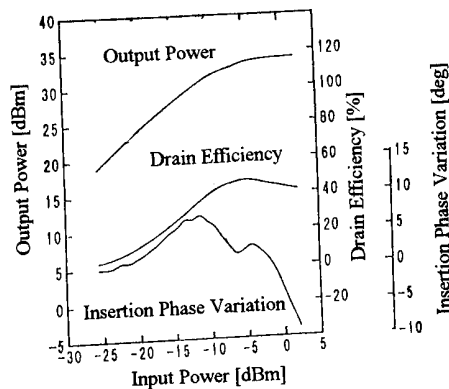


Fig.4 Measured power, power-added efficiency, and insertion phase variation

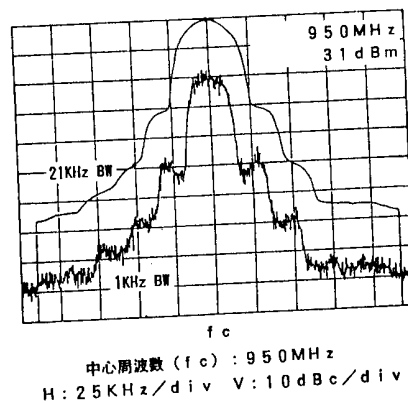


Fig.5 Measured output spectrum

3. High Power Amplifier Employing HMIC

A photograph of the UHF-band two-stage, high efficiency, linear amplifier module is shown in Fig.6 [7]. The gate peripheries of driver and power FETs were determined to 8.4 and 31.5mm, respectively, to achieve the maximum efficiency at an averaged output power of 31dBm for $\pi/4$ -shift QPSK modulated signals. The optimum load impedance providing the maximum efficiency at an averaged output power of 31dBm was obtained first for the power FET by the load-pull measurements using $\pi/4$ -shift QPSK modulated signals. Next, the optimum source impedance providing the minimum ACP (Adjacent Channel leakage Power) was obtained by the source-pull measurements using $\pi/4$ -shift QPSK modulated signals. The driver FET is biased under class A operation for high linearity. The power FET is biased under class AB operation for high efficiency. The drain voltage is 3.3 V.

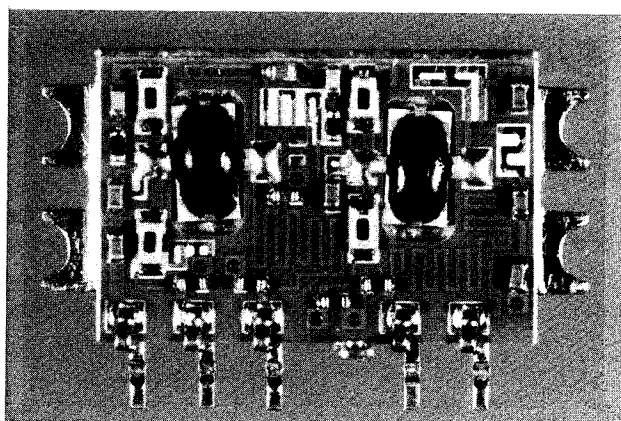


Fig.6 Photograph of the UHF-band two-stage, high efficiency, linear amplifier module

The circuit elements of the amplifier were designed by using lumped and distributed elements and fabricated on PPO (Poly Phelylen Oxide) substrates with the circuit dimensions of $11 \times 16\text{mm}^2$ for achieving low cost. The driver and power stage FETs employ a mold type package for low cost. The averaged output power, power-added efficiency, and ACP (50kHz offset) were measured for $\pi/4$ -shift QPSK modulated signals at UHF and plotted in Fig.7. A power-added efficiency of 44% and an ACP of -49.8dBc have been achieved for an averaged output power of 31dBm.

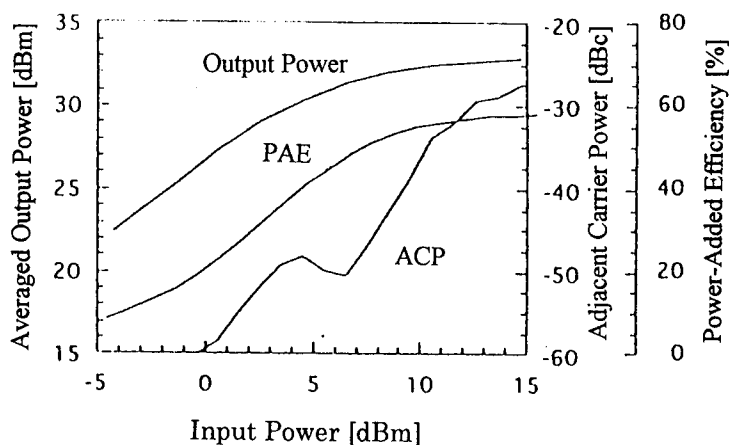


Fig.7 Measured output power, efficiency, and ACP

4. High Power Amplifier Employing MMIC

A photograph of the 1.9GHz three-stage high efficiency, linear MMIC amplifier is shown in Fig.8 [8]. The gate peripheries of the 1st, 2nd, and final stage FETs were determined to 0.3, 0.5, and 4mm, respectively, to achieve the maximum efficiency at an averaged output power of 22dBm for $\pi/4$ -shift QPSK modulated signals. The optimum load impedance providing the maximum efficiency at a 3dB backed off output power was obtained first for the final stage FET by load-pull measurements. Next, the optimum source impedance providing the minimum insertion phase variation with input power was obtained by source-pull measurements. The 1st and 2nd stage amplifier are biased under class A operation to prevent amplitude and phase distortion. The final stage amplifier is biased under class AB operation to improve efficiency. The drain voltage is 3.3V.

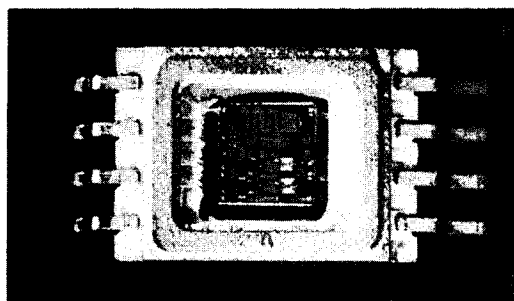


Fig.8 Photograph of the 1.9GHz three-stage high efficiency, linear MMIC amplifier

The circuit elements were fabricated by using lumped and distributed elements on GaAs substrates with the chip dimensions of $2.7 \times 2.7 \text{ mm}^2$. All matching and bias circuit elements are included in the MMIC chip. The averaged output power, power-added efficiency, and ACP (600kHz offset) were measured at 1.9GHz for $\pi/4$ -shift QPSK modulated signals (398kbps) and plotted in Fig.9. A power-added efficiency of 35% and an ACP of -55dBc have been achieved at an averaged power of 22dBm.

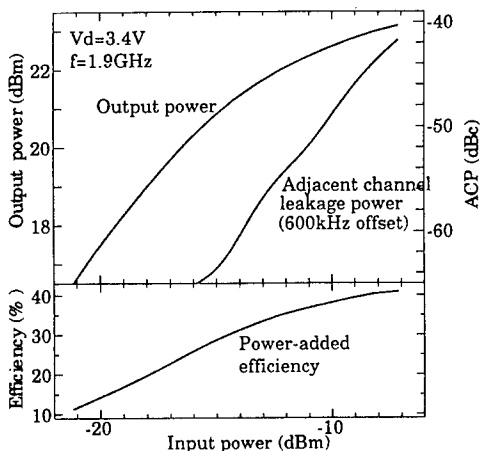


Fig.9 Measured output power, efficiency, and ACP

5. Conclusion

Three types of high power amplifier modules employing HMIC, MMIC, and a combination of HMIC and MMIC have been presented. It has been shown that these amplifier modules utilizing distinguished features of HMIC and MMIC technologies would be a candidate for high power amplifier modules with low cost, small size, low voltage operation, and high performance for use in mobile communication systems.

References

- [1] T.Takagi, Y.Ikeda, K.Seino, G.Toyoshima, A.Inoue, N.Kasai, and M.Takeda, "A UHF Band 1.3W Monolithic Amplifier with Efficiency of 63%", *1992 IEEE Microwave and Millimeter-Wave Monolithic Circuit Symposium Digest*, pp.35-38.
- [2] H.Hayashi, M.Nakatsugawa, and M.Muraguchi, "A Self Phase Distortion Compensation Technique for Linear Power Amplifiers," *1994 Asia-Pacific Microwave Conference Proceedings*, pp.555-558.
- [3] T.Yokoyama, T.Kunihisa, H.Fujimoto, H.Takehara, K.Ishida, H.Ikeda, and O.Ishikawa, "High-Efficiency Low Adjacent Channel Leakage GaAs Power

MMIC for 1.9 GHz Digital Cordless Phones," *IEEE Trans. MTT*, vol.42, No.12, pp.2623-2628, Dec. 1994.

- [4] K.Mori, M.Nakayama, Y.Itoh, S.Murakami, Y.Nakajima, and T.Takagi, "A UHF-Band High Efficiency and High Power Monolithic Amplifier Having Low Drain Bias Voltage," *1994 Asia-Pacific Microwave Conference Proceedings*, pp.663-666.
- [5] S.Nishiki and T.Nojima, "Harmonic Reaction Amplifier - A Novel High-Efficiency and High-Power Microwave Amplifier -," *1987 IEEE MTT-S Digest*, pp.963-966.
- [6] M.Mochizuki, Y.Ikeda, T.Okuda, Y.Yakajima, and T.Takagi, "900MHz Band Linear Amplifier Module with Low Power Consumption," *1993 IEICE NTCV Spring*, SC-1-3.
- [7] K.Nakahara, M.Mochizuki, H.Katayama, H.Hanai, Y.Itoh, T.Takagi, and Y.Mitsui, "900MHz-Band Low-Voltage Linear Amplifier Module," *1995 IEICE NTCV Spring*, SC-2-4.
- [8] M.Nakayama, T.Umemoto, Y.Itoh, and T.Takagi, "1.9 GHz High-Efficiency Linear MMIC Amplifier," *1994 Asia-Pacific Microwave Conference Proceedings*, pp.347-350.

VLSI ARCHITECTURES FOR VIDEO COMPRESSION

P. Pirsch, W. Gehrke

Laboratorium für Informationstechnologie
University of Hannover
Schneiderberg 32, 30167 Hannover, Germany

Abstract – This paper gives an overview on alternative approaches for the implementation of recent hybrid coding schemes. An efficiency measure is introduced and applied for the comparison of video signal processors, proposed in the literature. Concerning recent hybrid coding schemes, the comparison shows that adapted architectures achieve an efficiency gain by a factor of 6 to 7 compared to flexible architectures, applicable for a wider range of application fields. It is expounded that this efficiency might decrease for future video compression schemes, due to data dependent computational requirements of the applied algorithms.

1. INTRODUCTION

Video processing has been a rapidly evolving field for telecommunications, computer and media industries. In particular, for real time video compression applications a growing economical significance is expected for the next years. Besides digital TV broadcasting and videophone, services like multimedia education, teleshopping, or video mail will become audiovisual mass applications.

To facilitate world wide interchange of digitally encoded audiovisual data there is a demand for international standards, defining coding methods and transmission formats. International standardization committees have been working on the specification of several compression algorithms. The Joint Photographic Experts Group (JPEG) of the International Standards Organization (ISO) has specified an algorithm for compression of still images [4]. The ITU proposed the H.261 standard for video telephony and video conference [1]. The Motion Pictures Experts Group (MPEG) of ISO has completed its first standard MPEG-1, which will be used for interactive video and provides a picture quality comparable to VCR quality [2]. MPEG made substantial progress for the second

phase of standards MPEG-2, which will provide audiovisual quality of both broadcast TV and HDTV [3]. Besides the availability of international standards, the successful introduction of the named services depends on the availability of VLSI components, supporting a cost efficient implementation of video compression applications.

In this paper we give a short overview of recent coding schemes and discuss basic implementation alternatives in section 3. Section 4 provides a figure of merit for architectural efficiency of the alternative implementation strategies. Section 5 discusses future trends of video compression applications and their VLSI implementation.

2. RECENT CODING SCHEMES

Recent video coding standards are based on a hybrid coding scheme that combines transform coding and predictive coding. An overview of these hybrid encoding schemes is depicted in figure 1.

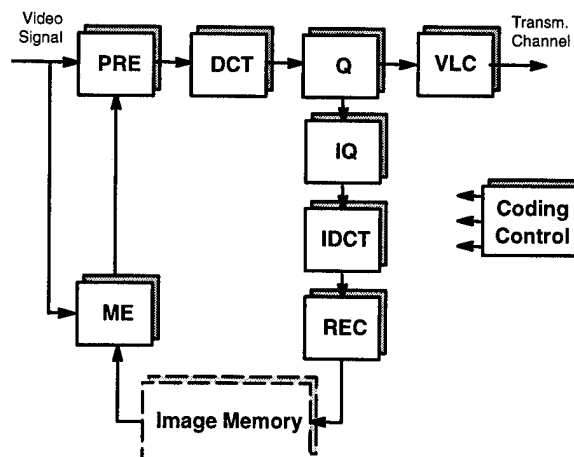


Fig. 1: Hybrid encoding scheme

The coding scheme consists of the tasks motion estimation (ME) typically based on blockmatching al-

gorithms, computation of the prediction error (PRE), discrete cosine transform (DCT), quantization (Q), variable length coding (VLC), inverse quantization (IQ), inverse discrete cosine transform (IDCT) and reconstruction (REC). The reconstructed image data are stored in an image memory for further predictions. The decoder performs the tasks variable length decoding, inverse quantization, and motion compensated reconstruction.

Generally, video processing algorithms can be classified in terms of regularity of computation and data access. This classification leads to three classes of algorithms:

Low-Level Algorithms

These algorithms are based on a predefined sequence of operations and a predefined amount of data at the input and output. Typical examples are block matching or transforms like the DCT.

Medium-Level Algorithms

The sequence of operations of medium-level algorithms depends on the data. Typically, the amount of input data is predefined, whereas the amount of output data varies according to the input data values. With respect to hybrid coding schemes, examples for these algorithms are quantization, inverse quantization or variable length coding.

High-Level Algorithms

High-level algorithms are associated with a variable amount of input and output data and a data dependent sequence of operations. Control tasks of the hybrid coding scheme are generally members of this class.

Since hybrid coding schemes are applied for varying video data rates, the required absolute processing power varies in the range from a few hundreds of MOPS (Mega Operations Per Second) for video signals in QCIF format to several GOPS (Giga Operations Per Second) for processing of TV or HDTV signals. Nevertheless, the relative computational power of each algorithmic class is nearly independent of the processed video format. In case of hybrid coding applications, approximately 90% of the overall processing power is required for low-level algorithms. The share of medium-level tasks is about 7% and nearly 3% is required for high-level algorithms.

3. ARCHITECTURAL ALTERNATIVES

In terms of a VLSI implementation of hybrid coding applications two major requirements can be identified. First, the high computational power requirements

have to be met by the hardware. Second, low manufacturing cost of video processing components is essential for the economic success of an architecture. Depending on the envisaged application field, implementation size and architectural flexibility might have to be taken into account.

Basically, implementations of video processing applications can either be based on standard processors from workstations or PCs or on specialized video signal processors. The major advantage of standard processors is their availability. Applying these architectures for implementation of video processing hardware, does not require the time consuming design of new VLSI components. The disadvantage of this implementation strategy is the insufficient processing power of recent standard processors. Video processing applications would still require the implementation of multiprocessor systems to meet the computational requirements.

To achieve compact implementations video processing hardware has to be based on specialized video signal processors, adapted to the requirements of the envisaged application field.

Although adaptation of the architecture leads to small implementation size and decreased manufacturing cost, the computational requirements of video processing applications demand for the exploitation of the algorithm-inherent independence of basic arithmetic operations to be performed. Independent operations can be processed concurrently, which enables the decrease of processing time and thus an increased through-put rate. For the architectural implementation of concurrency two basic strategies can be distinguished: pipelining and parallel processing.

In case of pipelining several tasks, operations, or parts of operations are processed in subsequent steps in different hardware modules. Depending on the selected granularity level for the implementation of pipelining, intermediate data of each step are stored in registers, register chains, FIFOs, or dual-port memories. Assuming a processing time of T_P for a non-pipelined processor module and $T_{D,IM}$ for the delay of intermediate memories we get in the ideal case the following estimation for the processing time $T_{P,Pipe}$ for a pipelined architecture with N_{Pipe} pipeline stages:

$$T_{P,Pipe} = \frac{T_P}{N_{Pipe}} + T_{D,IM} \quad (1)$$

From this follows, that the major limiting factor for the maximum applicable degree of pipelining is the access delay of these intermediate memories.

The alternative to pipelining is the implementation of parallel units, processing independent data

concurrently. Parallel processing can be applied on operation level as well as on task level. Assuming the ideal case, this strategy leads to a linear increase of processing power and we get:

$$T_{P,Par} = \frac{T_P}{N_{Par}} \quad (2)$$

where N_{Par} = Number of parallel units

According to the three ways for architectural optimization, adaptation, pipelining, and parallel processing, three architectural classes for the implementation of video signal processors can be distinguished:

Intensive Pipelined Architectures

These architectures are typically scalar architectures that achieve high clock frequencies of several hundreds of MHz due to the exploitation of pipelining.

Parallel Data Paths

These architectures exploit data distribution for the increase of computational power. Several parallel data paths are implemented on one processor die,

which leads in the ideal case to a linear increase of supported computational power. The number of parallel data paths is limited by the semiconductor process, since an increase of silicon area leads to an decrease of hardware yield.

Coprocessor Architectures

Coprocessors are known from general processor designs and are often used for specific tasks, e.g. floating point operations. The idea of the adaptation to specific tasks and increase computational power without an increase of the required semiconductor area has been applied by several designs. Due to their high regularity and the high processing power requirements low-level tasks are the most promising candidates for an adapted implementation. The main disadvantage of this architectural approach is the decrease of flexibility by an increase of adaptation.

A selection of proposed VLSI architectures for hybrid coding schemes and their implementation data are shown in table 1.

Ref.	Architectural Class	Technology [micron]	Chip Size [mm ²]	# Chips required for CIF-30Hz H.261 codec	Comments
[7]	Coprocessor	0.9	132 (Coder) 112 (Decod.)	2	
[8]	Coprocessor	0.5	312	1	w/o motion estimation. This chip has been designed for MPEG-2 applications
[9]	Coprocessor	0.8	160	3	frame rate 15 Hz
[10]	Coprocessor	1.0	77 (VP), 80 ? (VC)	2 VC + 3 VP	VC's chip size roughly estimated
[11]	Coprocessor	0.8	144	4	
[12]	Coprocessor	0.6	80	1	estimated chipsize
[13]	Intens. Pipelining	0.8	202	5	
[14]	Intens. Pipelining	0.5	281	1	
[15]	Parallel Data Paths	1.0	225	4	
[16]	Parallel Data Paths	0.8	231	4	
[17]	Parallel Data Paths	0.5	324	1	#Chips estimated
[18]	Parallel Data Paths	0.6	180	2	

Table 1 Overview of selected architectures for video coding applications

4. ASSESSMENT OF VLSI ARCHITECTURES

For a comparison of architectural alternatives an efficiency measure has to be defined. As a first approach efficiency E can be expressed by the ratio of through-put rate R_T and the required silicon area A_{Si} :

$$E = \frac{R_T}{A_{Si}} \quad (3)$$

Since the required silicon area and the through-put rate for an implementation of a specific application depend on the applied semiconductor technology, a realistic architectural assessment has to consider the gains provided by the progress in semiconductor technology. A sensible way to achieve a realistic assessment, is the normalization of the architecture parameters according to a reference technology. In the following we assume a reference process with a grid length $\lambda_0 = 1.0$ micron. Assuming the "constant field" model, the processing time of a given process with grid length λ scales as λ/λ_0 . This model supposes a linear scaling of voltages and doping concentration. In the "constant voltage" model of scaling of MOS transistors the gate delay scales as $(\lambda/\lambda_0)^2$. These two models do not take into account the long distance interconnection delay (which basically does not scale [19]), the short channel effects and the limitations due to the power dissipation issue. Reality is not well described by the traditional models of scaling (the voltage, at least for function specific architectures reported up to now, has not been reduced linearly with λ). Thus it is reasonable to use an empiric measure of processor speed vs. technology. Bakoglu produces a comprehensive list of microprocessors, with their clock frequency and their gate length λ [19]. From these data, it can be estimated that the cycle time of these processors, which results from a combination of all the factors mentioned above, scales approximately as $(\lambda/\lambda_0)^{1.6}$. Thus, for comparison of architecture alternatives we use in this paper a normalization by $(\lambda/\lambda_0)^2$ for the silicon area and $(\lambda_0/\lambda)^{1.6}$ for through-put.

$$A_{Si,0} = A_{Si} \left(\frac{\lambda_0}{\lambda} \right)^2 \quad (4)$$

$$R_{T,0} = R_T \left(\frac{\lambda}{\lambda_0} \right)^{1.6} \quad (5)$$

where the index 0 is used for the system with reference gate length λ_0 .

Equations (4) and (5) can be applied for the comparison of the architectural alternatives shown in

table 1. The result of this comparison is shown in figure 2, using the coding scheme according to ITU recommendation H.261 as a benchmark.

From figure 2, we can identify two groups of architectural classes. The first group consists of adapted architectures, optimized for hybrid coding applications, like ITU-H.261 or ISO MPEG-1. The architectures contain one or more adapted modules for computation intensive tasks, like DCT or block matching. It is obvious that the application field of these architectures is limited to a small range of applications. This limitation is avoided by the members of the second group of architectures. Most of these architectures do not contain function specific circuitry for specific tasks of the hybrid coding scheme. Thus, they can be applied for wider variety of applications without a significant loss of sustained computational power. On the other hand, these architectures are associated with a decreased architectural efficiency compared to the first group of proposed architectures: Adapted architectures achieve an efficiency gain of about 6 to 7.

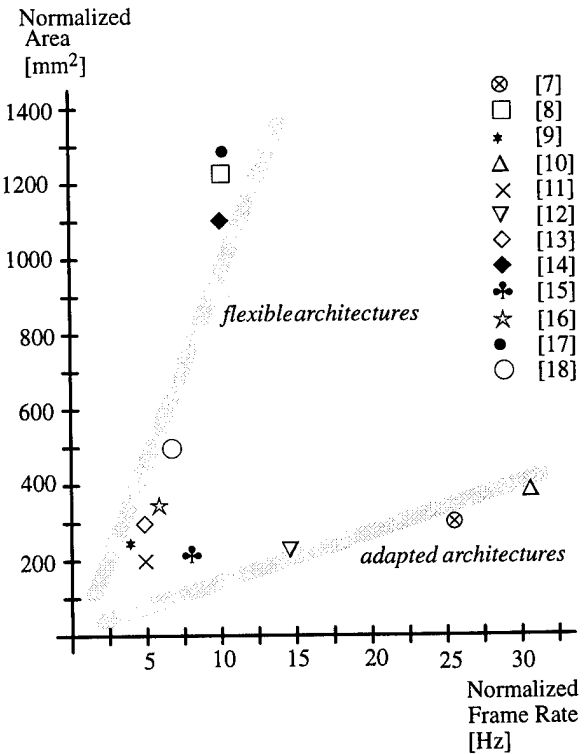


Fig. 2: Normalized silicon area and throughput (frame rate) for adapted and flexible programmable architectures for a H.261 codec

5. FUTURE TRENDS

The hybrid coding scheme is based on the segmentation of the input image into square blocks of equal size (typ. 16x16 pels). These blocks are encoded according to the scheme presented in section 2. It is obvious, that the predefined segmentation of the image will generally not correspond to the image content. As an alternative to hybrid coding approach, content based coding schemes are proposed. These approaches are based on a segmentation of the image data at runtime according to the image content. It is expected that content based video compression schemes will be the basis for the next generation of video coding standards. For example, content based video coding is proposed for the ISO MPEG4 standardization that is currently under progress and will be finished within this century [5].

Concerning the VLSI implementation of content based video coding schemes the major difference in comparison to hybrid coding scheme is the increased share of medium-level and high-level algorithms. It can be expected that the increased share of data dependent algorithms will lead to a decreased efficiency gain of adapted architectures in comparison to flexible programmable architectures. To clarify this statement, scheduling effects for the processing of hybrid coding schemes and coding schemes associated with data dependent computational requirements will be shortly discussed.

For simplification of the discussion we assume three different tasks. In case these tasks are associated with data independent computational requirements, each task can be processed by one adapted module. Generally, the processing power of each module can be adapted to the requirements of the applied algorithms. The utilization of the modules is maximized, if all the processing times T_{PI} of modules I are equal. In this case, a 100% utilization can be achieved, if the modules operate in a macropipeline mode. This is clarified by figure 3.

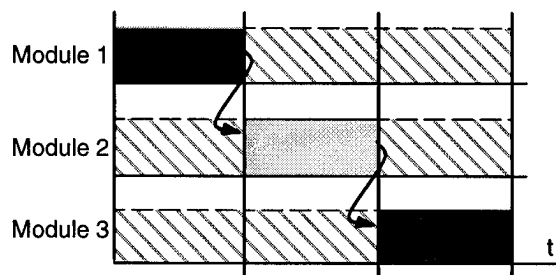
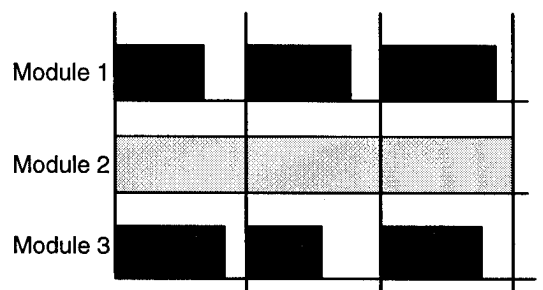


Fig. 3: Processing of algorithms associated with data independent computational requirements

Utilization of adapted modules might decrease if the tasks are associated with data dependent computational requirements. In this case the processing time of each task cannot not be determined at design time of the circuits. The result is varying idle times of the modules, according to the image content (Fig. 4 a).

In case of programmable architectures, the available hardware resources can be assigned according to the varying computational requirements at runtime and the impact of varying computational requirements is decreased. In consequence, the supported computational power of programmable architectures has to meet the overall computational power required to process the envisaged application in realtime (Fig. 4 b).

a) Adapted Architecture



b) Programmable Architecture



Fig. 4: Processing of algorithms associated with data dependent computational requirements processed with adapted architectures and programmable architectures

Due to the increased share of idle times, the advantages in terms of architectural efficiency of adapted architectures will become smaller for future sophisticated video compression schemes. Thus, it can be expected that flexible programmable architectures will become more attractive, even for mass applications.

6. CONCLUSION

The properties of recent hybrid coding schemes in terms of VLSI implementation have been presented. Architectural alternatives for the realization have been discussed. Based on a simplified efficiency modelling, it has been shown that adapted circuits achieve a 6-7

times higher efficiency than flexible programmable circuits. This efficiency gap might decrease for future coding schemes associated with a higher amount of medium-level and high-level algorithms. Due to their flexibility, programmable architectures will become more and more attractive for future VLSI implementations of video compression schemes.

REFERENCES

- [1] ITU-T Recommendation H.261, "Video Codec for Audiovisual Services at px64 kbit/s", 1990.
- [2] ISO-IEC IS 11172, "Coding of moving pictures and associated audio for digital storage media at up to about 1,5 Mbit/s", 1993.
- [3] ISO-IEC IS 13818, "Generic Coding of Moving Pictures and Associated Audio", 1994.
- [4] ISO-IEC IS 10918, "Digital compression and coding of continuous-tone still images", 1992.
- [5] ISO/IEC JTC1/SC29/WG11, "MPEG-4 Functionalities", November 1994.
- [6] P. Pirsch, N. Demassieux, W. Gehrke, "VLSI Architectures for Video Compression - A Survey", Proc. IEEE, vol.83, no.2, pp.220-246, Feb. 1995.
- [7] B. Ackland, "The Role of VLSI in Multimedia", IEEE Journal of Solid-State Circuits, Vol. 29, No. 4, S. 1886 - 1893, April 1994.
- [8] T. Akari, et. al., "Video DSP Architecture for MPEG2 Codec", Proc. ICASSP '94, vol.2, pp. 417-420, IEEE Press, 1994.
- [9] K. Aono, et. al., "A Video Digital Signal Processor with a Vector-Pipeline Architecture", IEEE Journal of Solid-State Circuits, Vol.27, No.12, pp.1886-1893, Dec. 1992.
- [10] D. Bailey, et. al., "Programmable Vision Processor/ Controller", IEEE MICRO, vol. 12, no. 5, pp. 33 - 39, October 1992.
- [11] K. Gaedke, H. Jeschke, P. Pirsch, "A VLSI Based MIMD Architecture of a Multiprocessor System for Real-Time Video Processing Applications", Journal of VLSI Signal Processing, vol. 5, pp. 159-169, April 1993.
- [12] W. Gehrke, R. Hoffer, P. Pirsch, "A hierarchical Multiprocessor Architecture based on Heterogeneous Processors for Video Coding Applications", Proc. ICASSP '94, vol.2, 1994.
- [13] J. Goto, et. al., "250-MHz BiCMOS Super-High-Speed Video Signal Processor (S-VSP) ULSI", IEEE Journal of Solid-State Circuits, vol. 26, no. 12, pp. 1876 - 1884, 1991.
- [14] T. Inoue, et. al., "A 300-MHz BiCMOS Video Signal Processor", IEEE Journal of Solid-State Circuits, vol. 28, no. 12, pp. 1321-1329, December 1993.
- [15] T. Mücke, D. Müller, R. Heiß, "ISDN-Bildtelefon auf der Grundlage eines Array-Prozessor-IC", mikroelektronik, vde-verlag, vol. 5, no. 3, pp. 116-119, May/June 1991. (in german)
- [16] H. Yamauchi, et. al., "Architecture and Implementation of a Highly Parallel Single Chip Video DSP", IEEE Trans. on Circuits and Systems for Videotechnology, vol.2, no. 2, pp. 207-220, June 1992.
- [17] K. Gutttag, "The multiprocessor video processor, MVP", Proc. IEEE Hot Chips V, Stanford CA, Aug. 1993.
- [18] J. Kneip, K. Rönner, P. Pirsch, "A single chip highly parallel architecture for image processing applications", Proc. SPIE Visual Communications and Image Processing, vol. 2308 (3), pp. 1753-1764, Sept. 1994.
- [19] H. B. Bakoglu, "Circuits Interconnections and Packaging for VLSI", Addison Wesley, 1987.

TRANSMISSION OF DCT-CODED IMAGES BY MULTICARRIER MODULATION FOR NOISY CHANNELS

Keang-Po Ho and Joseph M. Kahn

Department of Electrical Engineering and Computer Sciences
University of California, Berkeley, CA 94720

Abstract

We have proposed and analyzed a combined source-channel coding scheme using multicarrier modulation. By changing the power and modulation of subchannels carrying different bits of the quantized signal, the channel-induced distortion can be minimized. An algorithm for the subchannel power allocation is derived. For discrete cosine transform- (DCT-) coded images, multicarrier systems achieve more than a 9-dB improvement over single-carrier systems on very noisy channels.

1. Introduction

One of the most important results of Shannon's work was that source coding and channel coding can be treated separately without sacrificing fidelity [1]-[2]. Traditionally, the source and channel codes are designed separately and then cascaded together. However, Shannon's argument is true only if both transmitter and receiver are permitted to have an infinite degree of complexity. In practice, because of channel-induced additive noise, the probability of bit error (bit-error rate, BER) is not infinitesimally small. In typical communication systems, in order to transmit an analog source, the source is quantized into binary bits and all bits are transmitted via the same channel, and are thus afforded the same protection against error. However, some bits in the quantized signal (e.g., the most significant bit) are far more important than others. In such a situation, we can combine the source and channel codes into a single code in which the objective is to minimize the overall distortion between the original source at the transmitter and its reconstruction at the receiver.

The schematic diagram of a multicarrier modulation system is shown in Fig. 1. In transmission of a quantized analog source, each subchannel [3]-[4] can utilize different power, modulation constellation, channel encoding, and carrier $\phi_m(t)$, so that different error protection can be provided

This work was supported by National Science Foundation Presidential Young Investigator Award ECS-9157089 and The Hughes Aircraft Company.

for different bits. The distortion between the received signal and the original signal can thereby be minimized. In this paper, we will consider the using of multicarrier modulation to transmit discrete cosine transform- (DCT-) coded images.

2. Channel-Induced Distortion

Our combined source-channel scheme uses a fixed source encoder and changes the channel modulation to reduce the channel-induced distortion. The source encoder consists of a DCT followed by scalar quantizers. As the DCT coefficients are known to be accurately modeled as Laplacian-distributed random variables, the quantizer is optimized for a Laplacian source using the method of Lloyd [5] and Max [6]. The quantizer partitions the real axis into Q regions of $(-\infty, x_1]$, $(x_i, x_{i+1}]$, $i = 1, 2, \dots, Q-2$, $(x_{Q-1}, +\infty)$. Each region is quantized to the centroid of that region, y_i . For simplicity, we use the natural binary coding, i.e., the codeword y_i is mapped to binary codeword i .

Because a codeword represents the centroid of the respective partition, the overall distortion from the source at the transmitter to the reconstructed signal at the receiver is the sum of the quantization distortion and the channel-induced distortion [7]. Because the quantizer is given and fixed, in this paper, we seek to minimize the channel-induced distortion:

$$D_C = \sum_{i=0}^{Q-1} \sum_{j=0}^{Q-1} p_{y_i} P(j|i) (y_j - y_i)^2, \quad (1)$$

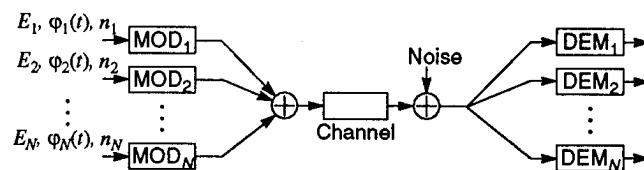


Fig. 1 Schematic diagram of a multicarrier system. E_m is the power transmitted in the m th subchannel, $\phi_m(t)$ is the carrier of the m th subchannel, and n_m is the number of bits per symbol of the m th subchannel.

where p_{y_i} is *a priori* probability of codeword y_i , and $P(j|i)$ is the transition probability for transmission of binary codeword i and reception of binary codeword j .

The binary codewords are binary numbers of $n = \log_2 Q$ bits. Each bit is transmitted over a different subchannel using multicarrier modulation. Assuming that the BER of each channel is p_{b_m} , $m = 1, 2, \dots, n$, the transition probabilities are

$$P(j|i) = \prod_{m=1}^n (1-p_{b_m})^{1-l_m(i,j)} p_{b_m}^{l_m(i,j)}, \quad (2)$$

where $l_m(i, j) = 1$ if the binary codewords represented by i and j differ in the m th position and otherwise $l_m(i, j) = 0$. Usually, the BERs p_{b_m} are small, so that the probability of multiple bit errors within the same binary codeword is small, and any terms having factors of $p_{b_{m1}} p_{b_{m2}}, m1, m2 = 1, 2, \dots, n$, can be ignored. The transition probabilities are thus simplified to

$$P(j|i) = \begin{cases} 1 & i = j \\ p_{b_m} & l_m(i, j) = 1 \\ 0 & \text{otherwise} \end{cases} \quad (3)$$

In this simplification, $P(j|i)$ is non-zero if i and j are equal, or are separated by a unit Hamming distance. For any n -bit binary number i , there are n different binary numbers separated from i by a Hamming distance of unity. If i_m is the m th bit in the binary representation of i , i.e., $i = \sum_{m=1}^n i_m 2^{n-m}$, those n binary numbers are

$$i_{e,m} = i + (1 - 2i_m) 2^{n-m}, m = 1, 2, \dots, n. \quad (4)$$

After some algebra, the channel-induced distortion is found to be:

$$D_C \approx \sum_{m=1}^n \sum_{i=0}^{Q-1} p_{b_m} p_{y_i} (y_{i_{e,m}} - y_i)^2 = \sum_{m=1}^n p_{b_m} w_{n,m}, \quad (5)$$

where

$$w_{n,m} = \sum_{i=0}^{Q-1} p_{y_i} (y_{i_{e,m}} - y_i)^2 \quad (6)$$

are the weighting factors of each bit.

The weighting factors $w_{n,m}$ and other parameters of optimal scalar quantizers of 1 to 9 bits, designed by Method I of Lloyd [5] for a zero mean, unit-variance Laplacian source, can be found in [8].

3. Subchannel Power Allocation

The 2-D DCT has been shown to provide relatively efficient and robust performance in a variety of image coding applications. The image is divided into small blocks of size $p \times q$, and a 2-D DCT is employed for each small block. The variances of transform coefficient $\sigma_{k,l}^2$, $0 \leq k < p$, $0 \leq l < q$, can be estimated from the image or derived from the image model.

Assume that $n_{k,l}$ is the bit allocation table determined by a bit allocation algorithm [9, pp. 501-504]. Assuming that the DCT coefficients are Laplacian-distributed, if $w_{n,m}$ are the weighting factors of the m th bit of an optimal quantizer for a unit-variance Laplacian source, obviously, the weighting factor of the corresponding source bit is $\sigma_{k,l}^2 w_{n_{k,l}}$. Let us assume that $p \times q$ 2-D DCT coefficients are quantized to N bits and transmitted by a N -subchannel multicarrier modulation system. Assuming that each subchannel has a power of $E_{n_{k,l}}$, the BER of the each subchannel is a function of $E_{n_{k,l}}$, or $p_{n_{k,l}} = P_{n_{k,l}}(E_{n_{k,l}})$, where $P_\gamma(E)$ is the BER function, which can be different for the individual subchannels if different modulation schemes are employed. Therefore, we would like to minimize the channel-induced distortion per pixel:

$$D_C = \frac{1}{pq} \sum_{k=1}^p \sum_{l=1}^q \sum_{i=1}^{n_{k,l}} P_{n_{k,l}}(E_{n_{k,l}}) \sigma_{k,l}^2 w_{n_{k,l}} \quad (7)$$

with the constraint that the total power is equal to E_T . Using a Lagrange multiplier, the solution of (7) is [8]

$$\sigma_{k,l}^2 w_{n_{k,l}} G_{n_{k,l}}(E_{n_{k,l}}) = \lambda, \quad (8)$$

where $G_\gamma(E) = dP_\gamma(E)/dE$ is the derivative of $P_\gamma(E)$ with respect to the power E , and λ is the Lagrange multiplier. For a fixed overall power, the multiplier λ can be found by solving

$$\sum_{k=1}^p \sum_{l=1}^q \sum_{i=1}^{n_{k,l}} G_{n_{k,l}}^{-1}(\lambda / (\sigma_{k,l}^2 w_{n_{k,l}})) = E_T, \quad (9)$$

where $G_\gamma^{-1}(E)$ are the inverse functions of $G_\gamma(E)$. After the multiplier λ is evaluated, the power allocation can be calculated by

$$E_{n_{k,l}} = G_{n_{k,l}}^{-1}(\lambda / (\sigma_{k,l}^2 w_{n_{k,l}})). \quad (10)$$

Although complicated, the expression (9) is a one-variable equation that can be solved easily by numerical methods [8].

4. Numerical Example

As a numerical example, we consider images transmitted over an additive white Gaussian-noise (AWGN) channel. Without loss of generality, we assume that all subchannels are identically modulated using BPSK. For Gaussian channel, the function $G_f(E)$ is a monotonic function so that (9) can be solved by the bisection method.

The original 256 gray-scale Lena image in Fig. 2 is employed for a demonstration. First, 128 is subtracted from the image, and then the image is divided into small square blocks of size 16×16 . The 2-D DCT is computed for each block and the variances of the DCT coefficients are estimated. The transform coefficients are normalized by their corresponding standard deviations $\sigma_{k,l}$ and quantized by the optimal quantizer for a unit-variance Laplacian distribution. The bit allocation table is determined by the integer bit-allocation algorithm [9, pp. 503-504].



Fig. 2 The original gray-scale image of Lena.

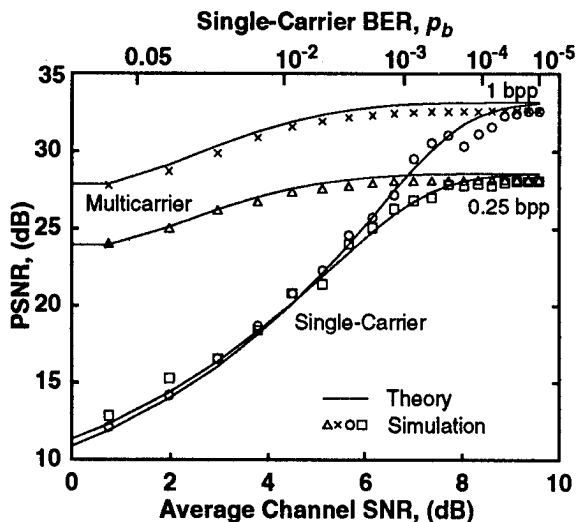


Fig. 3 PSNR as a function of average SNR of the channel and single-channel BER. Both theoretical and simulation results are shown for comparison.

Fig. 3 shows the peak signal-to-noise ratio (PSNR) as a function of average signal-to-noise ratio (SNR) of the channel, and the corresponding BER of the single-carrier system. The image is compressed to both 0.25 bpp (bit/pixel) and 1 bpp. Both theoretical results and simulation results are shown for comparison. In the calculation of the theoretical result, the channel distortion is computed using expression (5). The difference between the theoretical and simulation PSNR is smaller than 0.8 dB, allowing us to infer the validity of both the Laplacian distribution and the approximation of transition probabilities (3). For high channel SNRs, the PSNR of single-carrier and multicarrier systems are identical because the BER is small and the quantization distortion is much larger than the channel-induced distortion.

For low channel SNRs, the PSNR of the multicarrier system is much larger than that of the single-carrier system. At SNRs less than 3 dB, the improvement in the PSNR of the multicarrier over the single-carrier system is more than



Fig. 4 The compressed image of 0.25 bpp and the bit allocation table. PSNR = 28.05 dB.



Fig. 5 Reconstructed image at the receiver of single-carrier and multicarrier systems. The average SNR of the channel is 4.32 dB, corresponding to a single-carrier BER of $p_b = 10^{-2}$. (a) Transmitted through single-carrier system, PSNR = 20.52 dB. (b) Transmitted through multicarrier system, PSNR = 27.01 dB.

9.5 dB for the 0.25 bpp image and more than 13.5 dB for the 1 bpp image. Fig. 4 shows the compressed image of 0.25 bpp and the corresponding bit-allocation table. Fig. 5 compares the images transmitted over a single-carrier and a multicarrier system for SNR = 4.32 dB, which corresponds to a single-carrier BER of 10^{-2} . A 6.5-dB improvement in PSNR is achieved by use of multicarrier modulation. While channel errors cause the PSNR of the image transmitted over the single-carrier system to degrade by 7.5 dB, that of the image transmitted over the multicarrier system degrades by only 1 dB.

5. Conclusions

A combined source-channel coding scheme using multicarrier modulation is proposed and analyzed for DCT-coded images. Allocation of subchannel powers according to the importance of each bit achieves a large improvement over single-carrier modulation. A numerical example shows that on very noisy channels, multicarrier systems can achieve an improvement over single-carrier systems of more than 9 dB in terms of signal-to-distortion ratio.

In general, subband-coded images [10] have better quality than DCT-coded images. We are currently studying the application of the combined source-channel coding scheme to subband-coded images.

References

1. C. E. Shannon, "A mathematical theory of communication," *Bell System Tech. J.*, vol. 27, 1948, pp. 379-423, pp. 623-656.
2. C. E. Shannon, "Coding theorems for a discrete source with a fidelity criterion," *IRE Nat. Conv. Rec.*, Mar. 1959, pp. 142-163.
3. I. Kalet, "The multitone channel," *IEEE Trans. Commun.*, vol. 37, 1989, pp. 119-124.
4. J. A. C. Bingham, "Multicarrier modulation for data transmission: An idea whose time has come," *IEEE Commun. Mag.*, May 1990, pp. 5-14.
5. S. P. Lloyd, "Least squares quantization in PCM," Bell Laboratories Technical Note, 1957, published in *IEEE Trans. Inform. Theory*, vol. IT-28, 1982, pp. 129-137.
6. J. Max, "Quantizing for minimum distortion," *IRE Trans. Inform. Theory*, vol. IT-6, Mar. 1960, pp. 7-12.
7. R. E. Totty and G. C. Clark, "Reconstruction error in waveform transmission," *IEEE Trans. Inform. Theory*, vol. IT-13, 1967, pp. 336-338.
8. K.-P. Ho, Optimal Utilization in Subcarrier and Multicarrier Systems, Ph.D. Dissertation, University of California at Berkeley, 1995.
9. A. K. Jain, *Fundamentals of Digital Image Processing*, Englewood Cliffs, NJ: Prentice-Hall, 1989.
10. J. W. Woods, Ed., *Subband Image Coding*, Boston: Kluwer Academic, 1991.

Error Concealment Enhancement by Using the Reliability Outputs of a SOVA in MPEG-2 Video Decoder

Susanna Aign *

German Aerospace Research Establishment (DLR), Institute for Communications Technology
D-82234 Oberpfaffenhofen, Germany, Tel.: + 49-8153-28-2862, Fax: + 49-8153-28-1442

Abstract

The MPEG-2 source coding algorithm is very sensitive to channel disturbances. A single bit error in the bitstream will cause a high degradation of picture quality due to the use of variable length coding. Therefore, for picture replenishment error concealment techniques (ECT's) may be applied at the receiver.

The aim of this article is to study the error concealment (EC) enhancements due to the use of the soft output values of the SOVA (Soft Output Viterbi Algorithm) as an error detection technique (EDT) for MPEG-2 inter coded pictures applied for terrestrial broadcasting.

1 Introduction

The future terrestrial digital TV/HDTV signal will be a highly compressed signal because of the restricted bandwidth of the channels (UHF and VHF). The TV/HDTV source coding algorithms used for this applications will be based on MPEG-2 [1].

The TV layer should be highly protected. An example of a channel coding and modulation scheme for terrestrial hierarchical TV/HDTV-broadcasting is described in [2, 3]. At very long distances or at worst reception conditions, i.e. deep fades or impulsive noise, the portable receiver, which suffers from the non existence of a graceful degradation, may risk to receive nothing (the threshold effect). To avoid this or to enhance the picture quality, one may apply the ECT's at the receiver.

The aim of this article is to study the EC enhancements in MPEG-2 Video decoder due to the use of the reliability outputs of the SOVA, taking into account a real transmission medium [2]. For the simulations a Channel Model is used, which reproduces the errors and the appropriate reliability values for each bit at the receiver side.

The paper is organized as follows: In section 2 the Channel Model for the simulations is examined. In section 3 the different ED and temporal ECT's are described briefly. Simulation results are given in section 4 and section 5 is devoted to some conclusions.

2 The Channel Model

In this section a Channel Model, i.e. an error-pattern model for the whole terrestrial transmission scheme, is described. This model reproduces the error-pattern in the channel decoder. It is an easy way to simulate the error-pattern without the simulation of the whole system.

*The author is within the European dTTb-Race and the German ^HDTV_T projects

This model can also be used for a hierarchical scheme with different layers [2].

The channel encoder is based on a concatenated coding scheme. The inner code is a convolutional code with memory $m = 6$ and different rates for the different layers, and the outer code is a RS (204, 188, 17) code over $GF(2^8)$, which can handle up to $t_{max} = 8$ errors. The outer RS-codewords are adapted to the MPEG-2 Transport Packets of length 188 bytes.

The super channel comprises a channel encoder, a modulator, an OFDM multiplexer, the transmission channel, an OFDM demultiplexer, a demodulator and a channel decoder. The model can be described as follows:

One example for an interleaver between the inner and the outer code is given in Figure 1. The length of the outer code is $N = 204$ and the depth of the interleaver is $I = 8$. The bits of the inner decoder are mapped into symbols of 8 bits (one RS-symbol) and are then written out in rows into the interleaver-matrix. The RS-codewords from the outer code will be read out in columns.

The inner decoder is a Viterbi-decoder. This decoder generates burst-errors. Therefore, it is necessary to define two probabilities for the symbol-error-probability: First the probability $P(S_w|S'_r)$ that the current symbol S is wrong under the condition that the previous symbol S' was right, and on the other hand the probability $P(S_w|S'_w)$ that the current symbol is wrong under the condition that the previous symbol was also wrong.

The symbols in the interleaver-matrix consist of 8 bits. For these bits the probability $P(B_w|S_w)$, that one bit is wrong under the condition that the symbol is wrong, is defined. If the symbol is right, the Viterbi-decoder has corrected the wrong bits.

Now these three probabilities are used to produce a Channel Model. First one goes through the rows of the interleaver-matrix. The first symbol will be disturbed with the probability $P(S_w|S'_r)$. If the symbol is wrong, errors will be produced in the bits of this symbol with the probability $P(B_w|S_w)$. The next symbol will be disturbed with either $P(S_w|S'_r)$ or $P(S_w|S'_w)$ depending on whether the previous symbol was disturbed. Then the bits of this symbol will be disturbed with $P(B_w|S_w)$ and so on. If all symbols are handled, the errors of the inner-decoder are reproduced. The three probabilities will be obtained from computer simulations of the whole transmission scheme. They depend on the SNR, on the channel and on the code-rates.

To reproduce the error-patterns at the output of the outer-decoder, the RS-words are read out in columns and the wrong symbols will be counted. If the number of errors are equal or less than the number of correctable errors, all errors will be corrected by the outer RS-code, so they can

be deleted in the total column. If this number exceeds the number of correctable errors, the errors in that column remain. Only the first $k = 188$ information symbols from the RS-codeword are taken, to obtain the output error pattern.

For a hierarchical system with different inner and outer decoders, one can obtain a Channel Model by combining the corresponding models. This model is used for the simulations.

For ED this Channel Model can be extended for providing some reliability information for each bit. Assuming an inner SOVA [4] the inner decoder can provide reliability information for each bit. Because the outer RS-Decoder is a systematic code, the reliability information is also useful after the outer decoder. If the RS-decoder detects one wrong packet, this packet will be sent to the source decoder without change, so that the reliability information after the inner decoder is also legal for the bits after the outer decoder. This reliability information can also be used for ED.

The soft output values of the SOVA are the log-likelihood ratios for each bit. The definition of the log-likelihood ratio is:

$$L = \ln \left(\frac{P(x=1|y)}{P(x=-1|y)} \right) = \ln \left(\frac{P(x=1|y)}{1 - P(x=1|y)} \right), \quad (1)$$

where $P(x=1|y)$ denotes the probability that $x=1$ was sent under the condition that y was received. Assuming an AWGN-channel with variance σ_c^2 and the mean $\mu_c = 1$, the probability for the received symbol is:

$$P(y|x=1) = \frac{1}{\sqrt{2\pi}\sigma_c} e^{-\frac{(y-1)^2}{2\sigma_c^2}}, \quad (2)$$

For the probability that $x=1$ was sent under the condition that y is received one obtains with Bayes:

$$P(x=1|y) = \frac{P(x=1)P(y|x=1)}{P(x=1)P(y|x=1) + P(x=-1)P(y|x=-1)}. \quad (3)$$

With $P(x=1) = P(x=-1) = 1/2$ this reduces to

$$P(x=1|y) = \frac{P(y|x=1)}{P(y|x=1) + P(y|x=-1)}. \quad (4)$$

By inserting equation 2 one obtains:

$$P(x=1|y) = \frac{1}{1 + e^{-\frac{2y}{\sigma_c^2}}}. \quad (5)$$

With this equation the log-likelihood value (L-value) is:

$$L = \ln \left(\frac{P(x=1|y)}{P(x=-1|y)} \right) = \ln \left(\frac{\frac{1}{1 + e^{-\frac{2y}{\sigma_c^2}}}}{\frac{1}{1 + e^{\frac{2y}{\sigma_c^2}}}} \right) = \frac{2}{\sigma_c^2} \cdot y. \quad (6)$$

This is the L-value after the channel before the inner decoder. Because the received values y are gaussian distributed the L-values are also gaussian distributed with $\sigma_{Lc} = \frac{2}{\sigma_c^2} \cdot \sigma_c$ and $\mu_{Lc} = \frac{2}{\sigma_c^2} \cdot \mu_c$.

The soft-output values of the SOVA are also L-values. From simulations one can see that the power density function (pdf) of the L-values after the inner decoder can also be approximated by a gaussian distribution with $\sigma_{Ls} = \frac{2}{\sigma_s^2} \cdot \sigma_s$ and $\mu_{Ls} = \frac{2}{\sigma_s^2} \cdot \mu_s$ if assuming an AWGN-channel (Figure 2 where $x=1$ was sent). Therefore, for

the soft outputs one needs only the variance σ_s^2 and the mean μ_s of the outputs of the inner decoder, where for the mean it seems certain that $\mu_s = 1$ with the assumption that $x=1$ was sent.

The variance is determined by the BER after the inner decoder and by the corresponding E'_s/N_0 . The variance σ_s^2 to the corresponding BER can be obtained with the following equations:

$$BER = \frac{1}{2} * \operatorname{erfc} \left[\frac{E'_s}{N_0} \right] \quad \text{with} \quad \operatorname{erfc}[x] = 1 - \int_0^x e^{-t^2} dt$$

$$\sigma_s = \sqrt{\frac{N_0}{2 \cdot E'_s}}$$

With a given BER after the inner decoder the corresponding σ_s can be computed. Note, that the E'_s/N_0 after the inner decoder is not the E_s/N_0 of the channel. With the knowledge of the variance and the mean, one can obtain the pdf for the reliability informations.

The Channel Model is a model with two states: one state describing the right path and one describing the wrong path of the Viterbi-decoder. The reliability information for the bits in the wrong path is usually small. If $x=1$ was sent, the pdf of the L-values is the following:

$$pdf(L) = \begin{cases} \frac{1}{\sqrt{2\pi}\sigma_{Ls}} e^{-(L-\mu_{Ls})^2/2\sigma_{Ls}^2} & : L < 0 \wedge S_w \\ & \text{(wrong path, wrong bit)} \\ \frac{1}{\sqrt{2\pi}\sigma_{Ls}} e^{-(L+\mu_{Ls})^2/2\sigma_{Ls}^2} & : L \geq 0 \wedge S_w \\ & \text{(wrong path, right bit)} \\ 0 & : L < 0 \wedge S_r \\ & \text{(right path)} \\ \frac{1}{\sqrt{2\pi}\sigma_{Ls}} \left(e^{-(L-\mu_{Ls})^2/2\sigma_{Ls}^2} - e^{-(L+\mu_{Ls})^2/2\sigma_{Ls}^2} \right) & : L \geq 0 \wedge S_r \\ & \text{(right path)} \end{cases}$$

If one bit in the wrong path is correct, then the L-value is distributed in the positive side of the pdf, otherwise the L-value lies in the negative side of the pdf. It should be noted that the L-values for a sent $x=-1$ are gaussian distributed with σ_{Ls} and $\mu_{Ls} = \frac{2}{\sigma_s^2} \cdot (-1)$. Therefore, the mirrored pdf(L) has to be used.

If one simulates the L-values for each bit additionally in the Channel Model for the wrong and the right path respectively, one obtains a good approximation for the L-values after the SOVA. These reliabilities can also be used for ED.

For an Rayleigh fading channel the L-values after the SOVA are no more gaussian distributed. The pdf is then approximately the convolution of an Rayleigh distribution with an gaussian distribution. The computation of this function is more complex. The Channel Model should be so simple as possible and with the assumption that the L-values are gaussian it seems to be a good compromise between complexity and precision.

3 Error Detection and Error Concealment

3.1 Error Detection

For EC measures, proper ED is needed. Three ways of ED are considered: first the source decoder can detect errors [5], but with this method, many errors will still remain undetected and there is the risk of error propagation.

Therefore, another way already mentioned is: the channel decoder can also detect errors. The outer RS-decoder can detect wrong packets with high reliability [6]. A wrong packet will be indicated in the transport header. The header is about 4 bytes and the payload consists of 184 bytes. If the source decoder knows the errors in packets, the slices [1] where the packet errors are, will be concealed until the next synchronization point (the next slice). The worst case is that, if this packet would contain the slice start code. Then the rest of the current slice and the whole next slice must be concealed. This EDT finds the region where errors are in the bitstream. The region is at least 184 bytes long and these 184 bytes will cause the loss of synchronization until the next slice. This EDT gives no information about the exact location of the errors in the block. In many cases where the decoder failed, the RS-word has $t_{max} + 1$ errors. If these errors are at the end of the RS-word, decoding until another EDT finds errors could be better because the information, which could be correct in the bitstream, will be used. But this EDT must be a method with high reliability. One solution for using the correct part of a wrong packet is the use of the soft information at the output of the inner channel decoder [4] as a reliability for each symbol. The SOVA gives the log-likelihood values for each bit. From this information one can obtain the reliability for each symbol of the RS-word. With equation 1 one obtains for the probabilities for each bit:

$$P(x = 1|y) = \frac{e^L}{1 + e^L}$$

The probability $P(S)$, that one symbol of one RS-word is correct (with the assumption that the bits are statistically independent), is:

$$P(S) = \prod_{j=1}^8 \frac{e^{|L(j)|}}{1 + e^{|L(j)|}} \approx \frac{e^{|L'|}}{1 + e^{|L'|}} \quad \text{with } |L'| = \min_j L(j)$$

With this value one obtains a measure for the probability of each symbol in one Transport Packet. With a certain threshold one can say with high reliability, if the next symbol is wrong or not. The correct part of the erroneous packet can therefore be used until the first symbol is wrong in one packet.

3.2 Error Concealment

The ECT's used in this article for comparing the EDT's are temporal EC with and without motion compensation [5]. The simple temporal EC is a simple copy of the wrong parts of the previous anchor picture into the current picture. With this EC method shifts will be visible, if there is motion. The temporal ECT with motion compensation uses in addition the motion-vectors from one nearest macroblock in the current picture. The second method in the most cases is the best one, because high motion becomes not visible. But if the motion from the current macroblock is a motion with another direction than the surrounding macroblocks, this error becomes visible. This occurs also if there are burst errors which cause more than one disturbed slice, and the motion vectors which are considered are too far from the current macroblock. All ECT's will cause some remaining errors in the picture domain, because they could not be as good as the real picture data. Therefore, it seems worthwhile to use the soft information of the SOVA as an EDT, because there as much as errorfree data is used.

Other EC algorithms like spatial EC [7, 8] could have been used for comparing the EDT's, but they will lead to the similar results.

4 Simulation Results

Simulation results of different temporal ECT's with different EDT's in P- and B-pictures of MPEG-2 coded pictures are given in Table 1 and in Table 2. The different EDT's are ED in the channel decoder without soft information ('channel') and ED in the channel decoder with soft information ('sova'). Two different temporal ECT's are considered. One is simple temporal EC (simple copying from one previous picture, 'simple') and the other is temporal EC with motion compensation (with motion vectors from one nearest macroblock of the current picture, 'motion').

Error Concealment Comparison (PSNR)					
PER	simple-channel	simple-sova	motion-channel	motion-sova	without errors
10^{-1}					
Y	21.46	21.60	26.51	26.71	29.63
U	31.70	31.83	33.50	33.61	34.42
V	32.71	32.84	33.92	34.11	35.51
10^{-2}					
Y	27.10	27.13	29.03	29.06	29.63
U	33.94	33.95	34.29	34.30	34.43
V	34.93	34.94	35.17	35.18	35.51

Table 1: PSNR values for calendar (P-pictures)

Error Concealment Comparison (PSNR)					
PER	simple-channel	simple-sova	motion-channel	motion-sova	without errors
10^{-1}					
Y	25.45	25.68	28.07	28.19	29.12
U	33.96	34.00	34.18	34.14	34.34
V	35.17	35.21	35.30	35.34	35.54
10^{-2}					
Y	28.35	28.38	28.98	29.00	29.12
U	34.26	34.27	34.32	34.31	34.34
V	35.45	35.45	35.51	35.51	35.54

Table 2: PSNR values for calendar (B-pictures)

The simulation are carried out under the following conditions: the size of the TV picture of 4:2:0 format was 720x576 pixel. One slice consists of 44 macroblocks. The bit rate of 5 Mbit/sec is chosen, because it seems to be acceptable for a good TV quality (higher than PAL or SECAM). 20 P/B-pictures were disturbed with the packet error rate $PER = 10^{-1}$ and $PER = 10^{-2}$. The mean of the PSNR for the three components is shown in Table 1 and 2. The errors were simulated with the Channel Model, which reproduces the errors after the channel decoder (Rayleigh fading channel). The burst errors of the inner Viterbi-decoder were simulated.

The simulation results show that the main gain for ED with the soft output values is only 0.2 dB for the PSNR at $PER = 10^{-1}$ for the luminance component. One cause for these small improvements is that the slices are very long and that the amount of bits in the first part of the RS-word can be very small if one symbol error is at the beginning of one word. Because the synchronization point is at the next start of one slice, only a few macroblocks can be further decoded when using the remaining lossless part at the beginning of the RS-word. One way for obtaining better results is to make the slices shorter. Table 3 and 4 give the PSNR-values for the disturbed P- and B-pictures respectively, where the slice length is shorter (22 and 11 macroblocks instead of 44 macroblocks per slice).

Error Concealment Comparison (PSNR)						
PER	slice-length=22			slice-length=11		
	simple. sova	motion. sova	without errors	simple. sova	motion. sova	without errors
10^{-1} : U	Y 23.17	27.21	29.61	23.46	27.59	29.57
	32.03	33.38	34.41	32.52	33.78	34.39
	V 32.97	33.84	35.50	33.51	34.27	35.46
10^{-2} : U	Y 28.33	29.23	29.61	28.61	29.34	29.57
	34.11	34.34	34.41	34.17	34.33	34.39
	V 35.16	35.33	35.50	35.22	35.31	35.46

Table 3: PSNR values for calendar (P-pictures)

Error Concealment Comparison (PSNR)						
PER	slice-length=22			slice-length=11		
	simple. sova	motion. sova	without errors	simple. sova	motion. sova	without errors
10^{-1} : U	Y 26.74	28.55	29.08	26.88	28.61	28.99
	34.10	34.26	34.33	34.09	34.24	34.28
	V 35.31	35.40	35.52	35.31	35.39	35.46
10^{-2} : U	Y 28.64	29.00	29.08	28.75	28.92	28.99
	34.29	34.32	34.33	34.25	34.27	34.28
	V 35.48	35.51	35.52	35.44	35.44	35.46

Table 4: PSNR values for calendar (B-pictures)

The results show that for shorter slices the gain of using additional soft information is up to 2 dB for the luminance component for simple temporal EC at $PER = 10^{-1}$ whereas the gain for temporal EC with motion compensation is up to 1 dB. The temporal ECT with motion compensation is a very good ECT therefore, the gain is not so high. The reduced picture quality due to the use of more synchronization points in a video sequence with the bitrate of 5 Mbit/sec is negligible. In I-pictures, where no motion information exists, the gain will be higher because the ECT's like spatial EC and simple temporal EC will cause errors in the picture domain, therefore it seems worthwhile to use the correct part of one disturbed RS-word.

5 Conclusions

In this paper two different ECT's with two different ED methods for MPEG-2 compressed video sequences are studied. The first ECT is based on a simple temporal EC, where the previous anchor picture is copied into the current picture, where errors are detected. The second technique is the temporal EC with motion compensation. In this technique the motion vectors of a neighbouring macroblock are used for the EC of the current macroblock. The second technique is the best technique in the case of uniformly motion. With different high motion this technique can cause a few wrong blocks in the picture. The two EDT's are ED in the outer decoder of the channel decoder and the detection of wrong symbols by additionally using the soft information of the inner SOVA. It is shown that it is worthwhile to use the correct part of the RS-word until a symbol is wrong even if the ECT is not so good. It should be noted that the gain raises with shorter slices. For simple temporal EC the gain for the EDT with soft information is up to 2 dB for the luminance component at $PER = 10^{-1}$. For I-pictures the gain will be higher because no ECT is better than decoding on until the next symbol error.

Acknowledgement

I would like to thank Mr. L. Papke from DLR for helping me to define the Channel Model.

References

- [1] "MPEG-2 video and systems international standard." ISO-IEC/JTC1/SC29/WG11 MPEG 94, Nov. 1994.
- [2] K. Fazel and M. J. Ruf, "A hierarchical digital HDTV transmission scheme for terrestrial broadcasting," in *Proc. Globecom'93*, Dec. 1993.
- [3] G. Schamel, "Graceful degradation and scalability in digital coding for terrestrial transmission," in *Workshop on Digital HDTV*, 1993.
- [4] J. Hagenauer and P. Hoeher, "A Viterbi algorithm with soft-decision outputs and its application," in *IEEE Global Telecommunications Conference 1990 Conference Record*, vol. 3, pp. 47.1.1-47.1.7, November 1989.
- [5] S. Aign and K. Fazel, "Error detection & concealment measures in MPEG-2 video decoder," in *Proc. of the International Workshop on HDTV'94*, Torino, Oct. 1994.
- [6] R. J. McEliece and L. Swanson, "On the decoder error probability for Reed-Solomon codes," *IEEE Transaction on IT*, vol. IT-32, pp. 701-703, Sept. 1986.
- [7] S. Aign and K. Fazel, "Temporal & spatial error concealment techniques for hierarchical mpeg-2 video codec," in *Proceedings ICC'95*, Seattle, June 1995.
- [8] H. Sun and W. Kwok, "Error concealment with directional filtering for block transform coding," in *Proc. Globecom'93*, pp. 1304-1308, Dec. 1993.

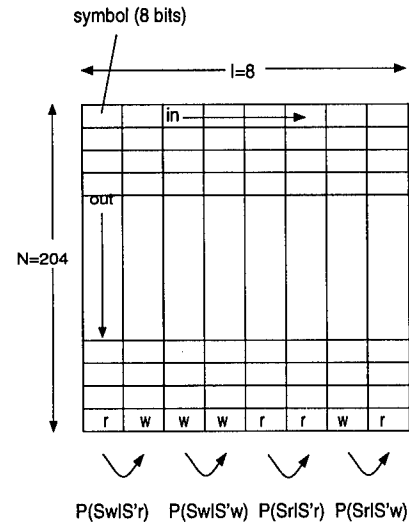


Figure 1: Interleaver

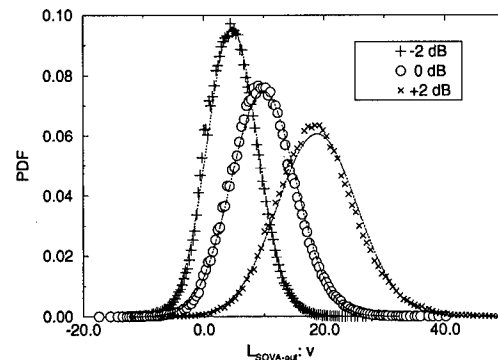


Figure 2: PDF(L) for different E_s/N_0

DCT/IDCT PROCESSOR DESIGN FOR HDTV APPLICATIONS

Avanindra Madiseti and Alan N. Willson Jr.

Integrated Circuits and Systems Laboratory
Department of Electrical Engineering
University of California at Los Angeles, CA 90024

1. INTRODUCTION

Transform coders, in particular the Discrete Cosine Transform (DCT), have been widely used in the implementation of low-rate codecs for video compression. The DCT has become an integral part of several standards such as MPEG [1], and CCITT Recommendations H. 261 and H.263 [2]. For real time implementation of the DCT at MPEG rates, general purpose DSP's [3] have been proposed. However, with the imminent arrival of High Definition Television and the considerably higher sample rates (75 MHz sampling frequencies) and higher throughput requirements, processors specific to the DCT (ASIC's) with highly parallel and/or pipelined architectures have been recently reported [4]. The use of such processors can be justified only if they result in a cost effective implementation. In this paper we will describe a simple but cost effective design of a combined DCT/IDCT processor. The implementation uses a parallel architecture that exploits symmetry properties in the DCT/IDCT algorithm and requires only simple *hardwired* multipliers. Clocking at 100 MHz, the processor is capable of handling real-time HDTV signals. The core area of the processor has been minimized while keeping the I/O requirements simple. Finite wordlength and accuracy studies have been carried out to ensure that the resulting implementation conforms to existing standards (H.261)[2].

2. COMPUTATION OF THE DCT/IDCT

The forward and inverse transforms can be written as a triple matrix product $Z = AXA^T$ and $X = A^TZA$ where $AA^T = I_N$ by virtue of the orthogonality of A , which is an $N \times N$ matrix. The decomposition to a triple matrix product requires $2N^3$ multiplications to be performed over N^2 clock cycles (or input sample periods) which requires $2N$ multiplies to be computed per input sample.

A standard block diagram of a DCT(IDCT) processor is shown in Fig. 1 where the computation of the 2D DCT has been broken down into two 1D DCT's (or IDCT's). The first computes $Y = AX$ (or A^TX) and the second computes $Z = YA^T$ (or YA). The $N \times N$ matrix-matrix multiply has been separated into N matrix-vector products. Thus, the basic computation performed by the DCT (or IDCT) is the evaluation of the $(N \times N)$ matrix by $(N \times 1)$ vector product. Each 1D DCT (or IDCT) unit must be capable

of computing N multiplies per input sample to perform a matrix-vector product.

If the input block X is scanned column by column, The intermediate product $Y = AX$ (or A^TX) is also computed column by column. However, since an entire row of Y has to be computed prior to the evaluation of the next 1D DCT, the intermediate result Y must be stored in an on-chip buffer. Since columns are written into the buffer and rows are read from it, it is commonly called the *transpose memory*.

The first 1D DCT/IDCT unit operates on rows of A (or A^T) and columns of X , while the second 1D DCT unit operates on a rows of Y and columns of A^T (or A). Since a column of A^T (A) is equivalent to a row of A (A^T), the second 1D DCT/IDCT unit is unnecessary if we can *multiplex* the first 1D DCT/IDCT unit between a column of X and a row of Y as shown in Fig. 2. However, the 1D DCT/IDCT unit must now process samples at *twice* the input sample rate, i.e, the 1D DCT/IDCT unit must be capable of computing $2N$ multiplies per input sample. We can exploit certain features of the 1D DCT/IDCT to reduce the computational overhead of the basic building block. The 8×8 DCT matrix can be written as

$$A = \begin{bmatrix} a & a & a & a & a & a & a & a \\ b & d & e & g & -g & -e & -d & -b \\ c & f & -f & -c & -c & -f & f & c \\ d & -g & -b & -e & e & b & g & -d \\ a & -a & -a & a & a & -a & -a & a \\ e & -b & g & d & -d & -g & b & -e \\ f & -c & c & -f & -f & c & -c & f \\ g & -e & d & -b & b & -d & e & -g \end{bmatrix}$$

where $a = \frac{1}{2} \cos \frac{\pi}{4}$, $b = \frac{1}{2} \cos \frac{\pi}{16}$, $c = \frac{1}{2} \cos \frac{\pi}{8}$, $d = \frac{1}{2} \cos \frac{3\pi}{16}$, $e = \frac{1}{2} \cos \frac{5\pi}{16}$, $f = \frac{1}{2} \cos \frac{3\pi}{8}$ and $g = \frac{1}{2} \cos \frac{7\pi}{16}$. Even rows of A are symmetric and odd rows are anti-symmetric. Thus, by exploiting this symmetry in the rows of A , and separating the even and odd rows, we get

$$\begin{bmatrix} Y(0) \\ Y(2) \\ Y(4) \\ Y(6) \end{bmatrix} = \begin{bmatrix} a & a & a & a \\ c & f & -f & -c \\ a & -a & -a & a \\ f & -c & c & -f \end{bmatrix} \begin{bmatrix} X(0) + X(7) \\ X(1) + X(6) \\ X(2) + X(5) \\ X(3) + X(4) \end{bmatrix}$$

$$\begin{bmatrix} Y(1) \\ Y(3) \\ Y(5) \\ Y(7) \end{bmatrix} = \begin{bmatrix} b & d & e & g \\ d & -g & -b & -e \\ e & -b & g & d \\ g & -e & d & -b \end{bmatrix} \begin{bmatrix} X(0) - X(7) \\ X(1) - X(6) \\ X(2) - X(5) \\ X(3) - X(4) \end{bmatrix}$$

This research was supported by the Office of Naval Research under Grant N00014-95-1-0231

Similarly, the 1D IDCT can be rewritten as:

$$\begin{bmatrix} Y(0) \\ Y(1) \\ Y(2) \\ Y(3) \end{bmatrix} = \begin{bmatrix} a & c & a & f \\ a & f & -a & -c \\ a & -f & -a & c \\ a & -c & a & -f \end{bmatrix} \begin{bmatrix} X(0) \\ X(2) \\ X(4) \\ X(6) \end{bmatrix} + \begin{bmatrix} b & d & e & g \\ d & -g & -b & -e \\ e & -b & g & d \\ g & -e & d & -b \end{bmatrix} \begin{bmatrix} X(1) \\ X(3) \\ X(5) \\ X(7) \end{bmatrix}$$

$$\begin{bmatrix} Y(7) \\ Y(6) \\ Y(5) \\ Y(4) \end{bmatrix} = \begin{bmatrix} a & c & a & f \\ a & f & -a & -c \\ a & -f & -a & c \\ a & -c & a & -f \end{bmatrix} \begin{bmatrix} X(0) \\ X(2) \\ X(4) \\ X(6) \end{bmatrix} - \begin{bmatrix} b & d & e & g \\ d & -g & -b & -e \\ e & -b & g & d \\ g & -e & d & -b \end{bmatrix} \begin{bmatrix} X(1) \\ X(3) \\ X(5) \\ X(7) \end{bmatrix}$$

The number of multiplies is halved since the $(N \times N) \times (N \times 1)$ matrix-vector multiply has been replaced by two $(\frac{N}{2} \times \frac{N}{2}) \times (\frac{N}{2} \times 1)$ matrix-vector multiplies which can be computed in parallel. Since the computation for both the DCT and the IDCT has been halved, the 1D DCT/IDCT unit in Fig. 2 now needs to compute only N multiplies per input sample. The savings in the multiplications comes at the expense of some data ordering and reordering that is required before and after the 1D DCT/IDCT unit.

3. ARCHITECTURE

Both the DCT and the IDCT require the computation of two (4×4) by (4×1) matrix-vector products. Our matrix-vector multipliers are designed to compute these matrix-vector products in parallel during four clock cycles. For four clock cycles, the matrix-vector multipliers operate on a column of X . For the next four clock cycles, the matrix-vector multipliers operate on a row of Y . This is the multiplex operation illustrated in Fig. 2. The DCT requires several additions/subtractions *prior* to the matrix-vector multiply whereas the IDCT requires the grouping of even and odd samples. This is performed by our Data Reorder Unit (DRU) which receives its inputs from the columns of X (off-chip) and the rows of Y (on-chip). Similarly, the DCT requires the regrouping of even and odd coefficients *after* the matrix-vector multiply while the IDCT requires some additions/subtractions. These are performed in the Inverse Data Reorder Unit (IDRU). The completed forward (reverse) transformed coefficients Z are written off-chip while Y is written into the transpose memory which is implemented as a 64-word DRAM. Each memory cell is implemented as a three-transistor RAM (3T-RAM). The pixels of Y are delayed by four clock cycles such that $Y(0)$ arrives four clock cycles after $X(0)$. Input pixels $X(n)$ and output pixels $Z(n)$ enter and leave the chip a single pixel at a time. The overall architecture (and floorplan) of the chip is shown in Fig. 3. It consists of the following blocks: (1) Data Reorder Unit (DRU) (2) Two Matrix-Vector Multiplier Units (3) Inverse Data Reorder Unit (IDRU) (4) Transpose Memory

3.1. Matrix-vector Multiplication

The computation of the 1D DCT/IDCT requires two 4×4 matrices. The first 4×4 matrix has elements that can assume one of three values: a, c, f (possibly negated). Any input to this matrix-vector multiplier can multiply only one of three coefficients. The second 4×4 matrix has elements that assume one of four values: b, d, e, g (possibly negated). Similarly, any input to this matrix-vector multiplier can multiply only one of four coefficients.

The architecture of the ACF matrix-vector multiplier is shown in Fig. 4. It consists of three *hardwired* multipliers implementing multiplications by fixed coefficients a, c and f . An input x_e to the ACF multiplier bank is broadcast to all three multipliers. The products ax_e, cx_e, fx_e are available in parallel. A bank of four accumulators then selects one of these products to perform the various linear combinations required for the matrix-vector multiply over four clock cycles. Thus, at the end of four clock cycles, ACC0 has computed the sum of products corresponding to the first row of the matrix, ACC1 has computed the sum of products corresponding to the second row of the matrix, and so on. The sequence of inputs to the ACF matrix-vector multiplier bank for the DCT is: $X(3) + X(4)$, $X(2) + X(5)$, $X(1) + X(6)$, $X(0) + X(7)$, $Y(3) + Y(4)$, $Y(2) + Y(5)$, $Y(1) + Y(6)$, $Y(0) + Y(7)$. For the IDCT, the sequence of inputs is: $X(4)$, $X(2)$, $X(6)$, $X(0)$, $Y(4)$, $Y(2)$, $Y(6)$, $Y(0)$.

The architecture for the BDEG matrix-vector multiplier is shown in Fig. 5. It consists of four *hardwired* multipliers implementing multiplications by b, d, e and g . An input x_o to the BDEG multiplier bank is broadcast to all four multipliers. The products bx_o, dx_o, ex_o and gx_o are available in parallel to all four accumulators. The bank of four accumulators then selects one of these products to perform the various linear combinations over four clock cycles. As before, ACC0 computes the first sum of products, ACC1 computes the second sum of products, and so on. The sequence of inputs to the BDEG matrix-vector multiplier bank for the DCT is: $X(3) - X(4)$, $X(2) - X(5)$, $X(1) - X(6)$, $X(0) - X(7)$, $Y(3) - Y(4)$, $Y(2) - Y(5)$, $Y(1) - Y(6)$, $Y(0) - Y(7)$. For the IDCT, the sequence of inputs is: $X(3)$, $X(5)$, $X(1)$, $X(7)$, $Y(3)$, $Y(5)$, $Y(1)$, $Y(7)$. The order in which the accumulators select their products is stored as control information in a small ROM. The outputs of the accumulators are multiplexed into the IDRU for further post-processing.

3.1.1. Hardwired Multipliers

Since the multiplier coefficients are fixed, we adopted a *hardwired* multiplier approach with the coefficients represented by a Signed Digit (SD) code. The primary advantage of the signed digit representation is that it allows most numbers to be represented with fewer non-zero digits. Table 1 lists the *hardwired* coefficients and their signed-digit representations. The number of non-zero bits is dictated by accuracy and finite wordlength specifications, and has been determined by simulation. The multiplier coefficients are accurate to four decimal places. From Table 1 we can see that four to six non-zero bits are adequate to represent the

coefficients, which *significantly* reduces the hardware complexity of the multiplier bank.

3.1.2. Accumulator

The accumulator shown in Fig. 6 consists of a 4-to-1 multiplexer that selects between one of the (three) four products at any given time instance. A negative coefficient requires that the selected product be subtracted from the current accumulated value. This is accomplished by the conditional invert (xor) unit. The contents of the accumulator are latched into the output register (OUTREG) once every four clock cycles and then reset to zero. This is accomplished by the signal *reset*. The controls for the 4-to-1 multiplexer *sel*[0 : 1], conditional invert, and reset for both the DCT/IDCT modes of operation, are stored in a ROM.

4. FINITE WORDLENGTH SIMULATIONS

We have carried out finite wordlength simulations to ensure that our implementation meets the specifications dictated by the standards (H.261). Simulations were carried out on a set of 10,000 8×8 blocks. These blocks were generated by the random number generator specified in [10]. Simulations were carried out for the three cases (a) $L = -256$, $H = 255$, (b) $L = H = 5$, and (c) $L = H = 300$, where L and H are the lower and upper bounds on the random numbers (i.e., $-L < X < H$). The peak mean square error and overall mean square error are illustrated in Figs.7-8 for the case $L = -256$, $H = 255$. An internal wordlength of 22 bits has been found to be adequate. The error characteristics of the core processor are summarized in Table 2.

5. IC CORE CHARACTERISTICS

Our DCT/IDCT processor has been designed using a $0.8\text{-}\mu\text{m}$ CMOS cell library. The library includes high-speed parameterizable carry-select adders, registers and multiplexers, among other cells. The 22-bit carry-select adder determines the critical path, which is well under 10 ns. This permits the realization of the 100 MHz clock and sample rate. The layout has been generated using the Mentor Graphics GDT design tools. The core measures under 10 mm^2 with a transistor count of 67,000 transistors. The core characteristics have been summarized in Table 3. A single pin determines the forward or inverse modes of operation. A single start pulse is required to initialize the chip. All other control signals are generated internally on-chip.

6. CONCLUSION

The 10 mm^2 core area of our 2D DCT/IDCT processor compares very favorably with core areas reported in the recent literature. This results from (a) the use of a fast algorithm that permits the use of only one 1D DCT/IDCT unit for the 2D transform, and (b) an architecture that results in a common datapath that is shared by both the DCT and the IDCT. The architecture requires seven hardwired multipliers and eight accumulators. A significant savings in area has been obtained by allocating just enough precision to the hardwired multipliers that the implementation

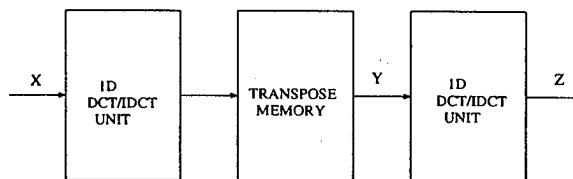


Figure 1: Basic DCT/IDCT Unit

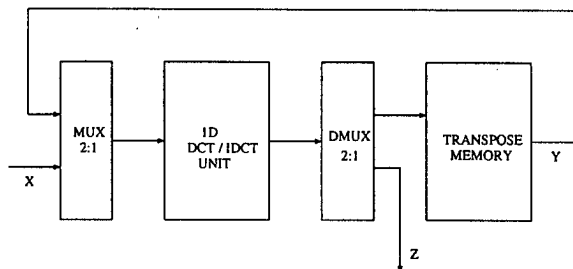


Figure 2: Multiplexed DCT/IDCT Unit

is compliant with the existing standards. The processor has been designed with a parameterizable input wordlength for applications that might need more precision. Clocking at 100 MHz, the processor can meet the real time processing requirements of currently proposed HDTV systems.

7. REFERENCES

- [1] ISO/IEC JTC1/SC29/WG11, MPEG Committee Draft CD11172, 1991
- [2] CCITT Recommendation H.261 (1990) & H.263 (1993)
- [3] K. Kikuchi *et al.*, "A single chip 16-bit 25 ns realtime video/image signal processor," *ISSCC Dig. Technical Papers*, pp. 170-171, Feb. 1989.
- [4] M. Matsui *et al.*, "200 MHz compression macrocells using low-swing differential logic," *ISSCC Dig. Technical Papers*, pp. 254-255, Feb. 1994.

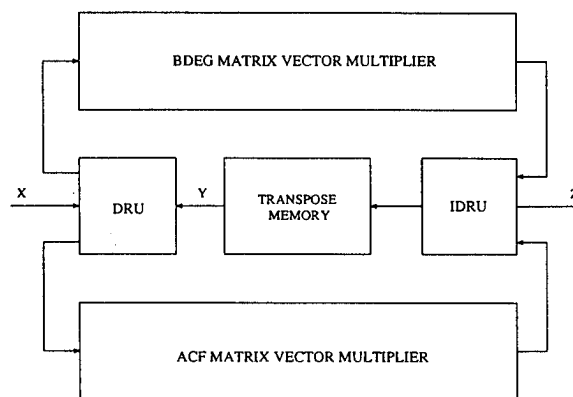


Figure 3: Floorplan and Architecture

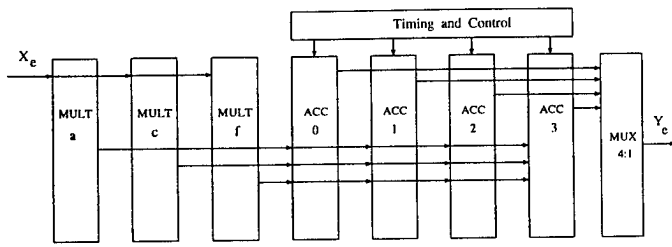


Figure 4: acf matrix vector multiplier

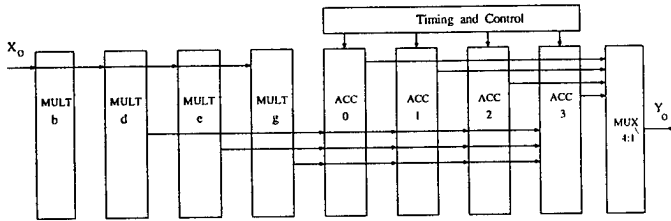


Figure 5: bdeg matrix vector multiplier

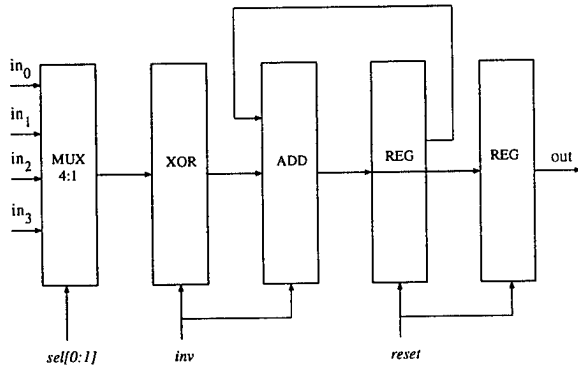


Figure 6: Accumulator

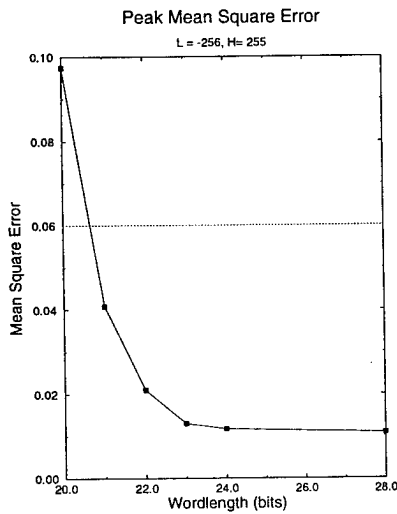


Figure 7: Peak Mean Square Error

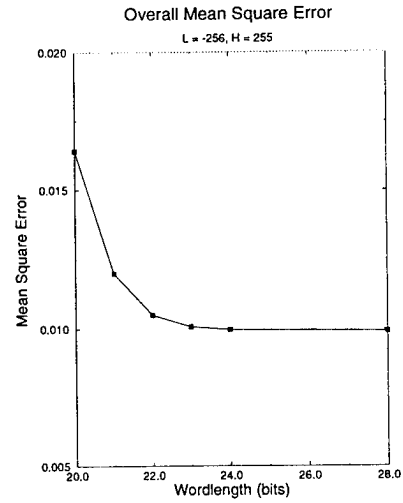


Figure 8: Overall Mean Square Error

	value	12 bit	SD representation	bits
a	0.35355	0.35351	$2^{-2} + 2^{-4} + 2^{-5} + 2^{-7} + 2^{-9} = 0.35352$	5
b	0.49039	0.49023	$2^{-1} - 2^{-7} - 2^{-9} + 2^{-13} = 0.49036$	4
c	0.46194	0.46191	$2^{-1} - 2^{-5} - 2^{-7} + 2^{-10} = 0.46191$	4
d	0.41573	0.41552	$2^{-2} + 2^{-3} + 2^{-5} + 2^{-7} + 2^{-9} - 2^{-12} = 0.41577$	6
e	0.27779	0.27734	$2^{-2} + 2^{-5} - 2^{-8} + 2^{-11} = 0.27783$	4
f	0.19134	0.19091	$2^{-3} + 2^{-4} + 2^{-8} - 2^{-14} = 0.19135$	4
g	0.09755	0.09716	$2^{-4} + 2^{-5} + 2^{-8} - 2^{-13} = 0.09753$	4

Table 1: Signed Digit Representation of the DCT Coefficients

	Spec.	L,H = -256,255	L,H = 300	L,H = 5
Peak Pixel Error	≤ 1	1	1	1
Peak Pixel M.S.E.	≤ 0.06	0.0134	0.0153	0.0139
Overall M.S.E.	≤ 0.02	0.0104	0.0101	0.0028
Peak Pixel Mean Error	≤ 0.015	0.0133	0.0125	0.0139
Overall Mean Error	≤ 0.0015	0.00096	0.0011	0.0011

Table 2: Accuracy of Processor

Inputs	9 bits (DCT), 12 bits (IDCT)
Outputs	12 bits (DCT), 9 bits (IDCT)
Internal Wordlength	22 bits
Technology	0.8- μ m CMOS, triple metal
No. of Transistors	67,000
Core Size	10 mm ²
Clock Rate	100 MHz
Mode Selection	DCT or IDCT
Block Size	8 \times 8
Accuracy	CCITT compliant

Table 3: Core Characteristics

IMPACT OF TROPOSPHERIC SCINTILLATION ON DIRECT-SEQUENCE SPREAD-SPECTRUM SATELLITE COMMUNICATION NETWORKS

Mohamed-Slim Alouini and Paul G. Steffes

School of Electrical and Computer Engineering
Georgia Institute of Technology
Atlanta, Georgia 30332-0250, USA
E-mail: paul.steffes@ee.gatech.edu

ABSTRACT

Tropospheric scintillation can seriously affect satellite links operating at K_a -band. The average bit error probability for a multiuser binary direct-sequence spread-spectrum satellite communication network operating under amplitude scintillation is evaluated. Numerical results are presented to illustrate performance comparisons of systems operating under typical scintillation statistics. As in the single user case, it is shown that the average system performance gradually degrades as the scintillation intensity increases and is worse for a high variability of these events. Results also indicate that the impact of amplitude tropospheric scintillations becomes less important as the number of asynchronous active users increases.

1. INTRODUCTION

New commercial applications are being promoted for the use of spread-spectrum (SS) techniques for satellite communication systems including: (i) Low- to medium-density traffic for interactive business transactions (credit card verifications, financial, and reservations services), (ii) Single-hop, very low response time links for voice, data, and facsimile direct communications, and (iii) Direct broadcasting from satellites (DBS). In the first application, asynchronous code-division multiple-access (CDMA) allows low-cost very small aperture terminals (VSATs) to communicate with a hub-station through a star network. The second application consists of a CDMA fully meshed network of small personal communications terminals (PCTs) conveying in demand-assignment multiple access (DAMA) fashion. The DBS application uses synchronous code domain multiplexed (CDM) signals to transmit different channels from a broadcasting ground station (cable company, satellite company, "sky-music", etc.) to fixed and/or mobile VSATs. Although there are two basic forms of SS, frequency hopping (FH) and direct sequence (DS), the latter is more frequently used for satellite communication networks.

Additionally, the next generation of geostationary communications satellites will take advantage of operation at K_a -band (20/30 GHz) with its large available bandwidths, and using high gain narrow spot beam antennas that will

be able to support smaller user terminals. Unfortunately, atmospheric effects including rain attenuation and tropospheric amplitude scintillation can seriously affect the quality of transmission at these high microwave frequencies. The scintillation degradation effect can even become predominant for low-margin VSAT and PCT systems operating at dry low-elevation sites.

Accurate evaluation of the performance of these networks is of interest in planning and designing efficient fading compensation methods such as (i) forward error correction (FEC), and automatic repeat request (ARQ) schemes, and (ii) adaptive modulations and power control techniques. As part of the Advanced Communications Technology Satellite (ACTS) propagation experiments program, the Georgia Institute of Technology has been involved in the K_a -band channel characterization and in the estimation of propagation impairments on the performance of VSATs [1]. Of key interest are experimental and theoretical studies of the impact of scintillation on SS signals.

This paper examines the performance of a direct sequence spread-spectrum (DS/SS) satellite communication system subject to tropospheric amplitude scintillation. The following section gives the statistical characterization of scintillation then describes the scintillating channel model. Section 3 presents the DS/SS system model and, the derivation of the average bit error probability (BER). The performance results calculated for specific scintillation statistics are reported in section 4. The paper concludes with a discussion of the results and directions for future research.

2. SCINTILLATING CHANNEL MODEL

Tropospheric scintillation results from random temporal variations and spatial inhomogeneities in the refractive index along the radio propagation path. It appears as an instability in both the amplitude and the phase of the signal. In this paper, we assume that the scintillation-induced phase jitter is small compared to the jitter generated by satellite and ground station frequency converters. The discussion is therefore limited to the impact of amplitude scintillation.

During a typical scintillation event, the received satellite signal amplitude fluctuates at a rate of approximately 1/3 Hz for a time period up to about one and a half hour. These events tend to occur in the early afternoon on hot humid summer days, and their effect is polarization inde-

This work was supported by NASA Lewis Research Center under Contract NAS3-27361.

pendent but is more pronounced at low-elevation angles, higher frequencies, and for small-diameter receiving antennas [2].

Based on the Rytov approximation and Tatarskii's theoretical formulation, one can characterize amplitude scintillations by the logarithmic stochastic process $\chi(t)$ [3]. Due to variations in meteorological conditions on the propagation path, $\chi(t)$ is a stationary zero mean Gaussian process only during short periods of time during which its intensity σ_χ remains constant. However as the weather conditions change, the refractive index structure parameter varies, inducing an inherent variability in σ_χ . This causes the scintillation long-term probability density function (pdf) to diverge from the normal distribution. This divergence is especially clear in the tails of the pdf. Since short-term statistics are insufficient for satellite communications system performance evaluations (in term of average BER and link availability), Mousley and Vilar [3] proposed a long term statistical model for $\chi(t)$ that was experimentally validated at the X-band and at the higher Ka-band [3]. According to this model, σ_χ^2 is itself considered to be a random variable following a log-normal distribution with $\ln(\sigma_m^2)$ mean and σ_σ standard deviation. The parameters σ_m and σ_σ have to be characterized for a particular site and depend mainly on its climatological conditions, the operating frequency, the receiver antenna diameter and the link elevation angle. This model prescribes the normal pdf for short-term log-amplitude fluctuations as a conditional pdf, conditioned on the random variable σ_χ ; the resulting long-term pdf is determined by averaging over the range of σ_χ . This pdf is the Mousley-Vilar pdf $p_\chi(\chi)$, and is given by [3]

$$p_\chi(\chi) = \int_0^{+\infty} \frac{1}{\pi \sigma_\sigma \sigma_\chi^2} \exp \left[-\frac{\chi^2}{2\sigma_\chi^2} - \frac{(\ln(\sigma_\chi^2/\sigma_m^2))^2}{2\sigma_\sigma^2} \right] d\sigma_\chi \quad (1)$$

Taking the mean variance of the Mousley-Vilar pdf the long-term (or average) variance σ_χ^2 of χ is related to σ_m and σ_σ by $\sigma_\chi^2 = \sigma_m^2 \exp(\sigma_\sigma^2/2)$.

The scintillating communication channel is modeled as an additive white Gaussian noise (AWGN) channel affected by tropospheric amplitude scintillation. At the output of the channel, the scintillating received signal $r(t)$ can therefore be written as

$$r(t) = r_o(t) \exp(\chi(t)) + n(t) \quad (2)$$

where $n(t)$ is the channel AWGN stochastic process with zero mean and two sided spectral density $N_o/2$, and $r_o(t)$ is the unperturbed "clear sky" signal in which the information is carried. We assume in our analysis that the tropospheric scintillating channel is not frequency selective since its coherence bandwidth is about a few GHz. The channel is also considered to be slowly time varying since the scintillation spectrum has the appearance of a band-limited white noise with a roll-off frequency of about 1/3 Hz. The stochastic process $\chi(t)$ is thus assumed to have the following characteristics: (i) statistically modeled by the Mousley-Vilar distribution, (ii) uncorrelated with the AWGN random process $n(t)$, (iii) constant over the total signal bandwidth, and (iv) remains constant during a bit time T .

3. PERFORMANCE ANALYSIS

The effect of amplitude scintillation on the performance of the satellite-earth channel had been initially accommodated by introducing an extra fixed degradation in the nominal budget link [4]. A more accurate method of BER evaluation in the presence of scintillation has been suggested by Banjo and Vilar [5]. This method was developed for single receivers using binary PSK modulation. In this section, we extend this method to a multi-user SS satellite communication system operating in a scintillating environment.

Assuming a binary DS/SS system such as described by Pursley [6], K users simultaneously share a channel, each transmitting with power P at a common carrier frequency $f_o = 2\pi\omega_o$, using a data rate $R = 1/T$ and a chip rate $R_c = 1/T_c$. Each transmitter k ($1 \leq k \leq K$) is assigned a specific code sequence ($a_j^{(k)}$) of chips elements (+1, -1), so that its code waveform is given by

$$a_k(t) = \sum_{j=-\infty}^{+\infty} a_j^{(k)} P_{T_c}(t - jT_c) \quad (3)$$

The function P_T denotes the unit rectangular pulse of duration T . The code sequence ($a_j^{(k)}$) is assumed to be periodic with period or processing gain $N = T/T_c$. The data signal $b_k(t)$ is binary PSK modulated onto the carrier at f_o then spread by the k^{th} users's code sequence. The resulting k^{th} users's transmitted signal $s_k(t)$ is thus given by

$$s_k(t) = \sqrt{2P} a_k(t) b_k(t) \cos(\omega_o t + \theta_k) \quad (4)$$

where the phase angle θ_k is a random variable uniformly distributed over $[0, 2\pi]$ to take into account that the K users are not phase synchronous. Moreover, for asynchronous DS/CDMA systems, the user k is randomly delayed relative to a reference signal by τ_k modeled as a uniformly distributed independent random variable in the interval $[0, T]$. The composite signal $s_{tot}(t)$ can then be expressed as

$$s_{tot}(t) = \sum_{k=0}^K \sqrt{2P} a_k(t - \tau_k) b_k(t - \tau_k) \cos(\omega_o(t - \tau_k) + \theta_k) \quad (5)$$

However, in case of synchronous transmission, the time delays τ_k are not random and can be set to $\tau_k = 0$ for all users.

Our analysis assumes that the channel responds in the same way for all users. This is the case for a VSAT and PCT networks subject to the following scintillation scenarios:

- Only the down-link is affected by scintillations with an average intensity $\sqrt{\sigma_{\chi_d}^2}$.
- Only the up-link is affected by scintillations with an average intensity $\sqrt{\sigma_{\chi_u}^2}$ and for a network supporting transmitters from the same geographical region (i.e., having the same scintillation statistics). This is typically the case for a high gain Ka-band narrow spot beam.
- Both the up-link and down-link are affected by scintillations with an estimated overall average intensity

$\sqrt{\sigma_{\chi_o}^2} = \sqrt{\sigma_{\chi_u}^2 + \sigma_{\chi_d}^2}$ for a network connecting transmitters in region A to a receiver in region B. A looped-back experimental link (A is the same as B), such as that being used in the Georgia Tech ACTS experiment, can be considered as a particular case of this scenario.

For all these scenarios, the received signal $r(t)$ at the output of the channel may be written as

$$r(t) = s_{tot}(t) \exp(\chi(t)) + n(t) \quad (6)$$

Let us consider the i^{th} user's receiver and assume that it is correctly synchronized, such as $\theta_i = \tau_i = 0$. The decision variable Z_i at the output of this matched receiver is

$$Z_i = \int_0^T r(t) a_i(t) \cos(\omega_o t) dt \quad (7)$$

By assuming slow scintillation, and by writing the data signal waveform as $b_i(t) = \sum_{j=-\infty}^{+\infty} b_{i,j} P_T(t - jT)$, Z_i is found to be equal to

$$Z_i = \sqrt{\frac{P}{2}} T \exp(\chi) [b_{i,0} + I] + \int_0^T n(t) a_i(t) \cos(\omega_o t) dt \quad (8)$$

where I is the multiple access interference term (MAI) defined in [6] as a function of the discrete aperiodic cross-correlation function. Under the standard Gaussian approximation (large number of users and high processing gain, i.e., $K \geq 10$ and $N \geq 200$) the MAI is modeled by a zero-mean normal distribution. Thus, Z_i may be considered to be a conditionally Gaussian random variable (conditioned on χ) so that

$$E[Z_i/\chi] = \sqrt{P/2} T \exp(\chi) \quad (9)$$

and

$$Var[Z_i/\chi] = \left[\frac{PT^2 \exp(2\chi)}{12N^3} \right] \sum_{\substack{k=1 \\ k \neq i}}^K r_{k,i} + \frac{N_o T}{4} \quad (10)$$

where $r_{k,i}$ is the average interference parameter between the i^{th} and k^{th} users and is expressed by Pursley [6] in terms of the aperiodic autocorrelation functions. In the above expressions, the conditional expectations have been taken with respect to the independent random variables θ_k , τ_k , $b_{k,-1}$, and $b_{k,0}$, assuming that there is an equal probability that the data symbols $b_{k,i}$ are equal to +1 or -1 for $k \neq i$. Let us now define the i^{th} user's average conditional signal-to-noise ratio $\overline{SNR}_i(\chi)$ as

$$\overline{SNR}_i(\chi) = \frac{E[Z_i/\chi]}{\sqrt{Var[Z_i/\chi]}} \quad (11)$$

After the substitution of expressions (9) and (10) in (11) and a simple rearrangement, we obtain the conditional $\overline{SNR}_i(\chi)$ conditioned on χ as

$$\overline{SNR}_i(\chi) = \left[\frac{R_i^K}{6 N^3} + \frac{\exp(-2\chi)}{2 (E_b/N_o)} \right]^{-1/2} \quad (12)$$

where $R_i^K = \sum_{k=1, k \neq i}^K r_{k,i}$ is the total interference parameter caused by the other $K - 1$ codes on the i^{th} one and $E_b = P T$ is the energy per bit. The i^{th} user's conditional bit error probability (BER_i) for a binary coherent PSK may then be written under the Gaussian approximation as

$$\overline{BER}_i(\chi) = Q(\overline{SNR}_i(\chi)) \quad (13)$$

where $Q(\cdot)$ is the Gaussian integral function defined as

$$Q(x) = \frac{1}{\sqrt{2\pi}} \int_x^{+\infty} \exp(-y^2/2) dy \quad (14)$$

Integrating (13) over the Mousley-Vilar pdf of the scintillation (1) yields the user i 's average BER

$$\langle \overline{BER}_i \rangle = \int_{-\infty}^{+\infty} Q(\overline{SNR}_i(\chi)) p_\chi(\chi) d\chi \quad (15)$$

We may note that when there is no scintillation ($\chi = 0$), then $\langle \overline{BER}_i \rangle = Q(\overline{SNR}_i(0))$, and the probability of error reduces to the expression derived by Pursley in a scintillation free channel [6]. In the same way, neglecting the multi-user's interference term in (15) yields the same expression for the average BER as the one computed in [5] for a single-user coherent binary PSK satellite digital link subject to scintillations and given by

$$\langle BER \rangle = \int_{-\infty}^{+\infty} Q(\sqrt{2(E_b/N_o)} \exp(\chi)) p_\chi(\chi) d\chi \quad (16)$$

This expression (16) holds for the transmission of K synchronous CDM signals spread by perfectly orthogonal codes (since the total interference parameter is equal to zero in this case).

The selected criterion for overall system performance is the $\langle \overline{BER}_{av} \rangle$, defined as the average bit error probability for an average user for which the total interference parameter is set to be equal to $R_{av}^K = \frac{1}{N} \sum_{k=1}^K R_i^K$. In addition, the user's average energy per bit to noise ratio (without multiple-access interference) $\langle E_b/N_o \rangle$ is given by

$$\langle E_b/N_o \rangle = (E_b/N_o) \int_{-\infty}^{+\infty} \exp(2\chi) p_\chi(\chi) d\chi \quad (17)$$

4. NUMERICAL RESULTS

A set of 50 Gold codes of length $N = 511$ bits were generated and assigned to 50 users. Initially, we study the effect of scintillation on a system with a fixed number ($K = 20$) of active users. The solid curve (a) in Figure 1 represents the scintillation-free channel reference case. In Figure 1, we have also plotted performance curves (b, c, d) for increasing scintillation intensities at a fixed index of variation, $\sigma_\sigma = 0$. As can be expected, performance degrades as σ_χ^2 increases. The curves (a, b, c, d) in Figure 2 illustrate the impact of the variability of the scintillation by keeping its long-term standard deviation constant at 0.8 dB and increasing σ_σ . These curves extend the conclusion found in [5], since they also show the worst degradation (at high SNR) for the highest scintillation variability statistics.

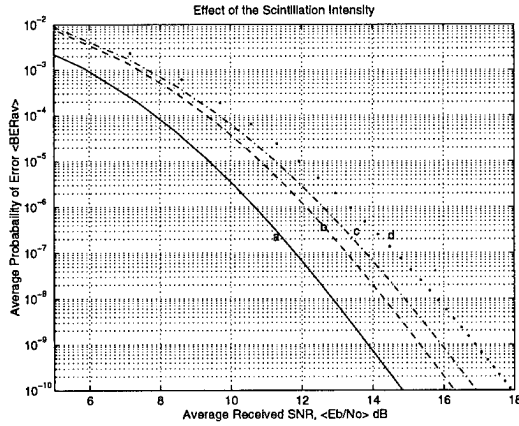


Figure 1: Average BER for increasing scintillation intensities ((a) $\sigma_m = 0$ dB, (b) $\sigma_m = 0.4$ dB, (c) $\sigma_m = 0.8$ dB, and (d) $\sigma_m = 1.2$ dB).

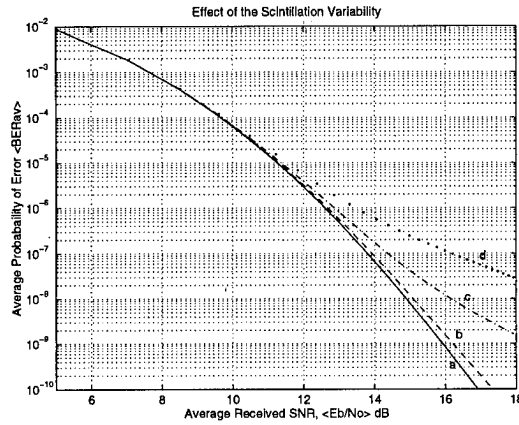


Figure 2: Average BER for increasing scintillation variability indices ((a) $\sigma_\sigma = 0$, (b) $\sigma_\sigma = 0.5$, (c) $\sigma_\sigma = 0.75$, and (d) $\sigma_\sigma = 1$).

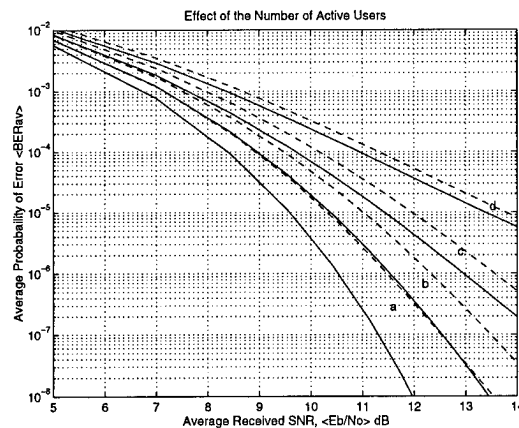


Figure 3: Average BER for different numbers of active users ((a) $K = 1$, (b) $K = 15$, (c) $K = 30$, and (d) $K = 50$).

Secondly, we study the impact of scintillation on a DS/SS channel with a variable number of active users. The average total interference parameter R_{av}^K was thus evaluated for different values of K . Figure 3 shows the performance achieved for an average user operating when, respectively, 1 (curve a), 15 (b), 30 (c), and 50 users (d), are simultaneously accessing a free fading channel (solid curves) or a scintillating channel (dashed curves). The parameter set used to obtain the curves of Figure 3 is $\sigma_m = 0.752$ dB and $\sigma_\sigma = 0.5$. It can be seen that as the number of active users increases, the scintillation induced $\langle E_b/N_o \rangle$ degradation (for a fixed $\langle BER_{av} \rangle$) decreases. As an example, the $\langle E_b/N_o \rangle$ degradation at $\langle BER_{av} \rangle = 10^{-6}$ is less than 0.1 dB for 50 active users, whereas it is 0.5 dB for 30 active users, 0.7 dB for 15 active users, and 0.85 dB for the single user case.

5. CONCLUSION

An analysis of the average BER performance of a binary DS/SS satellite communication system operating in a scintillating channel has been presented. Numerical results show that the performance is expected to degrade as the scintillation intensity increases and to be worse for sites with the highest scintillation variability statistics. It may also be concluded that the degradation is predominated by co-channel interference, rather than by signal fluctuations, when a high number of asynchronous users are simultaneously accessing a satellite. In the future, we plan to verify these theoretical predictions by experimental measurements conducted as part of the Georgia Tech ACTS propagation effects experiment.

6. REFERENCES

- [1] D. H. Howard and P. G. Steffes, "Georgia Tech ACTS class II experiment," in *Proceedings of the VI ACTS Propagation Studies Workshop (APSW VI)*, pp. 159–177, November 1994.
- [2] D. C. Cox, H. W. Arnold, and H. H. Hoffman, "Observations of cloud-produced amplitude scintillations on 19- and 28-GHz earth-space paths," *Radio Science*, vol. 16, no. 5, pp. 885–907, 1981.
- [3] T. J. Mousley and E. Vilar, "Experimental and theoretical statistics of microwave amplitude scintillations on satellite down-links," *IEEE Transactions on Antennas and Propagation*, vol. AP-30, no. 6, pp. 1099–1106, 1982.
- [4] R. K. Crane and D. W. Blood, "Handbook for the estimation of microwave propagation effects - Links calculations for earth-space paths (path loss and noise estimation)," Tech. Rep. P-7376-TR1, NASA Goddard Space Flight Center, 1979.
- [5] O. P. Banjo and E. Vilar, "Binary error probabilities on earth-space links subject to scintillation fading," *Electronics Letters*, vol. 21, no. 7, pp. 296–297, 1985.
- [6] M. B. Pursley, "Performance evaluation for phase-coded spread-spectrum multiple-access communication-Parts I & II," *IEEE Transactions on Communications*, vol. COM-25, no. 8, pp. 795–803, 1977.

FADE PREDICTION AND CONTROL SYSTEMS

Michele Luglio

Università di Roma "Tor Vergata" — Dipartimento di Ingegneria Elettronica
Via della Ricerca Scientifica 00133 - Roma - Italy
luglio@tovvx1.ccd.utovrm.it

ABSTRACT

The growing utilisation of high frequencies (Ka band) has made very important the use of one or more fade countermeasures (UPPC, Site Diversity, Frequency Diversity, Adaptive Coding, etc.) to overcome rain fading avoiding to overdimension the systems. Fade countermeasures could provide better performances if supported by a control system able to obtain the prediction of dynamic characteristics of rain fading in the instant in which the attenuation crosses a certain threshold. Such a system would allow to avoid overcompensation or false alarms as well as to optimise the available resources in case of multilevel compensation, with an efficiency as great as the prediction would be accurate. In this paper, after the description of the main techniques for real time measurement of the attenuation, a hypothesis of a new control system with the relative algorithm is presented. This system bases the prediction of the dynamic characteristics of fading on the observation of some initial parameters.

I. INTRODUCTION

Usually to determine attenuation level on a given link pre-elaborated models are used. The most used models are those of the CCIR [1] and those of the NASA [2]. These models are easy to implement and accurate in an average, global sense. On the other hand they suffer from limitations when applied to certain regions (e.g. tropics), or to the prediction of phenomena for which no systematic data exist (ice-crystal depolarisation), and to model boundary regions (low elevation angles) [3]. Most of the attenuation prediction models convert rainfall rate statistics into fade probability using the analytically derived specific attenuation per unit distance (dB/km) together with an effective path length and are developed using meteorological knowledge and limited sets of data.

In the case that one of the fade compensation methods is used, it's not very important the prediction of the probability with which fading overcomes a given threshold during the year, but the prediction of the value that some parameters can assume within a short interval. Thus it's important to get prediction models of dynamic characteristics of rain attenuation.

It would be necessary to have a control system that, according with a real time evaluation of channel quality and with a prediction of the rain parameters, taking eventually in account its past evolution, could determine the timing of the whole process.

The problems are two: instantaneous knowledge of fade

level, at the frequency of the link, and prediction of future characteristics of the attenuation.

The knowledge of channel conditions can be obtained observing primary parameters (attenuation, statistical distribution of rain) or secondary parameters (signal to noise ratio, BER, received signal characteristics) [4].

It is possible to know attenuation level by continuously measuring and scaling a known signal, transmitted by the satellite, with an additional receiver. If this signal is not available it's possible to use a radiometer or to note any reduction in link SNR. Monitoring only one carrier it is not possible to separate the contributions on the two links (in case of transparent payload). If the loopback signal is available an estimate of the attenuation at each frequency can be made. If many carriers from different stations are monitored, a fall in level of all carriers implies presence of fading on down link otherwise the fading affects a certain up link. Interference and variations due to equipment and to satellite instability can cause low precision.

To predict future characteristics of attenuation it is necessary to verify the correlation between one or more parameters linked to initial characteristics of rain fading and the dynamic characteristics of the phenomenon itself. Once this would be verified, the problem is to elaborate an algorithm able to provide a real time prediction.

In section V, taking hint from a system proposed at Coventry University (U.K.), a control system is introduced. This system would offer the possibility to obtain dynamic control and management of the resources utilising an algorithm to predict some parameters by real time observation and of the characteristics of previous events.

II. RAIN FADE OBSERVATION

To obtain and develop reliable statistical models for rain fade prediction very long observation time is necessary [7].

The most commonly observed parameters are the *duration* (time interval during which the attenuation is greater than a given threshold), the *depth* (peak level within the duration), the *rain rate* (absolute value of the derivative or as the intensity, mm/h), the *interfade time* (time interval during which the attenuation is lower than the threshold).

Slope

The attenuation is a continuous function of time and its slope, when a threshold is crossed, can be defined as the derivative (in the crossing point). Since we can

have only a sampled sequence, an optimum criterion to estimate the slope has to be found [8].

So far no correlation between slope and dynamic characteristics of fading has been demonstrated.

The research of the parameter linked to the initial characteristics of fading that more than others would be correlated with its dynamic characteristics is an open problem, in the sense that no accurate study has been conducted on the correlation between the initial instant and the time evolution of the phenomenon.

Empirical and theoretical distributions

A first step in analysing collected data is to verify if the empirical distributions (of rain fade or of one of the parameters) match one of the statistical distributions already known and characterised by means of one algorithm such as χ^2 , Kolmogorov Smirnov, etc.

The results referred to 4 years of measurements in Texas showed that the rain rate distribution well fits the normal distribution, while the year to year variability of the cumulative distribution, at a given percentage of time, fits a log-normal distribution. The distribution of the attenuation level in dB follows different statistics for different percentage of time [3].

Time variations of rain attenuation show that the rain rate grows as a function of attenuation, providing a further proof of the log-normality of the process [6]. Both fade and interfade duration follow a log-normal statistic both in K and Ka band [6] and in X band [3].

These results are confirmed in X band, for durations greater than 32 s [9][10], while for lower values they correspond to a power law model, not depending in both cases on the site or on the threshold. In [11] a software to analyse measured data at 30 GHz with Olympus is presented. The results referred to data at 30 GHz during 4 months (Sept. '91 - Jan. '92) with Olympus [12] agree with what is shown in [10].

III. PREDICTION OF THE DYNAMIC CHARACTERISTICS

The prediction of the evolution of rain fade can be obtained using one of the linear prediction techniques using auto-regressive series or utilising polynomial methods, with the observed samples. In both cases the precision of the prediction depends on the number of samples, on sampling frequency and on the margin introduced to take in account scintillation, variable during the 24 hours (greater during the afternoon [3]).

The prediction method presented in [5], based on the maximum entropy principle, is a type of linear prediction that implies the approximation of the signal level at any instant with of a linear combination of the previous n samples. The accuracy of this algorithm depends on the predict-ahead time intervals. For a 20 second prediction interval, the maximum error is within a range of about ± 1.5 dB.

In the framework of Sirio experiments, utilising the data collected at Spino d'Adda (within four years at

11.6 GHz with a sampling frequency of 2 s), it has been shown that two successive fade durations within a rain event or between different rain events are statistically independent [13].

IV - CONTROL SYSTEMS

Control system simulation

Utilising the measured data collected with Sirio in three sites (Spino d'Adda, Lario and Fucino) at 11.6 GHz a control system for fading compensation has been simulated at Politecnico of Milano making a real time prediction elaborating the previous samples with an algorithm based on linear regression [14]. The attenuation level is predicted with an anticipation equal to 2 s (expected response time of the system) and thus compared with a threshold (the minimum acceptable quality); if the predicted value is above the threshold the system starts with the procedure.

The performances of this algorithm depend on the sampling frequency, on the number of previous samples and on the value of the margin introduced to counteract scintillation. They are better (the percentage of outages is lower) if the number of samples is lower, because fast variations of attenuation are easier to predict with a small number of samples (even 2). On the other hand, with a too small number of samples or with a too high threshold for the scintillation a great number of false alarms occurs.

The control system efficiency (ratio between the effective utilisation time of the compensation and the utilisation time in an ideal system with no switching delay and no response time), is between 0.8 and 1.3. For values close to 2 the number of false alarms tends to zero.

FCMIS (Fade CounterMeasure Intelligent System)

An "intelligent" detection and control system is proposed in [7] (figure 2). The dynamic characteristics of fading and some prediction techniques can provide different informations for the management of the compensation procedure. These different informations concern some parameters that can have different characteristics and statistics, not excluding correlation among them.

A first parameter is the *duration*: the duration distribution can also be utilised in the system design phase to dimension the backup resource. A second parameter is the *interfade duration*: the distribution of interfade can be utilised to estimate the backup resources availability. A third parameter is the *fade rate*: the knowledge of this parameter can be useful for a dynamic management of the power margin. A fourth parameter is the *fade depth*: the distribution of fade depth allows the prediction of the occurrence of an attenuation amplitude peak; this information could be very important, both in design and in compensation management phase to estimate the compensation level in case of multilevel technique.

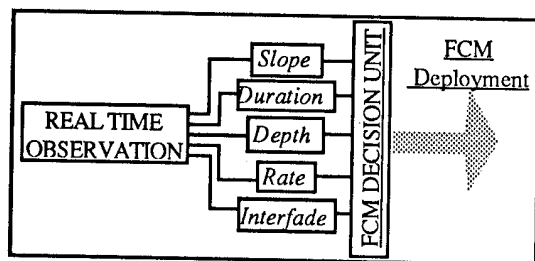


Figure 2 - FCMIS [7]

V. PROPOSAL OF A CONTROL SYSTEM

The intelligent control system (FCMIS) proposed in [7] suggests a hypothesis on how various informations regarding the estimate of several parameters, together with real time observation, can co-operate in deciding the activation of fade compensation techniques.

Starting from the FCMIS idea it's necessary, first of all, to define in greater details the functionality of the different blocks of figure 2 and how some of the informations can be utilised for dynamic control and management of the resources.

Control System with Dynamic Prediction

The FCMIS idea can be expanded and detailed in the *Control System with Dynamic Prediction* shown in figure 3, consisting of 5 stages.

The first stage consists in *real time observation* in which the parameters that characterise the rain event such as duration, depth, amplitude and interfade duration are detected and measured. In the *prediction and*

evaluation of statistical models stage, these parameters are stored, elaborated and compared with the statistics obtained with previously collected data. The statistical models are thus updated. Data are elaborated considering real time observation, previous events and attenuation curve characteristics.

The results of this stage are then utilised in the *decision* stage. Here the probability that the parameters could assume values greater than a threshold is compared with a prefixed value of probability. The results of this comparison are then utilised for the decision, with a logical AND type combination among the different inputs.

Thus the start of the compensation procedure depends on resource availability, verified in the *activation* stage and can be dynamically controlled utilising the predicted values of fade and interfade duration.

In the *management* stage the procedure is carried out. The amplitude and depth estimates can be utilised to control the amplitude of the utilised resources in case of multilevel compensation (quantized UPPC, multilevel gain coding, etc.), while fade and interfade duration estimates can be utilised to determine resource availability.

Dynamic Prediction Parameter

Statistical independence between two fade or interfade durations, as verified in [13], doesn't imply absence of correlation with the characteristics of past events. It might be possible to elaborate an algorithm to estimate these parameters on the basis of past events.

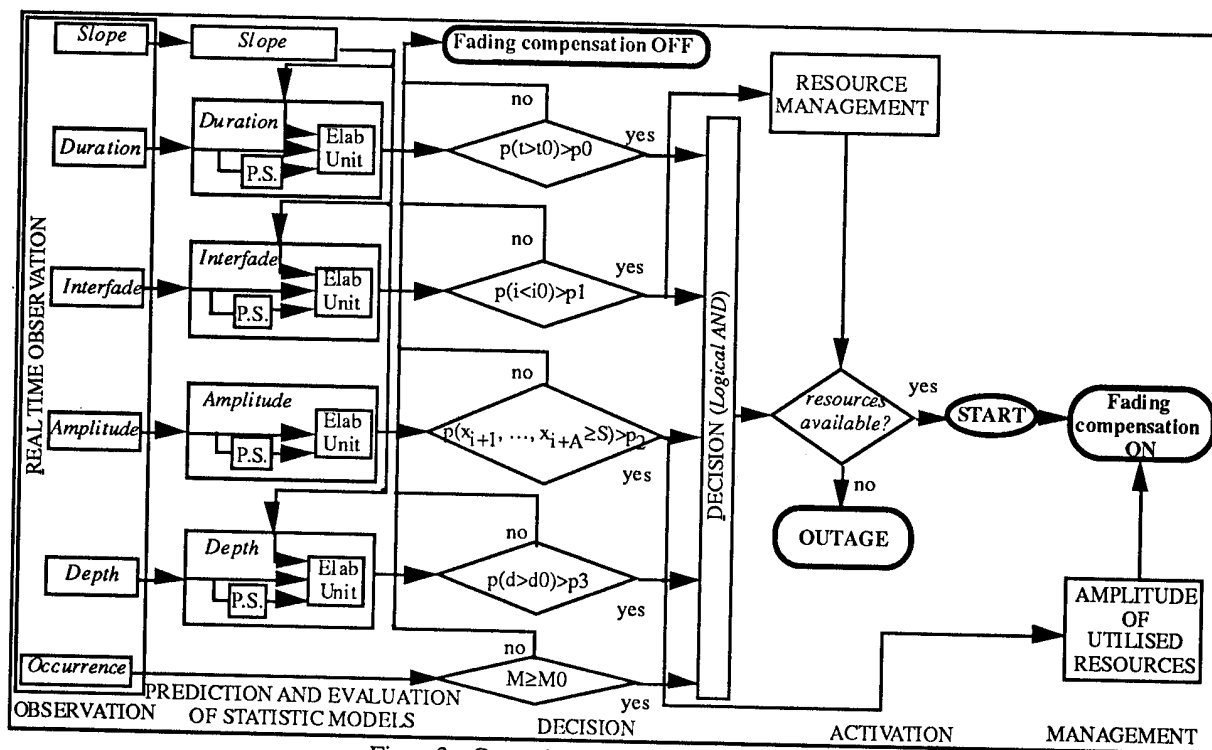


Figure 3 - Control system with dynamic prediction

An auto-regressive model able to fit rain evolution needs a great number of coefficients and very large matrices, as well as the polynomial interpolation of the sequence needs a polynomial with high degree and as many coefficients.

The prediction of fade or interfade duration or of depth is more accurate if a great number of samples is considered, taking in account long period statistics with a high enough sampling frequency. On the other hand, a too long sequence would cause such a complexity to require a not negligible computation power and elaboration delay.

Thus, to evaluate the next value it is possible to consider only the last two or three samples (according with [14]), while an efficient method to utilise data collected in many years, avoiding high and unacceptable complexity, could be the following.

Assuming the slope of the attenuation curve as a meaningful parameter for the prediction we could suppose that different parameters would correspond to different slopes.

The average and the variance of the collected data are dynamically calculated, updated and stored according to the slope at the beginning of the rain event.

In this way two tridimensional matrices are filled, with the columns corresponding to the parameters, the rows corresponding to different values of the slope and the third dimension to season or month (figure 4).

This sort of information can be meaningful considering that the statistical independence between two events verified in [13] and the randomness of the rain don't imply necessarily the statistical independence between two events that, occurring after a relatively long time, present common characteristics (season, slope, etc.).

With this procedure it is possible to obtain the data site by site because each station can detect and elaborate the statistics by itself.

The algorithm shown in figure 5, that represents the prediction and evaluation of statistical models stage of figure 3, implements the procedure described above.

In this diagram x_i is the i -th sample (last sample), S represents the threshold, or the fixed margin for the link, d, IN, X_{max} , are used to measure duration, interfade and peak values, while D, INT and P are the parameters and $\bar{D}, \bar{INT}, \bar{P}$, are the averages; σ^2 are the variances; A is the number of estimated samples.

After the detection, the i -th sample is compared with the threshold and the different counters are increased according to the result of the comparison. The value of the parameter for the current event, once calculated, is utilised to update the average and the variance of the distribution of the parameter itself.

The evaluation of the slope is made active only when the threshold is crossed. The estimated value is thus compared with the n_p values of slope to put, in the respective position of the matrices, the different values thus obtained. Dynamically updated averages and variances are obtained. The estimate of the A next values is made active only during the fade duration and

is performed using the last K samples with an auto-regressive algorithm.

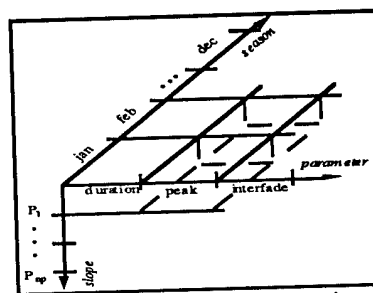


Figure 4 - Parameters matrix

Limits of the model

In this moment the assumption that the slope is correlated with the dynamic evolution of rain fading is not proved by any kind of empirical test, but this system could represent a significant step to demonstrate or not this statement. From this implementation we can expect one of the following results:

- a) data classified as a function of the slope are correlated with it;
- b) it's not possible to correlate the slope with the future evolution of rain fade;
- c) the slope shows correlation only with some of the parameters (for example peak, amplitude);
- d) the correlation with the future evolution exists only for some values of the slope (the relationship is not linear).

The system has been tested with the data collected at Politecnico of Milano with a 29 GHz station during 7 months of observation, but the very low number of events has not allowed to elaborate any result.

Prediction accuracy

The main factors of inaccuracy are: inaccuracy in the measurement, caused by equipment or by frequency scaling, correlation between the initial characteristics of rain fading (the slope in our case) and some parameters, the estimate procedure of the synthetic parameter of the initial characteristics (different methods to evaluate the slope of a sequence provide different results), the classification of the events according to the slope, the matching procedure performed between empirical probability distributions and theoretical ones.

CONCLUSIONS

The dynamic management and the optimisation of the resource, in case any rain fade compensation technique is used, are quite complex problems. Besides, it is not so far thoroughly studied.

A system based on the prediction of the dynamic characteristics of rain fade has been proposed and described.

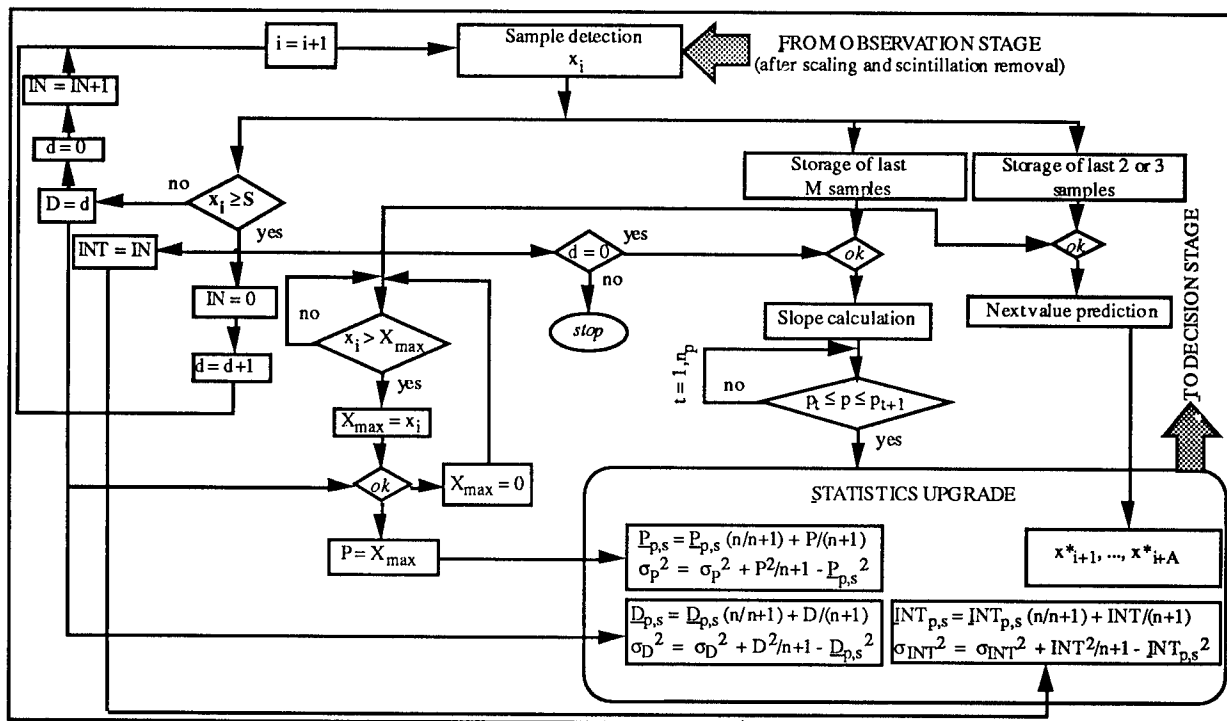


Figure 5 - Dynamic prediction algorithm

Before going forward with one of the dynamic prediction methods it is necessary to establish which parameter, referred to the initial conditions or to the past events, is more correlated with the future evolution of rain fade. The slope of the attenuation curve has been proposed, but this doesn't exclude that another parameter can better cooperate to the prediction. This aspect represents in this moment an open problem that shall be object of further studies. The idea of a control system with dynamic prediction could anyway be valid even if instead of the slope another parameter would be considered.

REFERENCES

- [1] Reports of the CCIR, "Propagation in Non-Ionised Media", Annex to vol. V, Int. Telecommunications, CCIR, Geneva, 1990.
- [2] L. J. Ippolito, "Propagation Effects Handbook for Satellite Systems Design", 4th Edition, Washington D.C., National Aeronautics and Space Administration, 1989.
- [3] W. Vogel, G. W. Torrence, J. E. Allnutt, "Rain Fades on Low Elevation Angle Earth-Satellite Paths: Comparative Assessment of the Austin, Texas, 11.2 GHz Experiment", Proceedings of IEEE, vol. 81, n. 6, June 1993, pp. 885-896.
- [4] M. Willis, B. Evans, "Fade Countermeasures at Ka Band for Olympus", Int. Journal of Satellite Communications, vol. 6, 1988, pp. 301-311.
- [5] A. Dissanayake, C. Zaks, "Implementation of Rain Fade Mitigation Techniques at Ka Band Frequencies", ACTS Conference '92, November 18-19 1992, Washington DC, pp. 210-221.
- [6] S. H. Lin, H. J. Bergmann, M. V. Pursley, "Attenuation on Earth-Satellite Paths - Summary of 10 years experiments and studies", Bell System Techn. Jour., vol. 59, n. 2, pp. 183-228, 1980.
- [7] TKP Chung, A. Gallois, "Fade Countermeasure Intelligent System (FCMIS), IEE Colloquium on Ka Band, Nov. 15th 1993, London.
- [8] S. Upton, J. R. Larsen, "Analysis of Fading Characteristics for Communications Applications", Olympus Utilisation Conference, Vienna 12-14 April 1989, pp. 247-250.
- [9] TKP Chung, A. P. Gallois, "The Characteristics of Fade Duration Distribution", Int. Symp. on Comm., Theory and Appl., July 1993.
- [10] "Project COST 205: Dynamic Characteristics of Rain Attenuation", Alta Frequenza, vol. LIV, n. 3, May-June 1985, pp. 194-202.
- [11] TKP Chung, A. P. Gallois, "Fade Duration Statistics: Results from Olympus Satellite", ICAP '93, 1993.
- [12] TKP Chung, A. P. Gallois, "Model Parameters of Fade Duration Statistics", Proceedings of 20th OPEX, Darmstadt, 23-25 Nov. 1993.
- [13] E. Matricciani, M. Mauri, "Rain Attenuation Successive Fade Durations and Time Intervals between Fades in a Satellite-Earth Link", Electr. Letters, vol. 22, n. 12, June 1986, pp. 656-658.
- [14] L. Dossi, "Real-Time Prediction of Attenuation for Applications to Fade Countermeasures in Satellite Communications", Electronics Letters, vol. 26, n. 4, 15th Feb. 1990, pp. 250-251.

RAIN ATTENUATION CHARACTERISTICS ON RADIO LINKS

Toshihiro Manabe and Teruaki Yoshida***

* NTT Advanced Technology Corp.
Yokohama-shi, Kanagawa, 244 Japan
manabe@kana.ntt-at.co.jp

** NTT Telecommunication Network Laboratory Group
Musashino-shi, Tokyo, 180 Japan
yoshida@magnet.netlab.ntt.jp

Abstract

This paper describes the rain attenuation characteristics of radio links and the possibility of outage free links. Since 1988, NTT has been conducting continuous rain attenuation measurements on experimental radio links. The experiments have been carried out in Tokyo. The measured frequencies are 15, 18, 20 and 26 GHz with transmission distances of 0.75, 2.8, 6 and 9 km. Rain attenuation characteristics are measured with 0.1 sec time accuracy. Field trial results show that the measured rain attenuation distribution has a maximum value, and radio links with fading margins that exceed the maximum rain attenuation become outage-free.

1. Introduction

Since 1984, NTT has provided high-speed digital leased line services using 26 GHz microwave links. This system possess a broad bandwidth and provides a good solution to the "last mile problem"[1]. On the other hand, microwaves especially those above 10 GHz, are susceptible to rainfall fading, which degrades transmission performance during rain.

Since 1988, NTT has been conducting continuous rain attenuation measurements on experimental links to study outage characteristics. In order to reduce estimation error, rain attenuation characteristics are being measured with 0.1 sec time accuracy. Field trial results show that

- (1) the rain attenuation distribution can not be described by the Gamma distribution at the upper end,

- (2) all measured rain attenuation distributions have maximum values,
- (3) the maximum values vary annually and depend on frequency and transmission distance,
- (4) radio links having fading margins that exceed the maximum rain attenuation are outage-free.

2. Rain attenuation characteristics

2.1 Prediction of attenuation due to rain

Estimation of rain attenuation is essential for the link design of radio systems. Rain attenuation Z between two points (point A and B) is expressed as

$$Z = \int_A^B R(x)^n dx \quad (1)$$

where $R(x)$ is the rain rate at point x between A and B, n is a constant that depends on frequency[2].

From eq.(1), rain attenuation is calculated from the rain rate and the rain attenuation distribution is estimated from the rain rate distribution.

Several ways have been proposed to estimate the rain rate and rain attenuation distributions. The Gamma distribution is widely used. Using the Gamma distribution, the rain rate distribution is expressed as follows[2];

$$f(R) = \frac{\beta^\nu}{\Gamma(\nu)} R^{\nu-1} e^{-\beta R} \quad (2)$$

where ν and β are Gamma distribution parameters.

For rain attenuation, the following equation is derived from eq. (2).

$$f(Z) = \frac{\beta_e^{\nu_e}}{\Gamma(\nu_e)} Z^{\nu_e-1} e^{-\beta_e Z} \quad (3)$$

where ν_e and β_e are Gamma distribution parameters.

Mathematically speaking, eqs. (2) and (3) are easy to calculate and suitable for computation. However, probabilities $f(R)$ and $f(Z)$ are never zero even if variables R and Z approach infinity. This means that eq.(3) requires the system to offer infinite fading margin against rainfall to make the link outage free. Is this realistic?

Let us consider rain and rain attenuation physically. Rain rate is defined as the amount of rain observed over an integration period. As the integration period, one minute is commonly used in Japan. It is obvious that the rainfall measured during this limited period cannot be infinite. The reasons are as follows;

- (1) Rain drops are generated from water vapor in the air. The amount of water vapor is limited.
- (2) Because the speed at which the rain drops fall is limited by air resistance, the number of rain drops observed during a fixed period is also limited.

If the rain rate distribution is limited, the rain attenuation distribution is also limited. This is easily explained from eq.(1).

From the above discussions, it is forecast that eqs.(2) and (3) cause excessive estimation error. Furthermore, the estimation of rain attenuation is based on the estimated one-minute rain rate, if the probability is less than one-minute, the estimation error will be increased.

2.2 Field trial system configuration

To achieve highly reliable radio systems, a field trial was begun in Tokyo in August 1988. Routes of the trial system are shown in Figure 1.

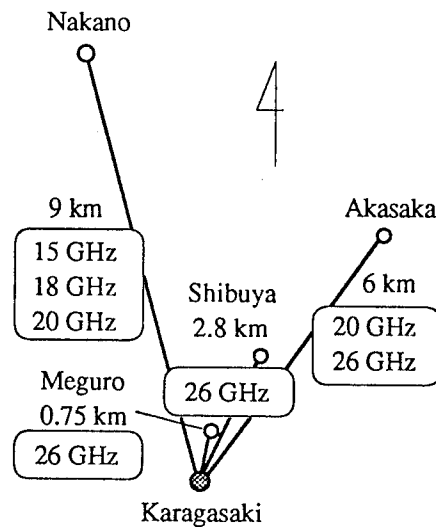


Fig. 1 Field trial routes

Four routes with transmission distances of 0.75, 2.8, 6 and 9 km were set around the Karagasaki central station. The frequencies were 15, 18, 20 and 26 GHz. Four 26 GHz links with different fading margins were set to Shibuya. The rain attenuation of each link was measured with 0.1 s accuracy and continuously recorded by a computer.

2.3 Measured rain attenuation

Figure 2 and 3 show measured rain attenuation at 26 GHz over the transmission distances of 0.75 km and 2.8 km, respectively. The dashed line is the estimated probability from the Gamma distribution. As the rain attenuation becomes large, the probability decreases between 10^{-1} and 10^{-3} . On the other hand, when the probability becomes small, it drops quite rapidly, indicating that the rain attenuation has reached a maximum limit; i.e., it is truncated. The maximum limits vary each year, but in each year the rain attenuation shows the same tendency to truncate. This result shows that there are some regions in which the probability of rain attenuation decreases rapidly, and if we can increase the fading margin so that it exceeds the highest

rain attenuation recorded, the links will be "outage-free".

Figures 4 and 5 show measured rain attenuation over transmission distances of 6 km. Frequencies are 20 and 26 GHz, respectively. The truncations shown in the 0.75 km and 2.8 km links at 26 GHz are also observed in the links of 6 km.

Figure 6 shows the measured rain attenuation distribution for the transmission distance of 9 km at 18 GHz. The truncations are also observed here.

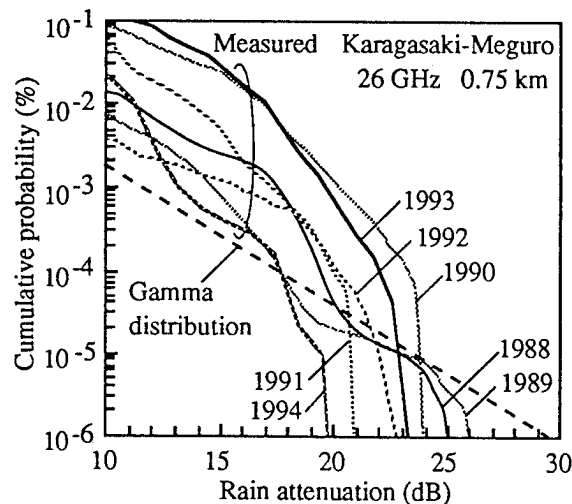


Fig. 2 Rain attenuation distribution over transmission distance of 0.75km

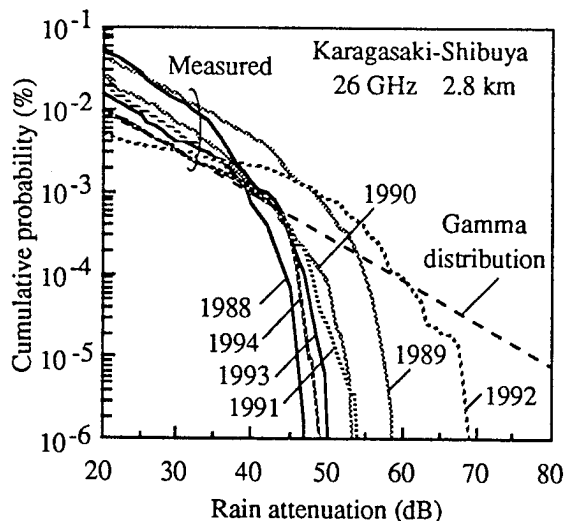


Fig. 3 Rain attenuation distribution over transmission distance of 2.8km

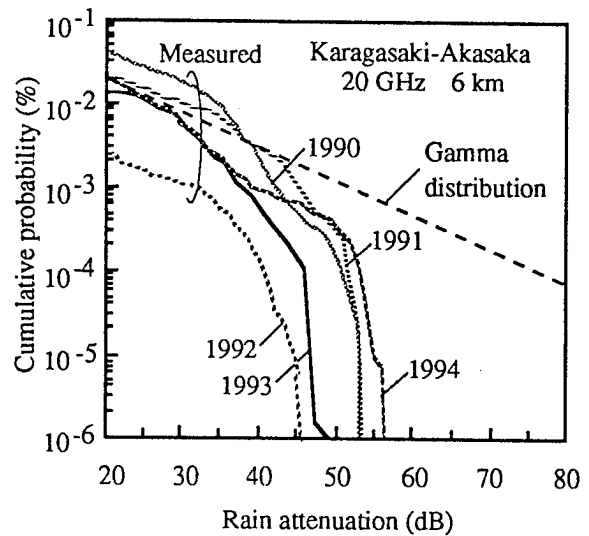


Fig. 4 Rain attenuation distribution over transmission distance of 6km

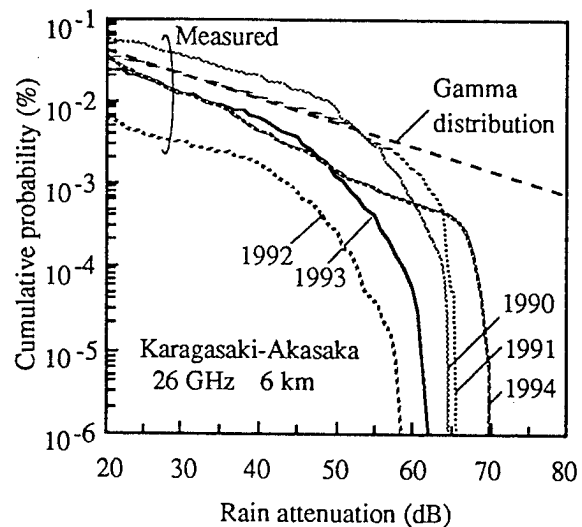


Fig. 5 Rain attenuation distribution over transmission distance of 6km

In Figures 2 to 6, the maximum values of the measured rain attenuation vary with frequency and transmission distance. They also vary from year to year.

3. Towards outage free radio systems

We set four links with different fading margins between Karagasaki and Shibuya to examine fading margin dependence on the BER characteristics. The margins are 24, 43, 55 and 60 dB.

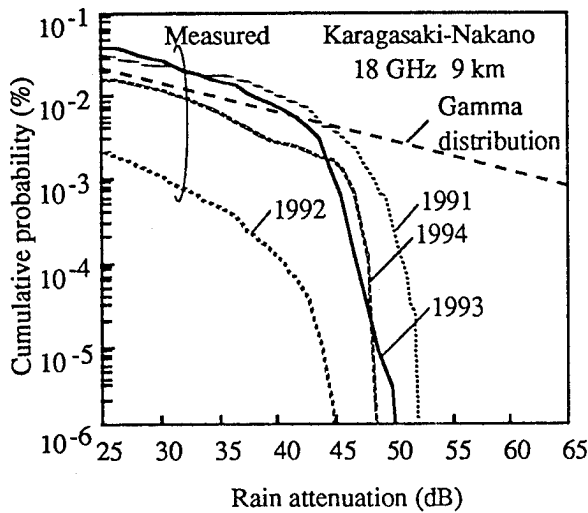


Fig. 6 Rain attenuation distribution over transmission distance of 9km

Figure 7 shows the cumulative time over which the measured BER of 10^{-4} was exceeded. The dashed line denotes the probability estimated using the Gamma distribution. In 1989, there was a major downpour on August 1. The downpour was so heavy that the meteorological observatory in Tokyo recorded the highest daily rainfall in Japanese history for that month. It is notable that many bit errors occurred in links with fading margin below 54 dB, but the link with the fading margin of 60 dB had no bit errors. In 1992, we also experienced heavy rainfall on December 8. In that year, total rainfall was small compared to another year. On December 8, however, extremely heavy rain was observed for several tens of minutes, and the link with fading margin of 60 dB suffered bit errors. Note that the outage was only 0.5 minutes over 7 years. Furthermore, if the link had 10 dB higher margin, the link would have remained outage free.

From the above discussion, it is clear that maintaining a high but practical margin makes radio links sufficiently robust against rainfall, they can be made outage-free.

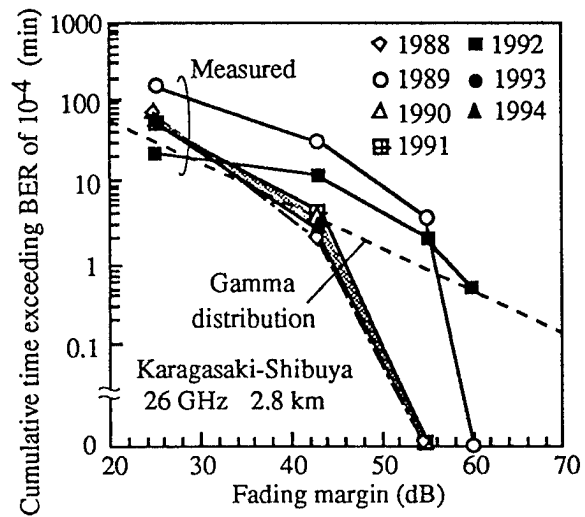


Fig. 7 Fading margin dependence of outage time

4. Conclusion

This paper described the rain attenuation characteristics of radio links and showed how to make outage-free-links. The results are summarized as follows;

- (1) the rain attenuation distribution can not be described by the Gamma distribution at the upper end,
- (2) all measured rain attenuation distributions have maximum values,
- (3) the maximum values vary annually and depend on frequency and transmission distance,
- (4) radio links having fading margins that exceed the maximum rain attenuation are outage-free.

Acknowledgment

Authors would like to thank Mr. Kozo Morita of NTT Advanced Technology for his helpful guidance. They also thank Dr. Kenji Kohiyama and Dr. Osamu Kurita of NTT Wireless Systems Laboratories for their corporation in the field trials.

References

- [1] G. Dickson : "23-GHz: New Dawn", Communication News, Sept., 1990
- [2] K. Morita and I. Higuchi : "Statistical Studies on Electromagnetic Wave Attenuation due to Rain", Rev. Elec. Commun. Lab., Vol. 19, No. 1, pp.97-150, 1970

An Overview of Quasi-optical Power Combining: Were We are and How We Got Here

James W. Mink *

North Carolina State University
Raleigh, North Carolina 27695-7911

Abstract

There is a continuing and unmet need for high power, solid-state sources at microwave and millimeter wavelengths. At microwave frequencies, transmission line or cavity combiners have been successful, but at millimeter wavelengths this approach has problems in terms of losses, power output and dimensional tolerances. In the past few years, significant efforts have been carried out to develop planar arrays of solid-state oscillators in order to produce spatial power combining. These structures have used open Fabry-Perot as well as conventional transmission lines for combining the active devices, to provide feedback for coherent locking of the individual oscillating devices and to couple energy to an electromagnetic wavebeam. In addition a new class of hybrid planar quasi-optical waveguides and resonators are under investigation for power combining. Active devices utilized have included two terminal GUNN or IMPATT diodes as oscillators, and three terminal devices such as FETs or HEMTs as both oscillators and amplifiers. With three terminal devices currently being more popular. This presentation discusses architectures under active investigation.

Introduction

For many years, there has been a need to obtain more power from solid-state devices, both sources and amplifiers. There exists many system applications in common use today and their range of applications is expanding. It is safe to predict that these systems will be utilized in the future across the spectrum of endeavors from communications, radar, to transportation, industrial and scientific applications. Satisfying this expanding demand mandates the utilization of previously unused, or little used, mm-wave and sub-mm-wave bands. In accordance with a long term trend toward systems operating at higher and higher frequencies, the necessary technology, however, is not very well developed at the present time. A fundamental limitation has been and continues to be the lack of convenient power sources and amplifiers. Component costs have been driven by the small size and tight tolerance associated for mm sources and in the case of waveguide components, by the need for hand assembly. This is more urgent at millimeter wave frequencies than at microwaves because microwave sources generally give better performance in terms of such parameters as power output, efficiency and / or spectral purity. Solid state devices are highly reliable, however, their output power tends to be very low due to their small physical size of the active region, resulting in the well known $1/f^2$ fall-off of available

* This work was supported by the Army Research office, Research Triangle Park, NC 27709

power. Hence, a need exists to combine the outputs of many individual elements to satisfy the system power requirement.

Many of the problems stated above may be resolved through the use of quasi-optical techniques. Quasi-optical devices typically have cross sectional dimensions in the order of 10 to 100 wavelengths and are relatively easy to fabricate. Tolerance requirements are greatly relaxed since boundary surfaces along the propagating directions of the guiding structure are not critical for mode selection and maintenance of mode purity. Rather, easily manufactured lenses or reflectors, and their spacing between them, establish the mode parameters. In addition, the rather large transverse dimensions of quasi-optical structures allow one the freedom to include numerous solid state sources to achieve the desired output power.

Architectures

All quasi-optical systems have several features in common: at least one transverse dimension is large compared to the wavelength; the longitudinal dimension is also large and may be large compared to the transverse dimension; hence, many individual solid-state sources may be integrated into the structure. While the dimensions are large compared to the wavelength, the mode structure is such that only a single mode, or at most a small number of modes may exist in the structure.¹

In recent years, research emphasis has been placed upon three principle classes of quasi-optical structures for oscillator design. The first structure to be investigated was that of an open resonator, commonly referred to as the Fabry-Perot resonator, with solid state sources located in a plane transverse to the direction of propagation. The electromagnetic mode structure of open resonators is well known and characterized.¹ Since, the physical size of each solid-state source is much smaller than the wavelength, a coupling device must be employed to extract energy from the active element and transfer it to the wave beam. Many coupling devices have been investigated including small dipoles², loop elements³, microstrip elements^{4,5}, and one dimensional waveguide structures⁶. In each case, the goal of such coupling elements is to impedance match between the active device and the electromagnetic wavebeam. An example of an open resonator structure is shown in figure 1. Feedback required for oscillation is obtained primarily through the electromagnetic wavebeam, with a small but measurable contribution due to direct mutual coupling between the coupling devices⁷.

The second structure to receive significant investigation is that of the grid oscillator and amplifier. In this case an array of active elements is placed in a uniform grid, which intercepts the electromagnetic wave beam, with each element connected to its nearest neighbors via a printed transmission line / antenna structure.^{8,9,10} When one considers the grid structures, feed-back to obtain oscillation is principally via the transmission line located between the active elements, with secondary coupling occurring via the electromagnetic beam. While the electromagnetic beam coupling is small, it is essential to insure all active elements oscillate coherently and in phase as opposed to anti-phase

oscillation¹¹. An example of the typical grid oscillator is shown in figure 2a⁸. Also shown in figure 2b a detailed depiction of one active element cell¹². To date, grid oscillators have produced the highest power level of about 10 watts in the X-band.¹³ Grid amplifiers are very similar to grid oscillators, only the feedback element, in this case a reflector is removed from the system. Grid amplifiers have shown relative gain, from the off state to the on state of about 15 dB operating at about 40 Ghz¹⁴.

The third class of quasi-optical systems are based upon the a hybrid dielectric slab-beam waveguide.^{15,16} The hybrid slab-beam waveguide consists of a thin dielectric slab, usually grounded on one side, into which phase correcting elements are inserted. The phase correcting element for an oscillator is usually a partially transparent curved reflector. Energy will be extracted through that reflector. The hybrid dielectric slab-beam waveguide confines the beam in dimension through wavebeam techniques as discussed above and in the second transverse direction (normal to the dielectric slab surface) through the technique total internal reflection as normally employed by slab dielectric waveguides. For this structure, one obtains a large area suitable for the integration of active elements along the direction of propagation and across the wavebeam. The advantage of this technique is that the active elements may be integrated as a component of the ground plane and coupled to the wavebeam through apertures in the ground plane. This technique provides adequate coupling to the wavebeam, while providing a mechanism for efficient cooling of the active elements. The hybrid dielectric slab-beam waveguide techniques continue to show promise, however, while they are the least developed of the three techniques discussed here an amplifier based upon these techniques have shown input to output gain of about 10 dB in the X-band¹⁷. An example of a hybrid dielectric slab / wave-beam oscillator is shown in figure 3a. Also shown in figure 3b is a detail of the coupling element.

Conclusion

Table I lists the specifications of reported quasi-optical spatial combiners. While the intention of quasi-optical techniques is to develop high power sources at millimeter wavelengths, most research to date has been conducted in the microwave region of the spectrum. It should be pointed out that research results shown in Table I has been primarily proof-of-concept demonstrations and additional development effort is required. However, several academic and industrial institutions currently have programs focused upon the millimeter spectrum. If one is interested in pursuing this technology, two extensive overview papers are available.^{18,19} These paper also extensively reference research that has been conducted for the interested investigator.

- ¹ G. Goubau and F. Schwering, "On the Guided Propagation of Electromagnetic Wavebeams," IRE Trans. Antennas and Propagation, vol. AP-9, May 1961, pp. 248-259.
- ² J. W. Mink, "Quasi-Optical Power Combining of Solid-State Millimeter Wave Sources," IEEE Trans. on Microwave Theory and Techniques, Vol. MTT-34, Feb. 1986, pp. 273-279.
- ³ K. J. Kogan, F. C. DeLucia and J. W. Mink, "Design of a Millimeter-Wave Quasi-Optical Power Combiner for IMPATT Diodes," Proceedings of the SPIE, Vol. 791, 21-22, May 1987, pp. 77-81.
- ⁴ G. P. Monahan, et.al., To be published
- ⁵ J.C. Wiltse, et.al., "Power Combining Arrays at Ka-Band," IEEE MTT-S International Microwave Symp. 1994.
- ⁶ Z. B. Popovic, R. M. Weikle, M. Kim, K. A. Potter, and D. B. Rutledge, "Bar-Grid Oscillators," IEEE Tans. on Microwave Theory and Techniques, Vol. MTT-38, pp. 225-230, March 1990.
- ⁷ P. L. Heron, G. P. Monahan, J. W. Mink, F. K. Schwering, and M. B. Steer, "Impedance Matrix of and Antenna Array in a Quasi-Optical Resonator," IEEE Trans. Microwave Theory and Tech., Special Issue on Quasi-Optical Techniques, Vol. MTT-41, pp. 1816-1826, Oct 1993.
- ⁸ Z.B. Popovic, R.M. Weikle II, M. Kim, and D.B. Rutledge, "A 100-MESFET Planar Grid Oscillator," IEEE Trans. Microwave Theory and Techniques, MTT-39, Feb. 1991, pp. 1930-200.
- ⁹ J. Birkeland and T. Itoh, "two-port FET Oscillators with Applications to Active Arrays," IEEE Microwave and Guided Wave Letters, Vol. 1 May 1991, pp. 112-113.
- ¹⁰ A. Mortazawi and B. C. DeLoach, "A Nine-MESFET two-dimensional Power Combining Array with Strongly Coupled Oscillators," IEEE Microwave and Guided Wave Letters, Vol. 3, pp. 214-216, July 1993.
- ¹¹ S. Nogi, J. Lin, and T. Itoh, "Mode Analysis and Stabilization of a Spatial Power-Combining Array with Strongly Coupled Oscillators," IEEE Trans. Microwave Theory and Tech., Special Issue on Quasi-Optical Techniques, Vol. MTT-41, pp. 1827-1837, Oct 1993.
- ¹² M. Kim, et.al., "A 100-element HBT Grid Amplifier," IEEE Trans. Microwave Theory and Techniques, Special Issue on Quasi-Optical Techniques, vol. MTT-41, pp. 1762-1771, October 1993.
- ¹³ J. B. Hacker, et.al. "A 10-Watt X-Band Grid Oscillator," IEEE MTT-S International Microwave Symp. 1994.
- ¹⁴ D. Rutledge, Private communications, June, 1995.
- ¹⁵ J.W. Mink and F.K. Schwering, "A Hybrid Dielectric Slab-Beam Waveguide for the Sub-Millimeter Wave Region," IEEE Trans. Microwave Theory and Techniques, Vol. 41. Oct. 1993, pp 1720-1729,
- ¹⁶ F. Poegel, et.al. "Demonstration of an Oscillating Quasi-optical Slab Power Combiner," IEEE MTT-S International Microwave Symposium, 1995.
- ¹⁷ H. Hwang, T. W. Nutseon, M. B. Steer, J. W. Mink, J. Harvey, and A Paoellaa "Quasi-optical Power Combining in a Dielectric Substrate, to be published, ISSSE'95 proceedings.
- ¹⁸ J.C. Wiltse and J.W. Mink, "Quasi-Optical Power Combining of Solid-State Sources," Microwave Journal, Vol. 35, pp. 144-156, Feb. 1992.
- ¹⁹ R.A. York, "Quasi-Optical Power Combining Techniques," International conference on IR&MMW, 1994. Also to be published by the SPIE.

FREQ (GHz)	ARRAY SIZE	DEVICE TYPE	POWER (mW)	REFERENCE
5.0	10X10	FET	550	Popovic, et.al.
7.3	3X3	FET	282	Mortazawi, et.al.
8.2	4X4	FET	184	York, et.al.
9.8	10X10	FET	10300	Hacker, et.al.
34.7	6X6	HBT	-	Kim, et.al.
37	4X4	HEMT	-	Wiltse, et.al.
60	2X4	IMPATT	2200	Compton, et.al.

TABLE I - REPORTED QUASI-OPTICAL SOURCES

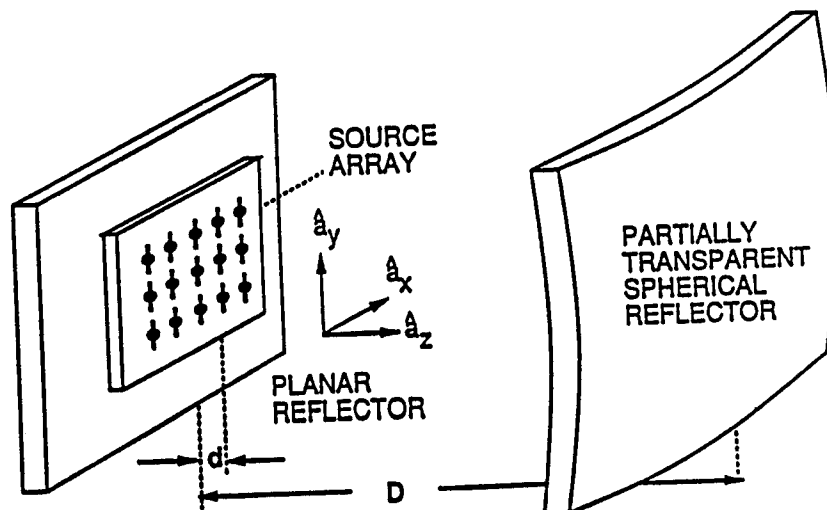
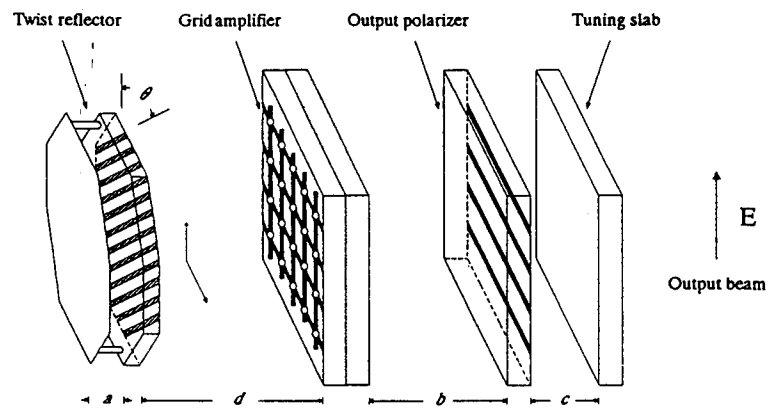
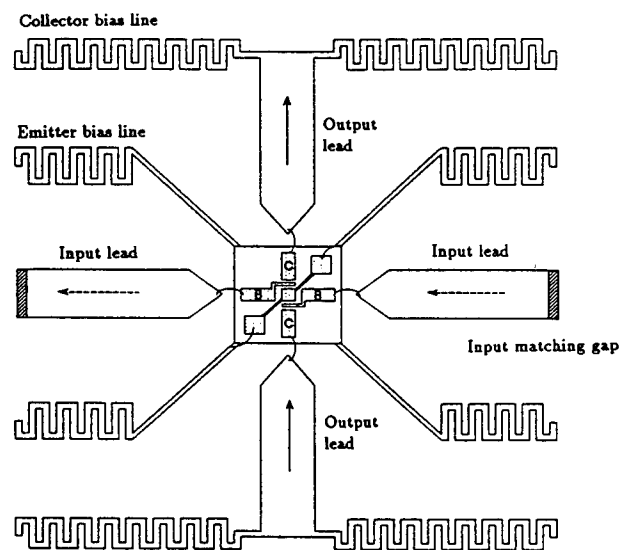


FIGURE 1 - OPEN RESONATOR CONFIGURATION

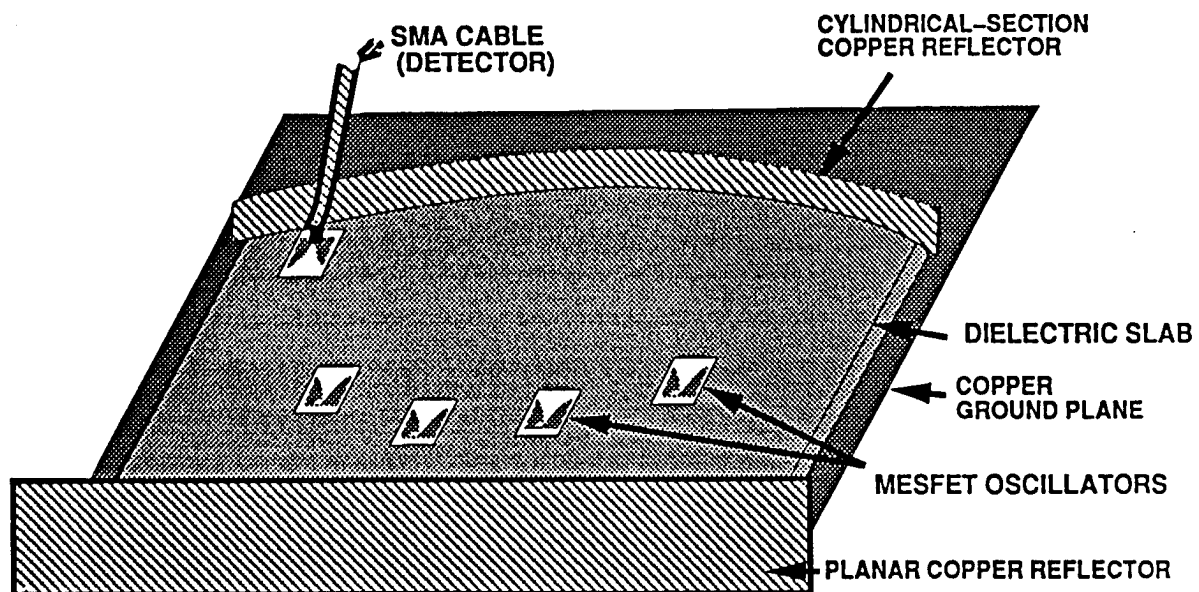


(a)

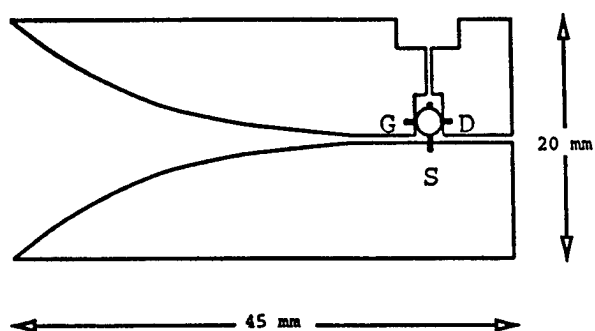


(b)

FIGURE 2 - GRID OSCILLATOR CONFIGURATION



(a)



(b)

FIGURE 3 - HYBRID SLAB-RESONATOR CONFIGURATION

QUASI-OPTICAL POWER COMBINING IN A DIELECTRIC SUBSTRATE

H. Hwang[†], T. W. Nuteson[†], M. B. Steer[†], J. W. Mink[†], J. Harvey[◇], and A. Paolletta[□]

[†] Electronics Research Laboratory, Department of Electrical and Computer Engineering,
North Carolina State University, Raleigh, NC 27695-7911

[◇] United States Army Research Office, PO Box 12211, Research Triangle Park, NC 27709

[□] Microwave & Lightwave Components Division, AMSRL-EP-MA, US Army Research Laboratory, NJ 07703

Abstract. This paper presents a quasi-optical MESFET-based dielectric slab waveguide with an amplifier array. Up to 19 dB amplifier gain and 9.5 dB system gain is obtained at 7.38 GHz. Measurements of amplifier and system gain, $|S_{21}|$, output power vs. input power and transverse power distribution are presented.

1. Introduction

Several quasi-optical structures have been reported, including wave beam type [1], grid type [2], microstrip coupling type [3], and dielectric slab beam waveguide type (DSBW) [4] for power combining. The dielectric slab system has the advantage of being two-dimensional and is thus more amenable to photolithographic reproduction than the conventional open quasi-optical power combining structures. Previous investigations of the quasi-optical dielectric slab cavity and waveguide [5], [6] demonstrated the suitability of this structure for the integration of quasi-optical power combining MMIC technology. In this work, the amplifier arrays are located on the ground plane to reduce perturbation and scattering loss of the beam-modes. Measurements of amplifier gain and system gain, output power vs. input power and transverse electric field distribution are presented. At 7.38 GHz, amplifier gain and system gain reach 19 dB and 9.5 dB, respectively.

2. Dielectric Slab Power Combining System

The dielectric slab waveguide amplifier system incorporates four MESFET amplifiers and two thin convex lenses as shown in Fig. 1. Detail of the active region is shown in Fig. 2. The waveguide system was adjusted with the transistors turned off so that the guided waves are focused near the aperture of the receiving horn ($d_1 = 12$ cm, $d_2 = 44$ cm, $d_3 = 16$ cm). The dielectric slab is Rexolite ($\epsilon = 2.57$, $\tan\delta = 0.0006$

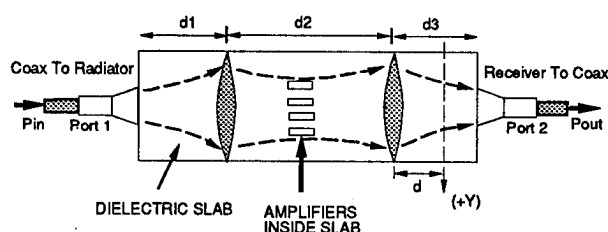


Figure 1: Dielectric slab waveguide system with MESFET amplifiers inside.

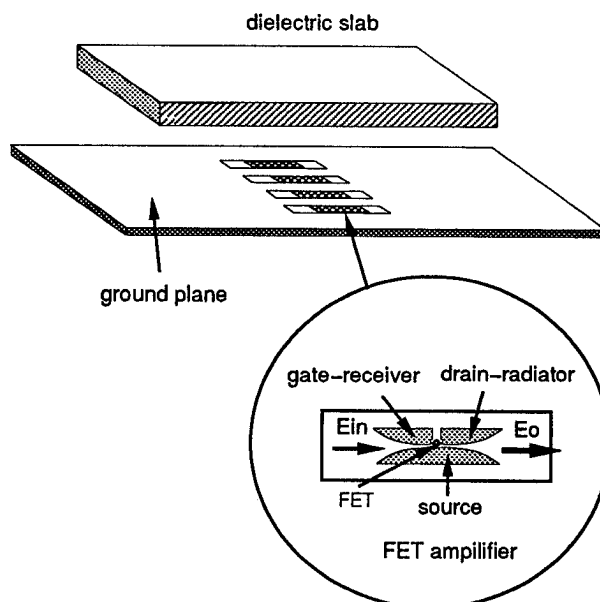


Figure 2: Amplifier array under dielectric slab waveguide.

at X-band), and it is 27.94 cm wide, 62 cm long, and 1.27 cm thick. The lenses are fabricated from Macor ($\epsilon = 5.9$, $\tan\delta = 0.0025$ at 100 kHz) with a radius of 30.48 cm, and the focal length, f , is 28.54 cm. The aperture width of both horn antennas is 9 cm, designed to be wide enough to catch most of the amplified power. Energy emitted from the input radiator propagates in a quasi-optical TE Gaussian mode in the dielectric slab waveguide, and is focused by the first lens in the middle area of the slab. This system is designed so that the amplifier unit cells are within the beam waist (the $1/e$ field points).

The amplifier unit cells are 7 cm x 1.5 cm and employ HP ATF-10235 MESFETs. This design was derived from the active slotline notch antenna by Leverich, et al. [7]. An amplifier unit includes two end-fire Vivaldi antenna tapers which are gate-receiver and drain-radiator, and is specifically designed to eliminate surface-of-slab to ground-plane resonance. The advantage of locating the amplifiers on the ground plane is that it reduces beammode perturbation, scattering losses, and reflection of the input energy due to the amplifier structure. These are problems with amplifiers mounted on the surface of the slab [6] and in the more conventional grid system.

3. Experimental Results and Discussions

The amplifier arrays were located at two locations, thus receiving different input power distributions. Figs. 3 and 4 show the amplifier gains with system input powers of -16 dBm, -13 dBm and -10 dBm. The amplifier gains are obtained by taking the ratio of the measured $|S_{21}|$ when the amplifiers are with and without bias. The highest amplifier gain is 19 dB in location 1 with a system input power -16 dBm. This amplifier gain can compensate the insertion loss due to the beammode energy scattered by the amplifiers.

In Fig. 5, the system loss and insertion loss are shown. The system loss includes beammode scattering by the lenses, and the horn radiation into the air. The insertion loss is due to beammode perturbation by the amplifier structure. In the frequency range of operation, the system loss is 9-10 dB when the system is without amplifiers, and the insertion loss is 2.5 dB due to the amplifiers inserted into the system.

After amplification, the guided waves spread out wider than horn aperture (see Fig. 9), and a small proportion of the amplified energy is captured by the receiving horn. As indicated in Fig. 6, the lenses do serve to focus energy to the receiving horn in spite of the scattering losses they induce.

Fig. 7 shows the system output power P_{out} vs. input power P_{in} when the amplifiers were with and without bias. The amplifier gain is the difference

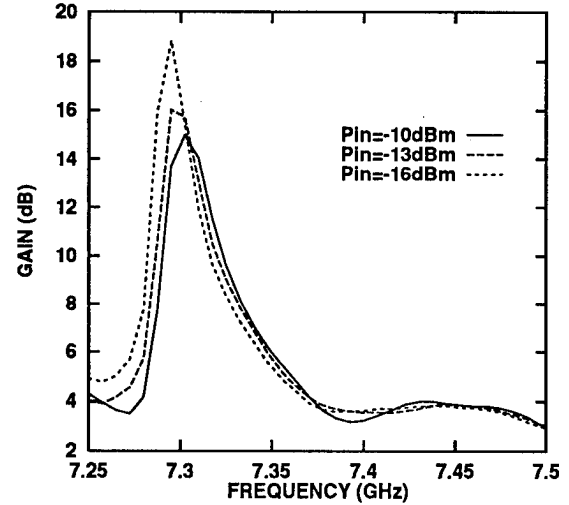


Figure 3: Amplifier gain for location 1. This location is 22cm away from the second lens.

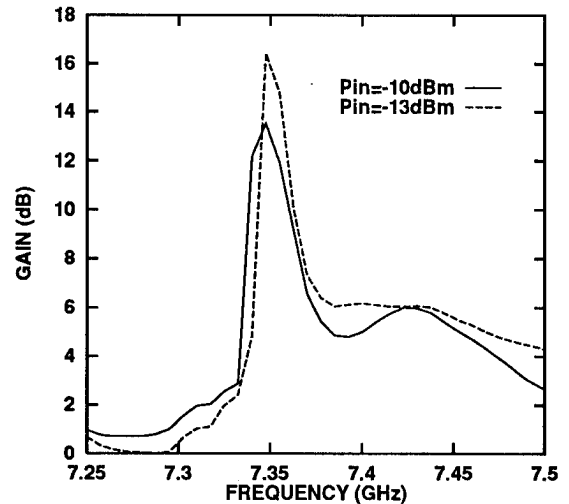


Figure 4: Amplifier gain for location 2. This location is 18cm away from the second lens.

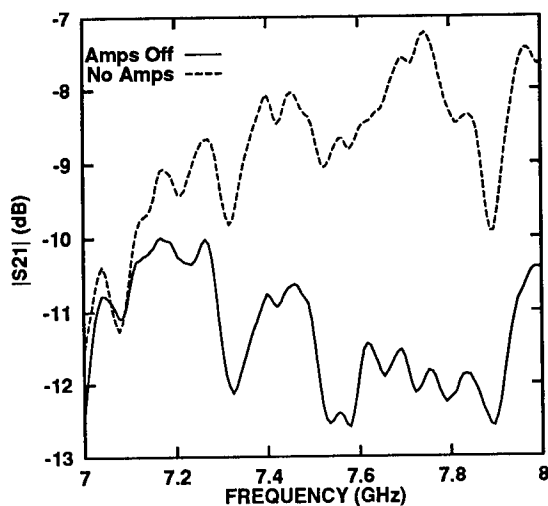


Figure 5: $|S_{21}|$ of the dielectric slab with/without amplifiers. The insertion loss of the unit cells alone is the difference between these two $|S_{21}|$ curves. This loss is believed to be due to field scattering.

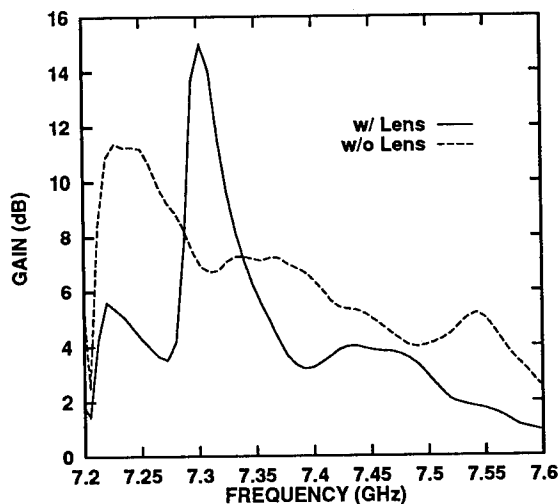


Figure 6: Comparison of amplifier gain with/without lenses.

between $P_{out}(\text{Amp ON})$ and $P_{out}(\text{Amp OFF})$. The system power gain is obtained by subtracting P_{in} from $P_{out}(\text{Amp ON})$. When $P_{out} = -16$ dBm, system power gain and amplifier gain are 9.5 dB and 19 dB, respectively. Note that the P_{out} does not saturate. This is a characteristic of the quasi-optical DSBW amplifier. When the amplifier cells saturate, the excess input power continues to propagate in the slab. The power added efficiency (PAE) of this system is 3.35%. However, we need to count the scattering loss from the second lens, which is about 3.5 dB. Therefore, the PAE is about 7.5%.

The system gain (defined as P_{out}/P_{in}) is shown in Fig. 8 with $P_{in} = 10$ dBm. The E-field distribution measured at $d = 13$ cm is shown in Fig. 9. Comparing the field distributions for amplifiers without biases and for no amplifiers inside the slab, we find that the $|E_y|$ decreases about 2 to 4 dB due to the insertion of the amplifier unit cells in the $-5 \text{ cm} < y < 5 \text{ cm}$ region. Analysis indicates that only 66% of the amplified energy is captured by the receiving horn. Considering 37% of amplified energy is not received, the power added efficiency should be 11.2%.

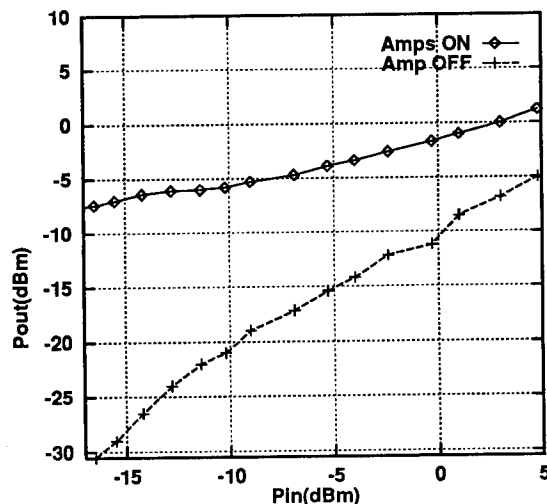


Figure 7: P_{out} vs P_{in} as amplifiers with/without bias

4. Conclusions

We have demonstrated quasi-optical power combining in a dielectric substrate with amplifiers located on ground plane. The maximum amplifier gain and system gain reach 19 dB and 9.5 dB, respectively, at 7.38 GHz.

Acknowledgment

This work was supported in part by the U.S. Army Research Office through grant DAAL03-89-G-0030.

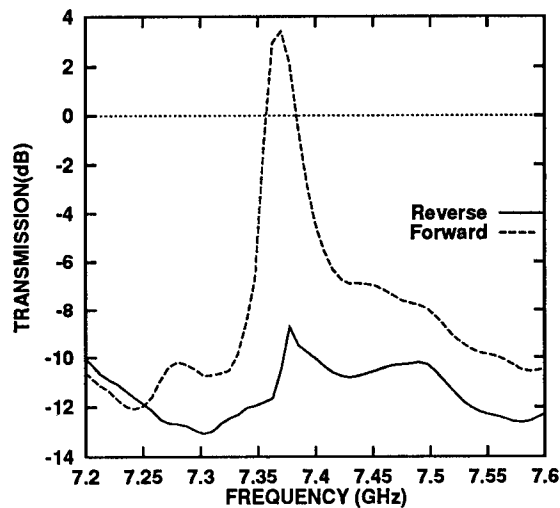


Figure 8: Transmission gain for the slab as amplifier with bias

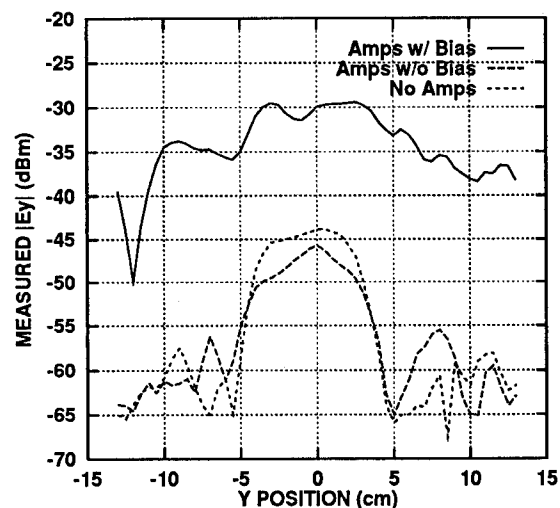


Figure 9: $|E_y|$ pattern on the top surface of slab. This pattern is measured at 7.38GHz with $P_{in} = 10$ dBm

We also thank R. Walter, A. Schaumke and K. Kojucharoff for their technical support in the early stages of this project.

References

- [1] J. W. Mink, "Quasi-optical power combining of solid-state millimeter-wave sources," *IEEE Trans. on Microwave Theory and Techniques*, vol. MTT-34, pp. 273-279, Feb. 1986.
- [2] Z. B. Popović, R. M. Weilke, M. Kim, and D. B. Rutledge, "A 100-MESFET planar grid oscillator," *IEEE Trans. Microwave Theory Tech.*, vol. MTT-39, pp. 193-200, Feb. 1991.
- [3] N. J. Koliass and R. C. Compton, "A microstrip-based quasi-optical polarization rotator array," *IEEE MTT-S Int. Microwave Symp. Dig.*, pp. 773-776, May 1995.
- [4] J. W. Mink and F. K. Scherwing, "A hybrid dielectric slab-beam waveguide for the sub-millimeter wave region," *IEEE Trans. Microwave Theory Tech.*, vol. MTT-41, pp. 1720-1729, Oct. 1993.
- [5] F. Poegel, S. Irrgang, S. Zeisberg, A. Schuene-mann, G. P. Monahan, H. Hwang, M. B. Steer, J. W. Mink, F. K. Scherwing, A. Paolletta, and J. Harvey, "Demonstration of an oscillating quasi-optical slab power combiner," *IEEE MTT-S Int. Microwave Symp. Dig.*, pp. 917-920, May 1995.
- [6] H. Hwang, G. P. Monahan, M. B. Steer, J. W. Mink, J. Harvey, A. Paolletta, and F. K. Scherwing, "A dielectric slab waveguide with four planar power amplifiers," *IEEE MTT-S Int. Microwave Symp. Dig.*, pp. 921-924, May 1995.
- [7] W. K. Leverich, X.-D. Wu, and K. Chang, "FET active slotline notch antenna for quasi-optical power combining," *IEEE Trans. Microwave Theory Tech.*, vol. MTT-41, pp. 1515-1517, Sept. 1993.

QUASI-OPTICAL COMPONENTS AND SUBSYSTEMS FOR COMMUNICATIONS

Zoya Popović,

Jon Schoenberg, Tom Mader, Wayne Shiroma, Stein Hollung, Milica Marković, Jonathan Dixon

Department of Electrical and Computer Engineering, University of Colorado, Boulder, CO

Scott Bundy

Superconducting Core Tech., Inc., Golden, CO

1. INTRODUCTION AND BACKGROUND

Although most wireless communications systems are now digital, they still require analog front ends, since the transmitted signal is a modulated sinusoid. Optimization of the analog transmitter and receiver can improve the digital system performance. In this paper we describe a new approach to what we believe are more reliable, less expensive, and more compact front ends for microwave and millimeter-wave communications. This new approach is based on quasi-optical components, which are printed surfaces loaded with active and/or passive devices.

Many active quasi-optical components have been demonstrated to date: oscillators [1-8], amplifiers [9-13], mixers [14], phase shifters [15,16], multipliers [17], and switches [18]. Although these demonstrations show the feasibility of a quasi-optical communication system, a practical demonstration combining the functions of several components has not yet been reported.

The most important front-end component of a communication system is the transmit/receive (T/R) module. A quasi-optical transceiver, consisting of a self-oscillating FET mixer, was reported in [19], but this circuit did not incorporate power amplification, low-noise amplification, or modulation functions. Here we describe analysis, design and measurements of the necessary quasi-optical T/R components. We also discuss a way to construct a quasi-optical transceiver from the presented components and present some demonstration results.

Originally developed to address the need for high-power millimeter wave sources [20], quasi-optical circuitry has several advantages for wireless communication applications:

- Millimeter waves offer more bandwidth, and the increased atmospheric attenuation forms a natural cell boundary, making these frequencies ideal for short-range, high-capacity indoor networks for high-speed data or multimedia transmission. The limited output

power of millimeter-wave solid-state devices is overcome by spatially power-combining hundreds of low-power devices [1,5]. This allows power levels in the tens of watts range, adequate for terrestrial and satellite communications.

- Quasi-optical active components are compact, lightweight, and amenable to monolithic integration. The antenna is an integral part of the circuit design, which allows for overall system size reduction.

- In a mobile environment where S/N ratios fluctuate wildly due to multipath and shadow-fading, dynamic power control and adaptive beam-steering techniques are needed to obtain energy-efficient systems. Recently, quasi-optical amplifiers with beam-steering and beam-forming capabilities have been demonstrated [12,13].

- The total output power is a result of combining a large number of devices. Hence, the reliability of quasi-optical components is good; a fraction of the devices can fail before the component fails [21,22].

2. SYSTEM COMPONENTS

The results presented here describe components which perform all of the functions that a quasi-optical transceiver requires: signal generation, amplification, reception, modulation and beam control.

Reliable, compact, solid-state oscillators are needed for signal generation and as LOs. In the first planar grid oscillator to demonstrate large-scale power combining [1], the powers of 100 MESFET oscillators were spatially combined to produce an effective radiated power of 21 W at 5 GHz. This type of device has demonstrated graceful degradation, as shown in [21,22]. In [7], a full-wave theory for analyzing grid oscillators consisting of arbitrarily shaped metal gratings printed on one or both sides of an arbitrary dielectric was presented. Several successful grid oscillators have been designed with this analysis tool, including C-band oscillators [7], X-band oscillators [12], and stacks of grid oscillators [6].

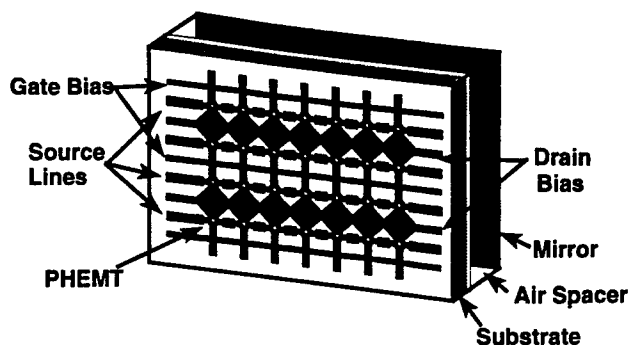


Figure 1: A 10.25-GHz grid oscillator (designed with our full-wave analysis program) operates exactly at the design frequency and is used as a focal-point feed for a lens amplifier combiner [12].

For example, Fig. 1 shows a grid oscillator designed to operate at 10.25 GHz as a feed for a narrowband free-space lens amplifier. This grid has a rectangular unit cell and an asymmetric metal geometry. It was built with 28 PHEMTs and oscillated exactly at the design frequency [12]. Another example is a millimeter-wave grid oscillator, fabricated and tested in collaboration with TLC Precision Wafer Technology Inc. and Honeywell (Minneapolis). The simulated oscillation frequency using small-signal device parameters is 31.25 GHz, while the 100-PHEMT monolithic grid locked at 31.1 GHz [23].

More recently, a theory for analyzing cascaded systems of multi-function grids, including fixed-frequency and tunable filters, and mode-selective grid oscillators was developed [24,25]. Filters, especially those with sharp rolloff characteristics, are essential for communication systems. Tunable filters offer additional system flexibility. A voltage-controlled frequency-selective surface (FSS) was designed using the theory presented in [24]. It consists of a printed grid loaded with varactor diodes. The resonance of this filter tunes in a 30% bandwidth when the bias across the diodes is changed, as shown in Fig. 2. This FSS was placed in front of a 25-PHEMT grid oscillator and allowed the locked frequency to be set at either 4 or 6 GHz [25]. The radiation patterns and cross-polarization levels for both frequencies are the same. The ability to selectively choose the carrier frequency is useful for frequency-diversity systems.

Low-loss circular polarizers which can be inserted in the transmission path are useful, as circular polarization has been shown to suppress multipath-delayed waves [26], resulting in improved transmission characteristics. In [25], a linear-to-circular polarization con-

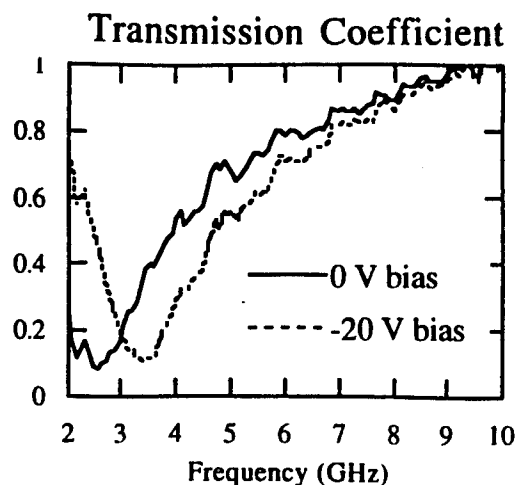


Figure 2: The measured electrical tuning of the resonance of a varactor-loaded tunable FSS shows a 30% bandwidth with very little change in resonance amplitude [25].

verter was presented which has a 1.2 dB axial ratio with only a 1-dB transmission loss at X-band.n

High gain, low noise and power amplifiers are necessary parts of every transceiver. A lens amplifier array using patch antennas is shown in Fig. 3. This amplifier demonstrated 8 dB of absolute power gain in a 3% bandwidth at 9.7 GHz [12]. The input side patches (shown in black) have variable delay lines across the array, allowing for a focal-point near-field feed. This enables efficient input feeding as well as simple transmitter design with the added capability of beam-steering and beam-forming.

In a mobile environment, where signal-to-noise ratios can fluctuate wildly, dynamic power control and adaptive beam-steering techniques can be used to maintain a low bit error rate and reduced sensitivity to multipath and shadow-fading. Beam-steering and beam-forming have been demonstrated with quasi-optical lens amplifiers [12,13]. The lens amplifier in Fig. 3 is fed by two identical grid oscillator sources positioned along a focal arc of the amplifying lens. When the two sources are turned on simultaneously, the fields are linearly superimposed at the amplifier output to produce a pattern with two distinct beams due to the two respective sources [13]. However, the two sources can also be switched on and off one at a time to produce a fixed number of discrete switchable beams for a steering system. We have measured a 5-kHz steering speed, limited by the settling time of the oscillator feeds.

High-efficiency quasi-optical amplifiers increase bat-

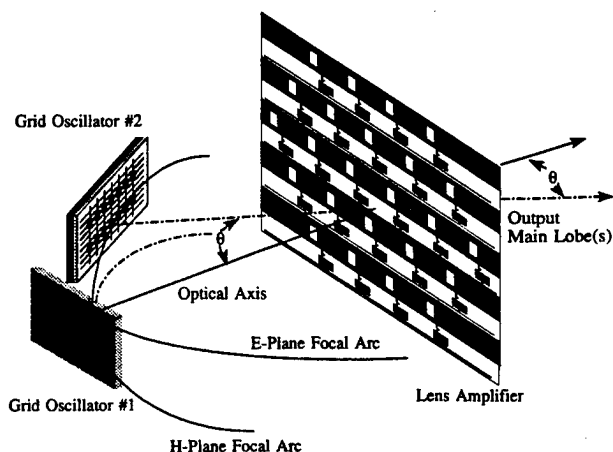


Figure 3: A quasi-optical planar lens amplifier fed by two identical grid oscillator sources positioned along a focal arc of the amplifying lens [13].

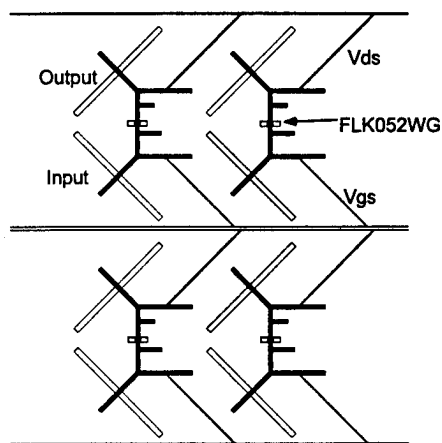


Figure 4: Layout of a plane-wave-fed slot antenna power amplifier. Unfilled rectangles show the positions of the slot antennas on the back of the substrate [27].

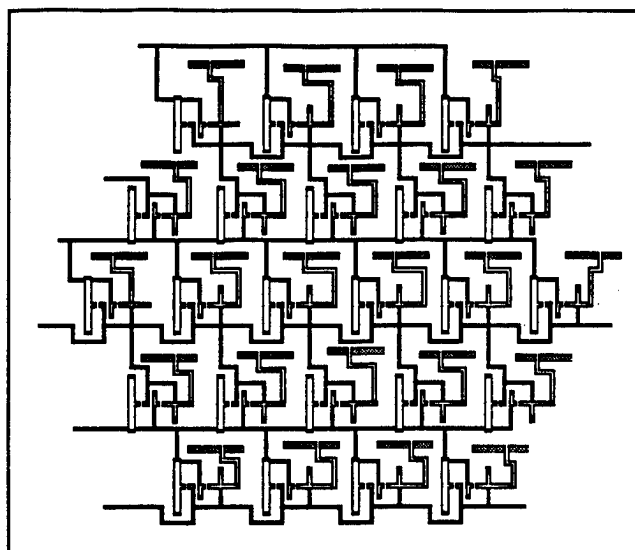


Figure 5: Layout of a slot antenna receiving low noise lens amplifier. The amplifiers in the array are two-stage PHEMT CPW circuits [13].

tery lifetime, and reduce overall size and weight due to lower heat-sinking requirements. By increasing the efficiency from 50% to 90%, the dissipated heat power is reduced by a factor of nine for the same amplifier output power. For two-dimensional amplifier antenna arrays, low heat dissipation is especially crucial, since the heat flow is lateral. A high-efficiency power amplifier array using anti-resonant slot antennas, shown in Fig. 4, exhibits 10 dB gain, 2.5 W of power with 65% power added efficiency at 5 GHz from only 4 MESFETs [27]. This concept can be extended to millimeter-wave frequencies, as was demonstrated in [28] for a Ka-band amplifier.

To demonstrate a receiving amplifier, an X-band low-noise PHEMT lens amplifier array using antiresonant slot antennas and two-stage low-noise CPW amplifiers has recently been reported [13]. The amplifier is shown in Fig. 5 and demonstrates 13 dB absolute power gain, a minimum 1.7 dB noise figure, and 11% 3-dB bandwidth with an average noise figure below 2.3 dB in this bandwidth, shown in Fig. 6. The high gain and low noise figure demonstrated by this amplifier are important for maintaining a high SNR, and thus a low bit error rate. The demonstrated 1.1-GHz bandwidth at 10 GHz demonstrates the applicability of quasi-optical amplifiers to broadband data communications.

3. DISCUSSION

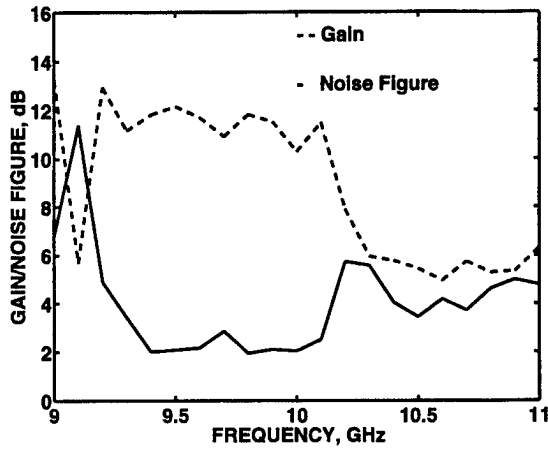


Figure 6: Measured gain and noise figure of the LNA array.

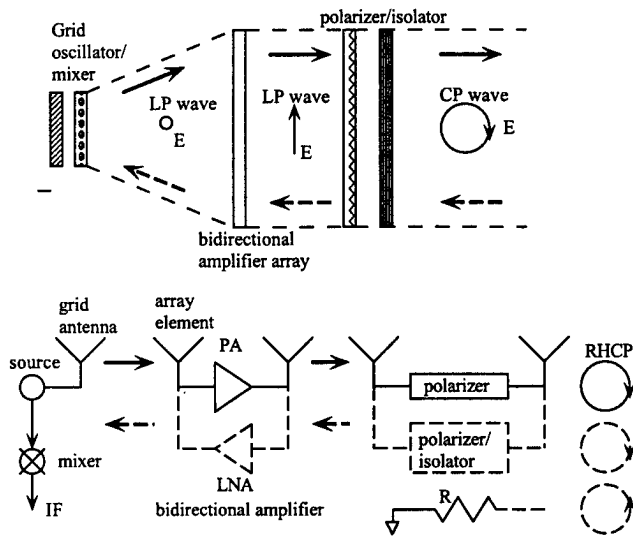


Figure 7: Block diagram of a quasi-optical transceiver. The transmitted signal is shown in solid-line arrows, and the receiving signal path in dashed-line.

The measured properties of basic components which make up a quasi-optical T/R module were discussed above. A block diagram of a possible quasi-optical transceiver is shown in Fig. 7. It consists of a grid oscillator, such as the one shown in Fig. 1, which acts as a solid-state power-combining source that generates the carrier frequency for the transmitter and also serves as the local oscillator and self-oscillating mixer for the receiver. A planar array of T/R active antennas, such as the ones from Figures 3, 4, or 5, performs the power amplification for the transmit and the low-noise amplification for the receive. Both the input and output waves are focused. Locating the source/mixer at the focal point of the amplifier reduces diffraction loss and thus increases system efficiency. The close proximity of the oscillator and amplifier also allows compact transceiver design. Reliability is improved since the degradation is graceful. This approach is modular, since individual grids or arrays serving different functions can be cascaded into systems.

Modulation can be achieved either through the gate bias of the oscillator or amplifier, or by cascading an external modulator with the amplifier. In [4], a quasi-optical VCO consisting of an array of transistor oscillators stacked with an array of varactor diodes demonstrated good frequency modulation characteristics in a 10% modulation bandwidth with low associated parasitic AM. However, since most modern communications systems are digital, it is important to have digital modulators. A quasi-optical digital phase modulator can be designed based on 3 antenna arrays connected with transistor SPDT switches, allowing 2 bits of phase shift in a single array. The 4 bits required for QPSK can be obtained with two cascaded arrays. We have demonstrated a unit cell of the BPSK modulator with phase shifts of 0° and 150° with no associated transmission loss, as the switches have some gain to overcome the losses.

In order for the quasi-optical amplifier to function as a T/R module, bidirectional amplifier elements need to be used, with transistors placed in opposite directions to amplify the outgoing and incoming waves independently. The transmit amplifier is impedance-matched for maximum power, while the receive amplifier is matched for low noise. (An alternative to using two amplifiers in each element is the grid approach [9], but in this case the amplifier needs to be simultaneously designed for high power/gain and low noise.)

The frequency-dependence of the antenna loads is included in the design. The choice of the antenna is an important consideration. Amplifier arrays using folded slots have demonstrated 8% bandwidth [29], while those

using a combination of loaded folded slots on the input and anti-resonant slots at the output have demonstrated 11% bandwidth [13]. The second-resonance slot itself has a convenient input impedance of 25 to 100 Ω and a 20% bandwidth (VSWR=2).

Antenna diversity is an important design option for wireless communications systems suffering from multipath effects. For example, in a recent article [30], it is shown theoretically that a significant increase in system capacity can be achieved by using spatial diversity and optimal combining. It has also been proven theoretically [31] that the power contained in the electric and magnetic field components are statistically independent after propagating through a multipath channel. An antenna which responds independently to the vector components of both the electric and the magnetic field can significantly reduce multipath effects [32]. The antennas themselves can therefore be designed to improve the overall system and effectively change the model of the multipath fading channel. As quasi-optical components are essentially active antennas, they are extremely suitable for spatial, frequency, polarization and field diversity architectures.

An important issue in local oscillator applications is the phase noise. The overall noise of a grid oscillator should be less than the noise contribution of an individual device, since the grid is self-injection-locked. In addition, since the phase noise of the devices are uncorrelated, the individual noise contribution of each device in the array should average out. Experimental verification for the single-sideband noise reduction in a 100-element grid was presented in [5].

In the two-level power combining approach shown in Fig. 7, advantages of both oscillator and amplifier combiners are used: the grid oscillator source has improved noise characteristics, while the amplifier array provides large dynamic range. For reception, the noise floor of the entire array is equal to the noise floor of each of the amplifier elements, provided the amplifier noises are uncorrelated. On the other hand, the input power of the array can be N times larger than that of a single element, as the power gets distributed. This means that for a 10 x 10 array, the dynamic range is increased by 20 dB. In addition, focusing on the receiver end with an LNA array allows for beam-forming in reception by placing mixers at different points along the focal surface. For example, with one mixer positioned at boresight, and two others placed at $\pm 45^\circ$, one could receive sum and difference patterns. The reciprocal beam-forming in transmission was already demonstrated with the array from Fig. 3. This allows adaptive processing at the receiver analog front end, increasing the dynamic range of the system.

4. ACKNOWLEDGEMENTS

The work presented in this paper was funded by the U.S. Army Research Office, the National Science Foundation under a Presidential faculty Fellow Award, Compact Software, Lockheed Martin and TLC Precision Wafer Techn., Inc. Jon Schoenberg holds an Air Force Institute of Technology Civilian Institution program fellowship. Jonathan Dixon holds an Office of Naval Research Graduate Fellowship.

5. REFERENCES

- [1] Z. B. Popović, R. M. Weikle II, M. Kim, and D. B. Rutledge, "A 100-MESFET planar grid oscillator," *IEEE Trans. Microwave Theory Tech.*, vol. 39, pp. 193-200, Feb. 1991.
- [2] R. A. York and R. C. Compton, "Quasi-optical power-combining using mutually synchronized oscillator arrays," *IEEE Trans. Microwave Theory Tech.*, vol. 39, pp. 1000-1009, June 1991.
- [3] J. Birkeland and T. Itoh, "A 16-element quasi-optical FET oscillator power-combining array with external injection locking," *IEEE Trans. Microwave Theory Tech.*, vol. 40, pp. 475-481, Mar. 1992.
- [4] T. B. Mader, S. C. Bundy, and Z. B. Popović, "Quasi-optical VCOs," *IEEE Trans. Microwave Theory Tech.*, vol. 41, pp. 1775-1781, Oct. 1993.
- [5] J. B. Hacker, et al., "A 10-Watt X-band grid oscillator," *1994 IEEE MTT-S Int. Microwave Symp. Dig. (San Diego, CA)*, pp. 823-826.
- [6] W. A. Shiroma, B. L. Shaw, and Z. B. Popović, "A 100-transistor quadruple grid oscillator," *IEEE Microwave and Guided Wave Lett.*, vol. 4, pp. 350-351, Oct. 1994.
- [7] S. C. Bundy and Z. B. Popović, "A generalized analysis for grid oscillator design," *IEEE Trans. Microwave Theory Tech.*, vol. 42, pp. 2486-2491, Dec. 1994.
- [8] P. Liao and R. A. York, "A new phase-shifterless beam-scanning technique using arrays of coupled oscillators," *IEEE Trans. Microwave Theory Tech.*, vol. 41, pp. 1810-1815, Oct. 1993.
- [9] M. Kim, E. A. Sovero, J. B. Hacker, M. P. De Lisio, J.-C. Chiao, S.-J. Li, D. R. Gagnon, J. J. Rosenberg, and D. B. Rutledge, "A 100-element HBT grid amplifier," *IEEE Trans. Microwave Theory Tech.*, vol. 41, pp. 1762-1771, Oct. 1993.
- [10] T. Mader, J. Schoenberg, L. Harmon, and Z. B. Popović, "Planar MESFET transmission wave amplifier," *Electronics Lett.*, vol. 28, no. 19, pp. 1699-1701, Sep. 1993.
- [11] N. Sheth, T. Ivanov, A. Balasudramaniyan, and A. Mortazawi, "A 9-HEMT spatial amplifier," *1994*

- IEEE MTT-S Int. Symp. Dig. (San Diego, CA)*, pp. 1239-1242, May 1994.
- [12] J. S. H. Schoenberg, S. C. Bundy, and Z. B. Popović, "Two-level power combining using a lens amplifier," *IEEE Trans. Microwave Theory Tech.*, vol. 42, pp. 2480-2486, Dec. 1994.
 - [13] J. S. H. Schoenberg, T. Mader, B. Shaw, and Z. B. Popović, "Quasi-optical antenna array amplifiers," *1995 IEEE MTT-S Int. Symp. Dig. (Orlando, FL)*, pp. 605-608.
 - [14] J. B. Hacker, R. M. Weikle II, M. Kim, M. P. De Lisio, and D. B. Rutledge, "A 100-element planar Schottky diode grid mixer," *IEEE Trans. Microwave Theory Tech.*, vol. 40, pp. 557-562, Mar. 1992.
 - [15] W. W. Lam, C. F. Jou, H. Z. Chen, K. S. Stolt, N. C. Luhmann Jr., and D. B. Rutledge, "Millimeter-wave diode-grid phase shifters," *IEEE Trans. Microwave Theory Tech.*, vol. 36, pp. 902-907, May 1988.
 - [16] L. B. Sjogren, H.-X. Liu, X. Qin, C. W. Domier, and N. C. Luhmann Jr., "Phased-array operation of a diode grid impedance surface," *IEEE Trans. Microwave Theory Tech.*, vol. 42, pp. 565-572, Apr. 1994.
 - [17] C. F. Jou, W. W. Lam, H. Z. Chen, K. S. Stolt, N. C. Luhmann Jr., and D. B. Rutledge, "Millimeter-wave diode-grid frequency doubler," *IEEE Trans. Microwave Theory Tech.*, vol. 36, pp. 1507-1514, Nov. 1988.
 - [18] K. D. Stephan and P. F. Goldsmith, "W-band quasi-optical integrated PIN diode switch," *1992 IEEE MTT-S Int. Symp. Dig. (Albuquerque, NM)*, pp. 591-594.
 - [19] J. Birkeland and T. Itoh, "FET-based planar circuits for quasi-optical sources and transceivers," *IEEE Trans. Microwave Theory Tech.*, vol. 37, pp. 1452-1459, Sep. 1989.
 - [20] J. W. Mink, "Quasi-optical power combining of solid-state millimeter-wave sources," *IEEE Trans. Microwave Theory Tech.*, vol. 34, pp. 273-279, Feb. 1986.
 - [21] Z. B. Popović, R. M. Weikle II, M. Kim, K. A. Potter, and D. B. Rutledge, "Bar-grid oscillators," *IEEE Trans. Microwave Theory Tech.*, vol. 38, pp. 225-230, Mar. 1990.
 - [22] J. Lin and T. Itoh, "Experiments of device failures in a spatial power-combining array," *IEEE Trans. Microwave Theory Tech.*, vol. 43, pp. 267-271, Feb. 1995.
 - [23] J. Geddes, TLC Precision Wafer Technology, Inc., private communication.
 - [24] S. Bundy, W. Shiroma, Z. Popović, "Analysis of cascaded quasi-optical grids," *1995 IEEE MTT-S Int. Symp. Dig. (Orlando, FL)*, pp. 601-604.
 - [25] W. A. Shiroma, S. C. Bundy, S. Hollung, B. D. Bauernfeind, and Z. B. Popović, "Cascaded Active and Passive Quasi-Optical Grids," to appear in *IEEE Trans. Microwave Theory Tech.*, Dec. 1995.
 - [26] T. Manabe and Y. Furuhashi, "Recent propagation studies in Japan," *IEEE Antennas and Propagation Magazine*, vol. 36, no. 5, pp. 7-13, Oct. 1994.
 - [27] T. B. Mader, *Quasi-Optical Class-E Power Amplifiers*, Ph. D. Dissertation, University of Colorado, Boulder, Aug. 1995.
 - [28] J. Hubert, J. Schoenberg, and Z. B. Popović, "A Ka-band quasi-optical amplifier," *1995 IEEE MTT-S Int. Symp. Dig. (Orlando, FL)*, pp. 585-588.
 - [29] H.-S. Tsai, M. J. W. Rodwell, and R. A. York, "Planar amplifier array with improved bandwidth using folded slots," *IEEE Microwave and Guided Wave Lett.*, vol. 4, pp. 112-114, Apr. 1994.
 - [30] J. H. Winters, J. Salz, and R. D. Gitlin, "The impact of antenna diversity on the capacity of wireless communications systems," *IEEE Trans. on Communications*, vol. 42, No. 2/3/4, pp. 1740-1750, April 1994.
 - [31] W. C. Jakes, ed., *Microwave Mobile Communications*, IEEE Press, 1993, (Copyright AT&T, 1974).
 - [32] W. S. Y. Lee, *Mobile Communications Design Fundamentals*, 2nd ed., John Wiley & Sons, Inc., 1994.

QUASI-OPTICAL MICROSTRIP AMPLIFIERS BASED ON MULTILAYER COUPLED STRUCTURES

Toni Ivanov and Amir Mortazawi

Department of Electrical and Computer Engineering
University of Central Florida,
Orlando, FL 32816-2450
tgi@engr.ucf.edu, amm@engr.ucf.edu

ABSTRACT

Single stage and double stage quasi-optical amplifiers are presented. The amplifiers are constructed on double layer back to back microstrip circuits with a shared ground plane. The ground plane provides an effective isolation between the receiving and the transmitting antenna arrays. Furthermore it serves as a heat sink in high power amplifier designs. The single stage quasi-optical amplifier had a gain of 7.54 dB at 10.04 GHz and the two stage quasi-optical amplifier had a gain of 18.0 dB at 9.95 GHz.

1. INTRODUCTION

The increasing demand for millimeter-wave communication and radar systems has lead to the need for solid state amplifiers working at these frequencies. However, in order to efficiently amplify electromagnetic waves at these frequencies, conventional amplifier circuits must be modified in order to reduce the losses in the guiding structures. This can be achieved by coupling the waves into and out of the amplifier through free space using radiating elements rather than by conventional waveguide coupling. This approach has lead to increased interest in the area of quasi optical power amplification [1-6]. This paper reports on microstrip quasi-optical amplifiers based on two types of coupling. These amplifiers were constructed on double layer back to back microstrip circuits with a shared ground plane. The continuous ground plane provides a very effective input-output isolation. The ground plane also serves as a heat sink. Furthermore, these circuits can be readily incorporated into multistage quasi-optical amplifiers.

2. THEORY AND DESIGN

2.1. A Single Stage Double Layer Quasi-Optical Amplifier Incorporating Microstrip-Via Hole-Microstrip Interconnects

The first circuit to be reported is a single stage quasi-optical amplifier based on a via-hole-coupled two layer microstrip structure. Figs. 1a and 1b show the layout of the amplifier incorporating nine HEMTs in a 3x3 array configuration. The input and output layers are placed back to back (with a shared ground plane) and the signal is coupled from one layer to the other through via-holes forming a three dimensional interconnect system. In order to design the input and output matching circuits, the simultaneous conjugate matched admittances are first determined. Open circuited stubs are used to provide simultaneous conjugate matched susceptances. These stubs effectively resonate the device admittances, hence the admittances seen looking into the input and output ports are purely real. These conductances are then matched to the input and output microstrip antennas using quarter wave transformers. Thus the simultaneous conjugate match conditions are fulfilled. The quasi-optical amplifier was fabricated on 31 mil thick RT - Duroid™ with $\epsilon_r = 2.3$. The active device used is a Fujitsu FHX06LG HEMT biased at $V_{ds} = 2$ V, and $I_{ds} = 10$ mA. The dimensions of the microstrip antennas used are 1.17 cm by 0.91 cm. The patch antennas were cross polarized to facilitate the gain measurements. The circuit was biased using high impedance lines connected to the center of the non radiating edges of microstrip antennas as shown in Fig. 1. The inter element spacing was chosen to be $0.67 \times 0.75 \lambda$ in order to obtain the optimum directivity from the antenna arrays. The far field measurement

procedure reported in [6] was used to determine the quasi-optical amplifier gain. The amplifier's gain was measured to be $G = 7.54$ dB at 10.04 GHz with a bandwidth of 0.4 GHz. Fig. 2 shows the gain versus frequency plot for the 3 x 3 quasi optical amplifier. This calculation takes into account the variation of the array gain with frequency. Fig. 3 shows a close match between the theoretical and experimental H-plane patterns. The E-plane pattern was also measured and good agreement with the theoretically predicted pattern was observed.

2.2. A Two Stage Double Layer Quasi-Optical Amplifier Incorporating Microstrip-Slot Line-Microstrip Interconnects

Here a two stage quasi-optical amplifier employing microstrip line - slot line - microstrip line interconnects is presented. The two layers are placed back to back with a shared ground plane. Fig. 4 shows a perspective view of the quasi-optical amplifier. The coupling between the two stages is accomplished through microstrip to slot transitions, therefore there is no electrical contact from one layer to another. This facilitates the monolithic fabrication of such amplifiers. Furthermore this provides DC isolation between the two amplifier stages. The common ground plane provides a very effective isolation between the receiving antenna array and the transmitting antenna array and it serves as a heat sink in high power amplifier designs. Separating the two stages may also play an important factor when the excess heat density is of concern. This type of structure allows the circuit designer to reduce the device density by spreading the devices between the two layers, thereby somewhat reducing the thermal power density. Therefore, this structure has the potential to address the heat flow, the isolation between input and output ports and MMIC compatibility problems simultaneously. The same active devices and substrate materials which were used to construct the amplifier described in section 2.1 were also employed here. The design procedure follows the same sequence, except that the output of the first stage and the input of the second stage are matched to the real impedance of the slot line. Fig. 5 shows the measured gain of a 3x3 two stage amplifier versus frequency. There are a total of 18 HEMTs used in this amplifier. Maximum gain of 18 dB was obtained at 9.95 GHz. The calculated and

measured E plane patterns of the 3x3 amplifier array are compared in Fig. 6.

3. CONCLUSION

Two quasi-optical microstrip circuits based on different multilayer coupled structures have been presented. The via hole coupled single stage amplifier had a gain of 7.54 dB at 10.04 GHz. The slot line coupled two stage quasi-optical amplifier had a gain of 18.0 dB at 9.95 GHz. Both structures address isolation and heat-sinking for MMIC implementation of these amplifiers at mm-wave frequencies.

ACKNOWLEDGMENTS

This work was supported in part by the Lockheed-Martin Corporation. The authors would also like to acknowledge Fujitsu Corporation for the donation of the devices and Rogers Corporation for the donation of the substrate materials.

REFERENCES

- [1] M. Kim, E.A. Soverro, J.B. Hacker, M.P. De Lisio, J.-C. Chiao, S.-J. Li, D.R. Cagnon, J.J. Rosenberg, and D.B. Rutledge, "A 100-Element HBT Grid Amplifier", *IEEE Trans. MTT*, Vol. 41, No. 10, pp. 1762-1771, Oct., 1993.
- [2] T. Mader, J. Schoenberg, L. Harmon and Z. B. Popovic, "Planar MESFET Transmission Wave Amplifier," *Electronic Letters*, vol. 29 No. 19, pp. 1699-1701, Sept., 1993.
- [3] C. Y. Chi and G. M. Rebeiz, "A Quasi-Optical Amplifier," *IEEE Microwave and Guided Wave Letters*, Vol. 3 No. 6, pp. 164-166, June 1993.
- [4] H.S. Tsai, M.J.W. Rodwell, and R.A. York, "Planar Amplifier Array with Improved Bandwidth Using Folded Slots", *IEEE Microwave and Guided Wave Lett.*, Vol. 4, pp. 112-114, Apr. 1994
- [5] T. Ivanov, and A. Mortazawi, "Two Stage Double Layer Microstrip Spatial Amplifiers", *IEEE MTT-S Int. Microwave Symp. Dig.*, pp. 589-592, May, 1995
- [6] T. Ivanov, A. Balasubramaniyan, and A. Mortazawi, "One and Two Stage Spatial Amplifiers", *IEEE Trans. Microwave Theory Tech.*, Vol. 43, no. 9, Sept., 1995

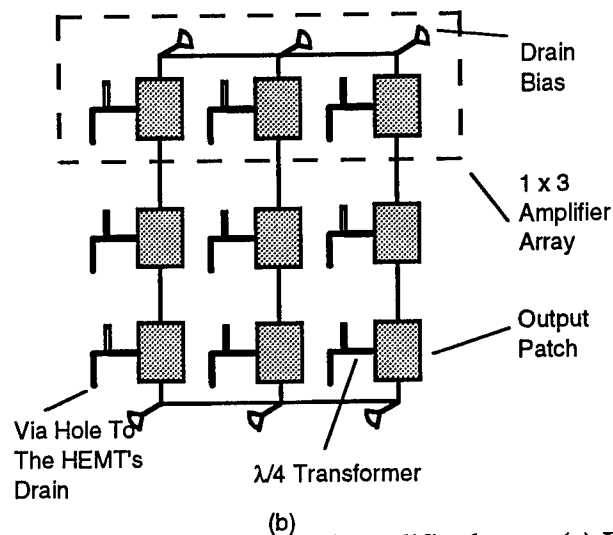
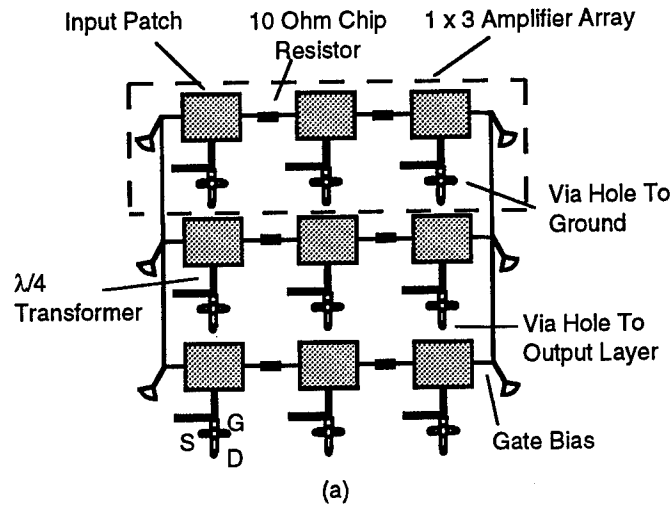


Fig.1 Single stage double layer quasi-optical amplifier layout (a) Input side, (b) Output side

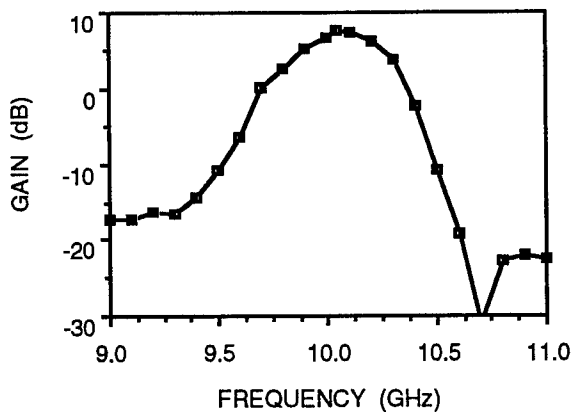


Fig. 2 Gain versus frequency response of the single stage quasi-optical amplifier

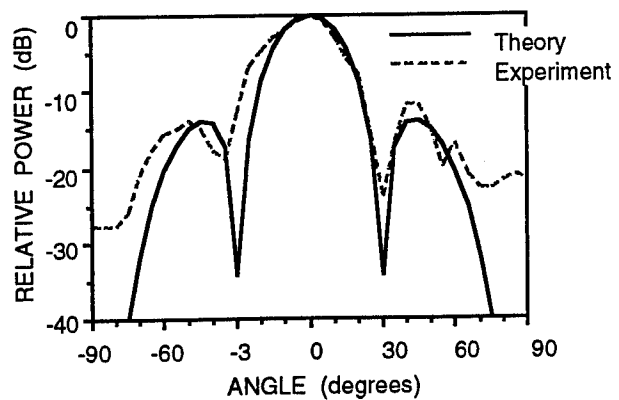


Fig. 3 Measured and calculated H-plane patterns of the single stage quasi-optical amplifier

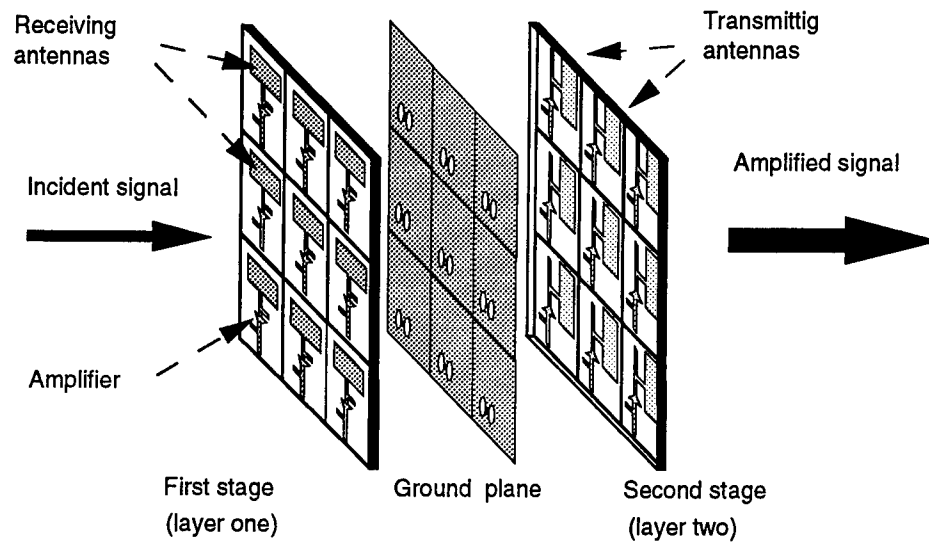


Fig. 4 Perspective view of the two stage quasi-optical amplifier

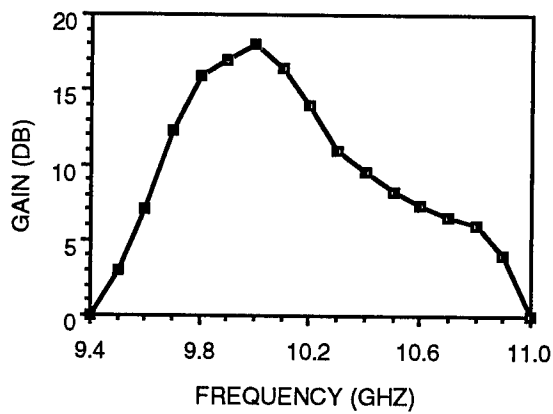


Fig. 5. Gain versus frequency plot of a 3x3 two stage amplifier array.

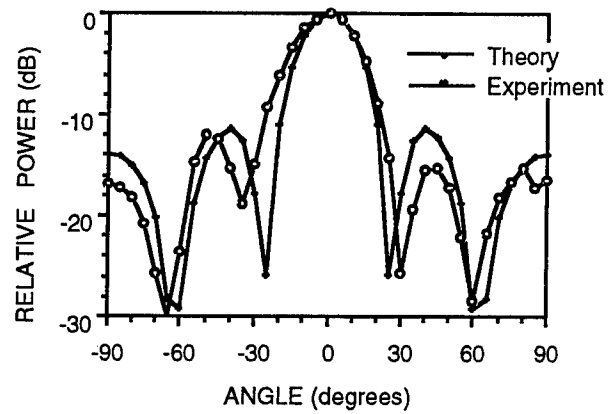


Fig. 6 Measured and calculated E-plane patterns of a 3x3 two stage amplifier array.

QUASI-OPTICAL GRID AMPLIFIERS AND OSCILLATORS

Robert M. Weikle, II

School of Engineering and Applied Science
Thornton Hall, University of Virginia
Charlottesville, VA 22903
weikle@virginia.edu

ABSTRACT

Recent work in active quasi-optical coupled arrays have shown this technology to be a feasible and promising method for achieving efficient and high-power solid state power combining. Quasi-optical techniques should find greatest use at millimeter-wave frequencies where waveguide circuits are lossy and difficult to build. In this paper, we examine some of the advantages of this technology and review the recent developments in active grid arrays. Because of their versatility, special emphasis is given to transistor grids and their use as oscillators and amplifiers.

I. INTRODUCTION

In recent years, engineers and scientists have intensified their efforts to find efficient and reliable methods for generating power at millimeter and submillimeter wavelengths. This work has been motivated largely by the wide variety of military, industrial, and research applications of this part of the electromagnetic spectrum. In spite of these efforts, the development and implementation of systems operating in the millimeter wave region has been slow and costly. This is due, in part, to the difficulties associated with fabricating and integrating circuit components that can operate at these wavelengths. Perhaps the most serious obstacle to the widespread development and use of millimeter and submillimeter wave systems, however, has been the lack of powerful and reliable solid state sources.

Although millimeter-wave semiconductor device technology has reached a high level of maturity over the past decade, vacuum tube sources remain the state-of-the-art with regard to power output and efficiency. Consequently, much effort has focussed on developing power combining techniques at millimeter-wave frequencies. Unfortunately, the traditional methods based on

waveguide cavities and "corporate" combiners suffer from increasing losses, decreasing combining efficiencies, and stricter tolerances when scaled to millimeter-wave frequencies. In great part, these problems arise from the application of standard RF and microwave engineering principles to a region where optical techniques may be more appropriate. As a result, researchers have begun to investigate the possibility of combining the outputs of large numbers of devices using quasi-optical techniques.

A number of distinct approaches to quasi-optical power combining have been demonstrated over the past several years [1]. Many of these are similar to classical spatial power combiners in which active devices, along with the necessary matching circuits, are integrated into an array of planar antennas (such as microstrip patches). The elements of these arrays typically interact through guided-wave coupling, weak radiative coupling, or are synchronized to an external signal. A different approach, which is more analogous to the laser, is the grid oscillator or amplifier.

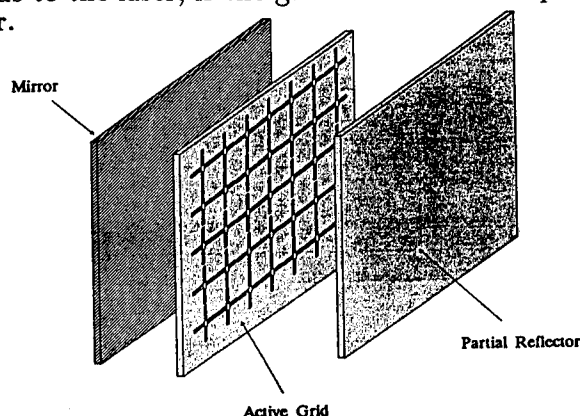


Figure 1. Diagram of a typical grid oscillator. A grid of active devices is placed in an open resonator

The essential difference between grid oscillators and amplifiers and the spatial power combiners described above is that the device spacing is a

small fraction of a wavelength. These grids, as a result, approximate a continuous, two dimensional gain medium in which the active devices are strongly coupled. An advantage of this approach is its amenability to modern IC fabrication technology and the relatively high device packing density. From a circuit point-of-view, a grid oscillator can be understood as a frequency-selective surface that contains active devices and presents a negative resistance to an incident electromagnetic wave. An oscillator is realized by placing the grid in a resonant cavity to provide positive feedback (see Figure 1).

II. CIRCUIT MODELLING

To understand the behavior of a quasi-optical array, it is necessary to determine the embedding impedances presented to devices placed in the grid. For finite grids of arbitrary geometry, this is a formidable task. Complications arise from the unknown behavior of the fields at the grid's edges. In addition, each device in the array couples to all other devices through the radiated fields. Even grids of moderate size can generate a large number of unknowns, making analysis very difficult.

The problem is made more tractable by assuming the array is infinite in extent and is illuminated by a uniform plane wave. With these assumptions, the symmetry of the array can be exploited to define an equivalent waveguide representing each unit cell of the grid (Figure 2). The boundary conditions on the equivalent waveguide are imposed by the grid symmetry and account for the interaction of all the devices in the array. In effect, the entire grid is reduced to a single waveguide circuit that can be modelled using any number of standard analysis techniques.

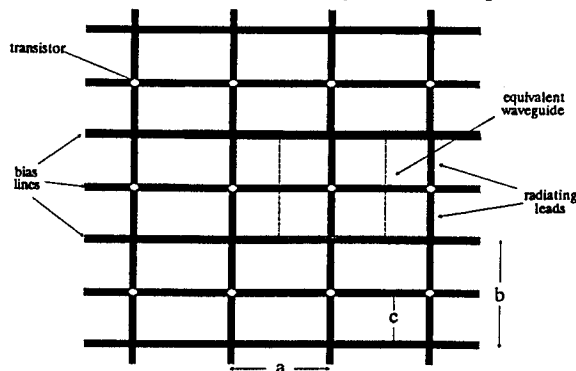


Figure 2. Illustration of a symmetric planar grid showing the equivalent waveguide. The waveguide has electric walls on the top and bottom and magnetic walls on the sides.

A simple technique for finding the embedding impedance for a grid unit cell is the induced EMF method. This method relies on an assumed current distribution from which the radiated fields are found. The driving-point impedance, Z , seen by a device in the unit cell is then found by applying Poynting's Theorem or reciprocity:

$$Z = -\frac{1}{|I|^2} \int_V \mathbf{E}(\mathbf{r}) \cdot \mathbf{J}(\mathbf{r}) dV$$

Because each device in the grid effectively sits in a TEM waveguide, the radiated field can be decomposed into a set of TEM, TM, and TE modes. An equivalent circuit model representing the grid embedding impedance is obtained by associating lumped elements with each waveguide mode that is excited (Figure 3). Including the device model with the grid equivalent circuit allows the behavior of the grid as an oscillator or amplifier to be predicted.

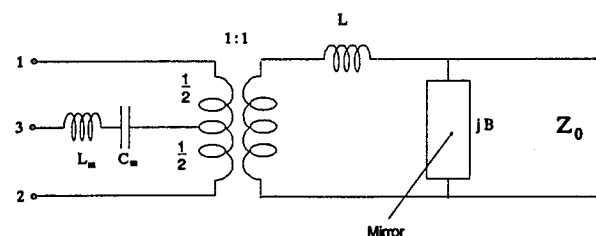


Figure 3. An equivalent circuit model for a planar grid. Propagating modes are represented with transmission lines and evanescent modes with reactive lumped components.

III. GRID OSCILLATORS

Although a variety of signal processing functions can be realized with active quasi-optical arrays, a primary motivation remains the realization of reliable, high-power solid state sources. Consequently, much work has focused on the development of grid oscillators for high-frequency power combining. In principle, any active device can be incorporated into a grid, including transferred electron devices and tunnel diodes. However, low DC-to-RF conversion efficiencies and the difficulties associated with stabilizing two-terminal active devices for coherent power combining has led most researchers to focus on planar transistor grids.

Most planar transistor grid oscillators that have been studied to date are based on two basic configurations. The first, demonstrated by Popović *et al.* in 1991, used packaged

MESFET's soldered to a grid of vertical and horizontal leads (Figure 4) [2]. The device package restricted the vertical leads to be the drain and gate, with the source connected to the horizontal (or common) lead. As a result, this configuration is known as a "common-source" grid oscillator. The grid was fabricated on a Duroid substrate and placed in front of a planar mirror to synchronize the devices and restrict radiation to the forward direction. When biased, the array produced a single frequency output at 5 GHz which could be tuned over a 10% bandwidth with the mirror position. The grid antenna pattern had a directivity of 16 dB and radiated 600 mW with a DC-to-RF efficiency of 20%.

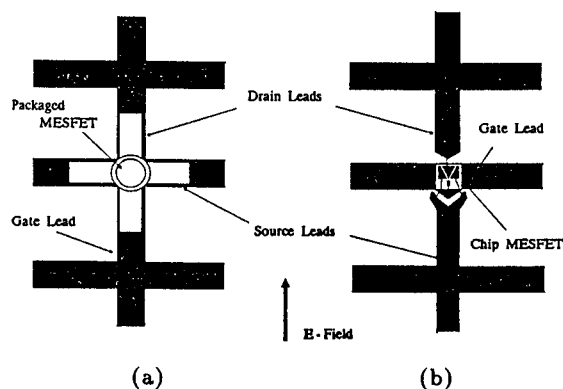


Figure 4. (a) Unit cell for a common-source grid which uses packaged FET's. (b) Unit cell for a common-gate grid oscillator with chip FET's. The gate lead is capacitively coupled to the incident electric field.

One potential disadvantage of the common-source grid is the gate lead is parallel (and strongly coupled) to the radiated field. As a result, the array may tend to oscillate at lower frequencies where the devices have high gain.

In the "common-gate" configuration, shown in Figure 4, the FET's are oriented so the drain and source leads radiate [3]. The gate is coupled to the radiated field through a series resonant circuit (Figure 3). The resonant frequency of this coupling circuit is the primary factor determining the oscillation frequency of the grid. Grid oscillator designs based on the common-gate configuration have been demonstrated operating over a wide range of frequencies and with relatively high power outputs. Initial work on common-gate grids was a proof-of-principle investigation using 16 chip MESFET's that produced 335 mW of power at 11.6 GHz with an efficiency of 20%. A scaled version of this array using 36 devices produced 235 mW at 17 GHz with 7%

efficiency. The first demonstrated monolithic millimeter-wave grid oscillator was a "common-base" heterojunction bipolar transistor (HBT) array operating at 35 GHz and producing an effective radiated power of 170 mW [4]. Hacker *et al.*, in 1992, built a hybrid 100-element common-gate grid oscillator using Fujitsu medium power MESFET's (FLK052XP) [5]. This grid was optimized for power output and produced 10.3 W of radiated power at 9.8 GHz with a DC-to-RF efficiency of 23%. Thus far, this is the highest power produced from a transistor grid oscillator.

Although the central goal of quasi-optical power combiners is high power and efficiency, other performance factors such as oscillator stability and noise, tuning bandwidth, and phase control are also important. It is expected (and has been verified experimentally) that the noise performance of grid oscillator arrays improves with an increasing number of devices. This results because the individual elements are mutually locked to a single frequency whereas the noise produced by each of these elements is uncorrelated. Locking the grid to an external, stable source can further reduce the phase noise of the oscillator.

Because a grid oscillator, in essence, is an array of active devices embedded in a frequency selective surface, the tuning bandwidth tends to be quite limited (typically less than 10%). Mader *et al.*, have shown that the operating bandwidth of a common-source array can be increased using an array of varactor diodes as a tuning element [6]. Oak demonstrated an improvement in the tuning bandwidth of a common-gate grid by integrating varactors directly into the gate lead of the array (Figure 5) [7]. In this case, the varactor was used to control the resonant frequency of the gate feedback circuit. Similar approaches to grid oscillator design may also be useful for beam steering applications or adjusting the impedance and frequency of individual unit cells to improve power and noise performance.

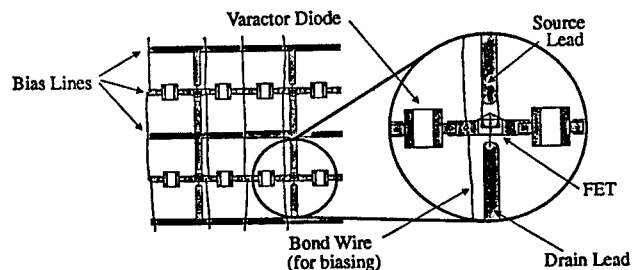


Figure 5. Diagram of a varactor tuned common-gate grid oscillator. Packaged varactors placed in the gate bias line tune the embedding impedance and frequency.

IV. GRID AMPLIFIERS

Much of the recent work on quasi-optical arrays has focussed on the development of amplifier grids as well as oscillators. Grid amplifiers, in essence, are active planar structures that accept an incident beam and re-radiate an amplified version. They offer the same advantages as grid oscillators: increased dynamic range, elimination of transmission line and waveguide losses, and robustness to device failure. Amplifiers, however, provide greater flexibility; with proper feedback they may be used as oscillators.

Kim *et al.*, demonstrated the first grid amplifier using 50 packaged low-noise FET's mounted on a crossed-dipole array [8]. The FET's are connected as differential pairs with the gate leads parallel with the polarization of the incident signal and the drain and source leads parallel with the output signal (Figure 6). Bias is fed to the devices

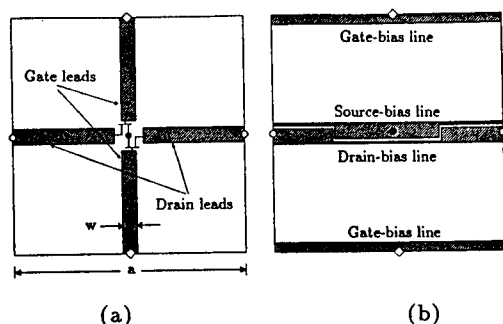


Figure 6. (a) A unit cell of the C-Band amplifier grid. (b) Bias lines run across the back of the substrate and feed the FET's with via holes.

through via holes from the back of the substrate. An advantage of this design is that the input and output of the amplifier have orthogonal polarizations. This feature permits high isolation between the input and output and is advantageous for stabilizing the amplifier. Elimination of spurious oscillations is perhaps the most difficult task in designing a grid amplifier. This initial proof-of-principle investigation gave a peak gain of 11 dB at 3.3 GHz and a 3 dB bandwidth of 90 MHz. Polarizers were used to provide separate input and output matching.

More recently, Kim demonstrated a 100-element grid amplifier using differential pair HBT chips manufactured by Rockwell [9]. An on-chip resistive bias network was provided for the bases and allowed the elimination of the base bias line. This array produced a peak gain of 10 dB at 10 GHz and a 3 dB bandwidth of 1 GHz. The noise performance and reliability of this grid amplifier were also investigated. It was found that

the grid noise figure was 7 to 8 dB, comparable to that for a single-device amplifier. Device failure was simulated by detuning the matching for several devices in the grid. The grid amplifier proved quite robust with respect to device failure; with 10% of the device detuned, the gain dropped by only 1%.

V. SUMMARY

In this paper, we have reviewed some of the important features and recent developments in quasi-optical active grids. In principle, this approach to millimeter wave circuit design should offer new advantages over traditional design techniques and be straightforward to incorporate into existing semiconductor fabrication processes. Although much of this initial work has demonstrated the feasibility and soundness of the approach, much work remains before complete systems will utilize this technology. More accurate design models and a better understanding of strongly coupled oscillators are needed. In addition, the effect of high dielectric substrates on finite grids at millimeter-wave frequencies and the thermal properties of high-power arrays require study. Nonetheless, quasi-optical grids remain a promising and exciting concept for future high power solid state sources.

REFERENCES

- [1] for example, see R.A. York, "Quasi-Optical Power Combining Techniques," to be published, *SPIE Critical Reviews of Emerging Technologies*, J. Wiltse, ed., 1994.
- [2] Z.B. Popović *et al.*, "A 100-MESFET Planar Grid Oscillator," *IEEE Trans. Microwave Theory Tech.*, MTT-39, pp. 193-200, Feb. 1991.
- [3] R.M. Weikle, *et al.*, "Planar MESFET Grid Oscillator Using Gate Feedback," *IEEE Trans. Microwave Theory Tech.*, MTT-40, pp. 1997-2003, Nov. 1992.
- [4] M. Kim *et al.*, "A 35 GHz HBT Monolithic Grid Oscillator," *17th Int. Conf. on Infrared and Millimeter Waves*, Proc., pp. 402-403, Dec. 1992.
- [5] J.B. Hacker *et al.*, "A 10-Watt X-Band Grid Oscillator," *IEEE MTT-S Internat. Microwave Symp. Digest*, vol. 2, pp. 823-826, May 1993.
- [6] T. Mader *et al.*, "Quasi-Optical VCO's," *IEEE Trans. Microwave Theory Tech.*, MTT-41, pp. 1775-1781, Oct. 1993.
- [7] A.C. Oak *et al.*, "A Varactor Tuned 16-Element MESFET Grid Oscillator," *IEEE Antennas Propag. Symp. Digest*, vol. 2, pp. 1296-1299, June 1995.
- [8] M. Kim *et al.*, "A Grid Amplifier," *IEEE Microwave and Guided Wave Lett.*, vol. 1, no. 11, pp. 322-324, Nov. 1991.
- [9] M. Kim, *et al.*, "A 100-Element HBT Grid Amplifier," *IEEE Trans. Microwave Theory Tech.*, MTT-41, pp. 1762-1771, Oct. 1993.

Low Temperature Grown GaAs Materials and Devices

Present Status and Trends

Erhard Kohn, Klaus-Michael Lipka

Dept. of Electron Devices and Circuits,
University of Ulm, D-89069 ULM, Germany
Tel.: +49 731 502 6150; Fax: +49 731 502 6155;
Email: dept-ebs@sunrise.e-technik.uni-ulm.de

Introduction

GaAs layers can be grown epitaxially over a wide range of temperature reaching from 180°C up to the thermal stability limit. While above 400°C growth temperature the stoichiometry is preserved within the ppm-range, at low growth temperature surplus As can be incorporated into the GaAs matrix within the percentage range. The material grown in this lower temperature range is called Low-Temperature-Grown GaAs. By high temperature annealing the solubility limit will be surpassed and most of the excess As precipitates. Thus, the material can have a variety of unusual properties. They have stimulated many investigations, also into related materials, resulting in more than 300 publications to date.

The first application was in the FET buffer layer structure virtually eliminating backgating and short channel effects. Using LTG-GaAs, the stability of GaAs FET devices has been improved dramatically and the Schottky gate breakdown limit has been surpassed for the first time. The second successful application are untrafast THz optoelectronic switches and detectors. Here the advances in FET's will be reviewed. However, the impact of this material is essentially deeper. LTG-GaAs can serve as raw model for a new class of materials: off-stoichiometric or composite semiconductors. They offer multifunction properties with metallic, magnetic, optically active or superconducting nano-clusters.

The As-Grown LTG-GaAs Material

Most of the excess As-atoms of LTG-GaAs will be found on interstitial sites widening the lattice [1]. However, a small fraction of the surplus As is located on the As_{Ga} position, where the As will form a deep multiple donor near mid gap similar to EL2 [2]. Since the concentration of surplus As is a function of growth condition, the properties of LTG-GaAs material may vary substantially and the lattice mismatch with the GaAs substrate may be used as a prime indicator when comparing materials.

At a growth temperature of 200°C to 250°C an As_{Ga} anti-site density between 10^{19}cm^{-3} and 10^{20}cm^{-3} is observed and wave function overlap occurs resulting in a deep donor mini band and hopping conduction. The Fermi-level is pinned at approx. 0.4eV below the conduction band [3,4]. Labeled σ -LT-GaAs [5], it is the only semiconductor with an energetically isolated miniband and hopping conduction. These two features control the electrical characteristics. What are the consequences?

- The carrier mobility in the miniband is low. Since the Fermi-level is pinned, the conduction band is essentially unpopulated. This results in a resistivity between 10k Ω cm and 1M Ω cm and a characteristic frequency of dielectric relaxation in the MHz-range. The activation energy for the hopping process is approx. 70meV. Therefore, the bias and temperature dependences are weak, and a linear IV-characteristic is observed up to high fields (see fig.1).
- Due to the high deep donor density, the material cannot be depleted noticeably, despite its high resistivity. 20nm thin surface layers have been found conductive; non-alloyed tunneling contacts can be formed [4] and the interface potential to bulk GaAs is the LTG-GaAs Fermi-level [5].
- The material cannot be doped in case the deep donor anti-site concentration is above the activation limit of common donors or acceptors. Doping profiles reaching into this layer are suppressed.
- Equilibrium for injected carriers is reached within fs due to fast trapping by the As_{Ga} -anti-site deep donor or the V_{Ga} -vacancy deep acceptor. Thus, the material is optically inactive [6].

As seen from fig.1, between 100 kV/cm and 200 kV/cm breakdown is observed. It is thought, that carriers are emitted into the conduction band by field emission and the material becomes highly conductive. Fig.2 shows a calculation of the density of conduction band electrons as function of applied field assuming a triangular barrier, confirming a transition to the highly conductive state in the correct field range [7]. The breakdown strength is therefore less than that of bulk GaAs.

Annealed LTG GaAs

Subjecting this material to a high temperature treatment, like for subsequent growth of active layers, the solubility limit for the excess As is surpassed. As will precipitate into clusters and the lattice mismatch disappears [8]. The clusters act as metallic inclusions forming internal Schottky barriers [9]. Accordingly, the clusters are surrounded by spherical depletion regions in a material with substantially reduced anti-site concentration. If the cluster density is high enough and the anti-site concentration low enough, these depletion regions may overlap forming an essentially depleted material of

high resistivity in the order of $10^9 \Omega\text{cm}$. The conduction through this material is rather complex, involving tunneling through the internal barriers or thermionic emission across them and hopping conductivity or space charge limited current between the barriers [10]. Growth and annealing conditions can be tailored to combine high resistivity and breakdown field. However, the breakdown field in the order of 300kV/cm is still within the limit of avalanche breakdown in undoped GaAs. But in contrast to bulk GaAs, injected carriers recombine fast and the Fermi-level is firmly pinned near midgap. Therefore, premature injection instabilities are suppressed. And indeed LTG-GaAs buffers have eliminated side gating and cross talk in digital circuits [11] and improved breakdown and backgating in power MESFET's [6].

Diffusion Barriers and Contacts

To be implemented into device structures the surplus As as well as the As-precipitates need to be confined to thin layers. However, the first experiments indicated an outdiffusion of As into active channels within the first 100nm. Thus, AlAs [12,13], InAlAs [13] and InGaP [14] have been deployed as diffusion barriers with a thickness down to 5nm. Fig.3 shows a TEM cross section of an active GaAs channel sandwiched between an annealed LTG-GaAs buffer layer and an unannealed σ -LT-GaAs passivation layer, separated by a top and bottom AlAs diffusion barrier. Also shown is the planar contact to this system by through-alloying of AuGe through the AlAs. Other techniques used are overlapping contacts [15] or selectively re-grown contacts [16]. The requisite for these contacts is the elimination of lateral exposed free surface areas. Since the free surface potential will differ from that of the LTG-GaAs/GaAs interface potential, these areas will determine the lateral field distribution and may cause severe high field instabilities.

Using the above heterostructure materials systems, not only active layers can be confined but also layers containing precipitates. AlGaAs/GaAs MQW's show for example precipitate accumulation in the GaAs layers [17]. But doping can also be used to steer precipitation [18]. This strongly indicates an influence of the solubility as well as the position of the Fermi-level on the defect formation.

Lossy Dielectric Passivation Concept

Controlling the electronic surface conditions has been one of the main difficult tasks of GaAs technology and surface related instabilities, noise and breakdown still limit device performance. Here LTG-GaAs passivation layers can offer distinct advantages. The LTG-GaAs/channel interface potential is well defined and the channel can be totally shielded from the surface. MESFET devices passivated by such layers have therefore shown reduced g_m -dispersion with drain bias, reduced $1/f$ noise and light immunity [19-21]. Used as a lossy dielectric, a σ -LT-GaAs passivation layer pins the lateral surface potential distribution and smoothes out lateral high field regions. In essence, the donor depletion charge in the channel can now be vertically compensated by surface charge provided by the conductive σ -LT-GaAs (see fig.4). This has two effects: (1) improving the Schottky gate/drain breakdown conditions and (2) extending the drift region. Indeed, extremely high drain breakdown voltages are observed in LTG-passivated MESFET's [22]; and an extremely small feed back capacitance and output conductance are observed causing extremely high f_{max} cut-off frequencies (see fig.5).

These results indicate that, by careful design of the device structure, the power limit of GaAs FET's of approx. 1.2W/mm (RF) can be surpassed. This limit is well characterized by the lateral spreading model [23], and states that due to lateral Schottky barrier breakdown the maximum source/drain voltage is inversely linked to the maximum open channel current. High gate/drain breakdown voltages can thus only be obtained at the expense of a low open-channel current.

A MISFET can overcome this Schottky-limit. However, GaAs-MISFET's with dielectrics of high breakdown strength like Si_3N_4 or SiO_2 suffer from severe interface state charging instabilities. To circumvent this problem a controlled interface charging current needs to be supplied modifying the MISFET concept by the leaky dielectric concept [24]. A conductivity can be introduced into the above dielectric materials, if they are made Si-rich. However, the IV-characteristics are essentially exponential due to Pool-Frenkel activation and the concept can only be implemented in a narrow bias range [25]. Here, LTG-GaAs offers a new alternative with its essentially linear IV-characteristics, however with a lower breakdown field than the channel material. On the other hand, the lateral leakage will enable high lateral breakdown voltages essentially independent of open channel current and it has indeed been possible to surpass the Schottky limit essentially [15]. However, an inherent property of the lossy dielectric MISFET is a frequency dispersion in g_m associated with the characteristic frequency of dielectric relaxation [26], which needs to be minimized.

Early experiments with LTG-GaAs MISFETs indicated an RF-power handling capability of 1.57 W/mm at 1.1 GHz [27], already outside the Schottky-limit. Recent experiments with σ -LT-GaAs recessed gate MISTs have yielded in DC characteristics as shown in fig. 6. Best results indicate an RF power density of 3.8W/mm , when operated below the dispersion frequency at 1MHz . However, above the dispersion frequency (indicated by a reduction in g_m of 15% between 50MHz and 500MHz), the potential in the device structure will redistribute and care has to be taken, that the limiting breakdown fields in the structure are not surpassed degrading the maximum power. Since detailed models are not yet available for this new device structure, the conditions have to be identified experimentally. This had proved difficult. An analysis of the gate/drain region at 2GHz indicates that the lossy dielectric passivation concept is also valid above the dielectric relaxation dispersion frequency, since breakdown did not degrade essentially. In a separate experiment 560m/mm maximum current could be modulated at 1GHz by the MIS diode. Combining both results, it can be predicted that properly designed LTG-GaAs FETs will handle RF power densities twice as high as the Schottky-limit.

LTG-InP Devices

InP grown at low temperatures contains a surplus of P and also a high P_{In} -anti-site density. However, in this material system the first excited state of the donor is in the conduction band (two localized P-ionization states are in the band gap) and LTG-InP will be highly conductive [28]. The material cannot be used as MISFET insulator. Instead, active n-type channels can be grown without doping at low temperature. This might be very attractive for optoelectronic applications. Here, fully processed optoelectronic device structures can be selectively overgrown with FET layers and the electronic circuit added using a low temperature budget for processing not degrading the optoelectronic components.

Conclusion

Low temperature grown off-stoichiometric materials offer many unusual properties. They may be defined by the growth process as well as by post growth annealing. It has been discussed, how LTG-GaAs layers can offer a new degree of freedom in the design of GaAs FETs. In perspective, the results shown also apply to related materials like AlGaAs and PMHEMT devices. Other materials, like LTG-InP will offer advantages in different directions. These have not been discussed in the open literature yet and concepts have still to be developed. The precipitate phase has up to now been used in buffer layer structures and optoelectronic switches. However, using their full potential means to modify our picture of a pure semiconductor towards that of a composite. This has only been attempted to a very limited extent. Thus, applications are still extensions of common concepts. However, composites offer multi-function properties combining semiconductor properties with magnetical, optical or even superconducting properties as suggested for example in the superconducting SUPERFET [29].

Acknowledgement

Many discussions with other researcher in this field are gratefully acknowledged. Special thanks are to R. Westfahlen, B. Splingart (Univ. Ulm), G. Salmer, D. Theron (IEMN, Lille), V. Morgan and H. Thomas (UWCC, Cardiff), who are partners in the ESPRIT project TAMPFETS. This project was supported through the European Union.

References

- [1] M. Kaminska et al., Appl. Phys. Lett. 54, 1989, 1881-1883
- [2] D.C. Look et al., J. Electrochem. Soc. 141, 1994, 747-750
- [3] A.C. Warren et al., J. Vac. Sci. Technol. B 10, 1992, 1904-1907
- [4] K.-M. Lipka et al., Inst. Phys. Conf. Series 136, 1993, 99-104
- [5] K.-M. Lipka et al., Materials Science and Engineering B22, 1993, 55-60
- [6] F.W. Smith et al., IEEE Electron Dev. Lett. 9, 1988, 77-80
- [7] G. Salmer, unpublished
- [8] R.S. Berg et al., J Electron. Mat. 19, 1990, 1323-1330
- [9] A.C. Warren et al., Appl. Phys. Lett. 57, 1990, 1331-1333
- [10] U.K. Mishra, Materials Science and Engineering B22, 1993, 72-77
- [11] C.-L. Chen et al., IEEE Trans. Electron. Dev. ED-36, 1989, 1546-1556
- [12] J.P. Ibbitson et al., Inst. Phys. Conf. Series 120, 1991, 37-43
- [13] K.-M. Lipka et al., 37th Electron. Materials Conf., 1995, paper F7
- [14] F. Scholz (Univ. Stuttgart), K.-M. Lipka (Univ. Ulm), private communication
- [15] K. Lipka et al., Electron. Lett. 29, 1993, 1170-1172
- [16] N.X. Nguyen et al., 1993 IEEE Cornell Conf. on Adv. Concepts in High Speed Semicon. Dev. and Circuits, Proc. 539-547
- [17] M.R. Melloch et al., J. Crystal Growth 127, 1993, 499-502
- [18] J.P. Ibbetson et al., Appl. Phys. Lett. 62, 1993, 169-171
- [19] C.L. Chen et al., Electron. Lett. 29, 1993, 499-501
- [20] A.D. van Rheene et al., Mat. Science and Eng. B22, 1993, 82-85
- [21] H. Thomas, unpublished
- [22] L.-W. Yin et al., IEEE Electron Dev. Lett. 11, 1990, 561-563
- [23] S.H. Wemple et al., IEEE Trans. Electron. Dev. ED-27, 1980, 1013-1018
- [24] T.L. Andrade et al., IEEE Trans. Electron. Dev. ED-28, 1981, 1244-1245
- [25] J.M. Dortu et al., Inst. Phys. Conf. Series 74, 1984, 563-568
- [26] K.-M. Lipka et al., 1993 IEEE Cornell Conf. on Adv. Concepts in High Speed Semicon. Dev. and Circuits, Proc. 103-110
- [27] C.-L. Chen et al., IEEE Electron Dev. Lett. 12, 1991, 306-308
- [28] P. Dreszer et al., Journ. Electron. Materials 22, 1993, 1487-1490
- [29] S. Tyc et al., MRS Proc. 241, 1992, 251-256
- [30] K.-M. Lipka et al., J Electron. Mat.
- [31] K.J. Luo et al., Inst. Phys. Conf. Series 141, 301-306
- [32] E. Kohn, WOCSDICE '93 (May 31-June 2, Parma, Italy), Abstracts 129-130

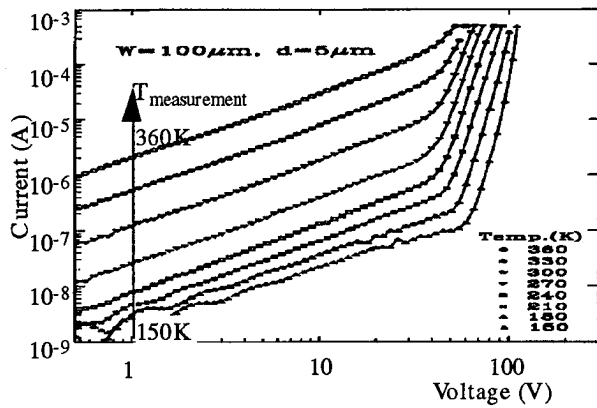


Fig.1
IV-characteristics of σ -LT-GaAs planar layer. Note the negative temperature coefficient for breakdown, indicating tunneling [30,31].

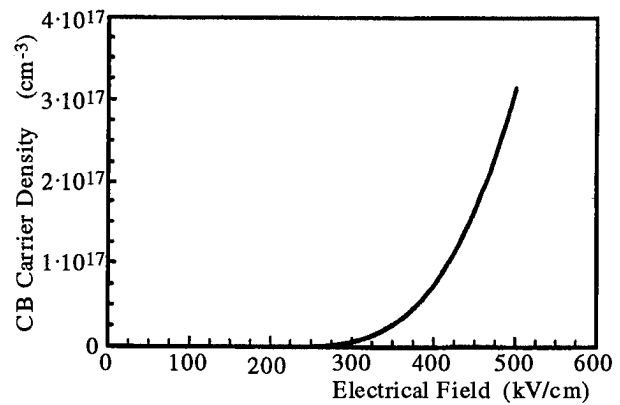


Fig.2
Conduction band electron density in σ -LT-GaAs as function of field, assuming tunneling from a triangular barrier [7].

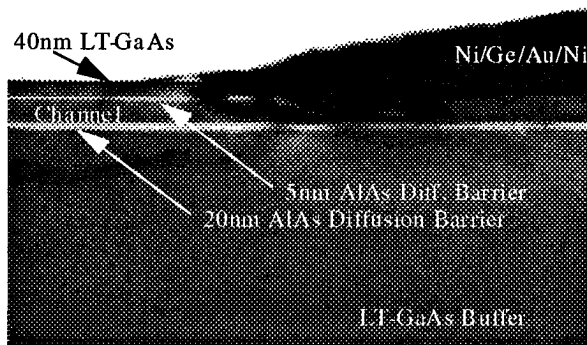


Fig.3
TEM cross section of planar FET contact region, showing through-alloyed contact, LTG- GaAs-buffer, AlAs diffusion barrier, GaAs active channel, top AlAs diffusion barrier and σ -LT-GaAs passivation layer.

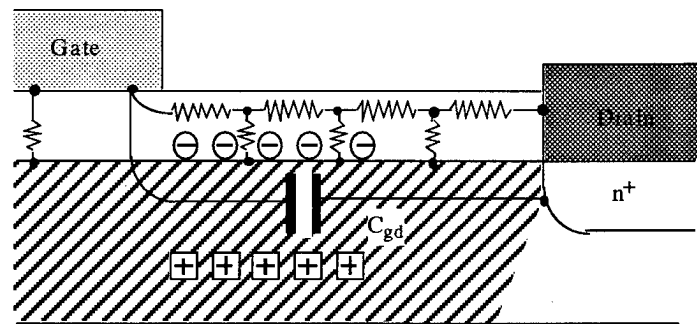


Fig.4
Equivalent circuit representation of LTG-GaAs passivated drift region with low conductive bypass on the surface [32].

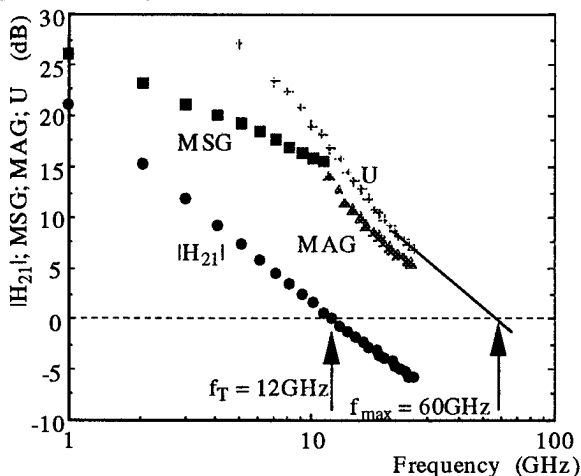


Fig.5
 f_T and f_{max} data for σ -LT-GaAs MISFET with $L_g=1\mu m$ and $V_D=3.5V$, $V_g=-0.3V$.

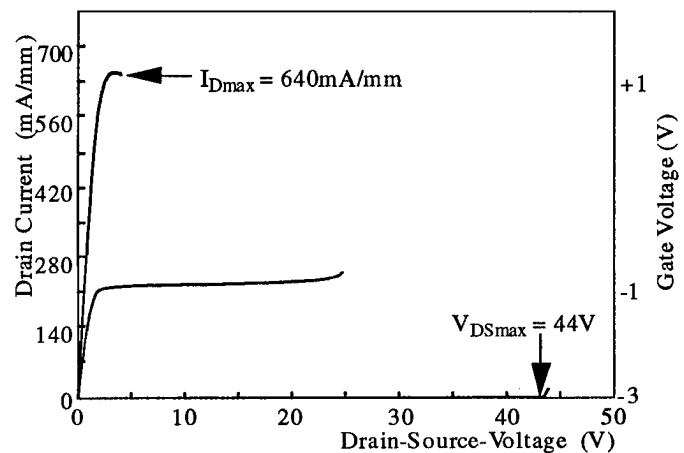


Fig.6
DC output characteristics of σ -LT-GaAs MISFET indicating 3.3W/mm power capability; $l_g = 1\mu m$, $w = 100\mu m$

RECENT APPLICATIONS OF 2D AND QUASI 2D SIMULATIONS : EVALUATION OF PERFORMANCE AND FUNDAMENTAL LIMITATION OF POWER FET

J.C. De Jaeger (invited paper)

I.E.M.N. - U.M.R. C.N.R.S. 9929 - Département Hyperfréquences et Semiconducteurs
Cité Scientifique, Avenue Poincaré, B.P. 69 - 59652 VILLENEUVE D'ASCQ CEDEX
Jean-Claude.DeJaeger@IEMN.Univ-Lille1.fr

ABSTRACT

In this paper, recent results concerning FETs for power applications are presented. The study is based on two kinds of simulation which make possible to perform exhaustive investigations : a physical two dimensional hydrodynamic energy model and a quasi two dimensional model. The study of the potentialities and limitations of HEMTs for applications beyond 60 GHz and LT GaAs MISFETs for low frequency ones is proposed for examples.

INTRODUCTION

The development of new power FET structures for microwave applications needs the determination of accurate predictions which involves improvements of the modeling due to the introduction of specific physical phenomena, the device complexity or high operating frequencies. As a first approach, the output power is proportional to the drain-source breakdown voltage V_{BR} and the maximum current I_{dso} . Usually, larger V_{BR} is obtained for devices made with high bandgap semiconductors. The current density is mainly depending on the carrier concentration in the channel and its transport properties. According to the operating frequency application, different new devices are developed at the present time. As an example, the study of the potentialities and limitations of two kinds of structure is proposed. First, conventional or δ -doped high electron mobility transistors (HEMTs) which constitutes the most promising structure beyond 60 GHz applications [1] and the low temperature (LT) GaAs MISFET which is a new structure for low frequency ones presenting high breakdown voltage [2].

Due to the complexity of the physical phenomena which must be taken into account and the large number of parameters to consider, two kinds of simulations are used. A two dimensional hydrodynamic energy model making possible to understand the physical mechanisms and a quasi two dimensional model from which it is possible to

perform device optimizations. The microwave performance of the devices is described and the main limitations are studied in particular the breakdown phenomena which constitute one of the most limitative effects for power devices.

MODELING DESCRIPTIONS

The proposed study is based on two different physical simulation tools :

A two dimensional hydrodynamic energy model which takes into account a large part of the physical phenomena which occur in the different structures. It is based upon the resolution of a set of equations derived from Boltzmann transport equation : the particule, momentum and energy conservation equations which are associated with Poisson's equation [3]. These equations are solved numerically using a finite difference method with non uniform meshes and a variable time step. The main advantage of this model is the results accuracy but it needs very long computing time due to a large number of mesh points and the use of small time steps. For this reason, programming techniques that include vectorial methods and parallel processors have been developed. This model uses a CRAY C98 computer.

A quasi two dimensional model where simplifying assumptions are introduced, but it accounts for the non stationary electron dynamic effects that take a particular importance in submicron gate devices [4]. The model is based under the successive resolution along the transversal and longitudinal axes. In a first time, the charge control law of the device is computed (transversal axis) and in a second time, the average values of the physical parameters in the device are calculated using the drain-source current equation, momentum and energy conservation equations and Poisson's equation (longitudinal axis). The validity of this simulation is prouved by a comparison with the results obtained from the 2D hydrodynamic model. Its main advantage is the relatively short computing time

which makes possible to optimise the power structure versus the different parameters.

HEMT STRUCTURES RESULTS

Mainly, two kinds of structure are investigated. The pseudomorphic AlGaAs/GaInAs HEMT on GaAs which constitutes the most promising structure for 60 GHz applications and the AlInAs/GaInAs HEMT on InP which has emerged as a device of choice for high microwave applications.

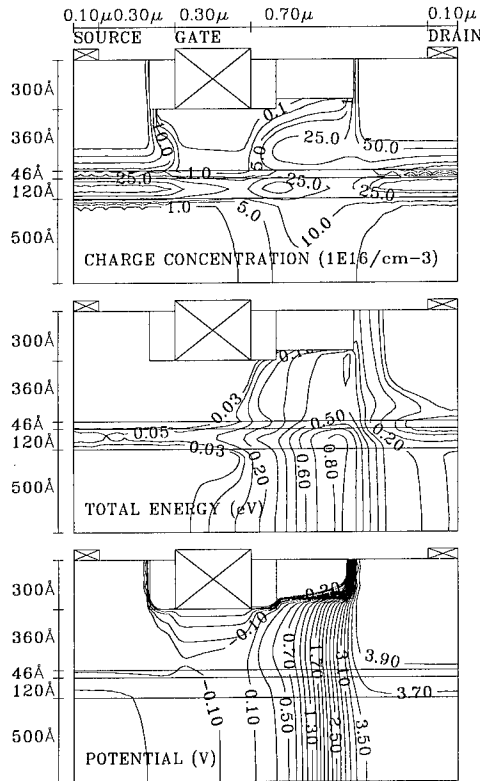


Fig. 1 : Distribution of physical quantities in a PMHEMT gate-recess device ($V_{gs} = 0V$; $V_{ds} = 4V$).

For the evaluation of power HEMTs performance, recent improvements have been introduced into the models. First, the impact ionisation phenomenon is taken into account. The minority carriers are considered and generation terms are added in the continuity equations. In order to simplify the calculation in the quasi 2D model, the hole effect is neglected in the charge control law [5]. The gate recess topology constitutes an important parameter that allows to improve the breakdown voltage. So, the real shape of the gate recess is introduced in the 2D model. It makes possible to study various gate recess configuration, so it constitutes a useful means for improving the device breakdown voltage optimisation.

For instance, figure 1 shows the distribution of physical quantities (charge concentration, total energy and potential) in a device where a double gate recess is introduced. The energy variation in the gate-drain zone allows to determine the location of the ionisation effect. In this case, it can be noted that electric field and average carrier energy remain uniform in the gate recess offset zone which is favourable to obtain a large breakdown voltage. Figure 2 represents the current-voltage characteristics deduced from the quasi 2D model for two devices with a different gate recess offset. An improvement is observed on the breakdown voltage for larger gate recess offsets. But it may cause a degradation of microwave performance and then, a compromise must be found. For this purpose, are also studied the microwave capabilities. For instance, figure 3 represents the intrinsic current gain cut-off frequency evolutions for two different structures.

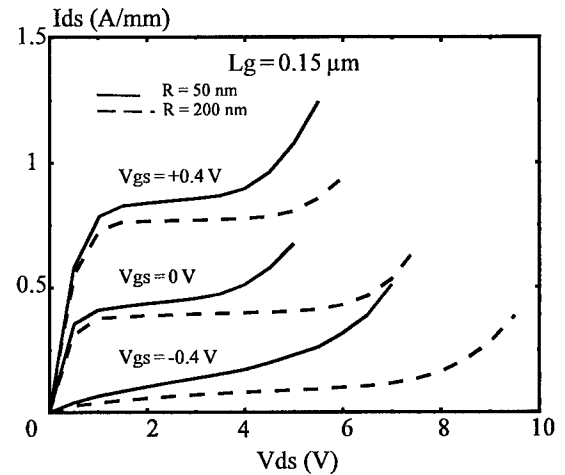


Fig. 2 : Current voltage characteristics for two gate recess offsets.

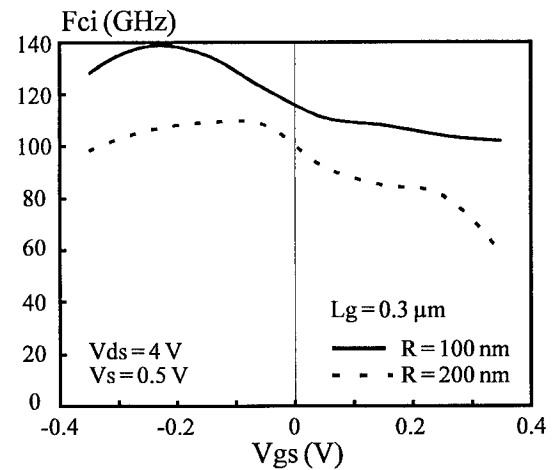


Fig. 3 : Influence of the gate-recess offset on the intrinsic cut-off frequency.

Recent improvement of the 2D model also consists in the determination of the gate current which constitutes a strong limitation for forward gate bias. Figure 4 shows the gate current versus the gate voltage V_{gs} for three doping levels of the doped AlGaAs zone in a conventional HEMT. The evolutions show that up to $V_{gs} = 0.5$ V, the gate current remains very small which confirms earlier assumptions of zero gate current at low V_{gs} . Moreover, the gate current is decreasing when the concentration of doped layer decreases. The main advantage of the AlInAs/GaInAs/InP structure is the possibility to obtain large carrier concentration N_s in the well due to larger conduction band discontinuity between $Al_{0.48}In_{0.52}As$ and $Ga_{0.47}In_{0.53}As$ than GaAs based HEMTs. A concentration of $4 \times 10^{12} \text{ cm}^{-2}$ is obtained for a single δ -doped device (fig. 5). Larger values can be obtained by dual δ -doped structures. Due to the higher electron velocity in the channel large drain-source current densities can be achieved. The main problem consists in the breakdown voltage but recent results show that a large improvement is obtained when an undoped $Al_{0.6}In_{0.4}As$ layer is inserted under the gate [6].

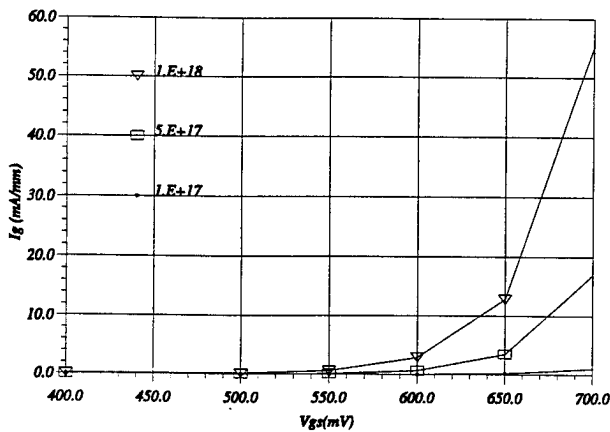


Fig. 4 : Gate current versus V_{gs}

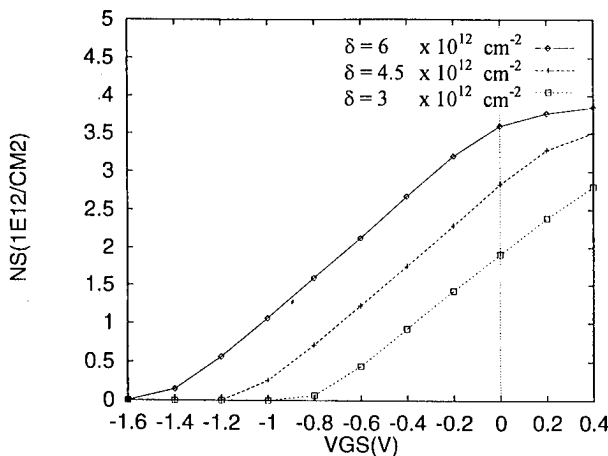


Fig. 5 : AlInAs/GaInAs/InP HEMTs charge control law

LT GaAs MISFET results

Modifications have been introduced in the simulations to take into account the specific physical phenomena which occur in the low temperature GaAs MISFET. The basic structure is shown in figure 6. Under static conditions, the LT GaAs zone is taken as conductive and under dynamic conditions the LT GaAs zone behaves as an insulator. This effect has been introduced in the quasi 2D model by a determination of a specific charge control in static and dynamic regimes (figure 7). From this simulation, the static and dynamic parameters can be determined. Figure 8 represents for instance the DC and microwave transconductances versus V_{gs} and figure 9 the C_{gs} capacitance evolutions. For the two regimes, the behaviour is different. The dynamic transconductance is lower than the static one. Concerning the capacitances C_{gs} , in static the evolution is similar to a MESFET structure but in dynamic a saturation is observed for forward biases as in MISFETs. Note that these evaluations are in good agreement with measurement.

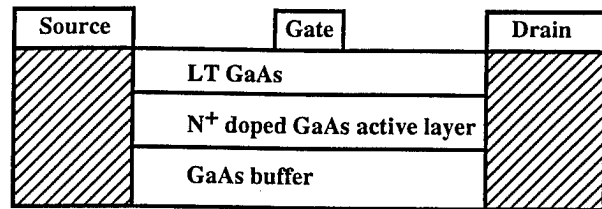


Fig. 6 : LT GaAs MISFET structure.

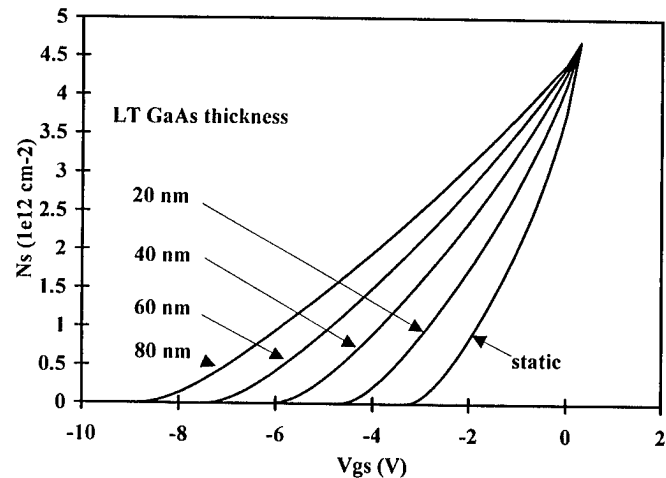


Fig. 7 : Charge control in static and dynamic for different LT GaAs zone thicknesses.

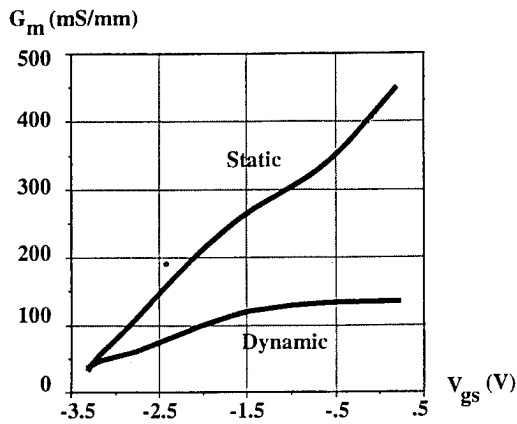


Fig. 8 : Static and dynamic transconductance for a LT GaAs MISFET

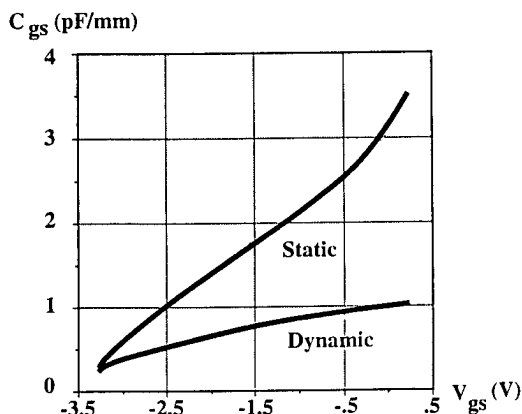


Fig. 9 : Static and dynamic capacitance C_{gs} for a LT GaAs MISFET.

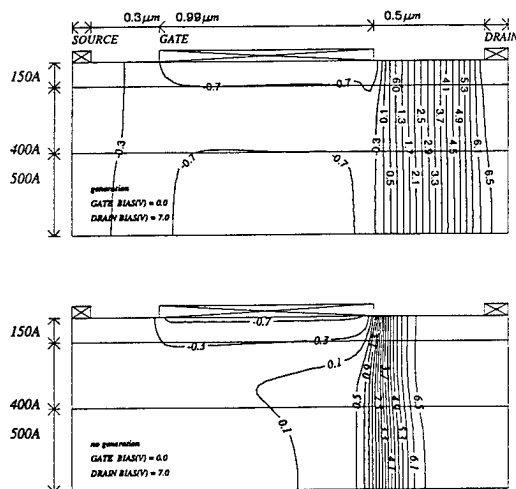


Fig. 10 : Effect of the carrier generation on the potential distribution.

LT GaAs devices present higher breakdown voltages than similar GaAs MESFETs. This can be explained by tunnelling of electrons from the trap

miniband located in the LT GaAs zone to the conduction band. These carriers will relax the local electric field peaks which involves an uniformisation of its distribution that can give more favourable breakdown conditions. This phenomenon introduced in the 2D model shows that an improvement of the electric field and potential distributions is obtained in the gate-drain zone (figure 10)

CONCLUSION

The simulation of complex structures by 2D and quasi 2D models allows to perform complete investigations of the physical understanding and the expected performance. Accurated results are obtained with a good agreement with those deduced from the experimental measurement. Improvements must be always brought to take into account new physical phenomena for devices operating at very high frequencies or close to breakdown (tunneling effect at the gate). In the future, other new devices can be studied such as those based on high bandgap semiconductors (SiC or GaN) from which a large breakdown voltage can be expected.

ACKNOWLEDGMENTS

The author would like to thank for their contributions : M. LEFEBVRE, J. HEDOIRE, Y. BUTEL, F. DUHAMEL, K. SHERIF, G. DIMA, J.D. DELEMER and G. SALMER.

REFERENCES

- [1] Y. CROSNIER, 24th European Microwave Conference, Cannes, France (1994)
- [2] M. LIPKA, B. SPLINGART and E. KOHN, Electronics Lett. 29 (13), pp. 1170-1171 (1993)
- [3] T. SHAWKI, G. SALMER and O. EL SAYED, IEEE Trans. on ED 37 (1) pp. 21-30 (1990).
- [4] H. HAPPY, G. DAMBRINE, J. ALAMKAN, F. DANNEVILLE, F. KAPTCHE-TAGNE and A. CAPPY, Int. J. of Micro and mm-waves comp. aided Eng. 3(1) pp. 14-27 (1993).
- [5] Y. BUTEL, J.C. DE JAEGER, K. SHERIF, M. LEFEBVRE and G. SALMER, 8th GaAs sim. workshop, Duisbourg, Germany (1994).
- [6] M. MATLOUBIAN, L.M. JELLOIAN, A.S. BROWN, L.D. NGUYEN, L.E. LARSON, M.J. DELANEY, M.A. THOMPSON, R.A. RHODES and J.E. PENCE
I.E.E.E. Trans on MTT 41 (12) pp. 2206-2209 (1993).

GaInP/GaAs HBTs: STATE OF THE ART

*S.L. Delage, H. Blanck, S. Cassette, D. Floriot, E. Chartier, and M.A. diForte-Poisson
and
E. Watrin* and P. Bourne**

THOMSON-CSF / Laboratoire Central de Recherches - F-91404 Orsay Cédex.

* TCS - BP46 - F-91401 Orsay Cédex

ABSTRACT: First, a review of the laboratories, which have studied the GaInP/GaAs HBT for electronic applications, is made. Then the peculiarities of this device are addressed compared to the more conventional GaAlAs/GaAs HBTs. Finally, a presentation of some recent Thomson-CSF X-band power results are presented and compared to the literature.

1. INTRODUCTION

GaInP/GaAs HBT is a new emerging challenger in the field of GaAs heterojunction bipolar transistors. Up-to recently, AlGaAs/GaAs heterostructures have been mainly used, giving rise to excellent results. All the current studies are focused on analogic microwave applications such as high power amplifiers and oscillators. The present results using GaInP/GaAs material are very close to the ones obtained using the GaAlAs/GaAs system, except for the reliability aspect, which seems to be better.

More than twenty laboratories have worked on the GaInP/GaAs HBT technology in Europe, USA, and Japan. These studies have explored all the topics required to produce devices from fundamental bandgap arrangement to MMICs and reliability. The table I shows a summary of the studies presented by various laboratories.

If one makes a review of all these papers, one could discover the following peculiarities for this heterojunction:

- * MOCVD growth is mostly used thanks to its high throughput capability and carbon doping;

- * Absence of aluminum and related effect;

- * Very high etching selectivity between GaInP and GaAs. That eases the emitter mesa etching by preserving the base layer. *This is not the case for the GaAlAs/GaAs system, which does not show such high selectivity.*

- * Favorable GaInP/GaAs band gap matching. *The composition grading is no longer necessary during the base-emitter interface growth, and a high injection efficiency is obtained.*

- * Limited dependence of the current gain versus collector current density and temperature without ledge passivation compared to GaAlAs/GaAs HBTs;

- * Low 1/f noise without any critical device-structure optimization, e.g.: Noise characterization of microwave devices has been performed by the team of Pr. Graffeuil at low and high frequencies. The 1/f noise is found to be lower than $1 \times 10^{-22} \text{ A}^2 \text{ Hz}^{-1}$ at 10 kHz for a $2 \times 30 \text{ } \mu\text{m}^2$ emitter at a collector current of 0.5 mA. This is obtained with a simple PECVD nitride passivation. The RF noise figure is about three dB between 2 and 20 GHz. The GaInP/GaAs HBT is therefore a good candidate for making microwave oscillators.

VCO MMICs working from 15 GHz to 34 GHz have been realized. Wideband monolithic VCOs are therefore achievable. For instance, -85 dBc/Hz at 100 kHz off carrier have been obtained at 17 GHz [8].

- * Better reliability compared to GaAlAs/GaAs thanks to phenomena not yet totally understood [20]. (10^6 hours at 200°C under bias)

University of California, Santa Barbara	DC characterization	MBE	[1]
Sony	DC characterization	MOCVD	[2]
T.I.	Physics of the heterostructure Power amplification	MOCVD MOCVD	[3] [4-5]
Thomson-CSF	X-Band Power amplifiers MMICs VCO	MOCVD MOCVD	[6-7] [8]
LAAS & Thomson-CSF	1/f & RF noise	MOCVD	[9-10]
University Paris VII & Thomson-CSF	Physics of heterojunction	MOCVD	[11]
Fraunhofer & Siemens Research	Device modeling	MOCVD	[12]
Daimler-Benz & Fraunhofer	RF performances VCO's	MOCVD MOCVD	[13] [14]
Daimler-Benz	X-Band Power amplifiers	MOCVD	[24]
University of Illinois, Urbana	D-HBT	MOCVD	[15]
Martin-Marietta & AT&T Bell Lab	RF performances	CBE & MOCVD	[16]
Tektronics	RF performances	MOCVD	[17]
CNET-Bagneux	DC characterization	CBE	[18]
NRC-Ottawa	DC characterization	CBE	[19]
Fujitsu	Reliability	MOCVD	[20]
University of Sheffield	Optoelectronics	MBE	[21]
Wright Patterson	High efficiency devices	MOCVD	[22]
University of Michigan & Thomson-CSF	DC characterization	MOCVD	[23]

Table I: Review of the main laboratories involved in the GaInP/GaAs HBT study

2. THOMSON-CSF POWER AMPLIFIERS

N-P-N GaInP/GaAs heterostructures are grown on 75mm wafers using LP-MOCVD technique. The collector thickness is kept close to 1 μm with a doping level of $2.0 \times 10^{16}\text{cm}^{-3}$. The current gain of microwave transistors is close to 20 which gives rise to a common emitter breakdown voltage BV_{CE0} of about 18V. This value has been up-to-now sufficiently high since the present limitation of HBT performances is mainly dominated by thermal behaviour. The current gain cut-off frequency f_t , which depends on the base and collector layer thicknesses, is about 55 GHz at the optimal bias point. The elementary emitter is 2 μm wide and 30 μm long. Two 2- μm wide 0.2- μm thick base contact stripes are used to give rise to a reasonably low base resistance.

Boron ion implantation is employed to decrease the parasitic element contribution and to realize the inter-device electrical isolation. All three electrodes are contacted using 3.5- μm thick gold air-bridges. Passive components and via hole technology are compatible with standard microwave GaAs MESFET foundry. Substrates are 100 μm thick for microstrip integration. The 10GHz small signal power gain of a monofinger HBT is close to 14 dB at 20 mA and 7V, which is our class-A bias point. At 10 GHz, the output power per finger is close to 90 mW and the collector efficiency is 60% for all topologies. Figure 1 shows a compilation of the power performances of GaAlAs/GaAs and GaInP/GaAs HBTs at 10 GHz.

One [7] or two stages X-band power amplifiers have been realized. Circuit characterizations are done either in CW or using 10 μ s pulses and a 10% duty cycle. Figure 2 shows the power performance of a 5W amplifier under pulsed conditions. 5W are reached with a power added efficiency of 33%. These results have to be compared to the recent Texas Instruments result obtained also using GaInP/GaAs, which indicates a 9.9W output power with a peak power added efficiency of 33.3% [5] or to Daimler-Benz [24] ones, which has obtained 40% and 8W CW. Figure 3 shows a comparison of our results with recent HBT publication.

3. CONCLUSION

GaInP/GaAs HBTs are now able to produce microwave oscillators and X-band high-power high-efficiency amplifiers. Higher reliability compared to GaAlAs/GaAs HBTs obtained by Takahashi et al from Fujitsu may be one of the major advantages for the future of this device. The high etching selectivity between GaInP and GaAs is very attractive for MMIC fabrication.

Thomson-CSF contribution is supported by DRET. We want to emphasize our ever growing with our colleagues from Daimler-Benz and DASA.

4. BIBLIOGRAPHY

- [1] M.J. Mondry et al, IEEE electron device letters, 175 (1985)6.
- [2] T. Kobayashi et al, J. Appl. Phys., 4898 (1989)65.
- [3] W. Liu et al, IEEE electron device letters, 510 (1992) 13.
- [4] W. Liu et al, IEEE electron device letters, 190 (1994) 15.
- [5] W. Liu et al, IEEE microwave and guided wave letters, 293 (1994)4.
- [6] S.L. Delage et al, Electronics letters, 253 (1991) 27.
- [7] S.L. Delage et al, 24th European Microwave Conference Proc., September 1994 , pp. 1143.
- [8] H. Blanck et al, IEEE MTT-S, San Diego, TU3A-3 (1994).
- [9] R. Plana et al, Electronics letters, 2354 (1992)28.
- [10] J.P. Roux et al, IEEE transactions on microwave theory and techniques, 293 (1995) 43.
- [11] J. Krinicki et al, J. Appl. Phys., 260 (1993)74.
- [12] U. Schaper et al, IEEE transactions on electron devices, 222 (1993) 40.
- [13] H. Leier et al, Electronics letters, 868 (1993)29.
- [14] U. Güttich et al, GaAs and related compounds, 15, Inst. Phys. Conf. Ser. 136.
- [15] A.W. Hanson et al, IEEE Electron Device Letters, 25 (1993)14.
- [16] L.W. Yang et al, InP and related materials 1994, page 563.
- [17] S.J. Prasad et al, Electronics letters, 2341 (1992) 28.
- [18] J.L. Benchimol et al, Electronics letters, 1344 (1992), 28.
- [19] Z. Abid et al, IEEE/Cornell conference on advanced concepts in high speed semiconductor devices and circuits, II-5 (1993).
- [20] T. Takahashi et al, IEDM 94, 191.
- [21] J.K. Twynam et al, Electronics letters, 85 (1988)25.
- [22] B. Bayraktaroglu et al, IEEE electron device letters, Vol.14, N°10, pp.493-495, October 1993.
- [23] M. Razeghi et al, Semiconductor Science and technology, 278 (1990), 5.
- [24] K. Riepe et al, IEEE microwave and guided wave letters, to be published.

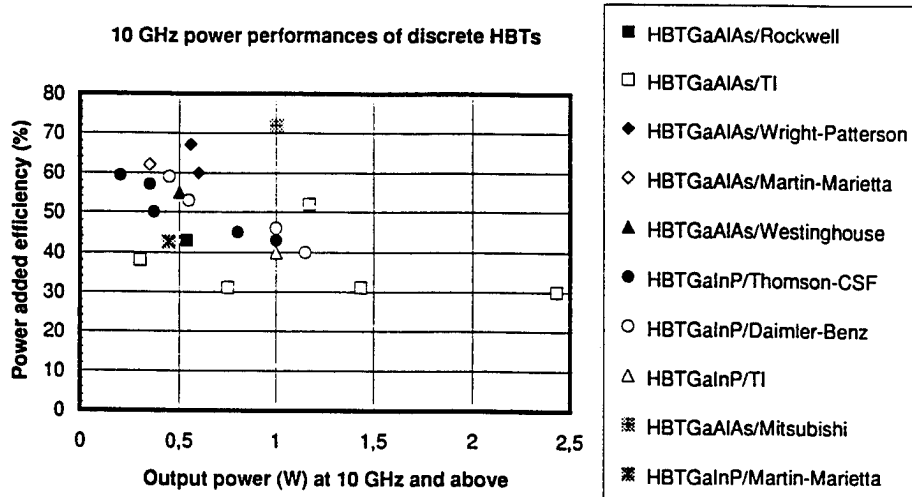


Figure 1: Power performances of discrete HBTs at 10 GHz

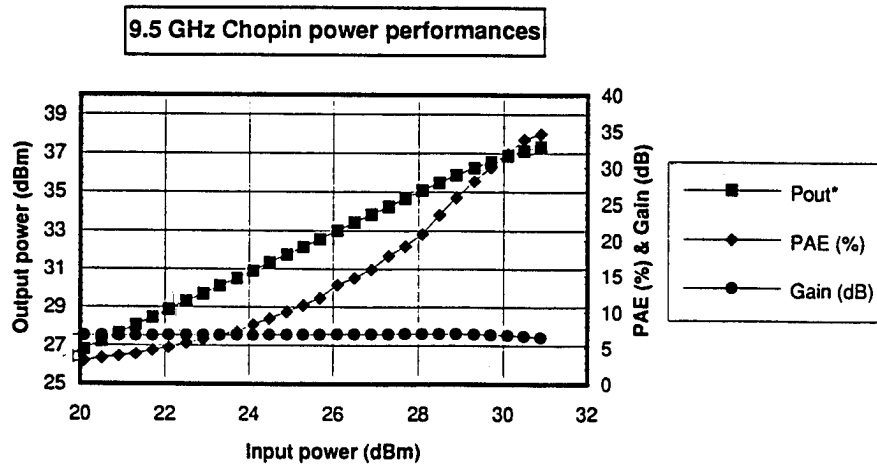


Figure 2: Output power versus input power at 10 GHz of a 5W amplifier (10 μ s, duty cycle: 10%)

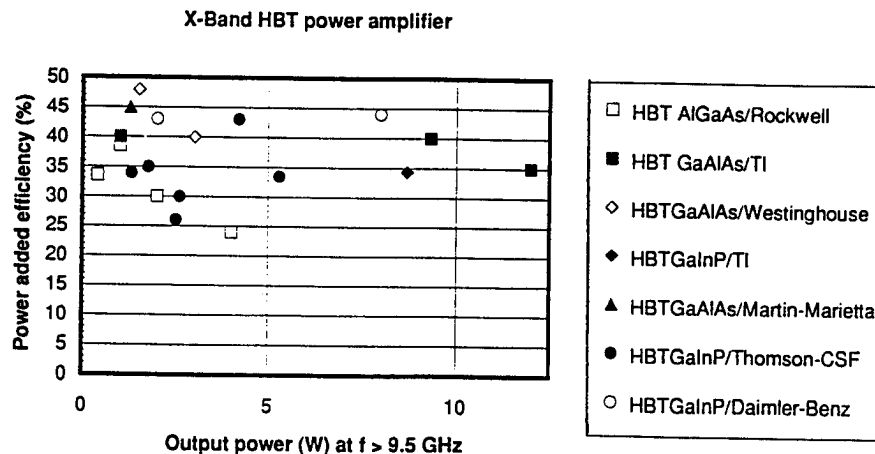


Figure 3: Comparison of X-band power amplifier performances

HIGH-PERFORMANCE MILLIMETER-WAVE MMIC'S FOR WIRELESS COMMUNICATION SYSTEMS

Keiichi Ohata* and Tamio Saito**

Advanced Millimeter Wave Technologies Co. Ltd.

*c/o NEC Corporation, 2-9-1 Seiran, Otsu, Shiga 520, Japan

**c/o Fujitsu Laboratories Ltd., 1015 Kamikodanaka, Nakahara-ku, Kawasaki 211, Japan

ABSTRACT

High-performance 60GHz-band MMIC's for wireless communication systems based on pseudomorphic heterojunction device technologies are presented. Dielectrically stabilized signal sources for FM/FSK modulators and LOs, such as a DRO with low phase noise of -90dBc/Hz at 100kHz off-carrier, 10.1dBm output power and 1.6ppm/°C stability, and a stabilized VCO with 55MHz/V modulation sensitivity, a 52.5-62.5GHz wide-band power amplifier with 14dB gain and 17.1dBm output power, and a low-noise high-gain down-converter consisting of an LNA and an active-gate mixer with 25.9dB gain and 2.8dB DSB noise figure, have been developed.

1. INTRODUCTION

Millimeter wave communication systems are attracting much attention for high speed wireless LANs, image data transmissions, contactless ID cards and so on because of high potential of realizing very compact equipment, of fine beam forming and of utilizing wide bandwidth[1]. 60GHz-band systems have an additional advantage of reduced mutual-interference among systems owing to high atmospheric attenuation loss of the radiated signals. In this paper, 60GHz-band monolithic integrated circuits based on InGaAs pseudomorphic heterojunction device technologies to be used for compact wireless communication

systems[2] are presented. High-performance MMIC chip sets for T/R modules of stabilized signal sources for FM/FSK modulators and LOs, wide-band power amplifiers, and low-noise high-gain downconverters have been developed.

2. DEVICE TECHNOLOGIES

For signal sources and power amplifiers where high output power is required, 0.15 μ m gate N-AlGaAs/InGaAs/N-AlGaAs double-doped double heterojunction FET (HJFET) with high f_{max} of 240GHz and high current drivability of 500mA/mm are adopted as the active elements. Figure 1 shows a cross sectional structure of an MMIC voltage controlled oscillator (VCO) for the FM/FSK modulator. In addition to the active HJFET, a drain DC-biased HJFET is adopted as a variable reactance element. The drain DC-biased HJFET varactor shows a reduced series resistance and gradually decreasing C-V characteristics near pinch-off, suitable for linear frequency control characteristics as shown in Fig.2, and can be fabricated in a simple process, completely compatible with active HJFETs for the oscillator itself and amplifiers[3].

For low noise MMIC's, 0.15 μ m gate N-InGaP/InGaAs/GaAs pseudomorphic HEMT's are adopted, which have superior performance to AlGaAs/GaAs based HEMT's[4]. The f_{max} is 180GHz.

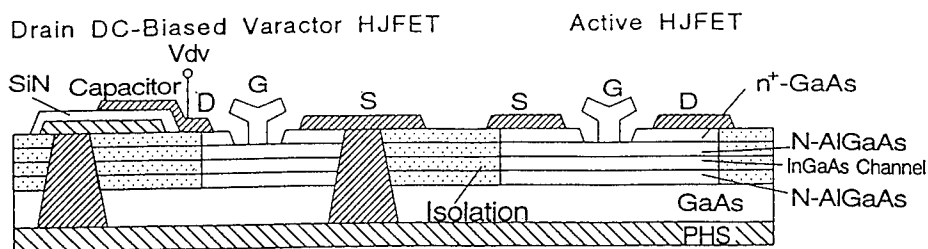


Fig.1 Cross sectional structure of the MMIC VCO.

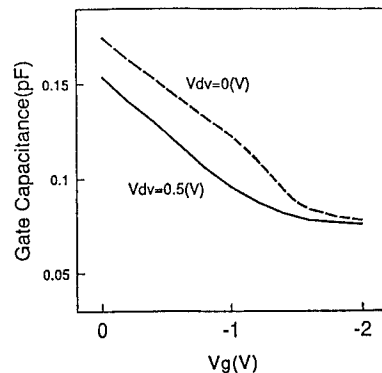


Fig.2 Varactor C-V curve.

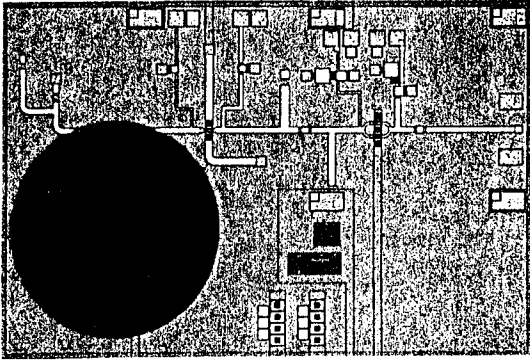


Fig.3 MMIC DRO chip.

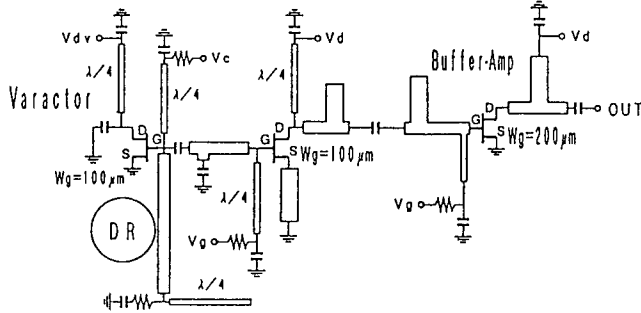


Fig.4 Circuit schematic of the VCO.

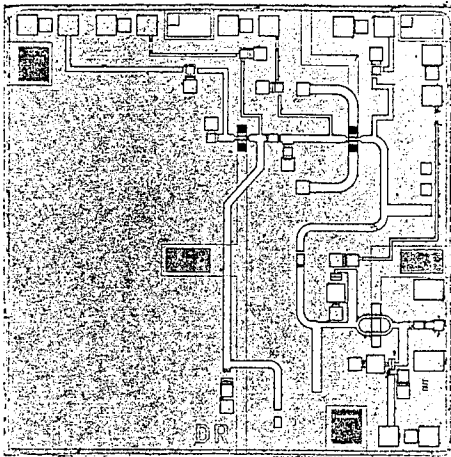


Fig.5 MMIC VCO chip. (DR is not placed.)

3. SIGNAL SOURCES

A 60GHz-band MMIC dielectric resonator oscillator (DRO) has been developed[5]. Figure 3 shows a chip photograph of a DRO with a buffer amplifier. The oscillator circuit has a series feedback topology. The capacitive stub is connected to the source of the FET as the series feedback element and the resonance circuit at the gate side is coupled to a dielectric resonator (DR). A rod shaped TE_{01δ} mode DR is placed directly on the

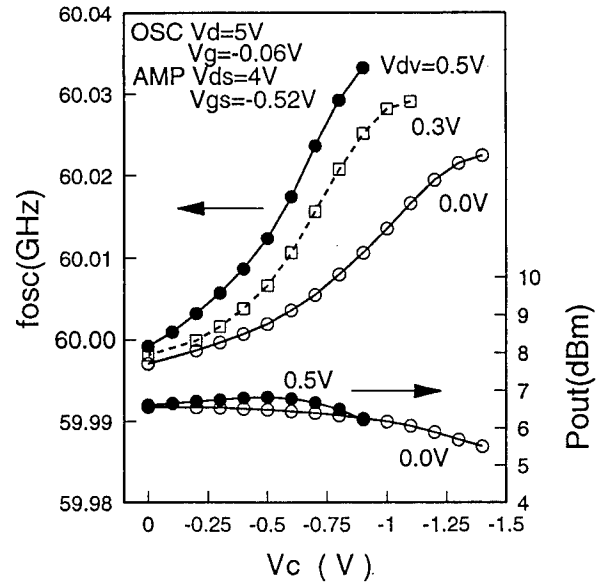


Fig.6 Oscillation frequency and output power vs. control voltage (V_c) with drain bias (V_{dv}) of the varactor as a parameter for the VCO.

MMIC chip. The MMIC chip size is $2.22 \times 3.37 \text{ mm}^2$. The MMIC DRO exhibits the state of the art performance of 10.1dBm output power and low phase noise of -90dBc/Hz at 100kHz off-carrier with the oscillation frequency of 59.157GHz. The frequency stability is high with the temperature coefficient of 1.6 ppm/°C. These performances are nearly comparable to those of Ka-band DROs [6], and suitable for signal sources and LOs.

In addition, a dielectrically stabilized VCO has been developed for the FM/FSK modulator[7]. The circuit schematic of the developed MMIC is shown in Fig.4. The circuit is composed of a VCO with an integrated varactor, stabilized with a DR, and a buffer amplifier. A resonance circuit is placed at the gate side of the active FET with a drain biased HJFET varactor circuit and a microstrip line coupled to a DR. The MMIC chip is shown in Fig.5. The chip size is $2.22 \times 2.22 \text{ mm}^2$. Figure 6 shows the oscillation frequency control characteristics and output power with the drain DC-bias (V_{dv}) of the varactor FET as a parameter. With increase in V_{dv} , the oscillation frequency variation and its linearity with regard to the control voltage (V_c) are improved. The modulation sensitivity of 55MHz/V at 60.0GHz is obtained for 0.5V V_{dv} . The output power is 6.9dBm and is fairly constant over the control voltage range. The phase noise is -80dBc/Hz at 100kHz off-carrier and the frequency stability is -4.1ppm/°C.

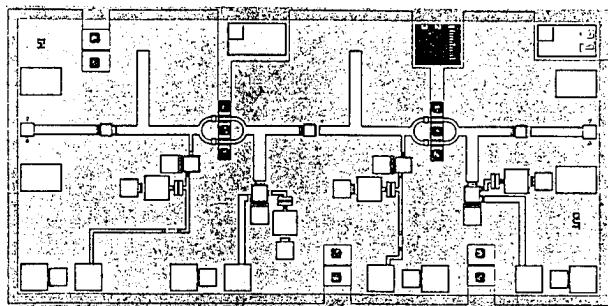


Fig.7 Two-stage wide-band power amplifier chip.

4. POWER AMPLIFIER

Wide-band power amplifiers have been developed for transmitters and LO buffer amplifiers. Figure 7 shows a MMIC chip of a two-stage amplifier with $200\mu\text{m}$ wide HJFET's. The chip size is $1.07 \times 2.22\text{mm}^2$. Both input and output matching circuits basically consist of a microstrip transmission line and an inductive shunt shorted stub grounded by a via-hole through an MIM capacitor. Due to these short length elements, the phase deviation with the frequency is small, resulting in wide-band operation capability [8]. An open stub in the input matching circuit and an RC network in the bias-line are introduced in order to prevent low frequency bias-line oscillations. The developed MMIC amplifier exhibits a very flat gain of 14dB from 52.5GHz to 62.5GHz with high isolation of 30dB as shown in Fig.8. The output power of 17.1dBm is obtained at 58.0GHz. This is sufficient for the transmitting power in the indoor communications.

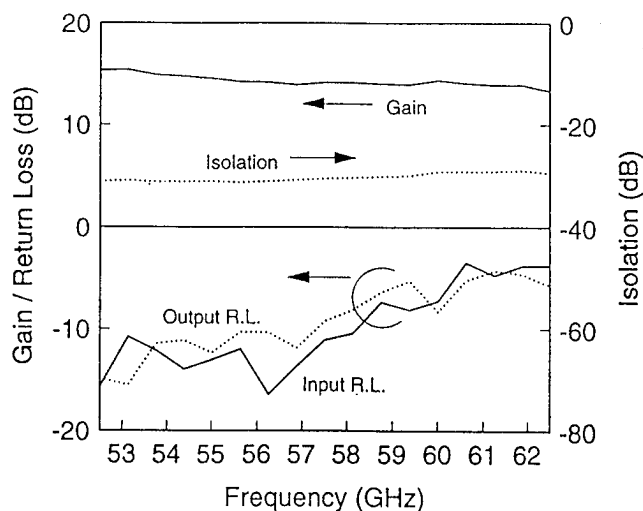


Fig.8 Frequency response of the wide-band power amplifier.

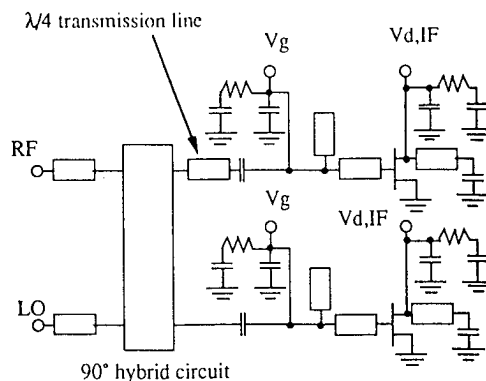
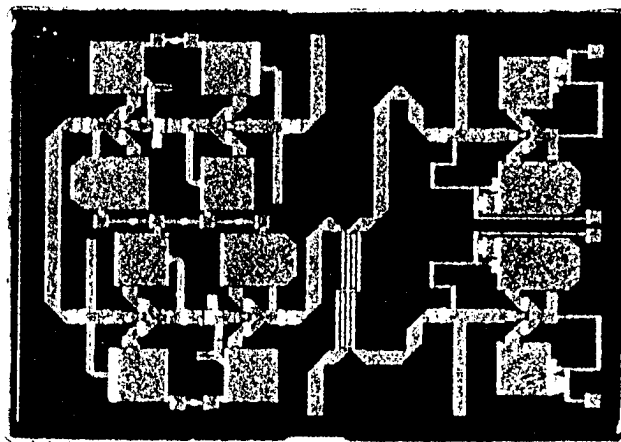


Fig.9 Circuit schematic of the SB gate mixer.



LNA Mixer
Fig.10 Downconverter chip.

5. LOW-NOISE DOWNCONVERTER

For receivers, low-noise downconverters consisting of an LNA and an active HEMT mixer have been developed[9]-[11]. A 60GHz-band one-chip downconverter integrated with a four-stage LNA and a single-balanced(SB) active-gate mixer has been demonstrated utilizing $0.15\mu\text{m}$ gate N-InGaP/InGaAs/GaAs pseudomorphic HEMT's[11]. The circuit schematic of the SB mixer is shown in Fig. 9. The mixer consists of a pair of HEMT's, a 90° hybrid circuit, and a $\lambda/4$ transmission line to make a 180° phase difference between the RF and LO signals for isolation. The MMIC chip is shown in Fig.10. The chip size is $1.75 \times 2.5\text{mm}^2$.

Figure 11 shows the LO power dependence of the active-gate mixer conversion gain. A maximum conversion gain of 1.5dB at 0dBm LO power is obtained. It is noted that the MMIC active-mixer has a positive gain for the first time over the millimeter wave developments. Figure 12 shows LO frequency dependences of the gain and noise

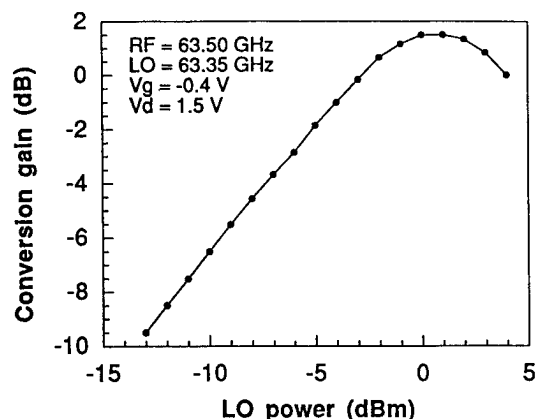


Fig. 11 LO power dependence of the mixer conversion gain.

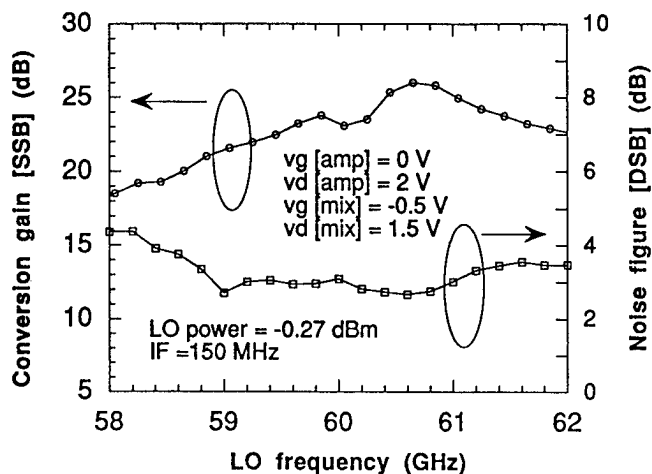


Fig. 12 Downconverter conversion gain and noise figure.

figure of the developed MMIC downconverter. The IF frequency is 150MHz. The downconverter has exhibited a high conversion gain of 25.9dB and a double side-band(DSB) noise figure of 2.8dB for low LO power of -0.27dBm at 60.8GHz.

6. CONCLUSION

High-performance MMIC chip sets for 60GHz-band wireless communication systems have been developed. 0.15 μ m gate N-AlGaAs/InGaAs/N-AlGaAs HJFET technologies are used for power MMIC's. A DRO exhibits low phase noise of -90dBc/Hz at 100kHz off-carrier and high stability of 1.6ppm/ $^{\circ}$ C. As the FM/FSK modulator, a dielectrically stabilized VCO with a drain biased HJFET varactor has realized 55MHz/V modulation sensitivity. Wide-band power amplifiers have been developed for transmitters and buffer amplifiers. A

two-stage amplifier exhibits a very flat gain of 14dB from 52.5GHz to 62.5GHz with 17.1 dBm output power. For receivers, low-noise downconverters consisting of an LNA and an active-gate mixer have been developed adopting 0.15 μ m gate N-InGaP/InGaAs/GaAs pseudomorphic HEMT technologies. The active-mixer has a positive gain for the first time, and the downconverter has exhibited a high conversion gain of 25.9dB and a DSB noise figure of 2.8dB. These MMIC's are suitable for compact wireless communication systems such as indoor wireless LANs, in which the transmitting power is planned to be 10dBm.

ACKNOWLEDGMENT

The authors wish to thank to Drs. T.Ishimine and Y.Takimoto for useful discussions and encouragements.

REFERENCES

- [1]Y.Takimoto and T.Ihara,"Research activities on millimeter wave indoor communication systems in Japan," 1993 IEEE MTT-S Microwave Symp. Dig.,pp.673-676.
- [2]Y.Takimoto and A.Inoue,"Minimum delay-spread millimeter wave indoor LAN system," SPIE Proc. Vol.2211, 1994, pp.278-281.
- [3]K.Ohata et al., "A millimeter wave monolithic VCO with an integrated heterojunction FET as a varactor," 1994 European Microwave Conf. Proc., pp.1667-1672.
- [4]M.Takikawa and K.Joshin,"Pseudomorphic N-InGaP/InGaAs/GaAs high electron mobility transistors for low-noise amplifiers," IEEE Electron Device Lett., 14, pp. 406-408, 1993.
- [5]M.Funabashi et al., "A V-band AlGaAs/InGaAs heterojunction FET MMIC dielectric resonator oscillator," 1994 IEEE GaAs IC Symp. Dig., pp.30-33.
- [6]U.Guttich and J.Wenger,"Design, fabrication, and performance of monolithic dielectrically stabilized PM-HFET oscillators up to 60GHz," 1994 European Microwave Conf. Proc., pp.361-365.
- [7]T.Inoue et al., "60GHz dielectrically stabilized monolithic voltage controlled oscillator," presented at 1995 European Microwave Conf.
- [8]M.Funabashi et al., "A 50-70GHz band heterojunction FET MMIC power amplifier," 1994 Int'l Conf. Infrared & Millimeter Waves Dig., pp.433-434.
- [9]T.Saito et al., "60-GHz MMIC downconverter using an image-rejection active HEMT mixer," 1994 IEEE MMWMC Symp. Dig., pp.77-80.
- [10]T.Saito et al., "60-GHz HEMT-based MMIC receiver with on-chip LO," 1994 IEEE GaAs IC Symp. Dig., pp.88-91.
- [11]T.Saito et al., "60GHz MMIC downconverter using a HEMT active-gate mixer," 1994 Asia Pacific Microwave Conf. Proc., pp.299-302.

ALGORITHMS FOR BLIND IDENTIFICATION OF TERRESTRIAL MICROWAVE CHANNELS

Javier Buisán Gómez del Moral Ezio Biglieri

Dipartimento di Elettronica, Politecnico di Torino
Corso Duca degli Abruzzi 24, I-10129 Torino (Italy).

ABSTRACT

Blind identification consists of estimating the impulse response of a linear, time-invariant channel used for transmission of digital data by observing the channel output without knowledge of the transmitted symbol sequence.

The aim of this paper is twofold. First we compare, in order to assess their applicability to the equalization of digital radio links affected by selective fading, some recently proposed algorithms based on the second-order statistics of the received signal. Further, one of these algorithms is modified to cope with correlated noise.

1. INTRODUCTION

By blind identification we mean here the estimate of the impulse response of a linear, time-invariant noisy channel used for transmission of digital data; this estimate is obtained by observing the channel output without knowledge of the transmitted symbol sequence. Our motivation for the present work was to assess the applicability of blind identification to the equalization of microwave radio links, to limit communication outages caused by severe selective fading. However, the conclusions drawn are applicable to other channels as well.

The desirable features of the ultimate blind identification algorithm are:

- Low identification error in the presence of noise.
- Fast convergence.
- Computational simplicity.
- Insensitivity to data-symbol correlation.
- Insensitivity to noise correlation.
- Possibility to make it adaptive.

This research was done in the framework of the "Human Capital and Mobility" program sponsored by the European Community.

Recent work on the subject was based on exploiting the cyclostationarity of digital signals, and was spurred by [4]. Tong, Xu, and Kailath [7, 8, 9, 10] have developed a blind identification algorithm (herewith referred to as TXK algorithm) which is based on an estimate of the autocorrelation function of the observed channel-output samples. This feature entails a convergence faster than other blind algorithms based on higher-order statistics [12], which is highly desirable when the channel is time-varying and its variations have to be tracked quickly in order to compensate for them. This algorithm converges globally, can resolve the non-minimum-phase zeros of the channel transfer function, and is robust with respect to timing recovery. However, it suffers from some drawbacks, viz.,

- It is computationally intensive, as it requires two singular-value matrix decompositions.
- It requires data symbols to be uncorrelated.
- It requires the noise to be uncorrelated.
- It is not adaptive.

An algorithm that improves on TXK (herewith referred to as MDCM) was proposed by Moulines *et al.* [5]. The advantages of this new algorithm over TXK are:

- A lower computational complexity.
- Convergence even with correlated data symbols.
- A lower identification error for the same observation length.

More recently, Baccalá and Roy [1, 2] have proposed a new algorithm (herewith referred to as BR) that presents a significantly lower computational complexity and an identification error close to that of TXK and MDCM algorithms.

The aim of this paper is twofold. First we compare, by combining analysis and simulation, the TXK, MDCM, and BR algorithms, in order to assess their

applicability to the equalization of digital radio links affected by selective fading. Our results show that in general these algorithms based on second order statistics outperform standard blind equalization in terms of convergence speed. Moreover, while the BR algorithm has a lower computational complexity, in this specific application the MDCM algorithm outperforms both TXK and BR in terms of robustness to source-data correlation and mean-square estimation error.

Further we present a modification of the MDCM algorithm in [5] in order to achieve blind identification in the presence of unknown correlated noise. Our algorithm is based on a matrix decomposition method proposed in [6].

2. CHANNEL MODEL AND IDENTIFICATION ALGORITHMS

We assume a digital signal linearly modulated by a symbol sequence $\{s_n\}$. The complex envelope $r(t)$ of the signal observed at the output of the channel can be expressed as

$$r(t) = \sum_{n=-\infty}^{\infty} s_n h(t - nT) + b(t), \quad (1)$$

where $\{s_n\}$ form a sequence of identically distributed complex random variables (the channel symbols), $h(t)$ is the channel impulse response, T is the symbol period, and $b(t)$ denotes additive noise.

The task of blind identification algorithms is to obtain an estimate of $h(t)$ based upon the observation of the process $r(t)$ during a finite time interval. We assume that $h(\cdot)$ has a finite duration, say $(M+1)T$, and that the conditions of identifiability based on second-order statistics [11] are satisfied by the channel impulse response.

The basic step in this approach consists of oversampling signal $r(t)$ with period Δ . Thus every T we get $L = T/\Delta$ samples of the observed process, taken at instants $t_0 + i\Delta$, $0 \leq i \leq L - 1$. This generates a vector process $\{r_n\}$.

2.1. The TXK algorithm.

The TXK algorithm is based on the further assumptions that

- The symbols s_n are uncorrelated, and
- The noise process $b(t)$ is white.

2.2. The MDCM algorithm.

This algorithm does not require the assumption that the symbol sequence be uncorrelated. Blind identification with the MDCM algorithm requires only one singular-value decomposition, along with the solution of an eigenvalue/eigenvector problem.

2.3. The BR algorithm.

This is based on the same assumptions as the MDCM algorithm, and provides identification by solving a system of linear equations.

2.4. Blind identification with correlated noise

None of the above algorithms works in the presence of correlated noise. We were able to modify the MDCM algorithm (which, as we shall see later on, provides the best performance for the problem we are considering here) in order to make it applicable to the case where the noise is not white. We use, with some adjustments, the matrix decomposition method proposed in [6].

3. RESULTS AND COMPARISONS

To model the fading radio channel transfer function $H(f)$, we use here the classical simplified three-ray model. Under normal propagation conditions, $H(f) = 1$, while during a fading event

$$H(f) = a(1 - be^{j\theta} e^{-j2\pi f\tau}) = a(1 - be^{-j2\pi(f-f_n)\tau}) \quad (2)$$

where a is the amplitude of the direct ray and accounts for flat fading (hereafter we shall assume $a = 1$), $0 \leq b \leq 1$ is the relative amplitude of the delayed ray, and $f_n \in (-1/2\tau, 1/2\tau)$ is the notch frequency, and τ is the difference of time delay between the two rays.

At the channel output the observed signal is $r(t) = x(t) + b(t)$, where $b(t)$ accounts for thermal noise (and possibly other interferences, which we shall disregard here.) With no fading the impulse response of the channel is a raised-cosine function with roll-off factor α , that is,

$$p(t) = A \frac{\sin \pi t/T}{\pi t/T} \cdot \frac{\cos \alpha \pi t/T}{1 - 4\alpha^2 t^2/T^2},$$

while in the presence of fading $h(t)$ is given by

$$h(t) = a [p(t) - be^{j2\pi(f_n - f_c)\tau} p(t - \tau)] \quad (3)$$

where f_c denotes the carrier frequency (note that $h(t)$ is generally complex.)

The following parameters values were selected as typical:

- Relative amplitude of the reflected ray:

$$B = 20 \log(1 - b) = 20 \text{ dB}$$

- Delay of the reflected ray:

$$\tau = 6.3 \text{ ns}$$

- Difference between the notch frequency and the carrier frequency:

$$f_n - f_c = 0$$

- Modulation scheme: 128-QAM at 140 Mbit/s, corresponding to a symbol interval 50 ns.
- Raised-cosine waveforms with roll-off α (in particular, we have examined the cases $\alpha = .11$ and $\alpha = .25$.)
- Oversampling factor L (we have chosen $L = 3$ and $L = 7$.)
- Observation length N .

The correlations were first estimated by using a time average over N symbol intervals. TXK, MDCM, and BR algorithms were then used to identify the channel impulse response. The quality of the identification was evaluated by computing the mean-square error

$$\text{MSE} = \frac{1}{LN} \sum_{i=1}^{LN} |h_i - \hat{h}_i|^2.$$

We also assume that the carrier phase is estimated exactly, that the duration of the impulse response is known, and that the unknown scalar complex multiplying factor inherent to all the algorithms examined here can be recovered in some way.

We hasten to say that the word “convergence” may not be fully appropriate when describing the behavior of these algorithms, which are not recursive in nature. Since they depend on a preliminary estimate of correlations, by “speed of convergence” we mean to describe how many samples are necessary for a correlation estimate that generates a good enough identification of the channel impulse response. Thus our “speed of convergence” actually reflects the robustness of an algorithm to the uncertainties in the knowledge of the correlation.

3.1. Equalization through channel identification

The estimate of the impulse response of the channel may be used to evaluate the tap gains of a linear transversal-filter equalizer. It was found in [3] that the TXK algorithm outperforms blind equalization in terms of speed of convergence, at the price of being computationally much more intensive than the latter.

3.2. Simulations with white noise and uncorrelated data

Table 1 summarizes the performance of the three algorithms in the presence of white noise and uncorrelated data. Here A_{TXK} , A_{MDCM} and A_{BR} denote the MSE of TXK, MDCM and BR algorithm, respectively. By $A_i \approx A_j$ we mean that at convergence the MSE performances of algorithms i and j are about the same. By $A_i < A_j$ we mean that at convergence the MSE of algorithm i is lower than for algorithm j . By $A_i \ll A_j$ we mean that at convergence the MSE of algorithm i is significantly lower (i.e., lower by more than one order of magnitude) than for algorithm j . N_C denotes the number of symbols needed to reach the convergence according to the criterion described in [3].

We can see that, for low signal-to-noise ratio E_b/N_0 (energy per bit over noise power spectral density), the MDCM algorithm gives always better estimates than the other two algorithms, and the BR algorithm gives similar MSE with respect to the TXK algorithm but with significantly lower computational cost.

For high E_b/N_0 , MDCM and BR give better estimates than the TXK algorithm, but always with a lower computational cost for the BR algorithm.

In general, we found that the convergence properties of these blind identification algorithms are very sensitive to the value of the roll-off factor α . In particular, for relatively small E_b/N_0 values the algorithms exhibit poorer convergence properties as α becomes larger. We may interpret this by looking at the shape of the raised-cosine pulse $p(t)$. If α is large, $p(t)$ exhibits a fatter central lobe and smaller sidelobes: therefore, the effect of the second ray is an almost complete cancellation of a portion of the impulse response for low values of τ/T . Conversely, for smaller α this cancellation effect is correspondingly reduced. We may say that the identification problem becomes better conditioned as α decreases.

3.3. Simulations with white noise and correlated data

The effect of data correlation was examined by choosing a binary symbol sequence $\{s_n\}$ with correlation $E[s_n s_{n-k}]$ equal to 1 for $k = 0$, to -1 for $k = \pm 1$, and zero elsewhere. The convergence of the MDCM algorithm is considerably slowed down, particularly for lower E_b/N_0 . Roughly, with 20,000 symbols the MSE is greater than for uncorrelated data by a factor of 2 for $E_b/N_0 = 50$ dB, by one order of magnitude for $E_b/N_0 = 30$ dB, and by two orders of magnitude for $E_b/N_0 = 20$ dB. On the other hand, the TXK and BR algorithms fail to converge, as expected.

α	L	E_b/N_0 (dB)	N_C	MSE
0.11	3	20	6000	$A_{\text{MDCM}} \ll A_{\text{TXK}} \approx A_{\text{BR}}$
0.11	7	20	1500	$A_{\text{MDCM}} \approx A_{\text{TXK}} < A_{\text{BR}}$
0.25	3	20	20000	$A_{\text{MDCM}} \ll A_{\text{TXK}} \approx A_{\text{BR}}$
0.25	7	20	8000	$A_{\text{MDCM}} < A_{\text{TXK}} \approx A_{\text{BR}}$
0.11	3	30	<500	$A_{\text{MDCM}} < A_{\text{BR}} < A_{\text{TXK}}$
0.11	7	30	<500	$A_{\text{MDCM}} < A_{\text{TXK}} \approx A_{\text{BR}}$
0.25	3	30	<500	$A_{\text{MDCM}} < A_{\text{BR}} < A_{\text{TXK}}$
0.25	7	30	<500	$A_{\text{MDCM}} \approx A_{\text{BR}} < A_{\text{TXK}}$
0.11	3	50	<500	$A_{\text{MDCM}} \approx A_{\text{BR}} \ll A_{\text{TXK}}$
0.11	7	50	<500	$A_{\text{MDCM}} \approx A_{\text{BR}} \ll A_{\text{TXK}}$
0.25	3	50	<500	$A_{\text{MDCM}} \approx A_{\text{BR}} \ll A_{\text{TXK}}$
0.25	7	50	<500	$A_{\text{MDCM}} \approx A_{\text{BR}} \ll A_{\text{TXK}}$

Table 1: Comparison among three blind identification algorithms.

3.4. Simulations with correlated noise

The effect of noise correlation was also examined. Colored noise was obtained by passing white noise through a single-pole filter. It was seen that the three algorithms considered here failed to converge.

The next step was modify the MDCM algorithm so as to achieve blind identification with correlated noise. It was seen from simulation that the channel estimates obtained from this modified MDCM algorithm are satisfactorily good, although the convergence was somewhat slowed down.

4. REFERENCES

- [1] L. A. Baccalá and S. Roy, "A new blind time-domain channel identification method based on cyclostationarity," *Signal Processing Letters*, Vol. 1, No. 6, pp. 89–91, 1994.
- [2] L. A. Baccalá and S. Roy, "Time-domain blind channel identification algorithms," *Proc. of 1994 CISS*, Princeton, NJ, March 1994.
- [3] E. Biglieri, G. Caire, and G. D'Aria, "Blind channel identification in terrestrial radio links," *Proceedings of ICC'93*, Geneva, Switzerland, May 1993.
- [4] W. A. Gardner, "A new method of channel identification," *IEEE Trans. Commun.*, Vol. 39, No. 6, pp. 813–817, June 1991.
- [5] E. Moulines, P. Duhamel, J.-F. Cardoso, and S. Mayrargue, "Subspace methods for the blind identification of multipath channels," *IEEE Trans. Signal Processing*, Vol. 43, No. 2, pp. 516–525, February 1995.
- [6] R. Rajagopal and P. Ramakrishna Rao, "DOA estimation with unknown noise fields: a matrix decomposition method," *IEE Proceedings-F*, vol. 138, No 5, October 1991.
- [7] L. Tong, G. Xu, and T. Kailath, "A new approach to blind identification and equalization of multipath channels," *Proc. of the 25th Asilomar Conference*, Pacific Grove, CA, pp. 856–860, Nov. 1991.
- [8] L. Tong, G. Xu, and T. Kailath, "Blind identification and equalization of multipath channels," *Proc. of ICC'92*, pp. 351.3.1–351.3.5, 1992.
- [9] L. Tong, G. Xu, and T. Kailath, "Blind identification and equalization based on second-order statistics: A time-domain approach," *IEEE Trans. Inform. Theory*, Vol. 40, pp. 340–349, March 1994.
- [10] L. Tong, G. Xu, B. Hassibi, and T. Kailath, "Blind identification based on second-order statistics: A frequency-domain approach," *IEEE Trans. Inform. Theory*, Vol. 41, pp. 329–333, January 1995.
- [11] J. K. Tugnait, "Fractionally Spaced Blind Equalization And Estimation Of FIR Channels," *Proc. 1993 Intern. Conf. on Communications*, Geneva, Switzerland, May 23–26, 1993.
- [12] J. K. Tugnait, "Fractionally spaced blind equalization of FIR channels under symbol timing offsets," *27th Conf. Signals Systems Computers*, Nov. 1–3, 1993, Pacific Grove, CA.

CHANNEL EVALUATION FROM PREDICTED ZERO CROSSING ANALYSIS

P. W. Piggin and M. Gallagher⁺

Department of Electronic and Electrical Engineering
The University of Leeds, Leeds, LS2 9JT, UK

M.Gallagher@elec-eng.leeds.ac.uk

ABSTRACT

This paper presents an investigation into Real-time Channel Evaluation (RTCE) from predicted zero crossing analysis of; (i) a pilot-tone, and, (ii) Frequency Shift Keying (FSK) modem tones within a HF (High Frequency) radio system. This work extends the initial investigations from the early 1970s which used an analogue implementation analysing phase perturbation by time-differential phase comparisons of a low-level pilot-tone inserted in-band. The results to be presented in this paper compare theoretical analysis and measured results in Gaussian and flat fading conditions, and hence identify the close relationship between phase threshold, zero crossing error rate and SNR (Signal to Noise Ratio). This type of non-parametric system measurement technique is widely applicable for other constant envelope modulation types, e.g. MFSK, and as such is suitable for incorporation into frequency management systems for various different radio systems operating in the HF, VHF and UHF bands.

1. INTRODUCTION AND BACKGROUND INFORMATION

The utilisation of a low-level, co-channel *pilot* tone as a diagnostic probe to facilitate monitoring of current channel state can provide an insight into communication system performance. Specifically, both the amplitude and phase of the tones are affected by underlying propagation conditions and co-channel interference; with phase sensitivity providing the best estimates of prevailing conditions [1]. Consequently, analysis of phase perturbation by time-differential phase-comparison can be used to estimate the prevailing SNR.

An original analogue implementation, (Darnell, 1975) [2] required long observation times (e.g. >200 seconds) to obtain a channel estimate for high SNRs. Latterly, by concentrating on reducing the observation time, (Grayson, 1991) [3] identified that, by using a Digital Signal Processing (DSP) based implementation, complete channel observations could be completed in 2.5 seconds. Work here with an enhanced DSP implementation optimises observation time still further to produce meaningful channel quality estimations in the region of 750 ms.

Application of this research is focused on effective spectrum management, since efficient system operation depends upon the ability to react to a range of parameters that characterise both propagation and channel noise. The use of RTCE in an automated communication system can reduce the use of high radiated powers by selecting frequencies and transmission times for which the received SNR is maximised and interference avoided. By effectively incorporating appropriate RTCE techniques, significant improvement in system performance can be achieved, as, in many instances, interference caused by congestion is the limiting factor in a communications system performance, rather than the propagation conditions.

2. RTCE FROM PREDICTED ZERO CROSSING ANALYSIS WITH A PILOT-TONE

Pilot-tone RTCE uses a low level tone placed in-band close to frequencies of interest. The pilot-tone is analysed to consider aspects such as instantaneous phase, amplitude, and other properties that are affected by the noise and channel perturbations. In this application the

⁺ Formerly with the Department of Electronic Engineering, University of Hull, Hull. UK.

pilot-tone is used to provide channel quality information to determine the required transmission SNR at a given instant in time. Although both the amplitude and phase of a pilot tone are affected by propagation conditions and interference, it is the phase that is more sensitive to the prevailing conditions [4]. Consequently, analysis of phase perturbation by time-differential phase comparison can provide insight into channel performance.

In a digital system, the incoming baseband signal is sampled and filtered to extract the highly-tuned pilot tone using a narrow-band FIR filter. The occurrence of a zero-crossing is predicted by adding a constant value of $(\pi/2)$ onto the previous detected crossing, (n being an integer and τ representing the period of the pilot tone). The timing of the predicted crossing point is used to calculate the phase error of the received tone and, if this is greater than a chosen threshold, a failure is recorded. The rate of phase comparison failure is then used to infer channel quality. This system does not require any form of decoding or demodulation to determine the channel quality and in this respect is *non-parametric* system, also no synchronisation of the zero-crossing of the pilot tone is required.

A pilot tone subject to additive Gaussian noise was used in initial tests. The theoretical results were derived from equation (3) in [1], given below in equation (1).

where; $P_e|_{SS+N}$ is the probability of zero crossing error for a signal in Gaussian-distributed noise, θ_{Th} is the pilot-tone phase threshold, σ_N RMS noise amplitude at the output of the RTCE filter (digital implementation), A_0 is the signal amplitude (normalised), and k_0 and envelope of autocovariance of the output noise of the RTCE filter.

Practical results were compared to the theoretical, and shown in Figure 1. As can be seen the results for both theory and experiment are in close agreement at all threshold values. It was noted that at high values of SNR, where the value of $P_e|_{SS+N}$ was very small, the measured results had a tendency to diverge from the theory. The general agreed reason for this phenomena is that the number of comparison possible at high SNRs is not statistically relevant when compared to the probability of error expressed in the theory.

$$\begin{aligned}
 P_e|_{SS+N} = & 1 - \int_{-\theta_{Th}}^{\theta_{Th}} \int_0^{\infty} \frac{1-k_0^2}{\pi} \cdot \frac{y}{(y^2 - 2k_0 y \cos \theta_{\tau} + 1)^2} \\
 & \left\{ 1 + \left\{ \frac{1}{2} \left(\frac{A_0}{\sigma_N} \right)^2 \frac{(1-k_0)}{(1+k_0)} \cdot \frac{y^2 + 2y \cos \theta_{\tau} + 1}{y^2 + 2yk_0 \cos \theta_{\tau} + 1} \right\} \right\} \\
 & \exp \left[-\frac{1}{1+k_0} \left(\frac{A_0}{\sigma_N} \right)^2 \left\{ 1 - \frac{1}{2} (1-k_0) \frac{y^2 + 2y \cos \theta_{\tau} + 1}{y^2 + 2yk_0 \cos \theta_{\tau} + 1} \right\} \right] dy d\theta_{\tau}
 \end{aligned} \tag{1}$$

3. OPTIMISING THE NUMBER OF PHASE COMPARISONS

In order to produce the results given above the number of averaged phase comparisons carried out to obtain a measure of the probability of pilot-tone phase error was varied as a function of the SNR (high number of comparisons for a low SNR), thus producing a statistically relevant result at low probabilities of error. An investigation was carried out into the *actual* number of phase comparisons required for optimal channel evaluation. It was found that an observation time of 750 ms was required, this is in comparison to 200 seconds for the original analogue implementation.

4. RTCE FROM PREDICTED ZERO CROSSING ANALYSIS WITH FSK MODEM TONES

In order to obtain the theoretical phase-error rates for an FSK modem, above that of a single pilot tone, equation (1) was considered, detailing the probability of zero-crossing error for a steady signal in Additive Gaussian white noise (AGWN). In order to adapt the equations given above to determine the zero crossing error rate for FSK modem tones with respect to a pilot tone, each tone was considered separately, and in the limit equi-probable.

Results shown in Figure 2 are similar to those shown in Figure 1, and show a strong correlation between calculated theoretical and measured results for both steady signal and Rayleigh fading channel conditions. It is clear, however, that at large window sizes the correlation is reduced. An explanation for the large window size (θ_{Th}) recording a lower error rate than expected in such in high noise situations is based on the DSP implementation being indiscriminate where subsequent valid zero crossing should occur. Hence invalid crossings are erroneously counted as correct.

5. CONCLUSIONS

Applications using this zero-crossing analysis RTCE technique would be best suited to using a narrow window size especially at low SNR values. This paper demonstrates that RTCE can be performed without the need for an inserted pilot-tone co-located with the information bearing modem tones. The advantages of this

are numerous: a reduction in system complexity and reduced power consumption within the transmitting system. RTCE from predicted zero crossing analysis is an important non-parametric channel quality and evaluation system, since it is possible to infer system performance without demodulation processes, e.g. synchronisation, error control or decryption. This research can be extended using in-band and out-of-band digital filters for constant envelope signalling methods e.g. MFSK. It is believed that this research has merits in a broad range of radio systems and forms an important part of channel spectrum management.

5. ACKNOWLEDGEMENTS

The support of the Engineering and Physical Sciences Research Council (EPSRC) and EDS Defence Ltd, Tewkesbury, is acknowledged.

REFERENCES

- [1] BETTS, J. A., et al, "*C.W. sounding and its use for control of HF (3-30 MHz) adaptive systems for data transmission*", Proc. IEE, Vol. 117, pp 2209-2215
- [2] BETTS, J. A., DARNELL, M., "*Real-time HF channel estimation by phase measurement on a low-level pilot-tones*", AGARD CP-173, 'Radio systems and the Ionosphere', Athens, 1975
- [3] GRAYSON, M., "*Real-time channel evaluation derived from predicted zero-crossing*", 3rd Bangor Symposium on Communications, 1991.
- [4] DAVID, F., FRANCO, A.G., SHERMAN, H., and SHUCAVAGE, L.B.: "*Correlation measurements on an H.F. transmission link*", IEEE trans Communications, 1969, COM-17, pp. 245-256

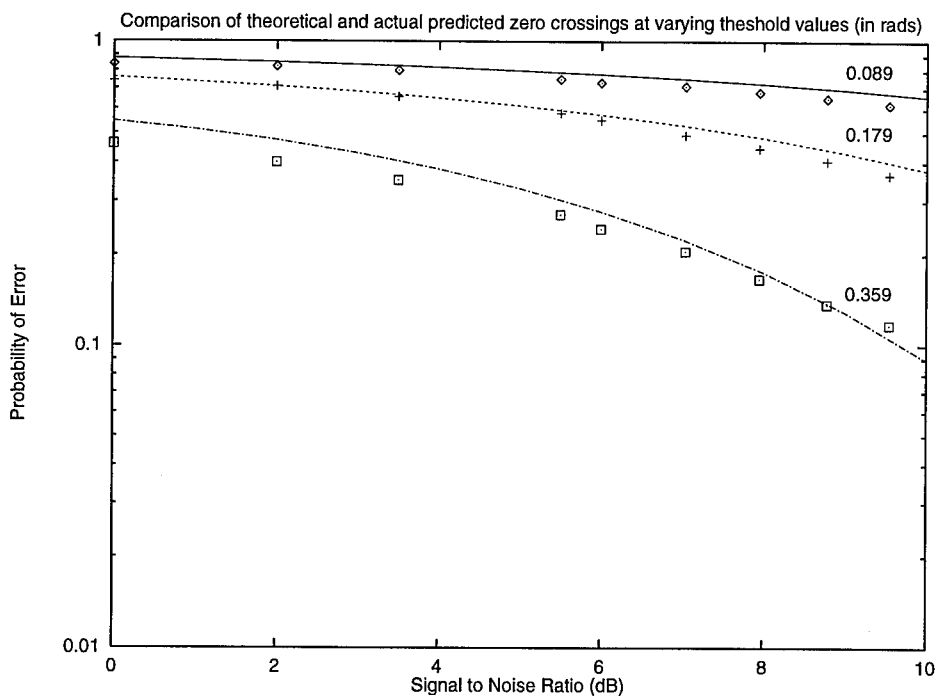


Figure 1 Comparison of theoretical and measured results for zero crossing error rates for a pilot-tone at various threshold values under Gaussian conditions

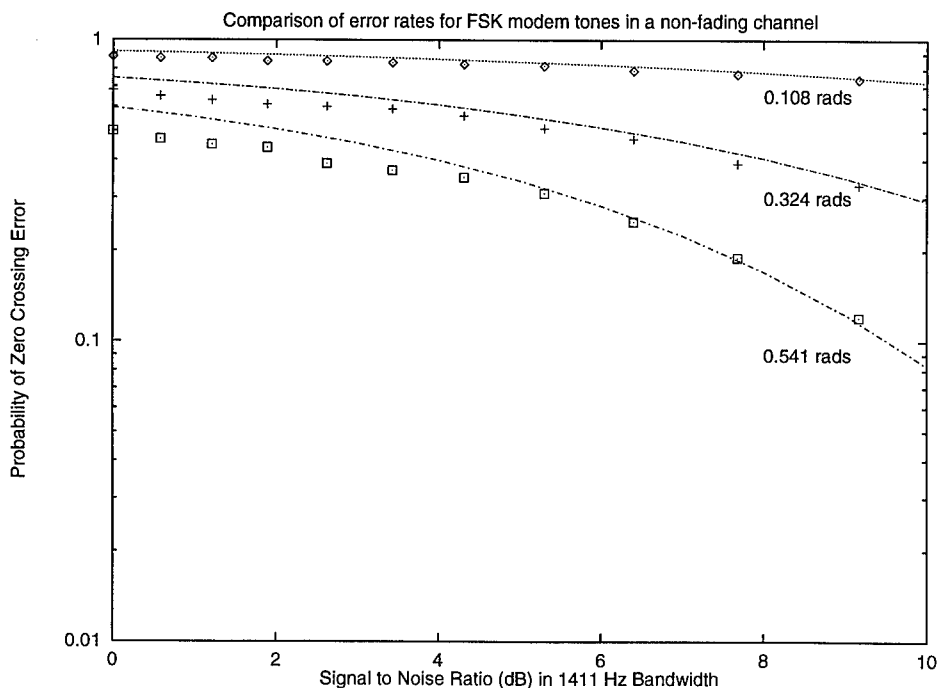


Figure 2 Comparison of theoretical and measured results for zero crossing error rates for FSK modem tones at various threshold values under Gaussian conditions

A NEW METHOD FOR FREQUENCY DETECTION BY LINEAR PREDICTION USING TOTAL LEAST SQUARES

Rodrigo Pinto Lemos and Amauri Lopes

State University of Campinas, UNICAMP/FEE/DECOM

Caixa Postal 6101, CEP 13083-970 Campinas, SP, Brazil.

E-mail: lemos@decom.fee.unicamp.br & amauri@decom.fee.unicamp.br .

ABSTRACT

This work is concerned with the use of Total Least Squares criterion in Forward-Backward Linear Prediction optimization, yielding a new frequency estimation method, named TLS-FBLP. A detailed comparison of our method to Tufts and Kumaresan's Modified FBLP, revealed that TLS-FBLP is better than Modified FBLP at low prediction orders, as well as they are similar for high orders.

1. INTRODUCTION

Studies in Signal Processing have paid special attention to the detection of sinusoids in the presence of white noise. The basic problem consists in estimating the sinusoids frequencies using a few signal samples.

This problem becomes critical either when the frequency separation is smaller than the reciprocal of the signal observation interval or when the signal-to-noise ratio (SNR) decreases.

The best performance for this situation is achieved by Maximum Likelihood (ML) based methods. However, its computational effort is prohibitive. Tufts and Kumaresan [6] introduced their Modified FBLP method, which solves Forward-Backward Linear Prediction (FBLP) in Least Squares (LS) sense and reduces noise effects by using Singular Value Decomposition (SVD). This method is computationally less expensive than ML, but its performance attains that of ML for high SNR's.

In 1980, Golub and Van Loan [3] presented Total Least Squares (TLS) criterion, which optimizes Linear Prediction (LP) by taking into account perturbation in both the observation vector \mathbf{b} and the data matrix \mathbf{A} .

The aim of this paper is to present a new frequency estimation method, named TLS-FBLP, which is based on the application of TLS criterion to FBLP optimization. Its performance is compared to that of Tufts and Kumaresan's Modified FBLP. Also, a new measure for the optimum value of prediction order is proposed.

2. FREQUENCY DETECTION BY LINEAR PREDICTION

Let us consider N uniformly spaced samples of the sum of M complex exponential signals, initially noiseless, as given by:

$$u[n] \triangleq \sum_{k=1}^M a_k \cdot \exp[j(\omega_k \cdot n + \phi_k)], \quad n = 1, 2, \dots, N \quad (1)$$

where the a_k are the amplitudes, the ω_k are the frequencies and the ϕ_k are the phases of the exponentials.

Linear Prediction allows us to estimate signal frequencies by using vector \mathbf{w} of coefficients of a prediction error filter (PEF), optimized in order to minimize the mean square error.

Ulrich and Clayton [7] have shown that the joint optimization of forward and backward PEF's, subject to the forward coefficients being the same as the complex conjugate of backward ones in reverse order (FBLP), yields better results when estimating the frequencies of undamped sinusoids.

The related optimum vector \mathbf{w} of coefficients, for a prediction order L , has dimensions $L \times 1$ and defines an L order polynomial $W(z)$, given by the formula:

$$W(z) = 1 - w_1^* z^{-1} - w_2^* z^{-2} - \dots - w_L^* z^{-L} \quad (2)$$

for the upper asterisk meaning complex conjugate.

Antunes [1] demonstrates that M of $W(z)$ zeros lie on the unit circle (UC), and are called *signal zeros*. The remaining ones are called *extraneous zeros* and are approximately uniformly distributed within the UC.

The desired frequencies can be estimated through the angular locations of the M signal zeros on the UC. These are the basic features of FBLP method.

The corruption of $u[n]$ by white noise leads the zeros of $W(z)$ to fluctuate around their ideal locations. This behavior is shown in Figure 1, where we superimpose the zeros of $W(z)$ for 50 experiments under the

following conditions:

$$\begin{aligned} N &= 25, & M &= 2, & L &= 24, & \text{SNR} &= 10 \text{ dB}. \\ a_1 &= 1.0, & \omega_1 &= (1, 00)\pi & \text{and} & \phi_1 &= (-1, 00)\pi. \\ a_2 &= 1.0, & \omega_2 &= (1, 04)\pi & \text{and} & \phi_2 &= (-0, 79)\pi. \end{aligned}$$

Each experiment uses a new realization of noise, added to the same signal samples.

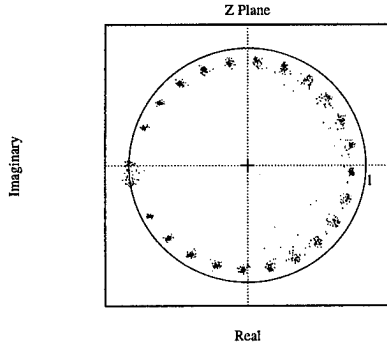


Figure 1: FBLP transfer function zeros.

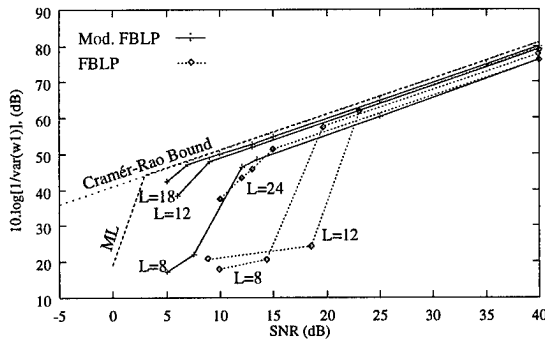


Figure 2: Comparison among performances of ML, FBLP and Modified FBLP methods.

These fluctuations degrade the detection performance. While SNR is greater than about 25 of dB's, performance degradation is due only to random fluctuations of the M signal zeros. However, the fluctuations of both types of zeros grow as SNR decreases, leading to the possibility of an extraneous zero to be located closer to UC than a signal zero. In this situation, this extraneous zero is interpreted as signal zero and a large error is produced. So, performance decreases rapidly, characterizing a threshold effect.

In Figure 2, we show the inverse of the estimates variance versus SNR. We also show the theoretical bound for the performance, namely, Cramér-Rao Bound, and the performance of Maximum Likelihood [6].

Focusing on the dotted line curves, we observe that they attain the ML performance at high SNR's. However, both curves and even Cramér-Rao Bound, decay

slowly as SNR decreases, until the threshold is reached. Consequently, their performances degrade rapidly.

3. MODIFIED FBLP METHOD

The general solution for vector \mathbf{w} , in least squares sense, is given by:

$$\mathbf{w}_{LS} = \mathbf{A}^\# \mathbf{b}. \quad (3)$$

where $\#$ means pseudo-inverse.

Singular Value Decomposition (SVD) [1] applied to data matrix \mathbf{A} , allows us to write (3) in the following form:

$$\mathbf{w}_{LS} = \sum_{k=1}^{\min[2(N-L), L]} \frac{1}{\sigma_{A(k)}} \mathbf{v}_{A(k)} \mathbf{u}_{A(k)}^H \mathbf{b} \quad (4)$$

where $\sigma_{A(k)}$ are the singular values, and $\mathbf{u}_{A(k)}$, $\mathbf{v}_{A(k)}$ the left and right singular vectors of \mathbf{A} , respectively.

In the noiseless case, $\text{rank}(\mathbf{A}) = M$. Thus, only the first M singular values are nonzero and, obviously, correspond to the signal. These are the *signal singular values*. In the presence of noise, \mathbf{A} has full rank and has others $\min[2(N-L), L] - M$ nonzero singular values, related to the noise. These are the *noise singular values*.

In Modified FBLP method, we take into account only the M largest $\sigma_{A(k)}$, i.e., the *signal singular values*, truncating the sum in (4) to M in order to approximate the noiseless case.

Continuous line curves in Figure 2 allows us to observe the lowering of threshold SNR's and the increasing of estimate precision, due to Modified FBLP method.

4. TOTAL LEAST SQUARES CRITERION

In the following, we develop a mathematical characterization of TLS criterion and describe the solution for the corresponding \mathbf{w} .

4.1. Analysis Through Perturbation Theory

When applying Perturbation Theory to Linear Prediction, we first write the LP set of equations as the approximation:

$$\mathbf{A} \mathbf{w} \approx \mathbf{b} \quad (5)$$

In order to have an equality, we can add an error vector \mathbf{e} to the right side of (5). So, we can write:

$$\mathbf{A} \mathbf{w} = (\mathbf{b} + \mathbf{e}) \quad (6)$$

The solution in least squares sense amounts to finding such a vector \mathbf{w} that minimizes the quadratic norm of \mathbf{e} , subject to (6).

TLS criterion takes into account perturbations in both \mathbf{b} and \mathbf{A} , in order to have an equality in (5). So, we can write:

$$(\mathbf{A} + \mathbf{E})\mathbf{w} = (\mathbf{b} + \mathbf{e}), \quad (7)$$

where \mathbf{E} is the perturbation matrix for \mathbf{A} , with dimensions $2(N-L) \times L$. We can rewrite (7) as:

$$([\mathbf{A} \mid \mathbf{b}] + [\mathbf{E} \mid \mathbf{e}]) \begin{bmatrix} \mathbf{w} \\ -1 \end{bmatrix} = \mathbf{0} \quad (8)$$

Thus, the solution to TLS problem amounts to finding such a vector \mathbf{w} that minimizes the quadratic norm of $[\mathbf{E} \mid \mathbf{e}]$, subject to (8).

4.2. Solving in Total Least Squares Sense

Define $\mathbf{P} \triangleq [\mathbf{A} \mid \mathbf{b}]$ and $\mathbf{Q} \triangleq [\mathbf{E} \mid \mathbf{e}]$, with dimensions $2(N-L) \times (L+1)$. TLS solution amounts to finding such a vector \mathbf{w} that assures:

$$\min \|\mathbf{Q}\|_F^2, \quad \text{subject to } (\mathbf{b} + \mathbf{e}) \in \mathcal{R}(\mathbf{A} + \mathbf{E}), \quad (9)$$

where $\mathcal{R}(\mathbf{A})$ denotes the *range* of \mathbf{A} .

Following the steps in [3], TLS estimate can be obtained from the SVD of \mathbf{P} for the case where $2(N-L) \geq (L+1)$:

$$\mathbf{P} = \sum_{k=1}^{L+1} \sigma_{P(k)} \mathbf{u}_{P(k)} \mathbf{v}_{P(k)}^H \quad (10)$$

for $\sigma_{P(1)} \geq \dots \geq \sigma_{P(M)} > \sigma_{P(M+1)} = \dots = \sigma_{P(L+1)} \geq 0$.

Golub and Van Loan [3] show that the minimum is attained when:

$$\mathbf{Q} = -\mathbf{P}\mathbf{v}\mathbf{v}^H \quad (11)$$

where \mathbf{v} is any unit vector in subspace \mathcal{S}_w , defined by the linear combination of $\{\mathbf{v}_{P(M+1)}, \dots, \mathbf{v}_{P(L+1)}\}$, i.e., the right singular vectors of \mathbf{P} corresponding to $\sigma_{P(L+1)}$.

For $\alpha \neq 0$ being the $(L+1)$ -st component of vector \mathbf{v} , we make:

$$\begin{bmatrix} \mathbf{w}_{TLS} \\ -1 \end{bmatrix} = -\frac{\mathbf{v}}{\alpha} \quad (12)$$

and substitute (11) and (12) in (8). Then we get:

$$\begin{aligned} ([\mathbf{A} \mid \mathbf{b}] + [\mathbf{E} \mid \mathbf{e}]) \begin{bmatrix} \mathbf{w}_{TLS} \\ -1 \end{bmatrix} &= \mathbf{P}(\mathbf{I} - \mathbf{v}\mathbf{v}^H) \left(-\frac{\mathbf{v}}{\alpha}\right) \\ &= \mathbf{0}, \end{aligned} \quad (13)$$

for $\mathbf{v}^H \mathbf{v} = 1$, i.e., \mathbf{v} is a unit vector.

Therefore, vector \mathbf{w}_{TLS} given by (12) satisfies equation (8) and assures that $\|\mathbf{Q}\|_F^2$ is minimal. Thus, it solves TLS problem. However, if there is no \mathbf{v} in \mathcal{S}_w such that $\alpha \neq 0$, TLS problem has no solution.

If $\sigma_{P(L+1)}$ is a repeated singular value of \mathbf{P} , we have infinite solutions. In this case, we can adopt minimum norm solution which is given by Golub and Van Loan [3] as:

$$\mathbf{w}_{TLS} = - \sum_{k=M+1}^{L+1} \left[\frac{v_{P[(L+1),k]}^*}{\sum_{i=M+1}^{L+1} |v_{P[(L+1),i]}|^2} \right] \mathbf{x}_k \quad (14)$$

where

$$\mathbf{v}_{P(k)} = \begin{bmatrix} \mathbf{x}_k \\ v_{P[(L+1),k]} \end{bmatrix} \quad (15)$$

For an underdetermined set of equations, i.e., $2(N-L) < (L+1)$, we have more unknowns than equations in (8). Lawson [4] states that this yields infinite solutions with null error. In this situation, TLS and LS solutions are the same. Thus, we can assume $\mathbf{w}_{TLS} = \mathbf{A}^\# \mathbf{b}$.

5. TLS-FBLP METHOD

TLS-FBLP method consists in the use of TLS criterion in order to find an optimum value for \mathbf{w} in *forward-backward* linear prediction, as stated by the formula:

$$\left(\begin{bmatrix} \mathbf{A}_f & \mathbf{b}_f \\ \mathbf{A}_b & \mathbf{b}_b \end{bmatrix} + \begin{bmatrix} \mathbf{E}_f & \mathbf{e}_f \\ \mathbf{E}_b & \mathbf{e}_b \end{bmatrix} \right) \begin{bmatrix} \mathbf{w} \\ -1 \end{bmatrix} = \mathbf{0} \quad (16)$$

where the indexes f and b refer to forward and to backward LP, respectively.

To the best of our knowledge, this approach is unpublished and yields a new frequency detection method.

5.1. Performances Under Perspective

In order to compare the performance of TLS-FBLP to that of Modified FBLP, we computed performance curves for prediction orders from $L = 2$ to $L = 24$. This allowed us to generate performance surfaces, as shown in Figure 3 and Figure 4. We observe the threshold SNR's through the shape of the cutting edge of the surface. At low prediction orders, Modified FBLP shows deep valleys even at high SNR's. However, the methods present the same performance curves for $L \geq 20$.

The shape of the threshold edge for TLS-FBLP is smoother than that for Modified FBLP. Threshold SNR values for TLS-FBLP are almost the same for L from 8 to 18, whereas the best performance of Modified FBLP is observed in the range $L = 14$ to $L = 18$, degrading significantly outside this interval. Also, the former is better than the latter at low prediction order values.

Therefore, TLS-FBLP method is less sensitive to prediction order changes than Modified FBLP.

The lowest threshold SNR value for TLS-FBLP is 8 dB at $L = 16$, whereas the lowest threshold SNR for

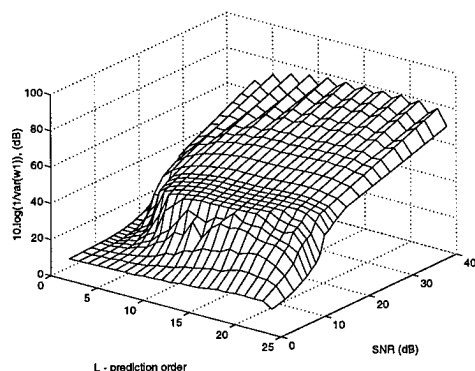


Figure 3: Performance surface for TLS-FBLP method.

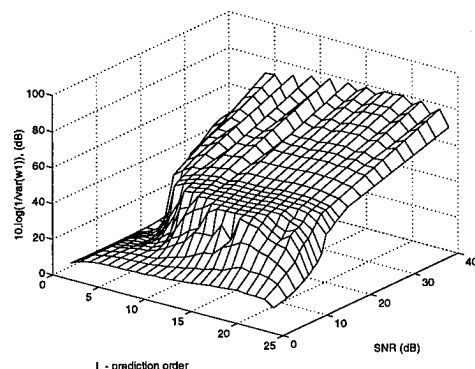


Figure 4: Performance surface for Modified FBLP method.

Modified FBLP had the value 7 dB and occurred at $L = 17$, as shown in Figure 5.

Although the best performance has been verified in Modified FBLP method, TLS-FBLP best performance is only 1 dB worse. So, we can say that TLS-FBLP shows performance comparable to Modified FBLP.

Both usual FBLP and TLS-FBLP do not make subspace restriction as Modified FBLP does, but TLS-FBLP performance is quite close to that of Modified FBLP, and significantly superior to that of FBLP.

The best performances of both TLS-FBLP and Modified FBLP occurred when data matrices \mathbf{P} and \mathbf{A} , respectively, became almost square. So, the empirical measure for the optimum prediction order in Modified FBLP, defined by Tufts and Kumaresan as $(3/4)N$, can be substituted by the measure that states: *the optimum prediction order value is such that it leads the data matrix or the extended data matrix to be approximately square.*

6. CONCLUDING REMARKS

Total Least Squares (TLS) criterion allows us to propose a new frequency detection method, which we called

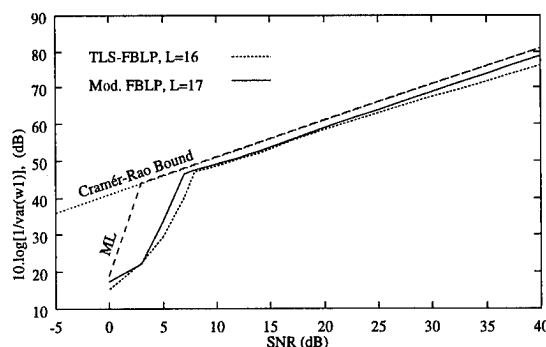


Figure 5: Comparison between the best performances for TLS-FBLP and Modified FBLP methods.

TLS-FBLP. This method lowers the threshold SNR's and its best performance is only 1 dB worse than the best result of Tufts and Kumaresan's Modified FBLP. Also, TLS-FBLP has shown to be less sensitive to prediction order changes and performed better than Modified FBLP for low prediction orders. Moreover, best performances occurred when the data matrix or extended data matrix were approximately square.

TLS-FBLP is similar to FBLP, as they do not make subspace restriction. However, its performance is comparable to that of Modified FBLP.

7. REFERENCES

- [1] E. J. B. Antunes, *Frequency Detection by Linear Prediction*, (in Portuguese) Master thesis, State University of Campinas, Brazil, 1992.
- [2] E. J. B. Antunes and A. Lopes, "Frequencies estimation of real sinusoids," *Proc. ISSSE (Paris)*, 1992.
- [3] G. Golub and C. F. Van Loan, "An analysis of the total least squares problem," *SIAM J. on Numerical Analysis*, vol. 17, 1980.
- [4] C. L. Lawson and R. J. Hanson, *Solving Least Squares Problems*. Englewood Cliffs, NJ: Prentice Hall, 1974.
- [5] R. P. Lemos, *High Resolution Methods with Subspace Restriction for Frequency Detection*, (in Portuguese) Master thesis, State University of Campinas, Brazil, 1995.
- [6] D. W. Tufts and R. Kumaresan, "Estimation of frequencies of multiple sinusoids: Making linear prediction perform like maximum likelihood," *Proc. IEEE*, vol. 70, pp. 975-89, 1982.
- [7] T. J. Ulrych and R. W. Clayton, "Time series modeling and maximum entropy," *Phys. Earth Planet. Int.*, vol. 12, pp. 188-200, 1976.

A PARAMETRIC SET OF NONLINEAR METHODS OF SPECTRAL ESTIMATIONS

Roman Ugrinovsky

Institute of Applied Physics, Russian Academy of Sciences
46 Uljanov Str., 603600 Nizhny Novgorod, Russia
E-mail: is77264@ltuvax.bitnet

ABSTRACT

A novel rigorous approach to the spectral density estimation problem based on the trigonometric moment problem technique is considered. Using the trigonometric moment problem results, all possible extrapolations of the autocorrelation function, which are in agreement with a set of known values are found. A wide set of spectral estimators is described in terms of polynomials orthogonal with respect to the given autocorrelation sequence. The parametric representation for this set is given.

1. Introduction

At present, there are several standard methods of dealing with the classical problem in digital signal and sensor array processing [1, 2, 3]. These methods include the conventional nonparametric Fourier approach and more recently developed parametric techniques such as maximum entropy (ME), maximum likelihood (ML), MUSIC, ESPRIT and others.

Until 1967, most of the procedures used for estimating the spectral density of a stochastic process were based on the Blackman-Tukey approach [1]. The expectation of an estimate is equivalent to the convolution of the true spectral density of the stochastic process with the spectral window. The statistical stability and resolution of the spectral density estimate using the Blackman-Tukey procedure are highly dependent on the choice of the window function [4]. Moreover, the spectral density estimator based on Blackman-Tukey approach is linear because it involves the use of linear operations on the available time series. A major problem with the Fourier transform is that the accuracy of the mode estimates is roughly inversely proportional to the total simulation time interval. Moreover, there

is problem with appropriate choice of the windowing function.

The windowing problem may be overcome by using the nonlinear estimators of spectral density based on ME approach, ML approach or others. But these approaches are not universal. Really, these approaches do not permit one to get other spectral estimations which corresponds to time series, whose autocorrelation functions agree with the same set of known values, i.e. to get other extrapolations of the correlation function.

Besides, when the spectral estimate with good resolution is necessary to solve a more concrete problem, for example, the power spectral density estimation problem with additional *a priori* information about the spectrum, it seems unreasonable to apply the known methods of spectral estimation, such as ME method, ML method or others in their original form, because these methods of spectral estimation are not intended to solve concrete problems [5].

So, in spite of the progress in spectral estimation and a list of successful practical application of the more popular methods of spectral estimation such as ME, MUSIC, ML and some others, new methods for effective spectral estimation are necessary. Besides, it is desired to have a common approach both for the construction of spectral estimation methods and for the investigation of their performance.

The aim of this paper is to propose and develop a novel rigorous approach to spectral density estimation problem. We describe all possible extrapolations of the autocorrelation function which agree with a set of known values. The set of possible spectral estimations is described as a parametric family of spectral estimators with parametrization function. The quantitative performance of the proposed spectral estimator's family is established.

This work was supported by the Russian Foundation of Fundamental Researches, Grant No. 93-02-16043.

2. Spectral density estimation problem

2.1. Problem formulation

Consider the problem of estimating a power spectral density function given only that it is positive on the spectral support, zero outside and compatible with the known values of the autocorrelation sequence.

The aim of spectral estimation is to find an estimate of the spectrum which agrees with the set of the known values of autocorrelation sequence c_k , $k = 1, 2, \dots, N$, i.e., spectral density estimation problem is to determine the nonnegative function $P(\theta)$ such that

$$P(\theta) \geq 0, \quad \text{for } \theta \in [-\pi, \pi], \quad (1)$$

and

$$\frac{1}{2\pi} \int_{-\pi}^{\pi} P(\theta) e^{-ik\theta} d\theta = c_k, \quad k = 0, 1, \dots, N. \quad (2)$$

Note that the considered problem (1)–(2) may be unsolvable for an arbitrary sequence of the values c_k if we strictly follow conditions (2). To become solvable, this problem has to be regularized.

There are two ways to attach a meaning to the problem (1)–(2). The first way is to replace conditions (2) by approximate relations. In this case the problem arises of choosing a good approximate relation. Another way to attach a meaning to the problem (1)–(2) is to relax the condition (1) and replace it by $P(\theta) \geq -\mu$, for $\theta \in [-\pi, \pi]$, where μ is a positive value. Then, the shifted spectral estimation $P_\mu(\theta) = P(\theta) + \mu$ will be nonnegative and problem transforms to problem (1)–(2) with modified autocorrelation sequence $c_k + \mu\delta_{k0}$, $k = 0, 1, \dots, N$, where δ_{k0} is the Kroneker symbol.

It is relevant to remark that the problem for shifted function $P_\mu(\theta)$ is not solvable for arbitrary positive value μ . However, we can always make the problem solvable by choosing a sufficiently large value μ .

The appearing item $\mu\delta_{k0}$ can be explained in a different way. First of all, the measurement data really may have a white noise with dispersion characteristic μ . Besides, by having added a component $\mu\delta_{k0}$ to regular autocorrelation coefficients c_k we imply an obvious method to impart regularity to the considered problem. In this way the value μ is a regularization parameter. Obviously, the regularized problem is equivalent to initial spectral density estimation problem (1)–(2) for new autocorrelation sequence $c_k + \mu\delta_{k0}$, $k = 0, 1, \dots, N$. Therefore, below we consider the spectral density estimation problem (1)–(2) with the regularization parameter μ , whenever the initial spectral density estimation

problem (1)–(2) for sequence c_k , $k = 0, 1, \dots, N$ is unsolvable.

2.2. Extrapolation of autocorrelation sequence

Let us now assume, that a solution of the spectral density estimation problem (1)–(2) is known. Then we may calculate the unknown terms of the autocorrelation sequence, i.e., c_k for all $k \geq N$ and so to extrapolate the autocorrelation sequence. The inverse is also true, i.e., if we have found an extrapolated autocorrelation sequence \hat{c}_k , $k = 0, 1, \dots$ such that its $N + 1$ first terms are equal to the known values of the autocorrelation sequence, i.e., the values

$$\hat{c}_k = c_k, \quad \text{for } k = 0, 1, \dots, N,$$

then the spectral estimate can be defined by means of the inverse Fourier transform

$$\hat{P}(\theta) = \sum_{k=-\infty}^{\infty} \hat{c}_k e^{ik\theta}, \quad (3)$$

where $\hat{c}_{-k} = \bar{\hat{c}}_k$ for all integers k .

Let us note, that the extrapolated autocorrelation sequence \hat{c}_k can be chosen arbitrary provided that the function $\hat{P}(\theta)$ is nonnegative. The last condition gives us a restriction for the possible extrapolations of the autocorrelation sequence c_k , $k = 0, 1, \dots, N$. Namely the autocorrelation sequence c_k , $k = 0, 1, \dots, N$ and the extrapolated autocorrelation sequences $\{\hat{c}_k\}_{k=0}^{\infty}$ have to be positive-definite [6, 7]. The set of all spectral estimations written in form (3) with an arbitrary positive definite extrapolated sequence \hat{c}_k , $k = 0, 1, 2, \dots$ forms the Carateodory class of function [8]. The Carateodory class is closely associated with the trigonometric moment problem [6], which plays an important part for the description of all solutions of the spectral density estimation problem.

2.3. The trigonometric moment problem

The trigonometric moment problem consists of a collection of complex numbers

$$c_k = \frac{1}{2\pi} \int_{-\pi}^{\pi} P(\theta) e^{ik\theta} d\theta, \quad k = 0, 1, \dots, N, \quad (4)$$

where $P(\theta)$ is an unknown positive function of θ . Assuming that the moments c_k , $k = 0, 1, \dots, N$ of $P(\theta)$ are exactly known, the problem is to determine the function $P(\theta)$. Let us note, not any set of numbers c_k , $k = 0, 1, \dots, N$ can be the moments of nonnegative

function, i.e., the trigonometric moment problem for an arbitrary sequence of moments c_k , $k = 0, 1, \dots, N$ can be unsolvable. We will assume that the Toeplitz determinants $\Delta_n = \det \|c_{n-k}\|$ are nonzero for all integer $n = 0, 1, \dots, N$.

Then there exists the system $\{P_n(z)\}$ of polynomials of the first type and the system $\{P_n^*(z)\}$ of polynomials of the second type orthogonal with respect to the unknown measure $P(\theta)$, which correspond to given moment sequence $\{c_k\}_{k=0}^N$ [6]. The monic polynomials $\{P_n(z)\}$ satisfy the recurrence relations for the orthogonal sets of polynomials:

$$P_{n+1}(z) = zP_n(z) + b_{n+1}P_n^*(z), \quad (5)$$

where $R^*(z) \stackrel{\text{def}}{=} z^k \overline{R}(1/z)$ for any polynomial $R(z)$ of degree k ; b_k are some constants for which formal analytic relations in determinant form can be obtained.

The following criterion of solvability of the moment problem (4) holds [9]:

Theorem 1 *The trigonometric moment problem (4) is solvable if and only if the inequalities*

$$|a_k| < 1, \quad k = 0, 1, \dots, N,$$

hold, where $\{a_k\}_{k=0}^N$ are the coefficients of the recurrence relation of polynomials orthogonal with respect to the moment sequences $\{c_k\}_{k=0}^N$.

To attach this theorem a constructive mean, a recurrence algorithms, for example, a Levinson algorithm has to be used to calculate the coefficients a_k of the recurrence relation for orthogonal polynomials [9].

Let us now assume that the necessary conditions of solvability of the trigonometric moment problem are true. Then all functions $P(\theta)$, for which the relation (4) is fulfilled for all $k = 0, 1, \dots, N$, can be described by means of the linear-fractional transformation [6].

Theorem 2 *Let $P_N(z)$ and $Q_N(z)$ be the monic polynomials of first and second type orthogonal with respect to given moment sequence $\{c_k\}_{k=0}^N$. Let the moment problem (4) be indeterminate. Then all solutions of the moment problem (4) can be described by means of the linear-fractional transformation*

$$P_\varepsilon(z) = \frac{c_0}{h_n} \cdot \operatorname{Re} \frac{zQ_N(z)\varepsilon(z) + Q_N^*(z)}{zP_N(z)\varepsilon(z) - P_N^*(z)}, \quad z = e^{i\theta} \quad (6)$$

of the function $\varepsilon(z) \in B$, where B is a class of functions holomorphic in C and bounded there in modulus by 1; $P_n^(z) = z^n \overline{P_n}(1/z)$, $Q_n^*(z) = z^n \overline{Q_n}(1/z)$, $h_n = \frac{\Delta_n}{\Delta_{n-1}}$.*

Due to Theorem 2 any solution $P(\theta)$ of the moment problem can be expressed by means of the linear-fractional transformation (6) with the holomorphic function $\varepsilon(z)$ corresponding to this solution.

Using the properties of the orthogonal polynomials [6] it is easy to transform (6) to form

$$P_\varepsilon(z) = \frac{1 - |\varepsilon(z)|^2}{|zP_N(z)\varepsilon(z) - P_N^*(z)|^2}, \quad z = e^{i\theta}. \quad (7)$$

3. Spectral estimator's family

In this section we consider the spectral estimation problem as a trigonometric moment problem.

As it follows from the previous section any solution of the spectral estimation problem (1)–(2) for the regularized sequence $c_k + \mu\delta_{k0}$, $k = 0, 1, \dots, N$ can be represented in form (7) where $\varepsilon(z)$ is a parametrization function corresponding to this spectral estimate, $P_N(z)$ is the polynomial with the coefficients satisfying to the Yule-Walker system and $P_N^*(z)$ is a polynomial conjugate to $P_N(z)$.

Using representation (7) and an effective algorithm for calculation of the orthogonal polynomial $P_N(z)$ and its conjugate by the given autocorrelation values one may obtain different spectral estimations. Obviously, the form and performance of a concrete spectral estimator depend on the choice of the parametrization function $\varepsilon(z)$. Using an appropriate parametrization function, the known spectral estimation can be obtained. For example, in the special case where $\varepsilon(z) \equiv 0$ relation (7) is simplified and passed to Burg's maximum entropy spectral estimation

$$P_{ME}(\theta) = |P_N(e^{i\theta})|^{-2},$$

where $P_N(z)$ is the polynomial with the coefficients satisfying to Yule-Walker system.

Another example is the maximum entropy solution of spectral density estimation problem with *a priori* information about spectrum [5, 10], where the aim of spectral estimation is to find the function which agrees with the set of the known values of autocorrelation function and given *a priori* information. In view of the given *a priori* information, the original spectral estimation problem reduces to spectral estimation problem with gaps in spectrum [10]. The spectral estimation with desired properties, can be found using relation (7). However, to find the solution of this spectral estimation problem, we have to choose the parametrization function $\varepsilon(z)$.

The algorithm choosing the parametrization function $\varepsilon(z)$ to construct the maximum entropy solution of the spectral estimation problem with *a priori* information about the spectrum can be found in [5, 10].

Let us now explain the way of choosing of the parametrization function $\varepsilon(z)$ to get the linear spectral estimator.

Obviously, any linear spectral estimate can be represented as a weight Fourier transform from the known correlation coefficients c_k

$$P(z) = 2\Re \sum_{k=0}^N \rho_k c_k z^k, \quad z = e^{i\theta} \quad (8)$$

where ρ_k is the weight coefficients, which are determined by the chosen windowing function. In the particular case $\rho_k = 0$ for all $k = 0, 1, \dots, N$ the relation (8) transforms to ordinary Fourier spectral estimate.

From relations (6) and (8) we have

$$\varepsilon(z) = \frac{A_{2N}(z)}{zB_{2N}(z)}, \quad z = e^{i\theta}, \quad (9)$$

where

$$A_{2N}(z) = \frac{h_N}{c_0} P_N^*(z) \sum_{k=0}^N c_k \rho_k z^k + Q_N^*(z)$$

and

$$B_{2N}(z) = \frac{h_N}{c_0} P_N(z) \sum_{k=0}^N c_k \rho_k z^k - Q_N(z)$$

are polynomials of power $2N$. The coefficients of this polynomials can be easily expressed through the initial correlation coefficients c_k and the given weights ρ_k .

From relation (9) it follows that the parametrization function ε is determined by the autocorrelation coefficients c_k and windowing function in unique way. Using varies windowing functions one can get any known linear spectral estimate. Thus, relations (7) and (9) give us a description of a class of linear spectral estimates by means of linear fractional representation.

Conclusion

We have considered a novel approach to the spectral density estimation problem based on the moment method technique. Using this approach all possible extrapolations of the autocorrelation function which are in agreement with a set of known values were found. A wide spectral estimator's family has been obtained in terms of polynomials orthogonal with respect to a given autocorrelation sequence.

1. REFERENCES

- [1] R.B. Blackman and J.W. Tukey. *The measurement of power spectra from the point of view of communications engineering*. Dover, New York, 1959.
- [2] J.P. Burg. Maximum entropy spectral analysis. In *Proc. 37th. Meeting Soc. Exploration Geophysicists*, Oklahoma City, OK, 1967.
- [3] J. Capon. *Nonlinear Methods of Spectral Analysis*, Ed.S. Haykin, volume 34 of *Topics in Applied Physics*, chapter Maximum Likelihood Spectral Estimation, pages 155–179. Springer-Verlag, 1983.
- [4] G.M. Jenkins and D.G. Watts. *Spectral Analysis and its Applications*. Holden-Day, San Francisco, 1969.
- [5] R. Ugrinovskiy. Maximum entropy algorithm for spectral estimation problem with a priori information. *J. Math. Phys.*, 35:4372, 1994.
- [6] N.I. Achieser. *The Classical Moment Problem and Some Related Questions in Analysis*. Oliver & Boyd, Edinburgh, 1965.
- [7] H.J. Landau. Maximum entropy and the moment problem. *Bulletin of the American Mathematical Society*, 16:47–77, 1987.
- [8] C. Carathéodory. Über den variabilitätsbereich der fourierschen konstanten von positiven harmonischen funktionen. *Rend. Palermo*, 32:193–217, 1911.
- [9] S.A. Korzh, I.E. Ovčarenko, and R.A. Ugrinovskiy. Chebyshev recursion — some analytical, computational and applied aspects. *Ukrainskii Matematicheskii Zhurnal*, 45:625–646, 1993. (English translation in: *Ukrainian Mathematical Journal*, 1993, 45:684–705 (1994)).
- [10] R. Ugrinovskiy. Maximum entropy algorithm for spectral estimation problem with gaps. In *ICASSP'94: Proc. Int. Conf. Acoust. Speech Sign. Proc.*, volume IV, pages 453–456, Adelaide, 19–22 April 1994.
- [11] N. Levinson. The wiener rms (root-mean-square) error criterion in filter design and prediction. *J. Math. Physics*, 25:261–278, 1947.

THE PRACTICAL DESIGN OF $\Sigma\Delta$ DATA CONVERTERS

Paul F. Ferguson, Jr.

Analog Devices
804 Woburn Street
Wilmington, Massachusetts 01887
Paul.Ferguson@analog.com

ABSTRACT

This tutorial-style talk will focus on the practical side of designing $\Sigma\Delta$ data converters. Topics to be discussed include an introduction to $\Sigma\Delta$ conversion, a comparison with other converter architectures, a discussion of the choice of circuit types, the design of circuit blocks, board level considerations, simulation and testing, and debugging of these converters.

1. INTRODUCTION AND MOTIVATION

There have been many papers published on $\Sigma\Delta$ conversion, most of which have focused on theory and architectural design. Some papers have also been published on particular IC implementations of these designs. There have been very few publications dealing with the practical implementation of these converters, discussing the wide variety of tradeoffs involved. This tutorial attempts to fill this need by discussing these converters from a practical point of view.

2. THEORY OF $\Sigma\Delta$ CONVERSION

In this section of the tutorial, the theory of quantization and noise shaping will be discussed, followed by time- and frequency-domain views of these loops. Considerations for the design of higher order loops will also be presented.

3. $\Sigma\Delta$ VS. TRADITIONAL CONVERSION

This section of the tutorial will compare $\Sigma\Delta$ conversion with more traditional approaches such as successive approximation and flash conversion. The comparison will focus on the issues of non-idealities and applications, and will include a demonstration of the effects of differential non-linearity in an audio recording.

This work was completed with much help from Robert W. Adams of Analog Devices.

4. $\Sigma\Delta$ A/D CONVERTER IMPLEMENTATION

This section will discuss the implementation of $\Sigma\Delta$ analog-to-digital converters. The discussion will include:

1. Design of the loop filter.
 - (a) Continuous- vs. discrete-time filtering.
 - (b) Breadboarding.
 - (c) Switched-capacitor implementation.
 - (d) Differential vs. single-ended implementation.
 - (e) Noise and error tolerance in the loop.
2. Opamp design considerations (with examples).
3. Integrator design considerations.
4. One-bit DAC design.
5. Comparator design.

5. INTERFACING TO THE $\Sigma\Delta$ CONVERTER

This section will present considerations in board-level design around a $\Sigma\Delta$ analog-to-digital converter. Discussion will focus on driving switched-capacitor signal and reference inputs and avoiding analog/digital interference.

6. SIMULATION, TESTING AND DEBUGGING A $\Sigma\Delta$ CONVERTER

This final section will explore the tradeoffs in the simulation, test, and IC debug phases of the converter design. Again, the focus will be on the analog-to-digital converter with obvious extension to the digital-to-analog converter.

ACTIVE GRIDS FOR QUASI-OPTICAL POWER COMBINING

David Rutledge, Jung-Chih Chiao, Michael DeLisio, Jeff Liu

Department of Electrical Engineering, Caltech, Pasadena, CA 91125

I. INTRODUCTION

Active grids are periodic structures loaded with transistors or diodes that interact with electromagnetic beams. These new quasi-optical components may make possible a new generation of low-cost, high-power solid-state millimeter-wave communications, broadcast, and radar systems. Quasi-optical power combining allows the output powers from large numbers of individual transistors and diodes to be combined in free space without transmission-line losses. These components can often be made as planar structures that are suitable for large-scale monolithic integration. This should allow these systems to have low cost. Often these devices are multi-mode devices that work with beams at different angles, or even with several beams simultaneously. This should make it possible to use these components in electronically-scanned systems. The devices can also tolerate high failure rates—a 10% transistor failure rate may only reduce the gain by 1 dB. This could give advantages in increasing the fabrication yield to lower the cost, or enabling the construction of ultra-reliable systems for space applications, or allowing a device to survive partial destruction in military use. These circuits are analyzed by equivalent waveguide circuits. The diameter of the equivalent waveguide is determined by the period of the structure, which is fixed by photolithography, rather than by fabrication of a metal waveguide. This makes it possible to make grids for the terahertz frequency range.

A variety of grids have been demonstrated, including detectors, phase shifters, multipliers, oscillators, and more recently, amplifiers and switches. In these grids, the power is proportional to the area, while the circuit impedances are determined by the dimensions of the unit cell. This allows great design flexibility. One can achieve high power and high efficiency simultaneously, or large dynamic range and low noise at the same time. I will discuss results for several recent grids. The first is a doubler with an output power of $330\ \mu\text{W}$ at 1 THz. The second is a 10×10 pHEMT hybrid grid amplifier with a 3-dB noise figure and 3.7-W output at 10 GHz. Finally I will discuss current results on monolithic grid amplifiers for millimeter wavelengths.

II. MILLIMETER-WAVES AND QUASI-OPTICS

This is an exciting time for millimeter-wave systems. For many years the major applications have been in military radar and radiometry. Millimeter waves are of special interest to the military, because millimeter-wave systems offer better resolution and ground-clutter rejection than microwave systems, and better fog and smoke penetration than infrared systems. More recently, commercial applications are becoming important. The FCC is considering a variety of allocations up to 140 GHz, and at 28-GHz television distribution systems are being established. Japanese companies are building 60-GHz computer networks. In Europe, a large number of millimeter-wave communications links have been established at frequencies between 31 GHz and 65 GHz [1]. Here in the United States, the Millitech Corporation has made excellent progress in passive imaging systems for detecting concealed weapons and for landing aircraft in the fog [2]. Several corporations are also making car radars for 76 GHz. At the same time as these new applications have appeared, there has been excellent technology development in monolithic millimeter-wave integrated circuits, much of it sponsored by the MIMIC program. Monolithic amplifiers that operate at 120 GHz have been demonstrated [3], and the Lockheed/Martin Corporation has built a 90-GHz radiometer on a chip [4].

In millimeter-wave research, quasi-optical devices have become a major focus. Quasi-optics research has a long history, going back to the development of beam waveguides by Goubau and Schwering [5], and a quasi-optical oscillator by Wandinger and Nalbandian [6]. Most of the early development was in *passive* devices like beam waveguides, diplexers, and frequency selective surfaces. This technology has reached a sophisticated level, and has seen applications in radio-astronomy telescopes and in NASA's Deep Space Network. Over the last ten years, however, *active* quasi-optical devices have developed. This new era of quasi-optics has attracted the attention of the microwave community, with a special issue of the *IEEE Transactions on Microwave Theory and Techniques* [7], and regular sessions on quasi-optics at the MTT Symposium. In addition, Robert York has written an excellent review paper of work [8].

III. OSCILLATORS

James Mink's 1986 paper on quasi-optical power combining of solid-state millimeter-wave sources [9] is often taken as the starting point for modern quasi-optical devices. Popović *et al.* demonstrated the first large-scale quasi-optical oscillator with a 100-MESFET oscillator grid [10] that produced a half watt at 5 GHz. Kim *et al.* also demonstrated a monolithic Ka-band oscillator grid, showing that these oscillators can be made in monolithic form [11]. However, the output power was small, in the range of 30 mW at 35 GHz, and the pattern was poor, indicating that the oscillation really was a substrate mode oscillation [12]. Hacker *et al.* recently built a grid with a 10-watt output at 10 GHz, showing that the grid approach is capable of substantial power (Figure 1). The next challenge is to produce watt-level outputs from a monolithic millimeter-wave grid oscillator.

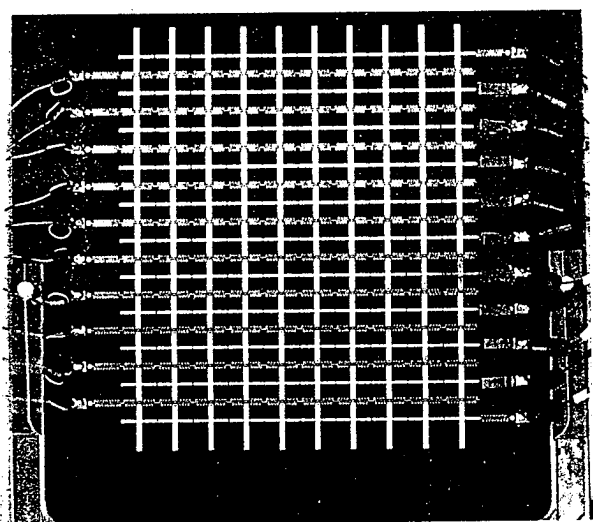


Figure 1. Photograph of the 10-watt grid oscillator demonstrated by Hacker *et al.* [13]. The beam propagates normal to the surface, and is vertically polarized. The horizontal leads are bias connections, and the vertical leads are the radiators.

IV. MULTIPLIERS

The first grid multiplier was demonstrated by Jou *et al.* (Figure 2) [14]. These multiplier grids are periodic structures loaded with planar Schottky diodes. These grids may contain thousands of diodes and can have substantial pulsed power. A grid by Liu *et al.* produced 5 W at 99 GHz [15]. This approach has recently been extended to the terahertz region by Chiao *et al.*, who demonstrated a pulsed output of 330 μ W at 1 THz. However, the efficiency of the terahertz devices is only 10^{-4} , and it will have to be greatly improved before these devices are useful for continuous operation.

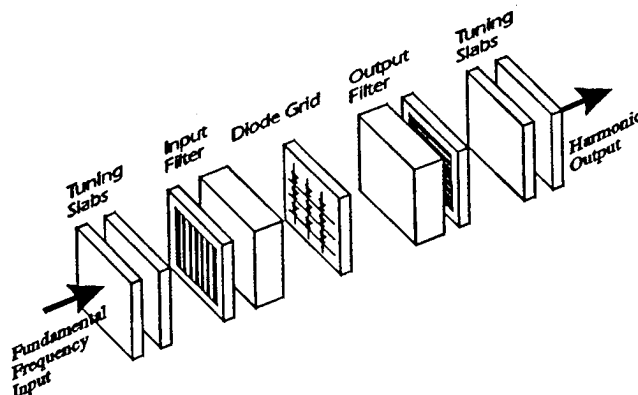


Figure 2. The grid multiplier [14]. The fundamental frequency wave enters on the left as a beam, passes through a filter, and is incident on a diode grid. The grid acts as a non-linear surface, and produces a beam at a harmonic frequency that passes through filters on the right.

V. AMPLIFIERS

In 1991, Moonil Kim *et al.* demonstrated the first grid amplifier [17]. The grid amplifier is an active quasi-optical device that amplifies a beam as it passes through it (Figure 3). The grid had a gain of 11 dB at 3.3 GHz. Our experience has been that it helps in several ways to have the input and output beams cross-polarized. It is easier to stabilize the grid against oscillations. In addition, the polarizers can tune the input and output circuits independently. We have also found that gain measurements are easier if the input and output beams are cross-polarized, because interference is reduced. This first grid was small, with only 25 differential-pairs elements, and the wiring arrangement was complicated, with radiating elements on one side of the board, bias lines on the other, and connecting feedthroughs. DeLisio *et al.* recently extended the original grid amplifier idea to a 100-element X-band HEMT amplifier. They reported 11 dB of gain at 9 GHz, 3-dB noise figure, and 3.7 W of output power [18]. Moreover, it was found that a grid amplifier can amplify beams at angles up to $\pm 30^\circ$, so that it could be used in an electronic beam-steering system.

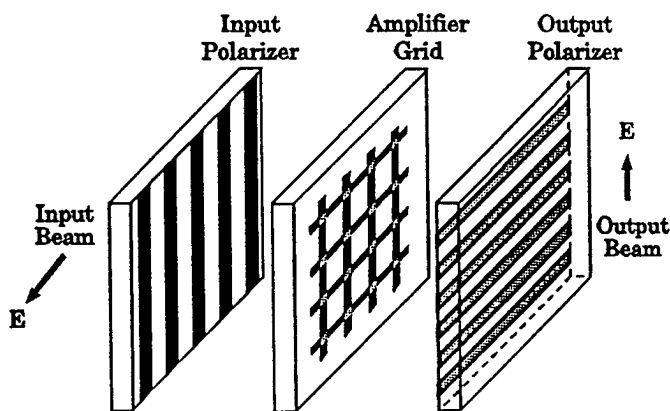


Figure 3. A grid amplifier [18]. In the figure, horizontally polarized power is incident from the left, and passes through the polarizer. The grid amplifier amplifies the beam and radiates it as vertically polarized power, which passes through the output polarizer on the right.

Amir Mortazawi's group has built a spatial amplifier based on the concept of extended resonance, with receiving and transmitting antennas on both sides of the printed circuit board [19]. Professor Mortazawi's design is particularly flexible with respect to input and output polarization. Zoya Popović's group has demonstrated a spatial amplifier with patch antennas on two sides of a printed-circuit board [20]. This approach is particularly flexible in the phasing of the radiating elements, so that the beam can be focused. Robert York's group has built a spatial amplifier with folded slots [8]. An excellent feature of Professor York's grid is that the connecting transmission line is coplanar waveguide, and this allows MIMIC amplifiers to be integrated conveniently.

VI. FUTURE WORK—MONOLITHIC GRID AMPLIFIERS

The goal of much current work is to demonstrate monolithic millimeter-wave quasi-optical amplifiers. Liu *et al.* reported 5 dB gain at 41 GHz from a 6×6 HBT amplifier (Figure 4) [21]. Research in monolithic quasi-optical amplifiers is just beginning, and the field is wide open, with several competing groups. Heat dissipation, high-power, and efficiency are major challenges.

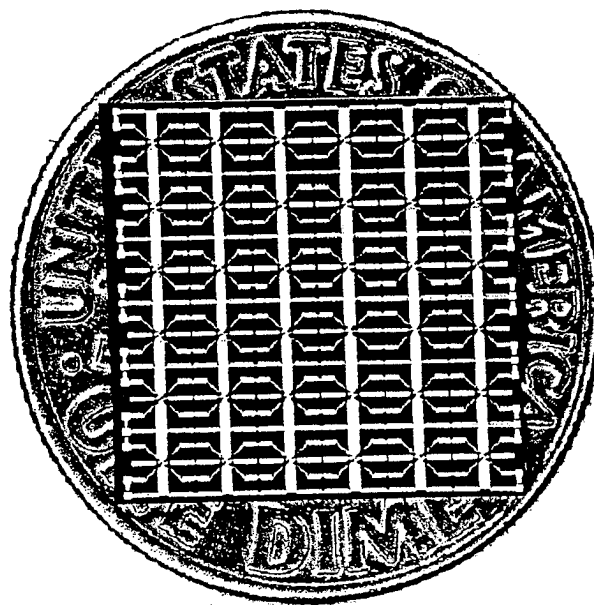


Figure 4. Photograph of a 36-element monolithic grid amplifier compared with a dime [21].

ACKNOWLEDGEMENTS

We appreciate the support of the Army Research Office and the Air Force Material Command/Rome Laboratory.

REFERENCES

- [1] John Burns, "The Application of Millimeter Wave Technology for Personal Communication Networks in the United Kingdom and Europe: A Technical and Regulatory Overview," Int. Microwave Symposium, San Diego CA, May 1994.
- [2] Paul Goldsmith *et al.*, "Focal Plane Imaging Systems for Millimeter Wavelengths," *IEEE Transactions on Microwave Theory and Techniques*, MTT-41 pp. 1664-1675, 1993.
- [3] R. Lai *et al.*, "A Monolithically Integrated 120-GHz InGaAs/InAlAs/InPh HEMT amplifier," *IEEE Microwave and Guided Wave Letters*, 4, pp. 194-195, 1994.
- [4] Tu, D-W. *et al.* "High-gain monolithic pHEMT W-band four stage low noise amplifier," 1994 International Microwave Symposium.
- [5] G. Goubau, F. Schwing, "On the guided propagation of electromagnetic wave-beams," *IRE Transactions Antennas Propagat.*, AP-9, pp. 248-256, 1961.
- [6] L. Wandering and V. Nalbandian, "MM-wave power combiner using quasi-optical techniques," *IEEE Trans. on Microwave Theory and Tech.*, MTT-31, pp. 189-193, 1983.
- [7] James Mink and David Rutledge, co-editors, "Special Issue on Quasi-Optic Techniques," *IEEE Transactions on Microwave Theory and Techniques*, MTT-41, October, 1993.
- [8] Robert W. York, "Quasi-Optical Power Combining Techniques," *SPIE Critical Reviews of Emerging Technologies*, 1994.
- [9] James W. Mink, "Quasi-optical Power Combining of Solid-State Millimeter-Wave Sources," *IEEE Trans. on Microwave Theory and Tech.*, MTT-34, pp. 273-279, 1986.
- [10] Z. B. Popović, R. M. Weikle II, M. Kim, and D. B. Rutledge, "A 100-MESFET Planar Grid Oscillator," *IEEE Trans. on Microwave Theory and Tech.*, MTT-39, pp. 193-200, 1991.
- [11] Moonil Kim, Emilio Sovero, Robert Weikle, Jon Hacker, Michael DeLisio, and David Rutledge, "A 35 GHz HBT monolithic grid oscillator," 17th Int. Conference on Infrared and Millimeter Waves, Pasadena CA, December 1992.
- [12] Donald Griffin, "Monolithic active array limitations due to substrate modes," IEEE Antennas and Propagation Society International Symposium, Newport Beach CA, June 1995, pp.1300-1303.
- [13] Jonathan B. Hacker, Michael P. DeLisio, Moonil Kim, Cheh-Ming Liu, Shi-Jie Li, Scott W. Wedge, and David B. Rutledge, "A 10-Watt X-band Grid Oscillator," International Microwave Symposium, San Diego CA, May 1994, pp. 823-826.
- [14] C. F. Jou, W. W. Lam, H. Z. Chen, K. J. Stolt, N. C. Luhmann, Jr., and D. B. Rutledge, "Millimeter-wave diode-grid frequency doubler," *IEEE Transactions on Microwave Theory and Techniques* 36, pp. 1507-1514, 1988.
- [15] "Monolithic quantum barrier based solid-state device arrays for millimeter wave frequency multiplication," Ph.D. Thesis by Hong-Xia Lantz Liu, UCLA, 1993.
- [16] Jung-Chih Chiao, Andrea Markelz, Yong-jun Li, Jonathan Hacker, Thomas Crowe, James Allen, and David Rutledge, "Terahertz Grid Frequency Doublers," 6th International Symposium on Space Terahertz Technology, Pasadena CA, March, 1995.
- [17] Moonil Kim, James J. Rosenberg, R. Peter Smith, Robert M. Weikle, II, Jonathan B. Hacker, Michael P. DeLisio, and David B. Rutledge, "A Grid Amplifier," *IEEE Microwave and Guided Wave Letters*, MGWL-1 pp. 322-324, November 1991.
- [18] Michael DeLisio, Scott Duncan, Der-Wei Tu, Cheh-Ming Liu, Alina Moussessian, James Rosenberg, and David Rutledge, "Modelling and Performance of a 100-Element pHEMT Grid Amplifier," submitted for publication.
- [19] N. Sheth, T. Ivanov, A. Balasubramanian, and A. Mortazawi, "A Nine HEMT Spatial Amplifier," International Microwave Symposium, San Diego, CA, May 1994, pp. 1239-1242.
- [20] J.S.H. Schoenberg and Z.B. Popović, "Planar Lens Amplifier," International Microwave Symposium, San Diego, CA, May 1994, pp. 429-432.
- [21] Cheh-Ming Liu, Emilio Sovero, and David Rutledge, "40-GHz Monolithic Grid Amplifier," submitted for publication.

TRANSFERRED ELECTRON OSCILLATORS FOR HETERODYNE RECEIVERS

S.H. Jones, J.E. Carlstrom, M.F. Zybura†*

Department of Electrical Engineering, University of Virginia, Charlottesville, VA 22903;

*Caltech, Pasadena, CA; †Litton Solid State, Santa Clara, CA

Millimeter Wave Radiometry and Devices Session

1.0 Introduction

Transferred Electron Oscillators (TEOs) are commonly used for local oscillator (LO) power in Heterodyne receivers. These sources can be used to directly pump mixer circuits up to 160 GHz or to drive varactor frequency multipliers for applications that require a higher frequency LO. The advantages of TEOs over other sources include low noise operation, moderate power (10-50 mW) up to at least 160 GHz, broad band operation, relatively low cost, high reliability, and easy integration with the receiver system. The disadvantage of these oscillators is the mechanical tuning for the frequency and power backshorts. The TEOs described in this presentation are all second-harmonic oscillators to insure reduced load pulling and lower noise than fundamental TEOs. Also, Efficient power generation from fundamental current oscillations is difficult to achieve at frequencies above 100 GHz with short InP TEDs. This report will focus on the theoretical and experimental results for a continuously tunable 115-145 GHz (20-50 mW) low noise source, and some preliminary theoretical and experimental results at 160 GHz.

2.0 Results and Discussion

2.1 Experimental Results

The 115-145 GHz second-harmonic TEO is similar to that described in reference 1. Half-height WR-8 wave guide perpendicularly intersects a similar diameter coaxial cavity. There is an adjustable backshort at one end of the WR-8 waveguide. The packaged Transferred Electron Device [2] is screwed into the waveguide floor and serves as the bottom wall of the coaxial cavity. Bias voltage is supplied to the diode through the coaxial cavity central conductor. A typical bias choke, center pin, and disc resonator connects to the top of the diode and serves as the cavity central conductor. The bias choke forms the top wall of the cavity. The coaxial cavity length is adjusted by mechanically sliding the bias choke up or down over the pin. By adjusting the coaxial frequency backshort the cavity length is varied over 50 mils and the oscillation frequency is smoothly

and continuously adjusted from 115-145 GHz. At the same time, the waveguide backshort is adjusted to optimize the output power. 20-50 mW of output power is achieved over the band, and the cavity operation is extremely reliable and reproducible. The cavity length essentially controls the frequency of oscillation at the fundamental. Since the fundamental (57.5-72.5 GHz) is cutoff by the output waveguide and the waveguide back short section, the fundamental is essentially reactively terminated. This leads to a strong fundamental voltage oscillation that is decoupled from the output waveguide and the waveguide backshort. The strong non-linearity of the diode combined with the large fundamental voltage oscillation creates efficient second harmonic power. The diode impedance at the second harmonic is tuned using the waveguide backshort and power is coupled to the output section. Tuning the second harmonic impedance for peak power has little effect on the fundamental impedance and operating frequency.

2.2 Numerical Simulations

Detailed simulations of the cavity have been completed using HP's High Frequency Structure Simulator. The entire oscillator cavity including the package have been simulated to extract the impedance seen by the diode at the fundamental and second harmonic frequencies (55-145 GHz). These results are used in our harmonic balance/numerical device-simulation code [3] to fully simulate the oscillator behavior. A detailed understanding of the oscillator operation and the tuning characteristics has resulted from these advanced simulation and will be explained.

3.0 References

1. J.E. Carlstrom, R. L. Plambeck, D.D. Thornton, IEEE Trans. MTT, vol. MTT-33, No. 7, July (1985).
2. M.F. Zybura, S.H. Jones, J. E. Carlstrom, J.D. Crowley, Proceedings of the Sixth International Symposium on Space Terahertz Technology, Caltech, (1995).
3. M.F. Zybura, J.R. Jones, S.H. Jones, G. Tait, IEEE Tans. MTT, vol. 43, No. 4, April (1995).

NOVEL HOT-ELECTRON BOLOMETER MIXERS FOR SUBMILLIMETER APPLICATIONS: AN OVERVIEW OF RECENT DEVELOPMENTS

William R. McGrath

Center for Space Microelectronics Technology, Jet Propulsion Laboratory,
California Institute of Technology, Pasadena, CA 91109

1. INTRODUCTION

Recently there has been a resurgence of interest in bolometers as heterodyne mixers at submillimeter wavelengths. This is due primarily to two new and innovative concepts [1,2] which result in bolometers with response times fast enough to allow for intermediate frequencies (IF) of 1 GHz - 10 GHz, as well as low mixer noise temperatures. These IF's are high enough for practical spectroscopy applications and thus these bolometers need to be seriously considered as heterodyne sensors. In this paper I will review briefly the basics of bolometer mixers. Then an overview will be given of the basic operation of the new high speed bolometers, along with a few recent results which demonstrate the performance. Finally, the role these sensors may be expected to fulfill will be discussed. I should emphasize that this paper is meant to provide a brief introduction to these new bolometer mixers, and reference will be made to the recent literature for the interested reader who wishes to delve more deeply into the details. This is not a review article, but rather an overview of recent developments, so no attempt is made to give a complete listing of results and publications.

2. BOLOMETER MIXERS

Bolometers have been used occasionally as heterodyne mixers primarily because of the advantages of high frequency operation (bolometers can be operated at millimeter through submillimeter wavelengths) as well as high sensitivity with near-quantum limited noise. Additionally, bolometers are simple square-law or total-power detectors. There is no instantaneous response at the rf as with an electronic mixer, such as a Schottky diode or SIS tunnel junction. There is also no harmonic response. The principle disadvantage of the bolometer mixer is the slow thermal response time. This limits the IF to low values, usually of order MHz. In general this is too low to be useful for many remote-sensing applications involving molecular line spectroscopy such as radioastronomy, atmospheric chemistry, and planetary science.

The limitation placed on the IF by the thermal response time can be understood by considering the basic operation of a bolometer mixer. The two basic elements of a

bolometer are shown in figure 1. There is an element which absorbs the incident rf power; typically an absorbing film. The absorber has a thermal heat capacity C , and as it absorbs power its temperature T increases. The absorber is connected to a thermal bath temperature T_{bath} by a thermal conductance G . The thermal response time is given by $\tau_{\text{th}} = C / G$, and represents the characteristic time over which the temperature of the bolometer can change for a sudden change in incident rf power.

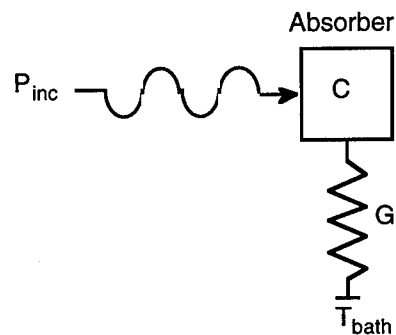


Fig. 1: Basic elements of a bolometer. C is the heat capacity of the absorber, typically a thin film. G is the thermal conductance to the bath temperature. P_{inc} is the incident rf power.

To operate the bolometer in a heterodyne mode, a local oscillator voltage, V_{LO} , at frequency ω_{LO} and a signal voltage, V_s , at frequency ω_s are applied to the absorber, which for simplicity we take to be a thin film of resistance R_n . The resulting dissipated power is:

$$P(t) = P_{\text{LO}} + P_s + 2(P_{\text{LO}}P_s)^{1/2} \cos(\omega_{\text{IF}} t) \quad (1)$$

where $\omega_{\text{IF}} = \omega_{\text{LO}} - \omega_s$ is the IF frequency, and $P_{\text{LO}} = (V_{\text{LO}}^2 / 2R_n)$ and $P_s = (V_s^2 / 2R_n)$ are the LO power and signal power respectively dissipated in the bolometer. The bolometer is not fast enough to follow the rf, so the power dissipated at these frequencies is the time averaged value. However, if the IF is low enough, the bolometer can follow this variation, so there can be a time dependent term at this frequency. The *Voltage Responsivity*, S , of the bolometer [3] gives the change in voltage across the bolometer for a change in absorbed power, and hence can be used to estimate the IF voltage amplitude:

$$V_{IF} = S \cdot 2(P_{LO}P_s)^{1/2} \quad (2)$$

The responsivity is given by:

$$S = I (dR / dT) / [G \cdot (1 + \omega_{IF}^2 \tau_{th}^2)^{1/2}] \quad (3)$$

where I is the bias current through the resistive film, and dR/dT is the derivative of film resistance with temperature. Thus for low enough IF, that is $\omega_{IF}^2 \tau_{th}^2 < 1$, the bolometer can follow the IF power swing; but for $\omega_{IF}^2 \tau_{th}^2 > 1$, the IF voltage will decrease and hence the conversion efficiency of the mixer will decrease. As mentioned above, τ_{th} for many conventional bolometers is large enough that the IF is limited to undesirably low values. However, the two new bolometers discussed below address this issue.

3. NEW APPROACHES

Recently, two new approaches [1,2] have been proposed for bolometers with very short thermal response times and hence a high IF rolloff frequency. Both bolometers utilize the resistive transition in a superconductive thin film which results in a large dR/dT and hence high responsivity. What is new however, is that these devices make use of very thin films: about 10 nm for Nb or NbN. Such thin films have a very high scattering rate due to surface effects and hence a short electron mean free path ℓ , which is about 1 nm - 10 nm. In these films, it is found that the electron-electron interaction is enhanced, resulting in a short electron-electron interaction time: $\tau_{ee} \propto \ell$; and the electron-phonon interaction is weakened: $\tau_{ep} \propto \ell^{-1}$ [2]. Hence the electrons can reach thermal equilibrium at a temperature different from the lattice temperature. Thus when absorbing rf power, the electrons can warm up relative to the lattice temperature. The electrical resistance in the film depends on the electron temperature and such a device is known as a hot-electron bolometer. Since only the electrons are heated, the heat capacity C can be very small, especially for a submicron-sized device. In addition, the hot-electron bolometer mixers discussed below employ novel mechanisms for cooling the electrons which results in a high thermal conductance and hence an overall short thermal relaxation time.

Before describing the details of the bolometers, it is useful to list the important advantages of these novel devices:

- 1) The thermal response time is very fast: ≈ 10 's ps. Thus IF's of 1 GHz - 10 GHz can be achieved.
- 2) These bolometer mixers should operate well to very high frequency: several THz. There is no energy gap limitation as in an SIS mixer. In fact, rf power is absorbed more uniformly above the energy gap frequency.

- 3) The mixer noise temperature is very low: near-quantum limited.
- 4) Very low LO power is required: nW's - μ W's. This is comparable to the requirements for SIS mixers and is an important issue at high submillimeter wave frequencies where LO power is difficult to generate.
- 5) The rf impedance of the device is essentially resistive and is determined by the geometry of the film; that is, the number of squares in a small strip. Typical values range from 20 Ω to 200 Ω . This greatly simplifies the rf circuit design. Unlike a Schottky diode or SIS tunnel junction, there are no parasitic reactances to tune out. The real rf resistance of the bolometer should be independent of frequency from about the energy gap frequency up to a frequency corresponding to the inverse electron-electron elastic scattering time (about 10^{-15} sec) which is approximately 160 THz [1].
- 6) In addition, these devices make use of existing materials and fabrication techniques: Nb, NbN, YBCO; micron-scale photolithography, and/or submicron E-beam lithography.

4. DIFFUSION-COOLED HOT-ELECTRON BOLOMETER MIXER

Figure 2 shows the basic geometry of this bolometer mixer which was proposed by D. Prober in 1993 [1]. The unique feature of this device is that it uses the rapid diffusion of hot electrons out of a submicron length strip (or microbridge) of superconductor into normal metal contacts as the cooling mechanism, or thermal conductance. In order for diffusion to dominate, over electron-phonon interactions, as the cooling mechanism, it is necessary for the microbridge to be short. The appropriate length L can be estimated [1] from the expression:

$$L \approx 2 (D \tau_{ee})^{1/2} \quad (4)$$

where D is the diffusion constant, and τ_{ee} is the electron-electron inelastic ("energy sharing") interaction time. Basically when an electron absorbs energy from an rf photon, it shares its energy in a time τ_{ee} and also diffuses a distance $L/2$. A hot electron in the middle of the bridge can thus go $L/2$ left or right. At that point, it encounters the normal metal contact which serves as a heat sink. These pads at the end of the microbridge must be normal metal since Andreev reflection [4] at the energy gap in a thick superconducting film would trap the hot-electrons inside the microbridge and substantially slow the response of the device. The electron-electron interaction time can be estimated from [5]:

$$\tau_{ee} \approx (10^8 R_s T_c)^{-1} \quad (5)$$

where R_s is the surface resistance and T_c is the superconductive transition temperature of the thin film. For the very thin (dirty limit) film used here, R_s is larger and T_c is smaller than the bulk values. For a 10 nm Nb film for example, $R_s \approx 20 \Omega/\text{sq}$, $T_c \approx 5 \text{ K}$, and the width of the transition is $\Delta T_c \approx 0.5 \text{ K}$. Substituting these values into eqn (4) and eqn (5), yields a length $L \approx 0.2 \mu\text{m}$. The microbridge can be somewhat longer (with a corresponding increase in τ_{th}), but should be less than $2(D\tau_{ep})^{1/2}$ where τ_{ep} is the electron-phonon interaction time. For this length and longer the electrons will remain in the bridge long enough to produce phonons which can alter the mode of operation (see section 5).

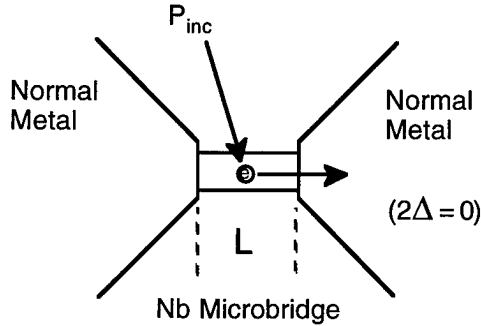


Fig. 2: Basic geometry of the diffusion-cooled hot-electron bolometer mixer.

The thermal response time can be calculated from the usual expression:

$$\tau_{th} = C / G \quad (6)$$

The thermal capacitance is given by the electron specific heat [6]:

$$C = \gamma T V \quad (7)$$

where $\gamma = 700 \text{ J/K}^2\text{m}^3$ for Nb, T is the electron temperature (which is always about T_c in a transition edge device), and V is the device volume. The thermal conductance G is given by the Wiedemann-Franz Law [6]. This law states that the ratio of thermal conductance to electrical conductance is proportional to temperature, if the electrons carry both the electrical current and the thermal current, which is the case for the diffusion-cooled microbridge. Thus:

$$G = (\pi^2/3) (k_B / q_e)^2 (T / R_{eff}) \quad (8)$$

where k_B is Boltzman's constant, q_e is the charge on the electron, T is the temperature ($\approx T_c$) and R_{eff} is the effective electrical resistance of the microbridge: $R_{eff} \approx R_n / 12$ [1]. R_n is the DC resistance of the microbridge for T just above T_c . The factor 1/12 arises because heat flows symmetrically out both ends of the microbridge.

For an actual bridge [7] with dimensions width = $0.14 \mu\text{m}$, length = $0.28 \mu\text{m}$, thickness = 10 nm and $R_n = 30 \Omega$, the estimated response time is 30 psec. The 3 dB IF rolloff frequency for the mixer conversion efficiency is then given by:

$$f_{rolloff} = (2 \cdot \pi \cdot \tau_{th})^{-1} \quad (9)$$

which is about 5 GHz in this case. However, due to self-heating effects [3] (and to a lesser extent by IF impedance mismatch effects [8]) the thermal conductance is reduced to a lower effective value:

$$G_{eff} = G (1 - A) \quad (10)$$

where typically $0.1 < A < 0.9$ for thermally stable operation. Thus the value of $f_{rolloff}$ can actually be in the range of about 2-5 GHz, which allows for IF's commonly used in heterodyne instruments.

Now we will estimate the mixer conversion efficiency η , the double-sideband receiver noise temperature $T_R(\text{DSB})$, and the LO power P_{LO} . The conversion efficiency for a bolometer mixer was originally worked out in detail by Arams et al [9] in 1966 and recently discussed in connection with these new hot-electron bolometers [8]. For convenience, we will follow the simplified approach given by Prober [1]. The conversion can be estimated using the voltage responsivity of the bolometer and the IF power amplitude. The result is:

$$\eta = P_{IF} / P_{cr} = [I^2 (dR/dT)^2 / G^2] \cdot [P_{LO} / 2R] \quad (11)$$

(note: this expression is valid for $\omega_{IF} \tau_{th} \ll 1$). For equal DC power ($P_{DC} = I^2 R$) and LO power dissipated in the bolometer, $\eta(\text{SSB}) = 1/8 = -9 \text{ dB}$ (note that $\eta > 0 \text{ dB}$ may be possible under some conditions [8]) It can be shown that the conversion efficiency in this case is independent of L , the length of the microbridge [1]. However, the response time $\tau_{th} \propto L^2$, thus $f_{rolloff} \propto 1/L^2$. Hence, as expected for a device that relies on diffusion out the ends, shorter is better for high speed. However, there is no sacrifice in conversion efficiency. While decreasing L will increase G and hence reduce the bolometric responsivity, in the heterodyne mode this can be compensated by increasing the LO power. Thus it is possible to have a bolometer mixer which is both *fast* and *sensitive*.

The best optimization of LO and DC power is a topic of current discussion [1,10]. In practice, the bolometer is thermally biased at a temperature somewhat below T_c , then a combination of DC and LO power is used to heat the electrons up to T_c . Prober [1] suggests setting $T_{bath} \approx T_c - \Delta T_c/2$ (that is, just below the transition width) and then applying enough LO to heat the electrons up by $\Delta T_c/4$ along with an equal amount of DC power. The LO power can then be readily approximated by $P_{LO} \approx \Delta T_c G / 4$ which is 4 nW for a 50Ω microbridge with $\Delta T_c = 0.5 \text{ K}$. Karasik and

Elantev [10] however suggest that the bath temperature should be made low and then the LO power should heat the electrons from T_{bath} up to $T_c - \Delta T_c/2$ and the DC power should then raise the temperature by $\Delta T_c/2$ in order to reach T_c . This implies an LO power of ≈ 70 nW for the same microbridge with $T_{\text{bath}} = 2.5$ K and $T_c = 5$ K. Since both the conversion efficiency and mixer noise improve with increasing LO power [10], the higher value may be desirable. In either case, the LO power requirement is extremely low; equal or less than that required for a submillimeter wave SIS mixer.

It is currently accepted that the main contributions to the noise in a bolometer mixer are due to Johnson noise and electron temperature fluctuation noise [11]. The latter being dominant. The Johnson noise temperature is, of course, T_c and arises from the film resistance at the transition temperature. The electron temperature fluctuation noise arises from the thermodynamic energy fluctuations in an electron gas at an average thermodynamic temperature T_c . The RMS electron temperature fluctuation can be expressed as [8]:

$$\Delta T_c = 4 k_B T^2 / G \quad (12)$$

This yields a DSB mixer input noise temperature of $T_c^2 G / P_{\text{LO}}$ according to Karasik and Elantev [10]. For the LO power level considered by Prober, this reduces to $T_c^2 / \Delta T_c$. The resulting DSB receiver noise temperature can be expressed as [1]:

$$T_R(\text{DSB}) = [(T_c^2 / \Delta T_c) + T_c + T_{\text{IF}}] / \eta \quad (13)$$

where T_{IF} is the IF amplifier system noise temperature. Thus for $T_c = 5$ K, $\Delta T_c = 0.5$ K, $T_{\text{IF}} = 4$ K, and $\eta(\text{DSB}) = -7$ dB (ie: 6 dB intrinsic mixer conversion loss and 1 dB of receiver optical path loss), we get $T_R(\text{DSB}) = 295$ K. However, reducing T_c just 1 K (a slightly thinner film) yields $T_R(\text{DSB}) = 200$ K. This performance becomes competitive with current state-of-the-art SIS receivers near frequencies of 500 GHz - 600 GHz. However, for the bolometer mixer there is no inherent frequency dependence of the performance above the energy gap frequency (except of course for the linear frequency dependence set by the quantum limit [12]). The same noise temperature, 200 K, should be possible at 0.5 THz or several THz (mechanisms which may ultimately limit the high frequency performance will be briefly discussed below).

To date, the diffusion-cooled hot-electron bolometer mixer has been rapidly developed by the Jet Propulsion Laboratory in collaboration with Yale University [7,13,14] (no other groups have yet reported results on this new device). A Nb device with dimensions 0.15 μm wide, 0.28 μm long, and 10 nm thick was tested in a waveguide mixer mount in a receiver at an LO frequency of 530 GHz (see references 7 and 14 for a complete discussion of these results). This LO frequency is well above the gap frequency

of ≈ 400 GHz for this thin Nb film with $T_c \approx 5.3$ K and $\Delta T_c \approx 0.5$ -1 K. The DSB receiver noise temperature is 650 K at an IF of 1.4 GHz. The estimated DSB mixer noise temperature is 560 K and mixer conversion efficiency is about -11 dB. The calculated receiver noise temperature is 570 K - 750 K (depending on the exact choice of ΔT_c from the R-T curve and using $\eta = -11$ dB), and similarly the predicted mixer conversion efficiency is about -9 dB [15]. Thus the calculated values agree well with experiment. The IF rolloff frequency was measured to be about 2 GHz, which represents superior performance for a low-noise bolometer mixer. This performance is comparable to the more mature submillimeter wave SIS receivers. It is thus clear from these results that this device works well as a submillimeter wave heterodyne mixer.

5. ELECTRON-PHONON COOLED HOT-ELECTRON BOLOMETER MIXER

Figure 3 shows the basic geometry of this bolometer which was proposed by E. Gershenzon, et al in 1990 [2]. The basic operation of this bolometer can be understood from fig. 3(b). An incident rf photon imparts its energy to an electron in the film. In a short time τ_{ee} this electron shares its energy with other electrons. The cumulative effect of absorbed rf power and the energy sharing process (ie: the enhanced electron-electron interaction) in these ultra-thin films is to create a hot-electron distribution. Then in a time τ_{ep} a hot electron creates a phonon which then escapes ballistically, for a sufficiently thin film, to the substrate in a short time τ_{ES} . In order for the hot-electron bolometric mechanism to proceed in this manner, there are some constraints which must be met. First $\tau_{ee} \ll \tau_{ep}$ to allow the electrons to heat up from absorbed power. This is usually satisfied for a thin (dirty limit) film at low temperatures $T < 10$ K ($\tau_{ee} \approx 10^{-10}$ sec to 10^{-12} sec) [16]. Next it is important for $\tau_{ES} \ll \tau_{pe}$, where τ_{pe} is the phonon-electron interaction time. That is, the phonons must escape to the substrate before they interact back with other electrons. This requires that the film be very thin since [2,16,17]:

$$\tau_{ES} = 4 d C_e / (v \alpha C_{ph}) \quad (14)$$

where d is the film thickness, C_e and C_{ph} are the electron and phonon specific heats respectively, v is the velocity of sound, and α is the coefficient of transmission of a phonon through the film-substrate interface. The thermal response time of the bolometer can then be written as:

$$\tau_{th} = \tau_{ep} + \tau_{ES} \quad (15)$$

Thus the limiting speed of this type of bolometer is set by τ_{ep} (this limit requires $\tau_{ES} \ll \tau_{ep}$ and thus the films should be thin, the phonon transmission at the substrate interface high, and the thermal conductivity of the substrate should also be high so that it remains a constant temperature bath). For a Nb bolometer, $\tau_{ep} \approx 1$ ns and hence $\text{IF}_{\text{rolloff}} \approx 160$ MHz,

which is higher than most bolometer mixers but still too low for many practical applications. For NbN operated at 7 K - 8 K, $\tau_{ep} \approx 15$ ps and hence $IF_{\text{rolloff}} \approx 10$ GHz. This is of course high enough to be of practical value.

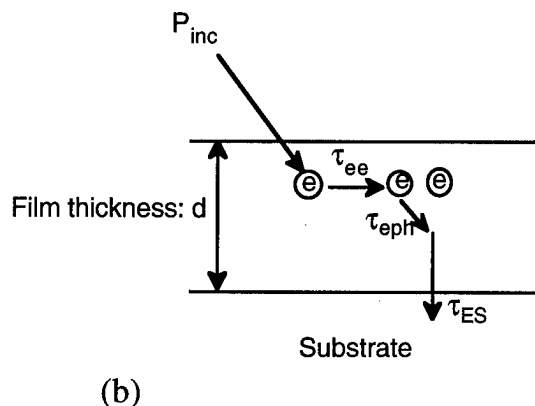
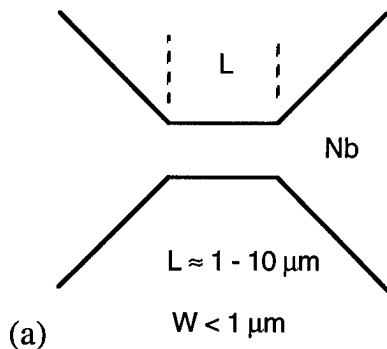


Fig. 3: Basic geometry of electron-phonon cooled bolometer mixer. (a) Top view showing geometry of microbridge. (b) Cross sectional view showing schematically the electron-phonon interactions described in the text.

The LO power requirements can be estimated in the same way as discussed in the previous section except G is now given by the electron-phonon thermal conductance ($G = 4 \times 10^4 \cdot T^3 \cdot V$ for thin Nb films [2], for example). It should be noted that G in this case depends on the volume V of the microbridge and thus it is advantageous to keep the volume small. The width of the microbridge should be less than about $1 \mu\text{m}$ to avoid a backflow of phonons from the substrate [2]. Then for a given film surface resistance R_s the length is chosen to give the appropriate resistance for an rf match to the mixer embedding circuit (waveguide, planar antenna, etc...). A typical size is $1 \mu\text{m} \times 5 \mu\text{m}$. The LO power then required for a Nb bolometer mixer is about 50-70 nW ($T_c = 4$ K and $\Delta T_c = 0.5$ K); and for NbN, $P_{LO} \approx 0.5$ -1 μW ($T_c = 7$ K and $\Delta T_c = 0.5$ K). These are extremely low and therefore very desirable for submillimeter operation.

The mixer noise temperature and conversion efficiency are calculated in the same way as previously discussed. However, the more detailed analysis in [8] suggests that under certain conditions, conversion efficiency greater than unity is possible. Also, as mentioned above, the exact choice of DC and LO power to optimize the mixer is still being theoretically analyzed.

Recent results have shown that the electron-phonon cooled bolometer mixer performs very well. Measurements on a Nb bolometer mixer [8] at an LO frequency of 20 GHz gave conversion efficiencies between -1 dB and -7 dB, an IF rolloff of 80-100 MHz, and an LO power of about 40 nW. These results are in close agreement with expected values. In addition, an NbN bolometer mixer operated in a waveguide mount at 100 GHz [18] has demonstrated an IF rolloff as high as 1.5-2 GHz, and a DSB receiver noise temperature of 450 K. This is extremely good performance, and is suitable for practical low-background spectroscopy applications.

Also, high- T_c yttrium-barium-copper oxide (YBCO) bolometers have been investigated [19-21] at wavelengths of $0.8 \mu\text{m}$ (375 THz), $1.56 \mu\text{m}$ (192 THz), and $10.6 \mu\text{m}$ (28 THz). The goal of these investigations was to demonstrate the high speed hot-electron response and the heterodyne mixing process (no attempt was made to produce a fully optimized mixer at such high frequencies, so the estimated conversion efficiency was low). Heterodyne mixing was clearly demonstrated in thin YBCO films with an IF up to 18 GHz (the limit of the measurement system). Since these bolometers operate at 80-90 K, the phonons play a more significant role which changes the device physics as compared to the low- T_c case (see references 10, 18-20 for a more detailed discussion).

6. DISCUSSION

The recent innovations in transition-edge hot-electron bolometers (micron and submicron sized, thin, dirty films) have led to ultra-fast, sensitive devices which are competitive as heterodyne mixers. Recent measurements have proven the concepts and even shown competitive performance. However, the most complete mixer measurement to date have been mainly below 1 THz (except for the YBCO bolometer mixer tests) where there already exist state-of-the-art SIS receivers with very low noise. These new bolometer mixers will play an important role at frequencies well above 1 THz where SIS and Schottky receivers become either extremely difficult or impossible (ie: above the energy gap frequency of NbN for example) to operate. In addition, the high- T_c bolometer will be useful in applications where sensitivity can be traded off against cooling requirements, as in a space-based mission.

Important development issues must be addressed for each bolometer. The diffusion-cooled bolometer will need

improved submicron definition and alignment of the normal metal contacts. Also, low-resistance normal-to-superconductor contacts are required. For the electron-phonon cooled bolometer, the phonon reflection at the film substrate interface must be minimized. This will be particularly important for materials like NbN (which have a high upper limit to the IF rolloff) which can react strongly with common rf substrates such as quartz, thereby producing a poor interface. In addition, both types of bolometers are resistive at the rf, so a very broadband match, to a planar antenna for example, should be easily achieved. The rf bandwidth can however be so broad that the mixer will be easily saturated. Unlike the common situation for an electronic mixer with reactive parasitics where the goal is to achieve a broadband rf match, these bolometer mixers will probably require bandpass filters at high submillimeter wave frequencies.

Finally, since the likely role for these bolometer mixers will be at very high frequencies, it is important to test as soon as possible the prediction that the performance is independent of frequency. Certain mechanisms may affect the high frequency performance. A high energy rf photon (several THz) will produce a high energy electron in the superconductive film. This hot electron can then either share its energy with other electrons, or break Cooper pairs, or produce hot phonons. In any case, the film will absorb rf power, but if the energy escapes, for example by the hot phonons rapidly leaving the film, before it is shared with the electron gas, then the electrons will not heat as efficiently and the sensitivity of the mixer will decrease. However, investigations of phonon processes in thin Nb films [22] suggest this will not be the case. The expectation is that the performance will not degrade until at least several THz. These detectors should thus have a significant impact on the field of THz heterodyne sensors.

7. ACKNOWLEDGEMENTS

This overview would not have been possible without the generous and fruitful discussions with the many researchers working on these detectors, and in related areas. I wish in particular to thank Bruce Bumble, Peter Burke, Hans Ekstrom, Eugene Gershenson, Gregory Gol'tsman, Sigfrid Yngvesson, Boris Karasik, Rick LeDuc, Tom Phillips, Dan Prober, Rob Schoelkopf, Anders Skalare, Lianne Verheijen, and Jonas Zmuidzinas.

The research described in this paper was performed by the Center for Space Microelectronics Technology, Jet Propulsion Laboratory, California Institute of Technology, and was sponsored by the National Aeronautics and Space Administration, Office of Space Access and Technology.

8. REFERENCES

- [1] D.E. Prober, "Superconducting terahertz mixer using a transition-edge microbolometer", *Appl. Phys. Lett.* **62** (17), pp. 2119-2121 (1993).
- [2] E.M. Gershenson, G.N. Gol'tsman, I.G. Gogidze, Y.P. Gusev, A.I. Elantev, B.S. Karasik, A.D. Semenov, "Millimeter and submillimeter range mixer based on electronic heating of superconductive films in the resistive state", *Superconductivity* **3** (10), pp. 1582-1597 (1990).
- [3] P.L. Richards, "Bolometers for infrared and millimeter waves", *J. Appl. Phys.* **76**, pp. 1-23 (1994).
- [4] A.F. Andreev, *Sov. phys. JETP* **19**, 1228 (1964).
- [5] P. Santhanam and D.E. Prober, "Inelastic electron scattering mechanisms in clean aluminum films", *Phys. Rev B* **29**, pp. 3733-3736 (1984).
- [6] C. Kittel, *Introduction to Solid State Physics*, 5th edition, John Wiley & Sons, Inc. New York (1976).
- [7] A. Skalare, W.R. McGrath, B. Bumble, H.G. LeDuc, P.J. Burke, A.A. Verheijen, D.E. Prober, "A heterodyne receiver at 533 GHz using a diffusion-cooled superconducting hot electron bolometer mixer", *IEEE Trans. Appl. Superconductivity* **5**, 2236 (1995).
- [8] H. Ekstrom, B. Karasik, E. Kollberg, K.S. Yngvesson, "Investigation of a superconducting hot electron mixer", *Proc. 5th Int'l. Symp. on Space Terahertz Technology*, Univ. of Michigan, pp. 169-188 (1994).
- [9] F. Arams, C. Allen, B. Peyton, E. Sard, "Millimeter mixing and detection in bulk InSb", *Proc. IEEE* **54**, pp. 308-318 (1966).
- [10] B.S. Karasik and A.I. Elantev, "Analysis of the noise performance of a hot-electron superconducting bolometer mixer", *Proc. 6th Int'l. Symposium on Space Terahertz Technology*, California Institute of Technology, Pasadena, CA, March 21-23, 1995.
- [11] J.C. Mather, "Bolometer noise: nonequilibrium theory", *Appl. Optics* **21**, p.1125 (1982).
- [12] C.M. Caves, *Phys. Rev D* **26**, p. 1817 (1982).
- [13] A. Skalare, W.R. McGrath, B. Bumble, H.G. LeDuc, P.J. Burke, A.A. Verheijen, D.E. Prober, "A superconducting hot-electron bolometer mixer for 530 GHz", *Proc. 5th Int'l. Symp. on Space Terahertz Technology*, Univ. of Michigan, pp. 157-168 (1994).
- [14] A. Skalare, W.R. McGrath, B. Bumble, H.G. LeDuc, P.J. Burke, A.A. Verheijen, D.E. Prober, "Noise temperature and IF bandwidth of a 530 GHz diffusion-cooled hot-electron bolometer mixer", *Proc. 6th Int'l. Symposium on Space Terahertz Technology*, California Institute of Technology, Pasadena, CA, March 21-23, 1995.
- [15] A. Skalare, JPL, Private communication on preliminary calculations of bolometer mixer performance using finite-difference formulation.
- [16] E.M. Gershenson, M.E. Gershenson, G.N. Gol'tsman, A.M. Lyul'kin, A.D. Semenov, and A.V. Sergeev, "On the limiting characteristics of high-speed superconducting bolometers", *Sov. Phys. Tech. Phys.* **34**, pp. 195-201 (1989).
- [17] G.N. Gol'tsman, A.I. Elant'iev, B.S. Karasik, and E.M. Gershenson, "Antenna-coupled superconducting electron-heating bolometer", unpublished.
- [18] O. Okunev, A. Dzardanov, G. Gol'tsman, and E.M. Gershenson, "Performance of hot-electron superconducting mixer for frequencies less than the gap frequency: NbN mixer for 100 GHz operation", *Proc. 6th Int'l. Symp. on Space Terahertz Technology*, California Institute of Technology, Pasadena, CA, March 21-23, 1995.
- [19] M. Lindgren, M.A. Zorin, V. Trifonov, M. Danerud, D. Winkler, B.S. Karasik, G.N. Gol'tsman, and E.M. Gershenson, "Optical mixing in a patterned YBa₂Cu₃O₇ thin film", *Appl. Phys. Lett.* **65**, pp.3398-3400 (1994).
- [20] M. Lindgren, V. Trifonov, M.A. Zorin, M. Danerud, D. Winkler, B.S. Karasik, G.N. Gol'tsman, and E.M. Gershenson, "Transient resistive photoresponse of YBa₂Cu₃O₇ films using low power 0.8 and 10.6 μ m laser radiation", *Appl. Phys. Lett.* **64**, 1 (1994).
- [21] M. Danerud, D. Winkler, M. Lindgren, M. Zorin, V. Trifonov, B.S. Karasik, G.N. Gol'tsman, and E.M. Gershenson, "Nonequilibrium and bolometric photoresponse in patterned YBa₂Cu₃O₇ thin films", *Journal of Applied Physics* **76**, (3) 1902 (1994).
- [22] E.M. Gershenson, M.E. Gershenson, G.N. Gol'tsman, A.M. Lyul'kin, A.D. Semenov, and A.V. Sergeev, "Electron-phonon interaction in ultrathin Nb films", *Sov. Phys. JETP* **70** (3), 505 (1990).

MILLIMETER-WAVE MIXERS WITH SCHOTTKY DIODES, FOR SUPERHETERODYNE SPACEBORNE RADIOMETERS - REVIEW AND PREDICTIONS

Israel Galin
Aerojet
P. O. Box 296
Azusa, California 91702

Abstract

Millimeter-wave (MMW) mixers employing Schottky diode (SD) devices are the only mixers implemented, to date, for spaceborne superheterodyne radiometry applications. Spaceborne missions impose high technical standards on such radiometers, lending special significance to MMW mixers employed for such applications. This paper reviews milestones in the developments of SDs and circuit technologies for spaceborne MMW mixers. The paper also suggests possible and desired future developments necessary to maintain and extend the dominance of mixers with SDs even to sub-millimeter-wave (SMMW) frequencies.

1.0 Introduction

Spaceborne observations, of the Earth's atmosphere and its surface, can be performed with radiometers employing superheterodyne receivers. Such radiometers require sensitivity often achievable, as shown in Figure 1, with "room-temperature" mixers employing SDs at MMW and SMMW frequencies [1].

Space-to-Earth MMW radiometry missions - typically unmanned, often of extended duration (several years), and always costly - have successfully driven the development of high quality, robust SD devices and mixer circuits. Evidence of this success are the mixers in dozens of different MMW radiometer instruments[2], listed in Figure 2, some of which have already been launched into space and several others, even at higher SMMW frequencies, to be launched in the future. Figure 2 also illustrates the mixer technology as a ladder with device and circuit technologies comprising its legs. Combinations of mixer device and circuit milestone accomplishments yield the steps of this ladder - climbing to ever higher frequencies with improved sensitivity, increased instantaneous bandwidth, improved reliability, and reduced complexity and costs - all through the MMW and the SMMW spectra.

Up-to-date developments of SD devices and mixer circuits are reviewed separately in the following two

sections. The concluding section attempts to predict the likely and desired future developments in devices and circuits for MMW/SMMW mixers.

2.0 Schottky Diode - Mixer Device Milestones

The recent half century of evolution in devices for MMW mixers, have led to improvements in the intrinsic non-linear resistor device required for mixer frequency convertors. Simultaneously, device improvements have optimized/minimized its packaging elements, which are neither a part of the intrinsic non-linear resistor nor an intended part of the mixer circuit.

Crystal, i.e. solid-state semiconductor, diodes emerged in the 40's as superior substitutes to vacuum tubes for mixers. In the late 50's, GaAs had replaced Si and Ge crystals yielding superior high frequency characteristics [3],[4]. Early mixer crystal devices had employed sharply pointed whisker wires to form a point-contact diode, at the whisker/crystal contact, and to couple this diode with the mixer circuit. After establishing the whisker-semiconductor pressure contact, a forward bias to the diode generated sufficient heat to weld the whisker and the semiconductor, de facto, forming a metal-semiconductor Schottky diode junction [5].

The progress in vacuum metal deposition and photolithography technologies, in the 60's, facilitated the production of semiconductor chips populated with small ($\sim 2\mu\text{m}$) discs of metal deposits - a group of SD junction anodes in a "honeycomb" layout, sharing one large ohmic contact cathode [6]. Each such preformed SD yields a mixer device with quality, predictability, and repeatability consistent with space application standards. However, the SD still requires, for coupling to the mixer circuit, a mechanically problematic and costly whisker pressure contact. For many years, SD "honeycomb" chips maintained only a 180° (lateral) anode/cathode orientation, compatible with machined coax/waveguide MMW mixers.

In the 70's, device manufacturers provided SDs whisker precontacted in "picopills" to simplify the assembly of up to 100 GHz machined mixers.

Also in the 70's, device technology matched new MMW mixer printed-circuits with SDs compatible with planar circuits: whisker contacted "honeycombs" were modified to include MMW notch-front SDs [7] with 90° (orthogonal) anode/cathode orientation, which improved the reliability of SD-circuit whisker contact on planar dielectric substrates; and, planar beam-lead SDs [8] altogether eliminated the need for whisker contacts for printed circuit mixers below 150 GHz.

In the 80's, beam-lead SDs evolved [9] into planar air-bridge finger, whiskerless SDs, successfully challenging the dominance of whisker contacted MMW mixers even above 150 GHz [10].

In the 90's, planar whiskerless SDs with sub-micron diameters promise to further reduce the role of whisker contacted SDs, even for SMMW mixers [11].

3.0 Mixer Configuration - Mixer Circuit Milestones

Mixer circuits embody the linear circuit residency for non-linear mixer devices. A mixer circuit provides filtering/matching interfaces for widely separated frequencies: at the highest frequencies, the mixer circuit interfaces between the mixer device and external RF and local-oscillator (LO) input sources; while at much lower frequencies, a mixer circuit interfaces between the mixer device and an external output IF load. Such circuit functions have governed developments in mixer circuit technology for more than fifty years.

One diode, single-ended mixers, with fundamental frequency pumping LOs, have traditionally employed high-Q directional cavities to channel the RF and the LO to the diode, and to suppress the LO noise. Balanced mixers employing two identical diodes, were introduced in the mid-40's [12], requiring balanced/unbalanced (balun) circuits for feeding the RF and the LO differently. The balun enables RF/LO isolation by virtue of orthogonality, and also the suppression of LO amplitude-modulated (AM) noise at frequencies of the RF. Fundamentally pumped, up to 190 GHz [13], balanced mixers were implemented with whisker contacted diodes. The same paper [12] also describes all sixteen possible mixers with two diodes, some of which feature high sensitivity [14] and efficient subharmonic pumping. Such MMW mixers [15] have bridged the gap created by a lagging MMW LO technology, and an inefficient and costly MMW frequency multipliers technology. For example, subharmonic x2 MMW mixers, requiring LOs at frequencies half that of the RF, were implemented in the 80's for MMW spaceborne applications [16]. They achieved wider instantaneous bandwidth relative to harmonic single-ended mixers [17], while requiring similar low frequency LOs as the latter.

Diverse MMW mixer circuit configurations have been implemented in a variety of transmission-line media. The first single-ended MMW mixers consisted of machined coaxial and waveguide filters. Early balanced mixers included a four-port waveguide magic-T with E and H ports as RF and LO inputs. The two remaining ports were terminated with coax/waveguide single ended mixers with their IF outputs feeding a coaxial power combiner.

Printed circuit mixers proliferated in the 60's and the 70's, yielding attractive planar compact balanced mixers: stripline and microstrip versions of 3-dB couplers and rate-race circuits replaced the waveguide magic-Ts; ultimately, the junction between a slotline and coplanar line yielded a wideband planar magic-T [18], variations of which are commonly used in monolithic mixers; and also inspired a particularly successful version of a machined strip guide MMW balanced mixers [19] with "picopill" SDs. Planar versions of MMW mixers were transformed into MMW monolithic integrated circuit (MMIC) mixers [20] eliminating, altogether, the circuit device mixer interconnects, and poising for penetration into SMMW frequencies.

4.0 Predictions and Conclusions

Mixer technology will continue to penetrate new and higher frequencies, and to improve mixer performance. However, GaAs device high frequency characteristics and circuit miniaturization capabilities are approaching their limits at SMMW frequencies. At the same time oscillator technology continues to lag in meeting MMW/SMMW LO requirements. Hence, it is critical for future progress to correctly identify, in advance, agents and patterns which will most likely succeed in carrying-out future changes in MMW/SMMW mixer technology. This review, which has thus far outlined portraits for agents and patterns of past changes in mixer technology, can also serve as an effective reference for such predictions.

Semiconductor submicron processes and materials with faster characteristics, e.g. InP, further developments of MMW/SMMW subharmonic mixers, and advances in MMIC technology are agents also likely to remain active in shaping future mixer technology.

MMICs and whiskerless SDs are technologies which can simplify the mixer assembly process, thereby, rendering practical MMW/SMMW mixer configurations otherwise considered too complex for implementation.

Whiskerless planar SDs have already rendered practical MMW subharmonic x2 mixers with two SDs in anti-parallel, and are considered for 600 GHz space missions [21] to operate with a frequency doubler and available 150 GHz LO. Subharmonic x4 600 GHz mixers [22]

eliminate the requirement for frequency doublers. Since mixer performance degrades with higher order LO subharmonic. Subharmonic x3 [23], with two SDs connected in series, promises new and superior mixers up to ~1 THz, requiring only a single doubler and available LOs.

MMICs have eliminated bond wire interconnects between various mixer elements, enhancing reliability and facilitating improved sensitivity and bandwidth. However, conventional MMW/SMMW MMICs yield relatively high effective ϵ_r lossy circuit media and support undesired modes. New variations of MMICs integrated with thin (~1-5 μ m) membranes [24], particularly in suspended configurations, yield lower effective ϵ_r and suppress undesired modes through higher and wider frequency bands. The continuing trend depicted in Figure 2 - toward MMW/SMMW multi-channel, wide bandwidth, spaceborne radiometers - is driven by cost, packaging, and performance considerations favoring advanced MMIC technology. This technology promises to render practical complex mixer configurations, like image rejection subharmonic mixers [25] and two SD subharmonic corner-cube mixers [26]. Such complex and advanced mixer configurations are important for meeting the future challenges awaiting MMW/SMMW mixer technology.

5.0 References

- [1] N. Keen, "On the Noise-Temperature of Cryogenically-Cooled Mixer Diodes at MMW", Workshop on Diode Technology at MMW, Univ of Bordeaux, April 1982.
- [2] M.A. Janssen, "Atmospheric Remote Sensing by Microwave Radiometry", John Wiley & Sons, Inc, 1993, pp. 266-267.
- [3] H.C. Torrey, et al, "Crystal Rectifiers", MIT Rad Lab Series Vol. 15, McGraw Hill, NY, 1948.
- [4] R.J. Bauer, et al, "MMW Semiconductor Diode Detectors, Mixers, and Frequency Multipliers", Proc IEEE, April 1966.
- [5] C.A. Burrus, "MMW Point-Contact and Junction Diodes", Proc IEEE, April 1966.
- [6] D.T. Young, et al, "MM Frequency Conversion Using Au-N-Type GaAs Schottky Barrier Epitaxial Diodes With Novel Contacting Techniques", Proc IEEE December 1965.
- [7] J. Paul, et al, "New Trends in MMW Mixers Technology", MW Journal, May 1980.
- [8] R.A. Murphy, et al, "SMMW Heterodyne Detection with Planar GaAs Schottky Barrier Diodes", IEEE Trans MTT, June 1977.

- [9] C.S. Setzer, et al, "High-Performance MMW GaAs Schottky Barrier Flip-Chip Diode", Electronics Letters, August 6, 1981.
- [10] P.H. Ostdiek, et al, "Integration of an Antiparallel Pair of Schottky Barrier Diodes in MMW Mixers", 15th International conference on IR and MMW, December 1990.
- [11] J. Hesler, et al, "The Design Construction & Evaluation of a 585 GHz Planar SD Receiver", 6th International Symp on Space THz Technology, March 1995.
- [12] M.J.O. Strutt, "Noise-Figure Reduction in Mixer Stages", Proc of I.R.E. and Wave Electrons, December 1946.
- [13] I. Galin, "A New Fundamentally Pumped Balanced Mixer for G-Band (140-220 GHz)", 13th Internat Conf on IR & MMW, December 1988.
- [14] J.D. Buchs, et al, "Frequency Conversion Using Harmonic Mixers", IEE Journal MW, Opt. Acoust., May 1978.
- [15] E.R. Carlson, et al, "Subharmonically Pumped MMW Receivers", 4th International Conference on IR & MMW, December 1979.
- [16] I. Galin, "Improved Structures For Subharmonically Pumped MMW Mixers", 12th International Conf. on IR and MMW, Orlando 1987.
- [17] N.R. Erickson, "Low-Noise SMMW Receivers Using Single-Diode Harmonic Mixers", Proc IEEE. November 1992.
- [18] J.K. hunton, et al, "A MW Integrated Circuit Balanced Mixer with Broad Bandwidth", Proc of Microelec. Symp., September 1969.
- [19] G. Spacek, "Strip Guide Balanced Mixer", US Patent NO. 3 584 306, 1970.
- [20] P.H. Siegel, et al, "Design & Measurements of a 210 GHz Subharmonically Pumped GaAs MMIC Mixer", IEEE MTT-S, June 1992.
- [21] P.H. Siegel, et al, "Heterodyne Radiometer Development For The Earth Observing System Microwave Limb Sounder", IR and MMW Engineering. SPIE Vol 1874, 1993.
- [22] R.E. Forsythe, et al, "Subharmonic Mixers for 183-225 GHz", 7th International conference on IR & MMW, December 1982.
- [23] B. Schuppert, "Analysis and Design of MW Balanced Mixers", IEEE Trans on MTT, January 1986.
- [24] S.S. Gearhart, et al, "A 250 GHz Monolithic Double-Slot SD Receiver", IEEE MTT-Trans, December 1994.
- [25] D. Weiner, et al, "The Image Rejection Harmonic Mixer", IEEE MTT-S Digest 1982.
- [26] Farran Technology 94-95 Product Catalogue, "Quasi-Optical Harmonic Mixer", Series CHM, pages 60-62.

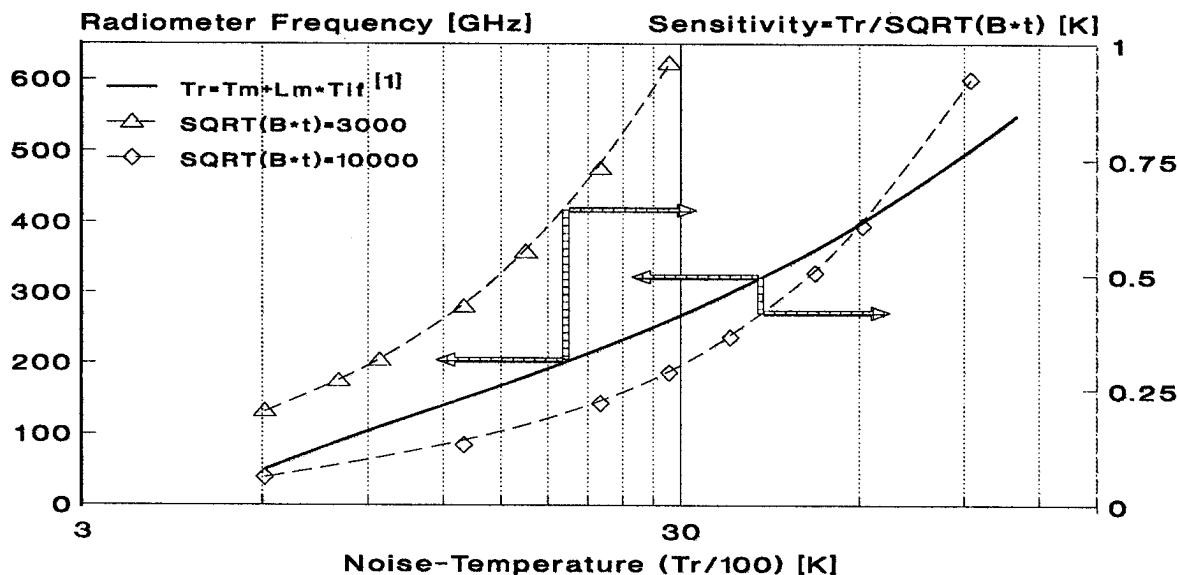


Figure 1: Possible SSB noise-temperature and achievable sensitivity, for practical MMW radiometers and mixers with Schottky diodes.
 ($T_{if} = 100K$; T_m = Mixer Noise-Temperature; L_m = Mixer Conversion-Loss; B = Predetection Bandwidth; t = Integration Time)

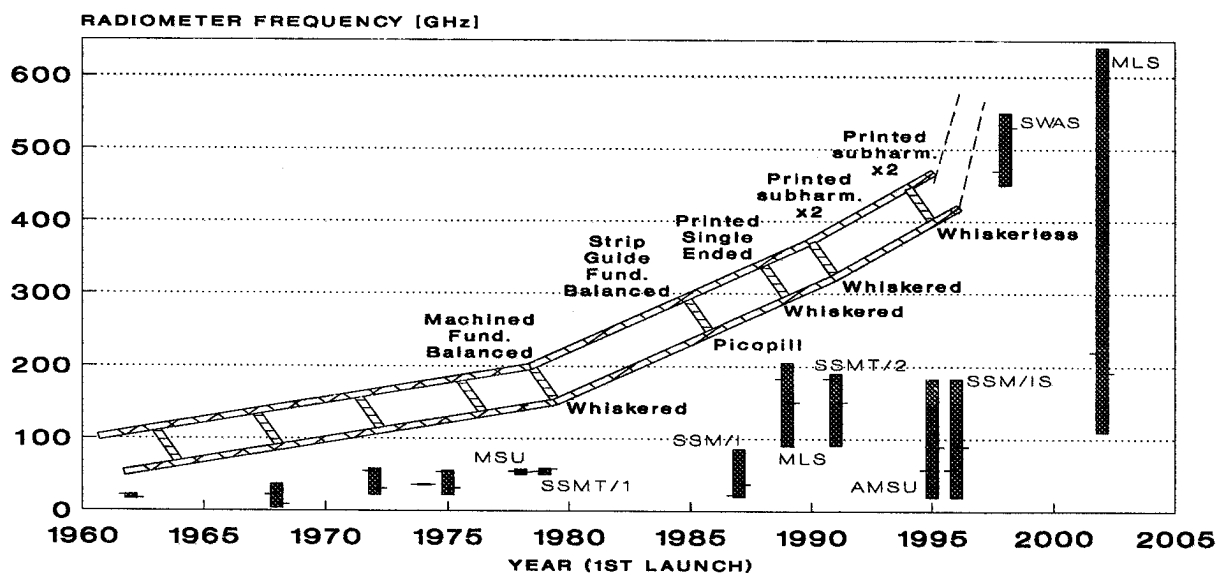


Figure 2: Radiometers launched and to be launched into orbit, and their implemented MMW mixer technology.

SILICON AND GALLIUM ARSENIDE IN HIGH TEMPERATURE ELECTRONICS APPLICATIONS

J. Winfried Klein

Institute for Electronics
Ruhr-Universität Bochum
D-44780 Bochum

Tutorial Paper

Abstract

Electronic circuits and systems which can operate at temperatures up to 250°C or even higher become more and more important. It can be shown that Si as semiconductor material can be used up to this temperature provided that circuit structures are optimized to handle the parasitic effects rising with temperature. For even higher temperatures up to 350°C GaAs can be used.

Other problems going along with high temperature applications arise from material characteristics as melting point, mechanical stability, insulating characteristics and migration problems.

This paper reports on a German Joint Research project dealing with the problems mentioned above. Some of them could be solved satisfactory, some problems are still existing.

1. Introduction

Some years ago High Temperature Resistant Electronic Circuits were a problem of some scientists and engineers for special sophisticated applications. But during the last years the situation has completely changed. The area of applications for high temperature electronic circuits and systems has dramatically increased. For example there is a great demand on high temperature electronics in the fields of automotive-, air- and spaceborne applications and especially in powerplants and harsh environment applications. In all these fields the main requirements are – additional to the high

temperature conditions – that the components and the circuits have to be both reliable and cheap.

To get the optimal solution for all fields of application it is necessary to know their different temperature ranges. Fig. 1 gives an overview of these applications as a function of temperature. In the same diagram we plot the intrinsic carrier concentration for different semiconductor materials versus temperature, which is a measure for leakage currents and other parasitic effects to be compensated by special circuit structures.

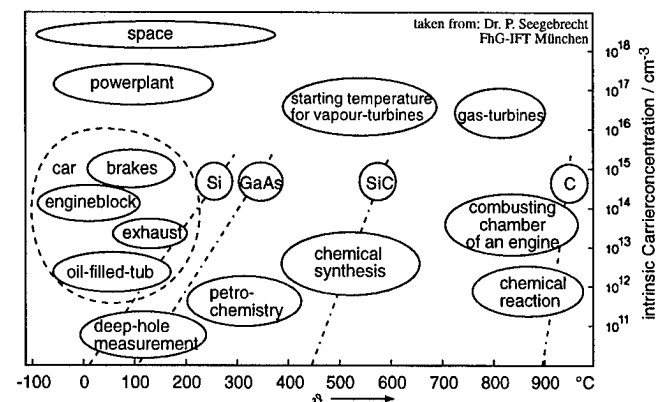


Figure 1: Temperature ranges for industrial applications.

If we consider that we can build circuits with a reliable operation up to an intrinsic carrier concentration of $10^{15}/\text{cm}^3$, we see that it should be possible to use silicon (bulk and SOI) as semiconductor material up to 250°C and GaAs up to 350°C. This means that it should be possible to cover the main application areas of car electronics, powerplant electronics, air- and space applications and the main part of petrochemistry.

2. The German Joint Research Project for High Temperature Electronics

In summer 1992 a German Joint Research Project for High Temperature Electronics was established using only silicon and gallium arsenide as semiconductor materials. Silicon carbide and diamond were not taken into further consideration for until now they do not fulfill the two limiting conditions mentioned above: to be reliable and cheap.

In this project 10 partners (4 companies, 2 Fraunhofer Institutes, 3 University Institutes and 1 Government Research Institute) came together to cooperate under the title „Microsystem Components for High Temperature Applications“. The total financial volume is 24 Million DM, sponsored by the German Ministry of Research and Technology. So this project gives a large variety of results some of which will be presented in this conference.

3. Some results achieved until now

I will now report on some of the results which were achieved in this joint project. For silicon investigations were made in Bulk technology as well as in SOI technology (SIMOX and BESOI). The principles of these technologies are shown in Fig. 2. As a result of the reduced leakage areas by application of SOI technologies a reasonable improvement of the high temperature behavior could be achieved.

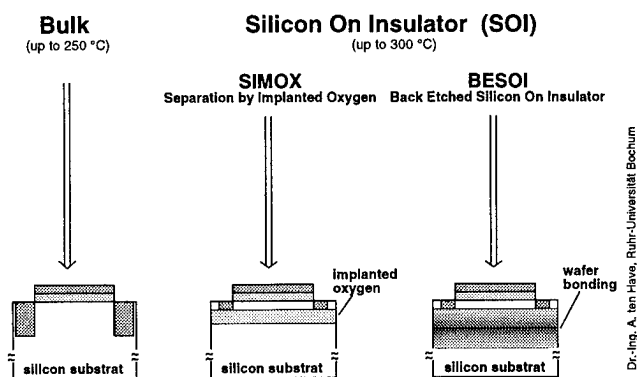


Figure 2: Silicon Technologies

Fig. 3 shows in comparison the transfer functions of a Bulk and a SOI N-MOSFET at a temperature of 300°C. It can be seen that the SIMOX-type is still in its active area while the bulk-type is out of control. Some other papers of this conference will report on operational amplifiers which were built in Bulk and SIMOX technologies.

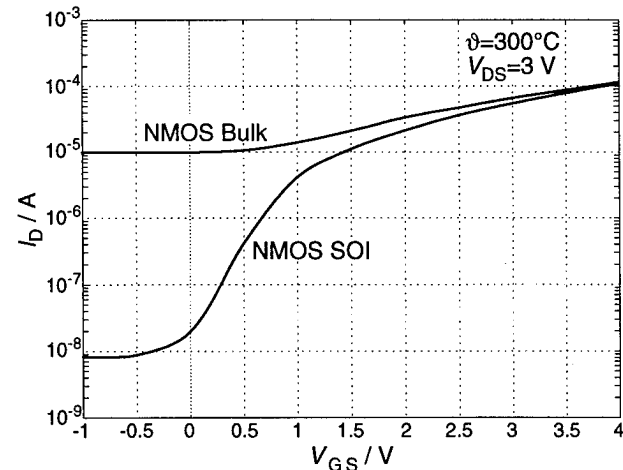


Figure 3: Comparison of Bulk- and SIMOX-Transistors.

For even higher temperature applications GaAs should be used because of its wider band gap. Fig. 4 shows the DC output characteristic of a GaAs-MES-FET in the temperature range of -196°C up to +500°C. It can be seen that the transistor can be used over this large range although there is a reasonable reduction in gain. As the main field of applications for GaAs components is in the high frequency domain Fig. 5 shows the S-parameters at different temperatures. The first demonstrator will be a FMCW-Radar system for high temperature application. It can be used for high temperature level measurement in chemical process control.

Regarding the complete problem of high temperature electronics one easily finds out that the semiconductor problem is only one of several others of equal importance. Fig. 6 shows that for example many materials used for passive components and devices as well as for metallisation and mounting and bonding technology in the normal temperature range cannot any longer be applied: Plastics as

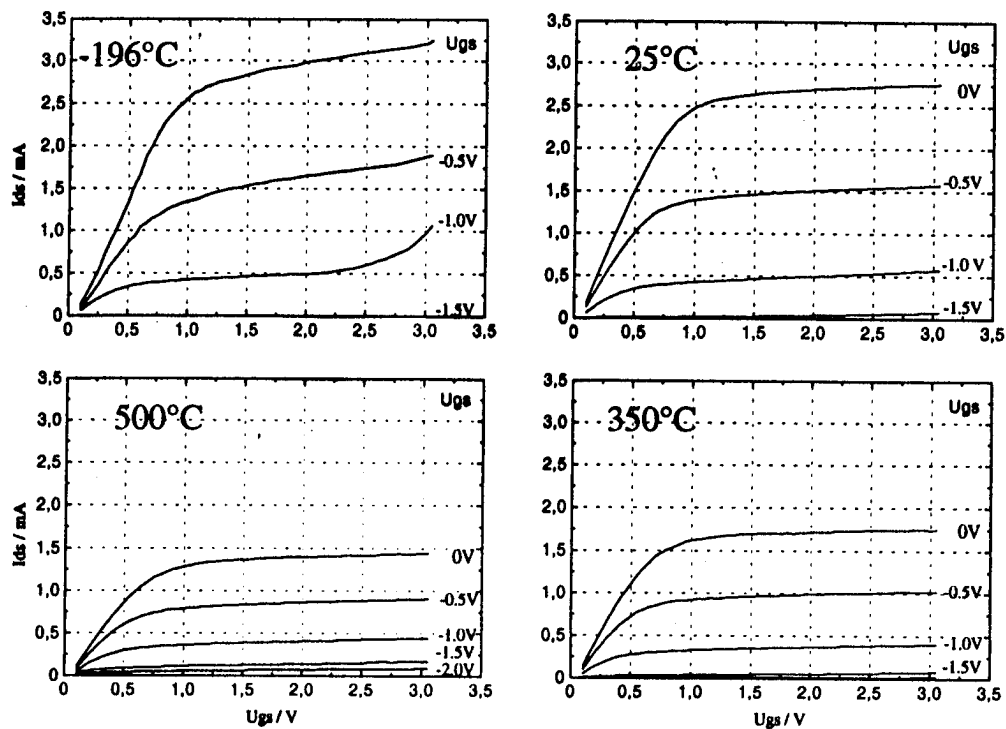


Figure 4: Output Characteristics of a $0.5 \times 10 \mu\text{m}^2$ GaAs-MESFET.

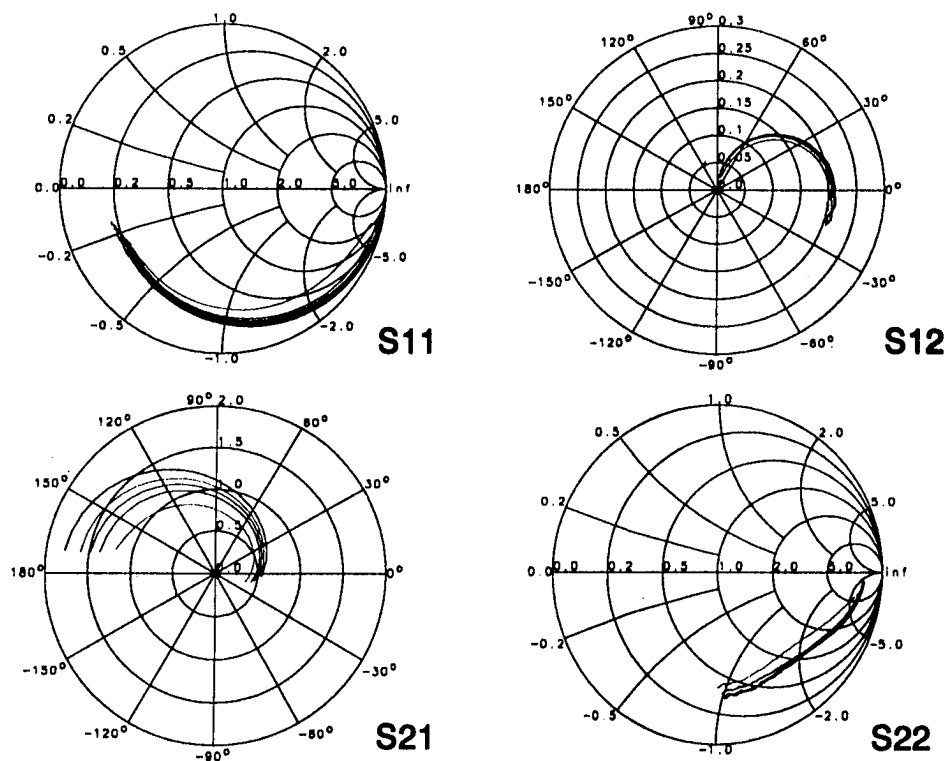


Figure 5: S-Parameters with $f = 1 \text{ GHz} \dots 50 \text{ GHz}$ for temperatures from RT to 250°C .

dielectric and insulating material melt. Normal solders melt, glass becomes conductive, flexible boards are destroyed and most of the materials corrode. Also material migration cannot be neglected.

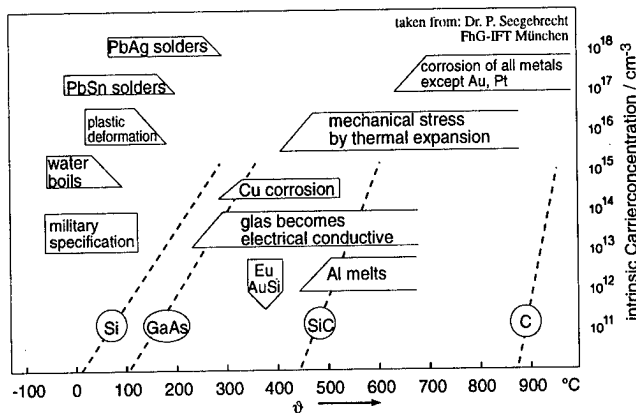


Figure 6: Characteristic temperature ranges for some materials.

This means that for example the usual AlSiCu for chip metallisation has to be replaced for example by W or Ti and the current density has to be reduced. All this requires more space on chip and so reduces package density. For interconnection of different devices thick film and thin film technologies have been proved to be reliable. Film resistors have a good temperature behavior and a good tracking, especially when being overglazed. Fig. 7 shows the long term behavior of a family of thick film resistors at a temperature of 300°C.

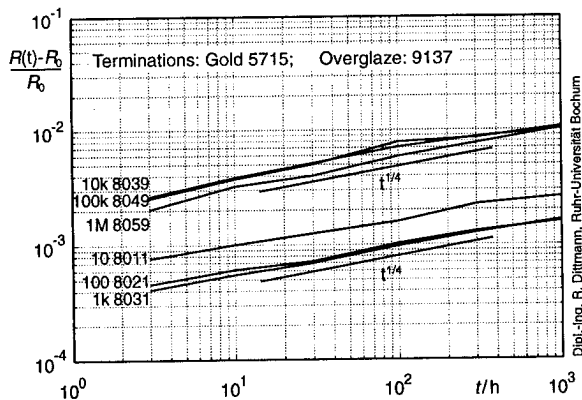


Figure 7: Irreversible resistance drift at 300°C up to 1,000 hours; survey of the HS80 thick film resistor family.

Wire bonding becomes a migration problem when different materials have to be connected. Fig. 8 shows the change in contact resistance at different high temperatures over a period of thousand hours.

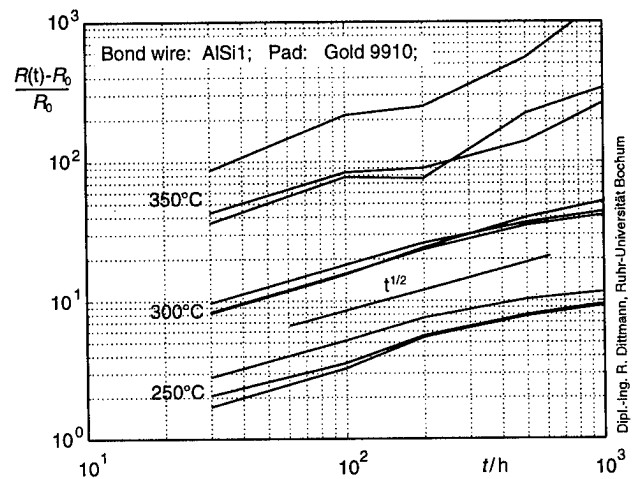


Figure 8: Irreversible contact resistance drift up to 1,000 hours for different temperatures; AlSi1 bond on DuPont's 9910 conductor.

Migration can be reduced by applying sandwich methods. Nevertheless pulltests and sheartests show that the stability of the connection is reduced to more than 1/2 by temperature treatment up to 300°C. Fig. 9 gives an example. All these effects can only be investigated in long term testloops of several thousand hours duration.

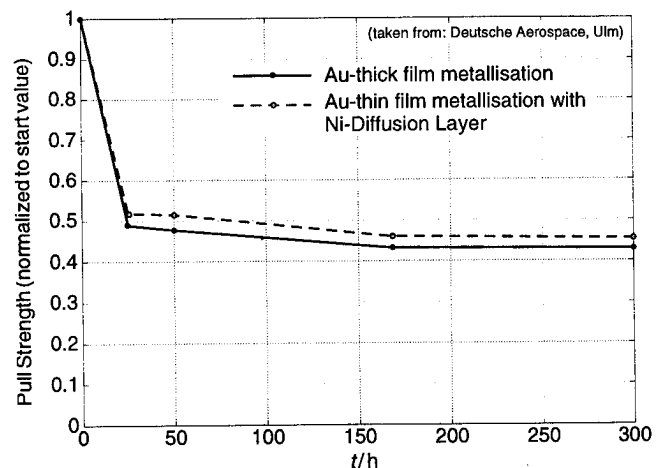


Figure 9: Pull strength drift after 300°C aging of 32 µm AlSi1-wires on Au-thick- and thin film metallisation.

This list of problems going ahead with high temperature applications cannot be closed without

mentioning the question of cheap and reliable housing and packaging of high temperature devices. The well known Covar and Cofired Ceramic Packages are reliable but so expensive that they could never be used in automotive or similar applications. But high temperature resistant cheap plastic packages are not available until now.

In conclusion we see that only the combination of high temperature components (active and passive ones) as well as a high temperature reliable mounting and bonding technology and last but not least high temperature circuit design can offer the possibility of building a high temperature electronic system (Fig. 10).

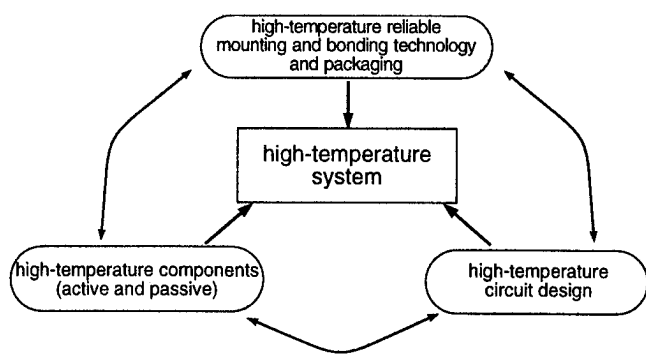


Figure 10: Activities for the development of high-temperature sensor-systems.

Discussing the question which circuits for high temperature application are needed let us look to a conventional control loop in the high temperature environment (Fig. 11).

We see that there are two ways to correspond with the high temperature range of the loop. The one is the sensor way to get information from the high temperature loop and the other one is the actor way to send control signals that means to send information to the high temperature area. If you want to do so with a minimum of information loss in both directions you have to use intelligent sensors (smart sensors) and intelligent actors (smart power actors). This means that in both ways you have to have high temperature resistant electronics.

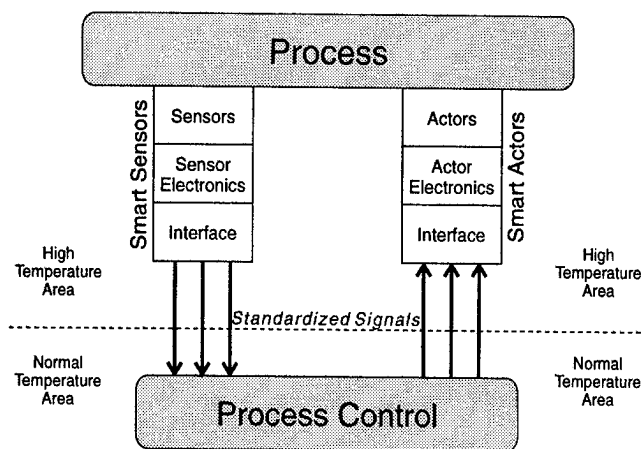


Figure 11: Process Control System.

Coming back to the German Research Project we here limited to the left area of Fig. 11, to the sensor area. Fig. 12 shows the smart sensors and the necessary sensor electronics which we have chosen as demonstrators.

4. Conclusions

The design of optimal circuits provides a coordinated research in three areas:

- Material and component selection including process optimization for the production of active and passive components,
- circuit structure optimization to tolerate the high temperature depending parasitic effects and, last but not least,
- mounting and packaging methods for reliable and cheap high temperature application.

These three areas of research and development are strongly influencing each other.

It could be shown, that for temperatures up to 250°C Silicon in Bulk and SOI technologies can be used as a semiconductor material and circuit design enables the production of most of the system components necessary to build high temperature resistant smart sensor systems. A similar situation is given for the use of GaAs up to temperatures of 350°C with the limitation that GaAs semiconductor technologies have some lack of experience compared with Silicon technologies.

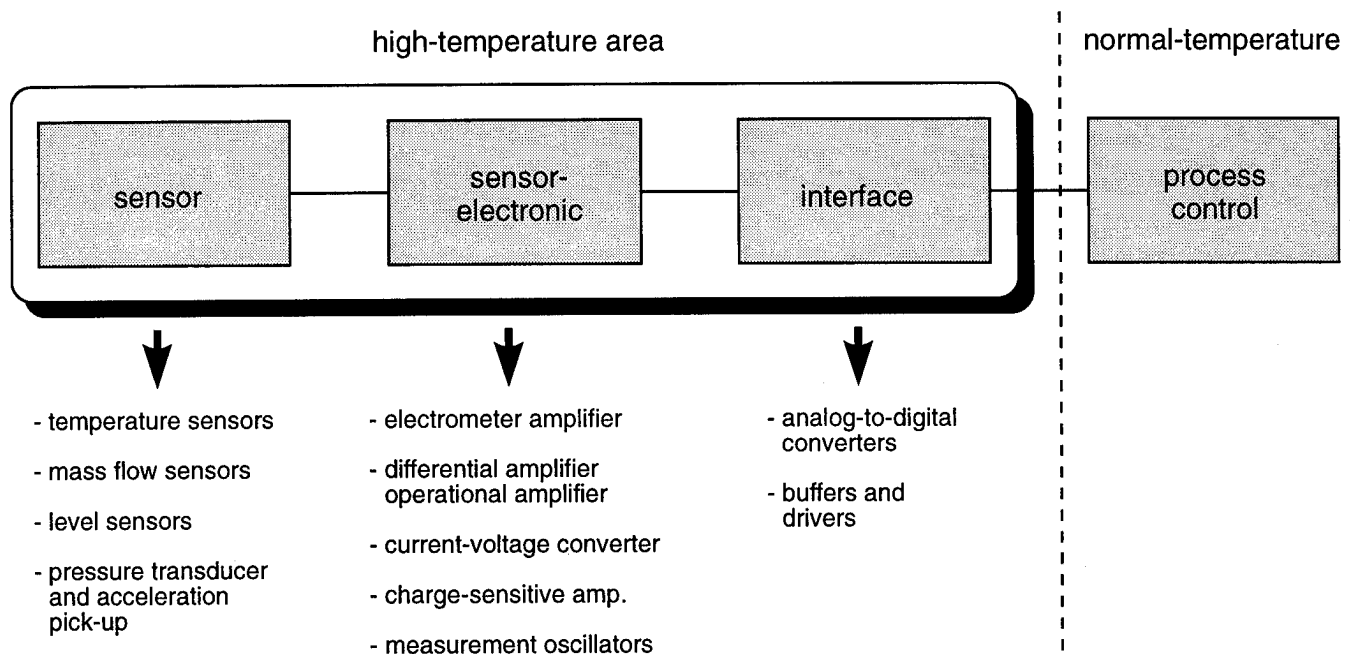


Figure 12: High-temperature sensor-system

Acknowledgement

The author is grateful for the support which he received from the partners of the German Research project:

- Deutsche Aerospace AG, Ulm,
- ELBAU GmbH, Berlin,
- ELMOS GmbH, Dortmund,
- Ferdinand-Braun-Institut, Berlin,
- Fraunhofer-Institut IFT, München,
- Fraunhofer-Institut IMS, Duisburg,
- KROHNE GmbH & Co. KG, Duisburg,
- Ruhr-Universität Bochum,
- Technische Hochschule Darmstadt,
- Technische Universität Chemnitz.

He also wants to thank the German Research Ministry and the VDI/VDE-Technologiezentrum Informationstechnik GmbH for financial and administrative support to do this research work.

HETERODIMENSIONAL TECHNOLOGY FOR ULTRA LOW POWER ELECTRONICS

W.C.B. Peatman¹, M. Hurt, R. Tsai, T. Ytterdal, H. Park, J. Gonzales and M. Shur

Department of Electrical Engineering, University of Virginia Charlottesville, VA 22903
¹on leave from UVA to Advanced Device Technologies, Inc. Charlottesville, VA 22901
TEL: (804) 979-4103, FAX: (804) 979-2653, E-mail: 75033.206@compuserve.com

ABSTRACT

We describe new heterodimensional technology suitable for ultra low power applications. This technology uses Schottky barrier contacts between three-dimensional metal and two-dimensional electron gas. The low power performance is due to a small capacitance of the 2D-3D junction, the concentration of the depletion layer electric field streamlines in the active channel, suppression of parasitic resistance, small leakage current, and, most of all, due to the total elimination of the narrow channel effect which allows us to scale the device width to submicron dimensions. We present, compare, and discuss measured and simulated I-V and C-V characteristics for the 2D-3D Schottky diode, 2D MESFET and Schottky Gated 2D-3D RTT.

1. INTRODUCTION

A major emphasis in IC technology over the last decade has been to increase the microprocessor speed and reduce memory access times. While speed performance continues to be an important metric for advances in ICs, increasing importance is given to overall energy efficiency, particularly for battery-powered applications such as wireless communications. An important figure-of-merit for low power electronics is the power-delay product. The power-delay product of a FET is determined by the energy $(C + C_p)\Delta V^2$ stored by the gate capacitor. Here, C is the gate-channel capacitance, C_p is the parasitic capacitance and ΔV is the gate voltage swing required to switch between on and off states (ΔV is proportional to the supply voltage V_{dd}). Future low power transistor technologies therefore must achieve the lowest possible reduction of both the switching capacitance and the supply voltage. Direct Coupled FET Logic (DCFL) and Complementary Heterostructure FET (CHFET) technology using GaAs-based FETs are among the most promising alternatives to conventional CMOS technology, due primarily to higher carrier mobilities in

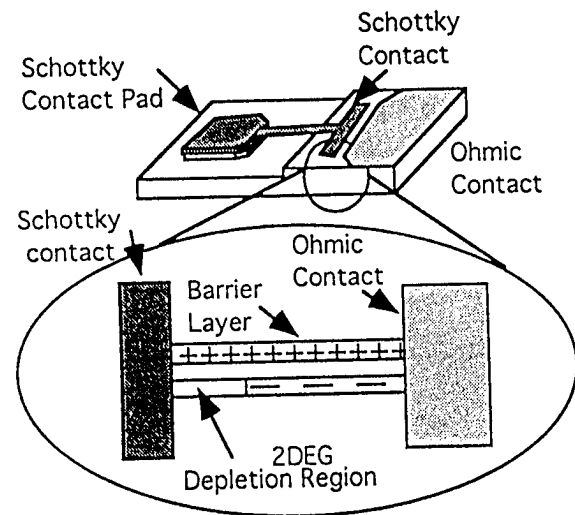


Fig. 1. Schematic structure of the heterodimensional Schottky diode.

GaAs and InGaAs where high carrier velocities can be achieved at lower voltages. While significant performance advances are being made by utilizing faster materials, further improvement may be achieved by optimizing the device geometry to simultaneously reduce power consumption and increase speed. In this paper, we review heterodimensional Schottky devices in which the Schottky contact is between the 3-d metal and the 2-d electron gas. The 3-d/2-d Schottky diode as well as two new field effect transistors will be discussed and recent results reported on each. These novel high speed devices offer unique and new approaches to the design of advanced semiconductor devices and circuits.

2. HETERODIMENSIONAL SCHOTTKY DIODE

A schematic of the heterodimensional 3-d/2-d Schottky diode and its non-linear capacitance-voltage characteristic are shown in Fig. 1. The Schottky contact is formed by plating metal into a trench etched in a heterostructure (e.g. $\text{Al}_{0.25}\text{Ga}_{0.75}\text{As}/\text{In}_{0.20}\text{Ga}_{0.80}\text{As}/$

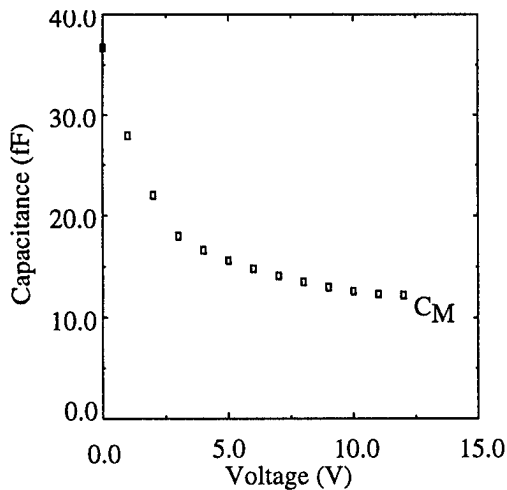


Fig. 2. Capacitance-voltage characteristic of the 100 μm wide heterodimensional Schottky diode.

GaAs) [1-3]. The Schottky barrier results in a depletion layer within the 2-dimensional quantum well. An important consequence of the direct contact is the 2-dimensional (vertical) spreading of the electric field in the depletion region. This leads to a stronger voltage dependence on the depletion depth and to a larger breakdown voltage [4]. Also, due to a small effective junction area, the capacitance is very low, 0.1 - 0.3 fF/ μm width, as shown in Fig. 2 (for comparison, a state-of-the-art 0.2 micron length heterostructure field effect transistor has a capacitance of about 1.0 fF/ μm). Together with low series resistance (0.8 Ω/mm) and large breakdown voltage (up to 20 V), the planar 3-d/2-d Schottky diode should be ideal for frequency multiplier applications in the millimeter/submillimeter wavelength regions. Tripler efficiencies greater than 1% at 225 GHz have been obtained and much higher efficiencies should be possible with better diode-to-circuit impedance matching [5].

3. SCHOTTKY-GATED RESONANT TUNNELING TRANSISTOR

A resonant tunneling transistor utilizing the heterodimensional Schottky gate contacts is illustrated in Fig. 3. The room temperature transistor characteristics are shown in Fig. 4. The Schottky gate metal was electroplated onto the side of a AlGaAs/GaAs double barrier heterostructure. The heterodimensional gate modulates the drain current by modulating the area of the quasi-2-dimensional accumulation layer which forms in the source-drain resonant tunneling diode under bias. This device exhibited record room temperature transconductance of 218 mS/mm with a peak current of 225 mA/mm [6]. The cutoff frequency was estimated to be 18.5 GHz.

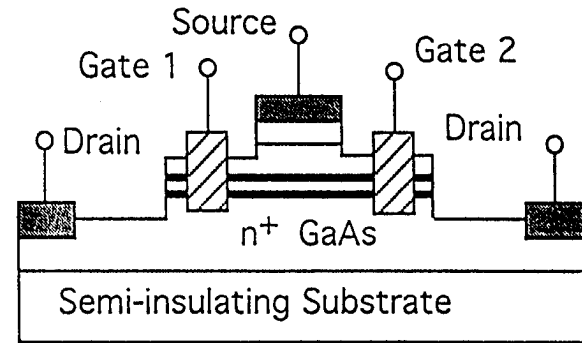


Fig. 3. Schematic of Schottky-gated Resonant Tunneling Transistor (SG-RTT).

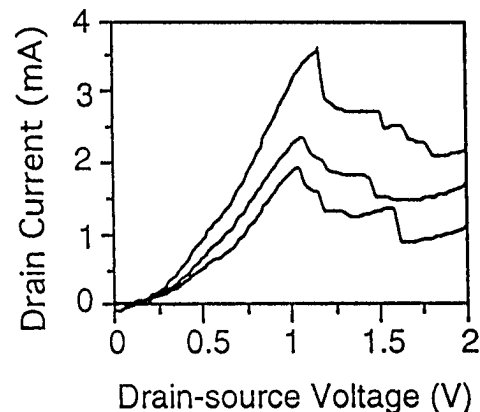


Fig. 4. Drain current versus drain-source voltage characteristics of SG-RTT (300K).

4. 2-D MESFET FOR LOW POWER ELECTRONICS

Low power digital ICs use device widths as small as 3-5 micron but rarely are smaller widths used. This is due to parasitic effects, known as the narrow channel effect (NCE), related to the poor control of charges at the edges of the channel [7]. These parasitics cause poor subthreshold ideality factor (which dictates larger gate voltage swing and therefore higher power consumption) and parasitic capacitances which limit switching speed. To address these problems, we are developing a new transistor technology, based on the heterodimensional Schottky sidegate technology, which permits width scaling to sub-micron dimensions without degradation due to the NCE. The 2-D METal-

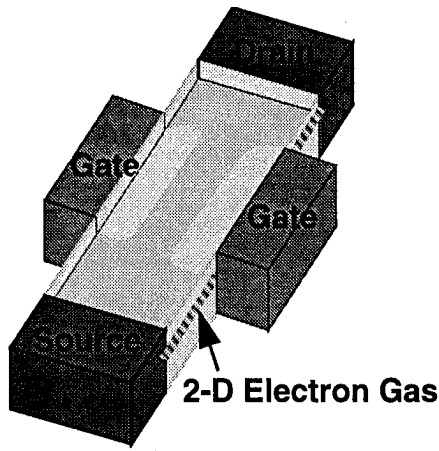


Fig.5. Perspective of 2-D MESFET (not to scale).

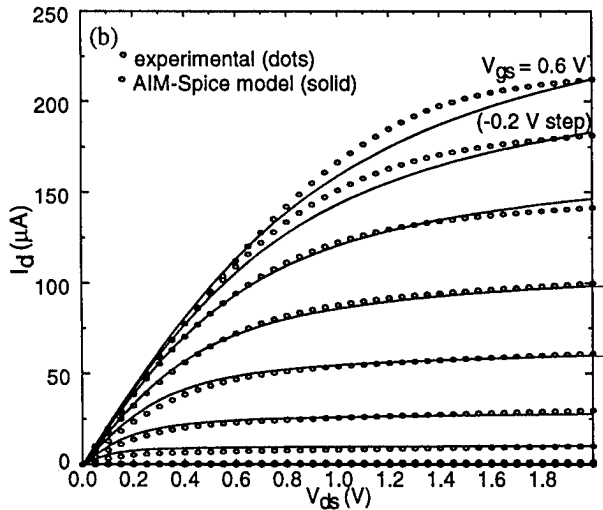


Fig. 6. Drain current versus drain-source voltage characteristics of the 1.0 micron wide device.

Semiconductor Field Effect Transistor (2-D MESFET) [2,8,9] is shown schematically in Fig. 5. The gate electric field streamlines are focussed onto the 2-DEG and pinch-off occurs when the two depletion regions merge together. Note that the gate metal physically eliminates the side channels, thereby eliminating the origin of the narrow channel effect. The two gates may be independently biased (for a "fan-in" of two) for greater functionality in digital applications.

Both enhancement (E) and depletion (D)-mode devices have been fabricated. The measured room temperature I_d - V_{ds} characteristics of a 1 micron wide D-mode 2-D MESFET are shown in Fig. 6. The threshold voltage was -1.0 V, the peak drain current and transconductance values were 370 $\mu\text{A}/\mu\text{m}$ and 225 $\mu\text{S}/\mu\text{m}$, respectively [9]. The I_d - V_{ds} and I_g - V_{gs} characteristics of a 0.5 micron wide E-mode 2-D MESFET

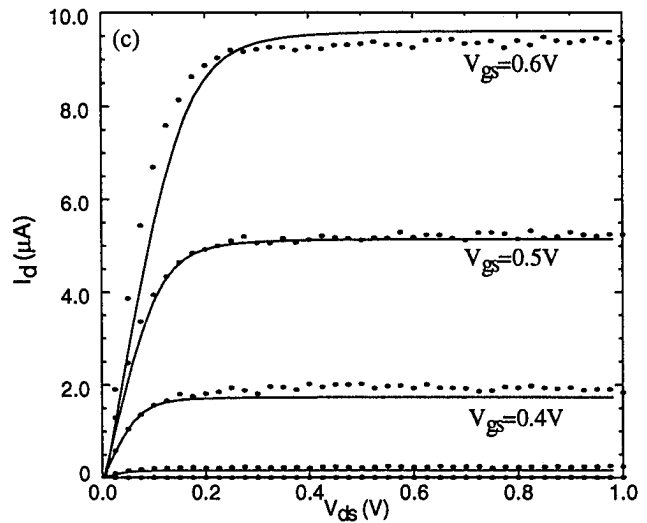


Fig. 7. Drain current versus drain-source voltage characteristics of 0.4 micron wide device.

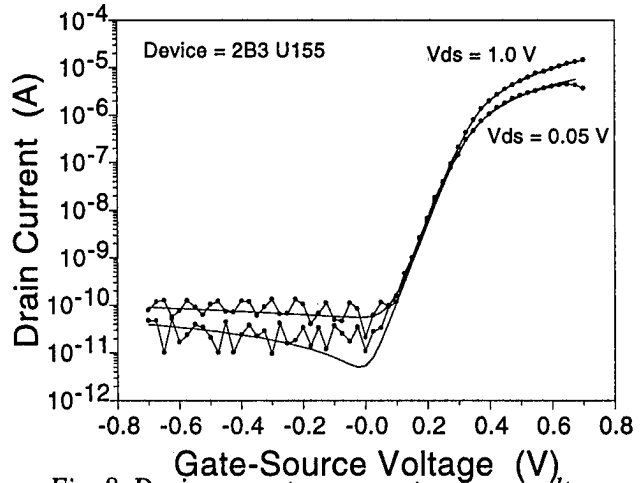


Fig. 8. Drain current versus gate-source voltage characteristics of 0.4 micron wide device.

are shown in Fig. 7 and 8, respectively. The threshold voltage was 0.3 V, the subthreshold ideality factor was 1.1, the output conductance was less than 1 mS/mm, the ON/OFF current ratio was greater than 10^5 and there is virtually no V_T shift for $0 < V_{gs} < 1$ V [10]. The DCFL 2-D MESFET transfer characteristics (using E-mode devices) are shown in Fig. 9 where a noise margin of 0.26 V was obtained. Using accurate 2-D MESFET I - V and C - V models implemented in AIM-SPICE [11], we simulated a three-stage ring oscillator and obtained per gate power-delay product of less than 0.1 fJ, shown in Fig. 10, which is about two orders of magnitude lower than that for competing technologies. The dramatic reduction in power-delay product is due to the fundamentally superior electrical properties of the heterodimensional Schottky technology in sub-micron dimension devices.

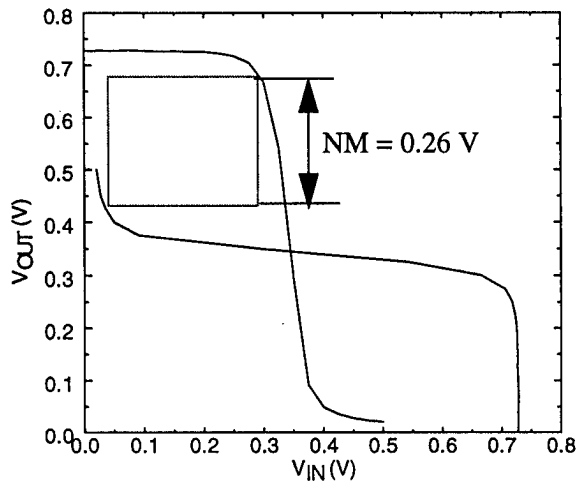


Fig. 9. Measured 2-D MESFET DCFL inverter transfer characteristics at 0.8 V supply voltage.

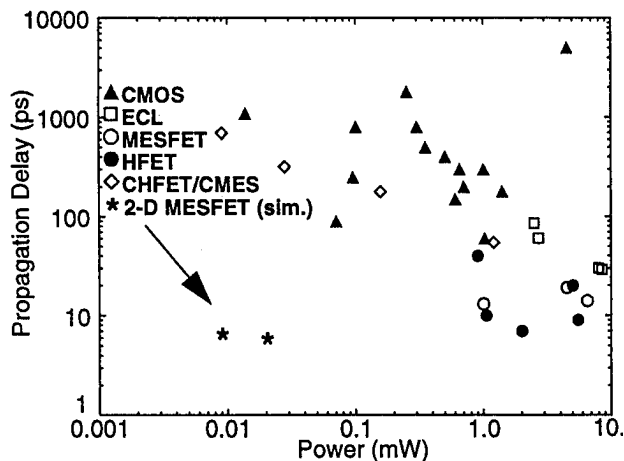


Fig. 10. Simulated 2-D MESFET ring oscillator has much lower power-delay product compared with existing transistor technologies.

5. SUMMARY

We have described the operation of several new devices based on the novel heterodimensional metal/2-d electron gas junction. The Schottky diode has low junction capacitance and high breakdown voltage, due to 2-dimensional spreading of the electric field in the depletion region. The Schottky-gated Resonant Tunneling Transistor uses the heterodimensional gate technology and achieved a record room temperature transconductance. The novel 2-D MESFET also uses the novel gate technology, to eliminate the narrow channel effect and drain-induced barrier lowering in devices scaled to sub-half micron channel widths. The 2-D MESFET was used to demonstrate a DCFL inverter gate having a noise margin of 0.26 V at 0.8 V supply voltage and voltage gain of 10. Finally, a power-

delay product of less than 0.1 fJ was predicted for a 3-stage 2-D MESFET DCFL ring oscillator.

ACKNOWLEDGEMENTS

This research was supported by the Office of Naval Research under Contracts N00014-90-J-4006 and N00014-94-C-0260, by the Wright Patterson Air Force Laboratory under contract F33615-95-C-1679, and by the Research Council of Norway.

REFERENCES

- [1] W.C.B. Peatman, T.W. Crowe, and M. Shur, "A novel Schottky/2-DEG diode for millimeter and submillimeter wave multiplier applications," *IEEE Elect. Dev. Lett.* 13, 11 (1992).
- [2] W.C.B. Peatman, B. Gelmont, W.J. Grimm, H. Park, M. Shur, E.R. Brown, and M.J. Rooks, "Heterodimensional Schottky-Gate Devices," *Proc. Int'l. Semic. Dev. Res. Symp.*, Charlottesville, VA, pp. 427-430, December 1993.
- [3] W.C.B. Peatman, T.W. Crowe, M. Shur, and B. Gelmont, "A Schottky/2-DEG Schottky Diode for Millimeter and Submillimeter Wave Multiplier Applications," in *3rd Int'l. Symp. Space THz Tech.*, Ann Arbor, MI, March 1992.
- [4] B. Gelmont, W. Peatman, and M. Shur, "Heterodimensional Schottky metal-two dimensional electron gas interfaces," *J. Vac. Sci. Tech. B* 11, 1670, (1993).
- [5] P.J. Koh, W.C.B. Peatman and T.W. Crowe, "Millimeter Wave Tripler Evaluation of a Metal/2-DEG Schottky Diodes Varactor," *IEEE Microwave Guided Wave Lett.* Vol. 5, No. 2, pp. 73-75, March 1995.
- [6] W.C.B. Peatman, E.R. Brown, M.J. Rooks, P. Maki, W.J. Grimm, and M. Shur, "Novel Resonant Tunneling Transistor with High Transconductance at Room Temperature," *IEEE Elect. Dev. Lett.*, Vol. 15, No. 7, pp. 236-238, July 1994.
- [7] C.T.M. Chang, Introduction to Semiconductor Technology: GaAs and Related Compounds, C.T. Wang (Editor), pp. 360, John Wiley & Sons, New York, 1990.
- [8] W.C.B. Peatman, H. Park and M. Shur, "Two-Dimensional Metal-Semiconductor Field Effect Transistor for Ultra Low Power Circuit Applications," *IEEE Elect. Dev. Lett.*, Vol. 15, No. 7, pp. 245-247, July 1994.
- [9] W.C.B. Peatman, M. Hurt, H. Park, T. Ytterdal, R. Tsai, and M. Shur, "Narrow Channel 2-D MESFET for Low Power Electronics," To be published, *IEEE Trans. Elect. Dev.*, Vol. 42, No. 9, Sept. 1995.
- [10] W.C.B. Peatman et al, Submitted to *IEEE Elect. Dev. Lett.*, June 1995.
- [11] K. Lee, M. Shur, T.A. Fjeldly and T. Ytterdal, Semiconductor Device Modeling for VLSI, Prentice Hall, p. 450, New Jersey, 1993.

ANALYSIS OF THE "HOT" ELECTRON REGIME OF OPERATION IN HETEROSTRUCTURE FIELD EFFECT TRANSISTORS

*E. Martinez^{**†}, M. Shur[†], and F. Schuermeyer^{*}*

^{*} Solid State Electronic Technology Directorate, Wright Laboratory
Wright-Patterson AFB, OH 45433-7331

[†] Dept. of Electrical Engineering, University of Virginia
Charlottesville, VA 22903-2442

I. Introduction

For years, circuit simulators have used idealistic models to describe the device characteristics ignoring the non-ideal behaviors such as the contribution of "warm" and "hot" electrons to the gate currents in Heterostructure Field Effect Transistors (HFETs)[1]. These non-ideal behaviors may affect the gate-switching characteristics introducing faults in high performance circuits. The purpose of this paper is to present experimental gate-current data, over a wide temperature range, and to introduce for the first time an analytical model that describes the contribution of heated electrons to the increase in gate current with drain-to-source voltage. The experimental data have been obtained at temperatures ranging from 198 K to 450 K from Heterostructure Insulated Gate Field Effect Transistors (HIGFETs) fabricated using $\text{Al}_{0.75}\text{Ga}_{0.25}\text{As}/\text{In}_{0.2}\text{Ga}_{0.8}\text{As}/\text{GaAs}$ and $\text{Al}_{0.48}\text{In}_{0.52}\text{As}/\text{In}_{0.53}\text{Ga}_{0.47}\text{As}/\text{InP}$. This regime of operation should be considered in the design of Heterostructure FETs intended for low power, high density, applications as well as in devices operated in the Charge Injection Transistor (CHINT-like) mode.

II. Experimental Observations

Figure 1 shows the experimental gate current characteristics as a function of the drain-to-source voltage for a $1.4 \times 10 \mu\text{m}^2$ HFET at room temperature. Three regions of importance can be identified when the gate current is observed as a function of drain-to-source voltage. The first region corresponds to low V_{ds} , where the electric field parallel to the heterointerface, F_{ds} , is linearly dependent on position, and the electron temperature, T_e , is nearly uniform everywhere in the channel,

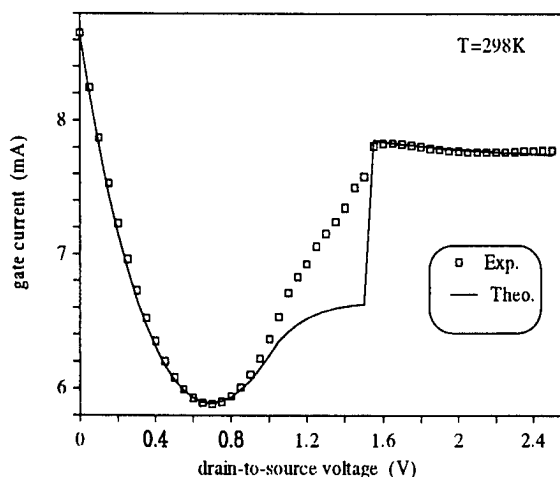


Figure 1 Gate current characteristics as a function of drain-to-source voltage for a $1.4 \times 10 \mu\text{m}^2$.

remaining close to the lattice temperature. In this case, the gate current is a contribution of the gate-to-source and the gate-to-drain current components, with the gate-to-source current component nearly independent of the parallel electric field in the channel.

The experimental data suggest that at low drain-to-source voltages, the electron contribution, from the drain to the gate current, decreases with a reverse in the drain-to-gate potential. A further increase in drain voltage increases the electron energy distribution causing the 2-D electrons to

accelerate in the channel, increasing their kinetic energy and therefore, contributing to a sharp increase in the gate current. Finally, the gate current saturates at high drain-to-source voltages. These abrupt changes in the gate current also affect the drain-current characteristics of the device and can not be reproduced with current device models [2,3,4]. Similar qualitative behavior is observed in both GaAs- and InP-based HFETs over a wide temperature range.

Figure 2 shows a qualitative description of the electric field, electron temperature, and barrier potential for each of the three regions described above. At very high drain-to-source voltages, the barrier increases near the drain, shifting the scattering distribution toward the middle region of

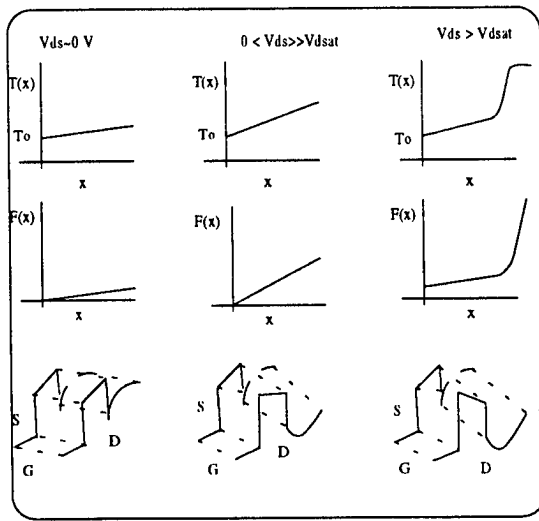


Figure 2. Qualitative description of the electron temperature, electric field, and the potential barrier under the gate for an HFET operated in the hot electron regime.

the channel. In that case, the contribution of hot electrons to the gate current decreases in the drain side of the channel but is maintained in the source-side and at the mid channel region. Therefore, the contribution of "superheated" electrons decreases with an increase in the drain-to-source voltages due to the increase in the barrier potential [5].

III. Theoretical Models

In order to understand the "hot" electron regime of operation in HFETs, we were motivated to develop an analytical model that can describe the dependence of the gate current on the drain-to-source voltage. This model is based in both the

Charge Control Model for FETs, and the CHINT-like theory of operation and real-space electron transfer in which the saturation of the gate current at high drain-to-source voltages is explained based on the rapid drop in the effective electron-energy relaxation time caused by the real-space transfer of hot electrons [6,7,8]. In our model, electrons are accelerated by the electric field parallel to the heterointerface. During the acceleration process, non-linear electric potential and electron temperature distributions are established in the channel area under the gate. These distributions are strongly dependent on the gate and drain-to-source voltages.

For drain-to-source voltages below the saturation voltage ($V_{ds} < V_{sat}$), the electric potential and the electric field distributions are expressed as quadratic and linear functions of position. Then, the electron temperature can also be estimated as a function of position and is given as

$$T_e(x) = T_o + \left(\frac{2q}{3K_b} \right) \tau_e(x) \mu_n(x) F(x)^2 \quad (1)$$

where T_o is the lattice temperature, q is the electron charge, K_b is the Boltzman constant, $\tau_e(x)$ is the energy relaxation time as a function of position, and $\mu_n(x)$ is the mobility as a function of position).

For drain-to-source voltages above saturation ($V_{ds} \geq V_{sat}$), the channel is divided in two separate regions, sub-critical and critical regions. The critical region under the gate, is where most of the electron transfer occurs. The position of the critical region is estimated as

$$x_{crit} = L_g - \lambda \ln \left(\frac{V_{ds} - V_{sat} + F_s \lambda}{F_s \lambda} \right) \quad (2)$$

where V_{sat} is the saturation voltage, L_g is the gate length, F_s is the saturation field, and λ is a fitting parameter dependent on the gate length.

In the subcritical region, the potential and electric field are given as

$$V(x) = V_{gt} - \sqrt{V_{gt}^2 - \frac{2I_{dssat}x}{\mu_n W_g C_d} \frac{x_{crit}}{L_g}} \quad (3)$$

and

$$F(x) = \frac{I_{dssat}}{\frac{\mu_n W_g C_i}{L_g} x_{crit} \sqrt{V_{gt}^2 - \frac{2 I_{dssat} x}{\frac{\mu_n W_g C_i}{L_g} x_{crit}}}} \quad (4)$$

where x_{crit} is estimated from equation 2, and I_{dssat} is the total drain saturation current given as

$$I_{dssat} = C_i F_s^2 L_g x_{crit} \left[\sqrt{1 + \left(\frac{V_{gt}}{F_s x_{crit}} \right)^2} - 1 \right] \quad (5)$$

where W_g is the gate width, and C_i is the insulator capacitance.

In the critical region, (for $x \geq x_{crit}$), the potential and the electric field are given as

$$V(x) = V_{gt} + F_s x_{crit} - \sqrt{V_{gt}^2 + (F_s x_{crit})^2} + F_s \lambda \left[e^{\left(\frac{x - x_{crit}}{\lambda} \right)} - 1 \right] \quad (6)$$

and

$$F(x) = F_s e^{\left(\frac{x - x_{crit}}{\lambda} \right)} \quad (7)$$

For ($V_{ds} > V_{sat}$), the electron temperature is estimated as

$$T_e(x) = T_o + \left(\frac{2q}{3K_b} \right) \tau_e(x) \mu_n(x) F(x) F_s \quad (8)$$

Therefore, the gate current as a function of drain-to-source voltage can be estimated by adding the contribution of scattered "hot" electrons under the gate and its given as

$$I_g = A \cdot T_o^2 W_g \int_0^{L_g} [A(x) * B(x) - C(x)] dx \quad (9)$$

where

$$A(x) = \exp\left(\frac{V_{gs} - V(x)}{\eta K_b T_e(x)}\right)$$

$$B(x) = \exp\left(\frac{-\Delta E_c}{K_b T_o(x)}\right)$$

$$C(x) = \exp\left(\frac{-\Delta E_c}{K_b T_o}\right)$$

where V_{gs} is the gate-to-source voltage, $V(x)$ is the potential as a function of position, K_b is the Boltzman constant, ΔE_c is the conduction band discontinuity, $T_e(x)$ is the electron temperature as a function of position, T_o is the lattice temperature, and η is the ideality factor of the potential barrier.

IV. Results

The results of our models were compared with experimental data. Figure 1 shows the room temperature gate current characteristics as a function of drain-to-source voltage for a $1.4 \times 10 \mu m^2$ $Al_{0.75}Ga_{0.25}As/In_2Ga_{0.8}As/GaAs$. In this figure, the gate voltage was measured at a constant gate-to-source voltage of 2.7 volts. As shown in this figure, our model is able to reproduce the three

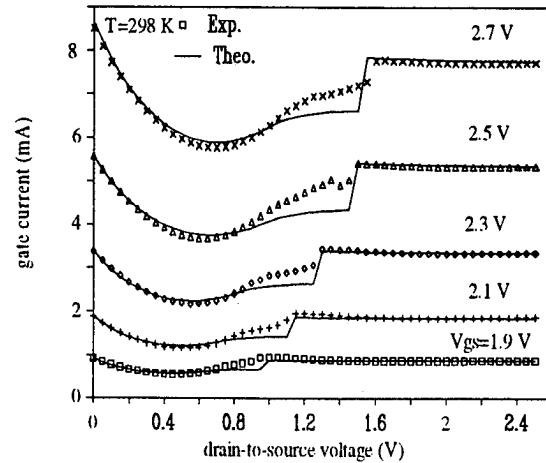


Figure 3. Comparison between the experimental and theoretical "hot" electron current as a function of gate voltage for a $1.4 \times 10 \mu m^2$.

regions observed in the experimental data. In the linear region ($V_{ds} \leq 0.85$ V), the experimental and theoretical data correlate well. The same results are obtained in the saturation region, ($V_{ds} > 1.5$ V). In the transition region, our model usually fails to describe the gate current accurately. The reason for this discrepancy between the theoretical and experimental data is due to the number of competing mechanisms in this transition region which are not accounted for in our model. A more sophisticated simulation, such as Monte Carlo, would be more accurately to describe the gate current in this region.

Similar results are obtained when the experimental and theoretical data as a function of gate-to-source voltage are compared. Figure 3 shows the family of curves as a function of gate-to-source voltage for the same device. As shown in

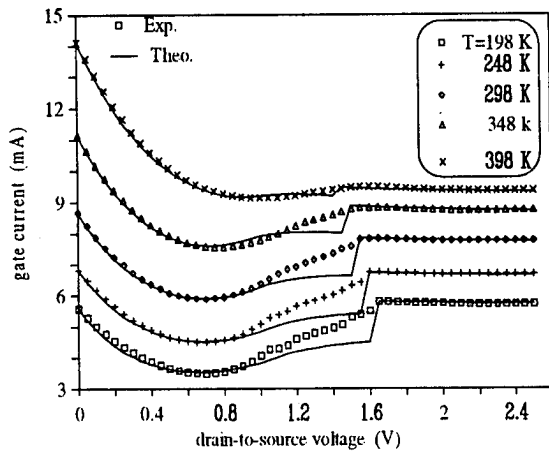


Figure 4. Comparison between the experimental and theoretical gate current as a function of temperature for the same device.

this figure, a good agreement between the experimental and theoretical data is maintained in the linear and saturation region over the entire range of gate voltages, in which the hot-electron effects are predominant.

As previously mentioned, modeling of the hot-electron gate current was also performed for a wide temperature range, and the theoretical results were also compared with the experimental data. Figure 4 shows the gate current as a function of drain-to-source voltage for temperatures ranging from 198 K to 398 K. As shown in this figure, good agreement between the experimental and

theoretical results was obtained over the entire temperature range.

V. Conclusions

An analytical model to describe the hot-electron regime of operation has been presented. This model was built on a Charge Control Model and a CHINT-like model in which the electron temperature is limited by the intervalley transfer and real-space transfer of electrons. Good agreement between the models and the experimental data was found over a wide temperature range, from 198 K to 398 K.

Understanding of these complex mechanisms is important to effectively reduce the gate leakage current in Complementary HFETs.

VI. References

- [1] E. Martinez, M. Shur, and F. Schuermeier, "Heterostructure Insulated Gate Field Effect Transistors Operated in the Hot Electron Regime", *IEEE Trans. Elec. Devices*, Vol. 41, No. 5, pp 854-856 (1994)
- [2] J. Laskar, J. Bigelow, J. Leburton, J. Kolodzey, "Experimental and Theoretical Investigation of the DC and High Frequency Characteristics of the Negative Differential Resistance in Pseudomorphic AlGaAs/InGaAs/GaAs MODFETs", *IEEE Trans. Elec. Devices*, Vol. 39, No. 2, pp 257-263 (1992)
- [3] M. Shur, D. Arch, R. Daniels, and J. Abrokwhah, "New Negative Resistance Regime of Heterostructure Insulated Gate Field Effect Transistors (HIGFET) Operation", *IEEE Electron Dev. Lett.*, Vol EDL-7, No. 2, pp 78-80 (1986)
- [4] K. Maezawa, and T. Mizutani, "High Frequency Characteristics of Charge Injection Transistor-mode Operation in AlGaAs/InGaAs/GaAs MESFETs", *Jap. J. Appl. Physics*, 30, No. 6, pp 1190-1193 (1991)
- [5] F. Schuermeier, M. Shur, E. Martinez, and C. Cerny, "Gate Current in HFETs Contribution by "Warm" Electrons", *Material Science and Engineering B* 28, pp 264-267 (1994)
- [6] M. Shur, *Physics of Semiconductor Devices*, Prentice Hall, pp 361-363 (1990)
- [7] A. Katalsky, and S. Luryi, "Novel Real-space Hot Electron Transfer Devices", *IEEE Electron Dev. Lett.*, EDL-9, pp 334-336 (1983)
- [8] M. Keever, H. Schichijo, K. Hess, S. Barnerjee, L. Witkowski, H. Morkoc, and B. Streetman, "Measurements of Hot-electron Conduction and Real-space Transfer in GaAs/AlGaAs Heterojunction Layers", *Appl. Phys. Lett.*, Vol. 38, pp 36 (1981)

60 GHz MMIC Mixer Using a Dual-Gate PM HEMT

R. Allam, C. Kolanowski, D. Langrez, P. Bourne, J.C. De Jaeger, Y. Crosnier and G. Salmer*

Institut d'Electronique et de Microélectronique du Nord
U.M.R. C.N.R.S. 9929 - Département Hyperfréquences et Semiconducteurs
Université Lille 1
Avenue Poincaré - B.P. 69
59652 VILLENEUVE D'ASCQ CEDEX - France

* Thomson TCS
B.P. 46, Route Départementale 128
91401 ORSAY CEDEX - France
Rachid.Allam@IEMN.Univ-Lille1.fr

2. MODELING OF THE DEVICE

ABSTRACT

A Dual-Gate PM HFET monolithic mixer has been developed, fabricated and measured at 60 GHz. This circuit uses a 0.15 μm gate length AlGaAs/InGaAs/GaAs pseudomorphic HEMT technology. The design optimization is performed from a complete extraction method of the dual-gate device and a non-linear electrical modeling. The mixer has a maximum conversion gain of -5 dB, a minimum noise figure of 11 dB at 5 dBm LO power, an output IMP3 of -2 dBm and a LO to RF isolation close to 35 dB.

1. INTRODUCTION

The fabrication of GaAs MMIC, for applications in 50-75 GHz frequency range has been developed these last years for linear and non-linear devices. In this perspective, we have developed a microstrip AlGaAs/InGaAs/GaAs dual-gate HEMT mixer. The main advantage of the dual-gate device is the suppression of the external wave guide coupler, required in single gate mixer, for the combination of LO and RF signals [1]. Furthermore, due to the natural isolation between the two gates, LO and RF signals can be combined with a good isolation. The first results of this MMIC shown in this paper give a conversion gain close to -5 dB for $F_{RF} = 59.8$ GHz and $F_{LO} = 54$ GHz with a flat bandwidth in the 58.5 - 62 GHz frequency range. The output third order intercept point (IMP3) is about -2 dBm. These results constitute a promising performance for a monolithic dual-gate PM HFET mixer operating at V band.

The dual-gate mixer design needs a good knowledge of the active device behaviour. For this aim, due to its complexity, a specific modeling has been developed in order to determine, in particular, the equivalent scheme of the transistor which can be considered as two equivalent single gate devices in cascode configuration [2]. The method is divided in two main sequences where the access and intrinsic elements are successively determined [3]. For this extraction, on wafer three-ports S parameter measurements are performed using a specific test bench developed in our laboratory. From this method it is possible to obtain with a good accuracy the main parameter evolutions versus the gate biases when the equivalent transistors are operating in linear or saturated regimes. Then, from this determination a dual-gate nonlinear electrical model has been performed for the mixer design.

3. CIRCUIT DESIGN AND FABRICATION

The mixer operates under low-noise conditions (LNM) [4]. In this configuration, the first equivalent transistor is linear and the second is saturated. Mixing occurs in the first transistor and the second one is working as an IF amplifier. The RF signal is applied on the gate 1 and the LO signal is applied on the gate 2. RF and LO matching are assumed by open stubs. The second gate is grounded, using a resonant circuit, in order to obtain an IF common gate amplifier. Two open stubs achieve LO and RF short-circuits at the drain. IF matching consists of a combination of a lumped spiral inductor and a capacitor. This circuit provides a low-pass filter and a real impedance at IF frequency. Gate bias

circuits using $\lambda/4$ lines, include $50\ \Omega$ resistances for the stabilization.

The MMIC was fabricated by THOMSON TCS Foundry using the $0.15\ \mu\text{m}$ gate length pseudomorphic AlGaAs/InGaAs/GaAs HEMT technology with three finger of $25\ \mu\text{m}$. The PM HFET is a one δ -doped layer device of $5 \times 10^{12}\ \text{cm}^{-2}$ with a InGaAs well of $120\ \text{\AA}$ depth. A photograph of the fabricated chip is shown in figure 1.

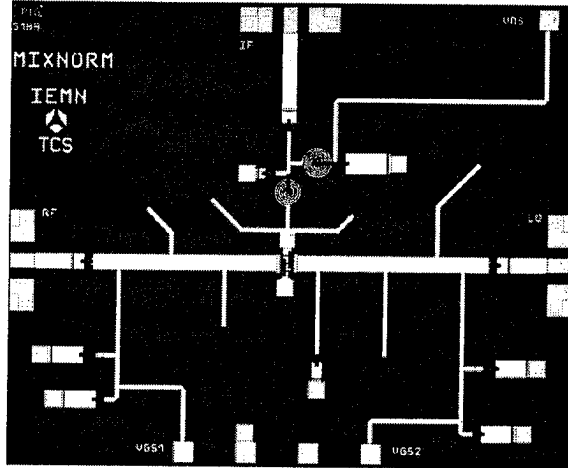


Fig. 1 : Photograph of dual-gate PM HEMT mixer

3. PERFORMANCE

The monolithic chip is mounted in a 50-75 GHz test fixture which has been developed in our laboratory [5] and that we have modified to include a specific insert with a third access for the IF output. Its characteristics are insertion losses lower than $0.75\ \text{dB}$ and return losses lower than $-20\ \text{dB}$ at each port.

The dual gate mixer optimization is very complex due to the two gate biases influence. The criteria chosen is the conversion gain. Figures 2 and 3 represent its dependance versus the gate biases V_{g1s} and V_{g2s} . It can be noted that the optimum condition is obtained for $0 \leq V_{g1s} \leq 0.15\ \text{V}$ and $0 \leq V_{g2s} \leq 0.2\ \text{V}$.

But the conversion gain is not the only parameter to consider. In a second step, a good compromise has to be found between the isolations RF to LO and LO to RF associated with a good matching impedance on the two input ports.

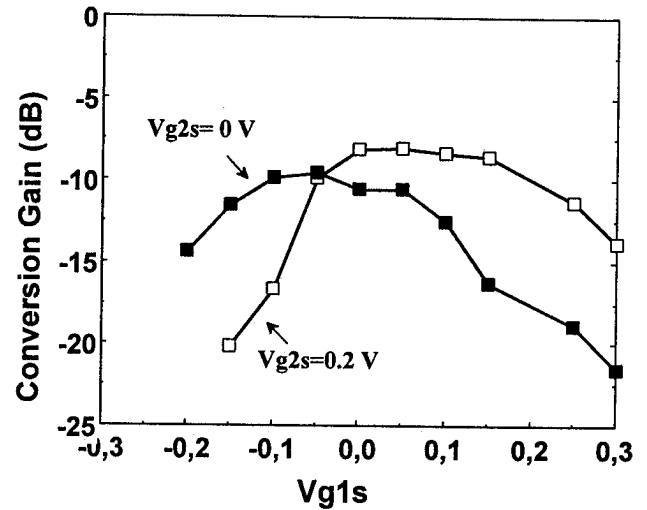


Fig. 2 : Dependence of the conversion gain versus V_{g1s} ($R_F=62.5\ \text{GHz}$; $L_O=56.7\ \text{GHz}$)

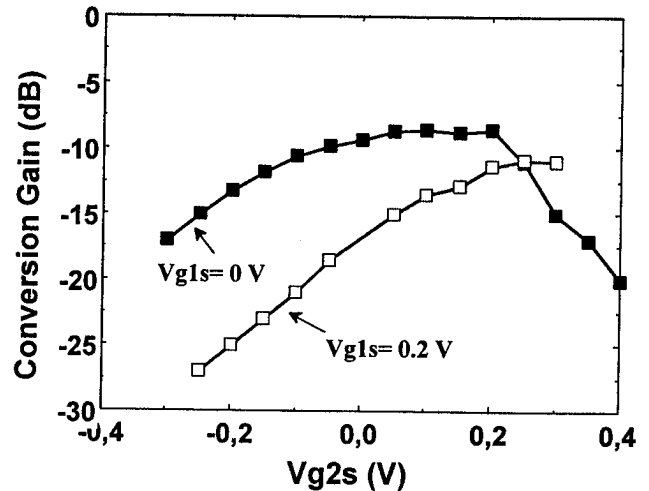


Fig. 3 : Dependence of the conversion gain versus V_{g2s} ($R_F=62.5\ \text{GHz}$; $L_O=56.7\ \text{GHz}$)

The optimum conditions are shown in figure 4 by the S_{ij} mixer parameters analysis. It can be noted that in this case, the LO to RF isolation is close to $30\ \text{dB}$ and the RF to LO isolation is better than $35\ \text{dB}$. These results are confirmed with measurement made with a LO signal pumped. The input return losses are about $15\ \text{dB}$ on the RF port and $6\ \text{dB}$ on the LO port

In this case, the LNM gate biases conditions are $V_{g1s} = 0\ \text{V}$ and $V_{g2s} = 0.15\ \text{V}$ and the drain bias is set to $3\ \text{V}$. Figure 5 gives the conversion gain evolution versus the LO power where $F_{RF} = 59.8\ \text{GHz}$, $F_{LO} = 54\ \text{GHz}$ and $P_{RF} = -23.5\ \text{dBm}$. A maximum conversion gain close to $-5\ \text{dB}$ is obtained with LO drive of $5\ \text{dBm}$.

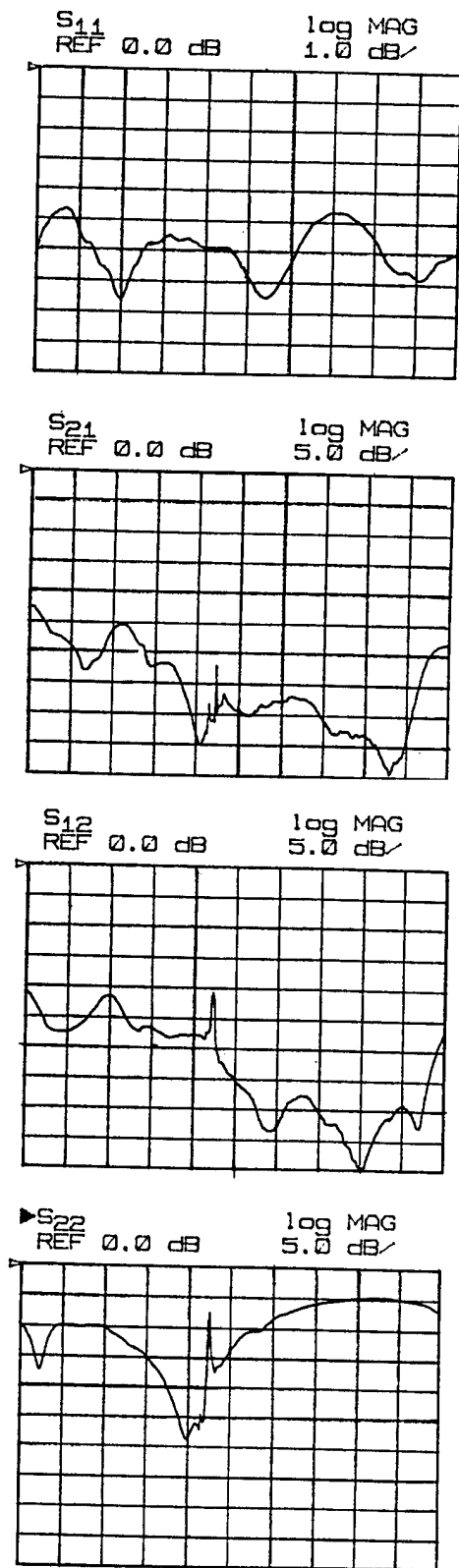


Fig. 4 : S_{ij} parameters measurement
(between 50 GHz and 75 GHz step 2.5 GHz)

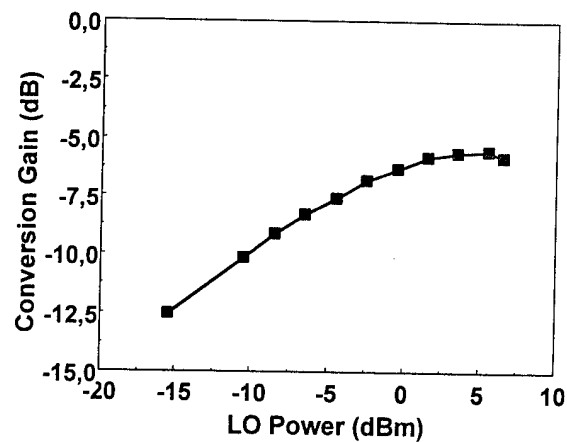


Fig. 5 : LO power dependance of conversion gain

For this LO power and $F_{LO} = 54$ GHz figure 6 shows the evolution of the conversion gain versus RF frequency. A flat bandwidth is obtained from 58.5 to 62 GHz.

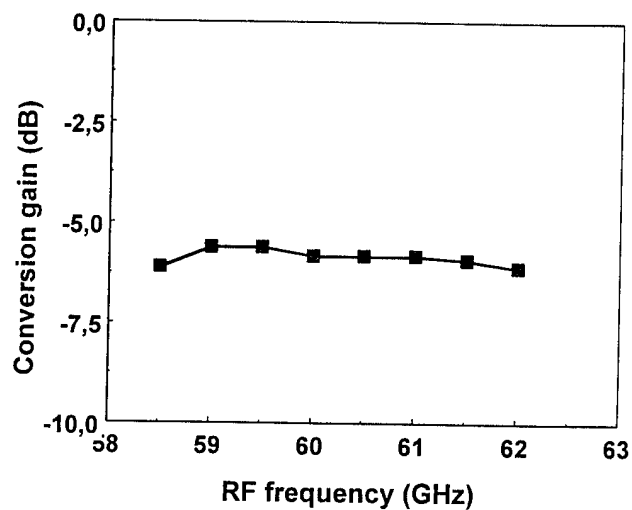


Fig. 6 : Conversion gain versus RF frequency

Intermodulation measurements are also made. The evolution of IMP3 versus the LO power is represented in Figure 7. A maximum value of -2 dBm is obtained at the output of the mixer.

CONCLUSION

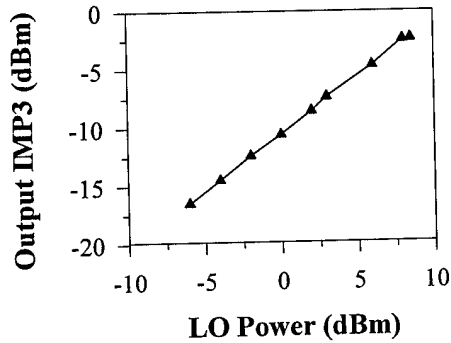


Fig. 7 : Output IMP3 versus LO power

The dual gate mixer noise figure is represented in figure 8 versus LO power. A minimum value close to 11 dB is observed.

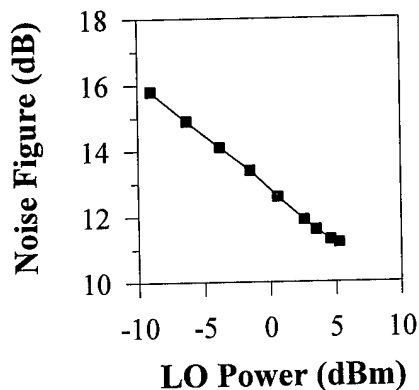


Fig. 8 : Noise Figure versus LO power

Performance of dual-gate microstrip PM HFET monolithic mixer has been reported in this paper. Operating under Low Noise Mixer configuration, this circuit exhibits -5 dB conversion gain with 5 dBm LO power from 58.5 to 60.5 GHz and an output third order intercept point of -2 dBm. This dual-gate device makes possible to obtain good isolations between LO and RF signals avoiding any external circuit which constitutes its main advantage. These results confirm the great interest of the pseudomorphic AlGaAs/GaInAs on GaAs based MMIC for V band mixer applications.

ACKNOWLEDGEMENT

The authors would like to thank J. Favre, C. Dourlens and E. Aubame, for the MMIC fabrication and helpful discussions, G. Dambrine and E. Delos for their support during the MMIC characterization. This work is supported by European Community on ESPRIT 6016 CLASSIC contract.

REFERENCES

- [1] Y. Know, D. Pavlidis, M. Tutt, G.I. Ng and T. Brock, "W-band Monolithic Mixer using InAlAs/InGaAs HEMT", IEEE GaAs IC Symposium 1990.
- [2] T. Furutsuka, M. Ogawa and N. Kawamura : « GaAs Dual Gate MESFET's » ; IEEE Trans. On Elect. Devices, Vol. ED-25, pp 580-586, June 1978.
- [3] D. Langrez, E. Delos, G. Salmer, "Modelling of 0.15 μ m Dual-Gate PM HEMTs by using experimental extraction", 24th European Microwave Conference, Cannes, Sept. 1994.
- [4] C. Tsironis, R. Meierer and R. Stahlmann, "Dual-Gate MESFET Mixers", IEEE Trans. Microwave Theory Tech, Vol. MMT-32, pp. 248-255, March 1984.
- [5] J.F. Kruck, G. Dambrine, A. Cappy, "Characterizations of Field Effect Devices in V band", 23th European Microwave Conference, Madrid, Sept. 1993.

Low-Frequency Noise performances of SiO₂/InP Metal-Insulator-Semiconductor Field-Effect Transistor

Y. K. Su, S. C. Shei, K. J. Gan, and M. Yokoyama

Department of Electrical Engineering
National Cheng Kung University
Tainan, Taiwan, R. O. C.

ABSTRACT

Low-frequency noise in SiO₂/InP metal-insulator-semiconductor field-effect transistor (MISFET) is studied systematically. In ohmic regime, the drain noise power density is proportional to the squared drain-source voltage, as $1/f$ resistor fluctuations. Hooge's constant α_H of 4×10^{-7} is obtained. The $1/f$ noise of the device attributed to number-fluctuation, mobility-fluctuation, and to trapping/detrapping in space-charge region and oxide/semiconductor interface are examined under various bias conditions. Moreover, a generation-recombination (G-R) noise corresponding to a deep energy level of 0.4 eV is observed.

1. INTRODUCTION

The InP metal-insulator-semiconductor field-effect transistors (MISFETs) are promising for the use in high-power devices, high-speed devices, digital circuits, and monolithic optoelectronic circuits due to its high saturation drift velocity, low ionization coefficient, and high mobility. However, the performance of MISFETs, critically depends upon the quality of MIS gate interface. To date, the best results for the InP MIS structure have been achieved with a deposited dielectric layer, silicon dioxide (SiO₂) has been the most widely used gate dielectric in InP MISFETs, because of its low leakage current, high breakdown field, and moderate interface state density.

Low-frequency spectroscopy technique is a very powerful tool to investigate the theoretical and practical information about the material and the devices [1]. Although, for high frequency or microwave linear applications we do not worry about the noise at low frequency, the low frequency noise does influence the performance of microwave nonlinear applications like diode, or FET mixers and oscillators [2]. Since low-frequency noise induces phase noise or frequency modulation (F.M.) and amplitude modulation (A.M.) noise microwave circuits, it is important to try to reduce the low-frequency noise of these devices by investigating its origins and mechanisms. Several low-frequency noise properties associated with these devices have been studied. Duh et al. studied the f^{-1} drain current noise in modulation-doped FETs (MODFETs) under a gate-biased condition [3]. Loreck et al. showed the generation-recombination (G-R) noise arising from the deep levels in AlGaAs [1], Zhang et

al. the burst noise in double-hetero bipolar transistors [4] and Liu et al. the gate f^{-1} noise in AlGaAs/GaAs MODFETs [5] and InGaAs quantum-well MODFETs [6]. However, to our knowledge, there is no investigations for the low-frequency noise performances of SiO₂/InP MISFET structure. In this letter, we have systematically studied the low-frequency drain-voltage noise in SiO₂/InP MISFET under various bias conditions for the purpose of determining the mechanism of the noise.

2. EXPERIMENTS

The n-channel depletion-mode SiO₂/InP MISFET structure is sketched in Fig. 1 and its transconductance is about 63 mS/mm for a 2x200 μ m gate. The gate oxide was deposited by direct photo-enhanced chemical vapor deposition (CVD) under the irradiation of deuterium (D₂) lamp at low-temperature range (<250 °C). The reactant gases were silane (SiH₄) and oxygen (O₂). The detailed description of process and a full summary of SiO₂/InP MISFET characteristics have been published elsewhere [7]. For measurement purposes, selected device chips were mounted on TO-5 headers and bounded with a thermo-compression ball bonder. The noise was measured in a brass-shielded box at room temperature, and a bias d.c. current was supplied by batteries through a 100-K resistor. The voltage noise across the current terminals was amplified by a low-noise preamplifier, and the outputs were fed to an HP 3652A spectrum analyzer. The analyzer was controlled automatically by a personal computer (PC). The smallest detectable circuit noise of the setup was about -172 dBV/Hz^{1/2} between 10 Hz and 100 kHz. The spectrum analyzer averaged 2⁶ noise spectra of every decade, and the computer further averaged the data and subtracted the a.c. line noise.

3. RESULTS and DISCUSSION

The drain noise power density of SiO₂/InP MISFET were measured by biasing the device in ohmic region. The measured noise spectra of the device with 2x200 μ m gate for a variety of drain voltages from 0.1 to 0.6 V and a fixed gate voltage of 0 V are shown in Fig. 1. We observed the noise spectrum density $S_{v_d}(f)$ of MISFET decreases with frequency at the rate of $f^{-0.8}$ below 60 Hz, and f^{-2} above it. This is typical of f^{-1} noise superimposed on the G-R noise. The turnover frequency of 60 Hz is observed. This has been previously reported for GaAs

MESFET [8,9]. Furthermore, the noise power density at frequencies lower than 1 kHz is at least ten times larger than the thermal noise and the background noise of the system. Figure 2 shows $S_{V_d}(f)$ versus drain voltage V_d at a frequency of 40 Hz calculated from Fig. 1. The noise spectra density has a squared voltage (V_d^2) dependence expected of a resistive mobility-fluctuation mechanism. The mobility-fluctuation noise is caused by interaction of electrons with slowly fluctuating longitudinal acoustical-phonon populations [10]. Already in 1969, Hooge had postulated [10], based on data obtained for many different materials, that

$$\frac{S_V(f)}{V_d^2} = \frac{\alpha_H}{fN}$$

where V_d is the voltage across the device, f and N are the frequency and the total carrier number, respectively, and α_H is the Hooge noise parameter. Recent measurements on a GaAs MESFET showed the value of 5.6×10^{-5} [11], and those on a quarter-micron GaAs Hall device a value of $\alpha_H = 4.5 \times 10^{-6}$ [12]. The proportionality constant α_H become thus a parameter to give the magnitude of the f^{-1} noise levels. Fitting the noise curve, a new empirical formula for f^{-1} was then proposed based on these experiments with the value α_H of 4×10^{-7} .

Fig. 3(a) and 3(b) show the noise power spectra versus frequency for various negative and positive gate voltages, respectively, in the drain voltage of 0.05 V. These spectra in Fig. 3 present pure f^{-1} noise without the f^{-2} in intermediate frequency as shown in Fig. 1. The noise power density versus gate voltage for the drain voltages of 0.05 V and 0.5 V, respectively, at frequency of 40 Hz is plotted in Fig. 4. For negative gate voltage, at low-field region ($V_d = 0.05$ V), the noise increases with the increase of the gate voltages. It indicates that the depletion layer near the gate electrode plays an important role in noise behaviour. The larger depletion layer results in the layer noise generation. Sah explained by the random fluctuations in the occupancy of deep traps in the depletion region [13]. For positive gate voltage, the noise increases with the increase of gate voltages as a result of trapping of carriers by oxide traps and the interface surface states as found for MOSFET [14]. Our data of $S_{V_d}(f)$ agrees well with the carrier density fluctuation model [15]. At high field region ($V_d = 0.5$ V) as shown in Fig. 4, however, there is no obvious variation in drain noise power density throughout the gate voltages. Because the mobility-fluctuation $1/f$ noise in high field field predominated over the $1/f$ noise attributed to trapping of the depletion region and interface surface states.

4. CONCLUSION

In conclusion, low-frequency noise measurements were performed in ohmic region of SiO_2/InP MISFET for various test conditions. The noise power density is proportional to V_d^2 , as $1/f$ resistor fluctuations. Hooge's constant α_H of 4×10^{-7} is obtained. The origins and

mechanisms of noise in MISFET were investigated and analyzed.

ACKNOWLEDGEMENT

The authors would like to express their thanks to Dr. J. Gong for his kindly assistance in the noise measurements. This work was supported by the National Science Council, Republic of China, under Contract: NSC 84-2215-E-006-013.

REFERENCES

- [1] L. Loreck, H. Dambkes, K. Heime, K. Plog and G. Weimann, "Deep-level analysis in (AlGa)As-GaAs 2-D electron gas devices by means of low-frequency noise measurement," IEEE Electron Device Lett. vol. EDL-5, pp. 9-11, 1984.
- [2] J. Graffeuil et al., "Comparative study of phase in HEMT and MESFET microwave oscillators," in IEEE MTT-S Int. Microwave Symp. Tech. Dig., vol. 2, pp. 557-560, 1987.
- [3] K. H. Duh, A. van der Ziel and H. Morkoc, "1/f noise in modulation-doped field-effect transistors," IEEE Electron Device Lett. EDL-4, pp. 12-13, 1983.
- [4] D. V. Zhang, A. van der Ziel, K. H. Duh and H. Morkoc, "Burst and low-frequency generation-recombination noise in double-heterojunction bipolar transistor," IEEE Electron Device Lett., vol. EDL-5, pp. 277-279, 1984.
- [5] S. J. Liu, M. B. Das, W. F. Kopp and H. Morkoc, "Noise behavior of 1- μm gate-length modulation-doped FETs from 10^2 and 10^8 Hz," IEEE Electron Device Lett., vol. EDL-6, pp. 453-455, 1985.
- [6] S. J. Liu, M. B. Das, C. P. Peng, J. Klem, T. S. Henderson, W. F. Kopp and H. Morkoc, "Low-noise behavior of InGaAs quantum-well-structured modulation-doped FETs from 10^2 to 10^8 Hz," IEEE Trans. Electron Dev., vol. ED-33, pp. 576-581, 1986.
- [7] S. C. Shei, Y. K. Su, C. J. Hwang, and M. Yokoyama, "SiO₂/InP structure prepared by direct photo-chemical vapor deposition using deuterium lamp and its applications to metal-oxide-semiconductor field-effect transistor," Jpn. J. Appl. Phys., vol. 34, pp. 476-481, 1995.
- [8] H. Tacano, Y. Sugiyuma, T. Taguchi and H. Soga, "Low-frequency noise GaAs layers grown by molecular beam epitaxy," Solid-State Electron., vol. 31, pp. 1215-1219, 1988.
- [9] H. Tacano and Y. Sugiyuma, "Comparison of 1/f noise of AlGaAs/GaAs HEMT and GaAs MESFETs," Solid-State Electron., vol. 34, pp. 1049-1053, 1991.
- [10] A. van der Ziel, Noise in Solid State Devices and Circuits, John Wiley & Sons, 1986, NY, Chapter 8.
- [11] K. H. Duh and A. van der Ziel, "Hooge parameters for various FET structures," IEEE Trans. Electron Dev., vol. ED-32, pp. 662-666, 1985.
- [12] A. van der Ziel, P. H. Handel and K. H. Duh, "Hooge parameters of Solid-state devices," IEEE Trans. Electron Dev., vol. ED-32, pp. 667-671, 1985.
- [13] Z. Celic and T. Y. Hsiang, "Study of 1/f noise in N-

MOSFET's: linear region," IEEE Trans. Electron Dev., vol.ED-32, pp.2797-2801, 1985.

- [14] C. T. Sah, "Theory of low-frequency generation noise in junction-gate field-effect transistors," Proc. IEEE, vol.52, pp.795-813, 1964.
- [15] P. A. Folkers, "Characteristics and mechanism of $1/f$ noise GaAs Schottky barrier field-effect transistors," Appl. Phys. Lett., vol.48, pp.344-346, 1986.

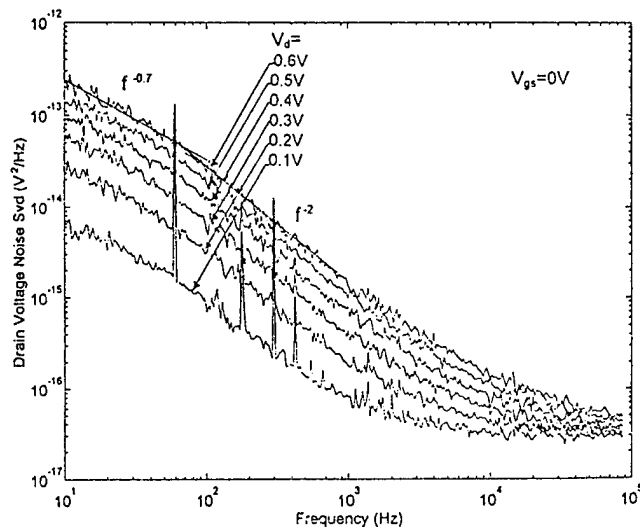


Fig.1 The noise spectra $S_{vd}(f)$ of SiO_2/InP MISFET for $V_{gs}=0$ V and V_d varied from 0.1V to 0.6 V.

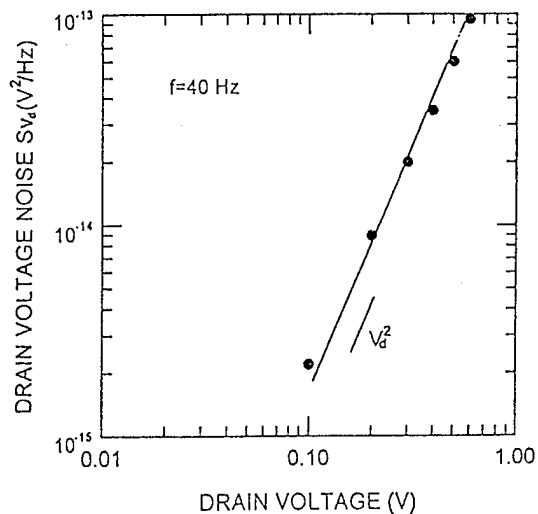
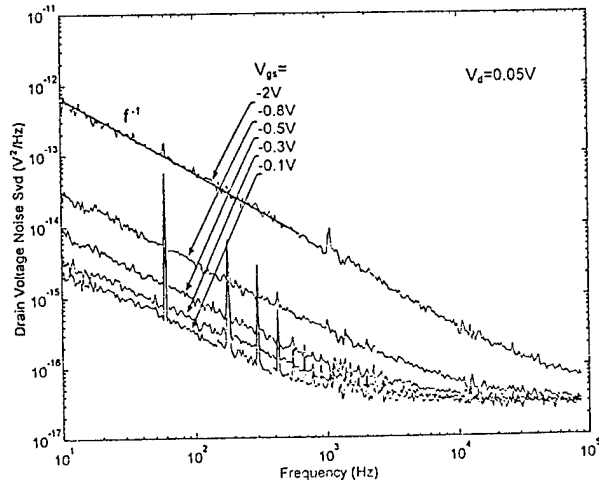
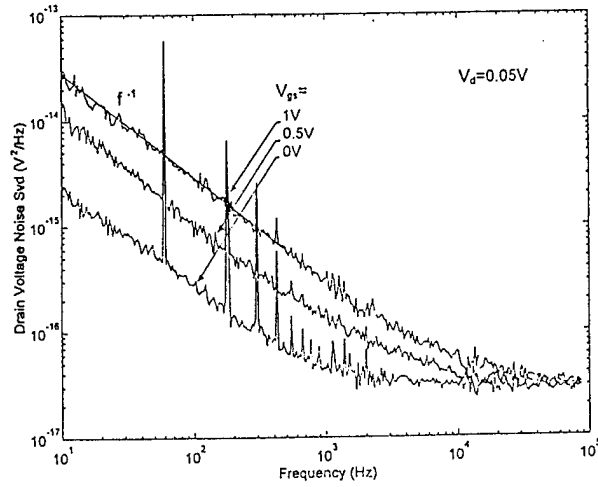


Fig.2 The noise spectra $S_{vd}(f)$ of SiO_2/InP MISFET versus drain voltage V_d at a frequency of 40 Hz calculated from Fig.1.



(a)



(b)

Fig.3 The noise spectra $S_{vd}(f)$ of SiO_2/InP MISFET versus frequency for (a) $V_{gs} = -0.1\text{V}, -0.3\text{V}, -0.5\text{V}, -0.8\text{V}$ and -2V ; and (b) $V_{gs} = 0\text{V}, 0.5\text{V}$ and 1V , respectively, at $V_d = 0.05\text{V}$.

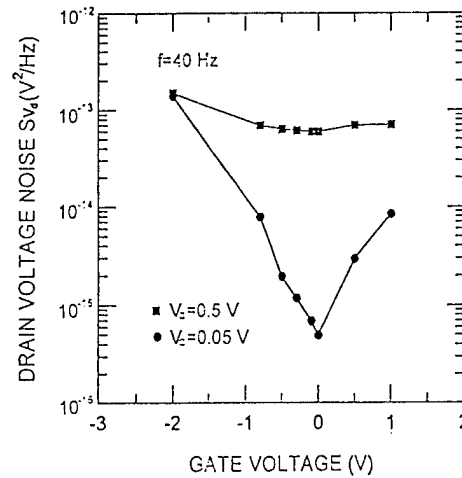


Fig.4 The noise power density of SiO_2/InP MISFET versus gate voltage at the frequency of 40 Hz and varied $V_d = 0.05\text{V}$ and 0.5V , respectively

A NEW FORM OF THE FOURIER TRANSFORM FOR TIME-VARYING FREQUENCY ESTIMATION*

Vladimir Katkovnik
Department of Statistics,
University of South Africa (UNISA),
P.O. Box 392, Pretoria 0001, RSA,
Tel: (012) 429-6210, FAX: (012) 429-3434,
E-Mail : katkov@risc6.unisa.ac.za

Abstract— The local polynomial Fourier transform (LPFT) and the local polynomial periodogram (LPP) are proposed in order to estimate the rapidly time-varying instantaneous frequency (IF) $\Omega(t)$ of a harmonic signal. The LPFT gives the time-frequency power distribution over the $t - (\Omega(t), d\Omega(t)/dt, \dots, d^{m-1}\Omega(t)/dt^{m-1})$ space, where m is a degree of the LPFT. The LPFT enables one to estimate both the time-varying frequency and its derivatives. The technique is based on fitting the local polynomial approximation of the frequency which implements a high-order nonparametric regression. The a priori information about bounds for the frequency and its derivatives can be incorporated to improve the accuracy of the estimation. The asymptotic mean square errors, bias and covariance, of the estimators of $d^s\Omega(t)/dt^s$, $s = 0, 1, 2, \dots, m-1$, are obtained. The considered estimators are high-order generalization of the short-time Fourier transform. The comparative study of the asymptotic variance and bias of the estimates is presented.

I. INTRODUCTION

By convention the term "frequency" is associated with the Fourier transform defined as an infinite integral over the time domain. Thus the time is removed, implying that the Fourier frequency is not a descriptor of a signal at a specific time-instant. For nonstationary signals the time variation of frequency information in $y(t)$ will be obscured since the spectrum is $I(\omega) = |Y(\omega)|^2$. An alternative representation is the short time Fourier transform (STFT) which is evaluated by applying a suitable windowing function to the original signal and evaluating the conventional Fourier

transform of the resulting length sequence. The STFT of the signal $y(t)$ can be given in particular by

$$Y_h(\omega, t) = \int_{-\infty}^{\infty} \rho_h(u) y(t+u) \exp(-j\omega u) du, \quad (1)$$

where ρ_h is a windowing function and h is a parameter which controls a length of the window. Using this technique, an approximation to the spectral content at the point t can be achieved by computing $I_h(\omega, t) = |Y_h(\omega, t)|^2$.

In recent years, time-frequency representations alternative to the STFT and based on time-frequency distributions have been developed. The time-frequency distributions, which indicate the energy content of a signal as a function of both time and the IF $\Omega(t)$, are powerful tools for time-varying signal analyses. They have been utilized to study a wide range of signals, including speech, music, and other acoustic signals, biological signals, radar and sonar signals, and geophysical signals. Recent reviews of the field are given in [1], [4].

Most time-frequency distributions of current interest are members of Cohen's bilinear (quadratic) class [3], which includes as a particular case the Wigner-Ville distribution (WVD).

The polynomial WVD was proposed [2] in order to improve the tracking ability of time-frequency distributions and has the similar optimal concentration in the $t-\omega$ plane for a polynomial IF of the complex harmonic signal.

Another approach to the problem and a new class of time-frequency distributions were studied in [5]-[9]. The local polynomial approximation of the time-varying phase was used in order to derive and to justify the local polynomial Fourier transform (LPFT). This transform is as follows

$$Y_h(\bar{\omega}, t) = \quad (2)$$

*This work was supported by the Foundation of Research Development of South Africa.

$$\int_{-\infty}^{\infty} \rho_h(u) y(t+u) \exp(-j\theta(u, \bar{\omega})) du,$$

$$\bar{\omega} = (\omega_1, \omega_2, \dots, \omega_m)' \in R^m,$$

where

$$\theta(u, \bar{\omega}) = \omega_1 \cdot u + \omega_2 \cdot u^2/2 + \dots + \omega_m \cdot u^m/m!. \quad (3)$$

The local polynomial periodogram (LPP) is then defined as follows

$$I_h(\bar{\omega}, t) = |Y_h(\bar{\omega}, t)|^2. \quad (4)$$

The quadratic and higher degree polynomials of the signal are used in the Cohen's and polynomial classes of time-frequency distributions with the exponential function $\exp(-j\omega u)$ by universal convention for the Fourier transform. The argument of this exponent is linear with respect to variable u . The LPFT on the other hand is linear with respect to the signal and the polynomial function of u , $\theta(u, \bar{\omega})$, appears in the argument of the complex exponent. This is a principal difference between the LPFT and the Cohen's and polynomial classes of time-frequency distributions.

The representation similar to (2), with a polynomial in the power of the complex exponent, appeared in the literature as a problem of estimating time-invariant coefficients of the polynomial phase of complex signals, which originated in radar applications [15]. The variance and the Cramer-Rao upper bounds of these estimates were studied in [14] and [15]. In contrast to the problem, considered in [14] and [15], the LPFT and the LPP in the form (2)-(4) have been developed with quite a different motivation.

In [10], [12] the LPFT and LPP have been derived within the local polynomial approximation (LPA) approach and interpreted as a generalization of the STFT and as a form of the time-frequency distribution. The accuracy of the LPA of the time-varying frequency and amplitude is studied in [9]. The accuracy of the LPP estimator of the time-varying frequency and its derivatives is considered in [11], [13].

II. ESTIMATION OF THE IF

The LPP estimator $\hat{\omega}(t, h)$ is introduced as a solution of the following constrained optimization problem [10]:

$$\hat{\omega}(t, h) = \arg \max_{\bar{\omega} \in Q \subset R^m} I_h(\bar{\omega}, t), \quad (5)$$

$$Q = \{\bar{\omega} : |\omega_s| \leq L_s, s = 1, 2, \dots, m\},$$

where L_s contain the a priori information about the IF, $|d^{s-1}\Omega/dt^{s-1}| \leq L_s, s = 1, 2, \dots, m$.

It was shown in [10]-[13] that the components of $\hat{\omega}(t, h)$ yield the following estimates: $\hat{\omega}_1(t, h)$ for the frequency $\Omega(t)$ and $\hat{\omega}_{s+1}(t, h)$ for the derivatives $\Omega^{(s)}(t)$, $s = 1, 2, \dots, m-1$. Both the convergence result, $\hat{\omega}(t, h) \rightarrow \bar{\omega}^0(t)$ as $h \rightarrow \infty$,

$$\bar{\omega}^0(t) = (\Omega(t), \Omega^{(1)}(t), \dots, \Omega^{(m-1)}(t))',$$

and the asymptotic accuracy of the estimator proves that the distribution $Y_h(\bar{\omega}, t)$ as a function of $\bar{\omega}$ concentrates in the point $\bar{\omega}^0(t)$.

III. ASYMPTOTIC ACCURACY

The accuracy results are given here for the discrete-time version of the LPFT. The vector-error is as follows

$$\Delta\hat{\omega}(kT, h) = \bar{\omega}^0(kT) - \hat{\omega}(kT, h), \quad \Delta\hat{\omega}(kT, h) \in R^m. \quad (6)$$

It is obvious that only asymptotic analytical results for the $\Delta\hat{\omega}(kT, h)$, where the estimator $\hat{\omega}(kT, h)$ is a solution of the awkward multimode optimization problem (5), can be obtained.

First of all let us make clear what kind asymptotic is studied. We will assume that the error $\Delta\hat{\omega}(kT, h)$, the noise ε and the derivatives $\Omega^{(s)}(t)$, $s \geq m$, are small. The last means that L_s are assumed to be small and therefore the frequency $\Omega(t)$ is close to a polynomial function of the power $(m-1)$. These assumptions are the basis for linearization of exponential functions which is used in the analysis.

We assume also that the window length is large ($h \rightarrow \infty$) so that a large number of harmonic circles is imbedded into the window. This is a long-time type asymptotics usual for most analytical results in the spectral analysis. The sampling interval T is not assumed to be small.

The first two moments of the vector-error $\Delta\hat{\omega}(kT, h)$ are used in the paper in order to characterize the accuracy of the estimation:

a) the covariance matrix

$$\text{cov}(\Delta\hat{\omega}(kT, h)) = \quad (7)$$

$$E((\Delta\hat{\omega}(kT, h) - E\Delta\hat{\omega}(kT, h)) \times (\Delta\hat{\omega}^*(kT, h) - E\Delta\hat{\omega}^*(kT, h))'),$$

where the prime (') stays for transpose and the asterisk means a complex conjugate value.

b) the bias, which is presented in the form of two expansions:

$$E\Delta\hat{\omega}(kT, h) = \sum_{s=0}^{\infty} B_s(h)\Omega^{(s)}(kT), \quad B_s(h) \in R^m, \quad (8)$$

and

$$|E\Delta\hat{\omega}(kT, h)| \leq B_m^{(A)}(h)L_m, \quad B_m^{(A)}(h) \in R^m, \quad (9)$$

where L_s are determined in (5). The inequality $|x| \leq |y|$, $x, y \in R^m$, in (9) means that $|x_j| \leq |y_j|$, $j = 1, 2, \dots, m$.

For the considered estimators $B_s(h) = 0$ for $s = 0, 1, \dots, m-1$, because the reproduction properties with respect to polynomial components of $\Omega(t)$ are insured by the local polynomial approximation estimates [5]-[8], thus (8) is as follows:

$$E\Delta\hat{\omega}(kT, h) = \sum_{s=m}^{\infty} B_s(h)\Omega^{(s)}(kT). \quad (10)$$

As a matter of fact (9) is a minimax upper bound.

The expansions (8)-(10) present quite a clear picture of the bias at the instant kT through the values of the derivatives of $\Omega(kT)$. Both the coefficients $B_s(h)$, $B_s^{(A)}(s)$ and $cov(\Delta\hat{\omega}(kT, h))$ appear to be a very convenient tool for a detailed comparison of the accuracy and the tracking ability of the different kinds of algorithms. The orders of the bias and the covariance matrix with respect to h and T can be given in clear analytical form.

The following results are given for the rectangular windows:

a) Symmetric window with $\rho_h(nT) = T/h$, if $|nT| \leq h/2$,

b) Nonsymmetric window with $\rho_h(nT) = T/h$, if $-h \leq nT \leq 0$, so that h is a window length, and h/T is a number of observation in the window

Let us present the asymptotic formulas derived for the covariance and bias of the estimates. These formulas enable us to compare the accuracy of the different algorithms in clear analytical form.

The following notation is used in what follows:

$$D(h) = \text{diag}(h, h^2, \dots, h^m),$$

$$W_\omega = \lim_{h \rightarrow \infty} D^{-1}(h) \left[\sum_{n=-\infty}^{\infty} \rho_h(nT) U(nT) U(nT)' - \sum_{n=-\infty}^{\infty} \rho_h(nT) U(nT) \sum_{n=-\infty}^{\infty} \rho_h(nT) U(nT)' \right] D^{-1}(h),$$

$$b(s) = -\frac{1}{(s+1)!} W_\omega^{-1} \lim_{h \rightarrow \infty} \frac{1}{h^{s+1}} D^{-1}(h) \times$$

$$\left(\sum_{n=-\infty}^{\infty} \rho_h(nT) U(nT) (nT)^{s+1} - \sum_{n=-\infty}^{\infty} \rho_h(nT) U(nT) \sum_{n=-\infty}^{\infty} \rho_h(nT) (nT)^{s+1} \right),$$

$$b^{(A)}(s) = \frac{1}{(s+1)!} |W_\omega^{-1}| \lim_{h \rightarrow \infty} \frac{1}{h^{s+1}} D^{-1}(h) \times$$

$$\left(\sum_{n=-\infty}^{\infty} \rho_h(nT) |U(nT)| |nT|^{s+1} + \right.$$

$$\left. | \sum_{n=-\infty}^{\infty} \rho_h(nT) U(nT) | \sum_{n=-\infty}^{\infty} \rho_h(nT) |nT|^{s+1} \right),$$

where

$$U(u) = (u, u^2/2, \dots, u^m/m!)',$$

and $|U|$ and $|W_\omega^{-1}|$ are a vector and a matrix of absolute values of U and W_ω^{-1} respectively.

Proposition 1 ¹⁰. Let $\hat{\omega}(kT, h)$ be a solution of (5), and L_{s+1} , $s = m, m+1, \dots$, such that as $h \rightarrow \infty$

$$L_{s+1} \cdot h^s \rightarrow 0, \quad (11)$$

then

$$\text{cov}(D(h)\Delta\hat{\omega}(kT, h)) = \frac{\sigma^2}{2|A|^2} W_\omega^{-1} \frac{T}{h}. \quad (12)$$

and (8) is of the form:

$$ED(h)\Delta\hat{\omega}(kT, h) = \sum_{s=m}^{\infty} \tilde{B}_s(h)\Omega^{(s)}(kT), \quad (13)$$

$$\tilde{B}_s(h) = h^{s+1} \cdot b(s).$$

²⁰. Let in ¹⁰ (11) hold for $s = m$, where $\sup_t |d^m \Omega/dt^m| \leq L_{m+1}$, then (9) is of the form:

$$|ED(\tilde{h})\Delta\hat{\omega}(t, h)| \leq \tilde{B}_m^{(A)}(h)L_{m+1}, \quad \tilde{B}_m^{(A)}(h) \in R^{14}$$

$$\tilde{B}_m^{(A)}(h) = h^{m+1} \cdot b^{(A)}(m).$$

■

Comment to the Proposition.

The formulas (12)-(14) determine the covariance matrix and the bias of the estimates. It follows that the asymptotic mean square errors are of the form:

$$E(\omega^{(s-1)}(kT) - \hat{\omega}_s(kT, h))^2 = \quad (15)$$

$$O\left(\frac{\sigma^2 \cdot h^{-(1+2s)}}{|A|^2} T + L_{m+1}^2 \cdot h^{2(m-s+1)}\right),$$

$$s = 1, 2, \dots, m.$$

The expression (15) gives a clear picture of the accuracy. The constants for (15), which depend on m , can be calculated from (12)-(14). The optimal choice of h in (15) yields the bias-variance trade-off and results in

$$\begin{aligned} h_0 &= O(B^{-\frac{2}{2m+3}}), \quad B = \frac{|A|L_{m+1}}{\sigma\sqrt{T}}, \\ E(\omega^{(s-1)}(kT) - \hat{\omega}_s(kT, h))^2 &= \frac{\sigma^2 T}{|A|^2} O(h_0^{-(2s+1)}), \\ s &= 1, 2, \dots, m, \end{aligned} \quad (16)$$

where B is assumed to be small.

Let us note that the variance is a linear function of the sampling interval T , but the bias does not depend on it. The accuracy results for the STFT follows from (15) and (16) if one assumes $m = 1$ in these formulas.

IV. CONCLUSION

A new form of the time-frequency transform LPFT and a new approach to the estimation of the rapidly time-varying frequency of a complex harmonic signal are proposed and justified. The most important distinctive feature of the new transform is that the degree of the complex exponential function generic for the Fourier transform is a polynomial function in the LPFT.

The LPFT is applied in order to propose a new form of the periodogram, the LPP, where the argument is a vector whose components provide estimates of the IF and its derivatives. The convergence results and asymptotic MSE for the estimator give an insight into properties of the LPP and LPFT.

For large h_0 the accuracy of the LPA estimates, characterized by the MSE values, has orders $O(h_0^{-(2k+1)})$ for the estimates of $d^{k-1}\Omega(t)/dt^{k-1}$, $k = 1, 2, \dots, m$.

The disadvantage of the developed approach is a complexity of the optimization problem (5). Nevertheless, the study and calculations show that there are a few quite prospective ways.

In particular, the following sequential algorithm, with a one-dimensional optimization for the every step, has been successfully tested for the linear LPA, $m = 2$. The first step assumes that $\omega_2 = 0$ and $I_h(\omega_1, \omega_2, t)$ is maximized over ω_1 , $\omega_1^{(1)} = \arg \max_{\omega_1} I_h(\omega_1, 0, t)$. The second step is maximization of $I_h(\omega_1^{(1)}, \omega_2, t)$ over ω_2 , $\omega_2^{(1)} = \arg \max_{\omega_2} I_h(\omega_1^{(1)}, \omega_2, t)$, and so on. Experiments show the fast convergence of this recursive procedure.

V. REFERENCE

- [1] B. Boashash, "Estimating and interpreting the instantaneous frequency of a signal- Part1: Fundamentals and Part 2: Algorithms and applications", *Proc. IEEE*, vol. 80, April, 1992, pp. 520-568.
- [2] B. Boashash and P. O'Shea, "Polynomial Wigner-Ville distributions and their relationship to time-varying higher order spectra", *IEEE Trans. Signal Processing*, vol. 42, 1994, pp. 216-220.
- [3] L. Cohen, "Time-frequency distributions - a review", *Proc. IEEE*, vol.77, July, 1989, pp. 941-981.
- [4] F. Hlawatsch and G. F. Boudreaux-Bartels, "Linear and quadratic time-frequency signal presentations", *IEEE Signal Processing Magazine*, vol. 9, February, 1992, pp. 21-68.
- [5] V. Katkovnik, "Homogeneous integral averaging operators obtained by the method of least squares", *Autom. Remote Control (trans. from Avtomatika i Telemekhanika)*, v.33, N , 1971, pp. 1767-1775.
- [6] V. Katkovnik, "Linear and nonlinear methods of nonparametric regression analysis", *Soviet Journal of Autom. and Inform. Sciences*, v.5, 1979, pp. 25-34.
- [7] V. Katkovnik, *Nonparametric identification and smoothing of data (Local approximation methods)*, Nauka, Moscow, 1985, 386 pp. (in Russian).
- [8] V. Katkovnik, "Identification of physical time-varying parameters", *Preprints of 10th IFAC Symposium on System Identification*, Copenhagen, Denmark, 4-6 July, 1994, vol.2, pp. 349-354.
- [9] V. Katkovnik, "Local polynomial approximation of rapidly time-varying frequency", UNISA, Pretoria, RSA, *Research report 94/1*, May, 1994.
- [10] V. Katkovnik, "New time-frequency transform for rapidly time-varying frequency estimation", UNISA, Pretoria, RSA, *Research report, 94/4*, November, 1994.
- [11] V. Katkovnik, "Local polynomial approximation of the instantaneous frequency: asymptotic accuracy", *Signal Processing*, 1994, Submitted.
- [12] V. Katkovnik, "Discrete-time local polynomial approximation of the instantaneous frequency", *IEEE Tran. on Signal Processing*, 1995, Submitted.
- [13] V. Katkovnik, "Local polynomial approximation of the instantaneous frequency: short-time asymptotic accuracy", *Signal Processing*, 1995, Submitted.
- [14] S. Peleg and B. Porat, "The Cramer-Rao lower bound for signals with constant amplitude and polynomial phase", *IEEE Trans. on Acoustics, Speech, and Signal Processing*, vol. 39, 1991, pp.749-752.
- [15] A.W.Rihaczek, *Principles of high-resolution radar*. Peninsula Publishing, California, 1985.

ESTIMATION OF THE SURFACE REFLECTIVITY OF SAR IMAGES BASED ON A MARKED POISSON POINT PROCESS MODEL

Jihad S. Daba

School of Electrical Engineering
University of Technology Sydney
Broadway, NSW, 2007, Australia
jdaba@ee.uts.edu.au

Mark R. Bell

School of Electrical Engineering
Purdue University
West Lafayette, Indiana, 47907, USA
mrb@ecn.purdue.edu

ABSTRACT

This paper presents stochastic models and estimation algorithms for speckled images. We treat speckle from a novel point of view: that of a carrier of useful surface information as opposed that of a contaminating noise. The stochastic models for surface scattering are based on a doubly stochastic marked Poisson point process. For each of these surface scattering statistical models, we present estimation algorithms to determine the average surface reflectivity and scatterer density within a resolution cell using intensity measurements of speckled images. We show that the maximum likelihood estimator is optimal in the sense that the variance of the error is the smallest possible using any other conceivable estimate having the same bias with the same data.

1. INTRODUCTION

In most prior work on speckle development in images, speckle has been viewed as a multiplicative noise that contaminates the image [1], making interpretation and image information extraction more difficult. As a result, a great deal of effort has been expended to look at ways of reducing speckle in images in order to improve their interpretation.

In our approach, we make use of the fact that speckle is a function of the spatial distribution of scatterers within the imaged resolution cell on a scale corresponding to the wavelength of the illuminating radiation. As a result, speckle can be viewed as a carrier of information about roughness characteristics of the imaged surface.

Our goal is not to reduce speckle per se, but to make use of it in developing techniques for modeling the scattering surface using random point processes influenced by an underlying information process and estimating the surface reflectivity and density of elemental scatterers (average number of scattering points per resolution cell) from Synthetic Aperture Radar (SAR) reflectivity measurements.

The estimation scheme under consideration is based on the marked Poisson point process and the resulting statistics of partially developed speckle which we derived in a separate paper [2].

Although the emphasis of this work is on synthetic aperture radar systems, we use SAR systems in our analysis to establish results that will serve as a basis for estimation problems in other coherent imaging systems where

the speckle phenomenon is present, such as medical ultrasound imaging systems.

2. SURFACE SCATTERING STOCHASTIC MODEL

2.1 Marked Point Process Speckle Model

In the single-look model, a radar resolution cell is assumed to contain a collection of N elemental point scatterers randomly distributed throughout the resolution cell, with each elementary scatterer position distributed independently of the positions of other scatterers. The random spatial distribution of the scatterers is described by a point process with a set of points having associated complex marks E_j , ($j = 1, \dots, N$) corresponding to the backscattered electric field from the j -th scatterer. Each backscattered electric field component E_j has a constant amplitude A_j equal to the size or reflectance strength of the j -th scatterer and a random phase ϕ_j uniformly distributed over the interval $[0, 2\pi)$. We assume that the number of scattering points within a resolution cell is Poisson distributed with a rate λA , where A is the area of a resolution cell.

When electromagnetic waves are scattered from such a surface, the resultant scattered field is the superposition of the electric fields scattered by each of the elemental scatterers. The resulting process is a marked Poisson point process and λ is the intensity of this process over a resolution cell with area A . When $\lambda(\cdot)$ is a random process, the point process is referred to as doubly stochastic marked Poisson point process [3].

SAR systems record intensity measurements of the mapped surface according to:

$$S_N = \left| \sum_{j=1}^N A_j e^{i\phi_j} \right|^2. \quad (1)$$

Speckle under this model is referred to as partially developed.

In the multilook model, L -independent diversity measurements are taken over the resolution cell by the radar. This technique involves the noncoherent sum of L statistically independent single realizations of the intensity measurements S_{Nl} ($l = 1, 2, \dots, L$) in Eq. (1) at each resolution cell:

$$T_{NL} = \sum_{l=1}^L S_{Nl}. \quad (2)$$

In a separate paper [2], we present a complete derivation for the intensity probability density function conditioned on N for the single look and multilook models.

2.2 Reflectance Amplitude Models

Since the surfaces mapped by SAR systems have varying roughness characteristics with respect to the wavelength of the illuminating radiation, we expect the amplitude (strength) of the scatterers to be governed by different models for different types of surfaces. We consider two models: (1) the reflectances of the elementary scatterers are constant (model discussed in the previous section), and (2) the reflectances are Rayleigh distributed.

In the case of Rayleigh distributed amplitudes, we consider the surface resolution cell as made up of a small number of scattering centers, with each center made up of a large number of elementary scattering points (Rayleigh center).

3. ESTIMATION TECHNIQUES

3.1 Constant Amplitude Model

3.1.1 Maximum Likelihood Estimation

The objective is to estimate the average reflectivity of SAR scattering surfaces, or equivalently, the rate λA of the Poisson process from the intensity measurements given by Eq. (1). This estimation problem is rather difficult since the parameter λA to be estimated is implicitly imbedded in the reflected signal intensity as the rate λA of the marked Poisson process.

Due to the mathematical complexity of the likelihood function for both single and multilook cases, we formulate an expectation-maximization (EM) algorithm [3] to produce a recursive ML estimate of λ .

We show that the EM algorithm is implemented recursively, starting with an admissible initial estimate $\hat{\lambda}^{[0]} \geq 0$, according to:

$$\hat{\lambda}^{[k+1]} = \begin{cases} \frac{1}{A}, & t = L \\ \frac{\psi(t, \hat{\lambda}^{[k]})}{A p_{\lambda}^c(t) |_{\lambda=\hat{\lambda}^{[k]}}}, & t \neq L \end{cases} \quad (3)$$

where

$$\begin{aligned} p_{\lambda}^c(t) &= \exp(-\lambda A) \left(\frac{(\lambda A)^2}{4\pi^2} K\left(\frac{1}{4}\sqrt{t(8-t)}\right) I_{[0,4) \cup (4,8]}(t) \delta_{L2} \right. \\ &+ \frac{1}{\Gamma(L)} t^{L-1} \sum_{n=n_0}^{n_L} \frac{(\lambda A)^n}{n! n^L} \exp\left(-\frac{t}{n}\right) \left(1 + \sum_{m=1}^{M_{nL}} c_m \mathcal{L}_m^{L-1}\left(\frac{t}{n}\right) \right) I_{[0,\infty)}(t) \\ &\left. + \frac{1}{\Gamma(L)} t^{L-1} \sum_{n=n_L+1}^{\infty} \frac{(\lambda A)^n}{n! n^L} \exp\left(-\frac{t}{n}\right) I_{[0,\infty)}(t) \right), \end{aligned} \quad (4)$$

and

$$\begin{aligned} \psi(t, \hat{\lambda}^{[k]}) &= \exp(-\lambda A) \left(\frac{(\lambda A)^2}{2\pi^2} K\left(\frac{1}{4}\sqrt{t(8-t)}\right) I_{[0,4) \cup (4,8]}(t) \delta_{L2} \right. \\ &+ \frac{1}{\Gamma(L)} t^{L-1} \sum_{n=n_0}^{n_L} \frac{(\lambda A)^n}{n! n^{(L-1)}} \exp\left(-\frac{t}{n}\right) \left(1 + \sum_{m=1}^{M_{nL}} c_m \mathcal{L}_m^{L-1}\left(\frac{t}{n}\right) \right) \\ &\left. + \frac{1}{\Gamma(L)} t^{L-1} \sum_{n=n_L+1}^{\infty} \frac{(\lambda A)^n}{n! n^{(L-1)}} \exp\left(-\frac{t}{n}\right) I_{[0,\infty)}(t) \right). \end{aligned} \quad (5)$$

We note that $\mathcal{L}_m^{L-1}(\cdot)$ are the generalized Laguerre polynomials, $K(\cdot)$ is the complete elliptic function, and the coefficients c_m are tabulated in a separate paper [2].

The EM algorithm was numerically implemented for various values of the parameter λ (assumed known). The results after k iterations are shown in Figs. 1 and 2 for different numbers of looks. In all cases, the sequence of estimates $\hat{\lambda}^{[k]}$ converges towards the maximum likelihood estimate. We assumed that the area of a resolution cell is 625 m² (25 m \times 25 m), which is a typical size for the resolution cell of Seasat SAR.

3.1.1 Performance of the ML estimator

The performance of the estimator is characterized by the bias $b(\lambda)$ and by comparing the variance of the error with the Cramer-Rao lower bound (CRLB) defined as [3]:

$$CRLB(\lambda) = \frac{\left(1 - \frac{db(\lambda)}{d\lambda}\right)^2}{J_L(\lambda)}, \quad (6)$$

where $J_L(\lambda)$ is the Fisher information matrix.

The expected value of the estimator $E[\hat{\lambda}]$ can be estimated using Monte Carlo simulation of the speckle intensity measurements. The numerical results are illustrated in Fig. 3 for 1 and 2 looks. We note that bias is reduced as the number of looks is increased. This is a direct result from the property that the maximum likelihood estimator is a consistent estimator [4].

We can estimate the variance of the estimator and the Cramer-Rao lower bound using Monte Carlo simulation of intensity measurements. Figure 4 provides a comparison between the estimated variance of the error and the estimated CRLB as a function of the rate λA , for various number of looks. For a given number of looks, the variance of the error and the CRLB increase as the rate gets larger. This follows from the fact that the rate and the variance of the Poisson process are equal. As the rate increases, so does the variance of the Poisson process, causing a lower performance of the estimator. As the number of looks is increased, the variance of the error and the CRLB decrease, and in addition, the variance of the error gets closer to the CRLB. The fact that the performance of the estimator improves with a larger number of looks is also a direct result of the consistency property of the ML estimator.

Overall, it is evident from these graphs that the performance of the ML estimator is very good. For rates lower than 20, the variance of the error is very close to the CRLB when 2 or more looks are used. For larger rates, only 4 looks are needed to bring the variance of the error much closer to the CRLB.

3.2 Rayleigh Amplitude Model

3.2.1 Maximum Likelihood Estimation

We derive the following recursive algorithm for the estimate:

$$\hat{\lambda}^{[k+1]} = \frac{1}{A} \frac{\sum_{n=1}^{\infty} \frac{(\hat{\lambda}^{[k]} A)^n \exp(-\frac{t}{n})}{n! n^{L-1}}}{\sum_{n=1}^{\infty} \frac{(\hat{\lambda}^{[k]} A)^n \exp(-\frac{t}{n})}{n! n^L}}. \quad (7)$$

The EM algorithm was numerically implemented for various values of λ (assumed known), starting with admissible initial estimates $\hat{\lambda}^{(0)} \geq 0$. The results after k iterations are shown in Fig. 5 for 4 looks. We chose $L = 4$ because this is the number of looks that is usually used for SAR systems in real-life applications.

3.2.2 Performance of the Maximum Likelihood Estimator

Using Monte Carlo simulation of the intensity measurements, we estimate the bias, error variance, and the CRLB. The results are illustrated in Figs. 6 and 7. Figure 6 shows that the bias is reduced as the number of looks increases. This follows from the fact that the ML estimator is consistent. We also note that as the rate increases, so does the variance of the Poisson process. This is evident in Fig. 6 since the statistical fluctuation in the estimate $\hat{E}(\hat{\lambda})$ gets larger as the rate λA is increased.

A comparison between the estimated error variance and the estimated CRLB is provided in Figure 7 for different numbers of looks. For a fixed number of looks, the variance of the error and the CRLB increase as the rate gets larger. As the number of looks increases, the variance of the error and the CRLB decrease, and the variance of the error gets closer to the CRLB. Again, this is expected because the ML estimator is consistent.

For large number of looks ($L = 4$), the error variance and the CRLB get very close and the ML estimator becomes optimal in the sense that no other conceivable estimator having the same bias with the same data can perform better.

4. DISCUSSION

In this section, we provide a comparison between the performance of the ML estimators in the constant amplitude and Rayleigh models.

The performance of the ML estimator over regions where the rate λA is not sufficiently large (≤ 20) is better in the constant amplitude model than in the Rayleigh amplitude model. This can be seen by comparing how close the error variance is to the CRLB in Fig. 4 versus Fig. 7, especially for the cases when $L = 2$ and 4.

Hence, the difference between the performances of the ML estimators for both models is notable when the rate λA is small. On the other hand, when the rate is sufficiently large (≥ 25), the performances of the estimators are quite comparable. This is justified by the fact that for large rates, the likelihood function in the constant amplitude model is very similar to the one in the Rayleigh model.

Finally, we mention that in the limit when the number of scatterers N gets very large (fully developed speckle), it follows from the central limit theorem that the likelihood function of the multilook intensity T obeys a Gamma law with parameters $(L, \lambda A)$. The statistic t is thus a complete sufficient statistic for the average reflectivity (or mean intensity) λA , and $\hat{\lambda} = t/(AL)$ is the minimum variance unbiased estimator (MVUE) and the maximum likelihood estimate of the parameter λ .

5. CONCLUSIONS AND SIGNIFICANCE

In this paper, we presented estimation algorithms to determine the average surface reflectivity and scatterer

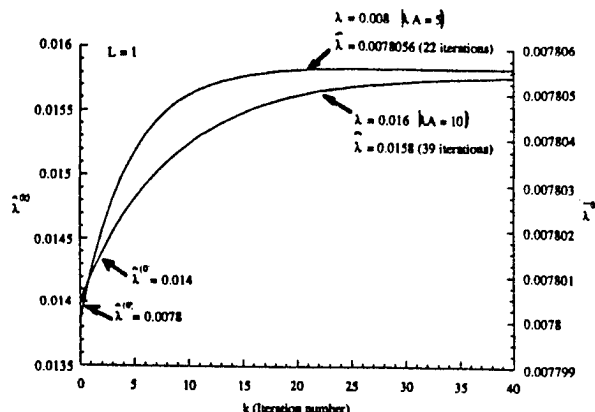


Figure 1: Sequences of EM estimates for a single look and different rates λA . (Constant amplitude model)

density (average number of scatterers within a resolution cell) using intensity measurements of speckled images. The estimation schemes were based on a marked Poisson point process model for partially developed speckle and were applied to the particular model of a constant mean reflectivity within the resolution cell.

The structure and performance of these estimators differ significantly from that of estimation in multiplicative and additive noise and are also a function of the particular point process parameters used to model partially developed speckle.

We showed that the performance of the estimators improved as the number of looks was increased. For 2 looks and rates λA less than 20, the maximum likelihood estimator was optimal in the sense that the variance of the error is the smallest possible using any other conceivable estimate having the same bias with the same data. The maximum likelihood becomes optimal for all rates λA as the number of looks is increased to 4 or more looks.

The techniques we developed to estimate the scatterer density serve as a powerful tool in SAR image classification, SAR image reconstruction, in addition to biological tissue classification and tomographic reconstruction in biomedical ultrasound imaging systems.

References

- [1] J. S. Lee, "Statistical Modeling and Suppression of Speckle in Synthetic Aperture Radar Images," *Proceedings of the IGARSS 87 Symposium*, May 18-21, pp. 1331-1339, 1987.
- [2] J. S. Daba and M. R. Bell, "Statistics of the Scattering Cross Section of a Small Number of Random Scatterers," to appear in *IEEE Transactions on Antennas and Propagation* (accepted 10/94).
- [3] D. L. Snyder and M. I. Miller, *Random Point Processes in Time and Space*, New York, NY: Springer-Verlag, 1991.
- [4] H. Sorenson, *Parameter Estimation*, Marcel Dekker, Inc.: New York, NY, 1980.

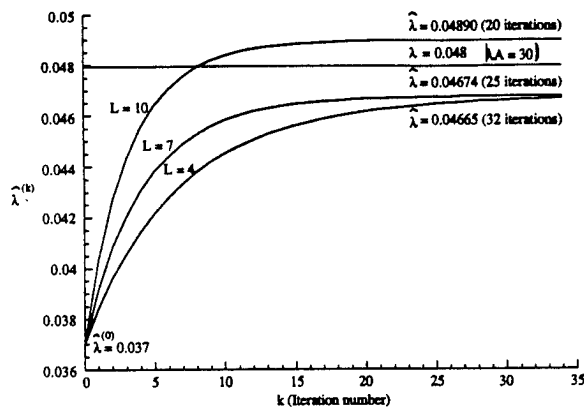


Figure 2: Sequences of EM estimates for a fixed rate λA and different looks. (Constant amplitude model)

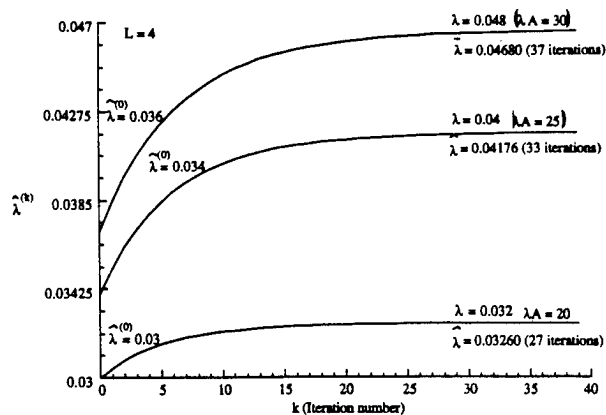


Figure 5: Sequences of EM estimates for 4 looks and different rates λA . (Rayleigh amplitude model)

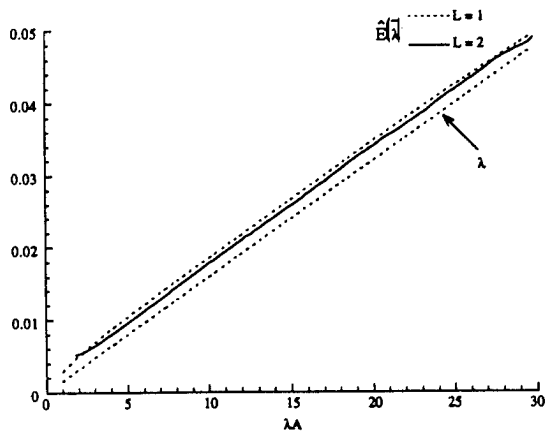


Figure 3: Estimated bias of the ML estimator as a function of the rate λA for 1 and 2 looks. (Constant amplitude model)

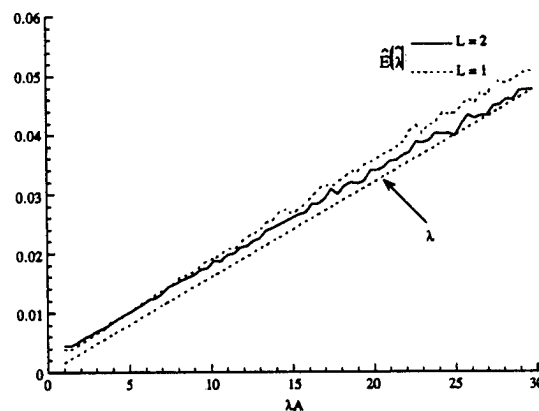


Figure 6: Estimated bias of the ML estimator as a function of the rate λA for 1 and 2 looks, using 3000 runs. (Rayleigh amplitude model)

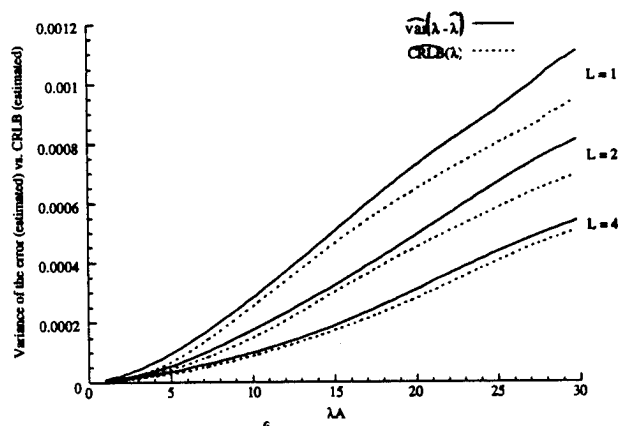


Figure 4: Estimated variance of the error of the ML estimator compared to the estimated CRLB as a function of the rate λA . (Constant amplitude model)

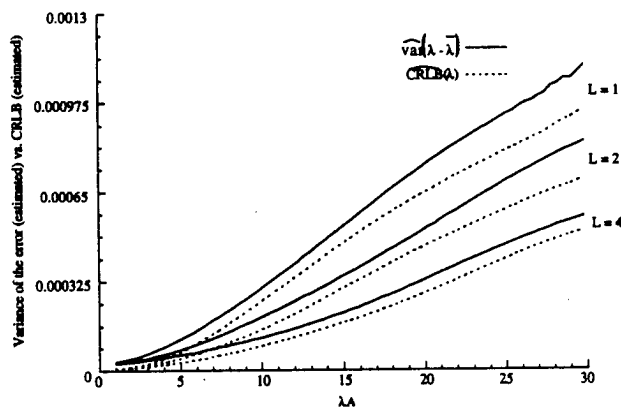


Figure 7: Estimated error variance of the ML estimator (using 10000 runs) compared to the estimated CRLB as a function of the rate λA . (Rayleigh amplitude model)

AN IMPROVED DIRECT INVERSE PROBLEM SOLVER FOR FRACTAL INTERPOLATION FUNCTIONS WITH APPLICATIONS TO SIGNAL COMPRESSION*

Jiangtao WEN Xuelong ZHU
Computer and Information Division
Dept. of Electronic Engineering
Tsinghua University
Beijing 100084
P.R. China

wen@king.dee.tsinghua.edu.cn, deezxl@tsinghua.edu.cn

ABSTRACT

In this paper, a novel direct algorithm to estimate parameters of fractal interpolation functions is proposed, and test results of its robustness and its performance in signal compression are reported.

IFS fractal interpolation function (FIF) is becoming an increasingly appealing class of models of such signals as the height distribution of sea floors, seismograph, and electrocardiograph signals, due to its inherent advantages.

Existing FIF-based signal compression algorithms usually use a FIF parameter estimation formula proposed by Mazel and Hayes ([1]), which is based on least square-error fitting techniques and needs to calculate the derivatives of such a error measure with respect to FIF parameters. It is very inconvenient to introduce many other useful error measures in real signal processing applications, such as Kullback entropy or Hausdorff distance, for they may endanger the computability of the derivatives.

In this paper, a computationally efficient, direct algorithm to solve the inverse problem of IFS interpolation signals is proposed. It can solve FIF parameters from its samples without calculating error function's derivatives. The algorithm's robustness in parameter estimation and usefulness in signal compression are shown with experimental results.

1. IFS Fractal Interpolation

Interpolation in pure mathematical sense is the problem of finding, from a given initial data set

$$\{(x_i, F_i): x_{i-1} < x_i, i = 1, 2, \dots, N\} \quad (1-1)$$

a continuous function $f(x)$ that satisfies,

$$f(x_i) = F_i, i = 0, 1, 2, \dots, N. \quad (1-2)$$

There are many ways to find the $f(x)$ in (1-2), for a N -th order IFS fractal interpolation function (FIF), $f(x)$ is the y -direction projection of a 2-D N -map hyperbolic IFS' attractor G . The maps of the IFS are affines of the form:

$$w_i \begin{pmatrix} x \\ y \end{pmatrix} = \begin{pmatrix} a_i & 0 \\ c_i & d_i \end{pmatrix} \begin{pmatrix} x \\ y \end{pmatrix} + \begin{pmatrix} e_i \\ f_i \end{pmatrix} \quad (1-3)$$

satisfying

$$w_i \begin{pmatrix} x_0 \\ y_0 \end{pmatrix} = \begin{pmatrix} x_{i-1} \\ y_{i-1} \end{pmatrix}, \quad w_i \begin{pmatrix} x_N \\ y_N \end{pmatrix} = \begin{pmatrix} x_i \\ y_i \end{pmatrix} \quad \forall i = 1, 2, \dots, N \quad (1-4)$$

From (1-1) to (1-4), one can find

$$\begin{cases} a_i = \frac{x_i - x_{i-1}}{x_N - x_0}, \\ c_i = \frac{F_i - F_{i-1}}{x_N - x_0} - d_i \frac{F_N - F_0}{x_N - x_0}, \\ e_i = \frac{x_N x_{i-1} - x_0 x_i}{x_N - x_0}, \\ f_i = \frac{x_N F_{i-1} - x_0 F_i}{x_N - x_0} - d_i \frac{F_0 x_N - x_0 F_N}{x_N - x_0}. \end{cases} \quad (1-5)$$

where $\{d_i: i = 1, 2, \dots, N\}$ is a set of free parameters that controls the box-counting dimension of G . To construct a hyperbolic IFS and have stable iteration, it is required that $\{|d_i| < 1: i = 1, 2, \dots, N\}$.

2. A Simple Inverse Problem Solver

In the discussions below, we suppose we are given a 1-D signal $f(x)$, $x \in [x_0, x_N]$, whose image $G = \{(x, f(x)): x \in [x_0, x_N]\}$ is the attractor of a hyperbolic IFS in the form of (1-3). From (1-4) and

* A research supported by the National Natural Science Foundation of China.

the affinity of maps, we know that, when x changes from x_0 to x_N , the y -component of w_i maps $f(x)$, $x \in [x_0, x_N]$ to the section between $[x_{i-1}, x_i]$, so we have

$$f(a_i x + e_i) = c_i x + d_i f(x) + f_i, \quad \forall x \in [x_0, x_N] \quad (2-1)$$

On the other hand, because the position of the first interpolation point x_0 is known, we can see from (1-5) that parameters a_i, c_i, e_i, f_i depend only on d_i and x_i . If we can find a relationship between d_i and x_i , then by using (1-4), (1-5) and testing if equation (2-1) holds, we will be able to solve x_i and then a_i, c_i, e_i, f_i . Similarly, once x_{i-1} is estimated, a_i, c_i, e_i, f_i depends only on d_i and x_i , by using a relationship of d_i and x_i and (1-4), (1-5), (2-1), we will also be able to solve x_i and a_i, c_i, e_i, f_i .

To derive a relationship between d_i and x_i , consider the integration

$$\begin{aligned} & \int_{x=x_0}^{x=x_N} f(a_i x + e_i) d(a_i x + e_i) \\ &= \int_{x=x_0}^{x=x_N} (c_i x + d_i f(x) + f_i) d(a_i x + e_i) \\ &= \int_{x_{i-1}}^{x_i} f(x') dx' \quad (x' = a_i x + e_i) \end{aligned} \quad (2-2)$$

so we have

$$\begin{aligned} \int_{x_{i-1}}^{x_i} f(x) dx &= a_i c_i \int_{x_0}^{x_N} x dx + a_i d_i \int_{x_0}^{x_N} f(x) dx \\ &\quad + a_i f_i \int_{x_0}^{x_N} dx \end{aligned} \quad (2-3)$$

From (1-5) and (2-3)

$$d_i = \frac{con1 + con4 \cdot k1 + con3 \cdot k2}{1 + k2 \cdot k3 + k1 \cdot k4} \quad (2-4)$$

where

$$\begin{aligned} con1 &= \frac{\int_{x_{i-1}}^{x_i} f(x) dx}{a_i \int_{x_0}^{x_N} f(x) dx}, \\ con3 &= \frac{F_i - F_{i-1}}{x_N - x_0}, \quad con4 = \frac{x_N F_{i-1} - x_0 F_i}{x_N - x_0}, \\ k1 &= -\frac{x_N - x_0}{\int_{x_0}^{x_N} f(x) dx}, \quad k2 = -\frac{x_N^2 - x_0^2}{2 \int_{x_0}^{x_N} f(x) dx}, \\ k3 &= \frac{F_N - F_0}{x_N - x_0}, \quad k4 = \frac{F_0 x_N - x_0 F_N}{x_N - x_0}. \end{aligned} \quad (2-5)$$

A complete algorithm to solve the parameters from a 1-D FIF signal is as follows:

1. Set a step s_i for searching, let $i=1$;
2. Choose $x_i = x_{i-1} + s_i$ as the i -th interpolation point;
3. Utilizing (2-4), (2-5) to compute the estimation of d_i associated with the current x_i . If $|d_i| \geq 1$, go back to step 2; else estimate a_i, c_i, e_i, f_i with (1-5);
4. Compute and temporarily store an error function $E(x_i) = D(A_i, B_i)$, where $A_i = \{f(x): x \in [x_{i-1}, x_i]\}$, $B_i = w_i(f)$, and $D(\cdot, \cdot)$ is a distance measure;
5. If $x_i \leq x_N - s_i$, let $x_i = x_i + s_i$ and go back to step 3; otherwise set the estimates of x_i and d_i (\hat{x}_i, \hat{d}_i) as the pair that yield the minimum value of $E(x_i)$ in step 4;
6. If $\hat{x}_i < x_N - s_2$, let $i = i + 1$, go back to step 2; otherwise, let $N = i$, $\hat{x}_N = x_N$ and terminate the algorithm.

In the above algorithm, s_i is a searching step which can be set to 1 for time discrete signals. s_2 is used to control the quality of signal compression, it can be determined from compression ratio requirements or *a priori* knowledge of the original signal ([3]).

The above algorithm does not need to calculate error function deviates in the estimation of any FIF parameters, as a result, there is virtually no limitation on the choice of error function.

The computational complexity of our algorithm is very small. As a matter of fact, it took a 486DX2/66 only a little over 10 seconds to solve a 1025 point FIF signal in our experiment.

3. Simulations and Conclusions

We present three examples of the applications of our algorithm. We use the sum of signal sample values to approximate integration and mean-square error to judge approximation.

In the first scenario, our algorithm is used to estimate the parameters of the 4th order FIF in Fig.1. The algorithm finds all the correct interpolation point positions, the estimated d_i 's are also very close to the original (Table.1). The reconstructed FIF is virtually indistinguishable from the original.

In the second scenario, our algorithm is used to estimate FIF components in the signals of Fig.2-1

and Fig.3-1. Fig.2-1 is constructed by adding a zero-mean white additive noise with uniform amplitude distribution to the FIF in Fig.1, while Fig.3-1 is the sum of Fig.1 and a period 25 samples sine wave. The SNRs for Fig.2-1 and Fig.3-1 are 0.06dB and 0.02dB respectively. The FIFs our algorithm reconstructs are plotted in Fig.2-2 and Fig.3-2, whose parameters are listed in Tables 2 and 3. The SNRs for reconstructed FIFs with respect to the original are 2.9dB and 3.5dB respectively.

Finally, we present the result of FIF/DFT hybrid compression of a short segment of real-world music signal $f(n)$ (Fig.4-1). We first approximate it with a 16th order FIF $f_1(n)$, then the difference between $f(n)$ and $f_1(n)$ is compressed with DFT transform coding. Preserving 291 DFT coefficients (corresponding to the DC component and 145 AC components) that are "furthest" away from the mean of all DFT coefficients and setting the rest of coefficients to the mean, we get signal $f_2(n)$. Reconstructed signal is the sum of $f_1(n)$ and $f_2(n)$.

Differential coding can compress DFT coefficient index and interpolation point position information to 4bits/index and 6bits/point respectively. Each d_i is quantized to 10bits, and the real and imaginative parts of DFT coefficients, sample values at interpolation points are saved with 16bits each. Because the original signal is a 1025-point 16bits/sample sequence, the overall compression ratio is a little over 3:1, and SNR is about 28.7dB. Using more complex quantization schemes and entropy coding techniques can achieve about 5:1 compression with approximately the same SNR.

In conclusion, we broaden the range of FIF-based signal modeling/compression by proposing an algorithm to solve the parameters of a FIF from its samples which relaxes the requirement to error metric derivability. Our algorithm can also be used to estimate fractal components in signals. It is able to reconstruct a fairly good "outlook" of the embedded FIF, even at very low SNRs. Though the algorithm realization is simple and our studies preliminary, the performance of the algorithm is encouraging.

i	$x_i(\hat{x}_i)$	$F_i(\hat{F}_i)$	d_i / \hat{d}_i
0	0	-3.000	/
1	256	-9.000	0.800 / 0.797
2	512	-5.000	0.800 / 0.819
3	768	-10.000	0.800 / 0.784

4	1024	-24.000	0.800 / 0.790
---	------	---------	---------------

Table.1 Original and Estimated FIF Parameters of Fig. 1

i	\hat{x}_i	\hat{F}_i	\hat{d}_i
0	0	-1.893	/
1	256	-6.296	0.840
2	512	-1.366	0.847
3	748	1.7601	0.774
4	1024	-33.998	0.785

Table.2 Estimated FIF Parameters From Fig.2-1

i	\hat{x}_i	\hat{F}_i	\hat{d}_i
0	0	-0.762	/
1	256	-0.159	0.394
2	511	1.276	0.209
3	762	-0.357	0.172
4	1024	-24.000	0.424

Table.3 Estimated FIF Parameters From Fig.3-1

REFERENCES

- [1] D.S.Mazel, H.M.Hayes, "Using iterated function systems to model discrete sequences", *IEEE Trans. Signal Processing*, Vol.40, No.7, pp1724-1734, July, 1992
- [2] D.S.Mazel, "Representation of discrete sequences with three-dimensional iterated function systems", *IEEE Trans. Signal Processing*, Vol.42, No.11, November, 1994
- [3] J.Wen, X.Zhu, "Recovering IFS interpolated signal from noise - a new simple inverse problem solver", in processing of *Chinese Journal of Electronics*

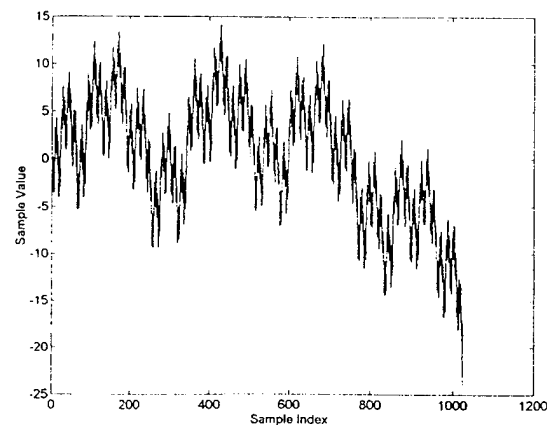


Fig.1 A 4th Order FIF

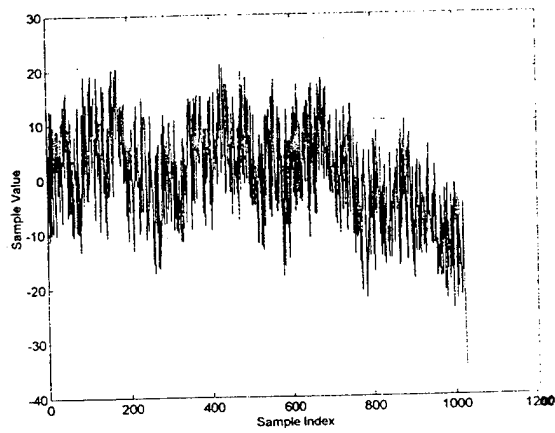


Fig. 2-1 FIF + Noise

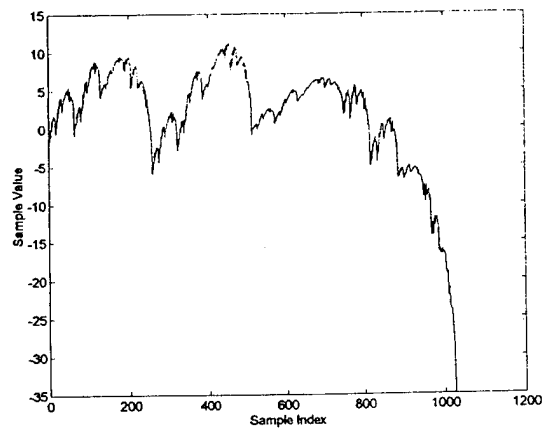


Fig. 2-2 Reconstructed FIF From Fig. 2-1

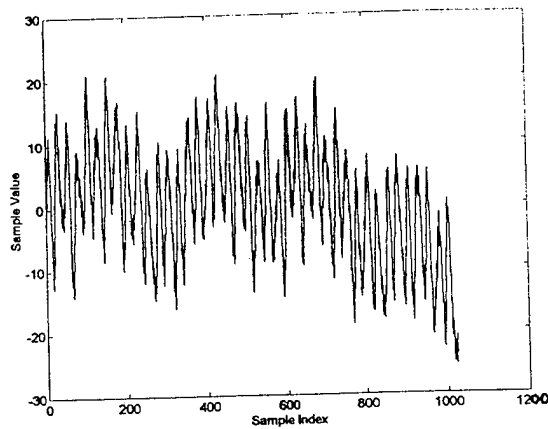


Fig. 3-1 FIF + Sine Wave

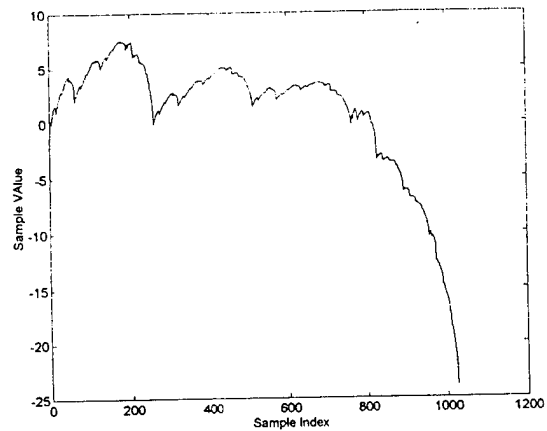


Fig. 3-2 Reconstructed FIF From Fig. 3-1

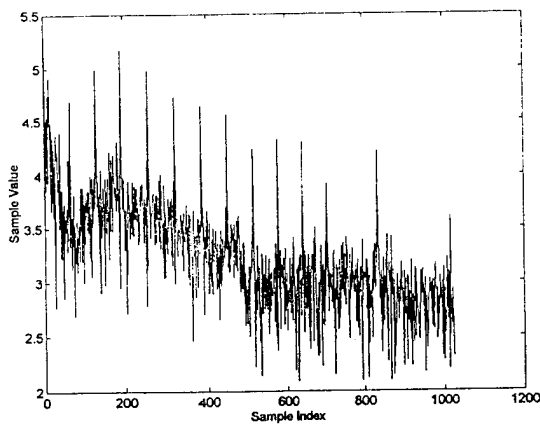


Fig. 4-1 Original Music Signal

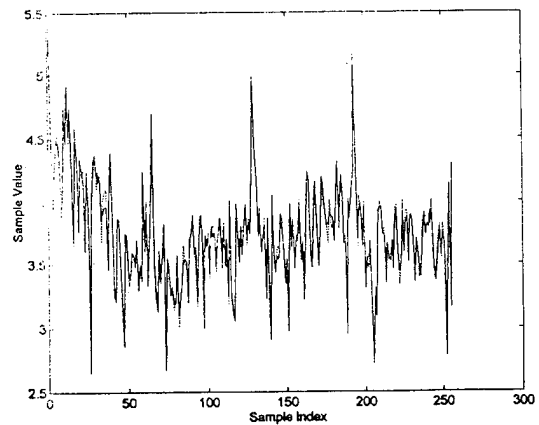


Fig. 4-2 Detailed Comparison of Original (Solid Line) and Reconstructed (Dash-Dotted Line) Music Signal

OPTIMUM CFAR DETECTION AGAINST CORRELATED K-DISTRIBUTED CLUTTER

Tullio Bucciarelli, Pierfrancesco Lombardo¹, Serena Tamburrini

Dpt. INFO-COM, University of Rome "La Sapienza"

Via Eudossiana 18, 00184 ROMA, ITALY

Ph. +39-6-44585865 Fax +39-6-4873300 e-mail: buccia@infocom.ing.uniroma1.it

1. Introduction

As well known the K-distributed clutter can be described as the product model of a texture variable, representing the properties of the observed surface, times an exponential component, usually named speckle, representing the effect of the coherent radar sensor. The performance of usual CFAR schemes for the detection of radar targets embedded in this clutter depends strictly on the algorithm used to select the detection threshold. In particular Watts pointed out in [1] that the exact knowledge of the texture value at each instant allows an ideal adaptive threshold to be set only on the speckle component. This selection, named 'ideal CFAR', is shown to widely outperform the fixed threshold detection scheme, especially for spiky clutter. The performance of the ideal CFAR defines an upper bound to the detection probability in K-distributed clutter, but it is purely theoretical since the knowledge of the texture variable is not available in practice. In the present paper we derive two estimators of the local texture value on the basis of the echoes received from the N range cells closest to the cell under test and use the estimated texture value, instead of the exact one, to set the detection threshold. The performance is clearly highly dependent on the range correlation, which determines the texture estimation accuracy, and its analysis allows us to assess how far is the 'ideal CFAR' from the practical implementation in the different conditions. The two estimators distinguish for using or not some prior information about the texture distribution. An evaluation of its importance can therefore be obtained from the comparison of their performances.

2. Correlated clutter model

As well known the K-distribution [2]-[3] is an adequate statistical description for sea clutter echoes received from a low grazing angle. According to this description the square-law detected intensity of the single received echo, $x = \tau \cdot z$, can be interpreted as the product model [2] of

the exponentially distributed variable z (with mean value 1), usually named 'speckle', times the variable τ , referred to as 'texture'. The texture variable, which modulates the variance of the speckle contribution, is a characteristic of the observed scene and has a gamma probability density function (pdf)

$$(1) \quad p_{\tau}(\tau) = \frac{1}{\Gamma(v)} \left(\frac{v}{\mu} \right)^v \tau^{v-1} e^{-\frac{v}{\mu}\tau}, \quad \tau > 0.$$

Its mean value μ is the mean reflected power and the order parameter v , which controls its variance, is a measure of the inhomogeneity of the scattering from the scene.

To derive the optimum estimation structures, we describe the model for the vector $\underline{x} = [x_{-L}, \dots, x_L]^T$ (for $L=N/2$), of the echoes $x_n = \tau_n \cdot z_n$, $n = -L, \dots, L$ received from $N+1$ adjacent range cells. With reference to a maritime search radar we can assume that the texture contributions from successive range cells show some partial correlation, depending on the sea swell configuration. On the contrary, at least as a first approximation, the speckle components in adjacent range cells can be considered decorrelated. In the presence of target the central component z_0 has a Rice pdf with gain factor 1 and noncentral parameter δ equal to the target signal power. Thus the multivariate pdf of \underline{x} can be written as

$$(2) \quad p_{\underline{x}}(\underline{x}) = \int_0^{\infty} \dots \int_0^{\infty} p_{\underline{x}/\underline{\tau}}(\underline{x}/\underline{\tau}) \cdot p_{\underline{\tau}}(\underline{\tau}) d\underline{\tau} \\ = \int_0^{\infty} \dots \int_0^{\infty} p_{\underline{\tau}}(\underline{\tau}) \prod_{n=-L}^L \tau_n^{-1} e^{-\frac{x_n}{\tau_n}} e^{-\delta} I_0 \left[2\sqrt{\delta \frac{x_0}{\tau_0}} \right] d\underline{\tau}$$

where the correlation structure of the texture component is implicit in the multivariate pdf $p_{\underline{\tau}}(\underline{\tau})$ of the vector $\underline{\tau} = [\tau_{-L}, \dots, \tau_L]^T$, representing the $N+1$ partially correlated texture variables. To simplify the analysis we

¹The author is currently at the Dept. of Electrical and Computer Engineering, Syracuse University, 121 Link Hall, Syracuse, NY, 13244, USA

assume a first order Markov structure for the texture component, which allows us to use the factorization

(3)

$$p_{\underline{\tau}}(\underline{\tau}) = p_{\tau_2/\tau_1}(\tau_2/\tau_1) \cdots p_{\tau_{L+1}/\tau_L}(\tau_{L+1}/\tau_L) \cdot p_{\tau}(\tau_L)$$

with conditional probability

(4)

$$p_{\tau_i/\tau_{i-1}}(\tau_i/\tau_{i-1}) = \frac{v}{\mu} \frac{1}{\rho^{v-1}(1-\rho^2)} \left(\frac{\tau_i}{\tau_{i-1}} \right)^{\frac{v-1}{2}} e^{-\frac{v}{\mu} \frac{\tau_i + \rho^2 \tau_{i-1}}{1-\rho^2}} I_{v-1} \left[\frac{v}{\mu} \frac{2\rho}{1-\rho^2} \sqrt{\tau_i \cdot \tau_{i-1}} \right]$$

where ρ is the one-lag correlation coefficient. For half-integer order parameters, the gamma correlated sequence with conditional pdf defined by eq. (4) can be derived as the sum of the squares of $2v$ gaussian exponentially correlated variables with one-lag correlation coefficient $\sqrt{\rho}$ and is itself exponentially correlated [4].

In the detection it is of high interest to assure the maximum probability of detection (Pd), maintaining the constant false alarm rate (CFAR) condition. Assuming an ideal knowledge of the texture in each cell, this is obtained by the ideal CFAR, by setting the detection threshold on the speckle component only. In practice this knowledge is not available and we replace the true value with its estimate, based on the N closest range cell. The work is therefore highly based on the joint pdf model of the $N+1$ received echoes in eq. (2), which will be exploited to derive optimum texture estimators. The performances obtained using the different estimators will be evaluated, showing their strong dependence on the correlation coefficient ρ .

3. Texture estimators

Using the pdf model in eq. (2)-(4) we can tackle the derivation of the texture estimators. We will derive two different estimators operating respectively in the domain of intensity and in the domain of the logarithm of intensity. The former is the more natural domain and will be considered first. The latter domain shows a series of desirable properties as much lower estimation errors for the parameters of the model [4]-[5]. Moreover it appears to be especially suited for variables with product model distribution, where the logarithmic transformation converts the product into a sum of variables. The estimators, derived below, make use of the N samples x_n , $n \neq 0$ around the central sample x_0 , which is the cell under test.

Since the estimation of the texture in the central range cell is obtained using the informations in the neighbor range cells only, sensible results can be achieved only if the

texture is highly correlated. According with this consideration, a first estimator will be obtained assuming it completely correlated: $x_n = \tau \cdot z_n$ and deriving the Maximum Likelihood (ML) estimate of τ . Namely we maximize the conditional pdf of the vector \underline{x} , given τ :

$$(5) \quad p_{\underline{x}}(\underline{x} / \tau) = \exp \left(-\frac{1}{\tau} \sum_{n=-L, n \neq 0}^L x_n \right)$$

Nulling the derivative of the logarithm of eq. (5) with respect to τ we get $\hat{\tau} = \frac{1}{N} \sum_{n=-L, n \neq 0}^L x_n$. This is coincident

with the usual cell-average (CA) CFAR scheme, which shows to be optimum for the estimation of the local texture variable, assuming a complete correlation. Even though the CA scheme has been derived for this specific case, it can be applied to every correlation condition. A loss in detection performance is expected, which grows as ρ decreases.

To obtain an accurate estimator when the texture is partially correlated, the prior pdf of the texture sequence must be properly represented in the model used for the optimization. This leads to complex equations in the domain of intensity. An approximate solution can be found in the logarithmic domain, where the product model is mapped in a sum: $w_n = \ln x_n = \ln \tau_n + \ln z_n = t_n + u_n$. A simplified texture estimator is obtained by approximating the pdf of the two logarithmic transformed variables by two gaussian distributions with the same first and second order statistics of the true distributions. Namely for $u = \ln z$ we have a mean value $m_u = -\gamma$ (γ is the Euler constant) and an identity covariance matrix $R_u = \sigma_u^2 I$, where $\sigma_u^2 = \pi^2 / 6$. $t = \ln \tau$ has a mean value $m_t = \langle \ln \tau \rangle = \psi(v) - \ln(v/\mu)$, where $\psi(v)$ is the digamma function and the element (n,k) of its covariance matrix R_t is $\langle \ln \tau_n \ln \tau_k \rangle - \langle \ln \tau \rangle^2$, derived analytically in [4]. Thus the approximate joint distribution of the logarithms of texture $\underline{t} = [t_{-L}, \dots, t_{-1}, t_0, t_1, \dots, t_L]^T$ and received data vector $\underline{w} = [w_{-N}, \dots, w_{-1}, 0, w_1, \dots, w_N]$, with a zero replacing the echo from the cell under test, can be written as

$$(6) \quad p_{\underline{w}, \underline{t}}(\underline{w}, \underline{t}) = p_{\underline{w} / \underline{t}}(\underline{w} / \underline{t}) p_{\underline{t}}(\underline{t}) = \\ = \frac{e^{-\frac{1}{2\sigma_u^2}(\underline{w} - \underline{t}' - m_u \mathbf{1})^T (\underline{w} - \underline{t}' - m_u \mathbf{1})}}{(2\pi)^{N/2} \sigma_u^N} \cdot \frac{e^{-\frac{1}{2}(\underline{t} - m_t)^T R_t^{-1} (\underline{t} - m_t)}}{(2\pi)^{N/2} |R_t|^{1/2}}$$

where $\underline{t}' = [t_{-L}, \dots, t_{-1}, 0, t_1, \dots, t_L]^T$ is obtained from \underline{t} nulling its central component. The vector $\underline{1}$ has all the components equal to 1, except for the central one, which is set to 0, and the vector \underline{m}_t has all the components equal to m_t . A Maximum a Posteriori (MAP) texture estimate, called LMAP, is found by nulling the $N+1$ derivatives of the logarithm of eq. (6) with respect to the components of \underline{t}

$$(7) \quad \frac{\partial}{\partial \underline{t}} \left[(\underline{w} - \underline{t}' - \underline{m}_u \underline{1})^T (\underline{w} - \underline{t}' - \underline{m}_u \underline{1}) + (\underline{t} - \underline{m}_t)^T R_t^{-1} (\underline{t} - \underline{m}_t) \right] = \underline{0}.$$

The system in eq. (7) can be solved as $\hat{\underline{t}} = (I' + R_t^{-1})^{-1} \underline{w} + (I' + R_t^{-1})^{-1} (R_t^{-1} \underline{m}_t - \underline{m}_u \underline{1})$,

where I' is obtained from the $(N+1)$ -dimensional identity matrix, by nulling the central component. Thus in the domain of the logarithm we obtain a linear estimator. The estimated texture intensity for the central range cell can therefore be expressed as $\hat{\tau}_0 = \exp(\hat{t}_0)$.

It is instructive to observe that CA doesn't require the knowledge of the covariance matrix of texture and is easily implemented in all correlation conditions, even though it is optimum only for completely correlated texture. On the contrary, LMAP uses the informations about the prior distribution of the texture to get a better estimation accuracy. It requires for practical application a map of correlation, or its adaptive estimation. Next Section will be devoted to the performance analysis of the proposed estimators, with special attention to the evaluation of the improvement obtained by using the prior information.

4. Detection performances

The analytical performance analysis can be tackled only in the completely correlated condition and even in that condition there are no closed form expressions [1]. Therefore we will resort to simulations to assess the detection performance of the different schemes. We generate the $N+1$ clutter samples with correlated texture and independent speckle components, according to the model of Section 2. A set of signals with different amplitudes are added coherently to the central range cell to obtain the performance as a function of the signal-to-clutter-ratio $SCR = \delta/\mu$. For each of the 10^6 trials the echoes from the $N=8$ external range cells are used to estimate the local texture value, in accordance with the proposed estimation schemes, and the central cell is compared to the detection threshold $\hat{\lambda} = G \cdot \hat{\tau}$. The prob-

ability of false alarm is maintained constant, $P_{fa} = 10^{-4}$, by adequate selection of the threshold gain G .

The simulated results for the CA are shown in Fig. 1 for $v = 0.5$, as functions of the signal-to-clutter ratio $SCR = \delta/\mu$. The performance of ideal CFAR and fixed threshold are also given for comparison. It is instructive to observe the decrease of the detection performance with decreasing texture correlation ρ . In fact, the neighbor cells are less and less representative of the texture value in the central range cell. In particular for $\rho=1$ the detection curve is not far from the curve obtained with the 'ideal CFAR'. In fact in this condition we have a good estimation of the local texture value. For lower ρ values the detection performance degrades, crossing the fixed threshold curve, because the estimation variance is much higher. Specifically for $\rho=0$ the estimation cells don't contain any informations about the texture in the central range cell; this causes the detection curve to be always lower than the fixed threshold curve. Fig. 2 and 3 show a comparison of the detection performances of CA and LMAP for $v=0.5$ and $\rho=0.7+0.95$ and for $v=5$ and $\rho=0.7+0.95$ respectively. LMAP detection curves are always contained between 'ideal-CFAR' and fixed threshold ones (from more extended simulation we can assess that this apply to every value of ρ). Moreover the LMAP estimator is less dependent on the correlation than the CA and provides always the best performance.

The improvement obtained with respect to the CA scheme depends on the texture variance, namely on the inverse of v . Moreover, it appears evident that for $v=5$ the spread of the detection performances with the correlation coefficient ρ is much reduced with respect to the condition of $v=0.5$. This can be explained in terms of the normalized texture variance, which is equal to $1/v$ and is reduced as v increases. For a high variance an accurate estimator is important. On the contrary, with a small texture variance, even though the detection scheme uses an estimate of the texture mean value instead of an estimate of the local texture, the detection performance is not highly affected. The analysis of accurate texture estimators is therefore of interest mainly for very spiky clutter distributions. In this condition we have shown that the new LMAP estimator achieves better performance than the more usual CA. This shows the importance of the use of prior information especially for the partially correlated case. From the behaviour of the plots we can also observe that for high correlation and high SCR the LMAP is close enough to the ideal CFAR. The validity of the latter for practical application is therefore assessed in this condition. It is evident, though, its purely theoretical significance for low texture correlations.

5. References

- [1] S. Watts, "Radar detection prediction in sea clutter using the compound K-distribution model", IEE Proc. Pt. F, Vol. 132, No. 7, Dec. 1985, pp. 613-620.
- [2] K.D. Ward, "Compound representation of high resolution sea clutter", Electronics Letters, Vol. 17, No.16, 6-th Aug. 1981, pp. 561-563.
- [3] T. Bucciarelli, "Sub clutter visibility in marine radars", Alta Frequenza, Vol. 54, No. 6, Nov 1985, pp. 359-366.
- [4] P. Lombardo, C.J. Oliver, "Comparison of estimators for correlation properties in K-distributed SAR images", The European Symposium on Satellite Remote Sensing, EUROPTO, Rome, Sept 1994, n. 2316-33.
- [5] P. Lombardo, C.J. Oliver, "Estimation of texture parameters in K-distributed clutter", IEE Proc. on Radar, Sonar and Navigation, Vol 141, No. 4, August 1994, pp.196-204.

Pd

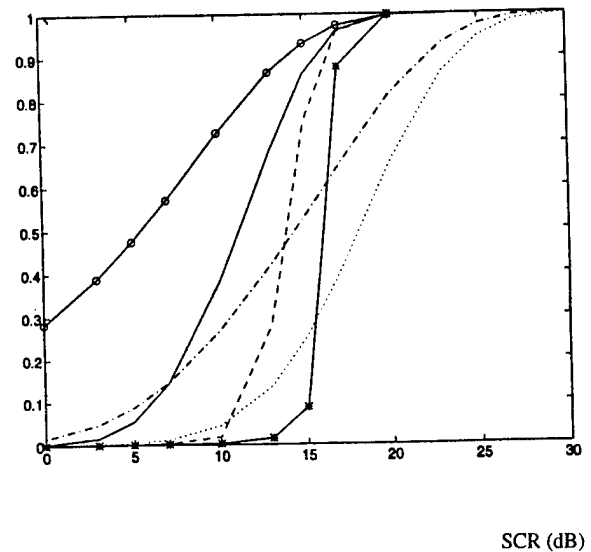


Fig. 2 - Comparison of the Pd as a function of the SCR for the CA and LMAP schemes for K-distributed clutter with $v=0.5$ and $N=8$ range cells. $\rho=0.95$: CA, (—○—), LMAP, (—); $\rho=0.7$, CA, (.....), LMAP, (- - -). For comparison 'ideal CFAR', (O), and fixed threshold, (*).

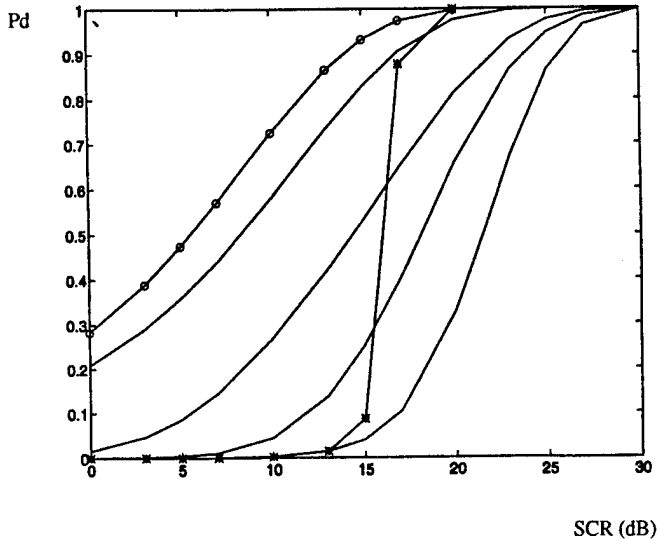


Fig. 1 - Pd as a function of the SCR for the CA scheme for K-distributed clutter with $v=0.5$, $N=8$ range cells and $\rho=1, 0.95, 0.7, 0$ (curves in decreasing order) compared to 'ideal CFAR', (O), and fixed threshold, (*).

Pd

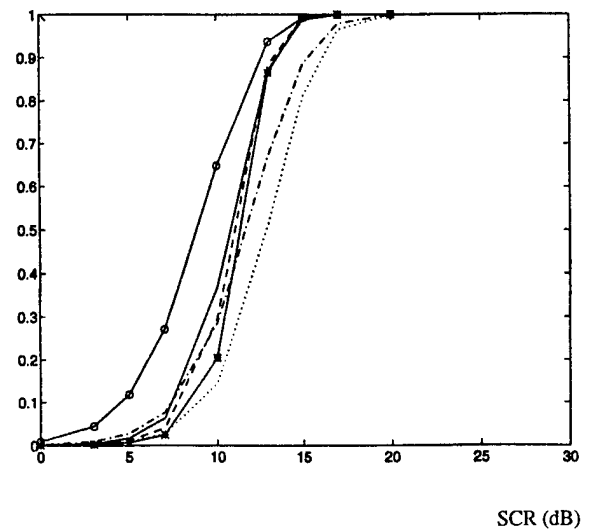


Fig. 3 - Comparison of the Pd as a function of the SCR for the CA and LMAP schemes for K-distributed clutter with $v=5$ and $N=8$ range cells. $\rho=0.95$: CA, (—○—), LMAP, (—); $\rho=0.7$, CA, (.....), LMAP, (- - -). For comparison 'ideal CFAR', (O), and fixed threshold, (*).

A DSP PERSPECTIVE OF SIGMA-DELTA TECHNIQUES AND APPLICATIONS IN COMMUNICATIONS

M. Bellanger
CNAM
292, rue Saint-Martin
F-75141 PARIS Cedex 03 FRANCE

Abstract:

Although originally analog, SIGMA-DELTA techniques have become a DSP tool. After a review of the basic principles, a design technique is presented for the bandpass loop filter of a high performance modulator and stability issues are discussed. Three applications linked to the area of communications are briefly discussed, a A/D converter for mobile radio, a direct digital synthesizer and a clock synchronization issue.

I - INTRODUCTION

SIGMA-DELTA is a feedback technique which was introduced for the digitization of telephone signals several decades ago [1]. Its most successful field of application has probably been the realization of high accuracy integrated analog/digital (A/D) converters [2]. Now, it is used in many technical fields, but the denomination of SIGMA-DELTA modulator has survived, from the initial application. Following the trend toward digital signal processing, it has become a DSP tool.

The concept is shown in fig.1.

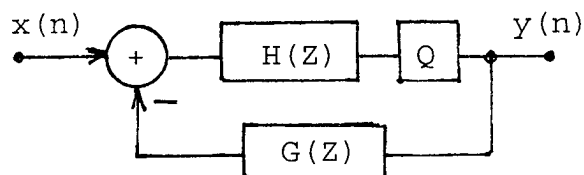


Fig.1 A SIGMA-DELTA modulator

The system output $y(n)$ is fed back and subtracted from the input $x(n)$. $G(Z)$ is the feedback filter and $H(Z)$ is called the loop filter. The box Q represents a non-linear operation, which generally corresponds to a quantization or rounding function. In a simplified analysis, it can be modelled as a source of an additive white noise $b(n)$ and the system operation is described, in terms of Z-transforms, by

$$Y(Z) = X(Z) \frac{H(Z)}{1+G(Z)H(Z)} + B(Z) \frac{1}{1+G(Z)H(Z)} \quad (1)$$

The input $X(Z)$ and the quantization noise $B(Z)$ are multiplied by two different transfer functions and, thus, the spectral distributions in the output of the input signal and the noise can be controlled. The following particular case is worth pointing out

$$H(Z) = \frac{1}{1 - G(Z)} \quad (2)$$

The diagram is shown in fig.2 and

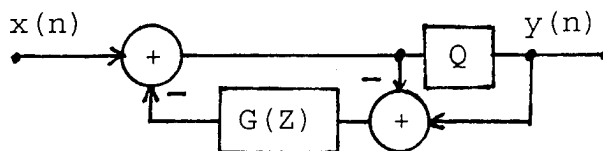


Fig.2. Noise shaping circuit

the equations become

$$Y(Z) = X(Z) + B(Z) [1 - G(Z)] \quad (3)$$

Only the quantization noise is affected by the system which is a noise shaping circuit. Both approaches in figures 1 and 2 are used in applications.

The performance of the system is critically dependent on the filters.

II-FILTER DESIGN-STABILITY

In some major applications, like A/D conversion, the feedback filter is often just a one sample delay, i.e. $G(Z) = Z^{-1}$ and the design problem concentrates on the loop filter. Then, stability analysis has to be included in the design process and the model shown in fig.3 is considered. The quantizer is

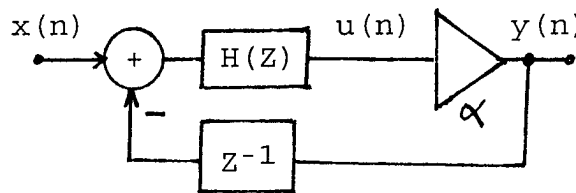


Fig.3. Model for stability analysis

replaced by an amplifier with gain α . Assuming that $H(Z)$ takes the form

$$H(Z) = N(Z) / D(Z) \quad (4)$$

the signal transfer function is

$$K(Z) = \frac{U(Z)}{X(Z)} = \frac{N(Z)}{D(Z) + \alpha Z^{-1}N(Z)} \quad (5)$$

The stability of the system depends on the poles of that function. Their locations in the complex plane in turn depends on the value α and a root locus analysis has to be carried out [3]. The system is stable, when it oscillates at half the sampling frequency $f_s/2$, i.e. a pole sits at -1, and all the other poles are

inside the unit circle. Then, the magnitude of the oscillation is $H(-1)$. In order to reject the noise out of the passband, the gain of the filter $H(Z)$ must be large and the poles must be located in the passband and close to the unit circle. An efficient approach for the filter design consists in using inverse notch sections defined by

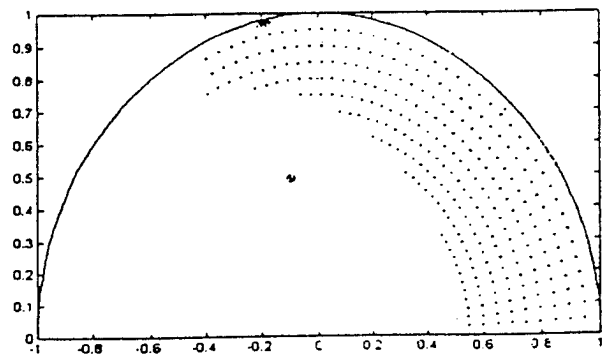
$$H_1(Z) = \frac{1 - 2(1-a)\cos\theta Z^{-1} + (1-a)^2 Z^{-2}}{1 - 2(1-b)\cos\theta Z^{-1} + (1-b)^2 Z^{-2}} \quad (6)$$

a and b being positive scalars such that: $0 < b < a < 1$.

The peak magnitude of the frequency response is approximately a/b .

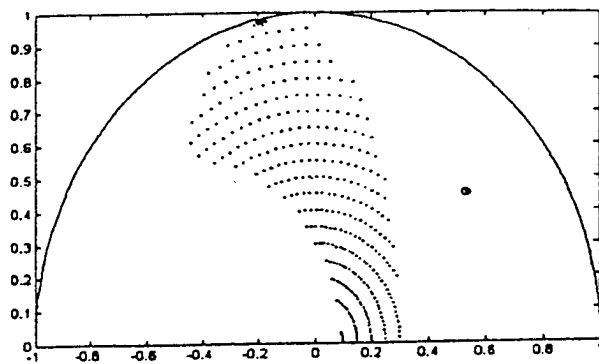
A procedure to include the stability in the design is as follows. The poles and the zeros of the filter sections are chosen to comply with the width of the passband and the gain objectives. Then, a pair of zeros is moved, so that all the other poles of $K(Z)$ are within the unit circle when α is such that the real pole reaches (-1).

As an illustration, the dotted area in fig.4 is the authorized domain



Poles	Zeros
$-0.2012 \pm 0.9693i$	$-0.0935 \pm 0.4912i$
$-0.1851 \pm 0.9725i$?

Fig.4-a. Authorized domain for the second zero pair in an order 4 filter, when a zero pair (and poles) is fixed.



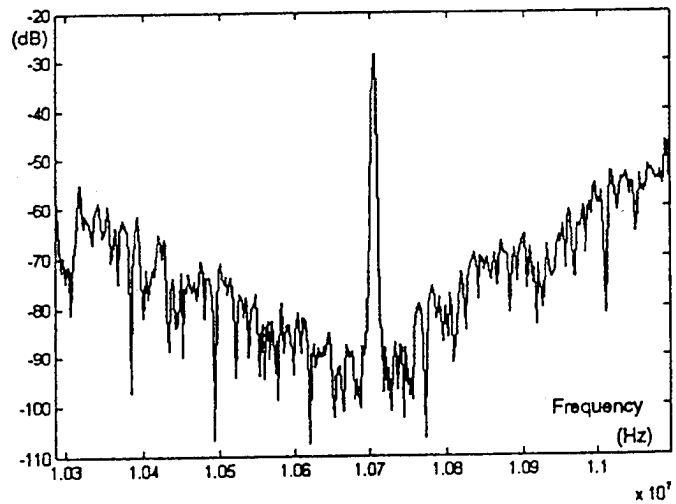
Poles	Zeros
$-0.2012 \pm 0.9693i$	$0.5354 \pm 0.4510i$
$-0.1851 \pm 0.9725i$?

Fig.4-b. Alternative authorized domain.

for a pair of zeros, when two pole pairs and a zero pair are fixed in a system of order 4. It is obtained by a systematic search on a grid. In fig.4-b, a different choice of the fixed zero pair yields a different domain. In an iterative procedure, all the poles and zeros can be moved to optimize the design.

III- A/D CONVERTER FOR MOBILE RADIO

This is a typical field of application[5]. The method described above has been applied to the design of an A/D converter for mobile radio data signals, in the vicinity of the 10.7 MHz intermediate frequency. Considering a filter with order $M=4$, the poles and zeros obtained are given in fig.5, as well as the spectrum of the output signal, when the input is a sinewave. The passband of the useful signal is approximately 50kHz and the loop filter gain exceeds 60 dB, which leads to an accuracy of about 10 bits for the A/D converter.



Poles	Zeros
$-0.1756 \pm 0.8827i$	$0.2268 \pm 0.4456i$
$-0.1970 \pm 0.9907i$	$0.4388 \pm 0.2397i$

Fig.5. Spectrum of the output signal for a filter of order $M=4$.

The procedure can be exploited to design filters with higher orders leading to A/D converters of greater accuracy. The practicality of such designs relies on the technology employed for the implementation and the context in which the equipment is operated.

IV- DIRECT DIGITAL FREQUENCY SYNTHESIZER

The flexibility of digital circuits can be exploited in frequency synthesis [6]. The bottleneck is generally the need for an accurate and extremely fast D/A converter. In some applications, like microwave communications, the frequency domain in which the sinewaves have to be generated is significantly smaller than the values of the frequencies of the sinewaves themselves, giving rise to a sort of reduced band DDS. For example, it can be 50 MHz around 200 MHz.

In those conditions, a SIGMA-DELTA

circuit can produce a quantization noise shaping and, thus, attenuate the noise in the critical band, which, for a given D/A converter, improves the spurious performance. The concept is shown in fig.6. The noise frequency above the loop filter bandwidth, through noise shaping. An efficient scheme is shown in fig.7, for order 3. It is a cascade of 3 sections and the noise produced by the decision circuit D is multiplied by $(1-Z^{-1})^3$.

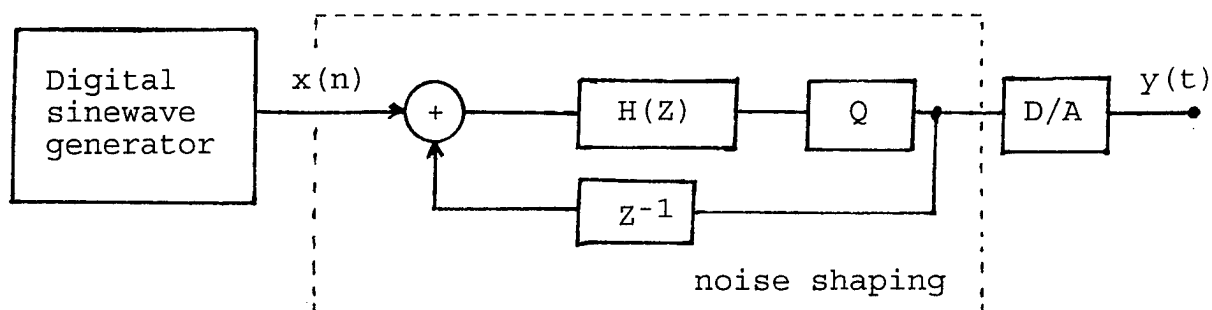


Fig.6. Reduced band Direct Digital Synthesizer with noise shaping

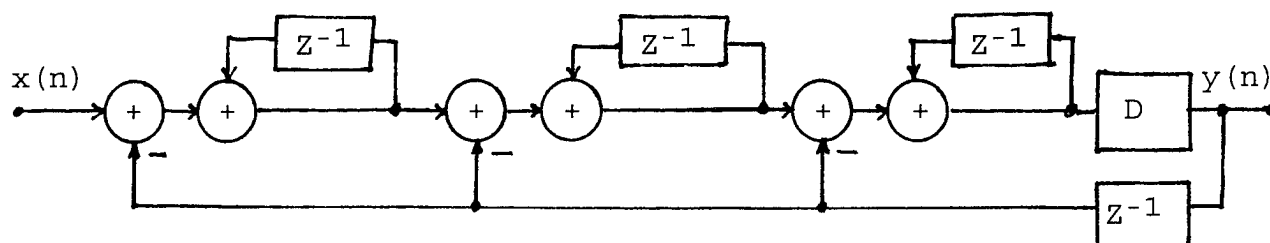


Fig.7. A cascade structure for noise shaping

rejection capacity of the filter, and its design, is related to the performance objectives and the characteristics of the D/A converter.

V - CLOCK SYNCHRONIZATION

In various applications, like broadcasting, digital storage, telephony or remote sensing, a clock produced by a source has to be transmitted over data channels and accurately restored at the receiving side, generally with the help of a phase lock loop. The quality of the recovered clock depends on the width of the lowpass loop filter and on the spectrum of the digital information transmitted, for example under the form of time stamps, stuffing bits, or other timing data [7]. In the spectrum of the transmitted signals, the undesirable components can be shifted in

To conclude, SIGMA-DELTA techniques can adjust to different contexts in terms of functionalities and performance and have a great potential.

References

- [1] R.Steele, "DELTA Modulation Systems", Pentech Press, London, 1975.
- [2] J.C.Candy and G.C.Themes, "Over-sampling DELTA-SIGMA Data Converters", IEEE Press, New York, 1991.
- [3] R.Van der Plassche, "Integrated A/D and D/A converters", Kluwer, 1994.
- [4] M.Bellanger et al., "Poles and Zeros of bandpass filters for $\Sigma\Delta$ Modulators", Int.J.of Circuit Theory and Applications, Vol.23, 1995.
- [5] S.Jantzi et al. "A 4-order band-pass $\Sigma\Delta$ Modulator", IEEE J.of S.S.C. Vol.28, No.3, March 1993, pp.282-291.
- [6] H.Nicolas et al. "A 150 MHz DDS in CMOS with -90 dBc Spurious Perf." IEEE J.of S.S.C., Vol.26, No.12, 1991.
- [7] ISO/IEC 13818-1, ITU-T Rec.H.222 Generic Coding of Moving Pictures & Audio Info., Part 1: Systems, 1994.

ADAPTIVE CHANGE OF CODE RATE IN DS-SSMA COMMUNICATION SYSTEMS

Youngkwon Ryu[†], Suk Chan Kim, Iickho Song*, Seong Ill Park*, and Hyung Myung Kim**

[†]WLL Research Lab., R/D Center, DACOM Co.

34 Gajeong Dong, Daejeon 305-350

Tel: +82-42-220-4165

e-mail: ryu@halla.dacom.co.kr

*Department of Electrical Engineering

Korea Advanced Institute of Science and Technology (KAIST)

373-1 Guseong Dong, Yuseong Gu, Daejeon 305-701, Korea

Phone : +82-42-869-3445, Fax : +82-42-869-3410

e-mail: isong@Sejong.kaist.ac.kr

Abstract - An adaptive code rate change scheme in DS-SSMA systems is proposed. In the proposed scheme, the error correcting code rate is changed according to the channel state, the effective number of users. The channel state is estimated based on retransmission requests. The criterion for the change of the code rate is to maximize the throughput under given error bound.

1 Introduction

In FH-SSMA systems using Reed-Solomon error correcting codes, optimum code rate and optimum number of users for maximum throughput can be obtained when the number of hopping frequencies and the packet error probability are given [1].

In DS-SSMA systems, however, neither optimum code rate nor optimum number of users has been obtained. In DS-SSMA systems, packet error probability and channel throughput are merely increasing functions of the code rate and number of users. In this paper, a transmission scheme is proposed which controls the error correcting code rate adaptively according to the channel states to maximize throughput when the packet error probability is fixed in DS-SSMA communication systems.

In this paper, retransmission requests is used to estimate the channel state, *i.e.*, the number of users, which has major effects on the bit error performance.

2 The System Model

The system considered here is shown in Figure 1.

In Figure 1, $a_k(t)$, $b_k(t)$, $d_k(t)$, and θ_k are the random signature signal with bit duration T_c , encoded signal with bit duration T , data signal, and phase of the k th carrier, respectively. The common carrier (angular) frequency ω_c is known, and K is the number of users. We assume that each signature sequence has an integer period $N = T/T_c$. The transmitted signal for the k th user can be written as

$$s_k(t) = \sqrt{2P} \text{Re} [a_k(t)b_k(t)\exp(j\omega_c t + j\theta_k)] \quad (1)$$

where P is the signal power.

Assuming that the channel is a Rician fading channel, the faded signal can be written as

$$y_k(t) = \text{Re} \{u_k(t - \tau_k)\exp[j\omega_c(t - \tau_k) + j\theta_k]\} + n_k(t) \quad (2)$$

where $n_k(t)$ is the additive white Gaussian noise (AWGN) term,

$$u_k(t) = \gamma \int_{-\infty}^{\infty} \beta_k(\tau, t) s_k(t - \tau) d\tau + s_k(t) \quad (3)$$

and γ is the transmission coefficient (or, fading intensity) of the fading channel, with $\beta_k(t, \tau)$ a zero-mean complex Gaussian random process. We assume that the effective number of users and the fading environment are varying slowly.

Figure 2 shows the receiver model, where it is assumed that the phase of the despreading signal is matched to the received signal, *i.e.* $\phi_k = \theta_k - \omega_c \tau_k$. It is assumed that Reed-Solomon code is used for error control, and the selective repeat request strategy is employed in the ARQ [2].

We change the code rate by changing the information bit length with the code word length fixed. We assume that backlogged packets, requested through an ideal backward channel, are retransmitted in the next packet transmission slot with probability 1. In any time slot, K packets are transmitted: if a user is requested for a retransmission the user is not allowed to send a new packet.

2.1 Bit Error Probability

Assuming the number of users is large enough to satisfy the central limit theorem, it has been shown in [3] that the approximation of multiple access interference (MAI) to AWGN results in quite close calculation of the bit error probability. Under the approximation, the bit error probability is

$$P_b = \frac{1}{\sqrt{2\pi}} \int_{\text{SNR}}^{\infty} \exp(-u^2/2) du \quad (4)$$

where SNR is the effective signal to noise ratio (SNR) with the approximation taken into account. The effective signal to noise ratio at the input of the decoder in Figure 2 has been calculated [4]. The estimation procedures in this paper are based on the observation that SNR in (4) can be expressed as

$$\text{SNR} = (CK' + D)^{-1/2}, \quad (5)$$

where K' is the effective number of users and C and D are determined by the fading types. Note that the parameters C and D are functions of the fading intensity, fading range, channel covariance, random signature sequence length, and SNR of AWGN.

2.2 Packet Error Probability

Let P_c , P_d , and P_u denote the probabilities that a decoded packet contains no error, detectable errors, and undetectable errors, respectively. Then we have $P_c + P_d + P_u = 1$.

Since Reed-Solomon code can correct up to $\lfloor (n-k)/2 \rfloor$ errors, it is easy to see that

$$P_c = \sum_{i=0}^{\lfloor (n-k)/2 \rfloor} \binom{n}{i} P_b^i (1 - P_b)^{n-i} \quad (6)$$

where $\lfloor x \rfloor$ is the largest integer not greater than x , n is the codeword length, and k is the information bit length. We also have

$$P_u = \sum_{i=n-k+1}^n A_i P_b^i (1 - P_b)^{n-i}, \quad (7)$$

where A_i is the weight distribution defined as [5]

$$A_i = \binom{n}{i} \sum_{j=0}^{i-n+k-1} (-1)^j \binom{i}{j} [(n+1)^{i-n+k-j} - 1]. \quad (8)$$

The probability P_E that the receiver commits an error when the ARQ strategy is used is given by

$$\begin{aligned} P_E &= \sum_{i=1}^{\infty} P_u P_d^{i-1} \\ &= \frac{P_u}{P_c + P_u}. \end{aligned} \quad (9)$$

3 Adaptive Code Rate Change Algorithms

In general, the error performance of the DS-SSMA system is worse than that would be caused by K (real) users counted by the base station because of near cell interference. The added error performance degradation effects result in increase of the number of users, the effective number of users K' . Note that P_E defined in (9) is now a function of the code rate k/n , the effective number of users K' , fading environment, and the ratio of pure AWGN power and signal power.

3.1 Code Rate for Maximum Throughput

In this paper, our performance criterion is to maximize the throughput when P_E is limited to a fixed value, where the throughput is defined as

$$E = \frac{K}{N} \frac{k}{n} (P_u + P_c). \quad (10)$$

Since P_E and the throughput are merely increasing functions of the number of effective users and code rate in DS-SSMA systems, the code rate which satisfies the P_E bound maximizes the channel throughput.

When the effective number of users is given and the fading environment is known, we calculate P_E for all code rates ($k = 1, 2, \dots, n$) by making use of (4), (6), (7), and (9). We then select the largest code rate which results in less P_E than the given bound. Some results are given in [6], assuming that the error correcting code length $n = 15$, the random signature sequence length $N = 1023$, the signal power $\mathcal{E} = PT$, and the pure AWGN power is N_0 . It is also shown in [6] that the code rate becomes high as the effective number of users decreases, and the effect of the pure AWGN on P_E is more severe when the fading intensity of MAI γ is smaller.

3.2 Estimation of Effective Number of Users

Figure 3 shows our estimation scheme, where we assume slotted communication: that is, each user transmits simultaneously one packet per slot. In Figure 3, T_s is the slot interval, $T_M = LT_s$ is the channel

monitoring interval, L is the channel monitoring slot number, R_i is the number of backlogged packets in the i th slot, and K'_i is the estimate of K' in the i th transmission slot. We assume that the code rate is constant during the channel monitoring interval and can be changed at the start of every channel monitoring interval. We assume the number of users K is constant over a channel monitoring interval, which can be achieved by not accepting new users until the end of a channel monitoring interval and allowing them to communicate at the beginning of the next channel monitoring interval. Once the estimation of the effective number of users is accomplished, we can optimize the code rate based on the estimated effective number of users.

More specifically, at the i th transmission slot, we can obtain K'_i from

$$K P_R(K'_i|k) = R_i, \quad (11)$$

where k is the information bit length trimmed to satisfy P_E limit for the previously estimated effective number of users and $P_R(K'_i|k)$ denotes the retransmission probability for K'_i effective users when the code rate is $r = k/n$. This probability can be calculated using (6) and (7), or

$$\begin{aligned} P_R(A|k) &= P_d|_{K'=A} \\ &= 1 - P_u|_{K'=A} - P_c|_{K'=A} \end{aligned} \quad (12)$$

for Reed-Solomon error correcting codes.

At the end of the channel monitoring interval, we take

$$\overline{K'_L} = \max \left\{ \frac{1}{L} \sum_{i=1}^L K'_i, K \right\} \quad (13)$$

as the estimate of the effective number of users. If the number of new calls minus that of dismissed calls during the channel monitoring interval is K_n , we assume that $\overline{K'_L} + K_n$ (effective) users are on the line in the next channel monitoring interval and change the code rate using the results in [6] based on this number.

Figures 4 and 5 show simulation results of the estimation where k_{opt} is the information bit length which results in the maximum throughput under the P_E bound 10^{-4} . In Figures 4 and 5, it is assumed that $L = 20$ and the fading is time selective with $\lambda = 1.5$, $\gamma = 1.0$, and $\frac{\epsilon}{N_0} = 10$ dB. In Figure 4, it is assumed that $K = 300$ and $K' = 350$. In Figure 5, it is assumed that $K = 400$ and $K' = 450$. We can see that even when the code rate was incorrectly selected in the present channel monitoring interval because the effective number of users had been estimated incorrectly in the previous channel monitoring interval, we can estimate the effective number of users to some degree of accuracy. The estimate of the effective number of users can then be used to change the code rate adaptively based on the results of [6].

4 Summary

In this paper, we proposed an adaptive code rate change scheme in DS-SSMA systems. In the proposed scheme, the error correcting code rate was changed according to an estimate of the effective number of users, which has significant effects on the bit error probability.

We estimated the effective number of users by making use of the retransmission requests. The criterion for the change of the code rate based on the estimated channel states was to maximize the throughput under given error bound.

Acknowledgement

This research was supported by Korea Science and Engineering Foundation under Grant 941-0900-040-2, and by the Ministry of Information and Communications under a Grant from University Basic Research Fund, for which the author would like to express their thanks.

References

- [1] S.W. Kim and W. Stark, "Optimum Rate Reed-Solomon Codes for Frequency-Hopped Spread-Spectrum Multiple-Access Communication Systems," *IEEE Trans. Comm.*, vol. COM-37, pp. 138-144, February 1989.
- [2] S. Lin and D.J. Costello, Jr., *Error Control Coding*, Prentice-Hall, Inc. Englewood Cliffs, NJ, 1983.
- [3] R.K. Morrow, Jr. and J.S. Lehnert, "Bit-to-Bit Error Dependence in Slotted DS/SSMA Packet Systems with Random Signature Sequences," *IEEE Trans. Comm.*, vol. COM-37, pp. 1052-1061, October 1989.
- [4] D.E. Borth and M.B. Pursley, "Analysis of Direct-Sequence Spread-Spectrum Multiple-Access Communication Over Rician Fading Channels," *IEEE Trans. Comm.*, vol. COM-27, pp. 1566-1577, October 1979.
- [5] T. Kassami, S. Lin, and W.W. Peterson, "Some Results on Weight Distributions of BCH Codes," *IEEE Trans. Inf. Theory*, vol. IT-12, p. 274, April 1966.
- [6] Y. Ryu, *An Adaptive Code Rate Change Technique in DS-SSMA Communication Systems*, M.S.E. Thesis, Department of Electrical Engineering, Korea Advanced Institute of Science and Technology (KAIST), Daejeon, Korea, December 1994.

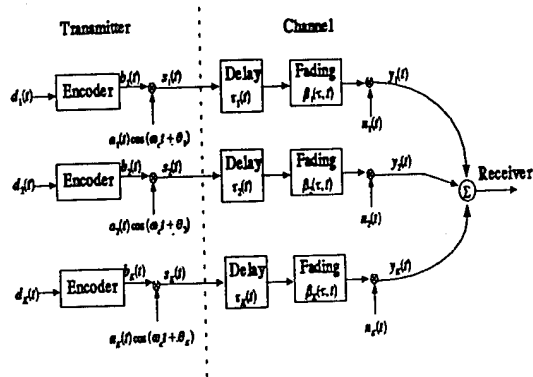


Figure 1. The System Model

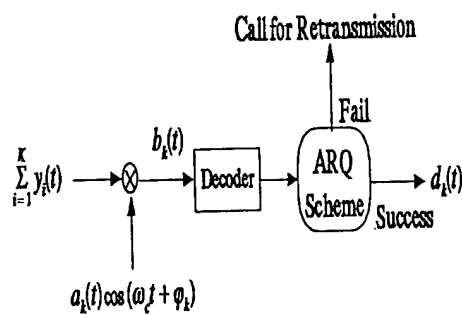


Figure 2. The Receiver Model

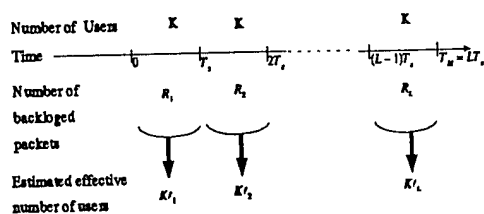


Figure 3. Estimation of Effective Users

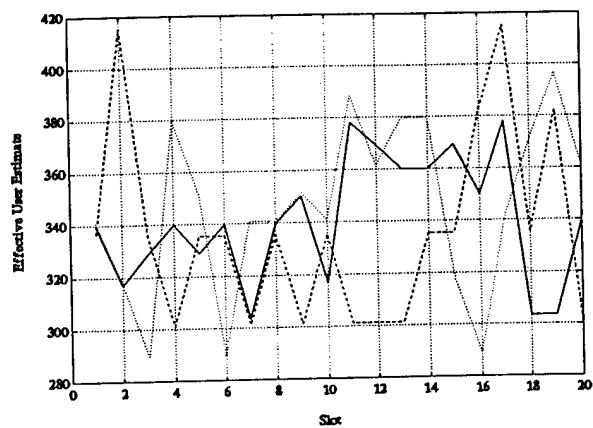


Figure 4. Simulation Results for $K = 300$ and $K' = 350$
(a) When k_{opt} is used $\Rightarrow \overline{K'_{20}} = 341$: ————
(b) When $k_{opt} - 1$ is used $\Rightarrow \overline{K'_{20}} = 336$: - - - - -
(c) When $k_{opt} + 1$ is used $\Rightarrow \overline{K'_{20}} = 346$:

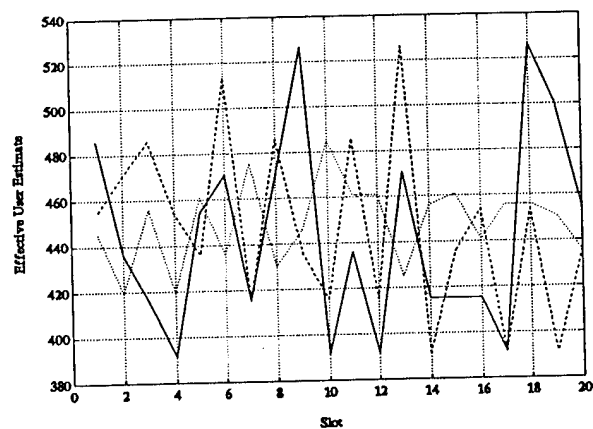


Figure 5. Simulation Results for $K = 400$ and $K' = 450$
(a) When k_{opt} is used $\Rightarrow \overline{K'_{20}} = 444$: ————
(b) When $k_{opt} - 1$ is used $\Rightarrow \overline{K'_{20}} = 443$: - - - - -
(c) When $k_{opt} + 1$ is used $\Rightarrow \overline{K'_{20}} = 449$:

MODIFIED DELAY-LOCKED LOOP FOR FADING CHANNELS

A. Wilde

Institute for Communications Technology
German Aerospace Research Establishment
D-82234 Wessling
Andreas.Wilde@dlr.de

ABSTRACT

The delay-locked loop (DLL) is well suited to guarantee fine synchronization for direct-sequence spread spectrum systems. In fading channels the mean time to lose lock (MTLL) of a DLL is very important because a loss of lock during a fade makes a re-acquisition process necessary. Using a two state model for the fading channel and a modified DLL will improve the MTLL considerably. The modified DLL operates in two different modes: a normal tracking mode for good channel conditions, and a "fade" mode for bad channel conditions, i.e. during a deep fade. The modified DLL is more robust against bad channel conditions.

INTRODUCTION

Spread spectrum techniques have become popular for various commercial applications, e.g. mobile communications based on Code Division Multiple Access (CDMA) and positioning systems (GPS). For direct sequence spread spectrum systems (DS-SSS) the exact code phase timing estimate is very important. The timing is influenced by clock offsets and by Doppler effects especially in mobile environments. In DS-systems, pseudo-noise (PN) code tracking with a delay-locked loop (DLL) is commonly used. The code phase estimate is produced by comparing the received signal with both early and late replicas of the locally generated PN reference sequence. The code phase timing error drives the clock of a PN-code generator to adjust the code phase timing. This is a closed-loop tracking control system. The conventional DLL has been studied in the literature in detail [1], [2], [3]. For the DLL there exist two com-

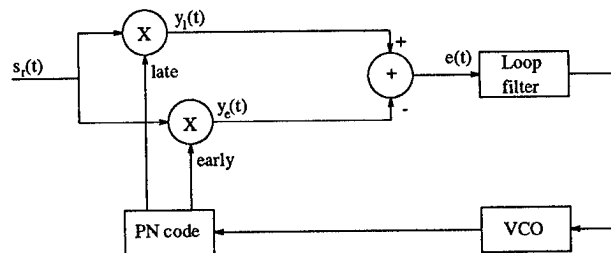


Fig. 1. Coherent conventional DLL

monly used performance criteria: the tracking jitter and the mean time to lose lock (MTLL). During normal operation the tracking jitter should be small enough to guarantee low error rates for spread spectrum data transmission and small delay errors for ranging systems. The tracking jitter is of main interest for sufficient high signal to noise ratios (SNR). The MTLL is very important for low SNR values. The MTLL characterizes the mean time that a DLL stays in its tracking range. When the DLL falls out of lock a re-acquisition process has to be started during which no data transmission or ranging is possible. The MTLL should be larger than the normal transmission time. The calculation of the MTLL is based on Fokker-Planck techniques for solving non-linear stochastic differential equations [1], [3], [4], [5]. In this paper a modified DLL for fading channels is proposed.

DLL DESCRIPTION

The conventional coherent DLL structure is shown in Figure 1. The received signal is multiplied by the early and late replicas of the local PN-code. The spacing between the early and late replicas is $2\delta T_c$, with T_c the chip duration and δ the normalized time offset of the early-late correlators. The error signal

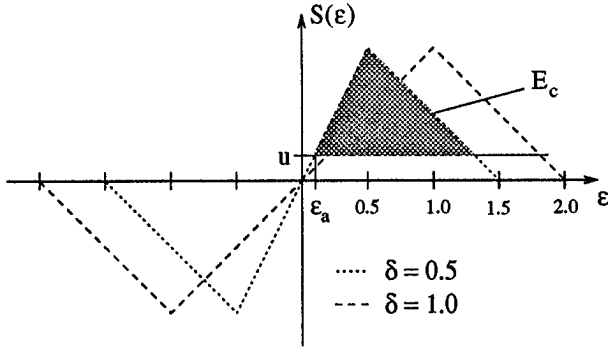


Fig. 2. S-curve for different coherent DLLs

$e(t)$ is the result of subtracting the despread early and late signals. The loop filter generates the input signal for the voltage controlled oscillator (VCO) steering the local PN-code generator. The loop filter is designed to keep the tracking error low. Due to the low bandwidth in the DLL an autocorrelation (ACF) over the PN-code is performed. The S-curve $S(\epsilon)$ for the conventional coherent DLL is shown in Figure 2 as a function of the timing error ϵ . The S-curves in Figure 2 are based on an ideal ACF which is the limit for the ACF of m-sequences as N , the sequence length tends to infinity.

The linear tracking range TR_{lin} is defined by the region around the origin where the relation between the delay discriminator output $S(\epsilon)$ depends linearly on the delay error ϵ . The linear tracking range is reduced when δ is reduced. The overall tracking range TR_{ov} is defined as the region where $S(\epsilon)$ produces a useful output signal to drive the VCO through the loop filter. The spreading waveform is denoted by $c(t - T_d)$. $T_d(t)$ is the timing offset between transmitter and receiver. $\hat{T}_d(t)$ is the receiver estimate of $T_d(t)$. The received signal in baseband is given by

$$s_r(t) = \sqrt{P}c(t - T_d) + n(t) \quad (1)$$

where P is the signal power and $n(t)$ is additive white Gaussian noise with two sided spectral power density $N_0/2$. The received signal $s_r(t)$ is correlated with the early and late reference spreading waveforms $c(t - \hat{T}_d \pm \delta T_c)$. The correlator outputs are given by

$$y_{e/l}(t) = \sqrt{P}c(t - T_d)c(t - \hat{T}_d \pm \delta T_c) + n(t)c(t - \hat{T}_d \pm \delta T_c) \quad (2)$$

The phase error is defined by

$$\epsilon = (T_d - \hat{T}_d)/T_c \quad (3)$$

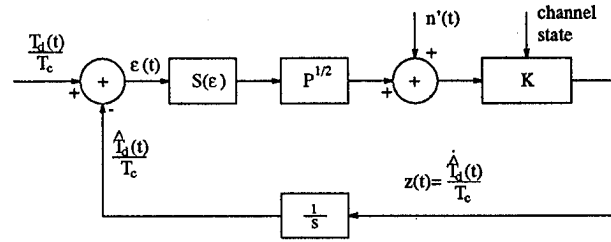


Fig. 3. Baseband equivalent DLL model

Assuming that the code self-noise [2] can be neglected and calculating the long term average $\bar{y}_{e/l}(t)$ yields

$$\begin{aligned} \bar{y}_{e/l}(t) &= \sqrt{P}R_c(T_d - \hat{T}_d \pm \delta T_c) + \bar{n}_{e/l}(t) \\ &= \sqrt{P}R_c(\epsilon \pm \delta T_c) + \bar{n}_{e/l}(t) \end{aligned} \quad (4)$$

with the idealized spreading code ACF defined by

$$R_c(x) = \begin{cases} 1 - |x|, & |x| < 1 \\ 0, & \text{else.} \end{cases} \quad (5)$$

Now the early and late branches are subtracted to give the error signal

$$e(t) = \bar{y}_l - \bar{y}_e = \sqrt{P}S(\epsilon) + n'(t) \quad (6)$$

which consists of the deterministic signal $\sqrt{P}S(\epsilon)$ and the white noise $n'(t)$. The noise characteristic of $n'(t)$ can be calculated via the autocorrelation function $R_{n'}(\tau)$ of $n'(t)$ as shown in [2] for the conventional DLL. The equivalent noise in the loop $n'(t)$ has two-sided power spectral density

$$S_{n'}(f) = N_0 \quad (7)$$

The equivalent baseband model for a first-order DLL is given in Figure 3. The nonlinearity $S(\epsilon)$ describes the discriminator characteristic (S-curve).

$$S(\epsilon) = R_c(\epsilon - \delta) - R_c(\epsilon + \delta) \quad (8)$$

$T_d(t)$ has the form

$$T_d(t) = T_0 + a_1 t \quad \text{with} \quad a_1 = \Delta R/R + v_0/c \quad (9)$$

where T_0 represents some constant time delay, ΔR the code clock mismatch, v_0 is a constant velocity relative to transmitter and receiver and c is the velocity of light. a_1 is the Doppler shift. The differential equation of the loop is given by

$$\dot{\epsilon}(t) = \frac{a_1}{T_c} - K\sqrt{P}S(\epsilon) - Kn'(t) \quad (10)$$

Some additional parameters are defined by

$$\tilde{K} = K\sqrt{P}, \quad u = \frac{a_1}{T_c \tilde{K}}, \quad \rho = \frac{\tilde{K} N_0}{2P} \quad (11)$$

For the noiseless case ($\rho = 0$) there exists one stable equilibrium point $(\epsilon_a, 0)$ with $S(\epsilon_a) = u$ and ϵ_a in the linear range of $S(\epsilon)$. Thus values $u \neq 0$ lead to a static error. The case $u = 0$ is only of theoretical interest because a_1 will never be exactly zero due to the code clock mismatch ΔR .

The closed loop transfer function $H(s)$ for the linearized loop is defined by

$$H(s) = \frac{\hat{T}_d(s)}{T_d(s)} = \frac{K_L}{s + K_L} \quad (12)$$

with

$$K_L = \sqrt{P} K S'(\epsilon_a) = \tilde{K} S'(\epsilon_a), \quad (13)$$

$S'(\epsilon_a) = 2$ being the slope of the S-curve at ϵ_a for the $\delta = 0.5$ DLL and the loop bandwidth is defined by

$$W_L = \int_{-\infty}^{\infty} |H(j2\pi f)|^2 df = \frac{K_L}{2} \quad (14)$$

MTLL AND TRACKING JITTER

Exact explicit solutions for the MTLL exist for the first order DLL. For the second order DLL with passive loop filter an approximation based on Kramers results is possible [5]. This approximation leads to a compact form for the MTLL. This is the reason why a slightly modified approximation based on the results by Kramers is used. The MTLL for the first order DLL is approximated by

$$\bar{t}_L = \frac{\sqrt{2}\pi}{\tilde{K}} \exp\left(\frac{E_c}{\rho}\right) \quad (15)$$

The minimal escape energy E_c is given by the area under the S-curve (see Figure 2)

$$\begin{aligned} E_c &= \int_{\epsilon_a}^{\epsilon_b} (S(\epsilon) - u) d\epsilon \\ &= \frac{3}{4}(1 - |u|)^2 \end{aligned} \quad (16)$$

The tracking jitter around the stable tracking point ϵ_a for the coherent DLL is given by [2]

$$\sigma_{\epsilon_a}^2 = \frac{N_0 W_L}{P} = \frac{N_0 K_L}{2P} \quad (17)$$

This shows that the parameter K leads to a tradeoff between small tracking jitter, large MTLL and small loop offset.

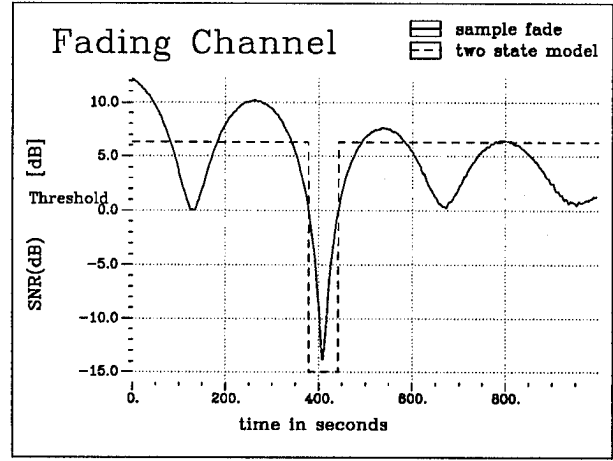


Fig. 4. Fading Channel

CHANNEL MODEL

To simplify the investigation, a two state channel model is used. The good channel condition corresponds to the normal tracking mode of the DLL, i.e. high SNR. The parameter K will be chosen to guarantee low tracking jitter in this mode. The bad channel condition corresponds to a deep fade, i.e. very low SNR. For this case the MTLL of the DLL is crucial. A real fading channel could be projected onto this model by introducing a threshold value. This is shown in Figure 4. If the received SNR is above the threshold value, then the channel condition is good, otherwise the channel condition is bad. In the simplified model $SNR_A = 6.3dB$ is assumed for the good state which lasts t_A . For the bad channel we have $SNR_B = -15dB$ and $t_B = 62sec$. The fade duration t_B is much smaller than the good state duration t_A and $SNR_A \gg SNR_B$. The threshold in the example is $0dB$. The mean SNR for both the real fading channel and for the two state channel model is $6dB$.

MODIFIED DLL

The problem for a conventional DLL is that the MTLL is reduced considerably during a fade. This increases the probability that it will lose lock during the fade. The assumption for proposing the modified DLL is that during the fade the timing offset between receiver and transmitter, i.e. the Doppler shift varies slowly. On the other hand the noise level is very high. To keep the DLL in lock with strong noise can

be achieved by a narrow loop bandwidth W_L . This is achieved by a small loop gain K . However, a small loop bandwidth is not able to track large Doppler shifts for a first order DLL. To bring together the two arguments the loop is opened, i.e. $K = 0$ during the fade. This corresponds to a loop bandwidth $W_L = 0$ which is optimal if there is no loop detuning. During the fade the timing offset increases due to the Doppler shift. As long as the fade duration t_B is not too long, the tracking error will still be in the overall tracking range TR_{ov} . When the fade is over, the loop is closed again and the DLL will drive the loop offset to zero.

Typical tracking error trajectories for a conventional DLL and for a modified DLL are shown in Figure 5. The two state channel model is used and Figure 5 shows details near the fade. The solid line shows the input dynamics, i.e. the constant Doppler shift. In this example it corresponds to a velocity of $3m/s$. The parameter $K = 0.08$ has been chosen as a trade-off between good Doppler tracking capabilities and low tracking jitter.

It is clear that during good channel conditions both DLLs perform equally good. During a fade, i.e. $SNR_B = -15dB$ the conventional DLL is very likely to lose lock because the MTLL is reduced drastically. This can be seen in Figure 5 as the dotted line oscillating strongly during the fade. After the fade the conventional DLL remains unlocked.

The modified DLL operates with $K = 0$, i.e. zero loop bandwidth during the fade. Thus it can not follow the Doppler shift a_1 . This leads to a loop detuning $\varepsilon_f = a_1 * t_B$. As far as the fade duration t_B is short enough, as in this example, the loop detuning will be inside the tracking range of the DLL at the end of the fade. The dashed line shows the trajectory of the modified DLL. It can be clearly seen, that the estimated timing offset \hat{T}_d remains constant during the fade, and how it approaches very fast the actual timing offset T_d after the loop has been closed again.

CONCLUSION

The modified DLL improves the lock performance in the two state channel model. This is achieved by adapting the DLL to the channel conditions. The investigation has been done for the coherent first or-

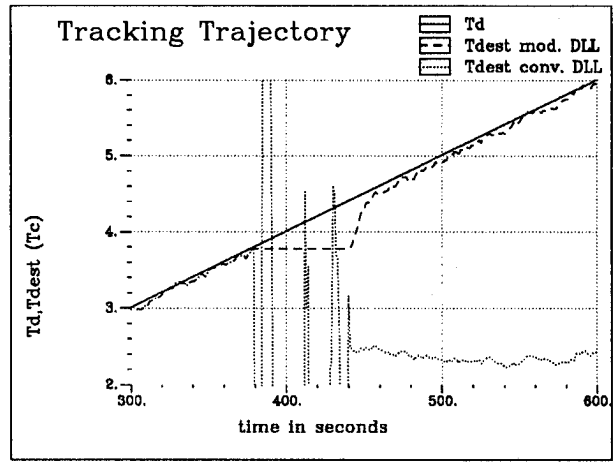


Fig. 5. Tracking Trajectory

der DLL. The modification can also be applied to the noncoherent DLL and to higher order DLLs. For higher order DLLs the opening of the loop means that timing estimates are extrapolated by the loop filter. The threshold based switching will make the loop robust against loss of lock in a fading channel. Further investigations for different fading channel models will be carried out.

REFERENCES

- [1] J.K. Holmes, "Coherent Spread Spectrum Systems", Wiley, NY 1982
- [2] R.E. Ziemer and R.L. Peterson, "Digital Communications and Spread Spectrum Systems", Macmillan, NY 1985
- [3] M.K. Simon, J.K. Omura, R.A. Scholtz, B.K. Levitt, "Spread Spectrum Communications", Vol. 3, Computer Science Press, Rockville, 1985
- [4] H.A. Kramers, "Brownian motion in field of force and the diffusion model of chemical reaction", Physica 7, pp. 284-304, 1940
- [5] A.L. Welti, B.Z. Bobrovsky, "Mean Time to Lose Lock for the Langevin-"Langevin"-Type Delay-Locked Loop", IEEE Trans. Commun., vol. COM-42, pp. 2526-2530, Aug. 1994

RAILWAY CAB SIGNALLING BY TRACK CIRCUITS AND SPREAD SPECTRUM MODULATIONS

Eugenio Costamagna (°) and Pier Franco Pellegrini ()*

(°) Dipartimento di Elettronica, Università di Pavia
Via Abbiategrasso, 209, 27100 Pavia, Italy

e-mail: eugenio@comell.unipv.it

(*) Dipartimento di Ingegneria Elettronica, Università di Firenze
Via di S. Marta, 3, 50139 Firenze, Italy
e-mail: pelle@labtel.ing.unifi.it

ABSTRACT

Track circuits are the traditional and perhaps the most important way to provide railway traffic control and train safety. However, electromagnetic interferences from solid state traction power applications and increased transmission capacity requirements are calling for new architecture and design. In this paper, spread spectrum modulations are considered, in order to provide interference rejection and multiple access capabilities. In particular, the possibility of provide track circuits suitable to work indifferently on networks equipped with different traction power systems is investigated.

1. INTRODUCTION

Cab Signalling (CS), Automatic Train Protection (ATP), and Automatic Train Control (ATC) systems via track circuits have been recently faced with severe electromagnetic compatibility (EMC) problems, both in rapid transit systems and in main line equipment cases. Problems arise both from solid-state power electronics, increasingly utilised in traction power and vehicle propulsion control applications, and from novel requirements of information bandwidths larger than already used.

Rapid transit equipment problems were considered, for instance, in [1] and [2]. New high speed main lines, requiring both refined train control and cab signalling systems and very large traction powers, are causing deep changes in technical requirement and design practices. As an example, the CS/ATC system adopted for the TGV lines in France and for the Channel tunnel was described in [3]. More generally, data transmission systems via track circuits allowing relatively large information bandwidths have been described, as, for instance, in [4] and [5].

In addition, new requirements are emerging in Europe, calling for easy interoperability of rolling stocks across boundaries of regions equipped with different electric traction and signalling systems. Traffic control interoperability was already allowed by parallel installation of dedicated equipment in a number of vehicles. However, more efficient solutions are needed today, in order to secure at a time both reduced equipment weights for high speed vehicles, and larger interoperability, extended to several different electric traction systems [6].

Radio transmission systems have been recommended to this purpose in various European studies, considering very demanding technical requirements: see for instance [6], and the ERWIN and TWIN projects, developed in the framework of the ESPRIT program. Radio transmissions are likely to be the only solution to the considered ground-to-train (and train-to-ground) communications scenarios.

However, it seems interesting to deserve some attention to a possible updated version of coded track circuit transmissions, which apparently was not considered in the previous technical literature.

In principle, spread spectrum (SS) modulations [7] are likely to offer effective solutions to CS, ATP and ATC track circuit design, as robustness against hostile EMC environments was already demonstrated in applications leading to similar problems, i.e., mobile radio and guided propagation trough power line wiring and intrabuilding power distribution circuits [8][9]. However, both the bandwidths allowed by the track circuit electrical characteristics (see, for instance, [10]) and the various interference signals make not straightforward any application of the customary processing gain and anti jamming margin evaluation procedures.

A first introduction to these problem was presented in [11], where different SS modulations were considered, anticipating that in this application too, as

usual, the relative merits of the Direct Sequence modulation (DS) and of the frequency hopping (FH) schemes cannot be assessed without concrete reference to the actual electromagnetic environment. Moreover, it was emphasised in [11] that the main benefit gained from SS modulations will be perhaps some insensitivity to the traction power supply techniques, more than any performance improvement with respect to traditional narrow band track circuits.

In this paper, attention is focused on low information rate signalling via track circuits for CS and ATP systems, mainly by means of DS modulations. Notable difficulties are not anticipated in considering various similar transmissions sharing the same circuits, and unconstrained multiple access schemes similar to those described in [12] can be easily conceived, in order to provide service to different mobiles on the same track section.

2. INTERFERENCES SPECTRA AND SPREAD SPECTRUM MODULATIONS ON TRACK CIRCUITS

Some examples of conducted emission spectra on tracks, to be faced by track circuit receivers, were shown in [11], Fig. 1, and some detailed spectra for various a.c. and d.c. traction power supply cases are provided in [13], [14], and in [1]. In particular, reference is made to Fig. 21/2 and 25/2 (a.c. 15 kV, 16 2/3 Hz thyristor locomotive, without and with filter), 22/2 and 23/2 (a.c., 25 kV, 50 Hz locomotives), Fig. 29/2 and 30/2 (calculated spectra for 2 four-quadrant controllers and 4 four-quadrant controllers, a.c. 25 kV, 50 Hz asynchronous motor locomotives) and Fig. 36/2 (d.c., chopper drive locomotive) in [13], to Fig. 2 and Table 1 in [14] and to Fig. 6 in [1] (chopper drive locomotives). Maximum envelopes for conducted emissions for a main line d.c., 3 kV system and for a rapid transit system are shown in [14], Fig. 1, and in [1], Fig. 8.

As seen, attention is normally restricted to harmonic spectra, as needed when considering traction currents which are not rapidly changing due to relatively slow train accelerations, and when chopper traction units are restricted to fixed-frequency operation.

Narrow band circuits secure immunity by rejecting spectral lines at harmonic frequencies. However, line frequencies are typical of the various electric traction systems, and so are the particular frequencies carrying the major interference contributions.

Considering the bandwidths available for tracks circuits, which are of the order of some 10 kHz, SS

modulations will offer in principle processing gains of the order of some 20 or 30 dB, depending on the information rate. The related interference margins will be largely independent from spectral details, in particular, from the interference fundamental and more dangerous frequencies. However, effective interference margins have to be carefully investigated, as no further protection is available to counteract major interference spectral lines if notch filter are not utilised (note that any notch filter is likely to limit standardisation and interoperability of equipment). From the above documentation, it appears that some low frequency regions, up to about 500 or 700 Hz, carry the larger interference lines both in the a.c. and in the d.c. supply cases. Higher frequency regions show some unconstrained harmonic levels in the Italian maximum envelope for conducted emission, and are used in various networks to carry ancillary signals.

Although considering the maximum envelope for d.c. traction systems is not realistic, as actual interferences show very sparse harmonic spectra, it is evident that the broad band nature of the DS signalling procedures is not likely to provide comfortable processing gains, and that a more realistic evaluation of the receiver performances will be based on white noise interference. This is suggested, in particular, by the near constant envelope of the a.c. locomotive spectra: when larger bandwidths are occupied by the modulation spectra, larger interference powers are collected by the receiver, and the performances of the optimum receiver will be near insensitive to the actual signal bandwidth.

With respect to narrow band systems, the protection of dedicated frequency channels is lost, and worst case interference conditions are probably worse. However, some insensitivity to particular condition is certainly gained, as insensitivity to the traction current fundamental frequency, which prevents interoperability of narrow band track circuit receivers. Moreover, continuous spectra and variable line frequency spectra are not in principle more harmful against a direct sequence receiver than fixed-frequency spectra, and probably the fixed-frequency operation constraint, already introduced in many networks to protect traditional track circuits, can be removed, allowing sweep frequency chopper drive operations.

To provide quantitative evaluation of the effects of the various interference spectra, a simulation program has been implemented. The first results on a.c. 16 2/3 Hz locomotive spectra, considering DS/PSK modulations at 5 or 10 bit/s information rates, show that proper operation conditions are provided at the same signalling current utilised in narrow band track

circuits. A chip rate of some hundred of Hz has been selected, with a carrier frequency of about 1 kHz, and a correlation receiver has been utilised. Out of band spectral lines have been filtered, as pre-filtering of any out of band (possibly strong) interference is clearly to be recommended in the system design.

As expected, the noise probability-distribution functions for levels comparable to 2 or 3 times the rms current values are similar to those of a gaussian noise, and the receiver performances, at least for low signal to noise power ratios and large bit error rates, are rather similar to those of a matched-filter/correlator receiver in the presence of white gaussian noise.

However, the periodic nature of the interference, which is likely to exhibit repetition periods of the same order of the bit duration, has to be taken into account: to provide comparison with the gaussian white noise case, the actual phases of the interference spectral lines have been periodically set to new pseudo-random values.

Further work is needed to complete the evaluation of the DS receiver with various interference spectra (processing gains of about 15 or 20 dB are expected against continuous wave interferences), and with various design parameters, and to provide comparison among different SS schemes and with narrow band systems.

In any case, it seems that signal acceptance checks similar to those utilised in narrow band circuits (as coding, detection hysteresis, on-off keying at very low rates followed by duty cycle evaluation, detection of unbalanced traction currents on tracks) have to be retained in the design of spread spectrum systems, which will be exposed to more unpredictable interference conditions.

To counteract unexpected strong interferences, which are the weakness of DS systems, frequency hopping modulation systems can provide effective solutions, because signal check and rejection mechanisms similar to those implemented in narrow band tracks circuits filtering can be utilised, and the low information rates allow to retain only signal received on clear frequency channels. Moreover, compatibility with current narrow band systems can be easily provided by tuneable fixed-frequency operation and adjustable detection procedures, easily provided, at low information rates, by means of digital signal processing techniques.

Similarly, diversity transmissions can be usefully investigated: in particular, multicarrier MSK modulation systems, already proposed for data transmission on track circuits [5], can provide diversity if the different carriers are modulated by the same low rate data sequence, as anticipated in [11].

A further possibility deserves some investigation. Considering a SS track circuit sharing the low frequency band of the current narrow band systems, compatible operations of the two systems calls for negligible mutual interference. This is likely to be feasible, but the accurate assessment of both system sensitivities and of the current levels needed for the SS system is needed. A frequency hopping system will be probably ignored by many narrow band traditional circuits; similarly, due to low power spectral densities, direct sequences systems will be not harmful, even considering the increased power levels needed to counteract the interference caused by the narrow band circuit itself.

3. CONCLUSIONS

A first assessment of the capabilities of spread spectrum modulated track circuit has been attempted, looking both for transmission performances comparable to those secured by means of the current narrow band track circuits, and for providing suitable operation by means of a sole standard equipment in different EMC conditions, as experienced in railway networks equipped with different electric traction systems. Although track circuit spread spectrum techniques seem not to be likely to provide performances similar to those expected from radio transmission systems, some interesting possibilities have been shown, and some future work outlined, which is needed to evaluate effective feasibility.

REFERENCES

- [1] L.A. Frasco and F. Ross Holmstrom, "EMC consequences of power electronics applied to rail transit," IEE International Conference on Railways in the Electronic Age, 17-20 Nov. 1981, pp. 117-127.
- [2] J. Hoelscher and R. Rudich, "Compatibility of rate-coded audio frequency track circuits with chopper propulsion drive in transit systems," IEE International Conference on Railways in the Electronic Age, 17-20 Nov. 1981, pp. 128-135.
- [3] G. Pascualt, "La transmission voie-machine," *Revue Generale des chemin de fer*, Février 1994, pp. 33-40.
- [4] P.F. Pellegrini, R. Marinetto, and L. Carli, "Some new techniques in the codification and transmission of data from ground to train,"

- Intern. Conference of the Institution of Railway Signal Engineers, London, Sept. 1984.
- [5] P.F. Pellegrini, G. Puliatti, and D. Novelli, "Alcune possibili soluzioni per la trasmissione di dati terra-treno su canale radio e rotaia," *Proceedings of the CIFI-DITEL Conference "Telematica e telecomunicazioni nei trasporti su rotaia"*, Genova, Nov. 1988.
 - [6] P. Winter, "Stratégie pour l'introduction du système européen unifié de contrôle/commande automatique de la marche des trains ETCS présentée à partir de l'exemple des Chemins Fédéraux Suisses," *Rail International*, Juin/Juillet 1993, pp. 67-74.
 - [7] R.C. Dixon, "Spread Spectrum Systems," J. Wiley & Sons, New York, 1984, II Ed..
 - [8] R.A. Piety, "Intrabuilding data transmission using power-line wiring," *Hewlett Packard Journal*, 1987, n. 5, p. 35-40.
 - [9] P.K. Van der Gracht and R.W. Donaldson, "Communication using pseudonoise modulation on electric power distribution circuits," *IEEE Trans. on Commun.*, vol. 33, 1985, N. 9, p. 964-974.
 - [10] D. Muzzioli, "Cibernetica della circolazione ferroviaria," *Ingegneria Ferroviaria*, Nov. 1985, p. 751-756 (in italian).
 - [11] E. Costamagna, "Ripetizione di segnali in macchina mediante circuito di binario e modulazioni Spread Spectrum," *Rendiconti 94^a Riunione Annuale AEI*, Ancona, 3-6 Ottobre 1993, p. 231-236 (in italian).
 - [12] E. Costamagna and S. Sanna, "Multiple access to a non linear satellite transponder by low bit rate spread spectrum data and telephone FDMA-MSK channels," *ISSSE'92, International Symposium on Signal, Systems and Electronics (URSI)*, Paris, 1-4 Sept. 1992, *Proceedings*, vol. 1, p. 397-400.
 - [13] CCITT Directives concerning the protection of telecommunication lines against harmful effects from electric power and electrified railway lines. Geneva, 1989, Vol. IV, chap. 2, p. 34-58.
 - [14] T. Franchini and A. Ventura, "Compatibilità elettromagnetica in ambiente ferroviario," *AEI*, vol.82, No. 5, 1955, p.440-444 (in italian).

MICROWAVE MODELLING OF A PHOTO-DETECTOR / AMPLIFIER FOR OPTICAL COMMUNICATION SYSTEMS

V. Anand

Department of Electronic Engineering
University College, London WC1, U.K.

ABSTRACT

Developments in techniques for modelling of photodiodes used in optical parametric receivers are examined in this paper. As parametric operation is non-linear and quasi-periodic in nature, special modelling techniques are required. The effect of diode parameters (eg. capacitance) on gain and bandwidth have been examined. Time domain techniques have been used for simulation. Different non-linear models for depicting the photodiode have been evolved during the course of analysis. A summarized analytical derivation is also presented. Finally, the results obtained from an experimental down converter are included.

1. INTRODUCTION

The concept of using parametric receivers for microwave amplification has been established for several years. This technique is now sought to be extended to receivers for optical carriers with microwave modulation. Since parametric operation is non-linear, the analysis of these circuits presents some difficulty. Various configurations such as up-converters, down converters and baseband amplifiers are possible in this system. One of the factors which is of paramount importance in governing receiver performance is the photodiode capacitance. This has some influence on the gain as well as the bandwidth. This receiver can principally be used fibre based microwave sub-carrier systems.

2. SYSTEM CONFIGURATION

The system has interaction of optical and microwave signals. The transmitter consists of a laser source which is amplitude modulated by RF or microwave signals. Specifically in a microwave sub-carrier system several microwave subcarriers are combined and modulated on the laser beam. The receiver consists of a photodiode which is operated in a parametric mode to perform amplification and to recover the baseband. Parametric operation is

effected by periodic variation of the diode capacitance. This is accomplished applying a microwave signal (level of 10-15 dBm) called pump across the diode. Manley and Rowe have developed the basic theory of electric parametric amplifiers and this can serve as a basis for this case¹. It is assumed that the level of the detected signal is much smaller than the pump and that the modulation of the capacitance is due to the pump. The profile of the diode's Capacitance Voltage characteristic and the ratio of the maximum to minimum capacitance is of significance in governing the performance of the amplifier.

3. ANALYSIS

A summarized analytical derivation is now presented for the down-converter. In the analysis, the periodic variation of the diode capacitance by electrical means is represented as a sinusoidally varying capacitance. Therefore, capacitance of a pumped photodiode can be approximately represented in the following manner [2].

$$C = C_0 \left[1 - \frac{V_p}{2(V_0 + V_b)} \sin \omega_p t \right] \quad (1)$$

where V_p is the pump voltage, V_0 is the barrier potential, V_b is the bias voltage, C_0 is the zero bias diode capacitance and ω_p the pump frequency. The photocurrent can be expressed as:

$$I_s = I_{s0} \sin \omega_s t \quad (2)$$

An expression can be derived for the total current in the photodiode as:

$$I = \frac{d(CV_s)}{dt} = V_s \frac{dC}{dt} + C \frac{dV_s}{dt} \quad (3)$$

Where V_s is the signal voltage across the diode due to the photocurrent I_s . Substituting from equations (1) and (2) into equation (3), the expression for the component of

the diode current I_d (peak value) at the down -converted frequency $\omega_p - \omega_s$ can be derived as:

$$I_d = \frac{I_{so} V_p}{4 (V_b + V_o)} \frac{[\omega_p - \omega_s]}{\omega_s} \quad (4)$$

If the load resistance at this frequency is R_o (normally 50 ohms), then the output voltage is given by $I_d R_o$. In accordance with normal microwave practice, the input voltage or power is measured across a 50 ohm load. Hence the input voltage can be written as $I_{so} R_o$ where $R_o = 50$ ohms. Therefore the gain of the Down -converter can be shown to be:

$$A_d = \frac{(\omega_p - \omega_s)}{\omega_s} \frac{V_p}{4 (V_b + V_o)} \quad (5)$$

Equation (5) shows that the gain is dependant on the ratio of the down-converted frequency to the signal frequency.

4. NON-LINEAR SIMULATION

Simulation can be effectively used to supplement analytical methods in investigating parametric systems. Because of the nature of the system, the simulation technique used should be able to tackle large signal non-linearity. For non-linear simulation time both domain and frequency domain methods are available. Time domain methods like transient analysis are quite versatile in tackling non-linearity and are used in packages like Spice3. As the amplitude of the harmonics are required at the end, spectrum analysis has to be performed. The circuit to be simulated is shown in fig. 1, where the photo-current is depicted as a current source.

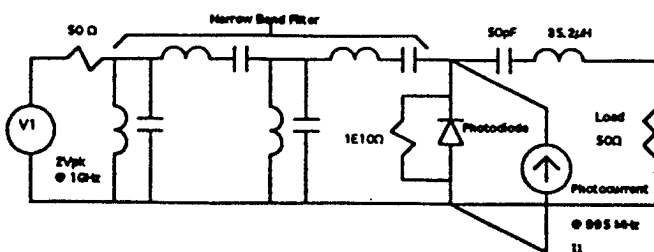


Fig.1 Simulated circuit of receiver

Two parameters which are important in transient analysis are the step size and the duration of analysis. These are to be fixed depending on the frequencies of interaction. In a typical case of a down-converter, the pump frequency may

be 1 GHz and the signal frequency 990 MHz which gives a down-converted frequency of 10 MHz. It would therefore necessary to resolve 10 MHz around a central frequency of 1GHz. To accomplish this, the duration of analysis should include several cycles of the smallest frequency to be resolved [3]. In addition transient analysis is performed at discrete points on the input waveform with interpolation in between. In order to minimize interpolation errors, step size should be chosen as a fraction of the pump period. Subsequently, during Fourier analysis on the transient analysis data, it should be remembered that only a finite data length is used which can result in amplitude errors [3]. This can be minimized by the choice of a proper window. A Hamming window offers a compromise between frequency resolution and leakage. On the other hand, a raised cosine window which has a small central lobe leading to better resolution and roll off characteristics has been used in the package.

5. MODEL DEVELOPMENT

Different models have been evolved for representing the non-linear diode behaviour. Initially the standard diode model in the package was used [4]. However for exactness, dedicated models have been evolved two of which are discussed here.

5.1 Non-linear capacitor model

As the name suggests the photodiode is represented as a non-linear capacitor. As a non-linear capacitor is not available as a standard model in Spice3 a model was synthesized as shown in fig 2. The non-linear capacitance is realized by having a non-linear source drive a current through a linear capacitor.

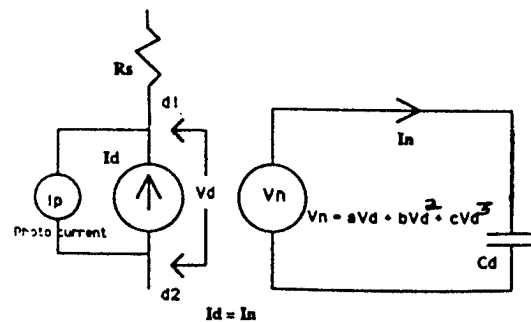


Fig. 2 Non-Linear capacitor model.

The non-linear source is dependent on the voltage between d1 and d2. The current through the capacitor is reflected

between d1 and d2 and this represents the non-linear capacitor. The series resistance of the diode is represented by R_s . If required a shunt resistance and series inductance can also be included. A Down-converting

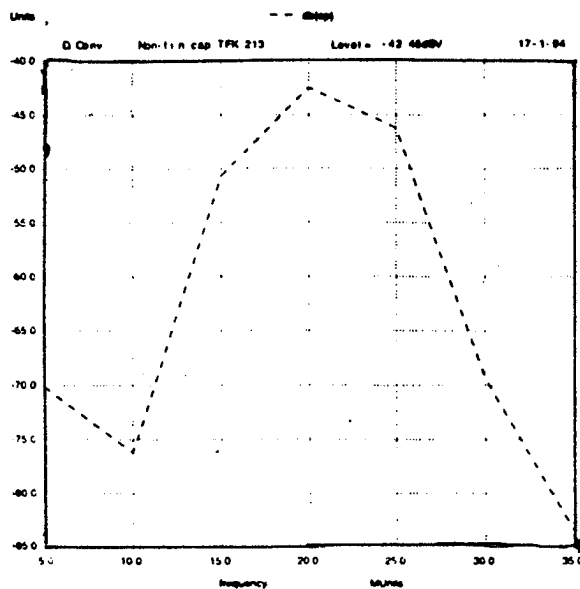


Fig.3 Output Spectrum Gain = 10.45dB

configuration was simulated using this model using the circuit shown in fig. 2. The C-V characteristic was measured using a parameter analyzer. The diode had a zero bias capacitance of 9.9 pF. The polynomial used for representing the non-linear capacitor was $C = 9.95 - 4.18V + 1.2 V^2$. The simulation was performed for a pump frequency of 1 GHz and a input frequency of 980 MHz (Level = -52 dBV). The output spectrum is shown in fig. 4 which indicates a gain of 10.45 dB at the down-converted frequency of 20 MHz.

5.2 Enhanced Model

The non-linear capacitor model works well in modelling normal junction diodes. However, photodiodes usually have a PIN structure. The enhanced model was developed with the intent of forming an exact representation of the diode structure. This is accomplished in the model shown in fig. 4. At zero bias, a portion of the intrinsic region is undepleted which is attempted to be represented in the enhanced model. Here, the diode structure is split into two parts, one representing the junction region and the other the undepleted part of the intrinsic region. At zero bias the capacitance of the junction region dominates by up to a factor of ten over the intrinsic region. With the application of bias, the capacitances of each region behave differently. The junction region can be modelled as before

with a polynomial. The undepleted intrinsic

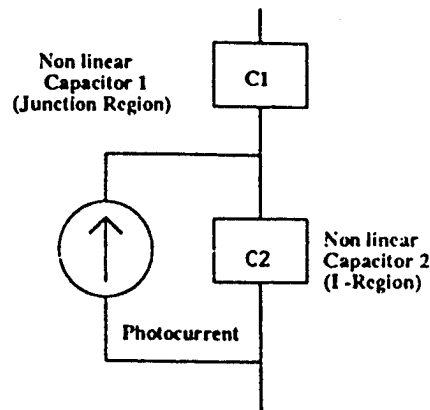


Fig. 4 Enhanced model of photodiode

region is represented as an exponentially increasing capacitance. The simulation was repeated on a down-converting configuration. At an input frequency of 980 MHz, the simulation predicted a gain of 6.0 dB at the output frequency of 20 MHz (fig. 5). This model can be used to balance intrinsic region properties of the photodiode which affects photodetection with those of the junction region which affects parametric performance.

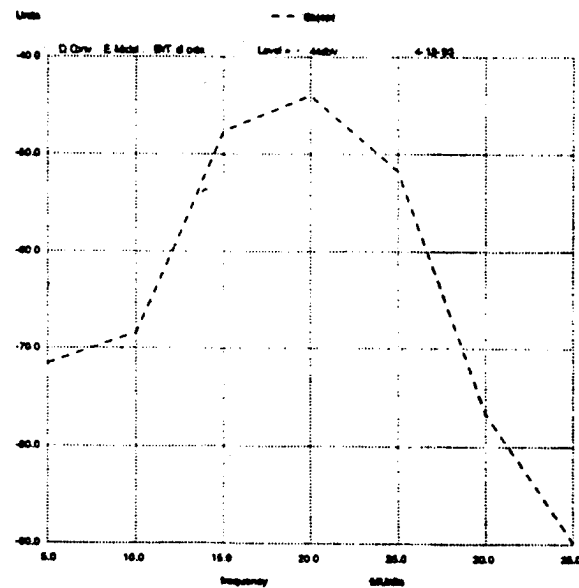


Fig. 5 Output Spectrum. Gain = 6.0 dB.
Input = -50 dBV

The simulation was also repeated to study the performance of up-converters. One of the factors of importance is amplifier bandwidth. Though a smaller diode capacitance (< 1 pF) would enable higher speed of operation, it was

observed that for improved parametric properties resulting in higher gain and bandwidth, a higher capacitance of around 10 pF is preferable.

6. PRACTICAL RESULTS

Practical down-converters and up-converters have been tested and these have performed well. A practical down-converter was built using a broad band laser transmitter which could accept modulation up to 1 GHz. The photodiode was built mounted in a micro-strip box. In a down-converting arrangement, using a 1 GHz pump and a 900 MHz signal the receiver gave a gain of 7.9 dB at the down-converted frequency of 100 MHz (fig 6)

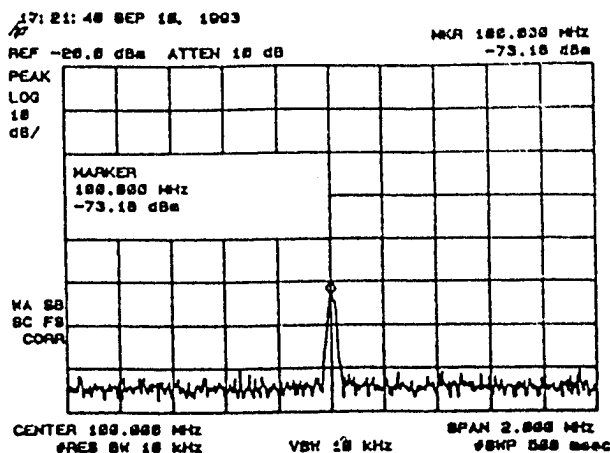


Fig 6. Output of Down-converter

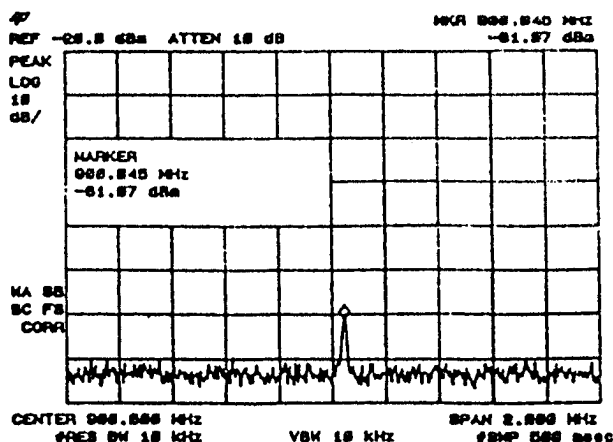


Fig 7 Input to Down-converter.

The performance can be improved by shorting the idlers which would otherwise dissipate some of the energy in the load. Up-converters earlier built which bandwidths of up to 100 MHz at a pump frequency of 1.5 GHz [4] A gain of 12.5 dB could be obtained at a signal frequency of 100 MHz

7. CONCLUSIONS

The development of simulation and modelling techniques for parametric receiver design is presented. The non-linear capacitor model helps in incorporating the measured Capacitance-Voltage characteristic of the photodiode in the simulation, while the enhanced model helps in modelling a more exact photodiode structure. The modelling of the down-converter has been a guide in the practical construction in predicting the down-conversion gain available for a range of input frequencies. The effect of diode capacitance in influencing parametric gain and bandwidth as indicated by simulation and practical experiments suggests that a value of 10 pF is desirable. The enhanced model will help in the evolution of a new diode structure which will balance photodetection and parametric properties

8. REFERENCES

1. Manley and Rowe, "Some general properties of non-linear elements- Part 1," *proc. I.R.E.*, vol. 44, pp 904-913, July 1956.
2. Paul F. Cencles, Jacques Graffeuil, *Microwave Components, Devices and Circuits*, chapter 9, pp 160-165.
3. Kindest K. S., Jacob White, Vincentelli A. S., "Steady State Methods for Simulating Analog & Microwave Circuits", chapter 5, *Kluwer Publishers*, 1990.
4. Khanifar A., Anand V., Parker A.E., "Photoparametric Amplifier / Converter in Lightwave Communication systems", *23rd European Microwave Conference proceedings, Madrid, September 93* pp 314-316.
5. R. Graver, "Microwave Control Devices," *Artech, Boston*, 1976, pp 326-329.

ON THE APPLICABILITY OF THE TRANSIMPEDANCE AMPLIFIER CONCEPT FOR 40Gb/s OPTOELECTRONIC RECEIVERS BASED ON InAlAs/InGaAs HETEROSTRUCTURE FIELDEFFECT TRANSISTORS

Ralf M. Bertenburg, Guido Janssen, Stefan van Waasen, Ralf Reuter,
Franz-Josef Tegude

Gerhard-Mercator-University Duisburg, Solid-State Electronics Department,
Kommandantenstr. 60, D-47057 Duisburg, Germany
phone: ++49 203 379 2987, ++49 203 379 3392
FAX: ++49 203 379 3400
e-mail: ralf@hlt.uni-duisburg.de

ABSTRACT

We will report on design considerations and general discussion of the applicability of the transimpedance amplifier concept for optoelectronic receivers at extremely high bit rates up to 40Gb/s. The investigated receiver design is based on a low gate-leakage InAlAs/InGaAs/InP heterostructure fieldeffect transistor (HFET) [1]. The very important noise modeling of these devices is done using an extended temperature noise model [2] in order to produce a reliable extrapolation far beyond frequency limits of common measurement setups. The fitted transistor model shows excellent agreement with measured data concerning rf as well as noise performance. The evidence of inductive peaking near the corner frequency of the transimpedance Z_T is correlated to a phase difference between the voltage gain V_u and Z_T itself. Furthermore, the distinct influence of the length of the feedback line on receiver performance is discussed. Based on 0.7 μ m gate HFETs produced by optical lithography and offering a current gain cut off frequency of $f_T=40$ GHz the following receiver features can be predicted: low frequency transimpedance $Z_{T0}=39.4$ dB Ω , corner frequency $f_{3dB}=22$ GHz, mean equivalent input noise current density $\overline{i_{na}} \approx 43$ pA/ $\sqrt{\text{Hz}}$. Thus the receiver shows an excellent calculated sensitivity of $\eta P_{\min} = -13.2$ dBm at 40Gb/s.

1. INTRODUCTION

The transimpedance amplifier concept for low noise preamplifiers in optoelectronic receivers is most common up to bit rates of 10Gb/s [3]. Recently, even 20Gb/s demonstrators can be found in literature. But this concept becomes more doubtful with increasing bit rate due to wave propagation effects within the circuit. Other approaches using impedance matched amplifier concepts like traveling wave amplifiers specially modified for

optoelectronic receiver applications [4] suffer from the bad power matching conditions at the input. From a pure physical point of view a photo detector (PD) is a capacitively shunted current source. All efforts to match this device to a low impedance wave guide result in a significant drop of responsivity of the PD [5]. Therefore, up to now the transimpedance amplifier seems to be the best concept for low noise preamplification in optoelectronic receivers.

Aim of this paper is to point out some very important design considerations for the development of such high bit rate receivers based on the transimpedance amplifier concept. Nevertheless, because all basic model data are derived from measured devices, the demonstrated amplifier design is suitable for technological realization. All simulations have been carried out using the *Microwave Design System (MDS)* by Hewlett Packard. Due to the significant influence of the noise modeling on sensitivity estimations, we have implemented a temperature noise model (TNM) [2] for the HFET devices. The calculation of receiver sensitivity is done in a measurement compatible way and hence direct correlation of simulated and measured data is possible.

2. HFET MODEL

The dc and rf model of the FET is based on the EEHEMT1 large signal model in *MDS*. Fig. 1 and 2 demonstrate the excellent agreement in both, dc and rf characteristics between measured and simulated data. Furthermore, that model shows very good agreement for a wide range of bias conditions. For the noise simulation the FETs were modeled using the TNM [2], which has the advantage of describing significant noise sources and small signal behavior at the same time. The comparison of measured and calculated noise data is shown in fig. 3. The TNM allows extrapolation far beyond measurement frequency limits without producing non physical results.

This is most significant for a valid prediction of receiver sensitivity. Low frequency 1/f-noise is not considered by the TNM. Nevertheless, sensitivity estimations will not be influenced significantly due to the very small bandwidth of 1/f-noise compared to the bit rate.

3. AMPLIFIER LAYOUT

The investigated transimpedance amplifier layout is straight forward as can be seen from fig. 4. It is based on a three stage concept with a first voltage amplifier stage (T_1) followed by a current amplifier and level shift (D_1 - D_3) driving stage (T_2) for bias adjustment. To achieve a suitable voltage gain bandwidth and to minimize additional noise contributions the first load (R_1) should be realized by a chip resistor rather than an active load. Within the second stage an active load (T_3) acting as current source results in more stable bias conditions without significantly increasing noise. For a circuit simulation according to a real chip design some physical line models (TL_1 , TL_2) have been added within the level shift and feedback path which obviously have the maximum length compared to all other interconnections. The third stage (T_4 , T_5) drives and matches a connected 50 Ω line termination.

4. CIRCUIT SIMULATION

Four types of simulations have been carried out. A dc simulation is used to examine bias conditions of all FETs. S-parameter simulation is used to derive all relevant small signal data like voltage gain V_u transimpedance Z_T (magnitude and phase) and power gain G . A noise voltage and current simulation in combination with the S-Parameter data allows direct calculation of the equivalent square input noise current $\langle i_{na}^2 \rangle$ and hence the prediction of receiver sensitivity after [6] as:

$$\eta P_{\min} = \frac{h\nu}{e} Q \sqrt{\langle i_{na}^2 \rangle} = \frac{h\nu}{e} Q \sqrt{\int_0^B \frac{S_{N,out} (1 - s_{11})^2}{Z_0 s_{21}^2} df},$$

where Q is the noise factor corresponding to the bit error rate ($Q \approx 6$ for BER = 10^{-9}), B the actual bit rate and Z_0 the characteristic impedance and load impedance, resp. $S_{N,out}$ the spectral noise power density at the terminated amplifier output, h Planck's constant and ν frequency of the optical input signal.

5. RESULTS AND CONCLUSIONS

In fig. 5 the transimpedance vs frequency is depicted. The influence of the length of transmission lines TL_1

and TL_2 is clearly demonstrated. With increasing line length inductive peaking occurs which significantly deteriorates impulse response as demonstrated in fig. 6. Scaling of these line lengths directly correlates with chip size. Therefore the total chip size should be as small as possible for high bit rate receivers. Inductive peaking of the transimpedance corresponds to a distinct phase difference between voltage gain and transimpedance function, hence the bandwidth of V_u should be larger than that of transimpedance Z_T itself (fig. 5). A flat characteristic of transimpedance is achieved with a corner frequency of $f_{3dB} \approx 22$ GHz corresponding to a bit rate of $B = 40$ Gb/s. Variations of group delay time are of the order of $|\Delta\tau_{gr}| < 10$ ps. The equivalent input noise current density is shown in fig. 7. The mean equivalent input noise current over bandwidth $\Delta f = B$ is $\overline{i_{na}} \approx 43$ pA/ $\sqrt{\text{Hz}}$. Thus receiver sensitivity can be calculated to $\eta P_{\min} = -13.2$ dBm. The receiver output signal shows a clearly open eye at that bit rate and an effective transimpedance corresponding to the eye opening of $Z_{T,eff} \approx 38$ dB Ω (fig. 8). Concluding it should be pointed out, that especially included lines within the feedback path deteriorate impuls behavior of the amplifier significantly.

LITERATURE

- [1] C. Heedt, F. Buchali, W. Prost, D. Fritzsche, H. Nickel, F.-J. Tegude, "Extremely Low Gate Leakage InAlAs/InGaAs HEMT", Int. Symp. on GaAs and Rel. Comp., Karuizawa, Japan 1992
- [2] R. Reuter, S. van Waasen, F.-J. Tegude, "A New Noise Model of HFET with Special Emphasis on Gate-Leakage", IEEE Elec. Dev. Let., Vol.16, No.2, Feb. 1995, pp.74-76
- [3] M.S. Park, R.A. Minasian, "Ultralow Noise 10 Gb/s p-i-n-HEMT Optical Receiver", IEEE Phot. Techn. Let., Vol.5, No.2, Feb. 1993, pp.161-162
- [4] C.S. Aitchison, "Potential of the Distributed Amplifier as a Photo-Diode Detector Amplifier in High Bit-Rate Optical Communication Systems", Electronic Let., Vol.26, Sept. 1990, pp.1693-1695
- [5] Y. Wey, K.S. Giboney et al., "108GHz GaInAs/InP p-i-n Photodiodes with Integrated Bias Tee & Matched Resistors", IEEE Phot. Techn. Let., Vol.5, Nov. 1993, pp.1310-1312
- [6] S.D. Personick, "Receiver Design for Digital Fiber Optic Communication Systems, I & II", Bell System Techn. J., Vol. 52, July-August 1973, pp.843-872, pp.875-886

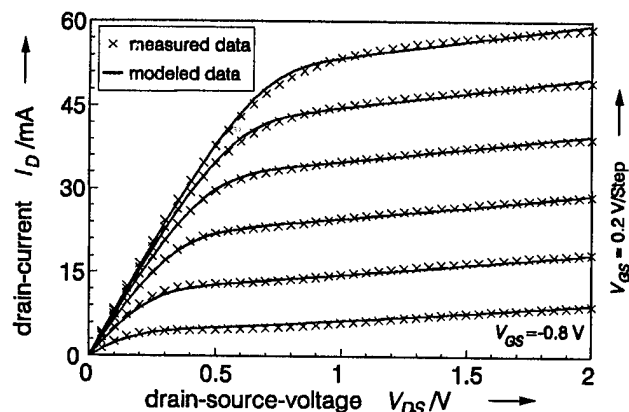


Fig. 1: Comparison of measured and modeled HFET output characteristics using the large signal EEHEMT1 model

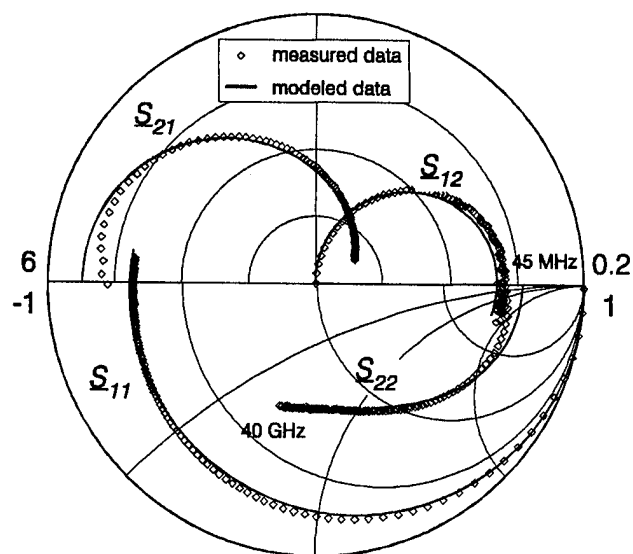


Fig. 2: Measured and modeled S-parameters using the EEHEMT1 model (\$V_{GS} = -0.2\$ V, \$V_{DS} = 1.2\$ V)

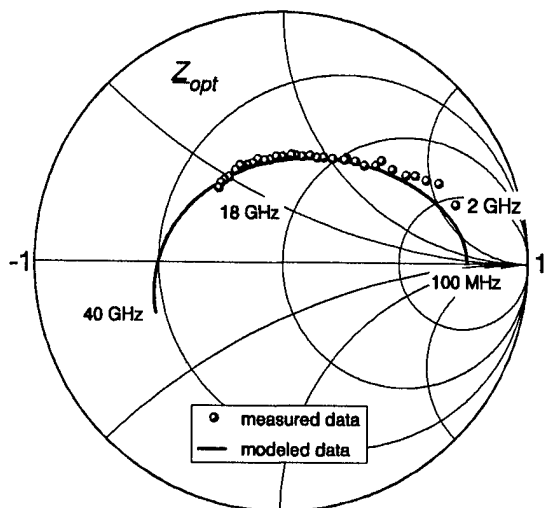
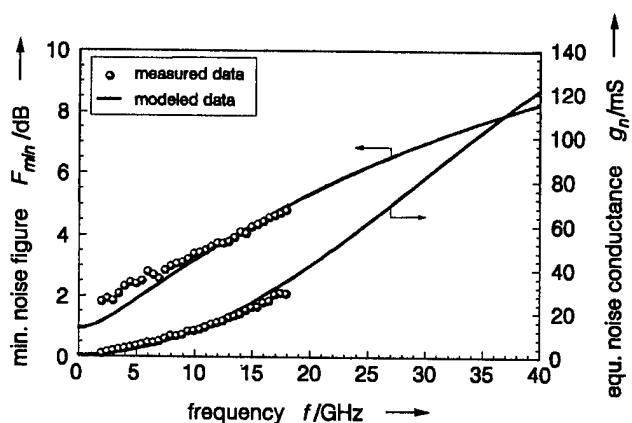


Fig. 3: Measured and calculated noise parameters based on the temperature noise model [2] (\$V_{GS} = -0.2\$ V, \$V_{DS} = 1.2\$ V)

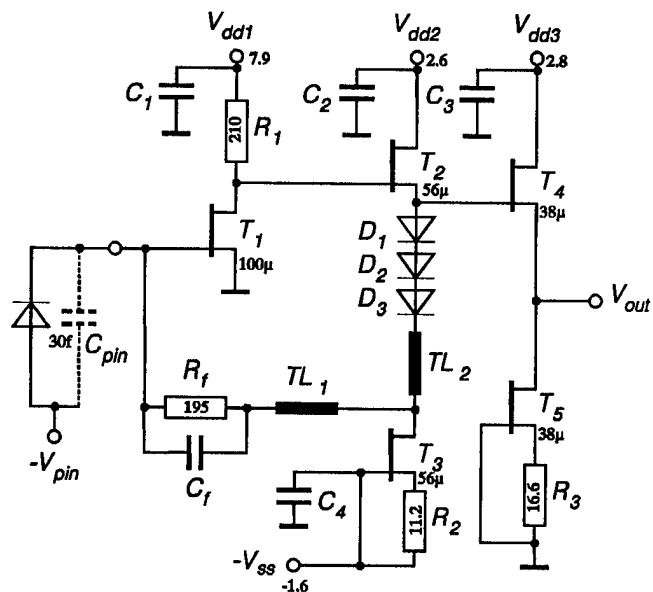


Fig. 4: Circuit diagram of the investigated transimpedance amplifier including transmission lines \$TL_1\$ and \$TL_2\$ with length \$l_1\$ and \$l_2\$, respectively.

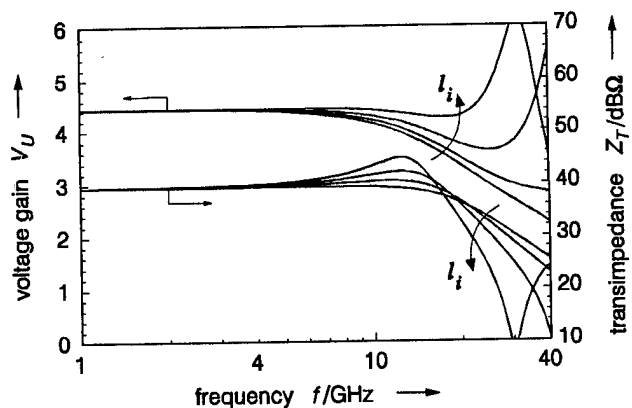


Fig. 5: Dependence of transimpedance and voltage gain on transmission line length ($l_i=0, 300\mu\text{m}, 600\mu\text{m}, 900\mu\text{m}$ and $l_1=l_i, l_2=3/2 l_i$)

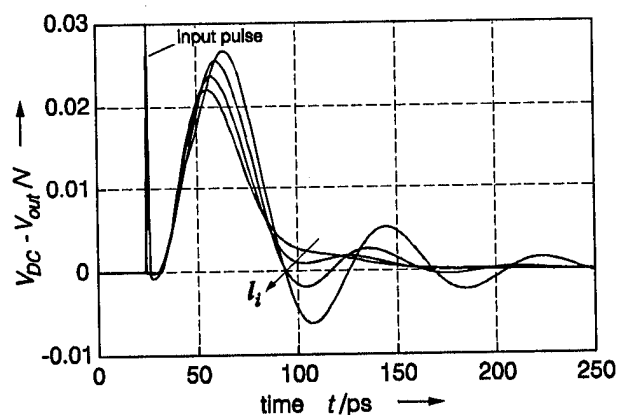


Fig. 6: Impulse response in dependence on the transmission line lengths ($l_i=0, 300\mu\text{m}, 600\mu\text{m}, 900\mu\text{m}$ and $l_1=l_i, l_2=3/2 l_i$)

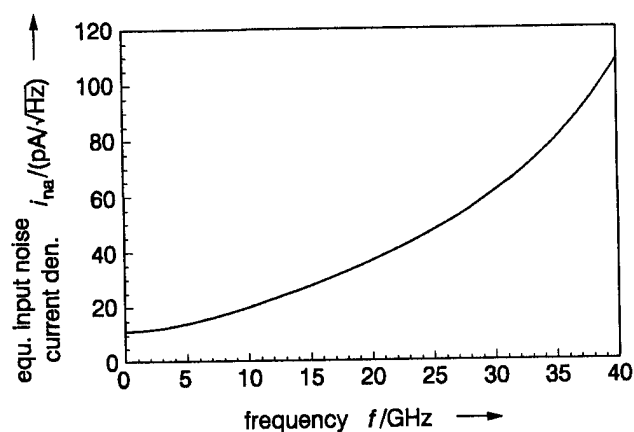


Fig. 7: Calculated equivalent input noise current density

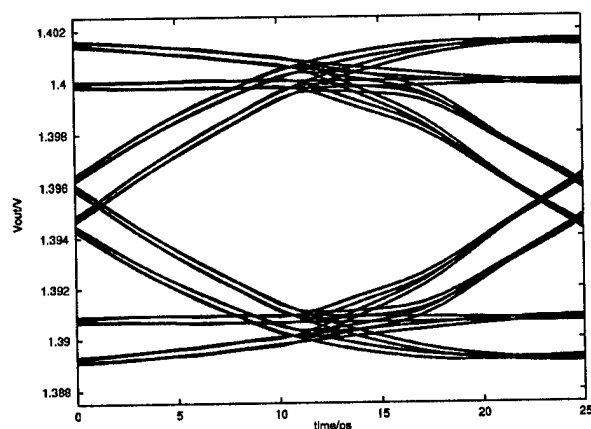
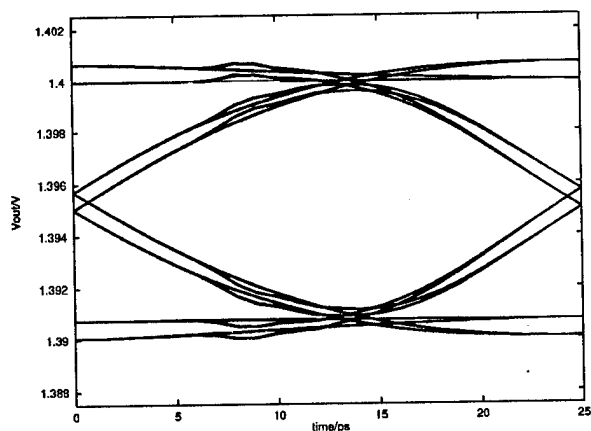


Fig. 8: Eye diagrams for 40Gb/s of the investigated transimpedance amplifier (above: without transmission lines, below: including transmission lines)

HIGH ELECTRON MOBILITY TRANSISTOR AS ELECTRONIC FLUTE

*M. I. Dyakonov and M. S. Shur**

A. F. Ioffe Physico-Technical Institute, St. Petersburg, 194021, Russia

*Department of Electrical Engineering, University of Virginia, Charlottesville, VA 22903-2442, USA
TEL: (804) 924 6109, FAX (804) 924 6109, E-MAIL: shur@virginia.edu

ABSTRACT

We discuss the similarity between the plasma waves in two dimensional systems and sound waves. We show that the behavior of both types of waves is governed by the same equations. Therefore, we may create resonant structures for plasma waves, similar to those in musical instruments, and plasma waves can be excited by a dc current, just like wind musical instruments are excited by air jets. However, the plasma wave velocity (on the order of 10^7 to 10^8 cm/s) is much higher than the sound velocity, and the sizes of devices with the two dimensional electron gas are very small (on the order of a micrometer or less). Thus, the plasma wave frequencies are in the terahertz range, and the plasma waves can be coupled to far infrared electromagnetic radiation.

1. INTRODUCTION.

When the electron mean free path for collisions with impurities and phonons is much greater than the mean free path for electron-electron collisions, electrons behave like a fluid, which may be described by hydrodynamic equations. In our recent papers ^{1,2}, we showed that this condition can be met for two dimensional (2D) electrons in a Field Effect Transistor (FET) and that the hydrodynamic equations describing this electron fluid coincide with those for shallow water. Furthermore, plasma waves in the FET channel are similar to shallow water waves. We also showed that in a short enough device, an instability should occur at a relatively small direct current because of spontaneous plasma wave generation. This provides a new mechanism for the emission of tunable far infrared electromagnetic radiation.

In this work, we discuss the similarity between the plasma waves in 2D systems and

sound waves. We show that the behavior of the plasma waves in 2D systems is governed by the same equations as for sound waves. Therefore, resonant structures, similar to those in musical instruments, may be realized for the plasma waves, and these waves can be excited by a direct current just like wind musical instruments are excited by air jets. However, the plasma wave velocity is much higher than the sound velocity and the FETs are very small. As a consequence, the plasma wave frequencies are in the terahertz range. These plasma waves are accompanied by a variation of a dipole moment created by charges in the FET channel and mirror image charges in the gate. This dipole moment variation should cause the emission of far infrared (terahertz range) electromagnetic radiation.

2. PLASMA WAVES AND SOUND WAVES

As was shown in ¹ and mentioned above, the 2D electron fluid in a FET is described by the hydrodynamic equations, which coincide with those for shallow water, with the gate-to-channel voltage, U , playing the role of the water level. In a FET, the plasma wave dispersion law is given by

$$\omega = sk$$

the plasma wave velocity, U is the gate-to-channel voltage swing, m is the effective mass, and e is the electronic charge. Plasma waves are similar to shallow water waves or to sound waves since they have a linear dispersion law.

Shallow water behavior is also similar to the dynamics of a gas with pressure proportional to the square of the gas density, (see, for example, ³). Thus, the nonlinear hydrodynamic

equations for the 2D electron fluid are similar to (but not identical with) the equations for a real gas, such as air. However, the linearized equations describing small-amplitude plasma waves in a FET and sound waves in a gas are identical. Since the linearized equations determine the instability threshold for a steady flow (i. e. the wave generation threshold), the instability conditions for a real gas and for a 2D electron fluid should be similar, provided that the Reynolds numbers and quality factors of resonance cavities are the same. Below, we will show that these parameters for our "electronic flute" may be of the same order of magnitude as for a conventional flute.

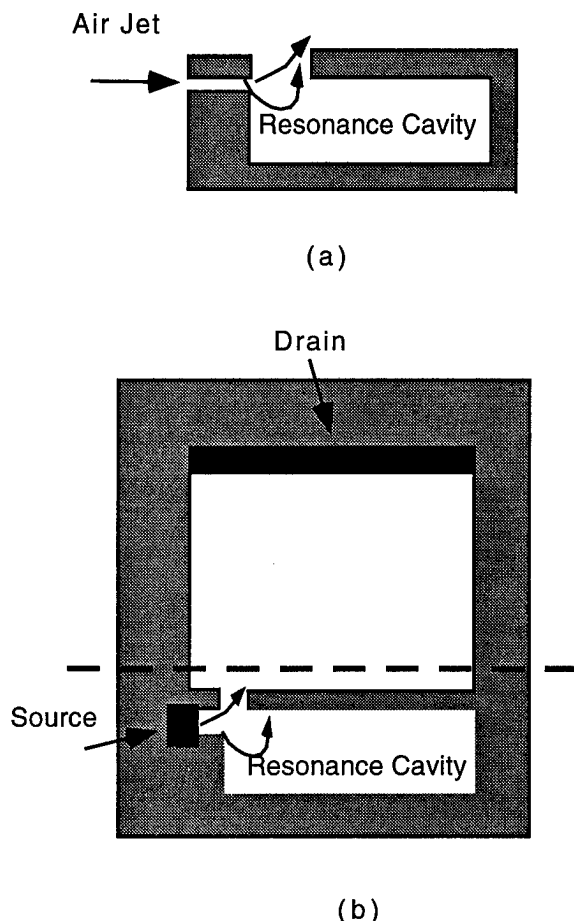


Fig. 1. Simplified diagram of a jet driven pipe musical instrument of a flute family (a.) and electronic flute (b). White areas in Fig. 1 b show the gated region of the device with the 2D electron fluid in the channel. ⁵

The part of the device in Fig. 1 b shown below the dashed line is the electronic flute.

Fig. 1a (from Ref. 4) shows the schematics of a jet driven pipe musical instrument of a flute family. In this instrument, an air jet excites a resonant cavity formed by the pipe closed at both ends. A similar structure can be realized using a modulation doped gated device (see Fig. 1b).

The top gated portion of the device connected to the drain is similar to the outside air space for a jet driven musical instrument. We call the part of this device shown below the dashed line in Fig. 1b an electronic flute. The remaining gated portion of the device connected to the drain is similar to the outside air space for a jet driven musical instrument. In the electronic flute, a direct current flow excites plasma waves in the resonance cavity in the same way as an air jet excites sound waves in an acoustic cavity.

In Table 1, we compare the relevant parameters, Reynolds numbers and quality factors for a conventional flute and for an electronic flute. One can see that the dimensionless parameters determining the wave generation, i. e. the Reynolds numbers and quality factors, for the electronic flute are not that different from those for a conventional flute, even though their dimensional parameters (size, flow and wave velocities, and frequency) differ by many orders of magnitude.

Parameter	Musical Instrument of Flute Family	Electronic Flute
relevant dimension	1 cm	10^{-4} cm
flow velocity	10 cm/s	10^7 cm/s
wave velocity	3×10^4 cm/s	10^8 cm/s
viscosity	$0.15 \text{ cm}^2/\text{s}$	$15 \text{ cm}^2/\text{s}$
frequency	100 - 10^4 Hz	10^{11} - 10^{13} Hz
Reynolds number	60	60
Quality factor	3-100	10

Table. 1. Parameter comparison for conventional and electronic flutes.

Therefore, we presume that the electronic flute will operate in a manner similar to a conventional flute but in a terahertz range of frequencies (see ⁵ for more details).

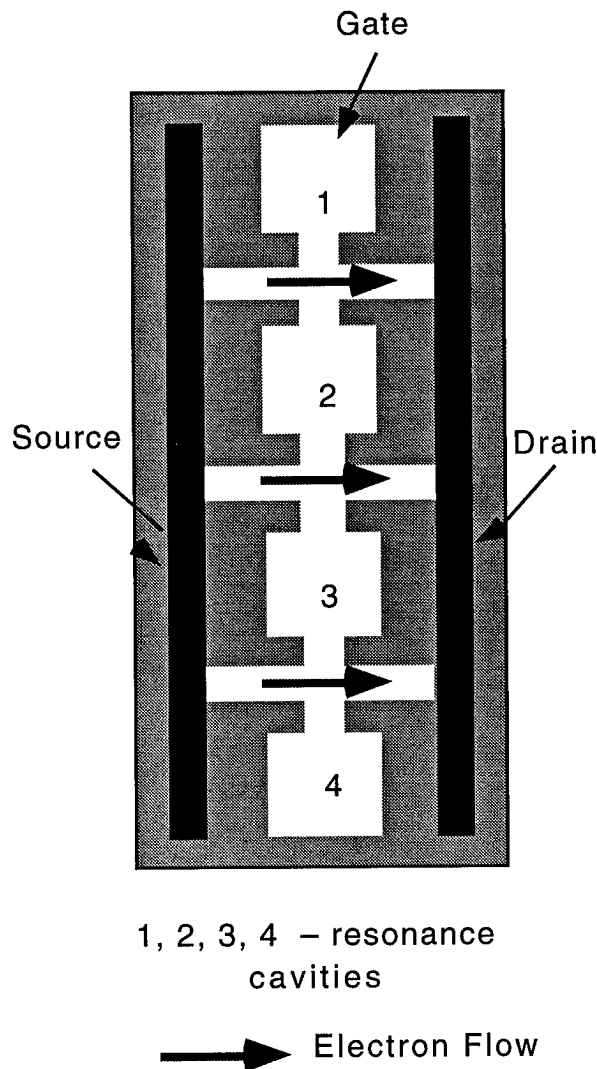


Fig. 2. Array of electronic flutes with a more efficient coupling of plasma waves to electromagnetic radiation. The plasma wave oscillations are excited in the peripheral resonance cavities by 2D electrons flowing from the source to the drain.⁵

The basic structure shown in Fig. 1 b can be modified and repeated many times, and this device may be made as an array with dimensions equal to a quarter of the wave length of the electromagnetic radiation with the frequency

coinciding with the plasma waves for the optimum coupling to the infrared radiation. For example, in the device shown in Fig. 2 ⁵, the plasma wave oscillations are excited in the resonance cavities by the current flowing between the source and drain. Even though only a few resonance cavities are shown in Fig. 2 (for simplicity), for the optimum coupling to the infrared radiation, the basic structure can be repeated many times and this device may be made as an array with dimensions equal to a quarter of the wave length of the electromagnetic radiation with the same frequency. (Of course, just as for musical instruments, the optimum design of the electronic flute may be both a matter of skill and art.)

Observations of infra-red absorption ⁶ and infra-red emission ⁷ in a silicon FET with a grating metal structure on the gate indirectly confirm the possibility of exciting the plasma waves in FETs and their coupling to electromagnetic radiation. The frequency of the observed electromagnetic radiation was equal to the frequency of the plasma waves which were excited by the drain-to-source current and were tuned by the gate bias.

In an ungated modulation doped structure

$$\omega = \sqrt{\frac{4\pi e^2 n}{\epsilon m}} k$$

and the plasma waves are equivalent to deep water waves. Even though for ungated structures, there is no such a strong similarity to sound waves as for a FET, we could speculate that similar effects may occur nevertheless.

6. SUMMARY

In conclusion, a complete similarity between the plasma waves in a FET and sound waves led us to believe in the possibility of realizing an electronic flute based on the excitation of plasma waves by a direct current in gated modulation doped structures and operating in a terahertz range of frequencies. Other similar devices, such as arrays, can be designed using the resonant structures for the plasma waves. These resonance properties should also allow us to use a HEMT as a detector or mixer ⁶ operating in a terahertz range with sensitivities, which may exceed the sensitivity of Schottky barrier diodes

4. ACKNOWLEDGMENT

The work at the Ioffe Institute has been partially supported by grant No. J4G100 from the International Science Foundation and the Russian Government and by the US Army through its European Research Office. The work at the University of Virginia has been partially supported by the US Army Research Office (Project Monitor Dr. John Zavada) and by the Office of the Naval Research (Project Monitor Dr. Yoon Soo Park).

5. REFERENCES

1. M. I. Dyakonov and M. S. Shur, Phys. Rev. Lett., 71, 2465 (1993)
2. M. Dyakonov and M. S. Shur, Choking of Electron Flow - A Mechanism of Current Saturation in Field Effect Transistors, Phys. Rev. B, vol. 51, No. 20, pp. 14341-14345, 15 May (1995)
3. L. D. Landau and E. M. Lifshitz, Fluid Mechanics (Pergamon, New York, 1966)
4. N. H. Fletcher and T. D. Rossing, The Physics of Musical Instruments, Springer-Verlag, New York (1991)
5. M. I. Dyakonov and M. S. Shur, Two Dimensional Electronic Flute, Applied Physics Letters, Aug. 21 (1995)
6. S. J. Allen, Jr., D. C. Tsui, and R. A. Logan, Phys. Rev. Lett., 38, 980 (1977)
7. D. C. Tsui, E. Gornik, and R. A. Logan, Solid State Comm., 35, 875 (1980)
8. M. Dyakonov and M. Shur, Detection and Mixing of Terahertz Radiation by Two Dimensional Electronic Fluid, in the Proceedings of 23th International Symposium on GaAs and Related Compounds, Cheju, Korea, Aug. 28-Sep. 1, 1995

AN ALGORITHM FOR FAST QUATERNARY A/D CONVERSION

A.S.Gandhi , A.M.Dighe

Department of Electronics and Computer Science
Visvesvaraya Regional College of Engineering
NAGPUR - 440011 (INDIA)
post@vrce.ernet.in

ABSTRACT

An algorithm for conversion of analog signals into quaternary numbers is described. Simulation results of the algorithm are reported. A flash type implementation of this algorithm is described.

1. INTRODUCTION

Systems based on multilevel logic and higher radix number systems, have the advantage of being faster by a factor of $\log_2 R$ over binary systems, where R is the radix of the number system.

The development of quaternary ADCs is taken up as a first step towards quaternary systems for data storage and transmission. The algorithm developed is quite parallel to the window algorithm for ternary systems reported in [1].

2. QUATERNARY NUMBERS AND CONVERSION ALGORITHM.

2.1 Quaternary numbers

Some of the 4 digit quaternary numbers and their decimal equivalents are shown in Table 2.1. It is observed that while Q_3 is fixed, Q_2 changes as 0, 1, 2 and 3 and the decimal equivalent changes as 0, 16, 32 etc. Similar pattern can be observed for Q_2 and Q_1 if we consider intermediate numbers, not shown in the table.

It is clear that, to resolve Q_3 , we must divide the input range into 4 regions (0,63.5), (63.5,127.5), (127.5,191.5) and (191.5,255.5) and assign values 0, 1, 2 and 3 to Q_3 , respectively, depending upon the region in which the input lies. This can be done by comparing the input with a 'window' centered at 127.5, and having lower threshold at $(127.5 - 64) = 63.5$ and upper threshold at $(127.5 + 64) = 191.5$. The comparison can be done in two ways. The input is directly compared with 127.5 ± 64 or the offset 127.5 is subtracted from the input and the resulting value is compared with ± 64 . We adopt the second strategy. It has the advantage of being simpler for flash type implementation.

We note from Table 2.1 that, given $Q_3 = 0$, then $Q_2 = 0$ for decimal equivalent < 16 and $Q_2 = 3$ for decimal equivalent > 48 . The next window is thus given by $W_2 = 31.5 \pm 16$. For $Q_3 = 1, 2$ and 3, the windows for resolving Q_2 are 63.5 ± 16 , 95.5 ± 16 and 127.5 ± 16 respectively. It is clear that the value of Q_3 decides the offset to be subtracted from the input before we compare it with ± 16 .

2.2 Symbol for window comparison.

We will now define a symbol for window comparison so that we identify two comparisons simultaneously. The symbol is "Z" which is to be interpreted as combination of the ">" and "<" signs. The statement " $Y Z \pm X$?" will mean " $Y > +X$? or $Y < -X$?" and will be read as "Y compared with $\pm X$ ". Similarly the statement " $Y Z X_1, X_2$?" means " $Y > X_1$? or $Y < X_2$?". Note the order of > and < signs as related to + and - sign of X or the values X_1 and X_2 .

2.3 Quaternary conversion algorithm.

We now define the windows and offsets for an n digit system.

INITIAL OFFSET	$F_{n-1} = (4^n - 1)/2$	$k = 0$
OFFSETS	$F_{n-k-1} = (4^{n-k})/2$	$k = 1, 2, 3, \dots, n$
WINDOWS	$\pm W_{n-k-1} = \pm (4^{n-k-1})$	$k = 0$ to $n-1$
ANALOG INPUT		
AT VARIOUS		
STAGES	N_{n-k-1}	$k = 0$ to n
SIGN BIT	$B = 0$ for positive input, 1 for negative input	

The bivalued variable B is used to keep track of the sign of the input at various stages.

The algorithm for n digit quaternary numbers is as below.

- 1) Initialize $k = 0$
- 2) Initial input $N_{n-k} = N$.
- 3) If $N_{n-k} > 0$, $B = 0$ else $B = 1$
- 4) $N_{n-k-1} = N_{n-k} - F_{n-k-1} (-1)^B \dots 2.1$
- 5) $N_{n-k-1} Z \pm W_{n-k-1}$? $Q_{n-k-1} = 3$ or $Q_{n-k-1} = 0$

- else
 $N_{n-k-1} Z 0 \quad ? \quad Q_{n-k-1} = 2 \text{ or } Q_{n-k-1} = 1$
 6) $f_1(Q_{n-k-1}) = (Q_{n-k-1} - 1)(Q_{n-k-1} - 2)/2$
 $f_2(Q_{n-k-1}) = (Q_{n-k-1})(Q_{n-k-1} - 3)/2$
 7) $N_{n-k-1} = (N_{n-k-1} - W_{n-k-1}(-1)^B)(f_1(Q_{n-k-1})) +$
 $(N_{n-k-1})(f_2(Q_{n-k-1})) \dots\dots 2.2$
 8) Increment k by 1.
 9) If k = n then $N_{-1} = N_0 - F_{-1}(-1)^B$ and STOP,
 else go to step 3.

Eqn 2.1 takes care of positive as well as negative inputs.

Whenever a digit at position (n-k-1) is 0 we have to add 4^{n-k-1} to the input before it is passed on to the next stage. If the digit is 3, then we have to subtract 4^{n-k-1} from the input. No such operation is required when the digit is 1 or 2. Eqn. 2.2 is used for this.

The value N_{-1} is the quantization error defined as

$$N - \sum_{m=0}^{n-1} Q_m 4^m$$

If the input to a stage is exactly equal to a threshold, it can be assumed to be higher or lower than the threshold. The same convention should be used throughout the conversion process.

The algorithm is illustrated for a 4 digit scheme as follows.

Offsets: $F_3 = 127.5, F_2 = 32, F_1 = 8, F_0 = 2, F_{-1} = 0.5$

Windows: $\pm W_3 = \pm 64, \pm W_2 = \pm 16,$
 $\pm W_1 = \pm 4, \pm W_0 = \pm 1$

k = 0

Let input $N = +59.3$ Thus $B = 0$.

$N_3 = N - F_3(-1)^B = 59.3 - 127.5 = -68.2$

$N_3 Z \pm W_3 \quad -68.2 Z \pm 64 \quad ?$

Hence $Q_3 = 0$ and $B = 1$

$f_1(Q_3) = 1$ and $f_2(Q_3) = 0$

$N_3 = -68.2 + 64 = -4.2$,

k = 1, B = 1.

$N_2 = N_3 - F_2(-1)^B = -4.2 - 32(-1)^1 = 27.8$

$N_2 Z \pm W_2 \quad 27.8 Z \pm 16 \quad ?$

Hence $Q_2 = 3$

$N_2 = 27.8 - 16 = 11.8,$

k = 2, B = 0.

$N_1 = N_2 - F_1(-1)^B = 11.8 - 8 = 3.8$

$N_1 Z \pm W_1 \quad 3.8 Z \pm 4 \quad ?$

Hence $Q_1 = 2$

$f_1(Q_1) = 0$ and $f_2(Q_1) = 1$

N_1 remains unchanged.

k = 3, B = 0

$N_0 = N_1 - F_0(-1)^B = 3.8 - 2 = 1.8$

$N_0 Z \pm W_0 \quad 1.8 Z \pm 1 \quad ?$

Hence $Q_0 = 3$ and the conversion is complete.

$f_1(Q_0) = 1$ and $f_2(Q_0) = 0$

$N_0 = N_0 - W_0 = 1.8 - 1 = 0.8$

k = 4

$N_{-1} = 0.8 - 0.5 = 0.3$

The quantization error is:

$59.3 - (3 \times 16 + 2 \times 4 + 3) = 0.3$

It is verified that N_{-1} is the quantization error. The algorithm produces complementary code for negative inputs.

3. SIMULATION RESULTS AND IMPLEMENTATION

The algorithm is simulated by means of a computer program. The error is computed according to step 9. It is found that the error is limited to $\pm 1/2$ of the least significant digit (LSD). Fig. 3.1 is the graph of quantization error vs. input.

The circuit to resolve the most significant digit is shown in Fig. 3.2. When two more such cells are cascaded, the complete circuit is a three digit quaternary ADC. The input range is ± 12.6 V and the LSD is 0.2 V. The quaternary digits 3, 2, 1 and 0 are represented by levels 0, -1, -2 and -3 V, respectively. The analog output of the last stage is the quantization error. Fig. 3.3 shows this output for a triangular wave input of 10 V amplitude. We see that the error is within ± 0.1 V. The circuit settles within 1.5 μ s for a step input.

There is no need of clocked operation and the circuit is essentially a flash ADC. The conversion time depends on the propagation speed of signals through the chain of digit cells. The complexity grows linearly with the number of quaternary digits. Hence the advantages are similar to those reported in [2] for the binary ADCs.

4. CONCLUSIONS.

It is possible to obtain a flash quaternary ADC with linearly increasing complexity. The simulation indicates that the error is within $\pm 1/2$ LSD. The error output of the circuit is also found to be mostly within ± 0.1 V.

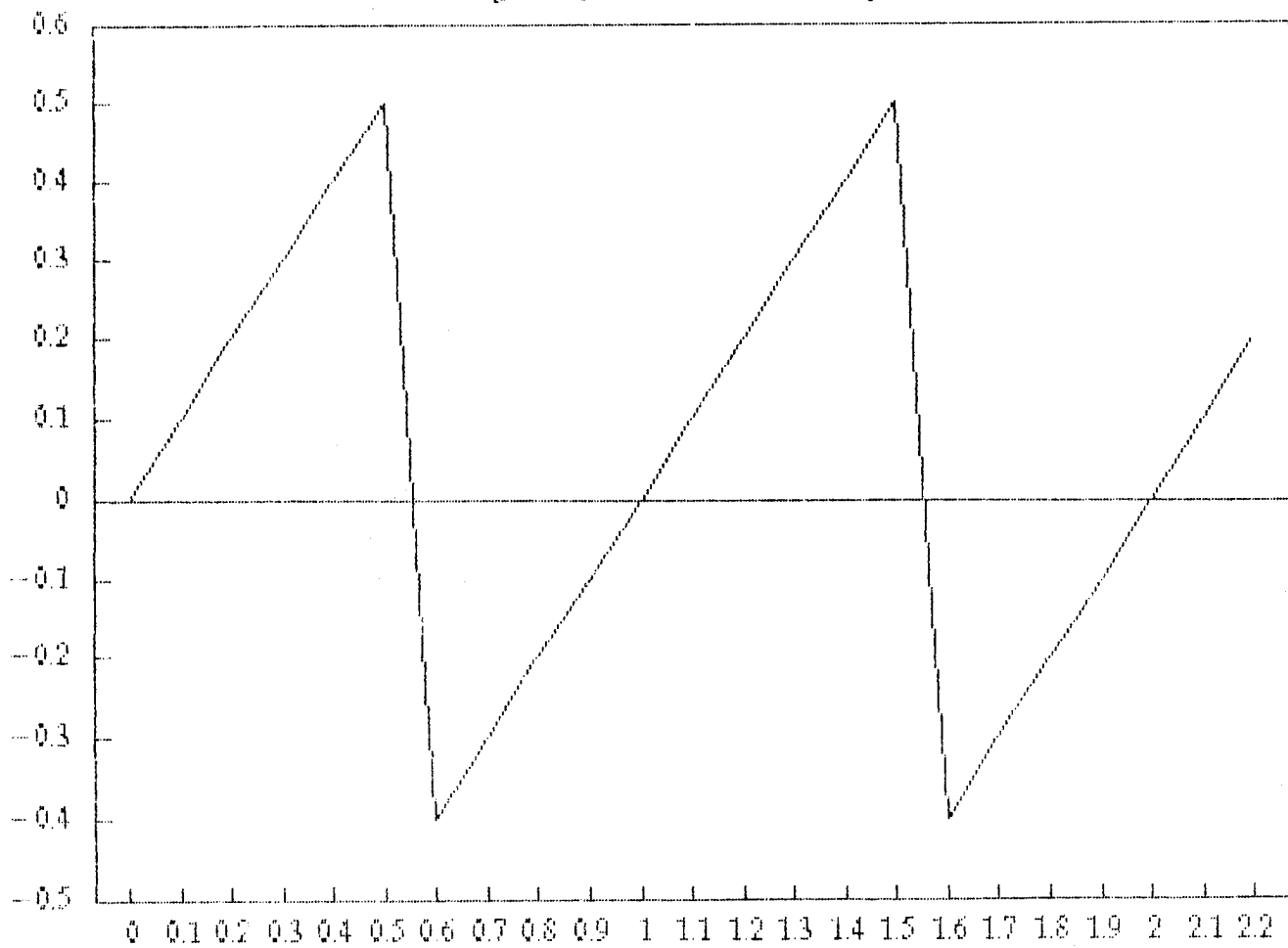
5. REFERENCES.

1. Dighe A.M., "An Algorithmic Ternary A/D, D/A Converter", ISCAS 93, IEEE International Symposium on Circuits and Systems, Chicago, May 3-6, 1993.
2. Dighe A.M., Kelkar A.R., "Flash Search A/D Converter", All India Conference on Applied Instrumentation, U.O.R. Roorkee, Feb. 14-15, 1992.

TABLE 2.1

$Q_3Q_2Q_1Q_0$	$D_2D_1D_0$
0 0 0 0	0 0 0
0 1 0 0	0 1 6
0 2 0 0	0 3 2
0 3 0 0	0 4 8
1 0 0 0	0 6 4
1 1 0 0	0 8 0
1 2 0 0	0 9 6
1 3 0 0	1 1 2
2 0 0 0	1 2 8
2 1 0 0	1 4 4
2 2 0 0	1 6 0
2 3 0 0	1 7 6
3 0 0 0	1 9 2
3 1 0 0	2 0 8
3 2 0 0	2 2 4
3 3 0 0	2 4 0

Fig. 3.1 Quantization error vs input.



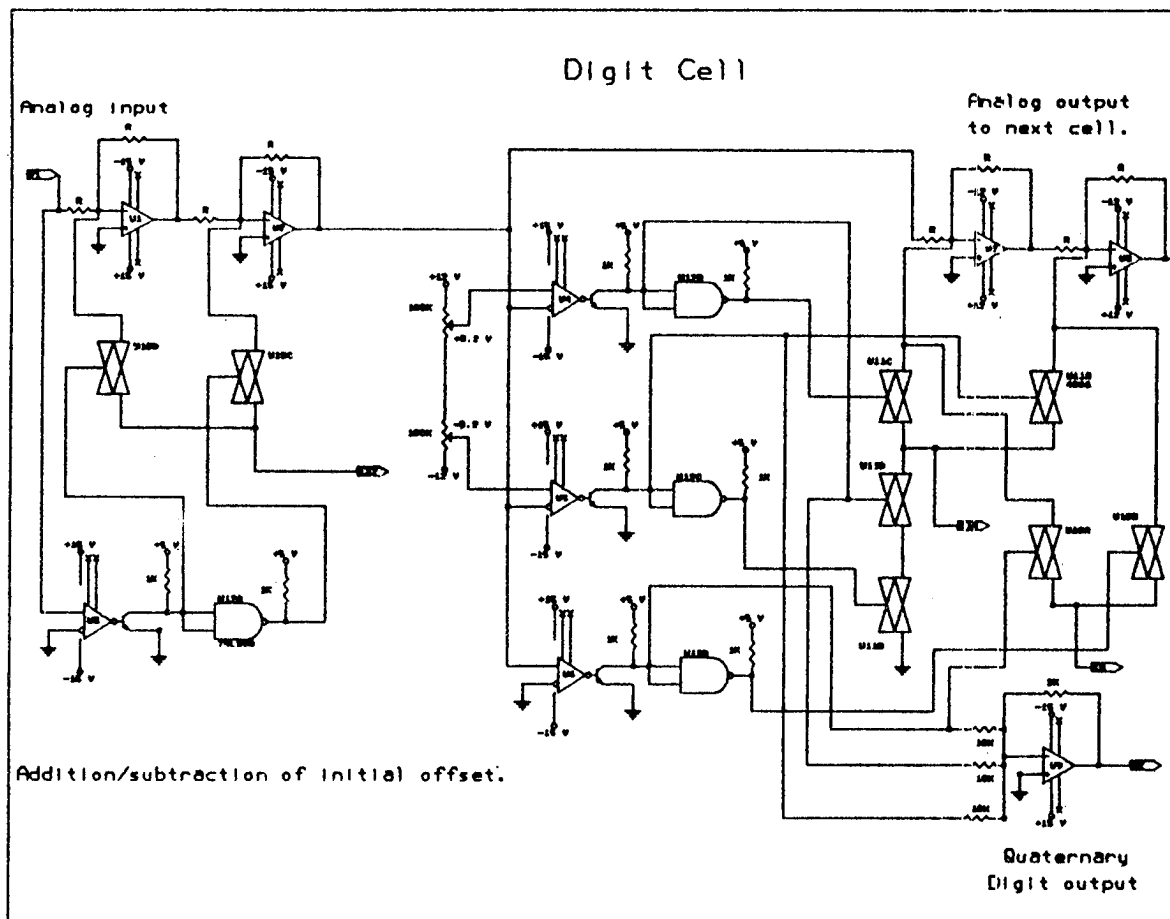


Fig. 3.2 Quaternary A/D conversion circuit.

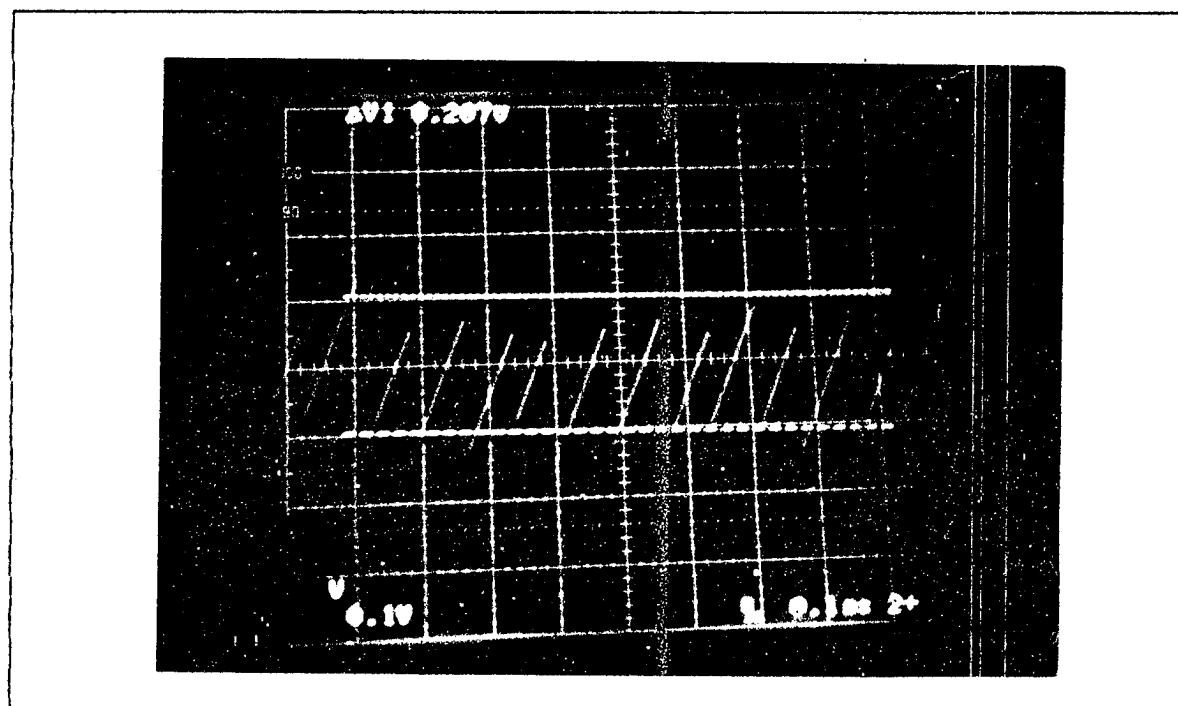


Fig. 3.3 Quantization error output of LSD Cell.

TIME DOMAIN IDENTIFICATION OF NON-LINEAR SYSTEMS

M.I. Sobhy, E.A. Hosny, M.W.R. Ng and El-Sayed A. Bakkar

The Electronic Engineering Laboratories,
The University of Kent at Canterbury
Canterbury, Kent, CT2 7NT, U.K.

Abstract

A new method of non-linear system design, and non-linear subsystem modelling is presented. The method is based on identifying a non-linear model for each subsystem and combining the individual models to solve the entire system. Time domain modelling and simulation is used throughout the procedure but frequency domain characteristics are also available. Modelling of non-linear subsystem is achieved by time domain measurement which offers considerable saving in measurement time. The identified models are not based on equivalent circuits and this offers flexibility and saving in the amount of data stored for each model.

I. New Approach to System Design

This paper describes a powerful technique of modelling linear and non-linear systems that leads to very efficient methods of measurement and simulation. The measurement are carried out in the time domain and this results in a much reduced effort and volume of the measured data compared to frequency domain measurements. In the frequency domain a large number of measurements have to be carried out to determine all four scattering parameters, in amplitude and phase, as functions of frequency and at a number of power levels. In the time domain the response is a real function (no phases) and usually much fewer power levels and time points are required to model non-linear systems.

The identification does not use equivalent electrical circuits. The basic elements of the identified systems are :

- . Multipliers which can be constant or non-linear functions of any signal in the system.
- . Delays which can also be non-linear.
- . Differentiators and Integrators.
- . Adders.

The identification is performed entirely in the time domain and produces a very efficient process that can identify any non-linear system with any non-linearity and with fewer elements than the usual equivalent circuit approach. If a transversal structure is used, then the stability of the

identified model is guaranteed.

In the developed procedure, subsystems such as amplifiers, mixers, filters ... etc are identified separately and then the subsystems are connected together to make a complete system. Measurements on the complete system are then performed and compared to the results of the simulations.

It should be also mentioned here that this technique will require separate identification of the transfer, feedback and reflection characteristics of each subsystem in order to simulate the interaction between the subsystems when connected together.

The advantages of this approach are summarized below:

- . A large system can be divided into smaller subsystems and the models for each subnetwork are derived separately.
- . A library of subsystems models can be developed and stored for future use without the need of an equivalent circuit. This includes amplifiers, mixers, oscillators, filters and couplers.
- . The model characterising a non-linear subsystem can be derived to match experimental data without the need to develop a physically realizable equivalent circuit. This gives a greater flexibility in modelling active devices.

II. Time Domain Identification of Non-Linear Subsystems

An example of time domain nonlinear model structure is shown in Fig. 1. This general non-linear model structure can simulate linear, non-linear, lumped and distributed system. The modelling process is to extract the parameters and the non-linear functions. This modelling method treats the subsystem as a black box. No internal information of the subsystem has to be known, but only the external measurable characteristics

As an example a receiver is to be constructed using an amplifier, a double balanced mixer and a band-pass filter. The system is to mix two signals at 0.277 Ghz and 0.347

Ghz and produce an IF signal at 0.07 Ghz.

First each of the subsystems is identified separately, then the whole system is constructed and the measured and simulated response of the overall system are compared.

a. Amplifier

An amplifier whose measurement and modelled pulse responses are shown in Fig. 2 and 3. The extracted non-linear model can simulate the saturation characteristics of the amplifier as shown in Fig. 4. The alternative frequency domain method requires a large number of frequency domain measurements at different input frequencies and power levels. Impulse response methods can be used to characterise linear circuits or systems. It is more complicated in non-linear system as the waveform of the identifying input are important and each system will have to be identified by a time domain function appropriate to its characteristics and degree of non-linearity.

b. Double Balanced Mixer

A double balanced diode mixer is also modelled in time domain and the measurement and modelled output spectrum are shown in Fig. 5. The nonlinear model can predict the conversion loss of the mixer as shown in Fig. 6.

c. Band-Pass Filter

A linear model of a band pass filter is extracted using time domain method and the measured and modelled frequency responses are shown in Fig. 7.

III. System Simulation

The characteristics of the complete system are obtained from simulation after the modelling of each subsystem is achieved. The overall gain of a receiver system composed of the above mixer, band pass filter and amplifier as shown in Fig. 8 is measured. The measurement and the simulation results are shown in Fig. 9 and 10. Simulated and measured waveforms at different check points of the system are shown in Fig. 11.

The procedure for system design can be summarised as follows:

- . The characteristics of each subsystem is measured using time domain measurements with an appropriate time function.
- . A linear or non-linear model is identified to fit the time domain measurements.

- . The whole system is then simulated using the identified subsystem models and the characteristics of the system is obtained in either the time or frequency domains.
- . Finally measurements on the whole system should confirm the simulated results.

IV. Conclusions

A new method of subsystem modelling and system simulation has been developed. Non-linear modelling and simulation are performed in time domain. Black box model is used instead of equivalent circuit model. The system simulation can deal with any number of subsystems and any arbitrary connection. A receiver system is modelled and the simulation results agree with measurements.

References

- [1] M.I. Sobhy, E.A. Hosny and M.A. Nassef "Multiport Approach for the Analysis of Microwave Non-linear Networks". International Journal of Numerical Modelling. Vol 28, No.1 Jan.1993
- [2] E.A. Hosny, M.A. Nassef and M.I. Sobhy. "Computer-aided Analysis of Non-linear Lumped distributed Multiport Networks". Proc. IEEE International Symposium on Circuits and Systems. Vol.1 pp. 418-431, New Orleans, May 1990

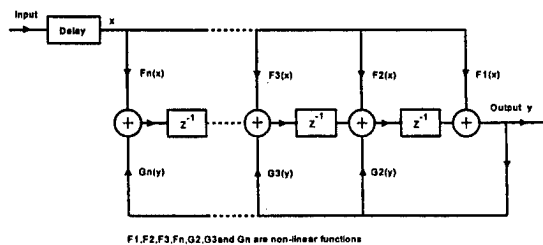


Fig. 1 Non-linear Model of Subsystem

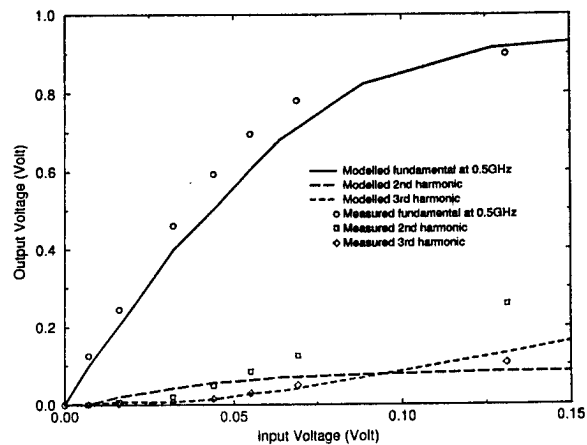


Fig. 4 Input-Output Responses of the Amplifier Model and Measurement

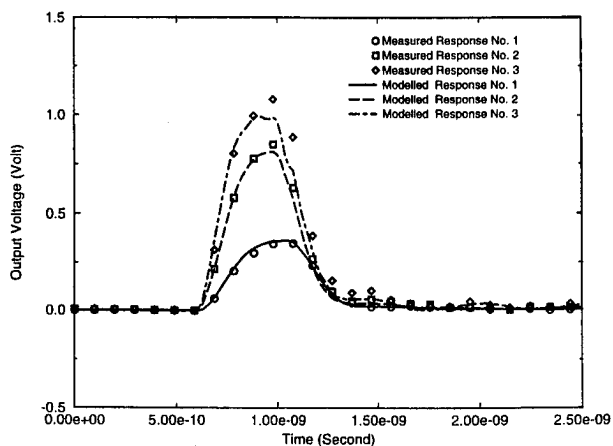


Fig. 2 Positive Pulse Response of Model and Measurement

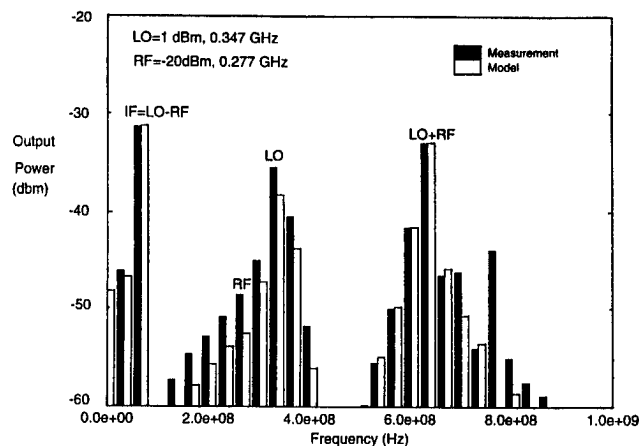


Fig. 5 Output Spectrum of The Mixer

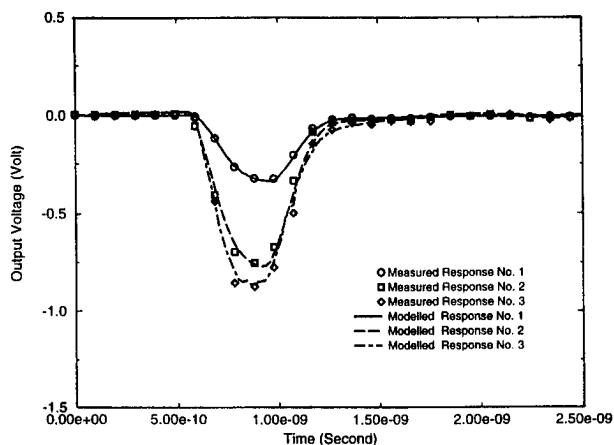


Fig. 3 Negative Pulse Response of Model and Measurement

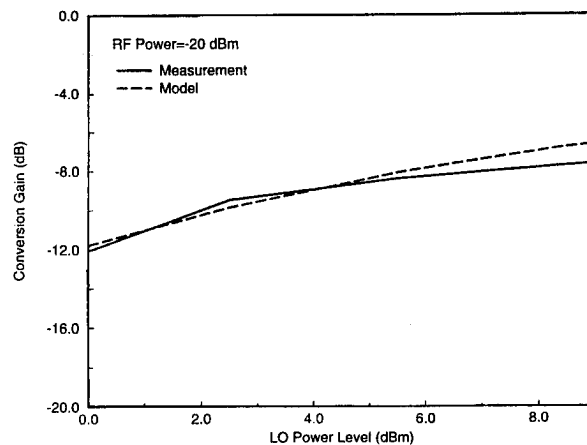


Fig. 6 Mixer Conversion Gain

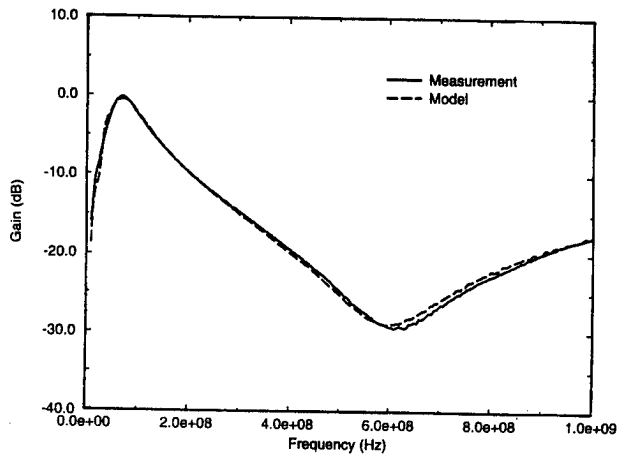


Fig. 7 Frequency Response of Band Pass Filter

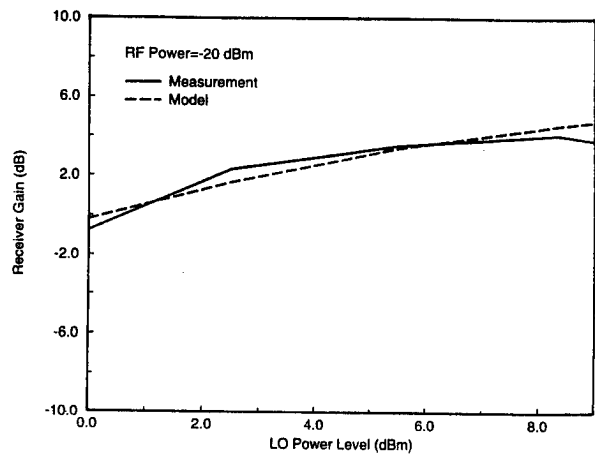


Fig. 10 Receiver Gain vs LO Power

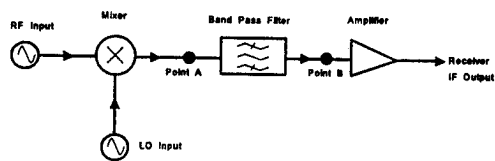


Fig. 8 The receiver system used for measurement and modelling

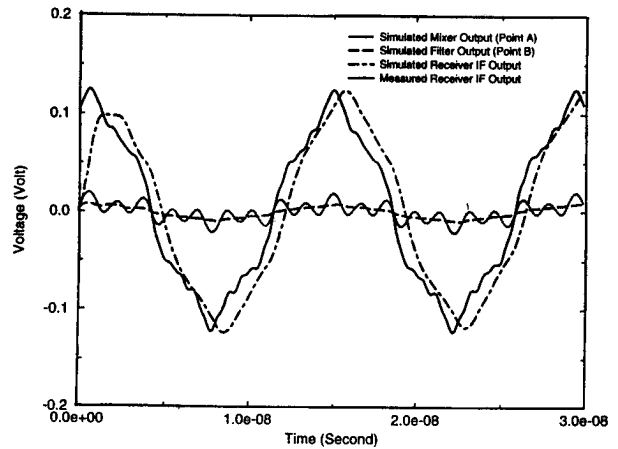


Fig. 11 Simulated and Measured Waveforms of The Receiver System

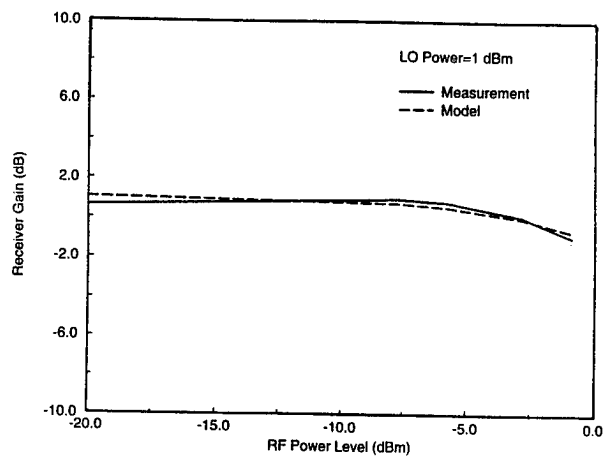


Fig. 9 Receiver Gain vs RF Power

A COMPUTER-AIDED IMPEDANCE CHARACTERIZATION FOR MICROWAVE RESONANT-CAP CIRCUITS

Subal Kar

Institute of Radio Physics & Electronics
University of Calcutta
92, A. P. C. Road
Calcutta: 700 009
India

ABSTRACT

A novel computer-aided impedance characterization has been done on the basis of analytical model equations and suitable computer programs for the microwave resonant-cap circuits used in IMPATT sources. This provides the dependence of the load impedance (terminating the cap cavity) and also of the real and imaginary parts of the cap circuit impedance (at the device plane) on the cavity parameters and frequency. The results are in good qualitative agreement with the previously reported experimental observations and can give a better physical insight regarding the important characteristics of the cap circuit and optimum performance of the cap-type IMPATT sources.

1. INTRODUCTION

The microwave and millimeter-wave IMPATT sources can be easily and efficiently designed by embedding the device in a resonant-cap cavity. Many researchers have carried out experimental studies on the various aspects of the cap-type IMPATT and also Gunn sources [1-4]. But a detailed and coherent analytical investigation and computed results for the important properties of the cap circuit and optimum performance of the cap-type sources are not readily available in published literatures.

The author has thus carried out the analytical modeling and computer-aided solution of the model equations to characterize the impedance properties

of the resonant-cap circuits. At first the analytical expressions have been derived for the real and imaginary parts of the cap circuit impedance at the device plane by approximating the resonant-cap cavity as a radial transmission line. The load impedance terminating the cap cavity has been obtained from resonance condition of the cap-type IMPATT oscillator. Computations were carried out to obtain the variation of the real part of the resonant-cap impedance with the cavity parameters i.e. cap height (h) and cap diameter (D). Also the frequency dependence of the imaginary part of the cap circuit impedance was computed for different parametric values of h & D . Finally, the normalized cap circuit impedance was plotted in an indigenously developed PC generated Smith Chart. On the basis of these analytically derived computed results many of the important properties of the resonant-cap circuit and of the cap-type sources including the experimental results of the earlier researchers are now understood more clearly.

2. THE MODEL EQUATIONS

In a resonant-cap type source the device is embedded in a high- Q cap cavity and the two together mounted in a rectangular waveguide through which the source is connected to the load as shown in Fig.1. The disc of the resonant-cap and the bottom broad wall of the rectangular waveguide forms the cap cavity which is basically a radial transmission line causing efficient power transfer

from the device to the load. The analytical solution of the e.m. fields within the cap cavity leads to the following expressions for the real and imaginary parts of the cap circuit impedance at the device plane (i.e. at $r = r_i$):

$$\text{Re}[Z_i] = Z_{\infty}(r_i) \frac{Z_L \eta}{Z_{\infty}(r_L)} \left[\frac{1 + v \zeta}{\eta^2 \zeta^2 + \left(\frac{Z_L}{Z_{\infty}(r_L)} \right)^2} \right] \dots(1)$$

$$\text{Im}[Z_i] = Z_{\infty}(r_i) \left[\frac{\eta^2 \zeta - \left(\frac{Z_L}{Z_{\infty}(r_L)} \right)^2 v}{\eta^2 \zeta^2 + \left(\frac{Z_L}{Z_{\infty}(r_L)} \right)^2} \right] \dots\dots\dots(2)$$

Where :

$$\begin{aligned} Z_{\infty}(r_{i,L}) &= 377 \frac{h}{2\pi r_{i,L}} \cdot \frac{G_0(kr_{i,L})}{G_1(kr_{i,L})} \\ \eta &= \frac{\text{Sin}(\theta_i - \theta_L)}{\text{Sin}(\psi_i - \psi_L)} \\ \zeta &= -\frac{\text{Cos}(\psi_i - \theta_L)}{\text{Sin}(\theta_i - \theta_L)} \\ v &= -\frac{\text{Cos}(\theta_i - \psi_L)}{\text{Sin}(\psi_i - \psi_L)} \end{aligned} \dots\dots(3)$$

$$G_0(kr_{i,L}) = [J_0^2(kr_{i,L}) + N_0^2(kr_{i,L})]^{0.5}$$

$$G_1(kr_{i,L}) = [J_1^2(kr_{i,L}) + N_1^2(kr_{i,L})]^{0.5}$$

$$\psi_{i,L} = \tan^{-1} \left[\frac{J_1(kr_{i,L})}{N_1(kr_{i,L})} \right]$$

$$\theta_{i,L} = \tan^{-1} \left[\frac{N_0(kr_{i,L})}{J_0(kr_{i,L})} \right]$$

$$k = \frac{2\pi}{\lambda_r}, \lambda_r \text{ is the resonant wavelength.}$$

h , r_i , r_L and Z_L are indicated in Fig. 1. While $J_m(kr)$ and $N_m(kr)$ are the m^{th} order Bessel and Neumann functions respectively.

The load impedance Z_L terminating the cap cavity can be obtained from the oscillation condition for an IMPATT device embedded in a resonant-cap cavity and is given by :

$$\begin{aligned} Z_L = & \frac{2\pi r_L}{h} Z_{\infty}(r_L) \eta \left[\frac{2\pi Z_{\infty}(r_i) \zeta f_r C_d - \zeta^2}{1 + 2\pi Z_{\infty}(r_i) v f_r C_d} \right]^{0.5} \end{aligned} \dots\dots\dots(4)$$

where C_d is the total diode capacitance and f_r is the resonant frequency of the oscillator.

3. COMPUTED RESULTS AND DISCUSSIONS

The analytically derived model equations have been evaluated through suitable computer programs. The values of Z_L for different cap diameter (D) and cap height (h) is computed from eqn.(4) utilizing the experimentally measured f_r for resonant-cap IMPATT oscillators and is shown in the following table :

D	Z_L	h	Z_L
425	397	80	324
475	385	90	341
500	360	100	360
525	354	120	371
550	329	140	369

(D & h in mils, Z_L in ohms.)

It may be seen that maximum power output is expected with a cap circuit having $D = 500$ mils and $h = 100$ mils for which $Z_L = 360 \Omega$, because of optimum impedance matching with the characteristic impedance ($Z_0 \sim 360 \Omega$) of rectangular waveguide (at $f \sim 10$ GHz) which is supported by the experimental observation by the author.

The plot of $\text{Re}[Z_i]$ vs D and h computed from eqn.(1) (wherein Z_L values are used from the above table) is shown in Fig.2. The value of $\text{Re}[Z_i]$ is found to change significantly ($0.105 \Omega / \text{mil}$) with cap height (h) while its change is comparatively insignificant ($0.018 \Omega / \text{mil}$) with cap diameter(D) which agrees qualitatively with the experimental observations of Doring and Seebald [5] and can also account for the experimentally observed predominant change of gain with cap height for the cap-type IMPATT amplifier as reported by Kar & Roy [6]. It may further be observed that the cap circuit resistance $R_c = 5.288 \Omega$ (for $D = 500$ mils and $h = 100$ mils, vide Fig. 2) nearly equals the negative resistance

of the IMPATT device $R_D \sim 5 \Omega$ (as specified by the diode manufacturers) thereby giving optimum oscillator performance.

The frequency dependence of the $\text{Im}[Z_i]$ with D or h as variable parameters are computed from eqn.(2) and plotted in Figs. 3 & 4 respectively. It is seen from Fig. 3 that each cap diameter corresponds to a specific resonant frequency (i.e. the frequency at which $\text{Im}[Z_i] = 0$) above which the cap circuit impedance is inductive and below which it is capacitive. These analytically computed results are in agreement with the experimental observations of Bates [3]. The nature of the curves in Figs. 3 & 4 can be understood with simple physical reasoning. The curves of Fig. 3 can be fitted to an empirical formula : $Df_c = \text{const.}$ (where f_c is the circuit determined resonance frequency) which is in agreement with the experimental observations by Kar et al. [2]. However, the clustering of the curves around a typical frequency of 10.55 GHz for different cap heights is due to the fact that in the theoretical analysis the post structure P_2 under the disc (vide Fig.1) was not considered. When the effect of P_2 is considered an extra inductance (which increases with cap height) comes into the circuit and hence : $f_c \propto 1/h$ as was observed experimentally.

A package for the Smith Chart has been developed on which the nature of the cap circuit impedance can be displayed with color graphics for different D and h values. The photographs showing the plot of the resonant-cap impedance (normalized w. r. t the characteristic impedance of the radial line at the device plane) for two different D and h values are shown in Figs. 5 (a) & (b) respectively. It is seen that the real part of the cap circuit impedance is predominantly determined by the cap height (vide Fig. 5(b)) while its change with cap diameter is very small (vide Fig. 5(a)). Also the cap circuit impedance is clearly seen to be capacitive below the resonant frequency (i.e. below $X = 0$ line in the Smith Chart) and it is inductive above the resonant frequency for different cap height or cap diameter.

4. CONCLUSION

The analytic model and the computed results representing the impedance characteristics of the cap-type microwave circuit presented in this paper is expected to be a sound basis for understanding the important properties of the cap circuit and the optimum performance of the cap-type IMPATT sources.

5. REFERENCES

1. I. S. Groves and D. E. Lewis, *Electronics Letts.*, vol. 8, pp. 98-99, Feb. 1972.
2. S. Kar, M. Mitra and S. K. Roy, *International J. of Elect.*, vol. 73, pp. 193-201, July 1992.
3. R. N. Bates, *Electronics Letts.*, vol. 18, pp. 198-199, March 1982.
4. W. H. Haydle, *IEEE Trans., Microwave Theory and Tech.*, vol. MTT-31, pp. 879-889, Nov. 1983.
5. K. H. Doring and E. Seebald, *Electronics Lett.*, vol. 16, pp. 50-51, Jan. 1980.
6. S. Kar and S. K. Roy, *Tech. review of Inst. of elect. and Tele. Commn. Engrs.*, vol. 8, pp. 333 - 338, Dec. 1991.

FIGURES

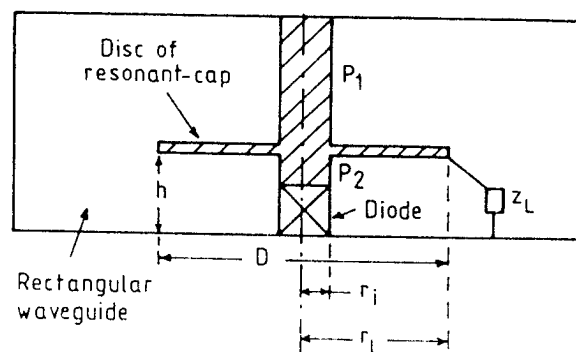


Fig. 1

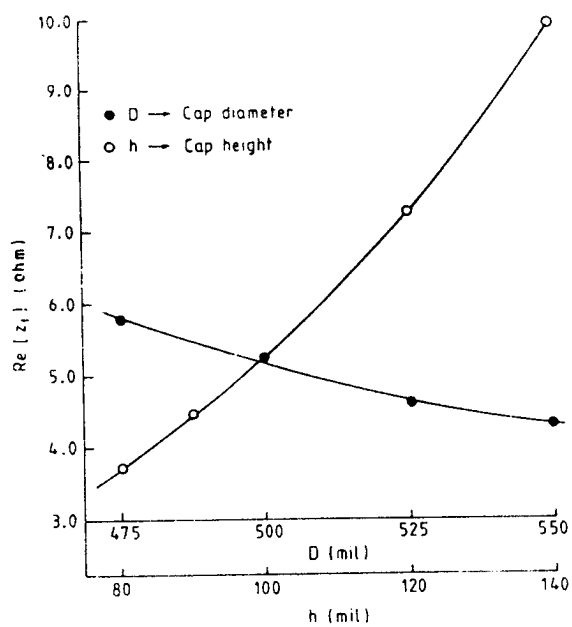


Fig. 2

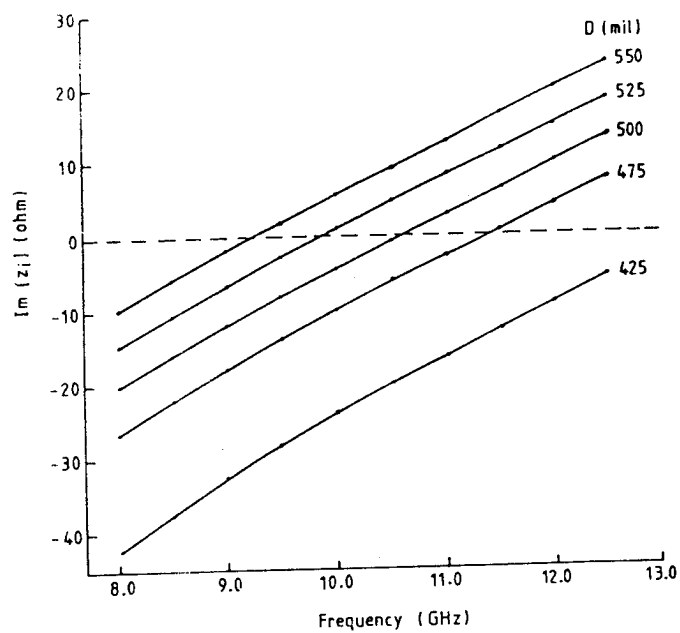


Fig. 3

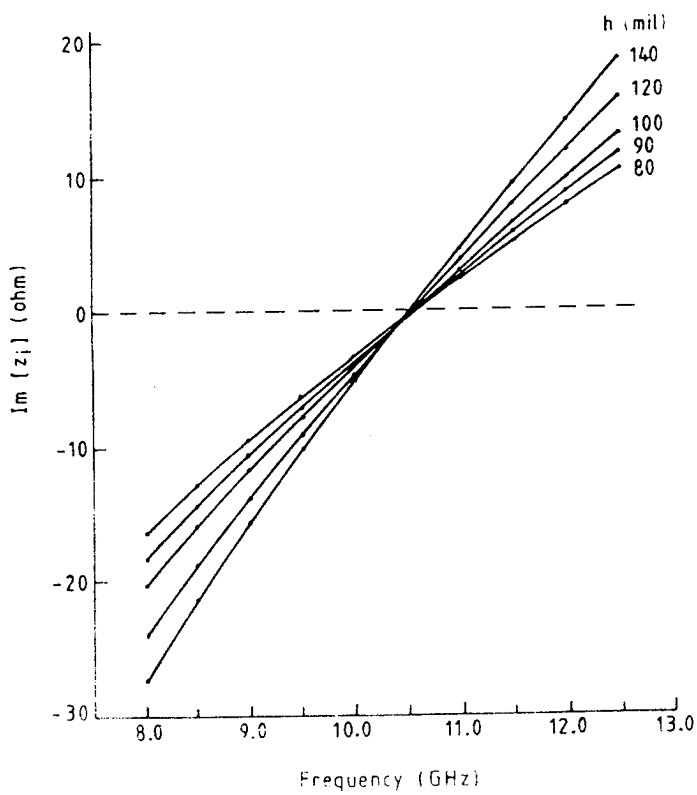


Fig. 4

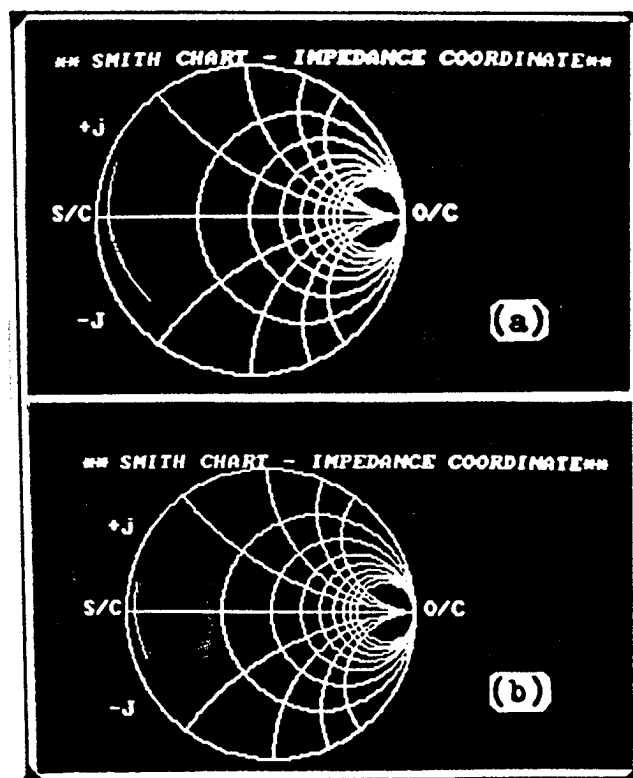


Fig. 5

A New Current Mode Universal Filter

R. Nandi, S.K. Sanyal, and S. K. Debroy

This paper was not available at the time of publication

A NEW TYPE CPW-RESONATOR BANDPASS FILTER WITH WIDE SUPPRESSION CHARACTERISTICS OF HARMONIC RESONANCE RESPONSES

*Yasumasa Noguchi **, *Kouji Wada ***, *Takanori Nakamine **
*and Nobuo Okamoto **

* Department of Electronic Engineering, Kinki University,
3-4-1 Kowakae, Higashi-Osaka City, Osaka 577, Japan

** Department of Electrical and Electronic Engineering, Yamaguchi University,
2557 Tokiwadai, Ube, Yamaguchi 755, Japan

ABSTRACT

In this paper, we present a newly developed bandpass filter (BPF) using a $\lambda_{g0}/2$ coplanar waveguide (CPW) resonator with the short ends and the input/output ports, which are constructed by the coupled shorted-short-line (C-SSL). The frequency characteristics of the input impedance of the filters are also specified. Next, a method for suppressing spurious resonance responses of the filters is discussed. Using the nodal analysis, the circuit simulation and the electromagnetic fields solver computation, the transmission characteristics of the spurious suppression over the wide frequency range of the CPW-BPF is specified. The spurious resonance responses of the CPW-BPF are suppressed more than -45.0 dB between 3.0 and 20.0 GHz.

1. INTRODUCTION

Recently, the mobile communication systems are changing from analog systems to digital systems. The microwave filters are required very severer specifications such as the suppressing harmonic resonance responses over the wide frequency range.

In this paper, we described the properties of the $\lambda_{g0}/2$ Coplanar Waveguide (CPW) resonator with the short ends and the input/output ports, which are constructed by the Coupled Shorted-Short-Line (C-SSL), and the transmission characteristics of the bandpass filters (BPFs) using the resonator. Using the nodal analysis, the circuit simulation and the electromagnetic fields solver com-

putation, the transmission characteristics of the spurious suppression over the wide frequency range of the CPW-BPF is specified. In the results of the theoretical analysis and calculation, the new type CPW-BPFs have the excellent spurious suppression characteristics.

2. BANDPASS FILTER USING $\lambda_{g0}/2$ CPW-RESONATOR WITH THE SHORT ENDS

As you well know the spurious harmonic resonance responses of the BPF using the $\lambda_{g0}/2$ resonators with the short ends arise at the frequencies of the integral multiples of the center frequency f_0 .

In the past, we used the transforming sections using the $\lambda_{g0}/4$ coupled transmission-lines or the tapping feed for input/output feeding in the conventional type $\lambda_{g0}/2$ CPW-resonator BPF. On the newly developed CPW-BPFs, we have been used C-SSL input/output instead of the above feeding structures. Using the C-SSL input/output configurations and the loaded capacitors, these CPW-BPFs can be achieved the wide suppression spurious harmonic resonance responses.

First, the circuit model #1 of the BPF using a $\lambda_{g0}/2$ CPW-resonator with the short ends and input/output ports, which are constructed by the C-SSL is shown in Figure 1. The ABCD-matrix K_a of the circuit model #1 is following equation (1).

Secondly, the circuit model #2 of the CPW-BPF using the very short resonator with the short ends attached shunt capacitor at the center of the one and the C-SSL input/

output structures is shown in Figure 2. The ABCD-matrix K_b of the circuit model #2 is following equation (2).

Finally, the circuit model #3 of the CPW-BPF using the very short resonator with the short ends attached shunt capacitor at the center of the one and furthermore the C-SSL attached the shunt capacitors at the input/output ports is shown in Figure 3. The ABCD-matrix K_c of the circuit model #3 is following equation (3).

The equivalent circuits of these CPW-BPFs are shown

in Figs. 1, 2 and 3, respectively. By the theoretical analysis and calculation for these configurations in the Figs. 1, 2 and 3, the input impedance characteristics of these BPF and the transmission characteristics of these ones are shown in Figs. 4 (a) and (b), 5(a) and 5(b) and 6(a) and 6(b), respectively. Fig. 7 shows the transmission characteristics of the CPW-BPF with the C-SSL in Fig.1 by the electromagnetic fields solver computation.

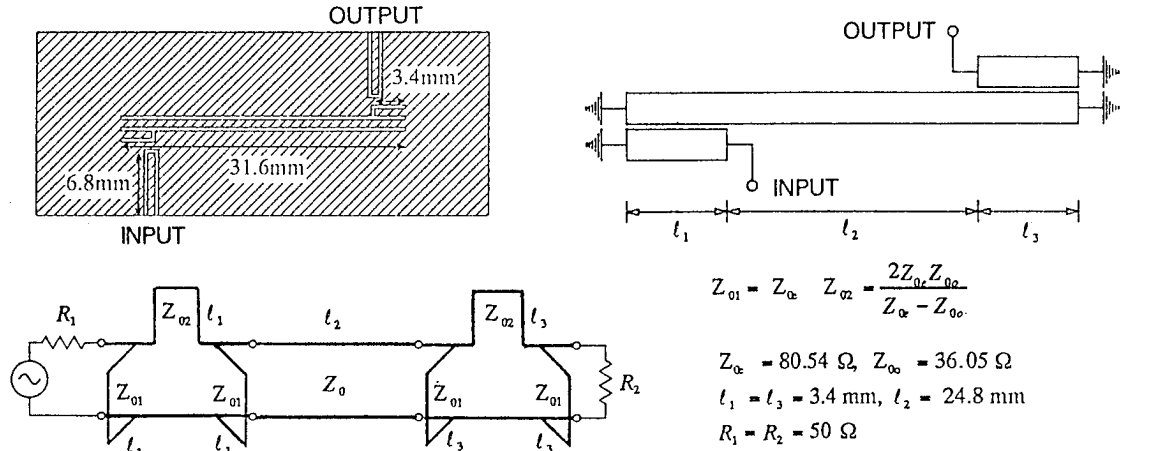


Fig.1 The circuit model #1 and its equivalent circuit of the BPF

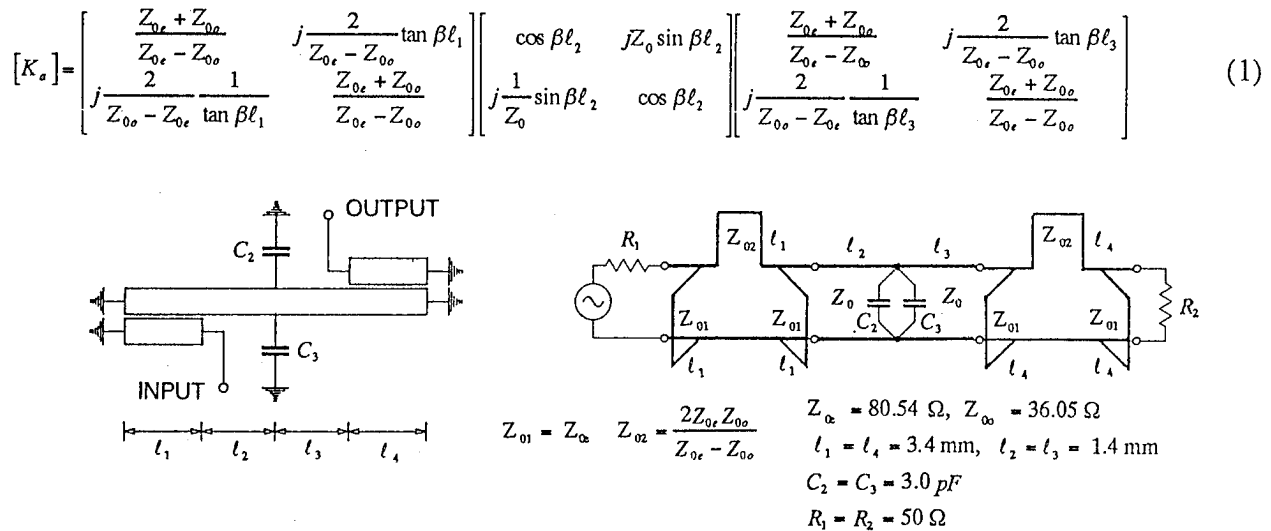


Fig.2 The circuit model #2 and its equivalent circuit of the BPF

$$[K_s] = [K_1][K_2][K_3], \quad [K_1] = \begin{bmatrix} \frac{Z_{0e} + Z_{0o}}{Z_{0e} - Z_{0o}} & j \frac{2}{Z_{0e} - Z_{0o}} \tan \beta \ell_1 \\ j \frac{2}{Z_{0e} - Z_{0o}} \tan \beta \ell_1 & \frac{Z_{0e} + Z_{0o}}{Z_{0e} - Z_{0o}} \end{bmatrix}$$

$$[K_2] = \begin{bmatrix} \cos \beta \ell_2 \cos \beta \ell_3 - \omega(C_2 + C_3) \sin \beta \ell_2 \cos \beta \ell_3 - \sin \beta \ell_2 \cos \beta \ell_3 & j Z_0 \sin \beta \ell_2 \cos \beta \ell_3 - j \omega(C_2 + C_3) Z_0^2 \sin \beta \ell_2 \sin \beta \ell_3 + j Z_0 \cos \beta \ell_2 \sin \beta \ell_3 \\ j \frac{\sin \beta \ell_2 \cos \beta \ell_3 + \cos \beta \ell_2 \sin \beta \ell_3}{Z_0} + j \omega(C_2 + C_3) \cos \beta \ell_2 \cos \beta \ell_3 & \cos \beta \ell_2 \cos \beta \ell_3 - \omega(C_2 + C_3) Z_0 \cos \beta \ell_2 \sin \beta \ell_3 - \sin \beta \ell_2 \sin \beta \ell_3 \end{bmatrix}$$

$$[K_3] = \begin{bmatrix} \frac{Z_{0e} + Z_{0o}}{Z_{0e} - Z_{0o}} & j \frac{2}{Z_{0e} - Z_{0o}} \tan \beta \ell_4 \\ j \frac{2}{Z_{0e} - Z_{0o}} \tan \beta \ell_4 & \frac{Z_{0e} + Z_{0o}}{Z_{0e} - Z_{0o}} \end{bmatrix} \quad (2)$$

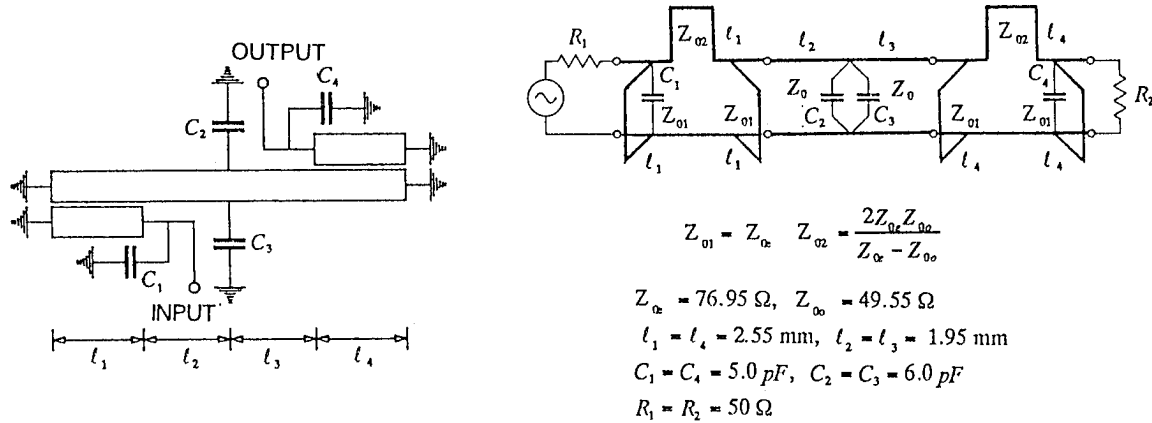


Fig.3 The circuit model #3 and its equivalent circuit of the BPF

$$[K_s] = [K_1][K_2][K_3], \quad [K_1] = \begin{bmatrix} \frac{Z_{0e} + Z_{0o}}{Z_{0e} - Z_{0o}} & j \frac{2Z_{0e}Z_{0o}}{Z_{0e} - Z_{0o}} \tan \beta \ell_1 \\ j \frac{2Z_{0e}Z_{0o}}{Z_{0e} - Z_{0o}} \tan \beta \ell_1 & \frac{Z_{0e} + Z_{0o}}{Z_{0e} - Z_{0o}} \end{bmatrix}$$

$$[K_2] = \begin{bmatrix} \cos \beta \ell_2 \cos \beta \ell_3 - \omega(C_2 + C_3) \sin \beta \ell_2 \cos \beta \ell_3 - \sin \beta \ell_2 \cos \beta \ell_3 & j Z_0 \sin \beta \ell_2 \cos \beta \ell_3 - j \omega(C_2 + C_3) Z_0^2 \sin \beta \ell_2 \sin \beta \ell_3 + j Z_0 \cos \beta \ell_2 \sin \beta \ell_3 \\ j \frac{\sin \beta \ell_2 \cos \beta \ell_3 + \cos \beta \ell_2 \sin \beta \ell_3}{Z_0} + j \omega(C_2 + C_3) \cos \beta \ell_2 \cos \beta \ell_3 & \cos \beta \ell_2 \cos \beta \ell_3 - \omega(C_2 + C_3) Z_0 \cos \beta \ell_2 \sin \beta \ell_3 - \sin \beta \ell_2 \sin \beta \ell_3 \end{bmatrix}$$

$$[K_3] = \begin{bmatrix} \frac{Z_{0e} + Z_{0o} - 2\omega C_4 Z_{0e} Z_{0o} \tan \beta \ell_4}{Z_{0e} - Z_{0o}} & j \frac{2Z_{0e}Z_{0o}}{Z_{0e} - Z_{0o}} \tan \beta \ell_4 \\ j \frac{2Z_{0e}Z_{0o}}{Z_{0e} - Z_{0o}} \tan \beta \ell_4 & \frac{Z_{0e} + Z_{0o}}{Z_{0e} - Z_{0o}} \end{bmatrix} \quad (3)$$

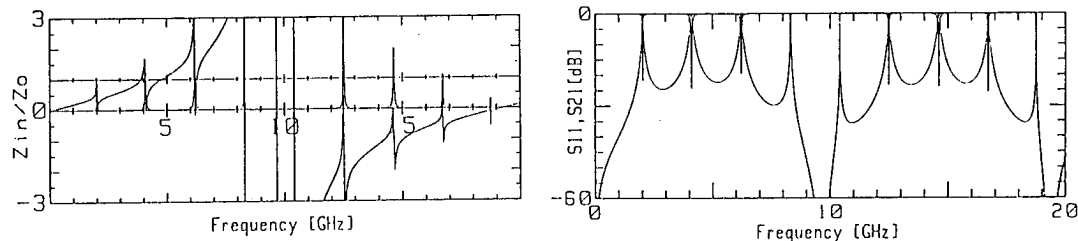


Fig. 4 (a) The normalized input impedance and (b) the transmission characteristics of the circuit model #1

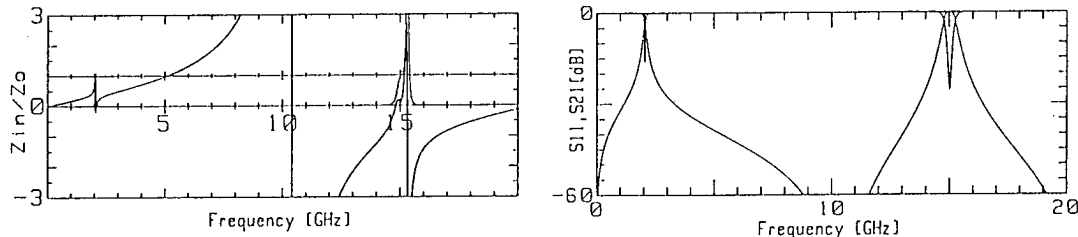


Fig.5 (a) The normalized input impedance and (b) the transmission characteristics of the circuit model #2

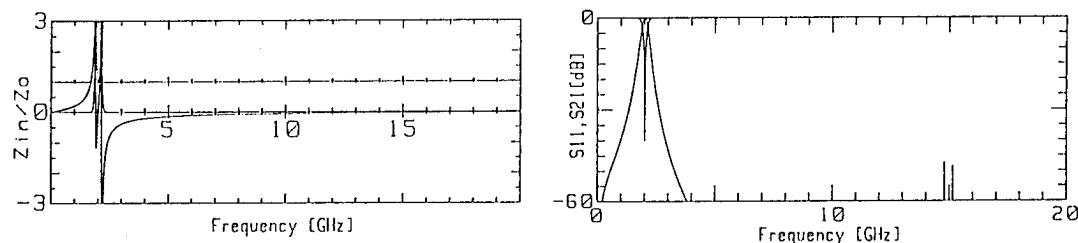
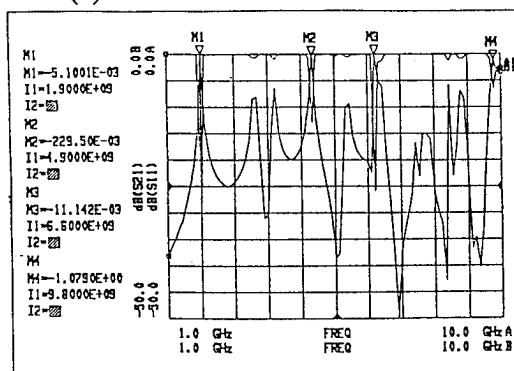


Fig.6 (a) The normalized input impedance and (b) the transmission characteristics of the circuit model #3

Fig.7 The transmission characteristics of the CPW-BPF in Fig.1 by the EM solver computation



CONCLUSION

We presented a newly developed CPW-BPF using a $\lambda_{g0}/2$ resonator with the short ends and the input/output ports, which were constructed by the C-SSL.

A method for suppressing spurious resonance responses of the CPW-BPFs was discussed. The spurious resonance responses of the CPW-BPF were suppressed more than -45.0dB between 3.0 and 20.0 GHz.

REFERENCES

- [1] Noguchi, Y., Ishii, J., et al., Proc. 1992 URSI ISSSE' 92, pp. 867-870, Paris, France, Sep., 1992.
- [2] Noguchi, Y., Wada, K., et al., Proc. 4th ISRAMT, pp. 610-614, New Delhi, India, Dec., 1993.
- [3] Wada, K., Noguchi, Y., et al., 1994 APMC Proc. pp. 763-766, Tokyo, Japan, Dec., 1994.

A Linear Sinewave VCO Design and its Digital Control

S.K. Sanyal, R. Nandi, S. K. Debroy, and D. Pal

This paper was not available at the time of publication

JOINT TIME-FREQUENCY ANALYSIS OF ELECTROMAGNETIC BACKSCATTERED DATA

Hao Ling

Department of Electrical and Computer Engineering
The University of Texas at Austin
Austin, TX 78712-1084
ling@ece.utexas.edu

ABSTRACT

The application of joint time-frequency techniques to extract the scattering mechanisms contained in electromagnetic backscattered data is reviewed. Research activities on interpreting the scattering phenomenology in the time-frequency plane, methods to improve the resolution of joint time-frequency processing, and imaging algorithms combining joint time-frequency techniques with conventional inverse synthetic aperture radar processing are discussed.

1. INTRODUCTION

In radar signature applications, the electromagnetic backscattered returns from a complex target are commonly processed in either the time or the frequency domain in order to extract useful target features for diagnostic and identification purposes. For example, scattering centers are manifested in the time domain as distinct pulses and can be related to the local features on the target. Similarly, the natural resonances of a target are manifested in the frequency domain as sharp, discrete events and can be attributed to the unique global features of the target. For target characteristics which are not immediately apparent in either the time or the frequency domain, the joint time-frequency representation of the electromagnetic backscattered data can sometimes provide more insight into the echo interpretation process. The usefulness of the time-frequency representation of signals, of course, has long been recognized in the signal processing arenas. In the electromagnetic scattering community, the joint time-frequency analysis was introduced by Moghaddar and Walton [1] to explain the measurement data from an open-ended waveguide cavity. The goal of this paper is to provide an overview of the progress made in the past several years in

the application of joint time-frequency techniques to electromagnetic signature data.

2. SCATTERING PHENOMENOLOGY IN THE JOINT TIME-FREQUENCY PLANE

The standard tool in generating the time-frequency representation of a signal is the short-time Fourier transform (STFT). It is basically a sliding window Fourier transform in time. By taking the Fourier transform of the windowed time data as the window is moved in time, a two-dimensional time-frequency image, or the spectrogram, is generated. Spectrogram provides information on the frequency content of the signal at different time instances. Alternatively, the STFT can also be interpreted as a sliding window Fourier transform in frequency where the frequency window function is given by the Fourier transform of the time window. In electromagnetic applications, the joint time-frequency image can be used to simultaneously display the different scattering phenomenology due to scattering centers, target resonances and dispersive mechanisms. Shown in Fig. 1 are the time-frequency features of the various mechanisms. A scattering center, which is a discrete event of time, shows up as a vertical line (Fig. 1(a)) as it occurs at a particular time instance but over all frequencies. A resonance, which is a discrete event of frequency, shows up as a horizontal line (Fig. 1(b)). Dispersive phenomena, on the other hand, are characterized by slanted curves in the time-frequency image. For example, surface wave mechanisms due to material coatings are characterized by curves with a positive slope in the time-frequency image (Fig. 1(c)). This is because as the frequency is increased, the surface wave becomes more tightly bound to the material layer, and consequently, propagates at a slower velocity and results in a longer time delay. Another type of dispersion is due to waveguide structures, such as those found in inlet ducts and slotted

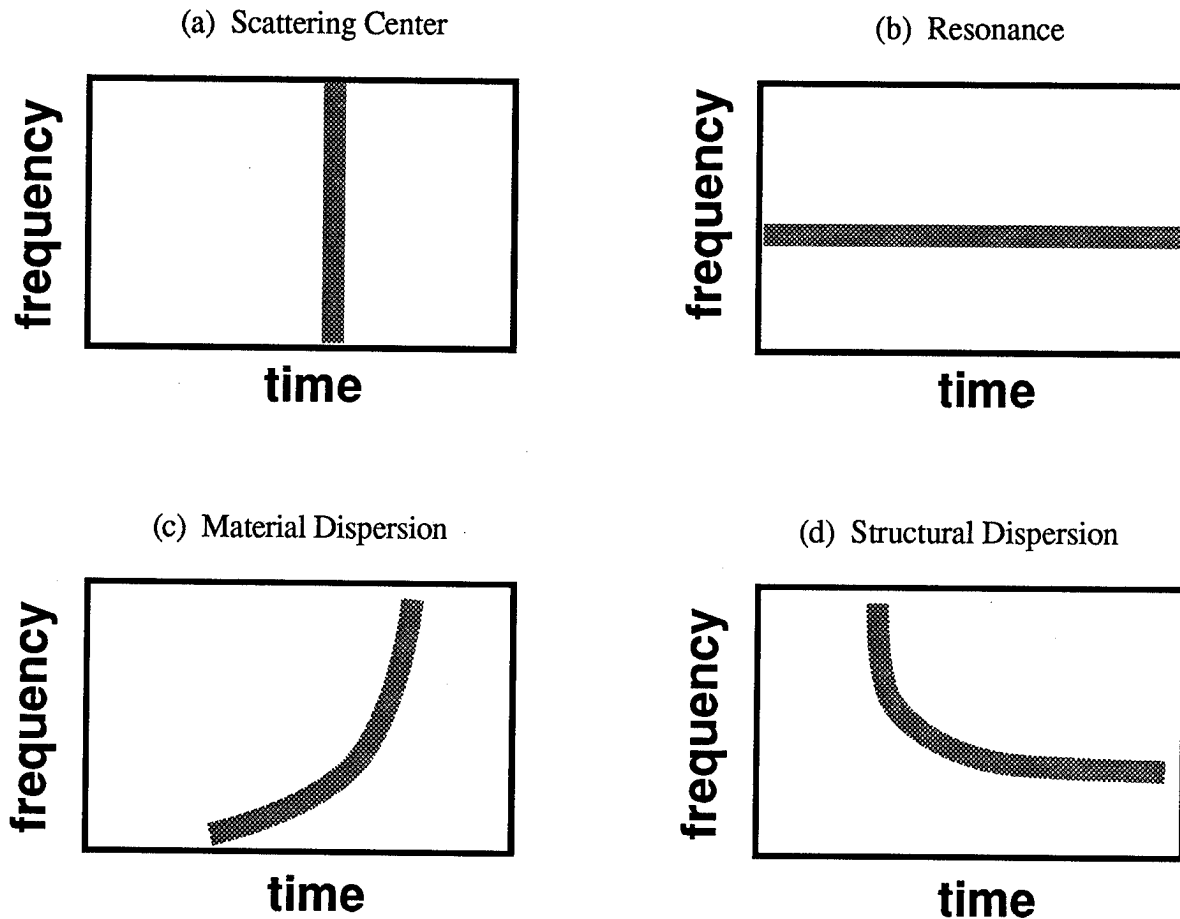


Fig. 1. Scattering mechanisms are manifested in the joint time-frequency image as distinct features.

waveguide antennas. These "structural dispersion" mechanisms are characterized by curves with a negative slope in the time-frequency image (Fig. 1(d)). This can be explained by the fact that as the frequency is lowered, one approaches the cutoff frequency of a waveguide mode and the propagation delay associated with this mechanism approaches infinity. All of the above mentioned phenomena have been observed in a wide variety of targets, from simulation data on canonical structures [1],[2],[4] to measurement data on complex platforms [1],[3]. In general, the time-frequency representation is particularly effective for identifying scattering mechanisms in targets containing "sub-skinline" structures such as inlet ducts, antenna windows and material coatings. For full-scale targets, these effects are most dominant in the UHF frequency ranges.

3. IMPROVEMENTS TO THE TIME-FREQUENCY PROCESSING ENGINE

The insights gained in the time-frequency plane come at the price of resolution. The time-frequency image generated by the STFT is limited in resolution by the extent of the sliding window function. Smaller time window results in better time resolution, but leads to worse frequency resolution. This is a well-known tradeoff of the time-frequency display. To overcome the resolution limit of the STFT, a number of alternative time-frequency representations developed in the signal processing community have been utilized to analyze electromagnetic scattering data. They include the Wigner-Ville distribution [1], the continuous wavelet transform [2], superresolution

algorithms [4] and adaptive techniques [5]. The well-known Wigner-Ville distribution provides good localization of scattering mechanisms at the expense of additional cross terms which lead to "ghosts" in the time-frequency image. The wavelet transform utilizes multi-scale basis functions to provide multiresolution capability. For frequency-domain radar echo which consists of both small-scale natural resonances and large-scale scattering center information, the wavelet transform defined in the frequency domain is better suited for resolving these multi-scale events of frequency than the STFT.

In either the STFT or the wavelet transform, the resolution in the time-frequency display is limited by the extent of the sliding window function as opposed to the full bandwidth of the signal. To further improve the Fourier-limited resolution in the time-frequency plane, the processing of the data within each time or frequency window using modern superresolution techniques such as ESPRIT, MUSIC or matrix-pencil algorithms have been investigated. Super-resolved parameterization retains the advantage of simultaneous time-frequency display while overcoming the resolution issue. However, additional processing is needed to fully parameterize the data, especially when dispersive mechanisms are present. Furthermore, the robustness of the algorithms to noise needs to be carefully considered.

The use of wavelet is a step towards variable resolution in the time-frequency plane. It is, however, rather rigid in its particular form of the time-frequency grid. Flexible resolution in the time-frequency plane to accommodate components of the signal with different resolution is highly desirable. Recently, a signal representation scheme that uses adaptive normalized Gaussian functions was introduced [5]. Unlike the STFT and wavelet decomposition, the time and frequency resolution as well as the time-frequency centers are adjusted to best match the signal. The adaptive spectrogram, a signal energy distribution in the joint time-frequency domain based on this adaptive representation, can be applied to backscattered signals containing scattering centers and resonances with very high resolution in both time and frequency. Issues that need to be further addressed include the uniqueness of the representation, computational complexity and efficient treatment of dispersive mechanisms.

4. JOINT TIME-FREQUENCY ISAR PROCESSING

While the joint time-frequency processing is applicable to single aspect data, it can also be combined with the traditional ISAR (inverse synthetic aperture radar) technique

to make use of the additional angular information. The ISAR imaging algorithm is basically a spatial mapping algorithm for point scatterers. For targets which can be well described by a collection of point scatterers, conventional ISAR imagery provides an ideal display of target features. However, when the target contains other non-point scattering mechanisms, the resulting ISAR image will contain artifacts which do not correspond to the spatial features on the target. For instance, the engine inlet return of an airplane usually shows up as a large cloud outside of the airframe structure in the ISAR image. A joint time-frequency ISAR can be formed by viewing the point scatterers in the conventional ISAR plane while placing other non-point scattering mechanisms in the time-frequency plane. Instead of the conventional (range)-(cross range) display, this is accomplished by applying joint time-frequency processing to the range (or time) axis to gain an additional frequency dimension. The resulting (range)-(cross range)-(frequency) ISAR allows us to view the frequency behavior of the scattering mechanisms not available in conventional ISAR. For aircraft signatures, for example, it is possible to remove the highly resonant engine inlet contribution from the ISAR image and view it separately in the joint time-frequency plane.

Similar to the above idea, the joint time-frequency processing can also be applied to the cross range (or Doppler frequency) axis of the ISAR image. This technique has been used to overcome motion compensation errors in stepped-frequency radar data [6]. For radars with long dwell time on fast-moving, close-in targets, the effect of motion compensation errors can be quite severe, resulting in cross range smearing in the ISAR image. If the joint time-frequency technique is applied to the Doppler frequency axis, an additional aspect dimension is generated. The resulting (range)-(cross range)-(aspect) display allows us to view the instantaneous ISAR images of the target at different aspect angles. Since motion compensation errors are reduced over smaller angular windows, the resulting sequence of images has less cross range blurring problem than the original ISAR image.

5. SUMMARY

Research in the last several years has shown that the joint time-frequency space is an attractive feature space for identifying target characteristics from electromagnetic backscattered data. Ongoing works are focused on applying multiresolution, superresolution and adaptive resolution techniques to enhance the resolution in the time-frequency image to facilitate feature identification. Incorporation of joint time-frequency processing to traditional ISAR

imaging also opens up a new avenue where multi-aspect data can be properly utilized. Once more fully developed, these processing techniques will be excellent tools for understanding the scattering phenomenology from computed or measured data. In addition, they should find applications in ultra-wideband radar target identification.

ACKNOWLEDGMENTS

This work was supported by the Joint Services Electronics Program under Contract No. AFSOR F49620-92-C-0027 and in part by NASA grant NAG3-1589.

REFERENCES

- [1] A. Moghaddar and E.K. Walton, "Time-frequency-distribution analysis of scattering from waveguide cavities," *IEEE Trans. Antennas Propagat.*, vol. AP-41, pp. 677-680, May 1993.
- [2] H. Kim and H. Ling, "Wavelet analysis of radar echo from finite-size targets," *IEEE Trans. Antennas Propagat.*, vol. AP-41, pp. 200-207, Feb. 1993.
- [3] W. Kent, R. Layden and J. Berrie, "Antenna scattering: measurements and time-frequency," presented at the annual Non-Cooperative Target Identification Program Review, Air Force Wright Laboratory, Oct. 28, 1993.
- [4] L. Carin, L.B. Felsen, D. Kralj, S.U. Pillai and W.C. Lee, "Dispersive modes in the time domain: analysis and time-frequency representation," *IEEE Microwave Guided Wave Lett.*, vol. 4, pp. 23-25, Jan. 1994.
- [5] S. Qian and D. Chen, "Signal representation using adaptive normalized Gaussian functions," *Signal Processing*, vol. 36, no. 1, pp. 1-11, Mar. 1994.
- [6] V. Chen, "Reconstruction of inverse synthetic aperture image using adaptive time-frequency wavelet transform," *SPIE* vol. 2491, pp. 373-386, 1995.

JOINT TIME-FREQUENCY ISAR ALGORITHM FOR IMAGING TARGETS WITH NON-POINT SCATTERING FEATURES

Luiz C. Trintinalia and Hao Ling

Department of Electrical and Computer Engineering
The University of Texas at Austin
Austin, Texas 78712-1084
luiz@ling1.ece.utexas.edu

ABSTRACT

In this paper we present a joint time-frequency ISAR algorithm. This algorithm allows the separation of the original ISAR image into two different images: an ISAR image containing only scattering center information, and a frequency-aspect image showing only resonance features associated with the target. We also show, as an example, the application of this technique to signal backscattered by a target containing a small open cavity.

1. INTRODUCTION

Inverse synthetic aperture radar (ISAR) imaging [1] has long been used in the radar community for signature diagnostic and target identification applications. It is a simple and very robust process for mapping the point scatterers present in the target. However, while simple targets can be modeled as a collection of point scatterers, real world targets contain many non-point scattering mechanisms such as resonances and dispersions. These scattering mechanisms appear in the ISAR image as blurred clouds which extend down-range, sometimes even obscuring other scattering centers. On the other hand, these mechanisms provide important features that can be used in the target classification process, if properly interpreted.

To address these issues, we present a new processing technique, the joint time frequency ISAR. This technique allows the separation of the original ISAR image into two different images: one ISAR image containing only scattering center information, and another frequency-aspect image showing strong frequency dependent features associated with the target. This separation is accomplished by using the adaptive Gaussian representation [2]. In this paper we give a brief introduction to the proposed algorithm and show its

application to signal backscattered by a target containing a small open cavity.

2. ISAR IMAGES OF TARGETS CONTAINING NON-POINT SCATTERING FEATURES

For targets that can be modeled as a collection of ideal point scatterers, it is well known that by gathering data at different frequencies and different aspect angles (and therefore at different values of k_x and k_y) it is possible to obtain an image in the x - y plane that will have peaks at the locations of these scattering centers. This image can be easily obtained by using the inverse Fourier transform, that will map the k_x - k_y plane into the x - y plane.

However, real targets contain many non-point scattering mechanisms, such as resonances and other dispersive phenomena, that cannot be focused in the x - y plane. For example if the target contains a very small cavity at the coordinates (x_0, y_0) , that resonates at the frequency f_0 , it can be shown that the scattered field due to this resonance can be written as:

$$S(f, \theta) = A \frac{\exp(-j2k_x x_0 - j2k_y y_0)}{\alpha + j2\pi(f - f_0)}$$
$$k_x = \frac{2\pi f}{c} \cos \theta, \quad k_y = \frac{2\pi f}{c} \sin \theta \quad (1a)$$

Under a small aspect aperture approximation this resonance would be mapped in the x - y plane as:

$$s(x, y) = B \delta(y - y_0) \exp(j2k_0 x) \exp(-2\alpha x/c) u(x - x_0) \quad (1b)$$

So we see that this kind of mechanism tends to spread over the down-range of the image, making the task of

locating scattering centers much more difficult. For example, Fig. 2 shows the ISAR image of a perfectly conducting plate containing a small cavity with an opening, as depicted in Fig. 1. The scattering data were simulated numerically using a method of moment electromagnetics code. We notice in the image that, in addition to the three scattering centers corresponding to the two edges of the plate and the cavity exterior, there is also a very strong return outside of the target. This return corresponds to the energy that is coupled into the cavity, and is re-radiated towards the radar at the resonance frequencies. This non-point scatterer contribution clearly complicates the image interpretation process since its location in the ISAR image does not correspond to the physical location of the scattering. In addition, it may obscure any other scattering centers located at these positions.

3. JOINT TIME-FREQUENCY ISAR

From the above discussion we conclude that it will be very useful to obtain a representation that can allow us not only to locate the frequency-independent scattering centers, but also to identify the frequency-dependent events in the signal. This can be accomplished by the use of the proposed joint time-frequency ISAR algorithm that combines the idea of standard ISAR with the joint time-frequency representation. In our recent work we have found the joint time-frequency display to be an excellent tool for visualizing signals that contain scattering centers, resonances as well as other dispersive mechanisms [3],[4]. To obtain the desired joint time-frequency ISAR representation, one choice is to apply the standard short-time Fourier transform (STFT) to each horizontal line of the ISAR image. For a fixed y (cross range), each horizontal line is a function of x (range), which is in turn directly proportional to the time (for small angular aperture). Therefore, the application of the STFT to each line of our image will generate a 3-dimensional matrix (x - y - f). Each (x - y) slice of this matrix is an ISAR image at a particular frequency. This display can thus show how the ISAR image varies with frequency. Furthermore, we can distinguish the frequency-independent part of the signal from frequency-dependent events by viewing the slices.

This implementation however presents three major problems. First, the frequency resolution is obtained at the cost of lower range resolution. This is a well-known property of the STFT. Second, it is difficult to automatically distinguish the frequency-dependent events from the frequency-independent ones. Third, we have to generate the whole cube before any feature identification

can be made, and that requires too much memory. In order to solve these problems we adopt a different algorithm based on the adaptive Gaussian basis function to process our ISAR image, as described next.

4. JTF-ISAR USING ADAPTIVE GAUSSIAN BASIS REPRESENTATION

The adaptive spectrogram is a signal representation scheme, recently introduced by Qian and Chen [2], that uses adaptive normalized Gaussian as basis functions. The objective of this method is to expand a signal $s(t)$ in terms of normalized Gaussian functions $h_p(t)$ with an adjustable standard deviation σ_p and a time-frequency center (t_p, f_p) :

$$s(t) = \sum_{p=1}^{\infty} B_p h_p(t) \quad (2)$$

where

$$h_p(t) = (\pi\sigma_p^2)^{-0.25} \exp\left[-\frac{(t-t_p)^2}{2\sigma_p^2}\right] \exp(j2\pi f_p t) \quad (3)$$

The coefficients B_p are found one at a time by an iterative procedure. One begins at the stage $p=1$ and chooses the parameters σ_p , t_p and f_p such that $h_p(t)$ is most "similar" to $s(t)$, that is:

$$|B_p|^2 = \max_{\sigma_p, t_p, f_p} \left| \int s_{p-1}(t) h_p^*(t) dt \right|^2$$

$$\sigma_p \in \mathbf{R}^+, \quad t_p, f_p \in \mathbf{R} \quad (4)$$

where $s_0(t) = s(t)$. For $p > 1$, $s_p(t)$ is the remainder after the orthogonal projection of $s_{p-1}(t)$ onto $h_p(t)$ has been removed from the signal:

$$s_p(t) = s_{p-1}(t) - B_p(t) h_p(t) \quad (5)$$

We see from expression (3) that scattering centers, i.e., signals with very narrow length in time, will be well represented by basis functions with very small σ_p . Frequency resonances, on the other hand, will be better depicted by large σ_p . Therefore the parameters extracted should give us the location and strength of these

scattering mechanisms with very high resolution. If we apply the above algorithm to each horizontal line of the ISAR image, instead of using the STFT, we will obtain a summation of Gaussians with different variances. Those Gaussian bases with small variances should be related to the scattering centers. Consequently if we reconstruct our ISAR image using only the functions in this group, we will obtain a much "cleaner" image that will show only the scattering centers. We can also reconstruct the ISAR image using only the large variance Gaussians, those related to the resonances and other discrete frequency events. It is, however, more meaningful to view these frequency-dependent mechanisms in the Fourier transform domain of the ISAR image. By doing so, we will obtain a frequency-aspect display that will allow us to precisely locate those frequencies.

5. EXAMPLES

Fig. 3 shows the enhanced ISAR image of Fig. 2, obtained by applying the above algorithm and keeping only the small variance Gaussians. Only the scattering center part of the original signal remains in the image, as expected. Fig. 4 shows the frequency-aspect display of the high variance Gaussians. Several equispaced vertical lines are observed. They correspond to the resonance frequencies of the cavity, which should occur at 5.30, 8.39, 11.86 and 13.52 GHz based on the dimensions of the cavity. Indeed, we see that they occur close to these frequencies and are almost aspect independent. Using our algorithm, we have also processed real measured data of a scaled model airplane taken inside a radar chamber and results will be presented.

6. CONCLUSIONS

In this paper we presented a new joint time-frequency ISAR image processing algorithm, that allows the analysis of multi-aspect multi-frequency scattered signals containing not only scattering centers but also other frequency dependent mechanisms. This technique allows the separation of the original ISAR image into two different images: one enhanced ISAR image with only scattering center features, and another frequency-aspect image showing only strong frequency dependent features. This is accomplished without any loss in resolution.

7. ACKNOWLEDGMENTS

This work was supported by the Joint Services Electronics Program under Contract No. AFOSR F49620-92-C-0027. L. C. T. is on leave from the

Department of Electronic Engineering of Escola Politécnica da Universidade de São Paulo, Brazil, and is also sponsored by CNPq.

8. REFERENCES

- [1] D. L. Mensa, *High Resolution Radar Imaging*. Artech House, Dedham, MA, 1981.
- [2] S. Qian and D. Chen, "Signal representation using adaptive normalized Gaussian functions," *Signal Processing*, vol. 36, no. 1, pp. 1-11, Mar. 1994.
- [3] H. Kim and H. Ling, "Wavelet analysis of radar echo from finite-size targets," *IEEE Trans. Antennas Propagat.*, vol. AP-41, pp. 200-207, Feb. 1993.
- [4] L. C. Trintinalia and H. Ling, "Interpretation of scattering phenomenology in slotted waveguide structures via time-frequency processing," to appear in *IEEE Trans. Antennas Propagat.*, 1995.

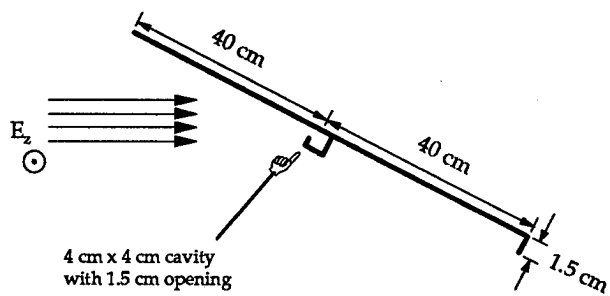


Fig. 1: Target geometry.

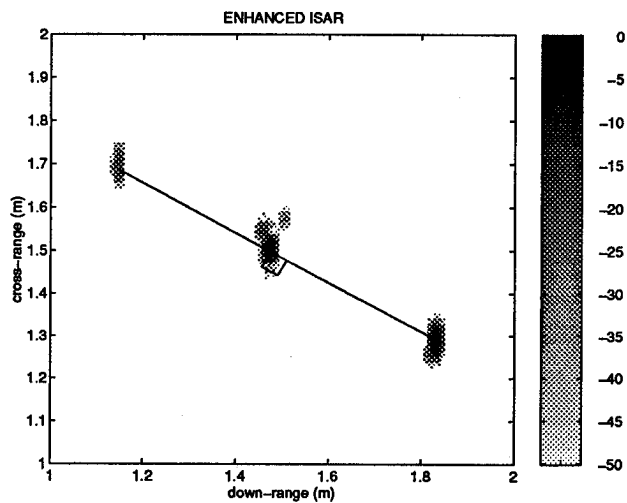


Fig. 3: Enhanced ISAR image of conducting plate containing a small cavity.

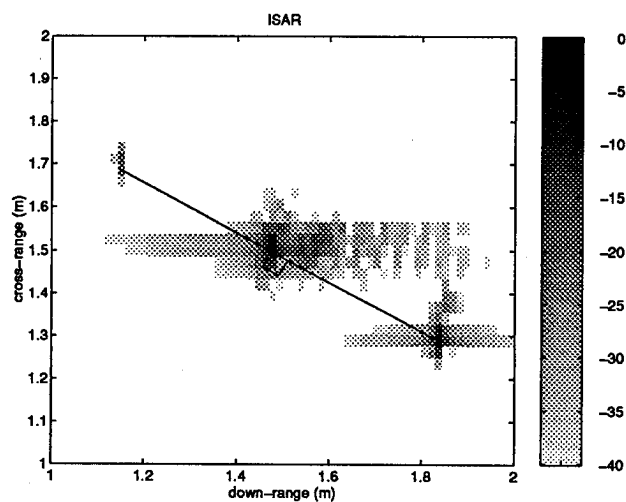


Fig. 2: ISAR image of a conducting plate containing a small cavity.

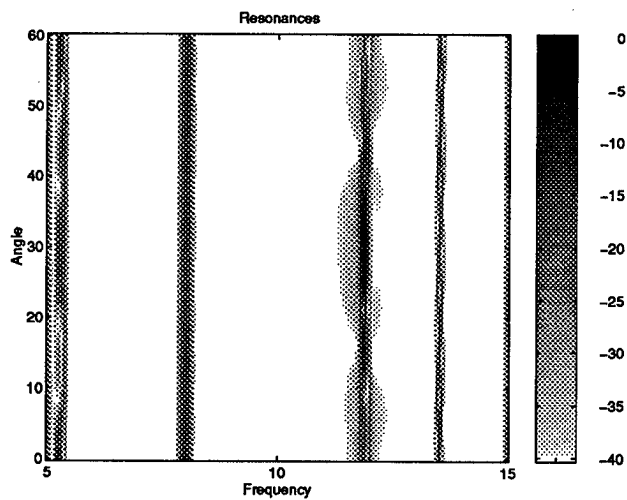


Fig. 4: Frequency aspect display obtained from ISAR image in Fig. 2, using only high variance Gaussians.

RECONSTRUCTION OF ISAR IMAGE BY TIME-FREQUENCY DISTRIBUTION SERIES

(Invited Paper)

Victor C. Chen

Airborne Brunch, Naval Research Laboratory
4555 Overlook Ave., Washington D.C. 20375

Shie Qian¹

DSP Group, National Instruments
6504 Bridge Point Parkway, Austin, Texas 78730
email: qian@eagle.natinst.com

ABSTRACT

Inverse synthetic aperture radar (ISAR) uses target's motion to generate images on the range-Doppler plane. In the conventional ISAR system, the Doppler spectra are computed by the Fourier transform. Due to the target irregular translational and rotational motion, the Doppler frequencies change over the time. Consequently, the Fourier transform based ISAR image may become blurred. To overcome this problem, the joint time-frequency transform is introduced to estimate the Doppler spectra. Because the joint time-frequency transform is able to resolve the instantaneous Doppler frequencies, the resolution of the resulting ISAR images are significantly improved. Moreover, the proposed ISAR system is not only effective, but also amenable to hardware implementation

1. INTRODUCTION

Inverse synthetic aperture radar (ISAR) is an imaging radar, which uses target's pitch, roll and yaw motions to generate image on range-Doppler plane. Figure 1 is a block diagram of the conventional stepped-frequency ISAR. As shown, the stepped-frequency ISAR first transmits a sequence of N bursts. Each burst consists of M narrow frequency band pulses. The center frequencies of successive M pulses are increased by a constant frequency step. When the target rotational and translational motion is mainly corrected, the received frequency signatures of bursts can be treated as the time history of the target reflectivity at discrete frequencies. Taking M -point inverse DFT for each received frequency signature will naturally yield N range profiles, each containing M range cells. The samples taking at the same range

cell for the N range profiles constitute a time history series. The DFT of the time history series gives N -point Doppler spectrum. Finally, by combining the M Doppler spectra at M range cells, the M -by- N ISAR image is formed. The range resolution of the stepped-frequency ISAR is determined by the burst bandwidth (M times the constant frequency step). The Doppler frequency (or cross-range) resolution is determined by the observation time (number of bursts N). Longer observation time provides better Doppler resolution and better signal-to-noise ratio, but causes more range and phase errors.

It is generally believed that the Doppler frequencies change over the time. The instantaneous Doppler frequency $f_D(t)$ is the function of target radial velocity $v_r(t)$, scattered rotation rate $\Omega(t)$, and scattered distance from the rotation center $r_c(t)$ as follows

$$f_D(t) = \frac{2f_0}{c} \vec{\Omega}(t) \times \vec{r}_c(t) + \frac{2f_0}{c} v_r(t) \quad (1)$$

where f_0 and c denote the radar carrier frequency and wave propagation velocity, respectively. Using the DFT to compute the Doppler spectra, we will obtain the global spectra rather than the instantaneous frequency $f_D(t)$. Consequently, the image will be blurred when target radial velocity $v_r(t)$, scattered rotation rate $\Omega(t)$, or scattered distance from the rotation center $r_c(t)$ change fast.

To overcome this problem, we employ the joint time-frequency transform to compute the Doppler spectra. Following a brief discussion of the joint time-frequency transform, numerical simulations are presented to demonstrate the effectiveness of the technique introduced in this paper.

¹ Corresponding author

2. TIME-FREQUENCY DISTRIBUTION SERIES

For signal $s(t)$, the Fourier power spectrum can be computed by

$$\begin{aligned} |S(\omega)|^2 &= \left| \int s(t) \exp\{-j\omega t\} dt \right|^2 \\ &= \int R(\tau) \exp\{-j\omega \tau\} d\tau \end{aligned} \quad (2)$$

Doppler spectra dramatically change over a short period.

If making the auto-correlation function time-dependent, for instance,

$$R(t, \tau) = s\left(t + \frac{\tau}{2}\right) s^*\left(t - \frac{\tau}{2}\right) \quad (3)$$

and inserting it into eq.(2), then we obtain a time-dependent spectrum

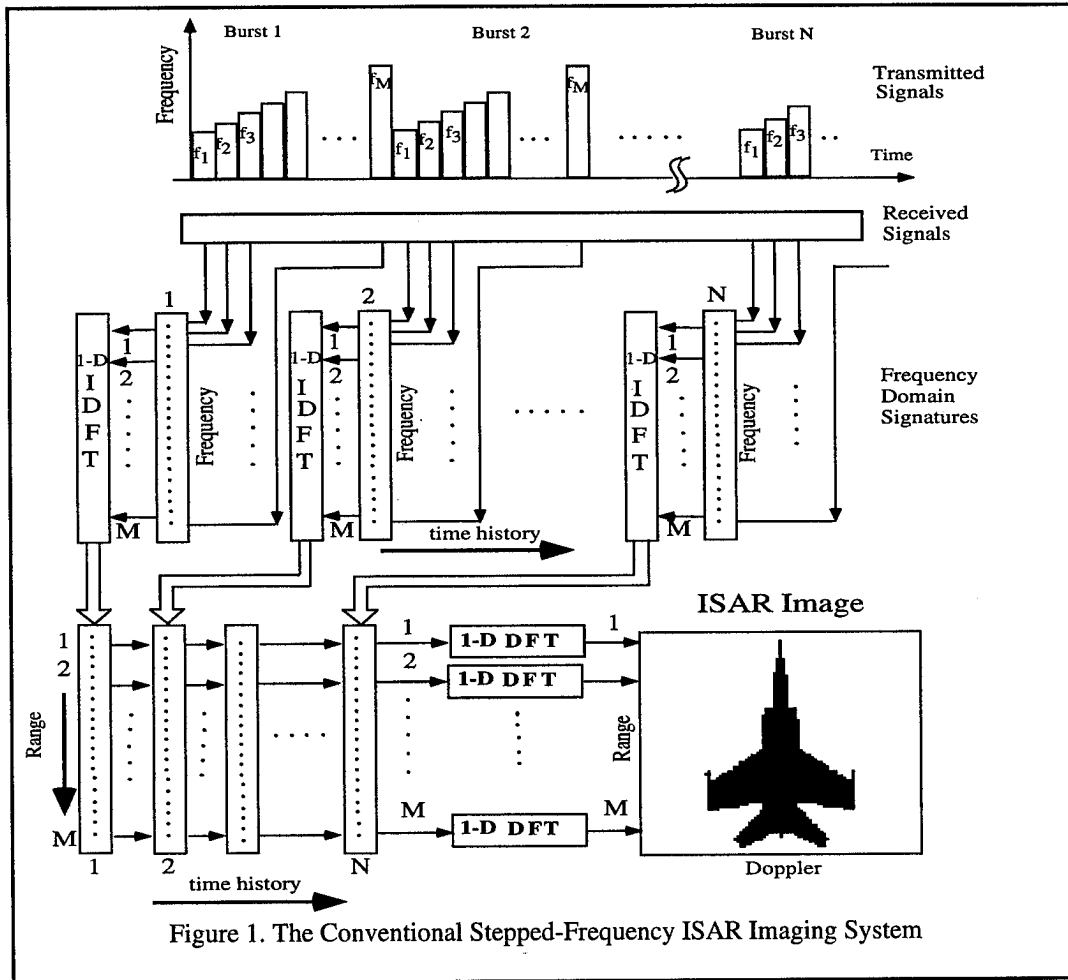


Figure 1. The Conventional Stepped-Frequency ISAR Imaging System

where $R(\tau)$ is called the auto-correlation function given by

$$R(\tau) = \int s(t) s(t - \tau) dt$$

which is time-independent. Although the power spectrum depicts how signal's energy distributes in the frequency domain, it does not give any indications how signal's frequency contents change over the time. Therefore, the image may be blurred when the

$$WVD(t, \omega) =$$

$$\int s\left(t + \frac{\tau}{2}\right) s^*\left(t - \frac{\tau}{2}\right) \exp\{-j\omega \tau\} d\tau \quad (4)$$

which is named the Wigner-Ville distribution (WVD). It is well known that the WVD better characterizes time-dependent spectra than any other algorithms known so far. Without loss of the generality, let's assume signal $s(t) = A(t) \exp\{j\phi(t)\}$, where $A(t)$ and $\phi(t)$

denote the amplitude and phase, respectively. Then, $\phi'(t)$ is traditionally considered as the instantaneous frequency. We can show that the mean frequency of the WVD at any time instant t is always equal to signal's instantaneous frequency, i.e.,

$$\frac{\int \omega WVD(t, \omega) d\omega}{\int WVD(t, \omega) d\omega} = \phi'(t) \quad (5)$$

The main problem of the WVD is the so-called the cross-term interference. When the analyzed signal has more than one frequency tone at time instant t , spurious peaks will appear in the middle of each pair of frequency tones. However, it is interesting to note that:

- Many useful properties possessed by the WVD, such as eq.(5), are determined by averaging the WVD;
- The cross-term interference is highly oscillated and localized;

These observations suggest that if the WVD is considered as the sum of harmonic series, than we can discard the high harmonics and use the lower order terms to well delineate the time-dependent spectrum. This is because that the high harmonic terms has smaller average.

Hence, they have limited influence to the useful properties. On the other hand, they are closely related to the cross term interference. The resulting presentation is named the *time-frequency distribution series* (TFDS) (also known as the Gabor spectrogram).

To compute the TFDS, the analyzed signal is first decomposed as the orthogonal-like Gabor expansion, i.e.,

$$s(t) = \sum_m \sum_n C_{m,n} h_{m,n}(t) \quad (6)$$

where the Gabor basis function $h_{m,n}(t)$ are time- and frequency-shifted Gaussian functions,

$$h_{m,n}(t) = (\pi\sigma^2)^{-0.25} \exp\left\{-\frac{(t-mT)^2}{2\sigma^2} + jn\Omega t\right\} \quad (7)$$

Taking the WVD with respect to eq.(6) yields

$$\begin{aligned} WVD(t, \omega) &= \sum_{m,n} \sum_{m',n'} C_{m,n} C_{m',n'}^* WVD_{h,h'}(t, \omega) \\ &= \sum_{m,n} \sum_{m',n'} C_{m,n} C_{m',n'}^* \exp\{jpT\omega_\mu\} \\ &\quad \exp\{-\sigma^{-2}(t-t_\mu)^2 - \sigma^2(\omega-\omega_\mu)^2\} \\ &\quad \exp\{-j(pT\omega - q\Omega t)\} \end{aligned} \quad (8)$$

where

$$t_\mu = \frac{m+m'}{2}T, \quad \omega_\mu = \frac{n+n'}{2}\Omega$$

and

$$p = m - m', \quad q = n - n'$$

Eq.(8) decomposes the WVD as the linear combination of localized two-dimensional harmonics that is named the *time-frequency distribution series* (TFDS).

When all terms are included, the TFDS manifestly converges to the WVD and thereby it holds all the properties of WVD. If we only retain the terms for $m=m'$ and $n=n'$, then we obtain the positive representation that is similar to the spectrogram. Because the useful properties are mainly determined by the low harmonics, one can selectively remove the high order harmonic

to well characterize time-dependent spectrum with limited cross-term interference.

3. TFDS BASED ISAR SYSTEM

Figure 2 depicts the part of the proposed ISAR imaging scheme. Note, the only difference of the new and traditional ISAR systems is that the Doppler frequencies in the proposed ISAR are computed by TFDS rather than by DFT. Since the Doppler spectrum is computed by the TFDS, one image frame

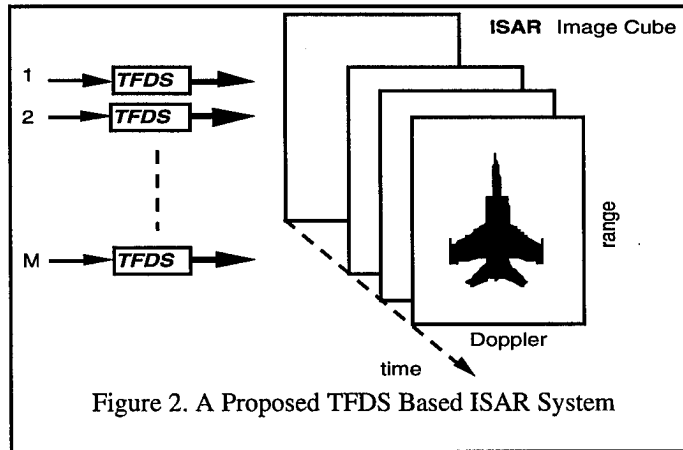


Figure 2. A Proposed TFDS Based ISAR System

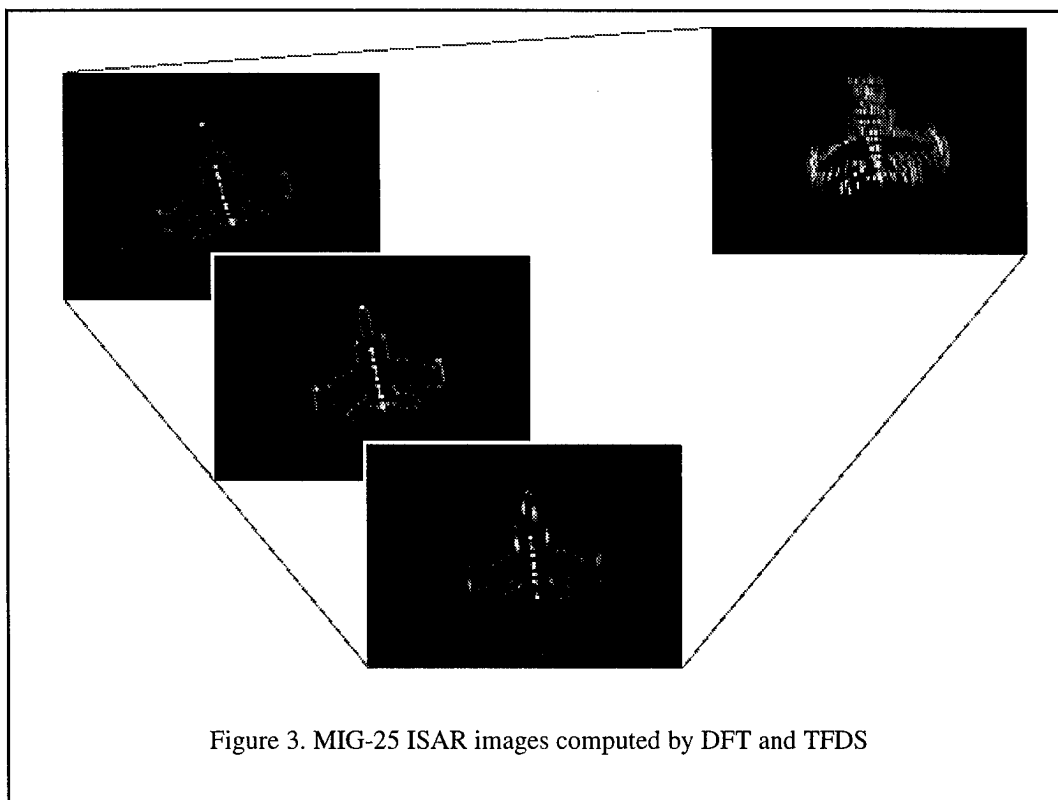


Figure 3. MIG-25 ISAR images computed by DFT and TFDS

in the traditional ISAR system is now decomposed into several instantaneous frames.

4. SIMULATION AND CONCLUSION

Extensive testing, on both the simulated and the real data, has been conducted in Naval Research Laboratory. All simulations indicate that the new scheme significantly improves the traditional ISAR performance. Figure 3 compares the simulated image of MIG-25 obtained by the traditional ISAR and one of the multiple frames generated by the new ISAR.

While the DFT based ISAR image is blurred due to the aircraft fast rotating, a clear aircraft image is observed by TFDS based ISAR. As far as the authors are aware, such result has not been achieved by any currently used methods. Moreover, it is worth to notice that the only difference between the new ISAR and the traditional ISAR is that the TFDS replaces the DFT. Therefore, the traditional ISAR can be easily up-dated without significantly altering the existent hardware structure.

Because of the effectiveness and simplicity of this new ISAR scheme, we believe that the technique discussed in this paper will strongly impact to future ISAR processor design.

REFERENCES:

- [1] C.C. Chen and H.C. Andrews, "Target-motion-induced radar imaging", *IEEE Trans. on Aerospace and Electronic Systems*, vol.16, No.1, pp.2-14, 1980.
- [2] V.C. Chen, "Radar ambiguity function, time-varying matched filter, and optimum wavelet correlator", *Optical Engineering*, vol.33, No.7, pp.2212-2217, 1994.
- [3] L. Cohen, *Time-Frequency Analysis*, Prentice Hall, Englewood Cliffs, New Jersey, 1995.
- [4] S.L. Marple, *Digital Spectral Analysis with Applications*, Prentice Hall, Englewood Cliffs, New Jersey, 1987
- [5] S. Qian and D. Chen, "Decomposition of the Wigner-Ville Distribution and Time-Frequency Distribution Series" *IEEE Trans. on Signal Processing*, vol.42, No.10, pp.2836-2842, Oct. 1994.
- [6] D.R. Wehner, *High-Resolution Radar*, 2nd edition, Artech House, 1994.

An Adaptive High Speed Wireless Transceiver for Personal Communications

Gregory J. Pottie¹

Electrical Engineering Dept.
University of California, Los Angeles

Abstract -- In personal communications systems, users contend for the resources of frequency and time, with re-use determined by spatial separation, power allocation, antenna beam patterns, data rate, and the required signal to interference ratio for reliable operation. We describe a highly adaptive transceiver which implements distributed control of power, channel assignments, and antenna weights, to maximize network throughput. That is, each link is optimized independently, with coupling only via the mutual interference.

I. Introduction

A high-performance experimental radio transceiver is under development at UCLA. It will include frequency hopping, variable bit and power allocation, channel coding, adaptive equalization, coherent M-QAM signaling, rapid channel probing, and adaptive transmitter and receiver antenna arrays. It will achieve data rates between 64 kb/s to 64 Mb/s, operating in the 2.4 GHz ISM band. A block diagram of the system architecture is given in Figure 1. The target application is communication among notebook computers, however, our principal objective is to develop a highly adaptive radio that enables experimentation with a wide variety of multimedia network control protocols. To this end, a combination of TDMA, FDMA, and frequency hopped CDMA will be supported. Most control functions for the link layer will be distributed, requiring at most feedback between a transmitter and its intended receiver, so that distributed network control protocols may also be supported. Each link independently attempts to achieve the highest possible signal to interference ratio (SIR). One of the challenges is to design a set of adaptive algorithms that will interact in a stable fashion, while increasing the robustness and throughput of the network. In the following sections, we outline the major adaptive subsystems.

II. Dynamic Power and Channel Allocation

In a radio network, frequency and time slots (channels) may be re-used at some distance due to propagation losses. Conventional designs re-use frequencies every four to seven cells in TDMA and FDMA systems. Such fixed assignments are wasteful of channel resources since they must be assigned based on 90% or 99% worst case channel conditions. As channel conditions vary widely due to shadowing,

this results in conservative re-use distances. In dynamic power and channel allocation (DPCA) algorithms, channels and transmitter powers are assigned to users so that all members of the network meet their own SIR requirement for reliable communication [e.g. 1-3]. Every channel is potentially available in every cell, with contention for the channels resolved using information on the mutual interference.

The basic mathematical statement of the problem is as follows. Let G_{ij} be the propagation gain between the j^{th} base station and the mobile to which the i^{th} base station is communicating directly for some time slot. Let P_i be the power transmitted by the user belonging to base station i . If $P_i=0$, there is no mobile communicating with base station i in the slot. The SIR for basestation i is then given by

$$R_i = \frac{G_{ii}P_i}{\sum_{j \neq i} G_{ij}P_j}$$

For reliable operation, we require $R_i > \gamma$, for all basestations. This set of conditions is equivalent to the following set of linear inequalities

$$G_{ii}P_i - \gamma \sum_{j \neq i} G_{ij}P_j > 0$$

where we must find whether there exists a set of positive powers $\{P_i\}$ for which all the inequalities are satisfied. It may be shown that this problem is equivalent to solving the matrix equation $G\Pi=1$, where Π is the vector of power assignments, $G_{ii} = G_{ii}$, and $G_{ij} = -\gamma G_{ij}$, with appropriate re-numbering of entries if not all basestations are active. Then if every component of the vector Π is positive, there is a feasible assignment. Moreover, the vector of powers is the best one to use apart from a scaling factor determined by the background noise, in the sense that it lies in the center of the region of feasible power assignments, and thus is least sensitive to perturbations.

To apply this single-channel algorithm to a multi-channel environment, we must in the worst case check among all possible combinations of users and find the assignment that leads to the largest number of users being admitted. However, we may instead employ any algorithm developed for performing dynamic channel assignment [e.g., 4], replacing the channel compatibility calculations of these algorithms

1. Supported by ARPA contract JFBI94-222/J4C942220

with solution of the system of equations above.

In the above, it was implicitly assumed that propagation data was reliably obtained at some central site. This is difficult to arrange, but fortunately unnecessary. In [5] a fully distributed form of the algorithm is presented, in which the only information exchange required is that between a mobile and its own base station, revealing their measurements of the interference power and the propagation loss in that single link. In the absence of dynamic range limitations on the power control, the algorithm not only converges to the optimum power vector if a feasible solution exists, but it also rejects new users in the absence of a feasible solution. Dynamic power range limitations can be accommodated by either limited centralized network control operations, or through voluntary termination of admission attempts when the resistance of other users is apparent from rapidly increasing interference levels [6].

III. Channel Probing

In distributed DPCA, each user increases or decreases its power by one step depending on whether the SIR is acceptable. Other users will react to power increments by increasing their power, which is then observed in the form of increased interference. The incremental increase of interference compared to the incremental increase of transmitted power may be viewed as the "resistance" of the channel to the entry of new user. The resistance of the channel together with the propagation loss on one's own link are powerful indicators of whether or not a feasible power assignment exists. A relatively small number of iterations of the algorithm at low power levels will yield a prediction of the maximum attainable SIR [6]; we refer to this as channel probing. We find that in cellular systems there is usually one dominant interferer. This case may be analyzed to yield a particularly simple rule for estimating the final SIR. Probing in this fashion permits more rapid evaluation of multiple channels, and reduces the disturbance of already active users by new users attempting to gain entry into the network.

IV. DPCA and Frequency Hopped Systems

The proposed transceiver is a frequency hopped system. There are many options for the application of DPCA, since each user accesses many channels. We may probe to predict the final SIR in each and assign bits and power to maximize the throughput for this expected SIR distribution. Channel coding with interleaving across the frequency slots could then serve to realize the frequency diversity, provide coding gain, and some smoothing of small SIR estimation errors. We may arrange the frequency hops to be synchronous among cells, so that the same set of interferers is encountered on each hop. DPCA then reduces to the single channel

form. A second option is to randomize the hopping patterns among the different cells. A combination of bit allocation and coding then produces a hybrid mix of interference averaging and interference avoidance, since we may choose not to allocate any power to those hops with large resistance. Simulation results for the simpler case of choosing M out of N hops to allocate an equal number of bits reveals that network throughput is very similar to the first option. However, this procedure is more robust with respect to channel variations since the set of channels occupied can be slowly changed, with the effect on any other being small since there is mutual interference in only one hop. Moreover, since hopping patterns are randomized among cells, each pattern encounters essentially the same ensemble of interference. Thus, choosing a new pattern is unlikely to lead to significantly better performance, and so we avoid the need to reprobe other patterns. This provides more tolerance to mobility for distributed algorithms than the first method.

For maximum flexibility, we will actually implement different bit assignments, i.e., different QAM constellations in different hops. The digital portion of the modem will support up to 256 QAM. The bit assignment problem for a frequency hopped system is very similar to that of discrete multitone transmission, except that we must probe to predict the final SIR for each hop, rather than use the value under the current power assignment. On all hops which get a non-zero number of bits, roughly the same power is assigned. We make a preliminary assignment of bits using the results of probing so that the transmitter power is minimized, and adjust as channel conditions change. In this case, the role of channel coding over the hops is not to realize frequency diversity but rather to provide some coding gain and smooth out errors that have been made in estimating the interference.

Finally, certain geographically disadvantaged users will require high transmission power, and in effect impose local frequency re-use restrictions in the channels they occupy comparable to what would be required in fixed channel assignments. These users couple several cells together, slowing convergence of distributed algorithms. One possible solution is for users with high transmitter power to drop to fixed assignment channels voluntarily, re-probing the channels with DPCA periodically to determine if they may be re-admitted with low power. We are presently investigating the dynamics of both this hybrid approach and a pure DPCA system.

V. Adaptive Antenna Array and Equalizer

Antenna arrays may also be used to suppress multipath and reduce interference [7]. We propose to adapt both transmitter and receiver arrays using least squares techniques. Switching between sets of fixed beam patterns is not feasible

for indoor systems, since we must gain some compromise benefit between diversity combining and interference cancellation, and the multipath has a very wide angular spread. Additionally, the human body interacts with the terminal to change the beam pattern.

The most interesting interaction is that between different pairs of communicating users. As the transmitter pattern of one array changes, so do the receiver patterns for all users in the vicinity. This in turn affects their transmitter patterns, as the latter may only be adapted based on the received signals. The antenna patterns must also react to changes in the power levels and/or channel assignments of the other users in the network. This is similar to the types of problems encountered in devising distributed DPCA schemes. Here, the transmitter and receiver beam patterns affect the gains G for both desired and interfering links. Due to the interference coupling, there is the possibility that the independently adapting antenna arrays will not converge.

We have investigated the dynamics of an adaptive antenna array with a variety of equalizer and transmitter adaptation options, with the happy conclusion that the ordinary LMS algorithm should be adequate. The imposition of orthogonality among channels within a cell together with the minimum SIR requirement for links to be declared feasible serve to decouple the users. With this requirement satisfied, the beam pattern of the partner on the desired link is the most important component of the signal to interference ratio. On the contrary, when the same frequency/time slots are shared within a cell, there often arise deadlock conditions. In this situation, it would be wise to use omnidirectional transmission and adapt only the receiver weights, even though when transmitters can be adapted significant extra gain is available. The antenna arrays should be adapted on a time scale faster than power control, since the antenna gain affects the perceived path gains between users. Following antenna adaptation, the radios can then probe to determine the bit allocation and final transmitted power levels.

The general problem of finding the best allocation of weights for transmission and reception in a large network with multipath resists closed form solution, and would in any case require (unavailable) reliable channel information and considerable cooperation among users. We have instead chosen to adapt receiver weights using a least squares algorithm, and then use these weights in transmission. A small number of iterations appears to give very good results, for typical indoor systems simulations providing a gain over omnidirectional transmission of 9 dB or more for a seven element array.

A variety of equalizer structures were investigated in combination with the antenna arrays. With perfect channel

knowledge, the best structure to use was found to be a multi-tap combiner, which consists of an (adaptive) FIR filter on each antenna branch followed by a summing junction. However, with LMS adaptation, this structure showed little performance improvement over using no equalizer at all, and we always found that under a constraint on the number of adaptive elements we were better off trading in the direction of increased antenna elements. The array already suppresses some undesired multipath components by placing nulls in certain directions, and thus already provides some equalization. Given the transmitter array adaptation strategy outlined above, we have decided to follow our antenna array with a DFE at baseband, which will be adapted on a slower time scale than the adaptive antenna array. This will serve the function of cleaning up residual ISI, as may be required for using large QAM constellations, or occasional pathological channel conditions.

VI. Adaptive Symbol Rates

The three orders of magnitude range of data rates will be achieved through a combination of three different symbols rates, variable constellation size, and TDMA subdivision of frequency slots. The number of symbol rates must be limited since each implies the need for a separate bandpass filter at IF. Thus we have tentatively decided upon symbol rates of 64 kbaud, 1 Mbaud, and 16 Mbaud. The high symbol rates could be used when line of sight (LOS) conditions exist in relatively short range transmission, while the lower symbol rates would be used for longer range transmission and for users demanding a lower throughput. Where possible, lower baud rate transmission is favored over TDMA division of a high baud rate stream due to reduced equalization requirements and increased resistance to noise and interference for a given power budget. The symbol rate would be chosen after performing a channel probe; users will not always be able to achieve the throughput they desire, but the system will attempt to give them the maximum throughput compatible with the ongoing traffic. Bit rates may on occasion have to be reduced as propagation conditions change.

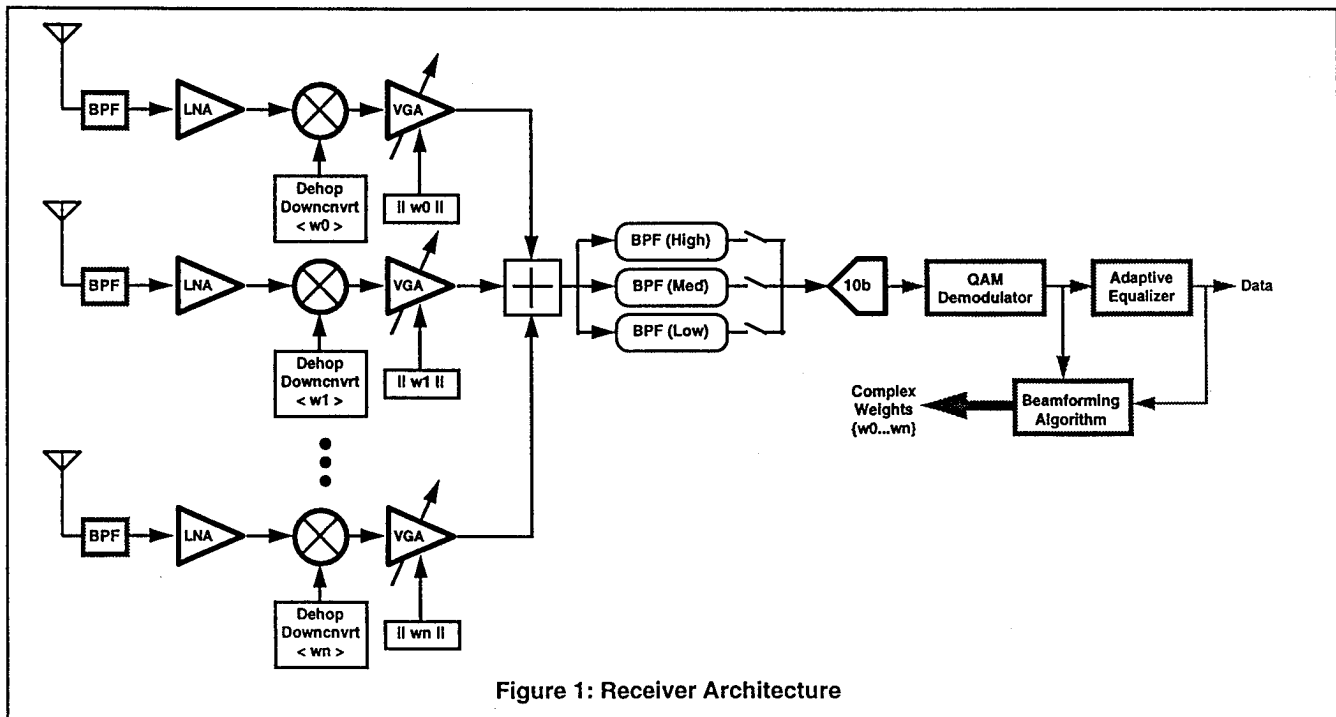
The coexistence of multiple symbol rate streams, with potentially widely divergent maximum power spectral densities, brings some additional problems. The lower symbol rate systems may cause extreme interference to the higher symbol rate systems if each operates under the same peak power constraint, since many low rate interferers may share the same band of frequencies as the high rate user. One obvious solution is to separate the different classes of users into different channels (hopping patterns) that are consistent across cells. The synchronization requirements are easily maintained with distributed algorithms. A variety of options which permit more flexibility in channel assignment are under investigation.

VII. Conclusion

The links in a multiple access radio system are coupled via their mutual interference. This and the signal for the desired link can be used to control essentially all adaptive functions of the radios, including symbol rate, bit allocation, power level, channel assignment, antenna transmitter and receiver weights, and equalizer settings. This presumes however that consistent timing information is distributed around the network, and further that in each cell orthogonal frequency assignments are made. Otherwise, adaptation may be extremely slow. Both functions require relatively little control traffic, operating at the level of frames. Thus, with minimal centralized control a highly capable set of adaptive algorithms can be enabled. The alternative of attempting optimum centralized control over all these functions, even if it were possible to gather all necessary propagation information, would be computationally intensive in the extreme and demand very high control traffic overhead. A fully asynchronous architecture would suffer from very slow adaptation, and would therefore be less able to cope with variable propagation and traffic conditions. Thus, some compromise between these extremes is required. We have opted for algorithms which we believe may operate with close to the minimum degree of centralized control required for robust operation.

References

- [1] R.D. Yates, "A framework for uplink power control in cellular radio systems," to appear, *IEEE J. Select. Areas in Comm.*, 1995
- [2] J. Zander, "Distributed cochannel interference control in cellular radio systems," *IEEE Trans. Vehic. Tech.*, vol. 41, pp. 305-311, Aug. 1992.
- [3] N. Bambos and G.J. Pottie, "Power control based admission policies in cellular radio networks", *IEEE Globecom*, Dec. 6-9, 1992, Orlando FL, pp. 863-867.
- [4] K.N. Sivarajan, R.S. McEliece, and J.W. Jackson, "Dynamic Channel Assignment in Cellular Radio," *IEEE Vehic. Tech. Conf.*, May 6-9, 1990, Orlando FL, pp. 631-637.
- [5] S. Chen, N. Bambos, and G.J. Pottie, "Radio link admission algorithms for wireless networks with power control and active link protection," technical report UCLA-ENG-94-25
- [6] V. Lin and G.J. Pottie, "Implementation of distributed power and access control for a frequency hopped wireless transceiver," *ICC 95*, Seattle, June 1995.
- [7] J.H. Winters, J. Salz, and R.D. Gitlin, "The impact of antenna diversity on the capacity of wireless communication systems," *IEEE Trans. Comm.*, vol. 42, pp. 1740-1751, April 1994.



HOMODYNE RECEIVER TECHNOLOGY FOR SMALL AND LOW-POWER CONSUMPTION MOBILE COMMUNICATIONS EQUIPMENT

*Makoto Hasegawa, Takashi Fukagawa
Masahiro Mimura, Mitsuo Makimoto*

Information and Communications Technology Laboratory,
Matsushita Electric Industrial Co., Ltd.,
3-10-1, Higashimita, Tama-ku, Kawasaki, 214 JAPAN
PHONE: +81-44-911-6671 FAX: +81-44-934-3107

ABSTRACT

The advantages of homodyne receivers and the problems necessary to overcome in order to realize the required performance have been reviewed. Some examples of our recent results and homodyne technologies are introduced as applied to pagers, wireless remote control equipment, and radio systems using reflected signals.

1. INTRODUCTION

Homodyne receivers are often called direct conversion receivers⁽¹⁾⁽²⁾ for mobile communications equipment. They are inherently suitable for circuit integration and small equipment because they have no IF circuits. A homodyne receiver can be regarded as a super high-speed analogue/digital converter because it can obtain the signal for digital processing from a propagating radio signal. This is the ultimately simplest radio receiver, but there are many barriers to get over and it has not yet been widely used. There are some examples of its use at this moment with reasonable receiver characteristics in low-power consumption such as our paging receivers. In radio communications systems using reflected signals or TDD(Time Division Duplex) or simplex transmitter/receivers, homodyne receivers enable one to use radio oscillator as both a transmitter and a local signal for receiver.

Usually, this configuration has some faults in characteristics, and can be adopted when circuit design and system design technologies for homodyne receivers are available to compensate its performance. These homodyne technologies are readily available for simple mobile equipment. Here, the merits and requirements of homodyne receivers and the recent results of our developments and technical features are presented.

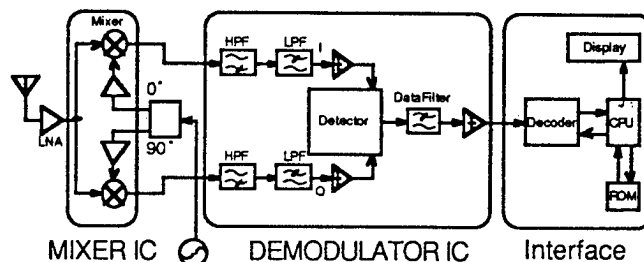


Fig.1 Block diagram of homodyne receiver

2. MERITS OF HOMODYNE RECEIVERS

A homodyne receiver is shown in Fig.1. The reason for features contributing to its small size, simple configuration, and suitability for circuit integration in low-power consumption are summarized as follows:

(1) Simple filter configuration

Since there are no IF circuits, image suppression is unnecessary, and channels can be selected using base band channel filters suitable for circuit integration. Not only a narrow band pass filter in the IF stage but also a band pass filter in the RF stage may be unnecessary when it has adequate AGC, frequency band width of antenna, and 3rd order IM of RF AMP/MIX.

(2) Minimum number of generators

Since the receiver has a simple configuration and needs only radio and base band frequency sections, which are theoretically necessary, there is little generation of erroneous signals. In the case of a homodyne receiver, there is no need for a 2nd local oscillator and its crystal element as compared with a double super heterodyne receiver.

(3) Suitability for multi-channel reception

In the case of a single super heterodyne receiver, a local oscillator is usually at a fixed frequency for

reinforcing channel filtering performance, although a variable frequency synthesizer can be used as a local oscillator in a double super heterodyne receiver or a homodyne receiver.

These merits result in a high-potential receiver with small size and low cost.

3. REQUIREMENTS AND TECHNOLOGIES OF HOMODYNE RECEIVERS

The requirements and corresponding technologies of homodyne receivers in low-power consumption are pointed out as follows in comparison with general heterodyne receivers:

- (1) The characteristic load to RF circuits is increased.

A considerable gain of front-end RF circuits is required to increase the RF signal level enough for the equivalent input conversion noise of base band circuits. Although the sensitivity of the receiver can be increased, the problem of distortion appears as the gain of RF circuits increases. Moreover, a spurious response of even order intermodulation distortion caused by undesired RF 2 signals and 2nd order harmonics of the local oscillator will appear in the demodulation band width, although it will not appear in the case of the super heterodyne receiver. Therefore, low distortion RF AMPs with low NF, and low distortion Mixers with low NF, are necessary. AGC circuits are effective for lowering the distortion in a strong electric field.

- (2) Ensuring high isolation is important.

The leakage of the LO signal in the receiver obstructs nearby sensitivity points in the receiver. Radiation from the LO signal directly obstructs sensitivity suppression in other receivers with almost the same frequency. Moreover large RF signal in a strong electric field obstructs a VCO of the LO just like as an injection lock. The required technologies include an IC circuit structure for high isolation at first, minimization of local oscillator power in order to reduce the LO signal leakage, layout of circuits, shield and housing design of equipment.

Since the output signal of the quadrature mixer is a base band signal, countermeasures such as low-frequency noise suppression by the voltage regulator are needed against low-frequency noise.

- (3) Degradation of sensitivity caused by $1/f$ noise should be minimized.

In directly converted base band signals, $1/f$ noise from zero frequency appears. The influence of base band $1/f$

noise at the output of the quadrature mixer may be reduced by arranging a high-pass filter in the channel filter, although it loses the low frequency signal information. This influence become greater at the higher C/N points.

- (4) Ensuring sensitivity band width for higher data-rate receiving is necessary.

The sensitivity band width depends upon the cutoff frequency of the channel low-pass filter and the performance of the demodulator in the case of a low equivalent modulation index. In particular, the adoption of circuit architecture that corresponds to maintain the sensitivity band width in a low equivalent modulation index with low power consumption is expected.

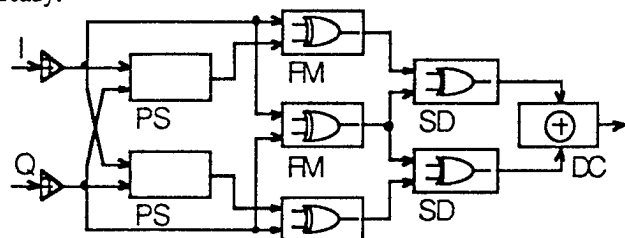
- (5) Rising time of the demodulator should be shortened in some cases.

Demodulation is performed in lower frequency than heterodyne receiver. Therefore, a large capacitance is essentially required for the demodulator. This results in a longer rising time.

4. SOME EXAMPLES OF OUR RESULTS AND TECHNOLOGIES

4.1 HOMODYNE RECEIVING PAGER

Paging receivers have an extreme demand for small size in mobile communications equipment. The modulation method is around 1,200bps data-rate FSK, so far, which is an advantage to designing a simple receiver configuration. In paging applications there are some barriers to realizing a practical homodyne receiver, although mainly heterodyne receivers are used. We developed an exclusively designed quadrature mixer IC with low distortion and high isolation for homodyne receivers and demodulator IC which adopt our proposed Frequency Multiplied Digital Phase-Shifting Demodulator^[4] shown in Fig.2 having a wide sensitivity band width using a multiplied signal in digital circuits. Several million homodyne receivers with the above mentioned 2 ICs, shown in Fig.3, are on the market already.



PS: Digital Phase Shifter SD: Signal Detecting Circuit
FM: Frequency Multiplier DC: Detected Signal Combining circuit
Fig.2 Detector of proposed demodulator for homodyne receiver I

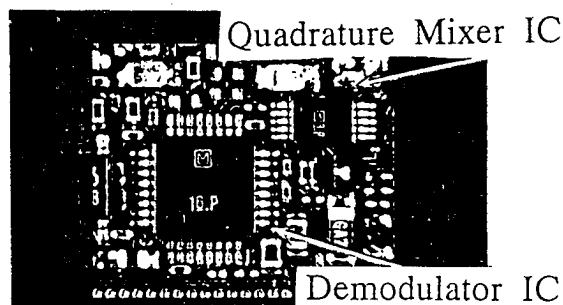


Fig.3 A photograph of the developed ICs

Higher data-rate multilevel FSK paging systems such as ERMES or FLEX are planned to be widely use in the next generation. Corresponding to such systems, the availability of our proposed Quadrature Frequency Digital (QFD) Demodulator⁵⁾ using a phase to frequency convertor in digital circuits, shown in Fig.4, is confirmed. As shown in Fig.5, the sensitivity around $BER=10^{-2}$ point, before error correction of the receiver using a QFD demodulator suitable for homodyne configuration, is obtained almost equivalent performance as a conventional heterodyne receiver.

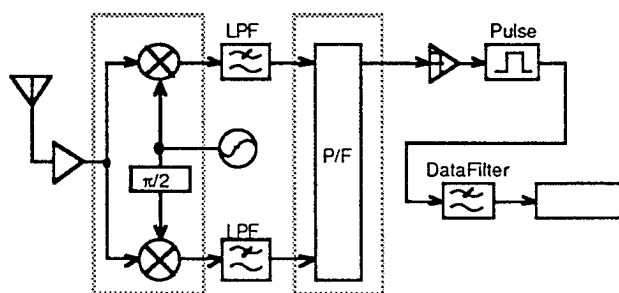


Fig.4 Block diagram of proposed receiver II

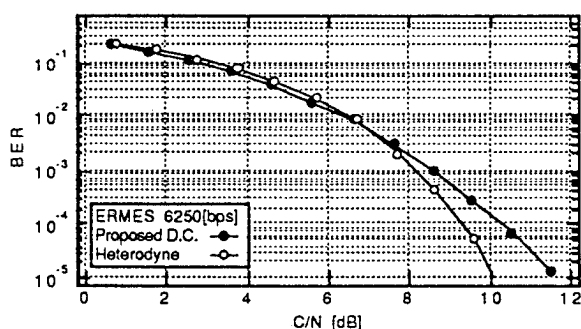


Fig.5 Experimental result

4.2 APPLICATION TO TRANSMITTER / RECEIVER

The RF oscillator can be used both as a transmitter and a local signal for receiver, especially in TDD (Time Division Duplex) or simplex radio equipment using the same frequency as shown in Fig.6. There is no need for additional frequency conversion by mixers, except for the homodyne quadrature mixers. Both transmitter and receiver are

homodyne. In this case, additional frequency cover range of the oscillator is not necessary.

One of the applications of this configuration is wireless remote control equipment which communicates relatively simple data. This equipment can use the regulatory applied for specified low power radio station in Japan.

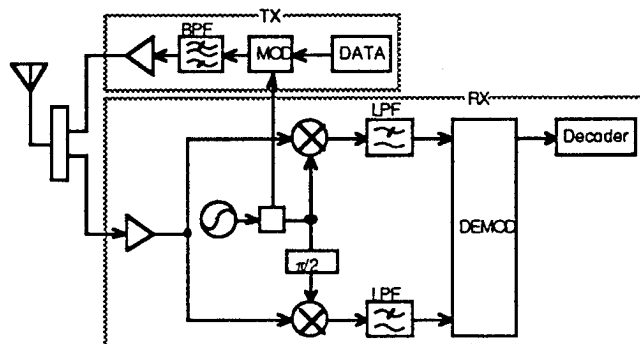


Fig.6 Homodyne Transmitter/Receiver

4.3 RADIO SYSTEM USING REFLECTED SIGNAL

Microwave AVI (Automatic Vehicle Identification) systems⁶⁾, especially those which feature access areas around 10m and high-speed data communication, have become somewhat popular. One of the examples of its practical use is management system of train movement. Usually, these systems have reading and writing function for two way communication using passive microwave cards, the principal operation is as follows.

- 1) An interrogator continuously sends microwave carrier during the reading operation, it receives a reflected modulated signal from the microwave card and a reflected carrier signal from other objects. Demodulation is performed from these signals and information of memorized data in the microwave card can be read.
- 2) The interrogator sends an ASK signal during the writing operation, and the microwave card detects the ASK signal and some information can be written into the card.

In these systems, basically, transmitting and receiving frequency is the same, and a homodyne receiver may be used. When many interrogators are placed nearby, interference between interrogators disturbs the communication between interrogators and microwave cards, and degrades communication quality. To solve this problem, the structure and main features of our proposed high interference immunity microwave card system is as follows:

- (1) The interrogator has a spread spectrum function in the transmitter and a despreading function in the receiver is performed using the same signal as the transmitted signal.

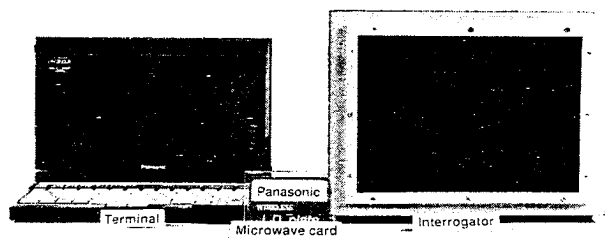


Fig.7 A photograph of the experimental system

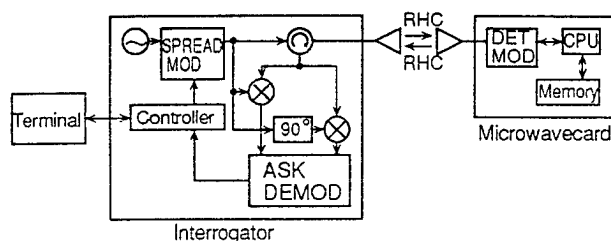


Fig.8 System diagram of proposed microwave card system

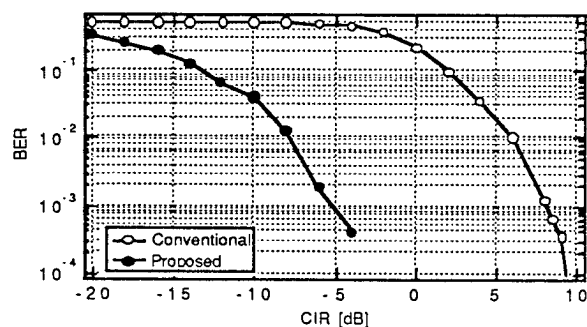


Fig.9 Interference immunity characteristics

(2) A quadrature homodyne configuration is adopted for the purpose of countermeasure of the demodulation level fluctuations caused by the phase relation between local signal and reflected received signal.

Fig.7 shows the photograph of a licensed radio station⁷⁾ for such experiments and the block diagram is shown in Fig.8. The oscillator is used as both a transmitter and a local signal for the receiver at the same time.

To confirm the interference immunity, the simulation of the relation between BER and CIR (carrier to interference ratio) is performed. Simulation results are shown in Fig.9.

Millimeter-wave vehicular radar for a collision warning or avoidance is another radio system using reflected signals. In this application, the homodyne receiver configuration is expected to be used for simple and low cost realization, which is a principal target at this moment, although the heterodyne configuration is also a candidate.

5. CONCLUSION

Although homodyne receivers are not widely used in present mobile communications equipment, this technology is effective for the simplification of radio communications equipment. Some examples of the results and technologies of our homodyne receivers in practical use were presented. This technology is expected to spread to various fields of mobile communications equipment through continuous study.

Acknowledgements

The authors gratefully acknowledge the assistance and support of their many colleagues at Information and Communications Technology Laboratory, Matsushita Electric Industrial Co., Ltd., and Personal Communication Division and Radio Telecommunication Division, Matsushita Communication Industrial Co., Ltd.

REFERENCE

- [1] K.Chiba and K.Murota. Performance of direct conversion FSK receiver. National Convention Record, I.E.I.C.E., Part 10, No.2232., 1987
- [2] I.A.W.Vance, B.Eng, and M. Sc. Fully integrated radio paging receiver. IEE Proc., 129, Pt.F,1,pp.2-6, Feb. 1982
- [3] M.Hasegawa, M.Ohba, and M.Makimoto. An FSK Quadrature Demodulator Using Digital Phase-Shifting Method with a Doubler. National Convention Record I.E.I.C.E., Japan, B-316, March 1991
- [4] K.Takahashi, M.Mimura, M.Hasegawa, M.Makimoto, and K.Yokozaki. A Direct Conversion Receiver Utilizing a Novel FSK demodulator and Low Power-Consumption Quadrature Mixer. IEEE Proc. VTC, pp.910-915, 1992
- [5] M.Hasegawa, M.Mimura and M.Makimoto. Direct conversion Receiver Technology for Pagers and Small Mobile Communications Equipment. Proc. International Workshop on Multi-dimensional Mobile Communications (MDMC), Japan, 2-2, pp.31-34, Nov. 1994
- [6] N.Adachi, Y.Namura, M.Mimura and M.Hasegawa. A study on the configuration of AVI system with high immunity. Proc. I.E.I.C.E., Japan, B-352, Autumn 1993
- [7] N.Adachi, K.Maeda, T.Fukagawa and M.Hasegawa. A Microwave Card System with a High Interference Immunity utilizing a Spread Spectrum Method. Asia Pacific Microwave Conference, 20-1, pp.463-466, 1994

SYSTEM DESIGN FOR CONTIGUOUS CELL COVERAGE IN HIGH DENSITY MICROCELLULAR NETWORKS

Brendan C. Jones and David J. Skellern

Electronics Department, School of Maths, Physics, Computing and Electronics
Macquarie University NSW 2109 Australia

email: brendan@mpce.mq.edu.au, daves@mpce.mq.edu.au

ABSTRACT

This paper examines whether microcellular networks can be designed to provide contiguous cell coverage for a given proportion of mobile terminals. Simulation results using a general microcellular interference model show that contiguous cell coverage may not be possible for an acceptable proportion of mobile terminals even if the call loss rate is low.

1. INTRODUCTION

System design methodologies for conventional (large cell) cellular networks have matured through a mix of theory and operational experience since the first systems were developed in the 1970s [1]–[2], but the applicability of these design techniques to the microcellular case is questionable [3]–[6].

The wide scale deployment of an extensive, high grade, wireless telephone system will require engineering tools and techniques that allow rapid and accurate system design [7]. The fundamental problem that needs to be addressed is of modelling the end result of multiple users propagating in a congested area [7],[8].

Some of the factors which affect the performance of microcells include adjacent channel interference, the distribution of user terminals, the close spacing of fixed stations, and spatial traffic variability [3]–[19].

One of the important system design issues for microcellular networks is the radio coverage quality. Users will increasingly demand wireline call quality [8] throughout the network and this will require reliable, contiguous radio coverage.

2. CELL COVERAGE MODEL

A general interference model has been developed that enables microcell coverage and cell radius distributions to be analysed in terms of the system design parameters [3]–[6].

The model takes a spatial approach to analysing the interference effects on a wanted link of an arbitrary number of interfering mobile terminals communicating with an arbitrary number of fixed stations.

An important aspect of the model is that it incorporates channel spill interference from all other users regardless of the magnitude of the interference at the source. Theoretical analysis and simulation results have demonstrated that even in the absence of cochannel and immediately adjacent channel interferers, interference from other users can be significant [6].

The model can be used to analyse cell coverage performance via a parameter called the 'interference to noise ratio' or INR, given the symbol η [3]. The INR is the total interference power at the input to a receiver divided by the receiver noise power and describes the extent of noise or interference dominance of the wanted link. Using this parameter, the maximum possible range r of a mobile terminal from its fixed station is given by a simple expression of the form [4]:

$$r^\gamma = \psi \left[\frac{1}{\eta_F + 1} \right] \quad (1)$$

where η_F is the uplink INR (i.e. the INR at the fixed station receiver). The parameter ψ is a system constant for a particular mobile technology and is a function of frequency, transmitter power, cochannel protection ratio and the receiver noise floor. γ is the path loss exponent in a simple distance-dependent path loss propagation model.

In a noise limited system, $\eta_F \ll 0.1$ and $1/(\eta_F + 1) \approx 1$, thus the maximum terminal range r is relatively stable. As a system becomes interference limited, $\eta_F \gg 10$, $1/(\eta_F + 1) \approx 1/\eta_F$, and the maximum terminal range r becomes sensitive to η_F and the arrangement of the interferers. The INR provides a means of computing cell radius distributions and thus the proportion of mobile terminals which meet some cell coverage criterion.

Previous papers [5]–[6] have examined the uplink INR and cell radius statistics in cellular and microcellular networks for example scenarios, both through Monte Carlo simulations and theoretical analysis. The next step is to consider how these statistics are affected by varying the user load and fixed station separation.

If a microcell network is to provide reliable, contiguous coverage, then a system design methodology needs to be developed so that the required proportion of mobile terminals continues to meet coverage targets as the user density increases.

3. CELL COVERAGE SIMULATION

The microcell simulation program used in [4]–[6] can be used to investigate cell size distributions as a function of user density. The program performs Monte Carlo simulations in accordance with the microcell interference model described in the previous section. The simulation provides call blocking and dropout estimates and Probability Density Functions (PDFs) and Cumulative Distribution Functions (CDFs) for the resultant INR and cell radii statistics.

The simulation was loaded with the technical specifications, call set up and channel allocation procedures for CT2 (an existing microcellular system). In each simulation 10 000 call attempts were made within a regular hexagonal arrangement of 19 CT2 fixed base stations, each 173.2 metres apart, so that the mobile terminal range required for contiguous coverage was 100 metres. A fixed number of mobile terminals were placed in random locations but with a uniform distribution in each cell. Transmitter power control was not used.

Call attempts in the simulation proceeded in a random sequence. A mobile terminal's call attempt would fail if it didn't meet the required $S/[N+I]$ at both the fixed and mobile ends of the link. An initially successful mobile terminal could also drop out if the success of other mobiles led to an increase in interference, causing its $S/[N+I]$ to fall below threshold. Channel reassignments and retries were allowed in accordance with the CT2 specifications. All calls were cleared and the process repeated after every terminal had completed a call attempt. The propagation exponent γ was set to 3 for both signal and interference.

Table 1 gives a summary of the call failure statistics, uplink INR (η_F) statistics, and contiguous coverage results as the traffic load was increased from 1 to 4 *simultaneous* users per CT2 cell. The cumulative η_F statistics for the *successful* calls are plotted on a lognormal probability scale (which amplifies the tails of the distribution) in figure 1. The cumulative cell radius statistics, computed from the η_F CDF using equation (1), are plotted on a log probability scale in figure 2.

Table 1 – Simulation Results for CT2 Network

PARAMETER	1 user/ cell	2 users/ cell	3 users/ cell	4 users/ cell
Call Blocking (%)	0.00	0.63	1.74	3.08
Call Dropping (%)	0.02	0.51	1.54	3.54
Total Call Loss (%)	0.02	1.14	3.28	6.62
Log Average η_F	0.050	0.375	0.869	1.410
Std Deviation log η_F	1.180	0.802	0.622	0.527
Terminals with contiguous coverage (%)	95.2	88.5	80.9	74.1

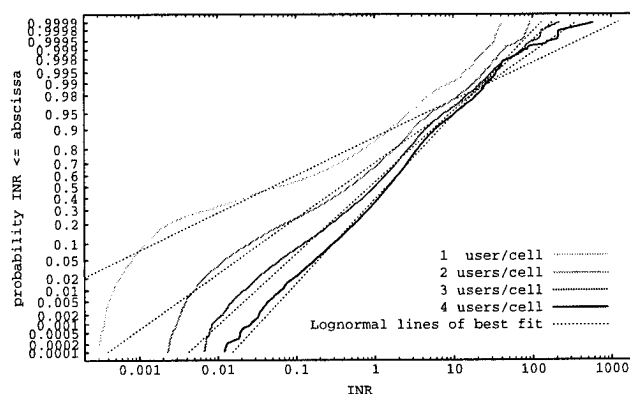


Figure 1 – η_F CDF vs cell load

Figure 1 shows that as the user loading per cell increased, the INR distribution approached a lognormal distribution, its log weighted average increased, but the standard deviation decreased (the dotted lines in figure 1 show the lognormal line of best fit to each simulated data). These results are consistent with the results presented in [6] for interferer ensembles.

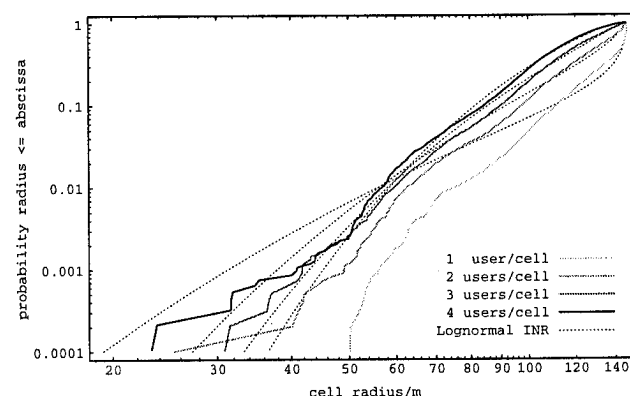


Figure 2 – Cell radius CDF vs cell load

The cell radius CDF (figure 2), derived from the η_F CDF using equation (1), shows that as the cell loading was increased, the proportion of terminals enjoying a cell radius sufficient to provide contiguous coverage (i.e. 100 m) reduced from 95% at 1 user/cell to an unacceptable 74% at 4 users/cell, even though the total call loss rate stayed well under 10% (see table 1).

The dotted lines in figure 2 show the cell radius CDF based upon the lognormal lines of best fit as shown in figure 1. The shape of these CDF curves varies substantially as a function of the mean and standard deviation of the lognormal estimate.

The question that needed to be answered was whether the coverage with 4 simultaneous users/cell could be improved by reducing the fixed station separation. Say a target is set that 90% of terminals should have contiguous coverage as determined by the fixed station layout. An iterative design strategy could then involve determining the 90% terminal range, reducing the fixed station separation in accordance with this

range, and performing the simulation again to establish whether the coverage target had been met.

In the above simulation, 90% of terminals had a cell radius of 84.5 metres or more. The fixed station separation was reduced so that contiguous coverage would have required a cell radius of 84.5 metres, and the simulation was performed again. Note that this also increased the user density as a fixed number of users made call attempts in each cell.

This simulation indicated that 90% of terminals had a cell radius of 72.7 metres or more, again insufficient for the coverage target. The fixed station separation was reduced again so that contiguous coverage would have required a cell radius of 72.7 metres, and the simulation repeated. This process was continued and the results are shown in figures 3 and 4.

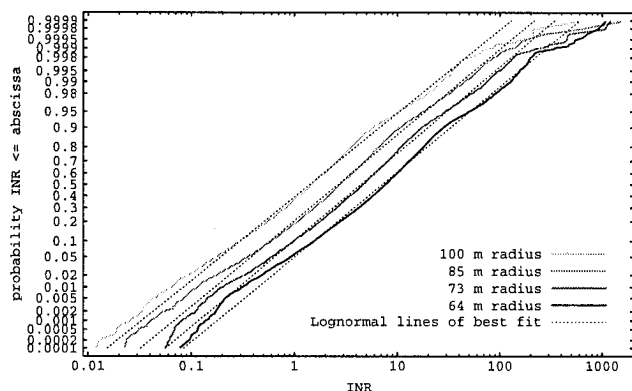


Figure 3 – η_F CDF vs cell spacing

Figure 3 shows that as the fixed stations were placed closer and closer together, the average uplink INR increased approximately in inverse proportion to the fixed station separation but the standard deviation of the INR samples essentially remained unchanged.

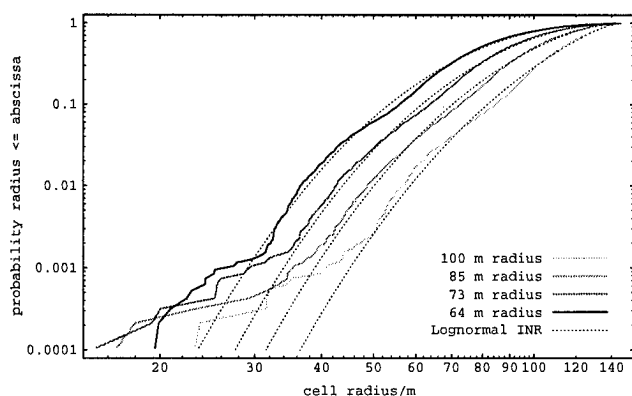


Figure 4 – Cell radius CDF vs cell spacing

This had the effect, as can be seen in figure 4, of increasing the spread of cell sizes. This only served to compete against the cell coverage improvement being attempted by this process.

Thus contiguous coverage was not achieved simply by reducing the fixed station separation, but it is not clear from figure 4 whether reducing the fixed station separation actually improved or reduced the proportion of terminals with contiguous coverage.

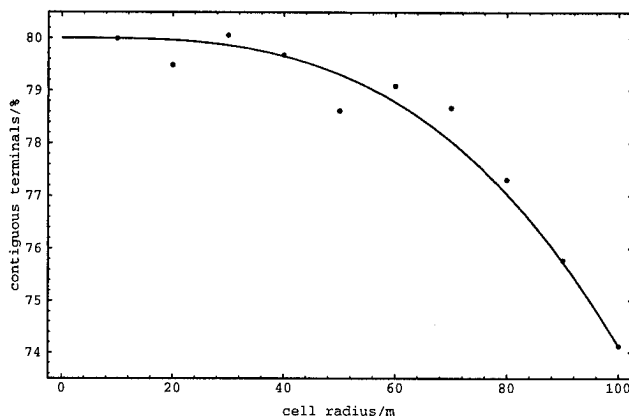


Figure 5 – Proportion of mobile terminals with contiguous coverage vs cell spacing

Figure 5 shows the proportion of mobile terminals which achieved contiguous coverage (as defined by the fixed station layout) versus the fixed station separation. With 4 simultaneous users/cell, the proportion of terminals with contiguous coverage increased slightly as the fixed station separation was reduced, but the proportion of terminals with contiguous coverage flattened out at approximately 80% at very small fixed station separations.

However, the total call loss rate improved slightly, from around 6.6% to 5.6%, as the fixed station separation was reduced. The rates for both call blocking and call dropping reduced as part of this reduction in total call loss.

Hence even with a low call loss rate and a very small fixed station separation contiguous coverage was not achieved. It would appear that the coverage quality limit is a function of the user load, the terminal distribution, and the cumulative off-adjacent channel spill from interfering users.

Cochannel and immediately adjacent channel interferers can largely be discounted from causing this limit because such interferers cause horizontal jumps in the INR and cell radius CDF traces. Examining figure 4, such jumps only occur in the last 0.5% of samples, thus coverage for the last 10% of terminals would mostly be determined by the effect of off-adjacent channel interference.

Overcoming a coverage limit may be difficult. Solutions could include a hard limit on the system capacity (i.e. controlling the number of fixed network trunks available per cell), or imposing stricter limits on system channel spill specifications. A better solution may be to develop new terminal admission controls that monitor and tailor the INR (and thus cell radius) statistics in order to maintain some coverage target.

4. CONCLUSION

Cell sizes experienced by individual mobile terminals in a cellular system are a function of the uplink "interference to noise ratio" or INR. The extent of contiguous coverage, or the proportion of terminals meeting a coverage target in a cellular or microcellular system, can be deduced from the INR statistics.

Simulations have shown that the proportion of mobile terminals meeting a contiguous coverage requirement in a microcell environment decreases as the per-cell load increases. Further, when the proportion of terminals with contiguous coverage drops below the target level, reducing the fixed station separation improves the proportion only slightly.

Hence contiguous cell coverage may not be possible for an acceptable proportion of mobile terminals in a microcell system even if the call loss rate is low. This coverage limit appears to be a function of the accumulated interference from off-adjacent channel spills of other users.

These results suggest that a system-wide microcellular design methodology will need to address the INR statistics in a system, and possibly tailor them through terminal admission controls, if contiguous coverage is required for a certain proportion of mobile terminals.

REFERENCES

- [1] V.H. MacDonald, "The Cellular Concept", *Bell System Technical Journal*, vol 58 no 1 pp 15-41, Jan 1979.
- [2] W.C.Y. Lee, *Mobile Communications Design Fundamentals*, 2nd ed., John Wiley and Sons, New York, 1993.
- [3] B.C. Jones and D.J. Skellern, "Interference modelling and outage contours in cellular and microcellular networks", *2nd MCRC Int. Conf. on Mobile and Personal Comm. Sys.*, pp 149-158, Adelaide, Australia, 10-11 April 1995.
- [4] B.C. Jones and D.J. Skellern, "Spatial outage analysis in cellular and microcellular networks", *Wireless '95*, Calgary, Canada, 10-12 July 1995, in press.
- [5] B.C. Jones and D.J. Skellern, "Outage contours and cell size distributions in cellular and microcellular networks", *45th IEEE Veh. Tech. Conf.*, Chicago, USA, 26-28 July 1995, in press.
- [6] B.C. Jones and D.J. Skellern, "Interference distributions in microcell ensembles", *6th IEEE Int. Symp. on Personal, Indoor and Mobile Radio Comm.*, Toronto, Canada, 27-29 September 1995, in press.
- [7] T.S. Rappaport, "Wireless personal communications: Trends and challenges", *IEEE Ant. Prop. Mag.*, vol 33 no 5, pp 19-29, Oct 1991.
- [8] J. Sarnecki, C. Vinodrai, A. Javed, P. O'Kelly and K. Dick, "Microcell design principles", *IEEE Comm. Mag.*, vol 31 no 4, pp 76-82, Apr 1993.
- [9] D.C. Cox, "Wireless network access for personal communications", *IEEE Comm. Mag.*, pp 96-115, Dec 1992.
- [10] D. Everitt and D. Manfield, "Performance analysis of cellular mobile communication systems with dynamic channel assignment", *IEEE J. Sel. Areas Comm.*, vol 7 no 8, pp 1172-1180, Oct 1989.
- [11] P.A. Ramsdale, A.D. Hadden and P.S. Gaskell, "DCS1800 - The standard for PCN", *6th IEEE Int. Conf. Mobile and Personal Comm.*, pp 175-179, Coventry, UK, 9-11 Dec 1991.
- [12] A.O. Fapojuwo, A. McGirr and S. Kazeminejad, "A simulation study of speech traffic capacity in digital cordless telecommunications systems", *IEEE Trans. Veh. Tech.*, vol 41 no 1, pp 6-16, Feb 1992.
- [13] W.T. Webb, "Modulation methods for PCNs", *IEEE Comm. Mag.*, vol 30 no 12, pp 90-95, Dec 1992.
- [14] S.S. Rappaport and S.-W. Wang, "Signal to interference calculations for balanced channel assignment patterns in cellular communications systems", *IEEE Trans. Com.*, vol 37 no 10, pp 1077-1087, Oct 1989.
- [15] J.P. Driscoll, "Relevance of receiver filter performance and operating range for CT2/CAI Telepoint systems", *Electron. Lett.*, vol 28 no 13, pp 1200-1201, 18 Jun 1992.
- [16] S. Sato, K. Takeo, M. Nishino, Y. Amezawa, T. Suzuki: "A performance analysis on nonuniform traffic in microcell systems", *IEEE Int. Conf. on Comm. (ICC 93)*, vol 3, pp 1960-1964, Geneva, Switzerland, 23-26 May 1993.
- [17] S.S. Rappaport and S.-W. Wang, "Signal to interference calculations for corner excited cellular communications systems", *IEEE Trans. Com.*, vol 39 no 12, pp 1886-1895, Dec 1991.
- [18] J.E. Button, "Asynchronous CT2/CAI Telepoint separation requirements", *Electron. Lett.*, vol 27 no 1, pp 48-49, 3 Jan 1991.
- [19] Y.-D. Yao and A.U.H. Sheikh, "Performance analysis of microcellular mobile radio systems with shadowed cochannel interferers", *Electron. Lett.*, vol 28 no 9, pp 839-841, 23 Apr 1992.

THE EFFECT OF RECEIVER COLLISIONS ON THROUGHPUT PERFORMANCE OF MULTICHANNEL MULTIAccess PROTOCOLS

Ioannis E. Pountourakis

National Technical University of Athens
Department of Electrical & Computer Engineering
Division of Computer Science
157 73 Zographou, Athens, Greece

Tel +30 1 7722426, Fax +30 1 7722530, E-mail ipount@theseas.softlab.ece.ntua.gr

ABSTRACT

The problem of receiver collisions in multichannel multiaccess communication systems is studied in this paper. Analytic solution is developed for throughput performance assuming receiver buffer with capacity of one packet. We calculate the average rejection probability at destination of a packet in order to estimate the effect of receiver collisions. The evaluations are carried out for Multichannel Slotted Aloha-type protocols with Poisson arrivals and finite population and examine the throughput degradation due to receiver collisions. Also numerical results are showing the throughput reduction as it compared with the protocol case without receiver collisions.

1. SYSTEM MODEL AND ASSUMPTIONS

A multichannel multiaccess communication system consisting of v parallel broadcast channels all of the same capacity is considered. A finite number, M , of stations each one connected by means of separate interface to every channel of the system is assumed. The time axis is considered to be divided into slots of equal length. Each station has access to all channels, i.e. it can transmit and/or receive constant length packets that fit to slot size. The round trip propagation delay is small enough (i.e. less than packet transmission time the slot duration). The set of rules that the proposed protocol implies for the stations in the multichannel system are as follows:

1) Every station is equipped with a receiver buffer and a transmitter buffer each one with capacity of one packet. If the transmitter buffer is empty, the station is said to be *free*, otherwise, it is *backlogged*.

Packets are collectively generated in a Poisson stream. If a station is backlogged and generates a new packet, the packet is lost and never returns. We assume a uniform distribution of retransmissions from backlogged stations. We also assume that the total offered traffic from new generated and retransmitted packets obeys to Poisson statistics.

2) We assume that each packet has a source and a destination address information. A station ready to (re)transmit selects randomly one among the v ($2 \leq v \leq M$) channels at the beginning of the slot in order to attempt its (re)transmission. Each channel is chosen with equal and constant probability $P_i = 1/v$. If more than one station select the same channel during a time slot to (re)transmit a collision will occur. In case of a successful (re)transmission the packet is uniformly distributed among M stations. If the receiver buffer of the randomly selected station as destination is 'full' the packet is rejected. This phenomenon is called *receiver collision*.

3) If a backlogged station retransmits successfully during a time slot and the retransmission is not aborted due to a receiver collision, it becomes free at the next time slot. A free station becomes backlogged in case of a unsuccessful transmission or receiver collisions.

4) The channels are error free and there are no capture phenomena. Thus, packets may be corrupted only because of their concurrent transmission or receiver collisions.

2. ANALYSIS

The throughput reduction induced by receiver collisions is related with the possibility of receiver buffer overflow and this is associated with buffer

capacity and the system throughput without the effect of receiver collisions. The possibility of receiver buffer overflow gives rise to rejection probability at destination in steady state which substantiates the throughput loss in quantitative fashion. The analysis is composed from two parts. a) Throughput evaluation of conventional multichannel system protocol and b) Throughput analysis of finite receiver buffer size protocol.

2.1 Multichannel Slotted Aloha Without Receiver Collisions

The traffic offered to i -th channel is given:

$$G_i = GP_i = G/v \quad (1)$$

For finite population of stations we adopt the Bertsekas's [1] assumptions for Poisson approximations of the overall traffic (G). Thus the throughput per channel in steady state is evaluated as:

$$S_i = G_i \exp(-G_i) = G/v \exp(-G/v) \quad (2)$$

Thus the total throughput is:

$$S = \sum_{i=1}^v S_i = G \exp(-G/v) \quad (3)$$

2.2. Multichannel Slotted Aloha With Receiver Collisions

Let

S_v = Random variable representing the number of successful (re)transmissions from multichannel system.

A_v = Random variable representing the number of correctly received packets at destination.

$S_v(G)$ = The number of successful (re)transmissions over the multichannel system, given that the total traffic is Poisson with a mean rate G packets/slot $1 \leq S_v(G) \leq v$.

$A_v(k)$ = The number of correctly received packets at destination, conditional that k successful (re)transmissions occurred, $1 \leq A_v(k) \leq S_v(r)$ for every $S_v(k) > 0$.

The probability $S_v(G) = r$, of finding r successfully (re)transmitted packets during a time slot obeys to binomial probability law.

$$\Pr[S_v(G) = r] = \left[\frac{v!}{(v-r)! r!} \right] (1 - P_{\text{suc}})^{(v-r)} [P_{\text{suc}}]^r \quad (4)$$

$$P_{\text{suc}} = \Pr\{ \text{a successful (re)transmission during a time slot in channel } i (i=1 \dots v) \} = G/v \exp(-G/v) \quad (5)$$

The probability $A_v(r) = k$, of finding k correctly received packets at destination given that r packets have been transmitted successfully during a time slot (see Appendix)

We define as conditional throughput $S_{RC}(k)$ the average number of different stations selected as destination chosen by a set of k successfully (re)transmitted packets from multichannel system during a time slot.

$$S_{RC}(k) = \sum_{r=k}^{\min(M,v)} \Pr[S_v(G)=r] \Pr[A_v(r)=k] \quad (6)$$

The expected value of $S_{RC}(k)$ is given by

$$S_{RC} = E\{S_{RC}(k)\} = \sum_{k=1}^{\min(M,v)} k S_{RC}(k) \quad (7)$$

Average Rejection Probability

We define P_{rej} , the average rejection probability at destination in steady state as the ratio of the average number of packet rejection at destination due to receivers buffer overflow, to the average number of successfully (re)transmitted packets.

$$P_{\text{rej}} = (S - S_{RC}) / S \quad (8)$$

4. NUMERICAL RESULTS

Figure 1 illustrates the throughput versus the offered traffic G for a $v=5, 10, 20$ (channel) systems with $M=50$ stations. It can be observed that throughput measures are on decrease as they compared with the protocol case without receiver collisions for all values of traffic rates. Also for a given value of traffic the difference $S - S_{RC}$ is increasing function of v . The explanation is that

as v grows, the throughput S increases, so the possibility of receiver collisions is large. For example let $G=4$, we have for $v=5$ ($S=1.797$, $S_{RC}=1.747$ and $P_{rej}=2.761\%$) for $v=10$ ($S=2.681$, $S_{RC}=2.559$ and $P_{rej}=4.543\%$) and for $v=20$ ($S=3.275$, $S_{RC}=3.085$ and $P_{rej}=5.772\%$).

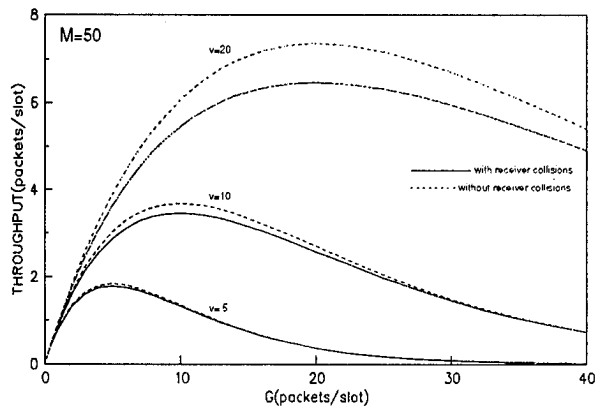


Figure 1: The throughput versus the offered traffic G characteristics for a $v=5,10,20$ (channel)systems with $M=50$ stations. Analytical results with and without receiver collisions schemes.

Figure 2 presents the histogram of the maximum average percent rejection probabilities for $v=2,5,10,20$ (channel)systems with $M=50,100$ stations. It is obvious that the maximum rejection probability $P_{rej(max)}$ in a multichannel system corresponds to maximum achievable throughput S_{max} . If we set the first derivative of the equation (3) with respect to G equal to zero, we find the optimal G that maximize the throughput of the system. Thus we take $G_{opt}=v$. From the Figure 2 is evident that as M increases the $P_{rej(max)}$ decreases. Also as v increases $P_{rej(max)}$ increases too. In case of $M=50$ we have for $v=5$, $P_{rej(max)}=2.825\%$ and for $v=20$, $P_{rej}=12.145\%$. We can say that three parameters characterize the performance behaviour of the multichannel system $\{v, M, P_{rej(max)}\}$.

Figure 3 illustrates the average rejection probabilities versus Traffic G (packets/slot) for $v=5,10,20$ (channel)systems with $M=50$ stations. For low value of the traffic G , the average rejection probability increases linearly with G (low values of the

throughput S). As the G increases approaching G_{opt} and the throughput approaching S_{max} , P_{rej} begins to saturate increasing slowly towards $P_{rej(max)}$. For higher values of G ($G > G_{opt}$) the S is reduced due to collisions over multichannel system so P_{rej} decreases because the possibility of collision at destination is low.

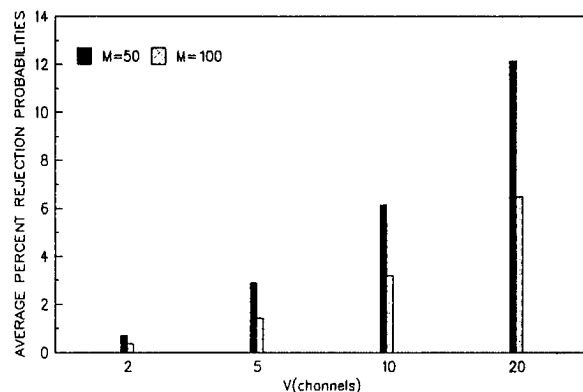


Figure 2: The histogram of maximum average percent rejection probabilities for $v=2,5,10,20$ (channel)systems with $M=50,100$ stations

CONCLUSIONS

The objective of this paper is to examine the effect of receiver collisions and to derive an accurate evaluation of the throughput performance of a parallel multichannel architecture with receiver buffer capacity of one packet. We have examined a model that based upon Poisson assumptions approximation for the total offered traffic over the multichannel system which reduces the computational complexity [2] for the throughput performance evaluation and the rejection probability at destination, for various number of stations and channels. Numerical results shows that for fixed M , as the number v of channels increases the probability of packet rejection P_{rej} at destination increases and this consists the main disadvantage on the performance behaviour of the multichannel system. Inversely for fixed v , the rejection probability reduces as M increases improving the performance approaching the performance of that without receiver collisions protocol.

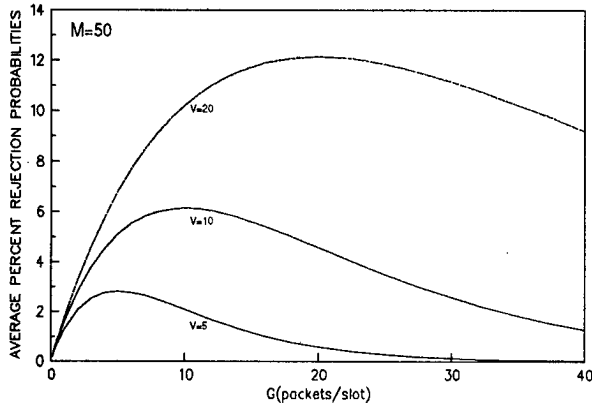


Figure 3: Average rejection probabilities versus Traffic $G(\text{packets/slot})$ for $v=5, 10, 20$ (channel) systems with $M=50$ stations

APPENDIX

The proposed uniform model corresponds to the occupancy problem of distribution indistinguishable balls (packets) to cells (destination stations) supposing that arrangements should have equal probabilities. We assume indistinguishable packets (re)transmitted to indistinguishable stations using Maxwell-Boltzman statistics [3]

Let M the number of stations in a v -channel system. We seek the probability $\Pr[A_v(k)=r]$ of finding r successfully received packets at destination when k free and/or backlogged stations have been correctly (re)transmitted from the multichannel system during a time slot.

It is obvious that $k-r$ packets are aborted due to destination conflicts phenomena while $M-r$ stations remain without any reception, then.

$\Pr[A_v(k)=r] = \{ \text{Probability of distribution } k \text{ packets to } r \text{ stations} \} \times$

$\{ \text{Probability that } r \text{ stations have received at least one packet} \}$

It is supposed that each station can transmit to and receive from every M station and according to

Maxwell-Boltzman statistics there are M^k possible arrangements of the k correctly (re)transmitted packets to M stations, each one with probability M^{-k} . Also the k packets can be distributed among the r ($r \leq k$) stations in r^k different ways.

The ratio of favourable to possible arrangements gives the probability P_{kr} of distribution k packets to r stations

$$P_{kr} = \frac{M!}{(M-r)!r!} \frac{r^k}{M^k} \quad \text{A.1}$$

Where $M!/(M-r)!$ are the ways in which r among M stations are chosen as destination.

Let $U(k,r)$ be the probability the r stations have received at least one packet at end of the time slot. Thus according to inclusion - exclusion method we take:

$$U(k,r) = \sum_{i=0}^r \frac{(-1)^i}{i!} \frac{r!}{(r-i)!} \frac{(r-i)^k}{M^k} \quad \text{A.2}$$

The probability that exactly r among k correctly (re)transmitted packets have successfully received at end of the time slot is given by

$$\begin{aligned} \Pr[A_v(k)=r] &= P_{kr} U(k,r) = \\ &= \frac{M!}{(M-r)!r!} \sum_{i=0}^r \frac{(-1)^i}{i!} \frac{r!}{(r-i)!} \left[\frac{(r-i)}{M} \right]^k \quad \text{A.3} \end{aligned}$$

REFERENCES

- [1] Dimitri Bertsekas and Robert Gallager, *Data Networks*, New Delhi: Prentice Hall of India, 1989.
- [2] I.E.Pountourakis and S.E.Hontas "Analysis of ALOHA-type Protocols for Multichannel Networks with Destination Conflicts" *Proceedings of Melecon'94*, vol.1 pp 325-328 April 1994.
- [3] William Feller, *An Introduction to Probability Theory and its Applications, Vol.1*, New York: Wiley, 1957,1968.

SILICON-ON-INSULATOR TECHNOLOGY FOR LOW POWER ELECTRONICS

Zachary J. Lemnios

Advanced Research Projects Agency
Microelectronics Technology Office
3701 N. Fairfax Drive
Arlington, VA 22203

1. Abstract

Low power electronics are the key enabling technology of a new class of highly functional portable information technology components and consumer products. The key challenge is to reduce power dissipation with minimal effect on computational performance. Silicon-on-insulator (SOI) technologies offer the capability to maintain high device integration levels, reduce power supply voltages to $<1V$, and concurrently reduce device capacitance, allowing high speed operation. Potential applications and technology insertion challenges for SOI are described.

2. Introduction

Advances and innovations in integrated circuit (IC) manufacturing and design technologies, including first generation low power techniques, are leading to new generations of wireless, portable information technology products and components. Increasing power dissipation levels by the most recent families of ICs is limiting their practical application in battery powered, portable microelectronic systems. System size and weight, along with functionality and cost, are also among the factors that differentiate these portable microelectronic systems. Additionally, in some cases, the spatial volume occupied by the microelectronics and associated support systems (i.e., power supplies, thermal mitigation, racks, etc.) is of a critical concern, especially in some non-consumer, noncommercial applications. Substantial reductions in IC power dissipation will allow smaller, lighter batteries with longer useful lifetimes, reduced electronic packaging costs, elimination of heat sinks and other thermal mitigation systems, enable reductions in the sizes and quantities of external power supplies, and may generally improve the reliability by reducing fatigue and breakdown.

Designs for portable products, or applications that require very low power dissipation but high performance are complicated by a lack of sophisticated design tools to fully explore trade-offs in design and manufacturing, optimize power (nominal, average, maximum), while remaining constrained by required performance. Present approaches to

low power system designs are mainly ad hoc and are not easily extended to future generations of products. In the past, some portable applications have included custom power management hardware and software to control unnecessary power dissipation by system components. This application-specific practice has allowed longer battery lifetimes, but has usually also compromised performance and ergonomics. The greatest general purpose reductions in power dissipation by an IC will result from decreasing the power supply voltage. However, dimensional and parametric scaling of conventional CMOS can not keep pace with the necessary voltage reductions, so conventional bulk CMOS technologies become too slow at low voltage and also exhibit relatively high current conduction below the threshold voltage.

The Advanced Research Projects Agency, working with the semiconductor industry recently began an aggressive program to develop enabling technologies for low power electronics, including ultra-shallow doping technologies, film silicon-on-insulator (SOI) substrate technologies, and new approaches to power management, circuit architectures and design.

3. Low Power Electronics Application Areas

Both commercial and noncommercial application areas are driving low power electronics technologies. The spatial volume of systems has decreased by 50% each five to seven year span, with superior or at least parity in functionality and performance. A number of commercial products are now demanding very low power dissipation to realize useful battery lifetimes and functionalities. Examples are in portable computers, digital assistants, cellular telephones and similar portable communication systems, "smart" cards, digital cameras, and medical devices (e.g., pacemakers and implants), and hand-held instruments. Portable, full speed, multi-media systems are on the horizon for commercial products, as are compact, high resolution, all electronic video cameras that may soon appear for commercial and industrial applications, all enabled by low power ICs and memory. As the information display unit is usually a large fraction of the power budget, it is likely that

voice commands and keyed inputs coupled with smaller, more dense flat panels will emerge.

Future industrial applications might couple low power electronic circuits with sensors and actuators and rf communication to provide intermittent, addressable, or continuous information on conditions or surroundings, especially applicable for hazardous environments or where fine granularity is important. The low power aspect allows very small form factors and long lifetimes. The location and status of mobile or distributed resources or inventories could be instantly updated through use of ubiquitous "smart" electronics unobtrusively embedded in appropriate structures or surroundings. As semiconductor technologies continue to improve, any number of additional embedded applications is likely to emerge as well.

The importance of low power enabling IC technologies to systems of military interest is also clear for both existing platforms and those under planning and development. In the portable, hand-held regime, there are applications for tactical information assistants, analogous to Personal Digital Assistants, but for assisting warfighters in completing mission requirements. Tactical information assistants might contain RF communications to upload or download appropriate information, such as terrain maps, target intelligence, positions, or orders.

Mixed signal applications are of great importance for military systems in such components as RADARs, SONARs, and communication systems. Power reduction here can improve reliability and allow greater functional signal processing densities. Most of the power dissipated by the analog section is in standby power of the operational amplifiers, roughly proportional to the circuit capacitance, including parasitics. There are ongoing research efforts to implement these analog and RF functions in low power CMOS, and the extension to SOI is both logical and highly possible.

The general electronic content of aircraft avionics, weapons, and detection systems has been increasing, limited in some cases by the power available from the generator. High power dissipation of certain electronics requires elaborate and expensive cooling techniques that add unnecessary weight and use up valuable space. Potentially, low power electronics could eliminate the external thermal mitigation systems and reduce the size or quantity of onboard generators. Munitions such as missiles have been moving toward smaller sizes, lighter weights, greater accuracy, greater velocity, and greater range. Battery powered, high computational processors and fast memories are required here, meeting a strict power budget between the target seeker and the guidance system. Ground based forces are also

relying more on electronic systems. Similar to aircraft, tanks and other vehicles have a limited capacity for generating power to run electronics and keep those systems thermally stable. Soldiers could use a variety of information and communication technology products to complete missions and aid in survival, but issues regarding form factor and useful battery lifetimes must be solved. In the future, the low power camera technology could enable complete, intimate, undetectable surveillance of a battlefield or other hostile territory. It is conceivable that a satellite could be miniaturized to the size of a wafer, easily and readily replicated, thus forming the backbone of an uninterrupted, inexpensive, highly redundant, highly reliable command, control, communication, and intelligence channel for global and highly localized application.

4. Technology Trends in Power Dissipation

Extrapolations contained within the Semiconductor Industry Association's National Technology Roadmap for IC voltage and power are summarized in Table 1.¹ Meeting both the power and power density projections will require integration of advanced technologies, especially in portable applications. Otherwise, large power dissipation will result in impractically short lifetimes for practical battery sources, expensive packaging, and heavy heat sinks or requirement of inconvenient cooling techniques. Trends in the power dissipation of commercial volume microprocessors are shown in Figure 1. These microprocessors were fabricated in bulk CMOS or BiCMOS technologies, and indicate an approximate tripling in dissipated power every generation. A typical recent microprocessor dissipates in the 10-30W range and operates around 100MHz.

TABLE 1: SIA Roadmap Extrapolations¹

	<u>1995</u>	<u>1998</u>	<u>2001</u>	<u>2004</u>
Desktop (V)	3.3	2.5	1.8	1.5
Battery (V)	2.5	1.8-2.5	0.9-1.8	0.9
High Performance [heatsink] (W)	80	100	120	140
Logic [no heatsink] (W/cm ²)	5	7	10	10
Battery Power (W)	2.5	2.5	3	3.5

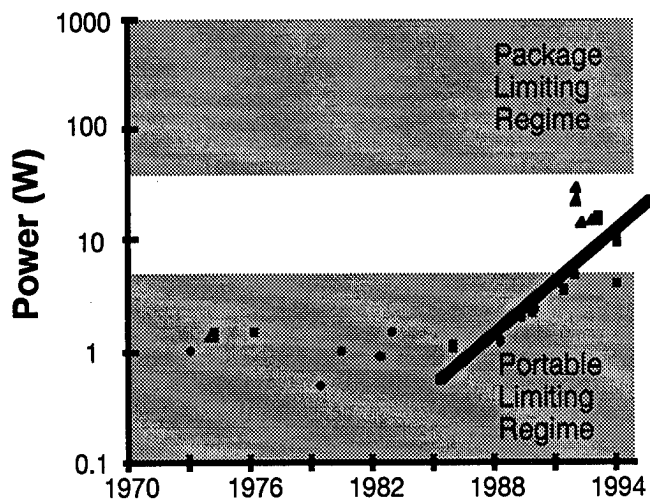


Figure 1: Microprocessor power trends.

5. Device Power Dissipation

CMOS is the dominant technology choice for digital applications. There are three principal components to the power dissipated in a CMOS device,

$$P_T = n_p C_{load} V_{out} V_{dd} f_{clock} + I_{sc} V_{dd} + I_{leakage} V_{dd} \quad (1)$$

where the activity factor n_p is determined by power management schemes and all other quantities have their usual meanings. The first term of (1) is the dynamic switching component and is often the dominant factor, but there is also a short circuit current during the switching transient, and a dc leakage current due to the diode dark current conduction. Careful device design and control of process parameters, such as threshold voltage, can minimize I_{sc} and $I_{leakage}$. There are four basic options available to reduce the switched power dissipation. The greatest reductions come from reducing the power supply voltage since power decreases nonlinearly as the square. But, reducing device and interconnect capacitance is necessary as well.

With architecture changes, the clock frequency may be reduced without sacrificing performance. In some fixed throughput applications, such as data compression/decompression, parallel circuits may be implemented to maintain bandwidth or functionality, while also enabling reductions in f_{clock} , which allows reductions in V_{dd} . Dynamic control of the clock frequency may provide dramatic reductions in power consumption. The underlying idea is to adaptively control the clock cycle to provide only as much throughput or bandwidth as is required at that instant. SOI material technology has several

compelling potential advantages to engineered-channel scaled CMOS structures.

6. Fabrication Technology Approaches

Conventional approaches to reducing the power of an integrated circuit are tantamount to reducing the power supply voltage. To retain performance, typically, device and process parameters are scaled by the same factor (as the power supply reduction). There are tremendous challenges in scaling as required critical dimensions are reaching practical limits, among them gate oxides are nearing tunneling limits, and junction depths are shallower than present technology can reproducibly manufacture. Junction depths are particularly critical since leakage and capacitance is directly proportional. A new approach to junction doping is under development based on a pseudo-lithography approach, called projection gas immersion laser doping (PGILD). A high power laser essentially images a device region and melts the silicon wafer in the presence of a dopant gas to form a very shallow junction. Preliminary experimental results have confirmed the ability to control junction depth through varying the laser pulse to increase or decrease the melt depth. Initial results indicate that the PGILD technology will be capable of reproducing junctions under 10nm. Development of a production prototype tool and unit process are now underway, as are process integration efforts.

While attractive and simple, scaling conventional bulk CMOS structures and parameters to reduce power supply voltages does not clearly provide a robust long-term solution of low power electronics. Although power certainly does scale, power density does not, so the thermal limitations remain. In addition, while minimum feature sizes have decreased, chip active areas have tended to increase, providing greater transistor integration levels and thereby increasing power dissipation. It is not altogether certain that bulk CMOS technologies, even with engineered channels, will work satisfactorily with supply voltages below about 1.5V.

Thin film SOI substrate technologies are attractive for use in applications that require low power, since SOI offers significant advantages in operating low voltage, short-channel transistors, from a speed-power perspective. SOI is also entirely compatible with conventional process technology and may also provide an opportunity for process simplification as compared to conventional bulk CMOS technology. It has been estimated that a nominal SOI process could use approximately 15% fewer steps than silicon CMOS, eliminate as many as three masks, and provide higher levels of device integration.² SOI starting substrates for future leading-edge microelectronics technology generations will require the development of

high-quality, thin buried oxide (BOX) layers and growth of gate oxide films near the tunneling limit. A series of comprehensive experiments is now underway in coordination with ARPA, SEMATECH, the semiconductor industry, and SOI wafer suppliers.³

The key issues for either SOI technology in commodity applications is wafer supply and wafer quality of acceptable material at affordable prices. A number of challenges must be solved for both SOI approaches before wide scale use in VLSI applications, such as integrity, defects and contamination in the oxide and the thin active region. The completeness and integrity of the bond is an issue for bonded, while the quality of buried oxide and the thin silicon region are a concern for SIMOX wafers. Particularly critical is the thickness control of the thin silicon layer, since that directly affects the threshold voltage for fully depleted devices. For SOI to remain a viable a technology option, competitively priced SOI wafers must be readily available with excellent thin silicon thickness (under 100nm) uniformity (< 3nm) to support fully and partially depleted transistor channels. Although the early indications from suppliers is positive, the control of intra-wafer, intra-lot and lot-to-lot material parameters must be improved and demonstrated for both technologies to gain long-term acceptance.

7. SOI Devices

The cross-section of an SOI transistor is shown in Figure 2. By making the silicon thickness very thin, under 600Å or so, the depletion layer extends entirely through the active area (fully depleted) and drastically improves the electrical characteristics, as compared to conventional CMOS or even thick film (partially-depleted) SOI (see Fig. 3). However, it is more difficult to fabricate substrates for fully depleted technologies and partially depleted devices can have a better subthreshold slope at high drain bias. Other potential advantages of SOI include a reduction in device and interconnect capacitance, as well as parasitics. It may be quite reasonable to employ doped buried layers to provide a means to electrically bias devices to compensate for process variations or possibly be used to control device conduction dynamically to turn on or off unnecessary areas of a chip. Since there are no well contacts, complementary circuits formed in SOI are not susceptible to the "latch-up" phenomena and device isolation is nearly total. The effects of the back-side oxide-silicon interface must be studied since that layer floats in voltage and interface states may trap holes leading to long term reliability problems or a number of first and second order modifications to device I-V performance. Susceptibility of SOI devices to electrostatic discharge (ESD) and methods to provide fast input protection need detailed investigations.

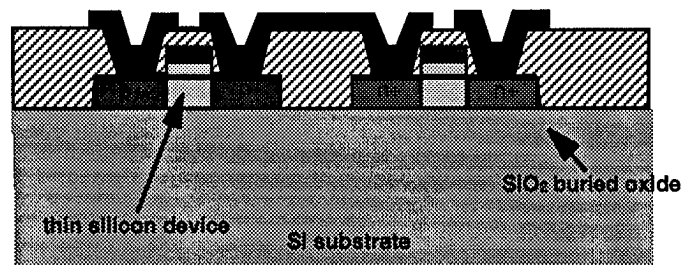


Figure 2 Cross Section of an SOI Inverter

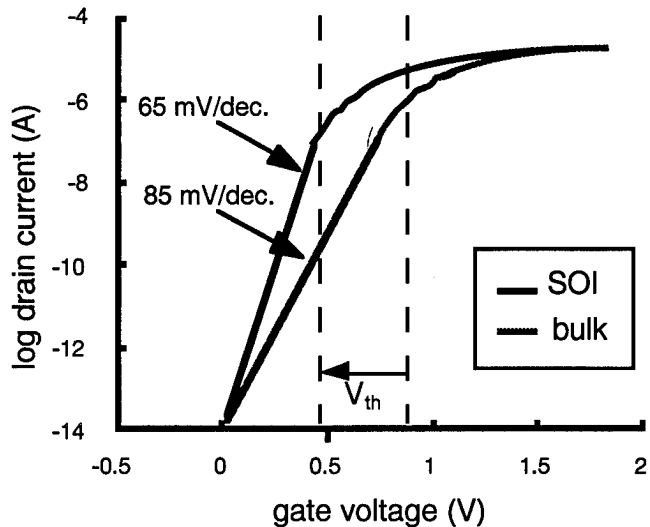


Figure 3: SOI and conventional CMOS thresholds voltages

8. Conclusion

Low power electronics technologies will have a tremendous impact on the performance and functionality of future systems. SOI is an attractive technology option for low power, high performance semiconductors. Efforts are underway to improve material properties and availability. Next steps in the development of an SOI technology base are better understanding of how materials issues affect device/circuit operation, and which device design paradigms are best.

9. References

1. "National Roadmap for Semiconductor Technology," Semiconductor Industry Association (1994).
2. T. D. Stanley, "SOI for Mainstream VLSI: Another Look at the Economic Incentive," Proceedings of the Electro-Chemical Society, 94(11), (1994).
3. SOI Material Specification and Design of Experiments, ARPA/SEMATECH Internal Report, (1995).

COMPLEMENTARY GAAS (CGaAsTM) TECHNOLOGY AND APPLICATIONS

Jerry Hallmark, Jon Abrokwhah, Bruce Bernhardt, Brian Crawforth**, Dave Foster**,
Jenn-Hwa Huang, Mike LaMacchia**, Rudy Lucero, Bill Mathes**, Bill Ooms*

Phoenix Corporate Research Labs, Motorola Inc., Tempe, AZ

* Compound Semiconductor Technologies

** Government, Space & Technologies Group

Abstract -- A self aligned complementary GaAs (CGaAsTM) technology has been developed for low-power, high-speed digital and mixed-mode applications. A single process flow has been used to build low-voltage, low-power, full-complementary digital circuits at 200MHz, high-speed SCFL digital circuits at 5GHz, RF MMIC and power circuits (900MHz), and combinations of these. Complementary digital circuits have demonstrated speed-power performance of 0.1 μ W/MHz/gate at 0.9V. A mixed SCFL/Complementary signal processor operated at > 1GHz with a speed-power performance of 0.16 μ W/MHz/gate.

I. INTRODUCTION

As the trend in electronic devices continues to move towards lower voltage, lower power, and higher integration, there will be an ever increasing demand for circuit technologies which do not sacrifice performance for low power. Ideally, this technology would be capable of operating at 0.9 to 1.5V which would require the use of only a single battery in portable applications. The CGaAsTM (Complementary heterostructure GaAs) process is ideal for very low voltage applications, and has an optimum speed-power performance at supply voltages near 0.9 V. Its flexibility allows a variety of circuit topologies to be used, and designs can be tailored to meet speed and power goals through both architecture and power partitioning. In addition, mixed mode applications can be considered which do not incur large sacrifices in either digital or RF performance and allow new circuit concepts to be used which take advantage of this integration.

II. CGaAs TECHNOLOGY DESCRIPTION

A. Epitaxial Material

CGaAs devices were fabricated on 4-inch epitaxial wafers consisting of a 30Å GaAs cap, 250Å undoped Al_{0.75}Ga_{0.25}As, 150Å undoped In_{0.2}Ga_{0.8}As, and a 2000Å GaAs buffer layer grown on LEC GaAs substrates (Figure 1). The threshold voltages of the NFET and PFET devices depend on the N- and P-Schottky barriers heights, the conduction and valence band discontinuities of the AlGaAs/InGaAs junction respectively, and the pinch-off voltage. N- & P-channel device threshold voltages were adjusted simultaneously with a Silicon pulse doping 30Å below the InGaAs channel. Thus the threshold voltages are set by the epitaxial material, not by ion-implantation. For small threshold voltage variations, precise

control of the layer thicknesses, mole fraction, and silicon delta doping were required. Molecular Beam Epitaxy (MBE) technology allows excellent control of layer dimensions and compositions and is ideal for such structures. Metalorganic Chemical Vapor Deposition (MOCVD) grown wafers have also been used with success.

B. Device Fabrication

A schematic cross-section of the CGaAs process is shown in Figure 1. The gate metal was RF sputtered TiWn (4000Å) which was etched with a low damage SF₆/CHF₃/He plasma to a nominal gate length of 1.0 μ m. The wafers were immediately capped with PECVD SiN to prevent oxidation of the GaAs/AlGaAs layers. N-channel (Si⁺) and P-channel (Be⁺/F⁺ co-implant) source/drain implants were self-aligned to the gates. The Fluorine improved activation of the Beryllium and also reduced the in-diffusion of Be under the gate and out-diffusion. The implants were rapid thermal annealed in a temperature range from 700°C to 800°C. The devices were then isolated via oxygen implant, and capped with PECVD SiO₂. A single refractory ohmic metal contacted both device types and was formed using dielectric-assisted lift-off. The refractory ohmics were stable up to a temperature range of 500°C to 600°C which allowed an interface with VLSI Aluminum interconnect metallization, where Al-Cu deposition took place at a temperature near 500°C.

The balance of the process was similar to standard Silicon processing. TEOS was deposited and then vias were formed to contact gate and ohmic regions. The first interconnect metal consisted of a TiW/AlCu/TiW sandwich. A TEOS interlevel

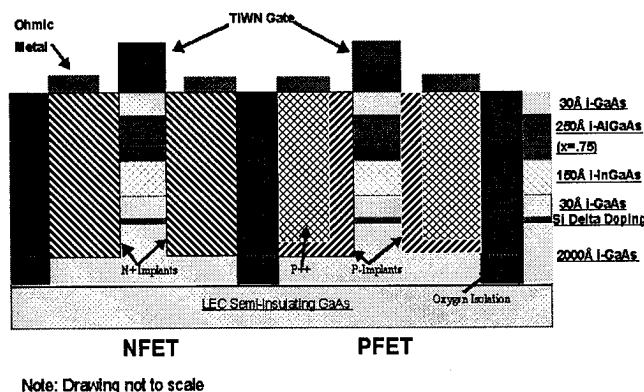


Figure 1: CGaAs Process Cross-Section

dielectric was deposited, a deposition/etchback planarization was performed, vias were formed, and an AlCu/TiW second metal was added. Finally, devices were passivated with SiO₂ and SiN [1].

III. DEVICE RESULTS

Typical I-V characteristics of 1 x 10 μm N- and P-channel devices are shown in Figures 2 & 3. Threshold voltages for these devices were designed to be +0.55V for NFETs and -0.55V for PFETs. While this gave about a 4:1 ratio of drain currents, it produced the optimum speed-power product in complementary circuits. The devices had very good pinch-off

characteristics and output conductances. Typical device parameters are shown in Table 1.

Parameter	NFET (1x10 μm)	PFET (1x10 μm)
V_t	+0.55 V	-0.55 V
I_{dss}	1.5 mA	0.4 mA
G_m	250 mS/mm	60mS/mm
Beta	250 mA/V ² -mm	55 mA/V ² -mm
Subth slope	75 mV/dec	90 mV/dec
Subth Current ($V_{gs}=0V$)	< 1nA	< 10nA

Table 1: Device Parameters

Due to the CGaAs devices' low threshold voltage and high current drive, performance is very good even at low voltages. Figure 4 shows unloaded ring oscillator delay versus supply voltage for several complementary technologies. The performance of the 1.0 μm CGaAs is superior to 0.5 μm CMOS or Thin-Film Silicon-on-Insulator (TFSOI) and the 0.5 μm CGaAs shows delays below 100ps at 1.2V.

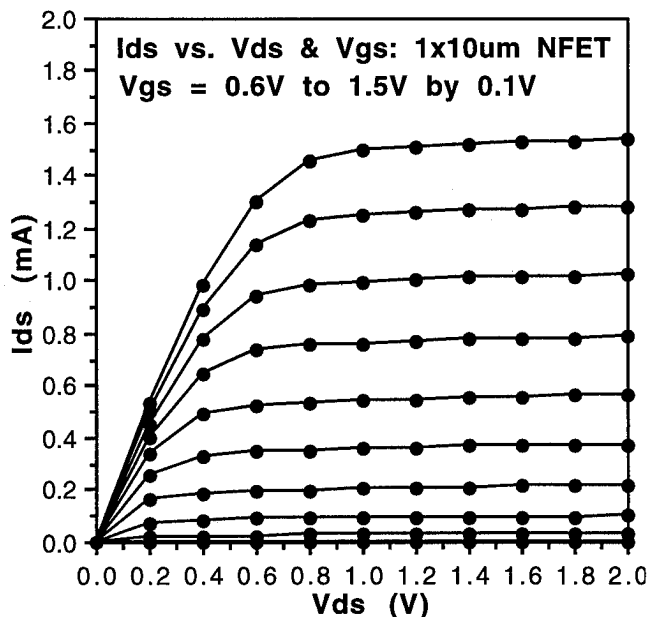


Figure 2: Drain current characteristics of 1x10 μm NFET

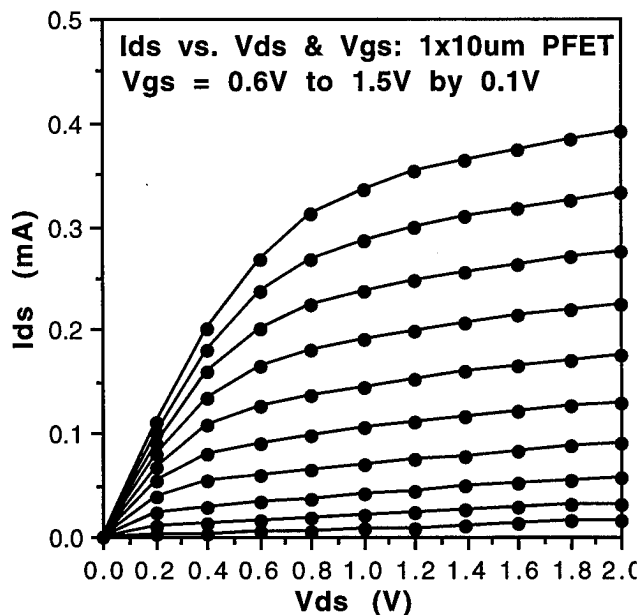


Figure 3: Drain current characteristics of 1x10 μm PFET

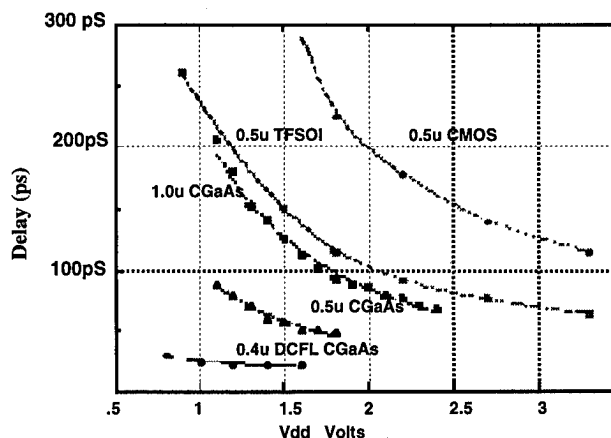


Figure 4: Ring Oscillator Delay vs. Voltage

IV. ARCHITECHTURE VERSATILITY

A variety of circuit design options are available using CGaAs technology. For digital designs, these include full complementary designs (CMOS-like), single-ended current steering logic (DCFL-like), and differential current steering logic (ECL/CML-like). Each of these styles present the designer trade-offs in power, speed, and gate complexity. The operating speed and power per gate for each style is shown in Figures 5 & 6. All of these styles may be used together on the standard CGaAs process and circuits can operate over a range from DC to greater than 5 Gb/s, with world class speed-power in each regime [2].

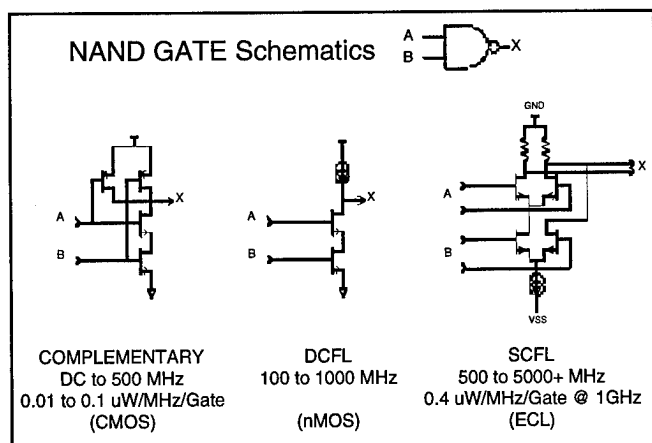


Figure 5: CGaAs Circuit Configurations

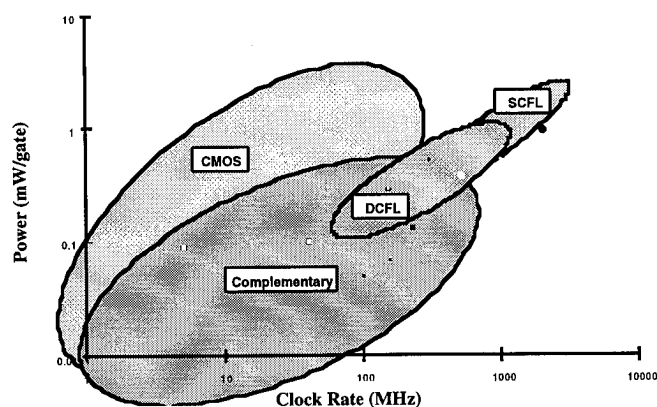


Figure 6: CGaAs Circuit Performance

This architectural versatility provides many of the advantages of BiCMOS, but with a much simpler process. A typical BiCMOS process flow adds the steps required to make a Bipolar transistor to an existing CMOS flow. This results in process flows with 25 or more mask steps. The standard CGaAs flow uses 13 masks through 3rd metal interconnect and provides all three types of circuit topologies if desired.

The complementary circuit style gives performance exceeding advanced CMOS processes while operating at 0.9 - 1.5 V. Complex logic gates can be built as in CMOS while layout is simplified. Since the CGaAs process does not require wells, tubs, or substrate contacts, devices can be laid out without the "normal" restrictions of putting all of one device type together in a common well. In fact, N- and P-type device contacts can even be butted together with the ohmic contact merged. This results in much simpler layouts and more compact designs. Most CMOS designs can be mapped directly into CGaAs designs, with little or no changes required. The only modifications typically required involve the lower supply voltage (limits on device stacking, etc.) and would also be needed for low-voltage CMOS design.

The DCFL-like circuit topology uses a PFET in place of a depletion-mode MESFET for the current source, and offers speed similar to E/D MESFET designs. Due to the higher gate diode turn-on voltage of the CGaAs devices, the high-level output of the gates are not clamped to 0.7V as is typical in E/D MESFET designs. This has several advantages including: higher noise margins, higher gate fan-in, the ability to stack input devices to make more complex gates, and the ability to directly interface with complementary circuits. Another advantage is that the P-load can be switched off when the circuit is not operating which reduces the standby power to a negligible level.

The source-coupled FET logic (SCFL) topology provides the highest operating speed at the expense of higher power. SCFL designs use differential current steering logic analogous to Silicon ECL or CML. Since only the very fast N-FET is used in SCFL, circuit speeds can exceed 5 Gb/s.

V. CIRCUIT RESULTS

Several circuits have been built using each of the design techniques and demonstrated the high performance and flexibility of CGaAs technology.

A. Complementary Designs

Several large circuits have been built with the full complementary design style. These include a 4K SRAM, a 16x16 bit multiply/accumulator, and a microprocessor core. These designs have demonstrated speed-power performance as low as 0.01 $\mu\text{W}/\text{MHz}/\text{gate}$ at 0.9V and 0.1 $\mu\text{W}/\text{MHz}/\text{gate}$ at 1.2V. Shift registers have operated at greater than 500MHz.

The 4K SRAM had nominal access delays of 5.3ns at 1.5 V and 15.0ns at 0.9 V. SRAM power ranged from 0.36 mW at 0.9 V to 16.2 mW at 1.5 V [3]. This power was significantly lower than other GaAs SRAM designs (Fig. 7) [4-12]. The SRAM was also tested over temperature and showed very little delay variation (< 7%) from -20°C to +120°C.

B. Mixed Digital Designs

A signal processor circuit was designed with a mix of high-speed SCFL and low power complementary blocks. It operated at over 1GHz over temperature (-35°C to +110°C) with a speed-power of 0.4 $\mu\text{W}/\text{MHz}/\text{gate}$. The SCFL circuits operated at -4 Volts while the complementary blocks used a -1.2V supply. Further testing showed that the SCFL supply could be reduced to -2.5V while maintaining operation at 1GHz and this reduced the speed-power to 0.16 $\mu\text{W}/\text{MHz}/\text{gate}$ [2].

C. Mixed Mode Designs

Some initial circuit design and characterization has begun using CGaAs devices for analog, MMIC, and RF power applications. While some device improvements still need to be made for precision analog circuits, there are many applications

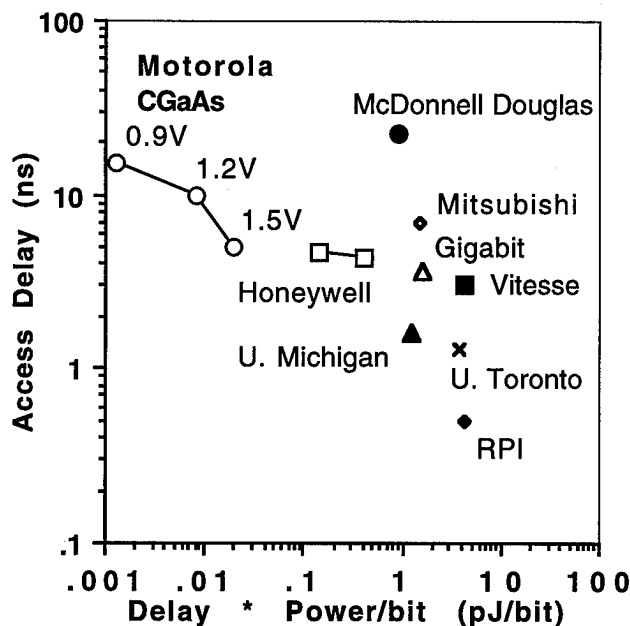


Figure 7: GaAs SRAM Delay and Power Comparison [4-10] which can be addressed including: digital filtering, A/D & D/A converters, ATM, etc. Since n-channel CGaAs devices are very similar to typical GaAs HFETs, both MMIC and power RF circuits can be designed. Table 2 shows typical RF device performance for 0.7 μ m gate length devices at 1.0V. A 0.7 μ m x 3mm NFET was used as a power amplifier in class AB operation with 26dBm output power at 1GHz for a 3V supply; power-added efficiency was greater than 60%.

Parameter	NFET (Lg=0.7 μ m)	PFET (Lg=0.7 μ m)
f_t (Vds=1.0V)	20 GHz	5GHz
f_{max} (Vds=1.0V)	30GHz	10GHz
MAG (Vds=1.0V)	20dB	6dB

Table 2: RF Device Parameters

VI. CONCLUSIONS

We have developed a complementary GaAs process which is ideal for low-power, high-speed digital and mixed-mode applications. The complementary operation along with the robust metal interconnect process allows large integration levels (10-30 K transistors) and provides a path for VLSI GaAs ICs in the future. A variety of circuit topologies gives the designer a wide range of options in both architecture and power partitioning.

ACKNOWLEDGMENT

The authors would like to acknowledge the contribution of the Motorola CS-1 GaAs fabrication personnel, whose dedicated efforts made this work possible.

CGaAsTM is a Motorola trademark.

REFERENCES

- [1] J.K. Abrokwha, J.H. Huang, W. Ooms, C. Shurboff, J.A. Hallmark, R. Lucero, J. Gilbert, B. Bernhardt, G. Hansell, "A Manufacturable Complementary GaAs Process," GaAs IC Symposium Digest, 1993, p. 127.
- [2] J. Hallmark, C. Shurboff, W. Ooms, R. Lucero, J. Abrokwha, J.H. Huang, "0.9V DSP Blocks, A 15ns 4K SRAM and a 45ns 16-bit Multiply/Accumulator," GaAs IC Symposium Digest, 1994, p. 55.
- [3] B. Bernhardt, M. LaMacchia, J. Abrokwha, K. Clauss, B. Crawford, S. Emmert, D. Foster, T. Lien, E. Lopez, B. Mathes, V. Mazzotta, B. Oh, J. Hallmark, R. Lucero, "Complementary GaAs (CGaAs), A High Performance BiCMOS Alternative," submitted to 1995 GaAs IC Symposium.
- [4] D.E. Grider, A. I. Akinwande, R. Mactaggart, P. P. Ruden, J. C. Nohava, T. E. Nohava, J. E. Breezley, P. Joslyn, and D. Tetzlaff, "Development of Static Random Access Memories Using Complementary Heterostructure Insulated Gate Field Effect Transistor Technology," GaAs IC Symposium Digest, 1990, p. 143.
- [5] D. E. Grider, I. R. Mactaggart, J. C. Nohava, J.J. Stroncz, P. P. Ruden, T. E. Nohava, D. Fulkerson, and D. E. Tetzlaff, "A 4Kbit Synchronous Random Access Memory Based Upon Delta-Doped Complementary Heterostructure Insulated Gate Field Effect Transistor Technology," GaAs IC Symposium Digest, 1991, p. 71.
- [6] A. Fielder, J. Chun, and D. Kang, "A 3ns 1Kx4 Static Self-Timed GaAs RAM," GaAs IC Symposium Digest, 1988, p. 67. (Gigabit)
- [7] H. Makino, S. Matsue, M. Noda, N. Tanino, S. Takano, K. Nishitani, and S. Kayano, "A 7ns/850mW GaAs 4Kb SRAM Fully Operative at 75°C," GaAs IC Symposium Digest, 1988, p. 71. (Mitsubishi)
- [8] C. Vogelsang, J. Castro, J. Notthoff, G. Troeger, J. Stephens, and R. Krein, "Complementary GaAs JFET 16K SRAM," GaAs IC Symposium Digest, 1988, p. 75. (McDonnell Douglas)
- [9] W. Terrell, C. Ho, and R. Hinds, "Direct Replacement of Silicon ECL and TTL SRAMs with High Performance GaAs Devices," GaAs IC Symposium Digest, 1988, p. 79. (Vitesse)
- [10] K. Nah, R. Philhower, H. Greub, and J. McDonald, "A 500ps 32X8 Register File Implemented in GaAs/AlGaAs HBTs," GaAs IC Symposium Digest, 1993, p. 71. (Rensselaer Polytechnic Institute)
- [11] A. Chanda and R. Brown, "An Asynchronous GaAs MESFET Static RAM Using A New Current Mirror Memory Cell," GaAs IC Symposium Digest, 1993, p. 79. (University of Michigan)
- [12] O. Law and C. Salama, "GaAs Schmitt Trigger memory Cell Design," GaAs IC Symposium Digest, 1993, p. 83. (University of Toronto)

A MANUFACTURABLE GaAs BiFET TECHNOLOGY FOR HIGH SPEED SIGNAL PROCESSING

M. F. Chang

Rockwell Science Center
1049 Camino Dos Rios
Thousand Oaks, CA 91360

Abstract

A GaAs BiFET LSI technology has been successfully developed for high speed and mixed signal circuit applications. High integration levels and functional circuit yield have been achieved. Excellent HBT and FET characteristics have been produced, with the noise figure of the FETs comparable to those of traditional MESFETs, enabling them to perform well in front-end receiver applications. Through this technology, several LSI circuits, including a 2 Gbps 2-bit prototype DRFM, a 2 GHz 32×2 bit shift register, a sample and hold circuit with 9-bit resolution at 200 Mbps and SRAMs with a record access time (330ps) have been successfully demonstrated.

1. Introduction

The integration of GaAs HBTs and MESFETs (Bipolar/FET or BiFET) can make a significant impact on the design of high speed and mixed signal integrated circuits and systems. BiFET technology offers great design flexibility and novel circuit opportunities by combining the device advantages of the HBT's high switching speed, high drive capability, excellent threshold voltage matching, and low $1/f$ noise; as well as the FET's low noise, high input impedance, high density, and low power dissipation on a single chip. In particular, the addition of MESFETs provides active loads, low voltage current sinks for minimizing power consumption, and floating current sources to provide high gain.

2. Device Structure and Fabrication

To achieve high integration level and high yield, a planar BiFET IC process has been developed. The typical material growth sequence and layer structure of the HBT are summarized in Fig. 1. The most obvious advantage of this process is the use of an already existing emitter epilayer to define the FET active channel. This eliminates the need

for material regrowth, provides a more planar structure, and avoids the need of forming p-type buried layer to reduce both short channel and sidgating effects.

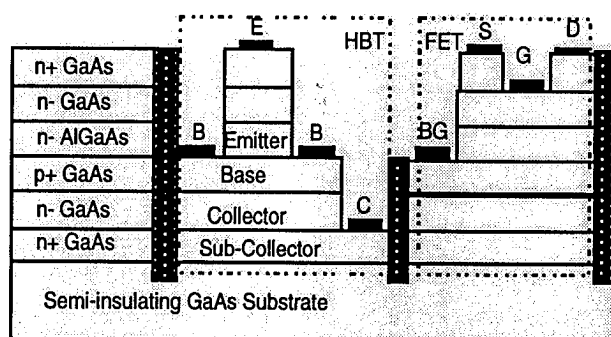


Fig. 1 Schematic cross section of the monolithic integrated GaAs HBT and MESFET.

The FET was fabricated from the emitter cap epilayers. During normal operation of the FET, the AlGaAs layer in the HBT emitter is fully depleted; thus the conduction paths remain primarily in the GaAs (rather than lower mobility AlGaAs) apart from real space transfer of electrons. The FET ohmic was on the heavily doped emitter cap layer. The backgate (BG) is a unique feature of the FET, which was formed on the p+ GaAs during the same fabrication process of the HBT base contact. Like the front gate, the backgate can also be used to modulate the FET channel. Gate recessing was performed using an $\text{NH}_4\text{OH}:\text{H}_2\text{O}_2:\text{H}_2\text{O}$ wet chemical etch with the end point determined by monitoring the channel current. Several steps in the MESFET fabrication process have been combined with the HBT process, including ion implantation for device isolation and all metalization for interconnects. A standard baseline HBT process was implemented for the device and circuit fabrication. In this process a Schottky diode was

formed on the collector layer; thin film NiCr resistors were also fabricated. The three level interconnects were processed along with the HBTs using standard Ti/Au metalizations and polyimide for intermetal isolation. All of the process steps are identical to the baseline HBT, with the exception of the gate definition.

3. BiFET Device Performance

The HBTs fabricated in this technology are comparable to those made by the HBT-only process. I-V characteristics are shown in Figure 2. Good current gain (> 50 at 1 mA) and excellent RF properties (f_t and $f_{max} > 50$ GHz at $I_c = 3$ mA) have been achieved for a $1.4 \times 3 \mu m^2$ device. This process has also produced both E-mode and D-mode MESFETs with excellent characteristics. Typical I-V characteristics for an E-mode MESFET are shown in Fig. 3. The f_t and f_{max} of a $0.5 \mu m$ FET were measured to be 40 and 35 GHz, respectively; the g_m of the FETs ranged from 250 to 350 mS/mm. Further reduction in the gate length will result in significant improvement of f_t , f_{max} .

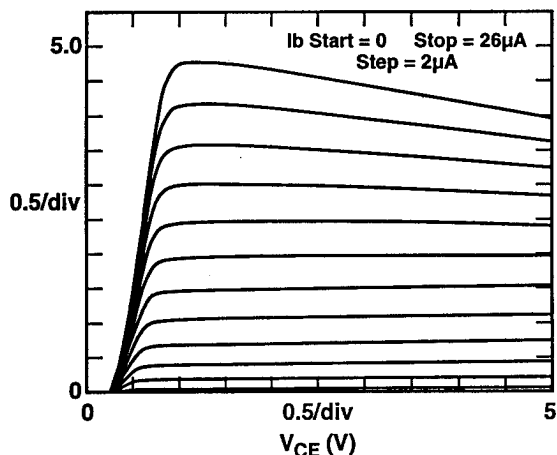


Fig. 2 I-V characteristics of (a) GaAs HBTs with emitter dimension of $1.4 \mu m \times 3 \mu m$.

4. Circuit Demonstrations

Several key GaAs BiFET circuits have been demonstrated. Those include the first LSI circuits: a single chip prototype DRFM, 200 Msp sample/hold circuits and ultra-fast SRAMs.

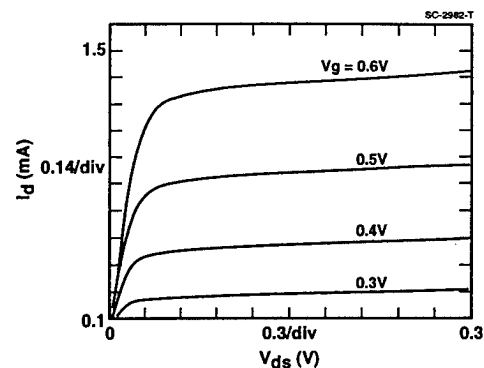


Fig. 3 I-V characteristics of GaAs MESFETs with gate length of $0.5 \mu m$ fabricated in the BiFET process.

5. DRFM on a Single Chip

The fabricated DRFM (Fig. 4) consists of a 2-bit ADC, a 2-bit DAC, 32×2 -bit word shift register and supporting circuitry. It contains 518 HBTs, 1572 FETs and 332 Schottky diodes. The DRFM system diagram is shown in Fig. 5. The designed system can be easily expanded in both length and width. Basic functionality consists of digitizing an input signal through a 2-bit analog to digital converter (ADC), selectively delaying (or storing) the pattern by using a 32×2 -bit word shift register, and then reconstituting it with a 2-bit DAC. The output waveforms of the DRFM are shown in Fig. 6. The DRFM was also found to be operational up to 2 GHz.

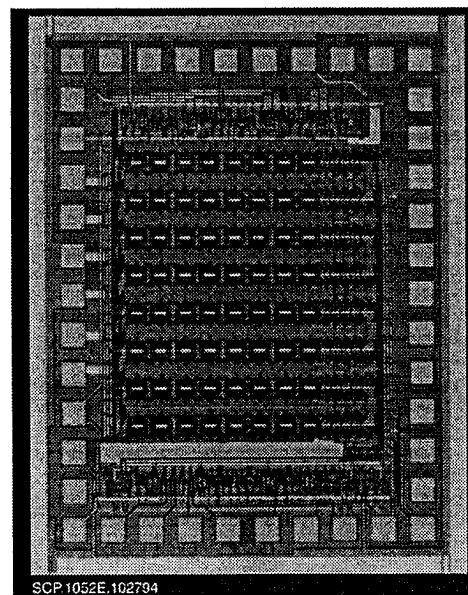


Fig. 4 Microphotograph of a fabricated BiFET DRFM.

6. Sample and Hold Circuit

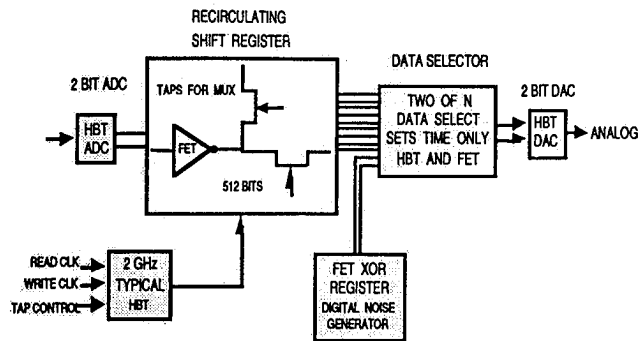
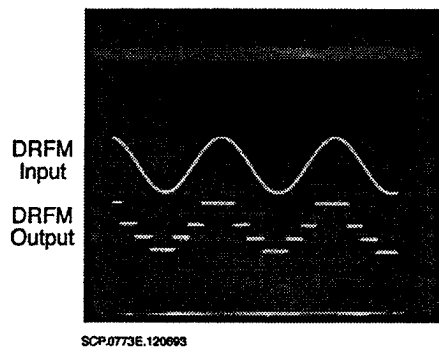
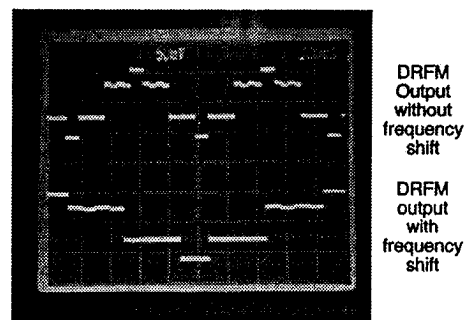


Fig. 5 DRFM system diagram, which consists of a two-bit ADC, a two-bit DAC, a 32-bit by 2-bit word shift register, and support circuitry.

A BiFET sample and hold circuit (Fig. 7) has been fabricated and evaluated. SINAD (Signal to Noise And Distortion) was measured to be greater than 55 dB (> 9 bit), but was limited by the test setup. The device accepts differential analog input and produces differential output. Clocks at up to 200 MHz are differential, but were driven single-ended for this test. Twelve-bit performance (74 dB) was expected from the simulation; and nearly 9-bit performance was observed at 200 Msps with an input frequency of 198 MHz, despite our test setup limitations. The very low droop rates (10 Msps) offered by the BiFET technology were also verified. The photos (Fig. 8) show the a signal with sampled output at 200 Msps and the spectrum of the beat frequency.



(a)



(b)

Fig. 6 (a) DRFM output waveform, (b) Input signal frequency down shifted by 2-bit DRFM.

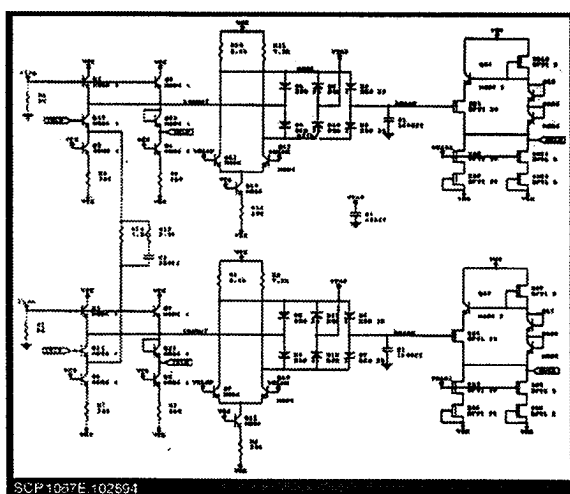


Fig. 7 BiFET sample and hold circuit schematic.

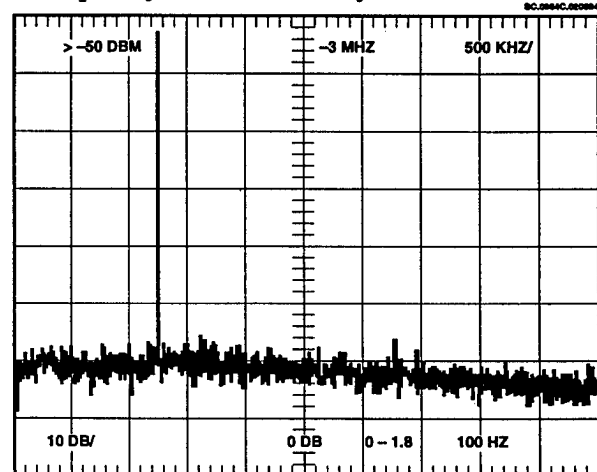
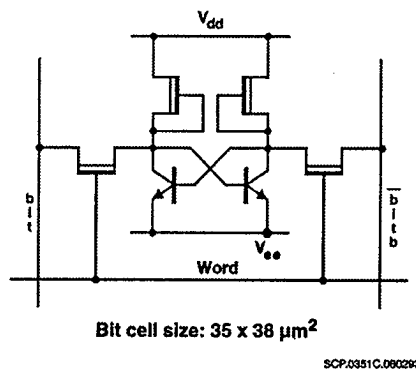


Fig. 8 BiFET sample/hold circuit output

7. Ultrafast BiFET SRAM

A small size (64 bits) SRAM was fabricated and tested. It is a conventional design in which six address lines, a WR strobe, D_{in} and Q_{out} control all function. The bit cell consists of four MESFETs and two HBTs (Fig. 9). The two HBTs and two MESFETs form a cross-coupled latch, while two MESFETs are pass elements to complementary bit lines. The pass elements have gates connected to word lines. All peripheral circuitry is implemented in HBTs, with Schottky diodes used for row decoding.



An access time test was performed. The access time test consists of selecting an arbitrary address line (A5) and toggling it a 1 GHz. This is a column select and ought to represent a worst-case read access time. An HP54120 oscilloscope was used to capture the output and measure the delay. Access time of around 330 ps to 360 ps was observed (Fig. 10). To our knowledge, this is the fastest SRAM ever demonstrated by any semiconductor technology.

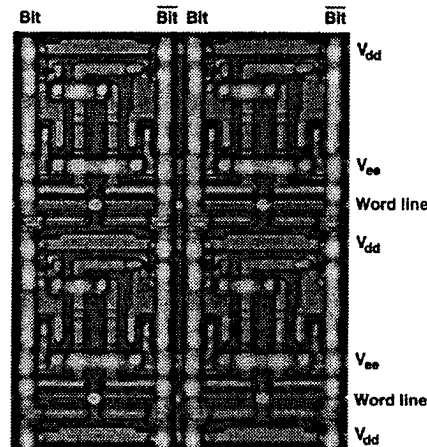


Fig. 9 Schematic and microphotograph of BiFET memory cell.

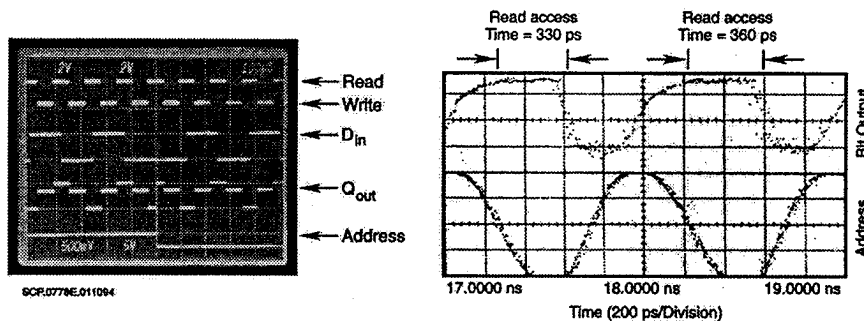


Fig. 10 BiFET SRAM with read access time of 330 ps.

8. Summary

In summary, we have developed a manufacturable, high speed BiFET technology for both analog and digital circuit applications. The technology is fully compatible with the standard HBT material growth and fabrication processes (only one additional mask needed to fabricate MESFETs and integrate them with HBTs). We have demonstrated various BiFET LSI circuits including: a 2 Gbps 2-bit prototype DRFM, sample and hold circuits with 9-bit resolution at 200 Mbps and SRAMs with

very fast access time (330ps). The developed BiFET technology is anticipated to impact both military and commercial circuits and systems in areas of functionality, speed, power, noise and system architecture.

9. Acknowledgments

The authors gratefully acknowledge the support of AFWL (contract # F33615-90-C-1505) in pursuing this work.

TECHNIQUES AND APPLICATIONS OF ANALOG FIBER OPTIC LINKS

Charles H. Cox, III

MIT Lincoln Laboratory
244 Wood Street
Lexington, MA 02173 USA

ABSTRACT

Analog fiber-optic links have a number of design challenges that are not found in their more popular digital link counterparts. This talk begins with a brief introduction to the field, then concentrates on the principals and experimental state of the art for both directly and externally modulated links. The utility of these links is then demonstrated by applications in cable television distribution, cellular telephone and phased array antennas.¹

1. INTRODUCTION

Transmission of signals over optical fiber has become common place. However probably 99% of all fiber optic links are digital links, i.e. links wherein the original data stream modulates the light without first being put on an RF carrier. There is a growing list of so called analog applications where the information to be conveyed over fiber is riding on an RF carrier, e.g. cable TV signals. The rationale for using analog fiber optic links is basically economic: by avoiding the need to convert the desired signal to or from its original format, it is possible to reduce the cost of the system. For example, high quality analog links can transmit an 80 channel CATV feed in the standard NTSC format thereby avoiding the need to digitize this signal at the head end and then reconvert the signal at each users TV.

Although there is clearly overlap in the design issues between digital and analog links, there are a number of issues that are unique to the analog link. Common to both types of links is the optical fiber and the wavelengths of operation. All optical links use silica glass fibers in which the attenuation at the wavelengths of interest has been reduced to about 1/10 that of clear air. Thus the fibers provide a transmission medium where the loss is independent of the signal frequency and only a weak function of length. All optical links use wavelengths in the near infrared. Since the first diode lasers operated at 0.85 μm , the first generation links used this wavelength. Second generation links operate at longer wavelengths, 1.3 and 1.55 μm , where the optical losses are lower by about a factor of 4 and 10 respectively. Further at these wavelengths the dispersion is, or can be

made zero, thereby increasing the length-bandwidth product of the fiber.

All analog links in use today convey the signal via intensity modulation of the optical carrier. The two general ways of imposing the intensity modulation are shown in Figure 1. In direct modulation the signal modulates the laser's optical power directly. Since laser diodes are the only laser with reasonable bandwidth for this type of modulation, they are the only type of laser used for direct modulation. For external modulation, the laser is operated CW and the desired intensity modulation is imposed using a separate device. Although there are a number of types of external modulators, an integrated-optic version of a Mach-Zehnder interferometer is the one that is used universally today. Since the modulator eliminates the modulation requirement on the laser, there is a broader choice of lasers for external modulation. Because of their high fiber-coupled optical power and low relative intensity noise, RIN, diode-pumped, neodymium doped yttrium aluminum garnet, Nd:YAG lasers are the most commonly used sources for externally modulated links.

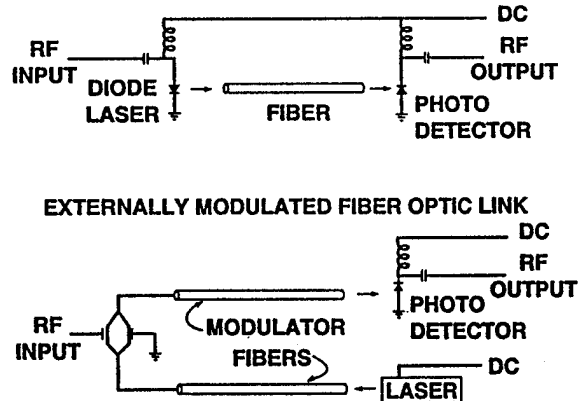


Figure 1: Analog Fiber-Optic Link Options

2. DIRECTLY MODULATED LINKS

As shown in Figure 2, there are basically two types of diode laser cavities in use today. The Fabry-Perot laser is the simpler of the two; the dominant reflections come from the cleaved end faces of the semiconductor substrate. Optical powers from microwatts to watts are commercially available. The cost of this type of laser is low, driven mainly by the market for lasers in every compact disk player. However the RIN and linearity do not meet the needs of demanding

1. This work was sponsored under Air Force Contract #F19628-95-C-0002. Opinions, interpretations, conclusions, and recommendations are those of the authors and are not necessarily endorsed by the United States Air Force.

analog link applications, such as CATV. Consequently there has been a substantial effort to develop a better diode laser. The distributed feedback, DFB, laser presently has higher linearity and lower RIN than a Fabry-Perot laser. In the DFB laser, the facet reflections are suppressed and the reflections come from a grating that is distributed along the length of the laser cavity. This and other processing changes have resulted in a diode laser that can meet the needs of CATV. However the more limited production and more complex structure result in a laser of significantly higher cost.

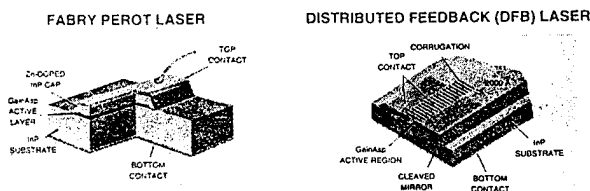


Figure 2: Diode Lasers for Direct Modulation

Link noise figure is one measure of the link improvement provided by a DFB laser. In Figure 3 the link noise figure is plotted vs. the average detector current for links using Fabry-Perot and DFB lasers. With careful setup, the Fabry-Perot based link can have a noise figure as low as 30 dB, whereas the DFB-based link has a noise figure of 20 dB over a wider range of operating currents. These data are valid for frequencies up to about 500 MHz. Above this frequency the DFB RIN begins to increase, thereby degrading the noise figure.

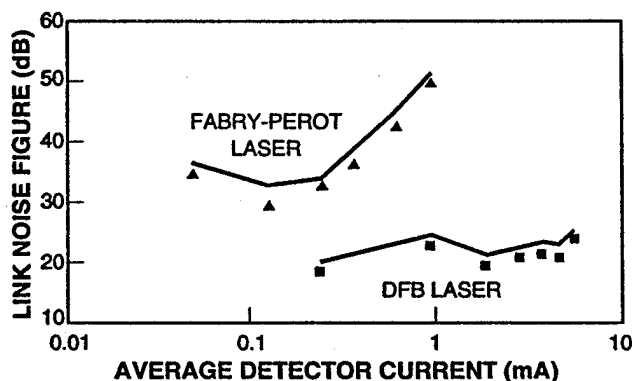


Figure 3: Link Noise Figure vs. Detector Current

Increased RIN is only one of the degrading effects as one goes to higher frequency links. Figure 4 shows the increase in link loss for some experimental high frequency links as well as the estimated link response if one were to use the latest diode lasers that have been reported in the literature. As will be seen below, the increase in link loss sets a lower bound on the minimum link noise figure. In principal any

link loss can be overcome via electronic amplifiers, however in practice the higher the link loss the more difficult it becomes to find an amplifier which has the gain and the dynamic range.

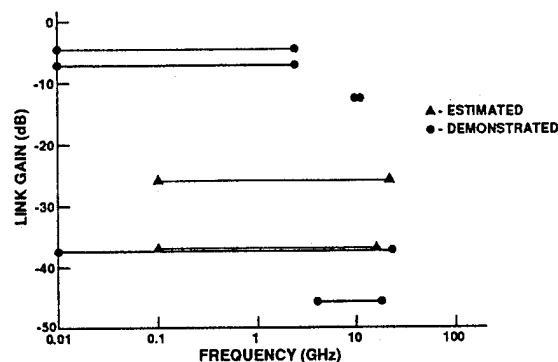


Figure 4: Link Gain vs. Frequency - Direct Modulation

Another important link parameter is dynamic range. There are several measures of dynamic range including maximum signal-to-noise floor or SNR, composite triple beat or CTB and intermodulation-free, IM-free, dynamic range. The limitation on dynamic range is imposed primarily by the modulation device, i.e., either the diode laser or the external modulator.

There are several factors that effect the dynamic range, among them are the laser structure - Fabry-Perot or DFB, laser design and the laser environment such as optical reflections into laser. Fabry Perot lasers typically have an IM-free dynamic range of 85-95 dB-Hz^{2/3} whereas DFB lasers generally have 100-110 dB-Hz^{2/3} of dynamic range. Controlling the reflections improves the dynamic range with either laser structure, however it more effective with DFBs. There are applications, especially the distribution of cable TV signals, where additional IM-free dynamic range is required. A variety of methods for increasing the dynamic range have been designed, however virtually all of them are propriety and so have received little or no public disclosure.

3. EXTERNALLY MODULATED LINKS

Virtually all externally modulated links use a modulator based on a Mach-Zehnder interferometer whose basic operation is shown in Figure 5. For modulations frequencies below about 3 GHz, it is reasonable to assume that changes in the modulation voltage are slow compared to the transit time of light in the waveguide arms. At higher frequencies, the transit time effects must be taken into account. This leads to the traveling wave modulator. The most efficient modulation is achieved when there is a match between the propagation velocities of the RF and optical fields. To date modulation up to 40 GHz has been obtained with such designs.

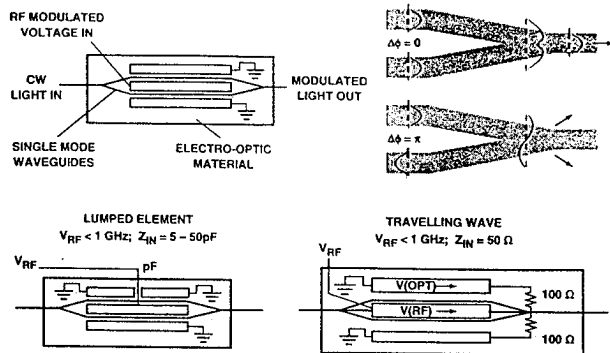


Figure 5: Mach Zehnder External Modulation

While link loss is also an issue with externally modulated links, this type of link has an additional degree of freedom which can be applied to overcoming the link loss. Link modeling has shown that unlike directly modulated links, the gain of externally modulated links increases as the square of the average optical power. Thus a 20 dB increase in optical power, for example from 100 μ W to 10 mW, results in a 40 dB increase in link gain. Using this approach, it is possible to have externally modulated links which are lossless or even have real power gain. The top two data points in Figure 6 show a bandpass link with about 10 dB of gain and a lossless broadband link. Present modulators have insufficient responsivity at higher frequencies to permit obtaining such results at higher frequencies using reasonable optical powers, as evidenced by the remaining curves in Figure 6. Also included are the estimated link gain using two recently reported modulators. Although both these modulators should provide previously unattainable link performance, neither has the link gain necessary for low noise performance.

Although the gain attracts attention, the link's RF insertion loss could easily be overcome using an RF amplifier. A more significant consequence of the links with low loss or gain is a lower link noise figure. For the link with 10 dB gain, the noise figure was 6 dB. While this is high compared with the state of the art for electronic amplifiers, it is a record low value for optical links. In fact this value may be low enough that no further low noise preamplifier is needed. Consider an application where the modulator will be used to remote the signal from a dipole antenna operating around 100 MHz. A 6 dB noise figure corresponds to a minimum detectable field strength of 2.3 μ V/m when the noise bandwidth is 1 MHz. Since the sky noise at 100 MHz produces a field of about 4 μ V/m, the sensitivity of this link is below the sky noise. Therefore the dipole terminals can be connected directly to the modulator electrodes, without any need for an electronic preamplifier. Several system applications, such as cable TV distribution and radar antenna remoting, require IM-free dynamic ranges beyond that attainable with present modulators. Thus there have been a number of methods proposed for increasing the IM-free dynamic range. Recently

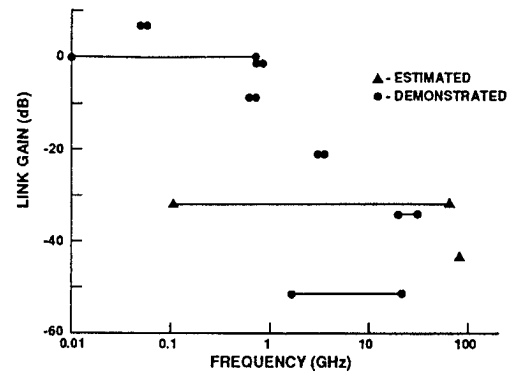


Figure 6: Link Gain vs. Frequency - External Modulation

Bridges and Schaffner () have written a link computer simulation which compared the IM-free dynamic range and noise figure of externally modulated links using any one of the various all-optical linearization techniques. The results of their calculations is shown in Figure 7. For the laser power and other link parameters they chose, the dynamic range of a simple Mach-Zehnder modulator, MZM, and a simple directional coupler, SDC, modulator come out to be about the same. Linearization either via a combination of MZMs or via multiple electrodes on a SDC improves the third order IM-free dynamic range, but at the penalty of increased noise figure. There is one case in their analysis that does not involve a noise figure penalty. By operating a SDC modulator at the bias point where the third derivative is zero, the third order distortion will be minimized; it will not be zero because third order distortion is also generated by the fifth order term in the SDC power series expansion. This bias point increases the second order distortion, which limits its application to systems whose bandwidth is less than an octave, so the second order distortion lies outside the bandwidth of interest. The interesting fact is that the noise figure is not degraded at this bias point, in fact it is actually improved slightly.

	MODULATOR	THIRD ORDER DYNAMIC RANGE (dB) IN 1 Hz BANDWIDTH	SECOND ORDER DYNAMIC RANGE (dB)* IN 1 Hz BANDWIDTH	NOISE FIGURE
	MZM	109.9	> THIRD ORDER	38.1
	DCM	109.4	> THIRD ORDER	38.0
	DCM (Special)	135.4	29.1	36.7
	2MZM	126.2	> THIRD ORDER	48.8
	3MZM	133.0	> THIRD ORDER	54.6
	LDCM + 1	126.3	> THIRD ORDER	45.9
	LDCM + 2	129.4	> THIRD ORDER	43.3

ALL ENTRIES IN dB
 *dB BELOW SIGNAL AT INPUT, MAKING IMD = NOISE
 REFERENCE: BRIDGES & SCHAFFNER

Figure 7: Optical Linearization Techniques

To give an overview of the state of the art in analog link performance, Figure 8 plots the published gain and noise figure for both directly and externally modulated links. Also

shown on this figure are two fundamental limits on link performance which have been derived by Cox (). From this plot it is clear that to reduce the link noise figure, it is essential to improve the link gain, i.e. to reduce the link loss. This will most likely require the development of modulation devices with higher responsivity.

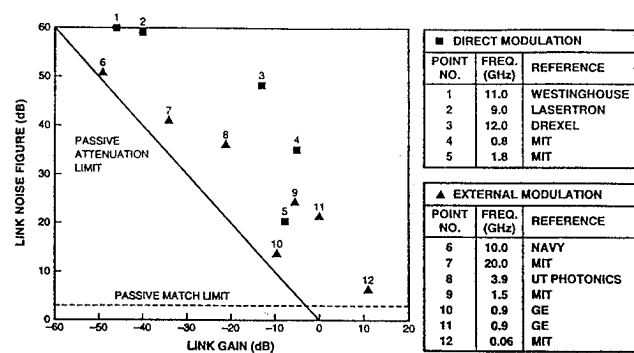


Figure 8: Summary of Recent Link Performance Results

4. APPLICATIONS

One of the first and probably most widespread applications of analog fiber optic links is to use fiber to replace the coaxial cable for the distribution of "cable" TV, CATV, signals. There are a number of ways to do this, the method employed by AEL () is shown in Figure 9. There block diagram is a little more complex than normal because they are using much of the same hardware to also distribute cellular telephone signals. There approach uses external modulation throughout. Wavelength division multiplexing permits full duplex operation, which is required for the telephone, and permits the CW lasers for both outgoing and incoming links to be located at the head end while using only two fibers. By using a proprietary linearization scheme, AEL is able to exceed the distortion requirements for CATV.

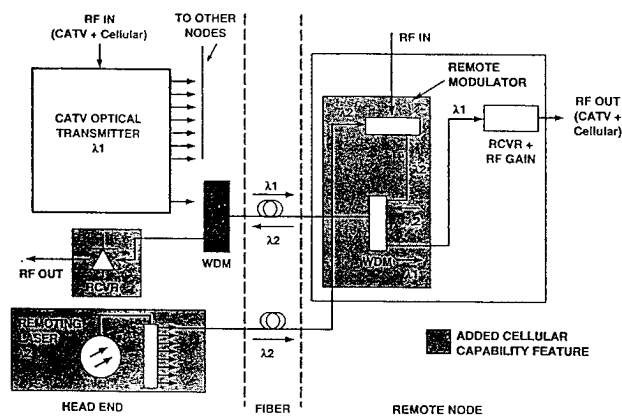


Figure 9: Duplex Fiber-Optic CATV - Block Diagram

Distribution of cellular signals from the telephone interface to the antenna site, even without CATV signals, is a

growing application area for fiber optics. The hardware offered by Allen Telecom Group uses direct modulation to remote the 16 telephone channels of the standard 900 MHz cellular band. A photograph of the pole mounted portion of their fiber-fed equipment is shown in Figure 10. Phased array radars are another potential application of analog fiber optics. ARPA and Rome Labs contracted Hughes build a prototype phased array antenna that used analog fiber optics. A block diagram of the radar is shown in Figure 11. This technology eliminated the change in beam direction, or beam squint, as the radar center frequency was changed. Direct modulation feeding various lengths of fiber was used to implement this time delay. Fiber optics was also used to distribute the radar wave form to all the subarrays. External modulation was used for this function because the output of a high power CW laser/external modulator combination could be divided, via an eight way splitter, to feed each of the subarrays.

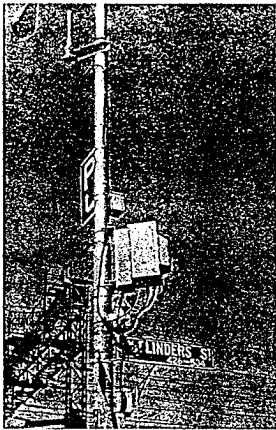


Figure 10: 16-Channel, 900-MHz Fiber-Fed Microcellular Base Station

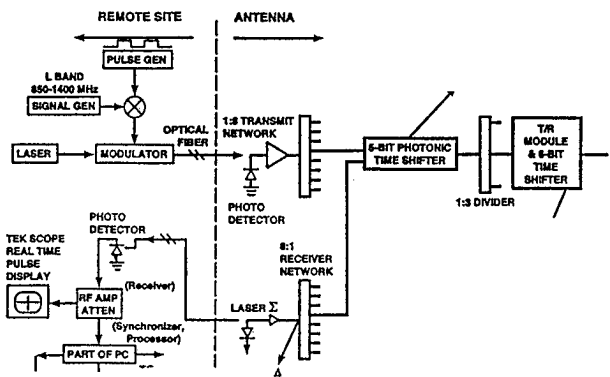


Figure 11: ARPA/Rome Labs/ Hughes - Photonic Phased Array Radar

REFERENCES

- [1] W. B. Bridges et al, Review of Linearized Integrated Optic Modulators. PSAA IV, Monterey, CA, Jan 1994.
- [2] C. H. Cox, Analog Fiber-Optic Link Performance: Status and Limits. PSAA IV, Monterey, CA, Jan 1994.

PHOTONIC SYSTEMS FOR ANTENNA CONTROL

Michael L. VanBlaricum, Catherine J. Swann

Toyon Research Corporation

75 Aero Camino, Suite A

Goleta, CA 93117

1. Introduction

There are many techniques for optically carrying an RF signal from an antenna element to its receiver, thus, optically isolating the antenna. However, if the antenna needs to be tuned or the matching network needs to be controlled then it is desirable to perform that function optically as well. We show that an optically-linked electrically-small loop can be tuned over almost an octave of bandwidth by using remote optical control via an optically variable reactance. Both theoretical and experimental results are presented.

2. Tuning of Photonically Linked Antennas

Connecting optical modulators and fiber optic links to an antenna allows flexibility in the system design beyond that available by conventional systems. This is due to two inherent properties of the optical links and modulators: 1) The broad bandwidth of optical modulators and optical links can be very large; and 2) The effective impedance of the optical modulator is reactive with a very small (a few ohms) resistive component.

The broad bandwidth allows the potential for connecting a broadband antenna to the link and remoting the receiver electronics. For example, in a measurement one might connect a probe antenna with more than a decade of bandwidth (such as the cavity backed spiral antenna) to the optical link. Using photonic modulators and links for this only makes use of the broad bandwidth and low loss of the optics. It still uses conventional antennas which must be mechanically supported and can have a fairly large interaction with the antenna or system under test.

The highly reactive impedance of the MZI modulator allows one to construct a field sensor system that has high sensitivity while small in both physical size and electromagnetic cross section. As mentioned above, the MZI impedance is generally capacitive with some resistive losses due to the small diameter of the electrodes and their leads. This difference in the load lends itself to narrow band matching with small antennas, such as short dipoles or small loops.

An electrically short dipole antenna or electrically small loop can be connected to an MZI with a matching / tuning circuit such that the overall circuit Q is very high and the voltage gain of the circuit can be 20 dB or more. This is possible because the resistive losses in an electrically short antenna due to radiation and attenuation are just a few Ohms. Hence, the impedance of the antenna can be combined with the impedance of the MZI and a tuning circuit to form a series resonant circuit with only a few Ohms of loss. This resonant circuit can then be tuned over a large band by changing the capacitance of the tuning circuit. **Figure 1** presents a block diagram of this concept using a small loop antenna connected through a matching network to an optical modulator. **Figure 2** presents a schematic diagram for the antenna system of **Figure 1**.

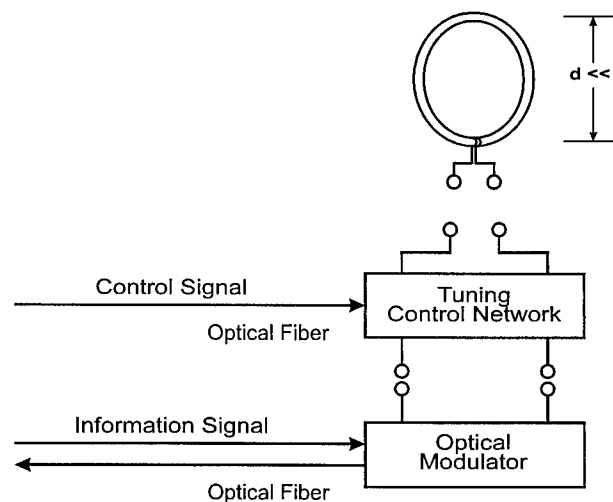


Figure 1 - Block diagram of a photonically connected and controlled electrically small loop antenna.

Conventional approaches for tuning the antenna / matching network described above require electrical (hard wire) connectivity to the tuning circuit. This is not appropriate for optical-based sensor systems because it defeats the passive nature of the fiber optical link. However, with the use of Toyon's optically variable capacitor (OVC™), it is possible to control the reactance of devices optically, while maintaining the all-dielectric characteristic of the link. The capacitance can be varied over almost a decade. Tuning

circuits have been built that allow an antenna's resonance to be swept over nearly an octave of bandwidth by changing the intensity of light incident on the tuning circuit.

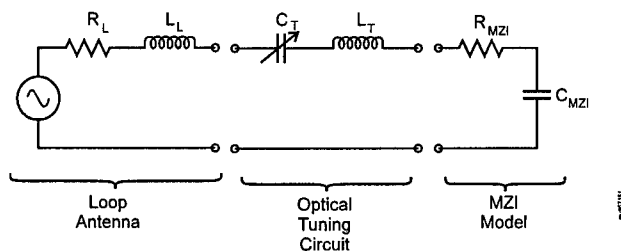


Figure 2. Schematic diagram of the equivalent circuit for the photonic antenna of Figure 1.

To test the complete photonic link and control of a loop antenna as shown in Figure 1, we built a half-loop antenna above a ground plane and reactively matched (See Figure 2) it to a MZI modulator using an OVC™. The diameter of the loop was 1.5 cm. A half loop antenna was used because we planned to illuminate it in a TEM (Crawford) cell [1] and needed to feed it against a ground plane.

Before performing the measurements, we modeled the entire system in our PHLASH™ code. PHLASH is a PC/Windows-based system engineering tool for predicting the performance of sensor and antenna systems which include a fiber optic link in their architecture. This particular link included an MZI with a V_π of 5.6 volts. The link was driven with only 6 mW of laser power. Hence, the link was not designed for optimal link gain or sensitivity. Figure 3 shows the predicted link gain values for the two extreme values of our OVC™. For the dark case the capacitance was 19 pF and the loop was tuned to 248 MHz. For the case of maximum light, the OVC™ produced a capacitance of 3 pF and the loop was tuned to 408 MHz.

Figure 4 shows the measured gain for the tuned half-loop link. The measured gain is uncalibrated because of the TEM cell measurements. The tuning range and the Q values were of principal interest to us. From Figure 4 the tuning range is seen to go from 242 MHz to 413 MHz or 71% which is greater than that which we had predicted. The measured Q is seen to be fairly close to the predicted value.

The above test was not optimized for link sensitivity. It was done to prove that a small antenna could be tuned and connected photonically. Subsequent to this test, we used

PHLASH to predict what the link gain and sensitivity for a loop antenna with a 4-cm loop diameter. We optimized the photonic link parameters to reflect the state-of-the-art available today. We used a MZI with a V_π of 0.75 volts and a laser with 150 mW of output power.

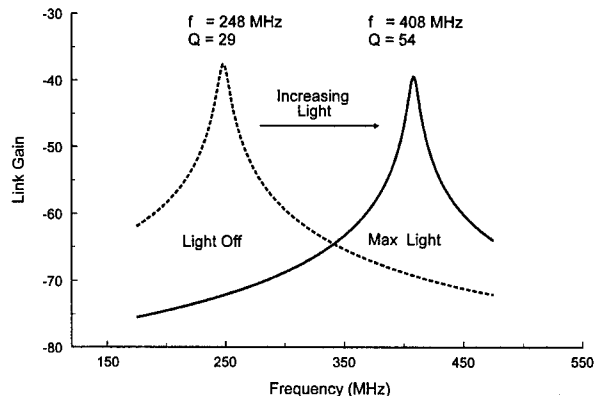


Figure 3. Predicted link gain for the 1.5-cm half-loop antenna reactively matched to the MZI-based link showing the two extreme states of the OVC™ tuning capacitor.

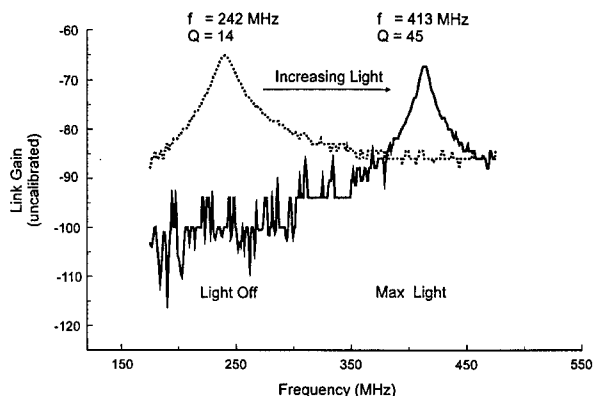


Figure 4. Measured link gain (uncalibrated) for the 1.5-cm diameter half-loop antenna reactively matched to the MZI-based link.

Figure 5 presents the predicted link gain for the 4-cm loop and optimized link. In this study, the same OVC™ was used. The larger antenna caused the tuning range to be lowered to 180 to 300 MHz. The tuning bandwidth was 66% which is the same as that predicted with the smaller antenna.

However, in this case, the link power gain is predicted to be about 22 dB. **Figure 6** shows that this translates into a minimum detectable field of less than 10 $\mu\text{V}/\text{meter}$ at the tuned value. It is interesting to note, for the light-off case, that the minimum sensitivity stays lower than 100 $\mu\text{V}/\text{meter}$ from below 100 MHz to above 350 MHz.

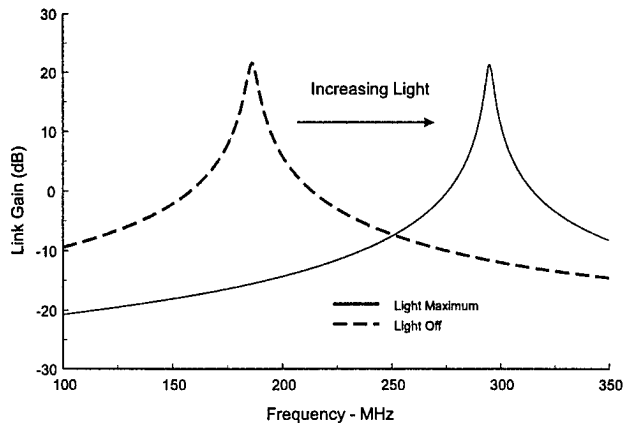


Figure 5. Predicted link gain for a 4-cm diameter loop antenna reactively matched to an optimized MZI-based photonic link. The gain is shown for the two extreme settings of the OVC™ capacitor.

Figure 7 presents the predicted dynamic range in a 10 kHz bandwidth for this system. The spurious-free dynamic range (SFDR) is nearly 90 dB everywhere except at the point of maximum link gain. The dynamic range, as it is calculated for the photonic link, is

$$\begin{aligned} SFDR &= \frac{2}{3} (IP3 - P_{o, mds}) \\ &= \frac{2}{3} (IP3 + 174 \text{ dBm} - NF - 10 \log(B) - G_a) , \end{aligned}$$

where $IP3$ is the third order intercept point for the MZI, $P_{o, mds}$ is the minimum detectable signal at the output of the link, NF is the link noise figure, G_a is the link gain, and $kT = -174 \text{ dB}$.

The minimum detectable signal at the output of the link is defined as

$$P_{o, mds} (\text{dBm}) = -174 \text{ dBm} + 10 \log B + NF + G_a$$

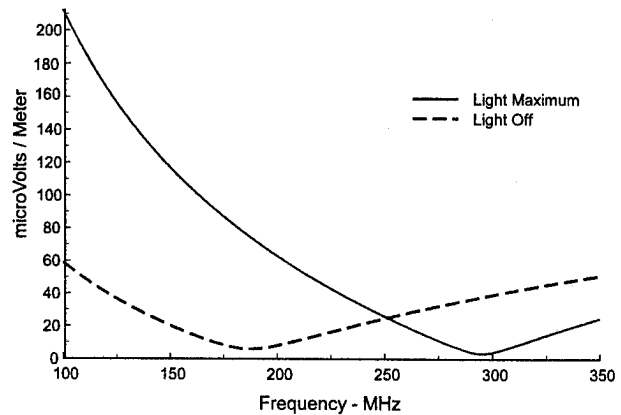


Figure 6. Predicted minimum detectable electric field for the 4-cm diameter loop antenna reactively matched / tuned to an optimized MZI-based photonic link.

From the expression for SFDR, it is clear that as the link gain goes up, the dynamic range goes down. Hence, design tradeoffs can be performed to maximize dynamic range at the expense of link gain.

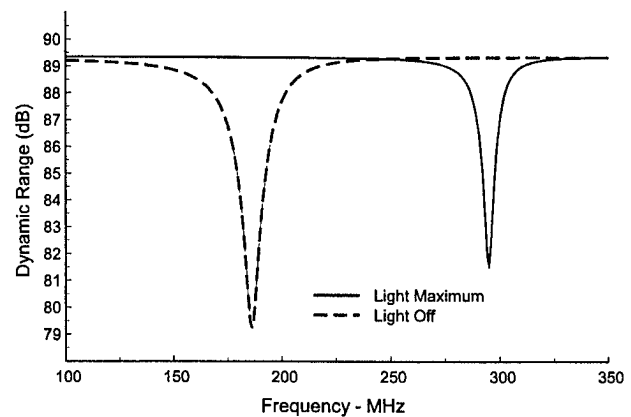


Figure 7. Predicted dynamic range for the 4-cm diameter loop antenna reactively matched/tuned to the optimized MZI-based photonic link.

3. Summary

In this paper we presented experimental data demonstrating that an photonically-linked electrically-small loop antenna can be tuned over a 71% bandwidth using an optically variable capacitor. We also showed theoretically that this technique can potentially give a very sensitive small receive antenna that is completely isolated optically. This bodes optimistically for building antenna near-field or chamber probes that do not greatly perturb the fields they are measuring.

4. References

- [1] M.L. Crawford, "Generation of Standard EM Fields Using TEM Transmission Cells," *IEEE Transactions on Electromagnetic Compatibility*, Vol. EMC-16, No. 4, Nov. 1974, pp 189-195.

PERFORMANCE ANALYSIS OF OPTICAL FIBER TDMA SYSTEMS

Jian-Guo Zhang

Telecommunications Program
School of Advanced Technologies
Asian Institute of Technology
G.P.O. Box 2754, Bangkok 10501, Thailand
jgzhang@cs4.ait.ac.th

ABSTRACT

In this paper, a simple model is presented to analyze the performance of optical fiber Time-Division Multiple Access (OF-TDMA) systems. The sensitivity analysis of OF-TDMA receivers is carried out by taking account of the effects of optical transmitter's extinction ratio, photodetector and electrical amplifier noise. It is shown that the non-zero extinction ratio is a major impairment which significantly degrades the receiver sensitivity when the number of users N is large. Compared with the single-user system, an OF-TDMA system requires far lower extinction ratio to alleviate the performance degradation when N is larger.

1. INTRODUCTION

Optical fiber Time-Division Multiple Access (TDMA) is a synchronous scheme which shares the huge bandwidth of single-mode optical fibers by dividing time into slots and specifying distinct time slots of a frame for different users. Optical fiber TDMA (OF-TDMA) can offer a high throughput by using optical signal processing and does not suffer from the cumulative delay as encountered when using asynchronous methods [1]. Thus, OF-TDMA networks are attractive to fixed data-rate or homogeneous services, continuous-type traffic, and high-data-rate terminals, such as digital TV or HDTV distributions and broadcasting, digital telephone, and circuit-switching based Synchronous Transfer Mode. In order to feasibly design OF-TDMA networks, the analysis of system performance would be required. In this paper, we develop a theoretical model for OF-TDMA systems and present an analytical expression to the receiver sensitivity of OF-TDMA systems, by which fast performance evaluation can be easily carried out.

2. SYSTEM MODEL

The block diagram of an OF-TDMA network is illustrated in Figure 1. A common clock of rate $1/T$ is used to synchronize all the OF-TDMA transmitters. Then N optical transmitters with the same wavelength operate at a data rate $F_b = 1/T$, and they are assumed to have the identical peak output power. Short optical pulses of width T/N are generated by each electrooptic (EO) modulator at a transmitter when data bits "ONEs" are issued. Each modulated pulse stream is further delayed to the assigned slot per data frame, and it is multiplexed with other $N - 1$ streams through a $N \times N$ optical star coupler with uniform outputs. On the other hand, an optical clock signal is distributed to N receivers through separate fibers. In order to achieve the correct frame synchronization, the length of optical fiber from each station (containing a transmitter-receiver pair) to the star coupler

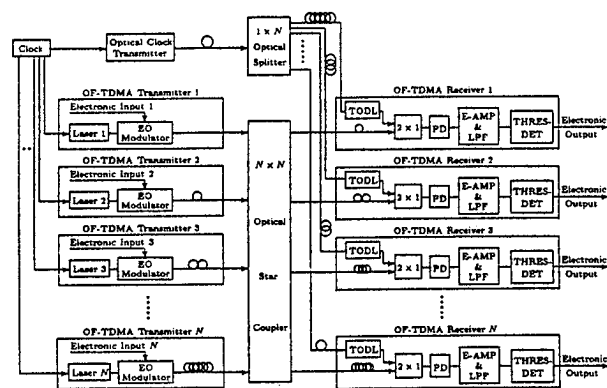


Figure 1: Block diagram of an OF-TDMA network using optical processing.

must be properly chosen [1]. At each receiver, the optical clock stream is appropriately delayed by a tunable optical delay line (TODL) as designed in [2], and therefore, is superimposed to the incoming OF-TDMA signal in the desired time slot by using a 2×1 optical combiner (see Figure 1). The combined optical signals are then converted into the electrical one at a wideband photodetector (PD) followed by the electrical amplifier (E-AMP) and low pass filter (LPF). Finally, a high-speed threshold detector (THRES-DET) is used to regenerate the data sent from the desired transmitter.

For the convenience of analysis, we assume that an optical transmitter consists of a continuous-wave (CW) laser and an ultrafast EO modulator. Then the extinction ratio r of optical transmitters is equal to that of EO modulators, while for the mode-locked laser scheme [1], we can still use an equivalent r which is normally very small [3]. For convenience, dispersion and distortion of fibers are neglected, and OF-TDMA decoders are treated as ideal incoherent optical signal processors. Moreover, optical pulses at each photodetector are assumed to be ideal rectangular.

Since all the transmitters are well synchronized, the multiplexed signal $Y(t)$ at the output of a $N \times N$ optical star coupler can be written as:

$$Y(t) = \sum_{i=1}^N \left\{ \sum_{j=-\infty}^{+\infty} d_j^{(i)} h_p(t - jT - (i-1)T_p) \right\} \quad (1)$$

where $d_j^{(i)}$ denotes the i -th user's optical power in the j -th OF-TDMA frame. It takes on a value E corresponding to the data bit 1 sent or rE corresponding to the data bit 0 sent. $T_p = T/N$ is the slot width. Here $h_p(t)$ represents a rectangular pulse in a time slot, i.e.,

$$h_p(t) = \begin{cases} 1 & -\frac{T_p}{2} \leq t \leq +\frac{T_p}{2} \\ 0 & \text{otherwise} \end{cases} \quad (2)$$

Without any loss of generality, we treat user 1 as the desired user. Considering periodical repetition characteristics of clock signal and TDMA frames, we can write the optical TDMA signal at the input of decoder 1 as

$$Y_1(t) = \sum_{j'=-\infty}^{+\infty} \left\{ \sum_{i=1}^N d_{j'-L}^{(i)} h_p(t - j'T - (i-1)T_p) \right\}$$

Similarly, the clock signal $Y_0(t)$ at the input of decoder 1 can be expressed as

$$Y_0(t) = \sum_{j'=-\infty}^{+\infty} \varphi h_p(t - j'T) \quad (3)$$

At receiver 1, TDMA decoder 1 adds $Y_0(t)$ to the received TDMA signal $Y_1(t)$, because the desired pulse and delayed clock signal occupy the same time slot per frame. The output of decoder 1 is given by

$$\begin{aligned} p_1(t) &= \varepsilon \{Y_1(t) + Y_0(t)\} \\ &= \sum_{j=-\infty}^{+\infty} \left\{ \left(\Phi_{j-L}^{(1)} + \Upsilon \right) h_p(t - jT) + \right. \\ &\quad \left. + \sum_{i=2}^N \Phi_{j-L}^{(i)} h_p(t - jT - (i-1)T_p) \right\} \\ &= \sum_{m=-\infty}^{+\infty} b_m h_p(t - mT_p) \end{aligned} \quad (4)$$

where L is a constant integer, $\Phi_{j-L}^{(1)} = rA$ or A , and $\Upsilon = rC$ or C , here A and C are peak optical power of TDMA and optical clock signals at the PD, respectively. b_m is the received optical power in the m -th slot, which can take one of four levels depending on the OF-TDMA pulse sequence pattern [4].

Since the received optical pulse is ideal rectangular, the intersymbol interference between optical pulses is zero. Then we can simply need to consider the isolated optical pulse $p(t) = b_0 h_p(t)$ instead of a sequence $p_1(t)$ when we analyze the noise. For the convenience of analysis, the filter is assumed to be an ideal low pass filter (LPF) and the intersymbol interference at the LPF is neglected.

3. RECEIVER SENSITIVITY OF OF-TDMA SYSTEMS

In this paper, we consider the APD-based optical receivers using a FET-front-end transimpedance amplifier of which the output noise power $< n_a^2 >$ is written as [4]

$$\begin{aligned} < n_a^2 > &= \left(\frac{4k\Theta}{R_b/R_f} + 2eI_g \right) B + \\ &\quad + \frac{8\pi^2 k\Theta \Gamma C_T^2 B^2}{g_m} \left(f_c + \frac{2B}{3} \right) \end{aligned} \quad (5)$$

where k is Boltzmann's constant, Θ is the absolute temperature, and B is the LPF bandwidth. e is the charge of an electron, C_T is the equivalent total input capacitance, R_b is the bias or load resistance, and R_f is the feedback resistance. Γ is a numerical constant. f_c is the $1/f$ -noise corner frequency. I_g is the FET gate leakage current, and g_m is the FET transconductance [5].

At the output of a LPF, the power of shot noise at the sampling time $t = 0$ is given by [4]

$$\begin{aligned} \langle n_s^2(0) \rangle &= \frac{4eRG^2F(G)b_0B}{\pi} \\ &\cdot \int_0^{2\pi T_p B} \frac{\sin(x)}{x} dx - \frac{2eRG^2F(G)}{\pi^2 T_p} \\ &\cdot b_0 [1 - \cos(2\pi T_p B)] \end{aligned} \quad (6)$$

and the average signal voltage $\langle V_s(t) \rangle$ at $t = 0$ is written as

$$\langle V_s(0) \rangle = \frac{2RGb_0}{\pi} \int_0^{\pi T_p B} \frac{\sin(y)}{y} dy \quad (7)$$

where $R \triangleq \frac{\eta e}{h\nu}$ is the photodetector responsivity [5]. G is the average value of the avalanche gain, and $F(G) = KG + (2 - 1/G)(1 - K)$ is the avalanche excess-noise factor, here K is the ratio of the ionization coefficients of electrons and holes of the APD.

The noise power due to the APD dark current is then written as

$$\langle n_d^2 \rangle = 2eB \{ I_{du} + G^2 F(G) I_{dm} \} \quad (8)$$

where I_{du} and I_{dm} are the dark current components which is not subject to and undergoes the avalanche multiplication process, respectively [5].

After the tediously mathematical treatment, the minimum peak optical power required to ensure a given bit error rate (BER) at OF-TDMA receivers is thus expressed as

$$\begin{aligned} P_m &= (Nr - r + q + 2) \left\{ \frac{U_1 + U_2}{\left(\frac{U_3 - U_4}{Q}\right)^2} + \frac{2}{\left(\frac{U_3 - U_4}{Q}\right)^2} \right. \\ &\quad \left. \cdot \sqrt{U_1 U_2 + \left(\frac{U_3 - U_4}{Q}\right)^2 U_0} \right\} \end{aligned} \quad (9)$$

where $q = \frac{C-A}{A}$ is the excess clock-to-TDMA signal ratio, and $Q = 6$ for $BER = 1 \times 10^{-9}$.

$$U_0 = 2eB \{ I_{du} + G^2 F(G) I_{dm} \} + \langle n_a^2 \rangle \quad (10)$$

$$\begin{aligned} U_1 &= (Nr - r + q + 2) \left\{ \frac{4eRG^2F(G)B}{\pi} \right. \\ &\quad \left. \cdot \int_0^{2\pi T_p B} \frac{\sin(x)}{x} dx - 2eRG^2F(G) \cdot \right. \end{aligned}$$

$$\left. \frac{1 - \cos(2\pi T_p B)}{\pi^2 T_p} \right\} \quad (11)$$

$$U_2 = \frac{(Nr + q + 1)U_1}{Nr - r + q + 2} \quad (12)$$

$$\begin{aligned} U_3 &= \frac{2RG(Nr - r + q + 2)}{\pi} \\ &\cdot \int_0^{\pi T_p B} \frac{\sin(y)}{y} dy \end{aligned} \quad (13)$$

and

$$U_4 = \frac{(Nr + q + 1)U_3}{Nr - r + q + 2} \quad (14)$$

The OF-TDMA receiver sensitivity S_r is thus defined as

$$S_r = 10 \log_{10} \frac{P_m}{10^{-3}} \quad (\text{dBm}) \quad (15)$$

4. NUMERICAL RESULTS AND DISCUSSIONS

At present, mature optical receivers can have a wide bandwidth of 10 GHz [6]. We can then reasonably choose $B = 10$ GHz and the chip rate $1/T_p = 10$ Gbit/s. The other parameters used for the calculation of receiver sensitivity are: $C_T = 0.5$ pf, $R_b = 10$ M Ω , $R_f = 390$ Ω , $\lambda = 1.55$ μm , and the parameters of InGaAsP APD and GaAs MES-FET are taken from [6]. Since $1/T_p$ is fixed, the data rate $1/T$ decreases as N increases.

Figures 2a and 3 show the effects of the non-zero extinction ratio r on the sensitivity of OF-TDMA receivers. For a fixed r , the OF-TDMA receiver sensitivity varies with the number of users N , which gets worse as N increases, because the effect of the accumulated DC optical power caused by the non-zero r is more severe when r or/and N becomes larger. For example, the degradation of optimum receiver sensitivity is 17.6 dBm when N increases to 2000 for $r = 0.01$, whereas the sensitivity degradation is only 5.2 dBm for $r = 0.001$ and N to 2000. Thus, for a given N the lower r is required to alleviate the performance degradation. Since using the mode-locked laser scheme as given in [1] can achieve a very low equivalent r , for the fixed output peak power of transmitters, this scheme can offer more users than the CW laser scheme. Figure 2b shows the effect of optical clock amplitude on the sensitivity of OF-TDMA receivers, which becomes more significant for a lower N , while the degradation is smaller when N is larger. It means that the receiver sensitivity can

be improved by separating OF-TDMA signal from clock pulses for the signal decision (i.e., $q = -1$), at the expense of increasing the receiver complexity. It is important to note that, as N increases, the optimum G decreases and the suboptimum G window becomes sharp. This requires the more critical control of G . Moreover, from Figure 2a, one can find that there would be no optimum G (> 1) if N becomes very large for $r = 0.01$, which means that there is no advantage to use APDs in this case.

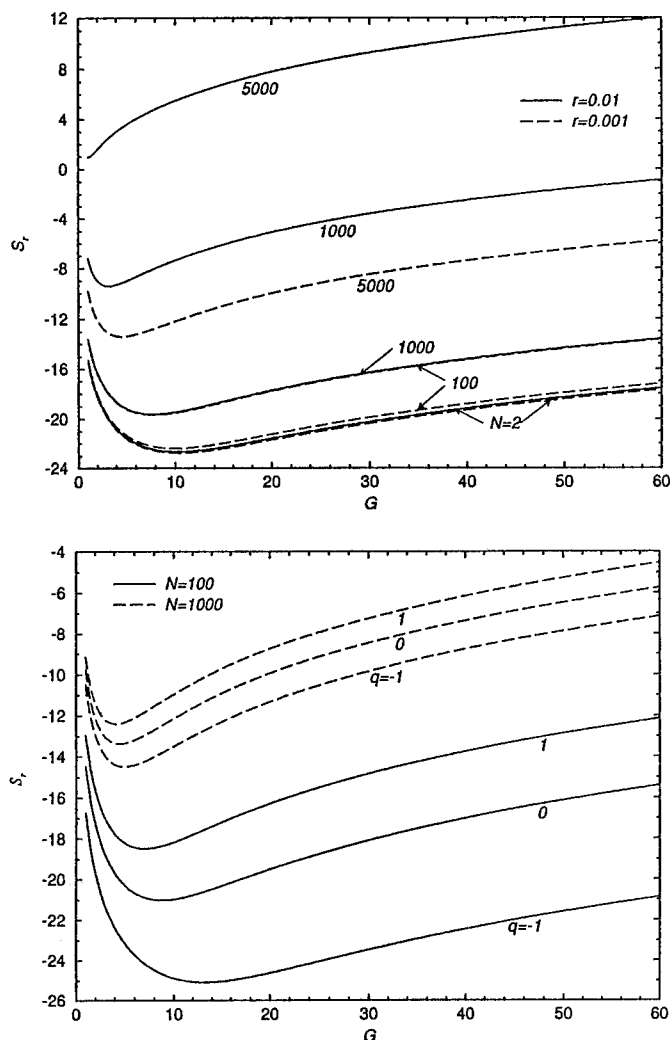


Figure 2: The OF-TDMA receiver sensitivity S_r versus the average APD gain G (a) as a function of N and r for $q = 0$ and (b) as a function of q and N for $r = 0.005$.

5. CONCLUSION

An explicit expression for the OF-TDMA receiver sensitivity has been presented in this pa-

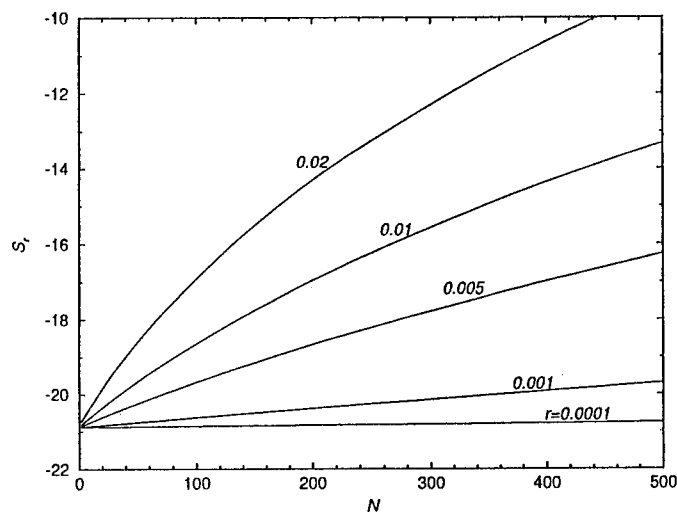


Figure 3: The OF-TDMA receiver sensitivity S_r versus the number of users, N , as a function of r for $q = 0$ and $G = 6$.

per, by which the fast performance evaluation can be easily obtained. Further improvement on the proposed model is to involve the effects of pulse spreading and distortion as well as timing jitter.

ACKNOWLEDGMENT

The author thanks Prof. G. Picchi of the University of Parma for helpful discussions. The author also acknowledges Dr. G. Migliorini for support.

References

- [1] P. R. Prucnal, M. A. Santoro, and S. K. Sehgal, "Ultrafast all-optical synchronous multiple access fiber networks," *IEEE J. Selec. Areas Commun.*, vol. SAC-4, pp. 1484-1493, Dec. 1986.
- [2] P. R. Prucnal, M. F. Krol, and J. L. Stacy, "Demonstration of a rapidly tunable optical time-division multiple-access coder," *IEEE Photonics Technol. Lett.*, vol. 3, pp. 170-172, Feb. 1991.
- [3] A. S. Hou, R. S. Tucker, and G. Eisenstein, "Pulse compression of an actively modelocked diode laser using linear dispersion in fiber," *IEEE Photonics Technol. Lett.*, vol. 2, pp. 322-324, 1990.
- [4] J.-G. Zhang and G. Picchi, "Performance analysis of optical time-division multiple access systems: Ideal rectangular optical pulses," Internal Report, Dept. Inform. Eng., University of Parma, 1992.
- [5] T. V. Muoi, "Receiver design of optical-fiber systems," Chapter 12 in *Optical-Fiber Transmission*, E. E. Bert Basch, ed. Indianapolis: Sams, 1987.
- [6] S. E. Miller and I. P. Kaminow, eds, *Optical Fiber Telecommunications II*. San Diego: Academic, 1988.

AN ERROR FLOOR REDUCTION SCHEME FOR DPSK RECEIVERS IMPAIRED BY PHASE NOISE

Kamran Kiasaleh, Member IEEE

The University of Texas at Dallas

P.O. Box 830688, EC 33, Richardson, TX 75083-0688

(214) 883-2990, FAX (214) 883-2710 E-mail: kamran@utdallas.edu

ABSTRACT

A technique for reducing the error floor of differential phase-shift-keying (DPSK) receivers impaired by phase noise is introduced and analyzed. In the proposed DPSK receiver, the bandwidth of integrate-and-dump (I&D) filters are decreased so that multiple samples per symbol duration of the received signal are made available to the post-detection and decision circuitry. The proposed post-detection circuitry, hereafter referred to as one-bit-shifted expanding-window (OBS-EW) post-detection processing scheme, correlates the acquired samples that are centered about the signal transition point in a two-symbol signaling interval. For a phase-noise-limited operation, it is shown that the proposed OBS-EW scheme achieves an error floor that is significantly smaller than that of a conventional DPSK receiver.

I. DPSK Signaling Format

DPSK receivers provide phase-coherent detection of differentially-encoded signals in the absence of phase synchronization when the phase ambiguity at the receiver is assumed to be constant for at least two consecutive symbol intervals [1, 2]. This, in turn, reduces receiver complexity, which ultimately results in a reduction in the receiver cost. Optical DPSK receivers have received a great deal of attention in recent years (for example, see [3, 4, 5]). The performance of a DPSK receiver, however, is quite sensitive to any fluctuations in the signal phase that may violate the aforementioned constant-phase assumption. In practice, phase instability that is commonly modelled as a Brownian motion is an ever-present feature of an optical or RF receiver. This impairment ultimately imposes an error floor on

the performance of DPSK systems, see [3]. To combat this effect, a number of techniques have been proposed [4, 6, 7, 8]. In [6], a post-detection strategy, hereafter referred to as fixed-window (FW) processing, was introduced, where the integration interval of I&D filters of a DPSK receiver is decreased. This results in the acquisition of multiple samples per symbol time. In this paper, an alternate scheme is introduced where the samples that are centered about the signal transition point in a two-symbol interval are correlated. In a DPSK receiver, the intermediate frequency (IF) version of a DPSK signal at the receiver is given by

$$x_{IF}(t) = A \cos [\omega_{IF}t + \psi(t) + \phi(t) + \theta] + n(t) \quad (1)$$

where A denotes the signal amplitude in V, ω_{IF} is the intermediate frequency in rad/sec, $\psi(t)$ signifies the total phase noise at the receiver, and $\phi(t) = \sum_{k=-\infty}^{\infty} \phi_k P(t - kT)$ is the information-bearing phase process with ϕ_k denoting the k th DPSK symbol taking on $\{0, \pi\}$ with equal probability, T representing the symbol interval, and $P(t)$ denoting a non-return-to-zero (NRZ) pulse with unit amplitude and a duration of T sec. Moreover, θ is an unknown (random), but constant phase that is uniformly distributed on $[-\pi, \pi]$ and $n(t)$ is an additive white Gaussian noise (AWGN) with a two-sided power spectral density (PSD) of $\frac{N_0}{2} V^2/Hz$, denoting the receiver thermal noise. Also, $\psi(t) = \int_0^t \mu(\tau) d\tau$, where $\mu(\tau)$ is a white Gaussian noise process with two-sided PSD level $2\pi\Delta\nu$ in $(rad/s)^2/Hz$ [$\Delta\nu$ denotes the full-width-at-half-maximum (FWHM) linewidth $\Delta\nu$ (in Hz) of the oscillator and flicker noise is assumed to be negligible]. Moreover,

$n(t) = \sqrt{2}n_c(t) \cos(\omega_{IF}t) - \sqrt{2}n_s(t) \sin(\omega_{IF}t)$. Next, we proceed to provide expressions for A and $\frac{N_0}{2}$ for the case of optical heterodyne detection. In this case, the above signal represents the amplified voltage across the photodetector's load resistance. Hence [5, 9], $A = 2Rr\sqrt{G_A P_s P_{LO}}$ in V and $\frac{N_0}{2} = G_A q r^2 R P_{LO}$ in V^2/Hz ; $f_L \leq |f| \leq f_H$, where r is the resistance in Ω of the photodetector's load resistor, G_A is the power gain of the IF amplifier, q is the charge of an electron, R is the photodetector's responsivity in amps/watt, P_{LO} is the power of the local laser, P_s is the received optical signal power, and f_L and f_H denote the 3 dB frequencies in Hz (about the IF frequency) of the IF amplifier's response. Based upon the above definition of $n(t)$ and assuming that the amplifier response is symmetrical about the IF frequency, $n_c(t)$ and $n_s(t)$ may be modelled as two independent, identically distributed Gaussian random processes with two-sided power spectral density levels $\frac{N_{oc}}{2}$ and $\frac{N_{os}}{2}$, respectively, which are given by $\frac{N_0}{2} = \frac{N_{oc}}{2} = \frac{N_{os}}{2} = G_A q r^2 R P_{LO}$ in V^2/Hz ; $0 \leq |f| \leq \frac{f_H - f_L}{2}$ Hz. Next, we resort to a complex representation of the DPSK receiver operation. To that end, we have

$$x_{IF}(t) = \text{Re}\{Y_{IF}(t) + Z(t)e^{j\omega_{IF}t}\} \quad (2)$$

where $Y_{IF}(t) = Ae^{j[\omega_{IF}t + \psi(t) + \phi(t) + \theta]}$ and $Z(t) = \sqrt{2}[n_c(t) + jn_s(t)]$. The upper case letters are used hereafter to represent complex signals. The IF signal is processed by the inphase and quadrature phase (I&Q) processing, followed by the I&D circuitry. This may be viewed as a shift to baseband followed by an integration of the IF signal. That is, we need to be concerned with $Y(t) = Y_{IF}(t)e^{-j\omega_{IF}t} = A \exp\{j[\psi(t) + \phi(t) + \theta]\}$ and $Z(t)$. At this point, we need to describe the operation of the I&D device. First, the symbol interval T is divided into N equally-spaced subintervals, hereafter referred to as the chip interval, each of duration $T_s = T/N$. The I&D circuit then provides an integration over N chip intervals of the signal at the output of the I&Q unit for later processing, as in [6]. Hence, for every symbol interval, N distinct samples are offered to the post-detection

device. Let the integration interval T_s be substantially smaller than the correlation time of the phase noise. The resulting sample for the k th signaling interval and the l th subinterval, $\Gamma_l^{(k)}$, is given by: $\Gamma_l^{(k)} \approx \gamma e^{j[\psi_l^{(k)} + \phi_k + \theta]} + Z_l^{(k)}$, where $\gamma = AT_s$, $\psi_l^{(k)}$ denotes the l th sample of the phase noise in the k th signaling interval, and $Z_l^{(k)} = \int_{kT+(l-1)T_s}^{kT+lT_s} Z(t)dt$.

II. Post-Detection Processing Schemes and Error Floor Calculation

Let $D_k^{(i)}$ be the decision variable of the i th post-detection processing technique for the k th signaling interval. For the FW scheme[6],

$$D_k^{(1)} = \frac{1}{N} \sum_{l=1}^N \text{Re}\{\Gamma_l^{(k)} \Gamma_l^{(k-1)*}\}. \quad (3)$$

For the proposed OBS-EW scheme (see Fig. 1),

$$D_k^{(2)} = \frac{1}{M} \sum_{l=1}^M \text{Re}\{\Gamma_l^{(k)} \Gamma_{N-l+1}^{(k-1)*}\} \quad (4)$$

where M is a design parameter that may be used to optimize performance. Since M may be varied for a fixed N , the proposed scheme may be referred to as an expanding window detection technique. An optimum receiver for the above post-detection processing schemes, in the absence of phase noise, then suggests the following decision rule: $D_k^{(i)} \underset{-1}{\overset{+1}{>}} 0$; $i \in \{1, 2\}$

for bipolar NRZ binary signaling. The receiver error floor for the i th DPSK receiver is $EF^{(i)} = Pr\left\{\sum_{l=1}^{L_i} \cos[\psi_l^{(k)} - \psi_{P_i}^{(k-1)}] < 0\right\}$, where $P_i = \begin{cases} l & i=1 \\ N-l+1 & i=2 \end{cases}$ and $L_i = \begin{cases} N & i=1 \\ M & i=2 \end{cases}$. Let $\Delta\psi_{i,j} = \psi_i^{(k)} - \psi_j^{(k-1)}$, $\underline{\Delta\psi}^{(1)} = [\Delta\psi_{1,1}, \Delta\psi_{2,2}, \dots, \Delta\psi_{N,N}]'$, $\underline{\Delta\psi}^{(2)} = [\Delta\psi_{1,N}, \Delta\psi_{2,N-1}, \dots, \Delta\psi_{M,N-M+1}]'$, and $\underline{K}^{(i)} = E\{\underline{\Delta\psi}^{(i)} \underline{\Delta\psi}^{(i)'}\}$.

With some effort, it may be shown that

$$EF^{(i)} \leq \frac{1}{\pi \sqrt{\prod_{n=1}^{L_i} (2\lambda_n^{(i)})}} \sum_{m=1}^{\lfloor \frac{L_i}{2} \rfloor} \int_{1/2\lambda_{2m-1}^{(i)}}^{1/2\lambda_{2m}^{(i)}} \frac{e^{-\frac{L_i\pi^2}{4}x}}{\sqrt{x^2 \prod_{i=1}^{2m-1} \left(x - \frac{1}{2\lambda_i^{(i)}}\right) \prod_{l=2m}^{L_i} \left(\frac{1}{2\lambda_l^{(i)}} - x\right)}} dx; \quad (5)$$

$i \in \{1, 2\}, L_i > 1,$

where $\lambda_n^{(i)}$ is the n th eigenvalue of the covariance matrix $\underline{\underline{K}}^{(i)}$ with

$$\begin{aligned} [\underline{\underline{K}}^{(1)}]_{j_1, j_2} &= \beta \min(j_1, j_2) + \\ &\quad \beta \min(N + j_1, N + j_2) - \\ &\quad \beta \min(j_1 + N, j_2) - \\ &\quad \beta \min(j_1, j_2 + N). \end{aligned} \quad (6)$$

and

$$\begin{aligned} [\underline{\underline{K}}^{(2)}]_{j_1, j_2} &= \beta \min(j_1 + N, j_2 + N) + \\ &\quad \beta \min(N - j_1 + 1, N - j_2 + 1) - \\ &\quad \beta \min(N - j_1 + 1, j_2 + N) - \\ &\quad \beta \min(N - j_2 + 1, j_1 + N). \end{aligned} \quad (7)$$

III. Significance of the Proposed Architecture

First, in Fig. 2, the error floors are depicted as a function of N . In this case, as expected, the error floors in general improve (i.e., decrease) as a result of increasing N . Recall that an increase in N directly increases the bandwidth of the I&D filters, which in the absence of additive noise (phase-noise-limited operation) does not increase the bit error rate. A rather remarkable result is the substantial improvement in the error floor that is gained by increasing N for the OBS-EW scheme. This confirms our earlier conjecture as to the effectiveness of the OBS-EW in reducing the error floor of a DPSK receiver. In fact,

as N is increased, the FW scheme offers little or no improvement in error performance, whereas the OBS-EW scheme offers an exponential-like decrease in the error floor with an increase in N . This result is of significant importance to the implementation of nearly noiseless DPSK optical communications systems that are impaired by phase noise due to non-ideal laser sources. In Fig. 3, the error floors of the OBS-EW and FW receivers are depicted as a function of linewidth-symbol-duration-product (LSDP). Once again, the OBS-EW scheme yields a performance that is far superior to the FW scheme for all values of $N > 1$ and for a wide range of phase noise levels. The effect of increasing N on the error performance for the FW scheme seems to be rather subtle. This is the main reason the plots for different values of N for the FW scheme in Fig. 3 almost overlap. However, for the OBS-EW scheme, an increase in N has a significant impact on the error performance. This is an encouraging result, which underscores the effectiveness of the OBS-EW technique in reducing the error floor of a DPSK receiver impaired by phase noise.

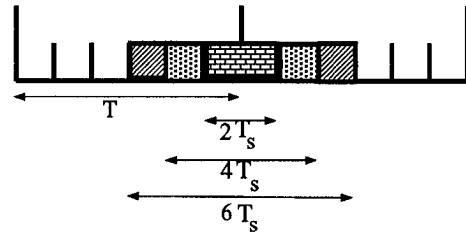


Fig. 1. The integration intervals for the proposed one-bit-shifted expanding-window (OBS-EW) post-detection processing schemes for $N = 6$ and $M = 3$.

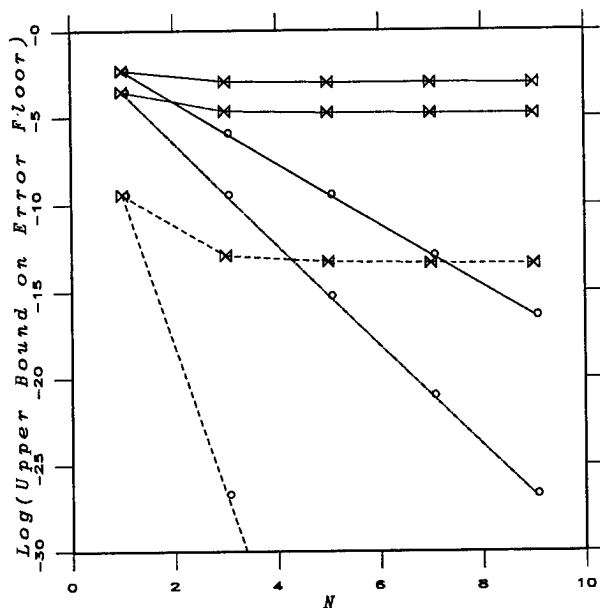


Fig. 2. Bit error floor as a function of N for DPSK receivers with the OBS-EW (O) and FW (Δ) post-detection processing for LSDP = 0.01 (---), 0.03(-.-), 0.05 (—).

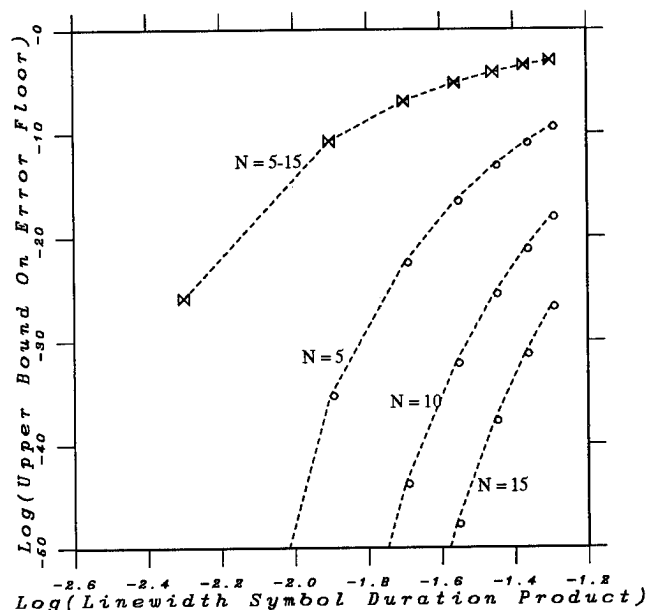


Fig. 3. Bit error floor as a function of LSDP for DPSK receivers with the OBS-EW (O) and FW (Δ) post-detection processing.

References

- [1] W. C. Lindsey and M. K. Simon, *Telecommunication Systems Engineering*. Information and System Sciences, Prentice-Hall, Inc., 1973.
- [2] J. G. Proakis, *Digital Communications*. McGraw-Hill, New York, 1989.
- [3] M. Azizoglu, P. A. Humblet, and J. S. Young, "Phase-noise-induced performance limits for dpsk modulation with and without frequency feedback," *IEEE/OSA Journal of Lightwave Technology*, vol. 11, pp. 290-302, Feb. 1993.
- [4] G. Jacobsen and I. Garrett, "Theory of optical heterodyne DPSK receivers with post detection filtering," *IEEE/OSA Journal of Lightwave Technology*, vol. LT-5, pp. 478-484, April 1987.
- [5] I. Garrett and G. Jacobsen, "Theoretical analysis of heterodyne optical receivers for transmission systems using (semiconductor) lasers with nonnegligible linewidth," *IEEE/OSA Journal of Lightwave Technology*, vol. LT-4, no. 3, pp. 323-334, Mar. 1986.
- [6] G. Jacobsen, "Performance of DPSK and CPFSK systems with significant post-detection filtering," *IEEE/OSA Journal of Lightwave Technology*, vol. 11, pp. 1622-1630, Oct. 1993.
- [7] Y. E. Dallah and S. Shamai(Shitz), "Coding for DPSK noisy phase channels," *IEEE Transactions on Communications*, vol. 42, no. 2/3/4, pp. 927-940, Feb./March/April, 1994.
- [8] Y. E. Dallah and S. Shamai(Shitz), "Time diversity in DPSK noisy phase channels," *IEEE Transactions on Communications*, vol. 40, no. 11, pp. 1703-1715, Nov., 1992.
- [9] L. G. Kazovsky, "Performance analysis and laser linewidth requirements for optical PSK heterodyne communications systems," *IEEE/OSA Journal of Lightwave Technology*, vol. LT-4, no. 4, pp. 415-425, Apr. 1986.

MULTI-WAVELENGTH, OPTICAL CODE-DIVISION-MULTIPLEXING BASED ON PASSIVE, LINEAR, UNITARY, FILTERS

Cedric F. Lam and Eli Yablonovitch

Electrical Engineering Dept., University of California, Los Angeles,
Los Angeles, CA 90095-1594

E-mail: flam@ee.ucla.edu and eliy@ee.ucla.edu

ABSTRACT

The opportunity exists to apply spread spectrum concepts into the enormous bandwidth of optical fibers. We introduce a new optical CDMA network architecture based on passive linear unitary filtering of the optical carrier signals.

1. INTRODUCTION

The opportunity exists to apply spread spectrum concepts into the enormous bandwidth of optical fibers. Recently we have seen the commercial emergence of spread-spectrum radio. In spite of radio being a relatively narrow band medium, the spread-spectrum concept has sufficient advantages in overall capacity and quality for it to compete commercially with

conventional time-division-multiplexed cellular telephones.

Surely if spread spectrum is viable in a narrow band medium such as radio, it should be even more promising in a broadband medium such as optical fibers. Included among the usual advantages of coded communications, are the prospects for Tera-bit switching and very high speed parallel signal processing.

The form of optical code division multiplexing which we have in mind is different from previous proposals employing so-called "optical codes"¹⁻³, which are non-negative, and therefore cannot be truly orthogonal. Instead we propose an optical code division multiplexed system which is mathematically and conceptually similar to

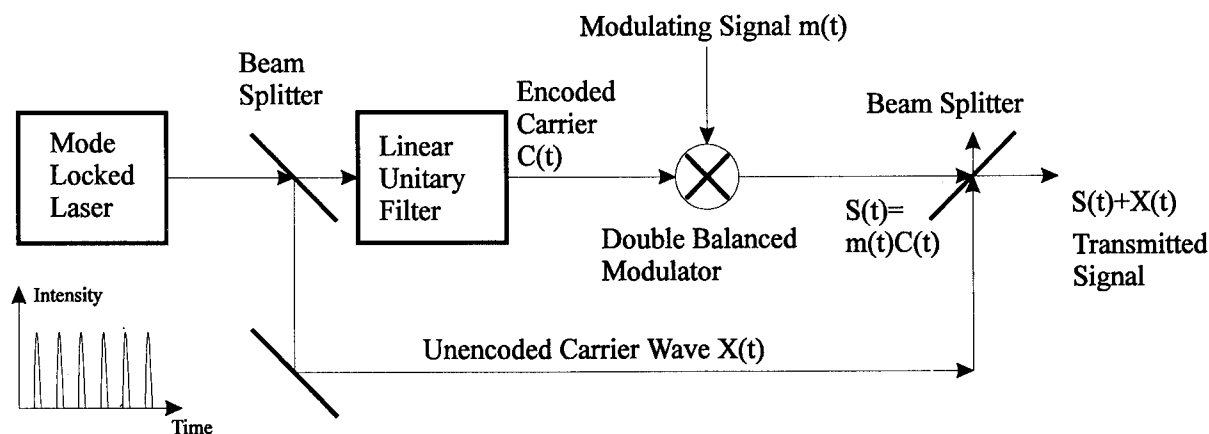


Fig.1 Transmitter Block Diagram

radio code-division multiplexing. The specific hardware implementation however must match the opportunities in modern optical components, but also their limitations.

2. THE TRANSMITTER

Figure 1 shows the block diagram of the transmitter in the proposed architecture. The transmitter uses a mode locked laser to generate the unencoded carrier waves at multiples of the laser repetition frequency. The unencoded carrier is passed through a linear filter which basically does a unitary transform to generate a linear combination of the components of the unencoded carriers.

Each user has a different linear filter and therefore a different linear code which is truly orthogonal to the codes of all other users. It has been recently shown by Reck⁴ et al that every unitary transformation can be implemented in optics using just mirrors, beam splitters and phase shifters. The encoded carrier is then modulated by the message signal through a double balanced modulator to obtain side bands on the modulated codes. All the user channel side bands and part of the unencoded carrier are combined together using a star coupler which is not shown in the block diagram. The unencoded carrier will be recovered at the receiver end to avoid the use of a local

oscillator.

The linear filters used in this system, apart from being the encoders for different channels, can also be used for some linear computations such as fourier transforms etc.. Because photons obey the superposition principle, instead of carrying out the operations sequentially as in digital computers, most of the linear computation can be parallized in a photonic system. This has significant implications for applications such as those involving image transformation because part of the computational load can be moved from the electronic system to the optical system.

One way to implement the double balanced modulator is to use an optical phase modulator inserted between two 50/50 biconical fused fiber beam splitters as shown in Fig. 3. By setting the phase modulation constant k_0 small, it can be shown that the modulator output will be the product of the carrier signal and the message signal.

3. THE RECEIVER

The receiver block diagram is shown in Figure 2. It takes the multiplexed signal side bands from different users and the unencoded carrier as the input. The multiplexed signal side bands are separated from the unencoded carrier signal by a

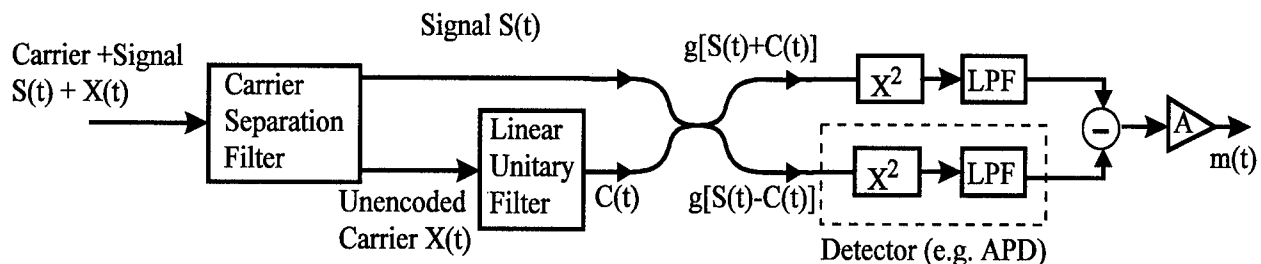


Fig.2 Receiver Block Diagram

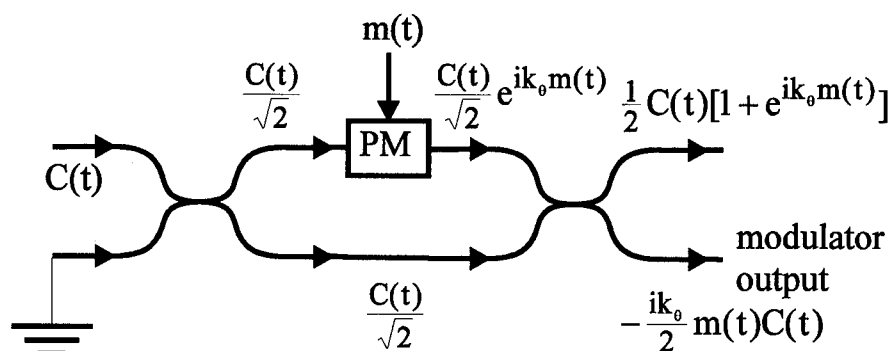


Fig. 3 An example implementation of a double balanced modulator

Fabry-Perot type filter which has very narrow pass bands centered at the pure carrier frequencies. By transmitting the unencoded carrier to the receiver and recovering it by the carrier separation filter, we can avoid the use of the local oscillator for signal detection which involves complicated phase locking mechanism and polarization tracking in the optical domain. The unencoded carrier and the signal side bands suffer the same phase shift, dispersion and polarization changes because they travel the same path. It thus maintains the CDMA system complexity to be compatible with a WDM system.

The code for the desired channel is generated from the recovered unencoded carrier by the same linear filter used in the transmitter. The multiplexed signal side bands and the carrier code are then passed to a double balanced mixer to obtain the message signal out. The double balanced mixer is composed of a 50/50 coupler and two square-law detectors which also function as low pass filters. The double balanced modulator output will give the product of the code and the multiplexed signal side bands. Because of the orthogonality between the codes, all the side bands from other channels will be rejected except the one which has the correct code.

3. CONCLUSION

To summarize, we proposed a novel optical CDMA architecture that uses truly orthogonal codes based on a passive linear filtering concept which in addition to code generation can also be explored for other linear computations in the optical domain. The proposed system involves no high speed coherent optical devices and uses direct detection at its output. The system complexity is compatible to a WDM system.

4. REFERENCES

- 1.F.R. Chung, J.A. Salehi, V.K. Wei, "Optical Orthogonal Codes: Design, Analysis and Applications", *IEEE Transactions on Information Theory*, Vol.35, No.3, May 1989, pp595-604
- 2.E. Park, A.J. Mendez, E.M. Gramire, "Temporal/Spacial Optical CDMA Networks-Design, Demonstration, and Comparison with Temporal Networks", *IEEE Photonics Tech. Letters*, Vol.4, No.10, Oct 1992, pp1160-1162
- 3.R.M. Gagliardi, A.J. Mendez, M.R. Dale, E. Park, "Fiber-Optic Digital Video Multiplexing Using Optical CDMA",

Journal of Lightwave Technology, Vol. 11,
No. 1, Jan 1993, pp20-26

4.M. Reck, A Zeilinger, "Experimental
Realization of Any Discrete Unitary
Operator", *Physical Review Letters*, Vol
73, No.1, 4 July 1994, pp58-61

5.P.E.Green, "Fiber Optic Networks",
Prentice Hall, 1993, N.J.

APPLICATION OF ANTENNA ARRAY PROCESSING TO PROBLEMS IN IMAGE UNDERSTANDING

Hamid K. Aghajan

Thomas Kailath

Information Systems Laboratory, Department of Electrical Engineering
Stanford University, Stanford, CA 94305

Abstract

A unifying framework for solving several problems in image understanding is proposed based on the exploitation of subspace fitting techniques originally developed for antenna array processing applications. The *SLIDE* (Subspace-based Line DEtection) algorithm is a framework for introducing the concept of subspace fitting into problems in image understanding and computer vision. The basic formulation of *SLIDE* provides a solution to the problem of multiple line fitting in binary or gray-scale images. However, as is shown in this paper, its modified versions can be applied to several other image analysis problems.

1. Introduction

An interesting relationship can be established between image analysis and the notion of subspace fitting by thinking of the image under consideration in a wave propagation context in which the digitized image is regarded as a snapshot of a spatial wave field at a fixed instant in time. This formulation leads to an efficient solution to several image understanding problems by exploiting ideas and tools from sensor array processing, communications theory, and projection-based transformations.

SLIDE is a model-based algorithm based on the partitioning of the induced measurement space into a signal subspace that is defined by the few desired parameters, and a noise subspace that includes all the undesired contributions. The signal subspace is determined by exploiting the spatial (and/or temporal) coherency that exists between contributions of the desired components, e.g. straight lines, in the image.

After establishing the framework for multiple straight line fitting applications, it is possible to extend the coherency accumulating notions of *SLIDE* to other vision applications by exploiting such tools of communications theory as chirping/dechirping and modulation. Circle and ellipse fitting, uniform motion estimation, linewidth measurement and alignment in microlithography for manufacturing of integrated circuits, skew de-

tection in text analysis, and estimation of the location of the axis of symmetry are examples of such extensions. In this paper, the fundamental form of the *SLIDE* algorithm will be briefly introduced first, followed by its application to several of the mentioned application areas.

2. The *SLIDE* Algorithm

Starting with a simplified case of fitting a straight line to a binary image with a set of colinear pixels, let us imagine that there is an array of sensors in front of the vertical axis of the image. A simple sketch of such arrangement is shown in Fig. 1. If we now consider the straight line to be the wavefront of a propagating wave, the measurements received at the sensors will have the form:

$$z(y) = e^{-j\mu x} = e^{-j\mu x_0} e^{j\mu y \tan \theta} \quad (1)$$

where μ is a constant parameter, and can be interpreted as the speed of propagation.

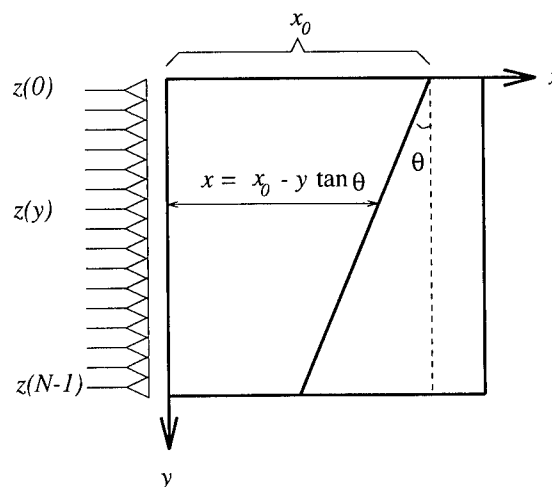


Figure 1: Image matrix and hypothetical sensors.

In our model, μ is free to choose, and its choice gives us a handle to develop different applications. The measurements $z(y)$ have the form of a complex sinusoid with

a frequency related to the line angle θ ; the line offset has been separated and encoded in a constant complex number. The varying part of the measurements can be lumped into a term $a_y(\theta) = e^{j\mu y \tan \theta}$, and be called the array response. The above formulation readily generalizes to the multiple line case,

$$z(y) = \sum_{k=1}^d e^{j\mu y \tan \theta_k} e^{-j\mu x_{0k}} + n(y) \quad (2)$$

$$= \sum_{k=1}^d a_y(\theta_k) s_k + n(y). \quad (3)$$

This equation is the starting point of extensive research in the last decade on the so-called subspace-based high resolution direction finding (and signal copy) algorithms (known as MUSIC, ESPRIT, WSF, etc., see *e.g.* [1]). In these methods, a sample covariance matrix is computed in a certain way from the measurements, and its eigendecomposition is examined. The basic concept of subspace fitting is that the d dominant eigenvectors of this covariance matrix span the same subspace that is spanned by the array response vectors for the desired angles.

The next step would be to estimate the line offsets. It can be shown that by modifying the propagation scenario, new measurements are obtained that contain chirp (quadratic frequency) contributions from the angles, and linear contributions from the offsets. In other words, the offsets will be encoded as frequencies of complex sinusoids. Dividing the *chirped* measurements $z(y)$ by the array response $a_y(\theta)$ results in new *dechirped* measurements $w(y)$

$$w(y) = \frac{z(y)}{a_y(\theta)} = \sum_{k=1}^d e^{-j\alpha y x_{0k}} + n'(y) \quad (4)$$

on which fast high resolution spectral estimation methods can be applied to obtain estimates of the line offsets. The above formulation also generalizes to gray-scale images by assigning the value of the gradient at each pixel to the amplitude of the wave emanating from it. Details of the implementation of the *SLIDE* algorithm can be found in [2].

3. 2D Motion Estimation

An interesting application of the *SLIDE* algorithm is in finding the velocities and positions of multiple moving objects in a frame sequence.

If the projections of the frames on one of the main (horizontal or vertical) axes are stacked up to produce a synthetic image in t and x , say, then the moving patterns in the original sequence will be represented by

skewed bands in this image. Fig. 2 shows a simple case, where there are two moving objects and a stationary object in the sequence. Propagating the image parallel to the x -axis produces measurements $z(t)$ that encode the x components of the velocities of the moving patterns as frequencies of complex sinusoids:

$$z(t) = e^{-j\mu v_z t} e^{-j\mu x_0} Mx(\mu). \quad (5)$$

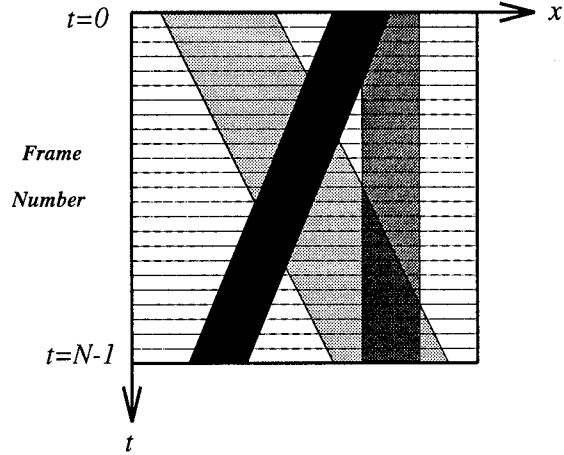


Figure 2: Stack of the frame projections.

A similar approach would result in the estimation of the positions of the moving patterns. An advantage of *SLIDE* is that it can handle multiple moving objects in the same frame sequence, whereas most other methods have to narrow down their working window such that only one moving pattern appears in it.

In Fig. 3, the first and last frames of a sequence are shown, in which two helicopters move and the background is stationary. The goal is to find the velocities and the positions of the helicopters.

Fig. 4 shows the synthetic images obtained by stacking the projections of the frames on the x and y axes. The derivative of the projections in time is taken by simply subtracting each frame projection from its neighboring projection. As we can observe, each helicopter is represented by a skewed band in these images. Then, the algorithm is applied to these synthetic images independently, and estimates of the velocities and locations of the center of gravity of the moving objects are obtained. These estimates have been used to plot the trajectories of the objects.

4. Text Skew Detection

Another application of the *SLIDE* algorithm is the estimation of the skew angle in scanned text images. Although the lines of text contribute to more than one pixel per image row, and the character pixels introduce fuzziness on the lines, the estimate obtained by *SLIDE* is accurate enough for pursuing the other steps of processing the text. This robustness stems from the fact



Figure 3: First and last frames of the test sequence.

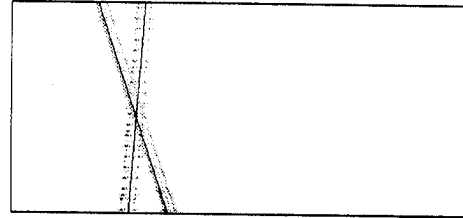
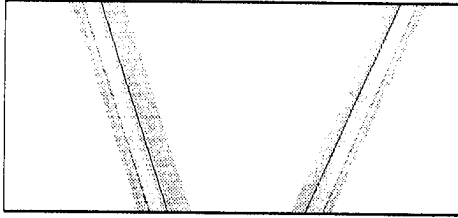


Figure 4: Stack of projections on the x and y axes, and detected motions.

that *SLIDE* exploits the great amount of coherency that exists in the text images between the locations of the pixels on parallel lines. This coherency contributes to enhancing the signal subspace component of the space spanned by the sample covariance matrix. An example of applying *SLIDE* to a scanned text image is shown in Fig. 5. The original image has been scanned with some amount of skew. The estimated value of the skew has been used to rotate the text image back to the proper orientation.

5. Axis of Symmetry

By exploiting the tools of communication theory, other application areas can be added to the framework of the *SLIDE* algorithm. One such tool is signal modulation, in which a passband signal can be represented by the location of a central carrier frequency, surrounded by two sidebands. A particular case of interest in this application category is the estimation of the axis of symmetry of patterns.

Consider the simple case of Fig. 6. Assuming that the pattern profile in each row of the image can be represented by

$$f(x - x_0 + y \tan \theta), \quad (6)$$

the measurements after dechirping would be

$$w(y) = e^{-j\alpha x_0 y} F(\alpha y) \quad (7)$$

which have the structure of a modulated signal with a central carrier frequency αx_0 . The shape of the sidebands around the carrier frequency in the frequency

domain of $w(y)$ is a scaled version of $f(\cdot)$, and hence is symmetric. It can be shown that applying subspace fitting techniques to such modulated signals results in an estimate of the mean frequency. In this application, the mean frequency is proportional to the position of the axis of symmetry, x_0 . Fig. 7 presents an example of applying the *SLIDE* algorithm to finding the axis of symmetry of an alignment mark on a wafer. The detected axis of symmetry has been superimposed on the original gray scale image taken from the wafer.

Detection of horizontal and vertical axes of symmetry can be extended to arbitrary symmetric shapes. The basic observation in applying subspace fitting methods is that due to the symmetry in the original shape, the measurements will have symmetric sidebands around the carrier frequency in the frequency domain. Subspace fitting results in an estimate of the carrier frequency. Fig. 8 shows an image with a pattern symmetric in the horizontal direction. The location of the detected axis of symmetry has been plotted on the image.

6. Circle and Ellipse Fitting

The circle is the most symmetric pattern. In addition to the estimation of the location of its center, it can be shown that *SLIDE* can also find an estimate for the value of the circle radius. This value appears as the carrier frequency of a modulated signal, which in this case is itself variable with the measurement index y . This technique is directly applicable to both hollow circles and disks, and can readily be applied to finding

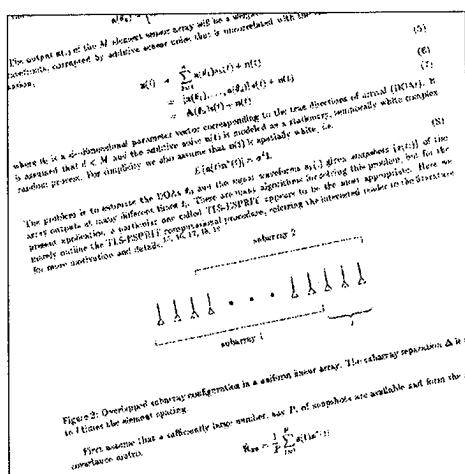


Figure 5: Scanned text image with a skew and the skew-compensated image.

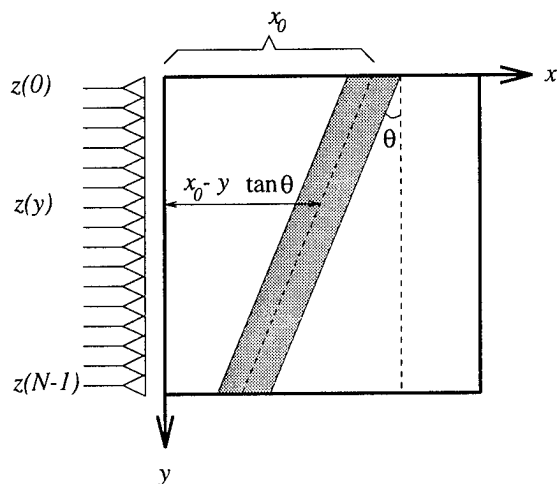


Figure 6: Image with a symmetric pattern.

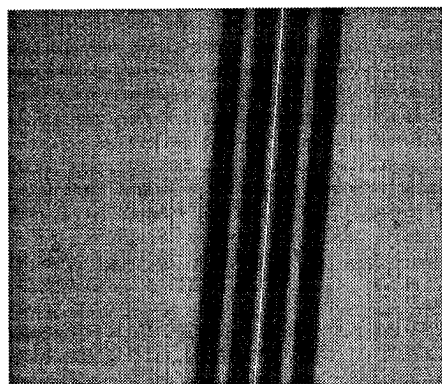


Figure 7: Semiconductor image used for alignment.

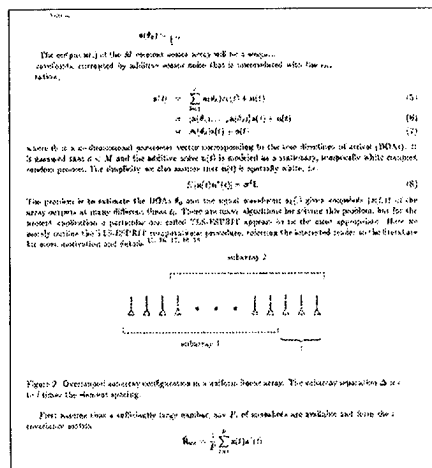


Figure 8: Image with a vertical axis of symmetry.

the parameters of ellipses as well.

Acknowledgments

The authors wish to thank the helpful discussions with and comments by Babak Khalaj and Professor A. Paulraj of the Information Systems Laboratory, Stanford University.

References

- [1] R. Roy and T. Kailath, "ESPRIT: Estimation of signal parameters via rotational invariance techniques", *IEEE Trans. on ASSP*, vol. 37, no. 7, pp. 984-995, July 1989.
- [2] H. K. Aghajan and T. Kailath, "SLIDE: subspace-based line detection", *IEEE Trans. on Pattern Analysis and Machine Intelligence*, vol. 16, no. 11, pp. 1057-1073, Nov. 1994.

PHASE RETRIEVAL ALGORITHM BASED ON MAXIMUM ENTROPY METHOD

Anisa T. Bajkova

Institute of Applied Astronomy of RAS,
8, Zhdanovskaya St., St. Petersburg, 197042
e-mail: bajkova@ipa.rssi.ru

ABSTRACT

The paper presented deals with phase retrieval problem for image reconstruction from only spectrum magnitude. Only two-dimensional spatially limited non-negative objects, which are characterized by analytical spectra, are considered assuming that the unique solution of phase problem exists. In this paper it is proposed to use nonlinear optimization approach, namely, well-known maximum entropy method (MEM) which has very good extrapolation features and high stability to noise. For solving phase retrieval problem we propose to introduce into the optimized entropy functional additional unknowns related to a real and imaginary parts of an object spectrum and represent the constraints, which are derived from measured spectrum magnitude data, as linear constraints, in order to reduce the optimization problem to the standard MEM. The whole computational algorithm is constructed as a combination of the standard MEM algorithm and additional nonlinear constraint for a real and imaginary parts of the spectrum data which is realized during computational iterations. Images reconstructed by the proposed MEM approach may be, if necessary, further improved by Fienup's iterations. In this case the previous image is used as a starting point ensuring reliable convergence of Fienup's algorithm to sought for solution. Numerous simulation results demonstrate validity and high efficiency of the approach proposed.

1. INTRODUCTION

Some problems of signal processing are connected with solving phase problem, i.e. image or signal reconstruction from only spectral magnitude. The most of physical instruments are able to register only spectrum intensity data, but for correct representation of an object it is necessary to have information both on spectral magnitude and phase. It is proved that in the case

of two-dimensional spatially limited non-negative functions, which have analytical spectra, the phase problem has, except of cases determined on null set, unique solution within a class of equivalent functions [1]. We will assume that solution of phase problem exists. But existence of the solution does not guarantee convergence of a phase retrieval algorithm to it. The problem of synthesis of the algorithms, which converge reliably to sought for solution, is a very difficult problem. At present the most popular algorithms are algorithms based on Fienup's iterations [2]. But it is known that sometimes Fienup's algorithm fails. The main possible reason, as was discussed in [3], is a starting point which is chosen in the iteration. In this paper we propose at first to seek for the solution of phase problem by maximum entropy method modified to spectrum magnitude data and then improve this result, if necessary, by Fienup's iterations using it as a starting point which ensures reliable convergence of the algorithm to sought for solution.

2. BASIC ALGORITHM

In this section the part of the combined phase retrieval algorithm, proposed in the section 4, which is based on maximum entropy method, is described. The standard MEM [4] for image reconstruction from complex spectrum can be represented as the following optimization problem. (We consider only discrete form.)

$$\min \sum_m \sum_l x_{ml} \ln(x_{ml}), \quad (1)$$

$$\sum_m \sum_l x_{ml} a_{ml}^{nk} = A_{nk}, \quad (2)$$

$$\sum_m \sum_l x_{ml} b_{ml}^{nk} = B_{nk}, \quad (3)$$

$$x_{ml} \geq 0. \quad (4)$$

where x_{ml} are unknowns; A_{nk} and B_{nk} are known spectrum data, real and imaginary parts respectively;

This work was supported by Russian Sciences Foundation under grant N 93-02-3079

a_{ml}^{nk} and b_{ml}^{nk} are constants, related to Discrete Fourier Transformation:

$$a_{ml}^{nk} = \cos(2\pi(mn + lk)/N)/N, \quad (5)$$

$$b_{ml}^{nk} = -\sin(2\pi(mn + lk)/N)/N. \quad (6)$$

A_{nk} and B_{nk} can be represented in the following way

$$A_{nk} = M_{nk} \cos \phi_{nk}, \quad (7)$$

$$B_{nk} = M_{nk} \sin \phi_{nk}, \quad (8)$$

where M_{nk} and ϕ_{nk} are spectral magnitude and phase respectively.

In the case of phaseless data let $\cos \phi_{nk}$ and $\sin \phi_{nk}$ be unknowns as well. Using the following identities

$$\cos \phi_{nk} = 2 \cos^2(\phi_{nk}/2) - 1, \quad (9)$$

$$\sin \phi_{nk} = (\sin(\phi_{nk}/2) + \cos(\phi_{nk}/2))^2 - 1, \quad (10)$$

and determining the following new variables

$$t_{nk} = 2 \cos^2(\phi_{nk}/2), \quad (11)$$

$$s_{nk} = (\sin(\phi_{nk}/2) + \cos(\phi_{nk}/2))^2, \quad (12)$$

which are nonnegative, it is possible to rewrite (1) - (4) as follows

$$\begin{aligned} \min \sum_m \sum_l x_{ml} \ln(x_{ml}) + \\ + \sum_n \sum_k t_{nk} \ln(t_{nk}) + s_{nk} \ln(s_{nk}), \end{aligned} \quad (13)$$

$$\sum_m \sum_l x_{ml} a_{ml}^{nk} - M_{nk} t_{nk} = -M_{nk}, \quad (14)$$

$$\sum_m \sum_l x_{ml} b_{ml}^{nk} - M_{nk} s_{nk} = -M_{nk}, \quad (15)$$

$$x_{ml}, t_{nk}, s_{nk} \geq 0. \quad (16)$$

In addition we demand meeting the following non-linear condition

$$(t_{nk} - 1)^2 + (s_{nk} - 1)^2 = 1. \quad (17)$$

For obtaining solution of considered phase problem it is proposed to solve (13) - (16) numerically using

steepest - descent method and require after each iteration meeting (17).

The optimization problem written as (13) - (16) looks like the standard one (1) - (4). Only additional variables t_{nk} and s_{nk} , which are non-negative as well as sought for function x_{ml} , are included into entropy functional and linear constraints.

Using Lagrange method it is easy to obtain the solution of the (13)-(16) expressed via dual factors

$$x_{ml} = \exp(-\sum_n \sum_k (\alpha_{nk} a_{ml}^{nk} + \beta_{nk} b_{ml}^{nk}) - 1), \quad (18)$$

$$t_{nk} = \exp(\alpha_{nk} M_{nk} - 1), \quad (19)$$

$$s_{nk} = \exp(\beta_{nk} M_{nk} - 1). \quad (20)$$

The dual factors α_{nk} and β_{nk} refer to (14) and (15) respectively.

As it is seen from (18)-(20), requirements of (16) are met.

Dual unconditional optimization problem appears as follows

$$\begin{aligned} \min \sum_m \sum_l x_{ml} + \sum_n \sum_k (t_{nk} + s_{nk}) - \\ - \sum_n \sum_k (\alpha_{nk} M_{nk} + \beta_{nk} M_{nk}). \end{aligned} \quad (21)$$

We propose to solve (21) using steepest-descent method. After each iteration dual factors get increases $z_{\alpha nk}(\beta_{nk})$:

$$\alpha_{nk} \leftarrow \alpha_{nk} + z_{\alpha nk}, \quad (22)$$

$$\beta_{nk} \leftarrow \beta_{nk} + z_{\beta nk}. \quad (23)$$

Simulation results for relatively simple image are shown in Fig.1. Analysis of simulation results [5] in the case of more complicate images shows that the solutions obtained only by MEM, i.e. (13)-(16), are characterized by good reconstruction of low-frequency region of spectrum which may be narrow. Supplement of the nonlinear constraint (17) allows to considerably widen the reconstructed region. Further improving is possible by Fienup's iterations if MEM-image is used as a starting point.

3.COMBINED MAXIMUM ENTROPY AND FIENUP'S ITERATION METHOD

The most well-known algorithm for phase retrieval is Fienup's iterative reconstruction [2]. It is proved that

Fienup's algorithm does not have a character of compressibility and error at each iteration can stay the same. In [3] a potential source of error in the numerical implementation of the algorithm is discussed. Besides it was established that Fienup's algorithm sometimes fails converging to a fixed-point. Authors of the paper have presented a conjecture that converging of the algorithm towards the fixed point depends on the starting point which is chosen in the iteration.

For avoiding failure of Fienup's algorithm caused by unsuccessful starting point it is proposed to combine phase retrieval algorithm from two parts. In the first part we propose to obtain the starting point using maximum entropy method which, as was mentioned in the Section 2, ensures good reconstruction of spectral phase in low frequency region. The second part assumes reconstruction by Fienup's algorithm using the image reconstructed by MEM as a starting point. As simulation results demonstrate, the combination proposed ensures reliable convergence of the algorithm to sought for solution. Error study shows high stability of the algorithm to noise [5].

may be, if necessary, further improved by Fienup's iterations. In this case the previous image is used as a starting point ensuring reliable convergence to sought for solution. Numerous simulation results demonstrate validity and high efficiency of the approach proposed.

5. REFERENCES

1. Bruck Yu.M., Sodin L.G. 1979, On the ambiguity of phase retrieval problem, *Optics Communications*, 30, pp.304-308
2. Fienup J.R. 1982, Phase retrieval algorithms: a comparison, *Applied Optics*, 21, 15, pp.2758-2769
3. Sanz J.L., Huang T.S., Wu T-F. 1984, A note on iterative Fourier transform phase reconstruction from magnitude, *IEEE Trans. on Acoustics, Speech, and Signal Processing*, 32, 6, pp.1251-1254
4. Frieden B.R. 1972, Restoring with maximum likelihood and maximum entropy, *J. Opt. Soc. Amer.*, 62, pp. 511-518
5. Bajkova A.T. 1994, Phaseless image reconstruction, *Communications of the Institute of Applied Astronomy*, 62, p. 23

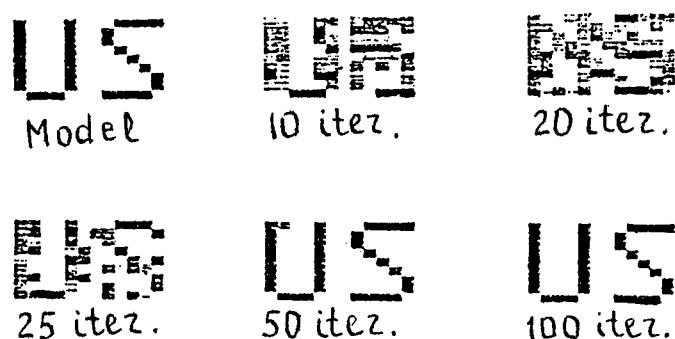


Fig.1.

4. CONCLUSION

In this paper the algorithm for image reconstruction from only spectrum magnitude based on maximum entropy method is proposed. It is suggested to introduce into the optimized entropy functional and linear constraints, which are derived from measured spectrum magnitude data, additional unknowns related to a real and imaginary parts of the spectrum of an object. The whole computational algorithm is constructed as a combination of the standard MEM algorithm and additional non-linear constraint for a real and imaginary parts of spectrum data, which should be realized during computational iterations of steepest-descent method. Images reconstructed by the proposed MEM approach

A METHOD TO DECREASE NONLINEAR IMAGE RECONSTRUCTION DISTORTIONS CAUSED BY MEASUREMENT ERRORS

Anisa T. Bajkova

Institute of Applied Astronomy of RAS
8, Zhdanovskaya St., St-Petersburg, 197042
e-mail: bajkova@ipa.rssi.ru

ABSTRACT

The problem of nonlinear distortions of images reconstructed from incomplete and noisy spectrum data using nonlinear optimization methods such as maximum entropy method is considered. To decrease the level of nonlinear distortions it is proposed to seek solution in the space of complex functions using generalized maximum entropy method instead of classical one.

1. STATEMENT OF THE PROBLEM

Let us consider the problem of image reconstruction from incomplete and noisy spectrum data. Images under the consideration are images of intensities and described by real non-negative distributions. In order to reconstruct missing spectrum components, especially in high frequency domain, it is appropriate to use nonlinear reconstruction procedures having super resolution effect. Such a problem arises, for example, in radio astronomy where aperture synthesis principle is used for high resolution source imaging. Most known and effective computational method for processing such images is maximum entropy method (MEM) [1]. Classical MEM ensures non-negative solution expressed as exponential function of an argument. MEM is characterized by high stability to input data noise. But when the level of noise becomes too large (such a situation is typical, for example, in radio astronomy where measurements of visibility function are made with low signal to noise ratio) classical MEM produces nonlinear distortions in the form of many artifacts with amplitudes commensurable with amplitude of sought signal. What is the cause of such distortions? The matter is that in spite of non-negativity of an actual object distribution, generally, a complex image corresponds to noisy input data. Therefore the solution of image reconstruction problem should be sought in the space of complex distributions. By the same token it is possible to reduce a level of nonlinear distortions moving them

to real negative and imaginary parts of output which should be rejected.

The aim of the paper is to show on the example of maximum entropy method how the generalization of output solution until complex functions can considerably improve the quality of reconstructed images.

2. GENERALIZED MAXIMUM ENTROPY METHOD FOR SOLVING THE PROBLEM

Originally generalized maximum entropy method (GMEM) was proposed for reconstruction of complex coherent images formed in accordance with radio holography principle [2,3]. In [4] the GMEM was considered for reconstruction of ISAR images. Below it will be shown that the GMEM is more preferable than classical MEM also in the case of real non-negative images of intensities if data are measured with low signal to noise ratio. Here let us recall basic aspects of the GMEM [2,3]. The GMEM assumes seeking solution in complex form: $r_{ml} + jq_{ml}$. Both a real and an imaginary parts of an image must be represented as a difference between two non-negatively determined sequences as follows:

$$r_{ml} = x_{ml} - y_{ml}, q_{ml} = z_{ml} - v_{ml}, \quad (1)$$

where $x_{ml}, y_{ml}, z_{ml}, v_{ml} \geq 0$.

If sequences x_{ml}, y_{ml} and z_{ml}, v_{ml} do not overlap, than x_{ml} and z_{ml} determine positive parts and y_{ml} and v_{ml} determine negative parts of the sequences r_{ml}, q_{ml} .

The GMEM assumes minimization of the functional which is written as follows:

$$\min \sum_m \sum_l x_{ml} \ln(ax_{ml}) + y_{ml} \ln(ay_{ml}) + z_{ml} \ln(az_{ml}) + v_{ml} \ln(av_{ml}), \quad (2)$$

where a is a positive parameter responsible for not overlapping positive and negative parts of the sought for sequences.

This work was supported by Russian Sciences Foundation under grant N93-02-3079

Linear constraints derived from measured spectrum data are written in the following way:

$$\sum_m \sum_l (x_{ml} - y_{ml}) a_{ml}^{nk} - (z_{ml} - v_{ml}) b_{ml}^{nk} = A_{nk}, \quad (3)$$

$$\sum_m \sum_l (x_{ml} - y_{ml}) b_{ml}^{nk} + (z_{ml} - v_{ml}) a_{ml}^{nk} = B_{nk}, \quad (4)$$

$$x_{ml}, y_{ml}, z_{ml}, v_{ml} \geq 0, \quad (5)$$

where a_{ml}^{nk}, b_{ml}^{nk} are constant coefficients which determine image formation system, A_{nk}, B_{nk} are measured real and imaginary parts of spectrum samples respectively.

Solutions for (x_{ml}, y_{ml}) and (z_{ml}, v_{ml}) are connected by the expression:

$$x_{ml} y_{ml} = z_{ml} v_{ml} = \exp(-1 - \ln(a)). \quad (6)$$

Making parameter a larger we can reach not overlapping effect. So, the GMEM approach allows to obtain solution of reconstruction problem in the space of complex functions. Because of the optimization problem (2)-(4) is solved with respect to non-negatively determined variables (5) the method possesses super resolution effect as classical MEM. If it is required to reconstruct an image of a real non-negative object x_{ml} it is necessary to represent the sought for sequence in complex form as (1). But as a final result, which must agree a priori information about non-negativity of an object, only a real non-negative part of the solution should be taken into account. Non-zero values of the sequences y_{ml}, z_{ml}, v_{ml} should be rejected because they arise only due to noise in input data and carry no information about real object distribution. So, by using the GMEM it is possible to transform most part of input noise to those parts of output solution which can be easily rejected. On the contrary, if we use classical MEM, we can not reject distortions, caused by input data noise, and they all appear in the form of nonlinear artifacts in the output image.

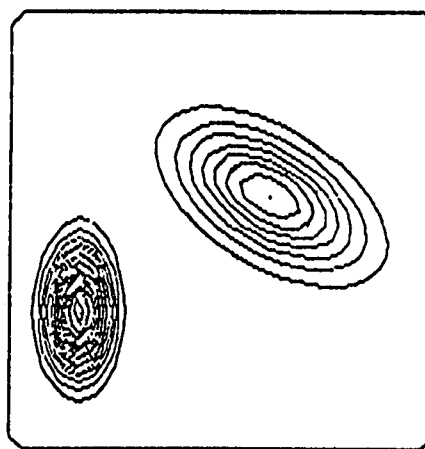
3. SIMULATION RESULTS

In Fig.1 simulation results proving advantage of the GMEM compared to classical MEM for reconstruction of intensity images from noisy spectrum data are shown. The model includes two gaussian components. The object spectrum with large "holes" in both low and high space frequency domain represents input data. Linearly estimated image obtained using inverse Fourier transform is characterized by linear distortions because

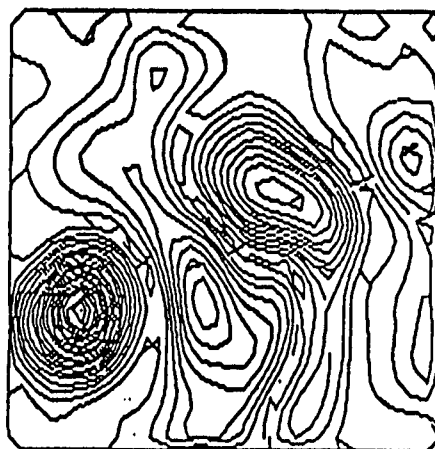
of missing spectrum data. As is seen, the image, reconstructed by classical MEM, has large non-linear distortions and the image, reconstructed by the GMEM, has much less distortions.

4. CONCLUSION

As is shown, using for reconstruction of intensity images instead of classical nonlinear optimization methods such as classical maximum entropy method with real non-negative output, their generalized forms with complex output, allows to considerably decrease the level of nonlinear distortions caused by noise in input data. As a final result only the real non-negative part of the corresponding complex solution should be taken into account.



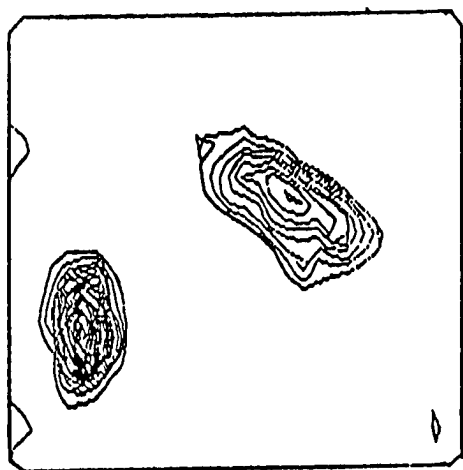
Model



Linear output



Reconstructed by MEM



Reconstructed by GMEM

Fig.1

5. REFERENCES

1. Frieden B.R. 1972, Restoring with maximum likelihood and maximum entropy, *J. Opt. Soc. Amer.*, 62, pp. 511-518
2. Bajkova A.T. 1992, The generalization of maximum entropy method for reconstruction of complex functions, *Astronomical and Astrophysical Transactions*, 1, p. 313
3. Bajkova A.T. 1992, Generalized maximum entropy. Comparison with classical maximum entropy, *"Maximum Entropy and Bayesian Methods"*, Ed. Mohammad - Djafari, G.Demoment, Kluwer Acad. Publ.,

SYNTHESIS OF DATA-DEPENDENT FILTERS FOR DIGITAL IMAGE PROCESSING AND RECOGNITION.

A.V.Kovalenko, V.N.Kurashov, N.G.Nakhodkin.

Taras Shevchenko Univ., Radiophysical Dept., Optical Proc. Lab., 64 Volodimirska Str., Kiev, 252017, Ukraine

Linear filtering remains an attractive method of image recognition because of simplicity of its performance in standard computing systems. Moreover, even nonlinear procedures of image processing include, as a rule, linear filtering for preliminary selection and transformation of classifying signs and compression of processed information to acceptable values. Efficiency of linear filtering is defined mainly by the proper choice of filter set, that must correspond to the peculiarities of the certain problem. Generally, it is desired that the total number of used filters would be as small as possible. From this point of view standard orthogonal transforms (Fourier, Haar, etc.) are usually not optimal and ineffective. It seems much more promising to use filters, constructed for some optimum criterion with account of statistical properties of image general population. The well known example of such approach is given by Karhunen-Loeve decomposition. Different authors differs in estimation of KL-transform efficiency for image processing and recognition, but in any case it is evident, that KL- decomposition is optimal for representation of the images, not for their discrimination. In the number of papers [1,2] there were suggested criteria of discriminant filters construction, based on a priori information about in-class and inter-class correlations of the general population. But practical application of these criteria, including KL-decomposition, involves some difficulties. Firstly, to construct the filters it is necessary to solve the spectral problem of matrix of dimension $M \times M$, defined by the number of samples M in the image. If M value is about $2^{16} - 2^{18}$, solution of such problem is possible only with strong additional suppositions. Secondly, the complete statistical information about image ensemble is never available to investigator, who has usually only limited number of experimentally obtained images on his disposal. Nevertheless, even the comparatively small set of images often is informative enough to obtain estimation of statistical parameters of general population, sufficient for constructing effective processing algorithm. In this paper we suggest the procedure of discriminant filters construction, based on a priori classified training set, and represent some results of its practical application.

We consider image ensemble $\{X\}$, that consists of m classes $\{X_\alpha\}$, $\alpha = \overline{1, m}$; each forming normal population with the average M_α and variance S . We suppose, that the ensemble is represented by a training set, consisting of N a priori classified images. In matrix representation dispersion of elements in each class is described by spread matrix Z_1 , and dispersion of classes is given by matrix Z_2 [3]. In terms of the training set the spread matrices are estimated approximately as:

$$\begin{aligned} Z_1 &= \frac{1}{m} \sum_{\alpha=1}^m \left[\frac{1}{N_\alpha} \sum_{k=1}^{N_\alpha} (M_\alpha - X_{\alpha k}) \otimes (M_\alpha - X_{\alpha k})^+ \right] \\ Z_\alpha &= \frac{1}{m} \sum_{\alpha=1}^m (M_0 - M_\alpha) \otimes (M_0 - M_\alpha)^+ \\ M_0 &= \frac{1}{m} \sum_{\alpha=1}^m M_\alpha \end{aligned} \quad (1)$$

where N_α is number of training set images, rated in α class, $\sum N_\alpha = N$. We construct filters for the criterion of maximum of some value J , that increases with divergence between classes and decreases with increasing in-class dispersion. To construct the set of K filters we define J_k as trace of the principle minor H_k of symmetric ratio of spread matrices H :

$$\begin{aligned} J &= \text{tr}[H_k] \\ H &= 0.5(Z_1^{-1}Z_2 + Z_2Z_1^{-1}) \end{aligned} \quad (2)$$

Criterion J achieves its maximum, when matrix H is represented in diagonal form, ordered in decreasing diagonal elements. As criterion matrix H is self-conjugate, it is brought to diagonal form with the unitary transform F :

$$F = [f_1, f_2, \dots, f_M] \quad (3)$$

where f_j are eigen vectors of H . Hence, as filters, optimal for J criterion one must choose the vectors f_j , corresponding to the maximal eigen values λ_j of matrix H .

We solve the spectral problem of matrix H , following the procedure, suggested by Kurashov and Chumakov for Karhunen-Loeve basis construction in approximation of training set [4]. This procedure radically decreases number of necessary operations, if number of images in the training set is much less than dimension of the image itself. According to this algorithm we orthogonalize the training set with Gram-Schmidt procedure with the resulting formation of some basis $\{e_i\}$, that consists of N vectors equal in dimension to the initial images $\{X\}$. Then we represent the training set in basis $\{e_i\}$:

$$\dot{X}_{ak} = \begin{bmatrix} \dot{X}_{ak}^{(1)} \\ \vdots \\ \dot{X}_{ak}^{(N)} \end{bmatrix} = [e_1, e_2, \dots, e_N]^+ \cdot X_{ak} \quad (4)$$

With representation (4) we receive according to (1), (2) the expressions for spread matrices \dot{Z}_1, \dot{Z}_2 and criterion matrix \dot{H} that have dimension $N \times N$, $N \times N \ll M \times M$. The important notice is, that the dimension is decreased with

no loss in information, and the recovery of original representation is performed with inverse transform $[e_i]^{-1}$. Hence the final expression for the required filters is:

$$f_j = [e_1, e_2, \dots, e_N] \cdot \dot{f}_j, \quad j = 1, \dots, M. \quad (5)$$

where \dot{f}_j are eigen vectors of matrix H , derived with any standard algorithm.

We studied the efficiency of the described procedure for recognition of images, formed by raster representation of binary coded harmonic and LFM signals (fig. 1). We have chosen such objects in order to have a chance of comparing the results with theoretical resolution limit. In our experiments the training set consisted of six groups of signals, with six realizations in each group (fig. 2).

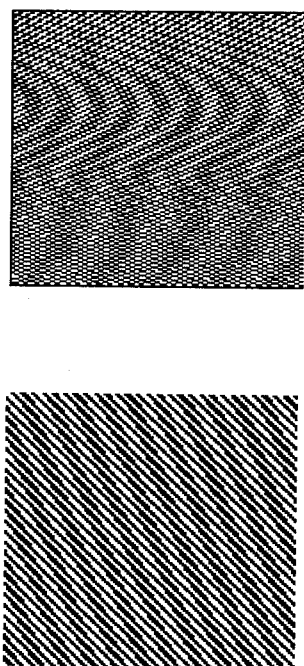


Fig. 1. Raster representation of binary coded LFM and harmonic signals without noise

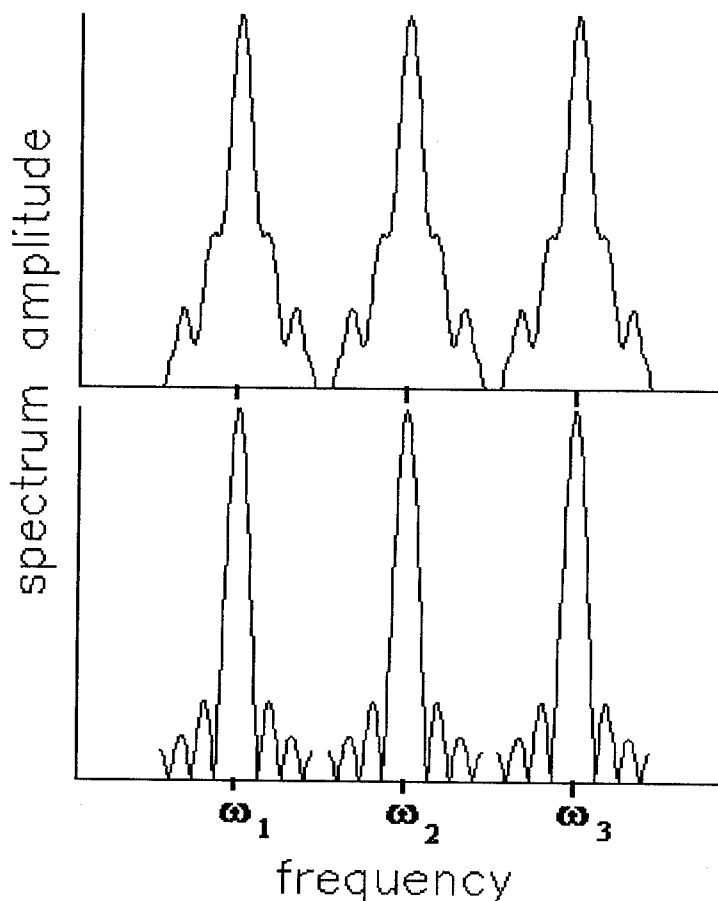


Fig. 2. Spectra of signals of the training set.
 $\omega_3 - \omega_2 = \omega_2 - \omega_1 = \Delta\omega = 7.5\omega_r$; $\omega_d = 2.5\omega_r$, ω_r is limiting resolution frequency, ω_d is frequency deviation in signals (1)-(3).

Each image had 128×128 samples and included wide band noise component, noise power was twice that of regular signal. It is evident, that such training set can be classified in three different manners: 1) for type of modulation - in two classes; 2) for central spectrum frequency - in three classes; 3) for both signs - in six classes. For each type of classification we found the respective set of discriminant filters, that were tested on the examining set. The examining set coincided in structure with the training one and differed by noise realizations. The results of recognition for modulation type and for central frequency are represented on the fig.3 as two-dimensional projection of the sign space. Good clustering of responses shows, that for such types of classification one can construct a deciding rule for

confident recognition with combination of two filters. As quantitative assessment of class discrimination we used Mahalanobis distance d [5]. The choice of such measure seems quite natural, because it is closely linked to probability of error of Bayes classifier. Particularly, for two normal classes, each including n images, error probability is $P = 0.5 \exp(-nd/8)$. In the case of several classes we determined Mahalanobis distance $d_{\alpha\beta}$ for each pair, recognition quality was assessed by the value of $d_0 = \min\{d_{\alpha\beta}\}$. The dependence of d on number of used filters (fig.4) shows, that the error of recognition of M classes approaches its low limit when $(M-1)$ filters are used, the further increase of their number has little effect on the recognition quality.

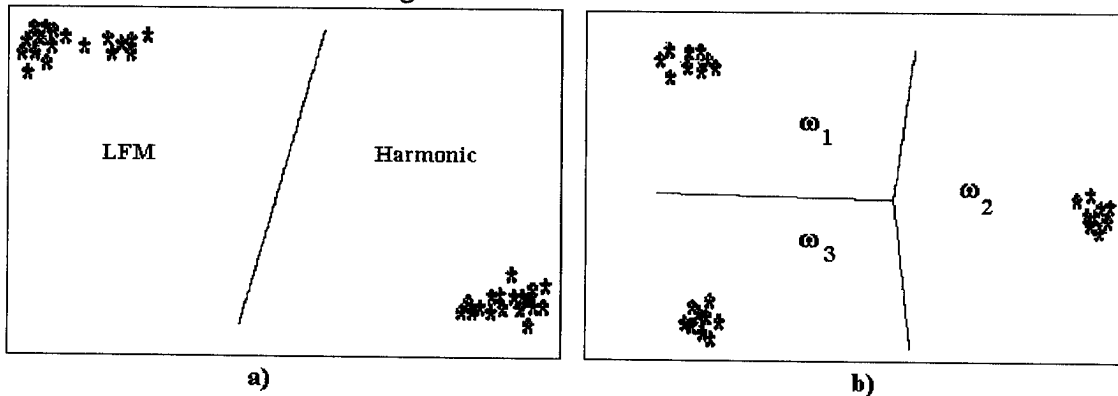


Fig.3. Two-dimensional projection of the sign space.
(a) - classification for type of modulation;
(b) - classification for central frequency.

Based on the described results we have arrived at two following conclusions. Firstly, a priori information about general population, derived from a training set, enables construction of the set of orthogonal filters, which provide effective recognition of images of very large dimension. Secondly, Mahalanobis distance is a good measure for quality of image recognition not only for two normal populations, but also for images with different statistics.

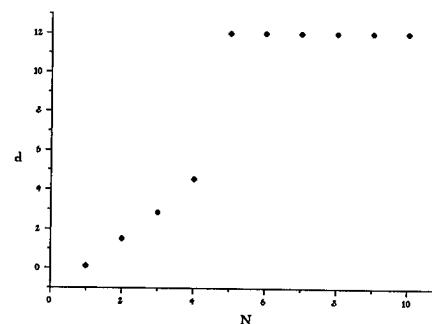


Fig.4. The dependence of the minimal Mahalanobis distance on number of used filters for the case of classification for six classes.

References

1. D.H.Foley, J.W.Sammon, IEEE Trans. Comput. 1975, C-24, 281-289.
2. Applications of Optical Fourier Transforms. Ed. H. Stark, Academic Press, New York, 1982.
3. K. Fukunaga. Introduction to Statistical Pattern Recognition. Academic Press, New York, 1972.
4. A.G.Chumakov, V.N.Kurashov. SPIE Proc., 1993, 2108, 338- 342.
5. T.W.Anderson. An Introduction to Multivariate Statistical Analysis. John Wiley & Sons, New York, 1958.

THE PRINCIPLE OF ANALYTIC CONTINUATION - HOW TO USE IT?

R.S. Adve and T.K. Sarkar

Department of Electrical and Computer Engineering,
Syracuse University, Syracuse, NY 13244.

S.M. Rao

Department of Electrical Engineering,
Auburn University, Auburn, AL 36849.

E.K. Miller

Los Alamos National Laboratory,
Los Alamos, NM 87545

Abstract

The principle analytic continuation is used to generate broadband information from narrow band data. The given information can be theoretical data-points or measured data. The given data, as a function of frequency, is modeled as a ratio of two polynomials. The Cauchy method can be used in numerical electromagnetics, optics, to reduce the size of large databases.

1. Introduction

In a host of applications in engineering, it is necessary to obtain information about a system over a broad range. In most cases it is not possible to evaluate the parameter of interest in closed form. However, either approximate or experimental data is available in a narrow band. Generation of the data over the broadband is not possible or may be extremely time consuming. The principle of analytic continuation is utilized to extrapolate/interpolate the data over a wide band. A variation on the method of Cauchy, as described in [1], has been chosen in this paper to implement the analytic continuation.

The Cauchy method deals with approximating an analytic function by a ratio of two polynomials. Given the value of the function and, optionally, its derivatives at a few points, the order of the polynomials and their coefficients are evaluated. Once

the coefficients of the two polynomials are known, they can be used to generate the parameter over the entire band of interest.

As an application, Cauchy's method has been utilized to generate broadband currents on a body from which its Radar Cross Section (RCS) is calculated. This is done from narrowband calculations of the currents. Particularly in the Method of Moments [2], [3] generation of the response at each frequency point is very time consuming. However, the current and its derivatives with respect to frequency can be calculated at a few points using the Method of Moments. Then Cauchy's method can be used to extrapolate/interpolate the current over a broad frequency range from which the RCS can be calculated.

Another area of application for the Cauchy method is that of device characterization. A very useful tool in computer aided design would be an online description of the characteristics of many devices. But, since each device could be used under different operating conditions, each with its own frequency characteristic, the memory required to describe all devices would be prohibitive. Here the Cauchy method could be used to generate broadband information while storing the measured data at only a few points.

In this paper the Cauchy technique is used to solve the above problems. In each of the cases mentioned above the Cauchy technique would save a signifi-

cant amount of program execution time or computer memory while still producing accurate results over broadband frequencies. We present, as examples, the application of the Cauchy method to generate broadband currents and to device characterization.

2. The Cauchy Method

Consider a system function $H(s)$. The objective is to approximate $H(s)$ by a ratio of two polynomials $A(s)$ and $B(s)$ so that $H(s)$ can be represented by a few variables.

Consider

$$H(s) \simeq \frac{A(s)}{B(s)} = \frac{\sum_{k=0}^P a_k s^k}{\sum_{k=0}^Q b_k s^k} \quad (1)$$

Here the given information could be the value of $H(s)$ and its N_j derivatives at some frequency points s_j , $j = 1, \dots, J$. If $H^n(s_j)$ represents the n^{th} derivative of $H(s)$ at point $s = s_j$, the Cauchy problem is:

Given $H^{(n)}(s_j)$ for $n = 0, \dots, N_j$, $j = 1, \dots, J$, find $P, Q, \{a_k, k = 0, \dots, P\}$, and $\{b_k, k = 0, \dots, Q\}$.

By enforcing the equality in equation (1), multiplying out, differentiating n times, and evaluating the expressions at point s_j , one obtains the binomial expansion,

$$A^{(n)}(s_j) = \sum_{i=0}^n {}^n C_i H^{(n-i)}(s_j) B^{(i)}(s_j) \quad (2)$$

Using the polynomial expansions for $A(s)$ and $B(s)$, equation (2) can be rewritten as

$$\sum_{k=0}^P A_{(j,n),k} a_k = \sum_{k=0}^Q B_{(j,n),k} b_k \quad (3)$$

where

$$A_{(j,n),k} = \frac{k!}{(k-n)!} s_j^{(k-n)} u(k-n) \quad (4)$$

$$B_{(j,n),k} = \sum_{i=0}^n {}^n C_i \frac{k!}{(k-i)!} H^{(n-i)}(s_j) s_j^{(k-i)} u(k-i) \quad (5)$$

$n = 0, 1, \dots, N_j$, $j = 1, \dots, J$, where $u(k) = 0$ for $k < 0$ and $= 1$ otherwise.

This can be written in the matrix form

$$[A| - B] \begin{bmatrix} a \\ b \end{bmatrix} = 0 \quad (6)$$

The order of matrix A is $N \times (P+1)$ and that of B is $N \times (Q+1)$ and $[a]$ and $[b]$ are the vectors with the polynomial coefficients.

This matrix equation can be solved using a singular value decomposition. The solution vector is the right eigenvector corresponding to the zero singular value. Hence, the number of non-zero singular values gives an estimate of the required orders of the polynomial coefficients.

3. Applications of the Cauchy Method

An example of the use the Cauchy method we interpolate the currents on a sphere being illuminated by a plane wave. The Method of Moments program evaluates the current and its first four derivatives with respect to frequency. This information was used as input to a Cauchy subroutine. The original Method of Moments program was used to calculate the RCS without the Cauchy method. The two RCS plots were compared to show the accuracy of the Cauchy method.

The current and its first four derivatives are evaluated at 5 frequency points in three ranges. $0.6m \leq \lambda \leq 1.0m$, $1.0m \leq \lambda \leq 1.8m$, $1.8m \leq \lambda \leq 6.0m$. Using this information the RCS on the sphere was calculated at 51 in the same range. Using the Method of Moments program to generate the same information would increase the execution time by a factor of eight. In Figure 1 we see the results of applying the Cauchy method to the evaluation of the RCS of a sphere. Here the RCS is plotted over a decade bandwidth.

Another application of the Cauchy method is in creating a database of many devices working in varying operating conditions. The Cauchy program would require the value of a parameter at a few frequency points and use this information to evaluate the parameter over a wide frequency band. Over many devices, and their operating conditions, this would yield significant savings in memory requirements.

To test this application the Y-parameters of a UM PHEMT were measured over the range of 1.0-

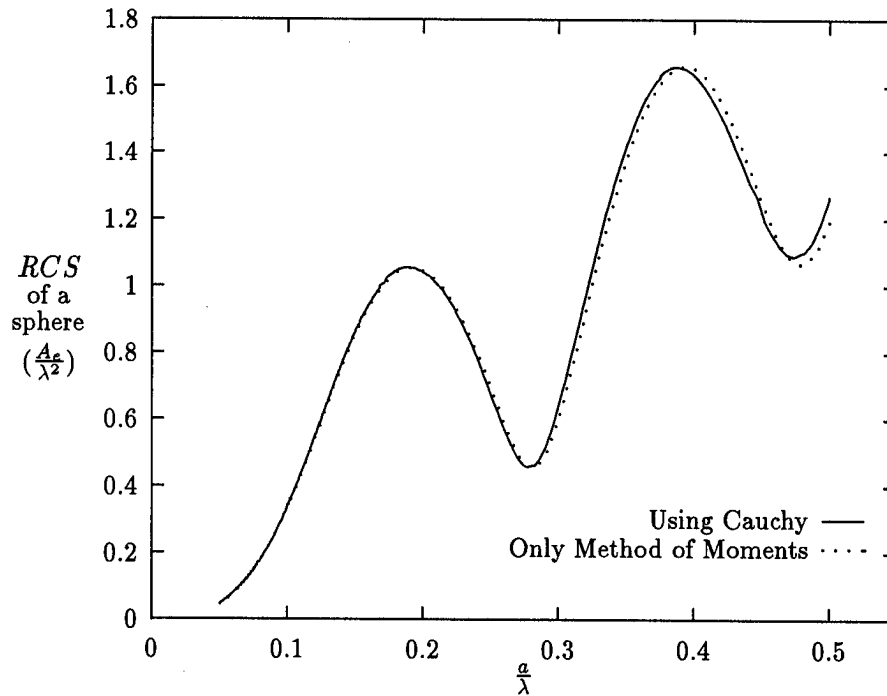


Figure 1: Radar Cross Section of a sphere

40.0GHz. Just five of these points were used as input to the Cauchy program. The points chosen were at the frequency points 1.0GHz, 10.0GHz, 20.0GHz, 30.0GHz, and 40.0GHz. This resulted in a numerator polynomial of order 1 and denominator polynomial of order 2. Figure 2(a) shows the magnitude ($|Y_{11}|$) reconstructed over this broad frequency range. Figure 2(b) shows the phase ($\angle Y_{11}$) over the same range. As can be seen the agreement with the measured values and the interpolated values is excellent.

4. Conclusions

This paper has presented a technique with many practical applications. The Cauchy method starts with assuming that the parameter of interest, as a function of frequency, can be approximated by a simple rational polynomial function. This technique has applications to many practical problems. In our research the technique is applied to the Method of Moments, optical systems, filter analysis, and de-

vice characterization. In all applications the Cauchy method has shown to save time and memory.

References

- [1] Kottapalli K., Sarkar T.K., Hua Y., Miller E. and Burke G.J. "Accurate Computation of Wide-band Response of Electromagnetic Systems Utilizing Narrowband Information" IEEE Trans. on MTT Vol.39,pp.682-688, April 1991
- [2] Harrington R.F. "Field Computation by Moment Methods" Robert E.Krieger Publishing Co., 1982
- [3] Rao S.M. "Electromagnetic Scattering and Radiation of Arbitrarily Shaped Surfaces By Triangular Patch Modeling", Ph.D. Dissertation, School of Engineering, University of Mississippi

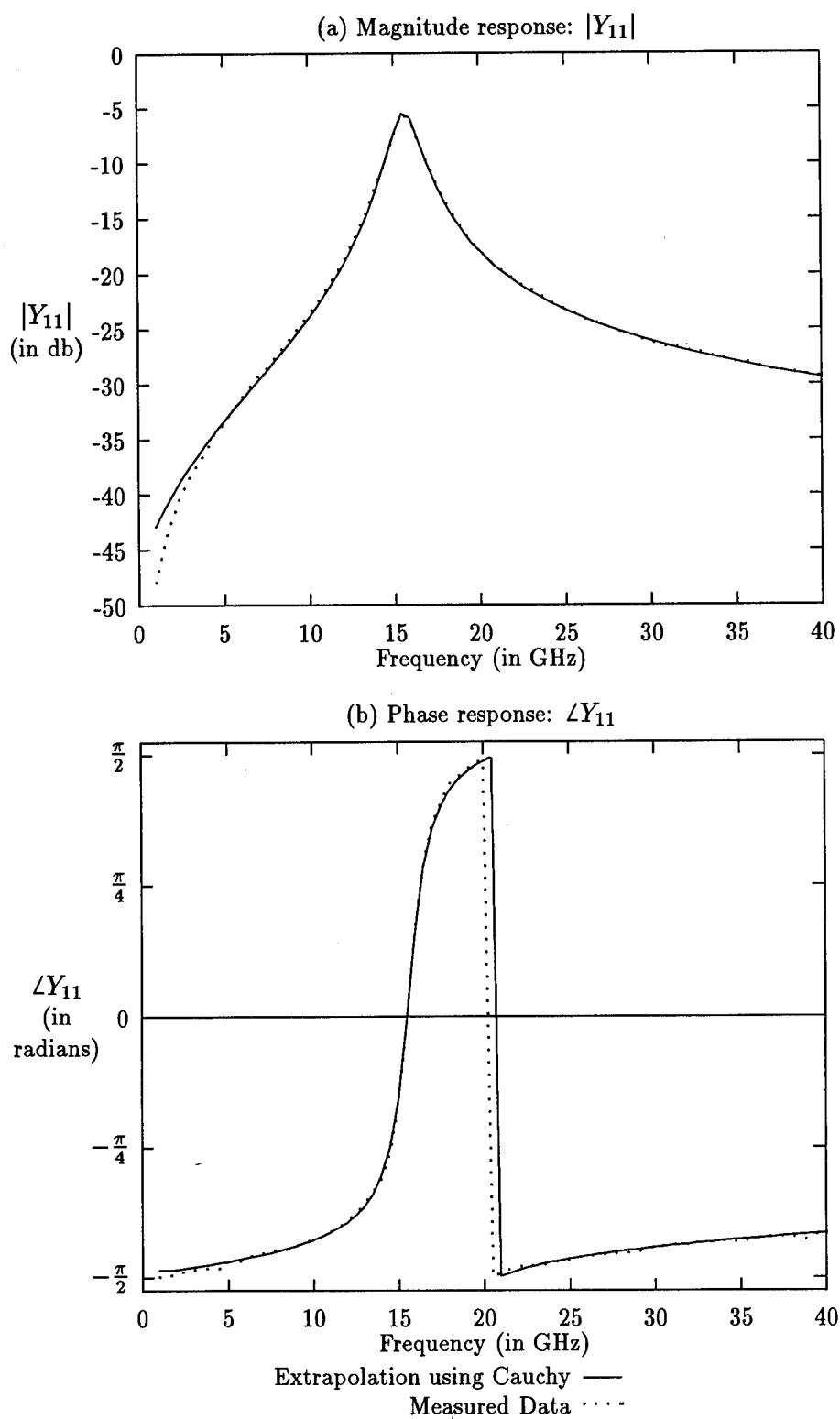


Figure 2: The Cauchy method applied to Device Characterization.

TIME-DOMAIN SIGNAL RESTORATION AND PARAMETER RECONSTRUCTION ON AN LCRG TRANSMISSION LINE.

J. Lundstedt, S. Ström and S. He

Royal Institute of Technology
Department of Electromagnetic Theory
S-100 44 STOCKHOLM, Sweden

ABSTRACT

In this paper the applicability of the compact Green functions technique in the problems of signal restoration and device characterization is discussed. It is shown that the compact Green functions, in a straightforward way, can be used to restore the incident signal from the distorted signal which is received at the other end of the line. Further, an exact method to reconstruct two of the electrical parameters of a nonuniform transmission line from the transient response is presented. This method may be used to characterize a microwave device in terms of transmission line parameters.

1. INTRODUCTION

The basic theoretical model of distributed linear networks and transmission lines is the telegrapher's equations. They describe the wave propagation characteristics of a transmission line (device) in terms of the distributed electrical parameters: the inductance $L(x)$, capacitance $C(x)$, resistance $R(x)$, and conductance $G(x)$. In this paper we present the latest results on using the wave-splitting technique and the compact Green functions technique for time-domain signal processing and device characterisation.

The signal processing problem we address is the problem of restoring signals that have been distorted by a nonuniform transmission line. The method we present is exact and works as long as the attenuation on the line is moderate, i.e., the method fails when the losses are so high that the signal propagation is more diffusion-like than wave-like.

In the device characterisation case, we assume that the telegrapher's equations can be used

as a model for the device, and focus on a reconstruction of the spatial dependence of two of the four electrical parameters of the transmission line from the time-domain transient response of the line.

2. THE MODEL EQUATIONS AND THE WAVE-SPLITTING TECHNIQUE

Consider a lossy nonuniform transmission line of length l between $x=0$ and l . The nonuniform line is assumed to be connected to two lossless uniform lines at the two ends. The voltage and current then satisfy the telegrapher's equations,

$$\begin{aligned} -\partial_x V(x,t) &= \frac{Z(x)}{c(x)} \partial_t I(x,t) + R(x)I(x,t) \\ -\partial_x I(x,t) &= \frac{1}{Z(x)c(x)} \partial_t V(x,t) + G(x)V(x,t) \end{aligned} \quad (1)$$

where ∂_x and ∂_t denote differentiation with respect to x and t , respectively, and where the characteristic impedance, $Z(x) = \sqrt{L(x)/C(x)}$, and the wavefront velocity, $c(x) = 1/\sqrt{L(x)C(x)}$, are substituted for the inductance and capacitance. The use of Z and c instead of L and C simplifies the mathematics and is in fact necessary in order to reconstruct the parameters L and C from the transient response.

The wave-splitting technique is based on transforming the voltage and current into right and left moving components V^+ and V^- . The choice of transform is arbitrary as long as it gives split components that are equal to the physical right and left moving signals at the lossless and uniform ends of the line. The

transform we use fulfil that criterion and gives simple mathematical expressions:

$$V^\pm(x, t) = \frac{1}{2}(V(x, t) \pm Z(x)I(x, t)) \quad (2)$$

From (1) we get the partial differential equations (PDEs) for V^\pm ,

$$\partial_x \begin{bmatrix} V^+(x, t) \\ V^-(x, t) \end{bmatrix} + \frac{1}{c(x)} \partial_t \begin{bmatrix} V^+(x, t) \\ -V^-(x, t) \end{bmatrix} = \begin{bmatrix} \alpha(x) & \beta(x) \\ \gamma(x) & \theta(x) \end{bmatrix} \begin{bmatrix} V^+(x, t) \\ V^-(x, t) \end{bmatrix} \quad (3)$$

where

$$\begin{aligned} \alpha(x) &= \frac{1}{2}(-GZ - RY + Z_x Y) \\ \beta(x) &= \frac{1}{2}(-GZ + RY - Z_x Y) \\ \gamma(x) &= \frac{1}{2}(GZ - RY - Z_x Y) \\ \theta(x) &= \frac{1}{2}(GZ + RY + Z_x Y) \end{aligned} \quad (4)$$

and where $Z_x \equiv \partial_x Z(x)$, $Y \equiv 1/Z(x)$.

By transforming the problem from voltage and current to right and left moving components, we get a mathematical system that is amenable to physical interpretations [1], and suitable for numerical treatment by the method of characteristics. But most important, we obtain natural boundary conditions for V^\pm at the ends of the nonuniform line, i.e., V^\pm are equal to outgoing and incoming waves at the boundaries. This means that we have exact absorbing boundary conditions for V^\pm in this one-dimensional problem.

3. THE COMPACT GREEN FUNCTIONS TECHNIQUE

A basic property of linear systems is that the response to a specific signal can be expressed as a convolution between the fundamental solution—the Green function—and the signal. In our case, the input is an incident signal, V^i , from the left at $x=0$, and the output is a reflected signal, V^r , at $x=0$, and a transmitted signal, V^t , at $x=l$. However, in one-dimensional wave propagation it is possible to

express all responses in terms of the transmitted signal instead of the incident signal. Using the transmitted signal is advantageous in both signal restoration and parameter reconstruction problems. It can be shown that the split components, $V^\pm(x, t)$, are given by the following expressions:

$$\begin{bmatrix} V^+(x, t + \tau(0, x)) \\ V^-(x, t + \tau(0, x)) \end{bmatrix} = \begin{bmatrix} a(x)V^t(t) \\ 0 \end{bmatrix} + \begin{bmatrix} G^{c+}(x, t) * V^t(t) \\ G^{c-}(x, t) * V^t(t) \end{bmatrix} \quad (5)$$

where $\tau(0, x)$ is the travel time from 0 to x ,

$$\tau(0, x) = \int_0^x \frac{dx'}{c(x')}$$

and $a(x)$ is the attenuation factor;

$$a(x) = \exp\left(\int_l^x \alpha(x') dx'\right) = \sqrt{\frac{Z(x)}{Z(l)}} \exp\left(\frac{1}{2} \int_x^l (GZ + RY) dx'\right) \quad (6)$$

$G^{c\pm}$ are compact Green functions, and $*$ denotes a convolution integral in time,

$$f(t) * g(t) \equiv \int_0^t f(t-t')g(t') dt'$$

The attenuation factor and the compact Green functions comprise all information of the scattering on the nonuniform line. $G^{c\pm}$ are called compact Green functions because they are equal to zero outside the time-interval from 0 to $2\tau(x, l)$. This property is explicitly used in the parameter reconstruction method. The compact Green functions satisfy,

$$\partial_x \begin{bmatrix} G^{c+}(x, t) \\ G^{c-}(x, t) \end{bmatrix} - \frac{2}{c(x)} \partial_t \begin{bmatrix} 0 \\ G^{c-}(x, t) \end{bmatrix} = \begin{bmatrix} \alpha(x) & \beta(x) \\ \gamma(x) & \theta(x) \end{bmatrix} \begin{bmatrix} G^{c+}(x, t) \\ G^{c-}(x, t) \end{bmatrix} \quad (7)$$

and the boundary conditions,

$$\begin{aligned} G_i^{c+}(x, 2\tau(x, l)) &= \frac{1}{2}c(x)\beta(x)G^{c-}(x, 2\tau(x, l)) \\ G^{c-}(x, 0) &= -\frac{1}{2}c(x)\gamma(x)a^+(x) \end{aligned} \quad (8)$$

4. SIGNAL RESTORATION

Assuming that we know the electrical parameters of the transmission line, by expressing the split components in the transmitted signal, the signal restoration problem is in fact solved. Note that the original signal $V^i(t) = V^+(0, t)$. According to equation (5), once the compact Green functions, $G^{c\pm}(x, t)$, and the attenuation factor, $a(x)$, have been calculated using equations (4), (6), (7) and (8), we get the original shape of the signal from the signal received at $x = l$ by,

$$V^i(t) = a(0)V^l(t) + G^{c+}(0, t) * V^l(t) \quad (9)$$

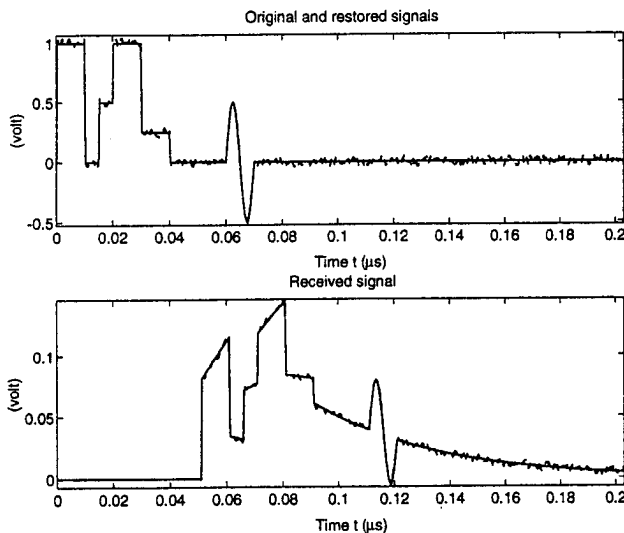


Figure 1. The upper graph shows the original and the restored signal. The lower graph shows the received signal with and without added noise.

The results of a numerical test is shown in figure 1. The test was based on a fictitious lossy nonuniform transmission line of 10 m length. The electrical parameters were chosen so that the signal was heavily distorted by the line. The solid lines in figure 1 represent the original and received signals. To illustrate the well-posedness of the restoration procedure, noise was added to the received signal (the broken line in the lower graph).

The result, given by equation (9), was the broken line in the upper figure. It is clearly seen that the restoration works well, which is a consequence of that the method is exact. For some lossy transmission lines a simple RC-circuit can be used for an instantaneous restoration of the signal [2].

5. PARAMETER RECONSTRUCTION, DEVICE CHARACTERISATION

Assuming that a device can be modelled by the telegrapher's equations, the compact Green functions technique can be used to reconstruct the transmission line parameters from the transient response of the device. If the device physically is not a transmission line, the algorithm provides the equivalent transmission line that corresponds to the given transient response.

From measurement (or specification, in design problems) of the transient response, in terms of $a(0)$, $G^{c+}(0, t)$ and $G^{c-}(0, t)$, the boundary conditions (8) and the PDEs (7) can be solved for two unknown parameters provided the other two are known. However, the reconstruction is only unique where the conditions in table I are satisfied [3].

Parameters	Condition for reconstruction
c and Z	$GZ - RY \neq 0$
c and R , c and G	$\partial_x Z(x) \neq 0$
Z and R , Z and G	no restriction
R and G	$\partial_x Z(x) \neq 0$ or $(GZ - RY) \neq 0$

Table I: Conditions for reconstruction of different pairs of parameters.

For example, the reconstruction of the characteristic impedance and the wavefront velocity is only possible where $GZ - RY \neq 0$. In the numerical example shown in figure 2, $GZ - RY = 0$ at $x \approx 0.85$ and it is seen that the reconstruction of Z and c fails around that point.

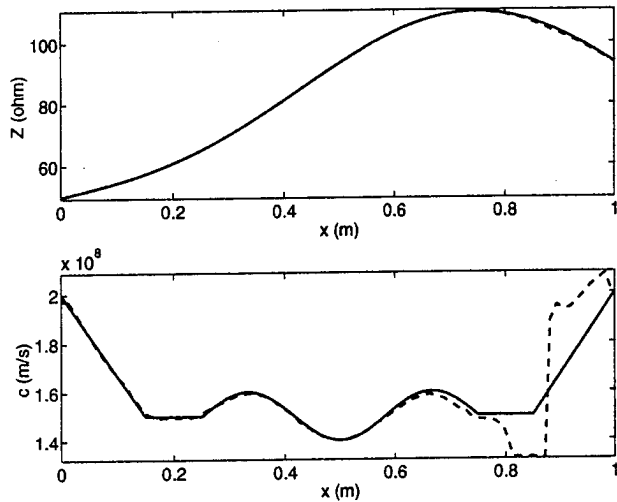


Figure 2. Reconstruction of Z and c . The error increases in the vicinity of $x \approx 0.85$ since $GZ - RY$ is zero there.

6. DISCUSSION

The objective of this paper was to show the usefulness of the wave-splitting technique and the compact Green functions technique in the area of signal processing and device characterization. An exact method to filter the distortion caused by a nonuniform transmission line was presented, as well as an exact method to reconstruct two of the transmission line parameters from the transient response of the line.

REFERENCES

- [1] J. Lundstedt, "Condition for distortionless transmission line with a nonuniform characteristic impedance", *IEEE Trans. Microwave Theory Tech.*, 43, 6, 1995.
- [2] J. Lundstedt and S. He, "Signal restoration after transmission through a nonuniform LCRG line", *IEEE Trans. Microwave Theory Tech.*, 42, 11, 2087-2092, 1994.
- [3] J. Lundstedt and S. Ström, "Simultaneous reconstruction of two parameters from the transient response of a nonuniform LCRG transmission line", *J. Electro. Waves and Applic.*, (in press),

On Incorporating Signal Processing and Neural Network Techniques with the FDTD Method for Solving Electromagnetic Problems

J. Litva C. Wu and E. Navarro

Communications Research Laboratory, McMaster University

1280 Main St. W., Hamilton, Ontario, Canada, L8S 4K1

Tel: 905-529-7070 ext. 23142, Fax: 905-521-29, e-mail: litva@mcmaster.ca

I. Introduction

The Finite Difference Time Domain Method (FDTD) is a very powerful numerical method for solving electromagnetic (EM) problems. Due to its flexibility, it can be used to solve problems which have very complex boundaries. It is well known that the FDTD method requires long computation times for simulating the resonant or high-Q structures. The reason for this is because the algorithm is based on the leap-frog formula. The quest to find good predictor for enhancing the method is very interested topic in EM modelling.

In this paper, the autoregressive model (AR) and Backpropagation (BP) Neural Network are designed as predictors. The Total Least Squares (TLS) method is applied to obtain AR coefficients. A waveguide filter is used as an example and modeled using the FDTD method. We demonstrate that a short segment of an FDTD data set can be used to train the predictors and the predictors can predict later information very well.

II. The Brief Background

The FDTD algorithm is a method in which the central difference scheme is used to discretize Maxwell's curl equations in both time and space. The central difference technique can contain the magnitude of the round-off errors so that second-order accuracy is achieved. To model the

electrical and magnetic fields in space, Yee introduced his cell system in 1966 [1]. The physical basis for Yee's cell system can be easily explained using Faraday's and Ampere's laws. After using Yee's cell system to describe the computational domain, which is bounded by electric, magnetic or application specific absorbing walls, Maxwell's equations are essentially replaced by a computer which calculates the fields at the grid points associated with the cells.

In this paper, a waveguide filter which is composed of a segment of rectangular waveguide and two metal walls with cross-iris (Fig. 1) is simulated using the FDTD method. The cavity between the two metal walls is a cross-iris coupled one-resonator filter. After a pulse is launched from input port, the time-sampled data are derived both the input and output ports. If modelling accuracy is to be realized, the simulation can not be stopped until the incident pulse totally passes the sampling points. If the device is a high-Q system, the sampling time is going to be very long. Fig. 2 gives the sampled data at output port. It can be observed that after 60000 time iterations, the output signal has still does not converged. In the following sections, we will demonstrate how AR process and BP neural networks can be used to predict FDTD data, based on using very short time samples.

III. Autoregressive Processes and Backpropagation Neural Networks

a. Autoregressive Processes [2]

An AR process is a random process, which is the output of an all-pole filter, when excited by white noise. In the time domain it can be described by,

$$b_i - \sum_{k=1}^K x_k a_{i-k} = n_i \quad (1)$$

where b_i is the i th time step signal, x_k is the AR coefficients, K is the order of AR model and n_i is white noise. Matrix A is covariance matrix. Equation (1) tells us that provided σ^2 is suitably small, the present value of output y can be predicted from a linear combination of past samples. The Least Squares solution can provide an estimate of best solution, x_{LS} , under certain conditions.

b. Total Least Squares (TLS) [3]

In the TLS case, there is error in both matrix A and b . Thus the regression equation $b = Ax + n$ may be written in the TLS case in the form

$$(A+E)x = b+r \quad (2)$$

where E is the error in A , r is the error in b . We wish to determine value for E , r and value x_{TLS} which satisfy,

$$\min_{(b+r) \in \text{range}(A+E)} \| [E, r] \|_F \quad (3)$$

One way to get the TLS solution is to carry out a SVD of $[A \ b]$ and assume that $\sigma_p > \sigma_{p+1} = \dots = \sigma_{K+1}$ with $p \leq K$. If not all $v_{K+1, i} = 0$, $i = p+1, \dots, K+1$, then the minimum

norm TLS solution is given by

$$x_{TLS} = - \frac{\sum_{i=p+1}^{K+1} v_{K+1, i} [v_{1, p} v_{2, p} \dots v_{k, p}]^T}{\sum_{i=p+1}^{K+1} v_{k+1, i}^2} \quad (4)$$

c. Multilayer Perceptron Neural Network [4]

Fig.3 depicts a portion of a multilayer perceptron. In this network, two kinds of signals are identified. First, Function Signal, which is an input signal that appears at the input end of the network and propagates forward through the network. Second, Error Signal, which originates at output neurons of the network, and propagate backward through the network. The error signal is computed by each neuron of the network involves an error-dependent function in one form or another. Each neuron in the network can be described by following pair of equations:

$$u_k = \sum_{j=1}^p w_{kj} x_j \quad (5)$$

$$b_k = \phi(u_k - \theta_k) \quad (6)$$

where k is the k th neuron in a network; $\{x_j\}$ are input signals; $\{w_{kj}\}$ are the synaptic weights for neuron k ; u_k is the linear output combiner; θ_k is the threshold; $\phi(\dots)$ is the activation function, which can be linear or nonlinear functions; and b_k is the output signal of the neuron. The first hidden layer outputs are the inputs of the second layer, etc. Basically, the BP process consists of two passes through the different layers of a network: a forwards pass and a backward pass. In the forward pass, the forward

signal is applied to the nodes of the network, and its effect propagates through the network, layer by layer. Finally a set of response is produced at the output layer. During the forward pass, the weights of the network are all fixed. On the other hand, during the backward pass, the weights are adjusted in accordance with the error-correction rule. Specifically, in the training procedure, the actual response of the network is subtracted from the desired response to produce an error signal, which propagates backwards through the network. The synaptic weights are adjusted so as to make the actual response of the network move closer to the desired response.

IV. Numerical Results and Discussions

In this section, the data from 2500 to 5000 iterations in Fig.2 is used to train AR coefficients based on TLS, because before 2500 iterations the system is in a period of transition. After taking the SVD of $[A \ b]$ ($K = 2$), we have $\Sigma = \text{diag}(0.01505, 0.0014044, 0.0000013519)$. Here again the order, p , of the TLS can be taken to be equal to 2. From Eq. (4) we have $x_{\text{TLS}} = [1.9988, -0.9999]^T$. Fig.4 shows a detailed comparison of real data (from 56500 to 57500 iterations) and predicted data, obtained using the AR model. The AR coefficients are obtained using TLS with $K = 2$. There is good agreement.

An neural network is designed with a input layer, 2 hidden layers and a output layer. In the network, the neurons on each layer are 6, 3, 3, 1. The activation function applied to the hidden layers is a sigmoidal nonlinearity defined by logistic function:

$$b_k = \frac{1}{1 + \exp(-u_k + \theta_k)} \quad (7)$$

and the activation function on the output layer is linear function. Again, the data from 2500 to 5000 iterations decimated by the factor 10 are used to train the network. Fig.5 shows the comparison between 56500 to 57500 iterations. Again a very good agreement is observed. More details will be presented on conference.

V. Conclusions

The TLS method is used to estimate AR coefficients, which are used in an AR model. A multilayer perceptron neural network is trained by the Error-Backpropagation Algorithm. The AR model and BP neural network are used as predictors and trained by a very small portion of early data set for the output of a waveguide. The results show that both predictors can give good predictions.

References

- [1] K. S. Yee, "Numerical solution of initial boundary value problems involving Maxwell's equation in isotropic media", IEEE Trans. AP Vol.14, pp 302-307, May 1966.
- [2] J. P. Reilly, "EE731 Lecture Notes: Matrix Computations for Signal Processing", version 1994.
- [3] G. H. Golub and C. F. Van Loan, Matrix Computations, Second Edition 1993.
- [4] Simon Haykin, Neural Networks - A Comprehensive Foundation, 1994.

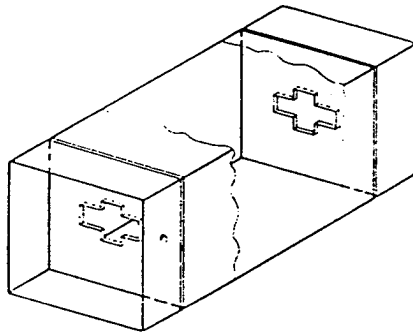


Fig.1 WR 62 waveguide housing.
Resonator length 12.155 mm.

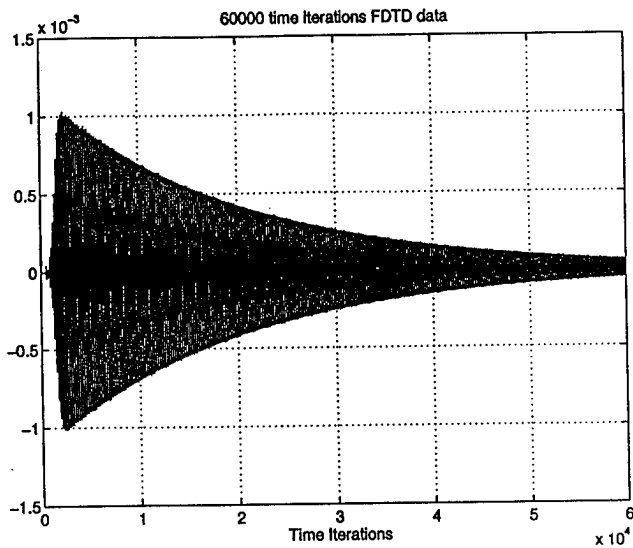


Fig.2 60000 iterations FDTD data sampled
at output port of the filter.

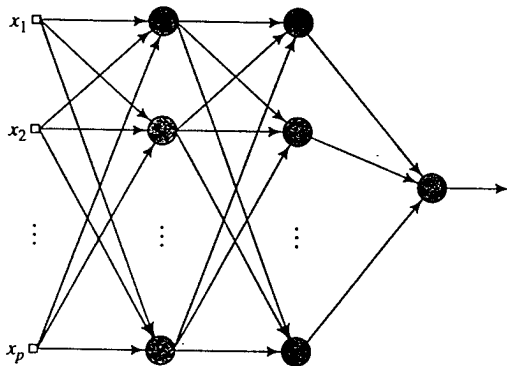


Fig.3 A multilayer Perceptron Network

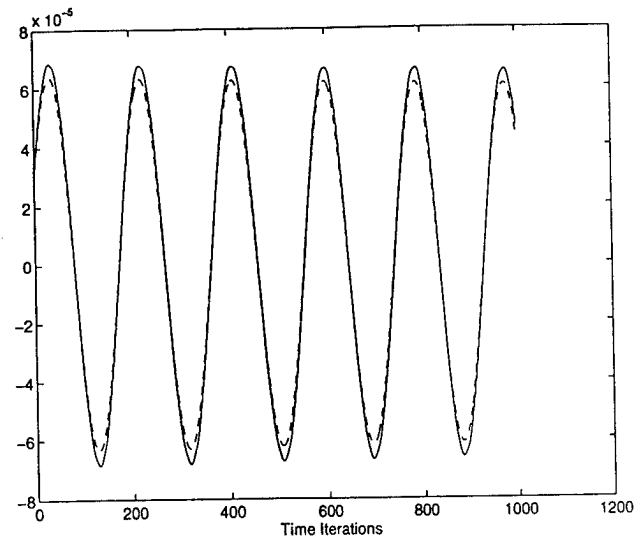


Fig.4 The comparison between FDTD and
AR model predicted data (from
10000 to 11000 iterations).

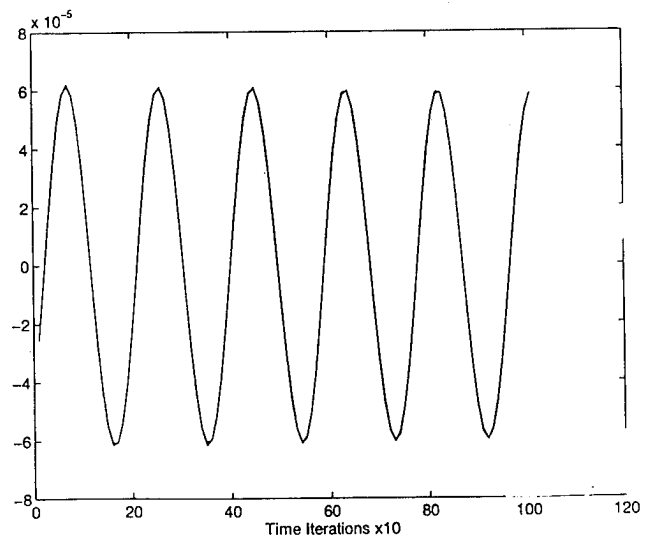


Fig.5 The comparison between FDTD
and BP network predicted data
(from 59000 to 60000 iterations).

SIMULATED IMAGES FOR GREEN'S FUNCTION OF MULTILAYER MEDIA, AN ALTERNATIVE TO COMPLEX IMAGES

Y.L. Chow, A. Torabian-Esfahani, N. Hojjat and S. Safavi-Naeini

Department of Electrical and Computer Engineering
University of Waterloo, Waterloo, Ontario, Canada N2L 3G1

Fax: (519) 746-3077, Phone: (519) 888-4567, X2822, email: ylchow@lenz.uwaterloo.ca

Area - Microwave Modeling and Simulation

1. ABSTRACT

Like most inverse problems the complex image solution of the Green's function of multilayer media is non-unique. The non-uniqueness makes the variations of the image amplitudes and locations unsteady with frequency. This is inconvenient for wideband, such as digital, circuit computations. Nevertheless, the non-uniqueness also points to the possibility of strong steadiness by fixing the image at *real* locations, say to those of the static images, without sacrificing convergence. These new images are renamed simulated. they are generated easily by the moment method in the spectral space without the Prony's method.

2. INTRODUCTION

Replacing the tedious Sommerfeld integrals in constructing the spatial Green's functions of a multilayer medium, Chow et al [1], [2] developed the quasi-analytic complex image technique. Requiring only 3 or 4 images with complex locations, the technique is accurate, and indeed rapidly convergent, and also general.

The underlying mathematics of the technique is the Prony's method which is really a curve fitting procedure, in the spectral space of the Green's function, for the images akin to remote sensing (i.e. inversion) of sources. The nonuniqueness of a inversion solution results in certain gives between image locations and amplitudes and means their unsteady variations over a frequency band. Happily, like other inversions, all variations give the correct values on the spatial Green's function fields. This tolerance is convenient for field evaluations at a single frequency, but not so for wide band, such that one can quickly and accurately interpolate the images at intermediate frequency points be-

tween salient frequency points.

On the other hand, the nonuniqueness also points to the possibility of having only a few *simulated images* with *real* locations, as opposed to complex images with complex locations, but still obtaining high accuracy in the Green's functions. To satisfy the low frequency asymptotes the real locations of the images can be the first 4 of the classical static images. With the locations fixed, we use *moment method in the spectral space*, and not Prony's method, to find the images amplitudes. The amplitudes are now indeed smooth varying function of frequency.

3. NUMERICAL RESULTS

The spatial Green's functions, from 4 simulated images and 4 complex images, are calculated for comparison. The microstrip structure has dielectric height of 1 mm with $\epsilon_r = 12.6$.

As we mentioned before the complex images are nonunique, both in amplitudes and in image locations. We shall show only the image locations of the first two out of four as a function of frequency in Figure 1. Since the locations are complex, we shall show only the *amplitudes* of the locations of G_A^{xx} the vector potential along the dielectric interface. We may call the image farther away from the source as image number 1 and the closer are as number 2. We see that the *amplitudes* of the locations indeed are unsteady. In fact images number 1 and number 2 appear to shift positions in Figure 1. Similar unsteadiness is observed for the image amplitudes, for all four images.

Despite such unsteadiness, the Green's functions from the complex images remain very steady and well behaved in Figure 2 and 3. The results of complex images in Figure 2 and 3 are circles, the results of

simulated images are dotted lines. We see that their agreements are excellent until distance $k_0\rho$ along the dielectric interface becomes unity.

The four simulated images in calculating the Green's functions in Figure 2 and the four in calculating in Figure 3 are perfectly steady. Both sets of the image locations are chosen to be those of electrostatic images and naturally they are steady. The amplitudes of the vector potential G_A^{xx} and scalar potential G_q are shown in Figure 4 and 5 and they are indeed steady and smooth as a function of frequency.

It is observed that beyond 6.7 GHz, when the first simulated image is one radian electrically from the source, the image amplitudes starts to vary with frequency. Below 6.7 GHz, the amplitudes of the simulated images are near constant but are not equal to those of the quasi-dynamic images in general, since for good accuracy the latter images may number 80 for $\epsilon_r = 12.6$ instead of just the first 4.

4. DISCUSSIONS

Near the source and at low frequencies, the simulated images are just as fast convergent and accurate as the complex images. At higher frequencies, however, since the images locations are fixed and real, we find that simulated images are not as accurate, until we double the image number.

This may not be a drawback for wide band (e.g. digital) signals since they are generally in a lower frequency than microwave. Then the advantage of smooth varying image amplitudes with frequency makes the simulated images a better choice for interpolation and rapid convergence.

5. REFERENCES

- [1] Y.L. Chow, J.J. Yang, D.G. Fang and G.E. Howard, "A closed form spatial Green's function for the thick microstrip substrate", *IEEE Trans. Microwave Theory and Techniques*, MTT-39, March 1991, pp. 588-592.
- [2] J.J. Yang, Y.L. Chow, G.E. Howard and D.G. Fang, "Complex images of an electric dipoles in Homogeneous and Layered dielectrics between two ground planes", *IEEE Trans. Microwave Theory and Techniques*, MTT-40, March 1992, pp. 595-600.

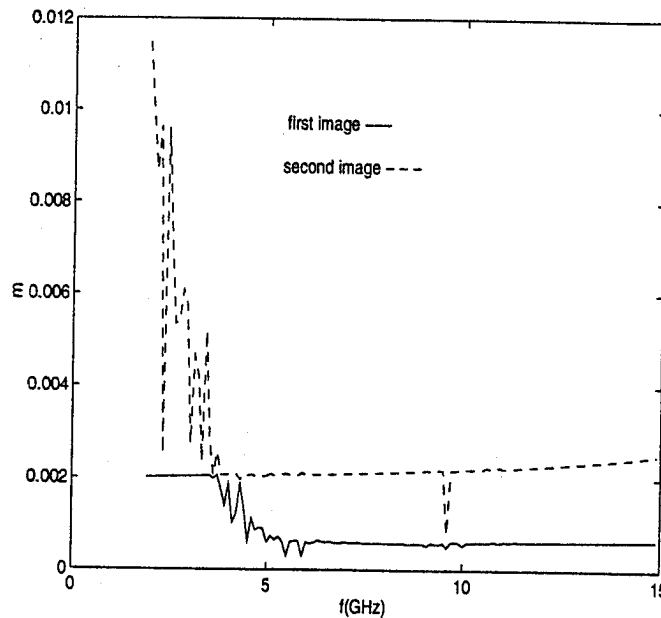


Figure 1: Amplitude of locations of complex images for G_A^{xx} .

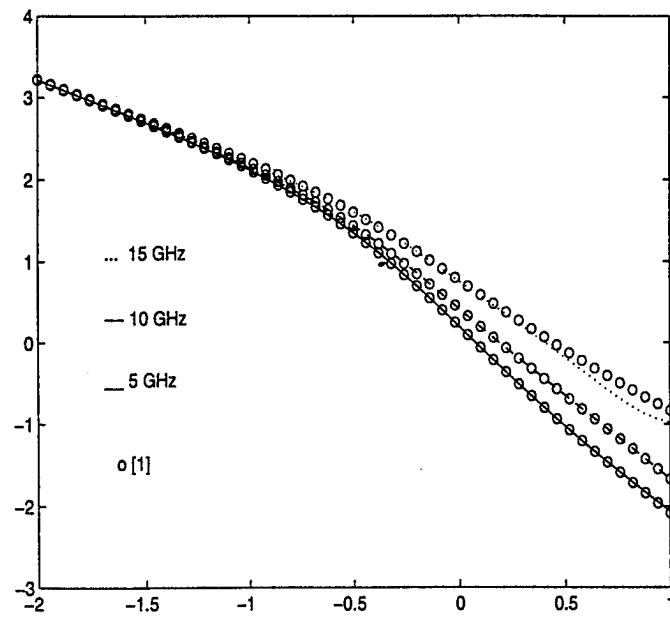


Figure 2: The amplitude of the vector potential G_A^{xx} .

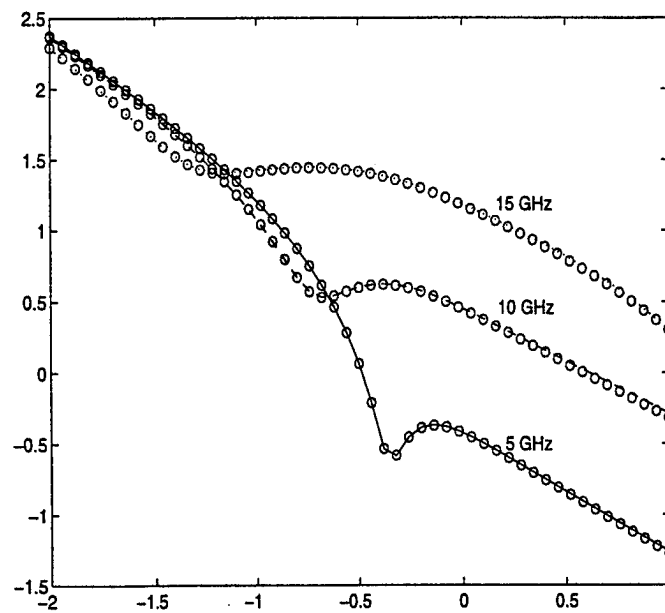


Figure 3: The amplitude of the scalar potential G_q .

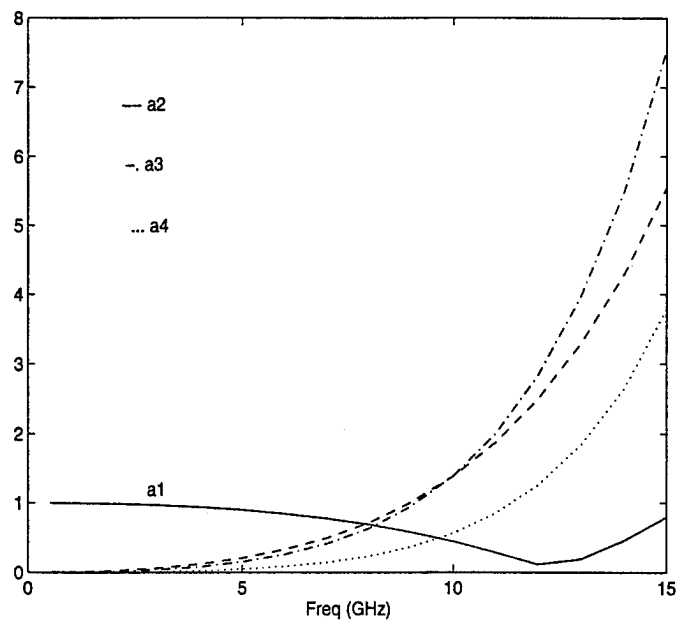


Figure 4: The relative amplitudes of images of G_A^{xx} .

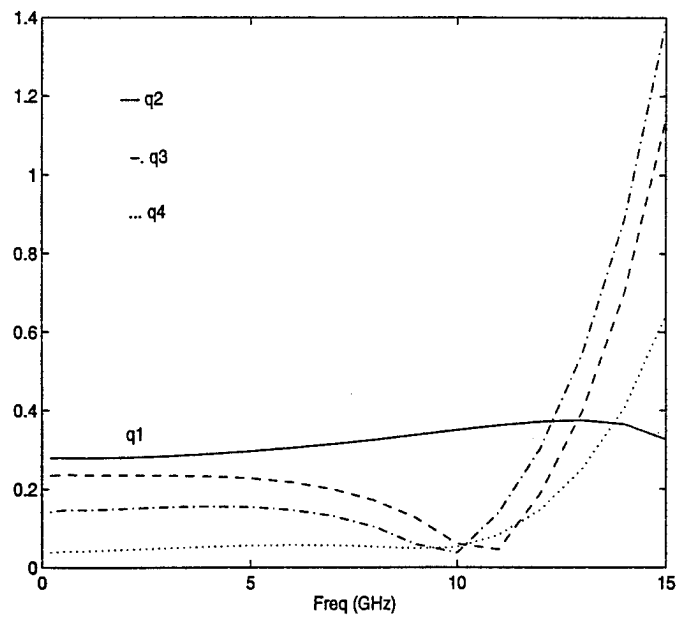


Figure 5: The relative amplitudes of images of G_q .

INTERPOLATION/EXTRAPOLATION OF FREQUENCY DOMAIN RESPONSES USING THE HILBERT TRANSFORM

S.M.Narayana, G.S. Rao, R.S. Adve and T.K. Sarkar
Department of Electrical and Computer Engineering,
Syracuse University, Syracuse, NY 13244.

M.C. Wicks and S.C. Scott
Rome Laboratory,
Rome, NY 13441.

Abstract

This paper shows that given frequency domain information over a limited frequency range, it is possible to extract information over a broad band and extract a real, causal time domain response. This is done through the use of the Hilbert transform. This technique for example can be implemented in network analyzers and waveform processing equipment.

1. Introduction

System measurements may be performed in either the time domain or the frequency domain. Time domain measurements are easier to perform since the waveforms of interest are all real. However, one disadvantage is the limited dynamic range of available systems. Frequency domain measurement equipment benefit from large dynamic range. Furthermore, frequency domain measurements may be carried out either over an entire range of frequencies or selectively over a band of frequencies. Theoretically, it is possible to extract a time domain response from these measurements by an inverse Fourier transform. But, if the measurements are made in a noisy environment, it is difficult to recover the true time domain response.

All physical time domain responses are causal, in that the signal is non-zero only for times greater than zero. However, since band-limited complex frequency domain data does not guarantee causality in the time domain, nor a real time domain response,

measurements carried out in the frequency domain do not truly represent the transient response of the system. Even so, we establish that it is possible to extract a causal response by extrapolating the complex frequency domain data under the premise that the time domain signal must be causal. The objective of this paper is to extrapolate/interpolate band-limited frequency domain data so as to facilitate the extraction of a causal time domain response.

In general, the real and imaginary parts of the complex frequency domain data are independent of each other. However, the causality of the time domain signal, denoted as $h(t)$, assures us that the real and imaginary components of the frequency domain are related through the Hilbert Transform [1].

Since we process discrete frequency domain data, we handle frequency and time domain signals in the form of sequences. A numerical example proves the usefulness of the technique.

2. Transform Relationships

This section briefly covers some of the properties of sequences and their Fourier and Hilbert transforms. Any periodic, real, time domain sequence $h[n]$ can be expressed as a sum of an even sequence $h_{pe}[n]$ and an odd sequence $h_{po}[n]$. Also, the Fourier transform of the even and odd parts of a sequence are the real and imaginary parts of the original sequence $h_p[n]$ [2].

Also, for real $h_p[n]$, $H_{\Re}(e^{j\omega}) = H_{\Re}(e^{-j\omega})$ which is an even function, and $H_{\Im}(e^{j\omega}) = -H_{\Im}(e^{-j\omega})$ which is an odd function.

Consider a periodic, real, time domain sequence $h_p[n]$ with period N , that is related to a finite length sequence $h[n]$ of length N by

$$h_p[n] = \sum_{i=-\infty}^{\infty} h[n + iN]$$

We know

$$h_{pe}[n] = \frac{1}{2} \{h_p[n] + h_p[-n]\}$$

and similarly

$$h_{po}[n] = \frac{1}{2} \{h_p[n] - h_p[-n]\}$$

If we have $N = 2r$ (where r is a positive integer) then, we can express $h_p[n]$ as

$$h_p[n] = h_{pe}[n]u_{pN}[n] \quad (1)$$

where

$$u_{pN}[n] = \begin{cases} 2 & n = 1, \dots, \frac{N}{2} - 1 \\ 1 & n = 0, \frac{N}{2} \\ 0 & n = \frac{N}{2} + 1, \dots, N - 1 \end{cases} \quad (2)$$

or

$$u_{pN}[n] = 2u[n] - 2u[n - \frac{N}{2}] - \delta[n] + \delta[n - \frac{N}{2}] \quad (3)$$

where $u[n]$ is the unit step sequence, and $\delta[n]$ is the unit sample sequence [2].

Also the odd part of the sequence can be expressed as,

$$h_{po}[n] = \begin{cases} h_{pe}[n] & n = 1, \dots, \frac{N}{2} - 1 \\ 0 & n = 0, \frac{N}{2} \\ -h_{pe}[n] & n = \frac{N}{2} + 1, \dots, N - 1 \end{cases} \quad (4)$$

Using some derivations and the definition of the Fourier Transform, we have

$$jH_{p\mathfrak{S}}[k] = \frac{1}{N} \sum_{m=0, m \neq k}^{N-1} H_{p\mathfrak{R}}V_{pN}[k - m] \quad (5)$$

This is the Hilbert transform relationship between the real and imaginary parts of the Fourier transform of a periodically causal sequence. If $h[n] = 0$ for $n < 0$ and for $n > N/2$ then the periodicity maybe removed and we have the same relationships between

the real and imaginary parts of the Fourier transform of $h[n]$.

$$jH_{\mathfrak{S}}[k] = \begin{cases} \frac{1}{N} \sum_{m=0, m \neq k}^{N-1} H_{\mathfrak{R}}[m]V_N[k - m] & 0 \leq k \leq N - 1 \\ 0 & \text{otherwise} \end{cases} \quad (6)$$

Equation (6) is the Hilbert transform relationship between $H_{\mathfrak{R}}[k]$ and $H_{\mathfrak{S}}[k]$. Thus with a knowledge of one the other can be evaluated. This procedure forms the basis of our technique for the extraction of a real, causal time domain response from band-limited complex frequency domain data. The theoretical development assures us that by computing the DFT's and IDFT's the original real time sequence will not lose its causal nature.

3. Extrapolation Of Frequency Domain Data

The method to generate a causal, finite duration time domain sequence $h[i]$, ($h[i] = 0$ for $i < 0$ and $i \geq N$) given a band-limited data samples of its Fourier transform is described. The iterative technique discussed in the subsequent part of the section describes a sequence of transformations between the time and frequency domains. To describe the algorithm utilized in our technique we shall assume that the band-limited frequency domain data is available between frequencies $f1$ and $f2$ and sampled at n frequency points in between $f1$ and $f2$. This data can be expressed as a row vector of length n , represented as

$$H(1 : n) = [H_1 H_2 H_3 \dots H_n]$$

where the notation $H(1 : n)$ indicates that samples 1 through n are elements of the row vector H . In general $H(p : q)$ indicates samples H_p through H_q .

In order to extract the real and causal time domain signal for which we have the complex frequency domain data in the frequency band $[f1, f2]$, we first extrapolate the available frequency domain data between frequencies $[0, f1]$ and from $[f2, f3]$, where $f3$ is a frequency chosen until which extrapolation is considered necessary. Since $H(e^{j\omega}) = H^*(e^{-j\omega})$ the extrapolated data between frequencies $[-f3, 0]$ will be symmetrical to that between frequencies $[0, f3]$. Therefore, extrapolation in the negative frequency domain will not require any additional computation.

The steps involved to extract the time domain sequence from a band-limited frequency domain data are explained below.

1. The available band-limited frequency domain data $H(1:n)$ is padded with zeros to the extent necessary. To extract a causal, time domain sequence of finite length n samples the frequency data has to be padded with zeros to a minimum of $2N$ points, providing a sequence of even length. Therefore the available frequency domain data has to be padded with $2N-n$ zeros. A zero padded vector $HZ(1:2N)$ is formed from $H(1:n)$ as

$$HZ(1:n) = [H_1, H_2, H_3 \dots H_n, 0, 0 \dots 0]$$

2. The zero padded complex frequency domain data is now split into corresponding real and imaginary parts.

$$HZ_{\Re} = \text{Real}(HZ)$$

$$HZ_{\Im} = \text{Imag}(HZ)$$

3. An inverse discrete Hilbert transform of the real part of the frequency data is performed which, gives us the imaginary sequence

$$HZ_{\Im(\text{new})} = [\mathcal{F}^{-\infty}(HZ_{\Re})]$$

4. The imaginary part of the band-limited frequency data extracted in step 2 is substituted into the data generated by the discrete Fourier transform of the odd sequence in the previous step.

$$HZ_{\Im(\text{subs})} = [HZ_{\Im}(1:n), HZ_{\Im(\text{new})}(n+1:2N)]$$

5. The new imaginary data $HZ_{\Im(\text{subs})}$ thus formed is subjected to a discrete Hilbert transform, which will return an improved version of the real sequence. The even sequence of samples are subjected to a discrete Fourier transform so as to recreate the real part of the spectrum.

$$HZ_{\Re(\text{new})} = [\mathcal{H}(HZ_{\Im(\text{subs})})]$$

6. The real part of the band-limited frequency data extracted in step 2 is substituted into the data generated by the discrete Fourier transform of the even sequence in the previous step.

$$HZ_{\Re(\text{subs})} = [HZ_{\Re}(1:n)HZ_{\Re(\text{new})}(n+1:2N)]$$

7. Subsequent processing is an iteration of the steps 2-11.

The results may not be absolutely convergent if sufficient amount of band-limited data is not available, however this also depends on the energy content of the spectral components in the band-limited data.

Subsequent sections illustrate the efficacy of this technique. We have provided several simulation results. We have also implemented this technique on actual frequency domain measurements performed on a Hewlett Packard network analyzer HP 8510B.

4. Simulation Results

The transfer characteristics of a band pass filter are measured at 415 points between 4.31 GHz and 7.415 GHz. 60 points (between points 200 and 260) were discarded. Using the Hilbert transform technique, the missing data was reconstructed. Figure 1 shows the comparison of the reconstruction of the real part with the original data. Figure 2 shows comparison of the reconstruction of the imaginary part with the original data. In both cases the reconstruction is very good.

5. CONCLUDING REMARKS

The Hilbert transform relationship between the real and imaginary parts of the frequency domain response for causal time domain signals proved to be a sound basis for the extrapolation of the frequency domain data and extraction of a causal and real time domain response. The reconstruction of the time domain signal is excellent given a sufficient number of iterations. Specifically, the peak value of the impulse response and the shape of the time domain response are accurately represented. The presence of an imaginary component in the time domain response as a result of the inverse Fourier transform of band-limited frequency domain data is nullified as a result of the processing.

Application of this technique in the case of noisy frequency domain data has been discussed. With an approximate knowledge of the bands of frequency data which have been corrupted by noise it was shown possible to extract the true time domain response. The technique was applied to measurements performed on the HP 8510B vector network analyzer

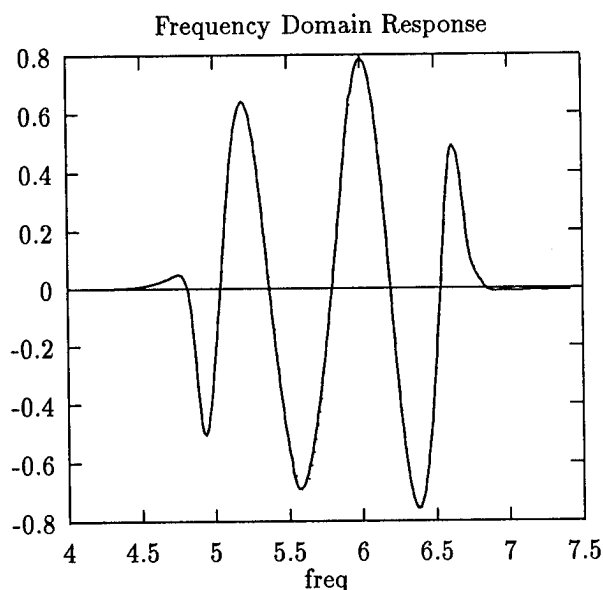


Figure 1. Real Part

for a Sliding load standard and the results have been discussed.

References

- [1] V. Čizěk, Discrete Hilbert transform, *IEEE Trans. Audio and Electroacoustics*, vol. AU-18, No. 4, pp. 340-343, Dec. 1970.
- [2] A. V. Oppenheim and R. W. Schaffer, *Discrete-time Signal Processing*, Prentice Hall, Englewood Cliffs, NJ, 1989.
- [3] Hewlett-Packard Company, HP 8510B Operating and Programming manual, HP Part No. 08510-90070, Hewlett-Packard, Santa Rosa, CA, 1987.

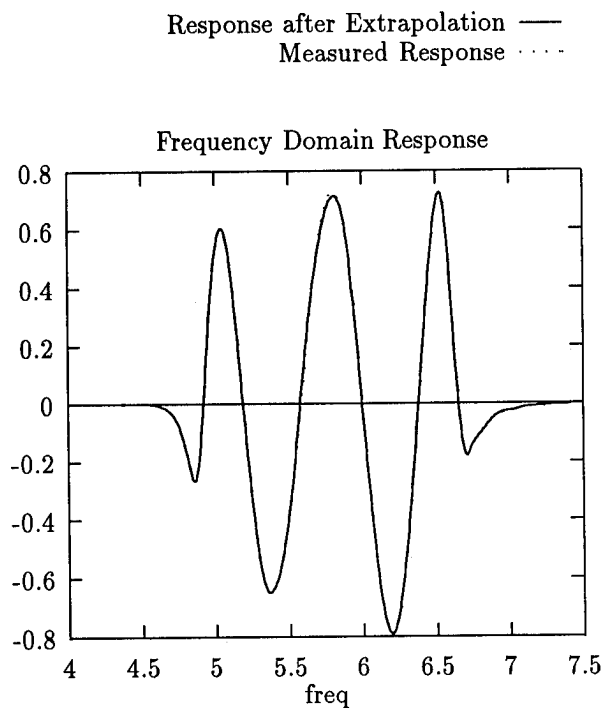


Figure 2. Imaginary Part

Cryogenically cooled HEMT's

From the device towards the applications

O. Llopis, L. Escotte*

LAAS-CNRS, 7 avenue du Colonel Roche, 31077 Toulouse, FRANCE

*Also with Université Paul Sabatier

Abstract

The essential low temperature electrical characteristics of HEMTs devices are presented. The emphasis is put on practical aspects of prime importance for the circuit designer such as the collapse preventing techniques or the noise behaviour. Some examples of cryogenic analog circuits are then described with their performances compared to their ambient temperature counterparts.

Introduction

The low temperature behavior of high electron mobility transistors (HEMTs) has been largely investigated since these devices have been introduced [1-4]. The aim of these studies was to check if the enhanced mobility in the undoped active channel of the HEMT could result in very high device performance. Even if the cut-off frequency, the gain and the high frequency noise figure have shown to improve largely at liquid nitrogen temperature with some devices, others were affected by parasitic effects such as the « collapse » of the I-V curves at low drain voltages [3-5]. A considerable work has thus been carried out to understand and circumvent this anomalous behavior [3-11]. Because preventing the collapse is a prerequisite for a HEMT device to be used in a cryogenic circuit, we will firstly present in this paper some possible solutions to circumvent this problem. We will also address others specific behaviors of cryogenically cooled HEMTs such as the transconductance and the noise figure improvement at low temperatures. These behaviors will be discussed in term of applications, enlightening the advantages of a HEMT based cryoelectronics. For example, the growing field of hybrid superconductor-semiconductor circuits needs a performant and reliable active device such as the HEMT. As an illustration, low noise HEMT amplifiers where the superconducting material is used to realize low loss band-pass filters, or low phase noise HEMT oscillators benefit from the high quality factor of superconducting passive elements.

1. The problem of collapse

Figure 1 illustrates the complexity of HEMTs I-V curves at low temperature. It represents the drain current characteristics of an AlGaAs/GaAs HEMT at 77K obtained with three different measurement procedures : DC in the dark, DC under light and pulsed in the dark with a pulsed width of 500 ns superimposed on a DC bias ($V_{ds} = 2$ V, $V_{gs} = -0.1$ V). The DC curve in the dark has been obtained after an initial plot of the $V_{gs} = 0$ V curve. This initial plot has induced the collapse phenomenon which consists in a strong reduction of the current at low drain voltages. It is caused by electron trapping on deep centers, particularly in the doped AlGaAs layer.

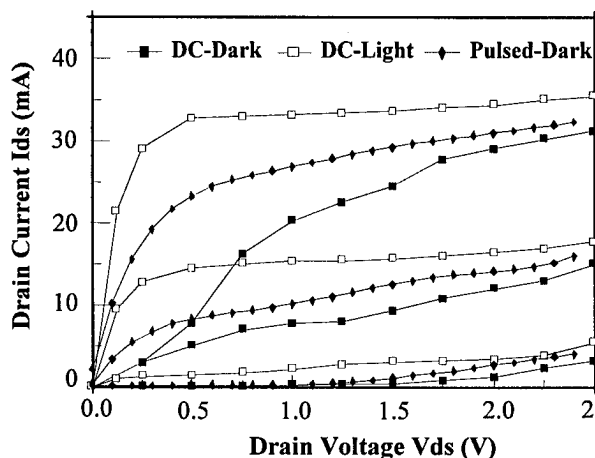


Figure 1 : HEMT TO8902 I-V curves at 77 K

The same experiment with other device structures such as pseudomorphic AlGaAs/GaInAs HEMTs (PHEMTs) would have shown different results with in some cases no collapse at all. This is due to a reduced trap density in these devices and/or better carrier confining in the channel [8,12]. However, even in these improved devices, the collapse may occur under specific bias conditions [10]. As an example, a few minutes stress at about $V_{ds} = 1$ V and $V_{gs} > 0$ V will cause carrier delocalisation and trapping ; the result is not always full collapse but a largely reduced density of free

carriers and hence of the drain current. Others technological solutions have been proposed such as superlattice HEMTs [9] or moving the gate toward the drain electrode [3,6]. However preventing any carrier trapping and hence collapse whatever the bias conditions is not an easy goal, even in these improved structures, and further work has still to be done.

To overcome these problems, it is possible to operate the device under light illumination [2]. Besides the practical difficulties related to this method, the noise properties under light are not well known. This is the reason why we have tried to take benefit of a different collapse recovery mechanism [10,11] : the high drain voltage recovery described by Hori [7]. An illustration of this recovery is provided by the HEMT pulsed I-V characteristic of Figure 1. This mechanism has also been observed in PHEMTs devices and occurs in these devices at lower drain voltages than in HEMTs. Figure 2 shows a PHEMT I-V characteristics measured after biasing the device five minutes at $V_{ds} = 1$ V and $V_{gs} = 0$ V. The collapse is clearly visible on the first curve ($V_{gs} = 0$ V) but has disappeared for the others gate bias.

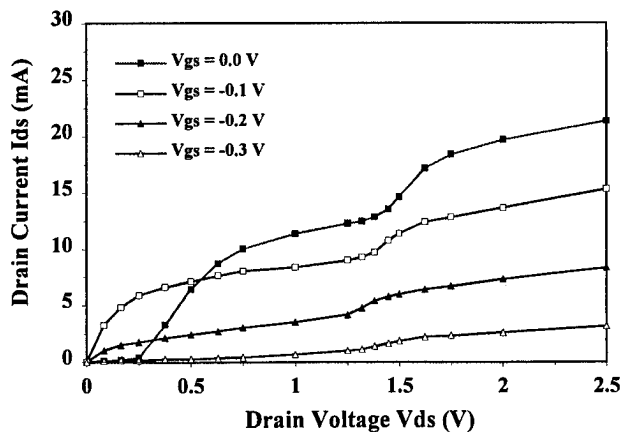


Figure 2 : PHEMT MGF4416 DC I-V curves at 77 K

The collapse suppression occurs since the drain voltage has been raised above the kink ($V_{ds} > 1.5$ V), i.e. in the impact ionization regime, during the initial plot at $V_{gs} = 0$ V [7]. The essential practical consequences of this behavior is that the HEMT nonlinear modeling at low temperature has to be carried out from I-V pulsed characteristics with a superimposed DC bias chosen in the collapse recovery zone, i.e. generally above 1.5 V.

2. Others specific behaviors at low temperature

The first high frequency parameter affected by the temperature is the transconductance g_m which is expected to increase while lowering the temperature because of the carrier mobility enhancement in the undoped

channel of the HEMT. It has been said that lowering the temperature is more or less like reducing the dimensions of the device. However, below a $0.1 \mu\text{m}$ gate length, new carrier transport phenomena are expected and this is what is actually observed at low temperature : the g_m improvement depends on the device gate length [13] and is more sensitive (about 50%) for a few tenth of micron devices than for $0.1 \mu\text{m}$ devices. This is due to short channel effects such as self heating or impact ionization. However, this behavior is largely dependent on the device structure [14] and an improvement of g_m has nevertheless been observed in $0.1 \mu\text{m}$ InP based HEMTs at low temperature [15]. Also note that the g_m enhancement goes with an enhancement of the non-linear behavior because of the increase of the threshold voltage V_t often observed at low temperature (Figure 3).

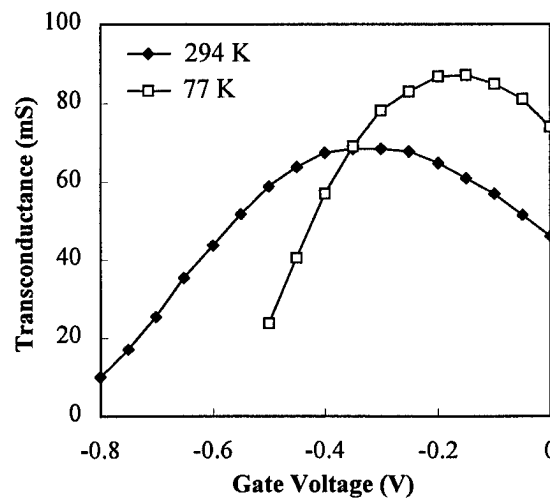


Figure 3 : FHX04 DC transconductance at $V_{ds} = 2$ V

The second parameter affected by the temperature is the output conductance. When a drain control is induced by the short channel effect or when the carriers are multiplied by impact ionization, the output conductance raises and this may be a serious drawback, specially when power output is needed.

Finally, the more interesting features at low temperature may be the reduction of the parasitic elements of the transistor [14,15], including the capacitances [6,15]. This results in very high cut-off frequencies [14,15] and should permit the development of a three terminal devices cryoelectronics above 100 GHz.

3. Low frequency noise

Low frequency (LF) noise is an important parameter in circuits where a mixing process is involved such as oscillators or mixers. It has been shown to be strongly

temperature dependent but, unlike thermal noise which is preeminent at high frequencies, LF noise is not systematically reduced at low temperature. Typical input referred LF noise spectra at ambient temperature show several bulges of generation-recombination (g-r) noise superimposed on $1/f$ noise [16]. Each g-r noise bulge corresponds to a trapping phenomenon, the frequency of the bulge being equal to $\frac{1}{2\pi\tau}$ where τ is the time

constant of the trap. When cooling the device, τ increases and this produces a bulge shift toward the low frequency range. This phenomenon is clearly shown on Figure 4 where a reduction of the noise above 1 kHz can be noticed at 110 K, but it goes with an increase of the noise under 1 kHz.

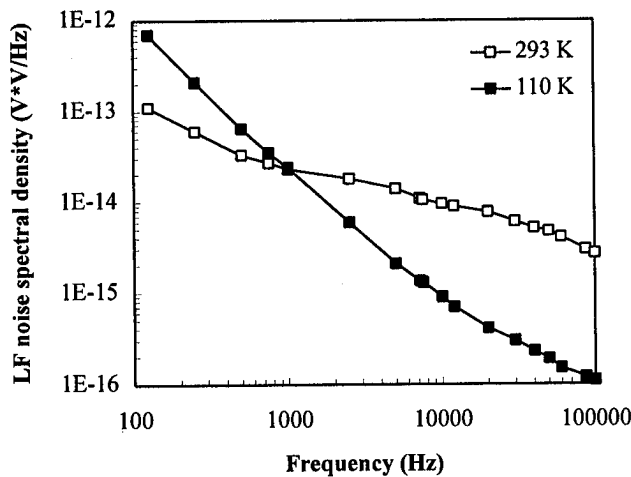


Figure 4 : Input LF noise spectral density for a PHEMT device at ambient and low temperatures

4. High frequency noise

The noise behavior of cryogenically cooled HEMT must be well characterized to design low-noise cooled amplifiers for radioastronomy or communication systems applications [17,18]. Cooling the device involves a decrease of the minimum noise figure F_{min} , and an increase of the associated gain G_a [19-21], mainly related to transconductance enhancement.

Figure 5 represents the variations of F_{min} against drain source voltage V_{ds} of a commercial AlGaAs/GaAs HEMT (Toshiba J8905) at 18 GHz and $V_{gs} = 0V$. The optimum value of V_{ds} is shifted towards higher values at 77 K, above the kink observed on the I-V curves. At both 294 K and 77 K the increase of F_{min} for small values of V_{ds} is attributed to a decrease of transconductance. The variations of F_{min} against normalized drain current, (I_{ds}/I_{dss}), are also reported on Figure 6 [22] for the same device at $V_{ds} = 2V$ and $f = 18$ GHz. The minimum noise figure exhibits a

minimum, both at room and cryogenic temperature, at about $I_{ds}/I_{dss} = 0.3$. F_{min} decreases from 1.3 dB to 0.4 dB at 77 K. For higher drain current values the benefit of cooling the device is reduced. This behavior is attributed to parallel conduction in the doped AlGaAs layer observed in DC measurement at 77 K.

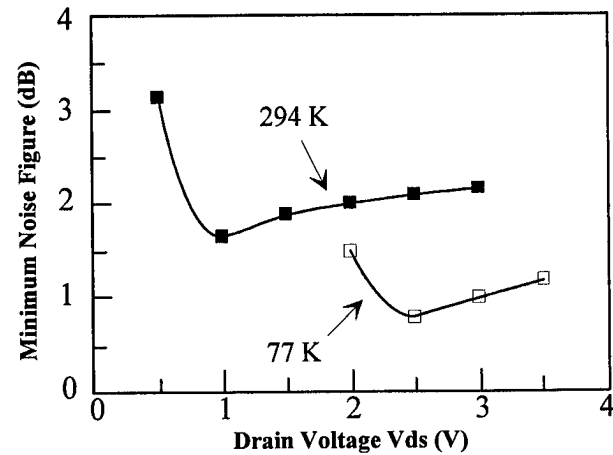


Figure 5 : JS8905 minimum noise figure versus drain voltage, $V_{gs} = 0V$, $f = 18$ GHz

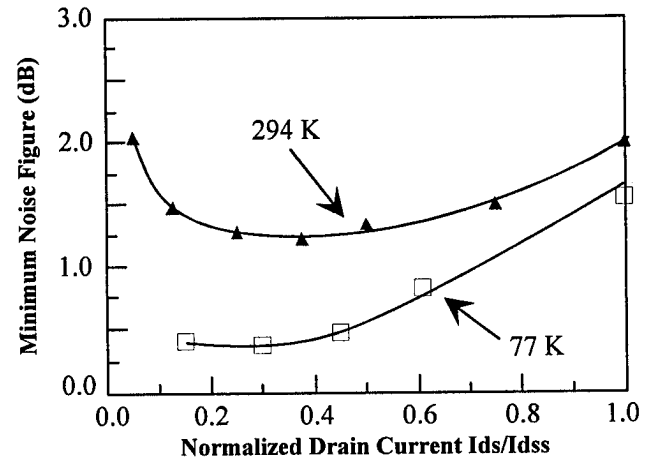


Figure 6 : JS8905 minimum noise figure versus drain current, $V_{ds} = 2V$, $f = 18$ GHz

When the devices are correctly biased, ultra-low noise cooled amplifiers have been realized with noise figure less than 0.7 dB (at $T = 12.5$ K) in the 26-36 GHz frequency range [17]. More recently, improved performances (noise figure less than 0.3 dB) have been obtained at 18 K using InP-based HEMT's in the 40-50 GHz frequency range [23].

5. Applications

Very low noise microwave amplifiers have already been presented. Apart from this obvious application of

cryogenically cooled HEMTs, many others low temperature electronics systems may be designed. The followings are only two examples.

5.1 Cryogenic oscillators :

The design of low phase noise cryogenic oscillators is possible thanks to the availability of very high Q factor resonators, even at liquid nitrogen temperature [24]. III-V semiconductor devices are well suited for this application because silicon BJTs cannot be used at these temperatures. However the noise performance of the oscillator will be directly related to the LF noise of the transistor. According to the results detailed in III, good performance may be expected at baseband frequencies in excess of 1 kHz but obtaining low noise very close from the carrier (< 100 Hz) will need a careful choice of the device [25,26,27]. In spite of this problem, cryogenic sapphire-superconductor resonator oscillators are today the best choice for extremely high spectral purity microwave sources [28].

5.2 Liquid helium temperature electronics :

III-V devices can operate at 4 K (or below) without carrier freeze out. One of the application, at these temperatures, is the amplification of infra-red (IR) detectors signals, also of SIS detectors signals. For IR detectors, the signal is usually at audio frequencies. Helium cooled MESFET amplifiers have been designed [29,30] and have proven to be competitive with 50 K silicon JFETs amplifiers. PHEMTs devices should be used in that field in a near future.

Conclusion

The essential features of cryogenically cooled HEMT's have been described. These devices are probably the best suited for the development of a 77 K electronics that should constitute an alternative to a high performance 4 K electronics which has always been too expensive to be largely used. The compared performances with respect to ambient temperature counterparts will definitely determines the interest of this field of investigations.

Acknowledgments

We would like to thanks Prof. J. GRAFFEUIL, Dr R. PLANA, Dr F. SEJALON and J. VERDIER for their contribution to the results presented in this paper.

References

[1] J.F. ROCHETTE et al., *1982 Symp. on GaAs and Related Compounds*, Inst. Phys. Conf. Ser., vol 65, pp. 385-392.
[2] T.J. DRUMMOND et al., *IEEE Trans. on Electron Dev.*, vol 30, n° 12, dec 1983, pp. 1806-1811.

[3] R. FISCHER et al., *IEEE Trans. on Electron. Dev.*, vol 31, n° 8, aug 1984, pp. 1028-1031.
[4] J. Y. CHI, R. P. HOLMSTROM, J.P. SALERNO, *IEEE Electron. Dev. Lett.*, vol 5, n° 9, sept 1984, pp. 381-384.
[5] A. KASTALSKY, R. KIEHL, *IEEE Trans. on Electron. Dev.*, vol 33, n° 3, march 1986, pp. 414-423.
[6] A. BELACHE et al., *IEEE Trans. on Electron. Dev.*, vol 38, n° 1, jan 1991, pp. 3-13.
[7] Y. HORI et al., *IEEE Trans. on Electron. Dev.*, vol 39, n° 12, dec 1992, pp. 2720-2725.
[8] S-M. J. LIU et al., *IEEE Trans. on Electron. Dev.*, vol 33, n° 5, may 1986, pp. 576-581.
[9] W. BROCKERHOFF et al., *IEEE Trans. on Microwave Theory and Tech.*, vol 37, n° 9, sept 1989, pp. 1380-1387.
[10] J. VERDIER et al., WOLTE 1994, *Journal de Physique IV*, Colloque C6, pp. 165-170.
[11] O. LLOPIS et al., *1994 IEEE Microwave Theory and Tech. Symp. Digest*, pp. 981-984.
[12] R. PLANA et al., *IEEE Trans. on Electron. Dev.*, vol 40, n° 5, may 1993, pp. 852-858.
[13] P. CROZAT et al., *Microelectronic Eng.*, 19 (1992), pp. 861-864.
[14] F. ANIEL, Ph.D. Thesis, Universite de Paris-Sud.
[15] D. YANG et al., *IEEE Electron. Dev. Lett.*, vol 15, n° 6, june 1994, pp. 209-211.
[16] J. R. KIRTLEY, T.N. THEIS, P.M. MOONEY, S.L. WRIGHT, *J. Appl. Phys.* 63(5), march 1988, pp. 1541-1548.
[17] M.W. POSPIESZALSKI, *1992 IEEE Microwave Theory and Tech. Symp. Digest*, pp.1369-1372.
[18] S.WEINREB, *IEEE Trans. on Microwave Theory and Tech.*, vol.28, pp.1041-1054, october 1980.
[19] M. W. POSPIESZALSKI et al, *IEEE Trans. on Microwave Theory and Tech.*, vol.36, n° 3, pp.552-560, march 1988.
[20] H. MESCHÉDE et al, *IEEE Trans. on Microwave Theory and Tech.*, vol.40, n° 12, pp. 2325-2330, dec. 1992.
[21] A. BAGDAD, E. PLAYEZ, G. SALMER, *Proc. of the 1992 European Microwave Conf.*, pp.576-581.
[22] L. ESCOTTE, F. SEJALON, J. GRAFFEUIL, *IEEE Trans. on Instrum. and Meas.*, vol.43, n° 4, pp.536-543, august 1994.
[23] M.W. POSPIESZALSKI et al, *1995 IEEE Microwave Theory and Tech. Symp. Digest*, pp.1121-1124.
[24] Z. Y. SHEN et al., *IEEE Trans. on Microwave Theory and Tech.*, vol. 40, dec. 1992, pp. 2424-2432.
[25] O. LLOPIS et al., *IEEE Trans. on Microwave Theory and Tech.*, vol 41, march 1993, pp. 369-374.
[26] C. P. LUSHER, W. N. HARDY, *IEEE Trans. on Microwave Theory and Tech.*, vol 37, march 1989, pp. 643-646.
[27] L. D. MANN, D. G. BLAIR, K. J. WELLINGTON, *Electron. Lett.*, vol 22, sept. 1986, pp. 1037-1038.
[28] M. E. TOBAR, D. G. BLAIR, *IEEE Trans. on Microwave Theory and Tech.*, vol 42, feb. 1994, pp. 344-347.
[29] A. T-J. LEE, *Rev. Sci. Instrum.*, 64(8), aug 1993, pp. 2373-2378.
[30] D. V. CAMIN, G. PESSINA, E. PREVITALI, WOLTE 1994, *Journal de Physique IV*, Colloque C6, pp. 159-164.

HIGH TEMPERATURE MICROWAVE MODELLING AND CIRCUIT DESIGN WITH MESFET'S AND HBT'S

V. Krozer, M. Schübler, K. Fricke, W.-Y. Lee, N. Stolte, M. Brand and Hans L. Hartnagel

Institut für Hochfrequenztechnik
Technische Hochschule Darmstadt

Merckstr. 25

D-64283 Darmstadt, Germany

Phone: +49 6151 162162

Fax: +49 6151 164367

email: dg9p@hrzpub.th-darmstadt.de

ABSTRACT

Novel microwave circuit structures have been designed and fabricated for application at high operating temperatures. The required simulation and characterization of MESFET and HBT devices at high ambient temperatures have been carried out. Novel physical analytical models for the high temperature performance of MESFET's and HBT's were developed. As an example a fully integrated radar front-end operating at temperatures up to 200°C is given in the paper.

1 INTRODUCTION

MMIC design and fabrication for high temperature applications have recently received increased attention. Most MMIC for high temperature applications considered up to date have been realized with MESFET or HEMT technologies. Also HBT devices have been proposed for high temperature applications [1, 2, 3, 4, 5].

The design of MMIC for high temperatures requires accurate modeling and characterization of devices at increased operating ambient temperatures. A number of physical and empirical models for MESFET devices have been presented in the literature. HBT device modeling has not yet reached this maturity and new results will be presented in this paper.

The scope of this contribution is to demonstrate novel MMIC designs intended for high temperature application and new results for the characterization of HBT devices for a temperature range up to 250°C.

2 MESFET BASED MMIC DESIGN

It is commonly accepted and has been confirmed by us earlier [1] that only S_{21} of MESFET devices decreases by approximately a factor of 2 with increasing temperature from room temperature to 200°C. As the other scattering parameters remain unchanged up to

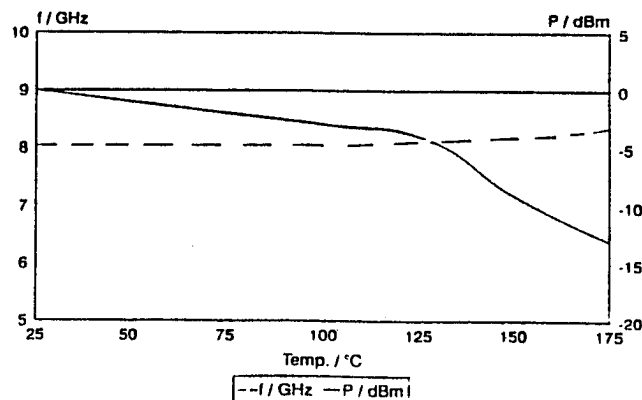
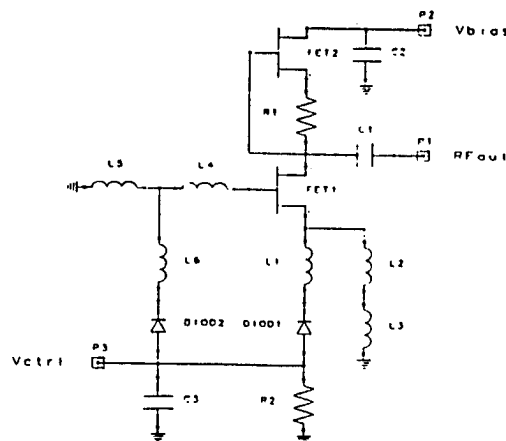


Figure 1: High temperature VCO and measured results for the frequency of oscillation and the output power as a function of ambient temperature.

reasoning a MMIC VCO has been designed and realized. In fig. 1 the design and the measured performance are illustrated. No special measures have been undertaken in this circuit to stabilize the output power versus temperature and therefore the output

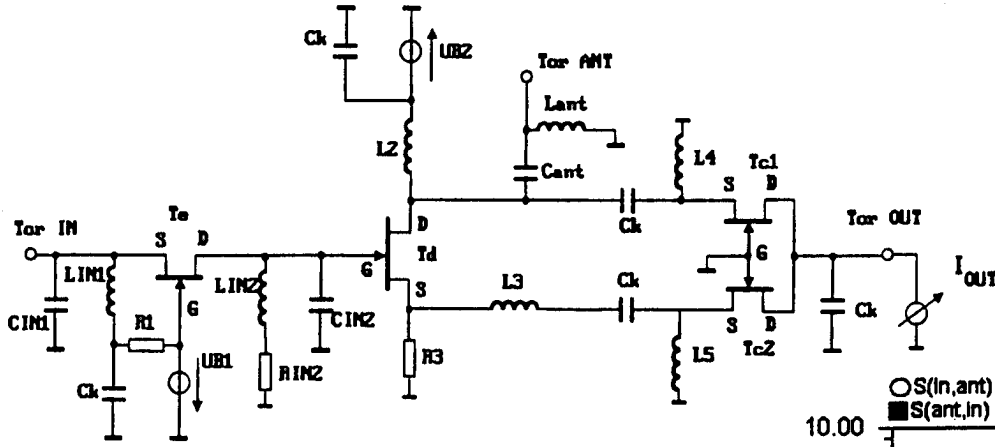


Figure 2: Active circulator with integrated mixer.

power drops at temperatures above 150°C .

A second circuit has been designed which comprises an active circulator with a mixer circuit designed to operate up to 200°C ambient temperature. The circuit is shown in fig. 2. The circulator utilizes a common-source configuration as an out-of-phase divider and a common gate pair as a mixer. The circulator does not exhibit a return path and could therefore also be called a diplexer because of its ability to deliver the signal from the input to the antenna port and from the antenna port to the mixer. The simulated performance of the circulator is summarized in fig. 3a and fig. 3b where the scattering parameters and the output IF current are indicated.

3 MODELLING AND CHARACTERIZATION OF HBT FOR HIGH TEMPERATURES

HBT devices offer a number of advantages with respect to high temperature applications when compared with MESFET devices. Most notably the vertical current flow and the possibility of heterostructuring yield higher flexibility in the design of HBT devices and circuits. Little is known on the high temperature microwave performance of HBT devices and there are no HBT device models available capable of accurately characterizing the HBT high temperature behavior. We have developed a DC and RF HBT model applicable for the simulation of the operation at increased temperatures [2, 3, 4, 5, 6, 7]. A comparison between measured and calculated DC characteristics at room temperature and at 200°C are given in fig. 4. Very good

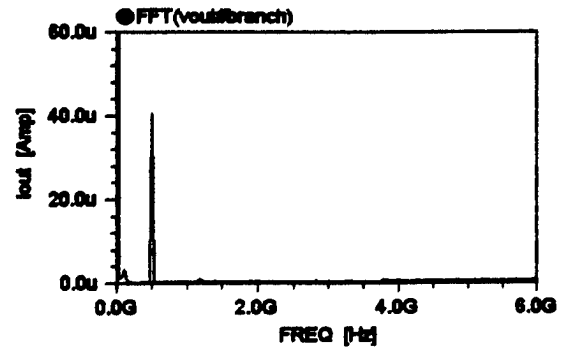
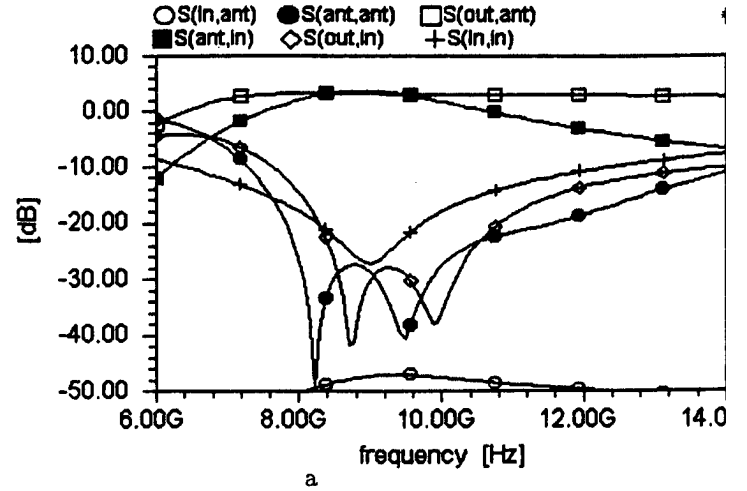
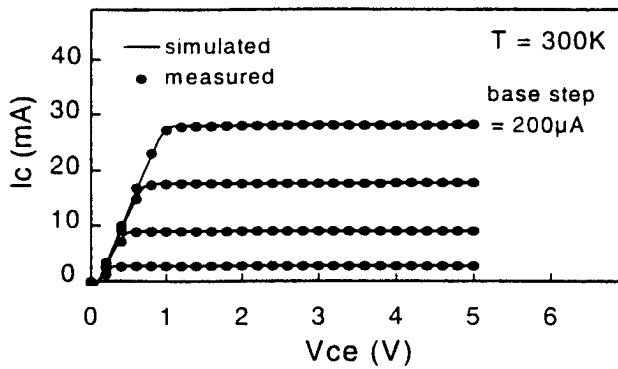


Figure 3: Simulated results for the a) scattering parameters and b) for the IF current at the output port of the circulator with integrated mixer.

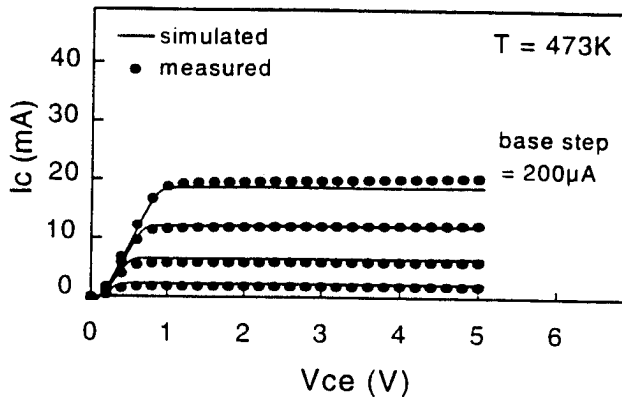
This work was supported in part by the Bundesministerium für Forschung und Technologie (BMFT), by the Deutsche Forschungsgemeinschaft (DFG). The authors are grateful to Dr. J. Würfl, Ferdinand-Braun-Institut für Höchstfrequenztechnik, Berlin for supplying DC data for the high temperature MESFET devices and for the fabrication of the MESFET circuits.

References

- [1] K. Fricke, W.Y. Lee, V. Krozer, J. Würfl, S. Bialas, and H.L. Hartnagel: Microwave Characterization and Comparison of Performance of *GaAs* based MESFETs, HEMTs and HBTs Operating at High Ambient Temperatures, *GAAS'92, European Gallium Arsenide and Related III-V Compounds Application Symp.*, Noordwijk, The Netherlands, April 27-29, 1992.
- [2] W.-Y. Lee, K. Fricke, V. Krozer, M. Schüßler, and H.L. Hartnagel: *AlGaAs/GaAs* HBT for Microwave Applications up to 240°C, *Workshop on High-Speed Bipolar Circuits and Devices*, Ulm, Germany, Oct. 11-12, 1993.
- [3] K. Fricke, V. Krozer, W.Y. Lee, M. Ruppert, M. Schüßler, G. Schweeger, A. Sigurdardottir, and H.L. Hartnagel: Design and Technology of *AlGaAs/GaAs* HBT for High Temperature Circuits, *GAAS'94, European Gallium Arsenide and Related III-V Compounds Application Symp.*, Torino, Italy, April 28-30, 1994.
- [4] V. Krozer, M. Ruppert, W.Y. Lee, J. Grajal, A. Goldhorn, M. Schüßler, K. Fricke, and H.L. Hartnagel: A Physics-Based Temperature-Dependent SPICE Model for the Simulation of High Temperature Microwave Performance of HBT's and Experimental Results, *1994 IEEE MTT-S, Intern. Microwave Symp. Dig.*, Mai 23-27, 1994.



a



b

Figure 4: Measured and Calculated I/V characteristics at a) room temperature and b) 200°C.

agreement between measured and calculated results can be achieved with this physical model. It will be demonstrated during the presentation that the RF performance of HBT resembles the high temperature operating conditions of MESFETs. For example the main deterioration in device performance is observed for the simulated as well as measured S_{21} .

4 CONCLUSIONS

We have demonstrated MMIC circuits based on MESFET devices operating at high ambient temperatures. It has also been shown that HBT devices exhibit a similar high temperature performance as the MESFET. A new model developed for the simulation of HBT devices greatly facilitates the temperature dependent design of MMIC based on HBT.

- [5] V. Krozer, M. Ruppert, J.-M. Miao, W.Y. Lee, M. Schüßler, K. Fricke, and H.L. Hartnagel: Modelling of High Temperature Performance of MES-FET's and HBT's, *HITEC'94, High Temperature Electronics Symposium*, Mai 23-27, 1994.
- [6] M. Schüßler, K. Fricke, W.-Y. Lee, V. Krozer, and H.L. Hartnagel: Collector Design for Improved Breakdown in High Temperature *AlGaAs/GaAs* HBT, *EDMO'93, Workshop on High Performance Electron Devices for Microwave and Optoelectronic Applications*, London, England, Oct. 18, 1993.
- [7] V. Krozer, M. Ruppert, M. Schüßler, K. Fricke, W.Y. Lee, and H.L. Hartnagel: Calculation of the Power Capabilities of HBT Amplifiers Based on a New Physical HBT Model, *INMMC'94, IEEE MTT/AP 3rd Intern. Workshop on Integrated Nonlinear Microwave and Millimeterwave Circuits*, Duisburg, Germany, 5th-7th Oct. 1994.

AlGaAs/GaAs and GaInP/GaAs HBT for High Temperature Microwave Operation

M. Schüßler, V. Krozer, J. Pfeiffer, T. Statzner, W.Y. Lee and H.L. Hartnagel

Technische Hochschule Darmstadt, Institut für Hochfrequenztechnik, Merckstr. 25
D-64283 Darmstadt, Germany, Tel. +49 6151 162162, Fax. +49 6151 164367

ABSTRACT

In this paper the basics of high temperature HBTs are described. Starting from the wafer structure, and ending with obligatory technological requirements. The paper is completed by a comparison between two very promising HBT material systems in terms of high frequency and high temperature performance.

1. Introduction

HBTs are very promising devices for power applications in the GHz-region[1,2,3]. The advantage of the high power density capability in comparison to field-effect-transistor based devices is at the same time a disadvantage because of device performance degradation due to selfheating effects. Since thermal resistances of conventional high frequency HBTs are in the order of some hundreds of Kelvin per Watt, an increase of intrinsic device temperature starting from 100°C is realistic for power applications.

Beside the above described HBT-application there is a

market for sensor-systems working with high frequency measurement methods in a high temperature environment. HBT based oscillators are here of interest because of their low phase noise in comparison with MESFET and HEMT based ones [4]. In this application it is the ambient temperature that influences the device performance.

These two examples should demonstrate the necessity of considering the high temperature aspects in design and technology of HBTs which will be discussed in this paper. Starting from the choice of the used material and the design of the wafer, followed by some remarks upon the influence on the design of the transistors and the used technology, and ending with the discussion of high-temperature microwave measurements of transistors up to 200°C ambient temperature.

2. Waferdesign

Aiming at high temperature operation AlGaAs/GaAs and GaInP/GaAs HBT have achieved very impressive results in the last years [5]. The standard structure for such a device is shown in fig. 1. This sketch also

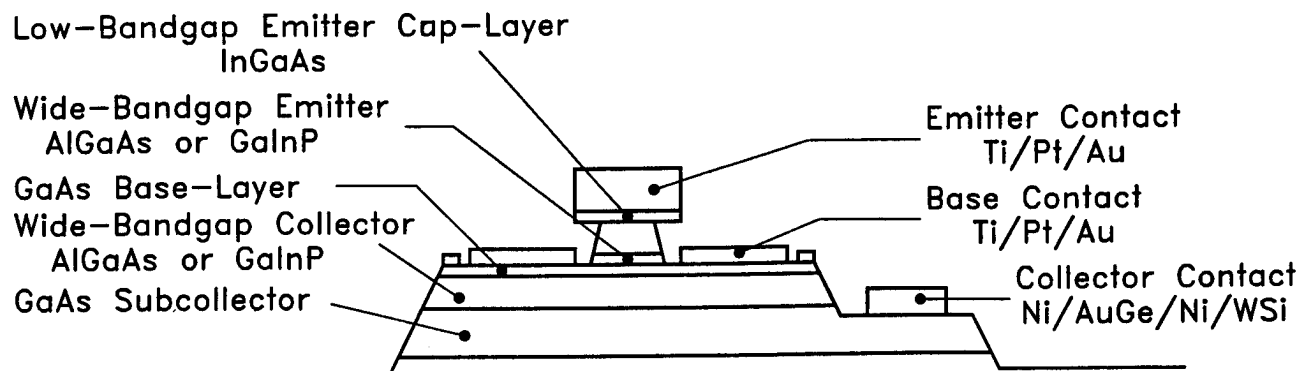


Fig. 1 Schematic cross section of a high temperature HBT

represents the structure of the fabricated AlGaAs/GaAs/GaInP and GaInP/GaAs/GaInP HBTs. Beside the conventional HBT-features such as low-bandgap emitter caplayer for very easy ohmic contact formation and wide-bandgap emitter for high base doping, there are two very important points for the wafer design.:

Thinking of high temperature operation the suppression of thermally generated charge carriers in the base collector space charge region is essential for a high output impedance. For temperatures above 200°C it is therefore recommendable to use a wide-bandgap collector material such as AlGaAs or GaInP. With $\text{Al}_{0.20}\text{Ga}_{0.80}\text{As}$ flat common-emitter output characteristics have been achieved up to 400°C even for large devices. The disadvantage of lower saturation velocity leading to increased collector delays of these materials in comparison with GaAs is compensated by the lower ionization coefficients, which allows to shrink the collector length with no change in breakdown voltage. To avoid a spike in the conduction band between base and wide-bandgap collector, an interfacial layer has to be inserted generally.

For a sufficient current gain even at elevated temperatures the valence band offset between base and emitter has to be large enough. This condition is automatically fulfilled for a GaInP emitter. For a AlGaAs emitter the Al mole fraction has to be adapted.

3. Technology

Technology of the devices has to take care of aspects of device reliability. For high operation temperatures degradation effects in ohmic contacts because of Au interdiffusion could have dramatic influence on device performance. Therefore special diffusion barrier layers in the ohmic contacts are necessary. In fig. 1 Pt and WSi is used for this purpose. For Ti/Pt/Au contact and Ni/AuGe/Ni/WSi contacts long time reliability at elevated temperatures has been proved already. But there are also some other concepts for n-ohmic contacts which avoid the use of Au for the ohmic contact layer, such as the Pd/In-System [6] and the Pd/Ge/Si-System which have achieved very promising results. For these concepts the use of a diffusion barrier is also obligatory.

Strongly related to device technology and very important for the thermal resistance of the device is the kind of emitter contacting technique. For the fabricated HBTs with $4 \times 20 \mu\text{m}^2$ emitterfingers nearly the whole part of the emitter contact is covered with a $2 \mu\text{m}$ thick plated gold layer used for the interconnection

metallization. This leads to the thermal resistance of about 300 K/W for a one emitter finger device for the fabricated transistors and a very good thermal coupling between the emitters of a multifinger-structure. This technique is very difficult for emitter widths of about $2 \mu\text{m}$ or smaller. For these transistors the contact to the plating is generally at the broadened end of an emitterfinger, leading to worse thermal resistance of one finger and worse coupling between emitterfingers.

4. Results

With the described technology HBTs with 1, 2 and 4 emitterfingers have been fabricated on an $\text{Al}_{0.38}\text{Ga}_{0.62}\text{As}/\text{GaAs}/\text{GaInP}$ wafer and a GaInP/GaAs/GaInP wafer with similar doping levels and layer thickness (emitter: $N_D = 7 \times 10^{17} \text{ cm}^{-3}$; base: $N_A = 4 \times 10^{19} \text{ cm}^{-3}$; collector: $N_D = 5 \times 10^{16} \text{ cm}^{-3}$). In fig. 2. the S-parameters of a GaInP/GaAs/GaInP one emitterfinger HBT are plotted for room temperature (RT), 100°C and 200°C from 45 MHz to 10 GHz. The bias point has been chosen in a way that the selfheating of the device is negligible and the collector current is constant. For the interpretation of the data a T-equivalent transistor circuit has been used. This parameter extraction technique has been performed in a similar way as described in [7].

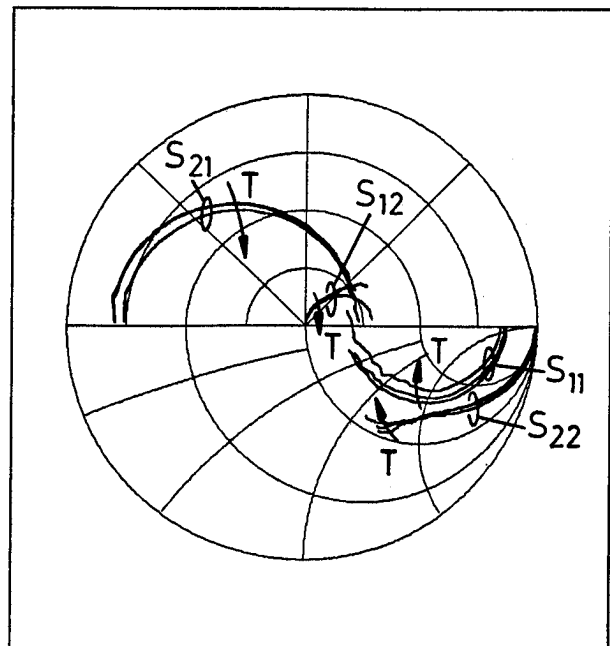


Fig. 2 Measured S-parameters of a one finger GaInP/GaAs/GaInP HBT from 45 MHz to 10 GHz for RT, 100°C and 200°C

Regarding S_{11} it is obvious that the real part of the input impedance is decreasing with temperature. From the simple approximation for the dynamic resistance of the base emitter diode

$$r_{eb} = h_{21} \cdot n \cdot V_t \cdot I_C^{-1}$$

an increase of this impedance would be expected (h_{21} =current gain, n =ideality factor of base emitter diode; I_C =DC-collector current, $V_t=k \cdot T \cdot q^{-1}$). Generally there are two temperature dependent factors which mask this effect. The current gain as shown in fig. 3 and the contact resistance of base contact. The decrease in current gain could be stabilised with an higher Al-mole fraction in the emitter. With 42%-Al a change from 66 at RT to 42 at 200°C has been reported by [8]. The temperature dependence of the base contact resistance is strongly related to technology.

Since the fabricated AlGaAs devices have larger variations in h_{21} with temperature the variations in S_{11} are more profound.

The variations in S_{21} are also strongly related to these two temperature dependent factors. Therefore for the AlGaAs based device this effect is again much more profound than for the GaInP based ones. Fig. 4 shows the normalized $S_{21}(T)$ for the two transistor types. The absolute values of plotted normalized transistor parameters at RT are listed in tab. 1.

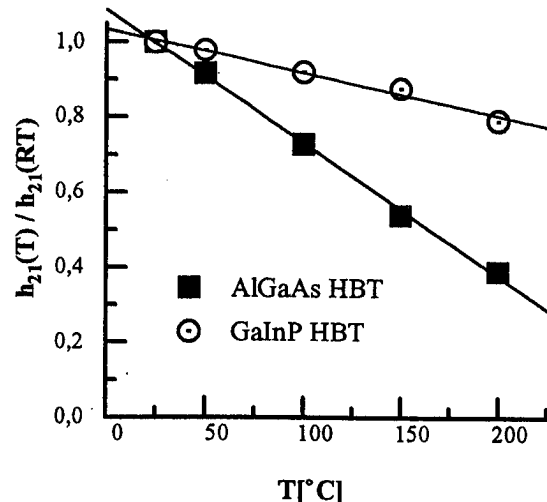


Fig. 3 Temperature dependence of normalized small signal current gain h_{21} for an AlGaAs/GaAs- and a GaInP/GaAs HBT

S_{22} is dominated by the intrinsic and the extrinsic base collector junction capacitance. The resulting impedance is nearly temperature independent as long as the thermally generated charge carriers in the space charge region of the base collector junction are negligible. For S_{12} it is basically the same effect.

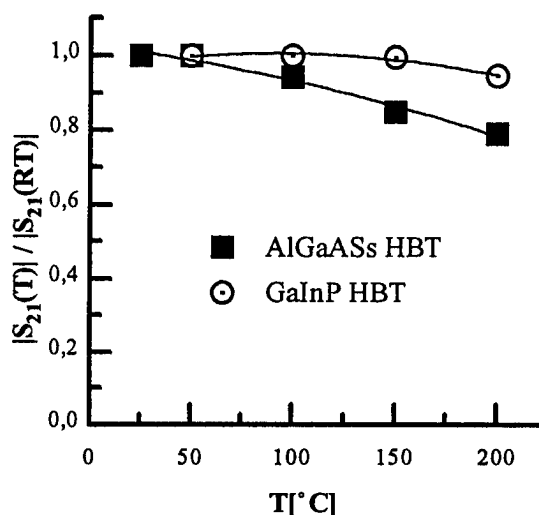


Fig. 4 Normalized $|S_{21}|$ versus temperature

The extracted normalized temperature dependence of f_T and f_{max} for the two wafer structures are plotted in fig. 5 and fig. 6 respectively. Again a bias point has been chosen where the self heating of the device is negligible.

The temperature dependence is quite similar for both material systems. The transit frequency decreases about 72% from RT to 200°C. Since the parasitics remain primarily constant, this effect originates from the increase of electron transfer time in the device and the increase of the differential resistance of the base emitter diode. Strongly related to f_T is the decrease in f_{max} which is also in the same order in this temperature range.

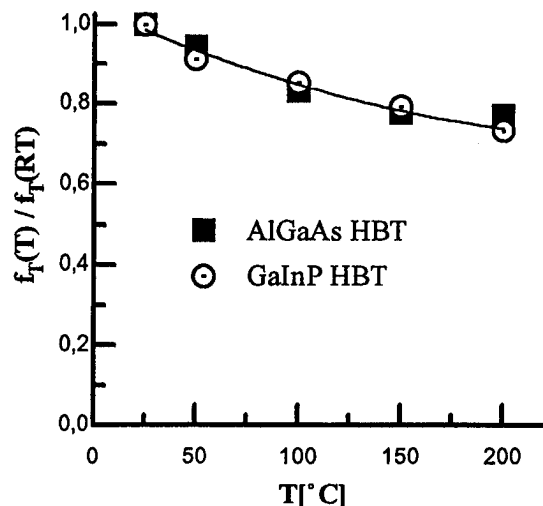


Fig. 5 Extracted normalized temperature dependence of f_T for an AlGaAs/GaAs- and a GaInP/GaAs HBT

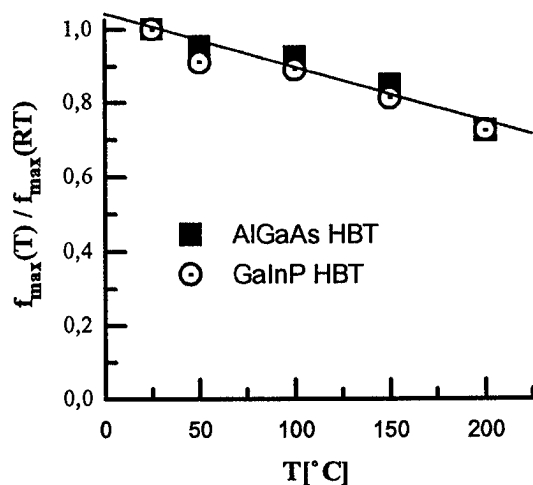


Fig. 6 Extracted normalized temperature dependence of f_{max} for an AlGaAs/GaAs- and a GaInP/GaAs HBT

Similar measurements for 2 and 4 emitter finger devices on both materials exhibit comparable results for power levels less than 100mW DC power Dissipation per emitterfinger, indicating a good thermal coupling between different fingers based on the already described technology. In this powerregion the transistors are scaleable in terms of collector current, rf-gain, etc. Only for high power level the thermal runaway of single emitters restrict device performance.

Values at RT	AlGaAs/GaAs-HBT	GaInP/GaAs-HBT
I_E	4 kA/cm ²	3 kA/cm ²
h_{21}	16.9	18.7
S_{21}	3.7	2.4
f_T	18.0 GHz	17.0 GHz
f_{max}	6.5 GHz	9.0 GHz

Tab. 1 Absolute values of plotted transistor parameters at room temperature.

5. Conclusions

In this paper aspects of HBT design with respect to requirements of elevated temperature operating conditions are pointed out. Microwave measurements from RT to 200°C exhibit similar high frequency properties for the fabricated AlGaAs/GaAs/GaInP and GaInP/GaAs/GaInP HBTs with only one difference. The HBTs with GaInP emitter offer nearly temperature independent gain origin from the weak temperature

dependence of small signal current gain. AlGaAs emitter based devices with an Al-mole fraction of more than 40% are also expected to offer this feature. Therefore comparable results concerning electrical performance should be achievable with both material systems. Similar investigations in the field of reliability may favour one transistor type.

Acknowledgement

We are grateful for financial support by the „Deutsche Forschungsgemeinschaft“ (DFG) (SFB241) and the „Bundesministerium für Forschung und Technologie“ (BMFT).

References

- [1] S.L. Delage, D. Floriot, H. Blanck, E. Chartier, M.-A. diForte Poisson, C. Brylinski, Y. Perreal, D. Pons, Power GaInP/GaAs HBT MMICs, 24th European Microwave Conference, Cannes, France, 1994
- [2] B. Bayraktaroglu, J. Barrette, L. Kehias, C.I. Huang, R. Fitch, R. Neidhard, R. Scherer, Very High Power Density CW Operation of GaAs/AlGaAs Microwave Heterojunction Bipolar Transistors, Electron Device Letters, October 1993
- [3] E.I. Song, C. Caneau, K.B. Chough, W.P. Hong, GaInP/GaAs Double Heterojunction Bipolar Transistor with High f_T and f_{max} , IEEE Electr. Device Letters, Vol. 15, No.1, Jan. 1994
- [4] U. Guttlich, J.-M. Dieudonne, K.Riepe, A. Marten, H. Leier, Ka-Band Monolithic VCOs for Low Noise Applications Using GaInP/GaAs HBTs, Proc. of IEEE MTT-Symposium, San Diego, USA, 1994
- [5] K. Fricke, H. L. Hartnagel, W.Y. Lee, and M. Schüßler, AlGaAs/GaAs/AlGaAs DHBTs for High-Temperature Stable Circuits, IEEE Electron Device Lett., vol. 15, pp. 88-90, March 1994.
- [6] K. Fricke, H.L. Hartnagel, W.Y. Lee, T. Pirling, M.Schüßler, J. Würfl, A Highly Reliable Ohmic Contact on GaAs Based on Pd/In, Proc. of Second International High Temperature Electronics Conference, Charlotte, USA, 1994
- [7] D.R. Pehlke, D. Pavlidis, Direct Calculation of the HBT Equivalent Circuit From Measured S-Parameters, MTT-S Digest, 1992
- [8] W.Y. Lee, M. Schüßler, V. Krozer, K. Fricke, H.L. Hartnagel, Influence of Thermal and Current Stress of AlGaAs/GaAs/AlGaAs DHBT at 400°C, Proc. of Second International High Temperature Electronics Conference, Charlotte, USA, 1994
- [9] W. Y. Lee, K. Fricke, V. Krozer, M. Schüßler, H. L. Hartnagel, AlGaAs/GaAs HBT for Microwave Application up to 240°C, IEEE Workshop on High-Speed Bipolar Circuits and Devices, Ulm, Germany, October 1993

HETEROJUNCTION BIPOLAR PHOTOTRANSISTORS FOR ANALOG MICROWAVE PHOTONIC SYSTEMS

A. Paolella, L.E.M.deBarros Jr, P.Herczfeld*, P.Enquist⁺ and W. Van Meerbeke*

Army Research Laboratory-PSD
AMSRL-EP-MA
Ft. Monmouth, NJ 07703
908-544-2825
paolella@arl.ftmon.mil

*Drexel University
Center for
Microwave/Lightwave
Technology
Philadelphia, PA

+Research Triangle Institute
Research Triangle Park, NC

ABSTRACT

The Heterojunction Bipolar Transistor (HBT) commonly used in GaAs MMICs for microwave and millimeter wave systems can perform as a high speed photodetector with inherent gain and high linearity. The use of the phototransistor will allow circuit designers to develop a new class of photonic/ millimeter wave circuits. A new model for the HBT has been developed which solves for the electrical and photogenerated currents. Experimental and theoretical curves relating to the device behavior are presented and compared.

1. INTRODUCTION

Three-terminal microwave devices for photodetection have been receiving increasing attention. Combining detection, amplification, and mixing in the same device results in considerable simplification of the receiver design, and provide an opportunity for new applications. The first devices investigated as photodetectors were microwave MESFETs [1,3] and HEMTs [2]. They exhibited high optical gain but poor frequency response. Further investigations [4,5] revealed that the principal mechanism of photodetection is a photovoltaic effect. This process provides for large gain, but it is inherently slow.

Heterojunction bipolar transistors are current-controlled-current-source devices where the photogenerated carriers contribute directly to the total photocurrent therefore the device is intrinsically fast. Recent studies [6] have shown that an active base terminal enhances the gain and frequency response compared to the floating base configuration. Furthermore HBTs provide for

integration, they sustain very high current densities (106 A/cm²), require low bias voltages and a single power supply.

2. EXPERIMENTAL INVESTIGATION

The device under test, comprises of a 5000Å subcollector doped at 2×10^{18} cm⁻³, 5000Å collector doped at 1.5×10^{16} cm⁻³, 800Å base Carbon doped at 2×10^{19} cm⁻³, 300Å AlGaAs emitter doped at 6×10^{17} cm⁻³, 400Å AlGaAs to GaAs graded doped layer at 2×10^{18} cm⁻³ and 2500Å GaAs emitter cap layer doped at 2×10^{18} cm⁻³. The base was exposed for illumination by etching the emitter cap layer and emitter. A modulated optical signal from a semiconductor laser at 850nm illuminated HBT's base region. Figure 1 shows DC output characteristics. The photocurrent at $V_{ce}=1.5V$ is about 300 mA. Fig. 2 compares the linearity of the HBT with the MESFET and shows that at optical intensities below 1 mW the MESFET is highly non-linear. As opposed to MESFETs and HEMTs [8] the HBT shows no shift in turn-on or saturation voltages, indicative of no photovoltaic behavior. This forecast that the photoresponse of HBT has a larger bandwidth. Experimental results confirm this prediction.

Figure 3 shows a comparison for two bias levels which indicates the an increase in the gain of the device with bias. The photoresponse shown is limited by the relaxation oscillations of the laser (at 7 GHz). The HBT has a potential response in excess of 10 GHz limited by the charging time of the base-emitter junction (~1.6ps) and the transit time on the base-collector space-charge region (~4.2ps).

3. THEORETICAL MODEL

The transport equation to be solved in the three regions of the device;

$$D_i \frac{d^2 n_i(x)}{dx^2} - \frac{n_i(x)}{\tau_i} + G_i(x) = 0 \quad (1)$$

where D_i is the diffusion coefficient, n_i is the minority carrier concentration (electrons or holes) and τ_i is the recombination lifetime, the index i refers to each specific region: emitter(e), base(b) and collector(c). The last term is the wavelength dependent generation term, which is assumed zero in the large band-gap emitter region. The transport equation is valid for neutral regions (zero E-field) inside the device whose boundaries are determined by Poisson's equation.

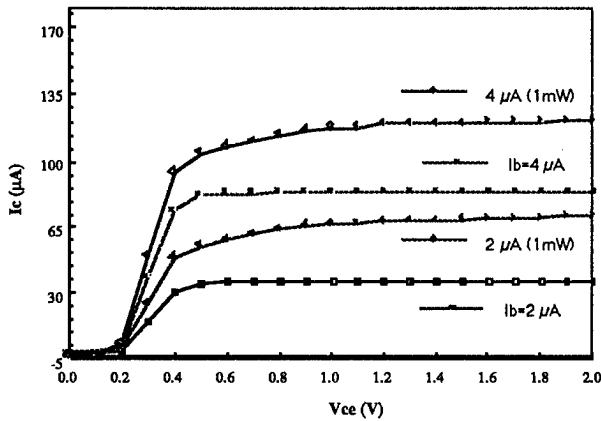


Figure 1. Measured DC output characteristics (dark and light) with optical power = 1 mW

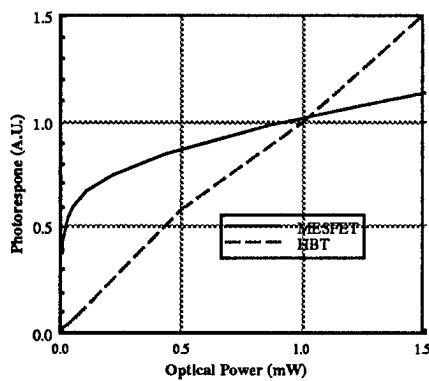


Figure 2. Comparison of MESFET and HBT linearity for the photoresponse

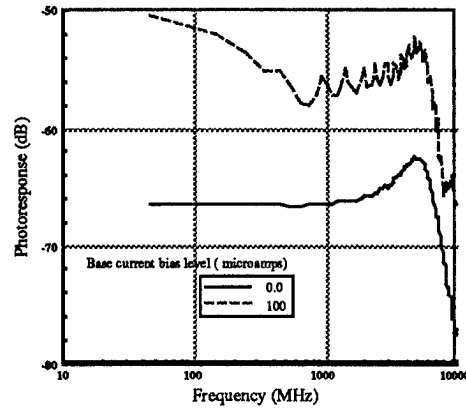


Figure 3. Microwave link gain as a function of bias.

The generation terms for base and collector region are best represented by

$$G_b(x) = \eta_b \alpha \phi_0 e^{-\alpha x} \quad \text{and}$$

$$G_c(x) = (\eta_b e^{-\alpha W_b} + \eta_c) \alpha \phi_0 e^{-\alpha x}$$

where by replacing back at equation (1) allows for the determination of minority carrier distribution at the neutral regions. To account for the effects of the bands discontinuities we use the approach of Parikh et al. [6] that defines an effective interface velocity for the carriers. Basically it introduces a correction term to the boundary value in the homojunction case such that :

$$n(x_{pe}) = n(x_{ne}) \exp \left[\frac{(-qV_{bi} + \Delta E_c)}{kT} \right] - \frac{F_{EN}}{S_{EN}} \quad (2)$$

where F_{EN} is the electron flux and S_{EN} is the effective velocity across the junction. In the case of a smooth heterojunction or a homojunction ΔE_c is small, which makes S_{EN} large, consequently eq.(2) reduces to the homojunction case. Since there is no spike in the valence band the boundary value for holes is the same as in a homojunction case. From drift-diffusion theory the total current across a junction is calculated based on the minority carrier currents at the edges of the depletion region plus any contributions from inside the space-charge region.

Only the base-collector junction is shown for the

abstract. The evaluation of the minority currents results in :

$$J_c = \frac{qD_b(\Gamma_{pe} + \Gamma_{pc}\cosh(\frac{W_b}{L_b}))}{L_b\sinh(\frac{W_b}{L_b})} - qD_bK_b'\alpha e^{-\alpha x_{pc}} + \frac{qD_cP_{nc}}{L_c\tanh(\frac{W_c}{L_c})} + \frac{qD_cK_c'(e^{-\alpha x_{pc}}e^{-\alpha x_{nc}}\cosh(\frac{W_c}{L_c}))}{L_c\sinh(\frac{W_c}{L_c})} + qD_cK_c'\alpha e^{-\alpha x_{nc}} + J_{g-r} \quad (3)$$

where the generation-recombination current J_{g-r} is given by

$$J_{g-r} = \int_{x_{pc}}^{x_{nc}} G_c(x)dx = q\eta'\phi_0 e^{-\alpha x_{pc}}[1 - e^{-\alpha W_{dc}}] \quad (4)$$

In the case where the photon flux is zero, the different components in the current expressions reduce to the well-known dark solution equations. The DC characteristics of the device are obtained by replacing the voltage dependent carrier densities and space charge boundaries in the current equations. The different parameters in expressions (3)-(4) are described in appendix A.

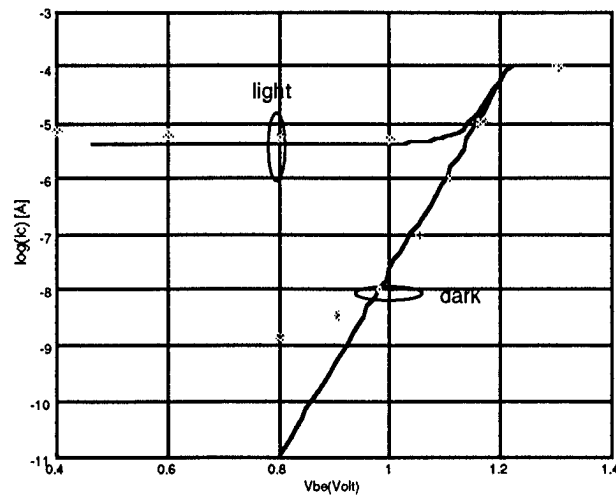


Figure 4. Gummel plots (I_c vs. V_{be}) with and without illumination.

In Fig. 4, collector current as a function of base-emitter voltage is shown. The solid lines represent theoretical results based on the equations given

above. Good agreement is noted between experimental and theoretical curves for moderate bias conditions. The discrepancy at higher bias voltages ($V_{be} > 1.2V$) is due to high injection, not included in the present model. For lower bias the curves diverge because of the non-ideal characteristics of the junctions.

4. CONCLUSIONS

A new analytical model is under development for heterojunction bipolar transistors under illumination. Good agreement between experiment and theory was observed within the ideal regions of the junctions. The results suggest no photovoltaic behavior which will lead to a faster optical response at the expense of gain. The high frequency response is limited by the transit time on the base-collector depletion region which potentially leads to results in excess of 10 GHz limited by the laser.

5. ACKNOWLEDGEMENTS

The development of the HBTs was supported by the Dr. M. Strocio at the Army Research Office and Mr. V.G. Gelnovatch at the Army Research Laboratory. This work was partially supported by the Brazilian research council (CAPES) through a Ph.D. fellowship program.

6. REFERENCES

- [1] A.A.deSalles, "Optical control of GaAs MESFETs", IEEE Trans.on MTT, Vol.MTT-31, No.10,Oct.1983, p.812
- [2] R.N.Simons, "Microwave performance of an optically controlled AlGaAs/GaAs high electron mobility transistor and GaAs MESFET", IEEE Trans.on MTT, Vol.MTT-35, No.12, Dec.1987, p.1444
- [3] W.D.Edwards, "Two and three terminal GaAs FET optical detectors", IEEE Trans.Elect.Dev.Lett., Vol.EDL-1,p.149, 1980
- [4] A.Madjar, A.Paoletta, P.Herczfeld, "Analytical model for optically generated currents in GaAs

MESFETs", IEEE Trans.on MTT, Vol.40, No.8, Aug.1992, p.1681

[5] G.J.Papaionannou, J.R.Forrest, "On the photoresponse of GaAs MESFET's: back gating and deep traps effect", IEEE Trans.Elect.Dev., Vol.ED-33, No.3, Mar 1986, p.373

[6] S.Chandrasekhar, M.K.Hoppe,A.Dentai, C.H.Joyner, G.J.Qua, "Demonstration of enhanced performance of an InP/InGaAs heterojunction phototransistor with a base terminal", IEEE Trans.Elect.Dev., Vol.12, No.10, Oct 1991, p.550

[7] C.D.Parikh, F.A.Lindholm, "A new charge-control model for single- and double-heterojunction bipolar transistors", IEEE Trans.Elect.Dev., Vol.39, No.6, Jun 1992, p.1303

[8] M.A.Romero, L.E.M.de Barros Jr and P.Herczfeld, "Internal photovoltaic effect in microwave devices", Proc. of the 1994 IEEE MTT-S, Vol.3, p.1505, San Diego, CA.

Appendix A

$$\Gamma_{pe} = n_{pe} + K'_b e^{-\alpha x_{pe}}$$

$$\Gamma_{pc} = n_{pc} - K'_b e^{-\alpha x_{pc}}$$

$$K'_b = \frac{\eta_b \alpha \phi_0 \tau_b}{1 - \alpha^2 L_h^2}$$

$$K'_c = \frac{\eta'_c \alpha \phi_0 \tau_c}{1 - \alpha^2 L_c^2}$$

$$\eta' = (\eta_b e^{-\alpha W_b} + \eta_c)$$

MODELING FOR DISPERSION OF SHIELDED MICROSTRIP LINE USING SLR TECHNIQUE

A.K. Verma and Raj Kumar

Department of Electronic Science
Delhi University of South Campus
New Delhi, India

ABSTRACT

We report a new dispersion model for shielded microstrip line in the range $1 \leq W/h_1 \leq 10$, $2 \leq h_2/h_1$, $0 \leq f \leq 20\text{GHz}$. Model has maximum deviation within 4% against the result of SDA. It has average of maximum deviation within 3.23%. Method is based upon reduction of shielded microstrip line into an equivalent open microstrip line with virtual permittivity which is a function of width of line, shield height and frequency. Over this equivalent virtual substrate Kirchning-Jansen dispersion model has been used. The present model is useful for fast interactive CAD, on the desk top computer

1. INTRODUCTION

The microstrip line based microstrip components and circuits are required to be placed within the shielding enclosure in order to reduce performance degradation from external influence. The top shield cover could also be used to some extent to compensate for the degrading effect of manufacturing tolerances [1]. The microstrip line with top shield is shown in Fig. (1). A closed form expression to account affect of top shield on the static effective permittivity and characteristic impedance has been reported [2]. However, no closed form expression suitable for the CAD application has been reported for frequency dependent effective permittivity $\epsilon_{\text{eff}}(f)$ of the shielded microstrip line. The top shield affects the dispersion behaviour in ways which is difficult to be modeled. A unified dispersion model for multilayer microstrip line, including top shielded microstrip line has been reported by the first author[3]. We have noticed that $\epsilon_{\text{eff}}(f)$ of the shielded microstrip structure determined from the unified dispersion model degrades very much for the close proximity of top shield to the microstrip line. This paper improves the previous model by incorporating some empirically determined factors in the single layer reduction (SLR) technique reported earlier[3]. The present model provides accuracy for $\epsilon_{\text{eff}}(f)$ within 4% against the results of SDA in the range of $1.05 \leq \epsilon_r \leq 20$, $1 \leq W/h_1 \leq 10$, $2 \leq h_2/h_1$ and $0 \leq f \leq 20\text{GHz}$.

2. MODEL

A careful examination of behaviour of the frequency dependent effective permittivity of shielded microstrip line reveals the following characteristic :

- * Proximity of the top shield alters dispersion of microstrip line such that with increase in frequency the $\epsilon_{\text{eff}}(f)$ moves towards a virtual permittivity having higher value than the actual permittivity of the substrate. This virtual permittivity of the substrate increases with nearness of the top shield to the central conductor.
- * The virtual permittivity of the substrate is also a function of operating frequency beyond one third of the lower cut off frequency f_p of the first higher order mode in the open microstrip line. With the increase of frequency the virtual permittivity should move towards the real permittivity of the substrate.
- * The virtual permittivity of the equivalent substrate is also a function of W/h_1 ratio of microstrip line.

To Model $\epsilon_{\text{eff}}(f)$ of the shielded microstrip line, we reduce the shielded microstrip line to an equivalent open microstrip line with virtual permittivity of the substrate. On such equivalent open microstrip line available dispersion formula could be used. The virtual permittivity can be written as

$$\epsilon_{\text{rv}} = \epsilon_r + \epsilon_{\text{radd}} \quad (1)$$

- ϵ_{rv} : Virtual permittivity of the substrate
- ϵ_r : Real permittivity of the substrate
- ϵ_{radd} : Additional permittivity which is function of W/h_1 , h_2/h_1 and frequency. ϵ_{radd} should meet the following requirements.

$$\begin{aligned} \epsilon_{\text{radd}}(W/h_1, h_2/h_1, f) &\longrightarrow 0, \text{ as } h_2/h_1 \longrightarrow \infty \\ \epsilon_{\text{radd}}(W/h_1, h_2/h_1, f) &\longrightarrow 0, \text{ as } f \longrightarrow \infty \end{aligned} \quad (2)$$

In the single layer reduction (SLR) technique the shielded microstrip line is reduced to an equivalent open microstrip line under the static condition. A difference in permittivity

$\Delta\epsilon_r$ of the substrate in presence of the top shield is obtained. $\Delta\epsilon_r$ forms the basis for the $\epsilon_{r_{\text{mod}}}$ which is to be empirically modified to take the above facts into account.

$$\text{Thus,} \quad \Delta\epsilon = \epsilon_r - \epsilon_r' \quad (3)$$

Where ϵ_r' is the permittivity of the equivalent substrate of the open microstrip line obtained from the SLR technique. However, this equivalent substrate is not our present virtual substrate of permittivity ϵ_r . We can write an expression for $\epsilon_{r_{\text{mod}}}$ as follows

$$\epsilon_{r_{\text{mod}}} = A \left[\frac{1.0 + \alpha(W/h_1)}{h_2/h_1} \right] \left[\frac{f_p}{3f} \right]^\beta \quad (4)$$

where

$$A = \sqrt{\Delta\epsilon_r}, \quad \text{for } \Delta\epsilon_r < 1 \quad (5)$$

$$= (\Delta\epsilon_r)^2, \quad \text{for } \Delta\epsilon_r \geq 1$$

$$f_p = Z_0/2\mu_0 h_1 \quad (6)$$

$$f_p/3f = 1, \quad \text{for } f \geq f_p/3$$

i.e. the frequency dependent term is neglected for the operating frequency $f \leq f_p/3$. Z_0 is the characteristic impedance of the shielded microstrip line determined from the variational technique. Constants α and β have been determined empirically from comparison of $\epsilon_{\text{eff}}(f)$ determined by the present model and the SDA. Table-I gives α and β for $1 \leq W/h_1 \leq 10$.

The Kirschning-Jansen dispersion model[4] for the open microstrip line has been used on this virtual substrate of equivalent open microstrip line. Any other dispersion model could be used in this virtual equivalent substrate.

3. RESULTS

Fig. (2a) and Fig. (2b) show dispersion results by the present model and SDA on plastic substrate of $\epsilon_r = 2.2$. Average maximum deviation in the range $1 \leq W/h_1 \leq 10$ for $h_2/h_1 = 2$ for frequency upto 20GHz is 1.1%. Maximum deviation is -1.8% at $W/h_1 = 3$, frequency 14GHz. For $h_2/h_1 = 6$, average maximum deviation in the range $1 \leq W/h_1 \leq 10$ is 1.4% and max. deviation is 2.2% at $W/h_1 = 10$, frequency 12GHz. Fig. (3a) and Fig. (3b) provide dispersion results on Alumina substrate, $\epsilon_r = 9.8$.

For $h_2/h_1 = 2$, max. deviation is -4% at $W/h_1 = 10$, frequency 8 GHz. For $h_2/h_1 = 2$, max. deviation is -3.9% at $W/h_1 = 6$, frequency 6GHz. Fig (4a) and Fig. (4b) show dispersion for the shielded microstrip line on $\epsilon_r = 20$. For $h_2/h_1 = 2$, max. deviation is 3.6% at $W/h_1 = 4$, frequency 20GHz and the average max deviation is 2.32% in the range $1 < W/h_1 \leq 10$. For $h_2/h_1 = 6$, max. deviation is 4.1% at $W/h_1 = 10$ frequency 2GHz. For $W/h_1 = 10$, variation in the static $\epsilon_{\text{eff}}(0)$ of variational method and SDA is about 2%. In most of the cases more deviation between the present model and SDA takes place for $h_2/h_1 = 3$ and in the middle frequency range. The average max. deviation for $\epsilon_r = 2.2, 12.95$ and 20 in the range $1 \leq W/h_1 < 10$ frequency upto 20GHz is shown in the table-2. It is possible to improve further accuracy of the model in this range. Range of W/h_1 , ϵ_r and frequency could also be enlarged.

REFERENCES

- [1] S.S. Bedair, M.I. Sobhya, "Tolerance analysis of shielded microstrip line", IEEE, Vol. MTT-32, No. 5, pp. 544-7, May 1994.
- [2] March, S. "Microstrip packaging : watch the last step", Microwave J., Vol. 20, No. 12, pp. 83-94, Dec. 1981.
- [3] A.K. Verma, G.H. Sadr, "Unified dispersion model for multilayer microstrip line", IEEE, Vol. MTT-40, No. 7, pp. 1887-91, July 1992.
- [4] M. Kirschning, R.H. Jansen, "Accurate model for effective dielectric constant of microstrip with validity upto millimeter frequencies", Electron Lett., No. 6, pp. 272-3, March 1982.

Table - I

W/h_1	α	β
1-3.5	1.00	1.0
3.5-6.5	0.30	0.70
6.5-8.5	0.22	0.62
8.5-10	0.20	0.85

Table - II

Average of max. deviation of present model from SDA

$$\text{Deviation} = \frac{\epsilon_{\text{eff}}(f)_{\text{SDA}} - \epsilon_{\text{eff}}(f)_{\text{Model}}}{\epsilon_{\text{eff}}(f)_{\text{SDA}}} \times 100$$

$\epsilon_{r \rightarrow}$	2.2	12.95	20
h_2/h_1 ↓			
2.0	1.10%	2.68%	2.32%
3.0	1.43%	2.59%	3.23%
4.0	1.41%	1.94%	2.74%

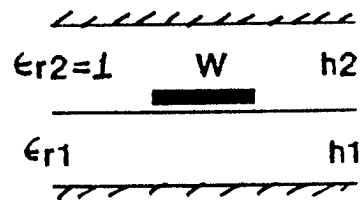


Fig. 1

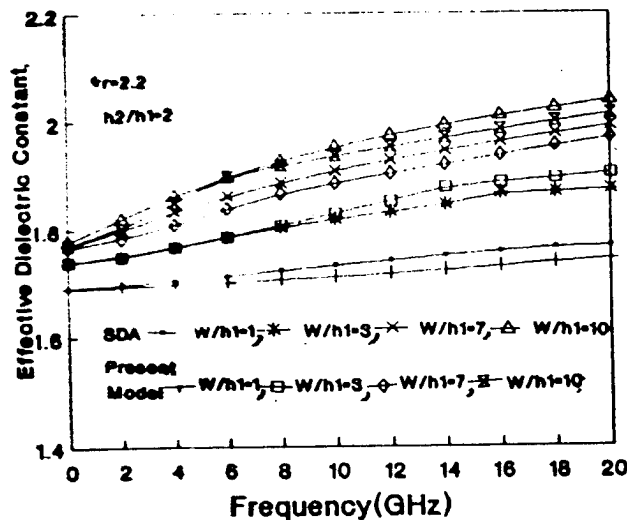


Fig. (2a). Dispersion Behaviour of Shielded Microstrip Line

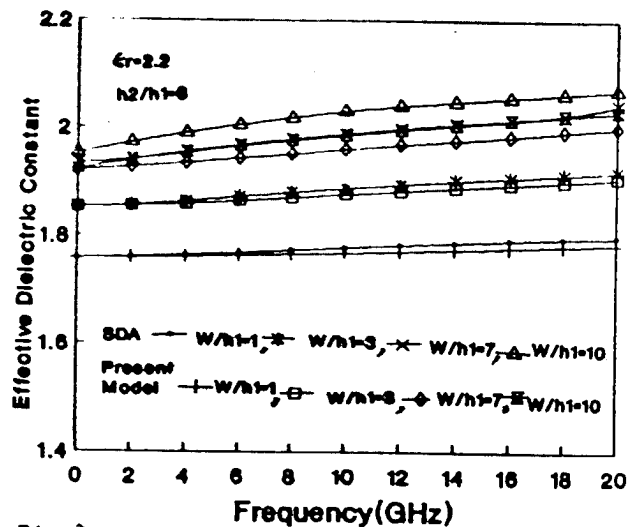


Fig. (2b). Dispersion Behaviour of Shielded Microstrip Line

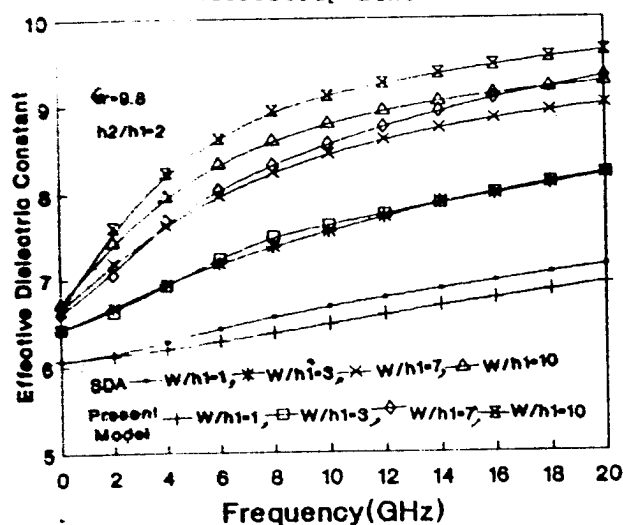


Fig. (3a). Dispersion Behaviour of Shielded Microstrip Line

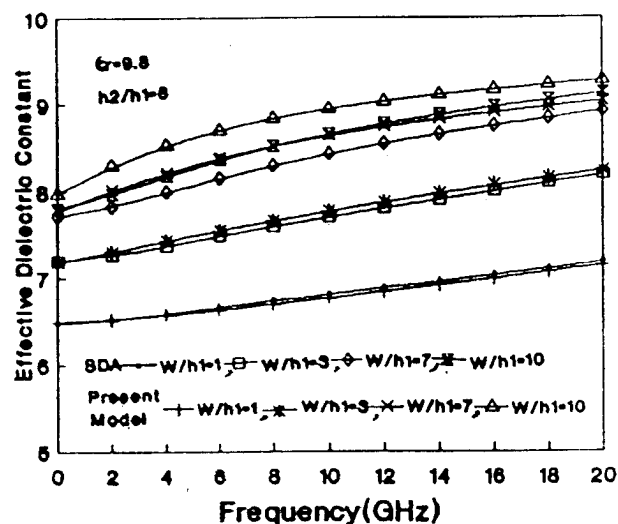


Fig. (3b). Dispersion Behaviour of Shielded Microstrip Line

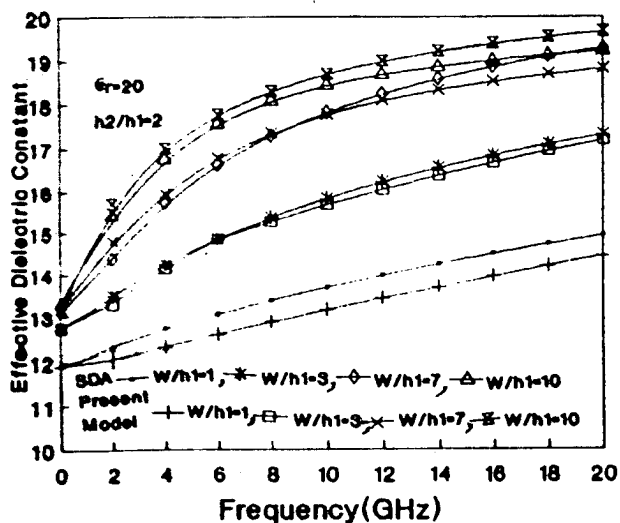


Fig. (4a). Dispersion Behaviour of Shielded Microstrip Line

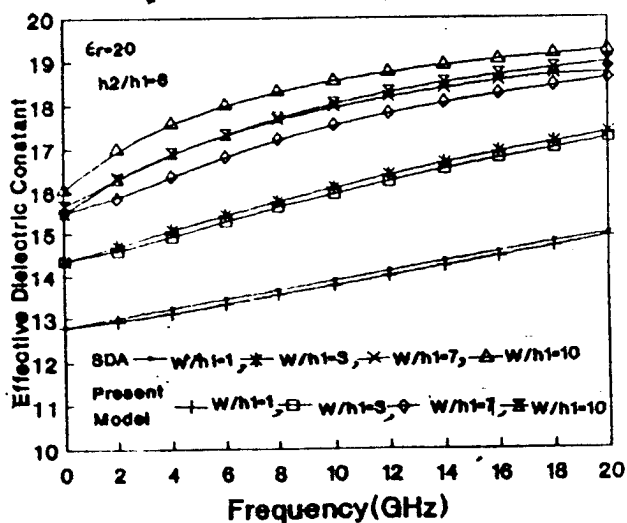


Fig. (4b). Dispersion Behaviour of Shielded Microstrip Line

ADAPTIVE ASYMPTOTIC OPTIMAL ALGORITHMS FOR DETECTING SIGNALS IN AUTOREGRESSIVE NOISE

B.B.Shishkov, Tz..P.Georgiev, S.N.Stoyanov

Technical University Sofia, 1618 Sofia, P.O.Box 104, Bulgaria

Phone: ++3592566123, Fax: ++3592877870, E-mail: bbshi @bgtus4.vmei.acad.bg

Abstract: Asymptotic optimal (AO) algorithms for detection of signals in additive autoregressive noise of order m (m -dependent Markov noise) are synthesized. The algorithms require the storage of m past data samples to achieve optimum performance. It is AO memory discrete-time detector of a deterministic or quasideterministic signal in autoregressive noise. To assure the change of the detector's parameters as a result of learning the AO algorithm was modified to adaptive one. Combining AO algorithm with adaptation it is a powerful approach to overcome a priori uncertainty in information systems. The investigations are carried out by common approach with many simulation results.

1. Introduction

In many works of Le Cam, Hajek, Roussas etc it has been proved that many important properties of the statistical criteria result from asymptotic normality of the logarithm of likelihood ratio for close hypotheses (for close values of the parameter) independently of the way of how observations are connected.

The asymptotic theory of statistical decisions applied to the problems of detection and estimation of signals on a background of noise permits to overcome the difficulties of interpreting statistics with finite measure of samples and to create more general and simpler methods in treatment of information.

2. Problem statement and assumptions

We consider the detection of signals in additive m -dependent Markov noise. Let us have a sequence $\mathbf{x} = \{x_i, i=1, \dots, n\}$ of real observations of a process $\mathbf{X} = \{x(t) = X_i, i=1, 2, \dots\}$ and, on the basis of \mathbf{x} , we wish to decide between the following pair of hypotheses concerning \mathbf{X} :

$$\begin{aligned} H_0: \mathbf{X}_{i-m}^i &= \mathbf{N}_{i-m}^i \\ H_1: \mathbf{X}_{i-m}^i &= \mathbf{N}_{i-m}^i + \lambda \mathbf{s}_{i-m}^i, \end{aligned} \quad (1)$$

where $\mathbf{N}_{i-m}^i = (N_{i-m}, \dots, N_i)$, $i=m+1, \dots$ is a stationary m -dependent Markov noise with an initial probability density $f(\mathbf{n}_1^m)$ and a transition probability density

$f(n_i | \mathbf{n}_{i-m}^{i-1})$. Here $\mathbf{s}_{i-m}^i = (s_{i-m}, \dots, s_i)$ is a deterministic periodic signal. The parameter λ is an unknown amplitude of the signal. Our study is restricted to the asymptotic (large-sample-size) case and, to avoid singularity, we will consider a sequence of alternatives $\{\lambda_n = \gamma / \sqrt{n}; n = 1, 2, \dots\}$, where $\gamma > 0$.

In [2] (see also [3, 1]) was derived an asymptotic optimal (AO) statistics for the problem (1)

$$\begin{aligned} T(\mathbf{x}) &= \frac{1}{\sqrt{n}} \sum_{i=m+1}^n \mathbf{s}_{i-m}^i{}^T \boldsymbol{\varphi}(\mathbf{x}_{i-m}^i) = \\ &= \frac{1}{\sqrt{n}} \sum_{i=m+1}^n \sum_{j=-m}^0 s_{i+j} \varphi_j(\mathbf{x}_{i-m}^i), \end{aligned} \quad (2)$$

where

$$\begin{aligned} \varphi_j(\mathbf{x}_{i-m}^i) &= \left. \frac{\partial}{\partial s_{i+j}} \log f(x_i | \mathbf{x}_{i-m}^{i-1}; \lambda \mathbf{s}_{i-m}^i) \right|_{\lambda \mathbf{s}_{i-m}^i = 0}, \\ & \quad j = -m, \dots, 0. \end{aligned} \quad (3)$$

The sufficient statistics (2) is asymptotic normal both on the hypothesis H_0 and the contiguous alternative H_1 with parameters

$$N(0, \text{tr}(\mathbf{SK})) \text{ and } N(\gamma \text{tr}(\mathbf{SK}), \text{tr}(\mathbf{SK}))$$

respectively, where

$$\mathbf{K} = (\mathbf{k}_{jv}) = E\{\varphi_j \varphi_v | H_0\}, j, v = -m, \dots, 0; \det \mathbf{K} < \infty \quad (4)$$

$$S = (s_{jv}) = \lim_{n \rightarrow \infty} \frac{1}{n} \sum_{i=m+1}^n s_{i+j} s_{i+v}, j, v = -m, \dots, 0; \det S < \infty.$$

AO algorithm can be presented as follows

$$\Phi(\mathbf{x}) = \begin{cases} 1 & (\text{there is a signal}) \text{ if } T(\mathbf{x}) \geq C \\ 0 & (\text{there isn't a signal}) \text{ if } T(\mathbf{x}) < C \end{cases} \quad (5)$$

Taking into account the asymptotic normality of the statistic (2) under H_0 and H_1 can be determined the threshold constant C and the performance of AO algorithm for given γ and $n \rightarrow \infty$.

3. Quasideterministic signals

Let us have again the problem (1), but useful signal is quasideterministic one:

$$s(t) = \sum_{q=1}^K v_q \psi_q(t) = \mathbf{v}^T \boldsymbol{\psi}(t); \quad (6)$$

$$s(t_i) = s_i = \mathbf{v}^T \boldsymbol{\psi}(t_i) = \mathbf{v}^T \boldsymbol{\psi}_i; i=1, n,$$

where $\mathbf{v}^T = (v_1, \dots, v_K)$ is a set of unknown random parameters and $\boldsymbol{\psi}^T = (\psi_1(t), \dots, \psi_K(t))$ are given basic functions. Further one can determine respectively (see [5]):

- likelihood ratio (LR)

$$l(\mathbf{x}; \frac{\gamma}{\sqrt{n}} \mathbf{v}^T \boldsymbol{\psi}_{-m,n}) \sim \exp \left\{ \frac{\gamma}{\sqrt{n}} \mathbf{v}^T \sum_{i=m+1}^n \boldsymbol{\psi}_{i-m,i} \boldsymbol{\phi}(\mathbf{x}_{i-m}^i) - 0.5 \gamma^2 \mathbf{v}^T \mathbf{B} \mathbf{v} \right\} \quad (7)$$

- k-dimensional vector statistic

$$\mathbf{T}(\mathbf{x}) = \frac{1}{\sqrt{n}} \sum_{i=m+1}^n \boldsymbol{\psi}_{i-m,i} \boldsymbol{\phi}(\mathbf{x}_{i-m}^i), \quad (8)$$

$$\Lambda[\mathbf{T}(\mathbf{x})] = \int_N l(\mathbf{x}|\mathbf{v}) f(\mathbf{v}) d\mathbf{v},$$

- by using decision function

$$\Phi[\mathbf{T}(\mathbf{x})] = \begin{cases} 1 & (\text{there is a signal}), \text{ if } \Lambda[\mathbf{T}(\mathbf{x})] \geq C \\ 0 & (\text{there isn't a signal}), \text{ if } \Lambda[\mathbf{T}(\mathbf{x})] < C. \end{cases} \quad (9)$$

4. Adaptive AO algorithms for detection of signals

Adaptive algorithms assure the change of the parameters and structure of the system as a result of learning. Let $\mathbf{Y}_1^L = (Y_1, \dots, Y_L)$ be a classified sample belonging to the distribution of the m-dependent Markov noise ($L > m$). With the help of a learning sample \mathbf{Y}_1^L a

parametric estimation of the basic characteristic $\hat{\phi}_j(\mathbf{x}_{i-m}^i)$ (see (3)) is derived

$$\hat{\phi}_j(\mathbf{x}_{i-m}^i) = g_j(\mathbf{x}_{i-m}^i, \mathbf{Y}_1^L), j = -m, \dots, 0 \quad (10)$$

and also the estimation of the matrix \hat{K} (see (4)) and the threshold constant $\hat{C} = z_\alpha \sqrt{\text{tr}(S\hat{K})}$. Here z_α is the upper α -th quantile of F , the d.f. of the standard normal. It can be proved that the adaptive algorithm is AO, if for any $j = -m, \dots, 0$ the convergence

$$\lim_{L \rightarrow \infty} E \left\{ \left| g_j(\mathbf{x}_{i-m}^i, \mathbf{Y}_1^L) - \phi_j(\mathbf{x}_{i-m}^i) \right|^2 \right\} = 0 \quad (11)$$

is fulfilled.

The additive m-dependent Markov sequence $\{N_i\}$ (see problem(1)) satisfies the linear autoregression's equation with unknown coefficients

$$\sum_{j=-m}^0 a_j N_{i+j} = \eta_i, i=1, \dots, n, \quad (12)$$

where a_j are arbitrary constants and η_i are i.i.d. random variables with common density function $f_\eta(z)$. It can be proved [4,5] that $X_i = N_i + \lambda s_i$ is a m-dependent Markov sequence with density function of a transition from \mathbf{x}_{i-m}^{i-1} to \mathbf{x}_i , which equals of

$$f(\mathbf{x}_i | \mathbf{x}_{i-m}^{i-1}; \lambda \mathbf{s}_{i-m}^i) = f_\eta \left(\mathbf{x}_i + \sum_{j=-m}^{-1} a_j \mathbf{x}_{i+j} - \lambda \sum_{j=-m}^0 a_j \mathbf{s}_{i+j} \right), \quad (13)$$

where $a_0 = 1$. Therefore, logarithmic derivative (see (3)) has an other representation as well

$$\phi_j(\mathbf{x}_{i-m}^i) = \frac{\partial}{\partial s_{i+j}} \log f(\mathbf{x}_i | \mathbf{x}_{i-m}^{i-1}; \lambda \mathbf{s}_{i-m}^i) \Big|_{\lambda \mathbf{s}_{i-m}^i = 0} = \quad (14)$$

$$= -a_j \frac{f'_\eta \left(\mathbf{x}_i + \sum_{j=-m}^{-1} a_j \mathbf{x}_{i+j} \right)}{f_\eta \left(\mathbf{x}_i + \sum_{j=-m}^{-1} a_j \mathbf{x}_{i+j} \right)}, j = -m, \dots, 0.$$

If we don't know the coefficients a_j , it can be found their maximum likelihood estimates using a learning sample of the autoregressive noise $\{N_i\}$. Finally it can be found out the parametric estimator $\hat{\phi}_j(\mathbf{x}_{i-m}^i)$ of the logarithmic derivative.

5. Communication systems

The basic algorithm-(8) is interpreted, when $m=1$ -Markov noise with unknown densities, and the useful signal is a quasideterministic one-a narrow band one (with an initial random phase φ_0) that is modulated by amplitude and by phase (frequency):

$$s(t) = a(t) \cos[\omega_0 t + \mu(t) - \varphi_0] = v_1 \psi_1(t) + v_2 \psi_2(t), \quad (15)$$

where $v_1 = \cos \varphi_0$; $v_2 = \sin \varphi_0$; $\psi_1(t) = a(t) \cos[\omega_0 t + \mu(t)]$, $\psi_2(t) = a(t) \sin[\omega_0 t + \mu(t)]$. Here the envelope $a(t)$ and the phase $\mu(t)$ are slowly changing deterministic functions; the random phase φ_0 is uniformly distributed in $[0, 2\pi]$.

The following algorithm is synthesized

$$|T(x)|^2 = \frac{1}{n} \left\{ \sum_{i=2}^n \sum_{j=1}^0 a(t_{i+j}) \cos[\omega_0 t_{i+j} + \mu(t_{i+j})] \hat{\varphi}_j(x_{i-1}) \right\}^2 + \frac{1}{n} \left\{ \sum_{i=2}^n \sum_{j=1}^0 a(t_{i+j}) \sin[\omega_0 t_{i+j} + \mu(t_{i+j})] \hat{\varphi}_j(x_{i-1}) \right\}^2 \quad (16)$$

and the structure scheme is presented as well (see Fig.1).

6. Simulation results

For the basic algorithm (2), (5) by simulation technique, were derived the curves of probability of correct detection $\hat{\beta}$ in dependence of signal to noise ratio, when $m=1$ and $m=3$ and α , n are fixed (see Fig.2-5).

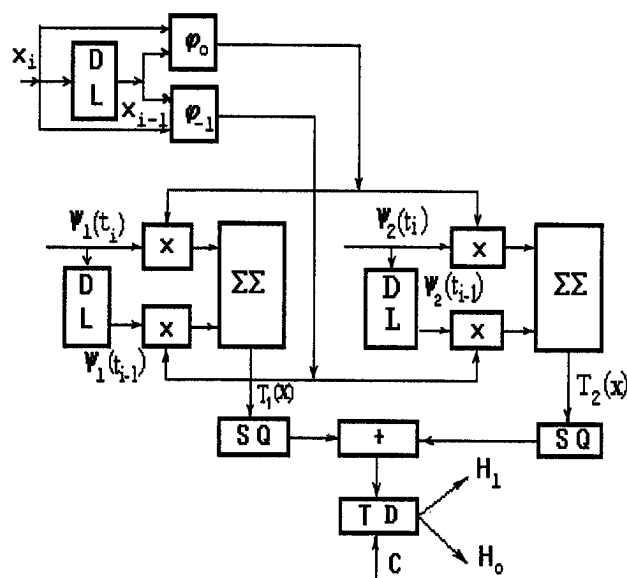


Fig.1 Structure of the detector for a narrow band modulated signal. DL-delay line; SQ-squared; TD-threshold device.

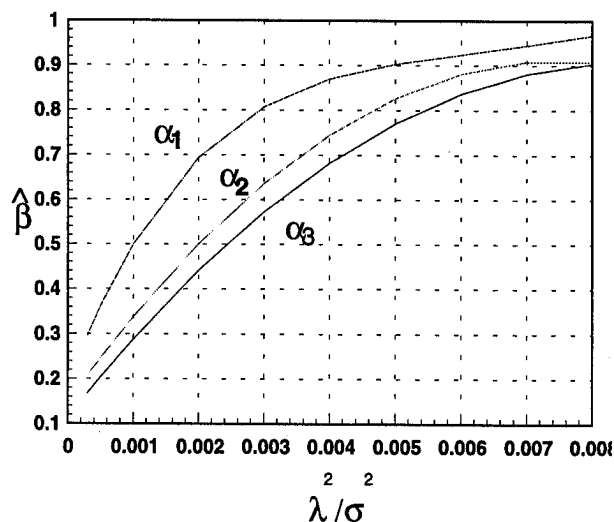


Fig.2. Estimation probability of correct detection; AR1, Const. signal, $\alpha_1=0.05$, $\alpha_2=0.01$, $\alpha_3=0.005$, $n=100$.

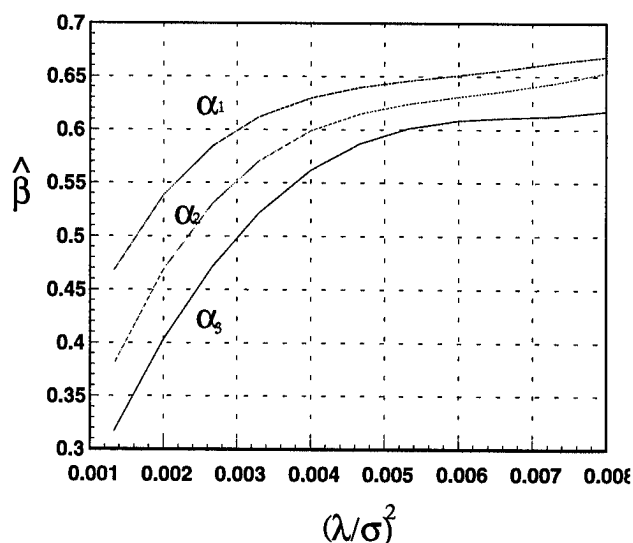


Fig.3. Estimation probability of correct detection; AR1, Pulse-signal, $\alpha_1=0.05$, $\alpha_2=0.01$, $\alpha_3=0.005$, $n=100$.

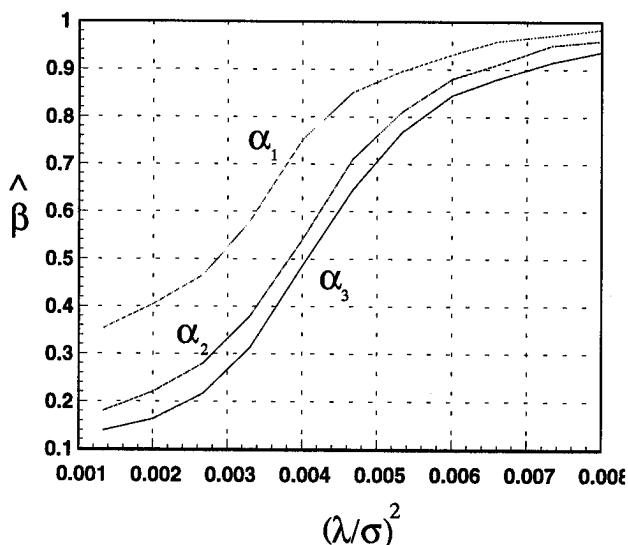


Fig.4. Estimation probability of correct detection; AR3, Const. signal, $\alpha_1=0.05$, $\alpha_2=0.01$, $\alpha_3=0.005$, $n=100$.

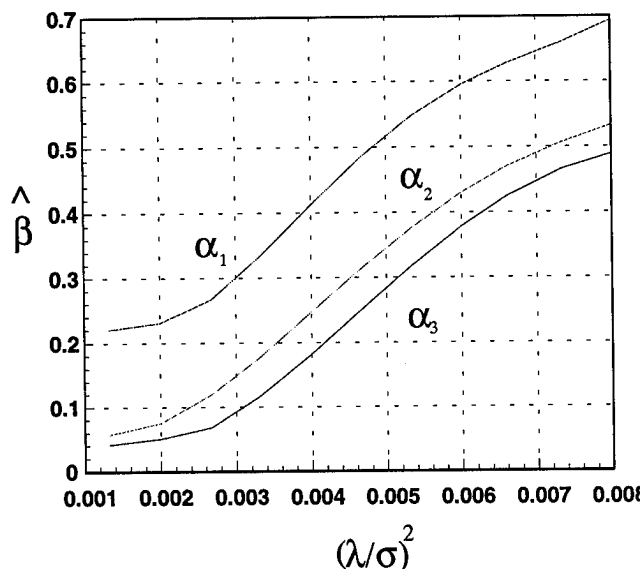


Fig.5. Estimation probability of correct detection; AR3, Pulse-signal, $\alpha_1=0.05$, $\alpha_2=0.01$, $\alpha_3=0.005$, $n=100$.

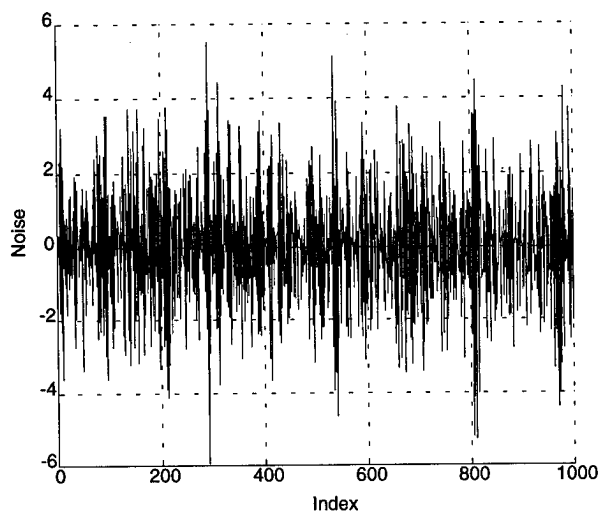


Fig.6. AR1, $N_i + 0.8N_{i-1} = \eta_i$, $\eta_i \sim N(0,1)$

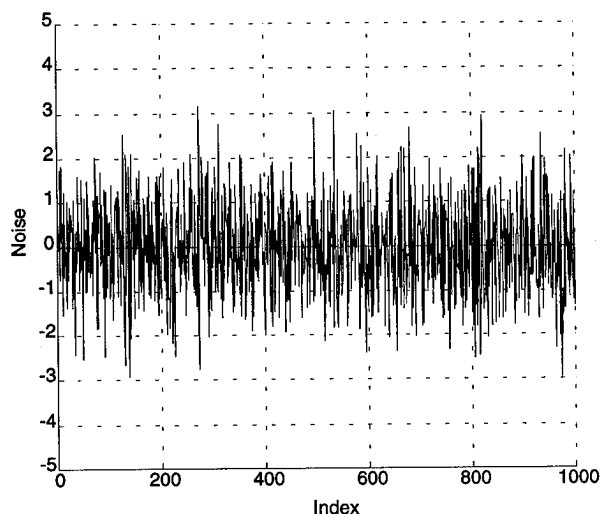


Fig.7. AR3, $N_i + 0.95N_{i-1} + 0.2996N_{i-2} + 0.0314N_{i-3} = \eta_i$, $\eta_i \sim N(0,1)$

7. Radar applications

The basic algorithm (8) is interpreted, when $m=0-\{N_i\}$ is nongaussian noise with unknown density function and independent samples. The useful signal can be written as follows:

$$s(t)=s(t,v)=a\cos(\omega_0 t - \varphi_0) \Rightarrow \quad (17)$$

$$a\cos(\omega_0 t_i - \varphi_{0j}) = a\cos\omega_0 t_i \cos\varphi_{0j} + a\sin\omega_0 t_i \sin\varphi_{0j} =$$

$$=v_1\psi_1(t_i) + v_2\psi_2(t_i), \quad i=1, \dots, n; \quad j=1, \dots, M,$$

where a is an unknown amplitude and φ_0 is uniformly distributed in $[0, 2\pi]$. Here M is a number of the impulses in radar's packet. The following algorithm is synthesized

$$\begin{aligned} |T(x_j)|^2 &= \frac{1}{n} \left[\sum_{i=1}^n a \cos \omega_0 t_i \hat{\phi}(x_{ij}) \right]^2 + \\ &+ \frac{1}{n} \left[\sum_{i=1}^n a \sin \omega_0 t_i \hat{\phi}(x_{ij}) \right]^2. \end{aligned} \quad (18)$$

The structure scheme is presented in [4].

Acknowledgments

This work was supported by National Science Fund under contract TH-414/1994.

References

- [1] Le Cam, L.M. On the Asymptotic Theory of Estimation and Testing Hypotheses. Proc. Third Berkley Sympos. Math. Statist. Probab., 1, pp. 129-156, 1956.
- [2] Kushnir, A.F., A.I. Pinski. Asymptotic Optimal Tests of Testing Hypotheses for an Interdependent Sample. Theor. Probab. Appl., 2, pp. 280-291, 1971.
- [3] Roussas, G.G. Contiguity of probability measures. Cambridge University Pres. p. 248, 1972.
- [4] Shishkov, B.B. Adaptive Technique in Signal Detection. Compt. Rend. Acad. Bulg. Sc., t. 45, No 10, pp. 29-32, 1992.
- [5] Shishkov, B.B. Testing Hypotheses on Distribution's Parameters of Time Series and Applications to Signal Detection. Radio Eng. Electron. Phys., t. XXXIX, No 3, pp. 411-423, 1994.

A FUZZY-RULE-BASED PHASE ERROR DETECTOR

Flavio Daffara

Laboratoires d'Electronique Philips
22 avenue Descartes, 94453 Limeil-Brévannes Cedex, France
Tel.: +33 1 45.10.67.11 - FAX: +33 1 45.10.69.60
e-mail: daffara@lep-philips.fr

ABSTRACT

This paper shows how fuzzy logic can be used to improve the behaviour of phase-locked loops. In particular, we have derived a fuzzy-rule-based phase error detector, which permits a decrease in the steady-state phase variance to be achieved.

1. INTRODUCTION

In modern digital communications, efficient synchronization techniques are required at the receiver side to fully exploit the potentiality of modulation/coding schemes without causing a bottleneck in the overall system performance.

One of the fundamental function in the receiver is the phase recovery unit, which generally consists in a phase-locked loop (PLL) [1] as depicted on Figure 1. A PLL is made up with three main blocks: a phase error detector (PD), a low-pass loop filter (LPF) and a voltage controlled oscillator (VCO). The phase detector provides an error signal ϵ_k whose average value is proportional to the phase error between the phase associated to the received signal $r(t)$ and the VCO's phase. The phase error ϵ_k is then low-pass filtered and the obtained signal $u(t)$ is used to drive the VCO in order to correct its phase. Usually, the performances of a phase recovery loop are given in terms of acquisition time and steady-state phase variance. The aim of this paper is to derive a fuzzy-rule-based PLL controller able to improve the synchronization loop performance.

The paper is organized as follows: Section 2 describes the general method for fuzzy-controlling a PLL. Section 3 develops a specific example of a fuzzy-rule-based phase detector designed to minimize the PLL steady-state phase variance. Finally, Section 4 is for our conclusions.

2. FUZZY-CONTROLLED PLL

Figure 2 shows how a fuzzy controller should be interfaced with a PLL. A set of rules describing the desired behaviour of the PLL constitutes the *Expert Data Base*. Such rules should be expressed as: if *condition* then *action*, where the *condition* and *action* parts are expressed in natural language and therefore contain some amount of uncertainty or inexactitude which are straightforwardly represented by subjective and not sharply defined classes of objects. For example the PLL controller could make use of the information: "the PLL is *almost locked*". Within fuzzy set theory [2] it is possible to give a meaning to such a sentence and a PLL can be in its lock-in state with a continuum of grades of membership (and not only locked or unlocked).

Once the rules have been set, the PLL state variables related to the *condition* part of the rules and the non-fuzzy controls dependent on the *action* part of the rules should be identified. Then the state variables (resp. non-fuzzy controls) should be mapped to ad-hoc fuzzy sets describing the *conditions* (resp. *actions*). Every possible value of the state variables or controls should belong to at least one of the fuzzy sets. It is then possible to combine all the different rules (depending on the PLL state variables) using a classical fuzzy logic method (Mamdani, Larsen, interpolation, etc. [3]) and obtain for each non-fuzzy control a value which is the most representative of the combination of all *actions*.

3. FUZZY-RULE-BASED PHASE DETECTOR

This section is an attempt to show the potentiality of the above mentioned method. For sake of simplicity we will only focus on improving the steady-state phase jitter by fuzzy-controlling the phase detector block.

Figure 3 shows the Minimum Mean-Square Error (MMSE) PD, which is currently known in literature [4]. The error signal is given by $\epsilon_k = \text{Im}\{p_k d_k^*\}$, where

$p_k = d_k e^{j\phi} + n_k = a_k + jb_k$ is the optimum sample of the signal at the output of the matched filter with d_k a random $M \times M$ -QAM symbol whose in-phase (I) and quadrature (Q) parts belong to the set $\{-(M-1)d, \dots, -d, d, \dots, (M-1)d\}$, ϕ the unknown phase error, n_k the noise which is a Gaussian complex random process whose variance is σ_n^2 and \hat{d}_k the decision taken on p_k .

A common way to evaluate the performance of a PD is to compare the steady-state variance of the phase measured in a closed loop configuration (for a given loop bandwidth B_L and at a given Signal-to-Noise Ratio, SNR) to the minimum achievable phase jitter in the same conditions. Such a minimum phase jitter is also known as the Cramer-Rao Bound (CRB) [5] and is given by

$$\sigma_{\text{CRB}}^2 = \frac{2B_L T}{\text{SNR}}$$

The MMSE phase detector gives very good performance (very close to the CRB) as far as the decision \hat{d}_k is correct, i.e. as far as the SNR is high. However, if the number of errors in the decisions increases (at low SNR) the PD performance worsens. The idea is to try to take into account only the decisions which are more likely to be correct and to discard the others. That is to say we try to use the following empiric rules:

- If the decision is correct then the PD should correct in the usual way i.e. using the MMSE algorithm (which is optimum).

- If the decision does not seem to be correct then it is better not to correct at all (or at least less than usually) rather than correcting in the wrong direction. In this case the *condition* is the "correctness of the decision" and the *action* can be identified as the "strength of the PD error signal". We arbitrarily chose to relate the "correctness of the decision" to two state variables x_1 and x_2 , which are the distances of the received point p_k from the closest I and Q decision thresholds respectively. We also chose to relate the "strength of the phase detector error signal" to one control γ_k , which is a gain factor ranging from 0 to 1. The new PD is shown on Figure 4 where $\epsilon'_k = \gamma_k \epsilon_k$ is the new error signal.

The membership functions [2] of the fuzzy sets corresponding to the "correctness of the decision" ($\mu_{CD_I}(x_1)$ and $\mu_{CD_Q}(x_2)$) and to the "strength of the PD error signal" ($\mu_{SE}(\gamma_k)$) are shown on Figure 5 as a function of x_1 , x_2 and γ_k in the case of a QPSK constellation.

The membership functions $\mu_{CD_I}(x_1)$ and $\mu_{CD_Q}(x_2)$ depend also on a parameter λ (see Figure 5), which has to be chosen carefully in order to optimize the fuzzy-controller. Such a parameter defines some uncertainty regions in the complex plane as shown in Figure

6. Since the membership functions characterising the state variables are monothonic, we used the interpolation method [3] to derive the non-fuzzy control γ_k , i.e. $\gamma_k = \mu_{SE}^{-1}\{\min[\mu_{CD_I}(x_1), \mu_{CD_Q}(x_2)]\}$. The empiric rules are implemented in the Control Logic block whose output γ_k is close to one if the decision is likely to be correct while is close to zero if the decision is likely to be erroneous.

The slope of the so obtained fuzzy-controlled PD has been evaluated by simulation and is plotted on Figure 7 for several values of λ in the case of a QPSK constellation. The degradation with respect to the CRB is given on Figure 8 for different values of SNR and λ . The values for $\lambda = 0$ correspond to the classical MMSE PD. The optimum value of λ is the one which minimizes the degradation and we can see that for this value the fuzzy-controlled MMSE PD outperforms the classical one. Predictably, the improvement is large at low SNR since the number of erroneous decisions is high, while it is small at high SNR because the decisions are almost completely correct.

4. CONCLUSIONS

In this paper we have shown the potentiality of applying fuzzy logic to improve the performance of tracking loops. In particular, we have developed a specific and very simple example of a fuzzy-rule-based phase detector. Even in this very simple case (only one rule) an improvement in the steady-state phase variance can be achieved by choosing an appropriate value of λ . Modifications in the shape of the membership functions or the use of more sophisticated rules taking into account other conditions (SNR level, speed of convergence, loop bandwidth, etc...) are expected to provide further improvement.

5. REFERENCES

- [1] H. Meyr and G. Ascheid, *Synchronization in Digital Communications*, Vol. 1, John Wiley & Sons, New York, 1990.
- [2] A. Kandel and W.J. Byatt, *Fuzzy Sets, Fuzzy Algebra, and Fuzzy Statics*, Proc. of the IEEE, Vol. 66, No. 12, December 1978, pp. 1619-1639.
- [3] D. Dubois and H. Prade, *Fuzzy Sets and Systems, Theory and Applications*, Academic Press, 1980.
- [4] M.K. Simon and J.G. Smith, *Carrier Synchronization and Detection of QASK Signal Sets*, IEEE Trans. Comm., COM-22, February 1974, pp. 98-106.

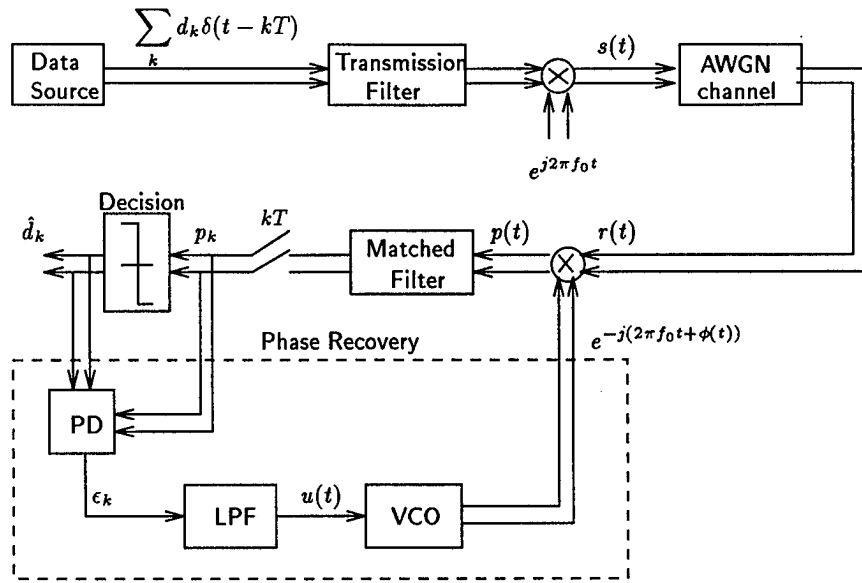


Figure 1: Digital transmission system.

- [5] H.L. Van Trees, *Detection, Estimation and Modulation Theory*, John Wiley & Sons, New York, 1968.

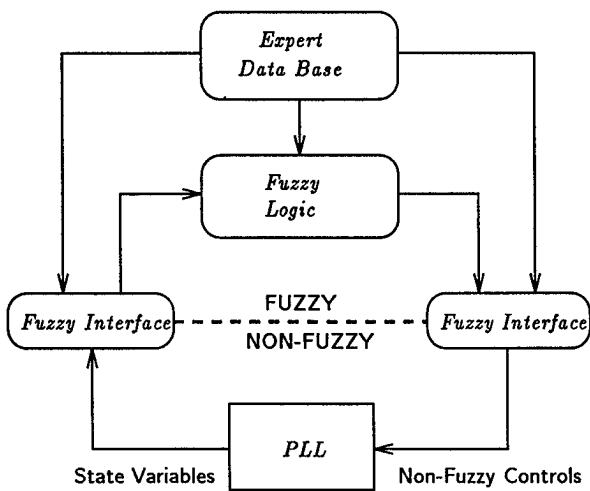


Figure 2: Fuzzy-rule-based phase-locked loop.

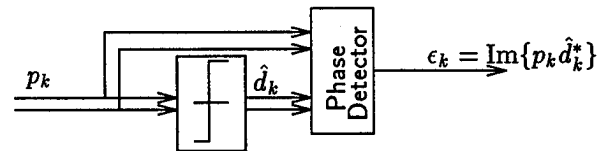


Figure 3: MMSE phase detector.

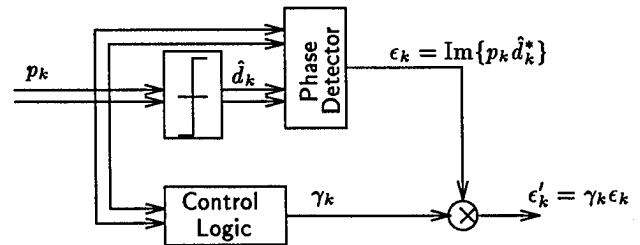


Figure 4: Fuzzy-controlled MMSE phase detector.

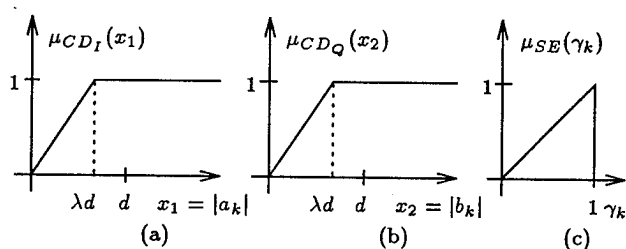


Figure 5: Membership functions of the fuzzy sets corresponding to the "correctness of the decision" (a) and (b) and to the "strength of the PD error signal" (c) in the case of a QPSK constellation.

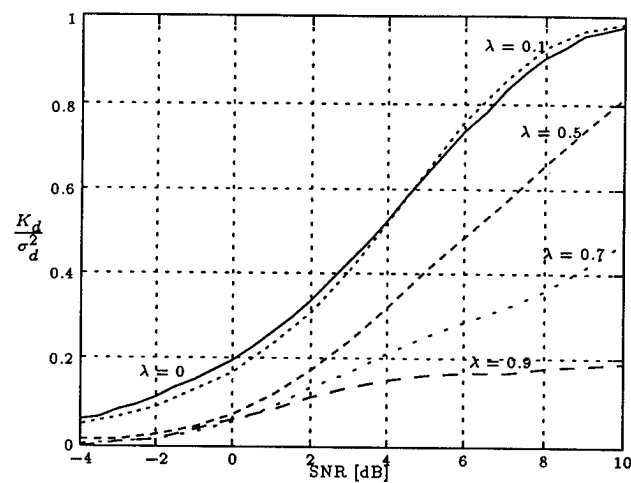


Figure 7: Phase Detector slope.

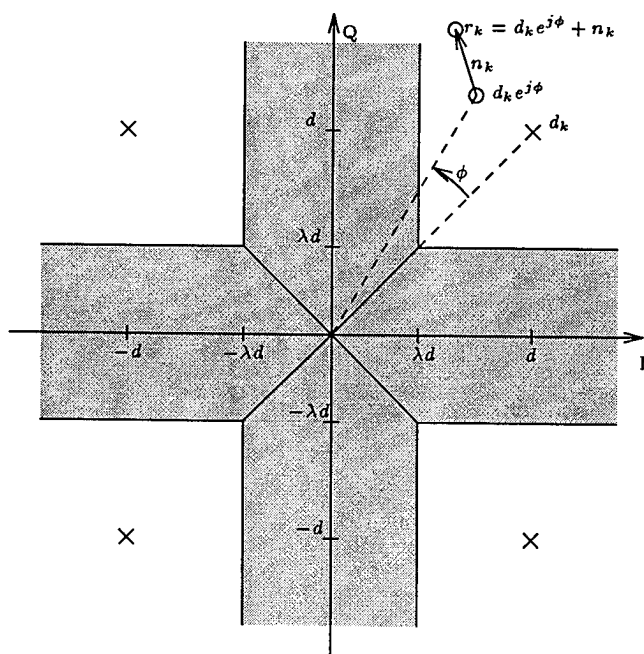


Figure 6: Uncertainty regions for a QPSK constellation.

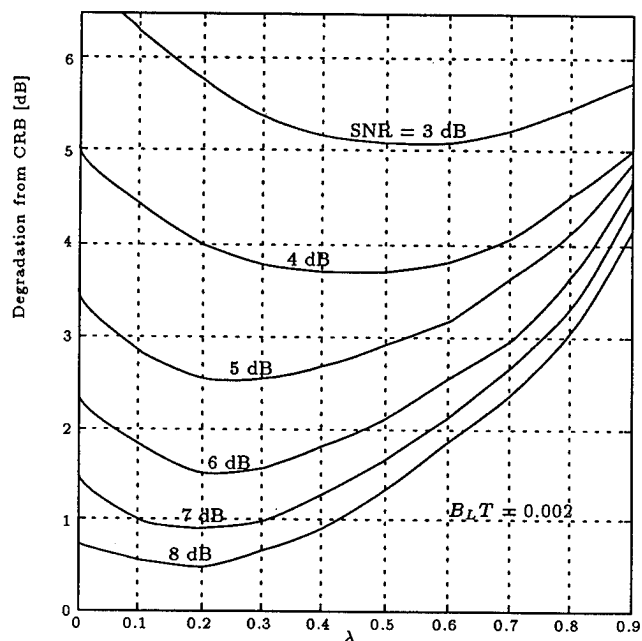


Figure 8: Degradation with respect to the Cramer-Rao Bound as a function of λ .

SPEECH PRODUCTION AND PERCEPTION MODELS AND THEIR APPLICATIONS TO SYNTHESIS, RECOGNITION, AND CODING

A. Alwan, S. Narayanan, B. Strobe, and A. Shen,

Department of Electrical Engineering, UCLA
405 Hilgard Ave.
Los Angeles, CA 90024

ABSTRACT

The last few decades have witnessed tremendous progress in the performance, reliability, and wide-spread use of speech-processing devices. Using mathematical models of human speech production and perception has been an important factor in the improved performance of these devices. In this tutorial paper, we review recent advances in speech production and perception modeling and summarize the challenges that lie ahead in developing fully parametric models.

1. INTRODUCTION

Quantitative models of human speech production and perception provide important insights into our speech production and perception mechanisms and lead to high-quality computer synthesis of speech, robust automatic speech recognition (ASR), and efficient speech and audio coders. These issues are of importance in the development of effective human-computer communications through the medium of human language.

Simplified linear models of speech production form the basis of several speech synthesizers [Klatt, 1987] and the most widely-used speech coder today: Code-excited-linear-prediction (CELP) [Schroeder and Atal, 1985]. Simple auditory models have been used successfully in optimizing the performance of speech and audio coders [Schroeder et al., 1979; Shen et al., 1995; Johnston, 1988]; these models are also embedded in the MPEG audio-coding standards [Brandenburg and Stoll, 1992]. Using auditory models as preprocessors has resulted in improving the performance of recognition systems in noise [Ghitza, 1986].

Supported in part by NSF, NIH, and ARPA/CSTO. Shrikanth Narayanan is now with ATT Bell Labs, and Albert Shen, with Intel. Inc., OR.

Recently, with rapid advances in hearing research, medical imaging, non-linear analysis, and computer technology, more sophisticated speech production and perception models are being proposed.

2. SPEECH PRODUCTION MODELS

Speech production research is directed towards better understanding and quantitative characterization of the acoustics, articulatory dynamics, and cognition of both normal and pathological human speech. Speech production modeling efforts, however, face at least two major challenges: (1) the lack of appropriate physical and physiological data which are crucial for developing quantitative models, and (2) the presence of articulatory and acoustic variabilities, both within and across speakers.

A great deal of attention is, hence, given to the development and use of novel measurement and instrumentation techniques that provide better insights into speech production mechanisms. Examples of such techniques include the use of magnetic resonance imaging (MRI) to study the 3D vocal-tract geometry, use of ultrasound [Stone, 1990], x-ray microbeam and electromagnetic midsagittal articulometer (EMMA) [Perkell, 1992] to study tongue dynamics, measuring linguopalatal interaction using electropalatography (EPG) [Hardcastle et al, 1989], and the use of microsensor-based aerodynamic and acoustic measurements in the vocal tract. Since most of these techniques provide information about certain specific attributes of speech production, data are typically collected using several of these techniques in parallel, if not simultaneously. Novel signal processing techniques are often required to process, visualize, and quantify the various physical and physiological speech production data thus obtained.

A major focus of speech production research is in modeling articulatory-acoustic relationships of speech

sounds. Physically and physiologically-based models for speech acoustics are particularly important for developing high-quality speech synthesis and low bit rate (articulatory) coding. Significant progress has been recently made towards developing improved articulatory-acoustic models. Extensive data from human subjects using techniques such as MRI were used to obtain accurate quantitative and qualitative characterizations of the vocal-tract geometry for vowels and consonants [Baer et al., 1991; Narayanan et al., 1995]. The information obtained from these experiments, such as accurate vocal-tract dimensions, were then employed in modeling the acoustics of these sounds. For example, physically-motivated 1D acoustic models for fricatives, showing good agreement with the spectra of natural fricatives, were recently reported [Narayanan, 1995].

Numerical simulation of the acoustic wave propagation in actual 3D vocal-tract models, particularly for 'static' scenarios corresponding to sustained sounds, using techniques such as finite element and/or finite time-difference methods has received wide attention [Miki et al., 1994; Cummings et al., 1995]. This is largely due to the vast improvements in computational capabilities and the availability of more realistic vocal-tract data. An alternative to numerical simulations for studying flow problems in the 3D vocal tract is to use mechanical analogs. It should, however, be noted that simulation of speech *dynamics* in 3D models is an extremely challenging problem, which is as yet largely untackled.

Considerable interest has also been devoted to the inverse problem in speech production i.e., the identification of articulatory parameters from the acoustic speech signal. Solution to the inverse problem has potential applications in low bit rate coding and speech recognition [Schroeter and Sondhi, 1992; Deng and Sun, 1994]. It is, however, important to bear in mind that the unconstrained inverse problem is non-unique. That is, the acoustic to articulatory transformation is not one-to-one. Identifying appropriate constraints to solve uniqueness is not a solved problem. Various techniques such as neural networks [Shirai, 1993] and genetic algorithms [McGowan, 1994] have been proposed for solving the inverse problem although their viability is yet to be fully demonstrated.

Novel approaches such as those drawn from nonlinear dynamical systems (chaos) theory have recently found applications in speech analysis. Such analyses have provided further insights into the production of pathological speech [Titze et al., 1993] and consonant

sounds such as fricatives which are characterized by turbulence formation in the vocal tract [Narayanan and Alwan, 1995].

Recently, there has also been an interest in understanding higher-level processing during speech production by monitoring brain activity using functional MRI [Shaywitz et al., 1995] in conjunction with other methods such as PET.

Considerable efforts directed towards modeling speech production are hoped to provide a clearer picture of the underlying mechanisms and help in the development of better engineering applications. The significance of efficient analysis schemes (identification of the articulatory parameters from the speech waveform) and synthesis schemes (generation of the acoustic speech waveform from the articulatory parameters) extends well beyond the realm of speech production modeling with clinical and linguistic implications.

3. SPEECH PERCEPTION MODELS

Much of the evidence for current auditory models are based on acoustic masking experiments. Static (or simultaneous) masking experiments have led to the definition of the critical bandwidth, and a non-uniform filter bank model of auditory perception [Fletcher, 1940; Zwicker et al, 1957; Zwicker and Terhardt, 1980]. Another well-quantified aspect of auditory processing is "loudness equalization" [Robinson and Dadson, 1956]. For example, the perceived loudness of two tones at different frequencies might be different even though their intensity levels (in dB SPL) are the same.

Dynamic (or non-simultaneous, forward) masking experiments [Plomb, 1964; Jesteadt et al, 1982; Moore and Glasberg, 1983] also provide significant insight for auditory modeling efforts. Specifically, forward masking experiments suggest that the relative levels of short-time spectral estimates are perceptually significant.

Further, perceptual experiments with spectrally complex speech-like stimuli indicate that human audition is particularly sensitive to the frequency location of local spectral peaks [Klatt, 1982]. Measurements of the timing detail of individual inner hair cell responses reveal firing responses which track dominant spectral features [Delgutte and Kiang, 1984] (instead of exclusively representing the spectral content at the fiber's center or best frequency as a filter bank model might predict) suggesting a possible mechanism for this spectral peak sensitivity.

Our understanding of auditory processing of speech signals is at an early stage; one of the major challenges in the next few decades is unraveling and modeling the neural mechanisms involved in speech processing [Pickles, 1994].

Auditory Models and Automatic Speech Recognition

Early efforts to build automatic speech recognition machines occurred in the 1950s at Bell Laboratories [Davis et al, 1952]. These systems relied on identifying the spectral resonances of vowels within isolated digits. Despite tremendous research focus, and many significant technical advances, a robust speech recognition system that approaches human performance still does not exist. Research, therefore, continues.

Typical speech recognition systems involve two fundamental steps: short-term spectral analysis, followed by pattern comparison with representative templates (or statistical models of templates). In the 1970s, LPC-based spectral analysis [Itakura, 1975], and the application of dynamic programming techniques to pattern comparison [Vintsyuk, 1968] led to successful isolated word recognition systems. Today many systems use Mel-Frequency Cepstral Coefficients (and their temporal derivatives) for spectral analysis, and Hidden Markov Models (HMM) of the templates for pattern comparison [Rabiner, 1989]. Mel-Frequency Cepstral Coefficients (MFCC) are defined as the DCT of log spectral estimation obtained with a critical bandwidth-like non-uniform filter bank model [Davis and Mermelstein, 1980]. The DCT provides an orthogonal transformation to a vector space with better energy compaction, which therefore requires fewer coefficients per acoustic vector. Including temporal derivatives of the cepstral coefficients in the acoustic observation vector is to account for dynamic sensitivity [Rabiner and Juang, 1993].

Providing a rigorous stochastic framework, HMMs and the techniques to train and apply them, have led to successful large-vocabulary speaker-independent systems [eg., Lee et al, 1991]. Unfortunately the performance of these systems still degrades significantly when the acoustic environment (amount and type of background noise, reverberation, competing sources, etc.) differs from the training data.

HMM systems [Rabiner, 1989] rely on a fundamental stochastic identity (Bayes Theorem). HMMs provide the probability of an acoustic observation for each specific template model. We then choose the template

model which generates the highest probability of the acoustic observation occurring.

If we are trying to answer the question: "What was most likely said?" it seems reasonable that we also want to characterize statistically the acoustic distinctions between sounds. Although recent efforts are addressing this issue, the formal derivation of a computationally tractable training procedure is much more difficult, and remains an open question.

Using MFCC and their temporal derivatives to represent the acoustic observation, current recognizers incorporate a suitable model of frequency selectivity and a rough approximation of short-term auditory adaptation. A number of researchers have proposed models with more explicit short-term auditory adaptation [Seneff, 1988; Lyon and Mead 1988; Hermansky and Morgan 1994], however parameterizing these models so that they are quantitatively consistent with measurable top-level functionality remains a consistent challenge.

The recent system we developed includes a model of short-term auditory adaptation parameterized through a series of perceptual forward-masking experiments, and a novel cepstral processing technique to isolate local spectral peaks [Strope, 1995]. Figure 1 illustrates different representations for the digits one, three, and nine, spoken by a male speaker. The top part of the figure is the time waveform, the middle part, a spectrogram computed using cepstral coefficients derived from a linear prediction model, and the third is a "perceptual" spectrogram computed using our dynamic perceptual model. Note how the perceptual representation highlights onsets and spectral transitions which are perceptually important. Using a dynamic-programming based recognition system, this representation leads to significantly more robust recognition performance when compared to common cepstral and cepstral derivative representations. Currently, we are also evaluating this representation with an HMM system.

Stochastic modeling provides a powerful tool to train recognition systems based on a sequence of acoustic observations. Future efforts will undoubtedly continue to improve these stochastic models and training techniques. We should also expect, however, increased performance by incorporating acoustic observation sequences that are more consistent with human perception.

Auditory Models and Speech and Audio Coding

Speech coding is the process of obtaining a compact representation of voice signals for efficient transmission and storage. Obtaining an efficient method of transmit-

ting speech signals over band-limited wired and wireless channels drives the research in speech coding. Today, in a software-controlled digital format, speech coders have become an essential component in telecommunications and in the multimedia infrastructure [Jayant and Cox, 1993]. Commercial systems which rely heavily on efficient speech coding include cellular communication, video conferencing, digital simultaneous voice and data (DSVD), as well as numerous PC-based games and multimedia applications.

To measure the overall effectiveness of digital speech coders, three metrics are commonly used: complexity, perceptual quality, and bit rate. The complexity of a speech coding algorithm is reflected in the number of machine instructions executed when operating in a real time environment, measured in millions of instructions per second (MIPS). The second criterion is perceptual quality. A common metric used to measure perceptual quality is the Mean Opinion Score (MOS). This measure is an average score derived from subjective listening tests using a five-point scale. A score of one is assigned to speech with 'poor' quality, while a score of five is given to speech with 'excellent' quality. The third metric is the operating bit rate of a coder, which is the rate at which data must be transmitted or stored in order to effectively reconstruct the original speech signal [Jayant and Noll, 1984].

Auditory modeling can aid in the design of speech and audio coders in two important ways: 1) developing an objective measure to rapidly and reliably assess the performance of a coder instead of conducting time-consuming and expensive subjective listening tests [Wang et al., 1992], and 2) optimizing the performance of perceptually-based speech and audio coding schemes [Shen, 1994; Shen et al, 1995].

Simplified auditory models have been used successfully in both areas (developing objective measures and designing speech and audio coders). These simplified models view speech as a sequence of unrelated static segments and exploit, predominantly, static masking effects. A more complete auditory model, especially one which takes into account *dynamic* spectral distortions, will undoubtedly have an important impact in speech coding research.

4. SUMMARY AND CONCLUSION

It is clear that our understanding of speech production and perception mechanisms has improved tremendously in the past few decades. Further multidisciplinary research in signal processing, acoustics, psy-

choacoustics, linguistics, imaging, and auditory physiology are needed to better model these mechanisms.

5. REFERENCES

- [1] Baer, T., Gore, J.C., Gracco, L.C., and P.W. Nye, "Analysis of vocal-tract shape and dimensions using MRI: Vowels", JASA 90, 799-828, 1991.
- [2] Brandenburg, K. and G. Stoll. "The ISO/MPEG Audio Codec: A Generic Standard for Coding of High Quality Digital Audio." Audio Engineering Society Preprint 3336, 1992.
- [3] Cummings, K., Maloney, J., and M. Clements, "Modeling Speech Production using Yee's Finite Difference Method," ICASSP Proc., Vol. 1, pp. 672-675, 1995.
- [4] Deng, L. and D.X. Sun, "A statistical approach to automatic speech recognition using the atomic speech units constructed from overlapping articulatory features," JASA 95, 2702-2719, 1994.
- [5] Davis, K. H., Bidduph, R., Balashek, S. "Automatic Recognition of Spoken Digits," JASA, 24, 637-642, 1952.
- [6] Davis, S. B., Mermelstein P., "Comparison of parametric representations for monosyllabic word recognition in continuously spoken sentences," IEEE Trans. ASSP 28, August, 357-366, 1980.
- [7] Delgutte, B. and Kiang, N. Y. S. "Speech coding in the auditory nerve: I. Vowel-like sounds," JASA 75, 866-878, 1984.
- [8] Fletcher, H. "Auditory Patterns," Rev. Mod. Physics 12, 47-65, 1940.
- [9] Ghitze, O. "Auditory nerve representation as a front-end for speech recognition in a noisy environment," Computer Speech and Language, 1(2):109-130, 1986.
- [10] Hardcastle, W.J., Jones, W., Knight, C., Trudgeon, A. and G. Calder, "New developments in electropalatography: A state of the art report," Clinical Linguistics and Phonetics, vol.3, pp. 1-38, 1989.
- [11] Hermansky, H., and N. Morgan "RASTA processing of speech," IEEE Trans. Speech and Audio Proc., vol. 2, no. 4, pp. 578-589, 1994.
- [12] Itakura, F. "Minimum Prediction Residual Applied to Speech Recognition," IEEE Trans. ASSP 23, February, 67-72, 1975.
- [13] Jayant, N.S. and P. Noll. *Digital Coding of Waveforms: Principles and Applications to Speech and Video*. Englewood Cliffs, NJ: Prentice-Hall, 1984.
- [14] Jayant, N.S. and R.V. Cox. "Speech Processing." IEEE Communications Magazine. Vol. 31, No. 11, 1993.
- [15] Jesteadt, W., Bacon, S., and Lehman, J. "Forward Masking as a function of frequency, masker level, and signal delay," JASA 71, 950-962, 1982.
- [16] Johnston, James D. "Transform Coding of Audio Signals Using Perceptual Noise Criteria." IEEE JSAC, Vol. 6, No. 2, 1988.
- [17] Kates, J., "An adaptive digital cochlear model," Proc. IEEE ICASSP, 3621-3624, Toronto, 1992.
- [18] Klatt, D. "Prediction of perceived phonetic distance from critical-band spectra: a first step," Proc. ICASSP, Paris, 1278-1281, 1982.

- [19] Klatt, D. "Review of text-to-speech conversion for English," JASA vol. 82, no. 3, pp. 737-793, 1987.
- [20] Lee, K. F., Hon, H. W., and Huang, X. "Speech recognition using Hidden Markov Models: a CMU perspective," Speech Communication, 9, 497-508, 1991.
- [21] Lyon, R. F., and Mead, C. "An Analog Electronic Cochlea," IEEE Trans. on Acoust., Speech, and Sig. Proc. 36, 1119-1133, 1988.
- [22] McGowan, R.S., "Recovering articulatory movement from formant frequency trajectories using task dynamics and a genetic algorithm," Speech Comm., 14, 19-48, 1994.
- [23] Miki, N., Badin, P., Ngoc, P-T, and Y. Ogawa, "Vocal tract model and 3-dimensional effect of articulation", ICSLP Proc., Yokohoma, Japan, 167-170, 1994.
- [24] Moore, B. C. J., and Glasberg, B. R. "Growth of forward masking for sinusoidal and noise maskers as a function of signal delay; implications for suppression in noise," JASA 73, 1249-1259, 1983.
- [25] Narayanan, S.S. "Fricative consonants: an articulatory, acoustic, and systems study," unpublished Ph.D. Dissertation, Dept. of Electrical Engineering, UCLA, June, 1995.
- [26] Narayanan, S.S., and A.A. Alwan, "A nonlinear dynamical systems analysis of fricative consonants", JASA 97, 2511-2524, 1995.
- [27] Narayanan, S.S., Alwan, A.A., and K. Haker, "An articulatory study of fricative consonants using MRI", to appear in the September issue of JASA, 1995.
- [28] Perkell, J., "Electromagnetic midsagittal articulometer systems for transducing speech articulatory movements", JASA 6, 3078-3096, 1992.
- [29] Pickles, J. *An Introduction to the Physiology of Hearing*. Second Edition, Academic Press, London, 1994.
- [30] Plomb, R. "Rate of Decay of Auditory Sensation," JASA 36, 277-282, 1964.
- [31] Rabiner, L. R. "A Tutorial on Hidden Markov Models and Selected Applications in Speech Recognition," Proc. IEEE, 77, February, 257-286, 1989.
- [32] Rabiner, L., and Juang, B. H. *Fundamentals of Speech Recognition*. Prentice-Hall, New Jersey, 1993.
- [33] Robinson, D., and R. Dadson, "A redetermination of the equal-loudness relations for pure tone," Brit. J. Appl. Phys., pp 166-181, 1956.
- [34] Schroeder, M. R., Atal, B. S., and Hall, J. L. "Optimizing digital speech coders by exploiting masking properties of the human ear," JASA, 66, 1647-1652, 1979.
- [35] Schroeder, M.R. and B.S. Atal. "Code-Excited Linear Prediction (CELP): High-Quality Speech at Very Low Bit Rates." Proc. IEEE ICASSP, pp. 937-940, 1985.
- [36] Schroeter, J., and M. M. Sondhi, "Speech Coding Based on Physiological Models of Speech Production", in *Advances in Speech Signal Processing*, edited by S. Furui and M. M. Sondhi, Marcel Decker, New York, 231-268, 1992.
- [37] Seneff, S., "A joint synchrony/mean-rate model of auditory speech processing," J. Phonetics, vol. 16, no. 1m pp 55-76, 1988.
- [38] Shaywitz, B.A. et al., "Sex differences in the functions organizational of the brain for language," Nature, 373, 607-609, 1995.
- [39] Shen, A. "Perceptually-based subband coding of speech signals," unpublished Master's thesis, Dept. of Electrical Engineering, UCLA, June, 1994.
- [40] Shen, B. Tang, A. Alwan, and G. Pottie, "A Robust and Variable-Rate Speech Coder," Proc. IEEE ICASSP 1995, Vol. I, 249-252.
- [41] Shirai, K. "Estimation and generation of articulatory motion using neural networks", Speech Comm. 13, 45-51, 1993.
- [42] Stone, M. "A three-dimensional model of tongue movement based on ultrasound and X-ray microbeam data", JASA 87, 2207-2217, 1990.
- [43] Strophe, B. "A Model of Dynamic Auditory Perception and its Application to Robust Speech Recognition," unpublished Master's thesis, Dept. of Electrical Engineering, UCLA, June, 1995.
- [44] Titze, I. R., Baken, R., and H. Herzel, "Evidence of chaos in vocal fold vibration," in *Vocal fold physiology: New Frontiers in basic science*, 143-188, Singular, San Diego, 1993.
- [45] Vintsyuk, T. K. "Speech Discrimination by Dynamic Programming," Kibernetika, 4, January-February, 81-88, 1968.
- [46] Wang, S., Sekey, A., and A. Gersho, "An objective measure for predicting subjective quality," IEEE JSAC, Vol. 10, No. 5, 1992.
- [47] Zwicker, E., Flottorp, G., and Stevens, S. "Critical Bandwidth in Loudness Summation," JASA 29, 548-557, 1957.
- [48] Zwicker, E., Terhardt, E. "Analytical expressions for critical-band rate and critical bandwidth as a function of frequency," JASA 68, 1523-1525, 1980.

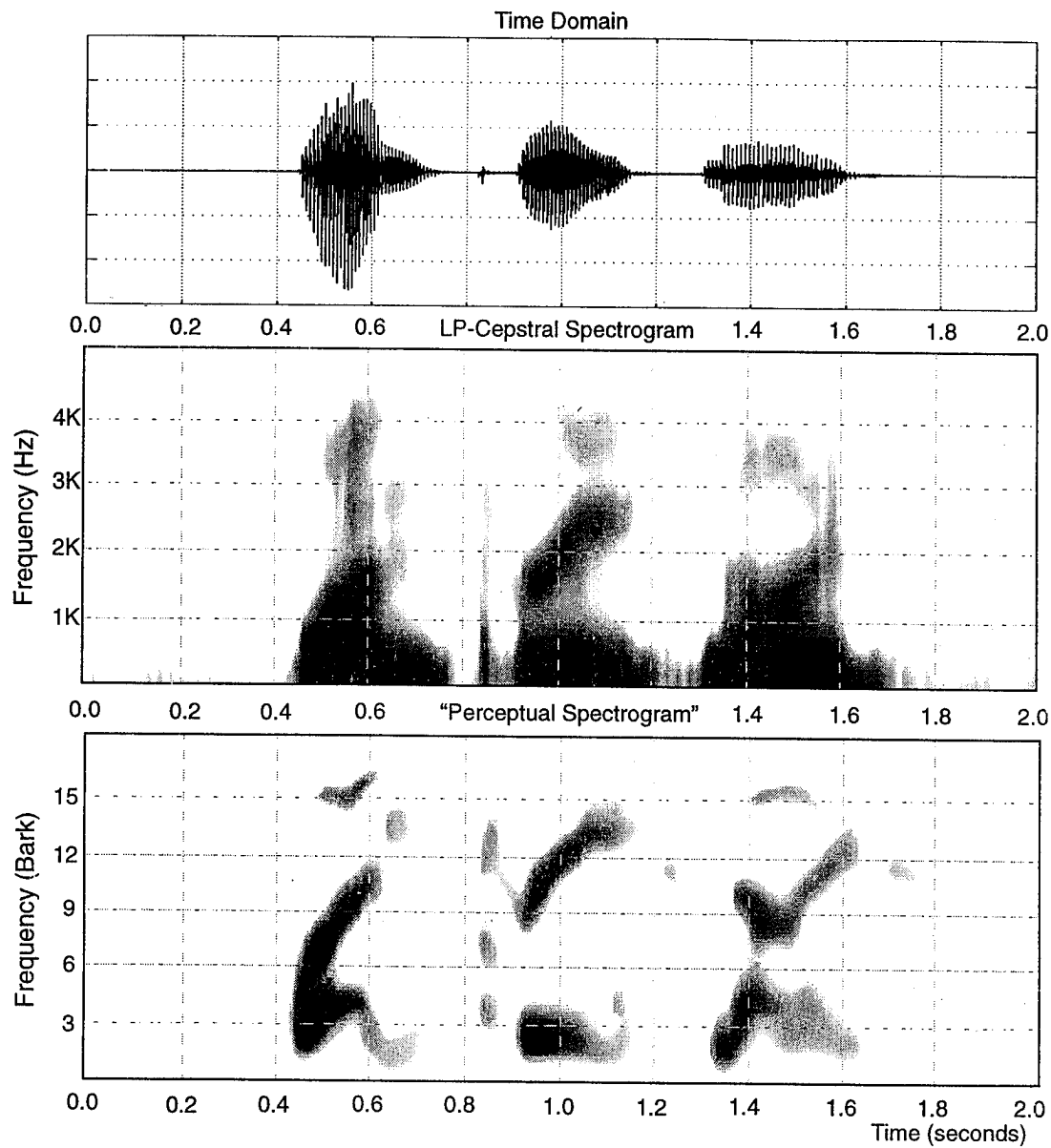


Figure 1. Different representations of the digits “one,” “three,” and “nine.” The top shows the time-domain waveform, the middle is the spectral estimation from short-time LP-Cepstral analysis, and the bottom shows the output of our dynamic perceptual model. The “perceptual spectrogram” highlights salient onsets, spectral transitions, and local spectral peaks, providing a more noise-robust representation.

Microphone Arrays for Speech Processing *

Ea-Ee Jan and James Flanagan
CAIP Center, Rutgers University, Piscataway, NJ 08855

ABSTRACT

Microphone arrays can capture desired signals and attenuate interfering noise and reverberation in multipath environments. Hands-free speech technologies can therefore be supported using microphone arrays. This report considers delay-and-sum beamformers, advanced array technology using matched-filters and hands-free speaker identification using microphone arrays.

I. Introduction

Microphones are used to detect and transduce sounds. However, the effectiveness of a microphone can be limited. Received sound quality can be degraded by deleterious properties of the acoustic environment, such as multipath distortion (reverberation) and ambient noise. In a teleconference, a microphone is able to pick up sounds of a talker seated close to the microphone better than one seated far away. Ideally, the teleconference should feel as natural as face-to-face conversation. This suggests the need for a hands-free sound capturing system that has neither a tether nor the encumbrance of hand-held or body-worn sound equipment. Acoustic noise and multipath distortion make hands-free sound capture particularly difficult to achieve. The ideal is to approach sound pickup comparable to that from a close-talking microphone. The microphone array is an attractive approach.

An array microphone system is constructed of a number of microphones distributed in space. The output of each individual microphone is processed and all outputs are summed. In a reverberant environment, the microphone array improves the quality of sound capture.

Today, advanced technology in electrets provides low-cost, high-performance transducers. In addition, the increased computational power and decreased cost of digital signal processors (DSPs) make computationally demanding systems implementable. By utilizing digital signal processing techniques, it is practical to design large scale microphone array systems for high quality sound capture for group conferences in large enclosures.

II. Delay-and-sum beamformer

The delay-and-sum beamformer delays the output of each transducer to cophase the sound arriving from

* This research is supported by NSF contracts MIP-9121541 and MIP-9314625

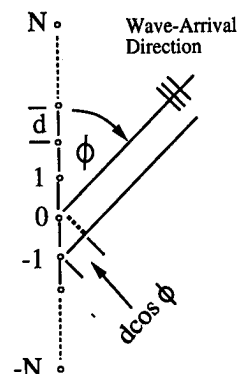


Figure 1: One dimensional microphone array of $(2N+1)$ elements.

a given direction. This technique has proved very effective for hands-free sound capture in moderately-reverberant auditoria and teleconference rooms [1, 3, 4]. Arrays for single beamforming may be one-, two- or three-dimensional in architecture depending upon the characteristics of the desired spatial selectivity. But, single beamformers are adversely affected by severe multipath distortion, and function best if the enclosure has at least a modest amount of sound treatment.

Fig. (1) depicts a line array of $(2N+1)$ omnidirectional microphones spaced equally by distance d . All microphones are identical with the same sensitivity. A typical omni-directional microphone is sensitive to pressure fluctuations of an acoustic wave with a flat frequency response over the audio frequency range for all incident angles of the arriving signal. For a plane wave from the direction of angle ϕ , the time-domain impulse response of a uniformly weighted line array is [3]

$$h(t) = \sum_{n=-N}^N \delta(t + nT) \quad (1)$$

where t is time, δ is the Dirac delta function, and T is the time difference of transit delay between adjacent microphones. The frequency response of Eq. (1) is the transform

$$H(j\omega) = \sum_{n=-N}^N e^{j\omega nT} = \frac{\sin[(2N+1)(\omega T/2)]}{\sin(\omega T/2)} \quad (2)$$

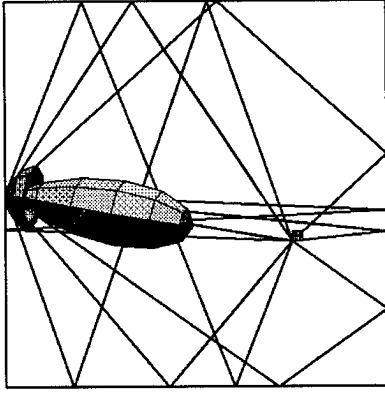


Figure 2: Simulation of a single beam formed by a 2-dimensional rectangular array steered to a source in a hard-walled room.

where ω is the radian frequency. The line array can be steered to angle ϕ_s if the output of the n^{th} microphone is delayed by $nd \cos(\phi_s)/c$, where c is speed of sound. The time difference between adjacent microphones is $T = (\cos(\phi) - \cos(\phi_s))d/c$. Therefore, the spatial response for a $(2N+1)$ element line array steered to angle ϕ_s is

$$H(\phi, \omega) = \frac{\sin[(2N+1)(d\omega[\cos(\phi) - \cos(\phi_s)]/(2c))]}{\sin[d\omega[\cos(\phi) - \cos(\phi_s)]/(2c)]} \quad (3)$$

The delay-and-sum system can direct a beam of sensitivity along the direction of the sound source, and can attenuate sound arriving from other directions. However, in the multipath environment, the beam will also pick up all reflected signals (images) along the beam direction. Fig. (2) shows a simulation of a two-dimensional rectangular array, which is single beamformed to a source in a hard-wall room. Rays up to second order images are plotted. From this figure, one can see that some images are along the "bore" of the beam, leading to degradation of the quality of sound pickup.

The beamwidth of the array spatial response (Eq. (3), Fig. (2)) is a function of frequency. To provide constant beam-width over a wide frequency range, harmonically nested sub-bands of sensors are used [4]. Research continues on constant beamwidth for delay-and-sum beamformers [2, 9].

III. Matched-Filter Arrays

Matched-filter techniques can be applied to microphone arrays to improve noise rejection and to achieve spatial selectivity in three dimensions [5, 6]. A matched-filter is a causal approximation to the time reverse of the impulse response of the system to be matched. In the array, a matched-filter is dedicated to each microphone. The array output is the summation of outputs from all matched-filters. Because the time-inverse impulse response, $h(-t)$, is typically non-causal, truncation and fixed delays are required to realize a causal filter which

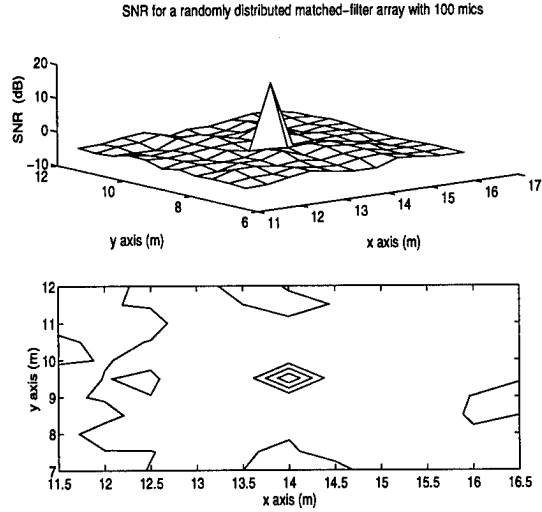


Figure 3: SNR of a 100 randomly-distributed MFA for sources located at various positions on the X-Y plane and passing through the focal point.

approximates the desired response.

The impulse response from the desired focal point to each receiver in the array is required to implement the Matched-Filter Array (MFA). This response can either be calculated from the room geometry or measured in actual rooms. For a source located at the focal point emitting a signal of $s(t)$, the temporal output of the MFA is

$$O(t) = \sum_{n=1}^N s(t) * h_{nf}(t) * h_{nf}(-t) = s(t) * \sum_{n=1}^N h_{nf}(t) * h_{nf}(-t) \quad (4)$$

where $h_{nf}(t)$ is the impulse response from the focal point to the n th sensor, N is the total number of sensors, and $*$ denotes convolution. When the source is off the focal position the temporal output of the array is

$$O(t) = s(t) * \sum_{n=1}^N h_{ns}(t) * h_{nf}(-t) \quad (5)$$

where $h_{ns}(t)$ is the impulse response from the source to the n th sensor. One can immediately notice that the size of the focal volume for the retrieval of low distortion signals is dependent on the spatial correlation of the impulse responses $h_{nf}(t)$ and $h_{ns}(t)$.

The configuration of the matched-filter array is of importance. A newly invented randomly distributed array with 100 sensors outperforms a 31×31 uniformly spaced 2-D array. The spatial volume selectivity of the MFA can be demonstrated using a ratio of undistorted signal power to reverberant (interfering) noise power (SNR). Fig. (3) shows the SNR for a 100 element randomly distributed MFA for various source locations on the X-Y plane. The SNR is displayed in decibels. The center of

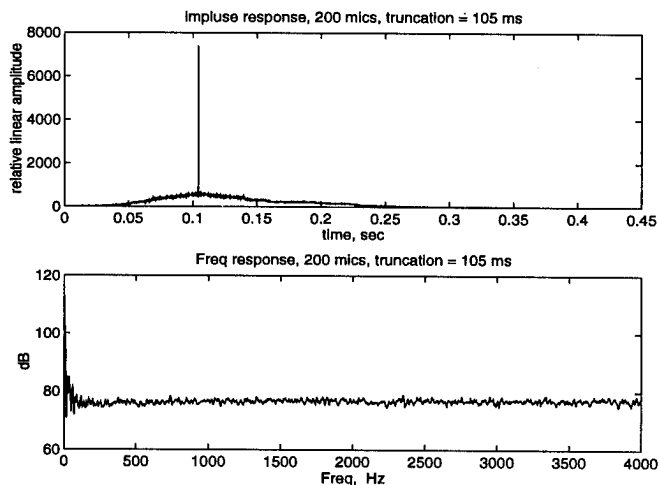


Figure 4: Impulse response of a two 100 randomly-distributed MFA with 105 ms truncation.

the array is located at (10,0,3) m in a 20x16x5 m room. The wall reflection coefficient is 0.9. The microphone spacing is 8 cm and the focal point of the MFA is fixed at (14,9,1.7)m. The source locations are sampled by an 11x11 rectangular grid, using the focal point as the center of the grid. The grid size is 0.5 m. The sampling rate is 8 kHz and up to fifth order images are included in the simulation. The lower graph in Fig. (3) is a contour plot of the SNR which presents equal SNR's. The peak is clearly located at the focal point. The SNR values drop dramatically even if the source is 50 cm away from the focus. This figure shows the acuteness of the spatial volume of the MFA which implies that those sources which are only 50 cm away or more from the focal point will be rejected by the array. Signal processing techniques permit control of the size of the focal volume.

Truncation of matched-filter for the MFA is usually required because of the following reasons. If the full length impulse response is employed,

- (1) the system delay is at least equal to reverberation time which is usually not tolerable.
- (2) large amounts of computation are required for convolution.
- (3) the sound quality is diminished by the long "tails" of the impulse response.

Fig. (4) shows the simulation results of the truncated MFA. The matched-filter is truncated at 105 ms. Up to fifth order images are included. Two 100 randomly-distributed arrays are mounted on two orthogonal walls. In time domain impulse responses, the magnitude of the major impulse is slightly smaller than the untruncated MFA and the tails after the major impulse are similar. However, the tails before the major impulse are much shorter. Therefore, the echoes before the desired signals are significantly reduced. Because the backward masking is always greater than forward masking, the truncated system provides a much better sound quality. In addition, the computation is reduced dramatically and

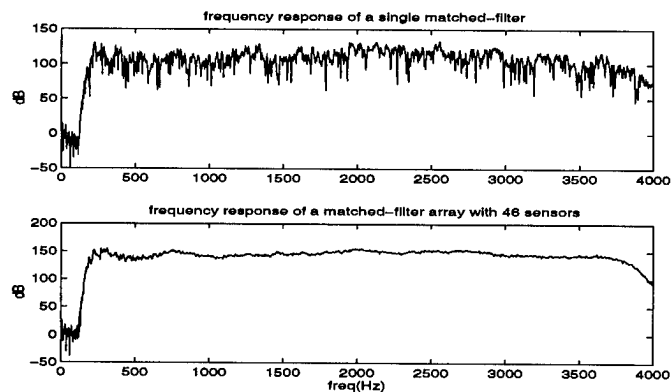


Figure 5: Frequency response of a single matched-filter and a MFA with 46 sensors in a real room.

the delay of the system is only 105ms. Significant improvement of sound capture quality is shown using real room data.

An experimental array with 46 channels was constructed in a real room. The data was collected in a regular hard-walled laboratory with dimensions 6x6x3m. The reverberation time is approximately 0.5 sec. The impulse response from the source to the microphone is measured using Maximum-Length Pseudo Random sequences. During the data collection, several computers generating fan noise were inside the room. Therefore, a high-pass filter with cut off frequency at 200 Hz is employed. Fig. (5) shows the frequency responses of a single matched-filter and of the composite of 46 matched-filters. The impulse response of 46 matched-filters is almost flat, explaining the reason for high quality audio output from the MFA in a multipath environment. The small amplitude in the low frequency range (0 Hz to 200 Hz) is due to the high-pass filtering. The amplitude drops around 4kHz is due to anti-aliasing filter of the D/A conversion.

Research continues to reduce the number of microphones by optimum array configurations to relieve the computational burden and to make hardware implementation more practical.

IV. Hands-free speaker identification

In this section, hands-free speaker identification (speaker ID) is presented. The reasons for pursuing this study are as follows. First, both spatial selectivity and speaker selectivity are often required in a teleconferencing environment. Speaker selectivity enables the array to capture the designated speaker in the enclosure. The speaker identification system aids this process. Also, in multi-point video conferencing, hands-free speaker ID assists participants in identifying remote talkers. This talker identification and localization contribute to realism.

Secondly, the error rate measurement for speaker ID can be used as an alternate index to demonstrate the performance of the array in comparison to a single microphone. The performance of the array is tested through

speaker recognition as opposed to speech recognition since a speaker recognition system is simpler and is less likely to be influenced by the details of the "back end", such as speaker dependency and the language model. Further, the text independent speaker identification relies exclusively on the acoustic information carried in individual frames of the time waveform. The result is more useful in evaluating speech enhancement of the microphone array [7]. Additionally, speaker ID permits security control for data access which is often desired in a multipoint conference.

Two parts are included in the design of the speaker ID system. For experimentation, the commonly used LPC derived cepstrum is used to provide measured features and a Vector Quantizer (VQ) with one codebook for each speaker is used as the classifier. The New England subset of the TIMIT database is used as the speech database. This subset is comprised of 24 males and 14 females. For each of the 38 speakers, the first five sentences are concatenated and used as the training data, and another five sentences are used as the testing data. The total number of trials is 190 (5×38). The TIMIT data, originally bandlimited to 8 kHz and sampled at 16 kHz, are low-pass filtered to 4 kHz and down sampled to 8 kHz. The hands-free speaker identification system is evaluated using speech signals impaired both by room reverberation and interfering noise. The degraded speech data is generated by computer simulation and the previously discussed MFA is used as a front-end sound capture device.

The dimensions of the room used in the simulation are $20 \times 16 \times 5$ m. The acoustic absorption coefficient for all of the walls is set to 0.1, representing a highly reverberant enclosure. Again, images up to the fifth order are included to generate the reverberant speech. The reverberation time of the enclosure is approximately 1.6 seconds. The speech input for the room simulation is a signal source placed at coordinates (14,9.5,1.7) m. The system performance is evaluated under various intensities of interfering noise power. The noise is generated by a Gaussian random number generator and is located at coordinates (3,0.5,0,1.0) m.

Fig. (6) shows the scores for correct identification from a single microphone and from two 31x31 MFA's placed on orthogonal walls of the room. Sensors of the arrays are uniformly spaced at 4 cm. The system is evaluated under matched condition where the acoustic conditions for training and testing section are identical. Four different values of interfering noise SNR'S are used, ranging from 20 dB to 0 dB. Fig. (6) shows that the correct identification score of the single microphone system decreases significantly as SNR decreases, while the performance of the MFA remains nearly unchanged, showing that the MFA can be used as an effective front-end device for hands-free speaker ID systems.

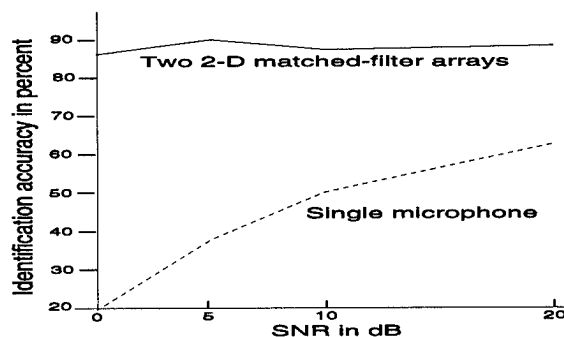


Figure 6: Speaker identification under a matched training and testing condition. An interfering noise is presented with varying SNR.

V. Conclusion

The matched-filter microphone array is able to provide high-quality hands-free sound capture in reverberant, distance talking environments. Conference participants are provided an environment approaching the naturalness of face-to-face conversation without tether or encumbrance by hand-held or body-worn microphones. Additionally, MFA's can be used as a front-end device for current speech technologies to provide hands-free operation and more natural human-machine-interfaces.

REFERENCES

- [1] M. S. Brandstein, J. E. Adcock, and H. F. Silverman, "A practical time-delay estimator for localizing speech sources with a microphone array", *Computer Speech and Language*, 1995, Vol. 9, pp. 153-169.
- [2] M. M. Goodwin and G. W. Elko, "Constant beamwidth beamforming" *Proceedings of IEEE ICASSP*, pages 169-172, April 1993.
- [3] J. L. Flanagan, J.D. Johnston, R. Zahn, and G.W. Elko, "Beamwidth and usable bandwidth of delay-steered microphone arrays", *AT&T Technical Journal*, 64:983-995, April 1985.
- [4] J. L. Flanagan, D. A. Berkley, G. W. Elko, and M. M. Sondhi, "Autodirective microphone systems", *Acustica*, 73:58-71, 1991.
- [5] J. L. Flanagan, A. C. Surendran and E. E. Jan, "Spatially selective sound capture for speech and audio processing" *Speech Communication* 13, 1993, pp. 207-222 .
- [6] E. E. Jan, P. Svaizer and J. L. Flanagan, "Matched-filter processing of microphone array for spatial volume selectivity" *Proc. IEEE ISCAS*, Seattle, 1995. pp. 1460-1463
- [7] Q. Lin, E. E. Jan, and J. L. Flanagan, "Microphone-array and speaker identification.", *IEEE Trans. on Speech and Audio Processing*, 2(4):622-629, Oct. 1994.
- [8] F. J. MacWilliams and N. J. A. Sloane, "Pseudo-random sequences and arrays", *Proceedings of IEEE*, volume 68, pages 593-619, 1980.
- [9] C. Sydow, "Broadband beamforming for a microphone array", *J. Acoust. Soc. Am.*, 96(2):845-849, Aug. 1994.

VOCAL-TRACT ACOUSTICS AND SPEECH SYNTHESIS

Shinji MAEDA

Ecole Nationale Supérieure de Télécommunication, Département SIGNAL
and Centre National de la Recherche Scientifique, URA 820
46, rue Barrault, 75634 Paris, France

ABSTRACT

Basic researches in speech communications have significantly progressed in the past four decades. Paradoxically, the most of currently developing text-to-speech systems is based on a "cut-and-paste" waveform concatenation method. Its main advantage seems to come from the fact that detail knowledge about speech is not necessary. The "dumb" but efficient engineering approach is actually taking over a more scientifically sound rule-based synthesis in the development and application of a high quality text-to-speech system. We overview these two different approaches and then try to demonstrate the feasibility of a vocal-tract synthesis method which is nothing but a retake of an old speech synthesis method called "vocal-tract analog". Some examples of vocal-tract synthesis of V_1CV_2 (vowel-consonant-vowel) utterances using an extremely simple phoneme concatenation by interpolation will be demonstrated.

1. INTRODUCTION: TEXT-TO-SPEECH SYSTEM

Since the number of different sentences a talker produces is practically infinite, any text-to-speech conversion system must produce speech concatenating a finite number of some segmental units. Sounds of world languages can be transcribed by only about 100 phonemes and 30 diacritics. English sounds can be transcribed by about 40 phonemes. The phoneme, therefore, is a phonetically well motivated unit. However, all efforts to directly concatenate phoneme-size segments of speech have badly failed. This failure was explained by the fact that the acoustic manifestation of phonemes highly depends on the segmental context, i.e., the well-known coarticulatory effects. The high context-dependent variability of phonemes motivated two different approaches for text-to-speech systems, (1) rule-based systems in which the coarticulatory effects are handled by a set of heuristic rules and (2) concatenation systems using a unit larger than the phoneme so that the units are concatenated at point where the coarticulatory effects are relatively small, for example at the middle of a vowel. We shall argue, in contrary to the "common" sense, that a straight forward phoneme concatenation might be possible if concatenations are done at the level of the vocal tract, instead of at the acoustic level.

The concatenation of segments is only one of components in text-to-speech systems. A correct assignment of prosodic patterns, such as voice fundamental frequency (F_0), segmental duration and pauses, is as important as segment concatenation to build a high quality system. Moreover, the phoneme is a

phonetically well motivated unit, yet describing sentences by phonemes is hardly practical. Systems, then, need a grapheme-to-phoneme converter in real applications. In this paper however, we describe only issues in segment concatenation, because it characterizes best the difference in the state of the art speech synthesis systems. A more general, comprehensive, and historical review on text-to-speech systems is given by Dennis Klatt [1].

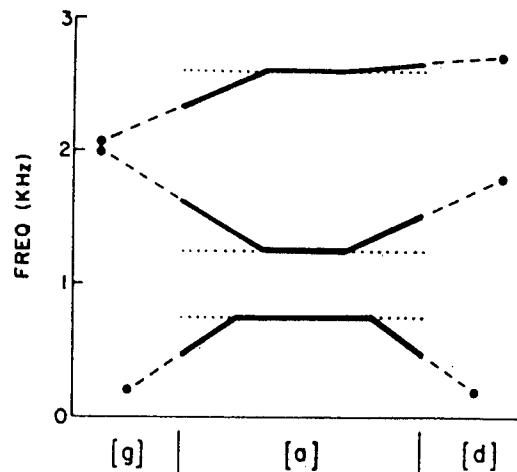


Figure 1. Specification of formant transitions by targets and rules formulated by Holmes [2] (after [1]).

2. RULE-BASED FORMANT SYNTHESIS

In a rule-based system, formant transitions observed in natural speech are simplified and stylized and then specified by heuristic rules. Let us describe how the formant transitions of "God", as an example, are determined by rules due to Holmes *et al.* [2] (described in [1]). Probably the most perceptually important formant transitions occur just after the vowel onset following a stop consonant and just before the offset preceding a stop. These transitions are important because they are one of cues signalling place of articulation and thus the identity of the consonants. First, the target values are read from a table: The target values of the first three formants of /a/ are shown in horizontal dotted lines in Figure 1. The targets for the stops /g/ and /d/ are indicated by the dots with dashed lines, which are called the "loci". Second, using these targets in combination of rules, the formant transitions indicated by the thick lines are determined. For example, the value of F_2 onset frequency is determined by,

$$F2_{\text{onset}} = k(F2_{\text{target}} - F2_{\text{locus}}) + F2_{\text{locus}}$$

which is a locus equation. In the case of Holmes' synthesis, a constant $k = 0.5$ was used. The value of k can be optimized to fit better with observed data. The specification of the transitions by loci is called locus theory [3]. This theory states that loci (the dots) are the points where the vowel formants emerge and converge, if the voicing were extended as indicated by the dashed lines, and they have fixed values for a given stop independently of the vowel context. However, a significant improvement in the intelligibility of stops is gained by the context dependent loci. Klatt [4] proposed the locus values varying depending on three vowel categories, front vowels, rounded vowels, and else.

Although it is possible to achieve a highly intelligible speech by concatenating phonemes with this kind of basic rules, a number of additional rules to handle phonetic details such as vowel reduction, vowel nasalization due to the coarticulatory effect from the adjacent nasal consonant, and so on, and detailed improvements in the excitation sources [5] are necessary to obtain human like speech. The formulation of concatenation rules requires knowledge and experience in acoustics and perception of speech. Often an improvement is gained after many tedious try-and-error experimentation. In short, concatenation of phonemes in formant synthesis is difficult to justify, unless there is another motivation or objective, beside the construction of a high quality system. The motivation was often to gain deeper understanding about which acoustic cues are important to distinguish a phoneme from another in speech. This is probably the main reason why rule-based phoneme concatenation systems using a formant synthesizer have been and are developed at highly regarded academic institutes, such as Haskins Laboratories in the earlier time, the MIT speech group, and speech communication department at Royal Institute of Technology (Stockholm), to mention a few.

3. WAVEFORM CONCATENATION: PSOLA

An engineering oriented method is to concatenate units larger than the size of phonemes, such as diphones to avoid the problem of the context variability altogether. The basic idea is that the transition part is extracted from speech continuum by cutting at the stable parts, for example at the middle of a vowel and stored in the inventory. The concatenation, therefore, can be done at the relatively stable edge of the transition. The smallest such unit is the diphone (or dyad), which is a segment corresponding to the middle part of a phoneme to that of the following phoneme. For example, "Paris" is synthesized by concatenating six diphones as $\langle \#p \rangle \langle pa \rangle \langle ar \rangle \langle ri \rangle \langle is \rangle \langle s\# \rangle$, where $\#$ denotes silence occurring at word boundaries. In certain cases, it is difficult to find a stable portion in a phoneme especially in a consonant, like $/r/$. Then we may

employ even longer unit and concatenation takes place only at the stable part of vowels: such a unit is called the "syllable dyad" or "triphone". Then "Paris" can be obtained by concatenating three triphones, $\langle \#pa \rangle \langle ari \rangle \langle is\# \rangle$. Increasing the size of concatenation segments might improve the quality of synthetic speech, the number of necessary segments would increase dramatically however. The number of phonemes, of diphones, and of triphones in English is, respectively, about 40, 1600, and 64000. A good compromise calls for mix units having different length. Using a relatively large speech database, necessary segments with different length are automatically extracted with a criterion for goodness of concatenation [6 and 7], thus keeping the number of segments manageable, say, in the order of 1000.

Earlier attempts in this kind of cut-and-paste synthesis did not always give satisfactory results however. A possible reason was that the parametric representation of speech segments did not have sufficient quality. The LPC encoded speech, for example, were stored in the inventory. For the prosodic control, a simplified excitation signal, consisting of pulse train for voiced sounds and white noise for voiceless consonants were modified to control prosody, thus degrading the quality. It is well known that LPC encoded speech can have a high quality only when the LPC filter is excited with the residual signal. An improvement was reported by using the multi-pulse LPC coding [7].

If one could modify pitch and duration of speech signals by manipulating the waveform, then extracted speech chunks are directly used as concatenable segments. If the modifications are perfect, we should be able to obtain concatenated speech whose quality is as high as the original human speech, at least, for the segmental characteristics.

One of such prosodic modification techniques is a non-parametric Pitch-Synchronous Overlap-Add (PSOLA). The development of PSOLA is traced back to the phase vocoder as a short-time Fourier analysis/synthesis scheme, which was to uniformly modify time-scale (speaking faster or slower with a constant rate) [8] or pitch-scale (speaking with a higher pitch or lower pitch) [9]. PSOLA is intended for non-uniform time-scaling (duration) and pitch-scaling. The key to the method is to use detected voice excitation points as analysis time instants, thus it can be used for prosodic control [10]. The method requires the detection of "instants" of voice excitation points. This is not really a handicap for a text-to-speech application, because pitch is detected and, if necessary, corrected during the construction of the waveform segment inventory. In synthesis, the synthesis time-instants are determined such that they exhibit the desired F_0 and duration patterns.

How PSOLA modifies pitch is illustrated in Figure 2. A short time window is applied to the original speech waveform at every analysis time-instants (pitch periods). Then synthesis

is done by simply placing these windowed waveforms (let us call it "wavelet") at desired synthesis time-instants as shown in Figure 2. Then, the wavelets are added together to obtain the pitch modified signal. The modification of duration is done by duplicating one or more wavelets to increase duration or by eliminating (discarding) one or more wavelets to shorten the duration. It may be noticed that this method operates strictly in the time domain and thus called TD-PSOLA. Why such a simple method works and how to determine the synthesis time-instants to derive desired prosodic patterns are explained in [10]. The pitch modification range of TD-PSOLA is of from 0.5 to 2, which is largely sufficient for the text-to-speech purpose, since the normal pitch range of a speaker is less than one octave.

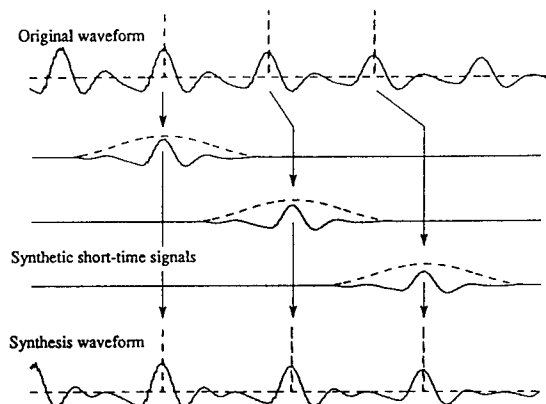


Figure 2. Pitch modification with TD-PSOLA (after [10]).

PSOLA technique significantly improved the quality of text-to-speech system. This is surprising from the scientific viewpoint, since the concatenation of segments from different utterance would destroy a physical coherence the stream of speech signal at every concatenation points. The quality in general is comparable to commercially available top-of-line rule-based systems. However, Klatt [1] stated "... the two types of systems seem to have a different set of perceived deficiencies in naturalness", which we think is still valid. Perhaps, a disadvantage of waveform concatenation approach is lack of flexibility, in contrary to the rule-based system. The waveform segment inventory is build from speech of a particular speaker. If we want a different voice, we have to build a new waveform inventory from a new speaker. Although some attempts to overcome this problem were carried out, it seems so far that an effective method is yet to be formulated however (e.g. [11]).

4. VOCAL-TRACT SYNTHESIS BY PHONEME CONCATENATION

Speech sounds are produced either by the vibration of the vocal folds for voiced source or by the turbulence of airflow at the downstream of the constriction for noise source. These sound

sources undergo spectral modification by the resonance characteristics of the vocal tract. Since, the human vocal-tract is a narrow tube, the major mode of resonance occurs along its length from the glottis to the lips (and/or to the nostrils in the case of nasal sounds). The generation and propagation inside the tract, therefore, can be simulated by an acoustic transmission line [12, 13, 14]. Values of the acoustic elements in the transmission line is calculated from the area function that describes the variation of cross-sectional areas along the length of the vocal tract. The simulator can be used for speech synthesis, although its computational load is much higher than acoustic synthesizers such as a formant synthesizer. This kind of synthesizers was called "vocal-tract analog", whereas the formant synthesizer "terminal analog" [12], because it specifies the input-output (source-radiated sound) relations which is actually the transfer function.

In a study of the acoustics of Arabic fricatives [15], the vocal-tract synthesizer [16] was used. In order to judge the perceptual adequacy of synthesized fricatives, it is necessary to set them in vowel contexts. The most technically simple way is to concatenate vowel-consonant-vowel (V_1CV_2) by target interpolation without pay any attention to the coarticulation phenomenon.

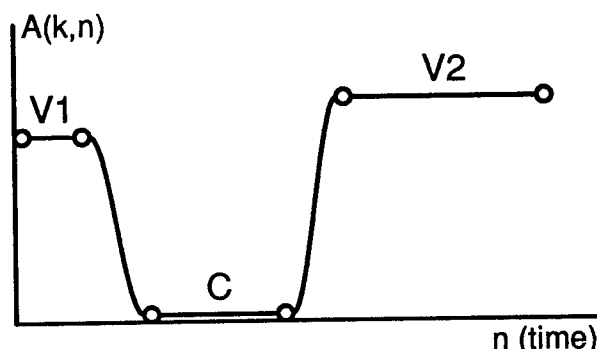


Figure 3. Interpolation of the k -th area of a vocal-tract area function in V_1CV_2 . The circles indicate targets.

In our synthesis, each phoneme is specified by a fixed area function as a target. The area function is specified by a fixed number of sections in which the k -th section is defined by the cross-sectional area, $A(k, n)$, and the length, $x(k, n)$. The index n denotes a discrete time. Obviously, a transition period from one phoneme to another is needed so that the area function varies smoothly between phonemes. The interpolation of A and x is done section-by-section independently. The interpolation of $A(k, n)$ is schematically illustrated in Figure 3. The stationary part in each phoneme is specified by the same target value at the onset and offset. The area (and length) between the offset of a phoneme and the onset of the following phoneme is interpolated by a cosine function. Since the k -th section in

this example corresponds to the constriction section during the fricative consonant /s/, the area becomes close to zero (actually 0.2 cm²). This is all we need to concatenate a V₁CV₂ sequence.

It may be interjected here that the target area function for /s/ is a uniform tube (corresponding to a neutral vowel) having a constriction with one section long at an appropriate place for the consonant. More importantly perhaps, the advantage of concatenation in the area-function domain is that both targets for consonants and those for vowels are specified by the area functions having only different values, thus the interpolation can be explicitly defined. In the acoustic domain however, oral vowels are characterized by only poles of the transfer function, whereas consonants requires poles and zeros [12, 14]. The interpolation in the acoustic domain, thus, would become complicated, if one wishes to interpolate the transition from a consonant to a vowel accurately.

The interpolated area function is fed into the vocal-tract synthesizer. The glottal area variation, parameterized glottal pulse shape representing the quasi-periodic vocal-fold oscillation for voicing and a slow opening/closing of the glottis during consonant to supply a sufficient airflow, is also calculated by the target interpolation scheme, and then fed into the synthesizer. The friction noise is automatically generated in the synthesizer. Pink noise, actually a sequence of low-pass filtered random numbers, is injected at one section downstream from the constriction section. The amplitude of the noise is modulated by a function of the cross sectional area of the constriction and the simulated airflow using either the square law [14] or cubic law [17].

Using the concatenation scheme described, various fricatives, such as /f, s, ʃ, and x/ and unvoiced stops, such as /p, t, and k/ with the different vowel contexts were synthesized. We did not perform any formal perceptual evaluation, but in casual listening, they sounded surprisingly natural and their intelligibility seems to be quite high. It is somewhat puzzling that the area-function interpolation in the earlier attempt by Kelly and Lochbaum [18] (described in [1]) resulted in a poor speech quality, which could not compete with a formant rule-based system in the same period. We suspect that the quality we obtained is primarily due to our vocal-tract synthesizer that simulates the vocal-tract acoustics more accurately than the Kelly-Lochbaum model.

5. CONCLUDING REMARKS

Although our experiment is preliminary concerning only isolated syllables with a limited number of consonants, it is tempted to state that the straight forward concatenation of phonemes might be adequate to obtain a high quality speech. If this is the case, it may possible to construct a text-to-speech synthesizer with some flexibility. For example, it is a simple

matter to convert a male speech to a female speech, and vice versa, with the vocal-tract synthesis.

REFERENCES

- [1] Klatt, D.H., "Review of text-to-speech conversion for English," *J. Acoust. Soc. Am.*, vol. 82(3), pp. 737-793, 1987.
- [2] Holmes, J.N., Mattingly, I.G., and Shearme, J.N., "Speech synthesis by rule," *Language and Speech*, vol. 7, pp. 127-143, 1964.
- [3] Dellatre, P., Liberman, A.M., and Cooper, F.S., "Acoustic loci and transition cues for consonants," *J. Acoust. Soc. Am.*, vol. 27, pp. 769-774, 1955.
- [4] Klatt, D.H., "Synthesis by rule of consonant-vowel syllables," *Speech Communication Group Working Papers 3*, MIT, Cambridge, MA, pp. 93-104, 1979.
- [5] Klatt, D.H. and Klatt, L.C., "Analysis, synthesis, and perception of voice quality variations among female and male talkers," *J. Acoust. Soc. Am.*, vol. 87, pp. 820-857, 1990.
- [6] Iwahashi, N., Kaiki, N., and Sagisaka, Y., "Concatenative speech synthesis by minimum distortion criteria," *Proc. of ICASSP*, vol. II, pp. 65-68, 1992.
- [7] Olive, J.P. and Liberman, M.Y., "Text-to-speech: An overview," *J. Acoust. Soc. Am.*, Suppl. 1, vol. 78, S6, 1985.
- [8] Portnoff, M., "Time-scale modifications of speech based on short-time Fourier analysis," *IEEE Trans. Acoust. Speech Signal Process.*, ASSP-29, 374-390, 1981.
- [9] Seneff, S., "System to independently modify excitation and/or spectrum of speech waveform without explicit pitch extraction," *IEEE Trans. Acoust. Speech Signal Process.*, ASSP-24, 358-365, 1982.
- [10] Moulines, E. and Laroche, J., "Non-parametric techniques for pitch-scale and time-scale modification of speech," *Speech Communication*, vol. 16, pp. 175-205, 1995.
- [11] Valbret, H., Moulines, E., and Tubach, J.P., "Voice transformation using PSOLA techniques," *Speech Communication*, vol. 11, pp. 175-187, 1992.
- [12] Fant, G. *Acoustic theory of speech production*, (Mouton, 's-Gravenhage), 1960.
- [13] Stevens, K.N. and House, A.S., "An acoustic theory of vowel production and some of its implications," *J. Speech Hear. Res.*, vol.4, pp. 303-320, 1961.
- [14] Flanagan, J.L., *Speech analysis, synthesis, and perception* (Springer, New York), 1972.
- [15] Yeou, M. and Maeda S., "Pharyngeal and uvular consonants are approximants: An acoustic modeling study," *Int. Congr. Phonetic Sciences*, Stockholm, 1995 (in press).
- [16] Maeda S. "A digital simulation method of the vocal-tract system," *Speech Communication*, vol. 1, pp. 199-229, 1982.
- [17] Stevens, K.N., "Modelling affricate consonants," *Speech Communication*, vol. 13, pp. 33-43, 1993.
- [18] Kelly, J. and Lochbaum, C., "Speech synthesis," *Proc. Fourth Int. Congr. Acoust.* paper G42, 1962.

Development of a Prototype Portable Binaural Digital Hearing Aid

Sigfrid D. Soli

House Ear Institute
Los Angeles, California

ABSTRACT¹

For a hearing aid user to perform binaural directional hearing in noisy environments, it is important to maintain at audible levels the binaural cues (interaural time and level differences) that would be present if the hearing aid were not in place. We have developed a wearable prototype digital hearing aid and personal computer (PC) based methods of digital filter design for evaluation of the effectiveness of this method. The body-worn prototype processor utilizes a Motorola 56000-series DSP chip to implement the filtering and amplification for both ears via cabled ITE ear modules. Up to four different user-selectable algorithms can be programmed in the processor.

Binaural fitting of the processor is accomplished in two steps: Hearing Aid Equalization (HAE) and Hearing Loss Compensation (HLC). HAE is achieved with an FIR filter which equalizes the amplitude and phase insertion effects of the ear modules and maintains the binaural cues with the modules in place. The HAE filter coefficients for each ear are obtained from in situ probe tube measurements of aided and unaided test signals using optimal filter calculations performed by the PC. HLC for each ear is also achieved with an FIR filter and associated gain. HLC filter coefficients are obtained with the PC using a weighted least-squares filter design technique. The target response for each HLC filter is determined from measures of auditory thresholds and soundfield reference signals, and is based on an adaptation of Articulation Theory for hearing aids. The HAE and HLC filters are convolved to produce a single filter. A detailed description of the processor, fitting algorithms, methods and accuracy of fittings, as determined from in situ probe tube measurements, and the hardware and software comprising the binaural hearing aid will be given. Results from field trials with the portable processors will also be reported.

¹Paper will be available at the time of the conference.

TOPOLOGICAL PULSE MODULATION OF FIELD AND NEW MICROWAVE CIRCUITS DESIGN FOR SUPERSPEED OPERATING DEVICES

G. A. Kouzaev and V.I. Gvozdev

Moscow State Institute of Electronics and Mathematics
Department of Laser & Microwave Information Systems
3/12 Bol Vuzovsky Per, Moscow 109028 Russia
Fax 007 095 9162807

ABSTRACT

In this paper a new type of electromagnetic field signals is considered. The signals have discretely modulated field structures (topologies). For their processing new logical passive circuits are proposed and results of numerical modelling are considered.

1. SIGNALS AND SWITCHES

Fundamental characteristics of signal processing devices are defined by physics of nonlinear switching phenomena and integrated circuits (ICs) technologies. Changing the physical effects it is possible to improve dissipative and time characteristics of digital circuits.

One of the approaches of electromagnetic field signal processing consists in writing digital information into a spatial structure (topology) of fields. The characteristic was named as topological chart of the electromagnetic field and it is an ordered set of separatrices and equilibrium points of field force lines. The topological chart can be changed discretely only. A particular case of the signal is modes of coupled strip transmission lines, which have different spatial structures of the electromagnetic fields [1]. According to the results of topological methods of electromagnetic fields design [2] a spatial switching is realized with passive circuits, which have nonlinear characteristics relative to the input field topologies.

Some experimental and theoretical results have been considered in [1], which touch upon microwave circuits on the base of coupled strip and slot transmission lines. For super high-speed applications rectangular time dependent impulses are preferable. In this area some new results have been obtained with the help of a switch which is shown in Fig. 1.

An input signal is a series of impulses of even

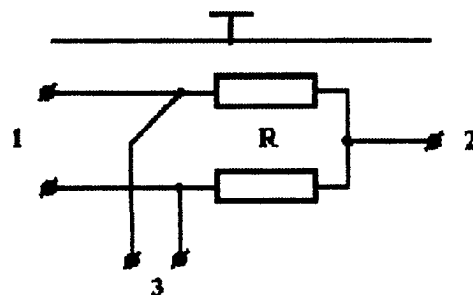


Fig. 1. Spatial switch for topologically modulated field signals.

$\begin{matrix} n \\ L \end{matrix}$	1	2	3
"0"			
"1"			

Fig. 2. Truth-table of the spatial switch.

(logical variable '1') and odd (logical variable '0') modes in coupled strip transmission lines (Fig. 1). The modes have different topologies of electromagnetic fields, equal phase and group velocities. The signals are switched at different outputs 2 and 3, according to truth-table (Fig. 2).

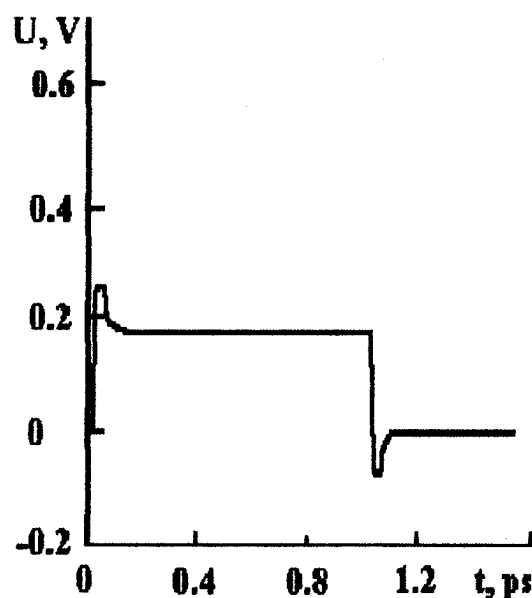


Fig. 3. Output signal on the port 2.

The switch is a device of triple reversible logic. Its switching time depends on linear dimensions and values of parasitic reactivities of the circuits.

2. TRANSIENT ANALYSIS

Simulation of transient processes with the help of equivalent circuits has shown switch delay time $t=0.1-0.3$ ps for linear dimensions of the switch about $4\text{ }\mu\text{m}$ (Fig. 3 and 4), if input signal is a rectangular time dependent impulse of even or odd modes with its duration $\Delta t=1$ ps and its amplitude $U=1$ V. Power losses P are defined by resistors $R=20$ Ohm and the ones are less than 20 mW for input current $I=0.1-1$ mA and do not depend on semiconductor physics. It is possible to reduce P to a minimum, if to drop the resistors. In this case the losses are equal approximately to 0.1 mW for alumina conductors which have a volume $V=100\text{ }\mu\text{m}^3$. The switching effect does not depend on semiconductor physics, due to that it is possible to overcome a part of fundamental limitations, which are typical for transistors.

Experimental studies of the switch have shown the outputs 2 and 3 isolation about 35-40 dB in the area of microwave frequencies. The switch was produced with MIC technology on Al_2O_3 -substrate.

On the base of the switch two types of logical circuits "AND", "OR", "NOT" are proposed. The first is based on interference effect [1, 2, 3], the second is hybrid circuits with semiconductor elements [3].

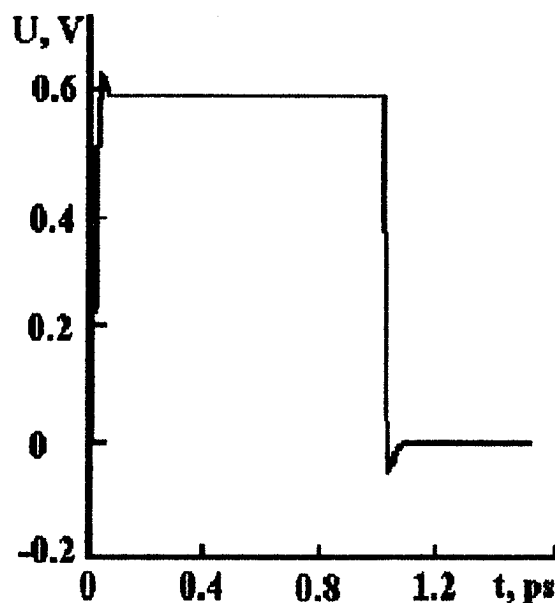


Fig. 4. Output signal on the port 3.

3. CONCLUSIONS

In this paper a new picosecond switch has been considered for electromagnetic signals which field structures are modulated discretely. The spatial switching is realized by a passive circuit. Typical time delay of the switch is equal to 0.1-0.3 ps and power losses are less than 20 mW. A field of applications of the new approach to field information processing is super high-speed circuits.

The work is supported in part by the Russia Foundation of Fundamental Investigations under Grant 94-0204979-a.

4. ACKNOWLEDGMENT

The authors thank I.V. Nazarov for his assistance in simulations of the switches.

REFERENCES

- [1] Kouzaev G.A. and Gvozdev V.I., 1993, "A new technology of signal processing for super high-speed microwave circuits". *Mikroelektronika*, 22, № 1, 37-50 (in Russian).
- [2] Kouzaev G.A. and Nazarov I.V. 1994, "On theory of hybrid logic microwave devices". *Radiotekhnika i elektronika*, 39, 1401-1407 (in Russian).
- [3] Kouzaev G.A. 1995, "Information features of electromagnetic fields superpositions". *Radiotekhnika i elektronika*, 40, 431-440 (in Russian).

LOW-POWER PSA TRANSISTORS FOR MICROWAVE COMMUNICATION SYSTEMS: COMPARISON AMONG BIAS-DEPENDENT MODELS EXTRACTED FROM MEASURED NOISE AND SCATTERING PARAMETERS

A. Caddemi, M. Sannino

Dipartimento di Ingegneria Elettrica - Università di Palermo

Viale delle Scienze - 90128, Palermo - ITALY

ABSTRACT

Due to the increasing interest in extending the frequency limits of silicon devices for telecommunication applications, we have analyzed the performance of different series of advanced polysilicon bipolar transistors.

The devices were grouped according to their emitter finger number and were characterized over the 2-6 GHz frequency range in terms of noise, gain and scattering parameters at different bias conditions.

A bias-dependent model extraction including noise sources has been subsequently performed for each series and a comparative analysis has been carried out. The results of this analysis point out distinguishing features of this advanced bipolar process which allows for realizing highly competitive bipolar devices for use in telecommunication equipment at low microwave frequencies.

1. INTRODUCTION

In portable communication systems operating over the low microwave range, devices and circuits must be designed to meet their best performance at very low current and voltage levels. The industry's trend is for developing advanced silicon bipolar processes to realize lower cost components, size and performance competitive with solution using GaAs. Among the most advanced bipolar processes for the realization of high speed silicon transistors, double-polysilicon self-aligned (PSA) schemes have definitively emerged as the most effective technique.

The adoption of polycrystalline silicon layers upon the base and the emitter single crystal zones allows for a remarkable increase of the common emitter current gain β and a smaller dependence of β itself on temperature than conventional BJT's. In addition, the self-alignment of the

extrinsic base and the emitter results in a substantial reduction of the base resistance and the collector-base capacitance thus allowing for an appreciable improvement in the gain-bandwidth product, maximum oscillation frequency, minimum noise figure, power dissipation and component integration level in VLSI application [1].

To the aim of exploring the features and performance of a commercially competitive PSA bipolar process, the manufacturer (CoRiMMe, an SGS-Thomson Research Center, Catania, Italy) has supplied us with several devices characterized by different emitter configurations. We had previously performed a complete analysis on a preliminary PSA device series from the same manufacturer aimed at the extraction of an accurate circuit model including noise sources [2].

We have recently characterized a total of 29 PSA transistors supporting 5 different chip topologies to gain a better insight on those effects related to emitter geometry which affect device operation. The features of the measured families (named Q_i) are the following:

- Q_2 4 emitters, 5 base contacts, 8 μm emitter length, with 4.6 μm pitch
- Q_3 8 emitters, 9 base contacts, 8 μm emitter length, with 4.6 μm pitch
- Q_4 16 emitters, 17 base contacts, 8 μm emitter length
- Q_6 same as Q_2 , with 3.8 μm pitch
- Q_7 same as Q_3 , with 3.8 μm pitch

The emitter finger pitch may be a critical parameter in improving the RF performance of

This work was supported by Italian Space Agency (ASI), National Research Council (CNR) and Ministry of University, Science and Technology Research (MURST).

BJT's since the transition frequency f_T can be increased by reducing its size. We performed the characterization and the model extraction of the transistor series in terms of noise, gain and scattering parameters over the 2÷6 GHz frequency range at the bias conditions suggested by the manufacturer which consisted of the fixed low voltage of 2.8 V and two I_C current values proportional to the emitter finger number n_e .

As a general result, F_0 takes on very low values as compared to conventional bipolar transistors: less than 1 dB at 2 GHz for Q_3 and around 2 dB up to 5 GHz for all families.

The noise performance at the lowest frequencies improves proportionally to n_e (which is expected since the base resistance decreases with increasing finger number) and deteriorates with increasing bias current. The maximum available gain is less affected by either n_e and the bias current level with typical values in the range of 11 to 14 dB. Also, this bipolar process has exhibited an average f_T around 10 GHz and no performance variations have been noticed between the device series having different emitter ptch.

2. DEVICE CHARACTERIZATION

The PSA devices were encapsulated in a standard 70-mil microstrip package which fits our measuring test fixture (Maury Microwave, mod. MT950) equipped with proper insert calibration elements (planar package-size devices supporting the *short* and *thru* layouts).

In our measurements, we refer to the representation in terms of the noise parameters which appear in the following relationship

$$F(\Gamma_s) = F_0 + 4 r_n \frac{|\Gamma_s - \Gamma_0|^2}{|1 + \Gamma_0|^2 (1 - |\Gamma_s|^2)}$$

where F and Γ_s are the noise figure and the input termination reflection coefficient of the device under test, respectively, and the four noise parameters are F_0 (minimum noise figure), Γ_0 (value of the complex variable Γ_s at which the minimum is located) and r_n (equivalent noise resistance normalized with respect to 50 Ω). A similar relationship holds for the reciprocal of the gain parameters which defines the conditions for the maximum value of the available gain (G_{opt}) vs. Γ_s .

By means of an automatic system whose measuring procedure has been developed in our

Lab, we perform measurements of the noise figure at the system output for either some properly selected values of Γ_s and, at each Γ_s value, for different values of system losses as introduced by a high repeatability step attenuator. From these noise data we derive both the noise and the gain parameter sets of the DUT by an accurate deembedding of the various stage contributions and by applying appropriate data processing techniques. The scattering parameters are then calculated by use of well-known relationships employing the gain parameters and, therefore, are not measured directly by a network analyzer (see [3] and references therein).

The transistor series were tested at the following bias conditions:

- Q_2 @ $V_{CE} = 2.8$ V, $I_C = 2$ and 8 mA;
- Q_3 @ $V_{CE} = 2.8$ V, $I_C = 4$ and 16 mA;
- Q_4 @ $V_{CE} = 2.8$ V, $I_C = 16$ and 64 mA;
- Q_6 same as Q_2 ;
- Q_7 same as Q_3 .

Since all the measured data for each group exhibited reduced spread, a Q_i typical device (bold line in the reported diagrams) to be employed during the modeling step has been determined by simple statistic functions for representing each transistor series. As an example, we report in Fig. 1 the four noise parameters of the Q_3 series at the above given bias conditions.

3. CIRCUIT MODEL EXTRACTION WITH NOISE SOURCES

The transistor chip model is a standard hybrid- π structure where the distributed base resistance and capacitance between intrinsic base and collector region have been introduced for an accurate representation of the transistor performance at microwave frequencies.

By deembedding the effects of the package from the measured parameter values, we obtained scattering and noise parameter sets which refer directly to the chip device performance. The optimization procedure has then been applied to the chip model network to determine the circuit element values as well as the noise sources by minimizing the scattering and the noise parameter error functions. The noise generators are represented by two correlated noise current sources at the input and the output port plus the thermal contribution arising from each of the physical resistors. The noisy model structure is shown in Fig. 2; the relevant element values, including noise generators, are reported in Tab.1. The model effectiveness has been verified by

deriving the element value variations at the different bias conditions for each series. All the model elements exhibit value trends in very good accordance with the physics-based predictions. In addition, numerical evaluation of F_O and r_n by use of well-assessed expressions has matched quite satisfactorily the measured values showing how the noise resistance is heavily affected by n_e as reported in Fig.3 at low current bias values, [4].

4. COMMENTS ON THE DEVICE PERFORMANCE

Some interesting remarks can be made with reference to the measured noise parameters:

- F_O increases and $|\Gamma_O|$ decreases with this four-fold increment of the bias current, whereas $R_n (\Omega) = 50 r_n$ and $|\Gamma_O|$ are affected by I_C to a very reduced extent;
 - F_O , R_n and $|\Gamma_O|$ decrease markedly with increasing n_e ; therefore, the Q_2 series exhibit values of the noise figure F_{50} measured in input matched conditions (i.e., @ $\Gamma_S = 0$) much higher than F_O . The quantity $\Delta F = F_{50} - F_O$ reduces at higher current values;
 - the slope of F_O vs. frequency increases proportionally to n_e . As a result, F_O approaches values around 2 dB for all Q_i families @ 5 GHz (lower bias current);
 - the slope of R_n vs. frequency vanishes with increasing n_e , thus becoming flat for higher n_e . The available gain G_a is less affected by either n_e and the bias current level than the corresponding noise figure F_{50} .
- By summarizing the best results, we measured typical values of F_O even lower than 1 dB and available gain values as high as 14 dB @ 2 GHz.

4. CONCLUSIONS

We here present the results of an extensive characterization activity performed on several PSA bipolar transistors.

The devices were grouped according to their emitter finger number and were tested over the 2-6 GHz frequency range in terms of noise, gain and scattering parameters at different bias conditions. A bias-dependent model extraction including the noise performance has been subsequently accomplished and a comparative analysis among the measured families has been carried out. Outstanding performances in terms of minimum noise figure and available gain have

been brought out for this advanced bipolar process for telecommunication applications up to 4-6 GHz.

REFERENCES

- [1] C.R. Selvakumar, "Theoretical and experimental aspects of polysilicon emitter bipolar transistors", in *Polysilicon Emitter Bipolar Transistors*, edited by A. Kapoor and D. Roulston, IEEE Press, New York, 1989.
- [2] A. Caddemi, M. Sannino, "Small signal and noise model determination for double polysilicon self-aligned bipolar transistor", 1994, *Active and Passive Electronic Components*, Vol. 17, pp. 167-175.
- [3] G. Martines and M. Sannino, "The determination of the noise, gain and scattering parameters of microwave transistors (HEMTs) using only an automatic noise figure test-set", 1994, *IEEE Trans. Microwave Theory Tech.*, Vol. MTT-42, pp. 1105-1113.
- [4] H. Fukui, "The noise performance of microwave transistors", *IEEE Trans. Electron Devices*, Vol. ED-13, pp. 329-341, Mar. 1966.

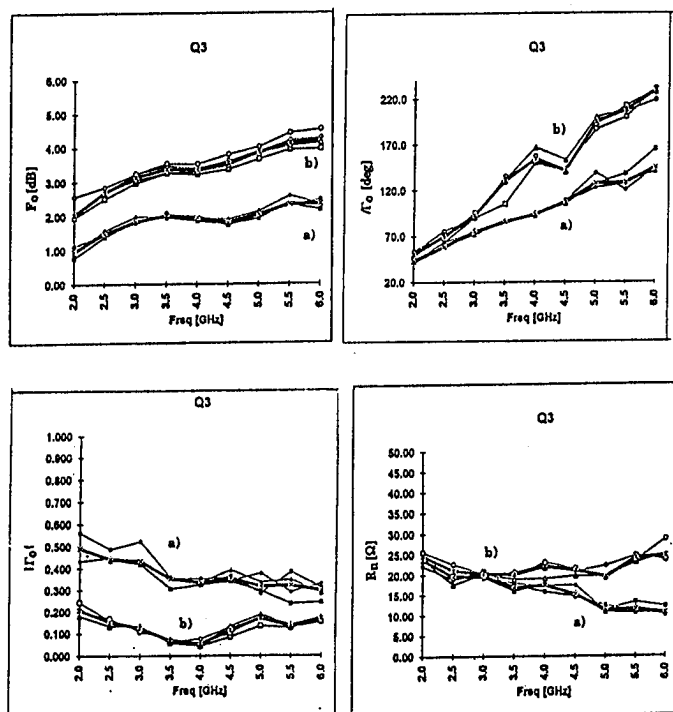


Fig. 1 - Noise parameters F_O , $|\Gamma_O|$, $|\Gamma_O|$ and R_n of the Q_3 series at the bias conditions: a) $V_{CE} = 2.8$ V, $I_C = 4$ mA; b) $V_{CE} = 2.8$ V, $I_C = 16$ mA.

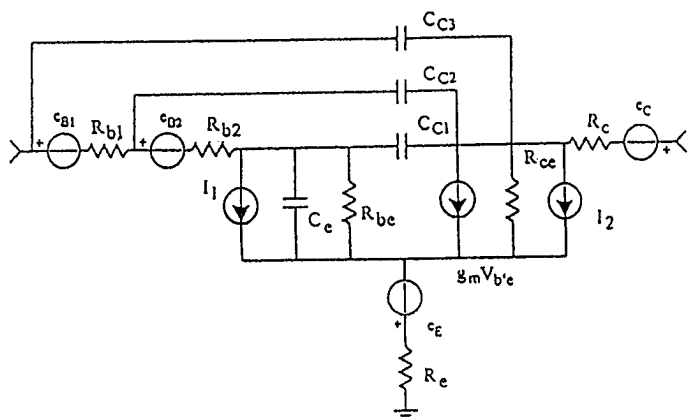


Fig.2 - Circuit model including noise sources.

	Q ₂ A	Q ₂ B	Q ₃ A	Q ₃ B	Q ₄ A	Q ₄ B
R _{b1} (Ω)	6	6	10	9	5	5
R _{b2} (Ω)	35	35	16	15	9	7
R _e (Ω)	3.3	3.3	1.8	1.8	0.5	0.5
R _c (Ω)	6	6	6	6	7	10
R _{ce} (Ω)	10000	10000	10000	10000	10000	10000
R _{be} (Ω)	1000	1000	1000	1000	1000	1000
C _e (μF)	0.8	4.4	1.6	9	5	20
C _{c1} (μF)	0.015	0.015	0.017	0.017	0.02	0.02
C _{c2} (μF)	0.09	0.1	0.12	0.13	0.3	0.35
C _{c3} (μF)	0.09	0.1	0.11	0.125	0.35	0.4
i ₁ ²	10	35	14	45	20	80
(pA ² /Hz)						
i ₂ ²	300	502	450	750	400	4000
(pA ² /Hz)						
Re (i ₁ i ₂ *)	0.8	0.8	0.6	0.6	0.15	0.8
Im (i ₁ i ₂)	0.2	0.26	0.4	0.2	0.85	0.3
T _{Re} (K)	297	297	297	297	1100	1000

Tab. 1 - Model element values.

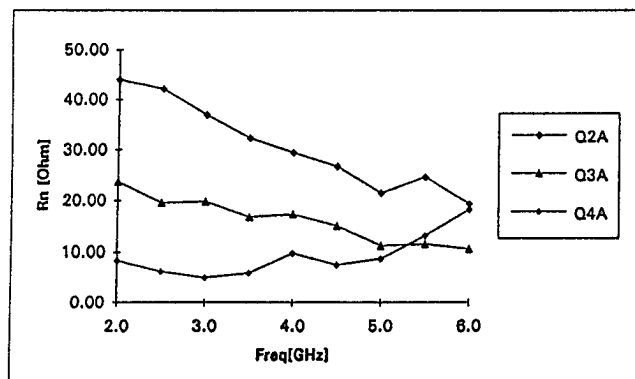


Fig. 3 - Values of R_n vs. frequency for the Q₂, Q₃ and Q₄ series at lower bias current.

RECENT ADVANCES IN TIME-DOMAIN SIMULATION

**B. Houshmand and T. Itoh*

*Jet Propulsion Laboratory
4800 Oak Grove Drive
Pasadena, CA 91109
Tel:(818) 354-5416 Email: bh@athena.jpl.nasa.gov

University of California, Los Angeles
Los Angeles, CA 90095
TEL:(310) 206-4820 Email: itoh@ee.ucla.edu

ABSTRACT

This paper presents the recent developments in the time domain simulation of microwave circuits. This approach is gaining attention mainly due to its ability for modeling realistic microwave structures which can include active and nonlinear devices. In particular, an overview of the Finite-Difference Time-Domain (FDTD) method with its recent additions such as Diakoptics and System Identification, and nonlinear circuit capabilities will be presented.

I. INTRODUCTION

Modeling of microwave structure has undergone a rapid growth in the past decade. The driving force for this growth has been a combination of factors ranging from the increase in the operating frequencies and integrating a complete system on a single module where the proximity coupling becomes important, to the need for reducing the design cycle where a design is expected to operate properly without further modifications after the initial fabrication. The accompanying increase in the available computation power has also provided a synergy for this growth. At this point a wealth of methodologies are available to address various modeling needs for microwave structures. These methodologies can be classified broadly as frequency and time domain methods. While the frequency domain techniques have been under development for the past four decades, the

time domain methods have recently been gaining attention mainly due its ability for modeling realistic microwave structures which can include active and nonlinear devices. This method is currently known as the Finite-Difference Time-Domain (FDTD). References [1] and [2] provide a general comparison of the numerical properties of the FDTD and other popular numerical methods. It is important to note that this algorithm provides both spatial and temporal interaction of the electromagnetic fields with the microwave structures. This information provides insights into microwave circuit operation. This algorithm has been successfully used for characterizing the performance of a broad class of microwave structures such as waveguides, multi-layer structures, discontinuities, transitions, filters, couplers and antennas. This paper provides an overview of this technique, and highlights some of the recent developments.

II. FDTD FORMULATION AND ALGORITHM

The FDTD algorithm is based on the discretization of the Maxwell's equations in time and space. A number of differencing schemes are available for discretization of the Maxwell's equations. A numerically stable method is the central differencing approach. Using a Taylor series expansion of the field values, it can be shown that the introduced errors are of second order with respect to discretization size in time and space. These difference equations are obtained directly from Maxwell's equations. A closer look at

these equations show that the E- and H-fields are updated on a dual grid which are displaced in time and space by half of the discretization length. In addition, the integral form of Faraday's and ampere's laws are satisfied on the E and H field cells, respectively. As a consequence, inhomogeneous media can be included with minor modifications to the updating algorithm.

These equations are suitable for direct implementation on a digital computer. The algorithm updates the field values throughout the discrete space for each time step. As a consequence of this approach, an iterative scheme is implemented which eliminates the need to store large matrices which results in large savings in computation requirements. An additional advantage of this algorithm is its ability to efficiently utilize the parallel computer architecture. This is a consequence of the Huygen's principle which requires the knowledge of field distribution over a surface for updating the fields within the volume enclosed by the surface. As a consequence, the communication among processors are limited to exchanging the surface information, while each processor updates the fields within a volume.

III. INFORMATION GENERATED BY THE FDTD ALGORITHM

This method of solution to the electromagnetic field equations provides both temporal and spatial field values throughout the computation domain. This information can be exploited both for extracting useful information regarding the circuit operation such as the S-parameters and resonance frequencies, and reducing the computation time and memory requirements. The spatial distribution is used for extracting the modes of the structure, and proximity coupling. The temporal variations is used for extracting the frequency response of the structure for a range of frequencies.

Reduction in computation requirements are achieved by invoking a number of the Linear Network concepts to the FDTD algorithm. The memory requirements is reduced by representing portions of the microwave structure by their respective impulse response matrices. The impulse response matrix is in effect the numerical Green's function and is computed in advance using the FDTD algorithm and an impulsive excitation. The details of this implementation is presented in [3]. This approach is particularly useful in optimization process where for portions of the microwave structure remain unchanged through the iterations and can be replaced by their pre-computed impulse response matrices. The reduction in computation time is obtained by applying the System Identification methods to the temporal variation of the field values at the locations of interest. Using this approach, an Auto-Regressive Moving Average (ARMA) model is used to describe the circuit behavior. The parameters of the ARMA model are computed using the FDTD generated field values. The Frequency response of the system is computed directly from the ARMA parameters thus eliminating the need for the Fourier Transformation. It is important to note that the time interval for computation of the ARMA model can be much smaller than the time interval required for the Fourier Transformation due to spectral resolution and truncation effects [4].

IV. APPLICATION TO ACTIVE DEVICES

An important utility of the FDTD algorithm has been its ability to characterize microwave structures which include active and nonlinear devices [5, 6]. Many practical microwave circuits are embedded with components which are both active and nonlinear (e.g., semiconductor devices), and realistic modeling of these circuits requires the inclusion of electromagnetic fields interaction with the passive circuit structure as well as devices. The device behavior is represented by its port

characteristics and is included in the FDTD algorithm via the Ampere's and Faraday's Laws. Figure 1 shows the layout of a typical microwave amplifier. The system under consideration is composed of distributed passive structures such as transmission line, matching stubs and DC biasing circuit, lumped passive devices such as capacitors and resistors, and an active device (GaAs MESFET). The lumped equivalent circuit small signal model of the active device is shown in Figure 2. Figure 3 shows the field distribution a plane under the metalization for a particular time. It is important to note that this methodology is applicable to structures which contain multiple devices as well as multi-layer metalization and dielectric discontinuities. This approach has also been applied to an oscillator circuit where the large signal characteristics of the active device is included. The structure is consist of two coupled patch antenna. Each patch is excited by a Gunn Diode which are coupled strongly through a transmission line. The FDTD simulation of the entire structure produced excellent agreement with the measurements [6].

V. SUMMARY

The time domain simulation of microwave structures using the FDTD has been successful for a wide class of microwave structures. This algorithm provides the spatial and temporal variations of the electromagnetic fields which can be used to gain additional insights into the circuit operations. The method also lends itself to a number of linear system techniques such as Diakoptics and System Identification which results in an efficient use of the computational resources for electromagnetic circuit simulation. This algorithm has also been extended to include active and nonlinear device models which provides the ability to simulate realistic microwave circuits.

- [1] Roberto Sorrentino, "Modeling and Design of Millimeter Passive Circuits: From 2 to 3D," 24th European Microwave Conference, Vol 1, pp. 48-61, 1994.
- [2] Allan Tran, B. Houshmand , and T. Itoh, "Analysis of Electromagnetic Coupling Through A Thick Aperture in Multi-layer Planar Circuits Using the Extended Spectral Domain Approach and Finite Difference Time Domain Method," to be published in IEEE AP-S Trans. special issue.
- [3] B. Houshmand, T.W. Huang, and T. Itoh, "Microwave structure characterization by a combination of FDTD and system identification methods," IEEE Microwave Guided Wave Lett., Vol. 3, No. 8, pp. 262-264, Aug. 1993.
- [4] B. Houshmand, T.W. Huang, and T. Itoh, "Microwave structure characterization by a combination of FDTD and system identification methods," IEEE Microwave Guided Wave Lett., Vol. 3, No. 8, pp. 262-264, Aug. 1993.
- [5] C. N. Kuo, V. A. Thomas, S. T. Chew, B. Houshmand and T. Itoh, "Small signal analysis of active Circuits Using FDTD Algorithm", "IEEE Microwave and Guided Wave Lett., vol. 5, no. 7, pp. 216-218, July 1995.
- [6] B.Toland, J. Lin, B. Houshmand, and T. Itoh, "FDTD analysis of an active antenna," IEEE Microwave and Guided Wave Lett., vol. 3, no. 11, pp. 423-425, Nov. 1993.

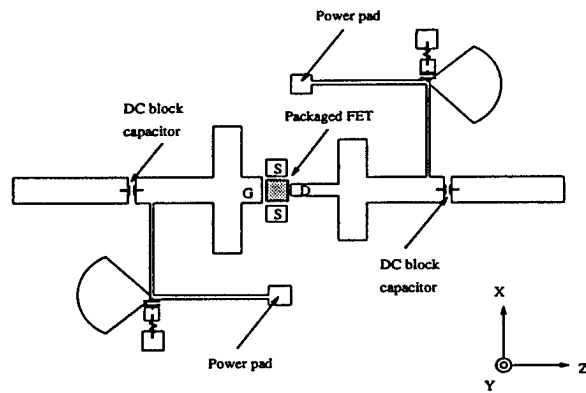


Figure 1: The layout of the microwave amplifier, which is designed at 6 GHz with 9 dB gain.

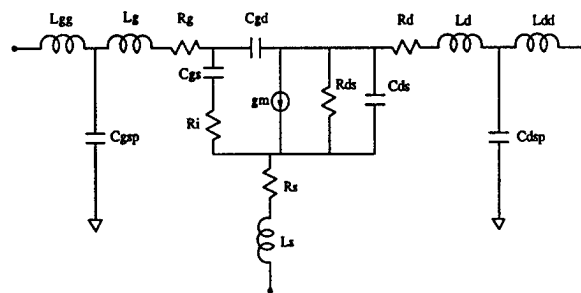


Figure 2: Lumped equivalent circuits of the GaAs MESFET.

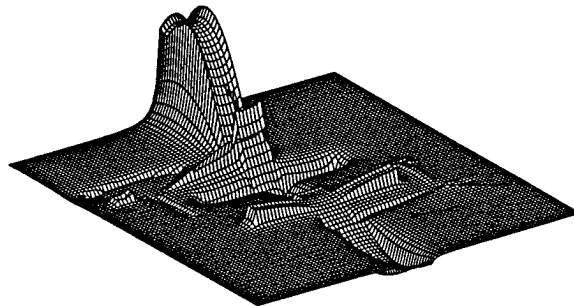


Figure 3: A snapshot of the field distribution of E_y component beneath the air-dielectric interface during the simulation.

SOLUTION OF EM FIELDS BY ASYMPTOTIC WAVEFORM TECHNIQUES

Ming Li, Qi-jun Zhang and Michel Nakhla
Department of Electronics
Carleton University
Ottawa, Canada, K1S 5B6

Abstract

A new numerical solution technique to electromagnetic (EM) field problems is presented in this paper. It is based on Complex-Frequency Hopping (CFH), which is an expanded asymptotic waveform evaluation approach recently proposed in the circuit simulation area with great success in solving large linear lumped and distributed circuits. The Helmholtz equations are formulated into a set of linear ordinary differential equations which are solved by asymptotic waveform evaluation. The technique offers speed or stability advantage over, e.g., the Finite Difference Frequency Domain (FDFD) and the Finite Difference Time Domain (FDTD) approaches for comparable accuracy. An example of waveguide frequency-domain analysis is provided.

1. INTRODUCTION

Modeling and simulation based on EM field formulations are important for accurate analysis and design of today's high-speed and high-frequency circuits and systems. Much research in efficient numerical techniques for EM problems has been conducted in the past [1]. However the task of numerically solving EM field problems is generally computationally intensive. For example, in the FDTD approach, the computation has to be done at a large number of time points to ensure stability [2][3]. In FDFD [4], it is required to solve a large set of linear equations at a large number of frequency points. For practical systems involving the modeling of many components and iterative optimization, the computation cost could be prohibitive.

Recently, Complex Frequency Hopping (CFH) [5]-[7], which is an expansion of asymptotic waveform evaluation [8], has been developed in the circuit simulation area, achieving CPU speedup of factor of hun-

dreds or even thousands over conventional circuit simulators. The technique received attention from the circuit simulation community and has been extended to solutions of static fields in VLSI interconnects [9], in ground/power planes [10] and thermal fields [11]. CFH techniques are particularly suitable for solving large sets of linear differential equations. However its potential to be a technique for solving nonstatic EM equations has not been addressed in the literature. This paper bridges this technical gap with a specific application of CFH techniques in solving the wave equations derived from Maxwell equations. A waveguide example based on the finite difference approach is used to illustrate the technique and to compare with conventional methods.

2. CFH FORMULATION OF MAXWELL'S EQUATIONS

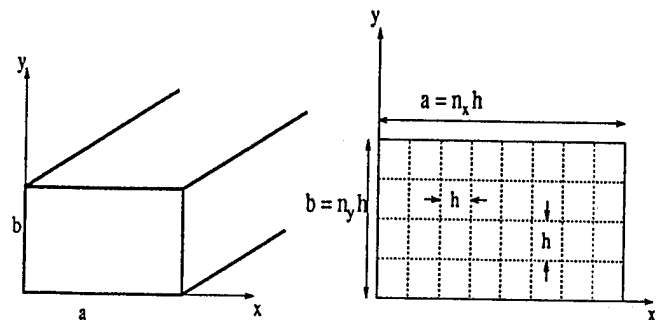


Figure 1: Infinite length waveguide

From the source-free Maxwell's equation, one can

obtain the vector wave equations:

$$\nabla \times \nabla \times \begin{bmatrix} E \\ H \end{bmatrix} - \mu \epsilon \frac{\partial^2}{\partial t^2} \begin{bmatrix} E \\ H \end{bmatrix} = 0 \quad (1)$$

Consider a two-dimension EM problem shown in Fig.1. For TM wave in a rectangular waveguide, the wave equation becomes

$$\frac{\partial^2 E_z(x, y, t)}{\partial t^2} = c^2 \left(\frac{\partial^2 E_z(x, y, t)}{\partial x^2} + \frac{\partial^2 E_z(x, y, t)}{\partial y^2} \right) \quad (2)$$

where c is the velocity of light.

Discretizing space and taking the Laplace transform, we get

$$\frac{h^2}{c^2} s^2 \hat{E}_z(i, j, s) + \hat{F}(i, j, s) = \frac{h^2}{c^2} s E_z(i, j, t)|_{t=0} \quad (3)$$

where

$$\begin{aligned} \hat{F}(i, j, s) = & 4\hat{E}_z(i, j, s) - \hat{E}_z(i+1, j, s) - \hat{E}_z(i-1, j, s) \\ & - \hat{E}_z(i, j+1, s) - \hat{E}_z(i, j-1, s) \end{aligned}$$

and $\hat{E}_z(i, j, s)$ is the Laplace transform of $E_z(i, j, t)$, $E_z(i, j, t) = E_z(x = ih, y = jh, t)$, and $h = \Delta x = \Delta y$.

Suppose n_x and n_y are the number of grids in the x and y directions respectively, and $N = (n_x - 1) \times (n_y - 1)$. Let $\mathbf{X}(s)$ be a N -vector containing $\hat{E}_z(i, j, s)$ for all i, j ; $i = 1, 2, \dots, n_x - 1$, $j = 1, 2, \dots, n_y - 1$.

Equation(3) can be rewritten in the form

$$[s^2 \mathbf{A} + \mathbf{G}] \mathbf{X}(s) = \mathbf{B}(s) \quad (4)$$

where \mathbf{A} and \mathbf{G} are $N \times N$ real matrices containing constants (such as 1's, 0's, 4's, $\frac{h^2}{c^2}$) which are derived from (3). In general, $\mathbf{B}(s)$ is a function of the initial conditions and external sources. For example, if an impulse input is added at grid point (i, j) , then the element of $\mathbf{B}(s)$ in the $[(i-1) \times (n_y - 1) + j]$ th position is equal to $\frac{h^2}{c^2} s$, and all other elements are equal to zero.

Equation (4) is usually very large. CFH uses a lower order Padé approximation to the solution of (4) which can be obtained by solving (4) at only a few selected frequency points [6], [7].

To use Padé approximation, $\mathbf{X}(s)$ is expanded into Taylor's series at frequency point $s = s_0$

$$\mathbf{X}(s) = \sum_{n=0}^{\infty} \mathbf{M}_n (s - s_0)^n \quad (5)$$

where \mathbf{M}_n is the n th moment vector of $\mathbf{X}(s)$.

When the expansion point is on the imaginary axis, $s_0 = jw_0$, then the moments \mathbf{M}_n can be solved recursively from

$$\begin{aligned} [-w_0^2 \mathbf{A} + \mathbf{G}] \mathbf{M}'_n = \\ \mathbf{A} [(-1)^{n+1} 2w_0 \mathbf{M}'_{n-1} - \mathbf{M}'_{n-2}], \\ n \geq 2 \end{aligned} \quad (6)$$

with

$$[-w_0^2 \mathbf{A} + \mathbf{G}] \mathbf{M}'_0 = w_0 \hat{\mathbf{B}} \quad (7)$$

$$[-w_0^2 \mathbf{A} + \mathbf{G}] \mathbf{M}'_1 = 2w_0 \mathbf{A} \mathbf{M}'_0 + \hat{\mathbf{B}} \quad (8)$$

where $\mathbf{B}(s) = s \hat{\mathbf{B}}$; $\mathbf{M}_n = \mathbf{M}'_n$, if n is odd; and $\mathbf{M}_n = j \mathbf{M}'_n$, if n is even.

For each expansion point, the moments $m_n = [\mathbf{M}_n]_{(i)}$; $n = 0, 1, 2, \dots, 2q - 1$ of an output i are matched to a lower order frequency domain function in the form of network transfer function

$$H(s) = \mathbf{X}_{[i]}(s) = \frac{\sum_{j=0}^l a_j s^j}{1 + \sum_{j=1}^q b_j s^j} \quad (9)$$

For given l and q , the coefficients of the numerator and denominator are related to the moments by

$$\begin{bmatrix} m_{l-q+1} & m_{l-q+2} & \dots & m_l \\ m_{l-q+2} & m_{l-q+3} & \dots & m_{l+1} \\ \vdots & \vdots & \ddots & \vdots \\ m_l & m_{l+1} & \dots & m_{l+q-1} \end{bmatrix} \begin{bmatrix} b_q \\ b_{q-1} \\ \vdots \\ b_1 \end{bmatrix} = \begin{bmatrix} m_{l+1} \\ m_{l+2} \\ \vdots \\ m_{l+q} \end{bmatrix} \quad (10)$$

$$b_0 = 1 \quad (11)$$

$$a_r = \sum_{j=0}^r m_{r-j} b_j \quad r = 0, 1, \dots, l. \quad (12)$$

where $m_j = 0$ if $j < 0$ and $l = q - 1$. Equation (10) is known as a Padé approximation which is the base for asymptotic waveform evaluation.

For accurating solutions of $\mathbf{X}(s)$ of EM problems, it is necessary to perform the Padé approximation at several expansion points, i.e., complex frequency hopping. Solutions from CFH is always stable and the accuracy can be easily controlled by hopping. Selection of the expansion points is described in details in [6], [7]. The computation cost of the moments defined by (6) is one LU factorization and $2q$ forward-backward substitutions of a REAL matrix for each expansion point. Therefore, significant CPU speed up can be achieved over conventional techniques such as FDFD where (4) is solved at a large number of frequency points.

3. NUMERICAL RESULTS

We use three different methods to calculate the frequency spectrum of a rectangular waveguide for the same problem given in Fig.1 . The three methods are the CFH technique, the FDTD and the FDFD approaches respectively.

We use Gaussian distribution pulses as the input source[2], i.e., when $t = 0$, $E_z(i, j) = e^{-\alpha^2[(i-i_0)^2+(j-j_0)^2]h^2}$, $\alpha h = 2.0$, (i_0, j_0) is the center input point and $i_0 = n_x/4$; $j_0 = n_y/2$. We chose $\rho = \frac{\epsilon_0}{h} \leq \frac{1}{\sqrt{2}}$, $h \leq \frac{c}{20f}$ for obtaining good stability and accuracy[1], where, f is the highest frequency of the system. In the CFH technique, $q = 8$ and the number of expansion points is 26.

To verify the proposed method, the cutoff frequency of the rectangular waveguide is also calculated by the analytical method [12] and compared with that from CFH in Table 1.

Fig. 2 shows the frequency responses of the waveguide for the different methods. Table 2 shows the CPU time for the different methods for different cases .

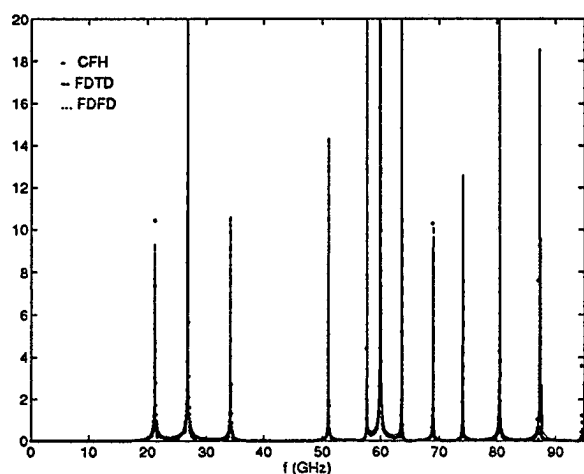


Figure 2: Frequency response

4. CONCLUSION

The concept of Complex Frequency Hopping has been used to derive an solution procedure to EM wave equations. The technique provides potential speed or stability advantages over conventional finite difference based techniques.

Table 1: Cutoff frequency

analytical fcut(GHz)	CFH	FDTD	FDFD
21.2281	21.2281	21.2217	21.2201
26.8526	26.8495	26.8494	26.8502
34.2310	34.2120	34.2231	34.2202
51.1253	51.1047	51.1094	51.1011
57.7478	57.7160	57.7080	57.7011
60.0444	59.9967	59.9887	59.9610
63.6859	63.6477	63.6477	63.6522
69.1162	69.0701	69.0542	68.9522
74.1487	74.1137	74.1153	73.9026
80.5579	80.5261	80.5340	80.4930
87.5289	87.4000	87.3506	87.2033
95.4118	95.3132	95.1715	95.0530
96.8188	96.7440	96.5816	96.1536
99.1185	98.9531	98.8973	98.8536

Table 2: CPU Time Consumption

parameter	method	CPU time(sec.)	CPU time normalized to CFH
$n_x=100$ $n_y=50$ $h=158.0\mu m$ $\rho=0.6$	CFH	765.98	1
	FDTD	1986.67	2.6
	FDFD	25950.0	34
$n_x=60$ $n_y=30$ $h=263.3\mu m$ $\rho=0.7$	CFH	102.48	1
	FDTD	440.64	4.3
	FDFD	17127.0	167
$n_x=60$ $n_y=30$ $h=263.3\mu m$ $\rho=0.6$	CFH	102.48	1
	FDTD	489.32	4.8
	FDFD	17127.0	167
$n_x=60$ $n_y=30$ $h=263.3\mu m$ $\rho=0.3$	CFH	102.48	1
	FDTD	979.14	9.6
	FDFD	17127.0	167

References

- [1] M.N.O. Sadiku, *Numerical Techniques in Electromagnetics*, Boca Raton: CRC Press, 1992.
- [2] R.C. Booton, JR. , *Computational Methods for Electromagnetics and Microwaves*, New York: John Wiley and Sons, 1992.
- [3] M. Mrozowski, "Stability condition for the explicit algorithms of the time domain analysis of Maxwell's equations," *IEEE Microwave and Guided Wave Letters*, Vol. 4, pp. 279-281, Aug. 1994.
- [4] S. Haffa, D. Hollmann and W. Wiesbeck, "The finite difference methods for S-parameter calculation of arbitrary three-dimensional structures," *IEEE Trans. Microwave Theory Tech.*, Vol. 40, pp. 1602-1610, 1992.
- [5] E. Chiprout and M. Nakhla, *Asymptotic Waveform Evaluation and Moment Matching for Interconnect Analysis*, Boston: Kluwer, 1993.
- [6] E. Chiprout and M. Nakhla, "Analysis of interconnect networks using complex frequency hopping," *IEEE Trans. Comput.-Aided Design*, Vol. 14, Jan. 1995.
- [7] R. Sanaie, E. Chiprout, M. Nakhla and Q.J. Zhang, "A fast method for frequency and time domain simulation of high-speed VLSI interconnects," *IEEE Trans. Microwave Theory Tech.* , Vol. 42, pp. 2562-2571, Dec. 1994.
- [8] L.T. Pillage and R.A. Rohrer, "Asymptotic waveform evaluation for timing analysis," *IEEE Trans. Comput.-Aided Design*, Vol. 9, pp. 352-366, Apr. 1990.
- [9] S. Kumashiro, R. Rohrer and A. Strojwas, "Asymptotic waveform evaluation for transient analysis of 3-D interconnect structures," *IEEE Trans. Comput.-Aided Design*, Vol. 12, pp. 988-996, 1993.
- [10] E. Chiprout, M. Heeb, M. Nakhla and A.E. Ruehli, "Simulating 3-D retarded interconnect models using complex frequency hopping(CFH)," *Proc. IEEE/ACM Int. Conf. Computer Aided-Design*, pp. 66-72, Nov. 1993.
- [11] D.G. Liu, V. Phanilatha, Q.J. Zhang and M. Nakhla, "Asymptotic thermal analysis of electronic packages and printed-circuit board," *IEEE Semi-Therm Symp. (San Jose, CA)*, Feb. 1995.
- [12] R.S. Elliott, *An Introduction to Guided Waves and Microwave Circuits*, Los Angeles: Prentice-Hall, 1993.

DESIGN AND SIMULATION OF MICROWAVE FILTER

A.M.NASSAR* A.M.MOSELHY** M.A.EL_GAZZAR***

* Faculty of Eng., Cairo University, Cairo, Egypt

** Air Defence Research Center, Cairo, Egypt

*** Egyptian Air Academy, 44632, Belbies, Sharkia, Egypt

ABSTRACT

A microwave filter has been designed. The designed filter has been simulated by using an efficient general purpose analysis program based on state space approach. The practical design has been built by using microstrip technology. The results of practical measurements and the simulated results are with good agreement.

1- Introduction

Microwave filters have many applications in radars, guidance, satellite communication and electronic warfare. The microstrip filters are very suitable for these applications because the microstrip has the advantage of small size, light weight, low cost and easy fabrication. Various kinds of filters can be realized by using microstrip type structures[1].

The objective of this paper is to introduce the analytical and practical design of microwave filter. A program based on state space approach has been applied for the analysis of the designed circuits in both time and frequency domains. Practical design and simulation results are compared.

2- Analytical Design

The design of microwave low pass filter with cutoff frequency of 2Ghz has been developed. Microstrip filters may be designed with maximally flat response or Chebyshev response in the pass band. The design is based upon the normalized g -values. These values must be converted into inductances and capacitances. The elements values g_1, g_2, \dots, g_n and g_{n+1} of the low pass

prototype filters for both maximally flat (Butter worth) and Chebyshev are given in [2]. In printed form, these types of filters will be realized as a series of high impedance and low impedance sections as shown in Fig.1. The length of the high impedance inductive sections may be calculated by[2].

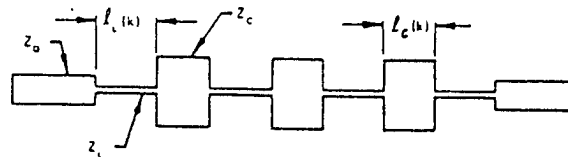


Fig.1 Microstrip L.P.F

$$l_i(k) = \frac{u}{w_0} \sin^{-1}(g(k) \cdot Z_0 / Z_L) \quad (1)$$

where u is the velocity of propagation in microstrip

$$u = \frac{C}{\sqrt{\epsilon_{eff}}} \quad (2)$$

$$C = 3E+8 \quad \text{m/sec}$$

ϵ_{eff} ...effective dielectric constant

Z_L is the characteristic impedance of the inductive section.

z_0 ... is the characteristic of the terminating resistance.

The length of the capacitive section is given by [2]

$$l_c(k) = X_{cc}(k) \frac{u}{w_0} \quad (3)$$

$$X_{cc} = \frac{g(k)}{Z_0} - [X_{cn}(k-1) + X_{cn}(k+1)], \quad (4)$$

and

$$X_{cn} = \frac{w_0 \ell_1(k)}{2w_0 Z_c(k)} \quad (5)$$

X_{cc}corrected value of capacitance susceptibility.

3- Simulation program

A general computer program for the analysis of microwave circuits has been applied. The program is based upon the formulation of the state and output equations using an efficient topological method with no restriction on the topology. The state and output equations for any network can be represented as the following.

(3a) The state and output equations :-

It has been shown [9] that the state variables of a distributed network are the reflected parameters at all the transmission line terminals or ports. The state variables of a lumped/distributed network are the voltages on all the independent capacitors, the currents in all the independent inductors and the reflected parameters (or the reflected voltages) at all the transmission-line ports.

The state equation is the differential-difference equation of the form:

$$\begin{bmatrix} \dot{X}_1(t) \\ X_2(t+T) \end{bmatrix} = \begin{bmatrix} A_{11} & A_{12} \\ A_{21} & A_{22} \end{bmatrix} \begin{bmatrix} X_1(t) \\ X_2(t) \end{bmatrix} + \begin{bmatrix} B_1 \\ B_2 \end{bmatrix} u(t), \quad (6)$$

where $X_1(t)$ and $X_2(t)$ are the state vectors of the lumped and distributed elements respectively and $u(t)$ is the input vector. The output equation is given by :-

$$y(t) = \begin{bmatrix} C_1 & C_2 \end{bmatrix} \begin{bmatrix} X_1(t) \\ X_2(t) \end{bmatrix} + E u(t) \quad (7)$$

Equations (6) and (7) are derived using topological methods with no

restriction on the network topology. Where A, B, C and E are the matrices of the state and output equation of the systems.

When the Laplace transform is applied to equations (6) and (7) we obtain the frequency-domain equations.

$$\begin{bmatrix} X_1(s) \\ X_2(s) \end{bmatrix} = \begin{bmatrix} sI_m - A_{11} & A_{12} \\ A_{21} & zI_{2n} - A_{22} \end{bmatrix}^{-1} \begin{bmatrix} B_1 \\ B_2 \end{bmatrix} U(s) \quad (8)$$

$$Y(s, z) = \begin{bmatrix} C_1 & C_2 \end{bmatrix} \begin{bmatrix} sI_m - A_{11} & A_{12} \\ A_{21} & zI_{2n} - A_{22} \end{bmatrix}^{-1} \begin{bmatrix} B_1 \\ B_2 \end{bmatrix} + E \quad U(s) \quad (9)$$

where $z = \exp sT$, I is the identity matrix, m, n are the number of lumped-state elements and transmission lines, respectively.

(3b) Network Analysis Using the State Equation

The previous results are used to analyze lumped/distributed networks in either the frequency or time domain.

(1) **Frequency domain analysis** : is Based on the expansion of the equation (9) to obtain the transfer function of the form.

$$F(s, z) = \frac{\sum_{i=0}^{2n} \sum_{j=0}^m A_{ij} s^j z^i}{\sum_{i=0}^{2n} \sum_{j=0}^m B_{ij} s^j z^i} \quad (10)$$

This expansion is achieved by using a modified faddeeva algorithm[7] for the inversion of the two variable matrix in equation (8).

(2) **Time domain analysis** : The output in the time domain is calculated from equation (7) when the state vector $[X_1(t) \ X_2(t)]^T$ is known. The state vector is first determined from the solution of (6). Equation (6) represents two simultaneous differential and difference equation :

$$X_1(t) = A_{11}X_1(t) + A_{12}X_2(t) + B_1u(t) \quad (11)$$

and

$$X_2(t) = A_{21}X_1(t-T) + A_{22}X_2(t-T) + B_2u(t-T) \quad (12)$$

The state vector $[X_1(t); X_2(t)]^T$ is assumed to be zero at $t < 0$. The vector $X_2(t)$ is calculated by substituting the values of $X_1(t-T)$, $X_2(t-T)$ and $u(t-T)$ in equation (12). The vector $X_1(t)$ is then calculated by solving the differential equation (11) numerically in each time period $kt < t < (k+1)T$, where $k = 0, 1, 2, \dots$

The state and output vectors have discontinuities at $t = KT$ and the initial values of the state vector at the start of each time period are obtained from the condition that the integral of the state vector is continuous.

The insertion loss predicated by simulation program is shown in Fig.1

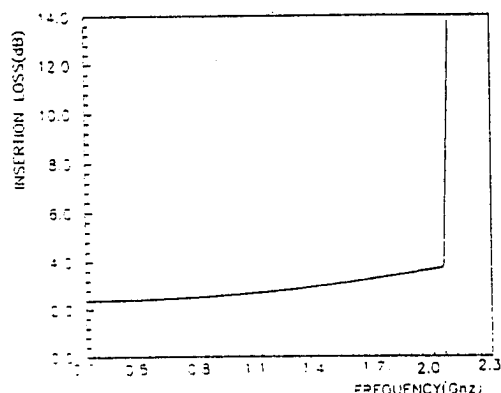


Fig.1 Insertion loss versus frequency(Ghz) of an L.P.F

4- Practical Design

The practical design of the microwave filter with cutoff frequency of 2Ghz has been developed in a stepped impedance form by using microstrip technology according to the following considerations.

- 1-The choice of the substrate material depends on the frequency of operation, cost, and applications. High dielectric constant substrates

result in small size circuits. RT-Duriod 5880 (Teflon) of $\epsilon_r = 2.33$ and $h = .787$ mm is chosen. The substrate with copper clad with is widely used in microwave integrated circuits.

- 2-A conventional microstrip synthesis technique described in [3] is carried out to calculate the dimension of microstrip circuits. The layout of the circuit is carefully prepared keeping in mind the microstrip discontinuity at step in width the mask layout is shown in Fig.2.

- 3- Fabrication process of thin film microwave integrated circuits using photolithographic technique is applied.

- 4-The circuits is measured by using direct measurement technique. An input signal ranging from 0.8 to 2.4 Ghz with varying amplitude is applied to the input port of the filter. The power of the output signal and spectrum of the fundamental and other harmonics are measured at the output port.

The insertion loss is given by:

$$IL(dB) = P_{out}(dBm) - P_{in}(dBm)$$

The insertion loss versus the frequency(Ghz) is shown in Fig.3.



Fig.2. The layout of the L.P.F

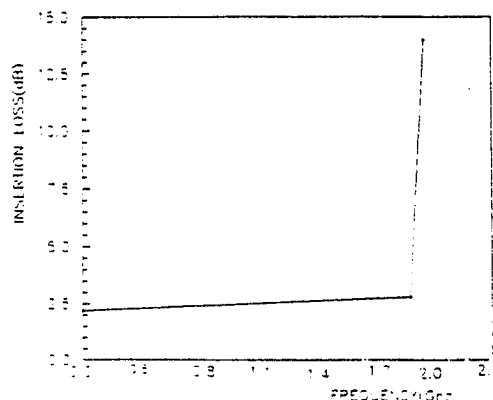


Fig.3. The insertion loss versus the frequency(Ghz)

5-Conclusion

The design procedure of microstrip low-pass filter is presented. The computer aided analysis adopted in this paper is with good stability and suitable computation time. The results show good agreements between simulation and measurements. The deviation between the measured and predicted simulated values was due to imperfection associated with the connectors used and the fabrication tolerances.

References

- [1]Gupata. k.C.R. Garg and I.J.Bahl, "Microstrip lines and slotlines",pretech house, Dedham, Mass.,1979
- [2]P.Bahartia. "Microwave Solid State Circuit design"
- [3]T.C. Edwards,"Foundations of Microstrip Circuits Design", Jon Widley & Sons.1992
- [4]L.O.CHua and P.Lin, "Computer- Aided Analysis of Electronic Circuits", Prentice-Hall,1975.
- [5]K.LeeandS.Park, "Reduced Modified Nodal Approach to circuit Analysis" ,IEEE TRAN. on Circuit and Systems, Vol. CAS-32, No.10, 1985.
- [6]I.R Bashkow,"The A Matrix, New Network Description" IRE Tran. Theory, Vol.CT-4, PP.117-119, 1957.
- [7]FADDEEVA, V.N.: "Computational methods of linear algebra" (Dover, New York, 1959)
- [8]WALTER BANZHAF, "Computer- Aided Circuit Analysis Using Spice", Prentice-hall ,1989.
- [9]SOBHY, M.I.: Topological derivation of the state equation of networks containing commensurate transmission lines, Proc. IEE, 1975, PP.1367-1371
- [10]J.K.Fidler, "Computer-Aided Circuit Design", Thomas Nelson, 1978
- [11]L.Kihell,"New General Approach to Commensurate TEM Transmission line Method Using State Space Approach", Int.J. Circuit Theory& Applications ,1974.
- [12]M.I.Sobhy and M.H Kerakos, " Computer-Aided Design of Commensurate and Non Commensurate Delay Lines Using State Space Technique", 1977 MTT-S Int. Microwave Symp.,1977
- [13]Esmat.A.F.Abdallah (Elect.Res. Inst.), E.A.Hosny (Kent.univ.U.K), M.A.Nassef and A.M.Moselhy (M.T.C) "Computer Aided Analysis of Microwave Integrated circuits using An Efficient Topological Method" proceeding of the Eighth National Radio Science Conference NRSC' 91, Cairo ,Egypt, Feb. 19-21,1991.
- [14] RABBAT,N.B.: "Efficient Computation of the Transient Response of Lumped/ Distributed Linear Active Network, IEEE Trans., 1975, CAS-22, PP.866-620.
- [15] A.M.NASSAR, A.M.MOSELHY, M.A. EL-GAZZAR, "Computer Aided Analysis And Design of Lumped/ Distributed Networks by Using Topological Algorithm", Twelfth National Radio Science Conference March 21-23, 1995 Faculty of Eng, Alexandria university, Alex. Egypt.

STATISTICAL MODELLING OF IDD TESTING EFFICIENCY OF ANALOGUE INTEGRATED CIRCUITS

Vladislav Musil

Technical University of Brno, Faculty of Electrical Engineering and Computer Science, Department of Microelectronics, Údolní 53, 602 00 Brno, Czech Republic,
e-mail: musil@gate.fee.vutbr.cz

ABSTRACT

The paper describes a new implementation of testing-algorithm model for analogue circuits. It is based on the possibilities of HSPICE and MATLAB to manage whole test simulation including the simulations of faulty or fault free circuits as well as post-processing of them. The approach takes account to tolerances deviations on parameters. Both the low-level and high-level modelling are assumed. Aim of this project is to model test techniques in order to classify their effectiveness in the sense of fault coverage, namely for test techniques using supply current monitoring.

1. INTRODUCTION

In the last few years, analogue and mixed-signal integrated circuits have grown in importance. Several new test ideas were introduced that provides a number of benefits in comparison with traditional analog test approaches. But at present there are still only few techniques available that can adequately test these devices, although the area has attracted considerable interest in recent years. There are three major problems in analog testability: the problem of modelling of faulty components, the problem of tolerances and the problem of limited number of test points (accessible nodes).

The approach, which is, at present, attracting a great deal of interest, is to monitor a supply current rather than functional outputs in order to observe faults. This approach covers fault detection in both the analogue and digital parts of the device. In this approach the current passing through the terminal is monitored during the application of test vectors. Originally these methods were proposed for digital testing and are widely worked out, providing effective solutions to increasingly difficult test problems. There are also several described techniques for analogue testing which also offer the advantage of direct detection of the defects obviating the necessity to propagate a defective voltage to an output port. It is also able to detect certain defects missed by traditional voltage test approaches based on the stuck-at fault model. Unfortunately, these methods are not worked out enough and we are also required to eliminate the

effect of tolerances of nonfaulty components and measurement errors, those problems have absolutely no equivalent in the digital circuits testing. Monte Carlo technique has been proved to be a powerful tool which is expected hopefully to reach the above goal.

2. PROBLEM OF TOLERANCES

In the testability area we deal with faulty models of devices for catastrophic and soft faults, but nevertheless, the effect of tolerances must be taken into account. Calculations only with the nominal values of nonfaulty elements parameters would be an oversimplification. The values of these parameters may lie anywhere inside of prescribed tolerance band. As a result of this, the faulty model of device will not be characterized by single voltage/current at accessible nodes (test points). Instead, the model will be characterized by allowed bands of each response, which can be considered as mapping of tolerance bands of nonfaulty components [2]. These bands are called the tolerance envelopes. The method of testing is said to be robust, if it is reliable also in the case, when the parameters have not nominal values, but lie in the prescribed tolerance bands.

The tolerance envelope (tolerance band) of supply current for fault free analogue circuit can be quite wide and it is difficult to establish border between fault free and faulty circuits (go/nogo test). A worst-case tolerance analysis is the identification of the extreme (i.e. worst) values of supply current (generally a performance) resulting from the variations in component values. The effect of tolerances can completely dominate the performance of a device under test. There is the lack of published data on Idd test limits. Some values are based on an engineering judgement and others are guessed. Unfortunately, the ideal situation with the defined gap (Fig. 6) or similarly with the frequency signature was not proved, esp. for soft faults. Of course, Idd should be tested at the highest possible voltage and after burn-in process (activation of hidden defects). Initial proposals, using off-chip current testing, were replaced for large circuits by on-chip testing (also with several sensors to get over the limited resolution).

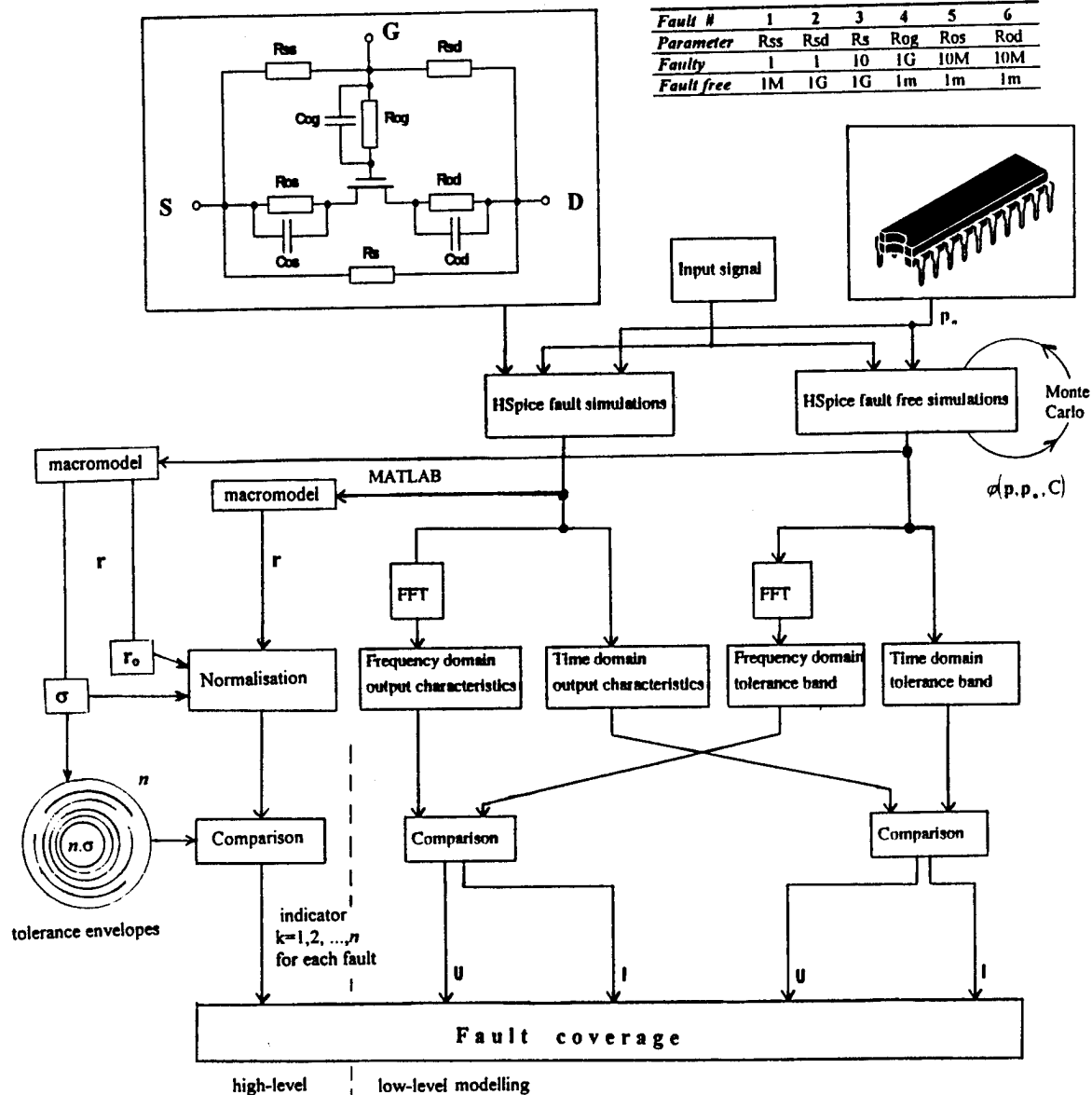


Fig. 1. HSPICE based flowchart of the proposed system

Analogue circuits can and do have a wide range of element values and topology. Direct simulation seems to be only way to obtain an exact behaviour of supply current or other responses. The only method we can use is the Monte Carlo analysis. This method is characterized by the use of pseudo-random numbers within statistical sampling experiments. Modelling for Monte Carlo analysis requires a statistical model capable of generating individual transistor models which are then used in an analysis programme. The statistical modelling problem considered below is how to construct a suitable statistical model which can accurately approximate both the spreads and correlations of parameters. An assumption is made that the parameters distribution functions (pdf) are well modeled by Gaussian distributions including inter-parameter correlations. The problem was approached

successfully for the cases to be described by a combination of theoretical considerations and the maximum practical use of experimental data. We have been handicapped by a lack of statistics about circuits.

The pdf $\phi(p)$ with expectations p_o and covariance matrix C , can be written as;

$$\phi(p, p_o, C) = \frac{1}{\sqrt{2^n \cdot \pi^n \cdot |C|}} \cdot \exp \left[-\frac{1}{2} (p - p_o)^T \cdot C^{-1} \cdot (p - p_o) \right]$$

Independent random parameters of statistical device models are often Gaussian. If their mapping to performance characteristic (inc. supply current) can be approximated by linear functions, then the performance characteristics will have Gaussian pdf.

The computer generation of the n -th random vectors p^n with the above pdf is performed as follows: first a normal vector x^n with a distribution $\phi(x, x_0, E)$, where E is the unit matrix, is generated and then it is transformed to p^n as follows

$$p^n = L \cdot (x^n - x_0) + p_0$$

where L is the lower triangular matrix resulting from the Cholesky decomposition of C , namely $C = L \cdot L^T$. In practice it turns out that it is easier to use the formula for the bootstrapped pdf (tracked pdf)

$$p_i = p_{i0} + \tau_i \cdot a_i + \sum_{j=1}^q k_j \cdot \lambda_j$$

where a_i and λ_j are random numbers from closed interval $(-1, 1)$ both with Gaussian pdf. Coefficients k_j (equals zero for uncorrelated parameters) express the tracking by variables λ_j . See Fig. 4.

3. METHOD DESCRIPTION

On fig. 1 we can see the flowchart of the simulation system. Only MOS circuits are simulated. Each transistor is replaced by its model for shorts and opens [1]. For circuit simulation the HSPICE programme is used. As outputs with benefit we can assume four different characteristics: supply current in time and frequency domains as well as output voltage in time and frequency domain. It has been noticed that processing of supply current characteristic by Fourier transform could bring interesting results (frequency domain approach) - a signature of the current status. But there is a problem about the best input stimuli for testing purposes. Some presumptions has existed and it could be possible to verify them. Our choice was a sine wave, a square wave, and a sawtooth wave.

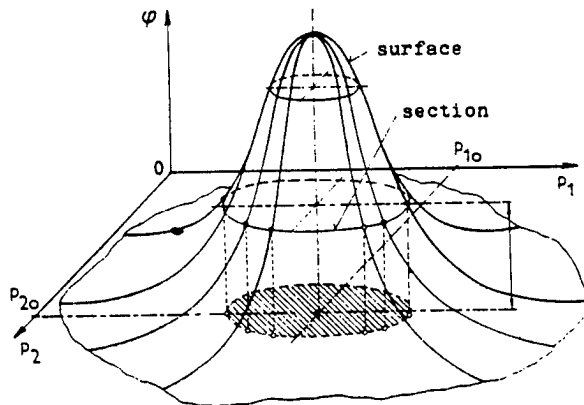


Fig. 2. Two dimension Gaussian distribution

First TR analysis runs for fault free circuit with parametr variation using Monte Carlo analysis for both supply current and output voltage. Then we can

estimate tolerance intervals for supply currents and frequency signatures. Now TR analysis runs for all possible (or supposed) faults. By comparing faulty characteristics with tolerance intervals and frequency signatures we obtain the final result - detectability for each fault (faults coverage).

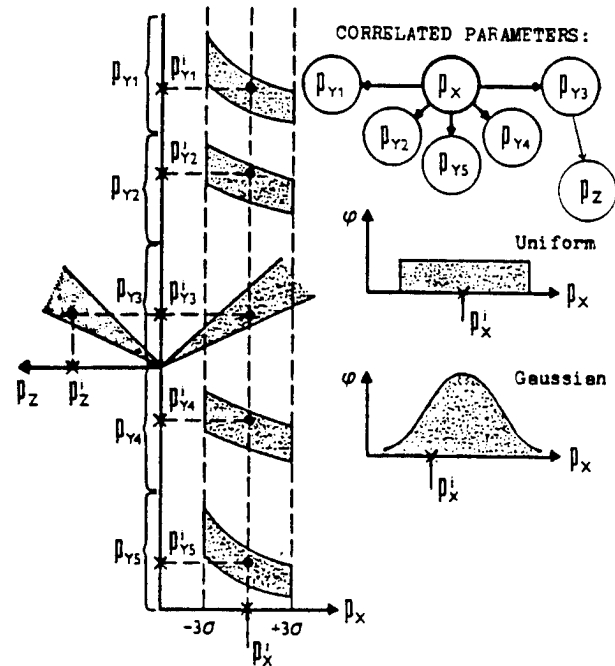


Fig. 3. An example of correlated parameters

A larger circuit can be modelled on a high level as a mathematical description of its behaviour. The fault free circuit and its tolerance envelope are transferred to the high level as a point with a sphere around (Figure 5). The idea was to do the same procedure for a faulty circuit to model a faulty circuit by use of the fault-free model. On the transistor level the faulty and fault-free circuits are represented by

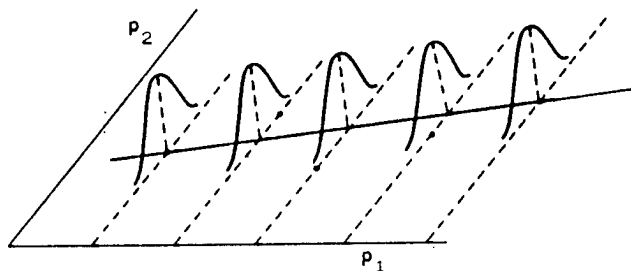


Fig. 4. Linearly correlated parameters

different connections (added or missing). This circuitry difference will be shifted to the high level as a parameter difference. The faulty behaviour can be placed to the same board as the fault free behaviour (Figure 5). Each fault is displayed as a point. Manufacturing parameter variation of the faulty circuit can be transferred and placed around the fault as a probability density cloud (the tolerance band is not defined for the faulty circuit). If the fault free envelope

(tolerance band) and faults are put together, a simple detection strategy can be found. The faults which are situated inside the envelope are "potentially" non-

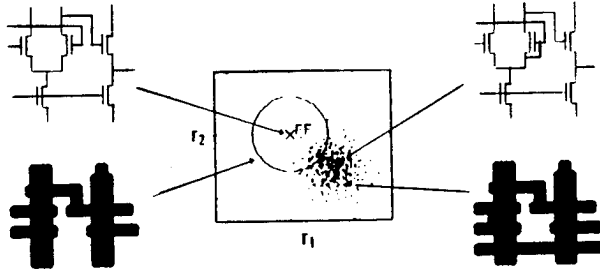


Fig. 5. Tolerance envelope for a fault free (FF) circuit and a scatter of high-level parameters for a faulty (F1) circuit

etectable. Faults that are placed outside are "potentially" detectable. This simple comparison does not demonstrate degree of detectability or respective non-detectability. To add this scaling, the variation of manufacturing parameters for faulty devices has to be taken in to account. The variation for a faulty device follows a Gaussian distribution. This enables us to calculate the probability of in- or out- envelope occurrence for each fault separately. The probability of occurrence, defined as an integral of probability density function apart from the envelope, is equal to the

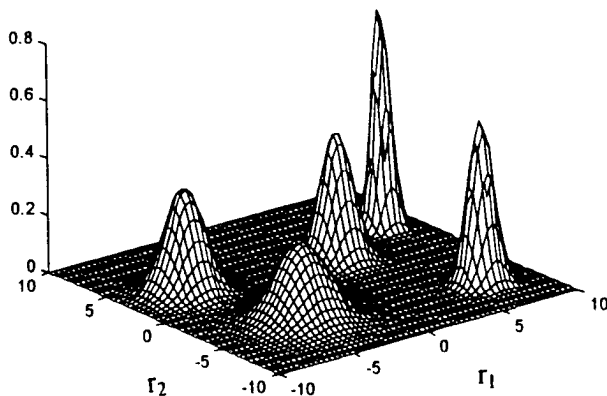


Fig. 6. Three dimensional map of faults with probability density values on the z-axis

potential detectability of the fault. By using the principles above the faults were transferred one by one to high-level space with their parameter variation. The

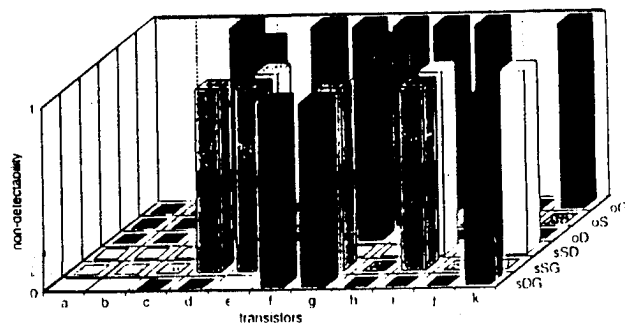


Fig. 7. Fault coverage for the supply current in time domain (input signal = sawtooth wave)

results are placed on to a two dimensional map as probability density clouds, and on a three dimensional map (Figure 6) with probability density on the z-axis. The potential detectability is calculated by a Monte-Carlo integration, the integral is a ratio of the points in the envelope to the total number of points. The map can be made only for two parameters, but the calculation is n-dimensional generally.

These topics will be discuss in more detail in the presentation as well as the results achieved. Examples will be given of three circuits, an inverter, an operational amplifier (Fig. 7), and a 2-bit flash ADC. These applications are representative of practical problems.

4. CONCLUSION

Testing is an essential part of each manufacturing process. Test methods for analogue circuits are not yet fully established. In this work, the inclusion of the effects of manufacturing tolerances of analogue and mixed-mode circuits to fault detectability has been presented. Here the test-process modelling system was described. It solves needs for wide flexibility during the test process modelling. Different fault models, input stimuli but mainly different analyses can be easily processed. Novel fault-processing algorithm with wide reprogramming features was designed. Both the low-level and high-level modelling are assumed. The importance of a supply current testing method was justified. This method is recommended in mass production of integrated circuits for inexpensive screening out of faulty circuits in the initial stages of testing.

The author would like to thank to Mr J. Povazanec from The Leeds Metropolitan University for his helpful discussions and suggestions.

REFERENCES

- [1] Eckersall, K.R. - Taylor, G.E. - Bell, I.M. - Toumazou, C.: Current monitoring for test. In: Toumazou, C.: Circuits & Systems, Tutorials. 1994 IEEE ISCAS, London, 30 May - 2 June, 1994, pp. 551-568.
- [2] Spence, R. - Soin, R.S.: Tolerance design of electronic circuits. Addison-Wesley Publishing Company, 1988.
- [3] Musil, V.: Methods of statistical circuit design. Slaboproudý obzor. Vol. 49, 1988, No. 2, pp. P1-P6 (in Czech).
- [4] Eshbaugh, K.S.: Generation of correlated parameters for statistical circuit simulation. IEEE Trans. on Computer-aided Design, Vol. 11. No. 10, Oct. 1992, pp. 1198-1206.
- [5] J. Povazanec, T. Volek, G. Taylor, "Analogue Test in Frequency and Time Domains", International Mixed Signal Testing Workshop, 1995

A SIMULATED ANNEALING ALGORITHM FOR THE OPTIMIZATION OF COMMUNICATION NETWORKS

Eugenio Costamagna (), Alessandra Fanni (+) and Giorgio Giacinto (+)*

- (*) Dipartimento di Elettronica, Universita' di Pavia, Via Abbiategrasso 209, 27100 - Pavia, Italy. Phone: +39-382-505200; Fax: +39-382-422583; e-mail: eugenio@comell.unipv.it
(+) Istituto di Elettrotecnica, Universita' di Cagliari, 09123 - Piazza d'Armi, Cagliari, Italy. Phone: +39-70-280327; Fax: +39-70-291619; e-mail: fanni@elettro1.unica.it

Abstract - A Simulated Annealing algorithm is presented for topological optimization of communication networks. An extensive testing over networks of various sizes and configurations is made in order to choose the best values of the parameters and to adapt the Simulated Annealing implementation to the specific problem. The performances of the algorithm are compared to that of other traditional techniques.

1. Introduction

Large attention has been recently devoted to various problems related to the optimization of network architecture, due to the impressive growth of communication services and to the need of larger frequency bandwidth and availability of new transmission media.

In particular, networks based on a unique exchange or hub facility connected to the users through multiplexed links seem to provide, in many cases, installation flexibility and costs suitable to fill the operational requirements of the so-called B-ISDN, Large Bandwidth Integrated Service Digital Network. The same topology is used in the computer networks using concentrators. Users are distributed over local or metropolitan areas, and are represented in the following by network access points at a level of about 2 Mbit/s.

To represent the topology of these multiplexer or traffic concentrators networks it is convenient to introduce a graph model. Let $G(N, A)$ be an undirected graph (the communication networks at hand allow simultaneous transmission in both the directions), where $N = \{1, 2, \dots, n\}$ is the set of nodes representing locations of both existing or possible multiplexers, and locations of users, and $A = \{(i, j)\}$ is the set of arcs of G . These represent the possible communication links that may be used to connect the users, the multiplexers and the exchange among them (cable conduit graph). This graph contains all the information about the particular area in which the net must be built, and can be derived examining the road map, the existing telephone network and any geographical constraint.

The design problem consists of choosing a spanning tree T of G connecting all the users to the multiplexers through the distribution network, and the multiplexers

to the exchange through the transport network, allowing the overall cost of the plant be minimised.

Considering the higher cost of the fiber-optic cables, compared with the costs of the equipment, it seems reasonable to realise a minimum path spanning tree. The optimization problem is so reduced to choose a sub-set M of N in which multiplexer centres have to be implemented. This fundamental scheme has been already proven to be suitable to use various objective functions, considering different terms of cost, and to investigate connectivity and reliability problems [1].

When the exchange site is selected and a number of multiplexers are made active, both the transport and the distribution networks can be obtained by means of the well-known minimum distance Dijkstra algorithm [2]. This leads immediately to model the network by a binary string, in which ones and zeroes indicate activation or no-activation of multiplexers in the n nodes.

2. Simulated Annealing

The objective function, representing the cost of the network, can be described as the sum of four components: the cost of the distribution network, the cost of the transport network, the cost of the multiplexers and the cost of the exchange. This function takes discrete values according to feasible configurations of the net, because the multiplexers have a finite number of inputs and one output, and are available in standard hierarchies, as the fiber optic cables. In addition, the topological variables are of binary nature. Summing up, the variables to be optimized are discrete and the objective function is not linear.

The resulting problem is a typical large size combinatorial optimization problem, falling in the class of the NP-hard problems, for which there is the need for heuristic algorithms. Among them, large attention has been recently devoted to the Simulated Annealing (S.A.) approach [3], based on an iterative improvement technique, suitably corrected introducing random moves.

To define such an algorithm, a generation and an acceptance procedure for the different network configurations must be introduced, or, better, a perturbation method has to be defined allowing to pass

from one configuration to another. The acceptance criterion is governed by a random number generator and a control parameter, called temperature.

Starting from an admissible solution of the problem, the search strategy in the neighbourhood of such a solution will be more intensive in the more promising regions, penalising the searches that move far from these regions but accepting with certain probability, also searches that worsen the solution. The temperature, slowly modifying its value, drives the system toward the final solution, which corresponds to a local minimum of the objective function. In Fig. 1 a typical implementation of the algorithm is shown.

1. Choose an initial solution S
2. Set $t = t_0$
3. Repeat until system is frozen.
 - 3.1 Do the following cycle l times.
 - 3.1.1 Make a perturbation in S and generate $S' \in R_S$
 - 3.1.2 Set $\Delta C = C(S') - C(S)$
 - 3.1.3 If $\Delta C \leq 0$, then set $S = S'$
 - 3.1.4 If $\Delta C > 0$ set $S = S'$ with probability $\exp(-\Delta C/t)$
 - 3.2 Set $t = r \cdot t$.
4. Show S .

Fig. 1 Typical implementation of Simulated Annealing

The core of this procedure is in step 3.1, known as *Metropolis algorithm*. It must be noted that $\exp(-\Delta C/t)$ is a number in $[0,1)$ when ΔC and t are positive, which may be correctly understood as a probability dependent on ΔC and t .

In the above implementation, it is of fundamental importance to introduce two additional parameters: the cooling ratio r and an integer number l that represent the number of iteration executed for each value of the temperature [4], i.e., the length of the Markov chain in the Metropolis algorithm.

3. Cooling schedule

To apply the S.A. algorithm to the problem at hand, we focus our attention on three main aspects: the goodness of the solutions, the computational time and the capability of the algorithm to cope with networks of different dimensions and topology.

As previously mentioned, the implementation requires to set various parameter values, following considerations of experimental nature.

To ensure the convergence of the algorithm, it is necessary to define the dimension of the neighbourhood of a configuration. A large number of experiments showed that the dimension of the neighbourhood affects only computational time, but not the final value of the objective function. As previously mentioned any feasible configuration has been represented with a

binary string of n elements: a '1' in a certain position of the string means that multiplexer has been activated in the corresponding node; '0' means that the node does not contain a multiplexer center. The neighbourhood is generated randomly choosing k elements of the string and changing '1's with '0's and '0's with '1's. The dimension of the neighbourhood is strictly linked with the value of k . Many trials showed that this value has to be changed with the number of nodes. In many cases k can be changed during the evolution of the algorithm, so that in the beginning large neighbourhood is visited, while in the proximity of frozen point neighbourhoods are restricted because only with small perturbations better solutions can be obtained.

One of the most important problem involved in the S.A. algorithm implementation is the definition of a proper *cooling schedule*, which is based on the choice of the following parameters: starting temperature, final temperature, length of Markov chains, the way of decreasing temperature. A correct choice of these parameters is crucial because the performances of the algorithm strongly depend on it. In literature many cooling schedule are mentioned [5]. In this paper, parameters have been chosen after a large number of tests.

The starting value of t , t_0 , has been chosen according to [5]. Let χ be the *acceptation ratio*, i.e. the ratio between the number of accepted transitions and the number of generated transitions, the value of t_0 is doubled until χ becomes higher than a fixed value χ_0 . Starting with $t_0=0.5$ and $\chi_0=0.8$ [5], the program has been optimized (in terms of the goodness of the solutions and of the computational time) with $t_0=0.4$ and $\chi_0=0.41$.

Another important problem, involved in the Metropolis criterion, consists in introducing a suitable normalisation of the costs. In fact, they have to be compared with the control parameter t . As can be seen in step 3.1.4 in Fig. 1, the values $\exp(-\Delta C/t)$ must be uniformly distributed in the interval $[0,1)$. This can be achieved assuming a different normalisation parameter in each step of the procedure, varying according to the variation of the costs of the solutions explored during the previous Markov chain.

The second parameter to be set is the length of Markov chains. It is polynomially linked to the problem' size [5], i.e. to the number n of nodes of the network. In particular the maximum number of accepted configurations have been set to $10 \cdot n$ while the maximum number of generated configurations has been set to $50 \cdot n$.

One of the most used strategy for varying t during the search is [5]: $t_{(k+1)} = r \cdot t_{(k)}$ with $0.5 \leq r \leq 0.99$. The best choice for r has been made considering the goodness of solutions and the amount of computational time needed. Best results have been obtained in the field of $0.95 \leq r \leq 0.97$. In fact, it has been noted that, assuming lower values it is possible to be trapped in

local minima, otherwise, with higher values a large amount of computational time is needed.

In Fig. 2 the results of three tests are shown: one with $r=0.99$, one with $r=0.95$ and another with $r=0.9$. As can be noted, in the first case a large amount of computational time is needed; in the second and in the third case the computational time is reduced: In particular setting $r=0.95$ results very close to optimum are found.

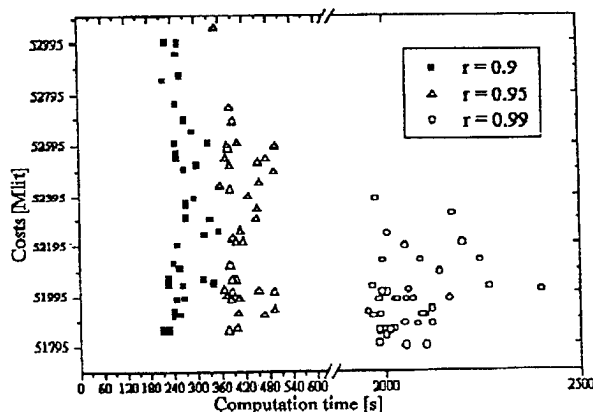


Fig. 2 Costs vs. computation time for different choices of r .

The final value of t is strictly linked to stop conditions. To be sure that no improvement is possible and that the system is frozen, two conditions must be verified together. Firstly t is decreased until it is less or equal to a fixed value t_f . Moreover, improvements in the objective function must be negligible.

The evolution of the solution values during the annealing process is shown in Fig. 3, for a network of large size (120 nodes), and for parameter values chosen with the previous criteria.

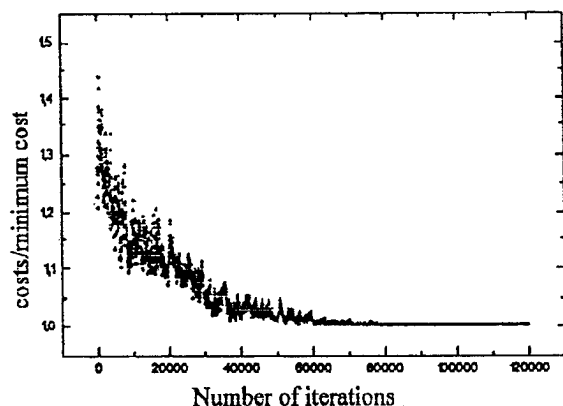


Fig. 3 Algorithm evolution for a 120 nodes network.

4. Results

Results of extensive testing over networks exhibiting different sizes and different topologies of the cable

conduit graph are reported. In particular, two topologies of random and geometrical graphs [4] with small (about 50 nodes), medium (about 100 nodes), and large (about 150 nodes) size are considered.

As a result, we have settled the optimum values of the parameters involved in the algorithm.

In Tab. I, we report the values of the optimised parameters.

Table I - Optimal cooling schedule

PARAMETERS	VALUES
Number of Changes k	1+5
Initial Temperature	0.4
Final Temperature	0.14
Length of Markov Chain	50*n
Cooling Ratio	0.95

As an example, we report the results obtained for a real network of large size (160 nodes), whose data have been supplied by the Italian Public Telephone Company. The cable conduit graph has been derived examining the existing telephone network and geographical constraints.

In Fig. 4, the results corresponding to 200 tests are reported. As can be noted, the larger part of the results falls in a range of $\pm 1\%$ around the minimum cost (44.724 MLit). The minimum was obtained with a frequency of 17%. In Fig. 4 we also report the result obtained with a local optimization algorithm (L.O.A.) [6], showing the improvement obtained with the S.A. approach.

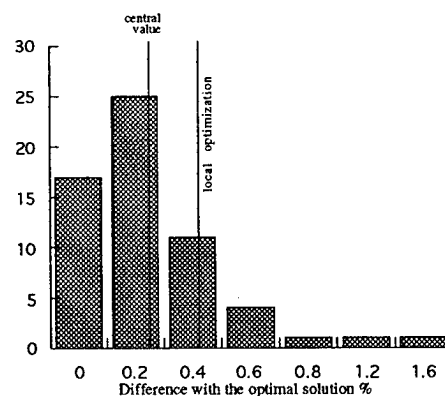


Fig. 4 Frequency occurrence of the solutions versus percent difference with respect to the optimal solution.

The computation time of the more frequent solutions range from 15 to 17 minutes on a HP/715 workstation. The results obtained applying the S.A. algorithm to a network of 58 nodes, corresponding to the telephone district of Oristano, Sardinia, are reported in Tab. II, for different choices of the location of the exchange, starting from random configurations or from the local

optimization algorithm result. The S.A. results are compared with those obtained with the L.O.A..

Table II - Comparison between S.A. and L.O.A. results for the Oristano network.

Exchange location	Starting configuration	Candidate sites for the multiplexers	Links layout	Cost improvement with respect to L.O.A.
fixed (Oristano)	result of L.O.A.	15	optimal	0 %
fixed (Oristano)	random	15	optimal	0 %
fixed (Oristano)	random	58	random	0.1 %
fixed (Oristano)	result of L.O.A.	58	optimal	1.3 %
random	random	58	complete graph	7 %

In Tab. III, all the statistics over the numerous networks considered are reported, together with comparison with those obtain with other optimization methods such as heuristic [6] and genetic [7], both in terms of cost and computation time.

Table III - Results of 21 test cases (*r* random networks, *g* geometric networks).

Networks	Star Config.	Heuristic		Genetic		Simulated Annealing	
	Cost [MLit]	Cost [MLit]	Time[s]	Cost [MLit]	Time [s]	Cost [MLit]	Time [s]
ORISTANO	82725.9	31306.70	0.71	31306.70	115.17	31306.70	35.79
45 nodes <i>r</i>	31566.30	19742.94	0.11	19440.79	58.75	19440.79	19.92
50 nodes <i>r</i>	30217.76	20083.49	0.19	19956.80	156.83	19956.80	21.7
54 nodes <i>r</i>	42621.92	26731.53	0.37	26057.90	58.75	26049.71	18.89
96 nodes <i>r</i>	79007.85	39748.11	1.84	39272.08	573.38	39163.73	172.7
100 nodes <i>r</i>	114315.5	51072.22	2.25	50240.43	851.74	50065.82	178.84
105 nodes <i>r</i>	230950.7	75139.37	2.99	72368.35	1130.33	72365.66	230.33
148 nodes <i>r</i>	174828	65912.76	11.33	64929.02	2673.84	63526.07	525.52
150 nodes <i>r</i>	166723.60	70526.54	7	69483.10	2978.06	67726.28	689.83
152 nodes <i>r</i>	284270.30	95534.58	15.43	96495.11	3165.80	95170.32	1008.27
48 nodes <i>g</i>	20630.60	12866.69	0.21	12853.94	130.45	12853.94	10.03
50 nodes <i>g</i>	27250.14	15998.17	0.09	15807.78	105.78	15807.78	11.75
54 nodes <i>g</i>	14891.19	11345.37	0.08	11286.37	162	11195.95	14.18
95 nodes <i>g</i>	52983.24	25553.40	0.63	24996.41	550.73	24600.07	83.38
100 nodes <i>g</i>	47029.95	28467.54	0.48	28330.15	448.79	27548.35	114.38
102 nodes <i>g</i>	26276.03	16969.90	0.54	16954.45	712.29	16928.37	123.59
120 nodes	142813.7	53263.67	6.2	51919.23	3180	51795.55	425
147 nodes <i>g</i>	50542.34	28121.80	2.01	27469.46	1858.41	27068.75	485.28
150 nodes <i>g</i>	53957.48	31550.54	1.91	31460.94	1580.45	31290.46	499.51
153 nodes <i>g</i>	62696.83	32389.70	1.97	31748.29	1720.48	31321.24	600.99
160 nodes	176382	44920.50	15.34	44904.60	5700	44724.50	955.98

5. Conclusions

A Simulated Annealing implementation for the topological optimization of communication networks design has been presented. Results over several test cases showed the crucial importance of a correct choice of the parameter values to obtain good solutions in a reasonable amount of time.

Furthermore, comparisons with other optimization techniques showed the suitability of the proposed algorithm to solve such problem.

References

- [1] E. Costamagna, A. Fanni, and R. Maestrini, "Connectivity and reliability of telecommunication networks," European Transactions on Telecommunications, vol. 4, no. 6, pp. 723-726, Dec. 1993.
- [2] G. Gallo and S. Pallottino, "Shortest path algorithms," Annals of Operation Research, vol. 13, pp. 3-79, 1988.
- [3] S. Kirkpatrick, C. D. Gelatt and M. P. Vecchi, "Optimization by Simulated Annealing," Science, vol. 220, no. 4598, pp. 671-680, May 1983.
- [4] D. S. Johnson, C. R. Aragon, L. A. Mc Geoch and C. Schevon, "Optimization by Simulated Annealing: an experimental evaluation; Part I, graph partitioning," Operation Research, vol.37, no. 6, pp. 865-892, Nov.- dec. 1989.
- [5] P. J. M. van Laarhoven and E. H. L. Aarts, (1989) "Simulated Annealing: Theory and Applications", Kluwer Academic Publishers, Dordrecht.

- [6] S. Costa, E. Costamagna and A. Fanni, "A heuristic optimization algorithm for multiplexed links telecommunication networks," Technical Report of the Electrical Eng. Inst., University of Cagliari, no. 37, pp. 1-9, May 1990.
- [7] G. Celli, E. Costamagna and A. Fanni, "Genetic algorithms for telecommunication network optimization," Proc. IEEE Int. Conf. on Systems, Man and Cybernetics, Vancouver, Oct. 1995.

ON OPTIMIZATION OF BROADBAND BEAMFORMER FOR HEARING AID APPLICATIONS

A. Wang, F. Lorenzelli, D. Korompis, R. E. Hudson, and K. Yao

E. E. Department, University of California
Los Angeles, CA 90095-1594

ABSTRACT

This paper considers various wideband signal model optimization techniques and associated performance results using steerable fixed beam microphone array processing for hearing aid applications in free-space and reverberant conditions. We first review and compare various conventional broadband and narrowband array optimization techniques. Then new results on maximum energy criterion broadband array optimization formulated for sub-band processing are presented. The uniformly spaced sub-band and the non-uniformly spaced sub-band using quadrature mirror filter approaches are treated. Then algorithms for implementing the hearing aid's search mode base on direction-of-arrival (DOA) estimation techniques for acoustic signals using sub-space methods are discussed. Finally, various simulation results under the maximum energy criterion and DOA estimation for free-space and reverberant conditions are presented to demonstrate the feasibility of the proposed techniques.

1. INTRODUCTION

Speech conversations in a room may be difficult due to several nearby simultaneous speakers, a number of independent noise sources in the background, and reverberation of all these sounds. For the hearing impaired, due to reduced dynamic range and sensitivity in amplitude and frequency, this problem is particularly severe. Direct amplification in a standard hearing aid with a single microphone is useful only in limited situations. It is known that increasing the desired speaker's SNR relative to all other received sound is a meaningful way to increase speech intelligibility. Indeed, in many critical cases near thresholds of intelligibility, a 4-5 dB SNR improvement may lead up to 50% improvement in intelligibility.

A microphone array, with the capability of forming a focused beam toward the desired speaker and possibly rejecting discrete spatial sources and attenuating general background reverberant noises, is a practical and effective method for enhancing the desired SNR. Besides the hearing aid problem, the desired feature of increasing the effective SNR of the speaker in an enclosed environment is also useful to the automatic speech/speaker recognition, the automobile hand-free telephone, and the teleconferencing problems. An array of sensors can be used to spatially and temporally sample an incoming field in order to synthesize an optimum beam pattern. This technique has been used exten-

sively and successfully in many aerospace/avionic direction finding and jammer/interference rejection applications [1] [2] [3]. These problems are modeled by microwave narrowband signals propagating in free-space. In contrast, the speech waveform must be modeled as a wideband signal, considerable amount of reverberation may exist in a typical indoor environment, and near-field effects must be considered. Clearly, microphone array processing based on a narrowband signal model is inadequate. Similarly, a direct application of the simple LMS type adaptive algorithm, known to be quite successful for microwave free-space beamformation applications, is also known to be inadequate for correlated reflections in reverberant room scenarios.

In this paper, we consider and compare various wideband signal model optimization techniques and associated performance results for steerable fixed beam microphone array processing. In Section 2, we first review and compare various conventional broadband and narrowband array optimization techniques. These include the minimization of the output array power subject to desired signal distortion constraint; the maximization of the array gain subject to white noise gain and linear constraints; and maximum energy criterion subject to norm, linear, and quadratic distortion constraints. In Section 3, we present our new results on maximum energy criterion broadband array optimization formulated for sub-band processing. We consider the uniform sub-band as well as the quadrature mirror filter sub-band approaches. In Section 4 we present the feasibility of using coherent signal subspace method to perform DOA estimation for the proposed hearing aid application. In Section 5, we present various simulation results under the maximum energy criterion and DOA estimation for both broadband and sub-band approaches for both free-space and reverberant conditions. A short conclusion is given in Section 6.

2. ARRAY OPTIMIZATION

In this section we review several known array optimization techniques. Consider an array with R sensors, each followed by a FIR filter with L taps. F is the (unnormalized) frequency, $F \in [-1/(2T), 1/(2T)]$ Hz, for a sampling frequency of $1/T$ Hz, while $f \equiv FT \in [-1/2, 1/2]$ is the normalized frequency. The range of look-directions ψ is in the half-hemisphere of $[-\pi/2, \pi/2]$. The desired signal angle and frequency region are given respectively by $\Delta\psi_0$ and Δf_0 , centered around ψ_0 and f_0 . Given a linear array of R sensors placed at locations d_i , $i = 0, \dots, R-1$, with a pla-

This work is partially supported by The House Ear Institute.

nar wave $x(t)$ impinging at angle ψ relative to the normal of the array, the signal received by the i th sensor is denoted by $x_r(t) = x(t - h_r)$, where $h_0 = \eta_0 T$, $h_r \equiv \eta_r T = h_0 + (d_r/c) \sin \psi$, $r = 1, \dots, R-1$. The array response function can then be written as

$$W(f, \psi) = \sum_{r=0}^{R-1} \sum_{\ell=0}^{L-1} w_{r\ell} e^{-j2\pi f(\ell + \eta_r)} = \mathbf{w}^H \mathbf{E}(f, \psi),$$

where the vectors \mathbf{w} and $\mathbf{E}(f, \psi)$ are defined as follows

$$\begin{aligned} \mathbf{w} &\equiv (w_{00}, \dots, w_{0,L-1}, w_{10}, \dots, w_{1,L-1}, \dots, \\ &\quad w_{R-1,L-1})^H, \\ \mathbf{E}(f, \psi) &\equiv (e^{-j2\pi f \eta_0}, \dots, e^{-j2\pi f(\eta_0 + L-1)}, e^{-j2\pi f \eta_1}, \dots, \\ &\quad e^{-j2\pi f(\eta_1 + L-1)}, \dots, e^{-j2\pi f(\eta_{R-1} + L-1)})^T. \end{aligned}$$

As we see in the following, for most array optimization criteria, we need to compute integrals of the form

$$\mathcal{I}(\Delta f, \Delta \psi) = \int_{\Delta f} \int_{\Delta \psi} |E(f, \psi)|^2 df d\psi.$$

2.1. Review of array optimization techniques

The array response can be optimized to achieve several objectives:

- Maximize the output power over the desired look region $(\Delta f_0, \Delta \psi_0)$ given by $\mathbf{w}^H A \mathbf{w}$, where $A = \mathcal{I}(\Delta f_0, \Delta \psi_0)$.
- Minimize the response to the noise. For fixed array design, if the noise is assumed to be arriving from some noise region $(\Delta f_n, \Delta \psi_n)$, the noise output power can be quantified as $\mathbf{w}^H B \mathbf{w}$, where $B = \mathcal{I}(\Delta f_n, \Delta \psi_n)$. For adaptive array design, the quantity considered is $\mathbf{w}^H R_x \mathbf{w}$, where R_x is the data correlation matrix.
- Minimize the white noise gain, which can be achieved by controlling the quantity $\mathbf{w}^H \mathbf{w}$.
- For broadband arrays, minimize the distortion of the desired signal. This distortion can be quantified by $(\mathbf{w} - \mathbf{w}_d)^H Q (\mathbf{w} - \mathbf{w}_d)$, where \mathbf{w}_d is the weight vector that most closely satisfy the desired look-region response. If the distortion is measured over the whole look region, then $Q = A$. In the next section, the distortion will also be quantified as $\mathbf{w}^H C \mathbf{w}$.
- Satisfy some linear constraints, which can be expressed as $D^H \mathbf{w} = \mathbf{f}$. The constraints can be placed on the the array response function's magnitude, its spatial derivative or its frequency derivative. Linear constraints are useful in cancelling narrowband interferers or to approximate any of the above quadratic forms.

Among the many formulations that have been considered are:

- Minimize the output power subject to constrained desired signal distortion [3]:

$$\min_{\mathbf{w}} \mathbf{w}^H R_x \mathbf{w}, \quad \text{with} \quad (\mathbf{w} - \mathbf{w}_d)^H Q (\mathbf{w} - \mathbf{w}_d) = \epsilon.$$

By using the Lagrange multiplier technique, the solution is given by $\hat{\mathbf{w}} = \lambda_o (R_x + \lambda_o Q)^{-1} Q \mathbf{w}_d$, where λ_o is the root of the equation

$$\mathbf{w}_d^H R_x (R_x + \lambda_o Q)^{-1} Q (R_x + \lambda_o Q)^{-1} R_x \mathbf{w}_d = \epsilon,$$

and can be solved by iterative techniques. It is also possible to impose linear constraints in addition to the above constraints[1].

- Maximize the array gain subject to constraining the norm of the weights and the linear constraints:

$$\max_{\mathbf{w}} \frac{\mathbf{w}^H A \mathbf{w}}{\mathbf{w}^H R_x \mathbf{w}}, \quad \text{with} \quad \mathbf{w}^H \mathbf{w} = \delta \quad \text{and} \quad D^H \mathbf{w} = \mathbf{f}.$$

For a narrowband array of frequency f_0 with a single look-direction, $A = \mathbf{d} \mathbf{d}^H$ where $\mathbf{d} = \mathbf{E}(f_0, \psi_0)$, one of the linear constraint is to ensure unity look direction $\mathbf{w}^H \mathbf{d} = 1$. Then the optimum weight is given by:

$$\mathbf{w} = (R_x + \lambda_o I)^{-1} D (D^H (R_x + \lambda_o I)^{-1} D)^{-1} \mathbf{f},$$

where λ_o is again the Lagrange multiplier. This yields the Minimum Variance Distortionless Response solution.

- Another class of formulation approximates the quadratic constraints by linear constraints. For instance, the constraint to keep $\mathbf{w}^H Q \mathbf{w}$ low can be achieved by taking the eigen-decomposition of the matrix Q :

$$Q = U_Q \Lambda_Q U_Q^H,$$

where $U_Q = [\mathbf{u}_1^Q, \dots, \mathbf{u}_{RL}^Q]$ is unitary and $\Lambda_Q = \text{diag}(\lambda_1^Q, \dots, \lambda_{RL}^Q)$, $\lambda_1^Q \geq \lambda_2^Q \geq \dots \geq \lambda_{RL}^Q \geq 0$. The constraint $\mathbf{w}^H Q \mathbf{w} < \epsilon$ corresponds to

$$(\mathbf{w}^H U_Q) \Lambda_Q (U_Q^H \mathbf{w}) = \sum_{i=1}^{RL} |\mathbf{w}^H \mathbf{u}_i^Q|^2 \lambda_i^Q < \epsilon.$$

By imposing $\mathbf{w}^H \mathbf{u}_i^Q = 0$, $i = 1, \dots, N_e$, where $N_e < RL$, we achieve $\mathbf{w}^H Q \mathbf{w} \leq \lambda_{N_e+1}^Q \|\mathbf{w}\|^2$.

2.2. Maximum Energy Array

The Maximum Energy Array (ME) criterion is as follows:[6]

$$\max_{\mathbf{w}} \frac{\mathbf{w}^H (A - \alpha C) \mathbf{w}}{\mathbf{w}^H (B + \sigma I) \mathbf{w}}, \quad \text{subj. to} \quad \mathbf{w}^H \mathbf{w} = 1 \quad \text{and} \quad D^H \mathbf{w} = \mathbf{0},$$

where α is the distortion controlling parameter and σ is the white noise controlling parameter. Equivalently, the norm constraint can be replaced by any quadratic constraint of the form $\mathbf{w}^H B \mathbf{w} = \epsilon$, just by scaling the weight vector. We note the following features of this approach:

- If the direction of interferer is unknown, then B is replaced by the matrix of isotropic noise field. For the adaptive case, B is replaced by the data correlation matrix R_x .

- The distortion is quantified by

$$\mathbf{w}^H \mathbf{C} \mathbf{w} = \int_{\Delta f_0} \int_{\Delta f_0} |\mathbf{w}^H (\mathbf{E}(f, \psi) - \mathbf{E}(f_0, \psi))|^2 df d\psi.$$

By choosing the appropriate value of α , the distortion can be controlled.

- The white noise gain, $\mathbf{w}^H \mathbf{w} / \mathbf{w}^H \mathbf{d} \mathbf{d}^H \mathbf{w}$, can be controlled by selecting the value σ .
- The linear constraints are used to impose zero constraints only. We can eliminate the linear constraints, by using the subspace orthogonal to the subspace spanned by the columns of D . If P_C is the $(RL) \times N_C$ matrix whose columns span the orthogonal subspace, the above maximization problem becomes

$$\max_{\mathbf{w}} \frac{\bar{\mathbf{w}}^H (P_C^H (A - \alpha C) P_C) \bar{\mathbf{w}}}{\bar{\mathbf{w}}^H (P_C^H (B + \sigma I) P_C) \bar{\mathbf{w}}}, \text{ subj. to } \bar{\mathbf{w}}^H \bar{\mathbf{w}} = 1,$$

where $\bar{\mathbf{w}}$ has N_C components, and $\mathbf{w} = P_C \bar{\mathbf{w}}$.

The optimum weight can be found as the generalized eigenvector corresponding to the largest eigenvalue of the problem $P_C^H (A - \alpha C) P_C \bar{\mathbf{w}} = \lambda P_C^H (B + \sigma I) P_C \bar{\mathbf{w}}$. Let $P_C^H (B + \sigma I) P_C = L L^H$, where L is a lower triangular matrix. Then the corresponding symmetrical eigenvalue problem is

$$\lambda \bar{\mathbf{w}} = L^{-1} P_C^H (A - \alpha C) P_C L^{-H} \bar{\mathbf{w}}.$$

Then $\bar{\mathbf{w}} = L^{-H} \hat{\mathbf{w}}$ and the weight vector is given by $\mathbf{w} = P_C L^{-H} \hat{\mathbf{w}}$.

If the matrix $(A - \alpha C)$ is positive definite, then the largest eigenvalue and the corresponding eigenvector can be found by using the power method. Otherwise, the Simultaneous Iterative Method [2] must be used.

3. SUB-BAND OPTIMIZATION TECHNIQUES

So far we have dealt with the broadband optimization problem over the entire speech frequency range. Now consider splitting the band into a number of adjacent subbands. The goal is to split the general problem into a number of subproblems, so that they will be less computationally demanding. Moreover, the task of locating the desired source and/or discrete interferers is much less challenging when the signals are narrowband. We shall show that the optimization cannot be reduced to a number of independent problems, since some global constraints have to be imposed in order to minimize signal distortion for enhancing intelligibility.

3.1. Uniform subbands

Consider Fig. 1, which displays a general scheme for subband processing of sensor arrays. Let us assume the K subbands are of uniform width, and define the k th subband as $\Phi_k \equiv [-(k+1)/(2K), -k/(2K)) \cup [k/(2K), (k+1)/(2K))$, $k = 0, \dots, K-1$. The signal at the output of the r th sensor, $r = 0, \dots, R-1$, is $x_r(nT) = x_0(nT + \eta_r T)$, $\eta_r = d_r \sin \psi / (cT)$, and its Fourier transform is denoted by $X_r(f) = X_0(f) e^{-j2\pi f \eta_r}$, $f \in [-1/2, 1/2]$. This signal is subsequently filtered by the K input subband filters $\tilde{G}_k(f)$,

$k = 0, \dots, K-1$. Each of these signals is downsampled by an integral factor $K_1 \leq K$ and passes through an L_k -tap FIR filter with coefficients $w_{r\ell k}$, $\ell = 0, \dots, L_k-1$ and transfer function $W_{rk}(f) = \sum_{\ell=0}^{L_k-1} w_{r\ell k} e^{-j2\pi f \ell}$. All the weighted signals at subband k are then added together, upsampled by a factor of K_1 , and filtered by the output subband filter, $G_k(f)$. Finally, at the output of subband k , we have the signal

$$Y_k(f, \psi) = \frac{G_k(f)}{K_1} \sum_{r=0}^{R-1} \sum_{m=0}^{K_1-1} W_{rk}(K_1 f) \tilde{G}_k(f + \frac{m}{K_1}) X_r(f + \frac{m}{K_1}).$$

In the desirable case where $G_k(f) \tilde{G}_k(f) = 1$, $G_k(f) \tilde{G}_k(f + m/K_1) = 0$, for $f \in \Phi_k$ and $m = 1, \dots, K_1-1$, then no aliased replicas of the signal are present at the output, and $Y_k(f, \psi)$ can be written simply as

$$Y_k(f, \psi) = \frac{1}{K_1} \sum_{r=0}^{R-1} W_{rk}(K_1 f) e^{-j2\pi f \eta_r} X_0(f),$$

for $f \in \Phi_k$. Note that due to the nonzero roll-off of the filters $G_k(f)$ and $\tilde{G}_k(f)$, the output $Y_k(f, \psi)$ contains contributions from frequencies outside the band Φ_k . The transfer function relative to subband Φ_k is given by

$$W_k(f, \psi) \equiv \frac{Y_k(f)}{X_0(f)} = \frac{1}{K_1} \sum_{r=0}^{R-1} \sum_{\ell=0}^{L_k-1} w_{r\ell k} e^{-j2\pi K_1 f \ell} e^{-j2\pi f \eta_r}.$$

For a uniform linear array where $\eta_r = rd \sin \psi / (cT)$,

$$W_k(f, \psi) = \frac{1}{K_1} \sum_{r=0}^{R-1} \sum_{\ell=0}^{L_k-1} w_{r\ell k} e^{-j2\pi r f d \sin \psi / (cT)} e^{-j2\pi K_1 \ell f},$$

for $f \in \Phi_k$. Note that the choice of $K_1 < K$ has the effect of relaxing the requirements on the input and output subband filters, $\tilde{G}_k(f)$ and $G_k(f)$, respectively.

For each of the K subbands, we can define matrices A_k and B_k as follows:

$$A_k \equiv \int_{\Phi_k \cap \Delta f_0} \int_{\Delta f_0} \mathbf{E}(f, \psi) \mathbf{E}(f, \psi)^H df d\psi,$$

$$B_k \equiv \int_{\Phi_k} \int_{[-\pi/2, \pi/2]} \mathbf{E}(f, \psi) \mathbf{E}(f, \psi)^H df d\psi,$$

for $k = 0, \dots, K-1$. Now, let

$$B_0 = \cup_k \{\Phi_k : \Phi_k \cap \Delta f_0 \neq \emptyset\}, \quad K_0 = \{k : \Phi_k \subseteq B_0\}.$$

In other words, B_0 is the union of all those subbands that intersect the frequency band, Δf_0 , of interest, while K_0 is the set of indices corresponding to the subbands in B_0 . Let β be defined as

$$\beta = \frac{\sum_{k \in K_0} \mathbf{w}_k^H A_k \mathbf{w}_k}{\sum_{\text{all } k} \mathbf{w}_k^H B_k \mathbf{w}_k}$$

$$= \frac{\sum_{k \in K_0} \mathbf{w}_k^H A_k \mathbf{w}_k}{\sum_{k \in K_0} \mathbf{w}_k^H B_k \mathbf{w}_k + \sum_{k \notin K_0} \mathbf{w}_k^H B_k \mathbf{w}_k}.$$

A first observation is that, in general, local optimization on each subband separately does not achieve the maximum β . Moreover, it is clear from the above expression for β , that when there are no non-zero constraints outside B_0 , then we can limit ourselves to the subbands that do overlap with Δf_0 , and put $w_k = 0$, $k \notin K_0$. In this case, the problem becomes

$$\max \frac{\sum_{k \in K_0} w_k^H A_k w_k}{\sum_{k \in K_0} w_k^H B_k w_k},$$

$$\text{subj. to } \begin{cases} D_k^H w_k = f_k, \\ \sum_{k \in K_0} w_k^H C_k w_k < \epsilon, \end{cases} \text{ where } k = 0, \dots, K-1.$$

Alternatively, the problem can be posed as

$$\max \frac{w^H A w}{w^H B w} \quad \text{subj. to } \begin{cases} D^H w = f, \\ w^H C w < \epsilon, \end{cases}$$

where now the matrices A , B , and C are block diagonal, with k th block equal to A_k , B_k , and C_k , respectively, and w is given by the stack of the $|K_0|$ vectors w_k , $k \in K_0$. This formulation allows us to obtain an interesting result which warns us against a direct maximization of β , which does not include global constraints of no distortion. Assume that we want to solve the maximization problem, where now we impose all the constraints locally on all the subbands. Following the general technique described earlier, we project all the matrices A_k and B_k onto a subspace orthogonal to the constraint space. But we apply the projections *separately*, for each subband. In other words, we have transformed the matrices A_k and B_k , $k = 0, \dots, K-1$, into $\bar{A}_k = P_k^H A_k P_k$ and $\bar{B}_k = P_k^H B_k P_k$, respectively, where P_k is the matrix whose columns are a basis for the subspace orthogonal to the constraint space for that subband. Then our maximization problem becomes the unconstrained problem

$$\max \frac{\sum_{k \in K_0} w_k^H \bar{A}_k w_k}{\sum_{k \in K_0} w_k^H \bar{B}_k w_k}.$$

As we discussed earlier, this is equivalent to finding the largest generalized eigenvalue and corresponding eigenvector for the matrix pencil $\bar{A} - \lambda \bar{B}$, where $\bar{A} = \text{diag}(\bar{A}_0, \dots, \bar{A}_{K-1})$, $\bar{B} = \text{diag}(\bar{B}_0, \dots, \bar{B}_{K-1})$. Also, let $\lambda_{\max}(\bar{A}_k, \bar{B}_k)$ be the largest generalized eigenvalue of the pencil $\bar{A}_k - \lambda \bar{B}_k$. The surprising result is that

$$\lambda_{\max}(\bar{A}, \bar{B}) = \max_{k=0, \dots, K-1} \lambda_{\max}(\bar{A}_k, \bar{B}_k) \equiv \lambda_{\max}(\bar{A}_{\bar{k}}, \bar{B}_{\bar{k}}),$$

and therefore the corresponding generalized eigenvector corresponds to having all the weights equal to zero except for subband \bar{k} . The maximum value for β is clearly obtained by picking the subband with the highest "average SNR", $\beta_k \equiv \lambda_{\max}(\bar{A}_k, \bar{B}_k)$, and putting to zero the weights in all the other subbands. Indeed, if we had performed local optimization on each subband, we would have obtained generally nonzero weights everywhere, and a β_{avg} given by

$$\beta_{\text{avg}} = \frac{\sum_{k=0}^{K-1} \gamma_k \lambda_{\max}(\bar{A}_k, \bar{B}_k)}{\sum_{k=0}^{K-1} \gamma_k},$$

which is smaller than $\lambda_{\max}(\bar{A}, \bar{B})$, for any set of weights $\{\gamma_k\}_{k=0}^{K-1}$. The danger of having only one "active" subband

is that the distortion may be intolerable. The solution to this problem clearly is to extend no-distortion (or flatness) constraints to the set of subbands of interest.

3.2. Using quadrature mirror filters

Quadrature mirror filters (QMFs) have encountered a wide range of image and speech applications due to the remarkable properties and relative ease of implementation of the multiresolution analysis capability. [7]. In this section, our aim is to explore the possibility of using QMF pairs for subband array processing.

Let $\tilde{H}_0(f)$ and $H_0(f)$ be the decomposition/reconstruction low pass filter pair, and $\tilde{H}_1(f)$ and $H_1(f)$ be the corresponding high pass filter pair. We assume that the conditions for perfect reconstruction are satisfied. In particular, we assume that

$$|H_0(f)\tilde{H}_0(f) + H_1(f)\tilde{H}_1(f)| = 2,$$

$$|H_0(f)\tilde{H}_0(f+1/2) + H_1(f)\tilde{H}_1(f+1/2)| = 0.$$

Consider a one-level decomposition. At the output of the filter $\tilde{H}_k(f)$, $k = 0, 1$, we have signals

$$X_{rk}(f) = \tilde{H}_k(f)X_r(f), \quad r = 0, \dots, R-1.$$

Analogously to the uniform subband approach, these signals are subsequently downsampled by 2 and passed through L_k -tap FIR filters, with coefficients $w_{r\ell k}$, $\ell = 0, \dots, L_k-1$, $k = 0, 1$, and transfer function $W_{rk}(f)$. The weighted signals pertaining to the same subband, $k = 0$ or 1 , are added together and then upsampled by 2. After filtering by $H_k(f)$, $k = 0, 1$, we have that the output of subband k is given by

$$Y_k(f, \psi) = \frac{1}{2} H_k(f) * \sum_{r=0}^{R-1} W_{rk}(2f) (\tilde{H}_k(f)X_r(f) + \tilde{H}_k(f+1/2)X_r(f+1/2))$$

The output of the array is given by

$$Y(f, \psi) = \frac{1}{2} \sum_{r=0}^{R-1} \left[W_{r0}(2f) \left(H'_0 \tilde{H}'_0 X'_r + H'_0 \tilde{H}'_0 \left(\frac{1}{2} \right) X'_r \left(\frac{1}{2} \right) \right) + W_{r1}(2f) \left(H'_1 \tilde{H}'_1 X'_r + H'_1 \tilde{H}'_1 \left(\frac{1}{2} \right) X'_r \left(\frac{1}{2} \right) \right) \right] =$$

$$(H'_0 \tilde{H}'_0 W'_0(f, \psi) + H'_1 \tilde{H}'_1 W'_1(f, \psi)) X'_0$$

$$+ \left(H'_0 \tilde{H}'_0 \left(\frac{1}{2} \right) W''_0(f, \psi) + H'_1 \tilde{H}'_1 \left(\frac{1}{2} \right) W''_1(f, \psi) \right) X'_0 \left(\frac{1}{2} \right),$$

where

$$H'_0 = H_0(f), \quad H'_1 = H_1(f), \quad H'_0 \left(\frac{1}{2} \right) = H_0 \left(f + \frac{1}{2} \right),$$

$$H'_1 \left(\frac{1}{2} \right) = H_1 \left(f + \frac{1}{2} \right), \quad X'_r = X_r(f), \quad X'_0 = X_0(f),$$

$$W'_0(f, \psi) = \frac{1}{2} \sum_{r=0}^{R-1} W_{r0}(2f) e^{-j2\pi f d_r \sin \psi / (cT)},$$

$$W'_1(f, \psi) = \frac{1}{2} \sum_{r=0}^{R-1} W_{r1}(2f) e^{-j2\pi f d_r \sin \psi / (cT)},$$

$W_0''(f, \psi) = W_0'(f + 1/2, \psi)$, $W_1''(f, \psi) = W_1'(f + 1/2, \psi)$. In only two cases aliasing is completely rejected. Either the filters $H_0(f)$ and $H_1(f)$ are ideal half-band filters, or $W_0''(f, \psi) \equiv W_1''(f, \psi)$. Neither situation is desirable, unless the condition $W_0''(f, \psi) \equiv W_1''(f, \psi)$ is imposed for one specific look direction ψ . With $\psi = 0$, this condition translates into

$$\sum_{r=0}^{R-1} W_{r0}(2f) = \sum_{r=0}^{R-1} W_{r1}(2f) \Rightarrow \sum_{r=0}^{R-1} w_{r\ell 0} = \sum_{r=0}^{R-1} w_{r\ell 1}.$$

The above implies that when the filter pairs $(\tilde{H}_0(f), H_0(f))$ and $(\tilde{H}_1(f), H_1(f))$ satisfy the perfect reconstruction condition, but are not ideal low (high) pass filters, it is still possible to achieve no aliasing for a given look direction. At $\psi = 0$, the array behaves as a perfectly linear filter, with a transfer function

$$W(f, 0) = \frac{Y(f, 0)}{X_0(f)} = W_0'(f, 0) = \frac{1}{2} \sum_{r=0}^{R-1} W_{r0}(2f).$$

Note that in this situation $W_{r0}(2f)$ has the period of $1/2$ and therefore it has identical behavior on $f \in [0, 1/2)$ and $f \in [1/2, 1)$, thus limiting our ability to shape the spectrum of $Y(f, \psi)$. This set of weights can be appropriately chosen to impose flatness on all the frequency range for the given look direction.

Consider now a two-level decomposition. The lowpass branch splits into two branches, respectively characterized by weight transfer functions $W_{r00}(f)$ and $W_{r01}(f)$. Note that we have slightly changed our notation, since now we identify the subbands with binary subscripts. For two-level decompositions, subscripts 1, 01, and 00, correspond to $k = 0$, $k = 1$, and $k = 2$, respectively. The global output is $Y(f, \psi) = Y_0(f, \psi) + Y_1(f, \psi)$. As before, we have

$$Y_1(f, \psi) = \frac{1}{2} H_1(f) \sum_{r=0}^{R-1} W_{r1}(2f) * [\tilde{H}_1(f) X_r(f) + \tilde{H}_0(f + 1/2) X_r(f + 1/2)].$$

For $Y_0(f, \psi)$, an analogous expression holds,

$$Y_0(f, \psi) = \frac{1}{2} H_0(f) \sum_{r=0}^{R-1} W_{r0}(2f) * [\tilde{H}_0(f) X_r(f) + \tilde{H}_0(f + 1/2) X_r(f + 1/2)],$$

where now $W_{r0}(f) = W_{r00}(2f)A_0(f) + W_{r01}(2f)A_1(f)$, and

$$A_0(f) = \frac{1}{2} H_0(f) [\tilde{H}_0(f) + \tilde{H}_0(f + 1/2)],$$

$$A_1(f) = \frac{1}{2} H_1(f) [\tilde{H}_1(f) + \tilde{H}_1(f + 1/2)].$$

It follows that the above equations are still valid. In particular, if one imposes the previous condition with equal weight transfer function, one finds that

$$\sum_{r=0}^{R-1} W_{r01}(f) = \sum_{r=0}^{R-1} W_{r00}(f), \quad \sum_{r=0}^{R-1} W_{r1}(f) = \sum_{r=0}^{R-1} W_{r00}(2f).$$

All of the previous equations can be directly extended to the case of multiple level decompositions, in an iterative manner.

Together with the no-aliasing conditions, the weights in each subband have to satisfy a set of additional conditions. When a discrete interferer at angle direction ψ_I has to be cancelled, a set of two constraints per subband has to be generated, each set cancelling both the interferer itself and its aliased image. For the case of a two-level decomposition, the following constraints must be satisfied

$$\sum_{r=0}^{R-1} W_{rb}(\mu_b f) e^{-j2\pi f d_r \sin \psi_I / (cT)} = 0, \quad b = 1, 01, 00,$$

with $\mu_1 = 2$, $\mu_{00} = \mu_{01} = 4$. A condition that ensures flatness of the frequency response for a given look direction has to be added. Then the constraint must be imposed on $W(f, 0) = \sum_{r=0}^{R-1} W_{r0}(2f)$.

The difficulty in dealing with the QMF-based subband approach is that the overall output is not a linear function of the input, due to the operations of down and upsampling. In the case where the decomposition/reconstruction filters are not ideal half-band filters, and the weights on each branch are different, the output is always affected by aliased versions of the signal. A possible strategy for achieving maximum energy concentration in the range of look directions of interest is to maximize the energy content in the angle range $\Delta\psi_0$, of the non-aliased component of the signals at the output of the weighting filters, $W_{rb}(f)$ ($b = 00, 01, 1$ for the two-level decomposition case), for one or (preferably) more frequencies within Δf_0 .

4. DOA ESTIMATION BY SUBBAND APPROACH

There is much recent interest in DOA estimation for broadband signals [9]. It is known that subspace DOA techniques such as MUSIC work efficiently when the signals are narrowband. The narrowband assumption is based on the product of the bandwidth B , and the propagation time through the array T , satisfying $BT \ll 1$. The traditional narrowband approach is based on the particular structure of the correlation matrix of the signals output from the R antennas. If \mathbf{x}_t is the $R \times 1$ vector of outputs at time t , then the correlation matrix, \mathcal{R}_x , is given by

$$\mathcal{R}_x = E\{\mathbf{x}_t \mathbf{x}_t^H\} = \mathcal{A} \mathcal{R}_s \mathcal{A}^H + \sigma_N^2 \mathbf{I},$$

where \mathcal{A} is the $R \times D$ steering matrix, \mathcal{R}_s is the $D \times D$ correlation matrix of the D impinging signals, and the noise is assumed white Gaussian with variance σ_N^2 . If \mathcal{A} is full rank and the SNR is sufficiently high, then \mathcal{R}_x has numerical rank equal to D , the number of impinging signals. The estimated DOA are then obtained by computing the noise subspace of \mathcal{R}_x , deriving the steering vectors orthogonal to it, and exploiting the one-to-one relationship between the steering vector and DOA parameters. In practical applications, the correlation matrix is estimated from the sample correlation matrix

$$\hat{\mathcal{R}}_{x,t} = \frac{1}{N} \mathbf{X}_t \mathbf{X}_t^H,$$

where X_t is the $R \times N$ matrix defined as $X_t = (x_{t-N+1}, x_{t-N+2}, \dots, x_t)$.

The above derivation is highly dependent upon the narrowband assumption. In fact, if the signals are not narrowband, the matrix R_x is always full-rank. Among the proposed approaches, is the so-called coherent signal subspace method (CSSM), and its variants. In this method, the broadband signals are first decomposed into a number of narrowband components, via pre-filtering, subsequently all the components are *focused* onto a predefined center frequency, and then a MUSIC-like algorithm is applied to the combined focused correlation matrices. Techniques such as CSSM are characterized by a rather high computational complexity. In the application of interest for a real-time DSP-based microphone array, it is necessary to keep the complexity to a minimum, without giving up the properties of the narrowband MUSIC algorithm. The technique used here is therefore summarized as follows: 1) the arriving broadband signals are filtered and decomposed into narrowband components; 2) the narrowband MUSIC algorithm is independently applied to each subband; 3) the number of signals and corresponding DOA's are estimated by using those highest subbands with sufficient energies capable of yielding the desired fine spatial resolutions.

5. PERFORMANCE — SIMULATION RESULTS

In this section, we present several simulation results for ME array designs as well as DOA estimations based on subband MUSIC approach for both free-space and reverberant conditions.

5.1. SNR measurement

Previous work in speech quality measurement [8] has shown the objective *segmental* SNR expression tracks well with subjective measurement of the quality of the coded speech waveforms. For hearing aid applications, we use a slightly modified expression defined as the *averaged* ΔSNR and given by

$$\Delta\text{SNR}^{\text{avg}} = \frac{1}{M} \sum_{m=0}^{M-1} \text{SNR}_{\text{out}}^m - \frac{1}{M} \sum_{m=0}^{M-1} \text{SNR}_{\text{in}}^m \quad (\text{dB}),$$

where $\text{SNR}_{\text{in}} = 20 \log_{10} \|x_s\|_2 / \|x_i\|_2$ (dB), $\text{SNR}_{\text{out}} = 20 \log_{10} \|y_s\|_2 / \|y_i\|_2$ (dB), and M is the number of short segments of the speech.

5.2. Conventional broadband simulation

Now, we investigate the relationship between the energy concentration index β and various linear constraints (magnitude, frequency derivative, and spatial derivative) imposed on the array. The simulation program generates impulse responses from the sources (speaker and interferer) to each microphone of the array using cubic interpolation to implement spatial propagation delays[4, 5]. A typical medium size reverberant room of size $5 \times 5 \times 2.48$ meter³ is modeled to have equal reflection coefficients of $\rho = 0.5$ for all six sides. Furthermore, we assume the desired and

the single interferer sources are both 1.8 meters from the center of the array and the image model of the room has perfect reflection of order three. The desired speaker is at angle $\psi_0 = 0^\circ$, the interferer is at angle $\psi_I = 50^\circ$, and the energy concentration region is given by $\Delta\psi_0 = \{\psi_s \pm 15^\circ\}$. Table 1 shows simulations with $R = 4$ sensors and different constraints and tap values. While β only measures the energy concentration in the look-direction with respect to isotropic noises, $\Delta\text{SNR}^{\text{avg}}$ incorporates the effect of the interferer on the array and thus is a good measurement of the improvement factor of the array. As expected, the reverberant performances are inferior compared to the corresponding free-space cases due to additional interferers generated by the reflections from the sides of the room.

5.3. Subband simulation

As shown in Fig. 1, uniform sub-band (USB) array partitions the incoming signals into K sub-bands by using a series of DCT-IDCT band-pass filter banks. Each band is then processed separately through an ME array with weights adjusted such that there is equal spectral response at the mid-point of each band in the desired look direction (i.e., $|W_k(f_{\text{mid}}^k, \psi_0)| = \text{const}$, for $k = 0, \dots, K-1$). Both magnitude and derivative constraints for rejecting the interferer at ψ_I , in the k th sub-band are set at two normalized frequencies f_1^k and f_2^k defined by

$$f_1^k = f_{\text{low}}^k + \frac{1}{4}(f_{\text{high}}^k - f_{\text{low}}^k), \quad f_2^k = f_{\text{low}}^k + \frac{3}{4}(f_{\text{high}}^k - f_{\text{low}}^k),$$

where $f_{\text{low}} = k/2K$, $f_{\text{high}} = (k+1)/2K$, $f_{\text{mid}} = (f_{\text{low}} + f_{\text{high}})/2$, such that the constraints are equally distributed in the speech band of interest as shown in Fig. 2a. We also find that the USB array has flatter look-direction response and also deeper null which results in better overall rejection than the conventional ME array response shown in Fig. 2b. In Table 2, both the conventional ME and USB arrays have $R = 4$ sensors, $L = 20$ taps, with the same array concentration region, speaker and interferer angle and distance relationships. An USB of $K = 8$ shows an $\Delta\text{SNR}^{\text{avg}}$ improvement as compared to a conventional ME array in free-space and reverberant conditions. We note the USB array is about 3 dB better in free-space and about 2 dB better in reverberant condition than the corresponding ME array. Furthermore, by comparing the attenuation of the interferer in Fig. 2 (computed from a far-field model) with Table 2 (obtained from simulation with a near-field model), we see the incomplete cancellations in Table 2 show the sensitivity of the interferer rejection due to the violation of the plane wave assumption. Better rejection can also be achieved by better matching the zero-constraints to the interferer spectrum through narrower and deeper nulls within each sub-band through a frequency decomposition approach. Finally, various HINT speech files [11] calibrated for equal intelligibility measurement¹ have been processed by the ME array for various field testings of human subjects with and without hearing impairments in free-space and reverberant environments. These experiments verify the effectiveness of the array for improving speech intelligibility.

¹Each sentence's RMS power is adjusted depending on its difficulty

5.4. Real room experiment

Here we present a real room experiment² to evaluate the potential performance degradation of performing spatial filtering (beamforming) due to real room environment and microphone array hardware implementation [10]. The system of digital acoustic array is illustrated in Fig. 3 where a large scale uniformly spaced microphone array with 8 omnidirectional elements is mounted on the center of one side of a medium reverberant room. The room size is $3.5 \times 4.7 \times 3 \text{ m}^3$. The desired and interfering sources are modeled by two speech files and are spatially separated by 50° . The cut off frequency is set at 5 kHz while the sampling frequency is set at 20 kHz. The microphone spacing is 16.5 cm and was chosen to perform source location with high resolution. However this distance results in spacial aliasing in the ME criterion for frequency band higher than 2 kHz. The near-field model has been incorporated to simulate the ideal case. The same set of weights is used in both ideal and real-room cases. Fig. 4a shows the waveform containing both sources at the input of the array, while Fig. 4b shows the processed waveform at the output of the array. The improved SNR's are 21.32 dB and 5.7 dB in ideal case and in real-room case respectively. Factors causing this difference are due to background noise, imperfections of array implementation, and room reverberations in the real-room case.

5.5. DOA estimation by CSSM

Lastly, we consider a narrowband MUSIC algorithm for performing DOA estimation of bandpassed broadband speech signals. The simulation results of a eight element array performing CSSM in free space and reverberant room of size $5 \times 5 \times 2.44 \text{ m}^3$. As shown in Fig. 5a, the true speaker DOA denoted by \circ at -60° and the true interferer DOA denoted by \star at $+20^\circ$ are well detected with high resolutions and low biasness by the proposed algorithm in free space. In the reverberant room case as shown in Fig. 5b, we observe the sources are still detected with lower resolutions and greater biasness. This technique requires the number of sources for DOA estimation to be less than the number of array sensors. For spatial aliasing-free requirement, arrays with low sensor spacing become inefficient for DOA estimation base on time-delay correlation techniques. On the other hand, MUSIC algorithm can be extended by using root-MUSIC and near-field MUSIC techniques for enhanced performance.

6. CONCLUSIONS

In this paper we first reviewed and compared the optimization of various fixed beam broadband arrays. Then we considered in some detail a steerable fixed array optimized under the maximum energy criterion. The purpose of this array is to concentrate the main lobe toward the desired signal, while rejecting interferences impinging from different directions. The resulting maximization turns out to be equivalent to a quadratically constrained maximization

problem. Additional constraints are added to further improve the overall performance of the array. We have shown that this optimization procedure provides encouraging results for the design of a microphone array for hearing aid application. Several simulation results are presented and show the usefulness of this scheme in free-space and reverberant environments. We have also explored splitting the frequency band of interest into a number of sub-bands. In particular, we have used the uniformly spaced and QMF sub-band techniques for improved array processing. Preliminary results indicate advantage in using the sub-band MUSIC technique for source locations. Currently, the above considered algorithms are under implementation with HEI for hearing aid pre-processing. Our future goals are to improve existing techniques and to find new challenging applications.

7. REFERENCES

- [1] M.H. Er and S.K. Hui, "Beamforming in Presence of Element Failure", *Electronics Letter*, vol. 27, no. 3, 1991.
- [2] G.H. Golub and C.F. Van Loan, *Matrix Computations*, Johns Hopkins Press, Baltimore, MD, second edition, 1989.
- [3] S. Haykin and A. Steinhardt, edit. *Adaptive Radar Detection and Estimation*, J. Wiley, New York, 1992.
- [4] D. Korompis, K. Yao, and F. Lorenzelli, "Broadband Maximum Energy Array with User Imposed Spatial and Frequency Constraints," *Proc. IEEE ICASSP*, 1994.
- [5] D. Korompis, K. Yao, R. Hudson, and F. Lorenzelli, "Microphone Array Signal Processing for Hearing Aid Applications," *VLSI Signal Processing VII*, IEEE Press, 1994.
- [6] K. Yao, "Maximum Energy Window with Constrained Spectral Values," *Journal of Signal Processing*, 1986.
- [7] A.N. Akansu and R.A. Haddad, *Multiresolution Signal Decomposition*, Acad. Press, 1992.
- [8] H. Cox, R. Zeskind, and M. Owen, "Robust Adaptive Beamforming," *IEEE Trans. on Acous., Speech and Signal Proc.*, 1987.
- [9] A. Paulraj, B. Ottersten, R. Roy, A. Swindlehurst, G. Xu and T. Kailath, "Subspace Methods for Directions-of-Arrival Estimation" *Handbook of Statistics Vol.10*, 1993.
- [10] S. E. Kirtman and H. F. Silverman, "A User-Friendly System for Microphone Array Research" *ICASSP*, 1995.
- [11] M. Nillson, S. D. Soli, and J. A. Sullivan, "Development of the Hearing In Noise Test for the Measurement of Speech Reception Thresholds in Quiet and in Noise" *JASA*, 1994.

²We appreciate the real-time measured data supplied by M. S. Brandstein of Brown University.

Sensors \times Taps	Zero magnitude constraints $[\psi, \omega/(c/d)]$	Zero freq. deriv. constraints $[\psi, \omega/(c/d)]$	Zero spa. deriv. constraints $[\psi, \omega/(c/d)]$	β	$\Delta\text{SNR}^{\text{avg}}$ in free- space (dB)	$\Delta\text{SNR}^{\text{avg}}$ in reverb. room (dB)
4×10	$[70, 0.25]$ $[70, 0.5]$	$[70, 0.25]$ $[70, 0.5]$		0.371	21.56	11.81
4×20	$[70, 0.25]$ $[70, 0.5]$	$[70, 0.25]$ $[70, 0.5]$		0.428	24.56	13.82
4×20				0.701	5.84	3.23
4×20	$[70, 0.25]$ $[70, 0.5]$		$[70, 0.25]$ $[70, 0.5]$	0.288	7.16	6.28

Table 1: Performance values for various arrays and parameters

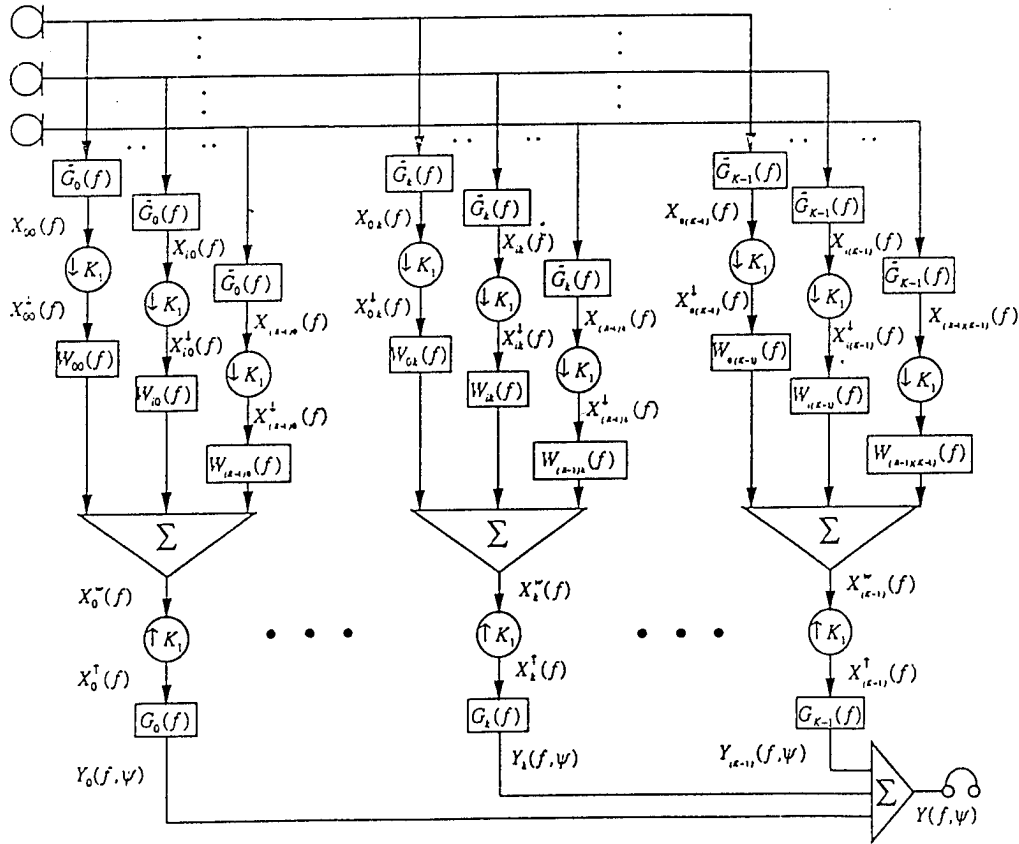


Figure 1: Subband array

$\Delta\text{SNR}^{\text{avg}}$ (dB)	Free-space	Reverberant room
ME array	21.75	10.43
USB array	24.64	12.51

Table 2: $\Delta\text{SNR}^{\text{avg}}$ for two arrays in free and reverberant conditions

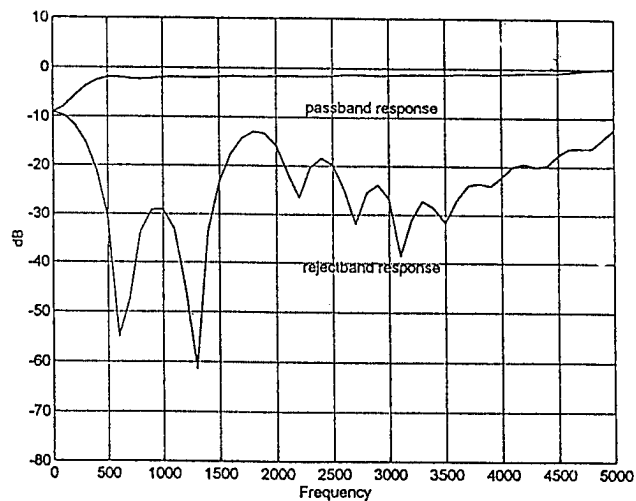
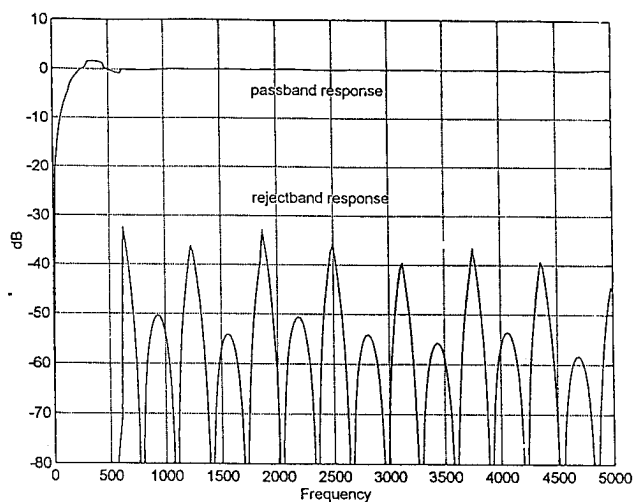


Figure 2: a. $|W(f)|$ of USB b. $|W(f)|$ of ME

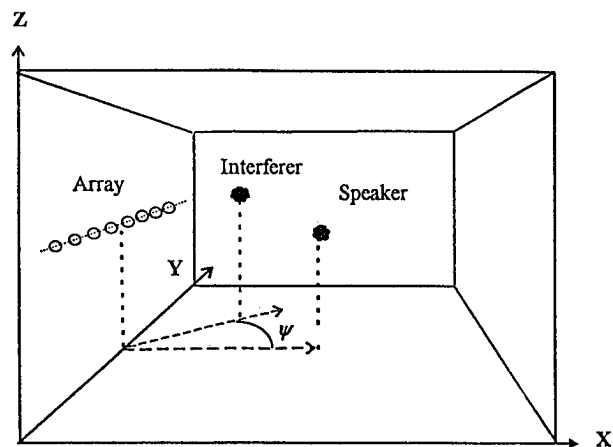


Figure 3: Real Time System Environment

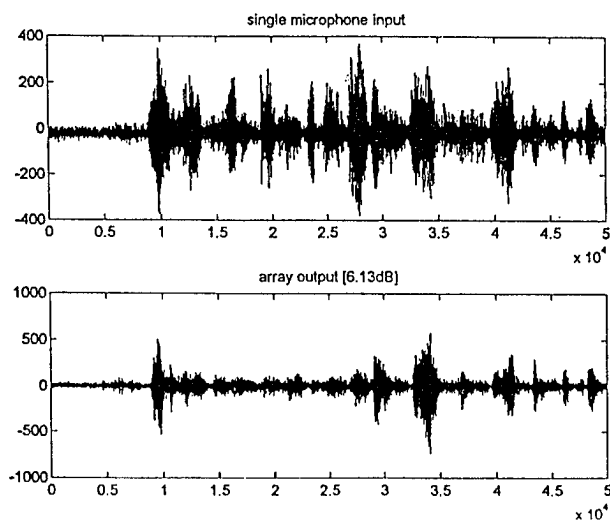


Figure 4: a. array input b. array output

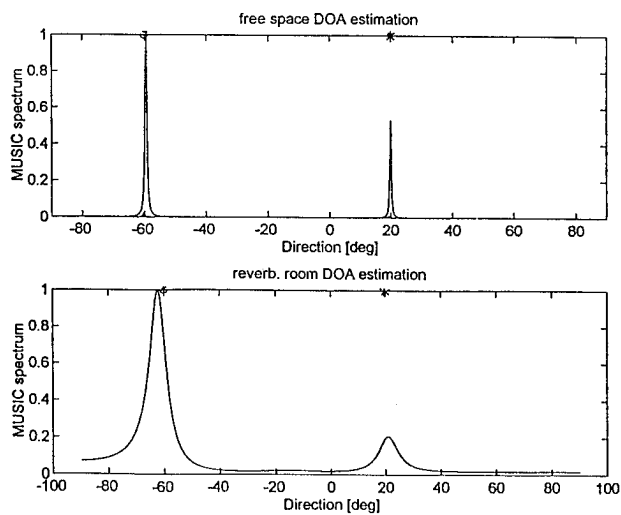


Figure 5: a. free-space DOA b. reverb.-room DOA

PSEUDO-RANDOM TURBO-CODES

Gérard Battail

Ecole Nationale Supérieure des Télécommunications,
Département Communications and URA 820 of CNRS,
46, rue Barrault, F-75634 Paris Cédex 13
e-mail: battail@com.enst.fr

ABSTRACT

Convolutional codes with a distance distribution close to that obtained in the average by random coding are necessarily recursive. We introduce pseudo-random recursive (PRR) codes with a weight distribution which fits well that of random coding, at least in its central part. Decoding these codes is simple only if their free distance is low and thus, the error-event high. However, combining such codes according to the turbo-code scheme may be used to decrease the bit error rate to meet the user's specification.

1. INTRODUCTION

We recently criticized the use of the minimum distance criterion in the search for good long codes. As an expected better criterion, we proposed a similarity measure of the distance distribution of a code with respect to that obtained in the average by random coding [1]. For the sake of brevity, we shall refer to it as "pseudo-random criterion". Some block codes satisfy this criterion, especially the iterated product of single-parity-check codes [1, 2] and the Reed-Solomon codes.

The main objection against applying the minimum distance criterion to long codes is that no account is taken of the proportion of word pairs at the minimum distance. If this proportion is very small, then an error in favour of a word at this distance of the transmitted word is unlikely. The minimum distance criterion appears as exceedingly pessimistic since it is based on the worst case, whose occurrence may be very infrequent. The examples of block codes meeting the pseudo-random criterion, especially the iterated product of single-parity-check codes, actually show that the proportion of codewords of minimum weight is very tiny [2]. Transposing such results to convolutional codes is however not straightforward.

Concerning the relevance of the pseudo-random criterion, it relies on the remark that random coding is asymptotically the best known means since it was used by Shannon to prove the channel capacity theorem. Since the performance of a code only depends on the

distances between its words, a deterministic code with a distance distribution close to that of random coding has similar performance, but its decoding does not demand exhaustive search, at variance with actual random coding [3].

A convolutional encoder generates coded sequences of arbitrarily large length, conveniently dealt with as infinite. The conventional notations thus consist of formal series in the unit-delay operator D which represent sequences with an origin at a finite time, but infinitely extending in the direction of positive indices. However, the performance and properties of conventional convolutional codes do not match those which may be expected from the asymptotic case where the codeword length tends to infinity. Their performance is mainly determined by the free distance and is not very different from that of a block code having this free distance as its minimum distance. On the contrary, the *turbo-codes* exhibit properties and performance in accordance with those which may be expected from a code whose length approaches infinity, especially near-capacity performance [4]. We tried to explain these features as resulting from the *recursivity* of turbo-codes, such that coded sequences of infinite length and weight are associated with finite-weight information sequences, at variance with non-recursive codes [5]. We shall now briefly review these ideas before examining the specific problems of decoding.

2. PSEUDO-RANDOM RECURSIVE CONVOLUTIONAL CODES

The linearity of a convolutional code implies that the set of distances of a codeword with respect to all others does not depend on this word. One may thus assume without loss of generality that the all-0 word was transmitted and study only the distribution of the word weights, for the sake of simplicity. We restrict ourselves to binary rate-1/2 convolutional codes but extensions to other alphabets and rates are straightforward.

The set of sequences generated by a convolutional encoder is conveniently described by a transition

graph where any branch represents a possible transition between states of the encoder, defined as its possible memory contents. Developing this graph in terms of the (discretized) time results in the trellis diagram. Each branch in this graph may be labelled by a monomial $D^w I^u L$ of the indeterminates D, I and L , where w indicates the weight of the corresponding output, u the information bit. The indeterminate L means that including this branch in a path increases its length by one. One usually considers the zero-to-zero transition graph, which describes the set of paths stemming from, and eventually merging again, with state 0. Then, the "transfer function" defined as the formal series

$$T(D, I, L) = \sum_i \sum_j \sum_k a_{ijk} D^{w_i} I^{u_j} L^{l_k} \quad (1)$$

is such that the coefficient a_{ijk} of the general term is the number of paths of weight w_i , corresponding to an information sequence of weight u_j and of length l_k in the zero-to-zero transition graph. One also considers the one-indeterminate transfer function $T(D) \triangleq T(D, I = 1, L = 1)$. Upper bounds on the probability that an erroneous path is chosen by the optimal decoder, as well as on the symbol error probability, can be derived from $T(D)$ and $\partial T(D, I, L = 1)/\partial I$, respectively, by replacing D by a real number depending on the channel (the inverse of the signal-to-noise ratio in the case of additive white Gaussian noise) [6].

Forney has shown that recursive and non-recursive codes are equivalent in the sense that the transfer function $T(D)$ is the same for codes of both types having the same parameters [7]. The free distance, in particular, is the same for both. This result has generally been interpreted as meaning that recursive codes have no particular advantage with respect to non-recursive ones. Forney thus writes: *... in fact feedback buys nothing*. We refute this conclusion, not because it relies on an incorrect result, but because at variance with non-recursive codes the transfer function of the zero-to-zero transition graph fails to properly represent the set of paths associated with a recursive convolutional code. Paradoxically, the very equivalence with respect to the transfer function $T(D)$ is the base of our argument showing that recursive codes outperform non-recursive ones.

When coded sequences are represented by polynomials or formal series of the indeterminate D , the entries of the generator matrix of a non-recursive code are polynomials, whereas those of a recursive code contain rational fractions. Let us for instance consider the systematic recursive encoder of rate 1/2 described by the generator matrix:

$$\mathbf{G} = [1 \quad N(D)/P(D)], \quad (2)$$

where $P(D)$ is a primitive polynomial of degree K and $N(D)$ is a polynomial of degree at most equal to K

(the constraint length of this code is thus $K + 1$). The encoder of such a code constitutes, in the absence of an input information sequence but assuming the encoder initial state to be different from 0, a generator of "maximum length sequences", often referred to as *pseudo-random*, so we shall refer to codes generated by this encoder as pseudo-random recursive (PRR).

Now the sequence of redundancy symbols transmitted in response to an information sequence represented by the polynomial $u(D)$ is $u(D)N(D)/P(D)$. Its development is a formal series when $u(D)N(D)/P(D)$ is a rational fraction, thus for any $u(D)$ non-multiple of $P(D)$, and its weight is then infinite (truncated in practice because one necessarily uses a coded sequence of finite length, but which we may assume to be arbitrarily large); merging with the 0-path never occurs in this case. If, on the contrary, $u(D)$ is a multiple of $P(D)$, this sequence is represented by a polynomial and the corresponding path converges to the 0-path. This case occurs only for a fraction 2^{-K} of all polynomials $u(D)$ of degree at least equal to K . For a non-recursive code, all entries of the generator matrix are polynomials: convergence to the 0-state always occurs.

For a recursive code with K large enough, merging with the 0-path does concern only a small fraction among all the paths, the only ones however which are taken into account by the transfer function $T(D)$. It is easily shown that the lengths of these paths are enumerated by the formal series development of

$$F(L) = \frac{L^{K+1}}{1 - L - L^2 - \dots - L^K} \quad (3)$$

which only depends on the size K of the encoder register, not on a particular code. The coefficient a_n in this formal series is equal to 1 for $n = K + 1$, equal to 2^{n-K-2} for $K + 1 < n < 2(K + 1)$, and smaller than 2^{n-K-2} for a larger value of n .

From the development of (3), a rough upper bound on the number a_n of paths of length n whose weight is enumerated by $T(D)$ is 2^{n-K-1} . The paths which have diverged from the 0-path at the initial instant and reach the node level $K + l$ without having visited the 0 state have a negligible probability of error since their weight increases with l . The source of possible errors then reduces to the set of paths which merge again with the 0-path after they have diverged from it. The number of such paths is less than 2^{l-1} , among a total number of $2^{K+l} - 1$ paths different from the 0-path. The estimates of the error probability based on the transfer function $T(D)$ ignore the other sequences. In order to actually take into account the set of all encoded sequences, they should be multiplied by the fraction of all sequences whose weights are enumerated by $T(D)$, a number less than $2^{l-1}/(2^{K+l} - 1)$. This bound is close to 2^{-K-1} , so the multiplying factor is very small if K is large.

3. DECODING PRR CODES

We now look at the problems of decoding PRR codes. It is well known, and by no means questioned here, that the *infinite* set of sequences generated by a non-recursive encoder and by the corresponding recursive one is the same [7]. For instance, the non-recursive generator matrix corresponding with (2) is

$$G = [P(D) \quad N(D)], \quad (4)$$

which differs only from (2) by the scalar factor $P(D)$. Clearly, it generates only finite-weight sequences in response to finite-weight information sequences. But a generator matrix just specifies the one-to-one mapping which associates the information sequences, which are necessarily in finite number, with a subset of all sequences which may be generated by the encoder. The difference between the non-recursive and the recursive encoders lies in the fact that this subset contains exclusively finite-weight sequences for the former, while it also contains infinite-weight sequences for the latter. Using PRR codes with a large register size K and a primitive polynomial as denominator of the rational fraction in (2) results in the fraction of finite-weight sequences in the subset being arbitrarily small.

The sequences generated by a non-recursive and by a recursive encoder belong to the same set and differ only as regards the probabilities associated to them for a given distribution of the input information sequences. A decoder searches in the infinite set of possibly generated sequences. It will find sequences which would often be generated by a non-recursive encoder, but very unlikely by the recursive equivalent one. One would wish to eliminate such "spurious sequences", but they belong to the infinite set of possible sequences, and two sequences close to each other may belong to this set if the minimum distance is small. From this point of view, the pseudo-random distance distribution property appears as misleading, since it refers to the *statistical* properties of a set of sequences although only a *single* joint realization of an encoded sequence and of the channel noise is available to a decoder.

The properties of PRR codes we described can nevertheless be exploited if the set of possible information sequences $\{u(D)\}$ is restricted to some distinctive subset. One is thus led to a concatenation scheme like the combination of PRR codes according to the turbo-code principle, as proposed in [5]. The pseudo-random distance distribution of the coded sequences is by this means made usable by a decoder. Before starting to describe it, we make a few remarks on decoding PRR codes by a conventional algorithm.

An obvious difficulty comes from the necessarily large size of the encoder memory K , which practically prohibits using the Viterbi algorithm. We realized that an iterated variant of replication decoding

could be used [8]. As for the Viterbi algorithm, decoding is described by a trellis, but the number of states is independent of K . In the simplest case, it equals 2^r , where r is the weight of the polynomial $P(D)$. For certain values of K , there exists a primitive polynomial of minimum weight i.e., $r = 3$, so the number of states is only 8.

Such a small value of r results in a poor error-event probability since the distance between two converging paths in the trellis is small. This distance equals the sum of the weights of $P(D)$ and $N(D)$. We take these two polynomials of same weight in order to keep at decoding a complete symmetry between the information and redundancy bits, so the free distance is $2r$. In case of error, the decoded sequence is the closer to the transmitted one, the smaller the weight of $P(D)$ since then the bit error rate in an erroneously decoded sequence is small. Using a larger value of r would both diminish the error-event probability and increase the bit error rate in case of error, but with an exponential increase of complexity.

Rather than to increase the weight r , we prefer to consider concatenated schemes. The decoded sequence is erroneous with a large probability for a single code but it is not far from the correct one, which is favourable in a concatenated system as will now be discussed.

4. PRR TURBO-CODES

Let us now combine two PRR encoders, of same rate R and memory K , with interleaving so as to make a turbo-code of rate $R' = R/(2 - R)$. One may cursorily analyse this system assuming that the two information sequences entering the encoders are random, equiprobable and independent. This last assumption is obviously false since interleaving makes a one-to-one correspondence between both sequences, but it is admissible inasmuch as it actually plays its expected role of "decorrelation". Then, the two encoders jointly generate a finite-weight coded sequence only if their input sequences are represented both by a polynomial multiple of the corresponding denominator in (2). Assuming independency, the proportion of such cases is raised to the square and thus becomes 2^{-2K} .

We find here the advantage of turbo-codes namely, that combining two short codes conciliates a good performance with the overall simplicity of decoding. Separate decoding of each component code is easy, and weighting the decoded symbols avoids losing information when the output of a decoder is used as the input of the other one. The performance is thus not far from that which would result from a single PRR code of memory twice the one which determines the decoding complexity, but where the specific properties of PRR codes are now taken into account. Indeed, interleaving results in avoiding with a large probability that the re-

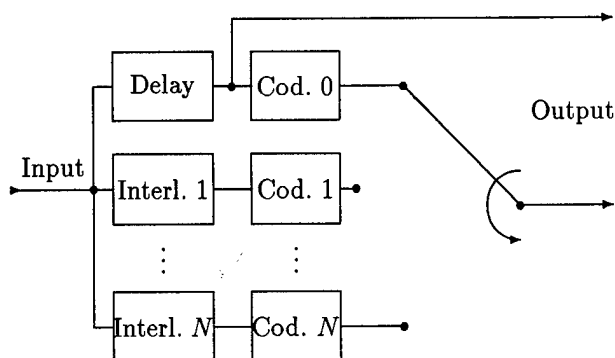


Figure 1: Encoder of a pseudo-random turbo-code of rate $1/2$. The boxes labelled "Cod. 0, Cod. 1, ..., Cod. N " generate the redundancy bits corresponding to the input sequence according to a pseudo-random code of rate $1/2$. The boxes labelled "Entrel. 1, ..., Entrel. N " represent interleavers, the delay of which is compensated for in the box labelled "Delay". Periodic puncturing keeps the rate.

sidual errors of a decoder, which occur according to patterns made of a small-weight multiple of the word of minimum weight, are a defavourable pattern also at the input of the other encoder [9].

We may interpret interleaving as a means for generating redundancy sequences which have as weight distribution the *convolution* of those of the component codes. The weight distribution of the redundancy sequence of a PRR code is close to that of random coding, except in its low-weight tail. The convolution results in little change in the central part of the distribution, but improves its tails since it gets closer to the Gaussian one. The rate decrease is compensated for by periodic puncturing. More than two pseudo-random encoders can be combined in this way, as depicted in Fig. 1, so the performance in terms of bit error rate can be adjusted to the user's specification by increasing N , as the central limit theorem makes its low-weight tail closer and closer to that of random coding.

5. CONCLUSION

Generating long encoded sequences is a necessary condition for near-capacity performance which is met by convolutional codes. Their historical development gave the main role to non-recursive ones, and we believe this was wrong. As could be foreseen from the performance of turbo-codes, the recursive codes, especially the PRR ones, actually outperform the non-recursive ones since they can generate long sequences, the weight distribution of which is very close to that obtained in the average by random coding. Near-capacity performance thus becomes possible. However, the deco-

ders do not deal differently with recursively and non-recursively encoded sequences (which differ only as regards their probability distribution). The information sequences should thus actually belong to some distinctive subset, which enables separating them from the added spurious sequences which result from decoding. One is thus led to concatenation, especially involving two or more PRR codes combined with interleaving according to the turbo-code scheme.

6. REFERENCES

- [1] G. Battail, "Construction explicite de bons codes longs," *Annales Télécommunic.*, Vol. 44, No. 7-8, pp. 392-404, Jul.-Aug. 1989.
- [2] G. Caire, G. Taricco, and G. Battail, "Weight distribution and performance of the iterated product of single-parity-check codes," *GLOBECOM'94, Communication Theory Mini-Conference*, pp. 206-211, San Francisco, U.S.A., Nov. 27-Dec. 1, 1994.
- [3] G. Battail, "We can think of good codes, and even decode them," *Eurocode'92*, Udine, Italy, 26-30 Oct. 1992; P. Camion, P. Charpin and S. Harari, Eds, *CISM Courses and Lectures* No. 339, pp. 353-368, Wien : Springer, 1993.
- [4] C. Berrou, A. Glavieux, and P. Thitimajshima, "Near Shannon Limit Error-Correcting Coding and Decoding : Turbo-Codes," *Proc. of ICC'93*, Geneva, Switzerland, pp. 1064-1070, 23-26 May 1993.
- [5] G. Battail, C. Berrou, and A. Glavieux, "Pseudo-random recursive convolutional coding for near-capacity performance," *Proc. GLOBECOM'93, Communication Theory Mini-Conference*, Vol. 4, pp. 23-27, Houston, U.S.A., Nov. 29-Dec. 2, 1993.
- [6] A.J. Viterbi, "Convolutional codes and their performance in communication systems," *IEEE Trans. on Commun. Tech.*, Vol. COM-19, 751-772, Oct. 1971.
- [7] G.D. Forney Jr, "Convolutional Codes I: Algebraic Structure," *IEEE Trans. Inf. Th.*, Vol. IT-16, No. 6, pp. 720-738, Nov. 1970.
- [8] G. Battail, M. Decouvelaere, and P. Godlewski, "Replication Decoding," *IEEE Trans. Inf. Th.*, Vol. IT-25, No. 3, pp. 332-345, May 1979.
- [9] P. Robertson, "Illuminating the structure of code and decoder of parallel concatenated recursive systematic (turbo) codes", *Proc. GLOBECOM'94*, pp. 1298-1303, San Francisco, U.S.A., Nov. 27- Dec. 1, 1994.

AN AUTOMATIC PROCEDURE TO CONSTRUCT THE OPTIMAL SOFT-DECISION QUANTIZERS AND BRANCH METRICS FOR VITERBI DECODERS

Tan F. Wong, David J. Skellern and L. H. C. Lee

Electronics Department,
School of Mathematics, Computing, Physics and Electronics,
Macquarie University,
NSW 2109 AUSTRALIA

ABSTRACT

In this paper, an automatic procedure is developed to construct the optimal soft-decision quantizer and branch metric, based on the cutoff rate criterion, for the Viterbi decoder over any memoryless channel. As only samples of the received symbols are required, this procedure finds applications in many practical channels.

1. INTRODUCTION

The selection of the soft-decision quantizers and branch metrics are critical issues in the design of high-speed soft-decision Viterbi decoders. For an additive white gaussian noise (AWGN) channel using QAM or MPSK signalling, the optimal branch metric is the Euclidean metric which is usually approximated using integer values in practical high-speed implementations. For soft-decision quantization, the traditional method is to quantize the in-phase and quadrature-phase components separately and uniformly (uniform scalar quantization) [5]. More recently, Parson [3] and Carden [1] suggested that a polar (phase) quantization scheme could be used for MPSK signals. Further, following the practice in uniform scalar quantization, Onyszchuk [2] pointed out that the step size of a uniform quantizer should be adjusted according to the noise power. Parson, Carden and Onyszchuk all based their work on the cutoff rate design criterion put forward by Wozencraft [10] and Massey [7].

All of the quantization schemes and the Euclidean metric above are derived for an AWGN channel. There is no guarantee of their suitability for other kinds of channels. Theoretically, the optimal branch metric can

be determined by calculating the conditional likelihood functions of the received symbols. It is also possible to design soft-decision quantization schemes, similar to those mentioned above, based on the cutoff rate criterion for memoryless channels (as the cutoff rate criterion is derived under the assumption of a discrete memoryless channel, DMC). However both of these require evaluation of the conditional density functions of the received symbols which, apart from a few cases, are extremely hard to obtain analytically. One point worthy of mention about the quantization schemes described above is that all impose fixed configurations on the shapes of the quantization regions, namely, rectangles and sectors. However, this is not an inherent restriction of the cutoff rate criterion, and the success of vector quantization techniques in speech and image compression, suggests that better performance might be achieved by removing the restriction on the configuration of the quantization regions. In this context, better performance means that fewer bits are needed in the branch metric and path metric calculators (Add-Compare-Select processors) in the Viterbi decoder for an acceptable error rate.

In this paper, we develop a practical procedure to automatically determine the optimal soft-decision quantization scheme and branch metric for any memoryless channel. Because the conditional density functions of the received symbols in general are difficult to obtain analytically, it will be assumed that only samples of the received symbols are given. These samples can be obtained easily by experimental measurements or computer simulations. We begin by outlining the cutoff rate design criterion in Section 2. In Section 3, an automatic procedure to determine the soft-decision quantization regions and the branch metrics is described. In Section 4, the procedure described in Section 3 is applied to find the soft-decision quantizers and branch

This work was funded by the CSIRO, Division of Radiophysics, Australia. The authors thank T. M. Percival of CSIRO for useful discussion throughout the investigation.

metrics for both a standard AWGN channel and an asymmetric AWGN channel. Section 4 also presents a comparison of the error-rate performance of the optimal vector quantization schemes and the uniform scalar quantization schemes, obtained by computer simulation.

2. THE CUTOFF RATE CRITERION

A continuous memoryless channel employing coded M -ary QAM or PSK modulation and soft-decision decoding with J quantization regions can be viewed as a M -input J -output DMC. This DMC is completely described by the transition probabilities $P(j|m)$, where $j = 0, 1, \dots, J-1$ and $m = 0, 1, \dots, M-1$. With equally probable input symbols, the cutoff rate, R_0 , of this DMC is given by [6][10],

$$R_0 = \log_2 M - \log_2 \left\{ \frac{1}{M} \sum_{j=0}^{J-1} \left[\sum_{m=0}^{M-1} \sqrt{P(j|m)} \right]^2 \right\} \quad (1)$$

Viterbi [9] showed that when convolutional coding is used with maximum likelihood decoding (Viterbi decoder), the error probability is bounded by,

$$P_e < C_R L 2^{-\nu R_0}, \quad \text{if } R < R_0 \quad (2)$$

where ν is the constraint length of the code, R is the code rate, L is the number of bits encoded and C_R is a constant independent of L and ν . Note that this bound is generally assumed to apply to trellis-coded modulation based on convolutional codes.

Equation (2) implies that the error probability is minimized by maximizing R_0 . Given a memoryless channel, from (1), R_0 depends on the arrangement of the quantization regions of the soft-decision quantizer. Lee [6] observed that maximizing R_0 is equivalent to minimizing S , where

$$S = \sum_{j=0}^{J-1} \left[\sum_{m=0}^{M-1} \sqrt{P(j|m)} \right]^2 \quad (3)$$

Lee worked out a necessary condition for the minimization of S which states that for every point $\mathbf{r} = \rho$ on the boundary of any two adjacent optimal quantization regions, say distinct a and b where $0 \leq a, b < J$, if \mathbf{r} is a point of continuity of conditional density functions $f(\mathbf{r}|m)$ for $0 \leq m < M$ and $P(a|m) \neq 0$ and $P(b|m) \neq 0$ for $0 \leq m < M$, then

$$\sum_{m=0}^{M-1} \left[\frac{1}{\sqrt{P(b|m)}} \sum_{i=0}^{M-1} \sqrt{P(b|i)} - \frac{1}{\sqrt{P(a|m)}} \sum_{i=0}^{M-1} \sqrt{P(a|i)} \right] f(\rho|m) = 0 \quad (4)$$

Lee went on to transform this necessary condition to constraints in a likelihood space and developed an iterative procedure to obtain the optimal quantization regions in that space. The major difficulty in implementing Lee's algorithm is that it is necessary to keep track of the adjacency of the quantization regions during the iterative process and convert the regions in likelihood space back to the signal space after an optimal partitioning of the likelihood space has been found. None of this is easy to implement automatically. Moreover convergence of the iterative process is not guaranteed. In the next section, we modify Lee's condition to allow us to perform the optimization process more easily.

3. THE AUTOMATIC PROCEDURE

Let us first assume that we know the conditional density functions $f(\mathbf{r}|m)$, for $0 \leq m < M$. This is determined by the channel. For $0 \leq j < J$, define

$$D_j(\mathbf{r}) = \sum_{m=0}^{M-1} \left[\frac{1}{\sqrt{P(j|m)}} \sum_{i=0}^{M-1} \sqrt{P(j|i)} \right] f(\mathbf{r}|m) \quad (5)$$

Then it can be shown that S will decrease if for every \mathbf{r} , we assign \mathbf{r} to region a such that

$$D_a(\mathbf{r}) < D_j(\mathbf{r}) \quad , \text{ for all } j \neq a \quad (6)$$

Hence by (6), a simple iterative procedure can be constructed to search for a minimum of S . Note that convergence is guaranteed as S is lower-bounded (see (3), every $P(j|m) \geq 0$).

Following this iterative process, we obtain a map of the optimal quantization regions. The optimal branch metrics (the likelihoods), $B(\cdot|\cdot)$, for the regions can be calculated easily by

$$B(j|m) = -\ln(P(j|m)) \quad (7)$$

for $0 \leq m < M$ and $0 \leq j < J$. For fixed-point implementation of the Viterbi decoder, if we employ the 2's complement roll-over method in the path metric calculator, no rescaling of the path metric is needed. However the maximum value in the branch metric, B_{max} , must be small enough such that

$$\nu B_{max} \leq 2^{n_b-1} + 1 \quad (8)$$

where ν is the constraint length of the code and n_b is the number of bits in the ACS calculator. Then to suit this implementation, the branch metrics in (7) can be linearly scaled and round off to $B'(j|m)$ as in (9).

$$B'(j|m) = \left\lceil \frac{B(j|m) - \min\{B(\cdot|\cdot)\}}{\max\{B(\cdot|\cdot)\} - \min\{B(\cdot|\cdot)\}} B_{max} \right\rceil \quad (9)$$

where $\lceil \cdot \rceil$ denotes rounding to the nearest integer.

As stated in Section 1, we assume that only samples of the received symbols are given. Under this assumption, we replace the conditional density functions required in the iterative process above by estimates obtained via the samples of the received symbols. While any reasonably good density estimation method [see 4] can be used, we adopt the 'pre-whiten' gaussian kernel method [4, pp. 77] in this paper. As in other applications of density estimation, the amount of smoothing introduced is the most important factor to be chosen. In this case, the amount of smoothing affects the retention of detail in the density functions, and hence in the shapes of the quantization regions. It is likely also to affect the rate of convergence of the iterative process.

Summarizing the discussion in this section, the steps of the automatic procedure generating the soft-decision quantization regions and the branch metric are as follows:

1. Obtain estimates of the conditional density functions from samples of the received symbols.
2. Choose an initial map of the quantization regions.
3. Assign each point, \mathbf{r} , in the map according to (6).
4. Calculate S by (3).
5. If the change in S is very small, obtain the map of the optimal quantization regions and go to the next step. Otherwise repeat Step 3.
6. Calculate the branch metric using (7).
7. Rescale the branch metric to integers by (9).

4. COMPUTER SIMULATIONS

In this section, we use the procedure in Section 3 to determine the optimal soft-decision quantizers and the branch metrics for two hypothetical channels, namely, the AWGN channel and the asymmetric AWGN channel. The asymmetric AWGN channel is similar to an AWGN channel, except that noise variance in the in-phase component is nine times of that of the quadrature-phase component. This channel serves as a simple example of one which has significantly different characteristics to an AWGN channel. The optimal branch metric of the asymmetric AWGN channel is not the Euclidean metric and, in fact, it is

$$B(\mathbf{r}|m) = \left(\frac{x - s_x^m}{3} \right)^2 + (y - s_y^m)^2 \quad (10)$$

where $\mathbf{r} = (x, y)$ and $\mathbf{s}^m = (s_x^m, s_y^m)$ are, respectively, the received symbol and the m -th transmitted symbol,

for $0 \leq m < M$. We assume QPSK signals with TCM is employed as shown in Figure 1 and fix the number of quantization regions to 32. Moreover, the number of bits, n_b , in the ACS calculator is set to 7 and this requires B_{max} to be set to 12. Ten thousand samples of the received symbols of the two channels, operating at 5 dB signal-to-noise ratio (SNR) per symbol, are fed to the automatic procedure to find the soft-decision quantization regions and the branch metrics. The maps of the quantization regions for the two channels are given in Figure 2.

Monte-Carlo simulations were performed to estimate the bit error rate performance of the TCM system in Figure 1 using these soft-decision quantizers and the branch metrics for the two channels, respectively. The Viterbi decoder is assumed to have a decision depth of 32. The results are shown in Figure 3(a) and (b) for the AWGN and the asymmetric AWGN channel respectively. Figure 3 also shows results for a system with uniform scalar quantizer (3 bits for each component) and Euclidean metric, and for a system with infinite precision and the optimal branch metric (Euclidean metric for the AWGN channel and the metric from Equation (10) for the asymmetric AWGN channel). From Figure 3(a), the performance of the vector quantizer is basically the same as that of the uniform scalar quantizer, which is about 0.4dB poorer than the unquantized system at a bit error rate of 10^{-4} . This agrees with results reported in [5]. So we save 1 bit by using the vector quantizer. For the asymmetric AWGN channel, the performance of the vector quantizer is much better (about 1.5 dB) than that of the uniform quantizer. In this case, the main reason for the better performance is that the branch metric of the vector quantizer is much closer to the optimal one (Equation (10)) than the Euclidean metric used in the uniform quantizer. This can be seen from Figure 2(b) which shows a map of the vector quantization regions similar to that of a uniform scalar quantizer (i.e. approximate partitioning into rectangular regions).

5. CONCLUSION

In this paper, we have developed for the Viterbi decoder a practical procedure based on the cutoff rate design criterion that determines, automatically, the optimal soft-decision vector quantization regions and the branch metric over any memoryless channel. Only samples of the received symbols are needed and no other prior knowledge of the channel is assumed. Computer simulations indicate that the vector quantizers perform better than their uniform scalar counterparts for both an AWGN channel and an asymmetric AWGN channel.

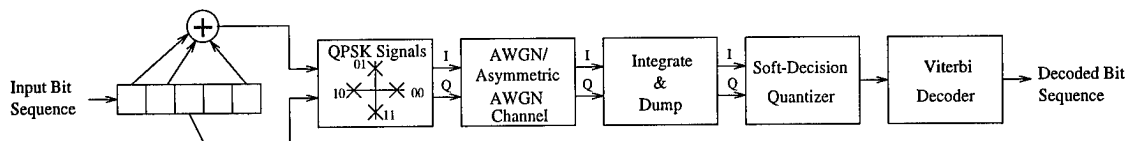


Figure 1: TCM system with soft-decision quantizer

6. REFERENCES

- [1] F. Carden, M. D. Ross, B. T. Koop, and W. P. Osborne, "Fast TCM Decoding: Phase Quantization And Integer Weighting," *IEEE Trans. Commun.*, Vol. 42, No. 2/3/4, pp. 808-812, Feb./Mar./Apr. 1994.
- [2] I. M. Onyszchuk, K. M. Chenug, and O. Collins, "Quantization Loss in Convolutional Decoding," *IEEE Trans. Commun.*, Vol. 41, No. 2, pp. 261-265, Feb. 1993.
- [3] R. D. Parsons, and S. G. Wilson, "Polar Quantization for Coded PSK Transmission," *IEEE Trans. Commun.*, Vol. 38, No. 9, pp. 1511-1519, Sep. 1990.
- [4] B. W. Silverman, *Density Estimation for Statistics and Data Analysis*, London: Chapman and Hall, 1986.
- [5] G. C. Clark, and J. B. Cain, *Error-Correction Coding for Digital Communications*, New York: Plenum Press, 1981.
- [6] L. Lee, "On Optimal Soft-Decision Demodulation," *IEEE Trans. Inform. Theory*, Vol. IT-22, No. 4, pp. 437-444, July 1976.
- [7] J. L. Massey, "Coding and modulation in digital communications," *Proc. Int. Zurich Seminar on Digital Communications*, pp. E2(1)-E2(4), 1974.
- [8] G. D. Forney, "The Viterbi Algorithm," *Proceedings of the IEEE*, Vol. 61, No. 3, pp. 268-278, Mar. 1973.
- [9] A. J. Viterbi, "Error bounds for convolutional codes and an asymptotically optimum decoding algorithm," *IEEE Trans. Inform. Theory*, Vol. IT-13, pp. 260-269, Apr. 1967.
- [10] J. M. Wozencraft, and R. S. Kennedy, "Modulation and demodulation for probabilistic coding," *IEEE Trans. Inform. Theory*, Vol. IT-12, pp. 291-297, July 1966.

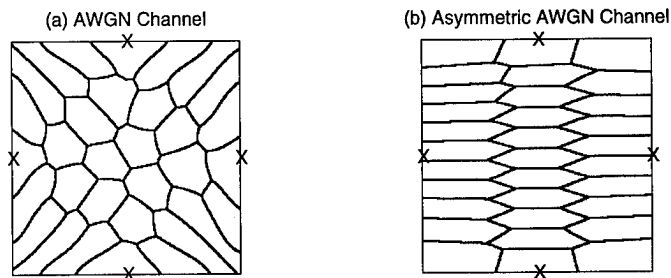


Figure 2: Quantization regions generated by the automatic procedure

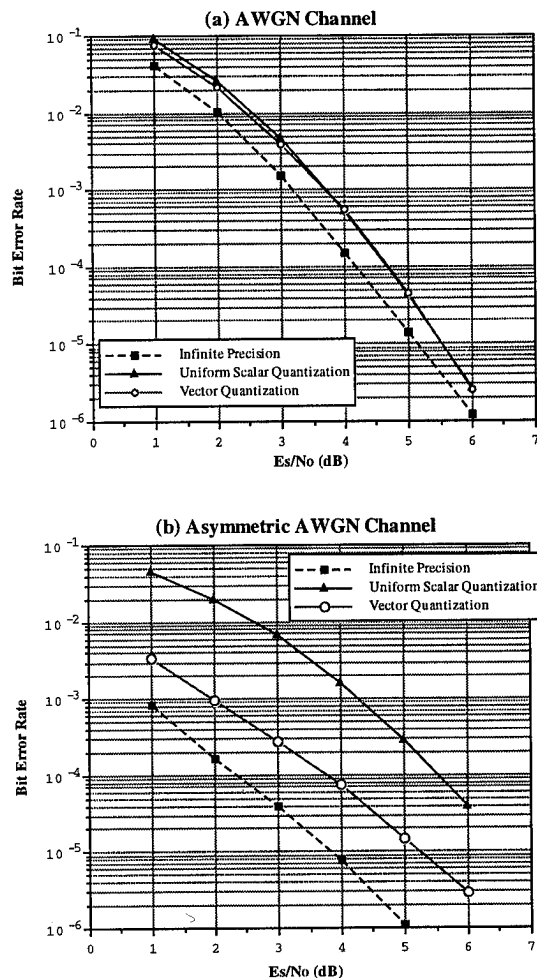


Figure 3: Bit error rate performances

STATE SPACE APPROACH IN TIME-VARYING BIORTHOGONAL FILTER BANKS

Aweke N. Lemma and Ed F. Deprettere

Abstract—Using state space representations of biorthogonal time varying filter banks, it is possible to derive conditions under which the transition between two time-invariant filter banks can be so controlled that both the decomposition filters and the reconstruction functions gently embrace. For a certain domain of filters, the transition interval can be made arbitrarily short. If it is zero, then the special case of instantaneous transition is reached.

I. Introduction

A biorthogonal filter bank (E, R) is a linear expansion of a sequence or signal. Thus if $u \in l_2^P(\mathbb{Z})$,¹ then $u = \sum \langle u, e_n \rangle r_{1,n}$, where e_n and $r_{1,n}$ are the rows and columns of bounded matrix operators E and R , respectively, with $RE = I$, the identity operator. We will assume throughout that e_n and $r_{1,n}$ are of finite lengths, and that E is lower triangular (causal) and R upper triangular (anti-causal). The entries of these operators will be finite dimensional matrices of dimensions $Q \times P$ and $P \times Q$, respectively, with the dimensions possibly time varying and $Q \geq P$. If $Q = P$, then also $RE = I$. If the filter bank is shift-invariant, then E and R are Toeplitz and characterized by the central row e and central column r , respectively. In this case we write $(E(e), R(r))$ instead of (E, R) .

$$E(e) = \begin{bmatrix} \ddots & & & \\ & \boxed{e} & & \\ & & \boxed{e} & \\ & & & \ddots \end{bmatrix} \quad (1)$$

$$R(r) = \begin{bmatrix} \ddots & & & \\ & \boxed{r} & & \\ & & \boxed{r} & \\ & & & \ddots \end{bmatrix} \quad (2)$$

In the context of filter banks, the rows of E are called *filter weight vectors* and the columns of R are called *impulse response vectors*. Moreover, they have the property that, with $F(x)$ the Fourier Transform of x , $F(e)$ and $F(r)$ are uniform spectral decompositions of the base band $[0, \pi]$.

In most applications a single biorthogonal filter bank $(E(e), R(r))$ is used to decompose and reconstruct certain

signals u . However, as most signals are not stationary, it may be expected that time varying filter banks will do a better job, especially when a quantization operator is inserted in between the two bank operators. In the latter case, for example, it is then also necessary to guarantee that the spectral decomposition properties of the time varying filter weight vectors are preserved and also that the time varying impulse response vectors remain good interpolation functions.

In this paper, we find perfect reconstruction filter banks giving signal expansions of the form

$$u = \sum_{n=-\infty}^{n_o-1} \langle u, e_{1n} \rangle r_{1,n} + \sum_{n=n_o}^{n_f-1} \langle u, e_n \rangle r_{1,n} + \sum_{n=n_f}^{+\infty} \langle u, e_{2n} \rangle r_{2,n}$$

where $n_f \geq n_o$, and the e_{1n} and e_{2n} are all shifted versions of e_1 and e_2 , respectively (and similarly for the $r_{1,n}$ and $r_{2,n}$). In other words, the behavior on the segments $[-\infty, n_o - 1]$ and $[n_f, +\infty]$ is shift invariant, whereas the segment $[n_o, n_f - 1]$ is the transition region on which e_n and $r_{1,n}$ have doubly indexed entries. Typically, the objective is to have small transition segment supporting smooth transitions between the stationary segments in both the E and R parts. Except when stated explicitly otherwise, we will have $Q = P$ throughout.

II. State Space Representation

Instead of using input-output maps E and R , the filter bank can also be represented by state space realizations. For the decomposition part E , the state space realization at time instant n maps present input $u(n) \in l_2^P(\mathbb{Z})$ and present state² $x(n) \in l_2^N(\mathbb{Z})$ to present output $y(n) \in l_2^Q(\mathbb{Z})$ and next state $x(n+1)$. Thus, denoting by $m(n)$ this map, we have

$$m(n) : \begin{bmatrix} x(n) \\ u(n) \end{bmatrix} \rightarrow \begin{bmatrix} x(n+1) \\ y(n) \end{bmatrix}$$

where the $(N+P) \times (N+P)$ matrix $m(n)$ is explicitly written as

$$m(n) = \begin{bmatrix} a(n) & b(n) \\ c(n) & d(n) \end{bmatrix} \quad (3)$$

This is shown in Fig.1. Let x represent the state sequence $\{x(n)\}$, $n \in [-\infty, \infty]$. Likewise let $y = \{y(n)\}$ and $u = \{u(n)\}$. Then we can write

$$\begin{bmatrix} Zx \\ y \end{bmatrix} = M \begin{bmatrix} x \\ u \end{bmatrix}$$

²Like P and Q , N (the dimension of $x(n)$) can be time varying.

The authors are with the Department of Electrical Engineering, Delft University of Technology, Delft, The Netherlands. This research was partly supported by Philips Research, The Netherlands.

¹That is, u is a finite energy sequence or column vector with P -dimensional column vector entries $u(n)$, $n \in \mathbb{Z}$.

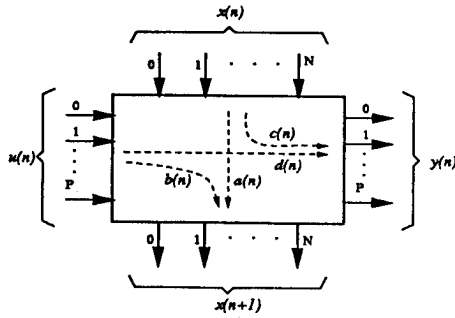


Fig. 1. The state space realization of the decomposition part of the Q-channel filter bank.

Where M , the state space realization map, is given as

$$M = \begin{bmatrix} A & B \\ C & D \end{bmatrix}, \quad (4)$$

with

$$\begin{aligned} A &= \text{diag}(\dots a(n-1) \ a(n) \ a(n+1) \dots), \\ B &= \text{diag}(\dots b(n-1) \ b(n) \ b(n+1) \dots), \\ C &= \text{diag}(\dots c(n-1) \ c(n) \ c(n+1) \dots) \text{ and} \\ D &= \text{diag}(\dots d(n-1) \ d(n) \ d(n+1) \dots), \end{aligned}$$

and Z is a shift operator

$$Z = \begin{bmatrix} \ddots & \ddots & \ddots & \\ & 0 & 1 & 0 \\ & & 0 & 1 & \ddots \\ & & & 0 & \ddots \\ & & & & \ddots \end{bmatrix}. \quad (5)$$

For the reconstruction part R we have, mutatis mutandis, similar relations³. In order to distinguish R from E , we add an overbar to the symbols when related to R : $\bar{m}(n), \bar{a}(n), \bar{b}(n), \bar{c}(n), \bar{d}(n)$. This is shown in Fig. 2. The state space realization map on the reconstruction side

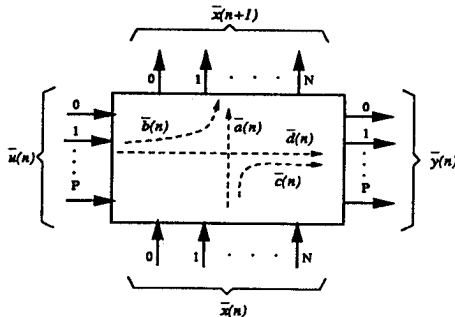


Fig. 2. The state space realization of the reconstruction part of the Q-channel filter bank.

³Recall that R is an anti-causal map, so 'next' becomes 'previous' and Z is to be replaced by Z^T .

is then \bar{M} . In the state realization domain, the "perfect reconstruction" property $RE = I$ transfers to $\bar{M}M = I$, or equivalently $\bar{m}(n)m(n) = 1^4$, for all n .

The decomposition map E and its corresponding state space realization map M are related as follows. Let

$$C(n) = \begin{bmatrix} \dots a(n-1) a(n-2) b(n-3) \\ a(n-1) b(n-2) \ b(n-1) \end{bmatrix} \quad (6)$$

$$O(n) = \begin{bmatrix} c(n) \\ c(n+1)a(n) \\ c(n+2)a(n+1)a(n) \\ \vdots \end{bmatrix}, \quad (7)$$

then $H(n) = O(n)C(n)$ is the so-called Hankel matrix⁵ of rank N at time instant n . It relates past inputs and future outputs as follows.

$$E = \begin{bmatrix} \vdots & \vdots & \vdots \\ \vdots & e_{(n-1)} & \vdots \\ \vdots & e_n & \vdots \\ \vdots & e_{(n+1)} & \vdots \\ \vdots & \vdots & \vdots \end{bmatrix} \quad (8)$$

$H(n)$

From these items we obtain the following relations.

- From $M \rightarrow E$

$$e_n = [c(n)C(n) \ d(n)] \quad (9)$$

$$e_{;n} = \begin{bmatrix} d(n) \\ O(n+1)b(n) \end{bmatrix} \quad (10)$$

- From $E \rightarrow M$

$$a(n) = O^\dagger(n+1)O^\dagger(n) = C(n+1)^{-}C^\dagger(n)$$

$$b(n) = \text{right-most } N \times P \text{ entry of } C(n+1)$$

$$c(n) = \text{top } P \times N \text{ entry of } O(n)$$

$$d(n) = \text{the common entry of } e_n; \text{ and } e_{;n}$$

where the superscript (\dagger) denotes pseudo inverse, and $C^{\leftarrow} = CS_-$, $O^\dagger = S_\dagger O$, with

$$S_\dagger = \begin{bmatrix} 0 & 1 \\ 0 & 0 & 1 \\ 0 & 0 & 0 & 1 \\ \vdots & \vdots & \vdots & \vdots \end{bmatrix}; \quad S_- = \begin{bmatrix} & & & 1 \\ & & 1 & 0 \\ 1 & 0 & 0 & \\ 0 & 0 & 0 & \end{bmatrix}.$$

Similar relations hold between R and \bar{M} . In this paper we address three classes of time varying filters; a) filters which

⁴where 1 stands for the identity matrix of appropriate order.

⁵ $C(n)$ and $O(n)$ are called the controllability and observability operators at time instant n , respectively.

come to existence at a certain time and extend to operate indefinitely (bounded from the top), b) filters which have been working since infinite time in the past and disappear at a certain time (bounded from the bottom), and c) filters of the second class being taken over by that of the first class (filters with transitions). In [1] the case of two-channel orthogonal filter banks is considered. There, orthogonal projectors are used to complete the basis for the right side sequence of the bounded filter bank. In contrast, our method uses the state space approach to find the boundary filters. The boundary filters so determined may happen to have smooth transitional behavior, at both the decomposition and reconstruction sides. However, in case the filters so obtained are not satisfactory, optimization procedures may be employed to suit the application. We address this in section III-C.2. In the third class, there is a special case where the takeover is instantaneous, that is, where the transition region $[n_o, n_f - 1]$ disappears. This case is addressed in section IV.

III. Generic Classes

In this section, we give conditions for the filter banks in each of the three classes mentioned in the previous section to guarantee perfect reconstruction as well as minimality of the transition region.

A. Filters bounded from the top

We start-off with bounding the doubly infinite matrices in (1) and (2) to the North and to the West, respectively.

$$E = \begin{bmatrix} \boxed{e} & & \\ & \boxed{e} & \\ & & \ddots \end{bmatrix} \quad (11)$$

$$R = \begin{bmatrix} \boxed{r} & & \\ & \boxed{r} & \\ & & \ddots \end{bmatrix} \quad (12)$$

Because of the sudden change in the filter coefficients, the perfect reconstruction behavior is lost in the process. We can re-establish the perfect reconstructiveness if we provide the system with the necessary state (vector) such that the map from past inputs to this state is equal to the controllability operator of the shift-invariant system. The initialization must be in such a way that we can recover the input at the reconstruction side from the outputs of the succeeding realizations.

The state space model of the switching process on the decomposition side is shown in Fig.3. At the initial time step, the state is initialized from the input. Therefore, the state space realization $m(0)$ at creation time $n = 0$ is such that $a(0) = []$, $c(0) = []$ and $d(0) = []$. Moreover, in order to perfectly recover the initial input vector at the

reconstruction side, its dimension must be at most equal to the state dimension of the target stationary filter. For maximally decimated systems ($P = Q$), the best choice would be to take the dimension of the initial input to be equal to the state dimension as indicated in Fig.3. In this case, $b(0)$ must be an $N \times N$ non-singular operator, where N is the state dimension of the target stationary filter.

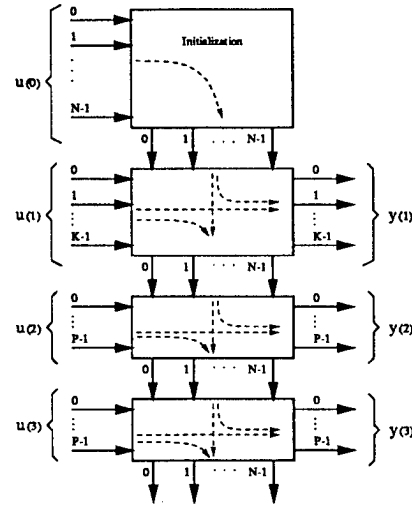


Fig. 3. Time varying system representation bounded from the top

Since the filter coefficients are given as in (9), the switching process on the decomposition side would be over if, at a certain point in time, the mapping from past inputs to the present states (the controllability operator) agrees with that of the target stationary filter[2]. This means that the number of inputs needed to establish the stationary filters depends on the length of the controllability operator.

The reconstruction version of Fig.3 can be obtained by reversing the directions of signal flows in it. For this reconstruction filter, the impulse response at time step n , which is the same as the n^{th} column of R , is given as

$$r_{;n} = \begin{bmatrix} \bar{O}(n-1)\bar{b}(n) \\ \bar{d}(n) \end{bmatrix}, \quad (13)$$

where $\bar{O}(n)$ is the observability operator of $\bar{m}(n)$. Clearly the impulse response at time step n would agree with that of the stationary filter if $\bar{O}(n-1)$ were the observability operator of the stationary target filter. In maximally decimated systems the controllability operator on the decomposition side and the observability operator on the reconstruction side have equal lengths. Therefore, in order to complete the switching process on the reconstruction side, we need as many outputs as the inputs on the decomposition side. The question remaining is how many boundary functions both on the decomposition and reconstruction sides are needed for the switching process.

Let the realization on the decomposition side at $n = 1$, $m(1)(a(1), b(1), c(1), d(1))$ be such that $[a(1)b(0) \ b(1)] = C(2) = C$, where C is the controllability operator for the

stationary filter, then all the filters for $n > 1$ will agree with that of the stationary filter. It is evident from here that, once $b(0)$ is chosen, the values of $a(1)$ and $b(1)$ are fixed. They are given by

$$a_1 = C(:, 1 : N)b_0^{-1}$$

and

$$b_1 = C(:, N + 1 : L)$$

where $C(:, i : j)$ stands for columns of C in the interval $[i, j]$, N = is state dimension of the target filter and L =length of C .

Once $a(1)$ and $b(1)$ are fixed, the choices of $c(1)$ and $d(1)$ must be such that the inverse realization $\bar{m}(1)(\bar{a}(1), \bar{b}(1), \bar{c}(1), \bar{d}(1))$ at $n = 1$ satisfies the requirements on the observability operator. Following we will show that, for a particular choice of $b(0)$, it is possible to come up with a simple procedure to design the realizations $m(1)$ and $\bar{m}(1)$ which satisfy the mentioned requirements.

Proposition III.1: Let $m(a, b, c, d)$ and $\bar{m}(\bar{a}, \bar{b}, \bar{c}, \bar{d})$ be the state space realizations of a Q -channel (with $Q=P$) stationary target filter bank on the decomposition and reconstruction sides, respectively. Let also be given $b(0) = C(:, (\mathcal{L} - N + 1) : \mathcal{L})$ (the N right most columns of C). Define $K = \lceil \frac{(\mathcal{L}-N)}{Q} \rceil Q < \mathcal{L}$. Then, if $a(1) = a^{K/Q}$ and $b(1) = C(:, (\mathcal{L} - K + 1) : \mathcal{L})$, we have $\begin{bmatrix} a(1)b(0) & b(1) \end{bmatrix} = C$. Moreover, if we choose $c(1) = O(1 : K, :)$ and $d(1)$ equal to the $K \times K$ matrix $E(1 : K, \mathcal{L} + 1 : \mathcal{L} + K)$, where E is as given in (11), then $\bar{m}(1)$ also satisfies the requirement on the observability operator at the reconstruction side. i.e.

$$\begin{bmatrix} \bar{c}(0)\bar{a}(1) \\ \bar{c}(1) \end{bmatrix} = \bar{O}(2) = \bar{O}.$$

Proof: The proofs of all the propositions are omitted because of lack of space. ■

Proposition III.2: Given the one sided infinite Q -channel decomposition/reconstruction pair of (11) and (12), The number of the boundary functions needed to re-establish the perfect reconstruction is equal to $\mathcal{L} - N \leq K$, where $K = \lceil \frac{(\mathcal{L}-N)}{Q} \rceil Q$, with N the state dimension and \mathcal{L} length of the controllability operator. ■

The following proposition fixes the maximum length of the boundary functions.

Proposition III.3: The maximum length of the boundary functions is $\mathcal{L} \leq N + K$, where N is the state dimension of the system, \mathcal{L} =length of C and K is as defined in proposition III.1. ■

B. Filters bounded from the bottom

Here, we consider the case when the stationary system has been working for indefinite time in the past and ends its operation at a certain time $n = 0$, say. The corresponding realization is depicted in Fig.4. Since our intention is to terminate the filtering, the boundary filter must use the present state and convert it into output as indicated in Fig.4. The generation of the output functions must be such that the map from the state provided by the

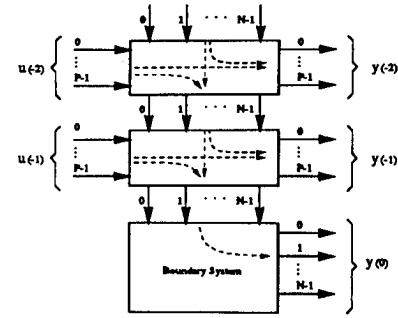


Fig. 4. Time varying system representation bounded from the bottom

stationary system to be terminated to the future outputs approaches \bar{O} as quickly as possible. This can be achieved by setting $c(0)$ equal to the top N rows of \bar{O} . The resulting output functions are such that at most the bottom K functions give the boundary filters and the rest have the same values as the stationary filter, where K is as defined in proposition III.1. This can easily be verified by generating the output functions of the boundary system using the relation $y(0) = c(0)C = O(1 : N, :)C$. Note that $c(0)$ must be non-singular in order to perfectly recover the past inputs using the output of the boundary system.

C. Transition between filter banks

In this case, the question we want to answer is: given two stationary filters with state space realizations m_1 and m_2 , we would like to design an intermediate realization m such that the transition durations on both the decomposition and reconstruction sides are minimal⁶ and equal. Let Fig.5 represent such a minimal system. Note that

$$m(n) = \begin{cases} m_1 & : n \in [-\infty, (n_o - 1)] \\ m & : n \in [n_o, (n_f - 1)] \\ m_2 & : n \in [n_f, +\infty] \end{cases}$$

with $n_o - 1 = -1$ and $n_f - 1 = n_o = 0$. If m is such that the map from the past inputs of $m(n_f)$ to its current state equals the controllability operator of the overtaking filter, then the outputs for $n \geq n_f$ will be equal to the stationary values of the overtaking filter. Since the initial filter is assumed to have been operating stationarily up to $n = n_o - 1$, the outputs for $n < n_o$ are unaffected by the intermediate system m . This means, the filter behaves the same way as the initial stationary system up to $n = n_o - 1$. On the reconstruction side, for the impulse responses to agree with the respective stationary values before and after the transition, the intermediate realization \bar{m} must satisfy $\bar{O} = \bar{O}(n)_{n \geq n_f} = \bar{O}_2$.

C.1 Minimal Structure for Switching Between Two Filter Banks

Consider the intermediate realization $m(a, b, c, d)$ shown in the middle part of Fig.5. Let the controllability oper-

⁶Minimal means Q , the number of transitional output functions related to m , is minimum.

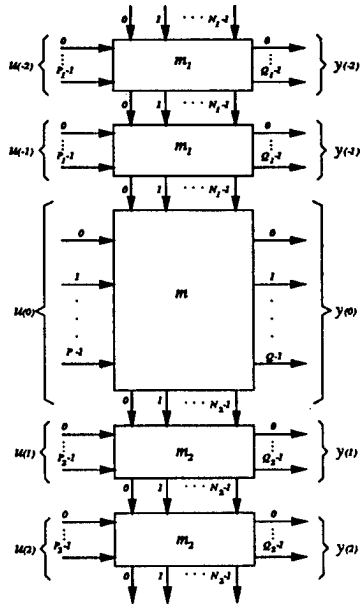


Fig. 5. Time varying system representation, transition between two filters.

ator on the decomposition side and the observability operator on the reconstruction side for the initial stationary filter and the final stationary filter be C_1, \bar{O}_1 and C_2, \bar{O}_2 , respectively. The following conditions must be satisfied by the transition system m and its inverse $\bar{m}(\bar{a}, \bar{b}, \bar{c}, \bar{d})$ if the time varying filter has to behave as the respective stationary filters outside the transition.

$$C_2 = [aC_1 \quad b] \quad (14)$$

$$\bar{O}_2 = \begin{bmatrix} \bar{O}_1 \bar{a} \\ \bar{c} \end{bmatrix}. \quad (15)$$

If $C_2 = SC_1$ for some invertible operator S , then it can be easily shown that there exist operators a and \bar{a} such that $aC_1 = C_2^*$ and $\bar{O}_1 \bar{a} = \bar{O}_2^*$. We address this sub-class of filter banks in sections IV and V. For now let us assume this is not the case.

Proposition III.4: Let $m(a, b, c, d)$ be the intermediate realization of the time varying system shown in Fig. 5. Also, assume that $C_2 \neq SC_1$ for all invertible S . Then, m and its inverse \bar{m} are minimal if and only if there exists an invertible matrix t , such that

$$m' = \begin{bmatrix} 0 & b' \\ c' & d' \end{bmatrix} = \begin{bmatrix} 1 & 0 \\ 0 & t \end{bmatrix} \cdot \begin{bmatrix} a & b \\ c & d \end{bmatrix} \quad (16)$$

Where m' is such that the time varying decomposition operator E' is a concatenation (along the main diagonal) of E_1 minimally bounded from the bottom and E_2 minimally bounded from the top. See (17). ■

Basically the above proposition is stating that, if the state space realization m (the middle part of Fig. 5) and its inverse \bar{m} represent minimal systems, then the state transition operators a and \bar{a} are zero. Consequently, we can redraw the detailed version of m as indicated in Fig. 6.

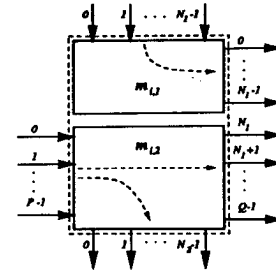


Fig. 6. Details of the intermediate state space realization.

This structure suggests that the decomposition operator E' of the time varying filter has the form shown below.

$$E' = \begin{bmatrix} & & & & & \\ & e_1 & & & & \\ & & e_1 & & & \\ & & & e'_{11} & 0 & \\ & & & & e'_{22} & \\ & & & & & e_2 \\ & & & & & & e_2 \\ & & & & & & & \ddots \end{bmatrix} \quad (17)$$

There is a similar structure on the reconstruction side also. In summary, the transition functions can be determined by terminating and starting the two filter banks before and after transition as described in sections III-A and III-B, respectively, and combining the so bounded filter banks as shown in (17). Taking proposition III.4 the other way around, overlap on the transition segment can then be achieved by applying an invertible output transform. We consider this in the next subsection. Because the structure of the transition functions is similar to the concatenation of independent bounded perfect reconstruction filters, the number of functions needed to switch between them is the sum of the boundary functions in the independent filters.

C.2 Controlling the Behavior of the Transition Filters

In real applications, in addition to perfect reconstruction, good filtering behavior is required. Therefore, we would like to know if we can alter the behavior of the transition functions as desired without violating its perfect reconstruction. Fortunately, we have some degree of freedoms to do so.

Consider the state space realization of the intermediate system shown in Fig. 6. Cascading this system with an invertible $Q \times Q$ constant matrix t does not affect the perfect reconstructing nature of the filter. If in addition, t is optimized to give good, desired, impulse response transitions on $[n_o, n_f - 1]$ in R , while maintaining smooth filter weight vector transition on $[n_o, n_f - 1]$ in E , we can improve the behavior of the transition filters without destroying the perfect reconstruction. Due to the mixing of the filter coefficients of the upper and the lower boundary filters (see equation 17) by the cascaded operator t ,

overlapped transition is resulted. For further reading on optimization methods the reader is advised to refer to [1] and [3].

In the remaining part of the paper we will show that, if the two filters under question are such that $C_b = SC_a$, as stated earlier, the transition between the filters can be made arbitrarily small. In the limiting case we can instantaneously switch from initial filter to the final one without any transition. For this subclass of filters, we first summarize, in the next section, results for the case $n_o = n_f$, which were presented in [4] and allow the construction of piecewise stationary biorthogonal banks. In section V, we extend these results to the case when $n_f > n_o$ by introducing an interpolation method which allow smooth transition between filter weight vectors in the decomposition part of the bank, and at the same time smooth transition between impulse response vectors in the reconstruction part of the bank. Examples that demonstrate the results are given in section VI.

IV. Instantaneous Transition in Perfect Reconstruction Filter Banks

The problem we want to address in this section is: given two stationary filters with state space realizations m_1 and m_2 , is it possible to instantaneously switch from initial to the final filter? Following we formally state the problem.

Let $(E(e), R(r))$ be a shift invariant biorthogonal filter bank. Put $E(e) = \begin{bmatrix} E_t \\ E_b \end{bmatrix}$ and $R(r) = [R_l | R_r]$, where E_t is the part of $E(e)$ above the central row e , and R_l is the part of $R(r)$ to the left of the central column r .

Now let be given $E_1(e_1) = \begin{bmatrix} E_{1,t} \\ E_{1,b} \end{bmatrix}$, $E_2(e_2) = \begin{bmatrix} E_{2,t} \\ E_{2,b} \end{bmatrix}$ and $R_1(r_1) = [R_{1,l} | R_{1,r}]$, $R_2(r_2) = [R_{2,l} | R_{2,r}]$. $R_1(r_1)E_1(e_1) = I$ and $R_2(r_2)E_2(e_2) = I$. The problem we want to address in this section is the following.

Problem.

Given the above two filter banks $(E_1(e_1), R_1(r_1))$ and $(E_2(e_2), R_2(r_2))$, does there exist a filter bank (E_{12}, R_{12}) such that

$$E_{12} = \begin{bmatrix} E_{1,t} \\ E_{2,b} \end{bmatrix} \quad (18)$$

and

$$R_{12} = [R_{1,l} | R_{2,r}] \quad (19)$$

and, of course, $R_{12}E_{12} = I$.

End problem.

The answer is partly contained in the following proposition, a proof of which can be found in [4].

Proposition IV.1: Let $(E_1(e_1), R_1(r_1))$ and $(E_2(e_2), R_2(r_2))$ be two shift-invariant perfect reconstruction filter banks with realization matrix pairs:

$$(m_1(a_1, b_1, c_1, d_1), \bar{m}_1(\bar{a}_1, \bar{b}_1, \bar{c}_1, \bar{d}_1))$$

and

$$(m_2(a_2, b_2, c_2, d_2), \bar{m}_2(\bar{a}_2, \bar{b}_2, \bar{c}_2, \bar{d}_2)),$$

respectively. If⁷

$$a_1 = a = a_2, b_1 = b = b_2, \bar{a}_1 = \bar{a} = \bar{a}_2, \bar{c}_1 = \bar{c} = \bar{c}_2, \\ c_2 = t \times c_1, d_2 = t \times d_1, \bar{b}_2 = \bar{b}_1 \times s, \bar{d}_2 = \bar{d}_1 \times s, \text{ and} \\ s \times t = I,$$

$$I = \begin{bmatrix} \bar{a} & \bar{b}_1 \\ \bar{c} & \bar{d}_1 \end{bmatrix} \cdot \begin{bmatrix} a & b \\ c_1 & d_1 \end{bmatrix} = \\ \begin{bmatrix} \bar{a} & \bar{b}_1 \\ \bar{c} & \bar{d}_1 \end{bmatrix} \cdot \begin{bmatrix} I & 0 \\ 0 & s \end{bmatrix} \cdot \begin{bmatrix} I & 0 \\ 0 & t \end{bmatrix} \cdot \begin{bmatrix} a & b \\ c_1 & d_1 \end{bmatrix} = \\ \begin{bmatrix} \bar{a} & \bar{b}_2 \\ \bar{c} & \bar{d}_2 \end{bmatrix} \cdot \begin{bmatrix} a & b \\ c_2 & d_2 \end{bmatrix}.$$

then $(\begin{bmatrix} E_{2,t} \\ E_{2,b} \end{bmatrix}, [R_{1,l} | R_{2,r}])$ is a biorthogonal filter bank with instantaneous filter weight vector transition in the decomposition part and instantaneous impulse response transition in the reconstruction part. ■

In the above proposition we have tacitly assumed that the two banks $(E_1(e_1), R_1(r_1))$ and $(E_2(e_2), R_2(r_2))$ have the same number of channels. This is, however, not a restriction. Indeed, if $m_1(a_1, b_1, c_1, d_1)$ is the realization matrix of - say - a p -channel filter, then a number of such realizations, r say, in (time) succession can be merged (by eliminating intermediate states) to obtain a realization matrix $m_1(a_1, b_1, c_1, d_1)$ of an $r \times p$ channel filter. The realization matrix $m_2(a_2, b_2, c_2, d_2)$ in the proposition will then also characterize an $r \times p$ filter bank. See the example in section VI.

In the next section, we start from this result to extend the transition behavior from instantaneous to graceful.

V. Interpolated Transition in Perfect Reconstruction Filter Banks

The matrix equation in the previous section expresses perfect reconstruction. The additional property is that the system is state stationary over all time including the time instant of instantaneous transition. The transition is instantaneous because the transformation matrices t and s are constant. If, on the other hand, we let these matrices be time varying, then the transition will follow a certain trajectory which we will have to control in case when we want to enforce meaning on the trajectories of the filter weight vectors in the operator E as well as the impulse response vectors in the operator R . One can envisage several strategies to control the transition behavior but we shall confine to one of them - spiral interpolation - which has proven to be simple and satisfactory.

Thus let $\{t(n)\}$ be the sequence of real $w \times w$ transformation matrices on the transition interval $[t_o, t_f]$, where $t(n_o) = I$ and $t(n_f) = t$, t being - for example - the matrix t in proposition IV.1. Associated with this sequence

⁷ Up to similarity transformations.

is the sequence of inverse matrices $\{s(n)\}$, $s(n)t(n) = I$. Now let $t = g\lambda g^{-1}$ and $s = g\lambda^{-1}g^{-1}$ be the eigenvalue decompositions of t and s . The eigenvalues are either real λ_i or appear in conjugate pairs ($|\lambda_k| e^{j\theta_k}, |\lambda_k| e^{-j\theta_k}$).

Proposition V.1: Let for $i = 1, \dots, w$, and $n_o \leq n \leq n_f$, $p_i(n)$ and $\gamma_i(n)$ be real and monotonically increasing functions from 0 at n_o to 1 at n_f . Put $t(n) = g[\text{diag}(p_i(n) | \lambda_i | + (1 - p_i(n)) e^{j\gamma_i(n)\theta_i})]g^{-1}$. $t(n)$ is real.

If $q_i(n) = \frac{p_i(n)|\lambda_i|}{p_i(n)|\lambda_i| + (1 - p_i(n))}$, then $q_i(n)$ is monotonically increasing from 0 at n_o to 1 at n_f , $s(n) = g[\text{diag}(q_i(n) | \lambda_i^{-1} | + (1 - q_i(n)) e^{-j\gamma_i(n)\theta_i})]g^{-1}$ is real, and $s(n) \times t(n) = I$. Moreover, the transition filters are such that the overall system remains perfect reconstruction. ■

VI. Illustrative Examples

A. Transition between filter banks

In this example, the transition behavior between two filters of lengths 18 and 10 are studied. the structures of both filters are as shown in Fig.7. In the initial case $f(z) = c_2 z^{-2} + c_1 z^{-1} - c_1 z^1 - c_2 z^2$ and $g(z) = c_4 z^{-2} + c_3 z^{-1} - c_3 z^1 - c_4 z^2$. The final filter has $f(z) = c_5 z^{-1} - c_5 z$ and $g(z) = c_6 z^{-1} - c_6 z$. The transition in the spec-

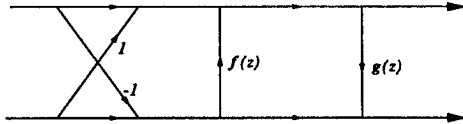


Fig. 7. A two channel ladder filter bank.

tral characteristics on the decomposition side is shown in Fig.8, and Fig.9 shows the transition between the impulse responses at the reconstruction side corresponding to the second channel. From the plots one can clearly see the decomposition behavior of the transition filter weight vectors and the gentle transition in impulse responses on the reconstruction side.

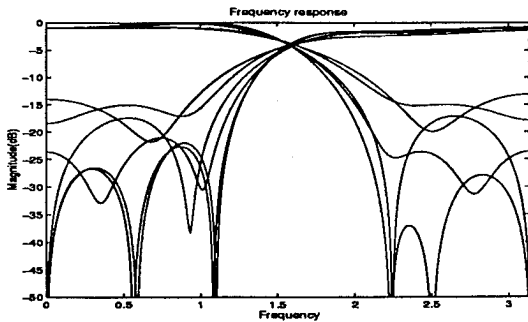


Fig. 8. Spectra of the transition filters on the decomposition side.

B. Instantaneous transition

Here, we consider the case when a 4-channel bank takes over from a 2-channel bank. The decomposition parts of the two banks are shown in Fig.10, in shift-invariant state. In this figure, $f(z) = -c_0 z + c_0 z^{-1}$, and $g(z) = -c_1 z + c_1 z^{-1}$. t is a constant 4×4 matrix.

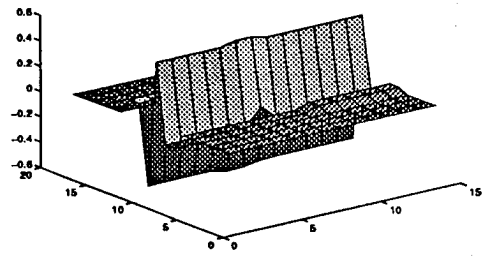


Fig. 9. Transitions in impulse responses of the second channel on the reconstruction side.

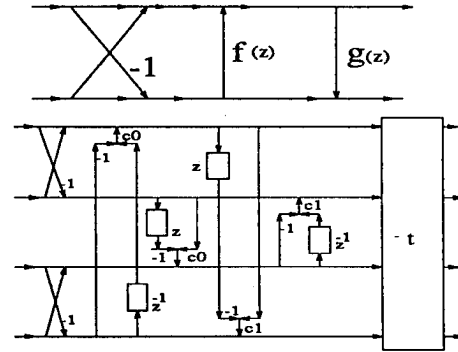


Fig. 10. A 2-channel and a 4-channel decomposition part of 2 perfect reconstruction filter banks

The Fourier transforms of the filter weight vectors of the two decomposition parts are shown in Fig.11.

If in the second filter in Fig.10 the matrix t is replaced by the identity, then the resulting flow graph is essentially twice the first filter. Thus if t is taken away from the second filter, then it represents two time steps of the 2-channel decomposition filter. This filter can be run for a while and then - at $n = n_o$ say - t can be cascades to the two 2-channel filters and start running as a single 4-channel decomposition filter. The take over is instantaneous. That is, the spectral characteristics switch instantly, at $n = n_o$, from the top spectra in Fig.11 to the bottom spectra. Moreover, the impulse responses of the reconstruction filters do also have an instantaneous transition at $n = n_o$, as shown in Fig.12 for the fourth channel of the two reconstruction filters⁸.

C. Interpolated transition

Instead of appending the constant matrix t at time instant n_o , we now 'spiral' - as explained in proposition V.1 - along the matrix trajectory $t(n) = g[\text{diag}(p_i(n) | \lambda_i | + (1 - p_i(n)) e^{j\gamma_i(n)\theta_i})]g^{-1}$, which takes off at $t(n_o) = I$ and is constant $t(n_f) = t$ from $n = n_f$ on. And similarly for the reconstruction filter: the input matrix starts off from $s(n_o) = I$ and spirals along the trajectory

⁸The reconstruction filters are not shown as they are easily obtained by reversing the direction of signal flow from output to input in the filters from Fig.10, [5].

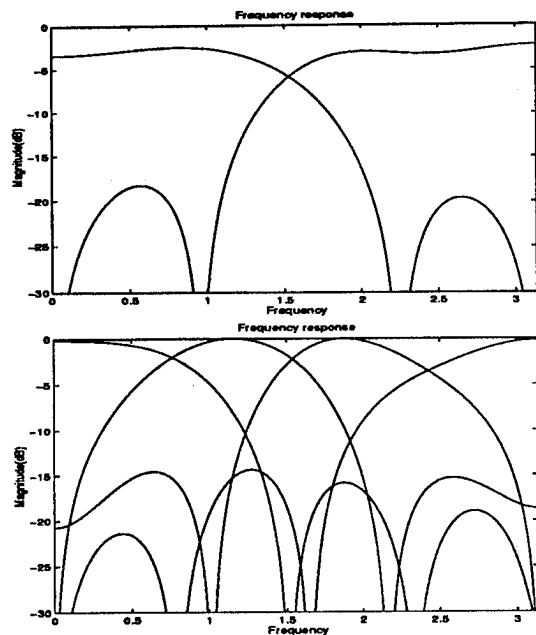


Fig. 11. Fourier transforms of filter weight vectors of 2 and 4-channel filters

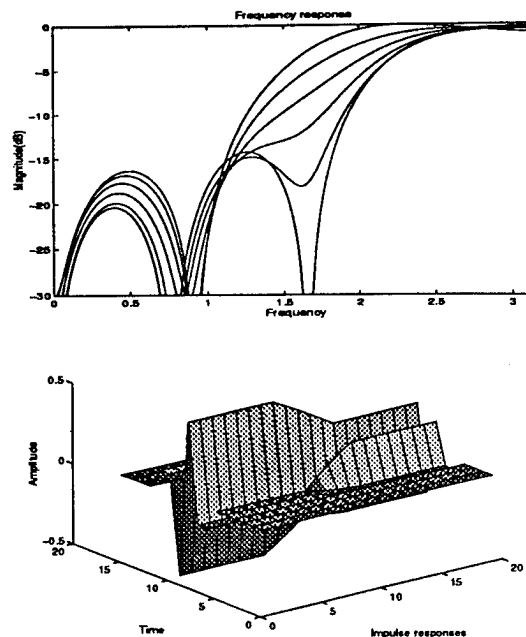


Fig. 13. Smooth transitions in the frequency and impulse responses corresponding to the fourth channel

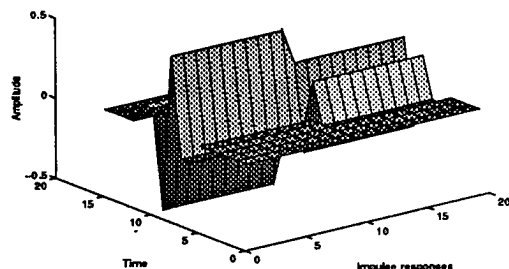


Fig. 12. Instantaneous switching in the impulse response corresponding to channel four

$s(n) = g[\text{diag}(q_i(n) | \lambda_i^{-1} | + (1 - q_i(n)))e^{j-\gamma_i(n)\theta_i}]g^{-1}$ to end at constant $s(n_f) = s$ at time instant $n = n_f$. As explained in proposition V.1, perfect reconstruction is guaranteed whenever $q_i(n) = \frac{p_i(n)|\lambda_i|}{p_i(n)|\lambda_i| + (1 - p_i(n))}$.

The smooth transitions of both the spectral characteristics at the decomposition side and the impulse responses at the reconstruction side are clearly seen in the plots shown in Fig.13 for channel four. The other channels transit in a likewise gentle way. As a final plot, the trajectories of the eigenvalues of $t(n)$ and $s(n)$ are shown in Fig.14.

Acknowledgement

The authors have appreciated the enlightening discussions with Dr. Ton Kalker while writing this paper.

REFERENCES

- [1] Cormac Herley and Martin Vetterli, "Orthogonal Time-Varying Filter Banks and Wavelet Packets," *IEEE Trans. on Signal*

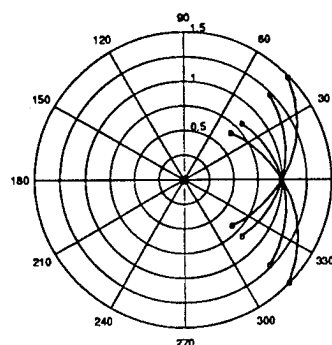


Fig. 14. Eigenvalue trajectories on the transition support. Initial values are all 1; end values are outside the unit circle for the decomposition filter and inside the unit circle for the reconstruction filter

- Processing*, **ASSP-42**(No. 10):pp. 2650-2663, October 1994.
- [2] Ed F. Deperetere, "Time Varying Filter Banks," Technical report, Philips Electronics N.V, The Netherlands, 1995.
- [3] Alfred Mertins, "Time-varying and Support Preservative Filter Banks: Design of Optimal Transition and Boundary Filters Via SVD," *IEEE Int. Conf. ICASSP-95*, Vol. 2: Digital Signal Processing:pp. 1316-1319, May 1995.
- [4] H.G.J. Theunis and Ed F. Deprettere, "Piecewise Stationary Perfect Reconstruction Filter Banks," *AEÜ*, Special Issue in Memory of Wilhelm Cauer, (to appear September 1995), 1995.
- [5] A.A. Bruekers and A.W. van den Enden, "New Networks for Perfect Inversion and Perfect Reconstruction," *IEEE J. Selected Areas in Communication*, 10(1), 1992.

PIECEWISE-LINEAR CHARACTERISTICS OF MSLMS FILTER

Hong-Qing Xu*

Ji-Nan Lin**

Rolf Unbehauen***

*Intelligent Automation Inc., 1370 Piccard Dr., Rockville, MD 20850, USA

**Thomson Consumer Electronics, Corporate Research Villingen, Hermann-Schwer-Str. 3, 78048 Villingen, Germany

***University Erlangen-Nürnberg, Cauerstrasse 7, 91058 Erlangen, Germany

ABSTRACT

The MSLMS filter is a new kind of nonlinear filter, which stems from the filter based on the threshold decomposition approach. In this paper, the MSLMS filter is studied from another point of view, i.e. that of the piecewise-linear (PWL) filtering theory. From this study it is seen that the MSLMS filter belongs to a subset of known PWL filters. It is theoretically investigated that the use of the MSLMS filter is limited since the subset it belongs to has a drawback in approximating a desired filtering operator. This drawback is overcome by another PWL filter, e.g. the so-called CPWL filter, which may be taken as a generalization of the MSLMS filter. An example of our simulations is presented, which verify the study.

1. INTRODUCTION

To overcome the limitations of the traditional linear filters in modern applications of signal processing, people are working to find more powerful nonlinear filters. Due to the lack of a general theory, various kinds of nonlinear filters are developed on different mathematical backgrounds. Among them the theory of threshold decomposition serves as the mathematical basis of a large family of nonlinear filters, including rank-order filters, the stacker filter and its generalized versions, which have been proved useful in many applications. The microstatistic (MS) filter is a new member of this family [1]. Instead of using nonlinear operations at the threshold level, the linear operation is adopted in the sub- (micro-) filters to reduce the computation complexity. As a result, the linear system theory can be used to analyze the filtering performance, although the whole operation is still nonlinear. The so-called MSLMS filter proposed in [2] modifies the MS filter with a real valued threshold decomposition and an adaptive feature, so that the complexity of the microstructured filters is further reduced and the performance is enhanced. The filter can "learn" to assign its parameters without requiring much a priori knowledge of the signal and noise statistics.

Considering a real, discrete-time sequence $\{x(n)\}$ which can be denoted for an N -long observation window as

$$x^T(n) = [x(n), x(n-1), \dots, x(n-N+1)] \quad (1)$$

an MSLMS filter is expressed as a sum of $2L$ microfilters

$$y(n) = \sum_{\substack{k=-L \\ k \neq 0}}^L y_k(n) = \sum_{\substack{k=-L \\ k \neq 0}}^L a_k^T T_k x(n) \quad (2)$$

where

$$y_k(n) = a_k^T T_k x(n) \quad (3)$$

with $a_k \in \mathbb{R}^N$ denotes the k -th (linear) microfilter.

$$T_k x(n) = [T_k[x(n)], T_k[x(n-1)], \dots, T_k[x(n-N+1)]]^T \quad (4)$$

where $T_k[\cdot]$ is the threshold operation

$$T_k[\xi] = \begin{cases} 0 & \xi \leq l_{k-1} \\ \xi - l_{k-1} & l_{k-1} < \xi \leq l_k \\ l_k - l_{k-1} & l_k < \xi \end{cases} \quad (5)$$

for $\xi \geq 0$ and

$$T_{-k}[\xi] = \begin{cases} 0 & \xi > l_{-k+1} \\ \xi - l_{-k+1} & l_{-k+1} > \xi \geq l_{-k} \\ l_{-k} - l_{-k+1} & l_{-k} > \xi \end{cases} \quad (6)$$

for $\xi < 0$ and $1 \leq k \leq L$. l_k , for $k = -L, \dots, L$, is the threshold, which satisfies

$$-\infty = l_{-L} < \dots < l_0 < l_1 < \dots < l_L = +\infty. \quad (7)$$

Static and dynamic methods have been introduced in [2] to estimate the thresholds, and an LMS algorithm was given to adjust the parameters a_k . The network structure of the MSLMS filter is depicted in Fig. 1. The superiority of the MSLMS filter over a conventional adaptive linear filter, i.e. the LMS filter in a non-Gaussian signal and/or non-Gaussian noise case has been shown in [2].

The authors of [2] have noticed that the MSLMS filter has a close relation to nonlinear filters based on the theory of piecewise-linear (PWL) systems, but they did not give any further discussion there. This paper studies the MSLMS filter from the viewpoint of the PWL theory. The PWL characteristics of the MSLMS filter are investigated. This study is thought of significant since it indicates a possibility of generalization of the MSLMS filter. Moreover, it may be taken as a part of the effort towards the goal of unifying different nonlinear filters.

This paper is organized as follows. In the following section we briefly introduce the theoretical framework

of PWL filters. Based on that, Section 3 studies the PWL characteristics of the MSLMS filter. This study reveals that the MSLMS filter mathematically belongs to a class of PWL filters, i.e. the so-called CPWL filter. It is also discussed there, that, as a subset of the CPWL filter, the MSLMS filter has some limitations which can be overcome by the latter. In Section 4, a simulation example is given to illustrate the result of our study.

2. PIECEWISE-LINEAR FILTERS

A filter is mathematically an operator between two signal spaces. We consider here only time-invariant digital filters with a finite support. Such a filter can be expressed by [8]

$$y(n) = f(x(n)) \quad (8)$$

where $f: \mathbb{R}^N \rightarrow \mathbb{R}$ is an N -variate real function. The main task in developing a general meaning of the nonlinear filter is to find a class of operators which should be able to represent or approximate, as many as possible, given filter operators and, on the other hand, which can be implemented in practice by usual physical components. To this end, PWL filters are developed. In a PWL filter a nonlinear filter function f as given in (8) is approximated in global by a series of linear subfunctions which are defined in properly partitioned, usually by hyperplanes (boundaries), subregions of the domain. A very important class of PWL functions is the so-called canonical PWL function [4] which is up to now the only method to represent all the local subfunctions as well as the domain partition of a PWL function in a compact explicit formula. The canonical PWL function takes the form:

$$f(x) = a + \langle b, x \rangle + \sum_{i=1}^{\sigma} c_i \langle a_i, x \rangle - \beta_i \quad (9)$$

where \langle, \rangle denotes the inner product of two vectors, and $a, c_i \in \mathbb{R}, b, a_i \in \mathbb{R}^N$. $\langle a_i, x \rangle - \beta_i = 0$ for $i = 1, 2, \dots, \sigma$ characterize the σ hyperplanes, which partition the domain in small subregions.

The existence condition of the canonical PWL function has been studied in [4]. Although it is not suitable for all kinds of PWL functions, the canonical PWL function has proved a "universal" approximant, that is, it is able to approximate any continuous function to an arbitrarily given precision [6].

Based on the canonical representation a nonlinear filter structure called CPWL filter is proposed in [5]. The CPWL filter is expressed as

$$y(n) = u_0(n) + \sum_{l=1}^L c_l |u_l(n)| \quad (10)$$

where c_l for $l = 1, 2, \dots, L$ are real parameters, and

$$u_l(n) = \bar{h}_l[x(n)] = h_{l0} + \sum_{i=0}^{N-1} h_{li}(i)x(n-i) \quad (11)$$

expresses a linear sub-filter with h_{l0} being its offset and $h_{li}(i)$ its impulse response.

Because of the universal approximation property of the canonical PWL function, the CPWL filter can be taken as a general meaning of filter which is used to approximate a desired nonlinear filtering operator on a given support. From the implementation point of view, the CPWL filter is also favorable, since, besides the basic operators which are necessary for a linear filter, only an "absolutor" is additionally required, which is easy to implement. An adaptive algorithm was developed in [5] to adjust the parameters as well as the weights of the linear sub-filters.

3. PWL CHARACTERISTICS OF MSLMS FILTER

The nonlinearity involved in the MSLMS filter is due to the threshold operators $T_k[\cdot]$ which is a continuous PWL function of one variable. Mathematically, a linear combination of PWL functions is still a PWL function where the domain partition is composed of the boundaries of the sub-functions. If the sub-functions are all univariate ones, the PWL function has a particular geometric property, i.e., it takes a lattice domain partition where the boundaries are only hyperplanes perpendicular to the coordinate axes. Such a function can always be represented as a canonical PWL function [4]. In fact, after a rearrangement of the formula (2) - (8) it is easy to find that the output of the MSLMS filter can be written as

$$y(n) = a_0 \sum_{i=0}^{N-1} b_i x(n-i) + \sum_{i=0}^{N-1} \sum_{\substack{j=-(L-1) \\ j \neq 0}}^{L-1} c_{ij} |x(n-i) - l_j| \quad (12)$$

where a_0, b_i , and c_{ij} for $i = 0, 1, \dots, N-1$; $j = -(L-1), \dots, (L-1)$, are a linear combination of the coefficients of the $2L$ micro-filters.

Comparing (12) with (10), it is seen that the MSLMS filter is a CPWL filter. As a special issue, the linear subfilters characterizing the lattice boundaries of the domain partition are those of $x(n-i) - l_j$.

This simplified issue has an advantage, i.e. it is easy to deal with the parameters, especially with that of the boundaries. Once all l_j being fixed, the determination of the parameters a_0, b_i , and c_{ij} is a linear programming problem and easy to solve. However, such filters constitute only a small subset of the CPWL family. It has been pointed out [6] that the universal approximation property of the canonical PWL function is lost by the subset which has a lattice domain partition. A PWL function of this subset is incapable of approximating an arbitrarily given function to a desired precision, no matter how finely the domain is partitioned. That means, unlike the CPWL filter, the MSLMS filter can in general not be used to achieve a desired nonlinear filtering operator. From this viewpoint, it can not be taken as a general meaning of nonlinear filter as the former.

4. A SIMULATION EXAMPLE

Simulations have been conducted to examine the above discussions. In all our simulations an MSLMS filter can always be implemented (or learned, in an adaptive case)

by a CPWL filter with a lattice domain partition. On the other hand, as a generalization of the MSLMS filter a CPWL filter improves the performance of the former. Here we present the results of an example of the simulations. In this example, a signal of a 8-state Markov chain is disturbed by a contaminated noise with the distribution.

$$F(a) = (1 - \epsilon)\Phi\left(\frac{a}{\sigma_1}\right) + \epsilon\Phi\left(\frac{a}{\sigma_2}\right)$$

where $\Phi(\cdot)$ is a normalized Gaussian distribution function, σ_1 is the variance of the nominal distribution and σ_2 is the variance of the outlier, and ϵ governs the proportion of contamination.

Three filters, i.e. a) the linear (LMS) filter, b) the MSLMS filter ($L = 4$), and c) the CPWL filter ($\sigma = 4$) were used to restore the signal. The results are compared in Fig. 2. One notices that, in this simulation, the MSLMS filter used more free parameters than the CPWL.

From this example we see that the MSLMS filter outperforms the conventional linear filter in achieving a smaller average error. On the other hand the performance of the MSLMS filter is improved by the CPWL filter, i.e. the latter can achieve a further smaller error with a relatively small number of free parameters. In addition, the CPWL filter has the best performance in restoring edges of the useful signal.

5. CONCLUSIONS

The study of the PWL characteristics of the MSLMS filter leads to the conclusion that this kind filter is mathematically equivalent to a subset of the CPWL filter. We do not mean that the former should already be replaced by the latter, (though, from the viewpoint of the implementation cost, such a replacement is by no means worthless.) In the CPWL implementation of an MSLMS filter, the original meaning of microstatistics, i.e. the linear filtering of the signal at different levels, becomes implicit, while this meaning may be significant in some applications. Nevertheless, the revelation of the PWL characteristics of the MSLMS filter can help us to analyze its behaviour, to improve its performance, and to generalize it for more application possibilities. Moreover, this study has opened a way to unify the two kinds of nonlinear filters developed on different theoretical backgrounds.

REFERENCES

- [1] Arce, G.R.: "Microstatistics in signal decomposition and the optimal filtering problem," *IEEE Trans. Signal Processing* **40** (1992), 2669-2682.
- [2] Chen, S., Arce, G.R.: "Microstatistic LMS filtering," *IEEE Trans. Signal Processing* **41** (1993), 1021-1034.
- [3] Fitch, J.P., Coyle, E.J., Gallagher, N.C.: "Median filtering by threshold decomposition," *IEEE Trans. Acoust., Speech, Signal Processing* **32** (1984), 1183-1188.
- [4] Chua, L.O., Deng, A.-C.: "Canonical piecewise-linear representation," *IEEE Trans. Circuits Syst.* **35** (1988), 101-111.
- [5] Lin, J.-N., Unbehauen, R.: "Adaptive nonlinear digital filter with canonical piecewise-linear structure," *IEEE Trans. Circuits Syst.* **37** (1990), 347-354.
- [6] Lin, J.-N., Unbehauen, R.: "Canonical piecewise-linear approximations," *IEEE Trans. Circuits Syst.* **39** (1992), 697-699.
- [7] Lin, J.-N., Unbehauen, R.: "Canonical piecewise-linear networks," *IEEE Trans. Neural Networks* **6** (1995), 43-50.
- [8] Lin, J.-N.: *Mapping-Netzwerke und adaptive nicht-lineare Filter*, Dissertation, University Erlangen-Nürnberg, 1993.

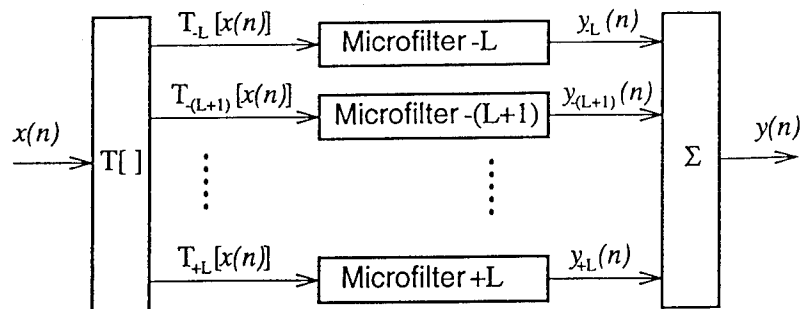


Fig. 1 Structure of a microstatistic filter

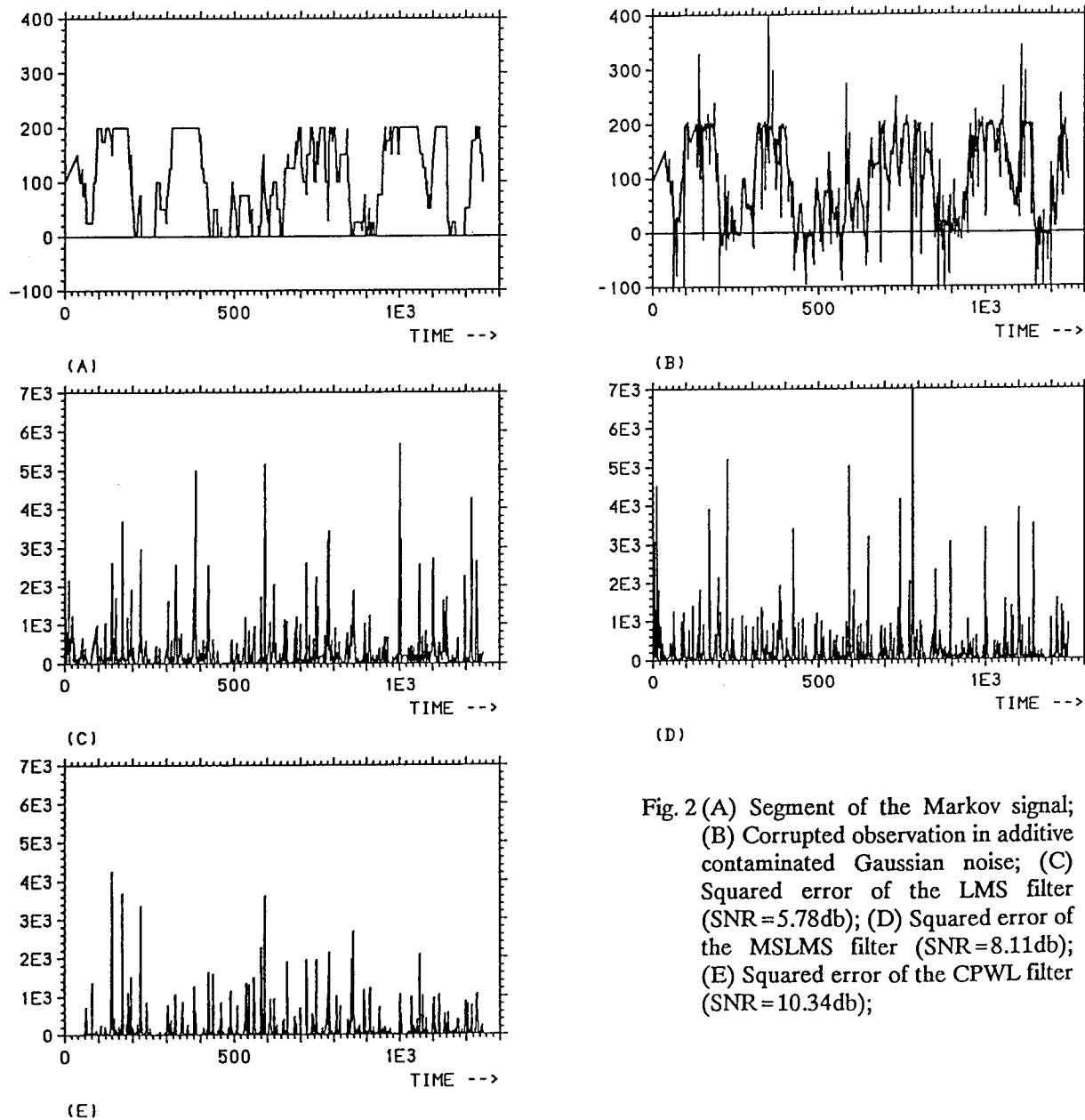


Fig. 2 (A) Segment of the Markov signal; (B) Corrupted observation in additive contaminated Gaussian noise; (C) Squared error of the LMS filter (SNR=5.78db); (D) Squared error of the MSLMS filter (SNR=8.11db); (E) Squared error of the CPWL filter (SNR=10.34db);

VARIANCE OF QUANTIZATION ERROR AT THE OUTPUT OF RECURSIVE DIGITAL FILTER

G. Mollova

Department of Computer Aided Design
Higher Institute of Architecture & Civil Engineering
1 Hr. Smirnenki Blvd., 1421 Sofia, Bulgaria
ttak%tu@bgcict.bitnet

ABSTRACT

A new analytical expression for the variance of resulting quantization error at the output of recursive cascade filter is proposed. The final results are given according to the filter's type and its order (even or odd). A design methodology for optimal recursive filters with minimum resulting error is presented aimed also to facilitate the computational process. A detailed numerical example is given, too.

1. INTRODUCTION

One basic problem in designing recursive digital filters is the roundoff effect in their fixed-point presentation. There are many papers dealing with the quantization error problem. Part of them are aimed to obtain new analytical expressions for the resulting error at the output of recursive digital filter [1,2]. Some authors look for variance approximation formulas to facilitate the computational process or apply heuristically approaches [3,4]. The "dynamic programming", "minimax noise" principle etc. are used as optimization methods for obtaining the cascade structure with a minimal variance of noise quantization.

The purpose of this paper is to derive a new analytical expression for the variance of resulting error for an even-or-odd-order recursive cascade filter. The derived relations depend on the coefficients of the first-and-second-order transfer functions and are oriented to CAD applications. The calculations are based on the transfer functions, directly found by means of Butterworth, Chebyshev and Elliptic approximations followed by the BLT pass, which implies the wide application of the derived expression. One essential difference between the new expression for the variance and the known ones is the introduction of a set of parameters describing the noise spectral density of each section.

2. SOLUTION

The variance of resulting quantization error at the output of the filter is [5]:

$$\sigma_r^2 = \frac{1}{2\pi} \oint_{|z|=1} \Phi_r(z) \cdot \frac{dz}{z} \quad (1)$$

where $\Phi_r(z)$ is the spectral density of the output resulting error:

$$\Phi_r(z) = \sum_{i=1}^{M-1} \Phi_r^i(z) + \Phi_\varepsilon^M(z) \quad (2)$$

$\Phi_r^i(z)$ describes the spectral density of resulting error at the output of cascaded filter caused by the quantization error of the i -th section, M is the number of sections. For even-order filter $M=N/2$, for odd-order filter $M=(N+1)/2$, where N is the order of filter. The function $\Phi_r^i(z)$ introduced above depends on the error spectral density at the output of the i -th section $\Phi_\varepsilon^i(z)$:

$$\Phi_r^i(z) = \Phi_\varepsilon^i(z) \cdot \prod_{s=i+1}^M W_s(z) \cdot W_s(z^{-1}) \quad (3)$$

where $W_s(z)$ is the transfer function of the S -th section from the cascade. Replacing (2) and (3) into (1) it is found:

$$\sigma_r^2 = \sum_{i=1}^{M-1} \sigma_i^2 + \sigma_M^2 \quad (4)$$

where: $\sigma_i^2 = \frac{1}{2\pi} \oint_{|z|=1} \Phi_\varepsilon^i(z) \cdot \prod_{s=i+1}^M W_s(z) \cdot W_s(z^{-1}) \cdot \frac{dz}{z}$,

$$\sigma_M^2 = \frac{1}{2\pi} \oint_{|z|=1} \Phi_\varepsilon^M(z) \cdot \frac{dz}{z}$$

To derive σ_r^2 it is necessary (eq.4) to be taken into account the $W_i(z)$ form (see Table 1). The examination process for lowpass filter will be shown here (the expressions for the other three types of filters are similarly derived).

Section i	Second order	First order
	$W_i(z)$	$W_i(z)$
Lowpass (LP)	$\frac{H_i(1+z^{-1})^2}{1+a_i \cdot z^{-1}+b_i \cdot z^{-2}}$	$\frac{H_i(1+z^{-1})}{1+a_i \cdot z^{-1}}$
Highpass (HP)	$\frac{H_i(1-z^{-1})^2}{1+a_i \cdot z^{-1}+b_i \cdot z^{-2}}$	$\frac{H_i(1-z^{-1})}{1+a_i \cdot z^{-1}}$
Bandpass (BP)	$\frac{H_i(1-z^{-2})}{1+a_i \cdot z^{-1}+b_i \cdot z^{-2}}$	
Bandstop (BS)	$\frac{H_i(1+c_i \cdot z^{-1}+z^{-2})^2}{1+a_i \cdot z^{-1}+b_i \cdot z^{-2}}$	

Table 1

Consider the product :

$$\prod_{s=2}^M W_s(z) \cdot W_s(z^{-1}) = W_2(z) \cdot W_2(z^{-1}) \dots W_M(z) \cdot W_M(z^{-1}) =$$

$$\frac{\prod_{s=2}^M H_s^2(1+z)^{2(M-1)} \cdot (1+z^{-1})^{2(M-1)}}{\prod_{s=2}^M (1+a_s \cdot z + b_s \cdot z^2) \cdot \prod_{s=2}^M (1+a_s \cdot z^{-1} + b_s \cdot z^{-2})}$$

The rest of products from (4) are evaluated at the same way. An important moment in deriving the final relation for the variance is presenting Φ_ε^i in the following form :

$$\Phi_\varepsilon^i = \frac{\sigma^2 \cdot (A_i + B_i \cdot z + C_i \cdot z^2) \cdot (A_i + B_i \cdot z^{-1} + C_i \cdot z^{-2})}{(1 + a_s \cdot z + b_s \cdot z^2) \cdot (1 + a_s \cdot z^{-1} + b_s \cdot z^{-2})}, \quad (5)$$

where A_i, B_i, C_i parameters describe the i -th circuit structure and σ^2 is the "white" noise variance. The correctness of the upper relation was proved out from the investigations of different circuit structures. Depending on the structure complexity and components' number (adders, multipliers, delay elements), some of the parameters A_i, B_i, C_i could be equal to zero. After replacing $\Phi_\varepsilon^i(z)$ $i = 1, 2, \dots, M$ (eq.5) into the common expression for the variance (4) it is obtained :

$$\sigma_r^2 = \frac{\sigma^2}{2\pi \cdot j} \left[\oint_{|z|=1} \sum_{i=1}^{M-1} M_i(z) \cdot \frac{dz}{z} + \oint_{|z|=1} M_M(z) \cdot \frac{dz}{z} \right], \quad (6)$$

where: $M_i(z) = \prod_{s=i+1}^M H_s^2 \cdot Y_i(z) \cdot Y_i(z^{-1})$,

$$M_M(z) = Y_M(z) = \frac{A_M + B_M \cdot z + C_M \cdot z^2}{1 + a_M \cdot z + b_M \cdot z^2},$$

$$Y_i(z) = \frac{(A_i + B_i \cdot z + C_i \cdot z^2) \cdot (1+z)^{2(M-i)}}{\prod_{s=i}^M (1 + a_s \cdot z + b_s \cdot z^2)}. \quad (7)$$

In order to be solved the circulation integrals in (6) it is necessary to prevent $Y_i(z)$ in fractional-rational form :

$$Y_i(z) = \frac{\sum_{s=0}^{2M-2i+2} (L_s \cdot z^s)}{\sum_{s=0}^{2M-2i+2} (F_s \cdot z^s)}, \quad i = 1, 2, \dots, M-1. \quad (8)$$

The binomial theorem was used to present the following product :

$$(A_i + B_i \cdot z + C_i \cdot z^2) \cdot (1+z)^{2(M-i)} = A_i +$$

$$+ z \cdot (A_i \cdot C_{2M-2i}^1 + B_i) + z^2 \cdot (A_i \cdot C_{2M-2i}^2 + B_i \cdot C_{2M-2i}^1 + C_i) +$$

$$+ z^3 \cdot (A_i \cdot C_{2M-2i}^3 + B_i \cdot C_{2M-2i}^2 + C_i \cdot C_{2M-2i}^1) + \dots +$$

$$+ z^{2M-2i-1} \cdot (A_i \cdot C_{2M-2i}^{2M-2i-1} + B_i \cdot C_{2M-2i}^{2M-2i-2} + C_i \cdot C_{2M-2i}^{2M-2i-3}) +$$

$+ z^{2M-2i} \cdot (A_i + B_i \cdot C_{2M-2i}^{2M-2i-1} + C_i \cdot C_{2M-2i}^{2M-2i-2}) +$
 $+ z^{2M-2i+1} \cdot (B_i + C_i \cdot C_{2M-2i}^{2M-2i-1}) + z^{2M-2i+2} \cdot C_i$, (9)
 where C_i^j are binomial coefficients. Comparing (8) and (9) the following common expression for the coefficients L_s (eq.8) was found :

$L_s = A_i \cdot C_{2M-2i}^s + B_i \cdot C_{2M-2i}^{s-1} + C_i \cdot C_{2M-2i}^{s-2}$,
 where $S = 0, 1, \dots, 2M-2i+2$. The denominator of $Y_i(z)$ do

not depend on the type of the filter. To determine F_s (eq.8) two types computational formulas were proposed [6], according to the S value (even or odd). Calculations of the product at the denominator of (7) have been done for $i = 1$ and $M = 1, 2, \dots, 10$. The observed tendency have been summarized for arbitrarily M with the aid of mathematical induction. In case of odd-order lowpass (highpass) filter three considerations were performed depending on the first-order section location in the cascade (at the input, output or inside - Table 3). The parameters $A_k^L, B_k^L, A_k^H, B_k^H$ describe the noise spectral density of lowpass (highpass) first-order sections, k denotes the place of the first-order section in the cascade filter. The L_s expressions for all types even-order filters are generalized in Table 2. Because of the more complex $W_i(z)$ for bandstop section the variance expression becomes too complicated. So, besides the exact variance formula a computationally more efficient relation is proposed (Table 2), based on the assumption that the coefficients C_i ($i=1, \dots, M$) at the nominator of the transfer functions $W_i(z)$ are equal. The investigations showed that these coefficients are nearly equal for some cases, so it is aptly to apply the simplified variance formula.

3. DESIGN METHODOLOGY

A design methodology for optimal recursive filters with minimum resulting error is proposed on the basis of previously derived expressions. This methodology is a part of the Program Package for Digital Filter Design [7] and its input data are as follows : the order of the filter N (number of sections M), the filter's type and $W_i(z)$ coefficients.

Step 1. Obtaining all circuit configurations for all possible pole-zero pairings. This step is obligatory for bandstop filters and for elliptically approximated filters. The exact number of pairings is $(M!)^2$. The displacement of the sections is taken into account at the next steps, so the number of pairings is $M!$

Step 2. Composing $M!$ structures for filter realization differ each other by the sequence of the sections into the cascade. Filters, built up from bandstop sections needs this step to be done for each structure, derived from step 1.

Step 3. For each circuit configuration as an output of Step 2 the following sub-steps are required :

Filter		Coefficients L_S ($i=1, \dots, M-1$; $S=0, \dots, 2M-2i+2$)
LP		$L_S = A_i \cdot C_{2M-2i}^S + B_i \cdot C_{2M-2i}^{S-1} + C_i \cdot C_{2M-2i}^{S-2}$
HP		$L_S = m \cdot A_i \cdot C_{2M-2i}^S - m \cdot B_i \cdot C_{2M-2i}^{S-1} + m \cdot C_i \cdot C_{2M-2i}^{S-2}$, $m = 1$ (s-even number); $m = -1$ (s-odd number)
BP	S-even	$L_S = m \cdot A_i \cdot C_{M-i}^{S/2} - m \cdot C_i \cdot C_{M-i}^{S/2-1}$, $m = 1$ (s/2-even number); $m = -1$ (s/2-odd number)
	S-odd	$L_S = m \cdot B_i \cdot C_{M-i}^{(S-1)/2}$, $m = 1$ for (s-1)/2 - even number; $m = -1$ for (s-1)/2 - odd number
BS	Exact formula	$L_S = F_S$ [6] for $s=i$: $a_i = B_i/A_i$, $b_i = C_i/A_i$; for $s \neq i$: $a_s = c_s$, $b_s = 1$
	Approx. formula	$L_S = A_i \cdot L'_S + B_i \cdot L'_{S-1} + C_i \cdot L'_{S-2}$, where: $L'_S = \sum_{t=0}^{S/2} c_i^{2t} \cdot C_{M-i}^{S/2+t} \cdot C_{S/2+t}^{S/2-t}, \quad S - \text{even number}$ $L'_S = \sum_{t=0}^{(S-1)/2} c_i^{2t+1} \cdot C_{M-i}^{(S+1)/2+t} \cdot C_{(S+1)/2+t}^{(S-1)/2-t}, \quad S - \text{odd number}$ $L'_S = 0, \quad 2M-2i < S < 0$

Table 2

Filter		Coefficients L_S
LP	$k=1$	$L_S = A_k^L \cdot C_{2M-2k}^S + B_k^L \cdot C_{2M-2k}^{S-1}$, for $i=k$, $S=0, \dots, 2M-2i+1$ $L_S = A_i \cdot C_{2M-2i}^S + B_i \cdot C_{2M-2i}^{S-1} + C_i \cdot C_{2M-2i}^{S-2}$, for $i=2, \dots, M-1$, $S=0, \dots, 2M-2i+2$
	$1 < k < M$	$L_S = A_k^L \cdot C_{2M-2k}^S + B_k^L \cdot C_{2M-2k}^{S-1}$, for $i=k$, $S=0, \dots, 2M-2i+1$ $L_S = A_i \cdot C_{2M-2i-1}^S + B_i \cdot C_{2M-2i-1}^{S-1} + C_i \cdot C_{2M-2i-1}^{S-2}$, for $1 \leq i < k$, $S=0, \dots, 2M-2i+1$ $L_S = A_i \cdot C_{2M-2i}^S + B_i \cdot C_{2M-2i}^{S-1} + C_i \cdot C_{2M-2i}^{S-2}$, for $k < i \leq M-1$, $S=0, \dots, 2M-2i+2$
	$k=M$	$L_S = A_i \cdot C_{2M-2i-1}^S + B_i \cdot C_{2M-2i-1}^{S-1} + C_i \cdot C_{2M-2i-1}^{S-2}$, for $i=1, \dots, M-1$, $S=0, \dots, 2M-2i+1$
HP	$k=1$	$L_S = m \cdot A_k^H \cdot C_{2M-2k}^S - m \cdot B_k^H \cdot C_{2M-2k}^{S-1}$, for $i=k$, $S=0, \dots, 2M-2i+1$ $L_S = m \cdot A_i \cdot C_{2M-2i}^S - m \cdot B_i \cdot C_{2M-2i}^{S-1} + m \cdot C_i \cdot C_{2M-2i}^{S-2}$, for $i=2, \dots, M-1$, $S=0, \dots, 2M-2i+2$
	$1 < k < M$	$L_S = m \cdot A_k^H \cdot C_{2M-2k}^S - m \cdot B_k^H \cdot C_{2M-2k}^{S-1}$, for $i=k$, $S=0, \dots, 2M-2i+1$ $L_S = m \cdot A_i \cdot C_{2M-2i-1}^S - m \cdot B_i \cdot C_{2M-2i-1}^{S-1} + m \cdot C_i \cdot C_{2M-2i-1}^{S-2}$, for $1 \leq i < k$, $S=0, \dots, 2M-2i+1$ $L_S = m \cdot A_i \cdot C_{2M-2i}^S - m \cdot B_i \cdot C_{2M-2i}^{S-1} + m \cdot C_i \cdot C_{2M-2i}^{S-2}$, for $k < i \leq M-1$, $S=0, \dots, 2M-2i+2$
	$k=M$	$L_S = m \cdot A_i \cdot C_{2M-2i-1}^S - m \cdot B_i \cdot C_{2M-2i-1}^{S-1} + m \cdot C_i \cdot C_{2M-2i-1}^{S-2}$, for $i=1, \dots, M-1$, $S=0, \dots, 2M-2i+1$ $m = 1$ when s - even, $m = -1$ when s - odd - for all HP cases

Table 3

3.1. Choice of an optimal low-noise structure for each section (from a knowledge-base [8] of elementary circuits).
 3.2. Computation of the coefficients, describing the noise spectral density of each section : A_i, B_i, C_i (second order) and $A_k^L, B_k^L, A_k^H, B_k^H$ (first order).

3.3. Derivation of the coefficients L_s and F_s from the Table 2 and Table 3.

3.4. Calculation of the circulation integrals :

$$I_i = \frac{1}{2\pi j} \oint_{|z|=1} Y_i(z) \cdot Y_i(z^{-1}) \frac{dz}{z}, \quad i = 1, 2, \dots, M$$

3.5. Variance $\sigma_r^2 = f(\sigma^2)$ calculation.

Step 4. The variances for different circuit configurations which was derived in the upper steps are compared to find this with the minimum value.

4. EXAMPLE

A great number of numerical examples based on the previously discussed methodology have been examined (with the Program Package PROSIS [7]). The next one will be given below : IIR bandpass filter with specifications - sampling rate 2π rad/s, stopband edges 2 rad/s and 3 rad/s, passband edges 2.5 rad/s and 2.8 rad/s, maximum passband ripple 2.5 dB, minimum stopband attenuation 30 dB. Applying Chebyshev approximation we obtain order $N=6$ and with the Elliptic one - order $N=4$. For filter, based on the Chebyshev approximation the optimal cascade consists of the P5LL, P10LL and P10LL elementary sections (fig.1) with a minimum value $\sigma_{rmin}^2 = 1.507 \cdot \sigma^2$ (according to step 2 from the design methodology six different connections are available with $\sigma_r^2 \in [1.507, 7.054] \cdot \sigma^2$). For elliptically approximated filter the variance depends on the pole-zero pairing and have a minimum value $\sigma_{rmin}^2 = 2.093 \cdot \sigma^2$ with an optimal structure consisting of two sections which circuit configuration is given in [9]. The parameters a, b and H from fig.1 correspond to the a_i, b_i and H_i from Table 1.

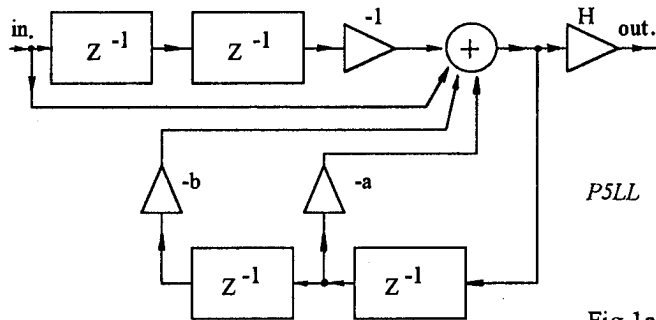
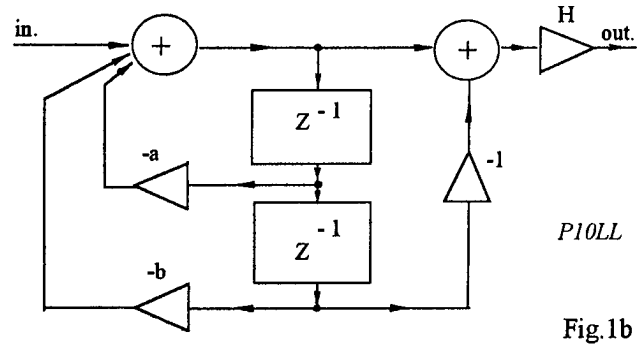


Fig.1a



P10LL

Fig.1b

5. CONCLUSION

This paper describes an alternative way for determination the variance of recursive cascade fixed-point digital filter, easy applicable in CAD design. The software tool available allows an optimal cascade structures to be realized as well as a new elementary low-noise circuits to be added to the knowledge-base in a view of engineering application.

REFERENCES :

- [1] Cappellini, V., Constantinides, A., Emiliani, P. "Digital Filters and Their Applications", Academic Press, London, 1978.
- [2] Jackson, L.B. "Roundoff-noise Analysis for Fixed-point Digital Filters Realized in Cascade or Parallel Form", IEEE Trans. Audio Electroacoustics, vol. AU-18, June 1970, pp.107-122.
- [3] Mondal, K., Mitra, S.K. "Roundoff Noise Upper Bounds for Cascaded Recursive Digital Filter Structures", IEE Proc., vol.129, Pt.G., No.5, Oct.1982, pp.250-255.
- [4] Kawai, S. "Advantageous Estimation Formula of the Least Roundoff Noise for the Cascade Fixed-point Digital Filters", Proc.of the Int. Symp.on Circuits and Systems., Kyoto, Japan, June 1985, pp.511-512.
- [5] Verechkin, A.E., Katkovic, V.J. "Linear Digital Filters and Methods for Realization", Moscow, Sov.Radio, 1973, p.140 (in Russian).
- [6] Mollova, G.S. "Optimal Cascade Structure Design of Recursive Digital Filter with Minimal Resulting Quantization Error", Izv.VUZ. Priborostroenie, No.12, 1991 (in Russian).
- [7] Shoikova, E.D., Mollova, G.S. "Integrated Environment for Digital Filters Design - Program Package 'PROSIS'", XXVI-th Science Session - "Communicational, Electronical and Computer Systems '93", Sofia, 1993 (in Bulgarian).
- [8] Mollova, G.S. "Knowledge-base for Engineering Design of Electronic Digital Filters", Proc. of the VIII-th Int. Conf. 'Systems for Automation of Engineering & Research', Varna, Bulgaria.
- [9] Verkroost, G., "A General Second-Order Digital Filter with Controlled Rounding to Exclude Limit Cycles for Constant Input Signals", IEEE Trans. on Circuits and Systems, vol.CAS-24, No.8, Aug.1977, pp.428-431.

RF CHARACTERIZATION OF A LOW COST MULTICHIP PACKAGING TECHNOLOGY FOR MONOLITHIC MICROWAVE AND MILLIMETER WAVE INTEGRATED CIRCUITS

K. (Jay) Jayaraj and Thomas E. Noll

Foster-Miller, Inc.

350 Second Avenue, Waltham, MA 02154

Phone: (617) 290-0992 FAX: (617) 290-0693

e-mail: jayaraj@world.std.com

and

Donald Singh

Honeywell Technology Center

3660 Technology Drive, Minneapolis, MN 55418

Phone: (612) 951-7874 FAX: (612) 951-7438

e-mail: singh_donald@htc.honeywell.com

ABSTRACT

This paper describes a unique multichip module technology based on highly impermeable *liquid crystal polymers* (LCPs) to interconnect and package Microwave and Millimeter Wave Monolithic Integrated Circuits (MIMICs). Because of the low moisture permeability of the LCPs, the packages can be made hermetic without heavy expensive housings, and can be two to four times lighter and one-fifth the cost of conventional ceramic based transmit/receive (T/R) modules. Preliminary results indicate that the LCP has a low dielectric constant, and low loss transmission lines can be manufactured on LCPs using large area processing techniques that provide a tremendous cost advantage over competing technologies. Using flip chip bonded MMICs attached to a high thermal conductivity, low coefficient of thermal expansion substrate, this innovative technology can meet a variety of commercial, military and space requirements.

1. INTRODUCTION

On account of their ability to form multiple beams and provide variable power among beams, phased array antennas using GaAs MIMICs are gaining significance in aircraft and space-based radar as well as communication applications. These systems require highly complex transmit/receive (T/R) modules, each containing a large number of GaAs MMICs required to meet the wide range of system performance, and also have the following properties: low cost, small size, high density housing and thin profile.

Although multichip packaging approaches have been in use for many years for digital ICs, packaging microwave and

millimeter wave MMICs is, in general, more demanding than packages typically encountered for digital and low frequency analog applications. These packages are characterized by a low lead count, high lead-to-lead isolation, tightly controlled transmission line impedance levels, and very low interconnect and transition losses.

At present, typical T/R modules contain several MIMICs which must be interconnected using single or multilayer RF substrates. The interconnect should have low insertion loss, wide bandwidth, low dispersion, small size and ease of reproducibility. In addition, the substrate should be able to incorporate both RF and control signal lines as well as DC bias lines without mutual interference and buried compact structures such as couplers, filters, power dividers, etc.

Traditionally these substrates have metallization of both sides and have either a thick film or a thin film circuitry on the top surface, whereas the bottom surface is either soldered or attached using epoxy to a metal base (4-5). Alumina ($\epsilon_r \sim 9.9$) is typically used as a substrate in the microwave frequencies whereas quartz ($\epsilon_r \sim 3.78$) is used in millimeter wave range. With increased system requirements it becomes necessary to include many GaAs MMICs as well as digital ICs together with thin film bypass capacitors and off-chip matching networks for power amplifiers on the same package. One method of solving this problem is by combining thick film and thin film metallization on the same substrate. The RF circuitry is on the top thin film, while a multilayer thick film interconnect circuit is at the bottom. Laser drilled via holes connect the thick film and thin film metal layers. Although such a technique has some advantages, these substrates do have many drawbacks of which the following are of prime importance:

- Increased overall cost due to non-compatibility of thick and thin film processes.
- Interconnection vias limit the chip density and also degrade the electrical performance.
- Thin film passive RF components and network occupy a large area resulting in further decrease in chip density, thereby increasing the overall package cost.
- Need for a hermetic package to protect the MMICs.

Our unique approach solves these problems by combining the RF, control signal lines and the DC bias lines on a single multilayer LCP substrate.

2. THE TECHNICAL APPROACH

Our approach is based on exploiting the barrier and dielectric properties of liquid crystal polymers to interconnect and package MMICs. To meet the permeability requirements the key is the utilization of the extremely low permeability of liquid crystalline polymers compared to other polymers. The permeability of Vectra™ and other LCP films has been measured because of the interest in their use as barrier films by the food packaging industry. Although unoriented films exhibit good barrier properties, biaxially-oriented films show orders of magnitude lower values. Foster-Miller has developed a unique extrusion process based on a patented counter-rotating die technology. This process differs from conventional extrusion processes in that it biaxially orients the polymer chains as they are being extruded, imparting balanced mechanical properties. Thus, due to the low moisture permeability of the LCPs, the packages can be made hermetic without heavy expensive housings, and can be *two to four times lighter* and *one-fifth* the cost of conventional ceramic based T/R modules.

2.1. RF Characterization

In order to fully exploit the dielectric properties of the LCP it is necessary to determine the dielectric constant and loss tangent of the LCP material as well as the characteristics of various planar transmission lines designed using this material in the microwave and millimeter wave region. Traditionally used microstrip lines and coplanar waveguides (CPWs), shown in Figure 1, were the planar transmission lines chosen to be characterized. Moreover, the highly accurate microstrip ring resonator techniques were used to measure the dielectric properties of the LCP material.

For measurement purposes the LCP films were bonded onto a 20 mils thick alumina substrate having metallization on one side and laminated with conventional high ductility copper foil of 9 μm thickness. The tooth structure of the copper file gives excellent adhesion over a wide range of temperature, although its roughness may increase losses at higher frequencies. Numerous microstrip and CPW structures having a wide range of

impedances were designed and placed on the LCP substrate (Table 1). These LCP substrates have thicknesses of approximately 4, 5, 6 and 20 mils, respectively.

These microstrip and CPW test structures were characterized (S-parameters) on-wafer, in the 0.5-40 GHz frequency range, using high frequency Cascade Microtech Probes and an HP 8510C network analyzer. The dielectric properties of the LCP were calculated using the multiple resonances in transmission ($|S_{21}|$) measurement in the ring resonator structures. Since the resonant frequencies are measured very precisely by the network analyzer, the calculated dielectric properties of the material are very accurate. Similarly, the complete characteristics of the transmission lines, namely, characteristic impedance (Z_0), effective dielectric constant (ϵ_{eff}) and loss (α) were calculated from the measured S-parameters.

Figure 2 shows the measured multiple resonances in a typical ring resonator structure and Table 2 shows for the first time the derived relative dielectric constant (ϵ_r) of the LCP substrate. From this it is clear that the LCP has a fairly uniform relative dielectric constant of 3.08 in the 0.5-40 GHz range. Figure 3 shows the measured ' Z_0 ', ' ϵ_{eff} ', and ' α ' of a 50 Ω microstrip line and an 80 Ω conductor-backed CPW. These results indicate that the lines have *extremely low dispersion* and *uniform characteristic impedance* in the 0.5-40 GHz region. Moreover, the line losses of ~0.3 dB/cm (@ 35 GHz), although slightly higher than similar lines on Duroid, are still low enough for packaging applications. In addition, these results were found to be in good agreement with theoretical predictions. We are highly encouraged by these initial results which represent first ever measurements on an unoptimized LCP package in the microwave and millimeter wave frequency band. Finally, since reducing the conductor surface roughness will result in lower losses, we believe that the RF performance of an optimized LCP package in a system will greatly exceed that of the state-of-the-art packages. Figure 4 shows the design process of LCP package technology.

2.2. Advantages of Our Approach Over Current Approaches

This unique and new approach provides many advantages over current packaging techniques. Our approach uses the highly reliable flip chip technology which is ideally suited for large volume applications compared to ribbon bonding. The interconnects can be designed either as microstrip lines or CPW. The need for a hermetic package is eliminated due to the highly impermeable characteristics of the LCP, which results in tremendous cost and weight savings. Finally, this new approach enjoys many advantages of the chips-first approach (separation of electrical and thermal paths, high device packaging density, low inductance, short chip interconnections) but overcomes the following limitations:

- Easier defective IC replacement - no need to rebuild the entire interconnect.
- ICs not subjected to processing stresses - chips last versus chips first.
- Weight and cost penalty due to the hermetic package.

3. CONCLUSIONS

This paper describes a novel technique for packaging MMIC devices which takes advantage of the unique dielectric and

barrier properties of LCPs. Preliminary data on microstrip line transmission lines on the LCP indicate that the material is suitable for microwave and millimeter wave system applications. Helium leak tests clearly indicate that near-hermetic packages can be achieved without using conventional metal or ceramic packages. Elimination of a conventional hermetic package coupled with large area processing techniques results in a low cost approach for MMIC based T/R module array systems.

Table 1. Dimensions of a Few Test Structures

Structure Type	Impedance (Ω)	W (μ m)	S (μ m)
Mstrip	20	965	
Mstrip	35	475	
Mstrip	50	275	
Matrip	75	150	
CBCPW	90	50	100
CBCPW	66	100	150
CBCPW	50	125	150
CPW	110	50	150
CPW	150	50	350

Length = 1250 μ m, 2500 μ m

Mstrip - Microstrip, CPW - coplanar waveguide.

CBCPW - Conductor backed CPW

Table 2. Results from Ring Resonator Measurements

Resonator Number	Resonant Frequency (GHz)	Relative Dielectric Constant
LCPRR-I-1	33.02	3.18
LCPRR-I-2	32.15	3.07
LCPRR-II-1	10.43	3.08
	20.81	3.08
	31.13	3.08
LCPRR-III-1	6.97	3.08
	13.93	3.08
	20.87	3.08
	27.78	3.08
	34.66	3.08

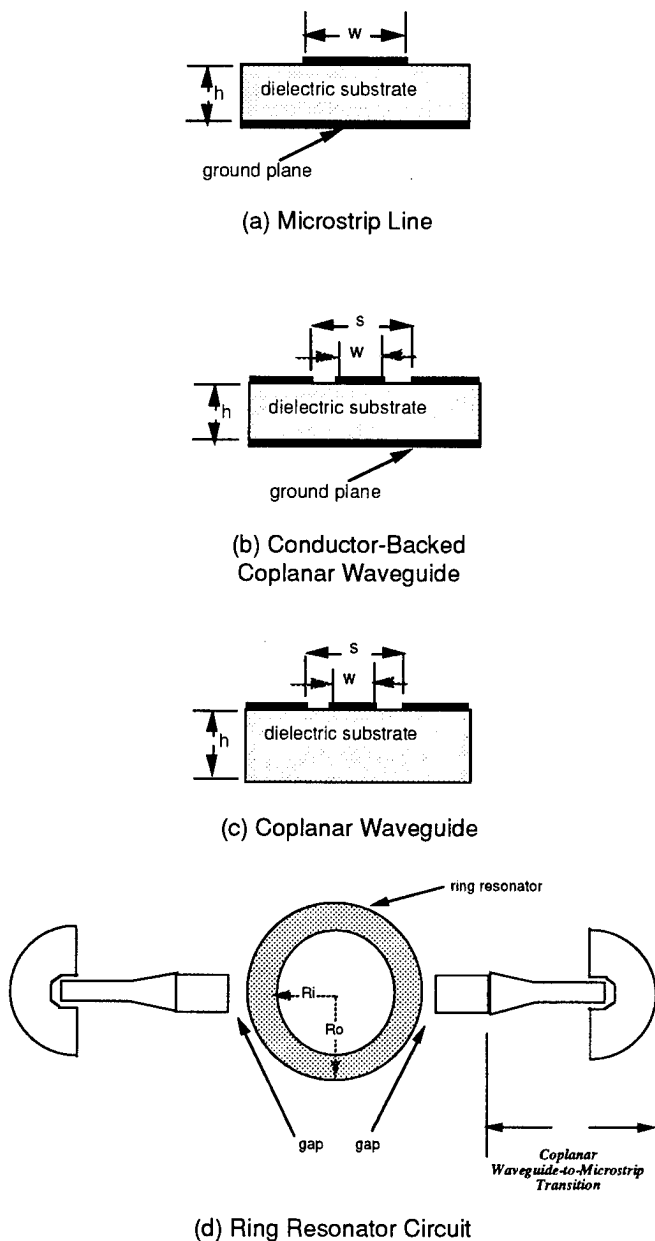


Figure 1. (a), (b) & (c) Cross-section of Microstrip Line, Conductor-Backed Coplanar Waveguide and Coplanar Waveguide Transmission Lines; (d) Ring Resonator Circuit Layout

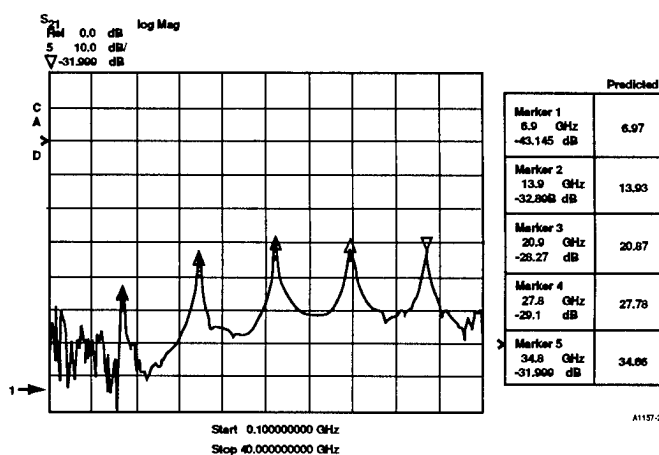
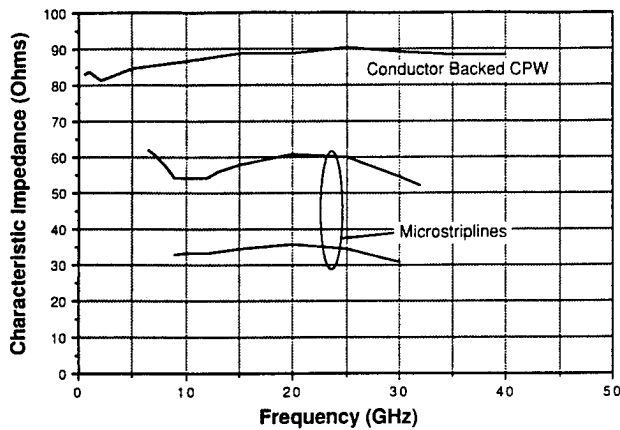
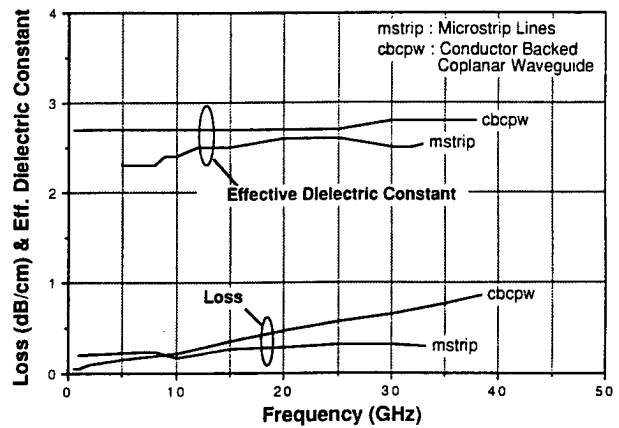


Figure 2. Measured Transmission Characteristics of Microstrip Ring Resonators



(a)



(b)

Figure 3. Measured Characteristics of Microstrip and Coplanar Waveguides on LCP

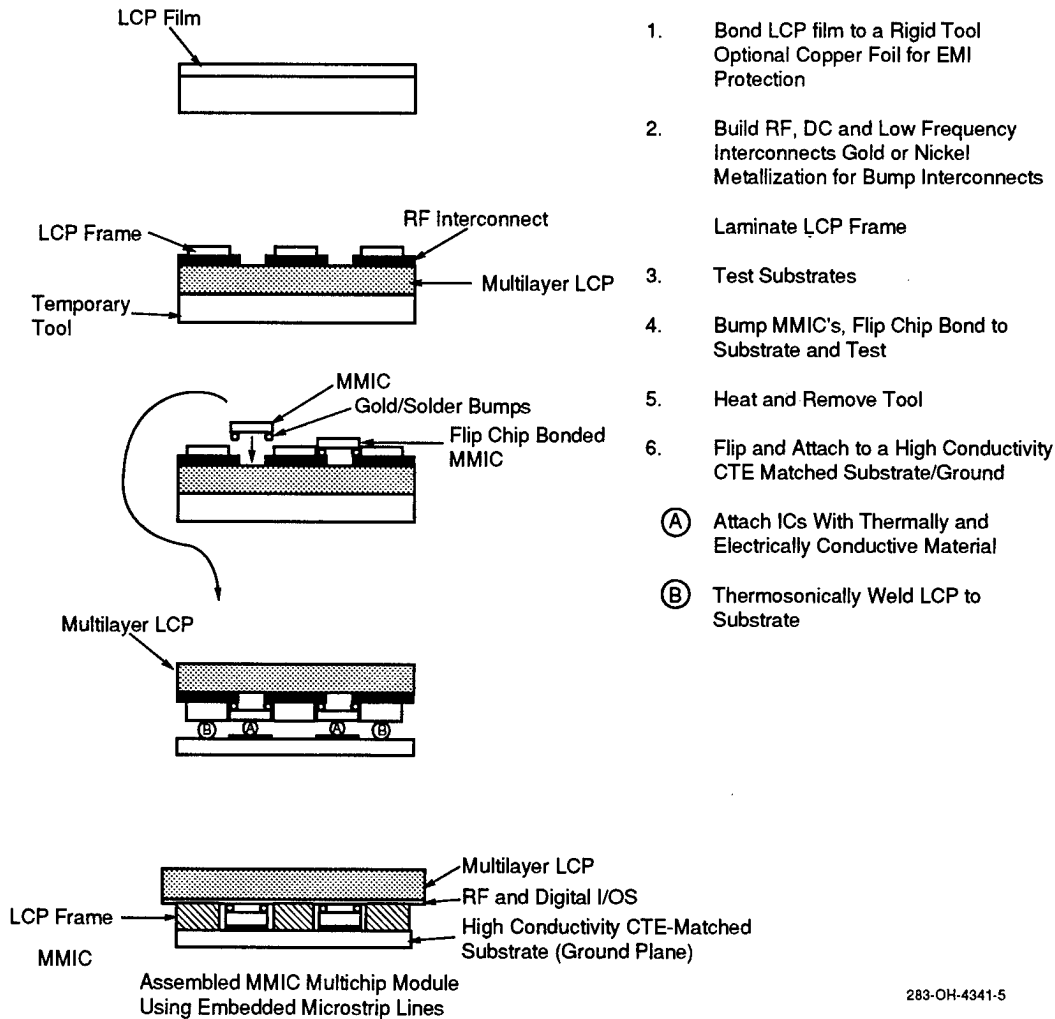


Figure 4. Process Flow of LCP Packaging Technology

NOVEL APPROACH USING TAPERS FOR HIGH POWER FET CHIPS CHARACTERIZATION

M. Zoyo, C. Galy*, A. Darbandi**, L. Lapierre***, JF. Sautereau*****

* Equipe Antennes Dispositif et Matériaux Microondes, UPS-LGE,
118 route de Narbonne 31068 Toulouse

** Alcatel Espace 26 av. JF.Champollion 31037 Toulouse

*** CNES 18 av. Ed.Belin 31055 Toulouse

**** UPS-LAAS/CNRS 7 av. Col. Roche 31400 Toulouse

ABSTRACT

This paper introduces a novel approach for the characterization of high power devices of total gate periphery (G.P.) around 20mm. Electrical models of two power FET chip devices (G.P.=4.8mm and 12.6mm) are obtained from scattering parameters measurements based on broadband impedance transformers and from DC pulsed measurements. A small scaling factor applied on these electrical models allows to get those of high power devices.

1. INTRODUCTION

High power chip devices with large G.P. around 20mm have been developed in order to deliver a high RF output power.

The characterization of these devices is required for the design of solid state power amplifiers.

These power devices are made by several elementary cells in parallel configuration, consequently the impedance values of device ports are quite small ($\approx 1\Omega$).

The usual technique consists of measuring S-parameters of a unit cell (G.P. ≈ 1 mm) on 50-ohms impedance environment, then a large scaling up (10~20 times) allows to achieve the equivalent electrical circuit.

The drawbacks of this technique are the following:

- Large scaling factor introduces a large error in the equivalent electrical circuits.
- Cells in power chip devices don't have the same environment as a single cell chip alone, such as electrical coupling effects, thermal coupling effects, dispersion in the processes manufacturing, ...etc.

In this paper we suggest a new technique of modelling the high power chip devices without the above mentioned drawbacks.

This technique is based on characterization of a big G.P. device and then using a small scaling factor for the very big devices (factor ≈ 2).

The use of test jig which transforms 50-ohms in few ohms at the ports of device is required for S-parameters measurements. This broadband transformation is realized by using exponential taper on microstrip technology.

A specific test bench is used for DC pulsed measurements.

We present the characterization of two power chip devices, a MESFET transistor with a G.P. of 12.6mm and a HFET transistor with a G.P. of 4.8mm.

2. TEST JIG CIRCUIT DESIGN

In standard techniques, S-parameters measurements of the device under test are made on 50 Ω impedance environment.

Power chip devices have low input and output impedances (few ohms) and specific test jig is required for the S-parameters measures. This test jig must remove, in wide band of frequency, high VSWR conditions. The impedance transformer can be obtained, for example, in using quarter-wave length cascaded transmission-line sections [1] or various forms of non-uniform transmission-lines [2,3].

Figure 1a shows the different forms of tapers (Tchebyscheff, hyperbolic, exponential) and figure 1b shows values of corresponding reflection coefficients [4].

The test jig used for the characterization of the power discrete chip devices, is made of two exponential tapers fabricated on microstrip alumina substrate of 0.254mm thickness (fig.2a), which drops significantly the high VSWR with a minimum of length [5]. In order to modelize the exponential form, each taper is discretized as ten same unit length tapered transmission-line sections.

The electrical model of the exponential taper has been verified by experimental measurements on two cascaded tapers for several configuration of connection with various bond wires or ribbons.

Figure 2b shows the measured and modelled insertion loss of two cascaded exponential tapers.

3. POWER CHIP DEVICES CHARACTERIZATION

RF tests and DC pulsed tests have been made on commercial power FET chip devices (a MESFET with G.P. of 12.6mm and a HFET with G.P. of 4.8mm), for several bias points.

A linear and non-linear electrical model of power FET transistors developed by Alcatel Espace are shown in figure 3.

The de-embedding method is applied to S-parameters measured on the previous test jig with input and output tapers, in order to extract S-parameters of device.

The linear model element values are optimized to fit calculated and extracted S-parameters. Figure 4a and 5a represent the modelled and measured small-signal S_{11} and S_{22} parameters of the MESFET and HFET devices.

The non-linear model parameters are determined by specific DC pulsed measurements [6] on power devices.

Four non-linearities have been taken into account. The breakdown current source, I_{dg} , and the direct current source, I_g , are modelled empirically by exponential equations. The capacitor C_{gs} is described by a hyperbolic tangent form versus the gate voltage, V_g . The drain current source, I_d , defined by bicubic spline function [7], allows to represent I-V characteristics.

Figure 4b and 5b shows the simulated and measured I-V relationship of these devices.

CONCLUSION

A specific test jig has been developed for broadband impedance transformation in order to measure scattering parameters of power chip devices with big G.P., in addition to the DC pulsed measurements. Power chip devices of type MESFET and HFET have been successfully characterized. High power chip devices (G.P. ≈ 20 mm) are obtained by a small scaling factor. This novel approach allows to reduce errors which happen in using a more large scaling up.

REFERENCES

- [1] S.B. COHN: "Optimum design of stepped transmission-line transformers" IRE Trans. On MTT Vol.3 n°4 April 1955 pp16-21
- [2] M.J. AHMED: "Impedance transformation equations for exponential, cosine-squared, and parabolic tapered transmission lines" IEEE Trans. On MTT Vol.29 n°1 Jan. 1981 pp67-68
- [3] P. PRAMANICK, P. BHARTIA: "Tapered microstrip transmission lines" IEEE MTT-S Digest 1983 pp242-244
- [4] T.S. SAAD: "Microwave engineer's handbook" Artech House Vol.1 1971
- [5] C.P. WOMACK: "The use of exponential transmission lines in microwave components" IRE Trans. On MTT Vol.10 March 1962 pp124-132
- [6] R. QUERE, J.P. VIAUD, J.P. TEYSSIER, J. OBREGON: "Nonlinear transistor modelling based on measurements results" European Microwave Conference 1994 pp136-141
- [7] A. PEDEN, R.A. PERICHON: "Table de données pour la description de modèles non-linéaires de MESFET" 7èmes Journées Nationales Microondes Grenoble 1991 pp279-280

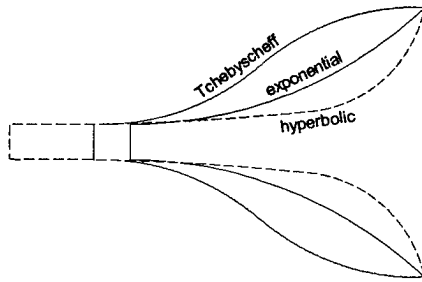


Figure 1a:
Geometric forms of tapers

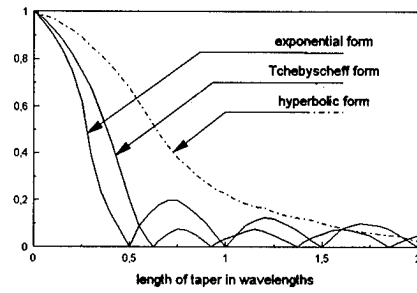


Figure 1b:
Magnitude of reflection coefficient for three tapers

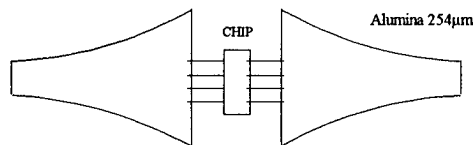


Figure 2a:
Test jig schematic

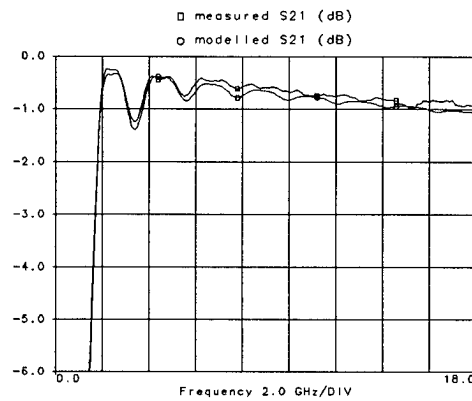


Figure 2b:
Insertion loss of two exponential tapers cascaded

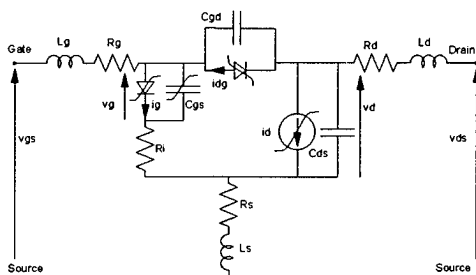


Figure 3:
Linear and non-linear model of the FET

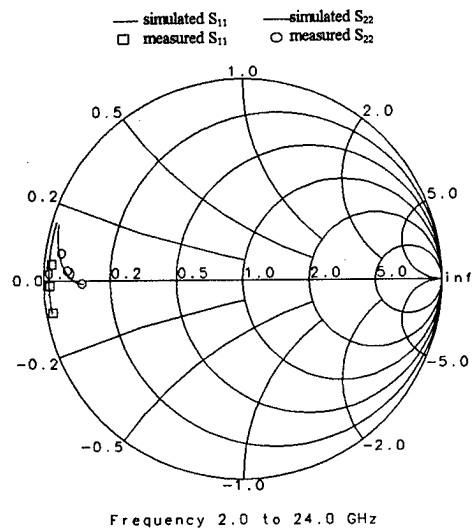


Figure 4a:
 S_{11} and S_{22} , measured and modelled values, of MESFET (G.P.=12.6mm)

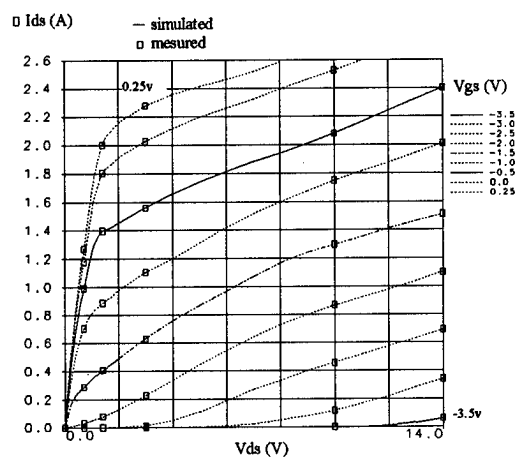


Figure 4b:
Measured and modelled I-V curves of MESFET (G.P.=12.6mm)

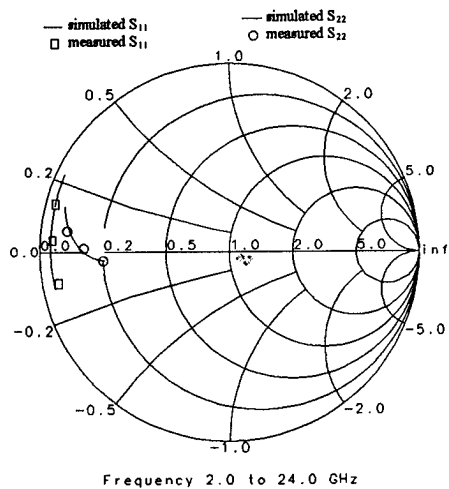


Figure 5a:
 S_{11} and S_{22} , measured and modelled values, of HFET (G.P.=4.8mm)

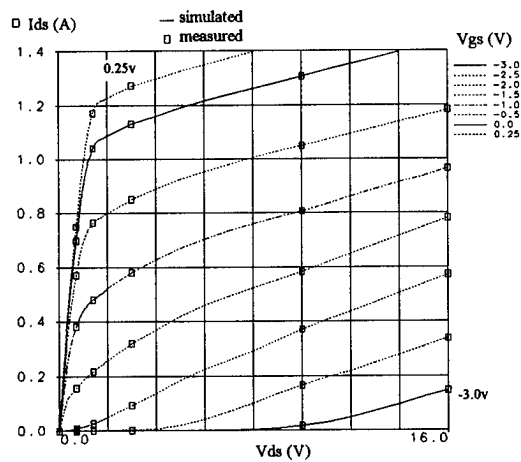


Figure 5b:
Measured and modelled I-V curves of HFET (G.P.=4.8mm)

HIGH TEMPERATURE OPERATIONAL AMPLIFIER WITH LOW OFFSET VOLTAGE

J. Bergmann and A. ten Have

Institute for Electronics
Ruhr-Universität Bochum
D-44780 Bochum
joachim.bergmann@rz.ruhr-uni-bochum.de

Abstract

In this paper circuit design techniques for high temperature electronics are presented. It will be shown that standard Bulk-CMOS technology may be suitable for circuits operating well at temperatures up to 250 °C, if special design techniques are considered.

While using standard circuits at elevated temperatures, main difficulties arise from the drain leakage current of MOSFETs which is amplified by a parasitic bipolar transistor (known from latch-up) and therefore becomes much higher than the original diffusion leakage current caused by the pn-junction of the drain-bulk diode. A low leakage current for MOSFETs can be achieved by a special circuit design technique. Further problems result from the drift of the threshold voltage depending on temperature and time.

As an example a Commutating Automatic Zero Operational Amplifier (CAZ-OPA) is presented in order to demonstrate the capabilities of standard Bulk-CMOS. This CAZ-OPA works with a digital circuit for offset compensation.

1. Introduction

In many fields of sensor-applications it is necessary to have an OPA for signal-conditioning close to the sensor to achieve a good signal to noise ratio. There are a lot of dc-coupled applications demanded for high temperature operation (up to 250 °C) which need OPAs with dc-characteristics like high input impedance, low input current and low input referred offset

voltage. We still have not found any commercially available amplifier fulfilling all these requirements at the same time while operating at high temperature.

We like to present a high temperature circuit-design technique for integrated MOS-circuits achieving good high temperature performance combined with a well known technology and low price. A high temperature OPA with a low input referred offset voltage will be taken as an example.

It should be stated that we are not working in the area of special materials and technologies like gallium-arsenide, silicon-carbide or diamond. Our objective is to find optimized circuit designs so that the circuit function becomes independent of device degradation due to high temperature.

2. High temperature performance of commercially available CMOS devices

The investigation of commercially available CMOS devices shows three main phenomena causing malfunction of systems at elevated temperatures:

- high input leakage currents,
- high input offset voltage and offset voltage drift,
- latch-up at high temperatures (in most cases at about 180 °C).

An analysis of these phenomena shows two main problems:

1st Problem: The leakage current of reversely biased diodes increases exponentially with rising

temperature and causes input currents (protection circuitry), operating point drifts and latch-up problems. The main problem is the parasitic bipolar transistor that can be found in MOS-transistors (figure 1). This bipolar transistor is well known from CMOS latch-up and causes an internal amplification of the drain leakage current at high temperatures (e. g. with a current gain of $B \approx 20$ @ $L = 2 \mu\text{m}$).

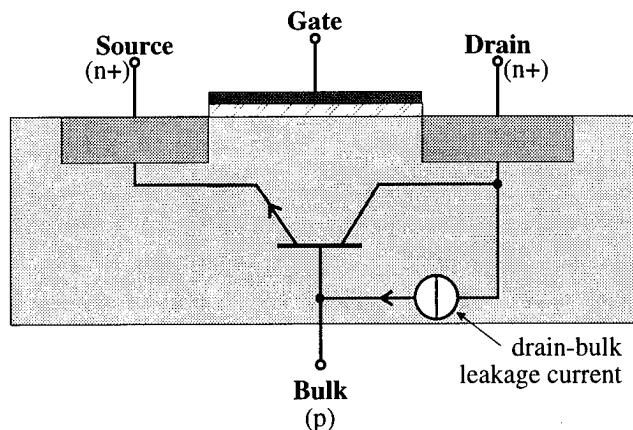


Figure 1: MOS-transistor with parasitic bipolar transistor.

Solution: By using a bulk-source reverse voltage it can be achieved that the leakage current itself will no longer be the base current of the parasitic bipolar transistor, so that no amplification will occur. Figure 2 shows the drain current of a n-channel MOSFET versus gate source voltage at 300 °C for different bulk-source reverse voltages.

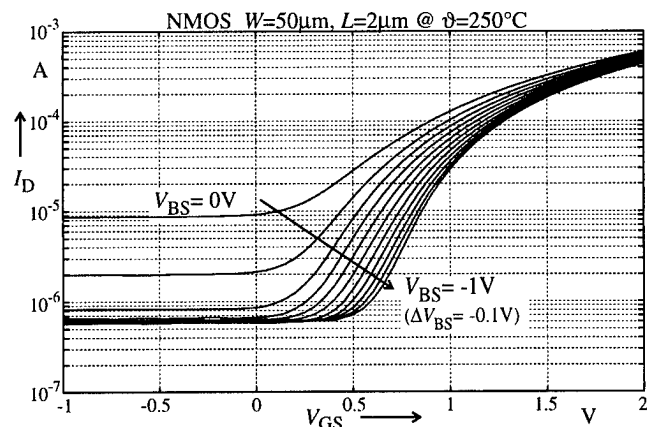


Figure 2: I_{DS} versus V_{GS} of MOS transistor for different Bulk-Source voltages V_{BS} at 250 °C.

Obviously a reverse voltage of about -400 mV is sufficient to prevent the amplification and to

minimize the drain leakage current. The introduction of a reverse voltage means that all existing cell libraries for integrated MOS circuits have to be modified in order to achieve a separation between V_{SS} and substrate potential. First test circuits built up with such cells have shown no latch-up with substrate biasing at temperatures up to 250 °C and even more (latch-up occurred at ≈ 180 °C without substrate biasing).

2nd Problem: A well known problem using MOS-transistors at high temperatures is the threshold voltage instability due to mobile ion contamination of the gate-oxide. For OPAs this instability causes a time and temperature dependent offset voltage in the range of $\pm 20\text{mV}$ or even more. Figure 3 shows the result of an offset voltage measurement done at 300 °C. The device was a simple integrated differential amplifier. It can be seen that an offset voltage drift in the range of 20 mV took place in less than 100 hours. The final offset voltage is not stable, but depends on the current operating conditions.

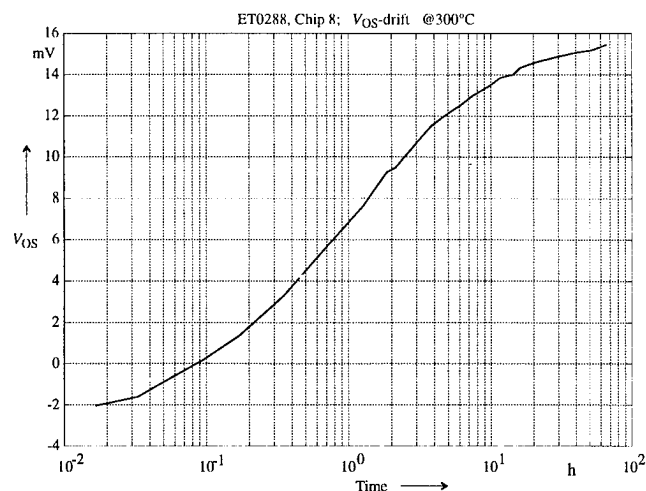


Figure 3: Offset voltage V_{OS} versus time at 300 °C (differential amplifier).

Solution: In order to get an OPA with low offset voltage over the full temperature range and independent of time, self-calibrating circuit designs have to be applied. A known principle for normal temperature applications is the Commutating Automatic Zero (CAZ) amplifier with a capacitor as analog offset correction storage (figure 4).

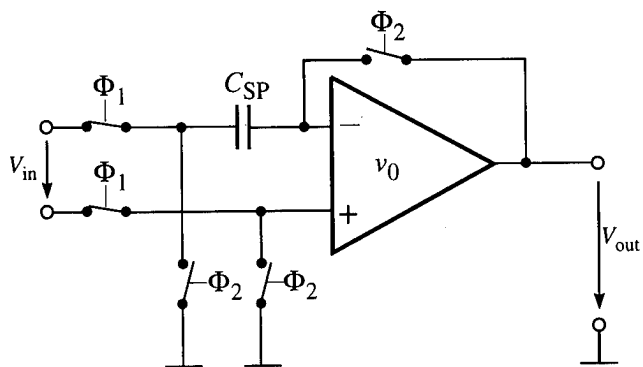


Figure 4: CAZ-Amplifier with analog offset-correction (one of two channels).

This CAZ-OPA does not work at elevated temperatures because of the rather low capacitance values available for high temperature application combined with the leakage currents of analog switches. The capacitor is discharged during amplifying mode (Φ_1 active), offset correction information is falsified and a high offset voltage ripple remains. Therefore we propose a digital storage which is rather independent of leakage currents.

3. A Commutating Automatic Zero Amplifier with digital offset correction

Figure 5 shows one of the two identical channels of a CAZ-OPA using a lossless digital storage for offset correction. With the input pins shorted the offset information at the output of the amplifier has to be converted to digital code. This is done by a simple analog-to-digital converter with Δ -modulator. It consists of the internal OPA itself, a comparator, a binary counter, a digital-to-analog converter (DAC) and control logic.

A main advantage of this circuit is that there is no need for any compensation capacitors with high capacitance values so it becomes suitable for complete monolithic integration.

Using the substrate biasing technique mentioned above we have had no problem to realize the internal OPA, the comparator, the switches and control logic for operation up to at least 250 °C. The influence of the comparator's offset voltage is

reduced by the open loop gain v_0 of the internal OPA.

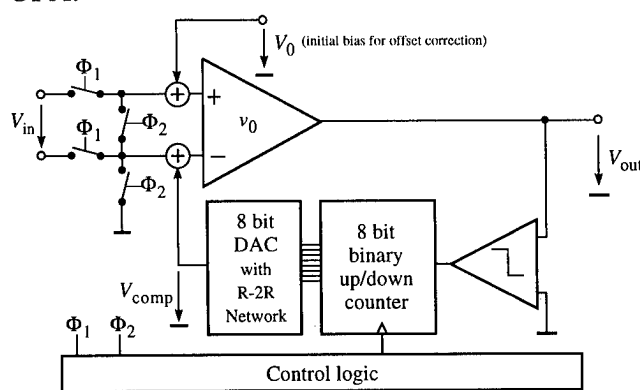


Figure 5: One channel of the CAZ amplifier with digital offset compensation.

The remaining problem for complete monolithic integration in a standard CMOS-technology was to design a suitable digital-to-analog converter.

Another advantage of the proposed CAZ-circuit is that there are no critical requirements for the DAC. Because of the closed loop operation we have no essential problems with offset voltage, gain error or integral linearity-error. The strongest restriction is the differential linearity-error that limits the useable resolution of the DAC and therefore the remaining offset voltage of the CAZ-OPA.

The digital-to-analog converter has been built up with a R-2R resistor network. For reducing the influence of the switches' leakage currents we have chosen the voltage switch mode. The matching errors due to the use of standard polysilicon resistors let us expect a maximum useful resolution of about 8 bits. For higher resolutions laser trimmable thin film resistors are recommended.

Because of a design-error in the resistor network the first converter realized has shown an initial differential linearity-error of more than 1 LSB at room-temperature. Nevertheless, the performance of the converter is rather independent of temperature. Actually a resolution of 7 bit is available for the offset compensation purpose up to 300 °C (figure 6).

Therefore with the proposed digital offset correction a supposed maximum amplifier offset voltage of ± 20 mV can be reduced to less than $240 \mu\text{V}$ over the full temperature range (worst case, but with low pass filter to reduce the influence of the alternating DAC output).

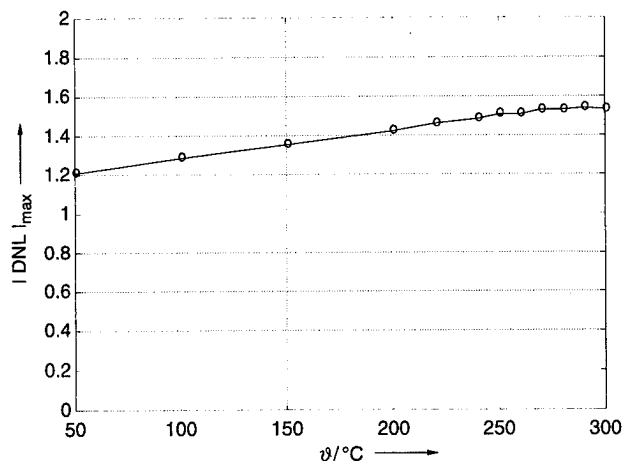


Figure 6: DAC's maximum differential-linearity error versus temperature for 8 bit operation.

A second attempt with corrected resistor network is still undergoing, but simulation promises 8 bit resolution over full temperature range which will lead to further reduction of the CAZ-OPA's offset voltage.

The investigation of a 14 bit DAC with thin film resistor network and substrate biasing has shown a differential linearity-error less than $\frac{1}{2}$ LSB up to 250°C . With the same assumptions this would lead to a remaining offset error of about $2 \mu\text{V}$ for the CAZ-OPA. Actually the decrease in offset-

voltage by increasing the DAC's resolution may be limited by the comparator's offset and the OPA's open loop gain which typically increases respectively decreases with rising temperature.

4. Conclusion

Operating electronic circuits and systems in a wide temperature range makes it necessary to use adapted circuit design techniques to make them independent of the devices' degradation properties. Especially bulk biasing and the consequent use of self-calibrating systems make standard CMOS-processes suitable for applications up to 250°C and even more. In the case of the presented CAZ-OPA (Commutating Automatic Zero Operational Amplifier) the digital offset compensation leads to another advantage compared to common CAZ-OPAs: a complete monolithic integration is possible without external capacitors for offset compensation purposes.

Acknowledgement

The authors want to thank the German Research Ministry and the VDI/VDE-Technologiezentrum Informationstechnik GmbH for financial and administrative support to do this research work.

Moreover they are grateful for the support which they received by ELMOS GmbH, Dortmund, where the monolithic integration took place.

DESIGN OF A HIGH GAIN POWER AMPLIFIER USING A BIAS DEPENDENT LARGE SIGNAL MESFET MODEL AND THE DESCRIBING FUNCTION TECHNIQUE.

*S. Muñoz, J. L. Sebastián and J. D. Gallego**

Facultad de Ciencias Físicas. U. C. M.

28040 Madrid (Spain).

* Centro Astronómico de Yebes.

Aptdo. 148. E19080 Guadalajara (Spain).

Abstract

A MESFET power amplifier has been designed using a large-signal quasi-static model with bias dependent elements. This model has been derived from experimental S parameters and dc measurements.

The analysis and gain optimization of the amplifier is performed by using the describing function technique. Optimum bias device conditions in C class are obtained for maximum gain. Experimental results show an excellent agreement with the theoretical analysis.

I. Introduction.

The knowledge of the small-signal equivalent circuit of the active device is an important part of any microwave design task that must have specific nonlinear requirements. In order to achieve good performance predictions, the appropriate device model parameters should be extracted as accurately as possible. Therefore, the bias dependency of the different elements of the model should be taken into account.

In this paper, a bias dependent nonlinear MESFET model has been derived for the design and analysis of a MESFET RF-power amplifier. The device bias conditions are optimized in order to achieve maximum gain. The RF- power transistor is characterized using the describing function technique where the terminal transistor currents are assumed sinusoidal.

II. Determination of the equivalent circuit elements.

Figure 1 shows the conventional small-signal equivalent circuit of a MESFET. The intrinsic elements are functions of the bias conditions whereas the extrinsic ones are considered to be independent of the operating point.

The element values for this equivalent circuit are found from dc and ac small signal measurements. These values are then optimized in order to fit the measured device scattering

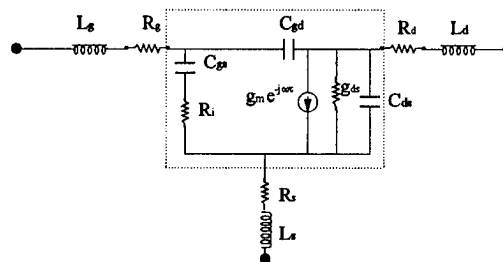


Fig. 1.

parameters. Large-signal information is obtained by the characterization of device S parameters over a broad range of operating bias conditions. In this work the measurements were performed at 100 different bias points within a range where the gate-source voltage varied from nearly pinch-off to slightly forward biased. The drain-source settings varied from low to high bias level values where the device was saturated. The S parameters for each particular bias condition were used to determine a unique set of values for the small-signal circuit elements.

In order to simplify the optimization process for the circuit elements, the extrinsic elements, (parasitic resistances and inductances), were first determined.

The values of the parasitic resistances were obtained under forward-bias gate conditions using the Fukui's method [1].

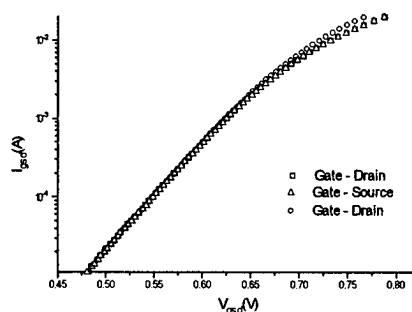


Fig. 2.

Figure 2 shows the three experimental dc current-voltage measurements for the NEC 71083. Although this transistor is not a power device, an appropriate test fixture was readily available and therefore it was used in this work. The values of R_d , R_g and R_s are obtained from the deviation of the slopes of the ideal diodes. The parasitic inductances are obtained using the cold-chip technique proposed by Diamant and Laviron [2]. The inductance values are computed from the imaginary components of the extrinsic device Z parameters at zero drain bias voltage. Figure 3 shows the values of L_d , L_g and L_s as a function of frequency.

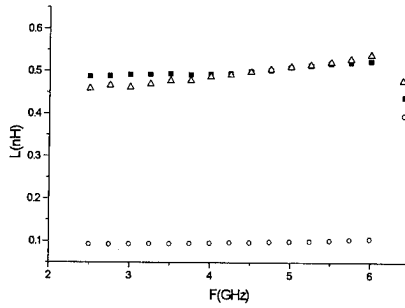


Fig. 3.

The experimental intrinsic y parameters are derived from the measured S parameters by de-embedding the extrinsic parameters. The bias dependent circuit elements are then determined by fitting the analytical y parameters of the equivalent circuit, shown in Figure 1, to the experimental ones. Figure 4 shows the imaginary parts of y_{12} , y_{22} and y_{11} versus frequency for a particular bias condition [3].

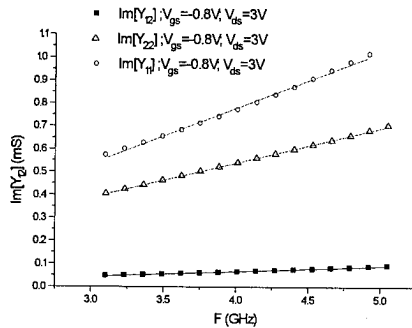


Fig. 4.

Device capacitances, C_{dg} and C_{gs} , are obtained from the slopes of the graphs. This process is repeated for different bias conditions in order to know the variation of the capacitances with the drain-source and gate-source voltages, as it is shown in figures 5 and 6.

The bias dependence of the capacitances is

obtained fitting the experimental results to the following expressions [4]:

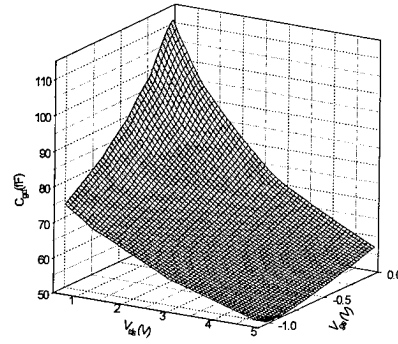


Fig. 5.

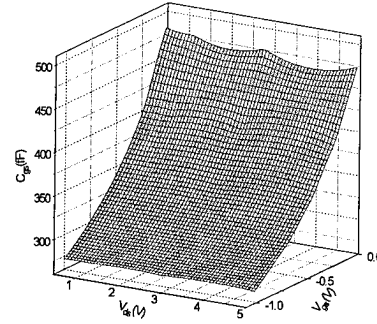


Fig. 6.

$$C_{dg} = C_{dg0} \frac{\exp(C_1 V_{ds}) + C_2 (V_{gs} + V_{ds}) 10^{C_3 (V_{gs} + V_{ds})}}{1 + C_4 V_{ds} 10^{C_3 V_{ds}}}$$

$$C_{gs} = C_{gs0} \frac{\exp(D_1 V_{ds}) + D_2 (V_{gs} + V_{ds}) 10^{D_3 (V_{gs} + V_{ds})}}{1 + D_4 V_{gs} 10^{D_3 V_{gs}}}$$

Finally, using the Curtice-Ettenberg model [5], the drain current, the transconductance and the output conductance are calculated as functions of the bias voltages.

III. Analysis and optimization of the amplifier.

A 4 GHz MESFET C-class amplifier was designed using the model previously obtained. For the analysis, the describing function characterization of the RF-power transistor was used assuming sinusoidal components for the terminal currents.

In order to apply the describing functions, the expressions for the mean-values and the different harmonic components of the transistor terminal voltages must be obtained.

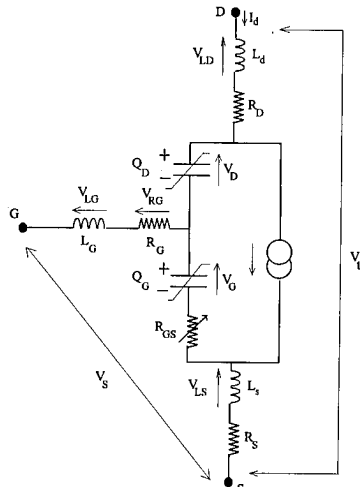


Fig. 7.

According to the model shown in Figure 7 and considering the drain and gate currents given by:

$$I_d = I_{d0} + I_{d1} \cos(\varphi - \varphi_d) \quad (3)$$

$$I_g = I_{g0} + I_{g1} \cos(\varphi - \varphi_g) \quad (4)$$

the transistor terminal voltage components, V_s and V_b , may be resolved in the following terms:

$$\left. \begin{aligned} V_{s0} &= V_{G0} + V_{RS0} + V_{RGS0} \\ V_{t0} &= V_{G0} + V_{D0} + V_{RS0} + V_{RD0} + V_{RGS0} \end{aligned} \right\} m. v.$$

$$\left. \begin{aligned} \vec{V}_{s1} &= \vec{V}_{LG1} + \vec{V}_{RG1} + \vec{V}_{G1} + \vec{V}_{RGS1} + \vec{V}_{LS1} + \vec{V}_{RS1} \\ \vec{V}_{t1} &= \vec{V}_{RS1} + \vec{V}_{LS1} + \vec{V}_{RGS1} + \vec{V}_{G1} + \vec{V}_{D1} + \vec{V}_{RD1} + \vec{V}_{LD1} \end{aligned} \right\} h. c$$

The contributions to the terminal voltages from the linear elements are obtained from straightforward circuit analysis and Fourier series calculations. The contributions, V_d and V_g , from the nonlinear elements are calculated as a function of the total charge Q_d and Q_g respectively, obtained from the experimental drain and gate C-V characteristics. For the device used in this work a parabolic approximation such as [6]:

$$V_{d,g} = \alpha_{d,g} Q_{d,g}^2 + \beta_{d,g} Q_{d,g} \quad (5)$$

gives an excellent fit for both charge-voltage relationships as shown in figures 8 and 9.

Once the device terminal currents and voltages are known, the describing functions are then calculated as the nonlinear impedances at each frequency component.

The complete amplifier is represented by a

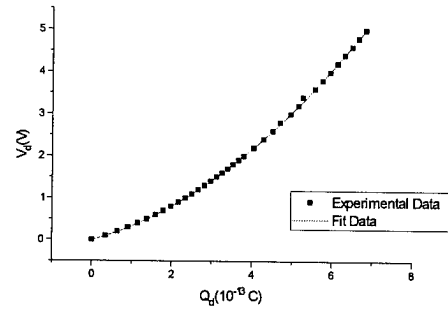


Fig. 8.

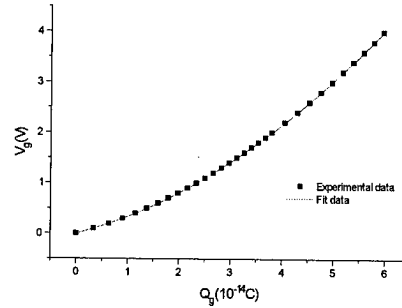


Fig. 9.

system of nonlinear equations that must be solved simultaneously for the unknown variables: terminal currents waveform parameters and the bias conditions V_{ds} and V_{gs} . For computational purposes, the system of nonlinear equations is divided into five subsystems as [7]:

$$S = \{S_{basic}, S_{bias}, S_{load}, S_{drive}, S_{opt}\} = 0 \quad (6)$$

where S_{basic} includes the charge balance equations at the gate terminal, S_{bias} is related to the bias circuit, S_{load} and S_{drive} include the input and output matching circuits and S_{opt} is the set of equations that provides the optimum bias conditions for maximum gain. A good efficiency can be obtained if the amplifier is made to operate in C-class. However, the design is generally quite complicated when using conventional methods. The describing function technique, used in this work, proves to be perfectly adequate to handle the mathematical complexity involved.

Figure 10 shows the amplifier output power for different bias conditions. A maximum output power of 19 dB is obtained at 4 GHz for the particular values of $V_{ds} = 3.5V$ and $V_{gs} = -1.55V$ provided by the solution of the system of nonlinear equations.

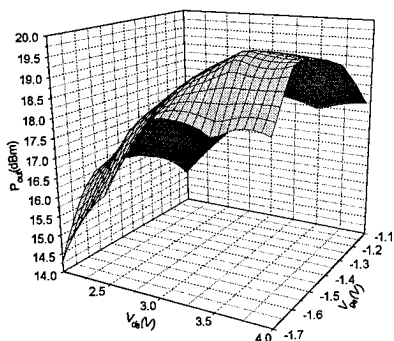


Fig. 10.

IV. Experimental results.

The microstrip layout of the experimental amplifier [8] is shown in Fig 11. The maximum output power value of 18 dBm is obtained at 4.3 GHz for the biasing conditions, $V_{gs} = -1.55$ V and $V_{ds} = 3.5$ V. These values are in excellent agreement with the theoretical results mentioned above.



Fig. 11.

Also, the optimum values of V_{ds} and V_{gs} provide the flattest gain as a function of the input power as well as low distortion as shown in Figure 12.

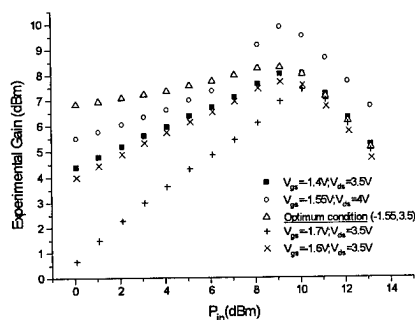


Fig. 12.

Conclusions

A C-class RF amplifier has been designed, analyzed and optimized by using a bias dependent large signal MESFET model. The large signal model has been obtained from experimental S parameters and dc measurements. The use of the describing function technique shows to be a very powerful

tool for the nonlinear analysis of the active device in C-class. This technique also makes possible the appropriate design of the input and output matching networks and the determination of the optimum bias conditions for maximum gain. The experimental results show the validity of the assumptions made a priori for the device terminal voltages and currents in order to solve the set of nonlinear equations.

References.

- [1] H. Fukui. "Determination of the Basic Parameters of a GaAs MESFET". Bell System Journal. Vol 58. n° 3. pp. 771-797. March 1979.
- [2] F. Diamant and M. Laviron. "Measurement of the Extrinsic Series Elements of a Microwave MESFET Under Zero Current Condition". Proc. 12th European Microwave Conference. pp. 451-456. 1982.
- [3] J. M. Golio. "Microwave MESFET's and HEMT's". Artech House 1991.
- [4] J. Rodriguez, K. A. Mezher, O. M. Conde, J. C. Luengo. "A Highly Accurate Microwave Nonlinear MESFET Model". Microwave Journal. pp. 280-285. May 1993.
- [5] W. R. Curtice and M. Ettenberg. "A Nonlinear GaAs FET Model for Use in the Design of Output Circuits for Power Amplifiers". IEEE Transactions on Microwave Theory and Techniques, Vol. MTT-33, n° 12. December 1985.
- [6] J. Vidkjaer. "A Describing Function Approach to Bipolar RF-Power Amplifier Simulation". IEEE Transactions on Circuits and Systems, Vol. CAS-28, n° 8. August 1981.
- [7] S. Muñoz, J. L. Sebastián. "Condición Óptima de Polarización y Principales Parámetros de un Amplificador MESFET-RF de Potencia." Actas del IX Simposium Nacional de la Unión Científica Internacional de Radio. URSI 94. pp. 317-322. Las Palmas 1994.
- [8] J. L. Sebastián and J. M. Miranda. "MWAVE: a Tool for Microwave Amplifier Design". Proc. 23rd European Microwave Conference. pp. 1009-1011. Sept. 1993.

SIMULATION AND CHARACTERIZATION OF A HIGH TEMPERATURE SIMOX-OPERATIONAL AMPLIFIER

P. Gehse and C. Eisenhut

Institute for Electronics
Ruhr-Universität Bochum
D-44780 Bochum

carsten.eisenhut@rz.ruhr-uni-bochum.de

ABSTRACT

For conventional junction isolated silicon integrated circuits, leakage currents increase with temperature. These currents across reverse bias junctions can easily modify circuit performance and even cause latch up. SOI (Silicon On Isolator) devices greatly minimize such leakage currents [1]. Realizing high temperature linear circuits the SIMOX (Separation by IMplantation of OXYgen) technology is used, because this technology can produce fully depleted thin-film MOSFETs with high electrical performance [2].

In this paper a simple SIMOX-model, which is verified in dependence on temperature and back-gate potential is presented. By the help of this model linear circuits (i.e.: operational amplifiers (OPA), voltage references, etc.) are developed, which can be operated up to 300°C.

Furthermore, first long-term examinations are accomplished to predict the reliability of SIMOX-MOSFETs at high temperatures.

1. INTRODUCTION

One of the research activities of the Institute for Electronics is circuit design for temperatures up to +300°C. In this temperature range SIMOX-MOSFETs may be used. These devices cannot be modelled sufficiently using standard SPICE MOSFET models.

We developed a simple macromodel, based on the SPICE MOS Level 1 model, which is capable of simulating a SIMOX-MOSFET in a wide range of operating conditions and uses physically established parameters. The quality of this macromodel is verified by different MOSFET circuit stages, and a high temperature SIMOX OPA with low offset voltage and offset voltage drift by operating temperatures up to 300°C has been realized.

2. SIMOX-MOSFET BASICS

In SIMOX-MOSFETs the film is separated from the bulk by a buried oxide layer (Fig. 1). Due to this the drain-bulk

junction area is much smaller than in conventional 'bulk-silicon' technology. Reduction of this area significantly decreases the leakage current. Furthermore, the fully depleted thin-film SIMOX-MOSFET possess the advantages of less threshold voltage temperature drift, higher integration density and the lack of latch-up [2]. Therefore, SOI-MOSFETs are very attractive for high temperature applications.

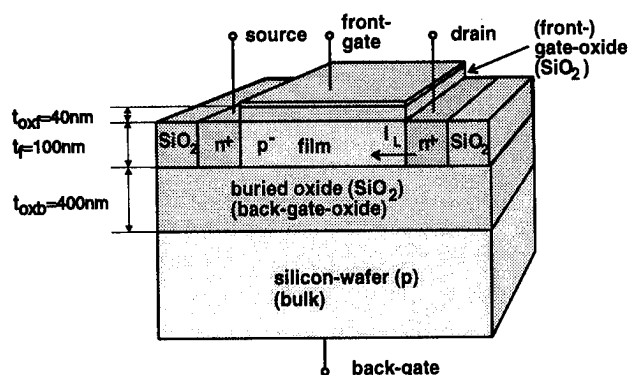


Fig. 1: N-Channel SIMOX-MOSFET

A parasitic property of these transistors is the 'back-gate-effect'. Regarding bulk as a second gate, a dependence of the frontgate threshold-voltage V_{TH} on back-gate potential can be observed [3].

2.1 SIMOX-MOSFET Macromodel and Parameter Extraction

In the used macromodel (Fig. 2) the back-gate-effect is considered using a back-gate-voltage controlled voltage source in series to the gate of a conventional MOSFET model (MOS Level 1 [4]). Due to the lack of temperature dependence of the drain and source resistors in SPICE MOS-models, external resistors have to be added, while the internal resistors have to be defaulted to zero ohms. This model has shown to be valid for temperatures up to 300°C in the regions of back-surface depletion and the beginning of the back-surface accumulation region [5].

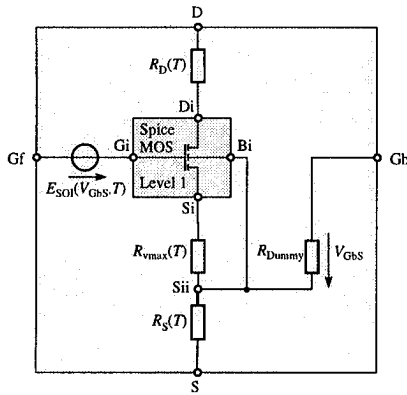


Fig. 2: SIMOX macromodel based on Bulk-MOS Level 1

Parameter determination for a macro-model like this may be a problem, because most of the existing model parameter extraction and optimization software tools are limited to conventional models or are pure extraction tools or are expensive and only available on workstations. Therefore a MS-Windows PC-based system called MIPEXOS (Modular Interactive Parameter EXtraction and Optimization System) has been developed, which is capable of extracting and optimizing parameters from measured data and is not limited to conventional semiconductor models [6]. In fact, models can be coded in a PASCAL-like description language making it possible to realize customized models like the presented macromodel as well as verifying new models.

By the help of MIPEXOS and the SIMOX macromodel we have simulated the transfer characteristics in dependence of back-gate-source voltage V_{Gb} (Fig. 3) and temperature (Fig. 4) to show the temperature independent operating point (ZTC). The transfer-characteristics with respect to V_{Gb} can be divided into three regions of the back-surface state:

back-surface state	electrical influence on front-channel	comparison between simulation and measurement
depletion	$\Delta V_{THf} \sim \Delta V_{Gb}$	good simulation of V_{THf} and g_{mf}
inversion	$V_{THf} = \text{const.}$, but $I_D = I_{Db} > 0$, although front-channel is in accumulation	no simulation of I_{Db}
accumulation	$V_{THf} = \text{const.}$, but $g_{mf} \downarrow$	good simulation of V_{THf} , but no simulation of the change of g_{mf}

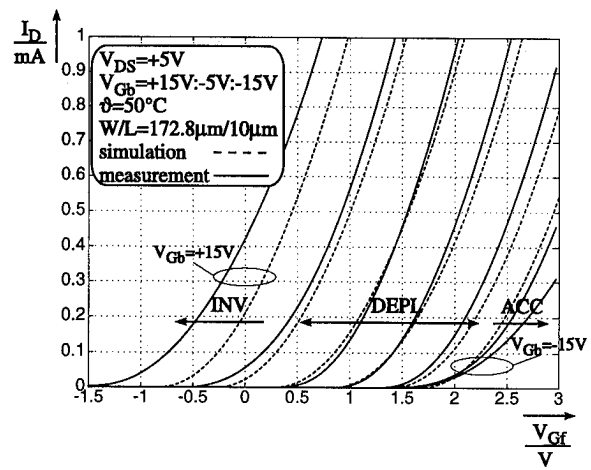


Fig. 3: Transfer characteristic of N-SIMOX-MOSFET depending on V_{Gb}

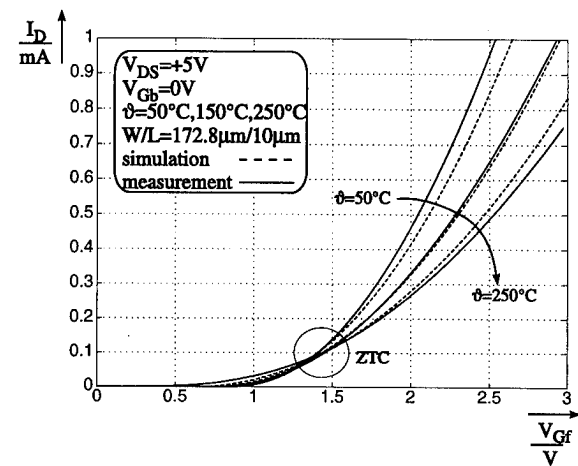


Fig. 4: Transfer characteristic of N-SIMOX-MOSFET depending on ϕ

2.2 SIMOX Circuits

By the help of simple circuits, i. e. current mirrors, differential amplifiers, inverters, output stages and transmission gates the performance of the expanded MOSFET model is examined with regard to temperature and back-gate influence. Fig. 5 and Fig. 6 present good correspondence between simulation and measurement characteristics of a source-stage in series to a source-follower (see transistors M7 - M10 in Fig. 7) in dependence on V_{Gb} , which is varied from 0V to -6V and temperature, which is varied from 50°C up to 290°C. The other stages show similar results.

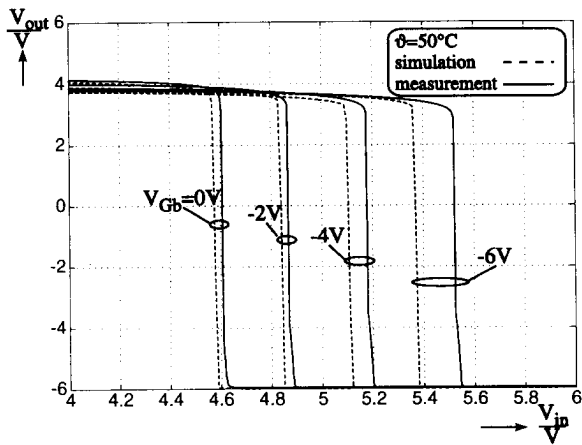


Fig. 5: Transfer characteristics of a source-stage with a source-follower depending on V_{Gb}

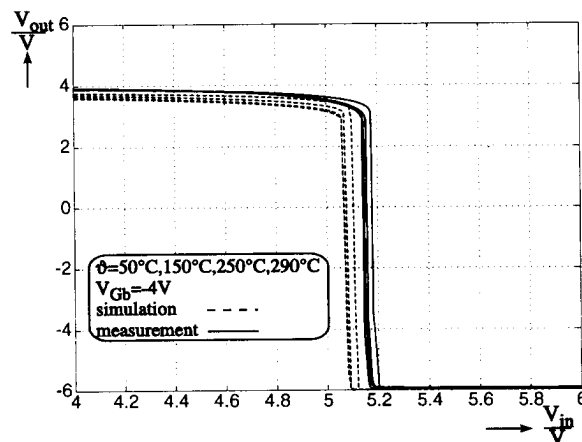


Fig. 6: Transfer characteristics of a source-stage with a source-follower depending on temperature

3. OFFSET-VOLTAGE DRIFT AND DEGRADATION OF A SIMOX-OPA

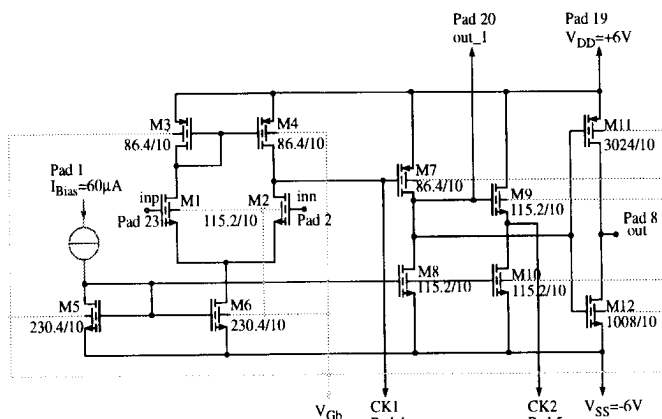


Fig. 7: Circuit diagram of the OPA

In Fig. 7 one of the first realized SIMOX-OPAs is presented. The transistors M1-M10 operate in the ZTC (Zero Temperature Coefficient)-operating point. To reduce the design and simulation effort, only parallel connected unit cells have been used. Furthermore an external current supply is necessary to influence the operating point. The frequency compensation is reached by an external connected capacitor. Tab. 1 gives an overview of the electrical characteristics of this universal frequency compensated OPA up to 300°C.

	20°C	150°C	250°C	300°C
U_{os}/mV	-4	-3	1	2
v_{oDC}/dB	96	92	89	76
CMRR/dB	127	128	129	-
I_{DP}/mA	48	31	22	19

Tab. 1: Electrical characteristics of the OPA

At each temperature the input bias current remains smaller than 1pA (without input protection circuit).

In spite of the small offset-voltage drift, the SIMOX-OPA possess an extreme high offset-voltage degradation at high temperatures under operating conditions (Fig. 8), which has to be examined more intensive on single transistors and single circuit-stages.

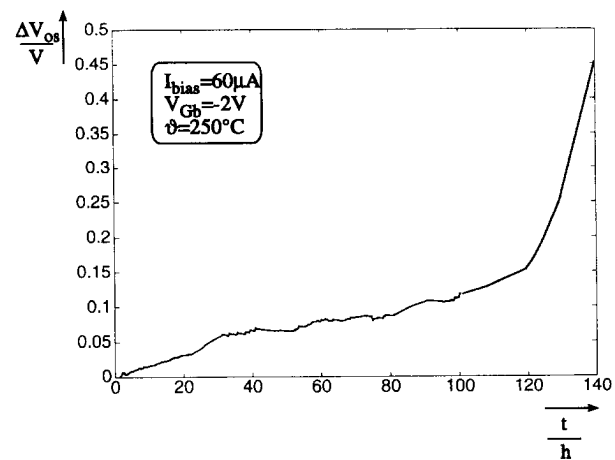


Fig. 8: Offset-voltage versus time at 250°C

3.1 Long-Term Degradation of the Electrical Behaviour of SIMOX-Components at High Temperatures

Concerning charge trapping effects near the Si/SiO₂ interface, MOSFETs are the most sensitive devices. These effects influence the threshold voltage V_{TH} and the transconductance g_m of MOSFETs in dependence on time, temperature and the operating point [7]. In the past decades, a lot of

measurement methods were developed to prove the quality of the Si/SiO₂ interface [8].

In this paper, degradation mechanisms which occur or are accelerated at realistic operating conditions and temperatures will be pointed out. First of all, the electrical degradation of single SIMOX-MOSFETs, which are operating in the ZTC, will be considered. This measurement method is called BTA (Biased Temperature Aging).

Reliable long-term measurements require a reliable mounting technology with small long-term degradation at high temperatures. Detailed examinations have shown, that the thick film technology, which uses Al₂O₃-ceramics as substrate, is excellently suitable for high temperature applications, if special paste systems are used [5, 9].

In Fig. 9 and 10 the results of long-term measurements of various transistors with different width are shown. Smaller transistors possess higher long-term degradation, which is caused by the existence of side-wall transistors.

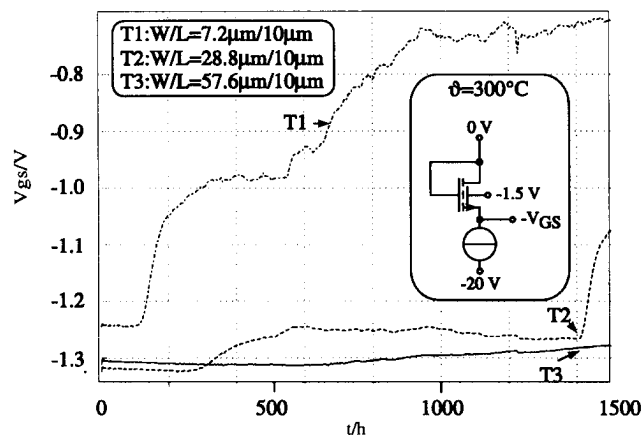


Fig. 9: N-SIMOX-MOSFET long-term drift at 300°C

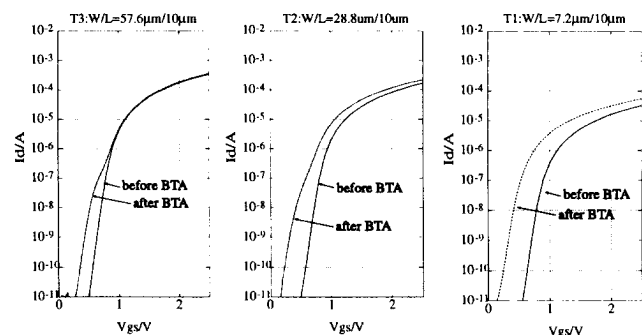


Fig. 10: Transfer characteristic before and after BTA

4. CONCLUSIONS

The presented macro-model has shown to be valid and useful for simple simulations under common operating

conditions with temperatures up to 300°C. For more detailed analysis specialized „native“ SOI-models (which include leakage currents, a wider range of operating conditions and other effects) have to be used.

The short-term measurements have shown, that it is possible to realize analog circuits, which can operate at temperatures up to 300°C. In further works the electrical characteristics, their temperature drift and their long-term degradation at high temperatures have to be improved.

ACKNOWLEDGEMENT

The authors want to thank the German Research Ministry and the VDI/VDE-Technologiezentrum Informationstechnik GmbH for financial and administrative support to do this research work.

Moreover they are grateful for the support which they received by ELMOS GmbH, Dortmund, where the monolithic integration took place.

REFERENCES

- [1] P. Brusius, et al, „Reliable High Temperature SOI Process“, 2nd Int. High Temperature Electronics Conference, Charlott, June 1994
- [2] J.-P. Colinge, „Silicon-on-Insulator Technology Materials to VLSI“, Kluwer Academic Publisher, 1991
- [3] H.-K. Lim, J.G. Fossum, "Threshold Voltage of Thin Film Silicon-on-Insulator (SOI) MOSFET's", IEEE Trans. Electron. Devices, Vol. ED-30, pp 1244-1251, October 1983
- [4] H. Shichman, D.A. Hodges, "Modeling of Insulated-Gate Field-Effect Transistor Switching Circuits", IEEE J. Solid-State Circuits, SC-3, 1968
- [5] 2. Statusbericht, Verbundvorhaben: „Mikrosystembausteine für Hochtemperaturanwendungen“, 1993
- [6] C. Eisenhut, A. ten Have, "MIPEXOS: Ein modulares, interaktives System zur Parameterextraktion und -optimierung", Tagungsbericht 3. GME/ITG Diskussionsitzung "Entwicklung von Analogschaltungen mit CAE-Methoden", Bremen September 1994
- [7] N. Shiono, C. Hashimoto, „Threshold-Voltage Instability of n-Channel MOSFET's under Bias-Temperature Aging“, Trans. Electron Devices, Vol. ED-29, No. 3, March 1982
- [8] M. W. Hillen, „Charge Trapping near the Si/SiO₂ Interface in Semiconductor Devices“, dissertation, University of Groningen, 1981
- [9] 3. Statusbericht, Verbundvorhaben: „Mikrosystembausteine für Hochtemperaturanwendungen“, 1994

CONFORMAL MAPPING ANALYSIS OF MICROSHIELD TRANSMISSION LINES

Eugenio Costamagna (*) and Alessandra Fanni (+)

- (*) Dipartimento di Elettronica, Universita' di Pavia, Via Abbiategrasso 209, 27100 - Pavia, Italy. Phone: +39-382-505200; Fax: +39-382-422583; e-mail: eugenio@comell1.unipv.it
(+) Istituto di Elettrotecnica, Universita' di Cagliari, 09123 - Piazza d'Armi, Cagliari, Italy. Phone: +39-70-280327; Fax: +39-70-291619; e-mail: fanni@elettro1.unica.it

Abstract - Due to features useful in microwave and millimeter wave integrated circuit design, unconventional planar transmission line geometries deserve large attention in the present technical literature. In particular, V-shaped and elliptic or circular-shaped microshield lines have been analysed in recent works. In this paper, accurate conformal mapping procedures are used to compare and to complete previous results on quasi TEM propagation characteristics, and to investigate useful coupled-line geometries.

I. Introduction

V-shaped and elliptic- or circular-shaped microshield lines have been recently proposed and analysed in the technical literature, considering both homogeneous and inhomogeneous dielectric media [1]-[3], and quasi TEM propagation models.

In [1], an inhomogeneous V-shaped structure was mapped into a rectangular geometry by means of numerical inversion of the Schwarz-Christoffel conformal transformation (SCNI). This allowed easy application of successive over-relaxation techniques (SOR) to the resulting smoothed inhomogeneous line structure, following a numerical procedure similar to the analytical one described in [4]. Moreover, no assumption was necessary on the field behavior at the dielectric-air interface.

In [2], a more complete analysis of a V-shaped structure was performed, including coupling characteristics, by a moment method procedure. In [3], the analysis was extended to elliptic- and circular-shaped microshield lines, by means of complex mapping procedures and assuming magnetic walls at the dielectric interfaces; top conductors at finite distance were considered.

As known, the magnetic wall model leads normally to good accuracy [5]-[8]. However, it seems interesting to compare various literature results with conformal mapping, using refined numerical techniques [9]-[11], both to allow transformation of complex geometries and to discuss the accuracy of the magnetic interface assumption. Moreover, flexible coupling characteristics are obtained by means of controlling the separation interval between coupled V-shaped microshield lines, and this generalises the coupled-line analysis presented in [2].

II. V-Shaped microshield line

V-shaped and elliptic or circular-shaped microshield lines geometries are shown in Fig. 1. Open sided structures are assumed for simplicity, but electric or magnetic wall can be easily introduced, and the upper conductor can be removed.

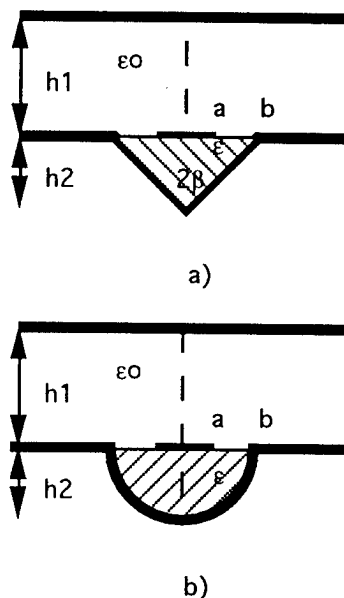


Fig. 1 Line geometries: a) V-shaped microshield line; b) elliptic-shaped microshield line.

In table I, some characteristic impedance values are reported for the V-shaped geometry considered in [2, Table I and Fig. 1]. No top conductor is considered. In [2] the geometrical parameters were $h = 240$ mils and $\alpha = 60$ degrees. The relative permittivity was $\epsilon_r = 2.55$. (α corresponds to 2β , w to $2a$, and h to h_2 of Fig. 1 a). Results obtained by applying a SOR procedure after a whole geometry conformal mapping, following [10], are also reported.

TABLE I
COMPUTED AND MEASURED CHARACTERISTIC IMPEDANCE VALUES

w/h	Z ₀ [Ω] (SCNI) Magnetic wall	Z ₀ [Ω] (SCNI + SOR) Whole geometry	Z ₀ [Ω] [2] Computed values	Z ₀ [Ω] [2] Measured values
0.2583	106.79	104.77	115	107
0.5208	73.20	71.70	78	76

The results show good agreement, further validating the magnetic wall assumption. However, it has to be noted that, for V-shaped structures, the field lines near the external ends of the dielectric interface are not likely to be almost parallel to the dielectric interface, even when interfaces lengths are small. This causes errors in magnetic wall computations more relevant than in traditional structures. Decreasing of errors due to increased relative permittivity is confirmed. Characteristic impedances have been computed for the V-shaped, top conductor line in Fig. 1 a), for various V angles in inhomogeneous dielectric. The results are reported in Fig. 2.

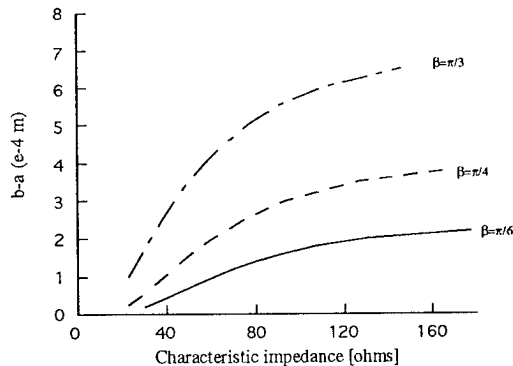


Fig. 2 Characteristic impedance of the V-shaped microshield line of Fig. 1 a) with $\epsilon_r=2.55$, $h_1=2$ mm, $h_2=0.4$ mm, for $\beta=\pi/3$, $\pi/4$ and $\pi/6$.

The effects of the different V angles on the characteristic impedance are well evident, showing saturation when the V-shaped ground is far away from the inner conductor.

III. Elliptic- and circular-shaped microshield lines

In Fig. 3, characteristic impedances are shown for the geometry in Fig. 1 b), i.e., the elliptic-shaped microshield line with top conductor and thin inner conductor. The curves are very similar to those derived from the formulas reported in [3]. Magnetic walls are assumed in the inhomogeneous dielectric computations, because this assumption is likely to lead to good results for this geometry. In fact, the accuracy was analysed in

air, and results similar to those derived in [8] for coplanar lines were found.

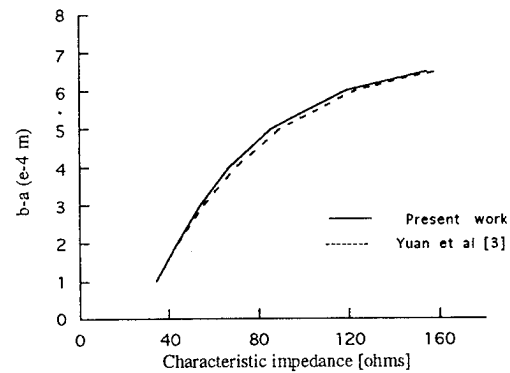


Fig. 3 Characteristic impedance of elliptic-shaped microshield line of Fig. 1 b) with $\epsilon_r=2.55$, $h_1=3$ mm, $h_2=0.4$ mm, for $b=h_2 \cdot \tan \beta$ ($\beta=\pi/3$).

The results obtained for the same geometry, but assuming thick inner conductors are shown in Fig. 4, where comparison is made with the lower and upper bounds supplied in [3]. Again the agreement is good, as conformal mapping results are found between the bounds.

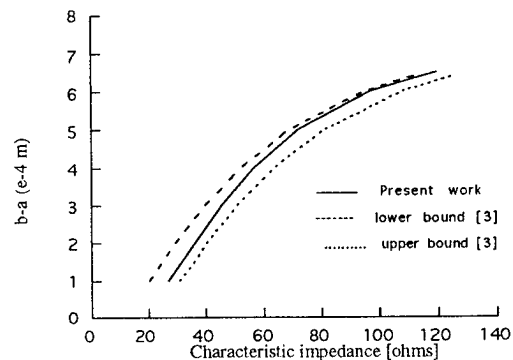


Fig. 4 Characteristic impedance of the elliptic-shaped microshield line of Fig. 1 b), inner conductor strip thickness 0.05 mm, $\epsilon_r=2.55$, $h_1=3$ mm, $h_2=0.4$ mm, $b=h_2 \cdot \tan \beta$ ($\beta=\pi/3$). Dotted lines show lower and upper bounds evaluated by means of formulas (14) and (15) in [3].

Similar results have been obtained for the circular-shaped, top conductor microstrip line, both for thin and thick strip conductors as shown in Fig. 5 and Fig. 6, where comparison is made with [3]. The agreement is good. The conformal mapping results are likely to provide reliable data, as they were compared in [14] and [15] with various data available for similar geometries, i.e. coaxial striplines and cross inner conductor, circular outer conductor coaxial lines.

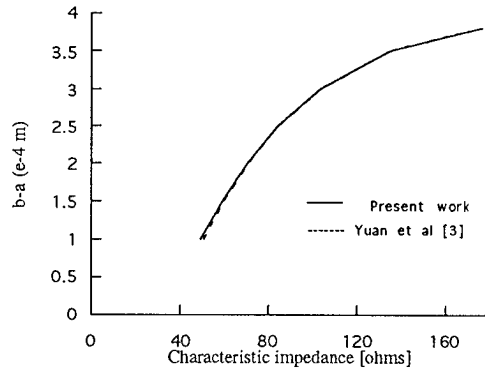


Fig. 5 Characteristic impedance of the circular-shaped microshield line of Fig. 1 b) with $\epsilon_r=2.55$, $h_1=3$ mm, $h_2=0.4$ mm, for $b=h_2 \cdot \tan\beta$ ($\beta=\pi/4$).

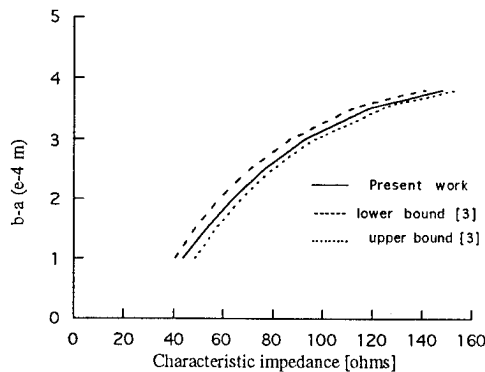


Fig. 6 Characteristic impedance of the circular-shaped microshield line of Fig. 1 b), with a conductor strip thickness 0.02 mm, $\epsilon_r=2.55$, $h_1=3$ mm, $h_2=0.4$ mm, $b=h_2 \cdot \tan\beta$ ($\beta=\pi/4$). Dotted lines show lower and upper bounds evaluated by means of formulas (14) and (15) in [3].

IV. Coupled V-shaped microshield lines

Coupled V-shaped microshield lines have been analysed, both with thin and with thick strip conductors, to discuss the thickness effects. The flexibility of the numerical conformal mapping procedures allows to discuss the effect of a slight modification of the geometry with respect to [2, Fig. 2].

This modification consists in providing a conductor surface coplanar to the dielectric interface between adjacent V-shaped outer conductor grounds, allowing more easy manufacturing of the whole structure.

The whole geometry is shown in Fig. 7, and coupling coefficients are shown in Fig. 8 and Fig. 9, where the coupling coefficient is expressed as

$$\text{coupling coefficient} = -20 \log \frac{Z_{\text{even}} Z_{\text{odd}}}{Z_{\text{even}} + Z_{\text{odd}}}$$

where Z_{even} and Z_{odd} are the even- and odd-mode impedances, respectively. These impedances as been computed by assuming a vertical electric or magnetic wall on the symmetry axes of the whole structure. Note that, due to the flexibility of the transformation procedure no assumption on magnetic wall in correspondence of the strip centre was necessary and that half structures are considered as a whole.

Fine adjustment of the coupling coefficient is allowed by selection of the distance $2c$, i.e., of the curve parameter. In fact, a centre ground conductor of adjustable dimension has been introduced, and the whole geometry is likely to provide a well-defined very low coupling with small overall dimensions, as the coplanar waveguide structure analysed in [16].

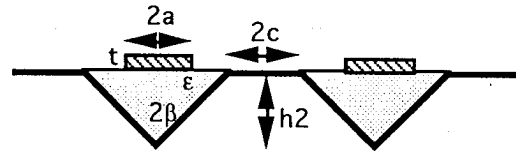


Fig. 7 Coupled V-shaped microshield line.

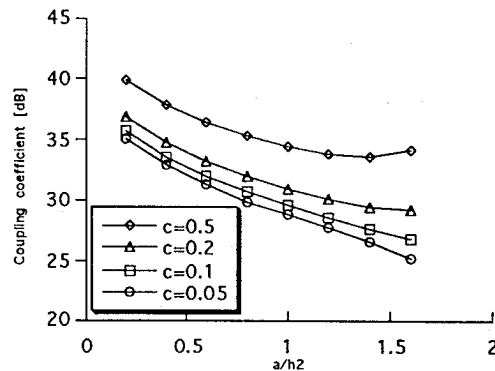


Fig. 8 Coupling coefficient for thick coupled V-shaped microshield line ($\beta=60^\circ$, $h_2=1$, $t=0.1$).

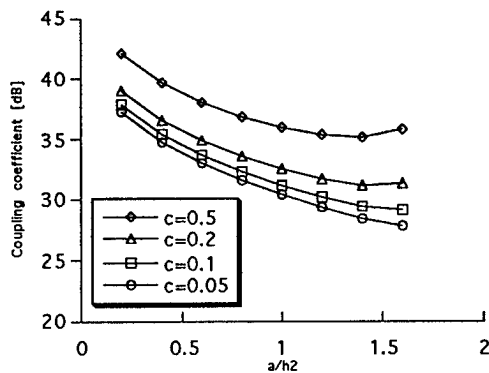


Fig. 9 Coupling coefficient for thin coupled V-shaped microshield line ($\beta=60^\circ$, $h_2=1$).

V. Conclusions

Numerical conformal mapping procedures have been applied to various microshield line geometries, and results have been presented which confirm and complete previous data. The same procedures are likely to be as well effective in analysing similar geometries and, among them, the new structures presented in [17].

References

- [1] E. Costamagna, "TEM parameters of angular offset strip lines," *Alta Frequenza*, vol. LVII, no. 5, May 1988, pp.193-201.
- [2] J. E. Schutt-Aine, "Static analysis of V transmission lines," *IEEE Trans. Microwave Theory Tech.*, vol. 40, no. 4, April 1992, pp. 659-664.
- [3] N. Yuan, C. Ruan, and W. Lin, "Analytical analyses of V, elliptic, and circular-shaped microshield transmission lines," *IEEE Trans. Microwave Theory Tech.*, vol. 42, no. 5, May 1994, pp. 855-859.
- [4] R. C. Callarotti and A. Gallo, "On the solution of a microstripline with two dielectrics," *IEEE Trans. Microwave Theory Tech.*, vol. 32, no. 4, April 1984, pp. 333-339.
- [5] G. Ghione and C. U. Naldi, "Coplanar waveguides for MMIC applications: effect of upper shielding, conductor backing, finite-extent ground planes, and line-to-line coupling," *IEEE Trans. Microwave Theory Tech.*, vol. 35, no. 3, March 1987, pp. 260-267.
- [6] E. Costamagna and A. Fanni, "Conductor-backed and upper-shielded coplanar waveguide with finite ground planes," *Microwave Opt. Technol. Lett.*, vol. 6, no. 16, Dec. 1993, pp. 879-882.
- [7] E. Costamagna and A. Fanni, "Lower bound algorithms for coplanar line and gap capacitance evaluations," *IEEE Trans. Magn.*, vol. 30, 1994.
- [8] C. Wan and W. Lin, "CAD-Oriented formulas for the quasi-TEM parameters of shielded and semi-enclosed (coupled) coplanar waveguides," *Int. J. Microwave and Millimeter-Wave Computer-Aided Eng.*, vol. 4, no. 4, 1994, pp. 336-348.
- [9] L.N. Trefethen, "Numerical computation of the Schwarz-Christoffel transformation," *SIAM J. Sci. Statist. Comput.*, Vol. 1, no. 1, March 1980, pp. 82-102.
- [10] E. Costamagna, "On the numerical inversion of the Schwarz-Christoffel conformal transformation," *IEEE Trans. Microwave Theory Tech.*, vol. 35, no. 1, Jan. 1987, pp. 35-40.
- [11] J.M. Chuang, Q.Y. Gui and C.C. Hsiung, "Numerical computation of Schwarz-Christoffel transformation for simply connected unbounded domain," *Comput. Methods in App. Mech. Engrg.*, vol. 105, 1993, pp. 93-109.
- [12] M. A. R. Gunston, *Microwave Transmission-Line Impedance Data*. London: Van Nostrand Reinhold, 1972, chapt.4.
- [13] E. Costamagna and A. Fanni, "Characteristic impedances of coaxial structures of various cross section by conformal mapping," *IEEE Trans. Microwave Theory Tech.*, vol. 39, no. 6, June 1991, pp. 1040-1043.
- [14] E. Costamagna and A. Fanni, "Characteristic impedances of coaxial structures of various cross section by conformal mapping," *IEEE Trans. Microwave Theory Tech.*, vol. 39, No. 6, June 1991, pp.1040-1043.
- [15] E. Costamagna, "Capacitance of rectangular lines with cross inner conductor, considering angular offset between conductors, side magnetic walls, and off-centered inner conductor," *Microwave Opt. Technol. Lett.*, Vol. 5, No. 11, Nov. 1992, pp. 553-557.
- [16] E. Costamagna and A. Fanni, "Accurate analysis of modal capacitances in coupled coplanar waveguides," *Microwave Opt. Technol. Lett.*, Vol. 8, No. 2, Feb. 1995, pp. 59-63.
- [17] N. Yuan, C. Ruan, W. Lin, J. He, and C. He, "Coplanar coupled lines: the effects of the presence of the lateral ground planes, upper and lower ground planes, and the V-shaped microshield ground walls," *IEE Proc. Microw. Antennas Propag.*, Vol. 142, No. 1, Feb. 1995, pp. 63-66.

DEVICE MODELS IN FDTD ANALYSIS OF MICROWAVE CIRCUITS

Chien-Nan Kuo,[†] Bijan Houshmand, and Tatsuo Itoh

Department of Electrical Engineering
University of California
Los Angeles, CA 90024-1595
Tel: (310) 206-4820
Fax: (310) 206-4819
itoh@ee.ucla.edu

[†]Jet Propulsion Laboratory
Pasadena, CA 91109

Abstract

This paper describes the investigation of two different approaches to model microwave active devices using the finite-difference time-domain (FDTD) analysis. Norton-equivalent and Thevenin-equivalent approaches are used in the extended FDTD method to model the interaction between the three-terminal active device and the electromagnetic field by placing equivalent sources in the active region. A typical microwave amplifier is analyzed, and the simulation results agree well with expectation.

region and the equivalent lumped circuit of the diode is incorporated into the FDTD grid. For a three-terminal active device, equivalent current sources are used to substitute for the device, and the value of the current source is specified by the device equivalent circuit model [5, 6].

The active device is the engine of microwave circuits. The simulation of microwave circuits heavily depends on the interaction between the active device and the electromagnetic field. This paper compares simulations of two different approaches of modeling active devices in the FDTD analysis. One is the Norton-equivalent approach using current sources, and the other is the Thevenin-equivalent approach using voltage sources. A typical microwave amplifier is analyzed using these two approaches.

1 Introduction

As the size of microwave circuits decreases, the Finite-Difference Time-Domain (FDTD) method provides a powerful solution to the simulation of electromagnetic phenomena of the entire circuit. The FDTD method solves Maxwell's equation in time domain directly and performs an accurate three-dimensional full-wave analysis. Therefore, the mutual coupling between elements are accounted for automatically. The transient behavior of the propagating wave can also be observed during the simulation.

The FDTD method has been generally applied to the analysis of microwave circuits. For passive circuits, frequency-dependent characteristics and the scattering parameters are studied [1, 2]. In addition, it is extended to include lumped passive devices and active devices. Passive components, such as resistors, capacitors, and inductors, are treated as distributed elements and incorporated into the coefficients of Yee's algorithm [3]. For two-terminal active devices, this methodology has been applied to analyze an active antenna [4]. A Gunn diode in the antenna is modeled as an equivalent active

2 Device Models in FDTD Analysis

To simulate microwave circuits, the FDTD algorithm is extended to include active elements. The idea used in [5, 6] is the Norton-equivalent approach which substitutes the active device with equivalent current sources in the active region. Since the equivalent current source fully characterizes scattering properties of the active device, the current source gives the same response of the reflected wave and the transmitted wave as that of the active device. Differently speaking, the current source also stands for the device current.

The implementation is to add the current source into Ampere's current law as a source term. The integral form of Ampere's law is then written as

$$I_{Total} = C \frac{dV}{dt} + I_{Device}, \quad (1)$$

where I_{Total} is the total current flowing through the FDTD cell, I_{Device} is the device current, V is the voltage drop across the FDTD cell, and C represents the space equivalent capacitance of the FDTD cell. The value of E field at integer time scale is evaluated from the voltage drop V . Since the value of I_{Device} is determined from the device equivalent circuit model, a straightforward way to solve V is to use the equivalent circuit of Eq.(1), as shown in Fig. 1(b).

The Norton-equivalent approach is suitable for current-controlled devices. For voltage-controlled devices, the Thevenin-equivalent approach is more appropriate. Instead of using current sources, equivalent voltage sources are placed in the active region to substitute for the active device. Similarly, because the voltage-current relationship at input ports of the device agrees with the scattering property, the voltage source behaves in the same way as the active device. The placement of the voltage source is shown in Fig. 1(c), where one end of the source connects to the microstrip line and the other end connects to the ground plane through vias.

The formulation for implementing the Thevenin-equivalent approach relies upon Faraday's Law. The integral form of Faraday's law is a dual form of Eq. (1),

$$V_{Total} = -L \frac{dI}{dt} + V_{Device}, \quad (2)$$

where V_{Total} is the total loop voltage of the FDTD meshes with voltage sources, V_{Device} is the device voltage, I is the mesh current of the FDTD cell, and L represents the space equivalent inductance of the FDTD cell. Note that the value of V_{Device} is related to the integration of the E field along the FDTD edge of the voltage source. Thus, when updating field values in the FDTD algorithm, the value of V_{Device} on an integer time scale needs to be determined as time increments.

3 Results

The system under consideration, as shown in Fig. 2, is an amplifier. The entire circuit contains DC biasing circuits, impedance matching circuits, lumped passive elements, and a three-terminal GaAs MESFET.

The FDTD simulation is performed with uniform grids, but the staircase approximation is used for radial stubs in the DC biasing circuits. The lumped resistors and capacitors are treated as distributed elements and incorporated into the FDTD algorithm. Norton-equivalent and Thevenin-equivalent approaches are applied to model the MESFET. Since the two approaches are duals of each other and both rely upon the implementation of equivalent sources, the simulation results are expected to be the

same. The observed time responses at port 1 and port 2 are shown in Fig. 3. According to these time waveforms, S-parameters are calculated and plotted in Fig. 4. Both results are very close to each other as expected.

4 Conclusion

Norton-equivalent and Thevenin-equivalent approaches for the modeling of the active device have been studied. With the use of equivalent sources, the FDTD method has been extended to include three-terminal active device and analyze the entire microwave circuit as a whole. The two approaches are duals of each other and produce the same results for the microwave amplifier. Both approaches maintain the features of the full-wave analysis and perform accurate electromagnetic field simulations of microwave and millimeter wave circuits.

5 Acknowledgement

This work was supported by Hughes Micro, JSEP contract F49620-92-C-0055, and Army Research Office contract DAAH04-93-G-0068.

References

- [1] X. Zhang and K. K. Mei, "Time-domain finite difference approach to the calculation of the frequency-dependent characteristics of microstrip discontinuities," *IEEE Trans. Microwave Theory and Tech.*, vol. 36, no. 12, pp 1775-1787, Dec. 1988.
- [2] D. M. Sheen, S. M. Ali, M. D. Abouzahra, J. A. Kong, "Application of the three-dimensional finite-difference time-domain method to the analysis of planar microstrip circuits," *IEEE Trans. Microwave Theory and Tech.*, vol. 38, no. 7, pp 849-857, July 1990.
- [3] W. Sui, D. A. Christensen and C. H. Durney, "Extending the two-dimensional FD-TD method to hybrid electromagnetic systems with active and passive lumped elements," *IEEE Trans. Microwave Theory Tech.*, vol. 40, pp. 724-730, Apr. 1992.
- [4] B. Toland, J. Lin, B. Houshmand, and T. Itoh, "FDTD analysis of an active antenna," *IEEE Microwave and Guided Wave Lett.*, vol. 3, no. 11, pp. 423-425, Nov. 1993.

- [5] V. A. Thomas, M. E. Jones, M. Piket-May, A. Taflove, and E. Harrigan, "The use of SPICE lumped circuits as sub-grid models for FDTD analysis," *IEEE Microwave and Guided Wave Lett.*, vol. 4, no. 5, pp. 141-143, May 1994.
- [6] C.-N. Kuo, S. T. Chew, B. Houshmand, and T. Itoh, "FDTD Simulation of a Microwave Amplifier," *IEEE MTT-S International Microwave Symposium*, May, 1995, Orlando, FL.

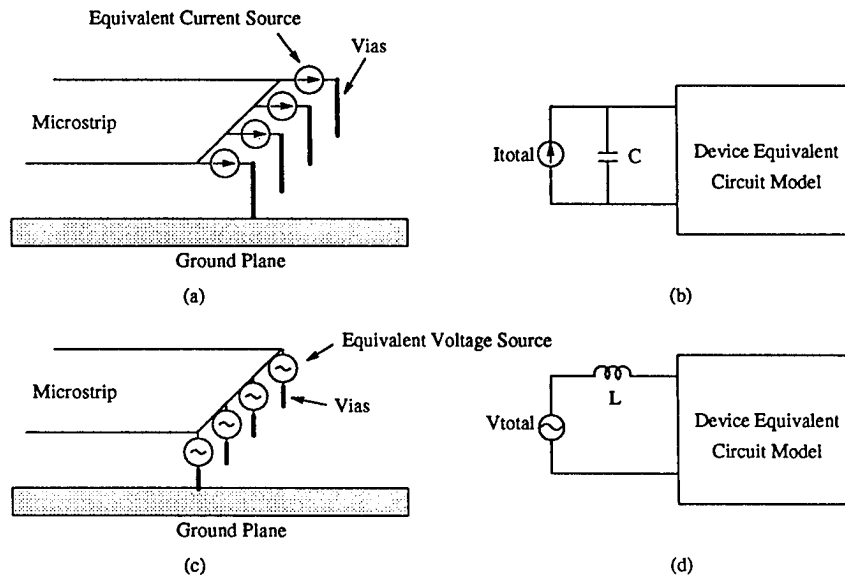


Figure 1: (a) The placement of equivalent current sources in the Norton-equivalent approach. (b) The equivalent circuit of the integral form of Ampere's law. (c) The placement of equivalent voltage sources in the Thevenin-equivalent approach. (d) The equivalent circuit of the integral form of Faraday's law.

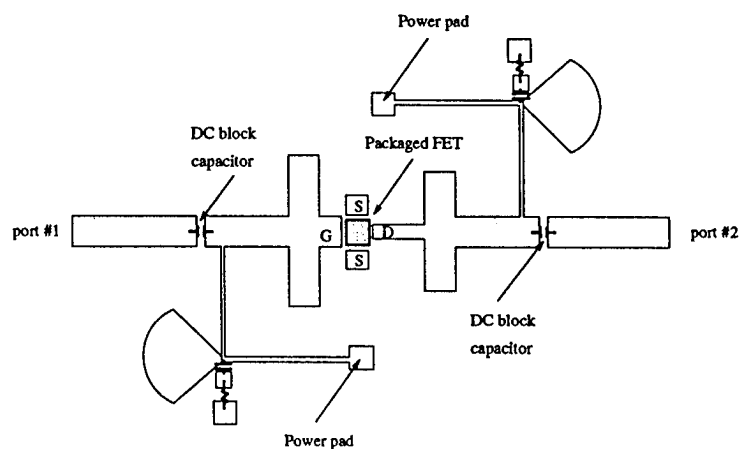


Figure 2: The layout of a typical microwave amplifier.

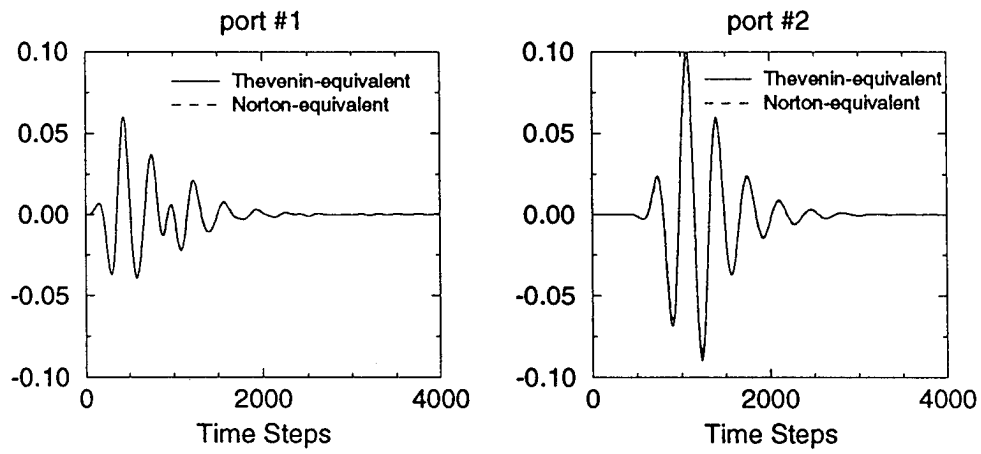


Figure 3: Time responses using Norton-equivalent and Thevenin-equivalent approaches observed at port #1 and port #2.

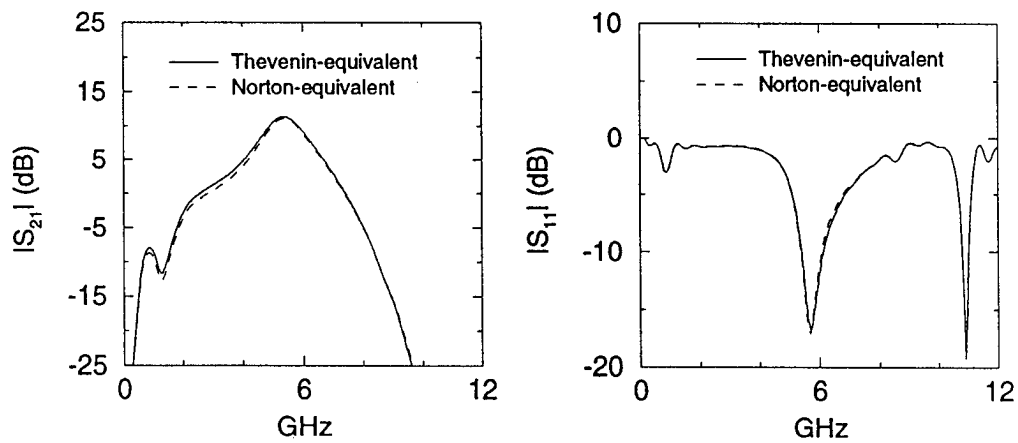


Figure 4: The calculated S-parameters from the time response.

A SIMPLE TECHNIQUE FOR DETERMINING TRANSMISSION LOSSES IN SAW DELAY LINES

T. E. TAHA
Faculty of Electronic Engineering
32952, Menouf, Egypt

ABSTRACT

Experimental data are analysed in order to determine the synchronous frequency at which the minimum insertion loss occurs in a surface Acoustic wave (SAW) delay line. The insertion loss of a locally fabricated delay line is measured to be 29.23 dB at a synchronous frequency in the order of 6 MHz. The transmission losses are deduced as a result of the comparison between the experimental data of the total insertion loss of the delay line and the theoretical results of the transducer losses. This technique can be considered as a base to the development of laboratory experiments to acquaint the undergraduate communication engineering major with SAW technology.

1. INTRODUCTION

SAW devices are now used in considerable range of applications in modern electronics [1],[2] and they play a key role in consumer communication applications [3]. One of the most important factors that influence the characteristics of these devices is the insertions loss [4],[5]. It is therefore, necessary to understand all the mechanisms contributing to the total insertion loss to accomplish the optimum design of such devices. Fig. 1, shows diagrammatically various contributions that make up the total insertion loss (IL). This loss is divided into two parts: the transducer losses (L_T) and

the transmission losses (L_P). L_T are the losses due to the conduction loss, the electrical mismatch loss and the bi-directional loss. On the other hand, L_P is the loss due to the interaction between the surface waves and thermal lattice wave, the effect of air loading, the presence of surface imperfections, radiation of bulk waves, beam steering and diffraction [6]. It is difficult to derive a theoretical loss L_P because it depends on the fabrication conditions of the device.

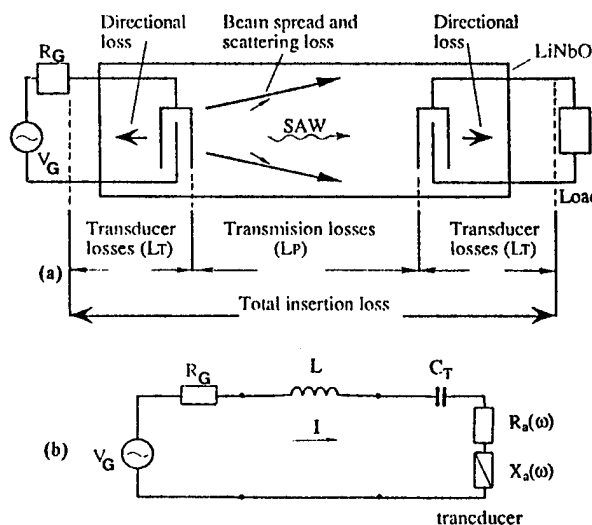


Fig. 1. (a) Losses in a SAW delay line. (b) Tuned transducer connected to source.

In this paper, we propose a simple technique for determining the transmission losses of SAW delay lines experimentally. This technique based upon the comparison between the experimental data of the total insertion loss of the delay line and the

simulation results of its transducer losses. Also, this technique can be considered as a base to the development of laboratory experiments to acquaint the undergraduate communication engineering major with SAW technology. It is the first approach indicated which has guided our work. In section 2, a simple model for calculation the transducer losses L_T is explained. In section 3, the measured delay line insertion loss is analysed and compared with the simulation results of L_T for estimating L_P experimentally, followed by the conclusions and the more relevant references.

2. THEORY

The basic building block element of any SAW device is the delay line. It consists of metallized interdigital transducers (IDT's) produced by photoetching aluminum on the surface of a piezoelectric substrate as shown in Fig.1 (a). The input IDT converts the received electromagnetic signal into two surface acoustic waves which travel in opposite directions. Only one of these waves is intercepted by the receiving transducer and this represents a 3 dB loss in power. A further loss occurs because the receiving IDT can not absorb all the energy from the surface wave. The electric load determines the amount of the loss, but at best 50% of the energy is observed; the balance is equally shared by a reflected wave and a transmitted wave. The minimum bi-directional loss in a two-transducer device is therefore 6 dB. If the transducer is interfaced directly with resistive source or load (untuned), the interelectrode capacitance superimposes a frequency mismatch in the desired acoustic response, and transducer insertion loss is excessive. A more mathematical description of these effects follows from an equivalent

circuit description of the transducer. A simple analysis, based on this circuit, will show that the minimum insertion loss for untuned device is > 6 dB.

According to Smith et al [7] the IDT can be represented by a series circuit consisting of the transducer capacitance C_T , a radiation resistance $R_a(\omega)$, and an acoustic reactance $X_a(\omega)$, Fig.1.(b). At the acoustic synchronism ω_0 , $X_a(\omega_0) = 0$ and $R_a(\omega_0) = (4/\pi)K^2N(1/\omega_0 C_T)$, where K^2 is the electromechanical coupling constant and N is the number of interdigital periods.

Transducer loss is defined as the ratio between the power which could be delivered to a load (transducer) from a matched signal generator and the actual power leaving the acoustic part in the desired direction [7]. Thus assuming a current I flow through the transducer circuit in Fig.1(b), and assuming for the moment zero resistance in the aluminum fingers, transducer efficiency (T_E) can be written as

$$T_E = \left[\frac{2 \left(\frac{4}{\pi} K^2 N \right) \omega_0 C_T R_G}{\left(\omega_0 C_T R_G + \frac{4}{\pi} K^2 N \right)^2 + 1} \right]^2 \quad (1)$$

where R_G is the source or load resistance. Because T_E is only the fractional power transmitted per transducer the delay line transducer insertion loss (L_T) then becomes

$$L_T = \frac{1}{(T_E)^2} = \left[\frac{\left(\omega_0 C_T R_G + \frac{4}{\pi} K^2 N \right)^2 + 1}{2 \left(\frac{4}{\pi} K^2 N \right) \omega_0 C_T R_G} \right]^2 \quad (2)$$

Minimum transducer insertion loss is obtained when the transducer capacitance is adjusted such that :

$$\omega_o C_T = \frac{1}{R_G} \sqrt{\left(\frac{4}{\pi} K^2 N\right)^2 + 1} \quad (3)$$

The transducers insertion loss is then :

$$L_T = \left[1 + \sqrt{1 + \frac{1}{\left(\frac{4}{\pi} K^2 N\right)^2}} \right]^2 \quad (4)$$

For $(4/\pi) K^2 N \ll 1$, these expressions reduced to :

$$\omega_o C_T = \frac{1}{R_G} \quad (5)$$

and

$$L_T = \left(\frac{4}{\pi} K^2 N\right)^{-2} \quad (6)$$

Using (6), the minimum insertion loss for a given substrate material and transducer finger pairs can be determined at the synchronous frequency (ω_o). The transducer capacitance required to obtain minimum insertion loss at (ω_o) can be calculated using (5). Because it is important to keep transducer insertion loss at a reasonable and predictable level and also to minimize phase and amplitude distortion across the acoustic passband, it is desirable in most cases to introduce a series L to tune out the effects of interelectrode capacitance C_T . Thus, the preceding simplified analysis could have been performed more exactly by assuming a nonzero transducer resistance from the

start and including the impedance of the lossy tuning inductor. In this case the delay line transducer insertion loss L_T is given by

$$L_T (dB) = 10 \log_{10} 4 \left\{ \left[1 + \frac{R_c}{R_a(\omega)} \right] [1 + X] \right\}^2 \quad (7)$$

Where R_c represents the conduction loss in the transducer fingers and in the tuning inductor,

$$R_a(\omega) = \frac{4k^2 N}{\pi \omega_o C_T} \left(\frac{\sin x}{x} \right)^2 \quad (8)$$

$$X = \frac{\left(\omega L - \frac{1}{\omega C_T} \right) + X_a(\omega)}{2 R_a(\omega) \left[1 + \frac{R_c}{R_a(\omega)} \right]} \quad (9)$$

$$X_a(\omega) = \frac{4K^2 N}{\pi \omega_o C_T} \left(\frac{\sin 2x - 2x}{2x^2} \right) \quad (10)$$

$$x = N \pi \left(\frac{\omega - \omega_o}{\omega_o} \right) \quad (11)$$

3. EXPERIMENTAL RESULTS

In order to determine the SAW delay line losses experimentally, insertion loss measurements are carried out on a delay line was locally fabricated with the available

technology in the Electronic Research institute, National Research Center, Cairo, Egypt. The transducers were fabricated by standard photoetching techniques of aluminum deposited on LiNbO_3 substrate. The available techniques are limited in resolution to line width of about $150\text{ }\mu\text{m}$, which corresponding to fundamental frequency of interdigital transducers of 6 MHz. The number of interdigital periods of each transducer is 4, the center-to-center distance between transducers is 16 mm. and transducer aperture width is 6 mm.

A pulsed sinusoidal voltage was applied to the input transducer and the output voltage from the output transducer was observed on the oscilloscope for each frequency variation of the input voltage. The tuning inductance was varied to maximize the voltage output on the scope at (ω_0) .

The experimental data of the total insertion loss versus frequency for the tuned 6 MHz delay line are given in Fig. 2. The following cubic polynomial form was found to fit the experimental points by the least-squares approximation.

$$IL = 61936 - 9.919F + 0.557F^2 + 0.031F^3 \quad (12)$$

Where IL is the insertion loss in dB and F is the frequency in MHz. Putting the first derivative of (12) equal to zero gives the synchronous frequency $F_0 = 5.93\text{ MHz}$, and the minimum insertion loss $IL_{\min} = 29.23\text{ dB}$.

A comparison of the measured insertion loss described by (12) with the theoretical loss calculated by using (7) is shown in Fig.2. The transducer losses L_T is determined to be 24.5 dB at F_0 . In order to obtain the experimental value of the transmission losses L_P at F_0 , we should

subtract L_T from IL_{\min} . The transmission losses L_P of the delay line are found to be 4.73 dB (see Fig.2.).

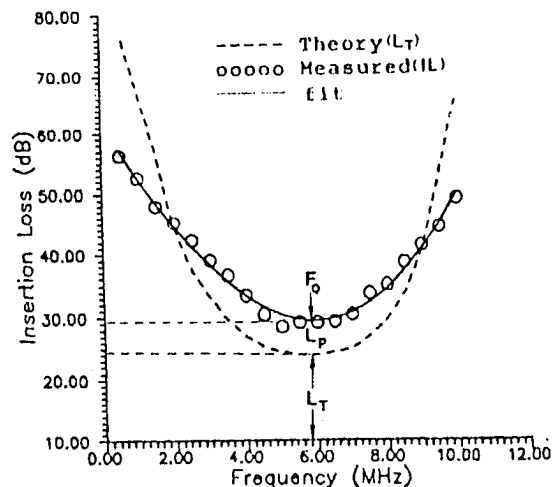


Fig.2 Theoretical and measured insertion loss versus frequency for a 6MHz LiNbO_3 SAW delay line.

4. CONCLUSIONS

A simple technique has been described to determine the synchronous frequency at which the minimum insertion loss occurs in a SAW delay line. Third order polynomial, obtained by a least-squares approximation, properly fit the experimental data of the delay line insertion loss versus frequency. Furthermore, a simple model for calculating the transducers losses of the delay line, based on the equivalent circuit of an interdigital electrode transducer, has been presented. The transmission losses of the delay line are deduced as a result of the comparison between the experimental delay line insertion loss and the simulation results of its transducer losses. The technique presented here not only to demonstrate the fundamental behavior of SAW devices, but also can be considered as a base for developing a laboratory experiments to acquaint the undergraduate communication engineering major with SAW technology.

REFERENCES

- [1] C.K. Cambell, "Applications of surface acoustic and shallow bulk acoustic wave devices", Proc. IEEE, Vol.77, No.10, pp.1453-1484, 1989 .
- [2] C.K. Cambell, "Surface acoustic wave Devices and Their Signal Processing applications," San Diego, Academic, 1989 .
- [3] C.W. Ruppel et al., "SAW devices for consumer communication applications", IEEE Trans. Ultrason. Ferroelec. Freq. Cont., Vol.40, No.5, pp.438-452, 1993 .
- [4] R. Huegle, "Harmonic GHz surface acoustic wave fillers with unidirectional transducers", IEEE Trans Ultrason. Ferroelec. Freq. Cont., Vol.40, No.3. 177-182, 1993 .
- [5] A.J. Slobodnik et al., "Microwave frequency acoustic surface wave loss mechanisms on LiNbO_3 ", J. App. phys., Vol.41, No.11, pp.4380-4387, 1970 .
- [6] D.P. Morgen, "Surface wave devices for signal processing", Elsevier, Amsterdam, 1985 .
- [7] W.R. Smith et al., "Analysis of interdigital surface wave transducer by use of an equivalent circuit model", IEEE Trans. Microwave Theory Tech., Vol.17, pp. 856-864, 1969 .

COMPARISON STUDY BETWEEN A COMPUTER AIDED ANALYSIS PROGRAM

USING STATE SPACE TECHNIQUE AND SPICE PROGRAM

A.M.NASSAR^{*}

A.M.MOSELHY^{**}

M.A.EL-GAZZAR^{***}

^{*} Faculty of Eng., Electronic Department, Cairo University, Egypt

^{**} Air Defence College, Alexandria, Egypt

^{***} Egyptian Air Academy, 44632, Belbies, Sharkia, Egypt

ABSTRACT:

In computer-aided analysis methods, the SPICE program is perhaps the most popular because of its simplicity and easy in programming. In lightly dampening systems the solution with SPICE program could extend over many periods making the computation costly. The modified nodal algorithm used with SPICE is poor in the analysis of distributed and lumped/distributed networks. In this paper the state space approach is a powerful technique in dealing with lumped / Distributed, linear dynamic networks in both time and frequency domains. The results show a considerable reduction in the amount of time necessary to compute the steady state response.

1-Introduction

Most circuit analysis is performed generally in two steps. The first step is to formulate the system of equations describing the circuit using two kirchhoff's laws and elements characteristics (laws of elements). The second step is to solve these equations using suitable graphical, analytical or numerical techniques. For linear networks, the nodal- analysis method [1]-[2] is perhaps the most popular because of its simplicity and easy in programming. However, this method has the following main disadvantages.

- (1)The nodal method cannot handle some types of dependent sources (only voltage controlled current sources are allowed).
- (2)Multiterminal elements that have no admittance matrix representation cause difficulty in nodal-analysis.
- (3)In frequency domain analysis using nodal method, the transfer function of the network must be known.

(4)There are problems at time discontinuities. Although the nodal -analysis method have been extended to analyze a lumped/ distributed networks, but its analysis of all types of lumped/distributed elements is still limited and its analysis of distributed elements is poor [1].

The state space approach is a powerful technique in dealing with lumped/ distributed, linear dynamic networks in both time and frequency domains. The state equations of networks containing lumped elements have been dealt with by numerous authors [3]-[4]. The state equations of networks containing transmission lines and resistive elements have been derived using topological approach [8]-[9]. The state space technique was extended for networks containing lumped and distributed elements.

The state space technique eliminates the need to know the transfer function in explicit form and removes any restriction on the topology. The same form of equations can be applied to either the time domain or frequency domain without the need of the fourier transform. The same technique can also be applied to purely distributed circuits and to lumped/distributed circuits whether the transmission lines are commensurate or not. No problems exist at the discontinuities of the time response , and the time response could be obtained for any arbitrary set of inputs without the use of convolution.

2- Simulation Program:-

(2a)The state and output equations :-

It has been shown [6] that the state variables of a distributed network are the reflected parameters at all the transmission line terminals or ports.

The state variables of a lumped/distributed network are the voltages on all the independent capacitors, the currents in all the independent inductors and the reflected parameters (or the reflected voltages) at all the transmission-line ports. The state equation is the differential-difference equation of the form:

$$\begin{bmatrix} \dot{X}_1(t) \\ X_2(t+T) \end{bmatrix} = \begin{bmatrix} A_{11} & A_{12} \\ A_{21} & A_{22} \end{bmatrix} \begin{bmatrix} X_1(t) \\ X_2(t) \end{bmatrix} + \begin{bmatrix} B_1 \\ B_2 \end{bmatrix} u(t) \quad (1)$$

Where $X_1(t)$ and $X_2(t)$ are the state vectors of the lumped and distributed elements respectively and $u(t)$ is the input vector.

The output equation is given by :-

$$y(t) = \begin{bmatrix} C_1 & C_2 \end{bmatrix} \begin{bmatrix} X_1(t) \\ X_2(t) \end{bmatrix} + Du(t) \quad (2)$$

Equations (1) and (2) are derived using topological methods with no restriction on the network topology. Where A, B, C and E are the matrices of the state and output equation of the systems.

When the Laplace transform is applied to equations (1) and (2) we obtain the frequency-domain equations.

$$\begin{bmatrix} X_1(s) \\ X_2(s) \end{bmatrix} = \begin{bmatrix} sI_m - A_{11} & A_{12} \\ A_{21} & zI_{2n} - A_{22} \end{bmatrix}^{-1} \begin{bmatrix} B_1 \\ B_2 \end{bmatrix} U(s) \quad (3)$$

$$Y(s, z) = \left\{ \begin{bmatrix} C_1 & C_2 \end{bmatrix} \begin{bmatrix} sI_m - A_{11} & A_{12} \\ A_{21} & zI_{2n} - A_{22} \end{bmatrix}^{-1} \begin{bmatrix} B_1 \\ B_2 \end{bmatrix} + E \right\} U(s) \quad (4)$$

where $z = \exp sT$, I is the identity matrix, m, n are the number of lumped-state elements and transmission lines, respectively.

(2b)- Network Analysis Using the State Equations

The previous results are used to analyze lumped/distributed networks in either the frequency or time domain.

(1) **Frequency domain analysis** : is Based on the expansion of the equation (4) to obtain the transfer function of the form.

$$F(s, z) = \frac{\sum_{i=0}^{2n} \sum_{j=0}^m A_{ij} S^j Z^i}{\sum_{i=0}^{2n} \sum_{j=0}^m B_{ij} S^j Z^i} \quad (5)$$

This expansion is achieved by using a modified faddeeva algorithm[4] for the inversion of the two variable matrix in equation (3).

(2) **Time domain analysis**: The output in the time domain is calculated from equation(2) when the state vector $[X_1(t); X_2(t)]^T$ is known. The state vector is first determined from the solution of Eq.(1). Equation(1) represents two simultaneous differential and difference equation :

$$\dot{X}_1(t) = A_{11}X_1(t) + A_{12}X_2(t) + B_1u(t) \quad (6)$$

and

$$X_2(t) = A_{21}X_1(t-T) + A_{22}X_2(t-T) + B_2u(t-T) \quad (7)$$

The state vector $[X_1(t); X_2(t)]^T$ is assumed to be zero at $t < 0$. The vector $X_2(t)$ is calculated by substituting the values of $X_1(t-T)$, $X_2(t-T)$ and $u(t-T)$ in equation(7). The vector $X_1(t)$ is then calculated by solving the differential equation(6) numerically in each time period $kt < t < (k+1)T$, where $k = 0, 1, 2, \dots$

The state and output vectors have discontinues at $t = KT$ and the initial values of the state vector at the start of each time period are obtained from the condition that the integral of the state vector is continuous.

Example 1: The simple circuit shown in Fig.1a was analyzed using the state space technique and the SPICE method to show the difference between them with respect to complete analysis (time

domain, frequency domain, computation time). The frequency response is given in Fig.1a. The impulse and step responses are shown in Fig.1b and Fig.1c. Where $R_1 = R_2 = 1\Omega$, $Z_{01} = 1.626$, $Z_{02} = 1.059\Omega$, $C = 1.377F$, $T = 1$ s.

Example 2: The normalized network shown in Fig.2a shows that the topology method is a powerful technique in dealing with lumped/distributed, linear dynamic networks and this method removes any restrictions on the topology. The SPICE program is still limited and its analysis of distributed elements is also poor. This example shows that the SPICE program can not compute like this topology of network.

3-Comparison study:-

Several examples were solved by using our state space analysis program and using SPICE program. The results show that SPICE program is still limited in dealing with some topology. The computation time for both STATE SPACE algorithm and SPICE program is given in table-1. It should be noted that the time given is the time of establishing the state equations and the solution of these equations to give the output. The results also show a considerable reduction in the computation time.

	Computation Time	
	Step Response	Frequency Response
Spice Program	10.27 Sec	9.7Sec
State Space Technique	5.27 Sec	6 Sec

Table-1

4- Conclusions

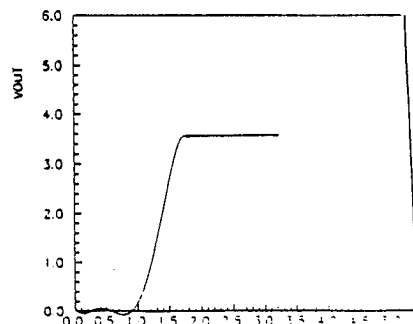
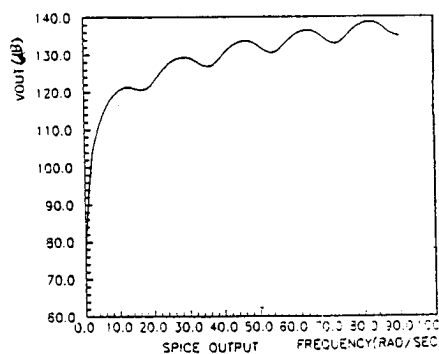
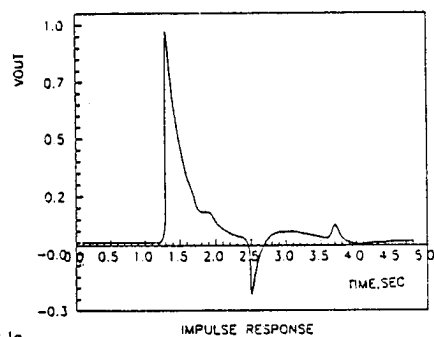
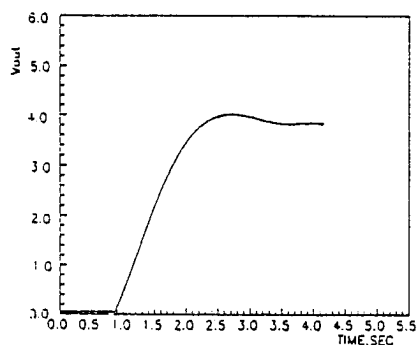
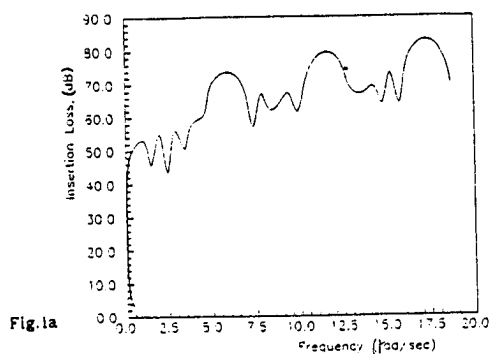
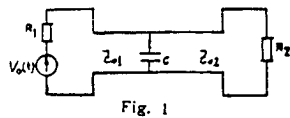
The state equation derived by topological methods can form the basis of powerful computer-aided technique for the analysis and design of networks containing both lumped/distributed

elements. The method is shown to be very effective in reducing the amount of computation time necessary for steady state solution of lumped/distributed networks than method used by SPICE program.

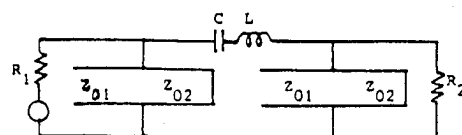
5 References

- [1] L.OCHua and P.Lin, "Computer- Aided Analysis of Electronic Circuits", Prentice -Hall, 1975.
- [2] K.Lee and S. Park, "Reduced Modified Nodal Approach to circuit Analysis", IEEE TRAN.on Circuit and Systems, Vol.CAS-32, No.10, 1985.
- [3] I.R Bashkow, "The A Matrix, New Network Description" IRE. Tran. Theory, Vol.CT -4, PP.117-119, 1957.
- [4] FADDEEVA, V.N.: Computational methods of linear algebra (Dover, New York, 1959)
- [5] WALTER BANTHAF, "Computer-Aided Circuit Analysis Using Spice", Prentice-hall, 1989.
- [6] SO B HY, M. I.: Topological derivation of the state equation of networks containing commensurate transmission lines, Proc. IEE, 1975, 122, (12), PP.1367-1371
- [7] J.K. Fidler, "Computer- Aided Circuit Design", Thomas Nelson, 1978
- [8] L.Kihell, "New General Approach to Commensurate TEM Transmission line Method Using State Space Approach", Int.J. Circuit Theory & Applications, 1974.
- [9] M.I.Sobhy and M.H Kerakos, " Computer-Aided Design of Commensurate and Non Commensurate Delay Lines Using State Space Technique", 1977 MTT-S Int. Microwave Symp., 1977
- [10] Esmat. A.F.Abdallah (Elect.Res.Inst.), E.A.Hosny (Kent.univ.U.K), M.A.Nassef and A.M.Moselhy (M.T.C) "Computer Aided Analysis of Microwave Integrated circuits using An Efficient Topological Method" proceeding of the Eighth National Radio Science Conference NRSC' 91, Cairo, Egypt, Feb. 19-21, 1991.
- [11] RABBAT, N.B.: "Efficient Computation of the Transient Response of Lumped/ Distributed Linear Active Network, IEEE Trans., 1975, CAS-22, PP.866-620.

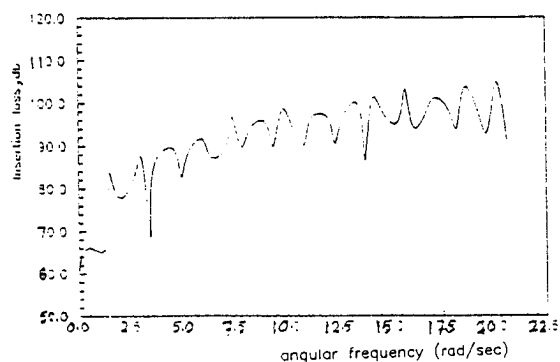
Example 1



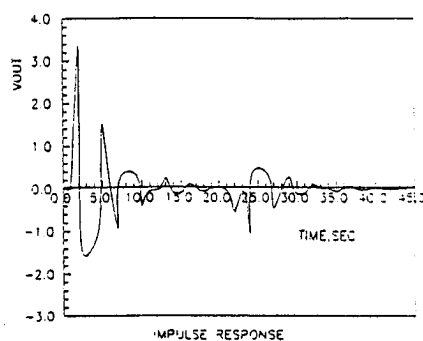
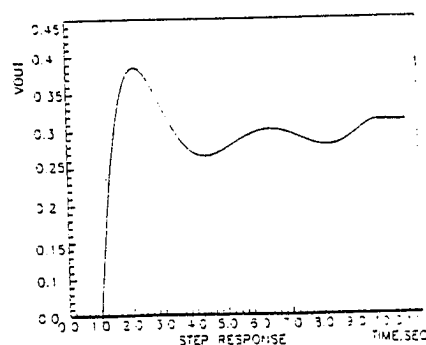
Example 2



$$\begin{aligned}
 T &= 0.20405 \text{ ns} & R_1 &= R_2 = 50 \Omega \\
 Z_{01} &= 44.2 \Omega & L &= 45 \text{ nH} \\
 Z_{02} &= 57.5 \Omega & C &= 0.062 \text{ pF}
 \end{aligned}$$



FREQUENCY RESPONSE



PERFORMANCE AND CONVERGENCE ANALYSIS OF A CM SIGNAL CANCELER WITH NOISE

Wookwon Lee and Raymond L. Pickholtz

Department of Electrical Engineering and Computer Science
The George Washington University
Washington, DC 20052

ABSTRACT

In this paper, we address the convergence model of a linear CM array in the presence of noise and demonstrate how the CMA performs for multiple signals in terms of output amplitude. We also derive an expression to evaluate the signal strength of a CM canceler output and present the SIR at each stage CMA output assuming uncorrelated signals and infinite SNR at the first stage.

1. INTRODUCTION

A new processing algorithm, Constant Modulus algorithm (CMA) is an algorithm which optimizes the output based on the *a priori* knowledge that the desired signal is of constant envelope. As such, it does not require neither a reference signal nor all signals to be linearly independent and is easily applicable to cellular environments where many dependent signals due to multipath exist and an array with standard adaptive algorithm may not converge properly if at all due to the correlation matrix processed by the array being close to singular.

In this paper, we address the convergence model of a linear CM array for narrowband signals in the presence of noise in Section 2. We also derive an expression to evaluate the signal strength at the output of a CM signal canceler. Some numerical results are presented in Section 3 and conclusions are made in Section 4.

2. CM SIGNAL CANCELER

Figure 1 shows a simplified block diagram of a two-stage N -element CM signal canceler. At the first stage, the complex signal $x_i(k)$, received by the i th element of the CM array in the k th sampling interval, is multiplied by an adjustable complex weight $w_i(k)$ and then, summed to form the array output $y(k)$ given by $y(k) = x^T(k)w(k)$. The CMA captures a desired signal and

suppresses all interferences by adjusting the weight vector w . The CMA is expressed as $w(k+1) = w(k) - \mu(|y(k)|^2 - 1)y(k)x^*(k)$, where μ is a positive step constant and the superscript $*$ denotes the complex conjugate. At the output of the first stage, the captured signal is subtracted from the received array input signals and the resulted signals are fed into the next stages for further processing.

2.1. Convergence Model with Noise

We derive an expression for the convergence of an N -element linear CM array with M narrowband signals arriving from spatial angles θ_m , $m = 1, \dots, M$, when zero mean, independent random noise processes, ξ_n , $n = 0, \dots, N-1$, exist at the CM array elements. Assume that the transmitted signals are complex, discrete-time processes given by $r_m(k) = A_m e^{j\varphi_m(k)}$, where $\varphi_m(k)$, $m = 1, \dots, M$, is the phase satisfying $e^{j\varphi_m(k)} = d_m(k)e^{j(\omega_k T_s + \psi_m)}$ where A_m is the amplitude of carrier signal, $d_m(\cdot)$ is the data signal, and ψ_m is an independent random variable uniformly distributed over the interval $[-\pi, \pi)$ for the m th carrier's unknown starting phase. We denote ζ_m as the phase difference of signal m between the first two array elements. Then, from Figure 1, the input to the n th CM array element

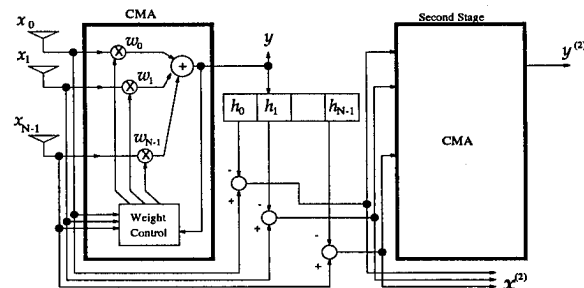


Figure 1: A simplified N -element two-stage CM signal canceler

$z_n(k)$, $n = 0, \dots, N-1$, which is the sum of signals and noise, can be represented in matrix form as follows :

$$z \triangleq x + d \triangleq ps + n \quad (1)$$

where $z \triangleq [z_0(k) \ z_1(k) \ \dots \ z_{N-1}(k)]^T$, p is the array matrix with its column $p_m \triangleq [A_m \ \dots \ A_m e^{-j(N-1)\zeta_m}]^T$, a signal vector $s \triangleq [e^{j\varphi_1(k)} \ \dots \ e^{j\varphi_M(k)}]^T$, and n is a noise vector independent at each array element. The array output with the input signals and noise is given by $y = w^T z = z^T w$ and the updating algorithm of a CM array is written as $w(k+1) = w(k) - \mu(|y(k)|^2 - 1)y(k)z^*$. Substituting y , we obtain $w(k+1) = w(k) - \mu(w^T z z^c w^* - 1)z^* z^T w$, where we used T for transpose, c for conjugate transpose, and $*$ for complex conjugate. Define the instantaneous array output amplitudes by $v \triangleq p^T w$ obtained from $y = x^T w = s^T p^T w = s^T v$ and similarly, the instantaneous noise at the array output by $\eta \triangleq n^T w$. Then multiplying p^T to $w(k+1)$ results in

$$\begin{aligned} v^{k+1} = & v - \mu p^T p^* (v^T s s^c v^* - 1) s^* s^T v \\ & - \mu p^T p^* (v^T s \eta^* - 1) s^* \eta \\ & - \mu p^T n^* (\eta^T s^c v^* - 1) s^T v \\ & - \mu p^T n^* (\eta^T \eta^* - 1) \eta \\ & - \mu \{ v^T s s^c v^* p^T n^* s^T + v^T s \eta^* p^T p^* s^* s^T \\ & + v^T s \eta^* p^T n^* s^T + \eta^T s^c v^* p^T p^* s^* s^T \\ & + \eta^T \eta^* p^T p^* s^* s^T + \eta^T \eta^* p^T n^* s^T \} v \\ & - \mu \{ v^T s s^c v^* p^T p^* s^* + v^T s s^c v^* p^T n^* \\ & + v^T s \eta^* p^T n^* + \eta^T s^c v^* p^T p^* s^* \\ & + \eta^T s^c v^* p^T n^* + \eta^T \eta^* p^T p^* s^* \} \eta \end{aligned} \quad (2)$$

where we dropped the time index k and denoted $v(k+1)$ by v^{k+1} for simplicity.

Assuming the signals and noise are independent, the mean output amplitude is obtained by taking expectation at both sides of (2) over signal $e^{j\varphi}$, which includes the data signal $d(\cdot)$, independently distributed phase ψ , and zero-mean independent noise ξ . We also notice that averaging over the product of signals results in a value of zero regardless of signal correlation due to independent, uniformly distributed random phase ψ , i.e., $E\{e^{j\varphi_l} e^{j\varphi_m}\} = 0$, $l \neq m = 1, \dots, M$. Thus, this analysis applies to both uncorrelated and correlated signals if the carriers with the same frequency differ in starting phase. We evaluate the expression in (2) term by term. With the commonly accepted assumption that $p^T p^* (v^T s s^c v^* - 1) s^* s^T$ is uncorrelated with v , and denoting $E[v_i]$ by \bar{v}_i , an expression for the expected value of the second term becomes

$$\begin{aligned} E\{2\text{nd term}\} &= \mu p^T p^* E\{(v^T s s^c v^* - 1) s^* s^T\} E\{v\} \\ &= \mu p^T p^* Q \bar{v} \end{aligned}$$

where $Q_{ii} \triangleq 2 \sum_{m=1}^M |\bar{v}_m|^2 - |\bar{v}_i|^2 - 1$ and $Q_{ij} = 0$ for $i \neq j$ and $i, j = 1, \dots, M$. The terms after the second term are due to the existence of noise. By similar manipulation for the rest of terms, we obtain the following expression of the mean array output amplitudes :

$$\bar{v}^{k+1} = \bar{v} - \mu N \tilde{R} \tilde{Q} \bar{v} - \bar{v}_\eta \quad (3)$$

where \bar{v}_η is the sum of $E\{3\text{rd term}\}$ through $E\{7\text{th term}\}$ survived and $(M \times M)$ matrices \tilde{R} and \tilde{Q} are defined with its elements $\tilde{R}_{ij} \triangleq \frac{A_i}{A_j} \frac{1}{N} \Lambda^c(\zeta_i) \Lambda(\zeta_j)$ for $i, j = 1, \dots, M$, and $\tilde{Q}_{ii} \triangleq A_i^2 (2 \sum_{m=1}^M |\bar{v}_m|^2 - |\bar{v}_i|^2 - 1)$ and $\tilde{Q}_{ij} = 0$ for $i \neq j$ and $i, j = 1, \dots, M$. The array matrix $\Lambda(\zeta_i)$ is defined by $\Lambda(\zeta_i) \triangleq [1 \ e^{j\zeta_i} \ \dots \ e^{j(N-1)\zeta_i}]^T$.

We also establish the relationship between the mean array output amplitude, denoted by $\bar{v}_{i,k}$, and the mean weight coefficients at a time instant k , given by

$$\bar{w}(k) = [\Lambda(\zeta_1) \ \dots \ \Lambda(\zeta_M)] R^{-1} \begin{bmatrix} \bar{v}_{1,k} \\ \bar{v}_{2,k} \\ \dots \\ \bar{v}_{M,k} \end{bmatrix}^T \quad (4)$$

where the each element of the array correlation matrix R is written by $R_{ij} \triangleq \Lambda^c(\zeta_i) \Lambda(\zeta_j)$, $i, j = 1, \dots, M$. Using (3) and (4), we iteratively calculate the weight coefficient vector w as follows : i) Calculate $w(0)$ with some initial values of v^0 , ii) Calculate v^{k+1} , iii) Calculate $w(k+1)$.

2.2. Output Amplitudes of a Canceler Stage

Since the CMA in each stage may not perfectly suppress interferences if the processing time is limited, the output of the canceler contains some residual power of the signals captured in the previous stages. In addition, when one signal power is much smaller than the others, the CMA takes much more time to suppress all the interferences than when all signals have the same power (see Section 3). If the first CM canceler stage does not remove the first desired signal completely, it passes some residual power of the signal to the second stage. Due to this residual signal, the second CM canceler again passes more residual signals to the next stage since imperfect capturing and deleting occur. As the number of canceler stages increases, the sum of residual power increases and eventually limit the performance of the signal canceler by capturing the same signal captured at one of the previous stages.

Denote the input to the l th element of the first stage CMA by $x_l^{(1)} = \sum_{m=1}^M C_{lm}^{(1)} r_m^{(1)}$, where the inter-element delay with respect to the first array element $C_{lm}^{(1)} \triangleq e^{-jl\zeta_m}$, $l = 0, \dots, N-1$, for the m th signal. The output of the first stage CMA is given by $y^{(1)} = \sum_{m=1}^M \alpha_m^{(1)} r_m^{(1)}$, where the array gain for the m th signal $\alpha_m^{(1)} \triangleq \sum_{l=0}^{N-1} C_{lm}^{(1)} w_l^{(1)}$. The output of the first canceler stage which is the input to the l th element of

the second stage CMA is given by $x_l^{(2)} = x_l^{(1)} - h_l^{(1)} y^{(1)}$. The canceler weight $h_l^{(1)}$ is obtained by minimizing the canceler output power, i.e., $\min E\{|x_l^{(2)}|^2\}$. With uncorrelated signals and no noise assumed, we obtain a general expression for the input signal to the k th stage CMA as

$$x_l^{(k)} = \sum_{m=1}^M C_{lm}^{(k-1)} r_m^{(1)} - \frac{\sum_{m=1}^M C_{lm}^{(k-1)} \alpha_m^{(k-1)*} P_{m,in}}{\sum_{m=1}^M |\alpha_m^{(k-1)}|^2 P_{m,in}} y^{(k-1)} \\ = \sum_{m=1}^M C_{lm}^{(k)} r_m^{(1)} \quad (5)$$

where $C_{lm}^{(k)} \triangleq C_{lm}^{(k-1)} - h_l^{(k-1)} \alpha_m^{(k-1)}$ and the signal power $P_{m,in} \triangleq \frac{1}{2} E[|r_m^{(1)}|^2]$. Notice for two signals that if the interference is completely suppressed at the first stage CMA output, i.e., $\alpha_2^{(1)} = 0$, then the canceler output contains only the interfering signal by eliminating the desired signal, i.e., $x_l^{(2)} = C_{l2}^{(1)} r_2^{(1)}$. We can also show that an equivalent general form can be expressed as

$$x_l^{(k)} = \sum_{m=1}^M C_{lm}^{(1)} \{r_m^{(1)} - \sum_{n=1}^{k-1} \frac{\alpha_m^{(n)*}}{D^{(n)}} E[|r_m^{(n)}|^2] y^{(n)}\} \\ = \sum_{m=1}^M C_{lm}^{(1)} \tilde{r}_m^{(k)} \quad (6)$$

where $D^{(n)} \triangleq \sum_{m=1}^M |\alpha_m^{(n)}|^2 E[|\tilde{r}_m^{(n)}|^2]$. The expression in (5) is represented in terms of $C_{lm}^{(k)}$, the equivalent inter-element phase delay taking the gain and the phase shift introduced at each stage into account while (6) is represented in terms of equivalent input amplitudes $\tilde{r}_m^{(k)}$. The CMA output at each stage then can be expressed as

$$y^{(k)} = \sum_{m=1}^M \alpha_m^{(k)} r_m^{(1)} \quad (7a)$$

$$\alpha_m^{(k)} = \sum_{l=1}^M C_{lm}^{(k)} w_l^{(k)} \quad (7b)$$

$$C_{lm}^{(k)} = C_{lm}^{(k-1)} - h_l^{(k-1)} \alpha_m^{(k-1)} \quad (7c)$$

$$h_l^{(k)} = \frac{\sum_{m=1}^M C_{lm}^{(k)} \alpha_m^{(k)*} P_{m,in}}{\sum_{m=1}^M |\alpha_m^{(k)}|^2 P_{m,in}} \quad (7d)$$

with an initial value of $C_{lm}^{(1)} = e^{-j l \zeta_m}$ for $l = 0, \dots, N-1$ and $m = 1, \dots, M$.

3. NUMERICAL RESULTS

We verify our convergence model in Section 2.1 by comparing numerical evaluation and computer simulation.

The simulation was performed with an eight-element array ($N = 8$) and two signals arriving from angles of $\theta_1 = 35.3^\circ$ and $\theta_2 = 23.8^\circ$. The signal power was 1.125 (i.e., amplitude of 1.5) for both signals and a CM array was initialized by $v^0 = [1.1 \ 0.9]^T$. Additive white Gaussian noise was added at each array element. Figure 2 shows the results of calculation and simulation. When SNR = 20 dB, the output amplitude of the captured signal approaches 1 and the interferer is successfully suppressed. For SNR = 0 dB, however, the output amplitude of the captured signal converges to the value less than 1 and the interferer has relatively big residual strength. In Figure 3, we show how much the noise affects to suppression of interferer. A dashed line represents captured signal-to-interference ratio (SIR) vs. input SNR. We also show the output SNR, which is less than the theoretical maximum, when an interferer exists (the solid line represents the SNR achieved by the array when no interferer exists). We observed for one signal that even though the array achieves the maximum gain in SNR, the amplitude of the captured signal may not be equal to 1. This is shown in Figure 4 along with the characteristic of Least Mean Square (LMS) array [4] (also see Figure 2 for two signals). This may be because the relatively strong noise limits the correction of error functions of the control algorithms. Notice that for the CMA the noise effect on the output amplitudes can be somewhat reduced by increasing the number of array elements while not for the LMS.

Figure 5 shows the suppression of an interferer with unequal power. When an interferer is much weaker than the other signals including the desired signal, it takes more time for the interferer to be completely suppressed. Finally, Figure 6 shows SIR at each canceler stage for signals shown in Figure 5 but with equal power and SNR = ∞ at the first stage. As one may expect, the SIR decreases as the number of stages increases. For iteration = 1000 and 1500 at each stage, interfer-

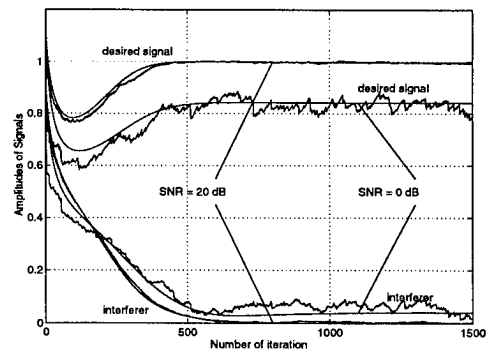


Figure 2: Output transients. $N = 8$, $M = 2$, $\theta_1 = 35.3^\circ$, $\theta_2 = 23.8^\circ$, $P_{1,in} = P_{2,in} = 1.125$, $v^0 = [1.1 \ 0.9]^T$.

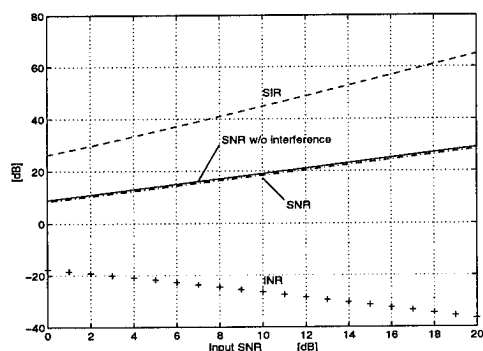


Figure 3: Noise effect on output power ratios. $N = 8$, $M = 2$, $SIR = 0$ dB, $\theta_1 = 35.3^\circ$, $\theta_2 = 23.8^\circ$, $P_{1,in} = P_{2,in} = 1.125$, $v^0 = [1.1 \ 0.9]^T$. (the solid line is for $N = 8$, $M = 1$, $\theta_1 = 35.3^\circ$, $P_{1,in} = 1.125$).

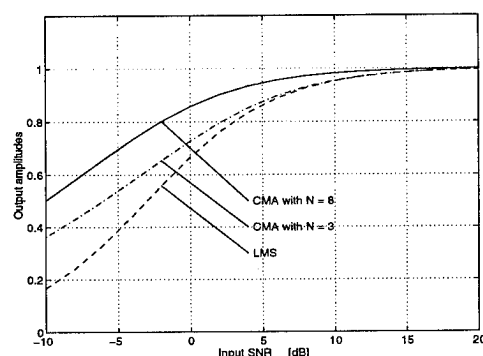


Figure 4: Noise effect on converged output amplitude. For the CMA, $N = 8$ and 3 , $\theta_1 = 35.3^\circ$, $P_{1,in} = 1.125$ (the dashed line for the LMS is obtained from [4]).

ences are relatively deeply suppressed at each CMA and the SIR linearly decreases. For iteration = 500, at the following CMA stages, relatively strong residual interferences are also further suppressed so that the slope of SIR deviates from the linearity.

4. CONCLUSIONS

We have presented the convergence model of a CM array in the presence of noise and demonstrated how the CMA performs for multiple signals in terms of output amplitude. We observed that the CMA achieves the array gain in SNR less than the theoretical maximum value when at least one interferer exists. We also noticed that for unequal power signals, it takes much longer time to suppress relatively small power interference if at least one interferer has relatively large power. These analytically derived conclusions are consistent with simulations. We also derived an expression to evaluate the signal strength of a CM canceler output

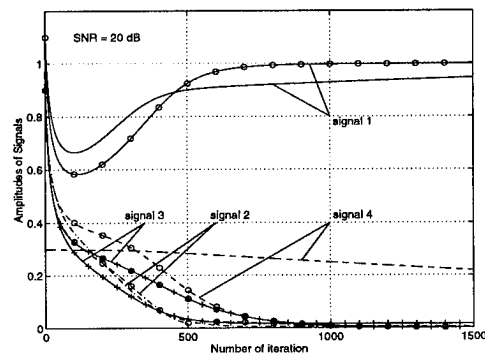


Figure 5: Convergence speed of the CMA for an equal and non-equal power interferer. $N = 8$, $M = 4$, $\theta_1 = 35.3^\circ$, $\theta_2 = 23.8^\circ$, $\theta_3 = 4.4^\circ$, $\theta_4 = -5.9^\circ$, $P_{1,in} = P_{2,in} = P_{3,in} = \text{constant} = 1.125$, $P_{4,in} = 1.125$ (lines with "o") or 0.045 (lines without "o")

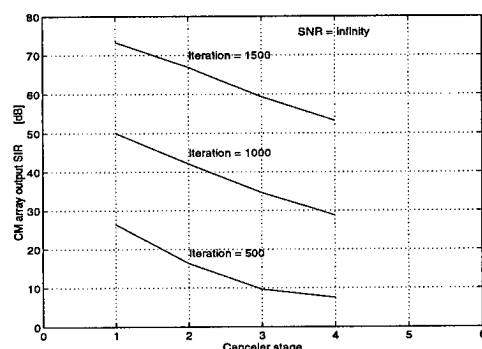


Figure 6: Signal-to-interference ratio at each stage. $N = 8$, $M = 4$, $\theta_1 = 35.3^\circ$, $\theta_2 = 23.8^\circ$, $\theta_3 = 4.4^\circ$, $\theta_4 = -5.9^\circ$, $P_{1,in} = P_{2,in} = P_{3,in} = P_{4,in} = 1.125$

and presented the SIR at each stage CMA output assuming uncorrelated received signals and infinite SNR.

5. REFERENCES

- [1] J. H. Treichler and M. G. Larimore, "The Tone Capture Properties of CMA-Based Interference Suppressors", *IEEE Trans. ASSP.*, Vol. ASSP-33, No. 4, pp. 946-958, Aug. 1985.
- [2] R. Gooch and J. Lundell, "The CM Array : An Adaptive Beamformer for Constant Modulus Signals", *ICASSP 86*, pp. 2523-2526, 1986.
- [3] B. J. Sublett, R. P. Gooch, and S. H. Goldberg, "Separation and Bearing Estimation of Co-channel Signals", *ICASSP 89*, pp. 629-634, 1989.
- [4] R. T. Compton, Jr., *Adaptive Antennas : Concept and Performance*, Prentice-Hall, pp. 29-30, 1988.

A WAVELET-BASED ALGORITHM FOR TIME DELAY AND DOPPLER MEASUREMENTS

X. X. Niu and P. C. Ching

Dept. of Electronic Engineering
Chinese University of Hong Kong
Shatin, Hong Kong
xxniu@ee.cuhk.hk pcching@ee.cuhk.hk

Y. T. Chan

Dept. of Electrical Engineering
Royal Military College of Canada
Kingston, Canada

ABSTRACT

This paper presents a wavelet-based algorithm for time delay estimation, specifically for linearly moving time delay estimation. The wideband cross ambiguity function (WBCAF) of the received signals at two spatially separated sensors is obtained by taking their cross wavelet transform. The global maximum of the WBCAF is then located which gives a direct measurement of the time delay and doppler compression. The performance of the estimation algorithm is analysed, and the mean values together with the variances of the estimates are derived. Simulation results are provided to illustrate the potential of the method. The major disadvantage of the algorithm is its excessive computation complexity.

1. INTRODUCTION

In radar and sonar signal processing, time delay estimation (TDE) has been widely used in target ranging and bearing measurements[1][2]. When the target and sensors are stationary, the time delay between two received signals is a constant. There are basically two methods that are commonly used to estimate the time difference between signals received from two spatially separated sensors, namely the cross-correlation method[3] and the parametric approach[4]. If the target and/or the sensors are moving, the time delay between the received signals will vary as a function of time. The simplest scenario being that the motion of the target or sensors is of constant speed and the target is far away from the sensors. In this case, the time delay becomes a linear time varying function. The algorithms that are capable of measuring time delay in the stationary condition have limitations in this non-stationary environment. If the time difference varies rapidly, most algorithms will fail to track the time varying delay.

The wideband cross ambiguity function (WBCAF) has been used to estimate the time delay and doppler shift by Jin *et al* [5]. The method is mainly applicable to active radar because the source signal must be known a priori. In passive sonar, the source signal is usually submerged in environment noise and is therefore not readily available. Weiss [6] has studied

the relationship between wavelet transforms and wideband correlation processing and their applications to source localization and channel modeling. By making use of this observation, we have developed a wavelet based algorithm to obtain the WBCAF of two received signals. This algorithm is then applied to solve the linearly moving time delay estimation problem.

2. THE ALGORITHM

In time delay estimation, if the target and/or the sensors are moving, the two received signals can be expressed as follows:

$$\begin{cases} f_1(t) = x(t) + n_1(t) \\ f_2(t) = x(t - D(t)) + n_2(t) \end{cases} \quad (1)$$

where $D(t) = D_0 + \beta t$ is the linear time varying delay. If the target is moving with constant velocity v in which $|v| < c$, where c is the speed of light in radar (or the speed of sound in sonar), the variables D_0 and β can be considered as the time delay and doppler shift respectively. The signals, $n_1(t)$ and $n_2(t)$, are additive white Gaussian noises with power spectral density N_0 in the two sensors. From (1), $f_2(t)$ can be expressed as:

$$\begin{aligned} f_2(t) &= x((1 - \beta)t - D_0) + n_2(t) \\ &= x\left(\frac{t - b_0}{a_0}\right) + n_2(t) \end{aligned} \quad (2)$$

where $a_0 = \frac{1}{1 - \beta}$ and $b_0 = \frac{D_0}{1 - \beta}$ are the scale and shift parameters respectively. The received signal $f_2(t)$ in this case is approximated by the wideband model and it is essentially a scaled and delayed version of the source input. Our task is to estimate a_0 and b_0 from the two data sequences, $f_1(t)$ and $f_2(t)$, and subsequently to compute the delay D_0 and the doppler factor β .

Weiss[6] and Young[7] have introduced the concept of the wideband cross ambiguity function (WBCAF) and its relationship with the wavelet transform. The WBCAF of two wideband signals, $f_1(t)$ and $f_2(t)$, is defined as

$$\text{WBCAF}(s, \tau) \triangleq \frac{1}{\sqrt{|s|}} \int_{-\infty}^{\infty} f_2(t) f_1^*\left(\frac{t - \tau}{s}\right) dt \quad (3)$$

In noise free environment, we obtain

$$\text{WBCAF}(s, \tau) = \frac{1}{\sqrt{|s|}} \int_{-\infty}^{\infty} x\left(\frac{t-b_0}{s}\right) x^*\left(\frac{t-\tau}{s}\right) dt \quad (4)$$

This WBCAF has a global maximum at $s = a_0$, $\tau = b_0$. However, it is very complicated to calculate the WBCAF directly because, for a data sequence $x(t)$, it is difficult to obtain an arbitrarily scaled and delayed version of $x(t)$. Though we may apply multirate signal processing methods to obtain $x(\frac{t-\tau}{s})$, the computation load is immense which makes the system impractical to be implemented for real time applications. Therefore, it is necessary to derive an efficient and effective way to find the WBCAF.

From [7], the cross wavelet transform indicates the extent of commonality between the two original signals or the two original wavelet transforms with respect to the same mother wavelet. The magnitude of the cross wavelet transform can be used to detect the presence of common signals. By definition, the cross wavelet transform is

$$W_g f(s, \tau) = \frac{1}{c_h} \int \int_{-\infty}^{\infty} W_h f(a, b) W_h^* g\left(\frac{a}{s}, \frac{b-\tau}{s}\right) \frac{da db}{a^2} \quad (5)$$

where $W_h f$ denotes the wavelet transform of $f(t)$ with respect to a particular mother wavelet, $h(t)$, which can be computed from

$$W_h f(a, b) \triangleq \frac{1}{\sqrt{|a|}} \int_{-\infty}^{\infty} f(t) h^*\left(\frac{t-b}{a}\right) dt \quad (6)$$

The parameter c_h is the admissible constant of the wavelet $h(t)$ which is given by

$$c_h \triangleq \int_{-\infty}^{\infty} \frac{|H(\omega)|^2}{|\omega|} d\omega \quad (7)$$

where $H(\omega)$ is the Fourier transform of $h(t)$. From (3), (6) and (5), the WBCAF can be written as

$$\begin{aligned} \text{WBCAF}(s, \tau) &= W_{f_1} f_2(s, \tau) \\ &= \frac{1}{c_h} \int \int_{-\infty}^{\infty} W_h f_2(a, b) W_h^* f_1\left(\frac{a}{s}, \frac{b-\tau}{s}\right) \frac{da db}{a^2} \end{aligned} \quad (8)$$

In this application, it is essential to find a mother wavelet $h(t)$ that is as close to the signal being transformed as possible and it will be an advantageous if such a mother wavelet is analytic so that $h(\frac{t-b-\tau}{s})$ can be calculated in advance for different values of s and τ . In addition, we need to derive two wavelet transforms for the received signals $f_1(t)$ and $f_2(t)$ separately,

$$W_h f_2(a, b) = \frac{1}{\sqrt{|a|}} \int_{-\infty}^{\infty} f_2(t) h^*\left(\frac{t-b}{a}\right) dt \quad (9)$$

$$W_h f_1\left(\frac{a}{s}, \frac{b-\tau}{s}\right) = \frac{1}{\sqrt{\left|\frac{a}{s}\right|}} \int_{-\infty}^{\infty} f_1(t) h^*\left(\frac{t-\frac{b-\tau}{s}}{\frac{a}{s}}\right) dt \quad (10)$$

Then by putting (9) and (10) into (8), the maximum point that corresponds to the required estimation of a_0 and b_0 at the (s, τ) plane of the WBCAF can be obtained.

3. PERFORMANCE ANALYSIS

The performance of this wavelet based WBCAF method can be analysed by computing the expectation and variance of the estimates of the scale and time delay parameter, viz. \hat{s} and $\hat{\tau}$. The mathematical derivation is tedious and it can be proved that the estimates of \hat{s} and $\hat{\tau}$ are asymptotically unbiased in high SNR condition. The variances of \hat{s} and $\hat{\tau}$ are fairly close to the CRLB for the case of high SNR, and they are dependent on the source/noise signal as well as the mother wavelet. In general,

$$\begin{cases} E[\hat{s}] \approx s_0 \\ E[\hat{\tau}] \approx \tau_0 \end{cases} \quad (11)$$

$$\begin{cases} \text{var}(\hat{s}) = \frac{N_0 s_0 (1+s_0)}{2\Delta(s)} B_s + K_1 \\ \text{var}(\hat{\tau}) = \frac{N_0 s_0 (1+s_0)}{2\Delta(s)} (D_s - \frac{E_s}{4}) + K_2 \end{cases} \quad (12)$$

where $\Delta(s)$, B_s , D_s and E_s are defined in a similar way as in [5]. The second terms in (12) are constants dependent on the noise power as well as the properties of the source signal and the wavelet function. It is noticed that the first terms of (12) are twice as large as that in [5]. This is deemed to be reasonable because, in this case, the time delay and doppler shift are being estimated in both sensors respectively. The strategy we have adopted in the proposed method is that we first design an optimum source signal to minimize the first terms of (12), and then select an optimum mother wavelet to make K_1 and K_2 as small as possible.

4. SEARCH METHOD AND SIMULATION RESULTS

In our simulations, we used two sinusoids with different frequencies as the source signal, viz. $x(t) = \sin(2\pi 0.45t) + \sin(2\pi 0.20t)$. The sampling period was chosen to be $\Delta T = 1$. Two uncorrelated wideband Gaussian sequences were generated for the noise signal $n_1(t)$ and $n_2(t)$. In sonar applications the ratio of the target speed and the velocity of sound is $\frac{v}{c} < 0.025$. So the scale [6] is within the range of $[0.95, 1.05]$. Here we chose the scale and time shift as $s_0 = 1.05$ and $\tau_0 = 0.15$ respectively. The corresponding time delay and doppler compression factor is $D_0 = 0.1429$ and $\beta = 0.0467$.

Three different mother wavelets have been tried,

$$\begin{aligned} h_1(t) &= (1-t^2)e^{-\frac{t^2}{2}} \\ h_2(t) &= 2\text{sinc}\left(\frac{t}{2}\right) - \text{sinc}\left(\frac{t}{4}\right) \\ h_3(t) &= e^{-0.0095t^2} \cos(2\pi 0.15t) \end{aligned} \quad (13)$$

It was found that the shape of the WBCAF was different for different mother wavelets. But for the particular source signal, $x(t)$, the mother wavelet $h_3(t)$, which was a Gaussian windowed sinusoid, produced the best result. The additional terms in (12), that increased the variance, are also smaller for $h_3(t)$ than for $h_1(t)$ and $h_2(t)$. Therefore $h_3(t)$ has been chosen as the mother wavelet in our study.

Fig.1 depicts the WBCAF of the source signal and its scaled and delayed version, and it can be seen that it is a smooth convex function in the range of $s \in [0.9, 1.1]$ and $\tau \in [-1, 1]$. However, if noise is present, the WBCAF becomes rugged and is no longer a smooth convex function as shown in Fig.2. In general, the steepest descent method is unable to locate accurately the maximum WBCAF. Instead, we used a grid search method to determine the maximum point which correspond to the scale and time shift of the signal.

Search Method

Assume that the initial range of s and τ for observation is $s \in [0.9, 1.1]$ and $\tau \in [-1, 1]$. The search procedure is as follows:

1. Make some grid on the (s, τ) plan, and find the maximum point of WBCAF.
2. Make a finer grid in a smaller range around the maximum point, then find the maximum point again.
3. Repeat step 2 until the resolution reaches the pre-defined value.

The performance of the method has been studied for different signal-to-noise ratio (SNR) and different observation data lengths. The SNR was varied from $-10, 0, 10$ to 20dB while the observation data length was changed from 50, 100, 200, 400 to 600 points, respectively. In each case 20 independent runs were performed to obtain the ensemble average.

Fig.3 and Fig.4 show the ensemble average of \hat{s} and $\hat{\tau}$, respectively, vs. the observation data length under different SNR conditions. While Fig.5 and Fig.6 show the variances of \hat{s} and $\hat{\tau}$ under the same conditions. In order to amplify the difference for ease of comparison, the variances of \hat{s} and $\hat{\tau}$ in Fig.5 and Fig.6 are plotted in logarithmic scale. It is seen that the scale and shift estimates are fairly close to the actual values of $s_0 = 1.05$ and $\tau_0 = 0.15$ when $\text{SNR} = 0\text{dB}, 10\text{dB}$ and 20dB , and the variances reduced as the observation length increased. But for noisy condition, say $\text{SNR} = -10\text{dB}$, the estimates had a large fluctuation about the actual values of s_0 and τ_0 , and the variance was significantly larger even a long observation data length was used.

It is found from Fig.3 to Fig.6 that under high SNR, less input points are required whilst for low SNR more input samples are needed to obtain better estimation of the scale and time shift of the received signals. For example, when $\text{SNR} \geq 10\text{dB}$, 200 input signal points are enough to get a reasonable result, whereas when $\text{SNR} = 0\text{dB}$, 400 points are required. It is also found from Fig.5 and Fig.6 that the shift estimate has a larger variance than the scale, that means the latter is more

sensitive to additive noise. The estimates of the delay \hat{D}_0 and the doppler factor $\hat{\beta}$ can be obtained easily from the unique relations between D_0, β and s, τ .

The major difference between this method and [8] is that in [8] the time delay is estimated iteratively and an inherent disadvantage of the method is that if the time delay varies rapidly, it will fail to track the delay. Whereas in the wavelet-based method, we use the whole data sequence to determine the scale and the shift between the two signals, and from there we are able to obtain accurate estimation of the delay and the doppler parameters irrespective of whether the time delay is changing rapidly or slowly.

5. CONCLUSION

In this paper we have used a wavelet-based method to estimate the scale and time shift between two received signals and subsequently to extract the time delay and doppler compression in the source localization problem. This method is based on the concept of wideband cross ambiguity function and the cross wavelet transform.

6. ACKNOWLEDGEMENT

Part of this work is supported by a research grant #CUHK 74/93E funded by the Hong Kong Research Grant Council.

7. REFERENCES

- [1] G. C. Carter, *Coherence and time delay estimation: an applied tutorial for research, development, test, and evaluation engineers*, IEEE Press, 1993.
- [2] *IEEE Trans. on Acoustics, Speech, Signal Processing, special issue on Time Delay Estimation*, vol. ASSP-29, no.3, 1981.
- [3] C. H. Knapp and G. C. Carter, "The generalized correlation method for estimation of time delay", *IEEE Trans. on Acoustics, Speech, Signal Processing*, vol. ASSP-24, no.4, pp.320-327, 1976.
- [4] Y. T. Chan J. M. F. Riley and J. B. Plant, "A parameter estimation approach to time-delay estimation and signal detection", *IEEE Trans. on Acoustics, Speech, Signal Processing*, vol. ASSP-28, no.1, pp.8-15, 1980.
- [5] Q. Jin K. M. Wong and Z. Q. Luo, "The estimation of time delay and doppler stretch of wideband signals", *IEEE Trans. on Signal Processing*, vol. SP-43, no.4, pp.904-916, 1995.
- [6] L. G. Weiss, "Wavelets and wideband correlation processing", *IEEE Signal Processing Magazine*, Jan. pp.13-32, 1994.
- [7] R. K. Young, *Wavelet theory and its applications*, Kluwer Academic Publishers, Boston, 1993.
- [8] H. C. So and P. C. Ching, "Comparative performance of LMSTDE and ETDE for delay and doppler estimation", *Proc. of 28th Asilomar Conference on signals, systems and computers*, Oct. 1994.

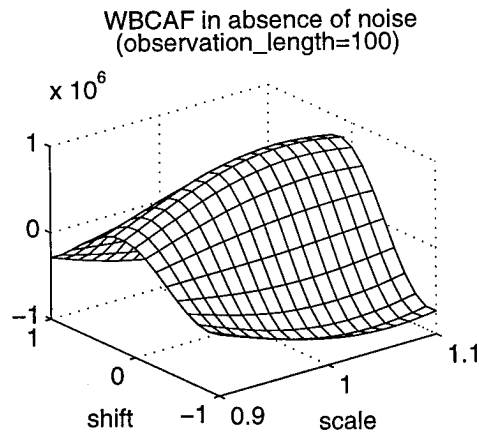


Figure 1: WBCAF is a smooth convex in the absence of noise

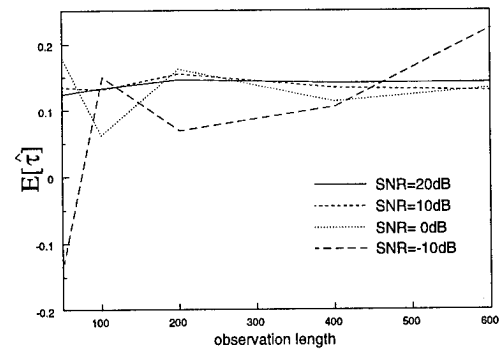


Figure 4: Ensemble average of shift estimations in different SNR conditions. ($\tau_0 = 0.15$)

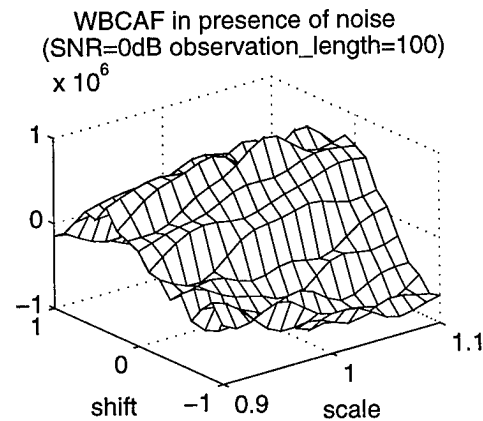


Figure 2: WBCAF is no longer a smooth convex in the presence of noise

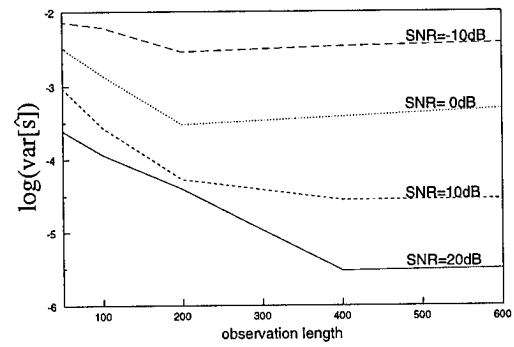


Figure 5: Logarithm of the variance of scale vs. observation length in different SNR condition.

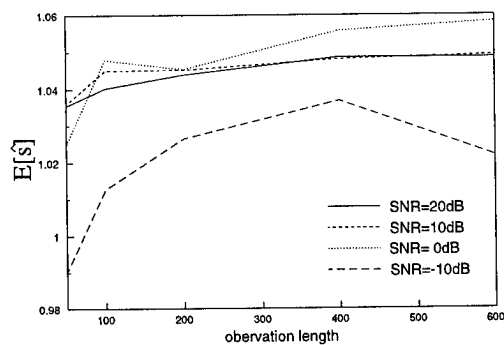


Figure 3: Ensemble average of scale estimations in different SNR conditions. ($s_0 = 1.05$)

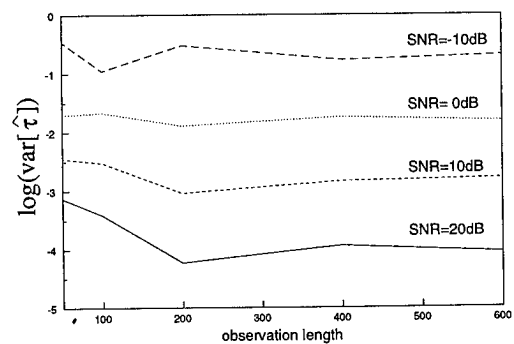


Figure 6: Logarithm of the variance of shift vs. observation length in different SNR condition.

Sampling Errors and the Influence of Processing after Sampling

by Eugen-Georg Woschni

Technische Universität Chemnitz-Zwickau
Fakultät für Elektrotechnik und Informationstechnik
09107 Chemnitz

ABSTRACT

As well-known it is not possible to fulfil the sampling-theorem exactly: Cut-off-errors because of the necessary low-pass-filtering before sampling - to get a band-limited input signal - and if this is not possible additionaly aliasing errors appear.

In the paper it is shown, that both cut-off- and aliasing-errors are depending of the algorithm of processing: Processing algorithms with an integral (I-) part - as typically mean operations - lead to decreasing errors in comparison with the - normally regarded - case of no operation after sampling; algorithms with a differential (D-) part on the other hand result in increasing errors. Final an example shows typical cases using a general signal model of the input.

1. INTRODUCTION - ERRORS WITHOUT SIGNAL PROCESSING

Investigations of the errors may be done either in the time or frequency domains. An approximation using the time domain is given by Churkin et al. 1966. If as a quality criterion the mean-square error \bar{e}^2 is used the frequency domain often is preferred (Zadeh and Desoer, 1963; Woschni, 1990; Woschni, 1993).

Fig. 1 shows the error components caused by ideal or real (non-ideal) anti-aliasing filtering $G_a(j\omega)$ including aliasing errors with ω_s = sampling frequency, $S_{xx}(\omega)$ spectral power density

$$\bar{e}^2 \approx \bar{e}_1^2 + \bar{e}_2^2 + \bar{e}_3^2 = 2 \left[\int_0^{\omega_s/2} S_{xx}(\omega) \cdot |1 - G_a(j\omega)|^2 d\omega + \int_{\omega_s/2}^{\infty} S_{xx}(\omega) d\omega + \int_{-\omega_s/2}^{+\omega_s/2} S_{xx}(\omega + \omega_s) |G_a(j[\omega + \omega_s])|^2 d\omega \right] \quad (1a)$$

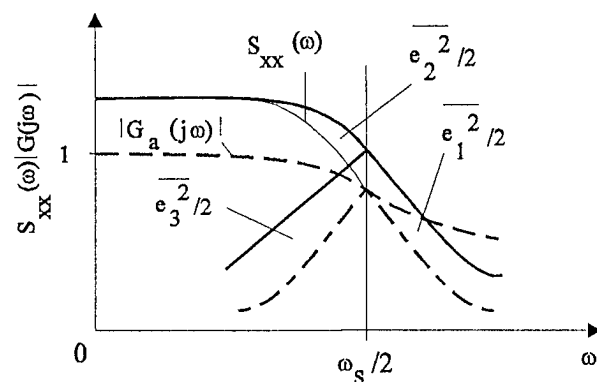


Fig. 1. \bar{e}_1^2 = damping error; \bar{e}_2^2 = cut-off error; \bar{e}_3^2 = aliasing error

It is assumed the error components to be not correlated - because of the mirror-effect this supposition may be fulfilled in practice approximately - and side-bands of higher than first order do not fall into the frequency range $-\omega_s/2 < \omega < \omega_s/2$. If the last mentioned condition is not fulfilled the last part in (1a) has to be changed using lag theorem of Fourier Transform (Woschni, 1990)

$$\overline{e_3^2} = \sum_{r=1}^{\infty} \int_{-\omega_s/2}^{+\omega_s/2} S_{XX}(\omega + r\omega_s) |G_a(j\omega + r\omega_s)|^2 d\omega. \quad (1b)$$

2. ERRORS WITH CONSIDERATION OF SIGNAL PROCESSING

A lot of important problems of signal processing as mean-value-, P-, PI-, PD-, PID-, FFT-algorithms and most of all filter-algorithms are linear. In these case the linear system theory yields and operations in the time domain $y = \{\text{Op } x(t)\}$ can be transformed by means of the Fourier-Transform to the frequency domain $\underline{Y}(j\omega) = G(j\omega)\underline{X}(j\omega)$.

2.1 Errors with fulfilled Sampling Theorem

Using the approach as given before we gain for the ideal algorithm of the processing procedure (the model) $G_{id}(j\omega) = F\{\text{Op}_{id}\}$ and for the real algorithm

$$G_{real}(j\omega) = F\{\text{Op}_{real}\}.$$

Now the results of linear system theory may be applied to calculate the mean-square error

$$\overline{e^2(t)} = 2 \left[\int_{\omega_s/2}^{\infty} S_{XX}(\omega) |G_{id}(j\omega)|^2 d\omega + \int_0^{\omega_s/2} S_{XX}(\omega) |G_{id}(j\omega) - G_{real}(j\omega)|^2 d\omega \right] \quad (2)$$

2.2 Errors with not fulfilled Sampling Theorem

Here we obtain - under the same suppositions as before approximately

$$\overline{e^2(t)} = 2 \left[\int_{\omega_s/2}^{\infty} S_{XX}(\omega) |G_{id}(j\omega)|^2 d\omega + \int_0^{\omega_s/2} S_{XX}(\omega) |G_{id}(j\omega) - G_{real}(j\omega)|^2 d\omega + \int_{-\omega_s/2}^{+\omega_s/2} S_{XX}(\omega + \omega_s) |G_{real}(j\omega)|^2 d\omega \right]. \quad (3a)$$

If side-bands of higher order are to be taken into consideration the last part has to be changed

$$\sum_{r=1}^{\infty} \int_{-\omega_s/2}^{+\omega_s/2} S_{XX}(\omega + r\omega_s) |G_{real}(j\omega)|^2 d\omega \quad (3b)$$

3. EXAMPLES

In most cases the power density of the signal is not known because of missing a-priori-information. Then $S_{XX}(\omega)$ is to be estimated - e.g. caused from a band-limited white noise by a low-pass of first order

$$S_{xx}(\omega) = \frac{S_0}{1 + (\omega/\omega_0)^2};$$

$$S_0 = 0 \quad \text{for } \omega \geq \omega_{x0}. \quad (4)$$

For this example it follows for the cases

- a) without signal processing
- with anti-aliasing filtering

$$\begin{aligned} \overline{\varepsilon^2} &= 2 \int_{\omega_s/2}^{\omega_{x0}} \frac{S_0}{1 + (\omega/\omega_0)^2} d\omega = \\ &= 2S_0\omega_0 (\arctan \omega_{x0}/\omega_0 - \arctan \omega_s/2\omega_0); \end{aligned} \quad (5a)$$

- without anti-aliasing filtering

$$\begin{aligned} \overline{\varepsilon^2} &= 4 \int_{\omega_s/2}^{\omega_{x0}} \frac{S_0}{1 + (\omega/\omega_0)^2} d\omega = \\ &= 4S_0\omega_0 (\arctan \omega_{x0}/\omega_0 - \arctan \omega_s/2\omega_0); \end{aligned} \quad (5b)$$

b) with signal processing $G(j\omega) = 1 + j\omega/\omega_0$ (PD-algorithm)

- with anti-aliasing filtering

$$\overline{\varepsilon^2} = 2S_0(\omega_{x0} - \omega_s/2); \quad (6a)$$

- without anti-aliasing filtering

$$\overline{\varepsilon^2} = 4S_0(\omega_{x0} - \omega_s/2); \quad (6b)$$

c) with low-pass filtering ω_{LP} after sampling (I-algorithm)

- with anti-aliasing filtering

$$\overline{\varepsilon^2} = 0 \quad \text{if} \quad \omega_{LP} < \omega_s/2; \quad (7a)$$

- without anti-aliasing filtering only aliasing errors appear and only if

$$\omega_{x0} > \omega_s - \omega_{LP}$$

$$\begin{aligned} \overline{\varepsilon_{al}^2} &= 2 \int_{\omega_s - \omega_{LP}}^{\omega_{x0}} \frac{S_0}{1 + (\omega/\omega_0)^2} d\omega = \\ &= 2S_0\omega_0 \left(\arctan \omega_{x0}/\omega_0 - \arctan \frac{\omega_s - \omega_{LP}}{\omega_0} \right) \end{aligned} \quad (7b)$$

Of special interest in practice is the case of mean operation after sampling, as for instance used in surface measurement. As Fig. 2 shows that means a low-pass-filtering ω_{LP} . In this case no aliasing error occurs as long as the limiting frequency of the signal ω_C is less than $(\omega_s - \omega_{LP})$. That means in this case the sampling frequency has to be only

$$\omega_s \geq \omega_C + \omega_{LP}. \quad (8)$$

Instead of the value due to the sampling theorem now the sampling frequency is allowed to be only half of this value for the extreme case $\omega_{LP} \rightarrow 0$ without errors!

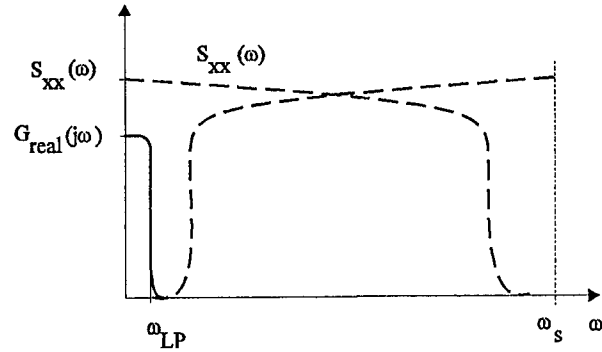


Fig. 2. Mean-operation after sampling

d) On the other hand additional errors due to non-ideal approximations appear:

For the rectangular approximation (T_s = sampling period) the mean-square error due to approximation can be calculated (Woschni, 1990)

$$\overline{\varepsilon^2} = 2 \int_0^{\pi/T_s} \frac{S_0}{(1 + \omega/\omega_0)^2} \left| \frac{1}{j\omega} - \frac{T_s}{1 - e^{-j\omega T_s}} \right|^2 d\omega \quad (9a)$$

The next better approximation is the trapezoidal one with the approximation error

$$\overline{\varepsilon^2} = 2 \int_0^{\pi/T_s} \frac{S_0}{(1 + \omega/\omega_0)^2} \left| \frac{1}{j\omega} - \frac{T_s}{2} \frac{1 + e^{-j\omega T_s}}{1 - e^{-j\omega T_s}} \right|^2 d\omega \quad (9b)$$

4. CONCLUSION

The sampling theorem and the sampling errors in the classical theory are treated without signal processing after sampling.

If signal processing after sampling is taken into consideration the situation is another one as shown in detail in the paper: In this case cut-off-errors as well as aliasing-errors are depending of the processing algorithm. These algorithms mean in the frequency domain an increasing or decreasing of the higher spectral frequencies. Due to this fact the errors - both

the cut-off and the aliasing parts - are decreasing, if the processing algorithm includes an integral (I-)part. On the other hand a differential (D-)part leads to increasing errors. In the extreme case of a mean-operation (i. e. an extreme low-pass-filtering after sampling) the sampling frequency is allowed to be half of the value due to the sampling theorem.

In the paper at least illustrative examples show the situation in typical cases of signal-processing as P-, PD- or I-algorithms.

Furthermore it has to be taken into consideration as well-known the condition for one-line processing. That means the computing time T_C must be less than the sampling period T_S .

T_C depends on the algorithm: In general T_C is the longer, the better the approximation. For the example of integration the trapezoidal approximation needs approximately the double of time in comparison with the rectangular approximation. For minimizing the overall error one has to make a compromise between sampling-period, degree of approximation and calculation error-components. Because due to the law that the computation speed increases one order of magnitude every 5...7 years in future the possible critical frequency will shift to higher frequencies that means the errors will be decreasing drastically.

Last not least it may be pointed out that the use of computers with higher bit-words (16 to 32 to 64 bit-computers) is only efficient if the errors are decreasing also drastically.

Woschni, E.-G. (1993). Cut-Off and Aliasing Errors - Exact Solutions and Approximations. Proc. XXIVth General Assembly of URSI, Kyoto, Sektion C2

Zadeh, L. A. and Desoer, C. A. (1963). Linear System Theory. McGraw-Hill, New York.

5. REFERENCES

Churkin, J. I.; Jakowlew, C. P. and Wunsch, G. (1966). Theorie und Anwendung der Signalabtastung. Verlag Technik, Berlin.

Woschni, E.-G. (1982). Signals and Systems in the time and frequency domains. In P. H. Sydenham (Ed.), Handbook of Measurement Science, Vol. 1. Wiley, London.

Woschni, E.-G. (1987). Minimising aliasing errors of sensors with digital output. J. phys. E: Sci. Instrum., 20, 119 -124.

Woschni, E.-G. (1990). Informationstechnik. Verlag Technik, Berlin.

OPTIMISATION OF ORTHOGONAL LOW-RATE CONVOLUTIONAL CODES IN A DS-CDMA SYSTEM

J.J. Maxey and R.F. Ormondroyd

School of Electronic & Electrical Engineering
University of Bath
Claverton Down, Bath
BA2 7AY, United Kingdom
eepjjm@bath.ac.uk, eesrfo@bath.ac.uk

ABSTRACT

The paper describes a novel approach to the use of direct-sequence spread-spectrum modulation for code division multiple access (DS-CDMA) applications by replacing the normal PN spreading code with an orthogonal low-rate convolutional code. This achieves both the spreading in bandwidth of the data and a powerful coding strategy within the output state of the convolutional shift register system, which maximises the number of simultaneous CDMA channels. In order to achieve orthogonality, Hadamard codes are incorporated within the convolutional coding strategy. The effects of using such a design within a DS-CDMA system are studied and the results show a direct increase in the capacity of the cellular system compared with a DS-CDMA using maximal length sequences. The importance of randomising the output symbols from the Hadamard encoder is also considered with respect to the spectral characteristics of the transmitted signal and the isolation between different simultaneously transmitting users.

1. INTRODUCTION

The field of spread spectrum multiple access is currently receiving considerable attention as a contender for the next generation mobile telephone system. DS-CDMA systems are at present looking very promising compared to advanced time division multiplex systems (TDMA) [1], as these systems offer increased flexibility in the frequency management of the cellular network, the prospect of temporary capacity overload and improved handover flexibility. The ultimate goal is to maximise the potential number of simultaneous users within a specific cell boundary.

Conventional DS-CDMA systems rely on an internally generated PN sequence, such as maximal length sequences or Gold codes, to spread the data in the transmitter by means of modulo-2 addition. This causes

the original data to be spread in bandwidth by a factor dependant on the PN sequence chip rate. If the PN data is of repetition length L , and one data period lasts for the whole repetition length, then the data will experience a spread in bandwidth proportional to L . The factor L , by which the data is increased in bandwidth can be termed the *spreading ratio* of the base-station transmitter.

This is not the only way of spreading the bandwidth of the data in the transmitter base-station, however. Using a convolutional encoder of rate $1/L$, as shown in figure 1, also introduces a redundancy of L symbols, hence this also provides bandwidth spreading.

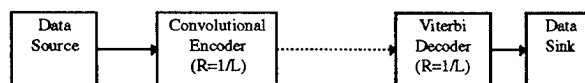


Figure 1 Spread-spectrum system using convolutional coding for signal spreading

Figure 2 shows the schematic of a CDMA base-station transmitter which is based on the use of low-rate convolutional codes rather than the more usual PN spreading sequences. The orthogonality of ordinary convolutional codes is very poor, and this would lead to a small number of simultaneous users when used in a CDMA system. This can be improved significantly by using low-rate orthogonal codes [2] which directly code and spread the data signal. This system provides an encoded bit sequence of length L on each bit transition from the data source and in effect provides complete spreading of bandwidth.

It is well known that orthogonal functions do not have good auto-correlation properties and therefore the direct use of orthogonal functions can lead to poor transmission spectral characteristics (e.g. non-uniform spreading) and large interference signals.

To reduce this problem, a second stage of randomisation is added to the encoded symbol set to improve the auto-correlation property of the orthogonal signals [2]. The PN sequence serves purely as a randomiser and introduces no further spreading of bandwidth. This encoded and spread signal is then modulated onto the carrier (using a technique such as QPSK) prior to transmission over the channel.

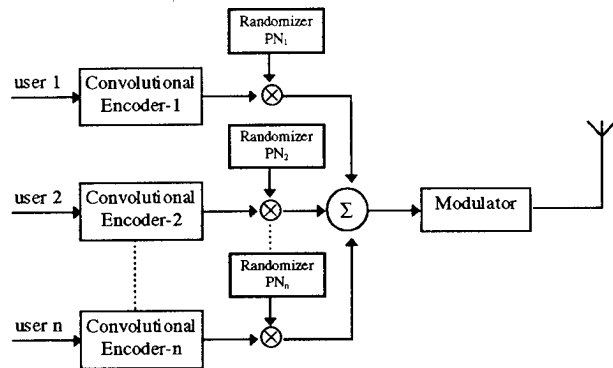


Figure 2 Simplified diagram of the proposed BS transmitter

The receiver structure performs the inverse operation by demodulating the received signal, then decoding the convolutionally encoded signal and providing an estimate of the most likely transmitted data bit. The decoding algorithm used by the receiver must use the maximum-likelihood decoding technique since the probability of any codeword being transmitted is equally likely. There are various decoding algorithms such as the Viterbi algorithm, sequential decoding (which is nearly maximum-likelihood) or concatenated coding schemes. One particular feature which is important to the decoding algorithm is its speed, especially if it is to be used for low rate codes in a DS-CDMA system where the throughput (i.e. the speed at which each data bit is processed) must be high. It will become apparent that a low rate code will inevitably slow down the speed of operation in the decoder since a large number of symbol comparisons per data bit will be made.

The Viterbi algorithm is a fast and efficient way of decoding convolutionally encoded data. It works by comparing the received sequence of encoded bits with the possible combinations of most likely transmitted bits and makes its decision after it has reached a decision on the most likely path through the trellis of the convolutional code. Thus it can be seen that this technique will yield an improvement over the simple correlating process in a conventional CDMA since a decoding decision is based not only on the complete set of L redundant symbols but

also takes into account the previous data bits which had been present in the shift register system. Hence, improved error detection is provided where the level of improvement depends on the constraint length K of the code (i.e. number of shift registers used). As K is increased, the decoding method becomes more historic since the number of possible states in the trellis diagram will increase exponentially. The higher the number of possible states in the trellis, the better the bit-error performance. The drawback, of course, is that the decoding procedure will slow down as the number of states in the trellis increases, as the decoder has to compare many more possible data bit transitions.

The level of improvement that a convolutional code will give compared to an uncoded system is given by the *coding gain*. The Viterbi algorithm offers the advantage of providing a high coding gain at low bit-error rates, which can range from 1.5 dB to 4 dB at a BER of 10^{-5} using hard decision limiting with constraint lengths 3 and 8 respectively.

2. DS-CDMA SIMULATIONS

Computer simulations of conventional DS-CDMA systems and the low-rate orthogonal code system were set up with identical basic parameters of code rate and spreading bandwidth for the two systems. In this way a fair comparison of bits/s/Hz/cell between the two systems can be established, hence it was possible to obtain a direct comparison of the number of simultaneous users between the two systems for a given bit-error rate (BER). For the case of the low-rate convolutional Hadamard encoder, shown in figure 3, the simulation provides an encoded sequence of 2^K output symbols for each consecutive input data bit. There are 2^K different sequence sets, each of length 2^K symbols and orthogonal to any other sequence. The inherent orthogonal properties of the Hadamard codes are based on the fact that any two sequences of length 2^K differ in 2^{K-1} bit positions, thus giving a 64 symbol length Hadamard code 32 different symbol combinations.

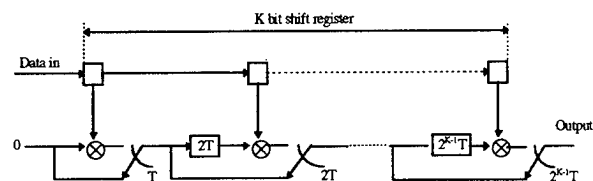


Figure 3 A low-rate convolutional encoder

To decode the received signal sequence with a Viterbi decoder it is necessary to find the most likely path

through the trellis state diagram. Since each user has a different unique mapping of state outputs in the shift register system to the inputs of the Hadamard block encoder, the trellis for each user will be considerably different, hence allowing all simultaneous users to be isolated from one another.

It is well known [3] that the BER performance of a Viterbi decoder is directly related to the free distance of the convolutional code, consequently the BER probability in the continuous additive white Gaussian noise channel is given as:

$$\text{BER} < \sum_{x=\text{dfree}}^{\infty} C_x P_x \quad (1)$$

where $P_x = Q\left(\sqrt{\frac{2xRE_b}{N_o}}\right)$, R is the rate of the code, E_b/N_o is

the required SNR at the output of the decoder and C_x is determined by the code structure of the Hadamard encoder. Equation (1) is the key to determining the structure of the most effective code performance for the continuous output additive white Gaussian noise channel. In order to use the same bandwidth in the most efficient way it is desirable to use a coding strategy which yields the highest free distance, ultimately governed by the code rate and constraint length of the encoder. The new code design featured in this paper will inevitably give a superior performance to a simple rate 1/2 encoder of same constraint length operating in a very noisy environment (i.e. high number of simultaneous users). At low user numbers the performance of both systems would yield an equal BER.

To obtain a result for the performance of such a system in "other-user" noise it is necessary to assume that a relatively large number of simultaneous users and a high spreading ratio will approximate the interference as normally distributed with a mean of zero and variance of

$$\sigma^2 = \frac{M-1}{1/R} \quad (2)$$

where M is the number of simultaneous users. This will lead to a new expression for P_x :

$$P_x = Q\left(\sqrt{\frac{2x}{M-1}}\right) \quad (3)$$

The free distance of the $K=6$ Hadamard convolutional code is governed by the total Hamming distance with respect to the "all-zero" path in the trellis and the

number of paths which will take the decoder decision to the all-zero state, given as $K+1$. For the Hadamard convolutional encoder used in this simulation the free distance is $7 \times 32 = 224$. The values for C_x have been obtained using a full search of the trellis structure and for a $K=6$ Hadamard code, neglecting the higher order terms, yield a bit-error probability of:

$$\text{BER} < P(224) + 2P(256) + 6P(288) + 16P(320) + 35P(352) + 60P(388) \dots \quad (4)$$

The results of equations 3 and 4 are displayed graphically in figure 4. It must be noted that BER values of greater than 1 serve only on a theoretical basis. A comparison between the uncoded conventional DS-CDMA system and the new Hadamard encoded system shows considerable improvements with the new implementation at a low number of simultaneous users. These results are also compared to the conventional rate $R=1/2$ coded DS-CDMA implementation and show that the Hadamard rate $R=1/64$ implementation performs better at a relative high number of users.

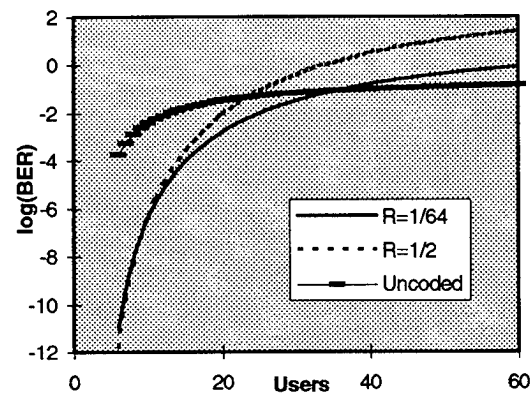


Figure 4 Theoretical performance of different coding schemes in other user noise

The resulting theoretical and simulated bit-error rate curves in "other-user" noise can be seen in figure 5. It is apparent that the theoretical prediction of the code matches the simulated results very closely, and a significant advantage in performance can be found when the number of simultaneous users is low.

To achieve a $\text{BER}=10^{-3}$ a maximum number of 7 users could be employed in a conventional DS-CDMA system but the use of low-rate convolutional coding can lead to an increase of nearly 130%, giving a new maximum number of users of 16.

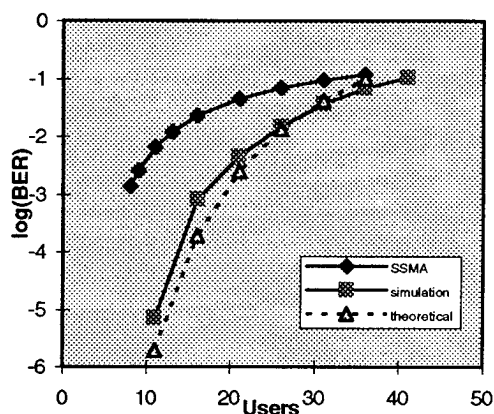


Figure 5 Performance of low-rate convolutional codes in other user noise

The use of PN sequences to randomise the output of the low-rate convolutional encoder is to improve the spectral characteristics of the orthogonal codes and provide better isolation between users without causing any further spreading of the encoded signal. This is done by using a PN sequence of the same rate as the orthogonal output sequence.

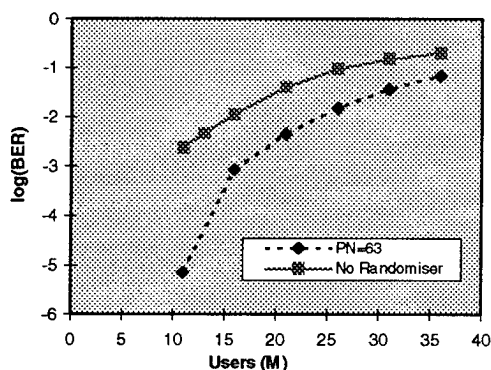


Figure 6 Graph displaying the advantages of using a randomiser

If $\delta \rightarrow 0$, where δ is the duration of one output symbol from the Hadamard encoder, the spectral density of a pseudo-random signal can be seen [2] to approach a constant value of E_s/T , where E_s is the symbol energy and T is the period of repeat of the pseudo-random noise sequence. It can therefore be seen that such a signal will give an almost uniform spectrum, which is desired in a DS-CDMA implementation. The sequence of output symbols from a low-rate orthogonal convolutional Hadamard encoder, however, have a periodic nature for

each sequence set of length 2^K . Thus the auto-correlation properties of orthogonal sequences is extremely poor and yields a spectrum with large variations in amplitude, which has the direct effect of degrading the performance of the decoder to other user noise since the signal sets are not independent random processes. To eliminate this problem a PN sequence of same rate can be used to smooth out the spectrum and randomise the interference created by other users as seen in figure 6.

It is clearly evident that the second stage of randomisation improves the performance of the cellular DS-CDMA system by at least 60%, giving an equivalent improvement in BER performance of about 2dB.

3. CONCLUSIONS

This paper has shown the feasibility of using low-rate orthogonal convolutional coding for DS-CDMA applications. It has been found that the number of simultaneous users per cell is increased by at least 70% and there is an additional improvement of 60% when a randomiser is used, giving a total improvement of 130%.

4. ACKNOWLEDGEMENTS

The authors would like to thank EPSRC for their financial support of this research project through the provision of research contract N°- GR/K27902 and also a research studentship.

5. REFERENCES

- [1] "A comparison of CDMA and TDMA systems"; CIRP TG 8/1 Washington; Ericsson May 1991.
- [2] A.J Viterbi; "Very Low Rate Convolutional Codes for Maximum Theoretical Performance of Spread-Spectrum Multiple-Access Channels"; IEEE Journal on Selected Areas in Communications, Vol 8, No.4, May 1990.
- [3] A.J. Viterbi; "Convolutional Codes and Their Performance in Communication Systems"; IEEE Transactions on Communications Technology, COM-19, No.5, Oct 1971.

AN EFFICIENT CONTINUATION METHOD FOR USE IN GLOBALLY CONVERGENT DC CIRCUIT SIMULATION

Michael M. Green

Department of Electrical Engineering
State University of New York
Stony Brook, NY 11794-2350
mgreen@ee.sunysb.edu

ABSTRACT

The use of continuation methods and various homotopies used for globally convergent dc operating point simulation are discussed. A new homotopy that gives the shortest possible arclength between the initial solution and the desired operating point is introduced. In addition, it is shown that for the case where a circuit possesses multiple operating points, this homotopy allows the user to choose which operating point is found first and is guaranteed to find at least three operating points in a single analysis.

1. BACKGROUND

Finding the dc operating points of a nonlinear circuit is one of the most important and difficult tasks in electrical circuit simulation. In the majority of circuit simulation programs the dc operating point is found (as in SPICE, for example) by using a Newton-Raphson-based iterative algorithm. Such algorithms have two shortcomings: First, convergence is in general not guaranteed; it is guaranteed only if the initial guess (specified by the user in SPICE by the `.nodeset` statement) is sufficiently close to the actual solution. Unfortunately the user either may not know the solution or cannot give a sufficiently accurate initial guess. Second, only one operating point can be found during an analysis; neither location nor even existence of other operating points are known once the algorithm has converged to a particular operating point.

A better approach to finding the solution of a set of nonlinear equations $F(x) = 0$, where $F: \mathcal{R}^n \rightarrow \mathcal{R}^n$ is smooth, is the use of a *continuation method*. In general, this method entails embedding the continuation parameter λ into a set of nonlinear equations $H(x, \lambda)$

where $H: \mathcal{R}^{n+1} \rightarrow \mathcal{R}^n$, $x \in \mathcal{R}^n$ and $\lambda \in [0, 1]$, which satisfies the following conditions:

1. $H(x, 1) = F(x)$.
2. The solution $x = a$ of $H(x, 0) = 0$, where $a \in \mathcal{R}^n$, is trivial or easily found.
3. There exists a continuous curve σ (called a "zero curve") in $\mathcal{R}^n \times [0, 1]$ such that $H(x, \lambda) = 0$ for every point on σ .

Since H gives a continuous deformation between the "easy" problem $H(x, 0) = 0$ and the "hard" problem $H(x, 1) = 0$, it is called a *homotopy*. In circuit simulation applications, $x \in \mathcal{R}^n$ is the vector of node voltages, $F(x)$ gives the set of Kirchhoff's Current Law equations at each node, and the continuation parameter λ can be chosen to control a circuit component, such as a voltage source, a resistor, or a transistor parameter.

A class of homotopies, known as "probability-one," has been found that can be applied to nonlinear circuits [1]. These homotopies have the property that the resulting zero curve will not exhibit a bifurcation, will remain bounded for $\lambda \in [0, 1]$ (achieved by keeping all circuits corresponding to $\lambda \in [0, 1]$ passive) and will not return to $\lambda = 0$ (achieved by arranging the operating point of the $\lambda = 0$ circuit to be unique). Hence in a probability-one homotopy the simulation is guaranteed to reach a solution at $\lambda = 1$.

Another important advantage of continuation methods using a probability-one homotopy is the possibility of finding more than one, or even all of circuit's operating points, since the zero curve can pass through $\lambda = 1$ more than once. Consider the Schmitt trigger shown in Fig. 1(a), biased in its hysteresis region. Using the circuit simulator SFRAME [2], developed at Bell Laboratories, a continuation method was used that employs the Variable Gain Homotopy to find the solution to this

This work was supported by the National Science Foundation under Grants MIP 94-12779 and MIP 94-57387.

circuit. The Variable Gain Homotopy is defined by

$$H(x, \lambda) = (1 - \lambda)(x - a) + F(\lambda\alpha, x), \quad (1)$$

where the vector a determines the $\lambda = 0$ solution, and $F(\lambda\alpha, x)$ corresponds to the nodal equations of the circuit that results when all of the transistor α 's are multiplied by λ . A simulation was run where each component of the a vector was set to 0. The resulting zero curve, projected onto the $V_{out} - \lambda$ plane, is shown in Fig 1(b). Notice that the curve intersects $\lambda = 1$ three times; hence, three operating points have been found in this one analysis. However, if another simulation is run where all components of a are set to 1, the curve shown in Fig. 1(c) results; in this case, only one operating point has been found. A third simulation was run where all components of a were set to 5, with the resulting curve shown in Fig. 1(d). In this case three operating points were again found, but in the *opposite* order of the run corresponding to Fig. 1(b). Notice also that a zero curve beginning at $\lambda = 0$ can "wander" before reaching $\lambda = 1$ for the first time - that is, the arclength can be long. Such a wandering zero curve requires more points to be calculated due to constraints from the curve-tracking algorithm [3] and thus will require a longer simulation time.

2. THE ARCLENGTH REDUCING HOMOTOPY

The above examples suggest three areas for improvement of current continuation methods in use:

- A. The user should be able to specify which operating point is found first (i.e., equivalent to the SPICE `.nodeset` command).
- B. The zero curve connecting $\lambda = 0$ to $\lambda = 1$ should have the shortest arclength possible.
- C. If multiple operating points exist, they should always be found.

We will now construct a homotopy that has these properties. We begin by deriving the Augmentation Principle:

Augmentation Principle: Consider the circuit shown in Fig. 2(a), where a set of open-circuit voltages V_1, \dots, V_k and short-circuit currents $I_{k+1} \dots I_n$ have been measured. The circuit in Fig. 2(b) is constructed as follows. Each open circuit in Fig. 2(a) where V_i , $i = 1, \dots, k$, has been measured is replaced with a voltage source of value V_i ; likewise, each short circuit in Fig. 2(a) where I_i , $i = k + 1, \dots, n$, has been measured is replaced with a current source of value I_i . By the Substitution Principle, the Fig. 2(b) circuit must possess

an operating point that is identical to the operating point measured from the Fig. 2(a) circuit. Moreover, at this operating point the current through each voltage source and the voltage across each current source must be zero. But if this is true, then augmenting each voltage source V_i with a series resistor R_i and augmenting each current source I_i with a shunt conductance G_i , as illustrated in Fig. 2(c), will not change this operating point, since none of these augmenting resistors and conductances will conduct any current. Therefore, the circuit constructed by replacing each open circuit having voltage V_i with a resistor R_i in series with voltage source V_i and replacing each short circuit having current I_i with a conductance G_i in parallel with current source I_i will possess the same operating point for any $R_i, G_i \in [0, +\infty]$.

The Augmentation Principle can be used to construct a homotopy as follows. If, at a certain operating point, a particular transistor is expected to be in the off state, then the pseudo-off model shown in Fig. 3(a) is used, where $r_{off} = +\infty$ at $\lambda = 0$ and goes to 0 as λ goes to 1; if a transistor is expected to be in saturation, then the pseudo-saturated model shown in Fig. 3(b) is used, where $g_{sat} = 0$ at $\lambda = 0$ and goes to $+\infty$ as λ goes to 1; if a transistor is expected to be in the forward active state, then the pseudo-forward active model shown in Fig. 3(c) is used, where $g_{fa} = 0$ at $\lambda = 0$ and goes to $+\infty$ as λ goes to 1. In this case, the value of V_{BE} is derived from the user's estimate of the collector current at the desired operating point. The resulting homotopy, called the Arclength Reducing Homotopy, has the following properties:

1. It is based on simply augmenting the existing BJT model with appropriate resistors; no change of the model itself is necessary.
2. The circuit corresponding to $\lambda = 0$ must possess a unique operating point by the Nielsen-Willson Theorem [4].
3. If the transistor states are chosen correctly, then the node voltages will be nearly constant with $\lambda \in [0, 1]$; hence, the arclength of the zero curve will be close to the minimum possible. This implies a small number of points that are needed to be calculated along the zero curve and thus a very fast simulation.
4. The first operating point encountered will always correspond to the selected transistor states, if such an operating point exists.
5. It exploits the designer's knowledge of the transistor states, which are typically known before

simulation. However, even if the expected states are incorrect or even randomly chosen, the global convergence property guarantees that an operating point will still eventually be found; it will just take longer to find.

Hence requirements A. and B. are fulfilled by use of the Arclength Reducing Homotopy. We will now investigate how multiple operating points can be found.

3. GUARANTEEING FINDING MULTIPLE OPERATING POINTS

We now allow λ to vary between 0 and 2 and place the following additional conditions on the Arclength Reducing Homotopy:

1. The curve is bounded for $\lambda \in [0, 2]$. This is easily arranged by constraining any circuit corresponding to $\lambda \in [0, 2]$ to be *passive*.
2. There exists some $\eta_0 > 0$ such that the circuit corresponding to any $\lambda \in [0, \eta_0]$ possesses a unique operating point.
3. There exists some $\eta_2 > 0$ such that the circuit corresponding to any $\lambda \in [2 - \eta_2, 2]$ possesses a unique operating point.
4. The unique operating point of the circuit corresponding to $\lambda = 0$ is "close" to an operating point of the original (i.e., $\lambda = 1$) circuit.
5. The unique operating point of the circuit corresponding to $\lambda = 2$ is "close" to an operating point, different from the one in Condition 4, of the original circuit.

Under these conditions, the only possible zero curve that can exist must pass through $\lambda = 1$ at least three times, as illustrated in Fig. 4. The shaded regions in this figure correspond to the homotopy's "regions of uniqueness." Notice that if $H(\lambda, x)$ were symmetric around $\lambda = 1$ (i.e., if $H(\lambda, x) = H(2 - \lambda, x)$), then any zero curve with one endpoint at $\lambda = 0$ would necessarily pass through $\lambda = 1$ only once. Thus, any homotopy that passes through $\lambda = 1$ more than once must have some degree of asymmetry around $\lambda = 1$. The five conditions given above guarantee this asymmetry.

To realize these conditions we simply extend the Arclength Reducing Homotopy by choosing another set of transistor states for $\lambda = 2$ that corresponds to a second expected potentially stable operating point. Hence each transistor model will have two augmenting resistors; for example, suppose a circuit possesses one operating point where a certain transistor is expected to be off and another operating point where the transistor is expected to be saturated. Then a model called *off_sat* would be used. The Fig. 1(a) Schmitt trigger was run again using the Arclength Reducing Homotopy where transistor Q_1 had continuation model *off_sat* and transistor Q_2 had continuation model *sat_off*. The resulting zero curve for V_{out} is shown in Fig. 5. Notice that the operating point corresponding to the first intersection with $\lambda = 1$ corresponds to Q_1 off and Q_2 saturated. Moreover, the variation in V_{out} (and, in fact, in all other node voltages) is very small along the zero curve between $\lambda = 0$ and $\lambda = 1$.

4. REFERENCES

- [1] R. C. Melville, Ljiljana Trajković, S-C. Fang & L. T. Watson, "Artificial parameter homotopy methods for the dc operating point problem," *IEEE Transactions on Computer-Aided Design of Integrated Circuits and Systems*, vol. 12, pp. 861-877, June 1993.
- [2] R. Melville, S. Moinian, P. Feldmann & L. Watson, "Sframe: An efficient system for detailed dc simulation of bipolar analog integrated circuits using continuation methods," *Analog Integrated Circuits and Signal Processing* 3, pp. 163 - 180, 1993.
- [3] L. Watson, S. Billups & A. Morgan, "ALGORITHM 652 HOMPACK: a suite of codes for globally convergent homotopy algorithms," *ACM Trans. Math. Software*, vol. 13, pp. 281-310, 1987.
- [4] R. O. Nielsen and A. N. Willson, Jr., "A fundamental result concerning the topology of transistor circuits with multiple equilibria," *Proc. IEEE*, vol. 68, pp. 196-208, Feb. 1980.

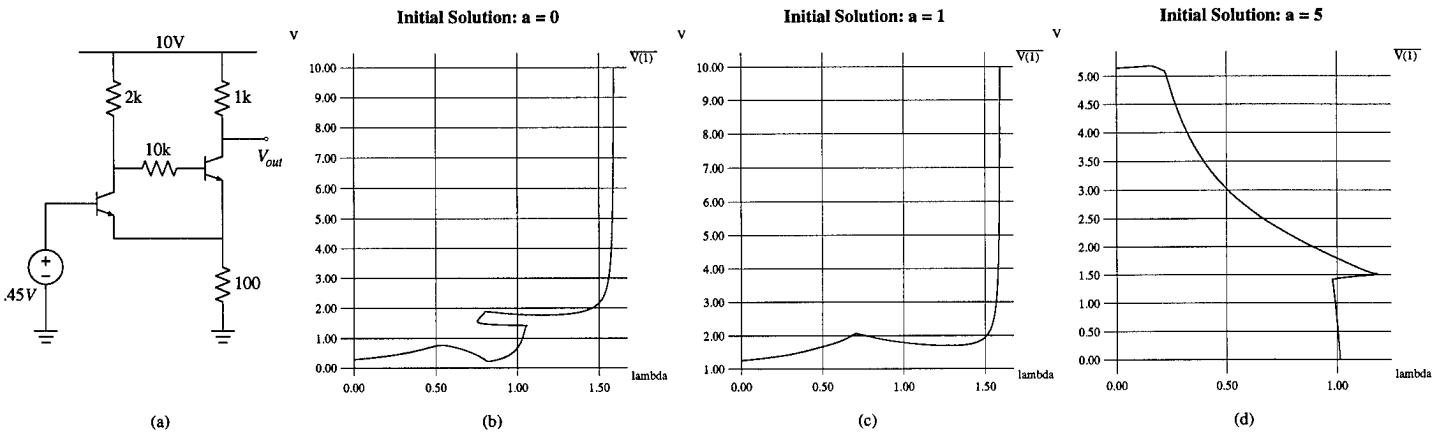


Figure 1: Zero curves for Schmitt trigger.

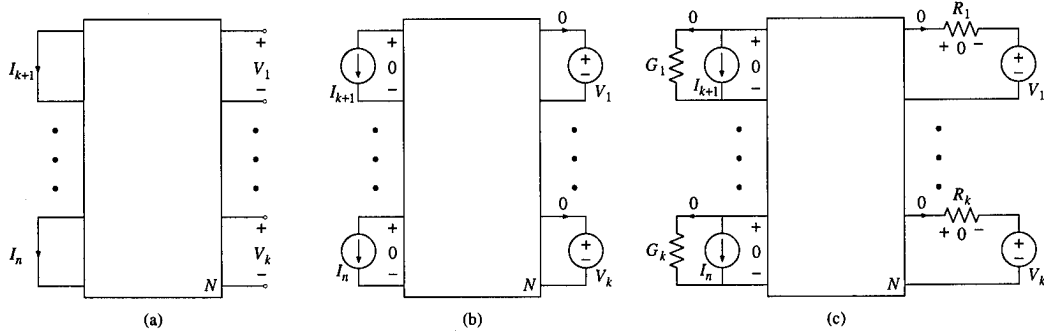


Figure 2: Derivation of the augmentation principle.

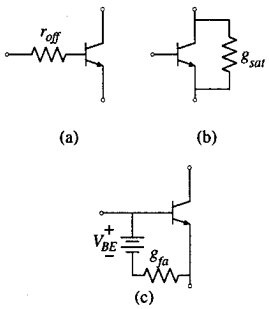


Figure 3: Transistor continuation models.

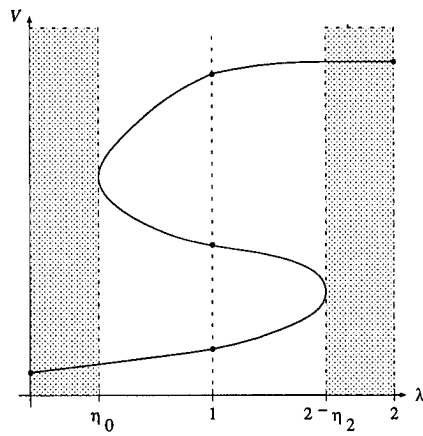


Figure 4: Illustration of criteria for finding multiple operating points.

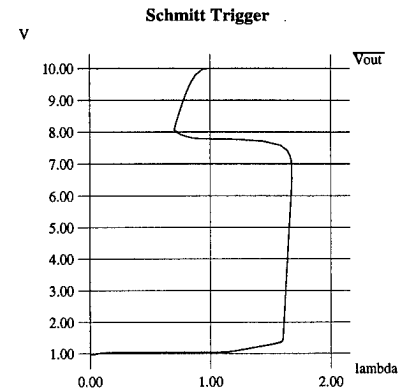


Figure 5: Schmitt trigger zero curve using Arclength Reducing Homotopy.

A LEARNING ALGORITHM FOR CELLULAR NEURAL NETWORKS (CNN) SOLVING NONLINEAR PARTIAL DIFFERENTIAL EQUATIONS

F. Puffer, R. Tetzlaff, and D. Wolf

Institut für Angewandte Physik, Universität Frankfurt
Robert Mayer-Straße 2-4, 60054 Frankfurt a. M., Germany
puffer@apx00.physik.uni-frankfurt.de, tetzlaff@apx00.physik.uni-frankfurt.de

ABSTRACT

A learning procedure for CNN is presented and applied in order to find the parameters of networks approximating the dynamics of certain nonlinear systems which are characterized by partial differential equations (PDE). Our results show that — depending on the training pattern — solutions of various PDE can be approximated with high accuracy by a simple CNN structure. Results for two nonlinear PDE, Burgers' equation and the Korteweg-de Vries equation, are discussed in detail.

1. INTRODUCTION

A CNN [2,3,4] is a system of simple nonlinear processors (cells) which are arranged in one or more layers on a regular grid. Interactions between cells are local and usually translation invariant, i.e. a connection from a cell j towards another cell i only exists if j is part of i 's neighborhood $\mathcal{N}(i)$ and its type and strength depend only on the relative position of j with respect to i . Thus the number of connections increases only linearly with the number of cells, a feature that makes hardware realization of CNN relatively simple when compared to other types of artificial neural networks. State $v_{x,i}^m$ and output $v_{y,i}^m$ of a cell i in layer m are real numbers, their dynamics being determined by state equations of the form

$$\begin{aligned} \frac{dv_{x,i}^m(t)}{dt} = & -g(v_{y,i}^m(t)) \\ & + \sum_{m'=1}^M \sum_{i+l \in \mathcal{N}(i)} a_l^{m'm} (v_{y,i+l}^{m'}(t), v_{y,i}^m(t); \mathbf{p}_{a,l}^{m'm}) \\ & + \sum_{i+l \in \mathcal{N}(i)} b_l^m (v_{u,i+l}^m(t), v_{u,i}^m(t); \mathbf{p}_{b,l}^m) \end{aligned} \quad (1)$$

with

$$v_{y,i}^m = f_{\text{out}}(v_{x,i}^m).$$

The feedback connection from a cell $i+l$ in layer m' towards another cell i in layer m is defined by the weight function $a_l^{m'm}$, while the functions b_l^m define the connection from an input node $v_{u,i+l}^m$ towards a cell i , the parameter vectors $\mathbf{p}_{a,l}^{m'm}$ and $\mathbf{p}_{b,l}^m$ have to be determined (e.g. by a learning algorithm) to achieve the desired

CNN behaviour. The cell output function is usually given by $f_{\text{out}}(y) = \frac{1}{2}(|y+c| - |y-c|)$ with positive c . The function $g(v_{x,i}^m(t))$ defines the local dynamics of a cell.

Up to now a large number of learning methods for CNN has been considered [5], most of them are modifications of the Recurrent Backpropagation and Backpropagation-through-Time algorithms for standard recurrent neural networks. But these methods are designed in order to find stable fixpoints of a network with linear weight functions. They are not applicable to the approximation of the dynamics of nonlinear systems.

2. SOLVING NONLINEAR PARTIAL DIFFERENTIAL EQUATIONS WITH CNN

The state equations (1) of a CNN, a system of locally interconnected ordinary differential equations, can be considered as a spatially discretized representation of a given PDE where the functions $a_l^{m'm}$ and b_l^m have to be chosen appropriately. Then the cell states $v_{x,i}^m(t)$ are approximations of the PDE's solution $u(x,t)$ at $x = x_i$ and the inputs $v_{u,i}^m(t)$ represent external forces.

Let the cell outputs be identical with the cell states, which can be achieved by choosing a sufficiently large parameter value c of the piecewise linear output function. Furthermore we set $g(v_{y,i}) \equiv 0$, and — as the PDE considered here are homogeneous — the network has no inputs. Then for a single layer network with $\mathcal{N}(i) = \{i-r, \dots, i+r\}$, the state equations are given by

$$\frac{dv_{x,i}(t)}{dt} = \sum_{l=-r}^r a_l (v_{x,i+l}(t), v_{x,i}(t); \mathbf{p}_{a,l}). \quad (2)$$

2.1. CNN design based on finite difference Methods

An approach for solving PDE with CNN, the so-called direct method, which has been used so far [7,8,9] is based on standard finite difference approximations of the spatial derivatives. This method is introduced for the example of the homogeneous Burgers equation [1,10]

$$\frac{\partial u(x,t)}{\partial t} = \frac{1}{R} \frac{\partial^2 u(x,t)}{\partial x^2} - \frac{1}{2} \frac{\partial (u(x,t))^2}{\partial x}. \quad (3)$$

After spatial discretization of Eq. (3) using three points to estimate the derivatives, the resulting set of equations

$$\frac{du_{x_i}(t)}{dt} = \frac{1}{R} \frac{u_{x_{i+1}}(t) - 2u_{x_i}(t) + u_{x_{i-1}}(t)}{(\Delta x)^2} - \frac{u_{x_{i+1}}^2(t) - u_{x_{i-1}}^2(t)}{4\Delta x} \quad (4)$$

can be represented by a single-layer CNN with state equations given by Eq. (2) with $r = 1$. By comparing Eq. (2) with Eq. (4) we obtain the weight functions

$$a_l = p_{a,l,1} v_{y,i+l} + p_{a,l,2} v_{y,i+l}^2$$

with

$$\begin{aligned} p_{a,-1,1} &= -\frac{1}{4\Delta x}, & p_{a,-1,2} &= \frac{1}{R(\Delta x)^2}, \\ p_{a,0,1} &= 0, & p_{a,0,2} &= -\frac{2}{R(\Delta x)^2}, \\ p_{a,1,1} &= \frac{1}{4\Delta x}, & p_{a,1,2} &= \frac{1}{R(\Delta x)^2}. \end{aligned}$$

We have shown previously [7,8] that for several PDE including Burgers' equation precise solutions can be obtained by this method.

While this well-known method is applicable if the entire PDE is given, our approach requires only a rough knowledge of the PDE's mathematical form — the highest order spatial derivative and the type of nonlinearity — and a few values of the system output. The learning method outlined in the following section is able to determine the PDE parameters — e.g. the coefficient R in Burgers' equation — and thus the complete system output.

2.2. CNN parameter learning

For learning the dynamics of a given nonlinear system, firstly the basic CNN structure has to be determined. This includes the choice of the neighborhood \mathcal{N} and of a class of nonlinear weight functions a_l . While the number of cells in the neighborhood has to be large enough to allow an estimation of the highest order spatial derivatives in the considered PDE, it is necessary that the nonlinearity of the PDE can be represented by the functions a_l .

Then let assume that the values of a special solution $u^*(x, t)$ of a PDE for an initial condition $u^*(x, 0)$ are known at the cell positions x_i for a few times t_m . These values are presented to the CNN as learning patterns. After choosing random initial values for the components of the parameter vector $\mathbf{p}_a = (p_{a,-r}, \dots, p_{a,r})$, the mean square error

$$e(\mathbf{p}_a) = \frac{1}{MN} \sum_{m=1}^M \sum_{i=1}^N [u_{\text{CNN}}(x_i, t_m, \mathbf{p}_a) - u^*(x_i, t_m)]^2$$

of the obtained CNN-solution $u_{\text{CNN}}(x_i, t_m, \mathbf{p}_a)$ is minimized for all cell positions x_i at times t_m . The minimization procedure is performed by using a standard technique, the downhill-simplex-method [6], which requires no explicit gradient information.

3. RESULTS

The learning method has been applied to determine solutions of the Burgers' equation (3) and the Korteweg-de Vries (KdV) equation [10]

$$\frac{\partial u(x, t)}{\partial t} = \frac{\partial^3 u(x, t)}{\partial x^3} - c \frac{\partial(u(x, t))^2}{\partial x}. \quad (5)$$

A CNN with a neighborhood radius $r = 2$ and polynomial weight functions

$$a_l(v_{u,i+j}; \mathbf{p}_{a,l}) = \sum_{k=1}^K p_{a,l,k} v_{u,i+j}^k.$$

with $K = 2$ has been used in all cases. Results obtained with the direct method and the learning method have been compared to reference solutions $u^*(x, t)$ which were calculated with high accuracy.

In order to determine the achieved approximation accuracy, the mean square error

$$e(t) = \frac{1}{N} \sum_{i=1}^N [u_{\text{CNN}}(x_i, t_m) - u^*(x_i, t_m)]^2$$

was calculated in all treated cases. A stepsize of $\Delta x = 0.5$ has been used for both CNN solutions.

Solutions of Burgers' equation with $R = 10$ are shown in Figs. 1 and 2. The values of the reference solution at $t_1 = 5$ and $t_2 = 15$ for the initial condition shown in Fig. 1 have been taken as the learning pattern.

The CNN with the same parameters has been applied to various other initial conditions including the square function shown in Fig. 2. Although the square function, due to its discontinuity, represents a numerically critical case and functions with discontinuities have not been taken as learning patterns, the error $e(t)$ of the solution obtained with the learning method is significantly smaller for a large range of t than that of the solution obtained with the direct method.

Figs. 3 and 4 show results for the KdV-equation with $c = 1/2$. The two-soliton solution shown in Fig. 3, which has been calculated analytically [10] at $t_1 = 1$, formed the learning pattern. The CNN has then been applied to calculate solutions of the KdV-equation for a gaussian initial condition, which cannot be solved analytically. Here both methods lead to the same approximation accuracy.

The learning process usually took about 1000 iterations in the case of Burgers' equation and about 3000 iterations for the KdV-equation.

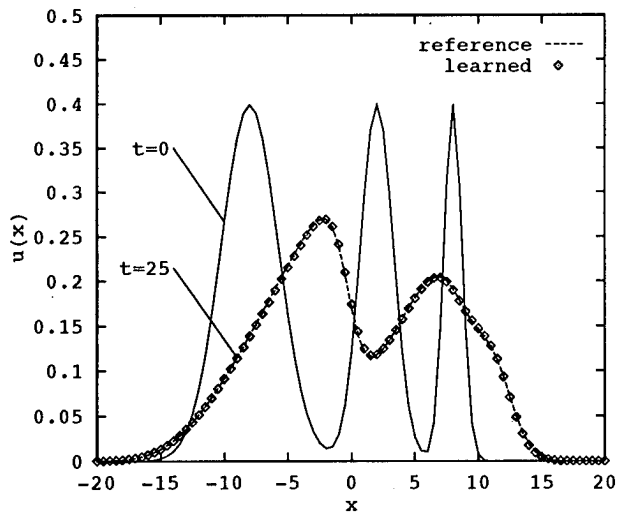


Figure 1a: Solutions of Burgers' equation at $t = 0$ and $t = 25$; values at $t_1 = 5$ and $t_2 = 15$ have been taken as the learning pattern

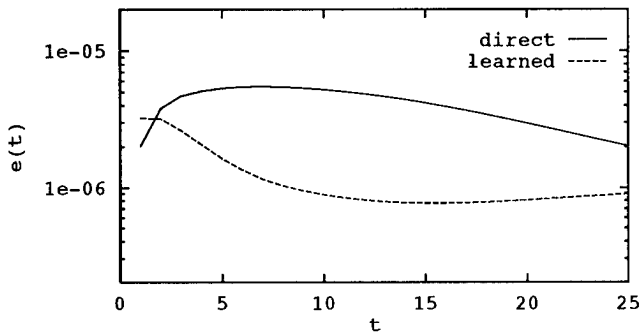


Figure 1b: Mean square error $e(t)$ of the solutions shown in Fig. 1a

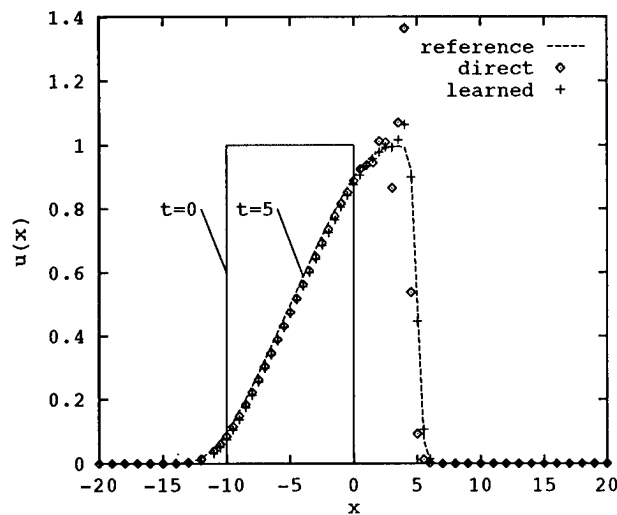


Figure 2a: Solutions of Burgers' equation at $t = 5$ for a square function as initial condition, which has not been taken in the learning process

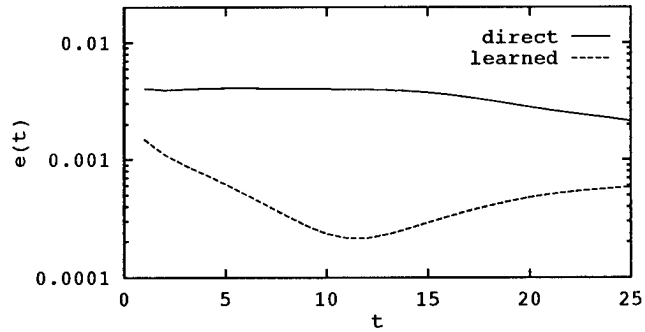


Figure 2b: Mean square error $e(t)$ of the solutions shown in Fig. 2a

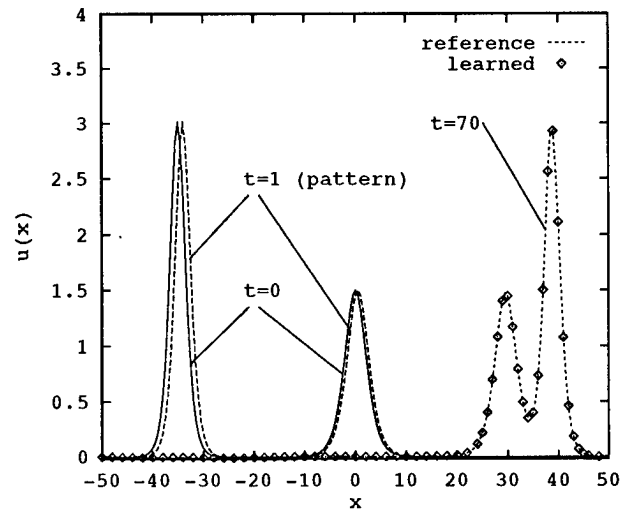


Figure 3a: Two-soliton solution of the KdV-equation; values at $t_1 = 1$ have been taken as the learning pattern

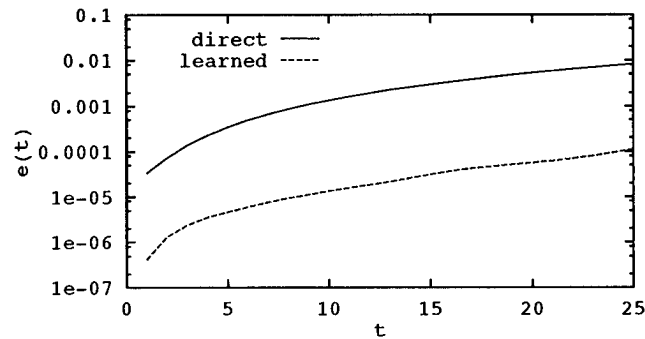


Figure 3b: Mean square error $e(t)$ of the solutions shown in Fig. 3a

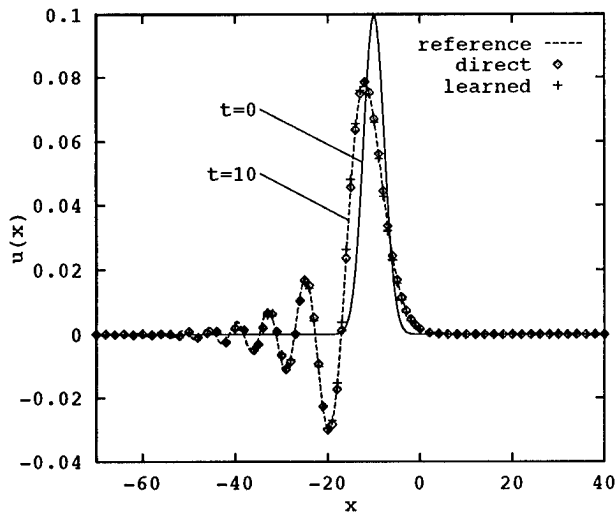


Figure 4a: Solutions of the KdV-equation at $t = 5$ for a gaussian function as initial condition, which has not been taken for the learning process

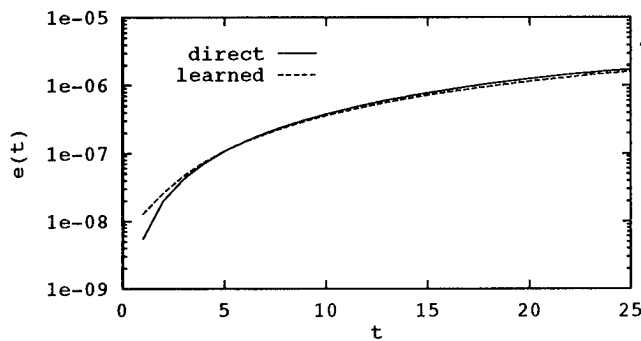


Figure 4b: Mean square error $e(t)$ of the solutions shown in Fig. 4a

4. CONCLUSION

Our results show that the dynamics of two nonlinear systems which are characterized by PDE, the Burgers equation and the KdV-equation, can be approximately solved by CNN with parameters optimized by a learning method. The solutions obtained by this approach were significantly more accurate than those using direct discretization. The learning method does not require the knowledge of the PDE's parameters.

REFERENCES

- [1] Anton, K., Tetzlaff, R. and Wolf, D.: Analysis of the Burgers Equation; Proc. 12th Int. Conf. on Noise in Physical Systems, St. Louis, pp. 599-602 (1993).
- [2] Chua, L.O. and Yang, L.: Cellular Neural Networks: Theory and Applications; IEEE Transactions on Circuits and Systems vol. 35, pp. 1257-1290 (1988)

- [3] Chua, L.O. and Roska, T.: The CNN Paradigm; IEEE Transactions on Circuits and Systems, vol. 40, pp. 147-156 (1993)
- [4] Cimagalli, V. and Balsi, M.: Cellular Neural Networks: A Review; Proc. 6th Italian Workshop on Parallel Architectures and Neural Networks, Vietri sul Mare, Italy (1993)
- [5] Nossek, J.A.: Design and Learning with Cellular Neural Networks; Proc. IEEE CNNA 94, pp. 137-146 (1994)
- [6] Press, W. H., Flannery, B. P. and Teukolsky, S. A.: Numerical recipes in C: The Art of Scientific Computing; New York, Cambridge University Press (1988)
- [7] Puffer, F., Tetzlaff, R. and Wolf, D.: Zur Genauigkeit der mit zeitdiskreten CNN gewonnenen Lösungen einiger Differentialgleichungen, Kleinheubacher Berichte, Band 37, Kleinheubach 1993, S. 245-252
- [8] Roska, T., Kozek, T., Wolf, D. and Chua, L.O.: Solving Partial Differential Equations by CNN; Proc. ECCTD '93, Davos, pp. 1477-1482 (1993)
- [9] Kozek, T., Chua, L.O., Roska, T., Wolf, D., Tetzlaff, R., Puffer, F., and Lotz, K.: Simulating Nonlinear Waves and Partial Differential Equations via CNN; IEEE Transactions on Circuits and Systems, in print
- [10] Witham, G. B.: Linear and Nonlinear Waves; Wiley, New York (1974)

AN ALGORITHM TO RECOGNIZE NUMERICAL HANDWRITTEN CHARACTERS ISOLATED AND OVERLAPPED

Edna L. Flôres, Eder N. Rezende*, Gilberto A. Carrijo* and João B. T. Yabu-uti***

*Departamento de Engenharia Elétrica - UFU

38.400-902 - Uberlândia - MG - Brasil

Tel.: (034)236-5099, FAX: (034)236-5099, e-mail:edna@brufu.bitnet

**Departamento de Comunicações - UNICAMP

Barão Geraldo - 13.081-970 - Campinas - SP - Brasil

Tel.: (0192)39-8324, FAX: 0055192391395, e-mail:yabuuti@decom.fee.unicamp.br

ABSTRACT

In this paper the authors describe the results of their investigation of the development of an algorithm for recognizing and identifying numerals which may be isolated or overlapped. These numerals may be continuous or fragmented. The features that the digits have in common and the intrinsic features of each one were considered. Such characteristics are used in the human recognition process and are the basis of the proposed algorithm. The principal idea of the algorithm is to start at the top of the image and group the pixels-on in horizontal and vertical lines that will characterize each one of the digits. Numerous experimental tests were carried out for recognition of handwritten numerical characters of bank checks and an accuracy of 99.88% was obtained.

1. INTRODUCTION

The recognition of human handwriting has been the subject of intensive research for more than three decades.

The principal motive for the development of recognition systems is the need to cope with the enormous flood of paper such as bank checks, commercial forms, postal address reading, etc.

Several high accuracy algorithms have recently been proposed for the recognition of handwritten numerals. Among the several techniques that have been proposed, the works of Shridhar et al. [1], Kimura et al. [2] and Lan et al. [3] should be mentioned.

The character segmentation algorithm used, separates the characters when there are blank spaces between them. The result of this segmentation may be isolated, overlapped and connected characters. After each segmentation between the characters, they are stored in a matrix (this matrix is named **original-matrix** in

this paper). Therefore, the **original-matrix** may have one, two or more characters at the same time, which may be isolated, overlapped and connected. Below we define these three types of characters:

Isolated Characters - characters in which the **original-matrix** is composed of only one character.

Overlapped Characters - characters with pixels-on (active pixel in one) in the same column, but apart. Therefore, the **original-matrix** may be composed of two or more characters depending on the way they are segmented.

Connected Characters - characters with pixels-on in common, i.e., one or more pixels belong to the two distinct characters, so the **original-matrix** may be composed of two or more characters depending on the way they are connected.

In this paper, the authors focused their attention on recognizing handwritten numerical characters, that are isolated or overlapped, which may be continuous or fragmented. The algorithm is presented considering intrinsic and common characteristics used by human beings. Then there are some comments about the data used to test the algorithm and the results obtained are shown. Finally, some conclusions concerning these results are presented.

2. DESCRIPTION OF THE ALGORITHM TO RECOGNIZE NUMERICAL HANDWRITTEN CHARACTERS ISOLATED AND OVERLAPPED

The main features utilized by the program to define each digit are:

Superior Horizontal Line

The superior horizontal line is obtained by the program scanning the bitmap from top-to-bottom and left-to-right until the first pixel-on is found. At this point the initial coordinate of the superior horizontal line is stored. This coordinate is denominated initial coordinate of the superior horizontal line (ICSHL). The ICSHL coordinate consists of: the row of the initial coordinate of the superior horizontal line (RICSHL) and the column of the initial coordinate of the superior horizontal line (CICSHL).

Handwritten numerals have various imperfections. As a result not all the pixels-on are in line on the superior horizontal, inferior horizontal or left vertical lines. With the intention of creating an algorithm with greater flexibility and in this way include the pixels-on that are not in line, variables were defined in the program to represent this flexibility. These variables are called "advantage-condition", "vertical-condition" and "horizontal-condition".

From the ICSHL coordinate a new pixel-on is searched for by the program to constitute the horizontal superior line. This pixel-on may be on the same row as the RICSHL or one row above or below, the pixel-on being one column to the right of the CICSHL (this condition will be referred to from now on as the first condition). In case the first condition is not verified then a pixel-on which may be in the directions 2 or 6 (i.e, being in the same column and one row above or below the pixel-on RICSHL) in accordance with the chain code of 8 directions [4] (this condition will be referred to from now on as the second condition). If the second condition occurs the program increases, by one unit, the "vertical-condition" variable. If this does not occur the program will increase by one the "advantage-condition" variable and move itself on the same row increasing the column by one. The process of searching for the pixels-on of the superior horizontal line repeats itself while the "vertical-condition" variable is less than 3 or the "advantage-condition" variable is less than 2. At the end of this search the final coordinate of the superior horizontal line denominated final coordinate of the superior horizontal line (FCSHL) is stored. The FCSHL coordinate consists of: the row of the final coordinate of the superior horizontal line (RFCSHL) and the column of the final coordinate of the superior horizontal line (CFCSHL). Figure 1 illustrates the superior horizontal line in two handwritten numbers.

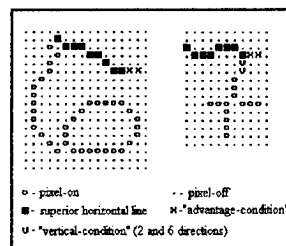


Figure 1- Superior horizontal line in two handwritten numbers.

Inferior Horizontal Line

The inferior horizontal line is obtained by the program scanning the bitmap from bottom-to-top and left-to-right until the first pixel-on is found. At this point the initial coordinate of the inferior horizontal line is stored. This coordinate is denominated initial coordinate of the inferior horizontal line (ICIHL). The ICIHL coordinate consists of: the row of the initial coordinate of the inferior horizontal line (RICIHL) and the column of the initial coordinate of the inferior horizontal line (CICIHL). From this point, the same process is utilized as in the superior horizontal line for the first condition. The only variation is the position of the RICIHL which may be on the same row or one row below or above. In the second condition the same process is repeated, therefore the first pixel-on should be searched for in direction 6 and then in direction 2, the rest of the process repeats itself. The final coordinate of the inferior horizontal line is denominated final coordinate of the inferior horizontal line (FCIHL). The FCIHL coordinate consists of: the row of the final coordinate of the inferior horizontal line (RFCIHL) and the column of the final coordinate of the inferior horizontal line (CFCIHL). Figure 2 illustrates the inferior horizontal line in two handwritten numbers.

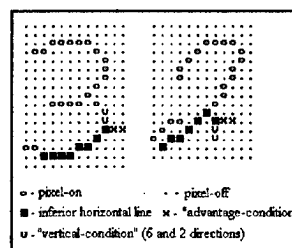


Figure 2 - Inferior horizontal line in two handwritten numbers.

Left Vertical Line

The left vertical line always begins at the ICSHL coordinate. From this point a new pixel-on of the left vertical line is searched for by the program and may

be in the same column of the pixel-on CICS HL or one column to the left or right, this pixel-on must be one row below RICS HL. When no neighbour is found, a pixel-on should be searched for which may be in the directions 4 or 0 (i.e., be on the same row and in the column before or in the next column of the pixel-on CICS HL) in accordance with the chain code. If this condition occurs the program will increase, by one unit, the "horizontal-condition" variable. If this does not occur the program will increase, by one unit, the "advantage-condition" variable and move itself in the same column increasing the line by one. The process to meet the pixels-on that constitute the left vertical line is repeated while the "horizontal-condition" variable is less than 3 or the "advantage-condition" variable is less than 1. When the "advantage-condition" variable is equal to 1 or the ICIHL coordinate is found, it is no longer necessary to scan the bitmap because the final coordinate of the left vertical line has been found. At the end of this search the final coordinate of the left vertical line (FCLVL) is stored. The FCLVL consists of: the row of the final coordinate of the left vertical line (RFCLVL) and the column of the final coordinate of the left vertical line (CFCLVL). Figure 3 illustrates the left vertical line in two handwritten numbers.

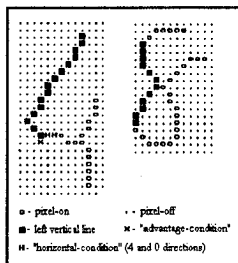


Figure 3 - Left vertical line in two handwritten numbers.

Elimination of the Comma and the Period

In the recognition of numerical characters of bank checks, the authors decided to eliminate the comma (,) and the period (.) between the numbers, since a lot of people do not use them when writing their checks and besides which the comma and period can be so small that the thinning algorithm for characters [5] considers them to be "noise". At times the comma may be of such a considerable size, that the thinning algorithm does not eliminate it. In this situation this algorithm is able to recognize it and eliminate it. In the program, the function which carries out the elimination of the comma is named comma-eliminator.

In order to recognize a handwritten numerical character of bank checks after obtaining its skeleton by the thinning algorithm, the program scans it to find the coordinates of the horizontal superior line (ICS HL and FCS HL); the coordinates of the inferior horizontal line (ICIHL and FCIHL) (this step will be referred to as STEP 1 from now on). The final coordinate of the left vertical line (FCLVL) will only be found after the comma-eliminator is executed. Later, the program performs STEP 1, executing the comma-eliminator function and then performing the following steps:

- If $(CFCSHL - CICS HL \leq 2)$ and if $(CFCIHL - CICIHL \neq 0)$ the function named verif-1-3-5-6-0 in the program is executed. The objective of this function is to recognize the digits 1, 3, 5, 6 and 0. Figure 4 illustrates some examples of numbers recognized by the function verif-1-3-5-6-0.

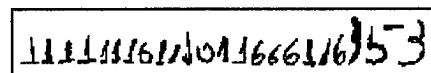


Figure 4 - Some examples of numbers recognized by the function verif-1-3-5-6-0.

- If the number is not recognized and if $(CICIHL \neq CFCIHL)$ and $(CICS HL \neq CFCSHL)$ and $((RFCLVL - RICIHL \leq 2)$ and $(CFCLVL - CICIHL \leq 2))$ or $(RFCLVL - RICIHL \leq 2)$ and $(CFCLVL - CFCIHL \leq 2))$ the function named verif-0-8-6-3-5-1-2 in the program is executed. The objective of this function is to recognize the digits 0, 8, 6, 3, 5, 1 and 2. Figure 5 illustrates some examples of numbers recognized by the function verif-0-8-6-3-5-1-2.

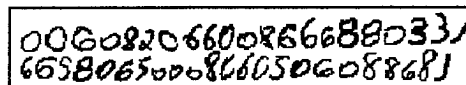


Figure 5 - Some examples of numbers recognized by the function verif-0-8-6-3-5-1-2.

- If the number is not recognized and $(CICS HL \neq CFCSHL)$ and $(CICIHL \neq CFCIHL)$, then the function named verif-2-3-5-7-9-8-0 in the program is executed. The objective of this function is to recognize the digits 2, 3, 5, 7, 9, 8 and 0. Figure 6 illustrates some examples of numbers recognized by the function verif-2-3-5-7-9-8-0.

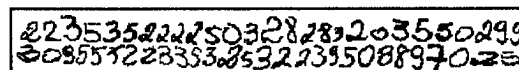


Figure 6 - Some examples of numbers recognized by the function verif-2-3-5-7-9-8-0.

- If the number is not recognized and ($CICSHL \neq CFCSHL$) and ($CFCIHL - CICIHL \leq 2$) the function named `verif-7-9-4-1-2` in the program is executed. The objective of this function is to recognize the digits 7, 9, 4, 1 and 2. Figure 7 illustrates some examples of numbers recognized by the function `verif-7-9-4-1-2`.

7779797797797777992711

Figure 7 - Some examples of numbers recognized by the function `verif-7-9-4-1-2`.

- If the number is not recognized and ($CFCSHL - CICSHL \leq 2$) and ($CFCIHL - CICIHL \leq 2$) the function named `verif-1-4-5-6-7` in the program is executed. The objective of this function is to recognize the digits 1, 4, 5, 6 and 7. Figure 8 illustrates some examples of numbers recognized by the function `verif-1-4-5-6-7`.

4411141144114411441144115566

Figure 8 - Some examples of numbers recognized by the function `verif-1-4-5-6-7`.

Should the number not be recognized by any of the mentioned functions, the program sends the message of nonrecognition.

Overlapped Characters Segmentation

To separate two or more overlapped characters, the program scans the whole character from the `ICIHL` coordinate (this step will be referred to as STEP 2 from now on). During this process, each pixel-on scanned is stored on a `new-matrix` and is deleted from the `original-matrix`. By the end of this procedure, the new matrix contains a copy of the scanned character. By scanning the whole character in STEP 2, the program verifies if the coordinates: `FICIHL`, `ICSHL` and `FCSHL`, found in the character, agree with the coordinates: `FICIHL`, `ICSHL` and `FCSHL` found in STEP 1. If this coincidence occurs, the algorithm recognizes the character contained in the `new-matrix` (this step will be referred to as STEP 3 from now on). If this coincidence does not occur, the program goes back to STEP 1 in order to find the coordinates of the superior and inferior horizontal lines of the character in the `new-matrix`. Then, STEP 3 is executed, in order to recognize the character. After recognizing the character, the program verifies if there are still pixels-on in the `original-matrix`. If so, it means that there are still one or more characters to

be recognized, so the algorithm carries out STEPS 1, 2 and 3 again. Figure 9 illustrates some overlapped numerals recognized by the algorithm explained above.

54 5300 0000 50 20 20 93 55 50 89 500 00
10 100 00 50 20 54 842 10 110 15 23 00

Figure 9 - Some overlapped numerals recognized by the algorithm explained above.

3. RESULTS OBTAINED

The algorithm was tested with over 820 handwritten numbers obtained from 164 checks written by 41 different people. They were asked to write random numerical characters on 4 checks. This algorithm was unable to deal with connected numbers. The check was simulated using white paper. 819 out of the 820 numbers handwritten were recognized successfully and one was recognized incorrectly. Results showed a recognition rate of 99.88%.

4. CONCLUSIONS

The results obtained showed that the algorithm utilized for the recognition of isolated or overlapped handwritten numerical characters presented an excellent recognition rate.

5. REFERENCES

- [1] - M. Shridhar and A. Badreldin, Recognition of isolated and simply connected handwritten numerals, *Pattern Recognition* 19, pp. 1-12, January 1986.
- [2] L. Lam and C. Y. Suen, Structural classification and relaxation matching of totally unconstrained handwritten Zip-code numbers, *Pattern Recognition* 21, pp. 19-31, January 1988
- [3] - S. N. Srihari, E. Cohen, J. J. Hull and L. Kuan, A system to locate and recognize ZIP codes in handwritten addresses, *IJRE* 1, pp. 37-45, January 1989.
- [4] - A. K. Jain, *Fundamentals of Digital Image Processing*. New York: Prentice Hall, Inc., USA., 1989, ch. 6, pp. 363.
- [5] - E. L. Flôres, E. N. Rezende, G. A. Carrijo and J. B. T. Yabu-uti, A fast thinning algorithm for characters, in *Proceedings of the Conference 1995 IEEE Workshop on Nonlinear Signal and Image Processing*, Neos Marmaras, Halkidiki, Greece, June, 1995, pp. 166-169.

NEURAL SYSTEM FOR TRACKING AND CLASSIFICATION OF PRIMARY RADAR ECHO SIGNALS

S. Cuomo, P.F.Pellegrini, E. Piazza

Dipartimento di Ingegneria Elettronica, University of Florence

Via di S.Marta 3 - 50139 Florence, Italy

phone: +39-55-4796267; fax: +39-55-494569

e-mail: labtel@ingfi1.ing.unifi.it

Abstract

This work presents a system designed to acquire primary echo radar from aircrafts and to operate a classification based upon spectral consideration on the retrieved echo. Fine spectral consideration are carried out exploiting the Jet Engine Modulation (JEM) phenomenon due to the modulation on the primary echo introduced by engines rotating parts. Classification efforts are obtained by the use of a Neural Network previously trained, put on the system as classification sub system.

Target parameters are investigated analyzing effective signals obtained by two operating radars with an experimental system specifically designed for real time tracking of civilian aircrafts using an acquisition sub-system, PC based, interfaced with the radar circuitry.

1. Introduction

Nowadays, because of the ever-growing number of aircraft in the areas to be controlled, the raising demand for security of passengers and cargoes and the greater care about the environment, the problem of improving the performances of traditional Airport Control systems must be faced. Research trend in future years is oriented towards the development of integrated systems, which collect information coming from various sensors, and distribute it both to ground air-traffic controllers and to moving vehicles. The realisation of a system for the automatic control of air space with non co-operative target recognition (NCTR) capability can play an important role in this context.

The automatic extraction in real time of the target features suitable to fulfil the requirements stated above can be carried out through innovative approaches to the processing of radar data based on neural network processing techniques.

It is well known that the rotating parts of aircraft engines introduce modulation on the aircraft echo

spectral response. With reference to jet powered aircraft these phenomena are known, in related literature, as Jet Engine Modulation (JEM) [1].

It has been observed that such phenomena are deterministic and supply a considerable contribution to the total energetic content of the signal and it is reasonable to think that these ones, being related to the particular couple "engine - aircraft body" may be regarded as a signature that may be used for a classification of the targets [2].

2. Experimental Measurements

In order to acquire real data, a flexible registration tool has been assembled. At each scan it samples, with a high data rate, the in-phase and quadrature components of the base-band signal in prefixed window of the radar sky and transfer it from the internal buffer into a mass storage for off-line analysis [2].

This tool has been designed with a particular consideration for aspects of portability and adaptivity to various radar systems. It is based upon a PC structure and a fast A/D converter which is able to acquire I, Q video channels (see Fig. 1).

Measurement campaigns were carried out at Fiumicino Airport in Rome and at Linate Airport in Milan (Italy). In Tab. 1 some of the parameters of the two radars involved in the experimental setup are reported.

Name	ATCR-33K	ATCR-44K
Location	Fiumicino	Linate
Frequency	2.76 GHz	1.27 GHz
Rotation speed	15 RPM	6 RPM
Beam Width	1.5 deg	1.2 deg
Pulse length	1 μ s	1.5 μ s
PRF (Average)	1000 Hz	446 Hz
Sweep on Target	17 Sweeps	15 Sweeps

Table 1 - Radar parameters

Results reported here are mainly concerned with

the S band radar [3], as the L band radar campaign was only recently performed and data analysis is still in progress. As previously pointed out, various types of aircraft in different operative conditions have been recorded. In the analysis of spectral response, the recordings have been mainly considered in Stagger OFF conditions in order to perform a sampling at the same time intervals.

In this work mainly are taken into account analysis of commercial aircrafts with turbojet engines and especially MD80, DC9, B747 types for which, by courtesy of Alitalia Airlines, it has been possible to obtain auxiliary information concerning constitutive and operative data.

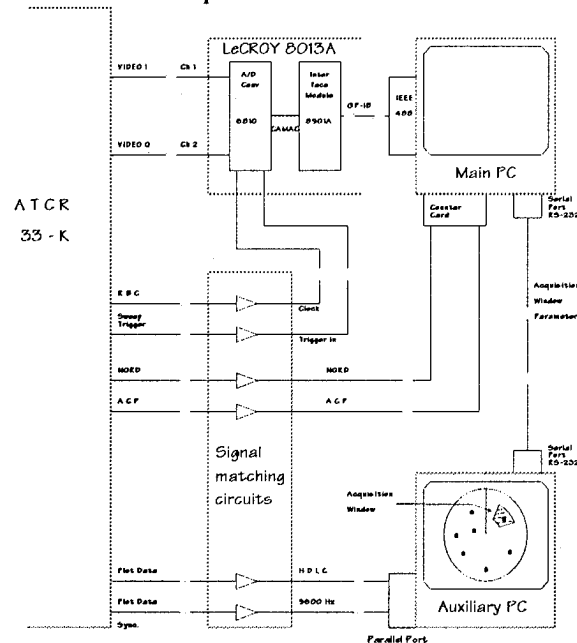


Fig. 1 - Recording tool as it result when connected to the ATCR-33K radar system

Few words about the recording procedure are useful. Once the target has been designated, automatically the recording equipment, using the information coming from the tracking PC, centers the window on the aircraft estimated position and records the I and Q signals belonging to the window. The process of centering the window and recording is repeated at any antenna turn, until the operator stops it. A number of auxiliary informations about the setting of the recording equipment and environment is recorded with raw data.

3. Spectral Analysis of ATC Radar echoes

In the case of JET-powered aircraft the rotating

blades of fan and turbines are internal to the engine ducts and thus the visibility depends on the aspect angle, while in turboprop-powered aircraft the rotating blades are always exposed. In either case the spectral signature is controlled - in addition to the RCS - by the dimensions, geometry, number of the rotating blades and by the rotation speed [1][3]. The phenomena called Jet Engine Modulations (JEM), have a general validity and they can be observed in a very large majority of measurement, at least for the S-band systems which where mainly considered. In any case, the characteristics of the ATC radar give rise to some problems for a correct interpretation of information present in the spectral response. In particular, the low PRF (about 1 KHz) typical of ATC systems, strongly limits the unambiguous band of the spectrum and cause aliasing effects which are present both for main Doppler line and for the JEM lines. Moreover a dwell time (related to the antenna main lobe) of few tens of milliseconds cause a poor spectral resolution.

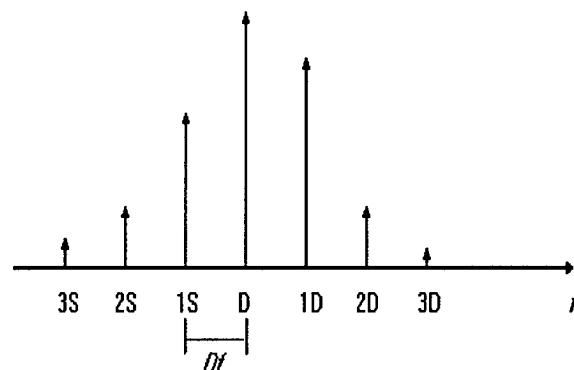


Fig. 2 - Theoretical spectrum showing the main Doppler line and side JEM lines

4. The NCTR problem

The problem of Non-Cooperative Target Recognition (NCTR) is not elementary. A lot of effort is spent trying to achieve NCTR with various types of sensors.

The problem to recognize a target with radar depends basically on which target characteristics to rely on. Some important target characteristics are: Radar Cross Section (RCS); target velocity; target fluctuation; dominant scatterers; Doppler spectrum. Probably a combination criteria based on a number of different characteristics will form a reliable method for target identification.

To carry out a kind of automatic classification some parameters characterizing the signal are needed. Particularly those parameters that they are invariant with respect to a number of variables characterizing the target and the sight geometry [4]. For example they can be invariant with respect to the position, speed or aspect angle of the target, or with respect to the type of the aircraft revealed or with respect to its engines[2].

The application of neural networks in signal classification has been receiving increased attention. Neural Network classifiers have shown, in a number of occasions [5], superior performance than other types of classifiers.

One of the most popular and well understood neural network paradigms is the multilayer network trained with the back propagation algorithm, specially in recognition/classification problems [6].

A multilayer neural network is a feed-forward network consisting of some layer of processing nodes called neurons (see Fig. 3) or adalines. Each neuron receives its inputs from the previous layer neurons output and put its output to all the neurons of the successive layer. The first layer is the input layer which receive input from external inputs, the last layer is the output layer which put its output to the external output and the intermediate layers are called hidden layers.

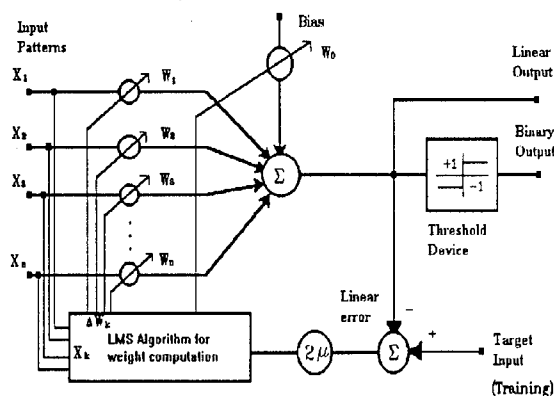


Fig. 3 - Single adaptive linear element (adaline) called neuron.

Although it has been demonstrated that only one hidden layer can realize any non linear mapping, two hidden layers can reduce the dimensions of the network and speed up the training process [6] [7]. Usually the input layer has as many neurons as available data for each record to classify, for instance signal samples of a signal, and the output layer has as many neurons as target classes. The neuron weights are automatically calculated by

the training algorithm. Once trained the network should be able to produce appropriate responses when presented with input vectors it has not seen before

When learning takes place, the actual output vector is compared to the desired output vector and the error between the two vectors is calculated and propagated back to the hidden and input layers to change the weights values in order to minimize the mean squared error.

This kind of learning is called training with supervision and requires a set of training inputs of which the expected output are known and called target output [6].

In this work, Neural Networks have been used to distinguish radar signals from 5 models of commercial aircrafts. Some preprocessing has been carried out on the raw signal to extract the pattern sets to be put into the network inputs. Five kinds of patterns have been tested:

- a) complex samples of the raw ATC signal;
- b) complex sample of the signal's spectrum;
- c) real samples of the spectrum amplitude;
- d) complex samples of the raw ATC signal and kinematic data;
- e) complex samples of the spectrum and kinematic data.

The raw ATC signal is made by 32 complex samples, taken with the sampling frequency of the radar, PRF, that is 1 KHz.

Two different networks have been tested, the first with only one hidden layer and the second with two hidden layers.

The whole set of recorded signal includes 164 records of turboprop powered aircraft and 23 records of turboprop aircrafts (see Tab. 2.)

Aircraft	Available	Training
DC9	76	12
MD80	66	12
B747	22	5
ATR42	18	5
C130	5	3

Tab. 2. - Available data set. and Training set composition.

The training set was made by choosing randomly a proportional number of records for each class. The composition of the training set is shown in Tab.2. The training set was the same for every test carried out. The test set was the whole set of available data, despite of the theory says to purge the training set from the test set.

For the software simulation has been used the program PDP Software included in the book "Exploration in parallel distributed processing" [8]. This software allow to simulate several neural network including Back Propagation networks and is available on both MSDOS and UNIX systems. The two network simulated are summarized in Tab. 4.

The classification is made on the basis of networks output. The PDP software produce outputs in the interval 0-1. If just an output is greater than 0.5, the record is assigned to that output class, if none or more than one output is greater than 0.5, the record is not classified.

Parameter	Net 1	Net 2
layers	3	4
1st hidden layer neurons	16	32
2nd hidden layer neurons	-	16
Total number of neurons	85	134
Number of weights	1104	2640

Tab. 4. - Parameters summary of the two used networks.

As was expected, the second network has achieved better result but with a much larger computational time, mainly in the training phase, while the classification time is almost the same.

	DC9	MD80	B747	AT42	C130	N.C.
DC9	57	14	5	4	0	20
MD80	26	42	5	11	2	15
B747	36	27	22	5	0	9
AT42	17	6	0	67	0	11
C130	0	0	0	40	60	0

Tab. 5. - Aircraft classification result for pattern e), Net 2, values in %. N.C. standing for Not Classified.

	a)	b)	c)	d)	e)
DC9	55	43	34	43	57
MD80	42	48	38	35	42
B747	22	22	27	23	22
AT42	11	33	39	33	67
C130	0	60	60	60	60
Average	41	42	36	37	51

Tab. 6. - Probability of aircraft correct classification versus the parameters taken into account. The network is the 2nd. Values in %

The best classification result was given by the

patterns a) and e), which represent the complex samples of the raw signal. An example of classification result is if Tab. 5. A global result, shown in Tab. 6. is the probability of correct classification.

The misclassification between DC9 and MD80 have to be remarked because that aircrafts have a very similar fuselage body and differ only for engines. Maybe the network uses information about the target RCS.

It is evident that the use of ancillary data or target features improve the classification performance. See the difference between pattern b) and e) results. These first results suggest that, with a further sophisticated system, a major increase in the capabilities of future radar systems could be developed.

References

- [1] Bell M.R., Grubbs R.A., "JEM Modelling and Measurement for Radar Target Identification", IEEE Transaction on Aerospace and Electronic Systems, Vol. 29, No. 1, p. 73, Jan. 1993
- [2] Pardini S., Pellegrini P.F., Piccini P., "Use of target spectrum for detection enhancement and identification", AGARD Conference proceedings 501, Ottawa, Canada, 1991
- [3] Pellegrini P.F., Cuomo S., Pardini S., "Radar Signal Analysis Oriented to Target Characterization applied to civilian ATC Radar", IEE RADAR92 Conference proceedings 365, p.438, Brighton, England, Oct. 1992
- [4] Le Chevalier F., "Principes de Traitement des Signaux Radar et Sonar", Masson, Paris, 1989
- [5] Nandagopal D., Johnson R.P., Martin N.M., Wright A.C., "Radar Target Recognition using Multilayer Back Propagation Neural Network (MLBPN)", IEE RADAR92 Conference proceedings 365, p.422, Brighton, England, Oct. 1992
- [6] Widrow B., Lehr M.A., "30 Years of Adaptive Neural Networks: Perceptron, Madaline, and Back propagation", IEEE Proceedings., Vol. 78, no. 9, 1990
- [7] Martinez Madrid J.J., Casar Corredera J.R., de Miguel Vela G., "A Neural Network Approach to Doppler based Target Classification", IEE RADAR92 Conference proceedings 365, p.450, Brighton, England, Oct. 1992
- [8] McClellan J.L., Rumelhart D.E., "Exploration in parallel distributed processing", The MIT Press, Cambridge, Massachusetts, 1987

Investigation of 1.3 μ m Pr-ion doped optical fiber amplifier for CATV subscriber network

Jieyuan Cao

The State Key Laboratory of Optical Fiber Local Communication Networks,
Shanghai Jiaotong University,
Shanghai, 200052, China
Fax: 0086-21-4330892

ABSTRACT

The application of 1.3 μ m Pr ion doped optical fiber amplifier (PDFA) for CATV subscriber network is reviewed. Design consideration and theoretical analysis of PDFA is conducted. Based on interaction between photon and electric field along the fiber, the numerical calculation of signal gain, effective fiber length and pump optimization are also made.

1. INTRODUCTION

Optical fiber CATV subscriber networks have been rapidly developed recently in China. Compared to coaxial cable transmission, optical fiber has evident advantages, such as extreme low loss and wide frequency band, therefore it saves cascade electrical amplifiers with equalizers which will accumulate noise, signal frequency nonlinear distortion over transmission line and improves system reliability. Optical CATV network will gradually become multi-media terminal network with development of people's needs to integrated service communication, data, computer, video and voice etc.

Generally speaking, the transform of coaxial cable to optical fiber CATV network in China will experience the following four steps:

Super-trunk architecture of optical cable for master headend to remote headend or sub-headend.

Fiber optic backbone trunk from sub-headend to feeder or node.

Fiber to the feeder through optical star radiation.

Fiber to the home (FTTH), a future CATV transmission style.

Among the architecture of fiber CATV network, passive optical network (PON) is an attractive and important one to realize the goal of FTTH. It is evident that PON shows low system cost, high stability and promise the further developing trends. There are two kinds of typical construction in PON distribution scheme, star-shape and tree shape. The former arranges the optical splitter near to the central TV station. The latter uses trunk optical cable to optical distribution network. In order to extending transmission distance and enlarging number of subscribers, applying in-line optical fiber amplifier into PON is an effective way as shown in Fig. 1.

Generally, light source for optical fiber CATV system may use 1310nm DFB-LD, 1550nm DFB-LD and solid state YAG Laser with external modulation. It is clear that the wavelength at which optical signal is amplified should be accordance with that of light source of optical CATV system. Although 1550nm is the communication window of low loss of single mode optical fiber and 1550nm Er ion doped optical fiber amplifiers have been used to practical optical systems, 1550nm LD in CATV will bring in the second term distortion resulted from frequency chirp during broadband modulation process. YAG laser and external modulator have characteristics of strong power and low noise, however, it needs complicated linear compensation technology to overcome the third term distortion. At the same time YAG laser with narrow line-width will produce stimulated Brillouin scattering and that will limit the injected optical power to optical fiber backbone.

Evidently, 1310nm DFB laser is most suitable to optical CATV because of its low cost, weak noise, mature technology and high reliability. At present Pr-ion doped fiber amplifier (PDFA)

which operated at wavelength of 1300nm with signal gain of 30dB has been reported. The result reveals that PDFA will be the best candidate to compensate splitting loss in passive optical fiber CATV systems.

2. THEORETICAL MODEL AND CALCULATION OF PDFA

2.1 Theoretical model

PDFA consists of a segment of Pr ion doped fluoride glass fiber, a pump laser operating at wavelength of 800nm or 1016nm, a WDM coupler for combining 1300nm optical signal and pump light and an isolator to prevent return light into light source. The typical construction of PDFA and the energy level diagram of Pr ion are shown in Fig. 2. The model of the four level transition of Pr ion for 1300nm amplification is denoted in the figure. Pump photon ground state absorption occurs between E_0 and E_3 energy level with pumping efficiency of W_p . Then Pr ions transfer swiftly to E_2 level without emission and some of them return to E_0 level spontaneously with spontaneous radiation probability A_{30} ($A_{30} \ll S_{32}$). The population inversion is formed and stimulated emission and amplification is realized between upper laser level E_2 and down level E_1 at emission rate of W_{21} . τ_{21} is lifetime of the stimulated ions. During above process, ions of E_2 level can also be absorbed to the higher level E_4 by excited state absorption (ESA) and transit to the lower level by the amplified spontaneous emission (ASE). These reduce the pump efficiency. The rate equation of ion population density are given by the following:

$$\frac{dn_0(r, \varphi, z)}{dt} = -(W_p + W_{gsa})n_0 + S_{10}n_1 + W_{sa}n_2 + A_{30}n_3$$

$$\frac{dn_1(r, \varphi, z)}{dt} = -S_{10}n_1 + (W_{sa} + W_{21} + 1/\tau_{21})n_2$$

$$\frac{dn_2(r, \varphi, z)}{dt} = W_{gsa}n_0 - (W_{sa} + W_{21} + W_{sa} + 1/\tau_{21})n_2 + S_{32}n_3$$

$$\frac{dn_3(r, \varphi, z)}{dt} = W_p n_0 - (A_{30} + S_{32})n_3$$

According to interaction between atoms and electric field, the basic equation of space distribution for light intensity in a fiber can be written as:

$$I(r, \varphi, z, \gamma) = p(z) |E(r, \varphi, \gamma)|^2$$

E is the normalized transverse distribution of electric field for definite LP mode in the fiber.

Thus, the power propagation equation along the fiber for pump and signal can be written as:

$$\frac{dP_p^+(z)}{dz} = \pm g_p(z)P_p^+(z)$$

$$g_p(z) = \sigma_{03} \int_0^{2\pi} \int_0^b |E(r, \varphi, \gamma_p)|^2 n_0(r, \varphi, z) r dr d\varphi$$

$$\frac{dP_s^+(z)}{dz} = \pm g_s(z)P_s^+(z)$$

$$g_s(z) = (\sigma_{21}(\gamma_s) - \sigma_{24}(\gamma_s)) \int_0^{2\pi} \int_0^b |E(r, \varphi, \gamma_s)|^2 n_2(r, \varphi, z) r dr d\varphi$$

where $P_p(z)$ and $P_s(z)$ are light intensity for pump and signal respectively, $g_p(z)$ is absorbance of pump light and $g_s(z)$ is gain coefficient of signal light. b is doping diameter of the ion in the fiber. \pm denotes the direction of $+z$ and $-z$ respectively. σ_{ij} is cross-section area between i and j level that denotes photon absorption or emission probability.

2.2 Numerical calculation of the gain

According to the above theoretical model the numerical calculation of gain can be made. Fig. 3 is the relation between signal gain and pump power. The wavelength of pump and signal are 1017 nm and 1300 nm respectively. The core diameter of the Pr ion doped fiber is 5 μ m. The numerical aperture is 0.19. Pr ion concentration is 500ppm. The gain of 0.025dB/mw can be obtained for fiber length of 23 m. The calculation results is in accordance with experimental results of ref. 9. Fig. 4 is the calculation results of the gain for different fiber length at the same pump power of 200 mw. The calculation shows that the signal power no longer increase while fiber length being 20 m. So the length of 20 m can be treated as effective fiber length.

The effect of pump operation on gain of in-line PDFA is also evaluated by the above theoretical model. Fig. 5 shows signal gain of PDFA at different power intensity distribution of fundamental mode of LP_{01} for pump. The 100% LP_{01} denotes pump power propagates completely in fundamental mode. The 0% LP_{01} denotes it propagates in higher order modes. Fig. 6 is a comparison between uni- and bi-direction pumping scheme. The results shows gain improvements can be obtained under bi-direction pumping scheme. This is because ESA of ($^1G_4 - ^3P_0$) for pump photon and co-operation upconversion of ($^1G_4 - ^1D_2$) - ($^1G_4 - ^3H_5$) for signal photon are suppressed. This results in an increase of population on G_4 energy level.

3. POTENTIAL APPLICATION SCHEME OF PDFA FOR FTTH

Optical fiber CATV network are rapidly developing in China and may be predicated that they will transit to FTTH by using new technology and facilities. An effective way to compensate splitting loss is use of PDFA which operates at the same light wavelength of 1300 nm in current fiber CATV systems as shown in Fig. 7.

4. SUMMARY

To increase the numbers of subscriber for current optical fiber CATV network and realize future FTTH in China. The application of in-line PDFA is an effective way to compensate splitting insertion loss. The design consideration and theoretical calculation of PDFA have been made in this paper. The calculation results denoted that the pumping efficiency of 0.025dB/mw can be obtained for fiber length of 20 m, NA of 0.19 and Pr doping concentration of 500 ppm. The theoretical analysis on pumping scheme confirmed that bi-direction pump is superior to uni-direction pump for improving signal gain.

REFERENCES

[1]F. Marcerou, H. A. Fevrier, J. Famos "General theoretical approach describing the complete behavior of the erbium-

doped fiber amplifier" SPIE Vol. 1373 PP168-186

[2]B. Pedersen et al. "Optimization of Pr^{3+} ZBLAN fiber amplifier" Photon Tech Lett. Vol. 4 No. 5 May 1992

[3]S. P. Bastien et al. "Theoretical modeling of erbium-doped amplifier pumped by the 800 nm band" SPIE Vol. 1587, Fiber Laser Source and Amplifiers II 1991.

[4]B. Pedersen et al. "The design of erbium doped fiber amplifier" J. L. T. Vol. 9 No. 9 Sept. 1991 PP1105-1112

[5]A. Biarklev et al. "Large signal modelling of an Erbium doped fiber amplifier" SPIE Vol. 1171 Fiber laser source and amplifiers (1988) PP118-129

[6]Yasutake chishi et al "A high gain, high output saturation power Pr^{3+} doped fluoride fiber amplifiers" IEEE Photon Tech Lett. Vol. 6 No. 2 1994 PP195-198

[7]Yasulake Chishi et al. "Investigation of efficient pump scheme for Pr^{3+} doped fluoride fiber amplifiers" IEEE Photon Tech Lett. Vol. 6 No. 2 1994 PP195-198

[8]Whitley et al. "Towards a practical 1.3 μm optical fiber amplifier" B. T. Tech. J 1993 No. 2 P115

[9]Cakter. S. F. Szebesta "Amplification at 1.3 μm in Pr^{3+} doped single-mode fluorozirconate fiber" Electron Lett 1991 27 PP 628-629

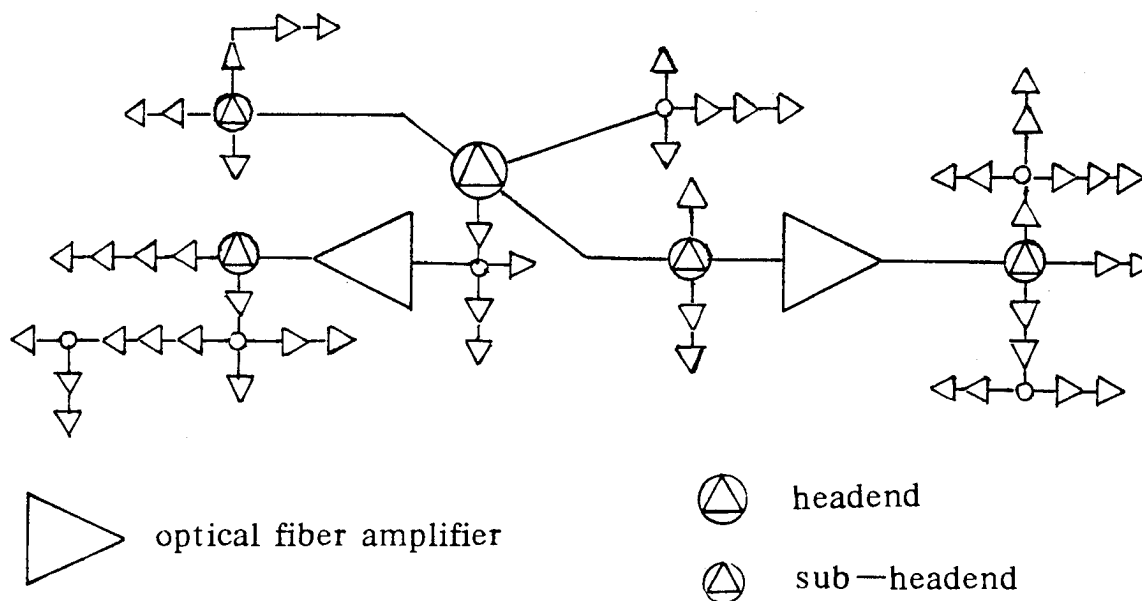


Fig. 1 Fiber optic backbone trunk with PDFA

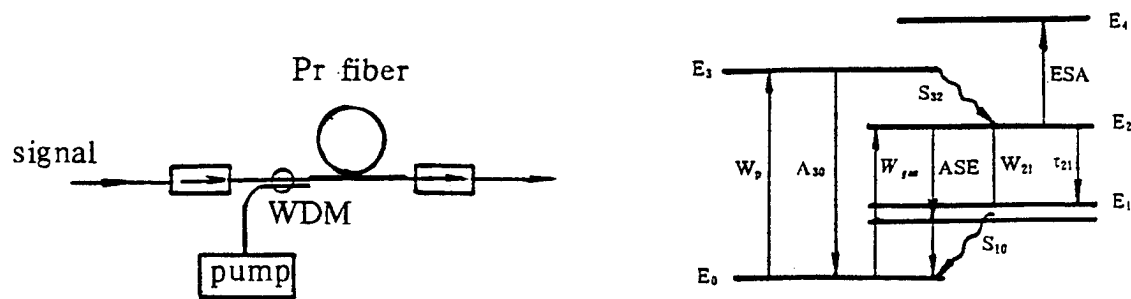


Fig. 2 Construction and principles of PDFA

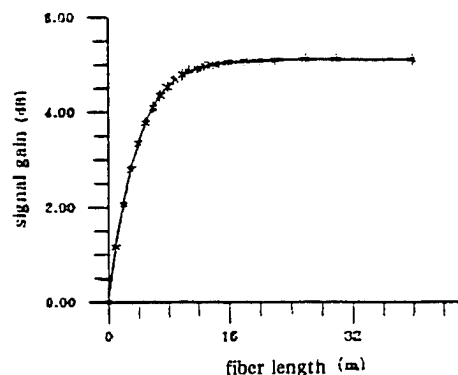
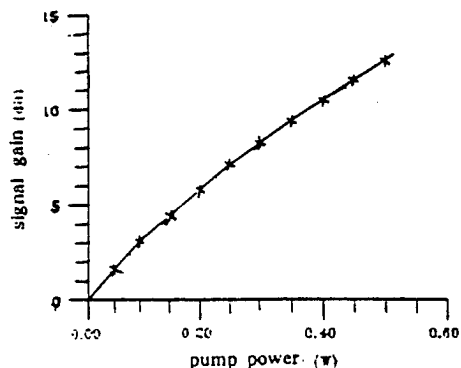


Fig. 3 Signal gain versus pump power Fig. 4 Signal gain at different length

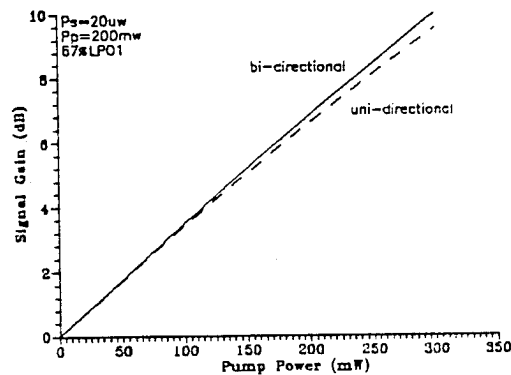
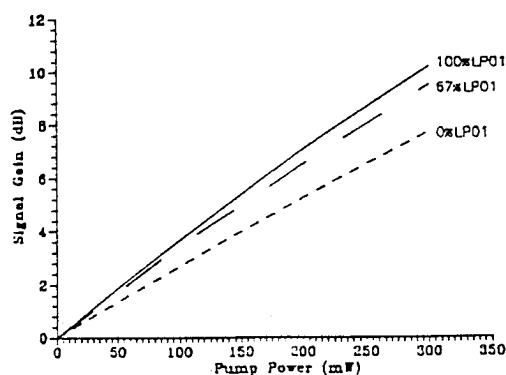


Fig. 5 The effect of power distribution of LP_{01} mode on signal gain Fig. 6 The comparison of gain between uni- and bi-direction pump scheme.

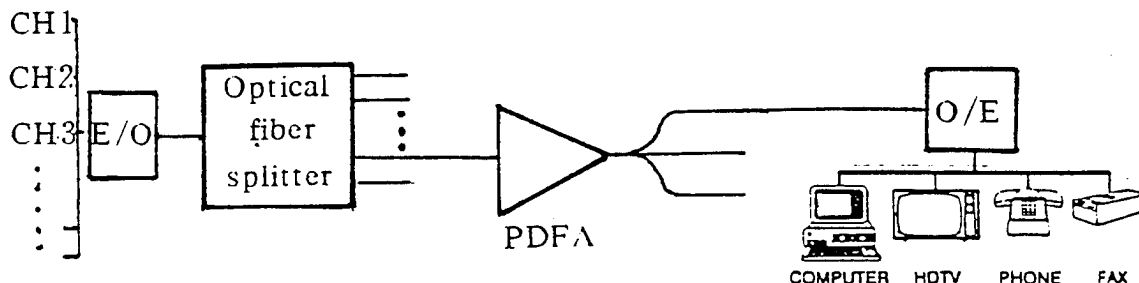


Fig. 7 The integrated service subscriber loop with PDFA

MODELLING OF SUB-SHOT NOISE OPTOCOUPERS USING RELATIVE NOISE DIFFERENCE

W. N. Cheung, P. J. Edwards and T. Zhang

Advanced Telecommunications Research Centre
Faculty of Information Sciences & Engineering
University of Canberra, PO Box 1, Belconnen, ACT 2616, Australia
wnc@ise.canberra.edu.au

ABSTRACT

From sub-shot noise photonic measurements in optocouplers we obtain the frequency characteristics of quantum noise reduction using the relative noise difference method. We have shown that the RND method enables us to remove the dependence of noise measurements on the noise and frequency response of the instrumentation amplifier. We have also attempted to derive the same frequency characteristics using a circuit-based model incorporating photonic noise sources. There is good agreement between measurement and modelling, hence lending experimental support to the use of the photonic noise model to other sub-shot noise optocoupler structures.

1. INTRODUCTION

Conventionally, the small-signal behaviour of an LED is modelled in the same way as for a semiconductor rectifier by a parallel RC circuit and its noise characteristics is determined by a shot noise current source connected in parallel with the RC circuit. While this representation is commonly used for describing the electrical behaviour of the device, it has been found inappropriate when dealing with photonic noise behaviour in an optocoupler. It is shown in this paper that the series equivalent noise voltage proposed by Edwards[1] yields results which agree with experimental observations whereas the parallel current source does not.

2. MODULATION RESPONSE

Consider the optocoupler as shown in Fig. 1. It is assumed that all photons generated by the LED are collected by the ideal photo detector and the amount of photo current generated at the detector is equal to the current responsible for generating the photons at the LED. Since electrons and holes are injected in

pairs and recombine in pairs in the LED, it is enough to consider the rate equation for only one type of charge carriers. Let $N=N_b+n$ and $I=I_b+i$, where N_b and I_b are the mean values, and n and i are the small signal quantities of the carrier number and junction modulation current, respectively. Since the mean rate of change of the carrier number is zero, the rate equation describing the excess charge number is given by [2]

$$\frac{dn}{dt} = \frac{i}{q} - \frac{n}{\tau_c} \quad (1)$$

where q is the electronic charge, and τ_c is the recombination time constant. Taking Laplace transform of eq. (1) and rearranging terms give the following:

$$\frac{qn(s)}{\tau_c} = \frac{i(s)}{1+s\tau_c} \quad (2)$$

Clearly the left-hand side of eq. (2) indicates that it is a measure of the rate of carrier recombination. If we assume that the quantum efficiency is 100% so that recombination is entirely radiative, then the right-hand side of (2), denoted by $I_p(s)$, may be regarded as the photon generating current. Also, eq. (2) expresses the frequency response of the device relating the photon current $I_p(s)$ to the modulation $i(s)$. We note that the frequency response is identical to that of a single-pole parallel RC circuit and the photon current is represented by the current through the resistance of the equivalent circuit. The modulation bandwidth is evidently given by $1/(2\pi\tau_c)$.

The current input to the device, i , is dependent on the modulating voltage v_m , the source impedance Z_s , and the electrical characteristic of the device. From junction diode theory, we note that the differential resistance for small signals at low frequencies is given by $R_d = \mu V_T / I_b$, where μ is the ideality factor,

V_T is the thermal voltage and I_b the bias current. We then arrive at the commonly used equivalent circuit of the LED as shown in Fig. 2 (omitting the noise for the moment), where C_j is given by τ_c/R_d which represents the storage capacitance of the junction. Any parasitic series inductance and resistance of the LED may be lumped with Z_s .

3. SHOT NOISE CURRENT

We have shown above that, for the modulation signal, photons are directly related to the current component through the junction resistance R_d . If we now follow convention to add a parallel noise current i_s as shown in Fig. 2(a), we would find ourselves in the dilemma that when the device is externally AC shorted (ie, $Z_s=0$), the shot noise current does not flow through the junction resistance, hence implying the absence of photonic noise. This is of course contrary to the fact that we should obtain full shot-noise in the photon intensity. This difficulty is apparently removed if we represent the shot noise by a voltage source, $v_s = i_s R_d$, in series with R_d as shown in Fig. 2(b). When the device is now AC shorted, we obtain the full shot-noise as can be verified in practice. Although one can transform the parallel combination of i_s and R_d into the series connection of v_s and R_d using Thevenin's Theorem, their equivalence holds only as far as any current or voltage external to the two equivalent circuits is concerned. Hence any external electrical measurement on the LED will not show the internal difference between the two equivalent circuits. However, the currents through the internal source resistance need not be the same in the two circuits. This apparent ambiguity can be resolved by measuring the photon number fluctuations generated by the currents through the differential resistance as we have done in the optocoupler.

At room temperature, the quantum efficiency of a practical optocoupler is usually much lower than unity so that the detector noise consists of two components, namely, the transmitted shot noise and the partition noise which is due to photon number deletion. That is, the detector noise spectral density is given by [3]:

$$\langle i_{no}^2 \rangle = \eta^2 \langle i_n^2 \rangle + \eta(1-\eta)2qI_b \quad (3)$$

where η is the transfer efficiency, q is the electronic charge, I_b the LED bias current, and $2qI_b = \langle i_s^2 \rangle$ is the mean square shot noise current spectral density. The partition noise is frequency independent. The transmitted noise, $\eta^2 \langle i_n^2 \rangle$, on the other hand, is

indicative of the process between photonic noise and the electronic shot noise current in the LED. Using the series equivalent circuit of Fig. 2(b) and with Z_s very large, $\langle i_n^2 \rangle$ can be expressed as

$$\begin{aligned} \langle i_n^2 \rangle &= \frac{[\langle v_s^2 \rangle / R_d^2](\omega\tau_c)^2}{1 + (\omega\tau_c)^2} \\ &= \frac{\langle i_s^2 \rangle (\omega\tau_c)^2}{1 + (\omega\tau_c)^2} \end{aligned} \quad (4)$$

Putting (4) into (3) yields the output noise relative to shot noise:

$$\frac{\langle i_{no}^2 \rangle}{\langle i_s^2 \rangle} = \frac{\eta^2 (\omega\tau_c)^2}{1 + (\omega\tau_c)^2} + \eta(1-\eta) \quad (5)$$

At low frequencies, the transmitted noise is very small and the output noise is said to be squeezed to below the shot noise level. The squeezing bandwidth can be defined as the frequency at which the output noise of the optocoupler is 3 dB below the shot noise level which appears at high frequencies. This frequency can be obtained from the first term of (5) and is given by $1/(2\pi\tau_c)$, which is the same as the modulation bandwidth. In practice, however, because of low quantum efficiency, the second term of (5) is quite large so that the total amount of squeezing is very small at room temperatures. One way to increase quantum efficiency is to work with the system at low temperatures.

4. PHOTONIC NOISE MEASUREMENTS

By cooling an optocoupler consisting of an IRED and high efficiency PIN diode detector we obtain quantum transfer efficiencies about 30% so that the output noise is not swamped by partition noise. Typical measurement results obtained at a temperature of 150 K and for different bias currents are as shown in Fig. 3. We consider the case for $I_b=2$ mA. Curve (a), denoted by $A(\omega)$, is obtained by illuminating the detector with Poissonian light having a constant intensity noise spectral density over the frequency range of measurement. The roll-off at high frequencies is due to the characteristics of the instrumentation amplifier response $G_a(\omega)$. Curve (b) gives the detector noise when the LED is used as the light source, and we represent it by $B(\omega)$. Both curves include a noise component, $\langle i_a^2 \rangle$, due to the

instrumentation amplifier. Thus the functions $A(\omega)$ and $B(\omega)$ may be expressed as follows:

$$[\langle i_{sn}^2 \rangle + \langle i_a^2 \rangle]G_a(\omega) = A(\omega) \quad (6)$$

$$[\langle i_{no}^2 \rangle + \langle i_a^2 \rangle]G_a(\omega) = B(\omega) \quad (7)$$

Taking the difference between (6) and (7) removes the amplifier noise and yields

$$[\langle i_{sn}^2 \rangle - \langle i_{no}^2 \rangle]G_a(\omega) = A(\omega) - B(\omega) \quad (8)$$

At very high frequencies, the detector noise reaches the shot noise level and from (3) and (4) we have $\langle i_{sn}^2 \rangle = \eta \langle i_s^2 \rangle$. Therefore eq. (8) simplifies to

$$\frac{\eta^2 \langle i_s^2 \rangle G_a(\omega)}{1 + (\omega\tau_c)^2} = A(\omega) - B(\omega) \quad (9)$$

Since $A(\omega)$ is proportional to the amplifier gain, or, $G_a(\omega) = K A(\omega)$, we may rewrite (9) as

$$\frac{\eta^2 \langle i_s^2 \rangle K}{1 + (\omega\tau_c)^2} = 1 - B(\omega)/A(\omega) \quad (10)$$

The right-hand side is referred to as the relative noise difference (RND). If the circuit model of Fig. 2(b) is correct, the RND characteristics should provide us with information regarding the squeezing bandwidth $1/(2\pi\tau_c)$. It is of interest to note that the squeezing bandwidth can also be thought of as the half-power point of the relative noise difference, as implied by (10).

Since both $A(\omega)$ and $B(\omega)$ are spectral plots in dBm, their ratio $B(\omega)/A(\omega)$ can be obtained from their dB difference and then linearised before the RND is obtained. A typical plot of the RND is as shown in Fig. 4 which corresponds to the case when $I_b = 2$ mA and a temperature of 150 K. By fitting a 1st order low-pass response (solid line) to the RND data, we find the squeezing bandwidth to be 650 kHz $\pm 15\%$, which is not significantly different from the modulation bandwidth of 616 kHz $\pm 5\%$ measured directly at the output of the PIN detector.

5. CONCLUSION

The method of relative noise difference is original and its use removes both the noise and frequency dependence of the amplifier used in the noise measurement. The apparent agreement between the squeezing and modulation bandwidths lends

experimental support to the validity of the series noise equivalent circuit for the LED in optocoupler applications [4-5].

ACKNOWLEDGMENT

The work is supported by the Australian DEET Targeted Institutional Link and ARC Grants.

REFERENCES

- [1] Edwards, P. J., "Reduction of optical shot noise from light-emitting diodes", IEEE J. Quantum Electronics, Vol. 29, 8, August 1993, pp. 2302-2305.
- [2] Carroll, J. E., Rate Equations in Semiconductor Electronics, Cambridge University Press (1985).
- [3] Edwards, P. J. and Pollard, G. H., "Quantum Noise-Correlated Operation of Electrically Coupled Semiconductor Light-Emitters" Phys. Rev. Letters 69, No.12, pp.1757-1760, 21 September 1992.
- [4] Cheung, W. N. and Edwards P. J., "Simulation of noise characteristics in optical devices using PSpice", Int. J. Electronics, 1994, Vol. 76, No.4, pp. 627-632.
- [5] Cheung, W. N. and Edwards, P. J., "Modelling and Analysis of Quantum Noise Suppressed Optocoupler Amplifiers", presented at the 10th Int. Conf. on Integrated Optics and Optical Fibre Communication, Hong Kong, June 26-30, 1995.

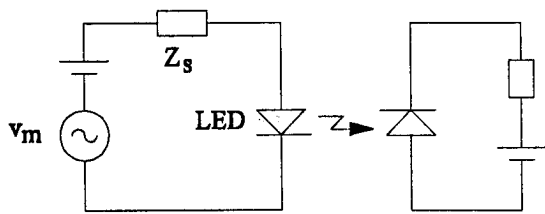
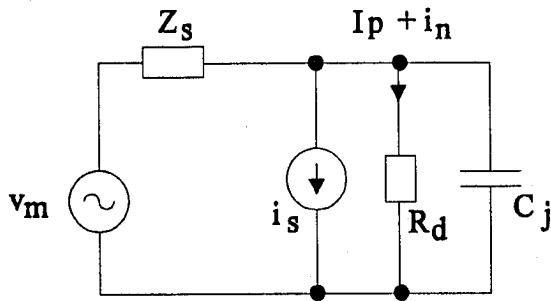
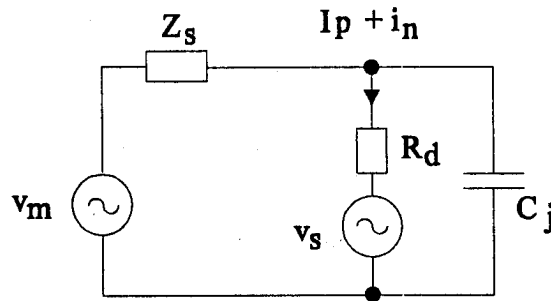


Fig. 1 Optocoupler circuit



(a)



(b)

Fig. 2 Electronic small-signal model of the LED with its internal shot-noise represented as (a) a current source, (b) a voltage source.

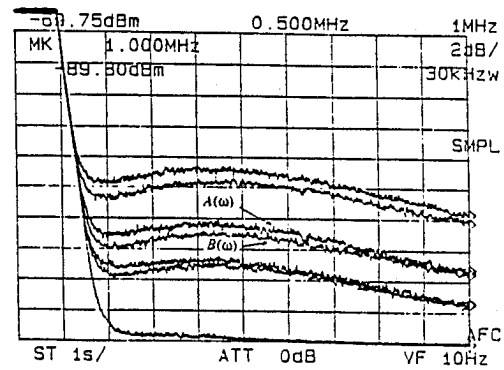


Fig. 3 Measurements of photonic noise spectral density at the output of the optocoupler with different LED bias currents.

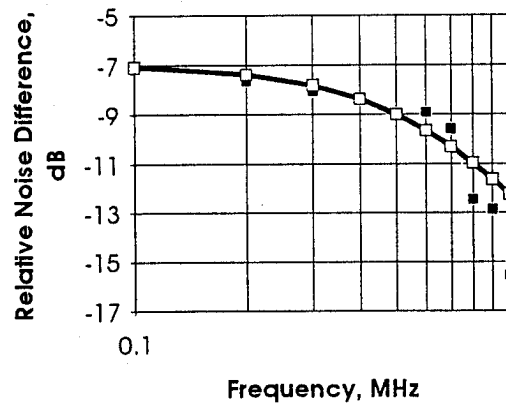


Fig. 4 RND data (dark squares) and a 1st order low-pass response (solid line) using circuit model.

MICROWAVE SIGNAL TRANSFORMATION IN A MAGNETOSTATIC WAVE TRANSMISSION LINE UNDER PULSED LASER IRRADIATION

Y. Fetisov, I. Romanov and V. Studenov

Moscow Institute of Radioengineering, Electronics and Automation
Vernadskogo 78, 117454 Moscow, Russia,
fax: 7(095)434-8665, e-mail: ber@glasnet.ru

ABSTRACT

A possibility to control parameters of microwave signals by pulsed optical heating of a ferrite film involved in a magnetostatic wave transmission line was demonstrated. Variations in the signal phase shift by 10π rad, delay time by 35 ns, and insertion loss by 5 dB were obtained in the 5.7 GHz frequency band using 5 ns laser pulses with the energy of 30 mJ.

1. INTRODUCTION

Recently, a great attention was paid to optically controlled devices for microwave signal processing and forming [1]. Such devices are considered very promising for application in phase array antennas and high-speed opto-electronic communication systems [2]. The optically controlled K-band oscillator containing PIN photodiode [3], optically tuned microwave phase-shifter/attenuator utilizing liquid crystal modulator [4] and optically controlled MESFET structures [5] have been designed and investigated.

This paper demonstrates for the first time an optical control of microwave signals parameters using a magnetostatic spin wave (MSW) propagating in an epitaxial yttrium-iron-garnet (YIG) film. It was shown that pulsed laser irradiation of the film resulted in a change in the MSW dispersion characteristic and gave rise to a considerable variation in the phase shift and delay time of microwave signal passed through a MSW transmission line.

2. EXPERIMENTAL SET-UP

Fig. 1 shows a schematic view of the MSW transmission line. The line contained an YIG film placed in a close contact with an alumina substrate. The film of the thickness $d=14.4 \mu\text{m}$ and magnetization $4\pi M=1750 \text{Gs}$ (at the room temperature) was grown on one side of a gallium-gadolinium-garnet (GGG) substrate of the thickness 0.5 mm and dimensions of 3.5 mm x 15 mm.

Two microstrip transducers of the width of $50 \mu\text{m}$ deposited on the alumina substrate at the distance $l=0.4 \text{cm}$ apart were used to excite and to receive MSWs. An external DC magnetic field $H=1276 \text{Oe}$ was applied tangentially to the film surface along the transducers. An input microwave signal $P(t)$ of the frequency $f=5-6 \text{GHz}$ fed to the first transducer excited the MSW propagating in the film, while the second transducer converted the MSW back into an output electromagnetic signal $P_{\text{out}}(t)$. At the same time the film was irradiated (through the transparent GGG substrate) with single optical pulses of the energy $W \approx 2-100 \text{mJ}$, duration about of 5 ns, and wavelength of $0.53 \mu\text{m}$ from a pulsed Nd-laser.

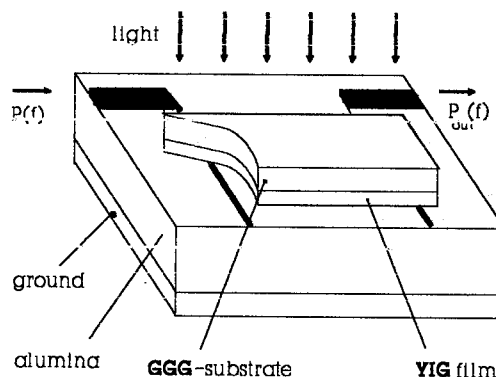


Fig. 1 MSW transmission line

Typical frequency response $I(f)=10\lg[P_{\text{out}}(f)/P(f)]$ and dispersion characteristic $f(k)$ of the MSW transmission line shown in Fig. 2 explain the nature of the light-microwave interaction in the YIG film. The MSW line dispersion characteristic is well described by the following dispersion equation [6]:

$$f^2 = f_H^2 + f_H f_M + \frac{f_M^2}{4}(1 - e^{-2kd}) \quad (1)$$

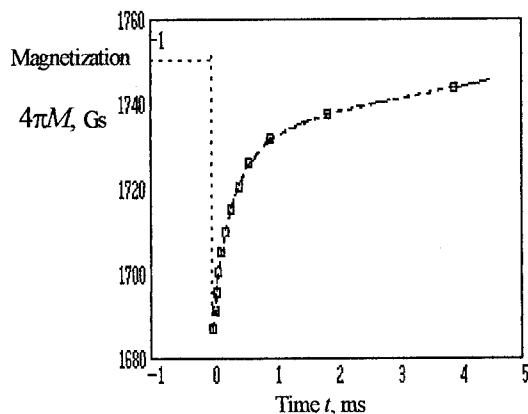


Fig. 5 Time-dependence of the YIG film magnetization $4\pi M(t)$.

Using dispersion equation (1) for MSW propagating in the ferrite film, measured or calculated frequency response $L(f)$ for the transmission line, and experimentally found time-dependence $4\pi M(t)$ for the film magnetization, one can calculate all characteristics of the microwave signal transformation in the MSW transmission line caused by pulsed laser irradiation of the YIG film.

For example, the delay time for microwave signal may be calculated using the following relation:

$$\tau = \frac{l}{V_g} = \frac{l}{2\pi d} \frac{f}{(f_h + f_m/2)^2 - f^2} \quad (3)$$

For our case the dependence $\tau(t)$ calculated using Eq.(3) and experimentally measured time-dependence for $4\pi M(t)$ is shown in Fig.6. The variation in the signal delay time from 95 ns up to 60 ns was accompanied by the changes in the transmission line insertion loss by 5 dB.

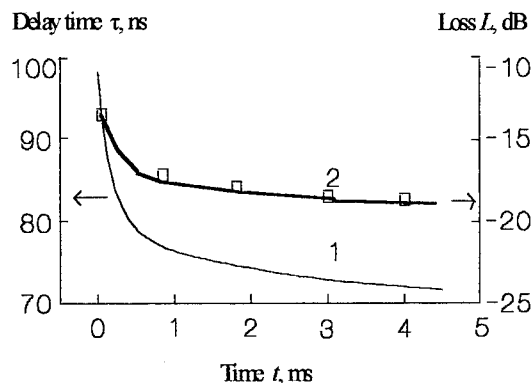


Fig. 6 Time-dependence of the microwave signal delay time $\tau(t)$ and insertion loss $L(t)$.

4. CONCLUSION

It was demonstrated that pulsed laser irradiation provided an effective control of the MSW transmission line characteristics. Laser pulses of the energy of 30 mJ and duration of 5 ns resulted in heating of the YIG film by $\Delta T = 17^\circ\text{C}$ and decrease in its magnetization by $\Delta(4\pi M) = 66$ Gs. For microwave signals with the frequency $f = 5.7$ GHz the optically induced variations in the phase shift by 10π rad and in the delay time by decades of percent have been obtained. These effects may be used to design optically controlled microwave phase shifters and delay lines.

5. ACKNOWLEDGMENT

The research described in this paper was made possible in part by the Grant No.M6Q300 from the International Science Foundation and Russian Government.

REFERENCES

1. T.Berceli "European research on optical-microwave interactions", APMC'94 Proc., Tokyo, 1994, p.953-956.
2. A.Seeds "Opto-electronic beam formers for phased arrays", APMC'94 Workshop Digest, Tokyo, 1994, p.47-52.
3. R.Saedi, T.Berceli, A.S. Daryosh, P.R.Herczfeld "Optically controlled K-band oscillator", MTT-S Symp. Digest, 1990, p.293-294.
4. O.Kobayashi, H.Ogawa "An opto-electronic RF/microwave variable attenuator/ phase shifter: the RF link performance", APMC'94 Proc., Tokyo, 1994, p.971-974.
5. M.Minegishi, J.Lin, T.Itoh "Electronic and optical control of MESFET for mode switching in an active antenna", APMC'94 Proc., Tokyo, 1994, p.963-965.
6. R.W.Damon and J.H.Eshbach "Magnetostatic modes of a ferromagnetic slab", J. Phys. Chem. Solids, 1961, v.19, p.308-320.

where $f_H = \gamma H$, $f_M = \gamma 4\pi M$, $\gamma = 2.8$ MHz/Oe is the gyromagnetic ratio, $4\pi M$ is the ferrite magnetization, f and k is the MSW frequency and wave number, respectively.

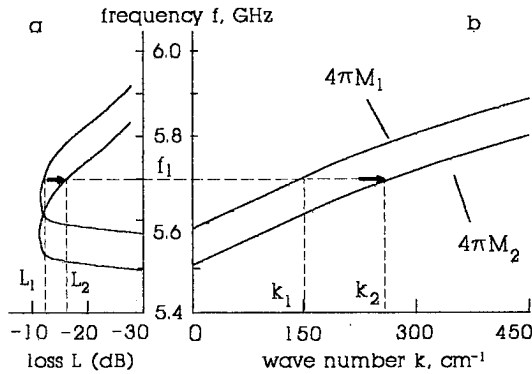


Fig. 2 MSW line frequency response (a) and dispersion characteristic (b).

A decrease in the film magnetization ($4\pi M_1 \rightarrow 4\pi M_2$) results in a down shift of both the frequency response $L(f)$ and the dispersion characteristic $f(k)$ of the line. Under pulsed laser irradiation the YIG film is heated and its magnetization is decreased with the coefficient $\partial(4\pi M)/\partial T \approx -3.8$ Gs/ $^\circ\text{C}$. It follows, that heating of the film with laser pulses have to change the phase shift $\Phi = kl$ as well as the insertion loss L of the microwave signal passed through the MSW transmission line.

3. RESULTS OF INVESTIGATION

The dispersion characteristic of MSW transmission line and transformation of microwave signal under pulsed laser irradiation of the ferrite film were measured by the interferometric method. The input signal $P(t)$ was divided and part of it was then mixed with the microwave signal from the transmission line output $P_{\text{out}}(t)$ having the phase shift $\Phi = kl$. Measured and calculated dispersion characteristics of the line under stationary conditions are shown in Fig. 3.

The time-dependence of the phase shift $\Phi(t)$ of output microwave signal (shown in Fig. 4) under pulsed laser irradiation was found by measuring the period of the beats at the line output. For laser pulse energy of $W \approx 30$ mJ and the signal frequency of $f = 5713$ MHz the phase shift of the output signal was increased from $\Phi_1 = 10\pi$ rad, up to $\Phi_2 = 17\pi$ rad during the time of the film heating (5 ns) and then it was decreased to its initial value at the cooling of the film.

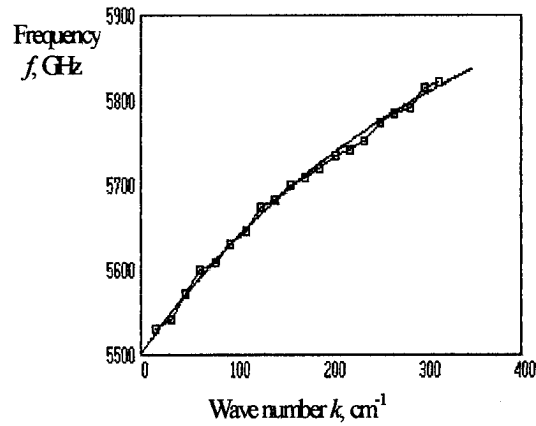


Fig. 3 Dispersion characteristic of the MSW transmission line.

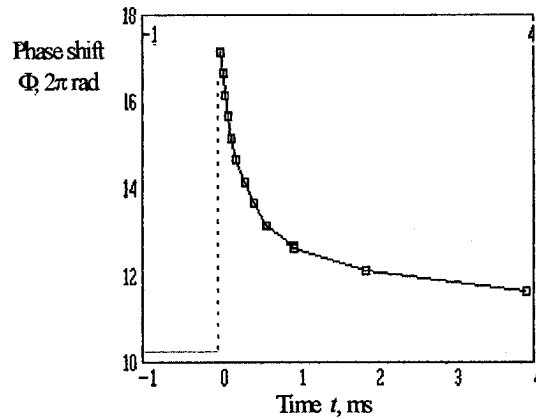


Fig. 4 Time-dependence of the signal phase shift.

Using dependence of the ferrite film magnetization on the MSW wave number:

$$4\pi M = \frac{2}{\gamma(1 - e^{-2kl})} \left[\sqrt{f_H^2 - (f_H^2 - f^2)(1 - e^{-2kl})} - f_H \right] \quad (2)$$

and experimentally obtained values for $k(t) = \Phi(t)/l$ at fixed f , we found the time-dependence for the film magnetization $4\pi M(t)$ which is shown in Fig. 5. In our experiments the maximum decrease of magnetization was equal to $\Delta(4\pi M)_{\text{max}} = 64$ Gs that corresponded to the maximum heating of the film by $\Delta T \approx 17^\circ\text{C}$. After the end of the laser pulse the magnetization was increased to its initial value approximately exponentially with a characteristic time about of 0.5 ms.

SELF-CONSISTENT BPM MODEL OF A WAVEGUIDE COUPLER WITH DISTRIBUTED GAIN

R F Ormondroyd

School of Electronic and Electrical Engineering,
University of Bath, Claverton Down,
Bath, BA2 7AY, U.K.
Tel. +44 1225 826826, e-mail r.f.ormondroyd@bath.ac.uk

ABSTRACT

A self-consistent model of coupling in an active twin-ridge waveguide coupler is presented, based on the beam propagation method. The coupler structure is assumed to be fabricated in double-heterostructure material which is electrically pumped to provide distributed gain. Stimulated recombination in the active region perturbs the complex refractive index of the structure and this results in non-linear coupling.

1. INTRODUCTION

There have been a number of significant recent developments in a range of advanced waveguide components such as: integrated laser/waveguide/detector structures, waveguide coupled DFB sources for WDM applications and switchable optical routing components for optical networks. A particular problem with integrated-optic waveguide components, particularly power splitters and couplers, is the accumulation of losses which invariably reduces the bit error rate performance of the system. A possible solution to this problem is to incorporate amplifying sections within the integrated-optic structure by the use of a conventional double heterostructure substrate (with a bulk or quantum well active layer) which can be locally pumped with injection current to provide a region of net gain. One consequence of this is that there is an interaction between the photons and the carriers in the active layer which gives rise to lateral and longitudinal

variations in the complex refractive index of the active layer of the waveguide and this affects the evolution of the guided modes. This effect is particularly strong at wavelengths close to the emission wavelength of the active layer. In certain applications, such as optical or current-controlled spatial switching, this interaction can be exploited.

Jensen [1] and Thylen *et al* [2] have examined the effect of non-linear coupling of the refractive index to the photon density in an otherwise passive twin-guide structure. In this paper, a self-consistent model of a twin-ridge coupler is presented in which there is distributed gain in each waveguide and the effects of lateral carrier diffusion and the interaction of the photons with the carriers are included.

2. THE MODEL

Figure 1 shows the structure of the waveguide. Each guide is independently pumped, with current confinement being provided by the etched ridges. It is assumed that there is good current confinement in the p-type cladding layer but there is electrical coupling between the guides due to lateral carrier diffusion in the active layer. This leads to a lateral variation in the real part of the effective refractive index due the ridge structure and an additional variation in both real and imaginary parts due to the carriers. In this model, good transverse optical confinement is assumed within the active layer of the DH substrate and only the lateral variation of the TE mode propagating along the guide is considered.

In common with many other authors, the effect of the ridge geometry is modelled using the effective index method [3] to reduce the computational overhead, and the longitudinal variation of the lateral mode is obtained by the beam propagation method [4-7].

The longitudinal variation in photon density gives rise to a longitudinal variation of the lateral carrier density distribution leading to possible gain saturation. This effect is specifically included in the model. The active waveguide problem may be split into two coupled sub-models, an electrical model and an optical model.

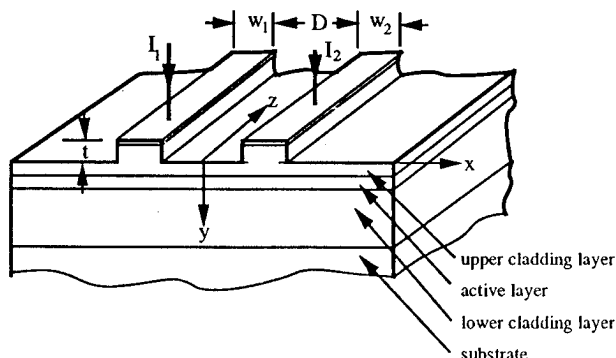


Figure 1. Structure of the active twin-ridge coupler

2.1. Electrical Model

The lateral carrier density distribution at some point z along the waveguide structure, $n(x, z)$ can be found from a solution of the diffusion equation:

$$D_{amb} \frac{d^2 n(x, z)}{dx^2} + \frac{J(x)}{e \cdot d} = R_{stim}(n, z) + R_{spont}(n, z) + R_{non-rad}(n, z) \quad (1)$$

where $J(x)$ is the current density distribution in the active layer, D_{amb} is the ambipolar diffusion coefficient, d is the thickness of the active layer. Carrier diffusion in the longitudinal direction has been neglected. The terms on the right hand side of the equation are recombination terms representing stimulated, spontaneous and non-radiative recombination. These are assumed to be of the form:

$$\begin{aligned} R_{stim}(n, z) &= \frac{c}{\eta_o} g(x, z) S(x, z) \\ R_{spont}(n, z) &= B_r n(n + p_o) \\ R_{non-rad}(n, z) &= \frac{n}{\tau} + C n(n + p_o)^2 \end{aligned} \quad (2)$$

where B_r is the bimolecular recombination coefficient, C is the Auger recombination term, p_o is the active layer doping density and τ is a characteristic lifetime. In the stimulated recombination term, $g(x, z) = an(x, z) - b$ is the optical gain of the material, c/η_o is the group velocity of the light in the waveguide, $S(x, z)$ is the photon density distribution and η_o is the background refractive index of the active layer.

2.2 Optical Model

For non-linear multi-guide structures, where the fields in each guide may not be phase matched, it is difficult to apply coupled mode theory. The beam propagation method is particularly appropriate to this type of problem because it provides a unified treatment of the various guided and radiation fields. It is assumed that the lateral field, $\Psi(x, z)$, satisfies the paraxial wave equation:

$$-2jk \frac{\partial \Psi}{\partial z} + \frac{\partial^2 \Psi}{\partial x^2} + (\epsilon_{eff}(x, z) k_0^2 - k^2) \Psi = 0 \quad (3)$$

where $k_0 = \omega/c$ and that the effective complex dielectric constant of the active layer in the lateral direction has been modified to take into account the effect of the carriers to yield:

$$\epsilon_{eff}(x, z) = \left(\epsilon_{act}(x) + (-R + j) \frac{\eta_o g(x, z)}{k} \right) \quad (4)$$

where $\epsilon_{act}(x)$ is the effective background dielectric constant of the active layer found by the EI method and R is the ratio of the change of the real part of the refractive index due to the carrier density. The evolution of the lateral field can now be found using the beam propagation method, with appropriate correction for the gain, as described qualitatively by Lagasse and Baets [5] and in greater detail in references [8] and [9]. The procedure is well known and involves splitting the guide longitudinally into a number of segments of length 2δ . In each of these segments, distributed gain is replaced by an equivalent value of lumped gain in the centre of the segment. The paraxial equation (3) is rewritten as $d\Psi/dz = (A + B(z))\Psi$ where A and B are non-commuting diffraction and complex gain operators, respectively. If Ψ_i is the lateral field at the i^{th} station, then the error in computing Ψ_{i+1} is minimised [7] when:

$$\Psi_{i+1} = \left[e^{\delta A} \exp \left(\int_0^{2\delta} B(z') dz' \right) e^{\delta A} \right] \Psi_i \quad (5)$$

This equation is solved by first free propagating the field Ψ_i over a distance δ to the edge of the gain sheet. This is achieved most conveniently by first expanding Ψ_i as its spectrum of plane waves. The resulting field at the centre of the segment is then operated on by a 'lens' of complex refractive index prior to further free propagation through a distance δ to the edge of the segment.

2.3 Solution method

A multi-layer effective index method was used to calculate the effective background indices of the guiding and cladding regions of the lateral active guide at the wavelength of interest. Longitudinally, the substrate was split into short [5] segments of typically $0.1 \mu\text{m}$ length. The arbitrary optical field at the input to the guide was propagated to the mid-point of the segment using the BPM algorithm with a 256 point FFT, and the photon density distribution, $S(x, z)$, obtained.

The carrier diffusion equation was then solved numerically at this point using $S(x, z)$ and an efficient iterative method with derivative boundary conditions, $dn/dx = 0$ was employed. From the solution of $n(x, z)$, the gain and complex refractive index profiles were then obtained. The optical field was then propagated to the end of the first segment using the new value of complex refractive index in the phase correction term of the BPM algorithm, as described above.

To prevent reflection of the propagating field at the outer edges of the structure, optical absorbing regions of graded absorptency were used in the usual way.

3. RESULTS

For the purpose of this paper, the method was applied to an active twin-ridge waveguide coupler assumed to be fabricated from GaAs/GaAlAs dh material. Table 1 lists the principal parameter values [10].

guide width, $w_1 = w_2$	$3\mu\text{m}$
guide spacing, D	$3\mu\text{m}$
active layer thickness, d	$0.2\mu\text{m}$ GaAs
cladding layer thicknesses	$2\mu\text{m}$ GaAlAs
ridge etch depth, t	$1.8\mu\text{m}$
percentage Al content in cladding layer	25%
non-radiative lifetime, τ	10^{-8} s
ambipolar diffusion coefficient, D_{amb}	$68 \text{ cm}^2\text{s}^{-1}$
bimolecular recombination rate, B_r	$10^{-16} \text{ m}^3\text{s}^{-1}$
gain coefficient, a	$8.9 \times 10^{-20} \text{ m}^2$
gain coefficient, b	$7.8 \times 10^4 \text{ m}^2$
transverse optical confinement factor Γ	0.75
wavelength, λ	$0.88\mu\text{m}$

Table 1 Parameters used in the simulation

Figure 2 shows the development of the optical field intensity of a passive twin-ridge waveguide structure, of dimensions given in table 1.

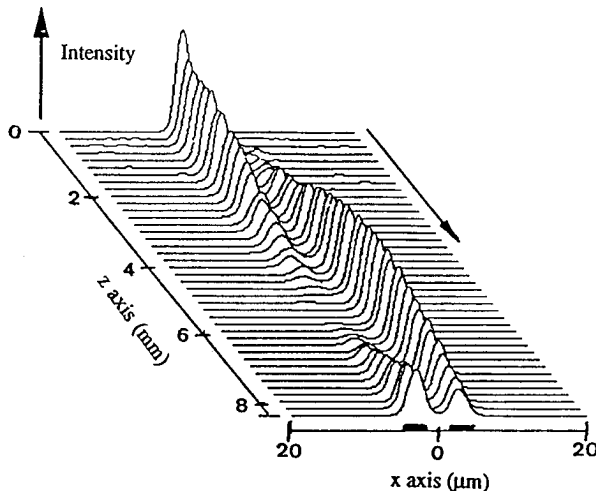


Figure 2. Evolution of the field intensity in a passive coupler, dimensions as Table 1 and effective refractive index step 0.0045

In this example, all the layers are assumed to be lossless. Optical injection is into guide 1 and classic coupling behaviour is observed. The coupling length is close to that obtained from coupled mode theory. This behaviour can now be contrasted with the case for the symmetrically pumped twin-ridge coupler electrically pumped just above its transparency value (measured between the input and output ports for an input power of 1mW), shown in figure 3. In this case, light is coupled from guide 1 into guide 2

within $100\mu\text{m}$. There is a rapid increase in intensity in guide 2 because the guide has excess gain for the initial levels of light coupled into it from guide 1, and there is amplification. As more light is coupled along the guide, the intensity builds up and causes significant stimulated recombination and the guide starts to saturate. Light couples back into guide 1, and this too is amplified and starts to saturate.

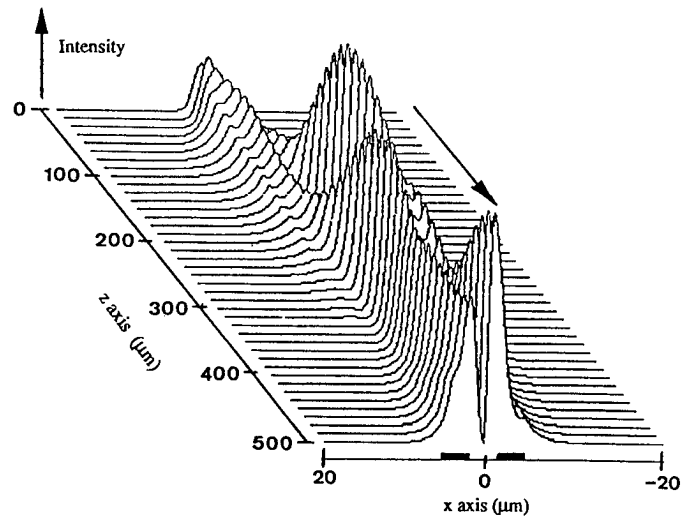


Figure 3. Beam propagation in a symmetrically pumped active twin-ridge coupler at input power of 1mW and $J_{\text{guide}} = 1.1 \times 10^8 \text{ Am}^{-2}$

Figure 4 shows the same structure extended over 3mm but with an optical input power of 10mW, where the two travelling wave amplifiers are now very heavily gain saturated.

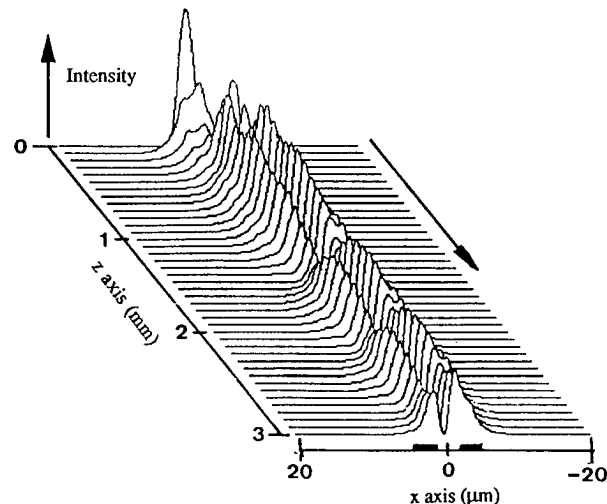


Figure 4. Evolution of field along symmetrically pumped active twin-ridge waveguide coupler. $J_{\text{guide}} = 1.5 \times 10^8 \text{ Am}^{-2}$, Optical input power = 10mW

Apart from the initial transient behaviour, shown in figure 3, once the light has coupled into guide 2, the light is effectively confined to both guides, and the intensity stays reasonably constant due to the effect of gain saturation.

By modifying the relative injection currents between the guides, a number of different coupling modes are observed, indicating that the device could be used as an electronically controllable spatial switch in OOK optical system. It is of practical benefit to note that the length of the active coupler is now no longer critical in obtaining the required coupled optical power into each guide.

Figure 5, shows how the coupler can be configured to couple from guide 1 to predominantly guide 2. In this case, guide 2 is relatively heavily pumped to provide gain whilst guide 1 is not pumped sufficiently to overcome the inherent loss in the active layer of the guide. Because of the strong coupling between the guides due to the effects of carrier diffusion on the complex refractive index, a significant proportion of the light has coupled across to guide 2 before it is totally absorbed in guide 1. The light that has coupled to guide 2 is then maintained by the gain in that guide.

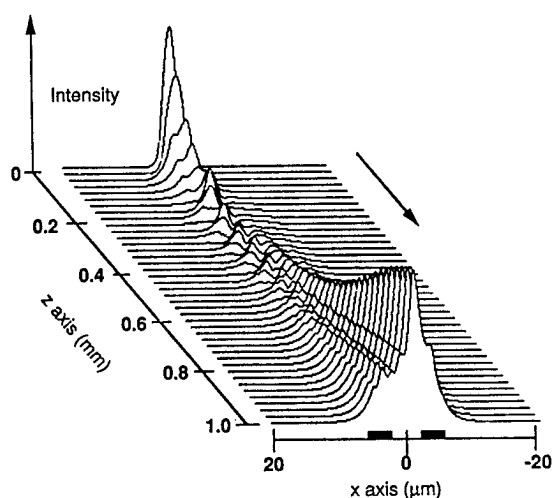


Figure 5. Evolution of the field in an asymmetrically pumped active coupler at 2mW input power ($J_{\text{guide1}} = 0.8 \times 10^8 \text{ Acm}^{-2}$ and $J_{\text{guide2}} = 1.3 \times 10^8 \text{ Acm}^{-2}$)

4. CONCLUSIONS

A self-consistent model of the active twin-ridge coupler has been presented which predicts the longitudinal evolution of the optical field. It is found that the strong electrical coupling between the guides significantly modifies the coupling length, compared with the passive case. Current injection into the two guides controls the intensity of the field beneath each guide extremely effectively by adjusting the complex refractive index profile and this can be exploited for optical routing applications. Gain saturation, however, provides a feedback

mechanism and this damps the transfer of optical power between the two guides, which implies that the physical length of the active component is no longer critical.

5. ACKNOWLEDGEMENTS

The author is pleased to acknowledge the financial support of the European Commission for the provision of contract SC1*-CT91-0634 (TSTS), and to Mr Raad Hassan for his help with the development of the computer program.

6. REFERENCES

1. S.M. Jensen, "The non-linear coherent coupler", IEEE J. Quantum Electronics, Vol. QE-18, no. 10, pp. 1580-1583, 1982.
2. L. Thylen, E.M. Wright, G.I. Stegeman, C.T. Seaton and J.V. Moloney, "Beam propagation method analysis of a non-linear directional coupler", Optics letters, Vol. 11, no. 11, pp. 739-741, 1986.
3. J. Buus, "The effective index method and its application to semiconductor lasers", IEEE J. Quantum Electronics, Vol. QE-18, no. 7, pp. 1083-1089, 1982.
4. G.P. Agrawal, "Fast-Fourier transform based beam propagation model for stripe-geometry semiconductor lasers: inclusion of axial effects", Applied Physics. Vol. 56, no. 11, pp. 3100-3109, 1984.
5. P.G. Lagasse and R. Baets, "Application of propagation beam methods to electromagnetic and acoustic wave propagation problems - A review", Radio Science, Vol. 22, no. 7, pp. 1225-1233, 1987.
6. G.P. Agrawal, W.B. Joyce, R.W. Dixon and M. Lax, "Beam propagation analysis of stripe-geometry semiconductor lasers: Threshold behaviour", Applied Physics letters, Vol. 43, no. 1, pp. 11-13, 1983.
7. M. Lax, J.H. Batteh and G.P. Agrawal, "Channelling of intense electromagnetic beams", J. Applied Physics, Vol. 52, no. 1, pp. 109-125, 1981.
8. A.E. Sziklas and A.E. Siegman, "Mode calculations in unstable resonators with flowing saturable gain - 2, FFT method", Applied Optics, Vol. 14, no. 8, pp. 1874-1889, 1975.
9. P.W. Milonni, "Criteria for the thin-sheet gain approximation" Applied Optics, Vol. 16, no. 11, pp. 2794-2795, 1977.
10. S. Adachi, "GaAs, AlAs and $\text{Al}_x\text{Ga}_{1-x}\text{As}$: material parameters for use in research and device applications", J. Applied Physics, Vol. 58, no. 3, pp. R1-R29, 1985.

AN ALL-OPTICAL CDMA COMMUNICATION NETWORK BY SPECTRAL ENCODING OF LED USING ACOUSTICALLY TUNABLE OPTICAL FILTERS

K. Iversen and O. Ziemann

Department of Communication and Measurement
Technical University of Ilmenau
P.O. Box 0565, 98684 Ilmenau, Germany
e-mail: iversen@e-technik.tu-ilmenau.de

ABSTRACT

The realization of spectral encoding of low-cost broadband light sources using acoustically tunable optical filters is discussed. We show the feasibility of source equalization and spectral code generation by some experiments. Finally, for the first time a polarization independent single-chip solution for transmitter and receiver is proposed.

1. INTRODUCTION

The first optical code division multiple access (CDMA) systems were proposed in the middle of the eighties by Hui [1], Prucnal et al. [2] and Tamura et al. [3] for third-generation communication networks. The basic idea was to employ the well known spread spectrum technic from radio frequency in an optical communication system to take advantage of the huge bandwidth of the transmission medium. Afterwards many new approaches were proposed [4] which make a better use of the special properties of light and fiber-optics.

In contrast to optical time division multiple access (TDMA) and wavelength division multiple access (WDMA) in CDMA systems no time synchronization or frequency stabilization and no preparatory information/coordination (tell-and-go) is necessary. While in a TDMA and WDMA environment the channel-allocation is static and has to be orientated at the maximum number of possible users, in CDMA a dynamic channel allocation depending on the number of active users is implemented. This could be an advantage at bursty traffic [5] and an easy network expansion is possible. Optical CDMA systems offer a greater immunity against fibre nonlinearities and have a high safety against interception. Moreover the use of optical standard components is possible.

Optical CDMA communication networks employing spectral encoded low-cost broadband light sources like

luminescence diodes (LED) have already been presented [6-8]. The concept is shown in Fig. 1. To every subscriber a cyclic shifted m-sequence is assigned. Other code families like Hadamard sequences are also possible. If the desired sequence (coded spectrum) arrives at the receiver the upper diode detects the energy of all ones, at the lower diode no energy is received because of the bandstop case (Fig. 1). If an undesired sequence arrives at the receiver both diodes detect the half of the one's and after the balanced receiver no signal is observed. Complete orthogonal transmission could be achieved, providing that the spectrum is properly equalized.

Drawbacks of the known system are the rather complicated construction of the bulk optic encoder/decoder as well as the address reconfiguration based either on fixed amplitude mask or LCD-arrangement. In [9] we show the feasibility of spectral encoding with acoustically tunable optical filters (ATOF). In the following the realization of an all-optical communication network is discussed.

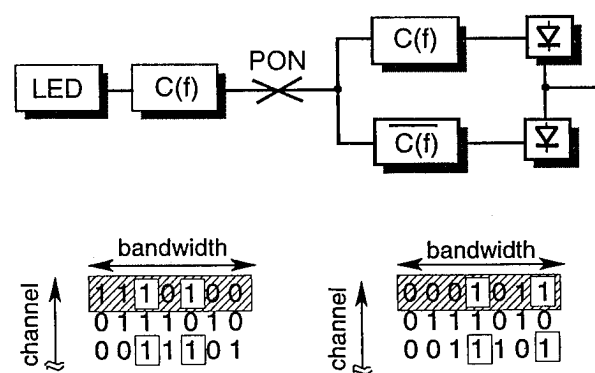


Figure 1: Block diagram of one transmitter and receiver, example for m-sequences of period 7

2. SPECTRAL ENCODING WITH ACOUSTICALLY TUNABLE OPTICAL FILTERS

2.1. Why using ATOF ?

The basic concept of ATOF is the interaction of an acoustic and an optic wave. In a LiNbO_3 -Chip an acoustic waveguide (with a width of about $100\mu\text{m}$) is integrated around an optical single mode waveguide. The propagation constants of the optical polarization modes (TE and TM) differs because of the birefringence. By applying of an acoustic wave with the same wavelength as the beat wavelength of the two polarization modes an interaction between these modes can occur and light will be converted from TE to TM for example. The birefringence is wavelength dependent. By applying a single electrical frequency to such an device, only for one optical wavelength conversion can be observed. If we assume a constant acoustic power between the transducer (transmitter of the acoustic wave) and the absorber, the filter characteristic is like a si^2 -function (according to the fourier transformation of a rectangle). The power of the acoustic wave, and therefore the voltage of the electrical drive signal determines the degree of conversion. For 100% conversion voltages of some 100mV will be enough (available filters for the first telecommunication window). Increase of the voltage over the 100% conversion point gives a back conversion into the incoming polarization mode.

By the use of TE polarized light at the input of an ATOF a passband filter or a band rejection filter can be realized, depending on the use of an TE or a TM polarization filter at the ATOF output. The linear characteristic of the acoustic wave transmitter allows the use of several drive frequencies (more than 100) at the same time. The limit is given by the maximum applied voltage at the transducer. By the choice of suitable drive frequencies and voltages, nearly every thinkable filter function can be realized. The spectral resolution is determined by the interaction length of the acoustic wave on the ATOF (some cm of length will give a resolution of some tens of nm in the first telecommunication window). This paper represents the realization of spectral encoding of a 20nm wide SLD-spectrum with a m-sequence of period 31. With variation of the voltage of the several drive frequencies a spectral flattening of the gaussian SLD-power spectrum was realized. So an ATOF has some important properties for the using as spectral encoder:

- the filter structure can be determined with the choice of the spectrum of the electrical drive signal,

- very long sequences are possible by the use of about 100 frequencies at the same time,
- only low drive powers (in the range of mW) are necessary,
- spectral flattening of the SLD spectrum is simple to made with variation of the drive voltages of the several lines,
- passband and rejection filters can be realized with different polarization filters (or more simple: a polarization dividing splitter gives inverse function at two outputs),
- because of using of only one waveguide without any free space optics the insertion loss of the element can be minimized,
- the size of the filter is in the cm range,
- the filter function can be changed in some μs only.

Disadvantages of the ATOF are:

- necessity of permanent drive signal,
- the temperature dependence of the birefringence.

2.2. Source and filter-parameters

For the described experiment we have used SLD with a spectral width of about 20nm and a center wavelength of 825nm. The spectral ripple was lower than 5% with a measurement resolution of 0.1nm. No spectral distortions are observable with modulation up to 100 Mbit/s. The used ATOF have an interaction length of 18mm and therefore a spectral resolution of 1/2 nm. Total conversion occurs with a driving voltage of $400\text{mV}_{\text{eff}}$. The tuning rate (dependence of optical filter wavelength from driving frequency) is $(2 \pm 0.1)\text{nm/MHz}$ over the used spectral range.

2.3. Spectral code generation

Fig. 2 shows the measured spectrum after the ATOF encoder, applying a m-sequence of period 31. For the generation of the 16 different frequencies we used an arbitrary function generator. The frequency shift of two direct adjacent frequencies are 270kHz. This gives a periodicity of the driving signal of $3.704\mu\text{s}$, matching to the propagation time of the acoustic wave on the chip. The whole driving spectrum has a bandwidth of 8.1MHz and was first generated in the 60 to 70 MHz region and then shifted in the required region of 350 to 360 MHz with a passive mixer. In order to minimize interference phenomena between the driving frequencies,

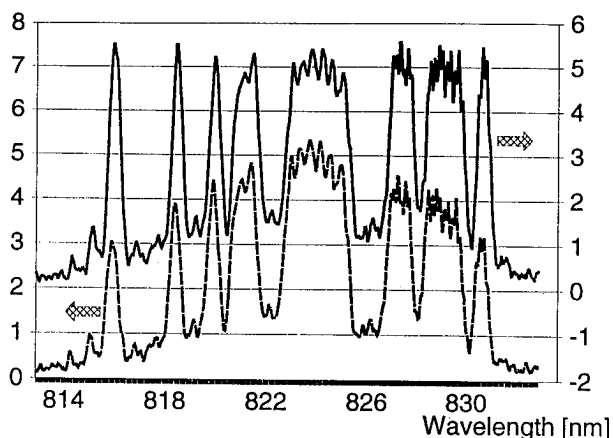


Figure 2: Measured spectrum after the ATOF encoder

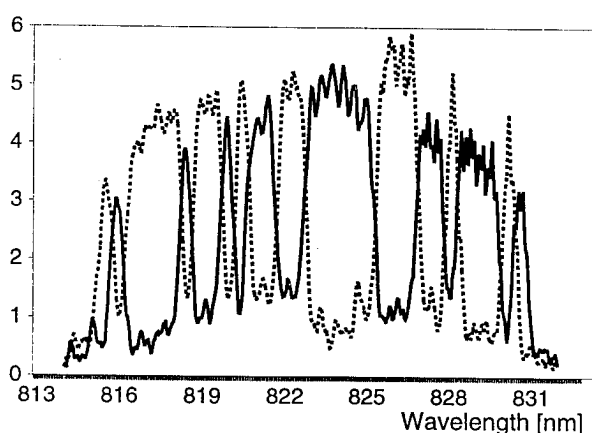


Figure 3: Two spectra and the inverted case

there phase positions were optimized. In Fig. 2 two spectra are shown. The first was get with the same driving voltage for every frequency. The envelope represents the spectrum of the SLD. For the second spectrum, the voltages of the outer lines were increased. By this we achieve a nearly flattened spectrum for the sequence. Fig. 3 shows two spectra for the same sequence and the inverted case.

2.4. Correlation properties

For a complete transmission system with spectral encoding, the processes of encoding and decoding have to be carried out afterwards. Fig. 4 shows a spectrum after an ATOF-pair. At both filters the same sequence was applied (without equalizing). The sequence can be identified by comparing with the inserted code in Fig. 4. The correlation properties of the use ATOF-

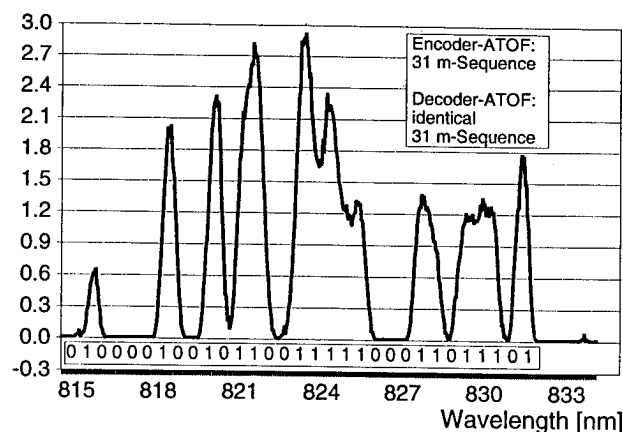


Figure 4: Spectrum after an ATOF-pair

pair were investigated by applying the original and the inverted sequence at the second filter. Than both driving signals were frequency shifted against the matched position (Fig. 5).

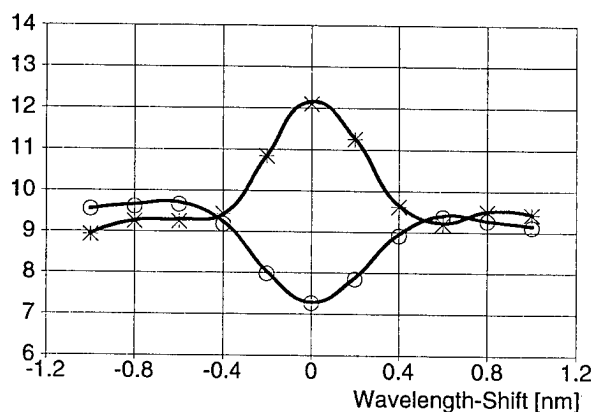


Figure 5: Frequency shifted m-sequence against the matched position. Y-values represents total optical power after the ATOF-pair

3. FURTHER INVESTIGATIONS

The disadvantage of the described solution is there polarization dependence. Fig. 6 shows a proposed conception with polarization splitter at the input and output. This filter works independent of polarization at the input, the two output ports give the converted and non converted fraction of the passed light, respectively. That's why the whole system has only the loss of the sequence (3dB because of the 50% share of "1"-chips in the sequence) and twice the additional insertion loss of

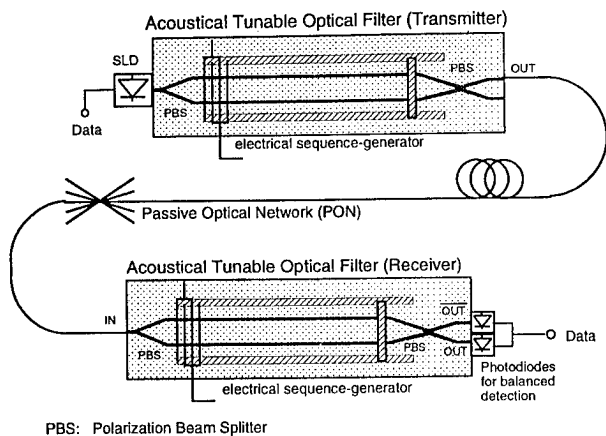


Figure 6: Proposed device with a polarization splitter at the input and output

the filters. The same device can be used in the transmitter and the receiver.

An important advantage of the ATOF is its simple tunability. The desired user can be selected in some μs . For applications with fixed channel arrangement no change of the filter function is necessary. Here the use of passive optical devices is preferred. We propose the use of arrayed waveguide structures or cascaded fibre bragg gratings. With arrayed waveguide the multiplexing of 64 channels [10] and a channel separation of 10GHz [11] was achieved. Fibre bragg grating can be realized as band rejection filters with a very low bandwidth, very high attenuation at the filter wavelength and a very low insertion loss far away from these wavelengths [12].

4. CONCLUSIONS

The advantages and the feasibility of spectral encoding with ATOF has been shown. The proposed concept offers an interesting alternative to future dense WDM-Systems. It appears that more users with higher signal-to-interference ratio are possible in comparison to a WDM-System with ATOF and low-cost broadband source. Moreover the CDMA concept allows a higher system stability.

5. ACKNOWLEDGEMENTS

We would like to thank Dr. V. Hinkov, I. Hinkov, P. Rauschenbach and Prof. D. Kress for discussion and support. Furthermore we thank LeCroy for providing the arbitrary function generator at our disposal. This project is under financial support of the Deutsche Telekom AG.

6. REFERENCES

- [1] J.Y. Hui, "Pattern Code Modulation and Optical Decoding - A Novel Code-Division Multiplexing Technique for Multifiber Networks," IEEE Journal on Selected Areas in Comm., Vol. SAC-3, No. 6, Nov. 1985, pp. 916-927
- [2] P.R. Prucnal, M.A. Santoro, "Spread Spectrum Fiber Optic Local Area Network Using Optical Processing," Digital Communications, Proceedings of the Second Tirrenia Int. Workshop, Sept. 1985, pp. 193-202
- [3] S. Tamura, S. Nakano, K. Okazaki, "Optical Code-Multiplex Transmission by Gold Sequences," IEEE Journal of Lightwave Technology, Vol. Lt-3, No. 1, February 1985
- [4] K. Iversen, "Comparison and Classification of All-Optical CDMA for Tera-Bit Networks," IOOC-95, Hong Kong, WC3-5
- [5] K. Iversen, H. Walle, K. Kluge, "Throughput, Capacity and Message Delay for different kinds of Optical CDMA Systems in Subscriber Loops," VII International Workshop on Optical Access Networks 1995, Nuernberg, P.10
- [6] D. Zaccarin, M. Kavehrad, "An Optical CDMA System Based on Spectral Encoding of LED," IEEE Photonic Technology Letters 4(1993)4, pp. 479-482
- [7] D. Zaccarin, M. Kavehrad, "Optical CDMA by Spectral Encoding of LED for Ultrafast ATM Switching," Proc. ICC'94, Vol.3, New Orleans, May 1994, pp. 1369-1373
- [8] M. Kavehrad, D. Zaccarin, "Optical Code Division Multiplexed System Based on Spectral Encoding of Noncoherent Sources," Journal of Lightwave Technology 13(1995)3, pp. 534-545
- [9] I. Hinkov, V. Hinkov, K. Iversen, O. Ziemann, "Feasibility of optical CDMA using spectral encoding by acoustically tunable optical filters," Electronics Letters, Vol. 31, No. 5, March 1995, pp. 384-385
- [10] K. Okamoto, K. Moriwaki, S. Suzuki, "Fabrication of 64x64 Arrayed Waveguide Grating Multiplexer on Silicon," Electr. Lett. 31(1995)3, pp. 184-186
- [11] H. Takahashi, I. Nishi, Y. Hibino, "10 GHz Spacing Optical Frequency Division Multiplexer based on Arrayed-Waveguide Grating," Electr. Lett. 28(1992)4, pp. 380-382
- [12] A.M. Vensarkar, P. I. Lemaire, J. B. Judkins, V. Bhatia, T. Erdogan, J. E. Sipe, "Long Period Fibre Gratings as Band Rejection Filters," OFC'95, pp. PD4-2

LONGITUDINAL ELECTRON TRANSPORT IN NON REGULAR ELECTRON WAVEGUIDES FOR FUTURE ULTRA FAST NANO-ELECTRONIC DEVICES.

A.S.Tager

SR&PC "Istok",
Frjazino, Moscow reg., 141120, Russia
asv335@ire216.msk.su

ABSTRACT

Quasiballistic longitudinal electron transport in the 2D and 1D heterostructures (or electron waveguides (EW)) can be effectively controlled by varying transverse potential distribution, dimensions or shape of an EW cross-section, since any such deformation appears as a "quasipotential" barrier or a "quasipotential" well. Specific properties of these quasipotential barriers and wells as well as their device applications are analyzed.

The examples include:

1. Control of electron transport through a short section of a 2D EW by varying its transverse dimensions or transverse potential distribution.
2. Formation of population inversion of the electron energy subbands in EWs with step-like discontinuities.
3. Interference of different electron "modes" in non regular EWs and application of this effect for design of: single channel interference transistors and electron energy filters.

1. INTRODUCTION

It is well known, that longitudinal ballistic electron transport in low dimensional (1D, 2D) semiconductor structures may be described as propagation of electron waves in EWs. Recently there was shown effectiveness of the analogy between electron and electromagnetic waves as a tool for calculation of electron waves propagation along EWs of different cross-sections. But as far as we know, all published works were devoted to analyses of regular EWs. Meanwhile one can suppose, that future quasiballistic nanoelectronics devices will be based on effects arising in non regular EWs, particularly, in the EWs with step-like discontinuities. Typical examples of these effects and devices will be presented in this report

Main effects to be considered are the quantum mechanical electron reflection and tunneling at quasipotential barriers and wells, electron waves interference and transformation in nonregular EWs. The use of the electron-electromagnetic waves analogy allowed us to apply software created earlier for dielectric or metallic waveguides. In the simplest way this

procedure may be applied to the plain 2D EW with infinitely high lateral barriers, where electron waves may be simulated by the electromagnetic TE_{0,n} (n=1,2,...) wave modes in a plain waveguides with metallic walls.

2. QUASIPOTENTIAL BARRIERS AND QUANTUM WELLS.

The high speed performance of electron devices is determined by the effectiveness of methods for electron current control. In common semiconductor devices this control is made by the help of potential barriers, formed by p-n junctions, metal-semiconductor junctions and so on. Quantum sized structures with electron gas of reduced dimensionality --1D and 2D electron waveguides open new possibilities. We will show that electron transport in the electron waveguides can be controlled by varying dimensions or form of its cross-section, because of any deformation of the waveguide cross-section is equivalent to a potential barrier or a quantum well appearance.

Let us consider the ballistic electron motion along the axis Z of rectilinear electron waveguide restricted at its boundaries by a potential barrier. At the absence of the longitudinal electric field a solution of the time independent Shrodinger equation can be written as

$$\psi(x, y, z, t) = \psi_{\perp}(x, y) \exp[i(\omega t - \gamma z)] \quad (1)$$

The transverse wave function $\psi_{\perp}(x, y)$ satisfies to Helmholtz equation

$$\Delta_{x,y} \psi_{\perp} + \beta^2 \psi_{\perp} = 0, \quad \beta^2 = k^2 - \gamma^2, k^2 = \frac{2m}{\hbar^2} (E - V). \quad (2)$$

Here $\omega = E/\hbar$, E-the total electron energy, $V = V(x, y)$ - potential electron energy, m- electron effective mass, $2\pi\hbar$ - Plank constant. If the boundary barriers are thick enough, the spectrum of the transverse wave numbers β would consist of the finite number of discrete values $\beta_{n,l}$ (n,l=1,2,...,N,L). for 1D structures and β_n (n=1,2,...,N) for 2D structures. The values of the wave number depend on the boundary barrier height and on the waveguide cross-section dimensions. Corresponding wave

functions determine the electron waves (wave modes) spectrum.

$$\psi_{n,l} = \exp[-i(\omega t - \gamma z)] \psi_{\perp n,l} \quad (3)$$

Each wave mode describes an electron state in an energy subband with a fixed transverse energy

$$E_{\perp n,l} = \frac{\hbar^2}{2m} \beta_{n,l}^2 \quad (4)$$

and with the longitudinal propagation constant equal, at $V(x,y) = V = \text{const}$, to

$$\gamma_{n,l} = \left[\frac{2m}{\hbar^2} \right]^{1/2} \left[E - (V + E_{\perp n,l}) \right]^{1/2} \quad (5)$$

Only lowest wave modes (having small n,l) propagate along waveguide without damping. They correspond to electrons having kinetic energy $E - V > E_{\perp}$. These electrons move in the waveguide along zigzag trajectories at angles $\alpha_{n,l} = \arctg\left(\frac{\beta_{n,l}}{\gamma_{n,l}}\right)$ to the waveguide axis.

Higher, exponentially damping wave modes are excited at waveguide discontinuities, they correspond to electrons scattered at angles other than $\alpha_{n,l}$. In equation (5) item

$E_{\perp n,l}$ is additive to the internal waveguide potential V and may be called "quasipotential". One can introduce into the waveguide a quasipotential barrier (QPB) or a quasipotential well (OPW) by varying at some place a form or dimensions of a waveguide crosssection and control by this way an electron transport. As example we will consider a 2D electron waveguide formed by two infinitely high potential barriers which are parallel one to another. Let us suppose that a waveguide section II having width W and length l is inserted in a regular waveguide I with width w . The inner potential V is supposed to be constant and equal to null. Section II forms for electrons in n -th subband a quasi potential barrier (if $W < w$) or quasipotential well (if $W > w$). For the evaluation of an electron transmission coefficient T of the section II it is necessary to "sew together", the wave functions of all wave modes at it's boundaries. This problem simplifies itself if the electron energy E lies in the interval $(E_{\perp 1})_I < E < (E_{\perp 2})_I$ so that only one lowest wave mode propagate through the input and output sections of the waveguide I. At this condition, one has, neglecting excitation of the higher modes:

$$T = \frac{2 \exp(-i\gamma_{ii} l)}{2 \cos \gamma_{ii} l - i \left(\frac{\gamma_{iI} w}{\gamma_{ii} W} + \frac{\gamma_{ii} W}{\gamma_{iI} w} \right) \sin \gamma_{ii} l} \quad (6)$$

where $\gamma_{i,ii}^2 = k^2 - \beta_{i,ii}^2$; indexes i and ii relate to waveguides I and II correspondingly. Formula (6) will

coincide with the well known expression for a flat potential barrier or potential well [1], if one put $W = w$,

$\beta_{1,i}^2 = 0, \beta_{1,ii}^2 = 2mV/\hbar^2$. We have investigated the features of the QPB in electron waveguides by the numerical simulation using algorithm derived earlier for electromagnetic wave waveguides, taking into account all wave modes [2]. There was found that electron scattering at QPB influences the electron transmission probability decreasing the steepness of its dependence on the electron energy because of higher modes excitation.

3. POPULATION INVERSION.

New effects arise in an enlarged waveguide section where two or more electron wave modes can propagate. One of the those effects is the population inversion between discrete energy levels (energy subbands) at longitudinal electron transport through nonregular quantum channels. Let us consider, for example, electron transport along a plane 2D electron waveguide, that width changes stepwise from a_I to $a_{II} > a_I$ at $Z = Z_I$. Suppose that the electron energy E lies between the first two discrete transverse energy levels in the first waveguide section I with the width a_I :

$$E_c \equiv E_{1,i} < E < E_{2,i}, \text{ where } E_{j,i} = \frac{\pi^2 \hbar^2}{m(a_I)^2} j^2$$

$$E > E_{j,ii} \text{ where } E_{j,ii} = \frac{\pi^2 \hbar^2}{m(a_{II})^2} j^2, \quad (7)$$

then the higher modes with $j = 2, 3, \dots$ can be excited in the second section II. In other words at these conditions electrons distribute themselves between several energy subbands that lower band-edges are determined by (7). Alignment of the electron numbers at different subbands is conditioned by the overlapping of the corresponding

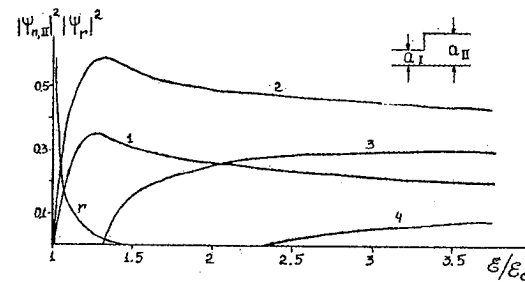


Fig.1 Relative electron populations in the first four energy subbands of the waveguide section II in dependence on the relative electron energy; $a_{II}/a_I = 2.2$.

transverse wave functions $\psi_{\perp j,ii}(x)$ and $\psi_{\perp 1,i}(x)$, namely by the integral:

$$Y_{1j} = \frac{1}{a_1} \int_0^{a_1} \psi_{1,1,i}(x) \psi_{1,j,ii}^*(x) dx. \quad (8)$$

The more is a value of this integral, the more is a number of electrons in a corresponding subband, proportional to $|\psi_j|^2$. The population inversion is determined as $|\psi_{j,ii}|^2 > |\psi_{(j-1),ii}|^2$.

In Fig.1 are shown, for example, functions $|\psi_{j,ii}|^2$ in dependence on the ratio of electron energy E to the critical energy $E_c \equiv E_1$, for 2D flat waveguide with asymmetrical rectangular step (see inset in Fig.1).. There are seen several regularities.

1. Probability of the electron reflection from a waveguide step $|\psi_r|^2$, which is near one at electron energy E close to the critical energy E_c , decreases sharply with increase of energy: $|\psi_r|^2 < 10^{-2}$, if $E/E_c > 1.4$.

2. After a symmetrical step only odd subbands are populated. The population inversion between these subbands is absent at any value of electron energy. At the same time population inversion exists between neighboring (odd and even) subbands.

3. The effectiveness of the electron transfer to the higher subbands is much greater for an asymmetrical step than for symmetrical one. The electron population at higher subbands is the larger the larger is a step height and an electron energy.

4. A ratio of the electron concentration in the higher subbands to that in the lowest one increases with electron energy. The population inversion occurs beginning from a certain threshold values of the electron energy. These threshold energies are the lower the larger is a step height.

5. If an asymmetrical step is large enough, the electron concentration in the second subband goes through a maximum at the electron energy, at which the occupation of the third subband begins. Degree of a population inversion can be greater than 2 (Fig.1).

Population inversion can also take place at electron transport along a quantum channel with constant crosssection if a profile of the transverse potential $V(x,y)$ changes abruptly in a certain plain.

A possibility of a population inversion formation at longitudinal electron transport opens a way to design lateral lasers as well as single channel interference transistors and other devices based on the interference of electron waves traveling along EWs.

4. SINGLE CHANNEL INTERFERENCE TRANSISTORS AND ELECTRON FILTERS.

The ballistic interference transistors were proposed about 10 years ago by S. Data et. al. [3]. Their idea was to use two separated quantum channels along which two electron waves propagate. This waves interfere at the common output of the channels. One can change an output electron current by the help of a transverse magnetic or electric fields that change an interference pattern (so called Aaronov-Bohm effect). But, as far as I know, this elegant idea didn't realized up to day because mainly of technological difficulties.

Meanwhile, as we have seen, two or more independent electron waves can be excited in a single quantum channel. This wave modes correspond to electrons, which move ballistically along a channel being in the different energy subbands. These electrons have different longitudinal velocities and the corresponding electron waves have different phase velocities. Their interference gives electron wave pattern, which depends on the relative wave amplitudes and phases. There was shown above, that the relative amplitudes of the electron waves, excited at the abrupt junction of two different electron waveguide sections, as well as their phase velocities can be changed by the changing the junction dimensions or a transverse electric field in one of these sections. This mechanism can be used for implementation of the single channel transistors, electron energy filters and other devices.

For better understanding of the waves interference picture we have analyzed the simple model which could be evaluated exactly by the help of algorithms that had been found earlier for electromagnetic waveguides simulations [4]. We have considered a 2D EW with asymmetrical quasipotential quantum well formed by a waveguide section II of length L and width W larger then width w of the input and output waveguide sections (see in set in Fig. 2). If the conditions

$$E_{1,i} \equiv E_c < E < 4E_c, \quad W/w < \frac{(n+1)}{2} \quad (9)$$

are fulfilled only one wave mode can propagate along a regular EW, but in enlarged section may propagate n modes with different propagation constants (5) There can exist different interference effects in the section II, aroused at repeated reflections and wave mode transformations at the input and output width steps. At each reflection one wave mode excites $(n+1)$ propagating waves (excepting infinite number of nonpropagating waves) - one wave which propagates in waveguide I, the second is the reflected wave of the same wave mode and besides - $(n-1)$ reflected waves corresponding to other wave modes. Therefore an interference pattern becomes rather intricate and can not be described analytically. Some results of numerical calculations accomplished on

the bases of the electromagnetic - electron wave analogy are presented on Fig.2, where transmission coefficient is given in dependence on the relative electron energy for two values of section II width.

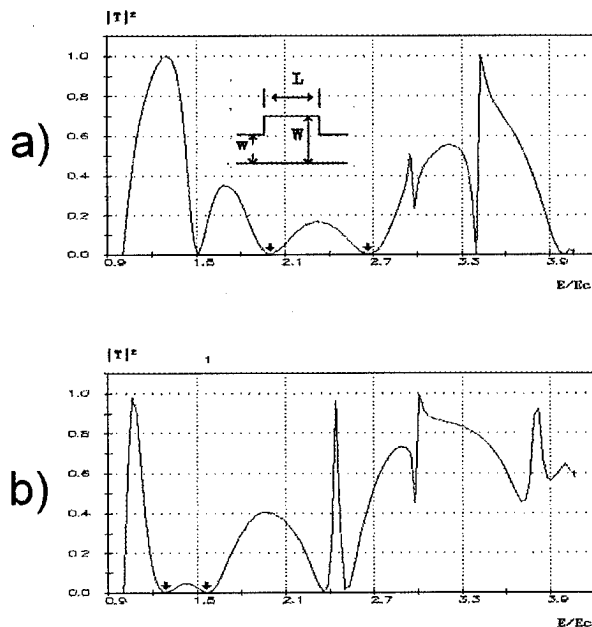


Fig 2 Dependence of electron transmission coefficient on relative electron energy: $L/w=2.2$; a) $W/w=2.0$, b) $W/w=2.2$.

According to (9) up to four subbands (wave modes) can exist in the section II at $2 < W/w < 2.5$. Distinctive peculiarity of this picture is the presence of more or less sharp resonances which number increases with the increasing of the propagating wave modes number. The extremal values of the transmission coefficient are, as a rule, near to one or to null. Resonance electron energies decrease gradually with the increasing of the EW width. It is difficult to identify in general case all extremums with the interference of the determined wave modes. However, two extremal electron energies which are shown at Fig.2 by the arrows, are apparently due to interference of two first forward wave modes. As is known, two plain waves propagating in the one and the same direction with equal amplitudes and different propagation constants $\gamma_1, \gamma_2 = \gamma_1 \pm \delta\gamma$ conceal at distance L determined by the condition: $\cos \delta\gamma L = -1$. This condition gives a series of single extremal energy values where transmission coefficient goes to null. But in considered case where two essentially non plain electron waves interfere at the junction of two EWs, the wave fadings could take place at pairs of two neighboring electron energies located near the same extremal energy values as it really takes place in Fig.2. Fig.2 testifies a principal possibility of the use of electron wave interference in a single quantum channel

for the effective control of electron transfer through this channel by changing a quasipotential well width. The similar result gives a change of the transverse potential distribution in a short section of a quantum channel with constant crosssection. Considered effects could be verified on the basis of a HEMT-like heterostructures with lateral hot electron injection and nanometer gate length [5]. As Fig.2 shows, on this way one can implement transistors with positive as well as with negative transconductance which value remains high enough at average electron injection energies about 0.2 - 0.3 eV dispersed over 0.03 - 0.05 eV. From the other side, the same effects may be applied for design of electrically controllable band pass and rejecting electron energy filters. A possibility of the frequency band tuning is important advantage of these filters in comparison with superlattice ones.

5. CONCLUSION

It is shown that there are at least two different way for effective control of the ballistic electron transport in quantum sized heterostructures: a creation of the quasipotential barriers by a local deformation of the quantum channel (electron waveguide) crosssection, as well as by its inner transverse electric field change, and the use of interference between several electron wave modes excited in a quantum channel at step-like discontinuities.

It is possible to make electron population inversion between electron energy subbands at the longitudinal electron transport along essentially non regular quantum channels.

It is possible to design single channel interference transistors and electrically tunable electron energy filters. These and similar devices should be suitable for the terahertz frequency band mastering.

The author wishes to thank V.I.Vasiliev and I.P.Chepurich for numerical calculations and helpful discussions. The work was partly sponsored by the Russian Scientific Foundation and the State Scientific Committee.

REFERENCES

1. D. Bohm Quantum theory, N.Y., 1952.
2. V.I.Vasiljev, A.S.Tager, Journ. of Techn.Phys.Lett., 1994, v.20, p.72, (in Russia).
3. S.Datta et. al., Phys. Rev. Lett., 1985, v55, p.3244
4. R.A.Silin, I.P.Chepurich, Radioengineering and Electronics, 1990, v.35, p.287, (in Russia).
5. A.B.Pashkovsky, A.S.Tager, Electron. Techn. ser.1, Electronica SVCH, 1992, v.5, p.21.

Analysis of the Monolithic SAW Memory by Using Green's Function

T. E. Taha and M. El-Kordy

Dept. of Electric Comm. Eng., Faculty of Electronics Eng., Menoufia University,
32953 Menouf, Egypt.

ABSTRACT

A detailed analysis of monolithic surface acoustic wave (SAW) Schottky diode memory correlator is presented. Based on Green's function concept, an efficient formalism for the calculation of the spatial charge density distribution of the diode is obtained. An equivalent circuit model has been proposed for determining the effective potential induced in the diode by the electric field associated with the SAW. The attenuation as well as the device efficiency are also calculated. The calculated results are verified by comparison with measured results.

1. INTRODUCTION

The concept of an acoustoelectric memory was first implemented with gap coupled device utilizing storage in surface states at the SiO₂/Si interface [1]. The surface states are difficult to control and they were soon replaced by Schottky barrier diode [2] and p-n diode [3-4]. Schottky diodes are majority carrier devices and exhibit very fast write time, suitable for wideband applications. The Green's function [5] technique has been used for studying the Schottky diode gap-coupled as well as strip coupled devices [6].

In this paper a detailed analysis of monolithic surface acoustic wave (SAW) Schottky diode memory correlator is presented. The Schottky diode charges are estimated through the solution of Poisson's equation by using Green's function. The depletion layer capacitance is determined by using the estimated charges. An equivalent circuit model has been used for determining the effective potential induced in the diode from the SAW electric field. The device efficiency as well as the output power delivered to 50 ohm load are calculated by solving the equivalent circuit. Good agreement between the obtained results and published data is achieved.

2. THEORY

The boundary conditions for the given configuration of Fig. 1 are assumed to be:

Magnetic wall: $\delta \Phi / \delta x = 0$ for $x = +P/2$

Electric wall: $\Phi = 0$ at the depletion layer boundary. The Green's function which satisfy the previous boundary condition has been found by using Fourier series as:

$$G(x/x_0, y/y_0) = -(1/2K) \text{Log}[1-2 \cosh B(x-x_0) \cdot \text{Exp}(-B(y-y_0)) + \text{Exp}(-2B(y-y_0))] + (j/2K) \text{Log}[1-2 \sinh B(x-x_0) \cdot \text{Exp}(-B(y-y_0)) + \text{Exp}(-2B(y-y_0))] \dots \dots \dots (1)$$

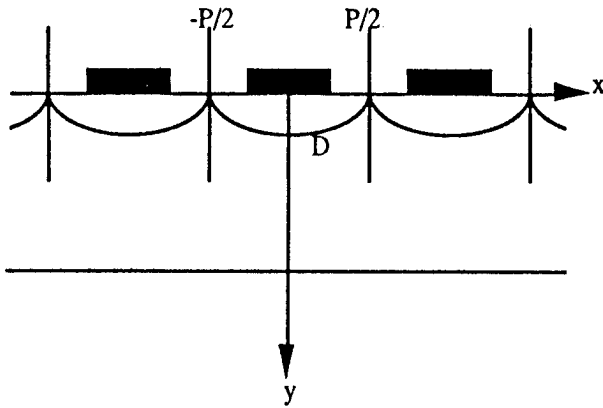


Fig.1 Periodic structure.

The Green's function has been used for solving the Poisson's equation in the following plain

$$D = [-p/2, p/2], [0, y(x)]$$

and the following expression is obtained

$$V(x, y) = \frac{1}{\epsilon} \int_D \rho(x, y) \cdot G(x/x_0, y/y_0) \cdot dx_0 \cdot dy_0 + \Gamma \dots \dots \dots (2)$$

$$\Gamma = \int \left(V \frac{\delta G}{\delta n} - G \frac{\delta V}{\delta n} \right) d\Gamma' \dots \dots \dots (3)$$

where Γ' is the contour of D

By solving the previous equation the quasi static charge has been determined. Also, eq. 2 can be write at the boundary of the depletion layer in the form:

$$\frac{\delta V}{\delta n} = \frac{1}{\epsilon} \int_D \rho(x_0, y_0) \frac{\delta G(x/x_0, y/y_0)}{\delta n} \cdot dx_0 \cdot dy_0 + \frac{\delta \Gamma}{\delta n} \dots \dots \dots (4)$$

and the surface impedance Z_s can be estimated as

$$Z_s = j \frac{K_s^2}{\epsilon_s} V \frac{\delta V}{\delta n} \dots \dots \dots (5)$$

The proposed equivalent circuit is shown in Fig.2 ;where R_L is load resistance, R_C is the sheet resistance of the metal-contact and Z_s is the surface impedance as calculated in eq. 5

The $V_{o.c}$ of fig. 2 is given by:

$$V_{o.c} = \sqrt{V_r \cdot V_s} \dots \dots \dots (6)$$

Where V_r and V_s are given by [7]:

$$V_r = \sqrt{2 \cdot (P_r/w) \cdot k^2 / \omega \cdot \epsilon_0 \cdot (1 + \epsilon_p)}$$

$$V_s = \sqrt{2 \cdot (P_s/w) \cdot k^2 / \omega \cdot \epsilon_0 \cdot (1 + \epsilon_p)}$$

w is the beamwidth of the acoustic signal

k is the wavenumber

P_r is the power of reading signal

P_s is the power of writing signal

The output power delivered to the load resistance is calculated by solving the circuit of fig. 2.

The efficiency as well as the attenuation due to the presence of Z_s have been also calculated.

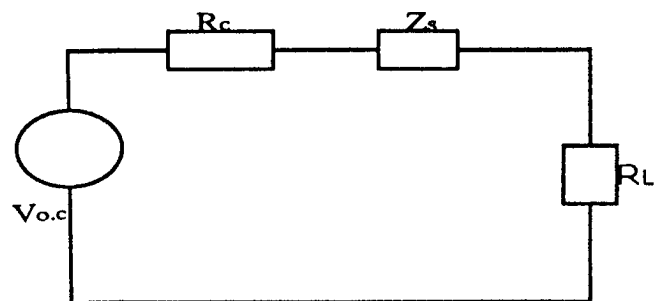


Fig.2 Equivalent circuit.

3. RESULTS AND DISCUSSION

The relation between real and imaginary part of Z_s is illustrated in fig. 3. The resistive part is increased to reach the maximum value at $5UT$ for doping concentration of $1. E17 \text{ cm}^{-3}$ and at $10 UT$ for doping concentraion of $2.5 E17 \text{ cm}^{-3}$.

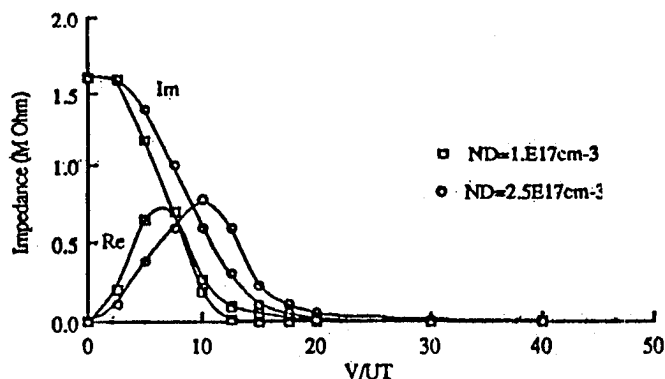


Fig. 3 Relation between surface impedance and diode surface potential

The variation of attenuation with peak value of storage impulse is illustrated in fig. 4. The attenuation can be minimized by varying the diode biase potential with doping density. It is greatly effected by varying the peak of the storage impulse in range less than $15UT$ in case of $ND=1.E17 \text{ cm}^{-3}$ and in range less than $18UT$ in case of $ND= 2.5E17 \text{ cm}^{-3}$. Over the previous range the storage impulse has littel effect on the attenuation.

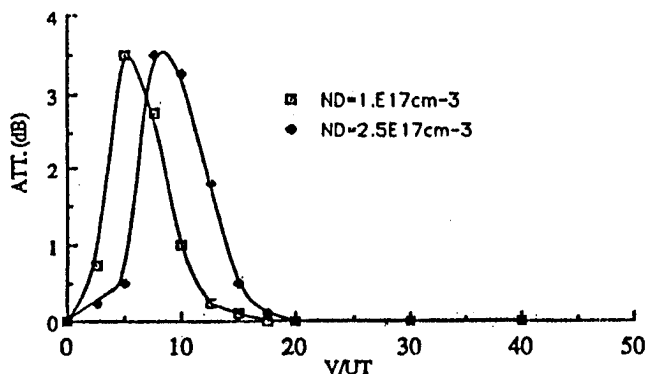


Fig. 4 Relation between attenuation and diode surface potential

Fig. 5 indicate the relation between the efficiency and peak value of the storage impulse. This relation is plotted at doping density of $ND= 1.6E17 \text{ cm}^{-3}$ as proposed by Wager [8]. It is can be noticed the value of the correlation response is greatly effected by the lower values of storage impulse while higher values has littel effects. The figure includes also the experimental data of Weger [8]. Our results gives good agreemnt at lower values of storage impulse while at values greater than $100UT$ there is divergence between our results and experimentals.

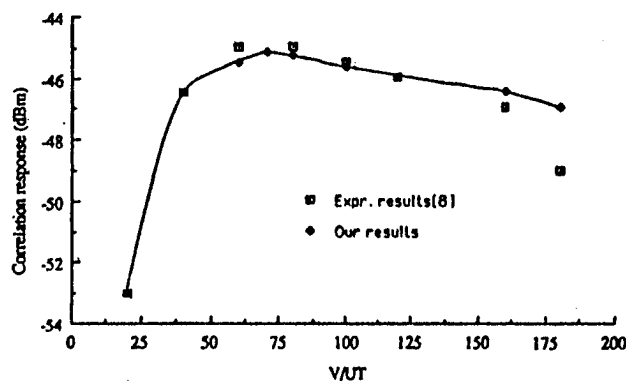


Fig. 5 Relation between the correlation response and diode surface potential

4. CONCLUSION

A new technique for calculating the output power of the monolithic SAW Schottky diode memory correlator has been presented. in this technique, an equivalent circuit model is proposed. The surface impedance has been calculated by using Green's function technique through new formula. It is found that the output power as well as the attenuation are greatly effected by small values of storage impulse while higher values has littel effect. The predication of this technique

given good results in comparison with published data specially at lower values of storage impulse.

REFERENCES

- [1] A. Bers and J. H. Cafarella, " Surface state memory in surface acoustoelectric correlator", Appl. Phys. Letters 25, pp.133-135 ,(1974).
- [2] K. A. Ingebrigtsen, R. A. Cohen, and R. W. Mountain, " ASchottky-diode acoustic memory and correlator," Appl. Phys. Letters 26, pp. 596-598 ,(1975).
- [3] C. Maerfeld, Ph. Defranould, and P. Tournois, "Acoustic storage and processing devices using p-n diodes", Appl. Phys. Letters 27, pp.577-578, (1975).
- [4] M. Elnokali, "Theory of the p-n diode SAW storage correlator in the flash mode", IEEE Trans. sonic ultrason. Vol. su-32, pp. 728-733, (1985).
- [5] M. El-kordy, "Some investigations on SAW devices for communication systems", Ph.D. Thesis, Menoufia University, Egypt, (1991).
- [6] M. El-kordy, A. Abou El-Fadl, and T. E. Taha, "Study of acoustoelectric memory for spread-spectrum communication by using Green's function", in Proc. of EUROEM94 conference , Bordeaux, France, (1994).
- [7] K. M. Lakin, "Perturbation theory for electromechanical coupling to electric surface wave on piezoelectric substrates", J. Appl. Phys. Vol. 42, pp.899-906, (1971).
- [8] R. Wager, "Principles of strip-coupled SAW memory correlator" IEEE Trans. Sonic Ultrason. Vol. su-32, pp. 716-727, (1985).

AN INTEGRATABLE CURRENT-TUNABLE R-L OSCILLATOR

B. Srisuchinwong and N.V. Trung

Department of Electrical Engineering
International Institute of Technology, Thammasat University
P.O.Box 22, Thammasat Rangsit Post Office, Patumthani 12121, Thailand
banlue@ipied.tu.ac.th

ABSTRACT

In this paper, a new integratable oscillator is presented through the use of a new current-tunable R-L filter. The oscillation frequency is current-tunable in excess of three orders of magnitude. Existing methods for on-chip inductors (L) are encouraged in implementing for this oscillator so as to enable very high oscillation frequencies. The paper suggests an alternative to integratable oscillators of "inductorless" types.

1. INTRODUCTION

High-frequency discrete-component oscillators use inductors (L) routinely. As inductors were not previously possible to fabricate in monolithic form [1], integratable oscillators were commonly of "inductorless" types [2,3]. Recently, methods for implementing inductors on-chip have been reported [4-6] and integratable high-frequency oscillators using inductors on-chip are increasingly of interest [1,5,7]. In this paper, a new integratable oscillator is presented through the use of a new current-tunable R-L filter (where R represents resistance). The existing methods [4-6] can also be suggested for implementing the on-chip inductors (L) of this oscillator.

2. CIRCUIT DESCRIPTIONS

Figure 1 shows the basic circuit configuration of the integratable current-tunable R-L oscillator. The four matched npn transistors Q1 to Q4 and the two matched inductors L1 and L2 of value L form a new R-L bandpass filter, where the input voltage is applied to the bases of Q3 and Q4, and the output voltage is taken across the emitters of Q1 and Q2.

The resonant frequency of the filter is tunable using a current-tunable resistance $R = 2r_e$, where r_e is the small-signal dynamic resistance of a forward-biased base-emitter junction of a bipolar transistor. Such a filter forms a counterpart of the current-tunable RC filter previously described in Pookaiyaudom et al [2]. The pair of Q10 and Q11 forms a differential amplifier that provides an appropriate gain for oscillation to be initiated and sustained. The matched npn transistors Q5 to Q9 form the Wilson current mirrors and convert the frequency setting current I_f to bias transistors Q1, Q2, Q3 and Q4. The loop-gain setting current I_g biases transistors Q10 and Q11. The output waveforms of the oscillator are taken across the collectors of Q10 and Q11, and can be amplified to appropriate levels for applications.

3. IDEAL ANALYSIS

Referring to Figure 1, assuming that the bases of Q3 and Q4 are temporarily disconnected with the collectors of Q10 and Q11. Let the small-signal input voltage across the bases of Q3 and Q4 be v_{in} , and the resulting small-signal output voltage across the collectors of Q10 and Q11 be v_o . One can show that the transfer function v_o/v_{in} can be expressed as

$$\frac{v_o}{v_{in}} = G \frac{s\tau}{(1 + s\tau)^2} \quad (1)$$

$$\text{where } \tau = \frac{L}{R} = \frac{L}{2(r_{e3,4})} = \frac{L}{2} \left(\frac{I_f}{V_T} \right) \quad (2)$$

G is equal to $R3/r_{e10,11}$, $r_{e10,11}$ is r_e of Q10 or Q11, $r_{e3,4}$ is r_e of Q3 or Q4, R3 is the load resistance of the differential amplifier, and V_T is the usual thermal

voltage associated with a pn junction and is approximately equal to 25 mV at room temperature.

By reconnecting the feedback loop, the steady-state sinusoidal oscillations can be sustained if the ratio v_o/v_{in} shown in (1) becomes unity. Therefore, one obtains

$$G = R3 \left(\frac{I_g}{2V_T} \right) = 2 \quad (3)$$

$$\omega_0 = \frac{1}{\tau} = \frac{2}{L} \left(\frac{V_T}{I_f} \right) \quad (4)$$

where (3) gives the required value of G to sustain steady-state sinusoidal oscillation, and (4) provides the angular frequency of oscillation.

4. SIMULATED RESULTS

The performance of the circuit shown in Figure 1 has been simulated using a circuit simulator package ViewSpice [8], running on a 32-bit personal computer. The npn and pnp transistors are modelled by QMPS2222A and QMPS3640, whose transition frequencies f_T are at 300 and 500 MHz, respectively [8]. For the simulation purposes, the value L is equal to 159 μ H. Figure 2 illustrates the simulated results

of the output waveforms versus I_f at $I_g = 4.4$ mA and $R3 = 25\Omega$. It can be seen from Figure 2 that the amplitude of the oscillation is well maintained at constant values for $I_f > 100$ μ A. Figure 3 depicts comparisons, between ideal and simulation cases, of plots of oscillation frequency versus the bias current I_f . It can be seen that oscillation frequencies obtained from both cases are almost similar and linearly tunable, through I_f , in excess of three orders of magnitude.

The spectrum of the output waveform at 60 KHz, for example, is shown in Figure 4. It can be seen that the second and third harmonics are approximately at 48 and 38 dB down, respectively, from the fundamental frequency. Figure 5 depicts comparisons, between ideal and simulation cases, of plots of oscillation frequency versus the inductance value L at $I_f = 1$ mA.

5. DISCUSSION AND CONCLUSIONS

A new current-tunable R-L Oscillator has been described. Oscillation frequencies are linearly tunable in excess of three orders of magnitude. By using better transistors with very high f_T (e.g. in the region of GHz) and much smaller value of L (e.g. in the region of nH using integratable bondwire inductance [5]), high oscillation frequencies (e.g. in the region of GHz using eq. 4) can be expected.

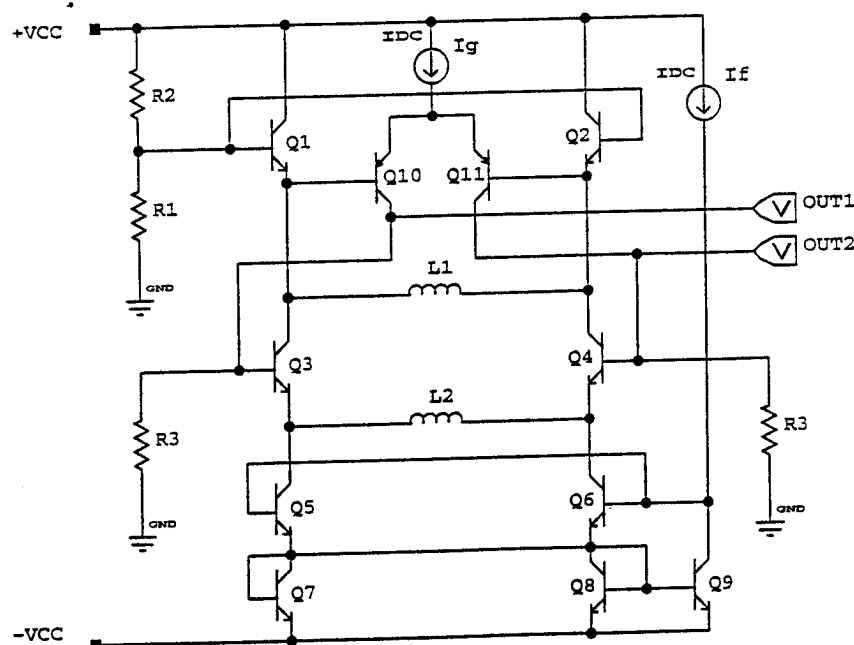


Figure 1: Schematic diagram of the integratable current-tunable R-L oscillator.

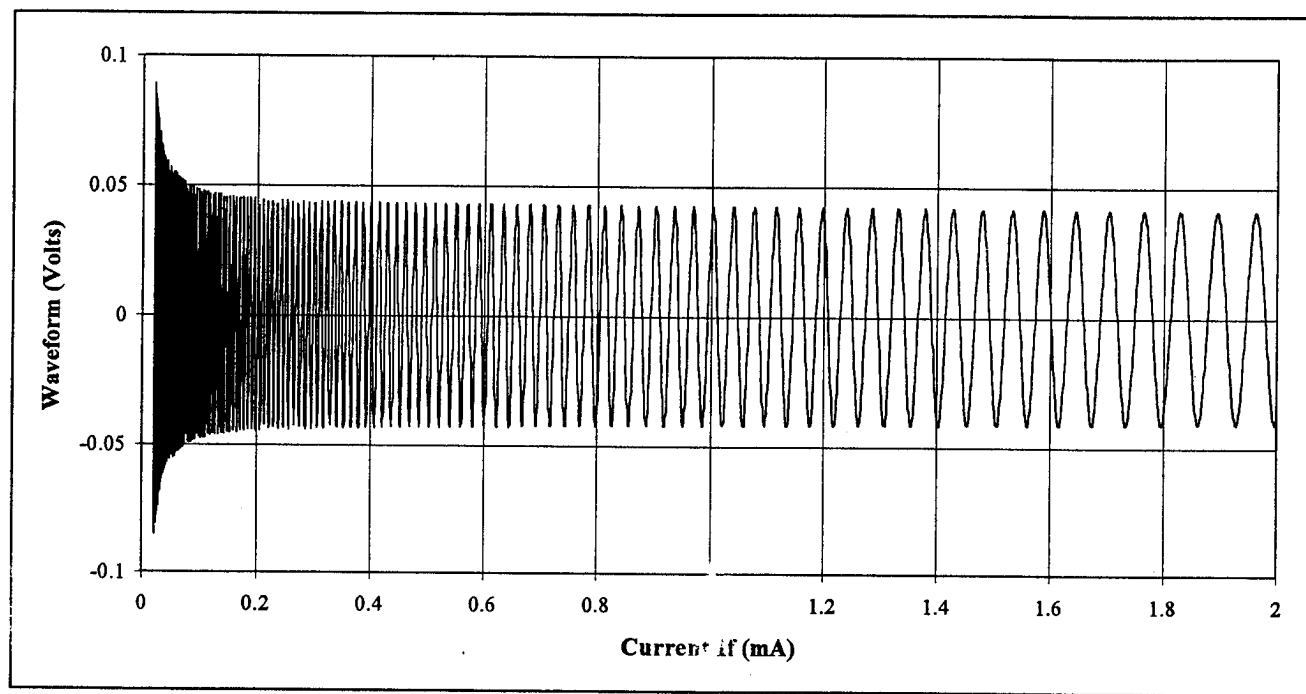


Figure 2: Oscillograms at various frequencies versus bias currents I_f

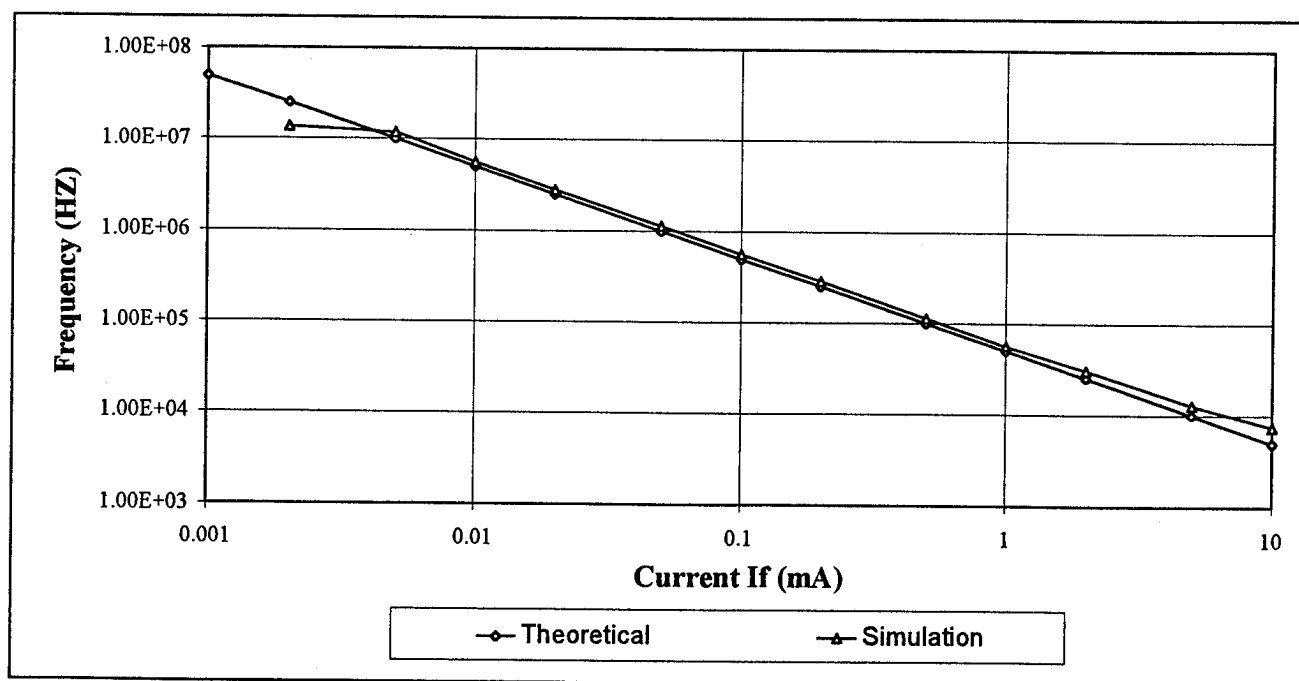


Figure 3: Plots of oscillation frequencies versus bias currents I_f

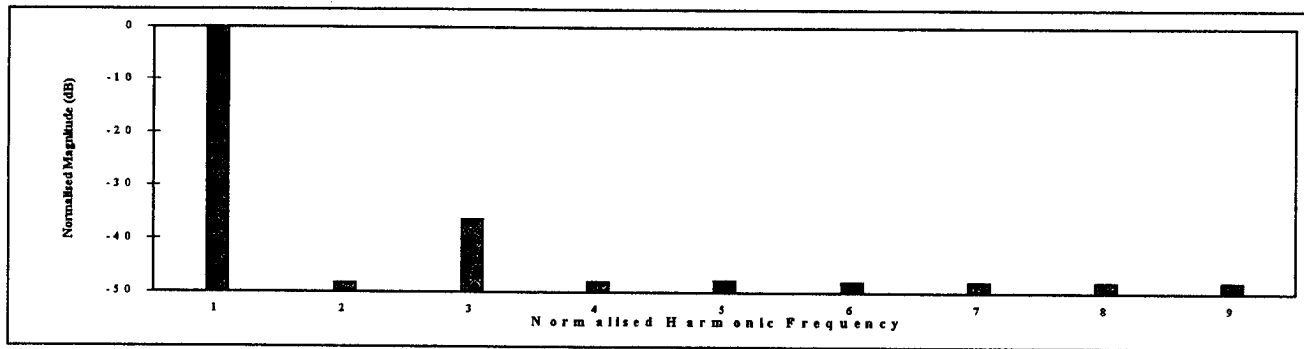


Figure 4: Frequency spectrum of output waveform at $I_f = 1\text{mA}$, $f_1 = 60\text{ KHz}$

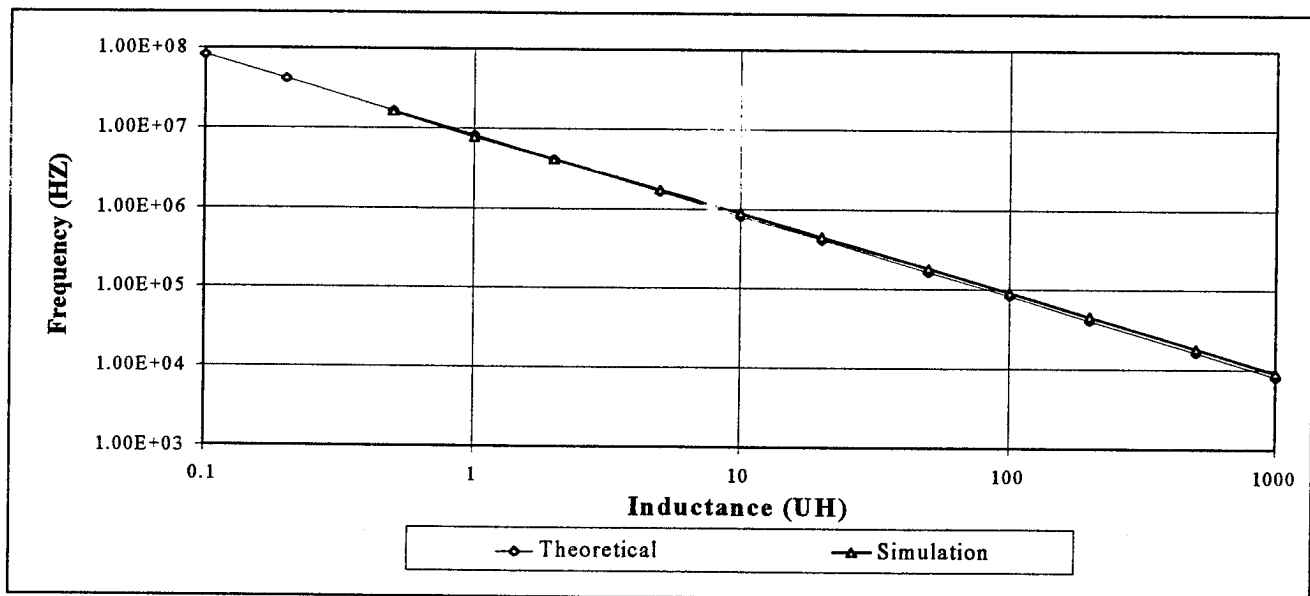


Figure 5 : Plots of oscillation frequencies versus values of inductance

REFERENCES

- [1] Nguyen, N.M. and Meyer, R.G., "A 1.8-GHz Monolithic LC Voltage-Controlled Oscillator", IEEE J. of Solid-State Circuits, vol. 27, no. 3, 1992, pp. 444-450.
- [2] Pookaiyaudom, S., Srisuchinwong, B. and Kurutach, W. "A Current-Tunable Sinusoidal Oscillator", IEEE Transactions on Instrumentation and Measurement, vol. IM-36, no. 3, 1987, pp. 725-729.
- [3] Verhoeven, C.J.M., "A High-Frequency Electronically Tunable Quadrature Oscillator", IEEE J. of Solid-State Circuits, vol. 27, no. 7, 1992, pp. 1097-1100.
- [4] Nguyen, N.M. and Meyer, R.G., "Si IC-Compatible Inductors and LC Passive Filters", IEEE J. of Solid-State Circuits, vol. 25, no. 4, 1990, pp. 1028-1031.
- [5] Steyaert, M. and Craninckx, J., "1.1 GHz Oscillator Using Bondwire Inductance", Electronics Letters, vol. 30, no. 3, 1994, pp. 244-245.
- [6] Kuhn, W.B., Elshabini-Riad, A. and Stephenson, F.W., "Centre-tapped spiral inductors for monolithic bandpass filters", Electronics Letters, vol. 31, no. 8, 1995, pp. 625-626.
- [7] Gerrits, J.F.M. and Pardoen, M.D., "1.6 GHz VCO with on-chip inductor and varactor diode", Electronics Letters, vol. 31, no. 4, 1995, pp. 293-294.
- [8] ViewSpice User's Manual, Workview PLUS on Windows, Viewlogic Systems, 1993.

ANALYSIS AND DESIGN OF MICROSTRIP POWER DIVIDER

A.M.MOSELHY*

A.M.NASSAR**

M.A.EL_GAZZAR***

* Air Defence Research Center,Cairo, Egypt

** Faculty of Eng., Cairo University, Cairo, Egypt

*** Egyptian Air Academy,44632, Belbies, Sharkia, Egypt

ABSTRACT

Two kinds of power splitter have been designed. The designed circuits have been simulated by using an efficient computer aided analysis program. The program is based on state space approach with no restriction on the network topology. The two circuits have been fabricated by using microstrip technology. The practical measurements and the simulated results are with good agreements

1-Introduction

Power dividers are used to divide the input power into a number of smaller amounts of powers for exciting the radiating elements in any array antenna. They are also used in multi-channel receivers to divide the input power into an equal values of powers for each channel. The power dividers can be used in balanced power amplifiers both as power dividers and power combiners[1].

A Wilkinson coupler offers broadband width and equal phase characteristic at each of its output ports. Fig.(1) shows the schematic diagram of Wilkinson coupler[2]. Wilkinson developed an N-way power divider that would split the input power into output powers at N-ports that would also provide isolation between the output ports[2].

The objective of this paper is to introduce the analytical design of power splitters, compensated and uncompensated power splitters. A computer-aided program based on state space approach has been developed and applied for analysis of the designed circuits in both time and frequency domains. The two circuits are practically fabricated by using microstrip technology. The measured and simulated results are compared.

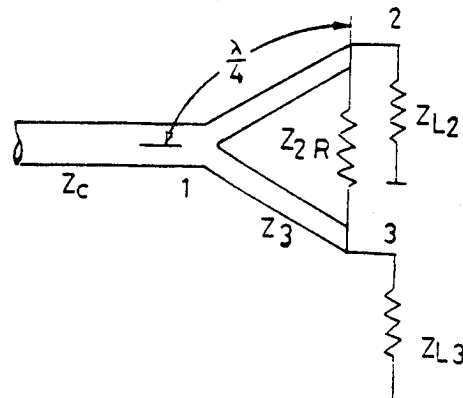


Fig.1 The Wilkinson power divider

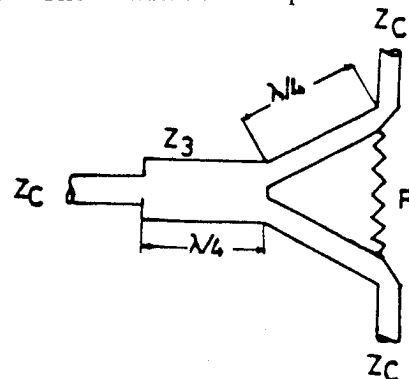


Fig.2. A compensated 3-dB power divider

2- Analytical Design

If we want to split the input power P_1 into output power P_2 and P_3 so that $P_3 = K^2 P_2$ and also maintain zero current in R , Wilkinson[1] express

$$R = \frac{Z_2 Z_3}{Z_c}, \quad (1)$$

$$Z_2 = K \sqrt{R Z_c}, \quad (2)$$

$$Z_{L2} = \frac{K^2 R}{K^2 + 1}, \quad (3)$$

$$Z_3 = \sqrt{\frac{R Z_c}{K}}, \quad (4)$$

and

$$Z_{L3} = \frac{R}{K^2 + 1} \quad (5)$$

Uncompensated 3-dB power splitters

A 3-dB power divider is obtained by choosing $K^2 = 1$ and $Z_{L2} = Z_{L3} = Z_c = 50 \Omega$. From equation (3) and (5), $R = 2 Z_c$ and from equation (2) and (4), we get $Z_2 = Z_3 = \sqrt{2} Z_c$

Compensated power splitters.

A modified design that incorporates an input quarter-wave transformer is shown in Fig(2). For good performance, we must choose[3]:

$$Z_c' = \left[\frac{k}{1+k^2} \right]^{1/4} Z_c, \quad (6)$$

$$Z_2 = K^{3/4} (1+K^2)^{1/4} Z_c, \quad (7)$$

$$Z_3 = \frac{(1+K^2)^{1/4}}{K^{5/4}} Z_c, \quad (8)$$

$$R = \frac{1+K^2}{K} Z_c \quad (9)$$

The performance of a Wilkinson power splitter is improved by the modified design.

3- Simulation Program

A general computer program for the analysis of microwave circuits has been applied. The program is based upon the formulation of the state and output equations using an efficient topological method with no restriction on the topology. The state and output equations for any network can be represented as the following.

(3a) The state and output equations :-

It has been shown [12] that the state variables of a distributed network are the reflected parameters at all the transmission line terminals or ports. The state variables of a lumped/distributed network are the voltages on all the independent capacitors, the currents in all the independent inductors and the reflected parameters (or the reflected voltages) at all the transmission-line ports.

The state equation is the differential - difference equation of the form:

$$\begin{bmatrix} \dot{X}_1(t) \\ X_2(t+T) \end{bmatrix} = \begin{bmatrix} A_{11} & A_{12} \\ A_{21} & A_{22} \end{bmatrix} \begin{bmatrix} X_1(t) \\ X_2(t) \end{bmatrix} + \begin{bmatrix} B_1 \\ B_2 \end{bmatrix} u(t) \quad (10)$$

Where $X_1(t)$ and $X_2(t)$ are the state vectors of the lumped and distributed elements respectively and $u(t)$ is the input vector. The output equation is given by :-

$$y(t) = \begin{bmatrix} C_1 & C_2 \end{bmatrix} \begin{bmatrix} X_1(t) \\ X_2(t) \end{bmatrix} + E u(t) \quad (11)$$

Equations (10) and (11) are derived using topological methods with no restriction on the network topology. Where A,B,C and E are the matrices of the state and output equation of the systems.

When Laplace transform is applied to equations (10) and (11) we obtain the frequency-domain equations.

$$\begin{bmatrix} X_1(s) \\ X_2(s) \end{bmatrix} = \begin{bmatrix} sI_m - A_{11} & A_{12} \\ A_{21} & zI_{2n} - A_{22} \end{bmatrix}^{-1} \begin{bmatrix} B_1 \\ B_2 \end{bmatrix} U(s) \quad (12)$$

$$Y(s,z) = \begin{bmatrix} C_1 & C_2 \end{bmatrix} \begin{bmatrix} sI_m - A_{11} & A_{12} \\ A_{21} & zI_{2n} - A_{22} \end{bmatrix}^{-1} \begin{bmatrix} B_1 \\ B_2 \end{bmatrix} + E U(s) \quad (13)$$

where $z = \exp sT$, I is the identity matrix, m, n are the number of lumped-state elements and transmission lines, respectively.

(3b) Network Analysis Using the State Equations

The previous results are used to analyze lumped/distributed networks in either the frequency or time domain.

(1) **Frequency domain analysis** : is Based on the expansion of the equation (13) to obtain the transfer function of the form.

$$F(s, z) = \frac{\sum_{i=0}^{2n} \sum_{j=0}^m A_{ij} S^j Z^i}{\sum_{i=0}^{2n} \sum_{j=0}^m B_{ij} S^j Z^i} \quad (14)$$

This expansion is achieved by using a modified faddeeva algorithm[10] for the inversion of the two variable matrix in equation (3).

(2)Time domain analysis: The output in the time domain is calculated from equation (11) when the state vector $[X_1(t); X_2(t)]^T$ is known. The state vector is first determined from the solution of (10). Equation (10) represents two simultaneous differential and difference equation :

$$\dot{X}_1(t) = A_{11}X_1(t) + A_{12}X_2(t) + B_1u(t) \quad (15)$$

and

$$\dot{X}_2(t) = A_{21}X_1(t-T) + A_{22}X_2(t-T) + B_2u(t-T) \quad (16)$$

The state vector $[X_1(t); X_2(t)]^T$ is assumed to be zero at $t \leq 0$. The vector $X_2(t)$ is calculated by substituting the values of $X_1(t-T)$, $X_2(t-T)$ and $u(t-T)$ in equation(6). The vector $X_1(t)$ is then calculated by solving the differential equation(15) numerically in each time period $kt < t < (k+1)T$, where $k = 0, 1, 2, \dots$

The state and output vectors have discontinues at $t=KT$ and the initial values of the state vector at the start of each time period are obtained from the condition that the integral of the state vector is continuous. The insertion loss for the compensated power splitter predicted by simulation program are given in Fig.(3).

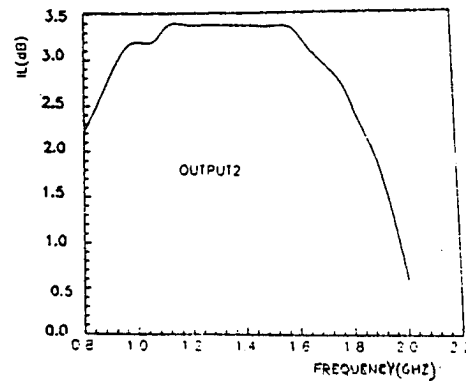
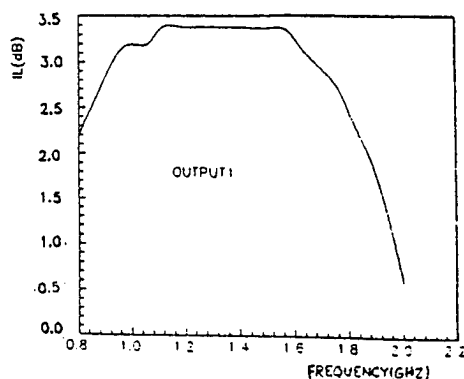


Fig.3.Insertion Loss Versus Frequency(Ghz) of a Compensated type

4- Practical Design

The practical design of two kinds of power splitters is performed according to the following considerations

1-Choice of materials:

Teflon of $\epsilon_r = 10.2$ and $h = 0.635$ mm is chosen for our design. The substrate is copper clad which is widely used in microwave IC'S. The dimension of the substrate is 50.8 mm x 50.8 mm .

2-Microstrip synthesis is carried out to calculate the width and length of the designed circuits according to the design formula obtained in [5]. The layout of the circuits are prepared keep in mind the size of the chip resistor and the microstrip discontinuity. The layout of 1.33 Ghz, 3-dB power divider is shown in Fig.(4)

3-Fabrication Procedures

The practical design is carried out using thin film technique. The chip resistor $R = 100 \Omega$ is connected to each circuit.

4-Practical measurements

The practical measurements are performed on the designed power splitters after fixing it by a substrate holder. Input signal ranging from 1Ghz to 1.5 Ghz is applied to the input port of the power divider. The output is measured at the two outputs by using spectrum analyzer. The IL versus frequency characteristic is shown in Fig.5. for the compensated type.

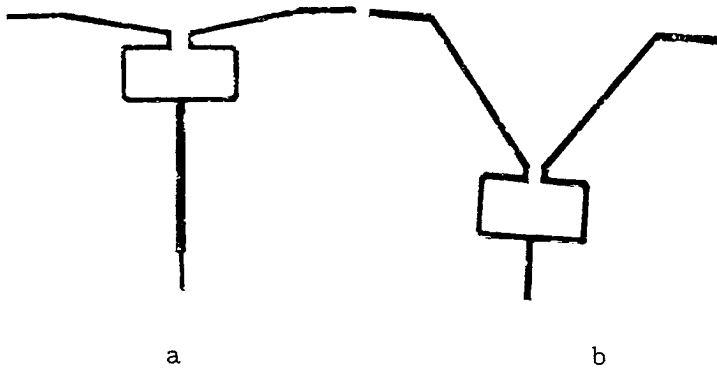


Fig.4. The layout of (a) Compensated type
(b) Uncompensated type

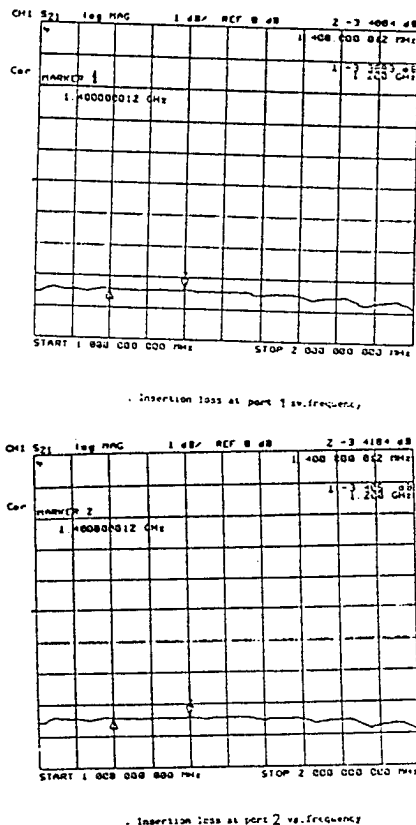


Fig.5.The insertion loss versus frequency
(Ghz) of compensated type

5-Conclusion

The design procedure of microstrip directional couplers are presented. The computer aided analysis adopted in this paper is with good stability and suitable computation time. The results show good agreements between predicted simulated values was due to imperfection associated with the connectors used and the fabrication tolerances.

6 References

- [1]R.E.Collin, "Foundation of microwave engineering", McGraw-Hill, Inc. 1992
- [2]I.Bahl and P.Bhart, "Microwave Solid State Circuit Design",John Wiley & Sons. 1988
- [3]S.B.Cohn , "A class of broadband 3-port TEM hybrids, " IEEE Transaction vol. MTT-16, PP.110-118.
- [4]Gupata. k.C.R. Garg and I.J.Bahl, "Microstrip lines and slot lines", pretech house, Dedham, Mass.,1979
- [5]P.Bahartia. " Microwave Solid State Circuit design"
- [6]T.C.Edwards, "Foundations of Microstrip Circuits Design", Jon Widley & Sons.1992
- [7]L.O CHua and P.Lin, "Computer- Aided Analysis of Electronic Circuits", Prentice-Hall,1975.
- [8]K.Lee and S.Park, "Reduced Modified Nodal Approach to circuit Analysis" ,IEEE TRAN. on Circuit and Systems, Vol.CAS-32,No.10,1985.
- [9]I.R Bashkow, "The A Matrix, New Network Description" IRE Tran. Theory, Vol.CT-4,PP.117-119,1957.
- [10]FADDEEVA, V.N.: " Computational methods of linear algebra" (Dover, New York, 1959)
- [11]WALTER BANSZAF, "Computer- Aided Circuit Analysis Using Spice",Prentice-hall ,1989.
- [12]SOBHY, M.I.: Topological derivation of the state equation of networks containing commensurate transmission lines, Proc. IEE, 1975, 122,(12), PP. 1367-1371
- [13]J.K. Fidler, "Computer-Aided Circuit Design", Thomas Nelson, 1978
- [14]Esmat.A.F. Abdallah (Elect.Res.Inst.), E.A.Hosny (Kentuniv.U.K), M.A.Nassef and A.M.Moselhy (M.T.C) "Computer Aided Analysis of Microwave Integrated circuits using An Efficient Topological Method" proceeding of the Eighth National Radio Science Conference NRSC'91, Cairo ,Egypt, Feb. 19-21,1991.
- [15]A.M.NASSAR,A.M.MOSELHY, M.M.EL-GAZZAR, "Computer Aided Analysis And Design of Linear Lumped/Distributed Networks Using Topological Algorithm", Twelfth National Radio Science Conference, March 21-23, 1995, Faculty of Eng. Alexandria, University,Egypt.

APPLICATION OF BWO FOR EXCITATION OF THE INTENSIVE NOISE SIGNALS OF MILLIMETER WAVE BAND

Vladimir A. Rakityansky

Institute of Radiophysics and Electronics
National Academy of Sciences of Ukraine
12, Acad. Proskura St.
310085 Kharkov, Ukraine
ire@ire.kharkov.ua

ABSTRACT

In the paper the problems connected with the intensive noise oscillation excitation in millimeter wave band are studied. With this aim in mind the O-type Backward Wave Oscillators, operating in chaotic oscillation regime, are proposed to use. The large advantages of the method suggested are the high efficiency, universal power spectrums and feasibility of electronic tuning of the noise oscillation frequency. Low voltage packaged noise sources, operating over the band from 30 to 60GHz, make possible output power of 8 – 25W and 4W respectively and 3 – dB power spectrum width more than 300MHz.

1. INTRODUCTION

Noise oscillations play an important role in modern microwave and millimeter environment. Noise oscillations, first and foremost, are the optimal kind of signals for radars, having high accuracy of measurement both distance and velocity simultaneously. Noise oscillation sources with output power of about some watts are used in jamming systems to confuse radars or communications, active radiometry and in measurements as a source of imitate signals. This raises the problem of creation of the compact and effective noise oscillation sources with power spectrum width and output power needed. The problem is especially urgent for millimeter wave band.

The various modulators are generally used for excitation of the oscillations with complicated power spectrum. The modulators act on the single-frequency sources, by random manner, or

on the passive super high frequency circuit elements (such as a pin-structures or its combination with circulator). The noise oscillation sources are known too, based on the Travelling Wave Tube with external delay feed back, or on the series network of solid noise source and Travelling Wave Tube Amplifier. The methods of the noise oscillations excitations, listed here, are of complex design and operating. An additional point to emphasize is that the wideband modulator realizing, for middle-power sources, is individual complex problem and the Travelling Wave Tube application encounters a difficulties in middle and higher frequency part of millimeter wave band.

In the papers [1 – 3] the automodulation processes in weak-resonant O-type Backward Wave Oscillators have been investigated and the new method of the millimeter noise oscillation excitation have been proposed. The method suggested uses dynamical properties of the such distributed autooscillation system as BWO and allows to excite with high efficiency intensive noise oscillations with power spectrum width of about 300 – 800MHz. The approach makes possible to extend spectrum of roles of the well-known oscillator. BWO has the universal power spectrums, depending on the working current values.

In the paper the peculiarities of the design and operation of millimeter packaged noise oscillation sources are considered. It is studied the properties of the low-voltage sources ($U \leq 4,5kV$) with two type of the slow-wave structures. The characteristics of the noise oscillation sources, operating in over the band from 30 to 60GHz, are presented.

2. SOURCE DESIGN

Two types of the slow-wave structures, such as vane-type circuit and double vane-type circuit, are used, in accordance with characteristics needed. The structures pointed have relatively large geometrical dimensions, sufficiently easy in fabrication and allows to use high power electron beams. Double vane-type circuit have a higher interaction efficiency of the non-uniform electric field with electron beams of finite thickness and its dispersion is lower that allows to devise more powerful and wide-band devices. Slow-wave structures of the noise oscillation sources have a greater electrical length of the interaction space in comparison with ones of the single-frequency sources. The vanes height, on the both terminals of the structure, is progressively decreased in size to zero, providing the surface waves transformation to waveguide ones. The needed mismatch is thereby introduced in order to form the weak-resonant oscillatory system with desired quality-factor. The diode electron gun with magnetic limitation on the electron beam is used as a source of electrons. Electron gun forms the strip beam with maximum current density of about $30A/cm^2$. Electron beam is introduced in interaction space through the anode opening, made in waveguide matching wedge. Electron beam is focused by *CoSa* system with plano-parallel gap. Inasmuch as the length of magnetic gap is too large, the weight of the system reaches to $10kg$.

The peculiarity of the design under consideration is the presence of the additional output waveguide at the collector end of noise oscillation sources. This fact allows to extend the branches of source application and to decrease the axial dimensions of the slow-wave structure. Output waveguides are on a perpendicular line to device axis and are matched with oscillatory system by using of the waveguides *E - bend*. Transition to output waveguides of standard size is performed by matching wedges. Collector waveguide, during experiments, is usually connected to matched load. The oscillations are radiated from the gun output waveguide, that is principal one for conventional *BWO*.

The frequency dependencies *VSWR* of output waveguides of millimeter noise signal source are the result of interference of the waves, reflected from the slow-wave structure terminals. Relatively great values of *VSWR* are compensated with distributed losses in the system. The losses achieve to $-10dB$ in higher frequency region. Electrodynamical circuit with characteristics listed can be considered as distributed oscillatory system with spaced spectrum of the eigen frequencies (minimal values of *VSWR* according to eigen frequencies).

3. OPERATION PECULIARITIES AND CHARACTERISTICS OF THE NOISE OSCILLATION SOURCES

Sources under consideration have the important special feature. The power spectrum shape of the source oscillations is determined by the values of working current, I_w . This can best be done in the lower frequency part of millimeter band, where the needed match quality and stringent magnetic focusing of electron beam is more easily provided. Thus, there is good reason to consider operation peculiarities of source of K_a band. It will be made in order of the working current increase.

3.1. Single-frequency oscillations

The single-frequency operating conditions is well known regime of *BWO*. The maximum values of threshold current I_{th} of source, in operating wave band, reaches to $I_{th\ max} = 4,5mA$. At the working current values $I_w \geq I_{th\ max}$ noise oscillation source operates as a source of single-frequency oscillations with wideband electronic tuning of the frequency. Output power is linearly built up with the enhancement of working current. The accelerating voltage dependencies of the output power and oscillation frequency of sources with vane-type and double vane-type slow-wave structures have essentially different aspects. Noise oscillation sources based on vane-type circuit provides output power to $280mW$ and relative electronic tuning range of about 10%. The application of the another type of circuit

allows to raise the output power up to $P = 600mW$, at the lesser working current, and to extend the electronic tuning range up to 15–20%. Power spectrum of the single-frequency oscillations radiated is similar to conventional *BWO* one. In the low voltage part of the sources working range the oscillations of the first upper pass-band of slow-wave structure on the bulk waves can be observed. This effect leads to the production of the discontinuity of electronic tuning even with good matching.

3.2. Multifrequency oscillations

At the values of working current $I_w = 22mA$ the amplitude of oscillations is taking a periodic modulation and in the power spectrum the additional components are appeared. The modulation is observed in over the operating frequency band of noise oscillation sources. The modulation frequency or the separation between neighbor spectral components can be varied in the range from 160MHz to 300MHz with the accelerating voltage U . With increasing of working current the power spectrum automodulation becomes more complicate and at $I_w = 33mA$ presents a set of equidistant spectral components. The power of the multifrequency oscillations is larger than the single-frequency one. At the $I_w = 45mA$ the output power is $P = 2,8W$. The accelerating voltage dependence of P , according to multifrequency oscillations, has essential nonuniform character. As a rule, the more complicate power spectrum oscillations have a larger power. The needed shape of the power spectrum can be received by choosing a corresponding values of U and I_w .

3.3. Noise oscillations

Excitation of the noise oscillations is observed at $I_w \geq 50mA$. In this case the power spectrum is strongly nonuniform and is placed near to earlier spectral line. At the $I_w \geq 110mA$ the excitation of the noise oscillations with continuous and wide spectrum is a taking place. The 3–dB bandwidth of power spectrum reaches to 250–300MHz at the maximum values of working current ($I_w = 180mA$). The overall power

spectrum bandwidth in this situation is up to 800MHz.

The distinguishing feature of the sources under discussion is the linear increase of the output power P with working current I_w . Interaction efficiency don't decrease for more complicate autooscillation regimes. Larger values of P are accomplished by the use of double vane-type circuit. The overall efficiency of the source mentioned is larger too and reaches to 5%.

Noise oscillation source based on the *BWO* allows to realize electronic tuning of the noise oscillation frequency. On account of operating peculiarities [3], the electronic tuning is not continuous. However, the band of the working frequencies is fully covered by means of electronic tuning as far as voltage intervals, according to wideband noise oscillation absence, are small ($\Delta U \leq 40V$) enough. Whereas the width of a power spectrum is too large. Relative band width of electronic tuning is commonly of about 4–10% and can be larger.

In order to provide the continuous electronic tuning of noise oscillation frequency it is necessary to improve the slow-wave structure matching with output arrangements. However, the essentially great values of I_w are needed, in this case, for excitation of the oscillations with complicate power spectrum. The special-purpose noise oscillation sources can provide the narrowband noise oscillations with power spectrum width of about 10MHz and frequency electronic tuning over the range from 34.2GHz to 37.7GHz at the working current $I_w = 90mA$.

3.4. Operating peculiarities of the higher frequency sources

Packaged constructions of the sources designed allow to excite the noise oscillations with frequencies up to 60GHz. The sources have a larger electrical length of the vane-type slow-wave structures. For excitation of the noise oscillations it is necessary to apply the electron beam with high density, that causes the necessity in larger values of focusing magnetic field.

Noise oscillations in sources of that range are excited at the isolated frequencies of the working band, that is caused by complexity of the good

matching of vane-type circuit with output arrangements. Output power and overall efficiency of the higher frequency sources are smaller, whereas the power spectrum width can be more than 1GHz.

4. THE MAIN SOURCES CHARACTERISTICS

At present time the packaged noise oscillation sources have been designed, operating in the needed band over the range from 30 to 60GHz. The main characteristics of sources are presented below. The characteristics pointed is not limit. There are the possibility of the output power significant increasing and the extending of the working band as in higher and lowest frequency range.

Technical Specification

Mean level of output power, W	4 - 25
Power spectrum density, mW/MHz	2 - 10
Spectrum width, MHz	
at power level $-3dB$	300
at power level $-10dB$	800
Electronic tuning, %	3 - 10
Voltage-frequency sensit. MHz/V	2 - 15
Cathode voltage, kV	2 - 4.5
Cathode current, A	0.1 - 0.18
Consumption of coolant, l/h	100
Mass of device, kg	9 - 12

5. CONCLUSION

Application of the dynamical properties of BWO allows to create the efficient and compact noise oscillation sources of millimeter wave band. The sources combine, in essence, the functions of the modulator and oscillation source. It should be particularly emphasized, that the source is powered by dc voltage only. Automodulation behaviors extend significantly the potentialities of BWO. A single source can provide, in dependence on the working current values, the single-frequency, multifrequency and noise oscillations. The electronic tuning of the oscillations radiated is possible in the all operating behaviors.

The noise oscillation source characteristics listed above are only partially shown the possibilities of the method under consideration. Its application allows to excite the noise oscillations of microwave and higher frequency range of millimeter wave band. Improvement of the electron gun and magnet makes possible the decreasing of the overall dimensions and weight of the sources, increasing of the power spectrum bandwidth and output power.

At present time the noise sources designed have been applied for development of the noise radars /4, 5/ and autodyne measurement systems and sensors /6, 7/ with high information capacitance.

REFERENCES

1. V.A. Rakityansky, "Frequency tuning ability of the BWO chaotic oscillations", Collective volume of IRE AS of Ukraine, Kharkov, 1990, pp. 85-89.
2. K.A. Lukin, V.A. Rakityansky, "Excitation of intensive chaotic oscillations of millimeter wave band", ISSSE, 1992, Paris, pp. 454-457.
3. V.A. Rakityansky, K.A. Lukin, "Excitation of the chaotic oscillations in millimeter BWO", International Journal of Infrared and Millimeters Waves, 1995, 6, pp. 13-26.
4. K.A. Lukin, V.A. Rakityansky, "Correlation reflectometry via noise signals", 2-nd International Conference on Millimeter Waves and Far-Infrared Technology, 1992, Beijing, pp. 57-60.
5. K.A. Lukin, Y.A. Alexandrov, V.V. Kulik, V.A. Rakityansky, "Broadband millimeter noise radar", International Conference Modern Radars, 1994, Kiev, Ukraine, pp. 30-31 (in Russian).
6. K.A. Lukin, V.V. Kulik, V.A. Rakityansky, "Autodyne effect in BWO operation in chaotic behavior", Proc. SPIE 2250, M. Afsar, Editor, 1994, pp. 207-208.
7. V.V. Kulik, K.A. Lukin, V.A. Rakityansky, "Application of non-coherent reflectometry method for a plasma diagnostic", Proc. SPIE 2250, M. Afsar, Editor, 1994, pp. 329-330.

MOSSIM : METAL OXIDE SEMI CONDUCTOR DEVICE SIMULATION PACKAGE

UMESH KUMAR

Senior Member, IEEE, Fellow, IETE, Deptt. of Elect. Engg.,
I.I.T., New Delhi-110016, INDIA

ABSTRACT

This paper discusses about the M.O.S. Device Simulator Developed by us, which simulates the device characteristic upto submicron channel length. It includes long channel, Short channel, subthreshold, field dependent mobility and punch through models.

1. INTRODUCTION:

MOSSIM includes long channel effect based on Gradual Channel Approximation, Short Channel effect based on two dimensional effect of applied terminal voltages, mobility degradation, and punch through effect. It computes the flat band voltage, zero biased threshold implantation adjustment dose and capacitances. It calculates the charge inside the bulk, channel thickness, body effect and channel length modulation parameters. It uses MOS modelling by analytical approximations ref (3) and (1) for surface potential, subthreshold current for short channel and long channel devices. Subthreshold region is important for low voltage and power application. While calculating current, it uses field dependent mobility model for two dimensional analysis ref (2) and ref. (4). While calculating the mobility, it computes both lateral and longitudinal electric fields, and then it computes the electron and hole mobility, because mobility effects directly effect the drains current. MOSSIM uses the two dimensional model to calculate the inversion layer mobility. It divides the drain characteristic in two different regions, these regions are linear and saturation regions in I-V characteristic of MOS transistor. We have considered

strong, moderate and weak inversion condition, because analog devices work in weak and moderate inversion. We have also included punch through effect, because for short channel devices punch through drain current will be dominated by space-charge limited current. Provision has been also added for interpolation of field independent mobility, which is based on substrate doping, and it can be used for drain current calculation. Subthreshold conduction occurs in weak inversion condition, and we can find very small changes in subthreshold current, while increasing the drain voltage.

It determines the long or short channel behaviour of device on the basis of calculated effective and minimum channel lengths. Junction depth can be specified either by user, or the program calculates it on the basis of doping. The user has to specify when he wants to drive the impurity deeper using subsequent thermal processes. It provides the choice for NPOLY, PPOLY or Al gate technology. We can use few of the calculated MOS Transistor parameters as an input to the circuit simulation, e.g. (Threshold Voltage, overlap and inter node capacitances, channel length modulation and body effect parameters for the same channel length, width and oxide thickness of MOS Transistors). We have simulated the MOS transistor's characteristics from 15 micron to 0.5 micron channel length devices. Device may be either N channel or P channel transistor, and oxide thickness used can be upto 130 Ang for submicron channel length devices. MOSSIM calculates MOS transistor parameters for zero biased and bias dependent conditions.

MOSSIM uses following expressions in the model for calculating various parameters of MOS transistor, and the currents following into the device.

Threshold voltage calculation:

$$V_{TH} = V_{FB} + 2U_B + \text{SORT} \left(\frac{2 * \text{EPSI}_{si} * N_A U_B}{C_{ox}} \right) \quad (1)$$

$$\text{here } U_B = V_T \log (N_A / n_i) \quad (2)$$

U_B : Fermi potential

Charge calculation in inversion layer:

$$Q_n(y) = Q_s(y) - Q_B(y) \quad (3)$$

Charge calculation inside the bulk:

$$Q_B(y) = -q N_A W_m \\ = -\text{SQRT} (2q N_A * \text{EPSI}_{si} (V_D + 2 U_B)) \quad (4)$$

Source and Drain depletion length calculation:

$$y_s = X_{JD} \text{SQRT} (V_{BI} + 2U_B) \quad (5)$$

$$y_D = X_{JD} \text{SQRT} (V_{BI} + 2U_B + V_{DS}) \quad (6)$$

where

$$V_{BI} = 0.0259 \log (N_A N_D / n_i^2) \quad (7)$$

$$\text{Left} = L - y_s - y_D \quad (8)$$

Transconductance calculation :

$$g_m = \omega m W / \mu C_{ox} (V_{GS} - V_{TH}) / L \quad (9)$$

where $m = 1/2$ at low dopings.

Drain current calculation :

$$I_{DS} = (W/L) \mu_n C_{ox} (V_{GS} - V_{TH}) V_{DS} - V_{DS}^2 / 2 \quad (10)$$

Expression for subthreshold current calculation

$$I_{subth} = \mu_n (W/L) * (a C_{ox} / 2 (\text{BETA}^2) * \\ (n_i / N_A)^2 * (1 - e^{-\text{BETA} * V}) * \text{BETA} * 2 U \\ * (\text{BETA} * 2 U_B)^{-1/2} \quad (11)$$

$$a = \text{SQRT} (2) * \text{EPSI} / L_D C_{ox} \quad (12)$$

$$\text{BETA} = q / K T$$

Capacitance calculation :

$$C_{DG} = C_{SG} = (1/3) C_{ox} W L \quad (13)$$

Punch Through Voltage Calculation:

$$V_{pt} = q N_A (L - y_s)^2 / 2 * \text{EPSI} - V_{BI} \quad (14)$$

Substrate Current Calculation:

$$I_{sub} = 2 I_{DS} \exp (-1.7 E_6 / E_m) \quad (15)$$

Since a MOSFET fundamentally operates under the influence of two external forces. One is the field which induces carriers in the inversion layer and constructs a narrow channel, the gate field. The other is the field which transports carriers from the source to the drain. Mobility which depends on both fields, is assumed to be expressed by the following formula (2) :

$$\mu (N_B, E, E_T) = \mu_0 f (N_B, E) g (E_T) \quad (16)$$

where N_B is the impurity concentration, and μ_0 is constant. The term of represent the property of bulk mobility. The bulk property in Si is approximated by the expression:

$$f (N_B, E) = 1 + (N_B / (N_B / S + N)) + \\ (E/A)^2 / (E/A + F) + (E/B)^2 - 1/2 \quad (17)$$

where

	S N (cm ⁻³)	A (V/cm)	F B (V/cm)
Electrons	350 3*10 ¹⁶	3.5*10 ³	8.8 7.4 * 10 ³
Holes	81 4*10 ¹⁶	6.1 * 10 ³	1.6 2.5 * 10 ⁴

The g term is introduced so as to represent the property of surface mobility. An approximate formula, which simulates the property can be expressed as follows:

$$g = (1 + k E_T) \quad (18)$$

The parameter k is determined to fit the experimental data. It is expressed as :

$$k = 1.539 * 10^{-5} \text{ cms/v, for}$$

n-channel device

$$= 5.35 * 10^{-5} \text{ cm/v, for}$$

$$\text{p-channel device} \quad (19)$$

Here, f and g are normalized to unity when N_B , E , and E_T are zero. Therefore μ_0 is low field mobility of an intrinsic crystal and given as

$$\mu_0 = 1600 \text{ cm}^2/\text{v-s, for electrons}$$

$$= 600 \text{ cm}^2/\text{V-s for holes} \quad (20)$$

Field can be expressed by the following expressions,

$$E = (V_D - V_{Dsat}) / \text{SQRT} (3 T_{ox} X_{JD}) \quad (21)$$

$$E_x = (Q_B + Q_n / 2) \text{EPSI}_{si} \quad (22)$$

Other MOS parameters are expressed as:

$$\text{GAMMA} = \text{SQRT} (2 * \text{EPSI}_{\text{si}} q N_A) / C_{\text{ox}} \quad (23)$$

$$\text{LAMDa} = (L/L_{\text{eff}}) * \text{SQRT} (\text{EPSI}_{\text{si}} (V_{\text{DS}} + 2 * \text{PERMI}) / 2 q N_A) \quad (24)$$

FERMI stands for Fermi Potential

EPSI stands for Epsilon

μ stands for Mobility

3. CONCLUSION

The program has been developed in Fortran-77, and it can be used on any personal computer. We have used this software to simulate the various characteristics of MOS transistor as shown in Figs. 2-5. The parameters of the device are also mentioned in the figures. The input to MOSSIM simulator is impurity concentration data and biasing condition of the transistor. Fig. 2-4 shows the drain characteristic of device at 2, 3, 4 and 5V gate voltages, while Fig. 5 shows the substrate current characteristic of NMOS transistor at various gate voltages.

4. REFERENCES:

1. Geoffrey W. Taylor, "Subthreshold conduction in MOSFET's," IEEE Transactions on Electron Devices, Vol. ED-25, No. 3, pp. 337-350, March 1978.
2. Ken Yamaguchi, "Field Dependent Mobility Model for Two Dimensional Numerical Analysis of MOSFET", "IEEE Transactions on Electron Devices, Vol. ED-26, No. 7, pp. 1968-1974, July 1979)
3. W. Fichtner and H.W. Potzl, "MOS modeling by analytical approximations", Int. J. Electronics, 1979, Vol. 46, No. 1, pp 33-55.
4. K.K. Thornber, "Relation of drift velocity to low-field mobility and high-field saturation velocity" J. Applied Phys. 51 (4), pp 2127-2136, April 1980.

5. J.R. Brews, "A Charge-Sheet Model of the MOSFET", Solid State Electron, 21, 345, (1978).
6. T. Kamata, K. Tanabashi, and K. Kobayashi "Substrate Current Due to Impact Ionization in MOSFET", Jpn. J. Appl. Phys. 15, 1127, 1976.
7. S.M.s Sze, Physics of Semiconductor Devices, Second Edition, Wileys Eastern Limited, 1981.
8. Umesh Kumar, "Comparison between two dimensional short channel MOSFET models IEE PROC., Vol. 130, Pt. I, PP. 37-46, February 1983.
9. Kit Man Cham et al., "Computer-Aided Design and VLSI Device Development", Kluwer Academic Press, 1986.
10. Paolo Antognetti et al., "Semiconductor Device Modelling with SPICE", McGraw Hill Book Company, 1988.
11. Yannis P. Tsividis, "Operation and Modeling of the MOS Transistor", McGraw Hill International Edition, 1988.

5. INPUT PARAMETERS

NA: Substrate Concentration

(/cm³) = 5.0e16

ND : Source/Drain Concentration

(/cm³) = 5.0e19

VGSF=2.0V VGSL = 5.0V VGSTEP = 1.0V

VDSF=0 VDSL = 7.0V VDSTEP = 0.1V

NSS (/cm²) = 1.0e11

Tox = 130 Ang L = 1.5 μ m W = 30.0 μ m

Vth = 1.0V; Gate is NPOLY

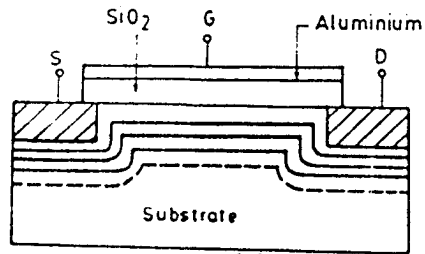


Fig. 1 - Depletion charge profile (---) and equipotential lines (—) in cross-section of long channel MOSFET

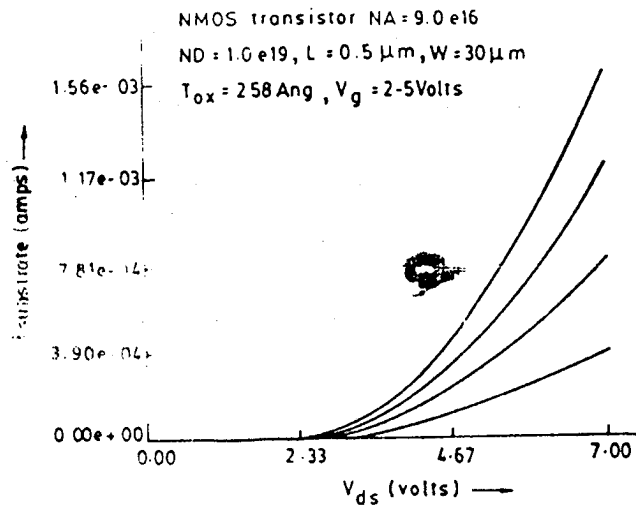


Fig. 2

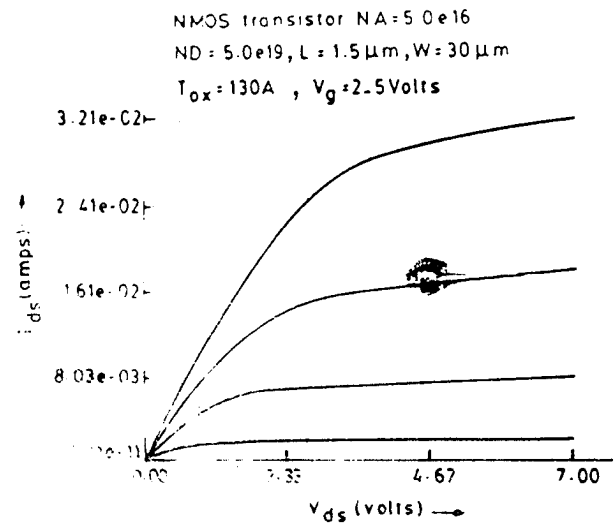


Fig. 3

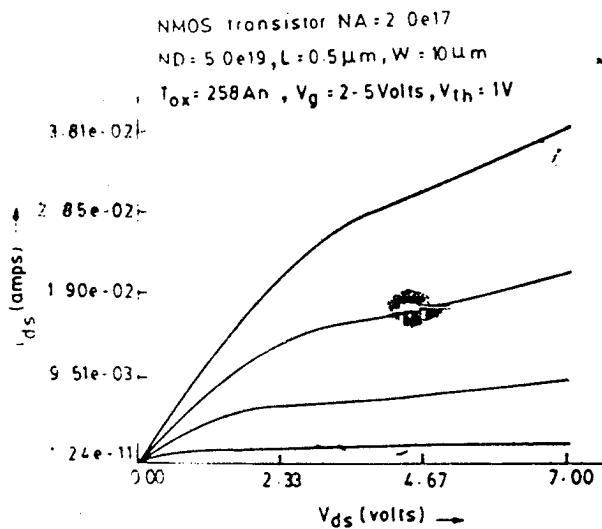


Fig. 4

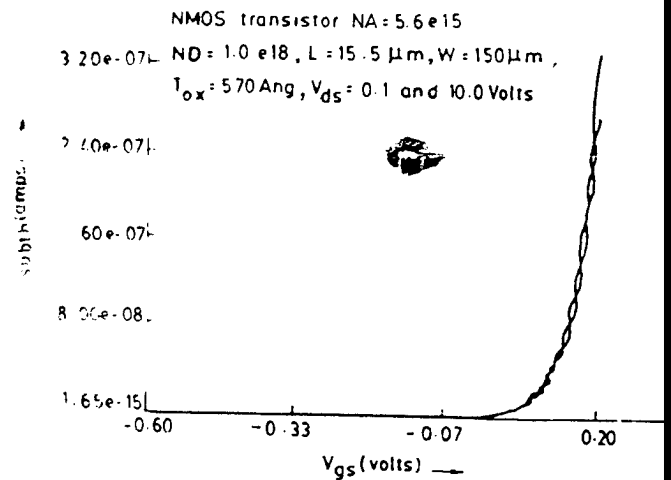


Fig. 5

OPERATIONAL AMPLIFIER FOR REDUNDANT ANALOG SYSTEMS

Vadim V. Ivanov and Michael V. Ivanov

OES Electronics Ltd.
P.O.Box 858, St.-Petersburg, 199397, Russia
Tel/fax +7-812-352-1268
E-mail michael@oes.leninf.spb.su

ABSTRACT

The operational amplifier for the creation of dependable analog systems and for median filtration is described. These OpAmps can be used in parallel connections with common or separate loads and inputs to achieve fault-tolerance, noise reduction, self-checkability and error indication, output power and accuracy rise of the analog systems.

1. INTRODUCTION

Median choice ("voting") of signals of subsystems was examined in [1, 2, 8] to reduce the influence of interferences, impairments and unpredictable faults of components in analog systems (AS) of measurement, communication and control. This algorithm was realized in the 1960's in a nonlinear feedback structure for ship and plane control

systems [2,3], particularly, using voting or "quorum-element" (QuE) (Fig. 1), recently reinvented for the image and speech median filtering in [4, 5]. But the median choice in the direct signal path is a non-linear operation of majority logic and therefore, because of deviations of signals and parameters of elements, has mutual drawbacks, such as [6, pp. 47-50]:

- it does not allow the implementation of a redundant open-loop gain or integrator element;
- it introduces nonlinear distortions in accurate systems;
- it is not effective in power system parts (power amplifiers or supplies);
- such ASs contain common non-redundant components and do not have fault diagnoses.

2. THE REDUNDANT ANALOG CONNECTION

The simplest operation to decrease input signal deviation is an arithmetical or weighted mean [8]. For input voltage sources V_i , this operation can be implemented in parallel connection of V_i with weighting resistors R_i (Fig. 2). For equal resistors

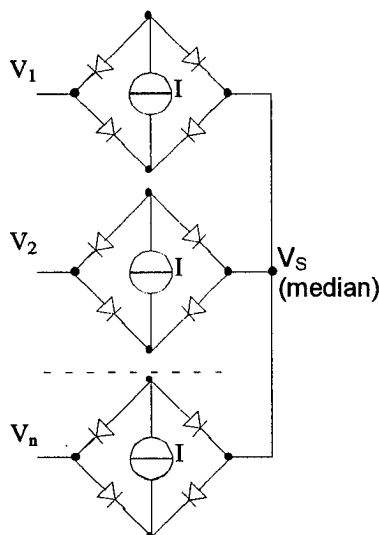


Fig. 1. Quorum-element

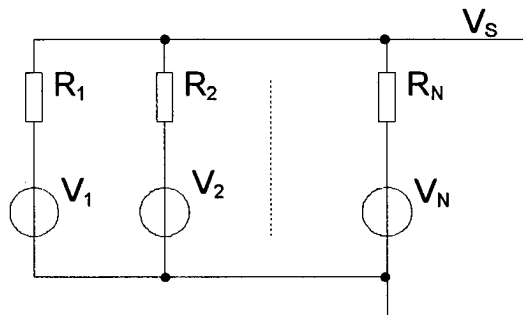


Fig. 2. Mean voltage circuit

R_i output voltage V_S is:

$$V_S = \frac{\sum_{i=1}^n R_i^{-1} V_i}{\sum_{i=1}^n R_i^{-1}} \Big|_{R_i = R} = \frac{1}{n} \sum_{i=1}^n V_i \quad (1)$$

To avoid the effect of large deviations caused by system faults, resistors R_i can be made non-linear, increasing with the rise of their currents. Diode bridges (Fig. 1) have this non-linear resistance. Also, it is necessary to limit possible signal levels in the circuit.

To implement a dependable structure and avoid mentioned drawbacks, authors suggest the redundant system structure (Fig. 3) and an example of the implementation of its subsystem in the form of an operational amplifier (Fig. 4).

Every subsystem consists of the input amplifier $A1_i$ with the output current limitation (Q1, Q2 and current source $I1$) and the output amplifier $A2_i$ also with a current limitation (it can be a power or temperature limitation) (Q11-Q18, R), and feedback Z_{1i} , Z_{2i} . In addition, every opamp includes feedback on the deviation of output signals from the median. The median is detected by the QuE, consisting of the diode bridge (Fig. 3) or transistor current limiter Q5-Q8 and I3 (Fig. 4). In [1] shown that voltage V_S of jointed outputs of QuE, is in limits (2):

$$\left| \frac{1}{m} \sum_{i=1}^m V_{Li} \right| \leq |V_S| \leq \left| \text{med}(V_{Li}) \right| \quad (2)$$

where $m \leq n$ is the quantity of V_{Li} , which are in the limitation area, $e \leq 2V_i = 2kT/q \sim 50$ mV for the diode QuE. Amplifiers A_S (Q3, Q4, I3) reduce the difference of output signals of subsystems, so

$$V_{Li} - V_S \leq \frac{I1}{G_S} \quad (3)$$

where G_S - transconductance of A_S , $I1$ - limitation level of $A1_i$. Deviations of V_{Li} from V_S are caused by: 1) process deviations of subsystem's production; 2) different input signals V_{INi} ; 3) different subsystem's feedbacks Z_{1i} , Z_{2i} ; 4) internal amplifier faults. V_{Li} can feed the subsequent redundant blocks of the system or the common

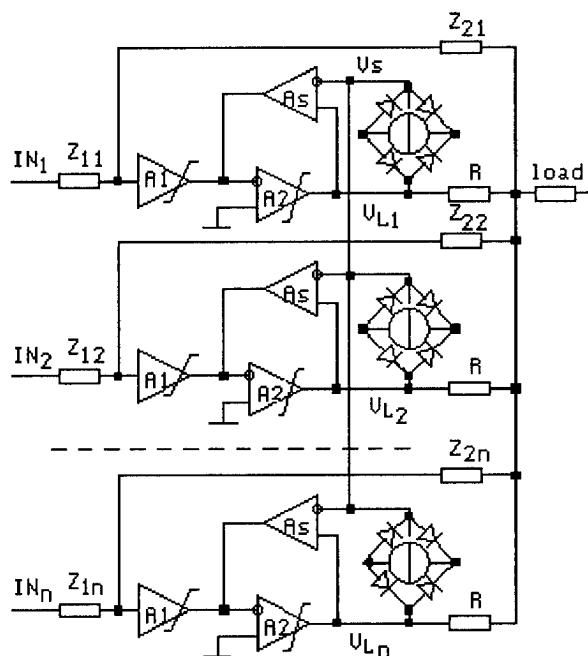


Fig. 3. Structure of the redundant analog system.

load of redundant connection through small resistors R .

The subsystem fault causes limitations of subsequent $A1_i$ and the break of its general feedback (rise of the $A1_i$'s input voltage) which can be detected by additional circuitry (not shown). Every subsystem can be used separately in non-redundant systems.

The single input or amplifier fault causes a disconnection of general feedback of this amplifier. In case of inner fault, this amplifier can produce the error on common load, which should be compensated by other amplifiers. This is the only damage of single or multiplicative (with appropriate redundancy coefficient) faults, while the system in general remains in a working state. With all active elements and the common load, this amplifier connection allows the summarization of all load currents and increases the power limitation in accordance with the parallel-joined amplifier quantity.

In test equipment, such connections of the standard and test blocks easily disclose defective devices with the help of fault diagnostic circuits without the difficult parameter measurements.

3. REALIZATION

As a general-use element for dependable redundant AS, the dual OA was produced on an analog bipolar array with vertical PNPs, $f_{iN-P-N} = 600$ MHz, $f_{iP-N-P} = 90$ MHz. Its parameters are as follows:

As a general-purpose OA:

- offset voltage < 3 mV;
- maximum output current 10 mA;
- unity-gain frequency 10 MHz;
- gain 90 dB;
- slew rate $5 \cdot 10^6$ V/s.

In parallel redundant connection:

- maximum difference of output voltage is < 50 mV in input error conditions;
- difference of output voltages is < 3 mV with equal input signals; input error indication level is 400 mV.

4. CONCLUSION

Our research resulted in the general nonlinear multiloop AS structure with median detection in feedback paths. This redundant structure can be realized from elementary levels to system levels of complexity and has the following properties:

- limitation of input and output signals in a safe or valid operating area;
- accuracy increase of the redundant connection through averaging over a set of m from n variables in the limited desirable area of the median;
- power enlargement in redundant power components [6];
- passivation of components whose variables

have been extended beyond the limited area of the connection median (neutralization of technological defects, additive noises, input and supply overloading, multiplicative failures);

- repairment or replacement of the failed units in an active state;
- diagnosis of the impairments, exceeding the tolerances;
- metrology attestation, appraisal of the degree of specification degradation by deviation from the reference subsystem without accurate measurements.

These features of redundant ASs and their components fully correspond with the dependability concept in [7].

Median feedback elements can be included in nearly any analog IC in any technology for the access to dependability properties. Multipliers, integrators, oscillators, instrumentation amplifiers, etc. can be created.

The most promising application is the creation of power fault-tolerant, solid-state amplifiers with the ability of unlimited parallel connection for the power enlargement. For redundant power amplifiers, deviations can cause an increase in local power dissipation and temperature in channels. By measuring signal deviations of local temperature sensors from the mean, the system can control the gain of the channels [6]. In this case, redundancy does not lead to hardware increment, but creates a power reserve.

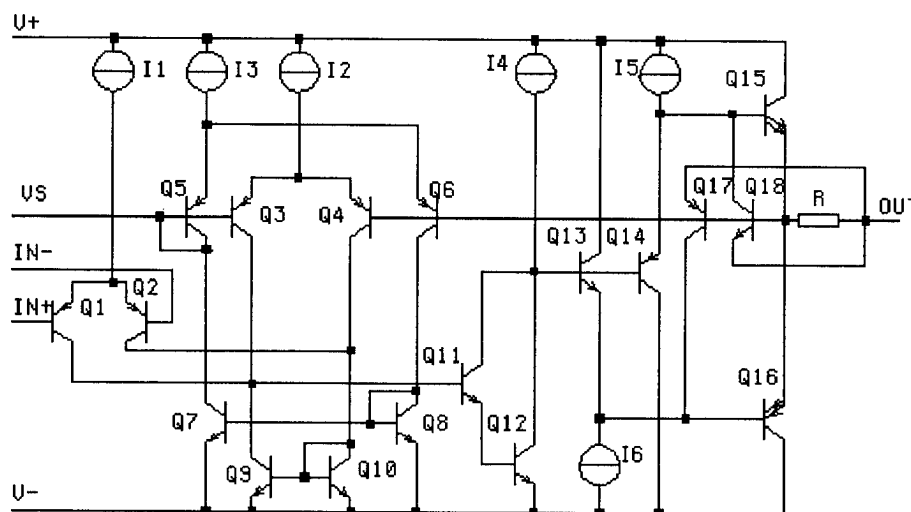


Fig. 4. Operational amplifier for redundant analog systems

5. ACKNOWLEDGMENTS

The authors would like to show their appreciation to Dr. Valery N. Ivanov for his basic ideas, works [1,2,6] and very useful discussions.

REFERENCES

1. ИВАНОВ В.Н., 'О реализации операции мажоритарного выбора в системах с обратной связью' (IVANOV, V.N., 'On realization of majority operation (function of voting) in feedback systems'), *Automatics and Telemechanics*, 1968, 7, pp. 112-117, USSR Academy of Science, Moscow. (in Russian)
2. ИВАНОВ В.Н., 'Принципы построения и элементы мажоритарных систем управления' (IVANOV, V.N., 'Design methods and elements of the majority control systems'), in "Технические средства автоматизации" ("Technical means of automation"), Nauka, Moscow, 1971, pp. 99-109. (in Russian)
3. БРАСЛАВСКИЙ Д.А., ЯКУБОВИЧ А.М., ЧЕШОКОВ Г.И., Авторское свидетельство №190664, (BRASLAVSKY, D.A., JAKUBOVICH, A.M., CHESNOKOV, G.I., USSR author certificate 190664), *USSR innovations bulletin*, 2, 1967. (in Russian)
4. DIETZ, P. H., CARLEY, L. R. 'An analog circuit technique for finding the median' in *Proc. 1993 Custom Integrated Circuits Conference*, May 1993, pp. 6.1.1-6.1.4.
5. DIETZ, P. H., CARLEY, L. R. 'Simple networks for pixel plane median filtering,' *IEEE Trans Circuits Syst.-II*, Vol.40, pp. 799-801, Dec. 1993.
6. ИВАНОВ В.Н., ИВАНОВ В.В., 'Мощные интегральные усилители' (IVANOV, V.N., IVANOV, V.V., 'Power integrated amplifiers'), Leningrad, CNII Rumb, 1987. (in Russian)
7. LAPRIE, J.C. 'Dependable computing: concepts and terminology' *Proc. FTSO*, 1987, pp. 44-53.
8. ГИЛЬБО Е.П., ЧЕЛПАНОВ И.Б. 'Обработка сигналов на основе упорядоченного выбора (мажоритарное и близкие к нему преобразования)' (GILBO, E.P. CHELPANOV, I.B., 'Signal processing based on the ranked choice (majority and related operations)'), Moscow, Sov. radio, 1978. (in Russian)

THE VOLUME-METRICAL MONOLITHIC INTEGRATED CIRCUITS FOR MICROVAWE BAND

V.I. Gvozdev, S.I. Podkovyrin, A.A. Lyalin

Moscow State Institute of Electronics and Mathematics
3/12 Bol Vuzovsky Per, Moscow 109028 Russia
Fax 007 095 9162807

The main principles of volume-metrical microvawe monolithic ICs design are discussed. The essential features of it are following:

1. Microwave transmission lines shold be chosen adequately providing the best total performance for each functional element and/or block.

2. It is important to involve 3 space dimensions in electromagnetic signal processing. In this case interlayer signal transmission can be obtained by means of local couplings. Coupling element could be used also as processing tool. A set of technological contradictions appeared when approaching submillimeter band will be pointed out below:

a) The active components of an IC should be very precisely mounted.

b) It is desirable that the transmission line insertion losses be low.

c) It is necessary that the relative layers position be precisely adjusted.

d) Unfavourable reactive parameters of active components are to be compensated.

These technological contradictions are resolved by taking advantage of the monolithic technique for volume-metrical ICs. Technological difficulties caused by semiconductor substrate size being restricted are avoided with the aid of monolithic ICs and distributed passive elements.

The volume-metrical monolithic ICs technique enables:

1. to combine several semiconductor structures for different active elements (Shottky diodes, transistores etc.)

2. to integrate physical processes of different nature (microwave, optical etc.) in one IC.

The emphasized above allows the usage of wide range of optoelectronic devices in microwave ICs.

In our report we discuss physical and technological design principles for basic waveguide and resonant elements. Attention was also paid to main functional elements for volume-metrical microwave ICs based on semi-isolating GaAs. The CAM/CAD methods are included too. Sample elements were investigated in our experiment and the results are shown in the report.

The comb dielectric waveguide designed for 90-300 GHz range was used as one of the possible versions.

It was manufactured of semi-isolating GaAs (<100> oriented) by means of liquid chemical processing. For the experiment it was made to be ring-shaped. Thus the low-radiation resonator used high-order azimuthal resonance.

Q~600 was achieved at 140 GHz. The special design features are determined taking in account that the technological process being anizotropic.

The plasmochemical technology has also great outlook.

The surface wave equalizing structures were also developed for semiconductor dielectric waveguiedes with lumb active elements. The basic waveguide elements and the metal-covered equalizers are placed on the opposite sides of the semiconductor layer.

The Shottky diode structure was offered with its terminals placed on the surface of semi-isolating GaAs sample open by the epitaxial technique. Antisipated parameters of the barrier are: capacity ~10 fF, leakage resistance ~5 Ohm. Several kinds of optoelectronic modulators and tuned attenuators based on monolithic ICs are suggested in our report. The fact that the devices are distributed ones allows to avoid undesirable elements interaction. The modulator performance (i.e. speed, modulation depth and control laser power) were analized too. Possible realization methods are given. The modulation depth ~35 dB and insertion losses ~0.5 dB were observed in the experiment with optoelectronic modulator designed like rejector filter.

The design methods are suggested for the specific distributed microwave amplifier based on the stable negative differential conductance phenomenon in GaAs.

In our report we concerned the problem of the 3D signal processing and special multi-layer monolithic ICs performing that. The technical solutions are shown taking in account the specific requirements.

AN IC FOR CLOSED-LOOP MICROMOTOR CONTROL

N. K. Rao, D. K. Hartsfield, A. Purushotham, and S. L. Garverick

Department of Electrical Engineering and Applied Physics
Case Western Reserve University
Cleveland, Ohio 44106
slg@pris.eeap.cwru.edu

Abstract

A Micromotor Control Integrated Circuit (MCIC) which enables closed-loop control of an electrostatic micromotor is described. The MCIC consists of low-noise sense electronics designed to detect critical rotor angles to a resolution of 0.5° (0.05° fF) at a 1 MHz sampling rate, and control logic which cycles the micromotor drive state during continuous rotation to maintain maximum torque, independent of loading.

The MCIC was fabricated using a 2- μm , n-well CMOS process and all circuits, analog and digital, function as expected. Preliminary measurements indicate that the input-referred noise of the sense amplifier is very close to the design objective of 32 μV rms.

1. Introduction

The ability to micromachine silicon, a material which is well understood for its electronic properties, is now being employed to fabricate miniature mechanical structures. In combination with the relatively mature silicon circuit technology and chemical/physical microsensors, the development of microactuators opens a pathway to closed-loop monolithic microelectromechanical systems (MEMS).

One such microactuator is the 12:8 salient-pole, electrostatic micromotor [1], depicted in Figure 1. Typically, the rotor diameter is 100 μm , the rotor-stator gap size is 1.5 μm , and the rotor thickness is 2.5 μm . Torque is generated using the electrostatic force between the rotor and three stator groups which are driven by three-phase excitation using a typical amplitude of 50 V. The step response of these micromotors is very underdamped with a peak overshoot that is about 7.5° for a step size of 15° and a natural frequency of approximately 10 kHz [2].

To date, these micromotors have been operated using open-loop stator excitation. To maintain synchronization between rotor position and stator phasing, the micromotor is operated in a stepped fashion. In other words, each time the phase of the excitation is advanced, the rotor is allowed to settle in its new rest orientation before advancing to the next phase. As a result, measured rotational speed has been limited to a few kRPM. On the other hand, our analysis and computer simulations using the models and data presented in [2] show that speeds in

excess of 100 kRPM are possible given optimum, closed-loop control.

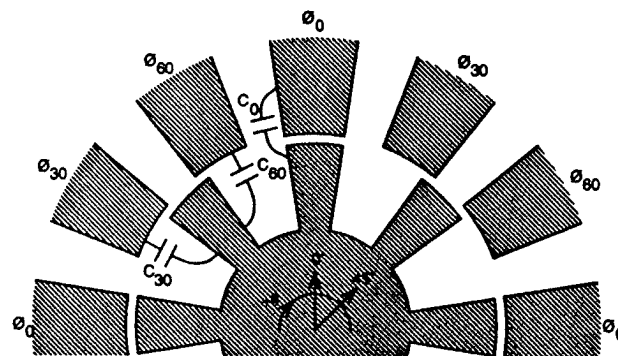


Figure 1. Schematic top view of a 12:8 salient-pole micromotor

The objective of this work is to develop closed-loop control electronics which maximize the torque/speed of this micromotor during continuous rotation. Our approach does not require modification to the micromotor structure and employs a technology which lends itself to future monolithic integration on the micromotor die. The sensing technique can be applied to a variety of capacitive microsensors and microactuators.

2. Control Principle

The torque produced by each of three drive phases, as a function of rotor angle of rotation, is sketched in Figure 2a. This qualitative sketch is based solely on symmetry arguments, but corresponds well to data obtained using 3D finite-element simulation [3]. To achieve maximum average torque, the drive electronics must switch a phase on when it contributes positive torque and switch it off when it contributes negative torque, as shown in Figure 2b. Drive torque is lost if the phase switching is not precise; we estimate that a switching resolution of 0.5° results in an average torque loss per phase switch of 0.4%. To achieve this sampling resolution for rotational speeds near 100 kRPM, a sampling rate of 1 MHz is used.

The angles of zero torque, i.e., the critical drive angles, occur when the rotor is either fully aligned or fully misaligned with a given stator phase. It is at these critical angles that the drive phase must switch. The critical drive angle for a given phase can be detected by differentially stimulating the capacitances between the other two phases and the rotor. This differential capacitance is zero at the

critical drive angle. Therefore, a comparator can be used to determine when the critical angle has been crossed, and advance the drive state when this occurs. For clockwise rotation, stimulus must be applied according to Figure 2b, which leads to a differential capacitance as sketched in Figure 2c.

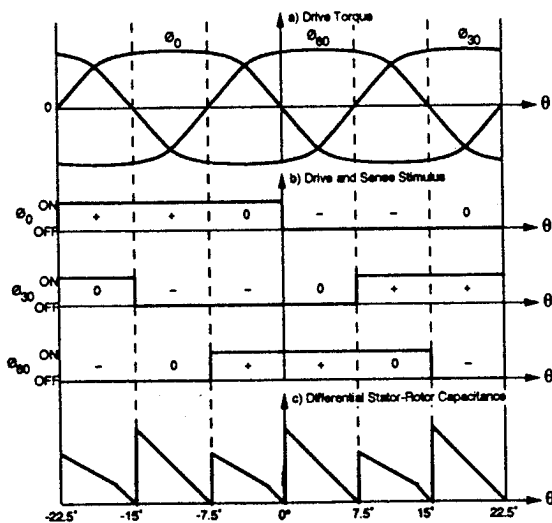


Figure 2. Principle of operation.

We therefore arrive at the state diagram shown in Figure 3 in which the drive state is represented by a 3-bit state variable $\langle \phi_0 \phi_{30} \phi_{60} \rangle$ where 1 means "on" and 0 means "off." There are six valid states through which the drive cycles as the crossing of critical angles is detected. There are two invalid states, 000 and 111, which are immediately exited should they occur due to circuit initialization or error.

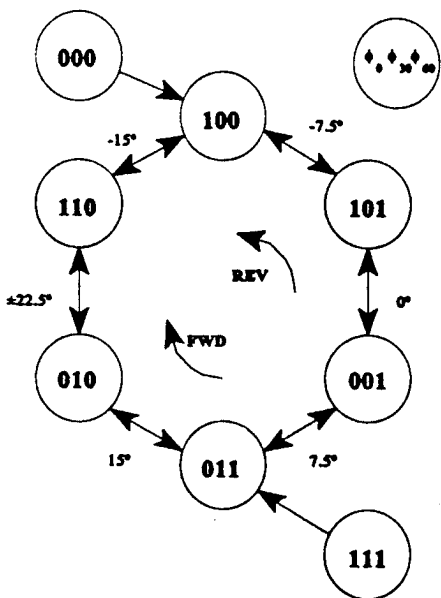


Figure 3. State diagram of the control algorithm.

Consider the start-up case in which the drive state is 100, and the rotor has been allowed to come to rest at 0° . When the control algorithm is activated, the ϕ_0 and ϕ_{30} stators will be stimulated to find that the rotor angle of rotation is greater than -7.5° , and the drive state will be immediately switched to 101. The ϕ_{60} stator now provides substantial forward torque to start the rotation of the rotor. The sense circuitry will soon determine that the critical angle of 0° has been exceeded, the drive state will be switched to 001, and the sense circuitry will begin to detect $+7.5^\circ$. At this time, the drive state is optimum given the rotor angle, and the rotor quickly gains speed. Computer simulations predict that the micromotor will reach more than 90 % of its steady-state speed by the time it has rotated 90° .

3. Sense Amplifier

Differential stator-rotor capacitance is sensed using the switched-capacitor integrating amplifier shown in Figure 4. A sense stimulus is applied by superimposing a high-frequency square wave on the stator drive voltages. This configuration holds the rotor at a virtual ground, and thus avoids electrostatic attraction between the rotor and the substrate of the micromotor which can cause a frictional force which inhibits micromotor operation.

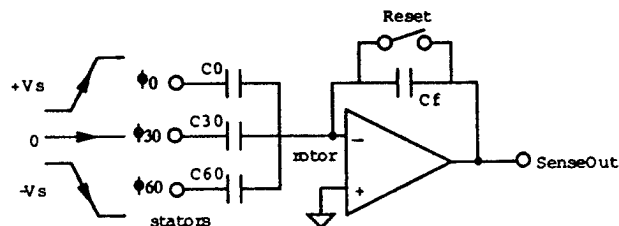


Figure 4. Simplified sense amplifier.

Each cycle of operation consists of a reset phase and a sense phase. During the reset phase, the feedback capacitor is discharged by the reset switch and the output of the sense amplifier is preset near ground, depending on its input-referred offset voltage. The reset switch is then opened and a differential stimulus is applied to two of the three phases. A charge proportional to the difference in capacitance of the two phases is driven across the feedback capacitor resulting in a voltage proportional to this differential capacitance.

Details of the sense amplifier are shown in Figure 5. A nominal timing diagram for clocks used by the sense amplifier and comparator is presented in Figure 6. As per the principle of correlated double sampling [4], the circuit that follows the initial switched-capacitor integrator detects the difference of the voltage before and after the sense stimulus has been applied. To reduce the error from charge injection from the NMOS transistors used as reset switches around the various amplifier stages, they are turned off in a skewed manner [5].

This micromotor has a differential stator-rotor capacitance of approximately 0.05 fF per 0.5°. To limit torque loss due to the superimposed sense stimulus to about 13%, its amplitude will be limited to 20% of the high-voltage supply, i.e. 10 V for a 50-V supply, corresponding to a signal of 3.1 ke⁻ into the integrator, i.e. 1 mV at the output of the initial integrator. The second-stage amplifier has a closed-loop gain of 10 and will therefore produce a 10-mV signal per 0.5° of rotation.

To permit adequate settling, the time constant of the first-order low-pass filter formed using a source follower with 20-k Ω output impedance has been set to 100 nsec (1.6 MHz). The op amp has been designed for an input-referred noise spectral density of 14 nV/ $\sqrt{\text{Hz}}$ and a noise corner frequency of 100 kHz. The double-sampled flicker noise

is negligible, and the thermal noise of the integrator, including spectral leakage through the first-order low-pass filter and double sampling, is 32 μV rms referred to the input of the sense amplifier, i.e. 5.4 mV when referred to the output of the second-stage amplifier assuming a parasitic input shunt capacitance of 8 pF. The op amp, therefore, has noise corresponding to about half the desired switching resolution.

A block diagram of the MCIC with key system components is presented in Figure 7. The sense amplifier receives its input from the rotor of the micromotor via the input Senseln. The output of the sense amplifier is compared to a threshold voltage, nominally 0 V, which can be adjusted during experimentation. The output of the comparator (Trip) is used by the control logic to determine an advancement in drive state.

The control loop is completed by the Drive/Stimulus Logic, which determines the correct differential stimulus, and the High-Voltage Converters, both of which are to be implemented using off-chip components. The high-voltage drive required by the micromotors exceed the capability of the availability of the available IC technology. By using off-chip Drive/Stimulus logic, the potentially disruptive switching signals output by the

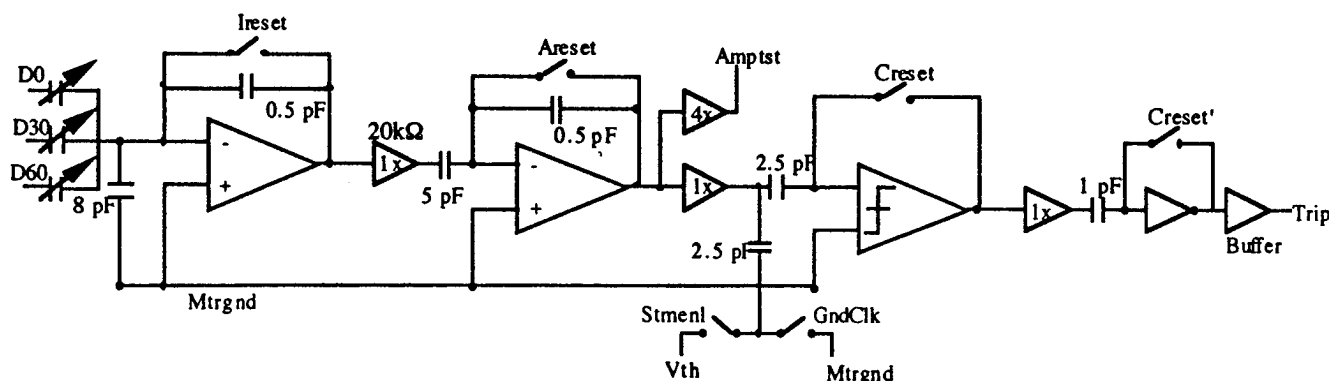


Figure 5. Detailed sense amplifier and comparator

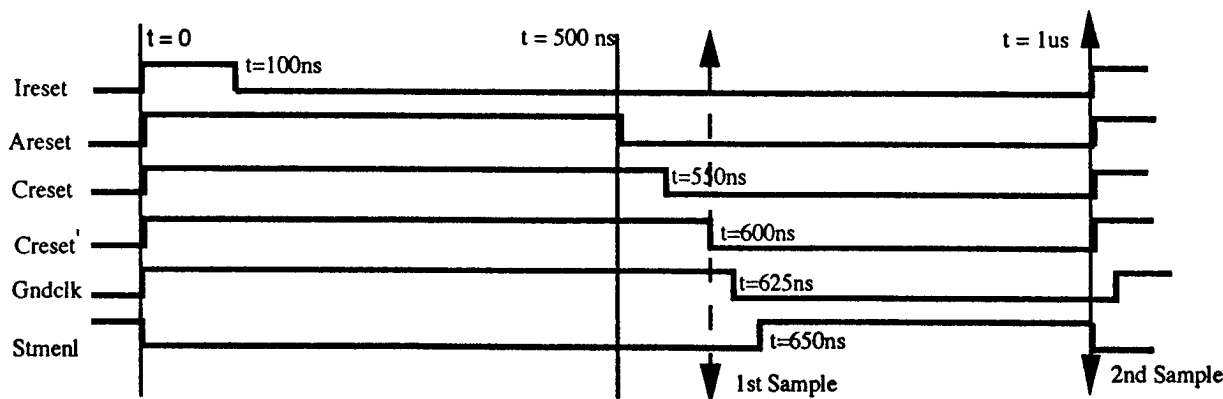


Figure 6. Nominal timing for the sense amplifier

MCIC is limited to the 3-bit drive state and a stimulus synchronization clock.

The user simply supplies a 1-MHz clock input which sets the sample rate, and supplies static control inputs which set the direction of rotation (Fwd) and toggle between continuous-rotation or stepper mode (Rot). The (analog) sense electronics is operated at $\pm 3.5\text{V}$ while the (digital) control logic is operated between 0 and 5V; level shifting is performed by latch-like circuits which drive the analog clocks, and by the AC-coupling within the comparator.

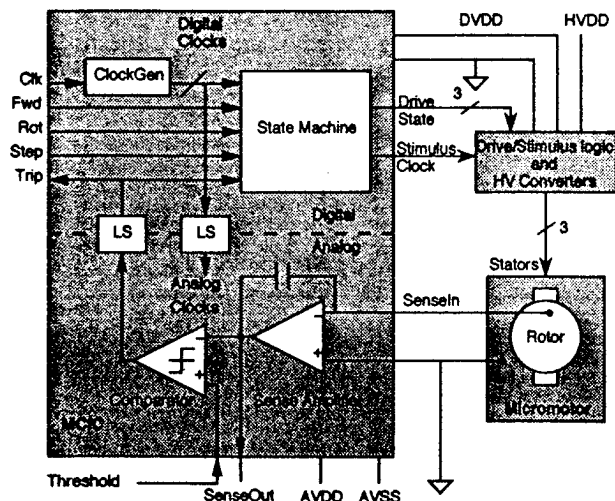


Figure 7. MCIC block diagram in system context.

5. Test Results

The MCIC has been fabricated using a 2- μm , n-well, double-poly CMOS process. A photomicrograph is presented in Figure 8. Coarse functionality was tested with a 0.5-pF capacitor between the stimulus clock and SenseIn to produce a strong positive charge input that caused the state machine to advance each clock cycle. The desired behavior of the drive state bits and the input clock is demonstrated in Figure 9.

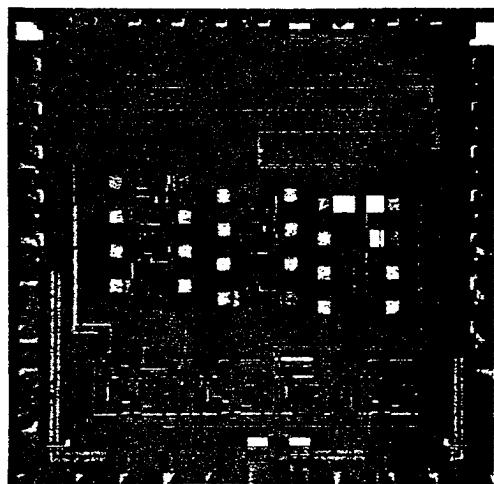


Figure 8. MCIC photomicrograph.

Noise performance was measured by varying the threshold input in 1-mV increments with the synthetic sense stimulus disconnected. For each setting of the comparator threshold input, the probability of a high Trip was determined by measuring the average (DC) value of the output from a CMOS flip-flop used to capture the MCIC Trip output. In principle, this measurement yields the Cumulative Distribution Function of the MCIC noise as referred to the output of the sense amplifier. The results obtained to date are roughly Gaussian, but exhibit non-monotonicity, an artifact, we believe, of the test setup. The difference in applied threshold voltage for 0.3% tripping and 99.7% tripping, i.e. 6σ assuming a Gaussian amplitude distribution, is 38 mV. Thus, rms noise referred to the output of the sense amplifier is about 6.3 mV, which is very close to the design goal.

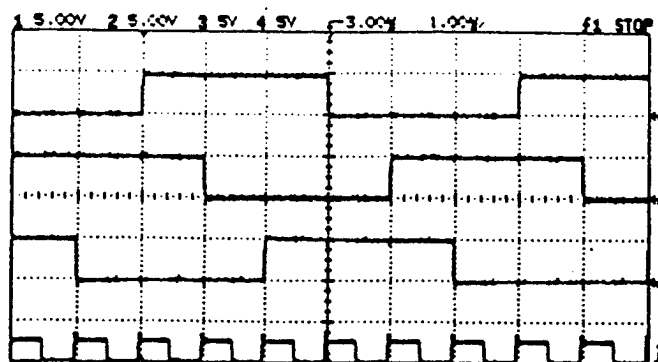


Figure 9. Measured state outputs for synthetic stimulus.

Acknowledgments

This material is based upon work supported, in part, by the National Science Foundation under Grant No. ECS-9309280. The MCIC was fabricated by Orbit Semiconductor through the MOSIS service.

References

- [1] M. Mehregany, *et al.*, "Micromotor Fabrication," *IEEE Trans. on Elec. Dev.*, vol. 39, no. 9, pp. 2060-2069, Sept. 1992.
- [2] S.F. Bart, *et al.*, "Electric Micromotor Dynamics," *IEEE Trans. on Elec. Dev.*, vol. 39, no. 3, pp. 566-575, March 1992.
- [3] M.P. Omar, *et al.*, "Electric and Fluid Field Analysis of Side-Drive Micromotors," *IEEE/ASME J. MEMS*, vol. 1, no. 3, pp. 130-140, Sept. 1992.
- [4] H.M. Wey and W. Guggenbuhl, "An Improved Correlated Double Sampling Circuit for Low Noise Charge-Coupled Devices," *IEEE Trans. Circuits Syst.*, vol. 37, no. 12, pp. 1559-1565, Dec. 1990.
- [5] Y.S. Lee, L.M. Terman, and L.O. Heller, "A 1mV MOS Comparator," *IEEE J. Solid-State Circuits*, vol. SC-13, pp. 294-297, June 1978.

A NOVEL DCT AND FTC BASED HYBRID STILL IMAGE COMPRESSION ALGORITHM

Jiangtao WEN Xuelong ZHU
Computer and Information Division
Dept. of Electronic Engineering
Tsinghua University, Beijing 100084
P.R. China

wen@king.dee.tsinghua.edu.cn deezxl@tsinghua.edu.cn

Abstract

In this paper, a novel DCT and FTC hybrid image compression algorithm is proposed, which dramatically improves the speed of FTC coding and JPEG's ability of preserving image details at high compression ratios. The overall subjective quality of the whole JPEG decoded image is also heightened.

1. Introduction

The ever widening adoption of information technology and improvements to the resolutions of image output devices have made it necessary for image compression algorithms to be able to preserve image details at high compression ratios.

The current still image compression standard JPEG, can not meet this demand. Dividing images into blocks which are compressed separately, JPEG can only remove redundancies within each individual block, all the redundancies rest between blocks remain. And because its compression relies on eliminating high frequency components of each image block, as the compression ratio gets high, JPEG has to sacrifice more and more high frequency components of each block to compensate for the redundancy remain between blocks. The more high frequency components it throws away, the more image details it loses. As a result, the quality of the decoded image drops quickly as the compression ratio rises for JPEG.

In this paper, a hybrid image compression algorithm that combines DCT based JPEG and IFS (iterated function systems) based FTC (fractal transform coding) is proposed, which has a compression quality that is much better than each individual algorithm can achieve, and is easy to realize.

2. Compression Algorithm

2.1 Pixel Classification

To overcome the inherent shortcomings of JPEG while maintaining compatibility, each pixel (i, j) (of gray-level $g(i, j)$) in the original image is first categorized into two groups, named low- d_f pixels and high- d_f pixels respectively, according to its fractal dimension $d_f(i, j)$, which can be calculated approximately as ([5]):

$$d_f(i, j) = 3 - \log_2 \left(\frac{V_2(i, j)}{V_1(i, j)} \right) \quad (1)$$

where

$$V_\varepsilon(i, j) = \sum_{(x, y) \in N(i, j)} [U(x, y, \varepsilon) - L(x, y, \varepsilon)] \quad (2)$$

$$U(x, y, 0) = L(x, y, 0) = g(x, y)$$

$$U(x, y, \varepsilon + 1) = \max \left\{ U(x, y, \varepsilon) + 1, \max_{(m, n) \in N(x, y)} \{ U(m, n, \varepsilon) \} \right\}$$

$$L(x, y, \varepsilon + 1) = \min \left\{ L(x, y, \varepsilon) - 1, \min_{(m, n) \in N(x, y)} \{ L(m, n, \varepsilon) \} \right\}$$

$$N(i, j) = \{ (m, n) : |m - i| \leq 1 \text{ and } |n - j| \leq 1 \} \quad (3)$$

In our experiment, the pixels with the highest 10%~15% of d_f are treated as high- d_f pixels.

The aim of pixel classification is to locate the part of image information that is most prone to be lost by JPEG compression. Pentland showed in [3], low- d_f pixels form the relatively smooth areas of an image, while the high- d_f areas are irregular. The higher the d_f , the more irregular the areas are. As a result, high- d_f pixels are usually distributed sparsely all over an image, and are the most likely to be divided into different blocks by JPEG, thus the redundancies within these pixels, such as the correlation between the pixels corresponding to the two opposite edges of the can in Fig.1, make up a large portion of the redundancies that can not be removed by JPEG. On the other hand, because high-

d_j areas are rich in high frequency components, the information loss at these positions are the most severe when high frequency components of each individual image block are discarded.

2.2 Compression of High-Dimensional Pixels

To have their redundancies removed, the gray levels of high- d_j pixels are extracted and written in scanning order to a data file with position information discarded. The file is then treated as a single-line "image" and compressed. Because to this "image", redundancies between segments are as important as redundancies within each segment, FTC is chosen to do the compression for it is good at searching for matching between segments.

The FTC coder we used in our experiments was based on the prototype source code in Chapter 6 of [2]. The form of the fractal transforms is the combination of contrast scaling, luminance shifting and horizontal flipping.

2.3 JPEG Compression of Whole Image

After high- d_j pixel gray levels are compressed, JPEG is used to compress the whole image to remove the redundancies among low- d_j pixels. Because these pixels are less sensitive to the loss of high frequency components, we can raise the compression ratio accordingly. We can even perform smoothing operations to low- d_j areas to further reduce the data rate after JPEG.

2.4 Transmission of Classification Information

Pixel classification information has to be transmitted to let the decoder know if the d_j of any pixel is high. In our experiment, we did this by assigning an even or odd quantization value to the DCT coefficient at the corresponding position to convey the information and divide the elements of the Q matrix by 2 so as not to degrade the overall precision of the quantization. Although such a scheme works in our experiment, it may cause undesirable increase to the data amount after run-length and entropy coding for "simple" images or at high compression ratios.

Now we are working on utilizing arithmetic coding to compress classification information. How to make full use of a JPEG compressed original image in the compression of classification information is still an open problem.

3. Decoding Process

The process at the decoder side is straightforward.

After JPEG decoding, gray levels of high- d_j pixels in the decoded image are extracted using pixel classification information and then used as the initial "image" for the following FTC decoding iteration.

Our FTC decoding process is a little different from the usual routine, for now the decoder has a reasonably good estimation of the "image" to be reconstructed, and thus the decoding can be seen as a progressive attempt to better such an estimation, one transform for the bettering of one range segment. Because the new "image" is very complex, some of the fractal transforms may not really be able to better the estimation. In such cases, we should leave the original estimation unchanged, and apply only those "good" fractal transforms.

Whether a transform is good can be determined by the encoder using the collage theorem, by seeing if the distance between domain and range segments is small. The parameters of the "bad" transforms can then be discarded at the encoder side and need not be transmitted.

After iteration, each FTC decoded gray level is averaged with the JPEG decoded value at its original position. Finally the resulted gray-levels are written back to the original positions.

4. Experimental Results

We tested our algorithm with a $320 \times 320 \times 8$ bits seaside scenery picture (Fig.2) which contains smooth objects such as sky as well as complex details in sands, rocks and sea waves. We label 11297 pixels as high- d_j pixel, which is about 11% of the total number of pixels.

Now that FTC coder is used to only a small portion of pixels, the requirement to its compression ratio is lowered. Experimental results in [4] show that the quality of a FTC coder is most sensitive to block sizes, so we set the length of range segments to a small value, 8, to improve FTC's quality. Scaling factors are chosen from $\{-0.9, -0.8, -0.7, 0, 0.7, 0.8, 0.9\}$. At the decoder side we only apply 1/3 of all possible fractal transforms, and the parameters of the rest 2/3 transforms are discarded at the encoder side. The overall compression ratio of FTC is about 8:1. Because the "image" to be compressed is small, the usually lengthy FTC coding can be done almost in real time without any software or hardware acceleration.

The improvement to RMSE by our algorithm over JPEG is listed in the Table, and we use the

product of compressed file size and decoded RMSE as another criterion to compare the performance of a compression algorithm. Obviously, the *smaller* the product, the *better* the compression.

5. Conclusions

It can be seen from the Table that although we are using the simplest FTC coder in our experiment, our algorithm is still able to vastly improve the RMSE and the size-RMSE product over the already fine-tuned JPEG.

Our algorithm can accommodate a number of modifications, e.g. it can be used to compress still images as well as image series, and for the latter, the cost of transmitting pixel classification information can be further reduced; contraction restrictions to fractal transforms can be relaxed, for now the decoding iteration starts from an reasonably good initial image and the local attractors of IFS iteration are thus less disastrous; at the decoder side, a fairly good image can be decoded from the JPEG part of code alone when the FTC part is not available; and finally, the same FTC code can be used with several JPEG coder operating at different compression ratios. This last feature is potentially useful in networks where different users have different need of image quality and different allocated bandwidth.

Our algorithm will improve RMSE at high- d_f pixels while keeping RMSE unchanged at low- d_f areas. Since there is no fixed relationship between a high- d_f pixel's position in the original image and in the new "image", as a result, although both JPEG and FTC have to divide image into blocks to compress, the write back of gray levels from the decoded new "image" to their original positions will alleviate some of the blocking artifacts induced by

JPEG, and thus improve the subjective quality of the whole decoded image.

Our algorithm is based on a careful analysis of the advantages and disadvantages of JPEG and FTC. The extraction of high- d_f pixel gray levels makes the removal of their redundancies possible, while the smaller size of the "new" image and the JPEG part of the code improve the speed and quality of FTC. Although still to be more extensively tested and more carefully studied, our preliminary results show that our approach is a promising way of more "wisely" applying IFS model to image compression.

Acknowledgment: The authors wish to thank the *National Natural Science Foundation of China* for its financial support to this research.

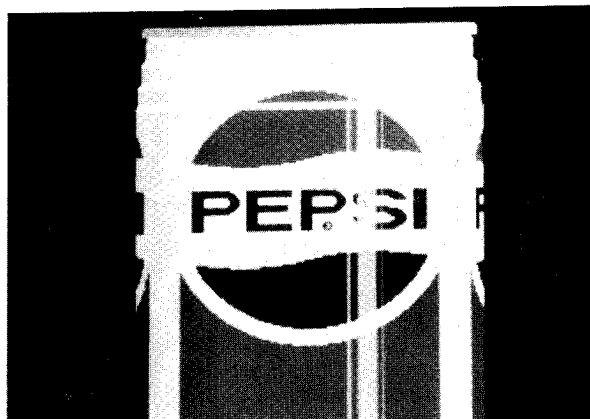
References:

- [1] G.K.Wallace, "The JPEG Still Picture Compression Standard", *Comm. of the ACM*, Vol.34, No.4, 1991
- [2] M.F.Barnsley, L.P.Hurd, *Fractal Image Compression*, AK Peters, Ltd., 1993
- [3] A.Pentland, "Fractal-based Description of Natural Scenes", *IEEE Trans, PAMI*, Vol.6, pp661-674, 1984
- [4] E.W.Jacobs, Y.Fisher, R.D.Boss, "Image Compression: A Study of the Iterated Transform Method", *Signal Processing*, Vol.29, pp251-263, 1992
- [5] T.Peli, V.Tom, B.Lee, "Multi-Scale Fractal and Correlation Signature for Image screening and Natural Clutter Suppression", *Proc. SPIE*, Vol.1199, *Visual Communication and Image Processing IV*, pp402-415, 1989

Image File	File Size (Bytes)	RMSE at high- d_f pixels	Size · RMSE	Rank of Size · RMSE
JPEG12*	8447	0.033391	282.054	8 (Worst)
JPEG12+FTC	10347	0.025346	262.255	5
JPEG14	7300	0.037065	270.575	7
JPEG14+FTC	9454	0.027023	255.475	4
JPEG16	6416	0.041376	265.468	6
JPEG16+FTC	8650	0.028517	246.672	2
JPEG18	5771	0.044165	254.876	3
JPEG18+FTC	8138	0.030020	244.303	1 (Best)

*JPEG12 means the decoded image of JPEG at a compression ratio near 12.

Table. Comparison of RMSE at high- d_f areas of JPEG and JPEG-FTC Compression



(a)



(b)

Fig.1 Pixel Classification
 (a) Original Image (b) Classification Result
 (in (b), gray levels of high- d_f pixels are set to either 0 or 255)



Fig.2 Test Image



Fig.3-1 JPEG16



Fig.3-2 JPEG16 + FTC

DISCRETE MULTIPLICATIVE SIGNALS AND THEIR RECOGNITION ALGORITHMS, BASED ON VILENKIN-KRESTENSON FUNCTIONS SPECTRAL TECHNIQUES

Lev Evgenievich Nazarov, Viacheslav Mihailovich Smolyaninov

Institute of Radioengineering and Electronics, Russian Academy of Sciences, Russia

Section Heading: **Signal and Information Theory. Modulation and Coding.**

The data transmission performance close to Shannons limit can be achieved by means of using optimal signal sets and their optimal recognition algorithms. For channels with additive white Gaussian noise the optimal performance criteria is based on Euclidean distance.

In our report the results of investigation of discrete multiplicative signal sets are presented. These signal sets were proved to have many useful properties for applications in digital communication systems.

The discrete signal sets $Sp(k)$, $k=0,1,\dots,L$, $p=0,1,\dots,q^n-1$ are algebraic multiplicative groups. Here L - signal length, q^n - number of signals in set. The signal sets have symmetry property. The multitudes of the signal cross-correlation coefficients, determining the set of Euclidean distances between signals and the tolerance to noise, are equivalent to multitudes of the signal dc components.

The construction methods of discrete multiplicative signal sets are based on Vilenkin-Krestenson functions. The corresponding column numbers of Vilenkin-Krestenson matrix, determining the signal sets, are signal address matrix. The conformity between signal sets $Sp(k)$ and groupe codes enable the groupe code properties to be used for construction corresponding signal sets $Sp(k)$ and for elaboration their recognition algorithms.

There is connection between metric characteristic of discrete binary ($q = 2$)

signals (Euclidean distance) and metric characteristic of corresponding binary codes (Hamming distance). In that case one can use the known optimal group codes to produce digital multiplicative signal sets with low value of cross correlation coefficients.

The construction procedure of original class of discrete multiplicative signal sets was performed. The constructed signals are equivalent to discrete frequency-modulated signals, investigation of the signal cross-correlation coefficient properties have found many of these signal sets practically perfect for criteria used optimal Euclidean distance.

It was proved the optimal signal recognition procedures can be implemented by means of Vilenkin-Krestenson functions spectral techniques, the analysed function is formed with help of address matrix. For realisation of recognition procedures one can use algorithms of fast spectral transforms more computationally efficient ($\sim n \cdot q^n$) than immediate spectral components computation ($\sim L \cdot q^n$). For signal sets corresponding Bose-Chaudhuri-Hocquenghem codes these optimal signal recognition procedures have been modified so that the required amount of storage ($q^{-1}, q^{l-1} < L < q^l$) and the number of operations ($\sim q^n \cdot \log_q L$) are decreased significantly relatively known optimal procedures. These recognition procedures are found to be used for recognition of common multiplicative

signal sets.

Suboptimal signal recognition procedures have been designed and investigated for broad class of discrete multiplicative signal sets. One can realize these procedures by means of using the $q^m \ll q^n$ spectral components and the required amount of storage and the number of operations are reduced greatly relatively known procedures but without significant degrading the

tolerance to noise.

The results of computer simulation tests of developed optimal and suboptimal signal recognition algorithms of constructed signal sets are presented. The results of comparison of tolerance to noise and of realisation complexity by means of digital techniques relatively known algorithms of algebraic decoding are presented too.

Rheolinear System Theory applied to the Problem of Generation of extremely low Frequencies and to Frequency Modulation

by Eugen-Georg Woschni

Technische Universität Chemnitz-Zwickau
Fakultät für Elektrotechnik und Informationstechnik
D-09107 Chemnitz

INTRODUKTION

The generation of extremely low frequencies often is realized by means of mixing of two low frequencies. Because of the inevitable interconnection between both generators problems arise covered by the rheolinear system theory and leading to consequences as described in the paper. The in principle same problems arise with frequency modulation as also shown in the paper.

2. GENERATION OF EXTREMELY LOW FREQUENCIES BY MIXING

Mixing two frequencies ω_1 and ω_2 the difference frequency $\Delta\omega = \omega_1 - \omega_2$ appears due to modulation theory. Because of the inevitable coupling of the generators rheolinear theory must be applicated leading to the result that with the synchronizing range $\Delta\omega_0$ the real difference frequency is (Woschni 1990; Barkhausen and Woschni 1956)

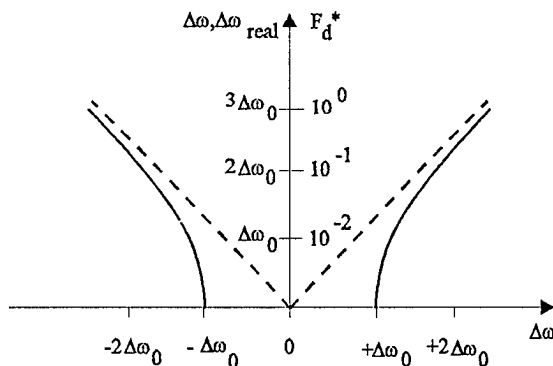


Fig. 1 Real (—) and ideal (---) difference Frequency; x measured values

$$\Delta\omega_{real} = \sqrt{\Delta\omega^2 - \Delta\omega_0^2} \quad (1)$$

as shown in Fig. 1 with the relative error

$$F_d^* \approx \frac{1}{2}(\Delta\omega_0 / \Delta\omega)^2 \quad (2)$$

Furthermore the output is not sinusoidal; the distortion is increasing with decreasing $\Delta\omega$, leading for $\Delta\omega \approx \Delta\omega_0$ (near the synchronisation limit) in the extreme case to bootstrap oscillations with $\Delta\omega_{real}$ as given by Equ. (1). Another application of the theory is frequency modulation.

3. FREQUENCY MODULATION

The implication of the solution of the differential equation of a sinusoidal modulated oscillator

$$u'' + \frac{1}{LC_0} \left(1 + \frac{\Delta C}{C} \sin \omega t \right)^2 u = 0 \quad (3a)$$

leads to the unequation

$$\frac{\Delta\Omega}{\Omega_0} \frac{\omega}{\Omega_0} \cos \omega t \cos \left(\Omega_0 t - \frac{\Delta\Omega}{\omega} \cos \omega t \right) \neq 0 \quad (3b)$$

showing that problems are increasing with increasing

$$\frac{\Delta\Omega \omega}{\Omega_0^2} \quad (4)$$

As given by the map of Ince-Strutt (Fig.2)

synchronizing effects appear in the synchronizing ranges of the order

$$2\Omega_0 / \omega = r. \quad (5)$$

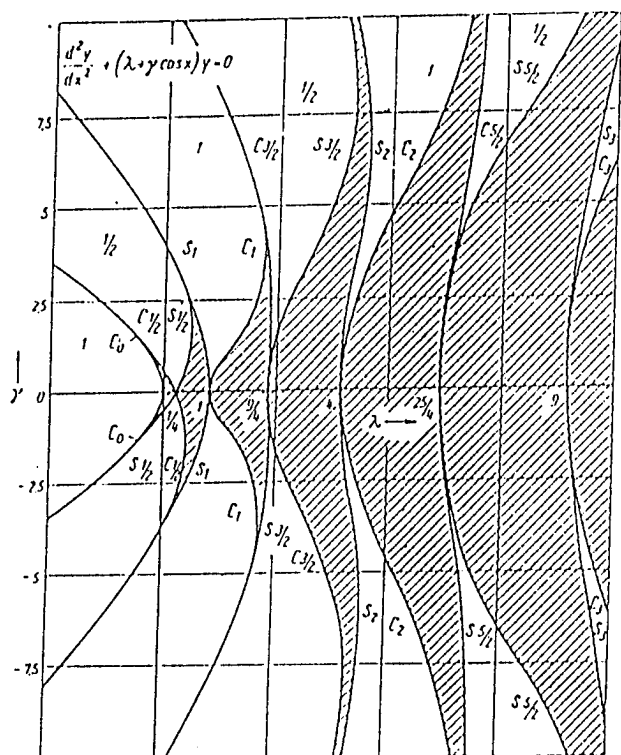


Fig. 2 Map of Ince-Strutt (Strutt 1932)

Fig. 3 shows the relations between the relative frequency swing $\Delta\Omega/\Omega_0$ and the relative limiting modulation frequency ω_p/Ω_0 with the relative synchronising range $\Delta\Omega/\Omega_0$ as parameter. In practice these effects are to be taken into consideration if $\Delta\Omega/\Omega_0$ and (or) ω_p/Ω_0 are not very small.

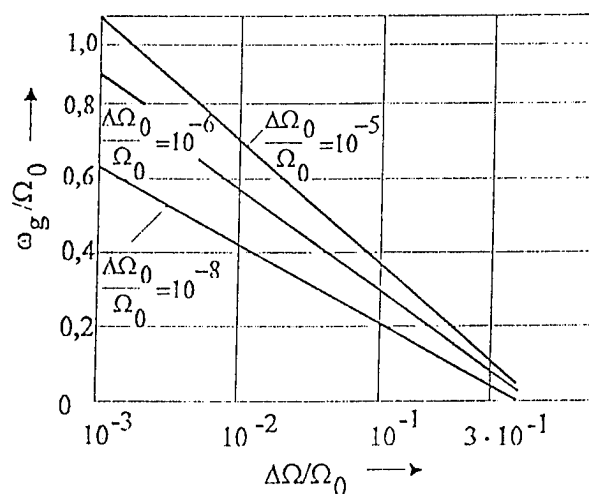


Fig. 3 Frequency modulation

DISCUSSION AND CONCLUSIONS

The generation of low frequencies by means of mixing is limited by synchronizing effects due to rheolinear theory. Especially here frequency errors are the consequence. Similar limitations arise in frequency modulation with reference to the limiting value of the modulation frequency and the relative frequency swing. Moreover distortions arise, increasing with decreasing difference frequency.

REFERENCES

- Barkhausen, H. and Woschni, E.-G.: HF-Technik und Elektroakustik 64, 180, 1956.
- Woschni, E.-G.: Frequenzmodulation, 2nd. Ed., Verlag Technik Berlin, 1962.
- Woschni, E.-G.: Informationstechnik, 4th. Ed., Verlag Technik Berlin, 1990.

NEW ARCHITECTURE FOR SELF-ROUTING PHOTONIC SWITCHING WITH SELF-SYNCHRONIZATION AND OPTICAL PROCESSING

Jian-Guo Zhang

Telecommunications Program
School of Advanced Technologies
Asian Institute of Technology

G.P.O. Box 2754, Bangkok 10501, Thailand
jgzhang@cs4.ait.ac.th

ABSTRACT

This paper presents a new architecture for self-routing photonic switching with self-synchronization and optical processing. Two wavelengths are used to carry the clock-data and address signals, respectively. This in turn allows to independently process both signals at each switching node. Thus, the complexity of optical routing controllers is reduced while the reliability of address decoding is significantly improved.

1. INTRODUCTION

Photonic switching is playing an important role in broadband communication networks. At present, conventional electronic processing and routing control are normally used in switching networks, which will impose a data flow bottleneck on the routing controller of each switching node. To achieve an ultrahigh throughput (e.g., ~ 100 Gbit/s), optical signal processing and optical routing control will be widely used in future photonic switching [1]. Self-routing switching is suitable for multistage networks, because self-routing control is totally distributed, and the outgoing link which the input packet will follow is determined by its destination address bit [2]-[4]. Self-routing can be performed packet-by-packet in real time by setting the state of a switching element during the entire packet, i.e., cross or bar state. Thus, it can handle very high-speed data streams.

Self-routing photonic switching with optical signal processing has been demonstrated [1][2]. The use of self-clocked packet-header encoding scheme can eliminate the requirement of synchronization

for decoding the destination address of the input packet at optical routing controllers. Therefore, it can simplify the network design and allow each switch to operate asynchronously [1].

In this paper, we propose a new architecture for ultrafast self-routing photonic switching with self-synchronization, which is based on the two-wavelength scheme. By using the proposed technique, the complexity of optical routing controllers is reduced, but the reliability of address decoding is significantly improved.

2. SELF-ROUTING PHOTONIC SWITCHES USING TWO WAVELENGTHS

Figure 1 illustrates the block diagram of the proposed photonic switching. It comprises three basic parts. The first part is an electrooptic (EO) switch which normally operates in one of two possible states (i.e., cross or bar), set by the electronic control signal [1]. The second part is an optical routing controller consisting of an optical address decoder and a gate controller. The optical routing controller optically decodes the incoming destination address on a packet-by-packet basis, and therefore, sends the electronic control signal to set the appropriate state of an EO switch according to the output of the address decoder. The last part is an optical phase adjuster which is used to compensate the propagation time difference due to using two-wavelength lights. It is also employed to match the processing delay of the optical routing controller at each switching node.

We use two different wavelengths to carry the

clock-data signal at wavelength λ_1 and the address signal at wavelength λ_2 , respectively. In order to

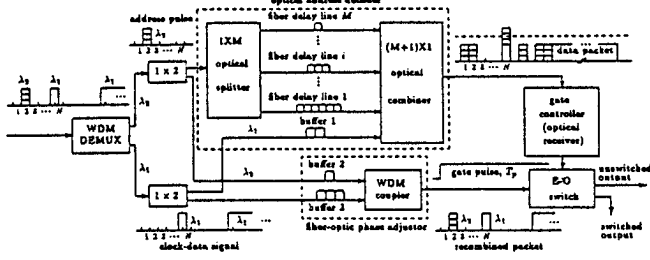


Figure 1: Block diagram of the proposed photonic switching.

achieve self-routing, the destination address of each packet is encoded in a packet header of length T by using the optical pulse-interval coding scheme [1]. This can be implemented at each transmitter by sending a short optical pulse of width T/N in the specific time slot with respect to an optical clock pulse of T/N being always in the N -th slot within a frame, as shown in Figure 2.

Let I_N be a positive integer set of which the elements are less than or equal to N . The time slots of a frame assigned to all the possible addresses which must correspond to the cross state of an EO switch form the **switched-output set** S [1], i.e., $S = \{a_i \mid \text{the } a_i\text{-th slot (per frame) corresponds to the cross state, } i = 1, 2, \dots, M\} \in I_N$, where $1 \leq a_1 < a_2 < \dots < a_M \leq N$ and $M \leq N$. As a result, all the remaining time slots of a frame form the **unswitched-output set** \bar{S} , i.e., $S \cup \bar{S} = I_N$. In order to eliminate the following data bits from the address decoding, a guard interval $\Delta t = (N - a_1)T/N$ is issued between the header and data signals as shown in Figure 2.

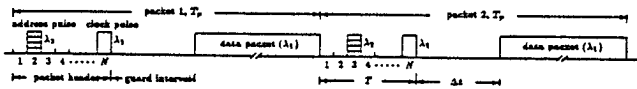


Figure 2: Structure of a packet header using optical pulse-interval coding scheme.

To efficiently perform self-synchronization for decoding addresses at each switching node, wavelength λ_2 is used to carry an address pulse if a packet is issued (see Figure 2). Then both clock-data and address signals are transmitted to a

switching node by using wavelength-division multiplexing (WDM) to efficiently share the common fiber. In order to avoid effects of fiber nonlinearities, the transmitted optical power on the fiber can be reasonable. However, the optical power budget could be improved if optical amplifiers are used.

At each switching node, the incoming optical clock-data and address signals are separated by using a WDM demultiplexer (DEMUX) whose output is split into two parts (see Figure 1). One is sent to the optical address decoder to read the destination address of the incoming packet. The other is fed into a fiber-optic phase adjuster.

An optical address decoder consists of $1 \times M$ power splitter, M fixed optical delay lines, optical buffer (i.e., a fixed optical delay line), and $(M + 1) \times 1$ wavelength-insensitive power combiner (i.e., a gating summer) as shown in Figure 1. The i -th delay line produces a delay of $(N - a_i)T/N$ with respect to an input optical address pulse at the address decoder, such that the delayed address pulse should superimpose on the phase-adjusted clock pulse by optical buffer 1 in the N -th time slot at the output of an optical address decoder if and only if the input address pulse is located in the slot $a_i \in S$, and therefore, a double-amplitude pulse results. This is because the maximum delay for address pulses is limited to $(N - a_i)T/N$ and a guard interval $(N - a_i)T/N$ is issued between data field and packet header, which in turn completely eliminates the following data bits from the address decoding. When this double-amplitude pulse is threshold detected, the gate controller (e.g., a wideband optical receiver) sends a gate pulse of duration T_p to set the EO switch in the cross state, otherwise the input address belongs to \bar{S} . Then the EO switch is set in the bar state because of no gate pulse. The entire packet is thus routed to the unswitched output. Recently, an EO switch operating in the wavelength range of $1.52 \mu\text{m}$ to $1.57 \mu\text{m}$ has been reported [5]. This can substantially support the proposed two-wavelength scheme.

Normally, a guard interval is also required for the switching architecture given in [1] to prevent the data pulses from the address decoding if the simple optical delay-line processing technique is used, otherwise the more complex address decoder or gate controller would be used. However, this may prevent the ultrafast processing because such implementation-related problems impose the throughput bottleneck at the interfaces. In this paper, we use two wavelengths for photonic switching, so it allows to independently process the clock-data

and address signals, respectively. The decoding reliability is then significantly improved compared with that scheme used in [1]. Furthermore, the proposed architecture for photonic packet switching does not require an inhibiting summer and the related optical delay lines as employed in [1]. Thus, the complexity of routing controllers is reduced. If M is far less than N , this new architecture would be much simpler than that given in [1].

The use of two wavelengths results in a difference between the propagation speeds of both lights in the optical fiber. If the propagation speed of the light at wavelength λ_1 is assumed to be faster than that of address light at wavelength λ_2 (this is always true in practical cases), we can use an optical buffer in the clock-data path before a $(M+1) \times 1$ combiner to fully compensate the time difference caused by two different propagation speeds in the fiber which is used just before the present switching node. Doing so, the output address pulse from the zero delay line (assuming $a_M = N$) and the phase-adjusted clock-data signal from optical buffer 1 maintain the same phase relationship at the gate controller as they were just sent from the transmitter as shown in Figure 2.

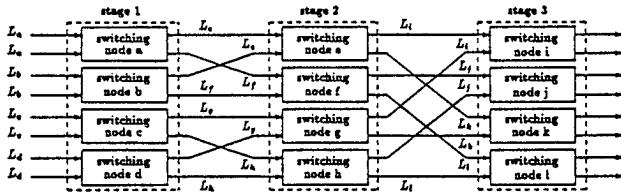


Figure 3: Multistage photonic switching network using the proposed switching architecture with equal-length input links to the same node.

To eliminate the accumulated time difference between two-wavelength lights through multistage switches, an optical phase adjuster comprising two fixed optical delay lines (i.e., buffers 2 and 3) and a WDM coupler is used to compensate the propagation time difference caused by the input link of each switching node as shown in Figure 1. As a result, the recombined clock-data and address signals at the input of an EO switch has the same phase relationship as given in Figure 2. The fiber lengths of the phase adjuster shall be also chosen to match the processing delay introduced by the routing controller to synchronize the arrival of the recombined entire packet with a gate pulse at the EO switch. Thus, the input links of a switching

node should have equal length. The use of a common phase adjuster can then fully compensate the propagation time difference from any input link of a switching node (see Figure 3). However, this requirement can be removed if multiple optical phase adjusters are used before each switching node, as shown in Figure 4. Each of the phase adjusters is designed to compensate the propagation time difference caused by its own input link.

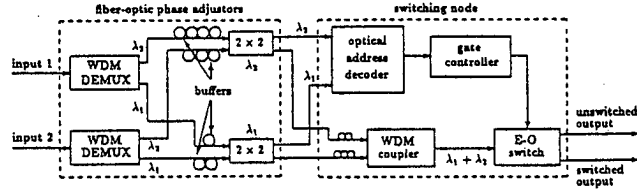


Figure 4: Photonic switching node using external fiber-optic phase adjusters.

3. SIMPLE PERFORMANCE ANALYSIS

In this section, we simply analyze the receiver sensitivity of gate controllers and the optical power budget of the proposed photonic switching.

For the convenience of analysis, we consider the single-wavelength case. It is because two wavelengths can be chosen closely and the performance difference between two-wavelength and single-wavelength systems would be insignificant.

Assume that optical clock and address pulses have identical pulsewidth T/N and the same peak power (see Figure 2). By using the similar approach given in [6], the minimum peak optical power, which is required by the gate controller of a switching node to guarantee a given bit error rate (BER), can be written as

$$P_m = (r+2) \left\{ \frac{U_1 + U_2}{\left(\frac{U_3 - U_4}{Q}\right)^2} + \frac{2}{\left(\frac{U_3 - U_4}{Q}\right)^2} \cdot \sqrt{U_1 U_2 + \left(\frac{U_3 - U_4}{Q}\right)^2 U_0} \right\} \quad (1)$$

where $Q = 6$ for $BER = 1 \times 10^{-9}$. $U_0 = 2eB \{I_{du} + G^2 F(G) I_{dm}\} + \langle n_a^2 \rangle$, $U_1 = (r+2) \left\{ \frac{4eRG^2 F(G) B}{\pi} \int_0^{2\pi T_p B} \frac{\sin(x)}{x} dx - 2eRG^2 F(G) \cdot \frac{1 - \cos(2\pi T_p B)}{\pi^2 T_p} \right\}$, $U_2 = \frac{(2r+1)U_1}{r+2}$, $U_3 =$

$\frac{2RG(r+2)}{\pi} \int_0^{\pi T_p B} \frac{\sin(y)}{y} dy$, and $U_4 = \frac{(2r+1)U_3}{r+2}$ [6]. Using the parameters of InGaAsP APD and GaAs MESFET given in [7], we can calculate the receiver sensitivity S_r for a chip rate of $N/T = 10$ Gbit/s, e.g., S_r is about -22.5 dBm.

From Figure 1, the power loss LOS_1 between the input of WDM demultiplexer and the output of EO switch at a switching node can be given by

$$LOS_1 = L_{wde} + L_{wco} + L_{eos} + 3 \text{ (dB)} \quad (2)$$

where L_{wde} , L_{wco} , and L_{eos} denote optical insertion power losses of WDM demultiplexer, WDM coupler, and EO switch, respectively. Note that the power losses of optical fibers, fiber splice, and optical buffers at switching nodes are neglected.

The power loss LOS_2 between the inputs of WDM demultiplexer and gate controller at a switching node is written as

$$LOS_2 = L_{wde} + 10 \log_{10} M + 10 \log_{10}(M+1) + 3 \text{ (dB)} \quad (3)$$

where $10 \log_{10} M$ and $10 \log_{10}(M+1)$ represent the power losses of a $1 \times M$ optical splitter and a $(M+1) \times 1$ optical combiner, respectively.

If once the S_r is obtained, the number of photonic-switching stages J_s (see Figure 3), limited by the power losses, for a given peak optical output power A_p from a transmitter can be given by

$$J_s \leq \left\lfloor \frac{10 \log_{10} A_p - LOS_2 - S_r}{LOS_1} + 1 \right\rfloor \quad (4)$$

where " $\lfloor x \rfloor$ " denote the largest integer $\leq x$.

For practical applications, the available A_p is substantially determined by the laser diodes used at the transmitting end, and is also limited by optical nonlinearities in the fiber.

4. CONCLUSION

We have presented a new architecture to ultrafast self-routing photonic switching with self-synchronization, which is based on a two-wavelength scheme. The use of the proposed technique can improve the reliability of address decoding and can reduce the complexity of optical routing controllers, because clock-data and address signals are independently processed at each switching node. An alternative design of photonic switching is to carry a packet header with any feasible coding scheme at wavelength λ_2 in parallel with the

data packet at λ_1 . In this case, it allows to use much wider pulses for the packet header to enable ultrafast signal processing. Therefore, we can use mature optical receivers with bandwidths around 10 GHz in this type of photonic switches.

We have also analyzed the receiver sensitivity of gate controllers at switching nodes and considered the optical power budget of the proposed photonic switching. A very simple equation has been presented to determine the number of switching stages for given peak output power of an optical transmitter and receiver sensitivity.

ACKNOWLEDGMENT

The author would like to thank Prof. G. Picchi of the University of Parma (Italy) for helpful discussions. The author also gratefully acknowledges Dr. G. Migliorini for support.

References

- [1] P. R. Prucnal and P. A. Perrier, "Optically-processed routing for fast packet switching," *IEEE LCS Mag.*, vol. 1, pp. 54-67, May 1990.
- [2] P. R. Prucnal, D. J. Blumenthal, and P. A. Perrier, "Photonic switch with optically self-routed bit switching," *IEEE Commun. Mag.*, vol. 25, pp. 50-55, May 1987.
- [3] R. Kishimoto and M. Ikeda, "Optical self-routing switch using integrated laser diode optical switch," *IEEE J. Sel. Areas Commun.*, vol. 6, pp. 1248-1254, August 1988.
- [4] M. Hashimoto, M. Fukui, and K.-I. Kitayama, "Self-routing optical crossbar switch," *IEEE Photon. Technol. Lett.*, vol. 2, pp. 522-524, July 1990.
- [5] J. F. Vinchant *et al.*, "Low driving voltage or current digital optical switch on InP for multi-wavelength system applications," *Electron. Lett.*, vol. 28, pp. 1135-1137, July 1992.
- [6] J.-G. Zhang, "Performance analysis of optical fiber TDMA systems," in *Proc. URSI/IEEE ISSSE'95*, San Francisco, USA, Oct. 25-27, 1995.
- [7] S. E. Miller and I. P. Kaminow, eds, *Optical Fiber Telecommunications II*. San Diego: Academic, 1988.

EFFECTS OF INCREASED CAPACITY IN CDMA CELLULAR SYSTEM

F.C.M. Lau & W.M. Tam

Department of Electronic Engineering

The Hong Kong Polytechnic University, Hunghom, Kowloon, Hong Kong

Tel: (852)-2766-6206; Fax: (852)-2362-8439; Email: encmlau@hkpucc.polyu.edu.hk

1. INTRODUCTION

In this paper, the effects on the increase in capacity of a desired cell in a CDMA cellular system has been investigated. The model used is the same as that used in [1] and refer to fig.1, the total mobile power from a cell having N mobile stations uniformly distributed in it to a base station at distance $d=kR$ is

$$P(d) = \frac{2\alpha NP_c}{\pi R^2} \int_0^R r^{m+1} \int_0^\pi \frac{d\theta}{(d^2 + r^2 + 2dr \cos \theta)^{\frac{m}{2}}} dr \quad (1)$$

where α is the voice activity factor;

P_c is the power of a CDMA user received at the base station of its own cell;

m is the path loss exponent typically ranging between 2 and 4.

The case for $m=4$ has been evaluated analytically [1] and the integral is equal to

$$P(d = kR)|_{m=4} = 2\alpha NP_c \left[2k^2 \ln \left(\frac{k^2}{k^2 - 1} \right) - \frac{4k^4 - 6k^2 + 1}{2(k^2 - 1)^2} \right] \quad (2)$$

When the cell size decreases, however, the fourth order exponential path loss assumption is no longer valid and the authors have investigated the cases for smaller values of m . For $m=2$, the analytical solution is found to be:

$$P(d = kR)|_{m=2} = 2\alpha NP_c \left[\frac{k^2}{2} \ln \left(\frac{k^2}{k^2 - 1} \right) - \frac{1}{2} \right] \quad (3)$$

When $m=3$, no analytical solution can be found and the authors evaluate equation (1) numerically by first expanding the function inside using binomial expansion.

Denoting the total interference from the first n -tiers of cells surrounding the desired cell as $I_{ext} = \alpha NP_c I(n)$ and assume that a CDMA cell can serve N users at the minimally required bit error rate level. Then the required C/I is given by

$$\left(\frac{C}{I} \right)_{req} = \frac{\alpha P_c}{(N-1)\alpha P_c + I_{ext}} = \frac{1}{(N-1) + NI(n)} \quad (4)$$

2. EFFECTS OF INCREASED CAPACITY ON C/I

When the number of users of the desired cell is increased by a factor of ΔN , the C/I ratio for the users in the desired cell becomes

$$\left(\frac{C}{I} \right) = \frac{1}{[N(1 + \Delta N) - 1] + NI(n)} \quad (5)$$

The degradation in performance is given by

$$\begin{aligned} \Delta \left(\frac{C}{I} \right) [dB] &= 10 \log \left(\frac{C}{I} \right)_{req} [dB] - 10 \log \left(\frac{C}{I} \right) [dB] \\ &= 10 \log \left[1 + \frac{N\Delta N}{(N-1) + NI(n)} \right] \\ &\approx 10 \log \left[1 + \frac{\Delta N}{1 + I(n)} \right] \quad (6) \end{aligned}$$

assuming $N \gg 1$. Then $\Delta C/I$ only relates to ΔN , the number of tiers n and of course the propagation path loss factor m .

3. EFFECTS OF INCREASED CAPACITY ON THE NUMBER OF USERS IN THE SURROUNDING CELLS

Maintaining the same required C/I ratio, when users are increased by a factor of ΔN in the desired cell, the number of users in each of the surrounding cells N_c will have to satisfy

$$\left(\frac{C}{I}\right)_{req} = \frac{1}{[N(1 + \Delta N) - 1] + N_c I(n)} \quad (7)$$

From (4) and (7), we have

$$N_c = \left[1 - \frac{\Delta N}{I(n)}\right] N \quad (8)$$

$$\text{where } 1 - \frac{\Delta N}{I(n)} \geq 0 \text{ or } \Delta N \leq I(n) \quad (9)$$

The maximum of ΔN is $I(n)$. In this case, the number of users in each of the surrounding cells will all reduce to zero. The desired cell becomes a single cell system to maintain the required C/I ratio. When $\Delta N > I(n)$ the C/I ratio for the users in the desired cell will reduce even without out-of-cell interference.

4. NUMERICAL RESULTS AND DISCUSSIONS

Equation (5) has been plotted as in fig.2. The cases for $n=1, 2, 3$ and 100 tiers of cells have been examined with $N=100$. The C/I decreases as ΔN increases as more in-cell interference has been introduced. For the same path loss factor m and ΔN , the C/I is always worse when n is larger. This can be understood because more outside-cell interference has been considered. For the same n and ΔN , the C/I is also better for a larger value of m . This is due to the smaller impact of the outside-cell interference when the path loss is large. Fig.3 plots the C/I ratio as a function of ΔN with $N=40$ to 200 users in steps of 40 users for $m=2, 3$ and 4, assuming that only 1-tier of cells is present. In general, the C/I decreases with a similar slope in all the cases, the change in C/I is insensitive to N . The C/I is smaller when N is larger because the interference is increased.

Table I shows the percentage change in the number of users of the surrounding cells to maintain the same C/I ratio of the desired cell when the number of users has been risen by ΔN . When the number of tiers of cells has been increased, the percentage change in the number of users in the surrounding cells decreases as the effect has been spread among a larger number of cells. For values less than -100 in the table, it merely indicates that the C/I ratio in the desired cell will decrease even if the number of users in the surrounding cells has been reduced to zero. For the same n and ΔN , the impact on the surrounding cells is smaller when the path loss factor is smaller. A smaller path loss factor indicates larger outside-cell interference which implies a larger N_c as given in equation (8).

5. CONCLUSIONS

In this paper, the effects of the increased capacity of a desired cell in a CDMA cellular system has been analysed. With propagation path loss factor of 2 or 4, analytical functions have been derived on the change in C/I ratio of the desired cell and also the change in the number of users in the surrounding cells to maintain the same C/I ratio in the desired cell. Approximate numerical results are obtained when the path loss factor is 3.

6. REFERENCES

- [1] W.C.Y.Lee, "Overview of Cellular CDMA, " *IEEE Trans. on Veh. Technol.*, vol.40, No.2, May 1991.
- [2] K.S.Gilhousen, I.M.Jacobs, R.Padovani and L.A.Weaver, "Increased Capacity Using CDMA for Mobile Satellite Communications, " *IEEE Trans. Select. Areas Commun.*, vol.8, pp 503-514, May 1990.
- [3] A.F.Naguib, A.Paulraj, T.Kailath, "Capacity Improvement with Base-Station Antenna Arrays in Cellular CDMA, " *IEEE Trans on Veh. Technol.*, vol. 43, No.3, August 1994.

[4] S.C.Swales, M.A.Beach, D.J.Edwards and J.P.Mcgeehan, "The Performance Enhancement of Multibeam Adaptive Base-Station Antennas for Cellular Land Mobile Radio Systems, " *IEEE Trans on Veh.Technol.*,vol.39, No.1, Feb.1990.

[5] K.I.Kim, "CDMA Cellular Engineering Issues, " *IEEE Trans on Veh. Technol.*, vol 42, No.3, August 1993.

ΔN	number of tiers				
	n = 1	n = 2	n = 3	n = 4	n=100
10%	-11.06	-7.33	-5.99	-5.27	-2.12
30%	-33.17	-21.98	-17.97	-15.81	-6.36
50%	-55.29	-36.63	-29.95	-26.36	-10.61
100%	-110.57	-73.27	-59.90	-52.72	-21.22

(a) m=2

ΔN	number of tiers				
	n = 1	n = 2	n = 3	n = 4	n=100
10%	-21.26	-17.29	-16.02	-15.39	-13.61
30%	-63.77	-51.87	-48.05	-46.17	-40.83
50%	-106.28	-86.45	-80.09	-76.95	-68.05
100%	-212.56	-172.90	-160.17	-153.89	-136.09

(b) m=3

ΔN	number of tiers				
	n = 1	n = 2	n = 3	n = 4	n=100
10%	-35.19	-32.10	-31.36	-31.06	-30.63
30%	-105.58	-96.29	-94.07	-93.19	-91.89
50%	-175.97	-160.48	-156.78	-155.31	-153.15
100%	-351.93	-320.97	-313.56	-310.63	-306.29

(c) m=4

Table I. Percentage change in the number of users in the surrounding cells to maintain the required C/I ratio when users are increased by a factor of ΔN in the desired cell (a) m=2, (b) m=3, (c) m=4.

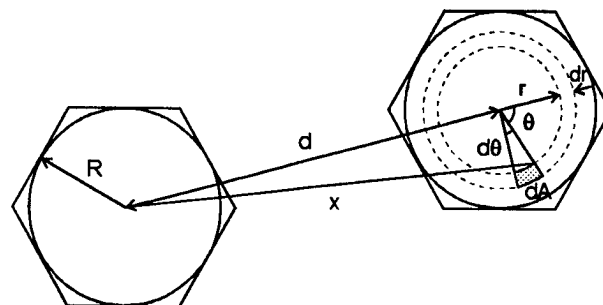


Fig. 1. Plot for calculation of the interference power

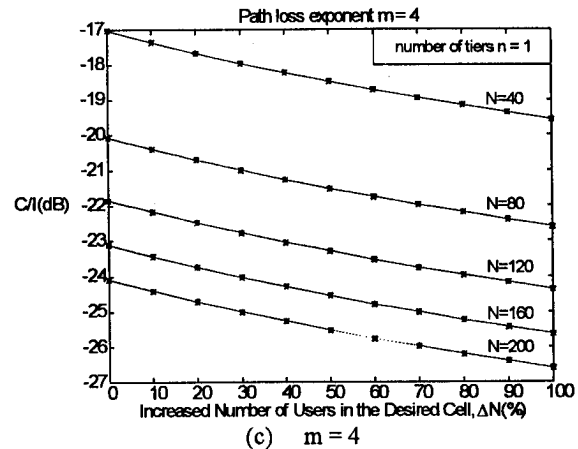
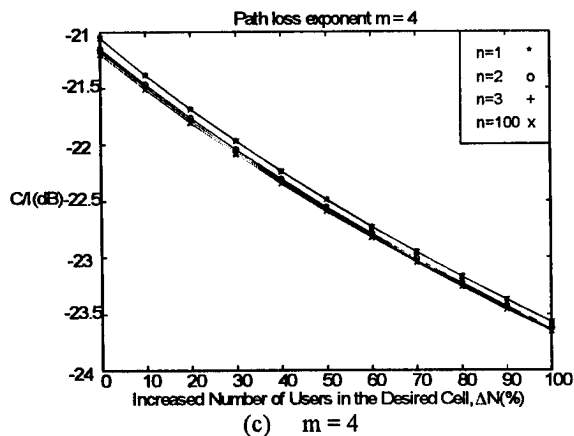
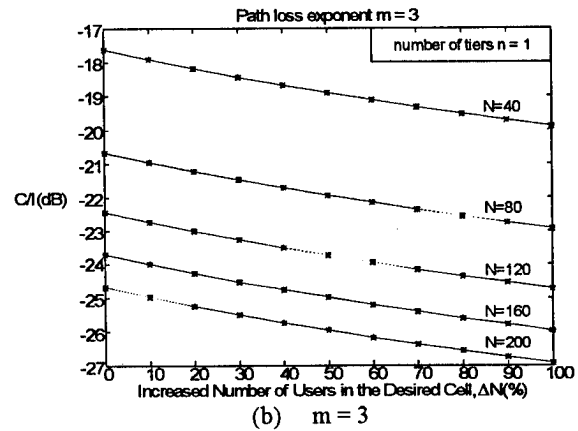
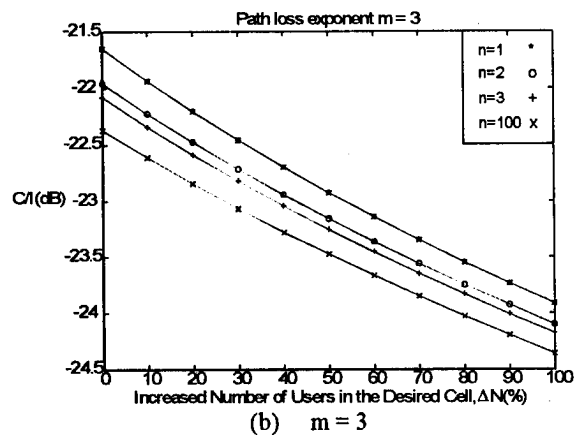
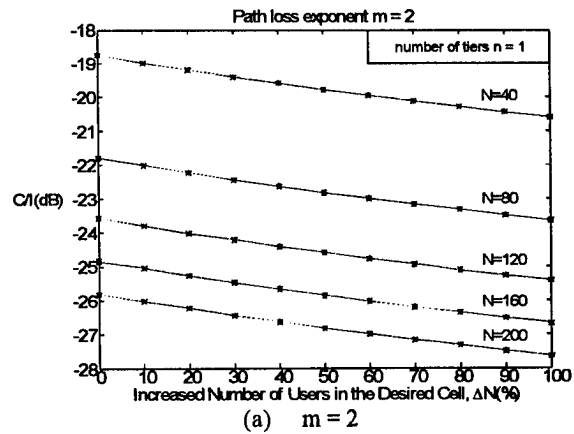
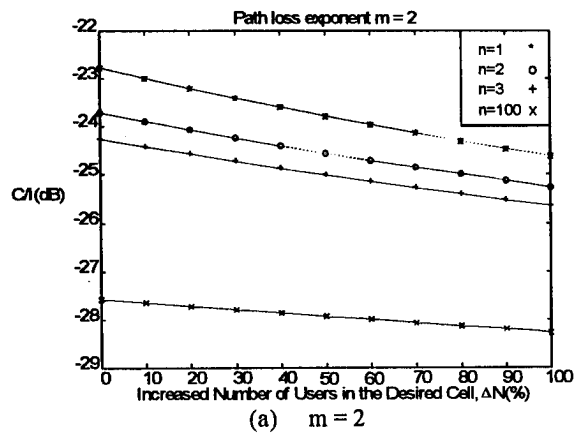


Fig. 2. Plot of C/I ratio as a function of ΔN (%) for various number of tiers of cells and propagation path loss exponent m (a) $m=2$, (b) $m=3$ and (c) $m=4$

Fig. 3. Plot of C/I ratio as a function of ΔN (%) with $N=40\sim 200$ users/cell and only 1 tier of cells for (a) $m=2$, (b) $m=3$ and (c) $m=4$

THE ALGORITHM FOR IMAGE DECOMPOSITION AND RECONSTRUCTION USING AMPLITUDE AND PHASE PATTERNS

A. Buchowicz

Institute of Radioelectronics, Warsaw University of Technology
ul. Nowowiejska 15/19, 00-665 Warszawa, POLAND
tel: +48 2 660 77 24, fax: +48 22 25 52 48
e-mail: A.Buchowicz@elka.pw.edu.pl

ABSTRACT

This paper investigates the decomposition of monochrome images into amplitude and phase functions and their reconstruction. The decomposition is based on single quadrant complex signals. Several examples of test images, their amplitude and phase functions and reconstructed images are shown.

1. INTRODUCTION

The images are represented by the function $u(x_1, x_2)$, where x_1, x_2 are Cartesian coordinates. The amplitudes and phases of the function $u(x_1, x_2)$ are defined by the 2-D complex signals with a nonzero spectrum only in a single quadrant of the spatial frequency space, as defined in [1]. Four such complex signals $\Psi_1, \Psi_2, \Psi_3, \Psi_4$ could be defined. However, signals Ψ_1, Ψ_3 and Ψ_2, Ψ_4 are complex conjugate so two amplitude functions $A_1(x_1, x_2), A_2(x_1, x_2)$ and two phase functions $\phi_1(x_1, x_2), \phi_2(x_1, x_2)$ are necessary to represent all four signals (1)

$$\begin{aligned}\Psi_1(x_1, x_2) &= A_1(x_1, x_2) \exp(j\phi_1(x_1, x_2)) \\ \Psi_2(x_1, x_2) &= A_2(x_1, x_2) \exp(j\phi_2(x_1, x_2)) \\ \Psi_3(x_1, x_2) &= A_1(x_1, x_2) \exp(-j\phi_1(x_1, x_2)) \\ \Psi_4(x_1, x_2) &= A_2(x_1, x_2) \exp(-j\phi_2(x_1, x_2))\end{aligned}\quad (1)$$

The original function $u(x_1, x_2)$ can be reconstructed from its amplitude and phase functions [1] using the formula (2)

$$u(x_1, x_2) = 0.5 [A_1 \cos(\phi_1(x_1, x_2)) + A_2 \cos(\phi_2(x_1, x_2))] \quad (2)$$

However, the reconstruction may not be complete since the DC term (mean value) and the "edge" samples are lost during decomposition [2].

2. AMPLITUDE AND PHASE PATTERNS CALCULATION ALGORITHM

The complex signals $\Psi_1, \Psi_2, \Psi_3, \Psi_4$ could be calculated by using either circular convolution [2] or Discrete Fourier Transform. Both algorithms deliver exactly the same patterns. The second method has been chosen. The input function is transformed with the use of FFT, then the proper quadrant of the spectrum is selected by zeroing all other quadrants and inverse FFT is calculated. Two complex signals: Ψ_1 with nonzero spectrum in the first quadrant and Ψ_2 with nonzero spectrum in second quadrant are calculated in this way. The reconstruction of the input signal $u(x_1, x_2)$ given by formula (2) is modified. The constant component U_{00} of the function $u(x_1, x_2)$ is stored during its spectrum calculation and added to the reconstructed function $u_{rec}(x_1, x_2)$ (3)

$$u_{rec}(x_1, x_2) = 0.5 [A_1 \cos(\phi_1(x_1, x_2)) + A_2 \cos(\phi_2(x_1, x_2))] + U_{00} \quad (3)$$

3. EXPERIMENTAL RESULTS

The algorithm presented in the previous section was used to calculate the amplitude and phase patterns of several test images. Two examples: well known image *Lenna* and random checkerboard are shown on Figures 1÷12. The grey levels in the images representing amplitude patterns were assigned as follows: the whole range of amplitude values in certain pattern was uniformly divided into 256 subranges, the lowest amplitude values (belonging to the first subrange) were assigned black colour and the highest white colour. The range $[-\pi, \pi]$ of phase values was uniformly divided into 256 subranges and again the lowest phase values were assigned black colour and the highest white colour. The zero phase angle is represented by grey colour (level 128).



Figure 1: Original image *Lenna*



Figure 4: Amplitude A_2 of the *Lenna*



Figure 2: Reconstructed *Lenna*



Figure 5: Phase ϕ_1 of the *Lenna*

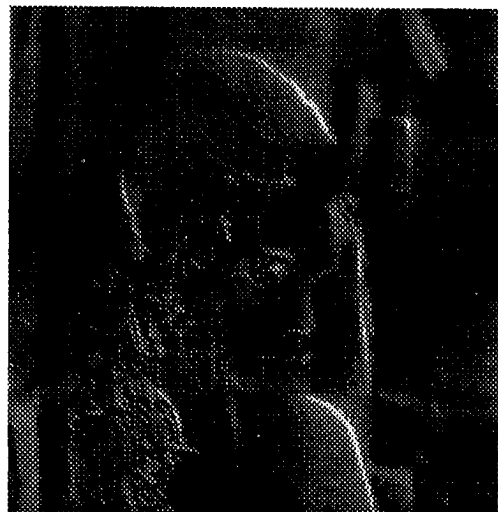


Figure 3: Amplitude A_1 of the *Lenna*

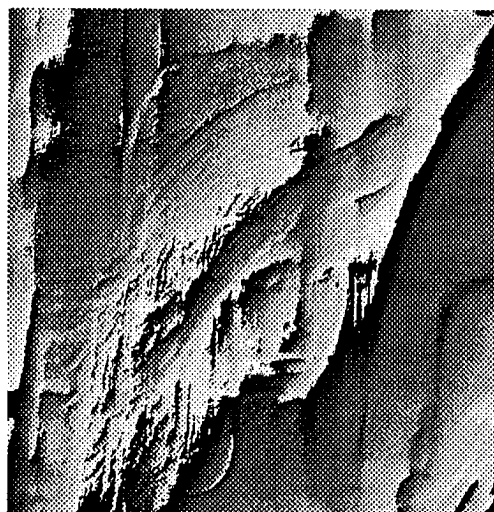


Figure 6: Phase ϕ_2 of the *Lenna*



Figure 7: Original random checkerboard

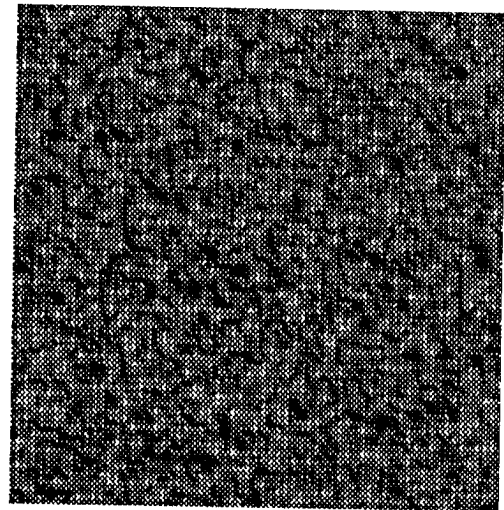


Figure 10: Ampl. A_2 of the checkerboard



Figure 8: Reconstructed checkerboard

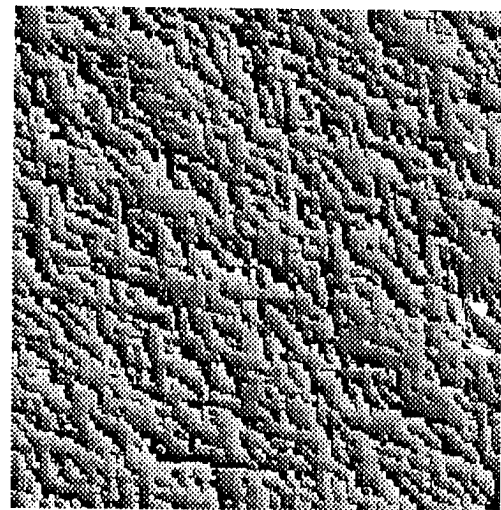


Figure 11: Phase ϕ_1 of the checkerboard

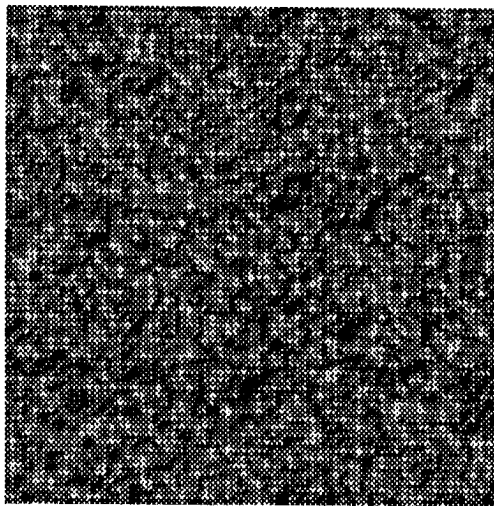


Figure 9: Ampl. A_1 of the checkerboard

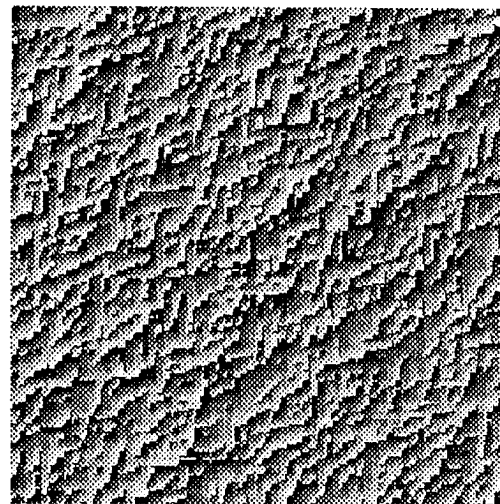


Figure 12: Phase ϕ_2 of the checkerboard

4. CONCLUSIONS

It has been shown that 2-D signals may be decomposed into amplitude and phase patterns. The original image may be reconstructed using these patterns. The algorithm presented in this paper is a straightforward one so it can create some distortions in the reconstructed images. These distortion are caused by the elimination of the edge samples of the 2-D discrete spectrum. The possibilities of the algorithm modification eliminating these distortions will be further studied. The application for amplitude and phase patterns will also be looked for.

Acknowledgements

I would like to thank Prof. Stefan Hahn for his assistance in preparing this paper.

5. REFERENCES

- [1] S. Hahn, "Multidimensional complex signals with single-orthant spectra", *Proceedings of the IEEE*, vol. 80, No. 8, August 1992, pp. 1286-1300
- [2] S. Hahn, K. Snopek, "Problems in the Computation of the 2-D Discrete Hilbert Transform", *Kleinheubacher Berichte*, Band 38, Deutsche Bundespost Telekom, Darmstadt 1994, ISSN 0343-5725, pp. 63-69

Conference Author Index

A

Abrokwah, J. 275
 Adve, R. S. 319, 335
 Aghajan, H. 303
 Aign, S. 59
 Aikawa, M. 25
 Allam, R. 171
 Alouini, M. S. 67
 Alwan, A. 367
 Anand, V. 211

B

Bajkova, A. 307, 311
 Bakkar, A., E-S 227
 Basu, A. 21
 Batchelor, R. A. 33
 Battail, G. 419
 Bell, M. R. 183
 Bellanger, M. 195
 Bergmann, J. 451
 Bernhardt, B. 275
 Bertenburg, R. M. 215
 Biglieri, E. 123
 Blanck, H. 115
 Bourne, P. 115, 171
 Bucciarelli, T. 191
 Buchowicz, A. 583

C

Caddemi, A. 385
 Cao, J. Y. 513
 Carlstrom, J. E. 145
 Carlstrom, J. 145
 Carrijo, A. 505
 Cassette, S. 115
 Chan, Y. T. 485
 Chang, F. 279
 Chang, K. 13
 Chartier, E. 115
 Chen, V. C. 251
 Cheung, W. N. 517
 Chiao, J.-C. 141
 Ching, P. C. 485
 Chow, Y. L. 331
 Compton, R. C. 9
 Costamagna, E. 207, 405, 463
 Cox, C. 283
 Crawforth, B. 275
 Crosnier, Y. 171
 Cuomo, S. 509

D

Daba, J. S. 183
 Daffara, F. 363
 Darbandi, A. 447
 David, G. 41
 deBarro, L. E. M. 351

De Jaeger, J. C. 111, 171
 DeLisio, M. 141
 Debroy, S. K. 241
 Delage, S. L. 115
 Delaney, M. 37
 Deprettere, E. 427
 Diforte-Poisson, M. A. 115
 Dighe, A. M. 223
 Dyakonov, M. I. 219

E

Edwards, P. J. 517
 Eisenhut, C. 459
 El-Gazzar, M. A. 397, 477, 545
 El-Kordy, M. 537
 Enquist, P. 351
 Escotte, L. 339
 Evgenievich, N. L. 571

F

Fanni, A. 405, 463
 Ferguson, P. 139
 Fetisov, Y. 521
 Flanagan, J. L. 373
 Flores, L. E. 505
 Floriot, D. 115
 Foster, D. 275
 Fricke, K. 343
 Fukagawa, T. 259

G

Galin, I. 153
 Gallagher, M. 127
 Galy, C. 447
 Gan, K. C. 175
 Gandhi, A. S. 223
 Garverick, S. L. 563
 Gehse, P. 459
 Georgiev, Y. P. 359
 Giacinto, G. 405
 Gomez del Moral, J. B. 123
 Gonzales, J. 163
 Green, M. M. 497
 Gvozdev, V. I. 383, 561

H

Hallmark, J. 275
 Hartnagel, H. L. 343, 347
 Hartsfield, K. D. 563
 Harvey, J. 89
 Hasegawa, M. 259
 Have ten, A. 451
 He, S. 323
 Herczfild, P. 351
 Ho, K. P. 55

Hojjat, N. 331
 Hollung, S. 93
 Hosny, E. A. 227
 Houshmand, B. 21, 389, 467
 Huang, J.-H. 275
 Hudson, R. E. 409
 Hurt, M. 163
 Hwang, H. 89

I

Isobe, R. 37
 Itoh, T. 1, 21, 389, 467
 Itoh, Y. 45
 Ivanov, M. V. 557
 Ivanov, T. 99
 Ivanov, V. V. 557
 Iversen, K. 529

J

Jager, D. 41
 Jan, E.-E. 373
 Janssen, G. 215
 Jayarai, K. 443
 Jones, B. C. 263
 Jones, S. H. 145

K

Kahn, M. 55
 Kailath, T. 303
 Kar, S. 231
 Katkovnik, V. 179
 Kato, E. 37
 Kiasaleh, K. 295
 Kim, H. M. 199
 Kim, S. C. 199
 Klein, J. W. 157
 Kobayashi, O. 17
 Kohn, E. 107
 Kolanowski, C. 171
 Korompis, D. 409
 Kovalenko, A. V. 315
 Krozer, V. 343, 347
 Kumar, R. 355
 Kumar, U. 553
 Kuo, C. N. 467
 Kurashov, V. N. 315
 Kuzaev, G. A. 383, 561

L

LaMacchia, M. 275
 Lam, C. F. 299
 Langrez, D. 171
 Lapierre, L. 447
 Lau, F. C. M. 579
 Lee, C. Y. 21

Lee, L. H. 423
 Lee, W. 481
 Lee, W. Y. 343, 347
 Lemma, A. N. 427
 Lemnios, Z. 271
 Lemos, R. P. 131
 Li, M. 393
 Liao, J. 21
 Lin, J. N. 435
 Lin, J. 1
 Ling, H. 243, 247
 Lipka, K.-M. 107
 Litva, J. 327
 Liu, J. 141
 Llopis, O. 339
 Lombardo, P. 191
 Lopes, A. 131
 Lorenselli, F. 409
 Lucero, R. 275
 Luglio, M. 71
 Lundstedt, J. 323
 Lyalin, A. A. 561

M

Mader, T. 93
 Madisetti, A. 63
 Maeda, S. 377
 Makimoto, M. 259
 Manabe, T. 77
 Markovic, M. 93
 Martinez, E. 167
 Mathes, B. 275
 Maxey, J. J. 493
 McGrath, W. R. 147
 Mihailovich, S. V. 571
 Miller, E. K. 319, 335
 Mimura, M. 259
 Mink, J. W. 89
 Mink, J. 81
 Mollova, G. 439
 Mortazawi, A. 99
 Moselhy, A. M. 397, 477, 545
 Munoz, S. 455
 Muraguchi, M. 25
 Musil, V. 401

N

Nakamine, T. 237
 Nakha, M. S. 393
 Nakhodkin, N. G. 315
 Nandi, R. 235, 241
 Narayana, S. M. 335
 Narayanan, S. 367
 Nassar, A. M. 397, 477, 545
 Navarro, E. 327
 Ng, M. W. R. 227
 Niu, X. X. 485
 Noguchi, Y. 237

Noll, T. E. 443
 Nuteson, T. W. 89

O

Ogawa, H. 17
 Ohata, K. 119
 Okamoto, N. 237
 Ooms, B. 275
 Ormondroyd, R. F. 493, 525

P

Pal, D. 241
 Paoletta, A. 351
 Paolletta, A. 89
 Park, H. 163
 Park, S. 199
 Peatman, W. C. B. 163
 Pellegrini, P. F. 207, 509
 Piazza, E. 509
 Pickholtz, R. L. 481
 Piggini, P. W. 127
 Pirsch, P. 49
 Pobanz, C. 1
 Podkovyrin, S. I. 561
 Popovic, Z. B. 93
 Pottie, G. 255
 Pountourakis, I. E. 267
 Puffer, F. 501
 Purushotham, A. 563

Q

Qian, S. 251

R

Rakityansky, V. A. 549
 Rao, G. S. 335
 Rao, N. K. 563
 Rao, S. M. 319
 Reuter, R. 215
 Rezende, E. N. 505
 Romanov, I. 521
 Rumelhard, C. 29
 Rutledge, D. 141
 Ryu, Y. 199

S

Safavi-Naeini, S. 331
 Saito, T. 119
 Salmer, G. 171
 Sannino, M. 385
 Sanyal, S. K. 241

Sarkar, T. K. 319, 335
 Sautereau, J. F. 447
 Schoenberg, J. 93
 Schuermeyer, F. 167
 Schuessler, M. 347
 Schuessler, V. M. 343
 Sebastian, J. L. 455
 Shei, S. C. 175
 Shen, A. 367
 Shih, Y. C. 37
 Shiroma, W. 93
 Shishkov, B. B. 359
 Shur, M. 163, 167, 219
 Singh, D. 443
 Singh, N. B. 553
 Skellern, D. J. 263, 423
 Sobhy, M. I. 227
 Soli, S. 381
 Song, I. 199
 Srisuchinwong, B. 541
 Steer, M. B. 89
 Steffes, P. G. 67
 Stoyanor, S. N. 359
 Stroem, S. 323
 Strophe, B. 367
 Studenov, V. 521
 Su, Y. K. 175
 Swann, C. 287

T

Tager, A. S. 533
 Taha, T. E. 471, 537
 Tamburrini, S. 191
 Tara, W. M. 579
 Tegude, F. J. 215
 Tetzlaff, R. 501
 Torabian-Esfahani, A. 331
 Trintinalia, L. C. 247
 Trung, N. V. 541
 Tsai, R. 163

U

Ugrinovskiy, R. 135
 Unbehauen, R. 435

V

VanBlaricam, M. 287
 VanMeerbeke, W. 351
 Vaughan, M. J. 9
 Verma, A. K. 355

W

Waasen Van, S. 215
 Wada, K. 237
 Wang, A. 409
 Watrin, E. 115
 Weikle, R. M. 103
 Wen, J. 187, 567
 Wicks, M. 335
 Wilde, A. 203
 Willson, A. N., Jr. 63
 Wolf, D. 501
 Wong, J. 21
 Wong, T. F. 423

Woschni, E. G. 489, 573
 Wright, W. 9

X

Xu, H. Q. 435

Y

Yablonovitch, E. 299
 Yabu-uti, J. B. T. 505
 Yao, K. 409

Yokoyama, M. 175
 York, R. 5
 Yoshida, T. 77
 Ytterdal, T. 163

Z

Zhang, J.-G. 291, 575
 Zhang, Q. J. 393
 Zhang, T. 517
 Zhu, X. 187, 567
 Ziemann, O. 529
 Zoyo, M. 447
 Zybura, M. F. 145